PL-TR-96-2153
Environmental Research Papers, No. 1195

PROCEEDINGS OF THE 18TH ANNUAL SEISMIC RESEARCH SYMPOSIUM ON MONITORING A COMPREHENSIVE TEST BAN TREATY, 4-6 SEPTEMBER 1996

Editors:
James F. Lewkowicz
Jeanne M. McPhetres
Delaine T. Reiter

17 July 1996

APPROVED FOR PUBLIC RELEASE; DISTRIBUTION UNLIMITED.

PHILLIPS LABORATORY
DIRECTORATE OF GEOPHYSICS
AIR FORCE MATERIEL COMMAND
HANSCOM AIR FORCE BASE, MA 01731-3010

AIR FORCE OFFICE OF SCIENTIFIC RESEARCH
DIRECTORATE OF MATHEMATICS & GEOSCIENCES
AIR FORCE MATERIEL COMMAND
BOLLING AIR FORCE BASE, DC 20332-0001

HQ AIR FORCE TECHNICAL APPLICATIONS CENTER
NUCLEAR TREATY MONITORING DIRECTORATE
PATRICK AIR FORCE BASE, FL 32925-3002

DEPARTMENT OF ENERGY
OFFICE OF NONPROLIFERATION & NATIONAL SECURITY
WASHINGTON, DC 20585

"This technical report has been reviewed and is approved for publication."

JOHN J. CIPAR
Task Scientist
Earth Sciences Division

DELAINE T. REITER
Program Manager
Earth Sciences Division

JAMES F. LEWKOWICZ
Director
Earth Sciences Division

This report has been reviewed by the ESC Public Affairs Office (PA) and is releasable to the National Technical Information Service (NTIS).

Qualified requestors may obtain additional copies from the Defense Technical Information Center. All others should apply to the National Technical Information Service.

If your address has changed, or if you wish to be removed from the mailing list, or if the addressee is no longer employed by your organization, please notify PL/IM, 29 Randolph Road, Hanscom AFB, MA 01731-3010. This will assist us in maintaining a current mailing list.

Do not return copies of this report unless contractual obligations or notices on a specific document requires that it be returned.

DISCLAIMER NOTICE

THIS DOCUMENT IS BEST QUALITY AVAILABLE. THE COPY FURNISHED TO DTIC CONTAINED A SIGNIFICANT NUMBER OF PAGES WHICH DO NOT REPRODUCE LEGIBLY.

REPORT DOCUMENTATION PAGE

Form Approved
OMB No. 0704-0188

Public reporting burden for this collection of information is estimated to average 1 hour per response, including the time for reviewing instructions, searching existing data sources, gathering and maintaining the data needed, and completing and reviewing the collection of information. Send comments regarding this burden estimate or any other aspect of this collection of information, including suggestions for reducing this burden, to Washington Headquarters Services, Directorate for Information Operations and Reports, 1215 Jefferson Davis Highway, Suite 1204, Arlington, VA 22202-4302, and to the Office of Management and Budget, Paperwork Reduction Project (0704-0188), Washington, DC 20503.

1. AGENCY USE ONLY (Leave blank)	2. REPORT DATE	3. REPORT TYPE AND DATES COVERED
	17 July 1996	Scientific, Final

4. TITLE AND SUBTITLE Proceedings of the 18th Annual Seismic Research Symposium on Monitoring a Comprehensive Test Ban Treaty, 4-6 September 1996

5. FUNDING NUMBERS

PE	61102F	621010
PR	2309	7600
TA	G2	09
WU	10	08

6. AUTHOR(S)
James F. Lewkowicz
Editors: Jeanne M. McPhetres
Delaine T. Reiter

7. PERFORMING ORGANIZATION NAME(S) AND ADDRESS(ES)
Phillips Laboratory (GPE)
29 Randolph Road
Hanscom AFB, MA 01731-3010

8. PERFORMING ORGANIZATION REPORT NUMBER
PL-TR-96-2153
ERP, No. 1195

9. SPONSORING/MONITORING AGENCY NAME(S) AND ADDRESS(ES)
Air Force Office of Scientific Research
HQ Air Force Technical Applications Center
Department of Energy

10. SPONSORING/MONITORING

19960909 010

11. SUPPLEMENTARY NOTES
This research was supported by PL under PE 621010, by AFOSR under PE 61102F, by AFTAC under PE 35999F, ARPA under PE 62301E, DOE and ACDA.

12a. DISTRIBUTION/AVAILABILITY STATEMENT
Approved for Public Release; distribution unlimited

12b. DISTRIBUTION CODE

13. ABSTRACT *(Maximum 200 words)*

These Proceedings contain papers presented at the Eighteenth Annual Seismic Research Symposium on Monitoring a Comprehensive Test Ban Treaty (CTBT), held 4-6 September 1996, in Annapolis, Maryland. This Symposium represents the combined annual review for the basic seismology program funded by the Air Force Office of Scientific Research (AFOSR) and the regional verification program funded by the Phillips Laboratory (PL), Hq Air Force Technical Applications Center (AFTAC), Department of Energy (DOE), the Advanced Research Projects Agency (ARPA) and the Arms Control and Disarmament Agency (ACDA). In addition, representatives from four of the DOE National Laboratories participate in the Symposium to provide insight on the internal DOE CTBT R&D program. The scientific objectives of the research programs are to improve the Air Force's capability to seismically detect, locate, identify, and characterize underground nuclear explosions under a potential CTBT. The purpose of these Symposia,

14. SUBJECT TERMS	15. NUMBER OF PAGES
underground nuclear explosions, discrimination, regional seismology, seismic sources, structure of the crust and upper mantle, mining practices, hydroacoustics, data processing and analysis	1068
	16. PRICE CODE

17. SECURITY CLASSIFICATION OF REPORT	18. SECURITY CLASSIFICATION OF THIS PAGE	19. SECURITY CLASSIFICATION OF ABSTRACT	20. LIMITATION OF ABSTRACT
UNCLASSIFIED	UNCLASSIFIED	UNCLASSIFIED	UL

Block 9 continued

AFOSR/NM
110 Duncan Avenue, Suite B115
Bolling AFB, DC 20332-0001

HQ AFTAC/TT
1030 South Highway A1A
Patrick AFB, FL 32925-3002

DOE
Office of R&D, NN-20
1000 Independence Avenue, S.W.
Washington, DC 20585

Block 13 continued

organized annually by GPE, is to provide the sponsoring agencies an opportunity to review research, particularly contractor research, accomplished during the preceding year and to outline areas of investigation for the coming year. For the researchers, it provides a forum for the exchange of scientific information to help achieve program goals, and an opportunity to meet AFOSR, PL, HQ AFTAC, DOE, ARPA and ACDA staff to discuss results and future plans. In addition, the Symposium and the technical presentations serve as an important avenue for technology transition to the Air Force user. The papers include studies of the identification and characterization of seismic sources (discrimination), the factors affecting regional wave propagation in various geological/geophysical settings, regional seismic wave propagation from both theoretical and empirical viewpoints, the determination of earth structure in selected areas of the world, various models of the physics of earthquake and explosion sources, hydroacoustic and infrasonic wave propagation, radionuclide monitoring, data processing and analysis.

Table Of Contents

Seismic Regionalization

Page

Abers, Geoffrey A. and Golam Sarker
Seismic Sources and Structure in Iran from Joint Seismic Program Array Data: Attenuation Variations at the Northern Margins of Eurasian Mountains 1

Anderson, Kevin K.
Regionalization Studies: Statistical Analysis of Detection Capability and Magnitude Scaling 10

Cong, Lianli; Jiangchuan Ni and Brian J. Mitchell
Seismic Surface Wave Attenuation Studies in the Middle East 16

Crotwell, H.P.; M.R. Powers; T.J. Owens and G. Zandt
Characterization of Seismic Structure and Wave Propagation within the Tibetan Plateau 26

Davis, Paul M. and Shangxing Gao
Teleseismic P- and S-wave Attenuation under the Baikal Rift Zone and Adjacent Areas: Method, Measurements, and Interpretation 36

Doser, Diane I.; G. Randy Keller; Kate C. Miller and Steven Harder
Development of a Lithospheric Model and Geophysical Data Base for North Africa 46

Dowla, F.; P. Goldstein; P. Harben; D. Harris; T. Hauk; S. Jarpe; E. Kansa; P. Lewis; D. McNamara; H. Patton; D. Rock; A. Ryall; C. Schultz; A. Smith; J. Sweeney; W. Walter and L. Wethern
Seismic Regionalization in the Middle East and North Africa 55

Keller, G. Randy; Kate Miller; Diane Doser; Steven Harder and Cathy Snelson
Lithospheric Profiles in the Southwestern U. S. 65

Levshin, A.L.; M.H. Ritzwoller and S.S. Smith
Group Velocity Variations Across Eurasia 70

Randall, G.E.; H.E. Hartse; W.S. Phillips and S.R. Taylor
Regional Characterization of Western China - II 80

Page

Rapine, Richard; Thomas Hearn; Jianxin Wu and James Ni
Sn and Lg Propagation Characteristics Beneath China 88

Ritzwoller, M.H.; A.L. Levshin; L.I. Ratnikova and D.M. Tremblay
High Resolution Group Velocity Variations Across Central Asia 98

Vernon, F. L.; R. J. Mellors; J. Berger; A. M. Al-Amri and J. Zollweg
Initial Results from the Deployment of Broadband Seismometers in the Saudi Arabian Shield 108

Seismic Wave Propagation

App, Fred N.; Randy J. Bos and James R. Kamm
Synthetic Seismograms at Regional Distances for May 1995 Earthquake and Explosion Sources in Western China 119

Archambeau, C.; J. Orrey and B. Kohl
3-D Seismic Wave Synthesis and Full Wavefield Inversion 129

Baker, G. Eli and J. Bernard Minster
Quantifying the Attenuation and Blockage of Lg and Robust Statistical Estimates of Site Amplifications at SCSN Stations 139

Boitnott, G. N.
Constructing a General Rheological Model for Rock Deformation 149

Cormier, Vernon F. and Tom Anderson
Lg Blockage and Scattering at CNET and KNET 159

Goldstein, Peter; Craig Schultz; Shawn Larsen and Lee Minner
Modeling of Regional Wave Propagation Phenomena in the Middle East and North Africa and New Analysis Capabilities in SAC2000 165

Husebye, Eystein S. and Bent O. Ruud
Wave Propagation in a Complex Crust - CTBT Implications 172

Jih, Rong-Song
Waveguide Effects of Large-Scale Structural Variation, Anelastic Attenuation, and Random Heterogeneity on SV Lg Propagation: A Finite-Difference Modeling Study 182

Johnson, Lane R.
The Effect of Damage on Explosion Generated Elastic Waves 195

Page

Keers, H.; K. Vogfjörd; G. Nolet and F. A. Dahlen
High Frequency Propagation of Crustal Waves 199

Lay, Thorne
Calibration of Regional Wave Discriminants in Diverse Geological Environments: Topographic Correlations 209

McLaughlin, Keith L. and Boris Shkoller
Calculation of Synthetic Seismograms Using PVM on a Network of Workstations 219

Morozov, Igor; Elena Morozova; Yuri Ganchin and Scott Smithson
Lg Propagation across Northern Eurasia Recorded by Profile "Quartz" 221

Nolte, B.; R. L. Gibson, Jr. and M. N. Toksöz
Irregular-Grid Modeling of Regional Wave Propagation 231

Park, Jeffrey; Vadim Levin and Liqiang Su
The Effects of Seismic Anisotropy on Regional Seismic Wave Propagation 241

Pavlis, Gary L.; Dimitri Repin; Stanley Radzevicius and Frank Vernon
Near-Surface Effects on High-Frequency Seismic Waves Observations from Dense, Three-Component Seismic Arrays 251

Schatzman, James C.
A Pseudo-Spectral Scheme for Viscoelastic Seismic Modeling 261

Wagner, Gregory S.
A Subspace Processing Approach for Three-Component Seismic Array Data 271

Wu, Ru-Shan; Xiaofei Chen and Thorne Lay
Modeling the Effects of Surface Topography on Lg Wave Propagation by a Hybrid Method 281

Wu, Ru-Shan; Shengwen Jin and Xiao-Bi Xie
Synthetic Seismograms in Heterogeneous Crustal Waveguides Using Screen Propagators 291

Xu, Heming; Steven M. Day and Jean-Bernard H. Minster
Two-Dimensional Nonlinear Wave Propagation in an Endochronic Material 301

Seismic Sources and Structure

Page

Ekström, Göran; Adam M. **Dziewonski**; Gideon P. **Smith** and Wei-jia **Su**
Elastic and Anelastic Structure Beneath Eurasia 309

Goff, John A. and Alan **Levander**
Simulating Crustal Heterogeneity Fields from Stochastic Models: A Performance Evaluation 319

Gupta, Indra N. and Tian-Run **Zhang**
Study of Low Frequency Lg from Explosions at Nevada, Kazakh, Lop Nor, and Azgir Test Sites 328

Harvey, Danny J.
Source and Structure Parameters from the Urals Event of 5 January 1995 Using Rayleigh Waves from Russian and Kazak Broadband Stations 338

Herrmann, Robert B. and Tao-Ming **Chang**
Progress in Waveform Inversion 347

Herrmann, Robert B.
Variability of the M_I - Y and ψ_∞ - Y Relations 354

Jordan, Thomas H.; James B. **Gaherty**; Mamoru **Kato** and Olav **Van Genabeek**
Regional Upper-Mantle Structures and their Interpretation in terms of Small-Scale, Anisotropic Heterogeneities 361

Langston, Charles A.; Andrew A. **Nyblade** and Ming **Zhao**
Seismic Wave Propagation in Southern and Central Africa 371

Levander, A.; S. **Pullammanappallil**; S.P. **Larkin**; L.M. **La Flame** and J.A. **Goff**
Estimation of Fine-Scale Crustal Heterogeneity from Seismic Exploration Data with Applications to the Basin and Range 380

Ni, James; Chris **Reese**; Jianxin **Wu** and Lian-She **Zhao**
Crustal Structure and Attenuation in Southern Tibet 390

Priestley, Keith and Steve **Mangino**
Structure of the Crust and Upper Mantle in the South Caspian Basin and Surrounding Region 400

Rodgers, Arthur and Susan **Schwartz**
Asian Lithospheric Structure from Waveform Modelling: Regional Pnl and Complete Waveforms, P and PP Triplications 410

Page

Xie, Jiakang
Excitation and Propagation of Pn in Central Asia 419

Zhang, Jiajun
Source Characterization Using Simplified Waveforms: Tests on Earthquakes and Nuclear Explosions in Xinjiang, China 429

Zhu, Lupei and Donald V. Helmberger
Crustal and Upper Mantle Structure of the Tibetan Plateau 439

Discrimination

Ahrens, Thomas J. and Cangli Liu
Shear Wave Generation from Contained Explosions 449

Anderson, D.N.; K.K. Anderson; D.N. Hagedorn; K.T. Higbee; N.E. Miller; T. Redgate; A.C. Rohay
Performance of Seismic Discrimination Frameworks 456

Barker, T.G.; K.L. McLaughlin and J.L. Stevens
Advanced Systems for Assessing the Performance of Regional Networks 462

Baumgardt, Douglas R.
Characterization of Regional-Phase Propagation and Seismic Discriminants for the Middle East 474

Bennett, T. J.; K. L. McLaughlin and M. E. Marshall
The Physical Basis for the Lg/P Discriminant 484

Bennett,T. J.; M. E. Marshall; B. W. Barker and J. R. Murphy
Transportability of Regional Phase Spectral Ratio Discriminants 494

Hartse, Hans E.; Steven R. Taylor; W. Scott Phillips and George E. Randall
Regional Seismic Discrimination in Central Asia with Emphasis on Western China 503

Hedlin, Michael A.H.; Frank L. Vernon; J.-Bernard Minster and John A. Orcutt
Experiments in Regional Monitoring of Small Seismo/Acoustic Events 515

Herrin, Eugene; G. G. Sorrells; Jessie Bonner; Valeriu Burlacu; Nancy Cunningham; Paul Golden; Chris Hayward; Jack Swanson; Karl Thomason and Ileana Tibuleac
Seismo-Acoustic Studies at TXAR 524

Page

Jenkins, Richard D.; Thomas J. **Sereno**; Donna J. **Williams** and Aaron A. **Velasco**
Attenuation at GSETT-3 Stations and the Lg/P Discriminant 534

Kim, W.-Y.; A. **Lerner-Lam** and P. **Richards**
Discrimination of Earthquakes and Explosions Using Three-Component Regional Records Corrected for the Free Surface Effect 544

Kushnir, A.F.; E. V. **Troitsky**; L.M. **Haikin** and A. **Dainty**
Study of Statistical Classification Approach to Discrimination Between Weak Earthquakes and Chemical Explosions Recorded by Israel Local Seismic Network 554

Lay, Thorne; Guangwei **Fan** and Arthur **Rodgers**
Crustal Waveguide Effects on Regional Phases in China and Southeast Asia 565

Li, Y.; M. N. **Toksöz** and W. L. **Rodi**
Discrimination of Small Earthquakes and Explosions 574

Murphy, J. R.; D. D. **Sultanov**; B. W. **Barker**; I. O. **Kitov** and M. E. **Marshall**
Application of Soviet PNE Data to the Assessment of the Transportability of Regional Discriminants 584

Pulli, Jay J.
Transportable Seismic Discriminants: Stable Estimates of Spectral Ratios 593

Sain, Stephan R.; H. L. **Gray** and Wayne A. **Woodward**
Outlier Detection without Ground Truth 602

Shapira, Avi; Yefim **Gitterman** and Vladimir **Pinsky**
Discrimination of Seismic Sources Using the Israel Seismic Network 612

Stevens, J. L. and K. L. **McLaughlin**
A Transportable Regional Discriminant Using a Maximum Likelihood Analysis of Surface Waves 622

Walter, William R.; Kevin M. **Mayeda**; David B. **Harris**; Howard J. **Patton**; Alan **Sicherman**; Craig **Schultz**; Peter **Goldstein**; Dan **McNamara** and Jerry **Sweeney**
LLNL's Seismic Magnitude and Discrimination Research 631

Woods, Bradley B. and Chandan K. **Saikia**
The Performance of Some Regional Seismic Discriminants to the Middle-East 641

Detection/Location/Identification

Page

Alexander, Shelton S. and Chih-Chieh **Yang**
Use of the Cepstral Stacking Method (CSM) for Improved Source Depth Determinations from Combined Single-Station and Array or Network Observations at Regional Distances 647

Bear, Lorie K. and Gary L. **Pavlis**
Multiwavelet Beamforming—A New Seismic Array Data Processing Method 657

Cipar, John J.
Event Location by Long-Period Surface Waveform Matching-Application to Earthquakes in Northeastern China and Korea 666

Claassen, John P.
Performance Estimates of the CD Proposed International Seismic Monitoring System 676

Cogbill, Allen H. and Lee K. **Steck**
Regional Location in Western China 685

Der, Zoltan A. and Robert H. **Shumway**
Investigation of Advanced Processing Techniques for Regional Array Data 695

Dreger, Douglas; Michael **Pasyanos**; Robert **Uhrhammer**; Barbara **Romanowicz** and Alan **Ryall**
Evaluation of the Performance of Broadband Networks and Short-Period Arrays in Global Monitoring 704

Edenburn, M.W.; M.L. **Bunting**; A.C. **Payne**; R.R. **Preston** and L.C. **Trost**
Synergy Among International Monitoring System Technologies 714

Kennett, B.L.N.
Understanding Seismic Wave Propagation at Regional and Teleseismic Distances 726

Kim, W. Y.; G. L. **Vsevolozhsky**; T. L. **Mulder** and P. G. **Richards**
Practical Analysis of Seismic Activity in Northwestern China During September 4-7, 1995 735

Mellors, Robert; Frank **Vernon** and David **Thomson**
Detection of Dispersive Signals Using Multitaper Double-Frequency Coherence 745

Murphy, J. R.; D. D. **Sultanov**; B. W. **Barker**; I. O. **Kitov** and M. E. **Marshall**
Detection Analyses of Low Yield Soviet PNE Explosions 754

Page

Saikia, Chandan K.; B.B. Woods and H.K. Thio
Path Calibration, Source Estimation and Regional Discrimination for the Middle East 763

Shoubik, B.M.; A.F. Kushnir; L.M. Haikin and A. Dainty
SCANLOC: Automatic Seismic Event Location Based on Local Seismic Network Data 774

Wallace, Terry C. and Mark A. Tinker
Location and Signal Identification With Broadband Arrays at Regional and Teleseismic Distances 782

Young, Christopher J.; Judy I. Beiriger; J. Mark Harris; Susan G. Moore; Julian R. Trujillo; Mitchell M. Withers and Richard C. Aster
The Waveform Correlation Event Detection System Project: Issues in System Refinement, Tuning, and Operation 789

Zhao, Lian-She and Cliff Frohlich
Single-Station Seismic Event Location: How Non-Horizontal Structure Affects Apparent Azimuth 799

Zollweg, J. E. and D. M. Childs
Empirical Identification of Depth-Related P Phases at Regional Distances 809

Hydroacoustics, Infrasound, Radionuclides and On-Site Inspection

Armstrong, W. Thomas and Rodney W. Whitaker
Estimates of Infrasonic Array Gain Patterns 819

Blackman, Donna K. and John A. Orcutt
Seismoacoustic Studies in the Norwegian Sea 826

Bowyer, T.W.; K.H. Abel; C.W. Hubbard; A.D. McKinnon; M.E. Panisko; R.W. Perkins; P.L. Reeder; R.C. Thompson and R.A. Warner
An Automated Radioxenon Analyzer for Possible CTBT Monitoring "The Xenon Xephyr" 833

Clarke, D.; D. Harris; T. Hauk; E. McDonald; G. Orris; J. White and R. Wong
IMS Hydroacoustic Network Site Selection and Performance 843

deGroot-Hedlin, Catherine D. and John A. Orcutt
Observations of T Phase Arrivals from North Pacific Events 853

Page

Farrell, Ted; Kevin LePage and Greg Duckworth
Development of the Hydroacoustic Coverage Assessment Model (HydroCAM) 861

Miley, H.S.; S.M. Bowyer; C.W. Hubbard; R.W. Perkins; R.C. Thompson and R.A. Warner
DOE Aerosol Radionuclide Monitoring System for the CTBT 871

Sweeney, J. J.; C. Carrigan; W. Pickles; C. Schultz and A. Smith
Results of the LLNL On Site Inspection Research Project 879

Mining Practices

Barker, T.G.; K.L. McLaughlin and J.L. Stevens
Physical Mechanisms of Quarry Blast Sources 891

Bennett, T. J.; M. E. Marshall; K. L. McLaughlin; B. W. Barker and J. R. Murphy
Seismic Investigations of Rockbursts 900

Glenn, L. A.; S. P. Jarpe and P. Goldstein
Seismic Characterization of Commercial Blasting Practice in an Open-Pit Gold Mine 908

Khalturin ,Vitaly I.; Tatyana G. Rautian and Paul G. Richards
Statistics on Mine Blasting and Blasting Signals for the Former Soviet Union 918

Leith, William; Alexander Spivak and Leonid Pernik
Large Mining Blasts from the Kursk Mining Region, Russia 926

Pearson, D. Craig; Brian W. Stump and W. Scott Phillips
The White Pine Mine Explosively Induced, Controlled Collapse Experiment 937

Srinivasan, C.
Blasting Induced Seismic Events in Kolar Gold Fields 947

Stump, Brian W. and D. Craig Pearson
Design and Utilization of a Portable Seismic/Acoustic Calibration System 956

Data Processing and Analysis

Page

Barron, Carole Craig; James G. **Fleming**; Stephen **Montague**; Dale L. **Hetherington**; Jeffry J. **Sniegowski**; Brady R. **Davies**; David L. **Armour**; and R. Patrick **Fleming**
Micromachined Silicon Seismic Accelerometer Development 967

Craft, R. L. and T. J. **Draelos**
Initial CTBT International Monitoring System Security Findings and Recommendations 977

Fisk, Mark D.; Steven **Bottone**; Richard J. **Carlson**; Henry L. **Gray** and Gary D. **McCartor**
Statistical Framework for Event Characterization and Assessment of Seismic CTBT Monitoring Capability 987

Grant, Lori; Flori **Ryall**; Ivan **Henson** and Wilmer **Rivers**
Ground Truth Database for Seismic Discrimination Research 997

Harris, J. Mark and Christopher J. **Young**
MatSeis: A Seismic Toolbox for MATLAB 1007

Hipp, Jim; Ralph **Keyser**; Chris **Young**; Ellen **Shepard-Dombroski** and Eric **Chael**
Knowledge Base Interpolation of Path-Dependent Data Using Irregularly Spaced Natural Neighbors 1014

Seber, Dogan; Eric **Sandvol**; Marisa **Vallvé**; Graham **Brew** and Muawia **Barazangi**
Development of a Geological and Geophysical Information System and Seismological Studies in the Middle East and North Africa 1026

Shumway, Robert H.
Array Processing of Delay-Fired Signals 1036

Simons, Randall W.; Christopher J. **Young** and Tony L. **Edwards**
Data Visualization for Comprehensive Test Ban Treaty Monitoring 1045

Seismic Sources and Structure in Iran from Joint Seismic Program Array Data: Attenuation Variations at the Northern Margins of Eurasian Mountains

Geoffrey A. Abers and Golam Sarker
Department of Geology, University of Kansas, Lawrence KS 66045
Grant No. F49620-95-1-0002
Sponsored by AFOSR

ABSTRACT

Seismic wave propagation is examined through mountain belts that bound the Iranian Plateau on the north, by studying records from a seismic network in the Greater Caucasus and an array in the Kopet Dagh. Attenuation is measured from spectral decay of body waves for paths 0-4° long, in a fitting procedure that simultaneously determines source and propagation parameters. From the Caucasus array, strong differences are recorded between waves that travel predominantly within the Russian Shield and those that traverse parts of the Greater Caucasus, for both *P* and *S* waves. The *S* wave attenuation factor Q_S is 775 ± 75 and 2060 ± 315 for mountain and shield paths, respectively, and typically $Q_P \sim Q_S$, for the 1-10 Hz body waves examined here. Inversions for spatial variation in *Q* show that near-station effects contribute significantly to observed loss of signals, particularly at stations on thick sedimentary piles in basins lying north of the Caucasus. Attenuation inversions also show that the boundary between high-*Q* and low-*Q* regions is sharp and follows the foothills of the Greater Caucasus. Thus the entire mountain range constitutes a region of high attenuation, not just the highly deformed southern flank. Preliminary results from the Geyokcha array, in the Turkmenistan Kopet Dagh foothills, show low Q_P and Q_S values near the array of 640 ± 70 and 900 ± 100 respectively, for paths ≤ 3° long. As in the Caucasus, these low *Q* (high attenuation) values are found in the foothills of this young mountain belt, the boundary between stable Eurasia and the Iranian plateau. Stations placed on the flanks of similar Alpine-Himalayan ranges may suffer similar attenuative loss of regional signals compared to nearby cratonic sites, complicating the use of these sites for seismic monitoring. On the other hand, nearby shield sites are likely to lie on young sedimentary basins, where site effects can severely distort signal. This combination of low *Q* beneath young mountains and adjacent thick sedimentary basins is common, and highlights the need for careful site evaluation in much of Eurasia.

Keywords: attenuation, regional seismic waves, tomography, Caucasus, Kopt Dagh

OBJECTIVES

We evaluate and characterize seismic data from digital network and array sites in and around the Former Soviet Union, in order to provide new constraints on seismic wave propagation characteristics in the Caucasus Ranges, Middle East and Iranian Plateau. Strong changes in the attenuation and velocity behavior of seismic waves are associated with the mountain belts here, and make it difficult to infer wave behavior from experiences gained within stable cratons. Seismograms from the IRIS-JSP networks and arrays in the northern Caucasus and Kopet Dagh collected since 1991 include a large number of local and regional events in the region. These waveforms are used for assessing the amplitude and phase of major wave groups along regional paths and for constraining earth structure beneath the network. Results provide information on the behavior of common event discriminants and detection thresholds for regional paths.

RESEARCH ACCOMPLISHED

Severe changes in wave behavior are observed between paths that cross the Caucasus and other Alpine-Himalayan mountain belts, and those that do not (Figure 1). These changes represent substantial attenuation of phases often used to discriminate explosions from earthquakes and to estimate event size and type. Work to date has concentrated on quantifying the behavior of seismic waves as they cross the Caucasus, mostly by examining phase amplitudes for events within 10° of the Caucasus Seismic Network (CNet). We have also made comparable measurements of body-wave attenuation for signals traveling to an array at Geyokcha, Turkmenistan, for events in and around the Kopet Dagh ranges. The main finding to date is a sharp boundary between regions of high Q found in stable continent, and regions of low Q in active Alpine-Himalayan mountain belts. These mountain ranges bound the northern flanks of the Iranian plateau, while most seismic monitoring facilities are north of them. Such barriers to wave propagation may play an important role in some detection scenarios.

Caucasus Network

The Caucasus network was established in 1991 through the Joint Seismic Program, as a cooperative project between Lamont-Doherty and the OME-Obninsk group (Abers, 1994). The stations are on the north side of the Greater Caucasus range, and straddle the transition from the Russian Shield to the Caucasus collisional zone. The northern stations lie on flat-lying, poorly consolidated Neogene sediments, while southern stations lie on tilted, well-lithified Mesozoic sediments. The network, based in Kislovodsk (KIV), consists of 5-6 digitally telemetered 3-component sensors with 0.2 Hz natural periods (Kinemetrics SV/SH1), digitized at 60 sps. Data were initially examined on site and later processed at Lamont-Doherty, before being forwarded to IRIS data management facilities. Waveforms for 1992 were picked and associated by the Joint Seismic Program Center (Harvey et al., 1994) and subsequent seismograms are distributed through IRIS. For 1993 and 1994, selected arrivals were picked and events were located at Kansas using JSP software. A total of 645 events were associated for 1992 (292 in the PDE), and 649 in 1993 (338 in the PDE), and 223 in the first half of 1994 (157 in the PDE).

Geyokcha Array

In 1993, a tight-aperature broadband array was deployed in the northern foothills of the Kopet Dagh mountains, near the Turkmenistan-Iran border (Figure 1B; Pavlis et al. 1994). Among numerous short-period sensors were deployed 12 broadband sensors over a 1.5 x 1.5 km area . The array lies ~20 km SW of the range-bounding faults that separate the Kopet Dagh, an actively deforming part of the Alpide-Himalayan collision zones, from the Turan depression where 10-15 km of Mesozoic and younger sediments remain undeformed. Teleseismic signals recorded by the array are complex, and vary dramatically

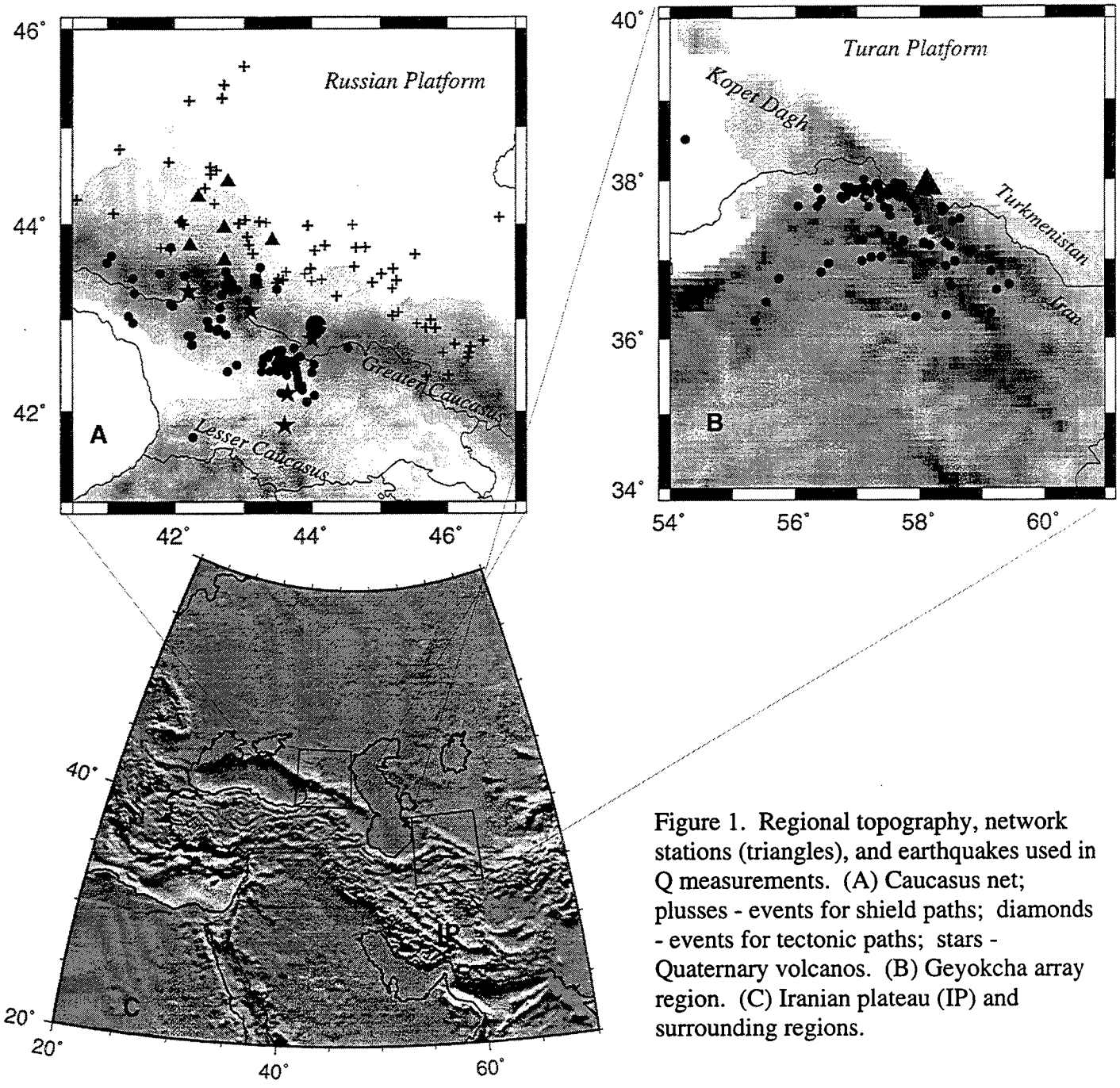

Figure 1. Regional topography, network stations (triangles), and earthquakes used in Q measurements. (A) Caucasus net; plusses - events for shield paths; diamonds - events for tectonic paths; stars - Quaternary volcanos. (B) Geyokcha array region. (C) Iranian plateau (IP) and surrounding regions.

between those that cross range-bounding fault system and those that do not (Abers and Garinger, 1996). For the attenuation analyses done here, we analyzed beams formed on the 250 sps recordings of the Streckheisen STS-2 sensor motions, and event locations determined from array analysis (G. Pavlis, pers. comm., 1996).

Attenuation measurements

For the short paths (<5°) examined here, spectral falloff of major body waves provides an adequate characterization of effective attenuation (Figure 2). We measure spectra of *P* and rotated *SH* waves in 2-5 s windows, depending upon event distance, using a multitaper algorithm. These spectra are compared to noise spectra of pre-event noise or late *P* coda, as appropriate, and are evaluated over the frequency band where signal levels are high (typically 0.5-10 or 1-20 Hz). These measurements of spectral amplitude variations with frequency (*f*) are fit to a simple model that includes both source and propagation effects:

$$A(f) = \frac{A_0 I(f) e^{-\pi t^* f}}{1 + (f / f_c)^2}$$

where A_0 is a frequency-independent term, t^* is a parameter that describes frequency-independent attenuation, f_c is a source corner frequency, and $I(f)$ is the known instrument response to ground displacement. We first determine t^* by least-squares regression on $\log[A(f)]$, and then invert the t^* measurements for attenuation. The small number of stations per event make it difficult to use most methods used for removing source effects, such as spectral ratio techniques. Hence, the t^* measurements suffer some tradeoffs with f_c. In several experiments f_c was held fixed for all records for each event, and in others f_c was set to an arbitrary high value. Overall the results were similar, suggesting that f_c - t^* tradeoffs do not grossly affect the results.

We invert each each log-amplitude spectrum for f_c, t^*, and A_0, and use measurements of t^* to describe attenuation using

$$t^* = \oint_{path} \frac{dr}{Q(r)c(r)}$$

for various parameterizations of attenuation Q. Here, $c(r)$ is the relevant phase velocity, estimated from previous work in the region. For each phase (*P* or *S*), Q^{-1} is estimated using standard tomographic inversion techniques as described below. In the simplest models, discussed first, Q^{-1} is assumed constant along each path and is readily estimated from linear regressions of t^* on r. In all work to date, Q is assumed to be independent of frequency.

Results: Greater Caucasus - Russian Platform

We examined records from 186 events recorded within 4° of the Caucasus network. Initially, these were subdivided into events with paths predominantly within the Russian platform and events with paths largely within the mountains (Figures 1, 3). The observations show gradual increase in t^* with increasing distance, and although at a higher rate for the mountain paths. Fitting a constant-Q model to these two subsets of data gives the values shown on Figure 3, with Q for mountain paths no more than half that for shield paths and Q for *S* waves roughly equal to that for *P*. In these fits, we also found an added constant-t* term was necessary to account for near-station effects which were found substantial at stations on soft sediments.

Results depend on fits to body-wave spectra in the 1-10 Hz range. Since the effect of Q on amplitude increases with frequency, the measurements probably reflect attenuation towards the high end of the frequency band. Hence, the somewhat lower Q values inferred from coda measurements (Rautian et al., 1979) may reflect differences in frequency (although the coda Q measurements are likely to be more sensitive to scattering).

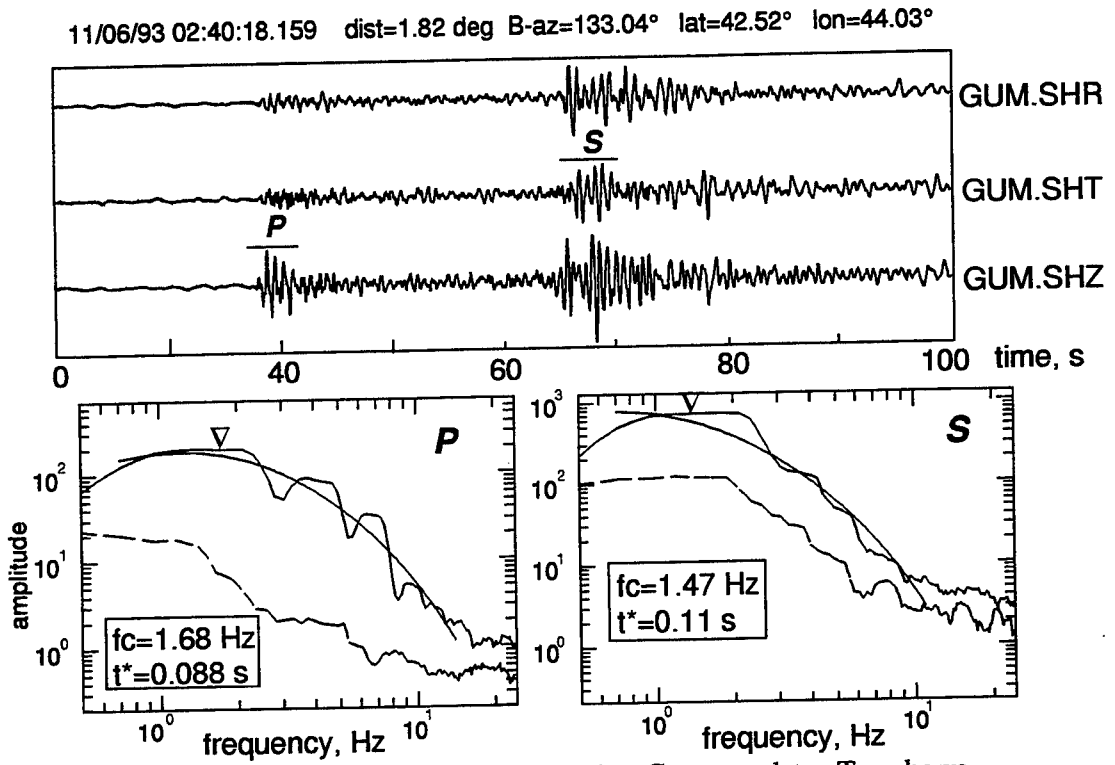

Figure 2. Example of fitting spectra to determine t* to Caucasus data. Top shows seismograms for a shield-type path. Bottom shows spectra for P and S windows, labelled. Inverted triangle shows estimated corner frequency, and t* estimates are shown in box. Noise curves are dashed, body-wave train solid.

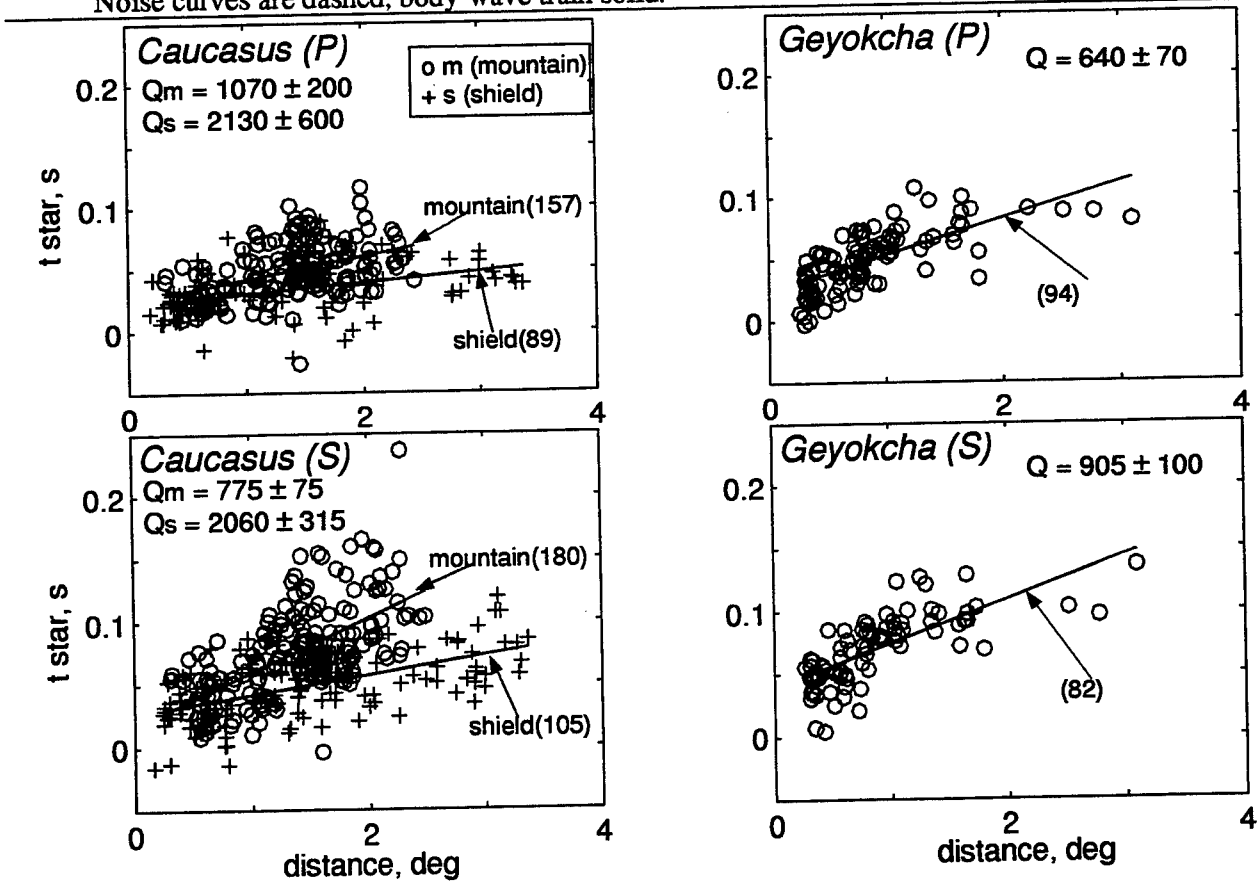

Figure 3. Results of fitting variations in t* with distance to a straight line (t* = a + br). Parameter a represents near-station effects, while b is used to calculate a path-averaged Q value, for each region.

In order to better understand the variations observed, the we modified the velocity inversion methods of Roecker (1993) to invert for spatial variations in Q^{-1} (Figure 4). Because t^* varies linearly with Q^{-1} many of the problems associated with velocity inversion are eliminated, and error assessment becomes much simpler. These inversions take into account a priori information on data uncertainties (calculated while determining t^*), model parameters, and methodological uncertainties. In some of these inversions the Earth is assumed to consist of a single layer, so that vertical variations in structure are ignored. In other inversions, a very thin low-velocity layer is included to mimic near-station effects of weak sediments.

Several inversions were done for models of increasing complexity (Figure 5). These show that only simple spatial variations are required in the data. In particular, near-site effects are important (inversions E-H), as estimated by placing a 200m thick block directly beneath each station and inverting for its Q^{-1}. These near-surface blocks show Q^{-1} values in the range 0.008 - 0.073, with the highest values seen at stations on weak young sediments. Inversions that allow bulk-earth attenuation to vary across the strike of the mountains (Figure 4) do significantly better (20-30% less variance) than those that require constant Q at depth (comparing inversions C, D, and F with A, B, and E respectively). Further complexity (inversions G, H) does not seem warranted by the present data although the images are suggestive of additional complications that might exist (Figure 4, bottom, shows inversion G).

The primary result of this study is that the factor-of-two boundary between cratonic-Q values and mountainous-Q values is sharp, and corresponds to the northern foothills of the Greater Caucasus. The point is illustrated by comparing inversions which are parameterized by one simple boundary between mountains and shield, but the location of this boundary is allowed to vary (Figure 6). For each inversion, the global variance of t* measurements to those predicted is calculated and compared to the "best" case (minimum variance). The location of this boundary is constrained in this way to lie in the northern foothills of the Greater Caucasus. The corresponding attenuation contrast is roughly a factor of 2 for both P and S.

Results: Turkmenistan-Iran Border Region

Preliminary work has begun to assess attenuation beneath the Geyokcha array. The same techniques are used here to determine attenuation, and show on average a $Q_P = 640 \pm 70$ for P waves and $Q_S = 900 \pm 100$ for S (Figure 3). These values are comparable to or somewhat lower than those seen in the Caucasus mountains, especially for P, and are much lower than common shield values. Again, within 20-30 km of the range front we are seeing attenuation values characteristic of tectonically active regions.

CONCLUSIONS AND RECOMMENDATIONS

The sharp boundary between high-Q and low-Q regions suggests that very small changes in raypath could have dramatically different signal characteristics. These variations are particularly of interest where body wave amplitudes are used for yield estimation and source discrimination. They also reflect similar variations in Lg and Sn propagation at longer distances (Abers et al., 1995; Rodgers et al., 1994). These variations make careful path corrections necessary in using any discriminant based on regional wave propagation near range fronts. Another practical implication of high attenuation in mountainous regions is that stations and arrays are better situated on adjacent shields, even though those sites may be somewhat farther away from sources of interest. This enhancement is to some extent counteracted by the increasing near-site attenuation effects observed at northern sites near the Caucasus, which tend to sit on thick piles of low-velocity sediment. Although we have no direct measurements, surface geology in the Turan depression (north of the Kopet Dagh) suggests that similarly complicated sediments may be present there.

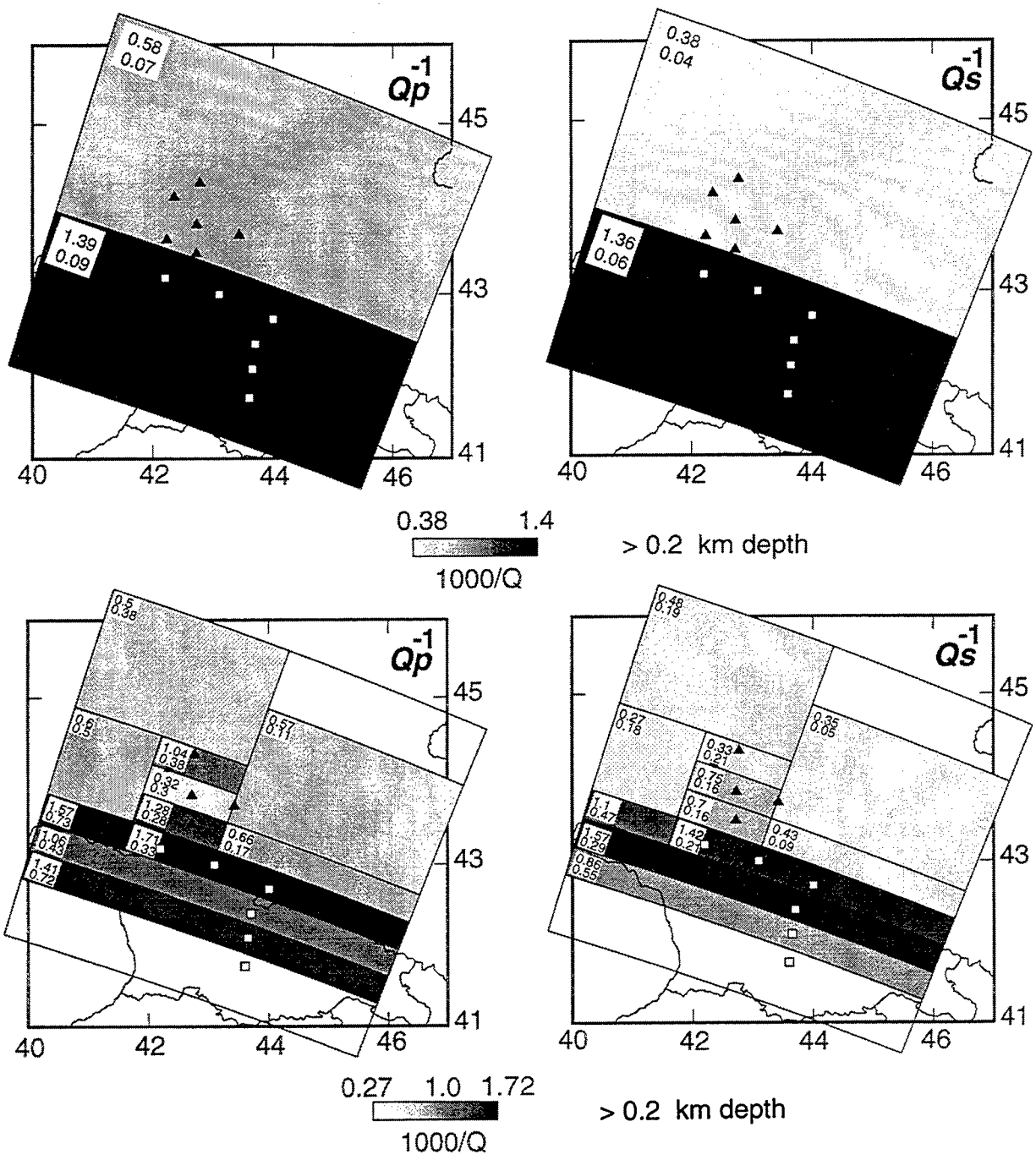

Figure 4. Results of attenuation inversion in the Caucasus, for two different parameterizations, corresponding to parameterization F (top) and G (bottom) of Figure 5. Each block is labeled by its value, 1000/Q, and formal uncertainty. Overall fit to data is similar for the two models. Both inversions constrain Q to be constant with depth below 200 m; a second layer makes up the topmost 200 m and is parameterized such that a separate block lies beneath each station. The upper layers, not shown, have $1/Q$ values 10-100 times larger than those shown here. Triangles show station locations, and open circles show Quaternary volcanic centers. Both show relatively high attenuation beneath the topography, indicated by the Russia-Georgia border which follows the crest of the Greater Caucasus ranges (also compare with Figure 1A). Events used are shown in Figure 1A.

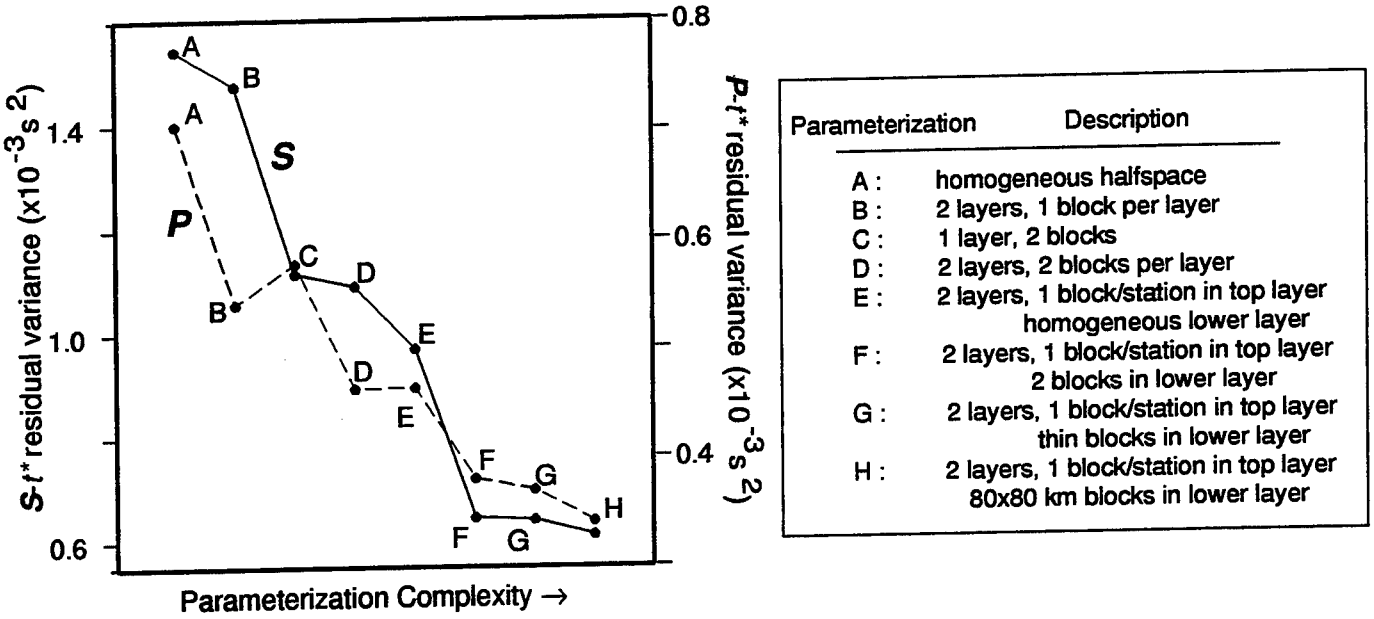

Figure 5. Variance reduction as a function of model complexity, for a variety of simple parameterizations. Parameterization A is a simple constant-Q halfspace; the number of free parameters increases to right. The models are described in the accompanying box. Note different scales for P and S on either side of plot; variances are in units of t*^2. For two-layer models, the upper layer is 200 m thick and has substantially larger a priori 1/Q values. In general two factors seem to dramatically affect residual variance: allowance of a top layer where 1/Q is allowed to be different beneath each station (effectively a station correction; models E-H), and allowance of different 1/Q values beneath the mountains from beneath the Russian shield (models C, D, F, G, H). Further complexity, such as small blocks, does not produce significant further variance reduction (compare G or H to F).

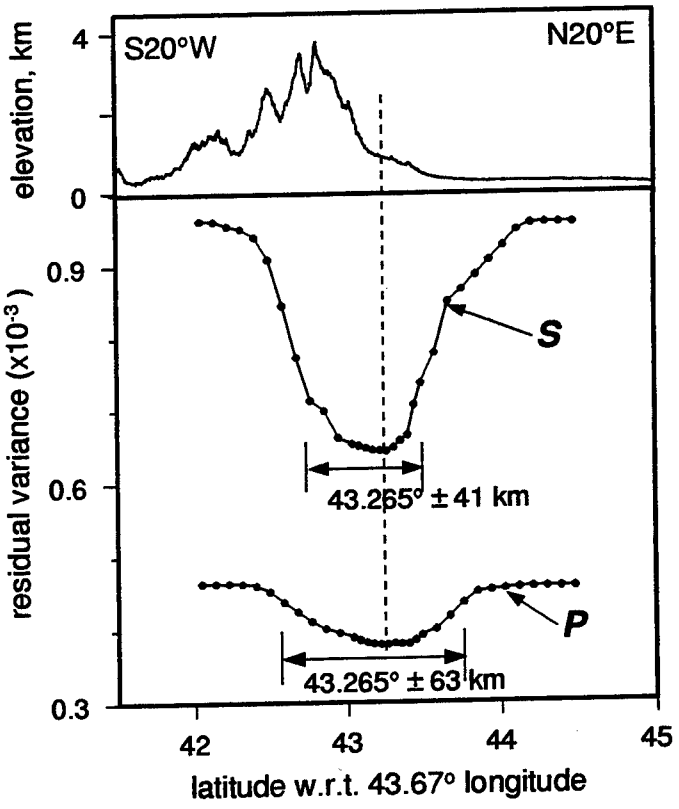

Figure 6. A test for the location of the boundary between high-Q and low-Q regions. Top shows topography of the Caucasus and Russian Shield, along a profile oriented N20°E. Bottom shows residual variance for P and S t* observations, to a simple model resembling F in Figures 4 and 5 (2 constant-Q regions, with boundary paralleling the range front). The data were inverted repeatedly, in each case shifting the boundary between the regions north or south. For both P and S, the boundary that produces a minimum residual crosses 43.67°E at 43.265°N (dashed line), in the lower foothills on the north flanks of the Greater Caucasus. Double arrows indicate 95% confidence limits calculated from F tests on the residual variances.

These observations also have tectonic implications for the generation of deep structure beneath mountains. Our Q estimates are vertical averages in a sense, and at the distance ranges studied probably represent Q averaged throughout the crust and perhaps the uppermost mantle. They show low Q wherever high topography is found. In the case of the Caucasus this boundary is represented geologically by a simple monocline with little surficial deformation, while the active deformation front lies south of the ranges (Triep et al., 1995). If interpreted in terms of temperature, the Q measurements along with observations of Quaternary volcanism suggest significantly greater lithospheric heating within the Greater Caucasus than expected over a region of monoclinal folding. It is reasonable to infer, although not required by the observations, that for some reason the mantle part of the lithosphere has been reheated everywhere beneath high topography, perhaps reflecting convective instability within the mantle. Analysis of gravity measurements in the Caucasus would help confirm or refute such a scenario. Regardless, simple observations of elevation seem to be revealing more about the nature of crustal structures here than does surface geology.

REFERENCES

Abers, G.A., and L. Garinger, Estimating structure beneath IRIS array sites from teleseismic multichannel receiver functions, *IRIS Workshop Abstracts*, Spring 1996.

Abers, G.A., The Caucasus Seismic Network, *IRIS Newsletter, 13*, 16-17, 1994.

Abers, G.A., W.-Y. Kim, and A. Lerner-Lam, Seismic sources and structure in Iran and the Caucasus from Joint Seismic Program array data, in *Proceedings of the 17th Annual Seismic Research Symposium* 12-15 September 1995, Scottsdale, Arizona, PL-TR-95-2108, p. 602-608, 1995.

Harvey, D, and others, Caucasus Network Information Product Triggered events from January 1, 1992 to November 9, 1992, Version 1.0, IRIS-JSPC, 1994.

Kadinsky-Cade, K., M. Barazangi, J. Oliver, and B. Isacks, Lateral variations of high-frequency seismic wave propagation at regional distances across the Turkish and Iranian plateaux, *J. Geophys. Res., 86*, 9377-9396, 1981.

Kim, W.-Y., V. Aharonian, G. Abers, A. Lerner-Lam, and P. Richards, Discrimination of earthquakes and explosions in southern Russia using regional high-frequency data from IRIS/JSP Caucasus Network, in *Proceedings of the 17th Annual Seismic Research Symposium* 12-15 September 1995, Scottsdale, Arizona, PL-TR-95-2108, 68-77, 1995.

Pavlis, G., H. Al-Shukri, H. Mahdi, D. Repkin, F. Vernon, JSP arrays and networks in central Asia, *IRIS Newsletter, 13*, 9-12, 1994.

Rautian, TG, VI Khalturin, and IS Shengeliya, Seismic coda envelopes and assessment of earthquake magnitudes in the Caucasus, *Phys. Solid Earth, 15*, 393-398, 1979.

Rodgers AJ, TM Hearn, and JF Ni, Pn, Sn and Lg propagation in the Middle East, *EOS Trans AGU, 75(44)*, 463, Fall, 1994.

Sarker, G., G.A. Abers, and A. Lerner-Lam, Seismic Q and tegional tectonism in the Greater Caucasus continental collision zone, *EOS Trans. AGU*, Fall 1995.

Triep, E., G.A. Abers, A. Lerner-Lam, V. Mishatkin, N. Zhacherenko, and O. Staravoit, Active thrust front at the south slope of the greater Caucasus: The 29 April, 1991 earthquake and its aftershock sequence, *J. Geophys. Res , 100*, 4011-4034, 1995.

Roecker, S.W., Tomography in zones of collision: practical considerations and examples, in *Seismic Tomography, Theory and Practice*, H.M. Iyer and K. Hirahara, eds., Chapman and Hall, London, p. 584-612, 1993.

Regionalization Studies: Statistical Analysis of Detection Capability and Magnitude Scaling

Kevin K. Anderson
Pacific Northwest National Laboratory
Sponsored by U.S. Department of Energy, Contract DE-AC06-76RLO 1830
Comprehensive Test Ban Treaty Research and Development Program, ST482C

Abstract

Statistical methods are needed to assess the performance of seismic stations in regions of interest, both for determining the value of a station's contribution to the primary or secondary network and for determining the quality of its data for the regional characterization efforts of the U.S. Department of Energy Comprehensive Test Ban Treaty research program. This paper considers the problems of estimating the regional detection capability using noise studies and scaling regional amplitudes to the global m_b scale. The indirect method of estimating a station's regional detection capability is based on measuring the seismic noise level and estimating the signal-to-noise ratio required for detection. Magnitude scaling is calibrating station magnitudes to the worldwide m_b scale. It involves estimating the station-dependent distance corrections in the relationship $m_b = a + b\log(amp) + c\log(dist)$, where amp is the frequency-adjusted P-phase amplitude and $dist$ is the great circle distance between station and regional event. A methodology is presented that jointly estimates the scaling coefficients for multiple regional stations. In both problems, statistically incorporating the uncertainty in worldwide m_b magnitudes of observed events improves the estimation.

Key words: distance correction, seismic noise, measurement error modeling.

Objective

The Department of Energy Comprehensive Test Ban Treaty (DOE CTBT) research program (DOE 1994) currently provides to the monitoring community the detailed characterization of two regions of interest. Included in these characterizations are estimates of the regional detection capabilities. Seismic noise studies will be used to assess individual station detection capability for primary and secondary stations in the global seismic monitoring network. The regional amplitudes also need proper distance correction for future network magnitude measurements. Magnitude scaling ensures that the regional magnitudes are comparable to the global m_b magnitudes.

This paper presents statistical methods that can improve the estimation of individual station detection capability. The paper also discusses how those methods can be applied to joint magnitude scaling of multiple regional stations. Statistical techniques based on *measurement error modeling* (Fuller 1987) allow us to adjust for the effect of measurement error (uncertainty) in the worldwide m_b measurements of the calibration events.

Detection capability is referred to in terms of the probability of detecting an event as a function of the event magnitude. In an automated monitoring process, this detection probability function has two parameters – the detection threshold and a signal variance. The latter parameter is usually estimated using seismic noise studies (Sereno and Bratt 1989). These noise studies typically ignore the uncertainty in measured magnitudes of the subject events causing the signal variance to be overestimated. Measurement error modeling allows us to account for this uncertainty.

Magnitude scaling involves estimating the station-dependent coefficients in the relationship $m_b = a + b\log(amp) + c\log(dist)$, where *amp* is the frequency-adjusted P-phase amplitude and *dist* is the great circle distance between station and regional event. Calibration data include the m_b measurements whose uncertainty can be taken into account through measurement error modeling. Further, multiple stations can be scaled at the same time in a joint analysis.

Research Accomplished: Station Detection Capability

The *indirect method* of estimating station detection capability is based on the statistical assumption that observed signal-to-noise ratios divided by the detection thresholds are log-Gaussian distributed (Ringdal 1975). A detection is assumed to occur when

$$SNR > th,$$

where th is the automatic detection threshold. If SNR/th is log-Gaussian distributed, then the probability of a detection is

$$P(SNR > th) = P((\log(SNR/th) - \mu)/\sigma) > -\mu/\sigma) = \Phi(\mu/\sigma), \tag{1}$$

where $\Phi(x)$ is the Gaussian cumulative distribution function and μ and σ^2 are the mean and the variance of $\log(SNR/th)$, respectively. Usually, μ is assumed to be a function of the magnitude and location of the event, while σ^2 is assumed to be independent of source of the event (Kelly and Lacoss 1969; Ringdal 1975). Detection thresholds are determined from Equation (1) through inversion. The $p \times 100\%$ detection threshold is the magnitude which satisfies the equation

$$\mu = \sigma\Phi^{-1}(p), \tag{2}$$

where $\Phi^{-1}(x)$ is the inverse Gaussian cumulative distribution function. For example, the 90% detection threshold is the magnitude which satisfies $\mu = 1.28\sigma$.

Sereno and Bratt (1989) modeled μ as a function of range (in km from station to event) and used least-squares to estimate the parameters of this function and to estimate σ^2. A statistical framework for their approach is as follows; adapting their terminology and notation. Let us assume that, for an event with true magnitude m at range r, $\log(SNR/th)$ has a Gaussian distribution with mean

$$\mu = \alpha m + a + b\log(r)$$

and variance σ^2, where a and b are unknown constants and α is chosen such that $\log(SNR/th) - \alpha m$ does not depend on the source. Sereno and Bratt (1989) used a local magnitude measurement M_L as an estimate of the true magnitude of the events. Given a set of n events, they used least-squares to regress the values of $\log(SNR/th) - \alpha M_L$ on $\log(r)$, which provided estimates of a and b. However, the mean squared error (MSE) from this regression (the "regression variance") overestimates σ^2 because of the measurement error in M_L. For example, if we assume M_L is independent of $\log(SNR/th)$ and has a Gaussian distribution with mean m and variance σ_L^2, then the mean and variance of $\log(SNR/th) - \alpha M_L$ is

$$a + b\log(r) \qquad \text{and} \qquad \sigma^2 + \sigma_L^2,$$

respectively. The regression MSE is an estimate of the variance $\sigma^2 + \sigma_L^2$ in this case. If M_L is dependent on $\log(SNR/th)$ (which is more likely than not), then the variance of $\log(SNR/th) - \alpha M_L$ is even more complicated. Instead of M_L, Taylor and Hartse (1995) in a study of detection thresholds at WMQ CSSN station used a worldwide m_b that can be treated as independent of $\log(SNR/th)$. Thus, the mean and variance of $\log(SNR/th) - \alpha m_b$ is

$$a + b\log(r) \qquad \text{and} \qquad \sigma^2 + \sigma_b^2,$$

respectively, where σ_b^2 is the variance of the worldwide m_b. With this statistical framework in place, estimation of detection thresholds and their uncertainties is possible.

Estimation of Detection Thresholds

With the above statistical framework and by Equation (2), the $p \times 100\%$ detection threshold for events at range r, $m(p, r, \alpha)$, is

$$m(p, r, \alpha) = \left(\sigma\Phi^{-1}(p) - a - b\log(r)\right)/\alpha.$$

The detection thresholds are expressed in this way, $m(p, r, \alpha)$, to make explicit their dependence on the level p, the range r, and the value of α. They are estimated by inserting estimates of σ, a, and b:

$$\hat{m}(p, r, \alpha) = \left(\hat{\sigma}\Phi^{-1}(p) - \hat{a} - \hat{b}\log(r)\right)/\alpha. \tag{3}$$

Estimates of a and b are provided by the regression of $\log(SNR/th) - \alpha m_b$ on $\log(r)$. An estimate of σ is

$$\hat{\sigma} = \sqrt{s^2 - \hat{\sigma}_b^2},$$

where s^2 is the regression MSE and $\hat{\sigma}_b^2$ is an estimate of the variance of a worldwide m_b (which is roughly 0.04 magnitude units).

Uncertainty Analysis for Estimates of Detection Thresholds

The uncertainty associated with estimates of detection thresholds $\hat{m}(p, r, \alpha)$ in Equation (3) can be estimated straightforwardly from the variances of $\hat{\sigma}$, $\hat{a}$, and $\hat{b}$.

If we model the uncertainty in the estimate of the variance of the worldwide m_b by assuming that $\hat{\sigma}_b^2$ has a Chi-squared distribution with K degrees of freedom, then the variance of $\hat{\sigma}$ is approximately

$$\frac{1}{\hat{\sigma}^2}\left(\frac{s^4}{(n-1)} + \frac{\hat{\sigma}_b^4}{K}\right).$$

(The larger K is, the more certain one is of σ_b^2.) The variance of the estimate of the $p \times 100\%$ detection threshold can be estimated by

$$\frac{1}{\alpha^2}\left(\frac{1}{\hat{\sigma}^2}\left(\frac{s^4}{(n-1)}+\frac{\hat{\sigma}_b^4}{K}\right)\left(\Phi^{-1}(p)\right)^2+s_a^2+2s_{ab}\log(r)+s_b^2(\log(r))^2\right), \tag{4}$$

where

$$\begin{pmatrix} s_a^2 & s_{ab} \\ s_{ab} & s_b^2 \end{pmatrix} = s^2 \begin{pmatrix} n & \sum_{j=1}^n \log(r_j) \\ \sum_{j=1}^n \log(r_j) & \sum_{j=1}^n (\log(r_j))^2 \end{pmatrix}^{-1}$$

is the covariance matrix of the regression estimates of a and b.

This formulation does not take into account the uncertainty in α. If we treat the uncertainty in α as independent of the data (the values of $\log(SNR/th) - \alpha m_b$) and with variance equal to σ_α^2, then

$$(\hat{m}(p,r,\alpha)\sigma_\alpha/\alpha)^2$$

should be added to the estimated variance in Equation (4) to take into account uncertainty in α.

Approximate confidence limits can be placed on detection threshold estimates $\hat{m}(p,r,\alpha)$ by assuming the Gaussian distribution and using their estimated variance. "Quick-and-dirty" 95% confidence limits are $\hat{m}(p,r,\alpha)$ plus/minus 2 times the standard deviation (the square root of Equation (4)).

Research Accomplished: Regional Magnitude Scaling

CTBT monitoring of events in a new region of interest will require calibration of new (or not previously used) stations. Detection and identification of events in the region may be based entirely on data from these uncalibrated stations. Regional magnitude scaling involves calibrating the amplitudes from the regional stations to the worldwide m_b magnitudes using a model very similar to that of the previous section of this paper. That is, we want to determine the station-dependent values of a, b, and c such that, for each station,

$$a + b\log(A) + c\log(D) \tag{5}$$

is scaled to the worldwide m_b magnitude scale, where A is the frequency-adjusted station amplitude and D is the distance from the station to the event. A regional path effect term could be included if an analysis of the residuals after scaling shows spatial structure. The parameter b is often assumed to be constant across stations. By modeling b as station-dependent, this assumption can be examined.

This section considers the problem of calibrating a set of regional stations to the worldwide m_b magnitude for a large set of events. The statistical approach taken is known as measurement error modeling (Fuller 1987) and is similar to the approach used by Anderson and Nicholson (1993) to determine relative regional magnitude-yield relationships. The approach takes into account the uncertainty (or measurement error) in the m_b values and in the distances (due to location errors). We introduce the statistical model and discuss parameter estimation in the next subsections.

Statistical Model

A number of regional stations can be scaled jointly. It makes sense to do so because the stations observe many of the same events, especially with well-balanced data. The statistical model includes the station-dependent parameter b as presented in Equation (5). Scaling the stations jointly allows us to test whether parameter b is the same for each station and just one value is needed.

We assume that data from n events are available to scale K regional stations whose locations are known. The necessary data fill a table such as Table 1 (shown with five events and three stations). The station amplitude data are modeled as

$$\log(A_{ij}) = (m_i - a_j - c_j\log(d_{ij}))/b_j + \epsilon_{ij}, \quad i = 1,2,\ldots,n, \quad j = 1,2,\ldots,K, \tag{6}$$

Table 1: Regional Magnitude Scaling Data Table: Example

	Station 1 Amplitude	Station 2 Amplitude	Station 3 Amplitude	m_b	Event Location	
Event 1	A_{11}	A_{12}	A_{13}	m_{b1}	LON_1	LAT_1
Event 2	A_{21}	A_{22}	A_{23}	m_{b2}	LON_2	LAT_2
Event 2	A_{31}	A_{32}	A_{33}	m_{b3}	LON_3	LAT_3
Event 4	A_{41}	A_{42}	A_{43}	m_{b4}	LON_4	LAT_4
Event 5	A_{51}	A_{52}	A_{53}	m_{b5}	LON_5	LAT_5

where d_{ij} are the true great circle distances, m_i are the true event magnitudes, and ϵ_{ij} are independent Gaussian random variables with zero means and variances that may depend on the station, σ_j^2.

The observed event locations are modeled as the true locations (lon_i, lat_i) plus independent measurement error,

$$LON_i = lon_i + v_{1i}, \qquad LAT_i = lat_i + v_{2i}, \tag{7}$$

where (v_{1i}, v_{2i}) are independent bivariate Gaussian random variables with zero mean and common covariance Σ_L. The great circle distance (ignoring depth and elevation) between two points on the earth is a well-known function of the longitudes and latitudes of the points. The assumption of unbiased errors in the event locations is questionable. In many regions, systematic errors in location are observed; however, those errors generally are not well understood. Our initial studies show that the errors in the log-distances are nearly negligible compared to the errors in the magnitudes and that reasonable results are achieved by ignoring errors in log-distances.

The worldwide m_b measurements for these n regional events are assumed to be independent of the individual station amplitudes and distances and are direct measurements of the true event magnitudes m_i,

$$m_{bi} = m_i + u_i, \tag{8}$$

where u_i are independent Gaussian random variables with zero mean and common variance σ_b^2.

The unknown parameters a_j, b_j, and c_j are the scaling constants for station j. The true event magnitudes m_i and the event locations are considered *nuisance parameters* in this problem; they must be estimated at the same time as the scaling constants but are of secondary interest. (The nuisance parameters could be viewed as being reestimated during this scaling process, as the magnitudes and locations were already estimated.) For estimation purposes, the variances σ_j^2, σ_b^2, and Σ_L must be known at least up to a constant multiple; that is, we need to know their relative sizes.

Joint Estimation of the Scaling Constants

Assuming the independence and Gaussian distribution of all of the measurement errors in Equations (6-8), the maximum likelihood estimates of the unknown scaling constants a_j, b_j, and c_j, the true event locations (lon_i, lat_i), and the true event magnitudes m_i can be found by least-squares estimation. That is, minimize the weighted sum of squares objective function

$$\frac{1}{2}\sum_{i=1}^{n}\sum_{j=1}^{K}\left(\log(A_{ij}) - (m_i - a_j - c_j \log(d_{ij}))/b_j\right)^2/\sigma_j^2 + \frac{1}{2}\sum_{i=1}^{n}(m_{bi} - m_i)^2/\sigma_b^2 + \tag{9}$$

$$\frac{1}{2}\sum_{i=1}^{n}\begin{pmatrix} LON_i - lon_i \\ LAT_i - lat_i \end{pmatrix}' \Sigma_L^{-1} \begin{pmatrix} LON_i - lon_i \\ LAT_i - lat_i \end{pmatrix}$$

with respect to the model parameters. The three major sums contributing to the objective function correspond to the measurement errors in the log-amplitudes, the worldwide m_b magnitudes, and the event locations, respectively. All three contributions are minimized together. The variances σ_j^2, σ_b^2, and Σ_L serve as the weights.

The weighted sum of squares is a nonlinear function of the parameters and requires an iterative optimization scheme. The possibly large number of parameters may give standard optimization routines trouble, however. Some iterative shortcut, like that used by Anderson and Nicholson (1993), may be needed. The covariance of the estimates can be calculated using the classical maximum likelihood approach (via the Hessian of the likelihood function).

Conclusions and Recommendations

The statistical methods presented in this paper can provide better estimates of detection thresholds and magnitude distance corrections by taking into account the uncertainties in event magnitudes. The author intends to apply the statistical methods to data from the two regions of interest in the DOE CTBT research program – the first region being western China and then the Middle East/North Africa.

Future work will extend the regional detection threshold estimation to include estimation of α by merging the analysis with the multi-station magnitude scaling. We will also incorporate small magnitude biases in the worldwide m_b measurements.

References

Anderson, K. K., and W. L. Nicholson (1993). A relative magnitude model for measurements of Soviet underground nuclear explosions from regional stations, *Bull. Seism. Soc. Am.* **83**, 1563-1573.

DOE (1994), *Comprehensive Test Ban Treaty Research and Development FY95-96 Program Plan*, United States Department of Energy, Washington, D.C., DOE/NN-0003.

Fuller, W. A. (1987). *Measurement Error Models*, John Wiley & Sons, New York.

Kelly, E. J., and R. T. Lacoss (1969). Estimation of seismicity and network detection capability, Technical Note 1969-41, Lincoln Laboratory, MIT, Lexington, Massachusetts. **ESD-TR-69-250, ADA695044**

Ringdal, F. (1975). On the estimation of seismic detection thresholds, *Bull. Seism. Soc. Am.* **65**, 1631-1642.

Sereno, T. J., and S. R. Bratt (1989). Seismic detection capability at NORESS and implications for the detection threshold of a hypothetical network in the Soviet Union, *J. Geophys. Res.* **94**, 10,397-10,414.

Taylor, S.R., and H.E. Hartse (1996), Regional phase detection thresholds at WMQ, Los Alamos National Laboratory, Los Alamos, New Mexico, LAUR-96-395.

SEISMIC SURFACE WAVE ATTENUATION STUDIES IN THE MIDDLE EAST

Lianli Cong, Jiangchuan Ni, and Brian J. Mitchell
Department of Earth and Atmospheric Sciences
Saint Louis University

Contract No. F19628-95-K-0004
Sponsored by DOE

ABSTRACT

Surface wave phase and group velocities, as well as attenuation coefficients, are determined for 12 earthquakes and six station pairs in the Middle East. The velocities, especially group velocities, show very large path-dependent variations at periods shorter than about 25 seconds. The highest Rayleigh wave group velocities at short periods are similar to those in the Basin and Range province of the western United States (~ 2.9 km/s at a period of 10 s) but others, at the same period, are much lower (as low as 2.3 km/s). The highest Rayleigh wave group velocities, at short periods, occur consistently over the path between stations GNI and KIV just west of the Black Sea. These observations suggest either a smaller than normal crustal thickness or higher than normal crustal velocities along that path. Mean attenuation coefficients at periods greater than about 25 s are about 0.4 x 10^{-3} km^{-1}. At shorter periods they increase rapidly with decreasing period to 0.7 x 10^{-3} km^{-1} at 20 s and 1.7 x 10^{-3} km^{-1} at 10 s. These values are about twice as large as mean attenuation coefficient values found earlier for the Basin and Range province.

The large variations in surface wave velocity and attenuation coefficient determinations for different paths in this region and the complexity of many of the surface-wave wave forms suggest than many of our measurements, especially attenuation coefficient measurements, may be affected by complex crustal structure and possibly biased because waves depart from the great circle path between event and station or because of mode conversion. For that reason we have developed a new interactive computer code for determining both dispersion and polarization parameters of seismic surface waves. The program, SPAN (Surface-wave Polarization Analysis), is now complete and will be used to determine the particle motion of the Rayleigh and Love waves that we use in our studies.

Key Words Attenuation, surface waves, Middle East

OBJECTIVE

Our ultimate objective is to derive crustal models of attenuation structure in the Middle East, a region undergoing intense compressional deformation (e.g. Molnar and Tapponnier, 1975; Sengör, 1987). Past studies of seismic wave attenuation have indicated that the efficiency of wave propagation there is poor (Nuttli, 1980; Seber and Mitchell, 1992; Ghalib, 1992; Mitchell et al., 1996). That poor efficiency of propagation is probably due both to high intrinsic attenuation and by a high degree of lateral complexity that scatters seismic energy. In addition, that lateral complexity may further complicate wave propagation by focusing seismic energy in some cases, defocusing it in others, and by causing mode conversion between various Rayleigh and Love modes. This complexity may introduce biases into surface wave dispersion and attenuation measurements making it difficult to model anelasticity as function of depth.

Before using surface-wave data to invert for crustal anelastic structure we need to be sure that it is not contaminated by the effects produced by severe lateral crustal complexity. In order to assure that our data is of sufficient quality we have developed a frequency-time domain code for analyzing the dispersion and polarization properties of surface waves. Measurements of surface-wave polarization will allow us to select only those recordings that are clearly Rayleigh or Love waves arriving along, or close to, great-circle paths.

RESEARCH ACCOMPLISHED

Interstation Determinations of phase velocity, group velocity, and attenuation

We searched for earthquakes near great-circle paths that pass between various pairs of digital broad-band seismograph stations in the Middle East. Twelve earthquakes selected in this way are plotted on the map in Figure 1. Differences between the directions of approach at each station and the great-circle path between stations range between 1.0 and 7.6 degrees, with most deviations being between about 2 and 6 degrees. Of the stations shown in Figure 1, 6 pairs (GNI-ABKT, ABKT-KIV, GNI-ANTO, ANTO-GNI, ANTO-KIV, and GNI-KIV) have, up to now, yielded useful data. Four of the earthquakes occurred beneath the Mediterranean Sea; for that reason paths between the earthquakes cross oceanic-continental margins that may laterally refract the recorded surface waves at one or both stations, causing wave propagation directions to differ from the deviations given in Table 1. In addition, some paths, such as that between ANTO and KIV and between GNI and ABKT cross regions known to be characterized by oceanic crust (in the former case the Black Sea and in the latter the southern Caspian Sea).

Figure 2 presents 12 interstation determinations of Rayleigh wave phase and group velocity. Large variations, especially for group velocities at shorter periods, occur from path to path. At longer periods velocities are similar to those of the Basin and Range province in the western United States (Lin, 1989), another tectonically active region. At periods shorter than about 25 s the fastest group velocities are about 2.9 km/s, values that are again similar to those in the Basin and Range. Several velocities are, however, much lower (as small as 2.2 km/s) than the Basin and Range velocities of Lin (1989). The fastest Rayleigh wave group velocities are those between stations GNI and KIV west of the Black Sea, suggesting that the crust is either thinner or faster than normal in that region.

We assume, after removing effects of wavefront spreading, that the spectral amplitudes (A) of seismic surface waves attenuate as $A(f) \sim e^{-\gamma(f)x}$ where f is frequency, γ is the

attenuation coefficient in km^{-1}, and x is distance in km. The attenuation coefficients determined as a function of period appear in Figure 3. As with velocities the attenuation coefficient values exhibit large variations from path to path. Mean values at periods of 30 s and greater are about 0.4×10^{-3} km^{-1}. At shorter periods they increase rapidly with decreasing period reaching about 0.7×10^{-3} km^{-1} at 20 s and 1.7×10^{-3} km^{-1} at 10 s. These can be compared to the mean interstation values of Lin (1989) for the Basin and Range province, a region of crustal extension (with moderate tectonic activity), where seismic wave attenuation in the upper crust is known to be high (Lin, 1989; Mitchell and Xie, 1994). Attenuation coefficients in the Basin and Range are about 0.3×10^{-3} km^{-1} at periods greater than about 30 s, 0.35×10^{-3} km^{-1} at 20 s, and 0.66×10^{-3} km^{-1} at 10 s.

Attenuation coefficients obtained from interstation measurements in the Middle East are therefore higher at all periods than those determined for the Basin and Range using the same method. Mitchell (1995) has proposed that seismic Q (a quantity proportional to the inverse of attenuation) in any region is proportional to the length of time that has passed since the last episode of major tectonic activity there. For both the Middle East and Basin and Range to conform to that rule they should both be characterized by the same attenuation since both are both currently active. Since attenuation in the Middle East is higher than that in the Basin and Range, another factor, probably the greater intensity of deformation in the Middle East, must be responsible.

A New Tool for Surface Wave Dispersion and Polarization Analysis

The large variations of surface wave velocities and attenuation throughout the Middle East that are apparent in Figures 2 and 3 suggest that our measured values could be significantly biased by deviations from assumed great-circle paths and by scattering due to lateral complexities in the crust and upper mantle. In addition, the wave forms of many of the surface waves that we found sometimes exhibit choppiness and other departures from the smooth character that we find in many other regions. Because of these complexities it will be important to determine the particle motion of the surface waves that we study. We have recently completed coding for a new program to determine surface wave dispersion and polarization as a function of period or frequency. The program SPAN (surface-wave polarization analysis), is a GUI program written for an X-window environment. Dispersion can be determined using single-component records whereas polarization measurements require records of three components of motion. The computational procedures follow Levshin et al. (1992) but our implementation differs from that work by permitting researchers to proceed interactively through the process using results of each step to decide on parameters to be used in the next step. The procedure includes (1) plotting digital time series and displaying a dynamic plot of particle motion within any selected time window , (2) providing a view of the selected trace(s) in which one can select a time window of interest and apply selected window parameters (length of time window and slopes at the ends of the window) as shown in Figure 4, (3) determining the Fourier spectra for the selected portions of all traces, also shown in Figure 4, (4) displaying dispersion, obtained by means of the multiple-filter method, using color shading for various amplitude ranges (See Figure 5 for a gray-scale version), and (5) plotting deviations of particle motion polarization (including inclination, tilt, and slope of the polarization ellipse), again with color shading, from that expected for a plane-layered earth model (Figure 5). For Rayleigh waves ellipticity is also determined. In each step the user controls the process interactively using control panels in the active window.

Results are displayed for each step and can be saved and/or printed at the users discretion. Messages are displayed that prompt the user for the next step and manual instructions are accessible using help buttons. Dispersion curves are presented as contoured

normalized amplitudes on a group velocity-period (or frequency) plot, where the amplitude maxima correspond to group velocities. Phase-equalization and time-variable filtration are used to isolate the desired mode for improved determinations of group or phase velocity.

Our future work will use SPAN to routinely determine particle motion in our surface wave analyses. Surface waves that are found to deviate greatly from a great circle path or exhibit particle motion that does not correspond to expected Rayleigh wave or Love wave motion, perhaps because of mode conversion, will not be used in our modeling of velocity or Q structure in the Middle East.

CONCLUSIONS AND RECOMMENDATIONS

Seismic surface wave attenuation coefficients in the Middle East determined so far indicate that attenuation is unusually high. In addition, lateral complexities in structure produce a large spread in surface wave velocities and attenuation from path to path within that region. Both factors will contribute to difficulty in detecting small nuclear events that are detonated in that region. Work in modeling anelasticity in the Middle East will require selective gleaning of data to make sure that factors such as departures from great circle paths or conversions between modes to not lead to biased results.

Our research suggests that successful nuclear test monitoring in the Middle East will require well-placed stations in sites that are as quiet as possible. Seismic arrays may be required at selected sites to completely understand wave propagation in that region and to detect small events.

REFERENCES

Ghalib, H. Seismic velocity structure and attenuation of the Arabian plate, *Ph.D. dissertation*, 314 pp., Saint Louis University, St. Louis, MO, 1992.

Levshin, A., L. Ratnikova, and J. Berger, Peculiarities of surface-wave propagation across central Eurasia, *Bull. Seism. Soc. Am.*, *82*, 2464-2493, 1992.

Lin, W.J., Rayleigh attenuation in the Basin and Range province, *M.S. thesis*, 55 pp. Saint Louis University, St. Louis, MO, 1989.

Mitchell, B.J., Anelastic structure and evolution of the continental crust and upper mantle from seismic surface wave attenuation, *Rev. Geophys.*, *33*, 441-462, 1995.

Mitchell, B.J., Y. Pan, and J. Xie, The variation of Lg coda Q across Eurasia and its relation to continental evolution, *J. Geophys. Res.*, submitted, 1996.

Molnar, P., and Tapponnier, Cenozoic tectonics of Asia: Effects of a continental collision, *Science*, *189*, 419-426, 1975.

Nuttli, O.W., The excitation and attenuation of seismic crustal phases in Iran, *Bull. Seism. Soc. Am.*, *70*, 469-485, 1980.

Seber, D., and B.J. Mitchell, Attenuation of surface waves across the Arabian peninsula, *Tectonophysics*, *204*, 137-150, 1992.

Sengör, A.M.C., Tectonics of the Tethysides: Orogenic collage development in a collisional setting, in *Ann. Rev. Earth Planet. Sci.*, *15*, 213-244, 1987.

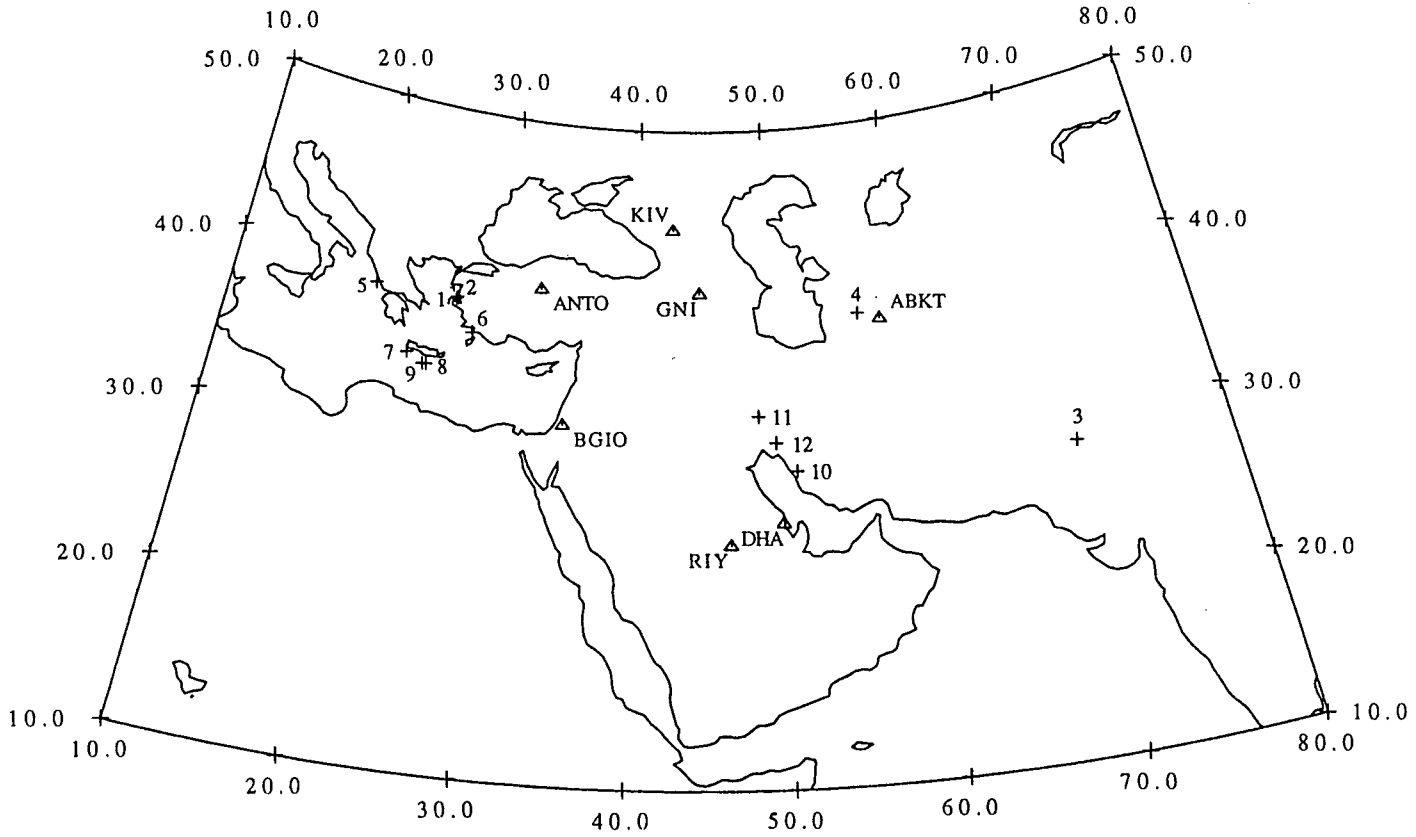

Figure 1. Map of events (+) and stations used for two-station determinations of phase velocity, group velocity, and attenuation in the Middle East.

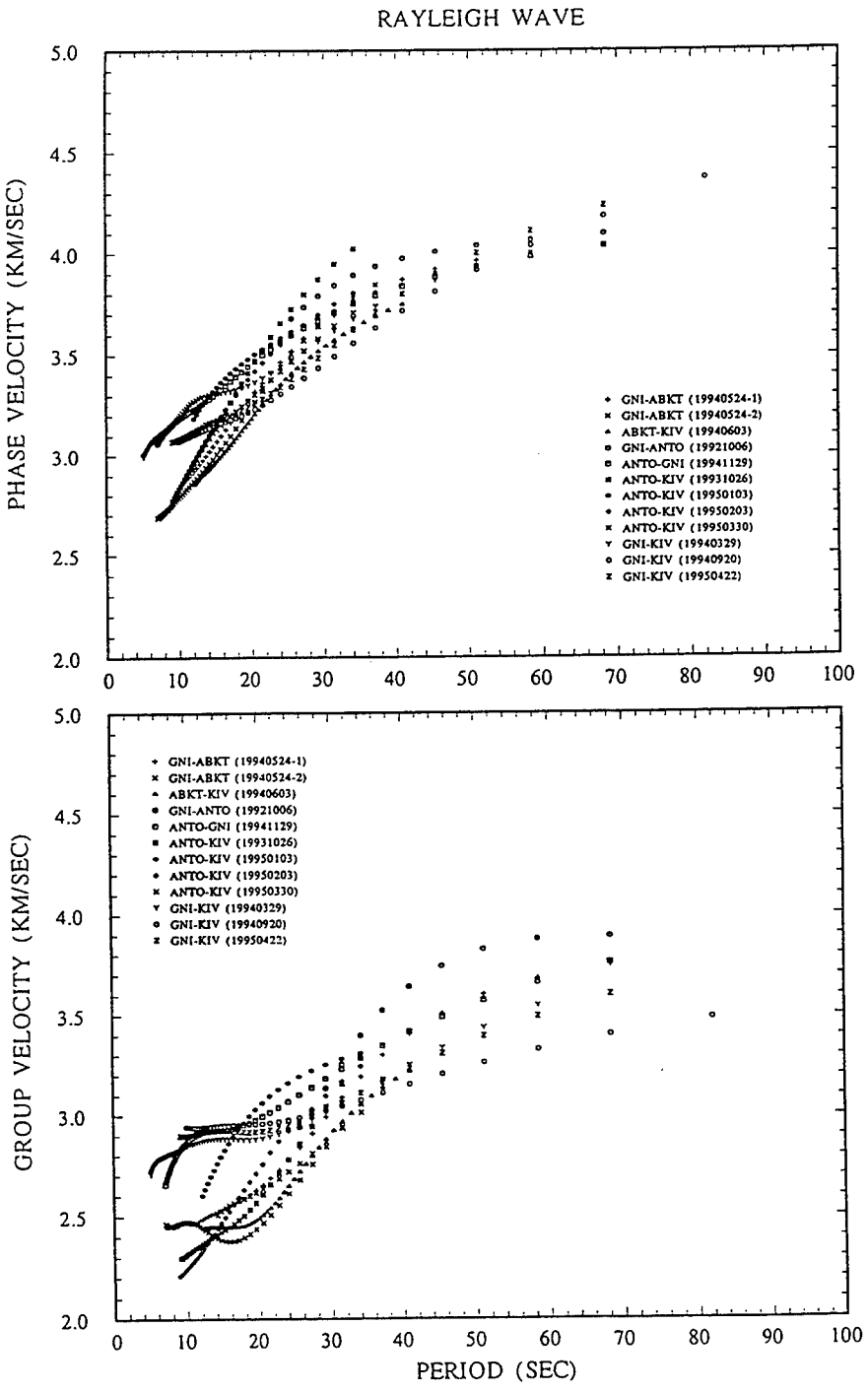

Figure 2. Inter-station phase and group velocities for selected station pairs.

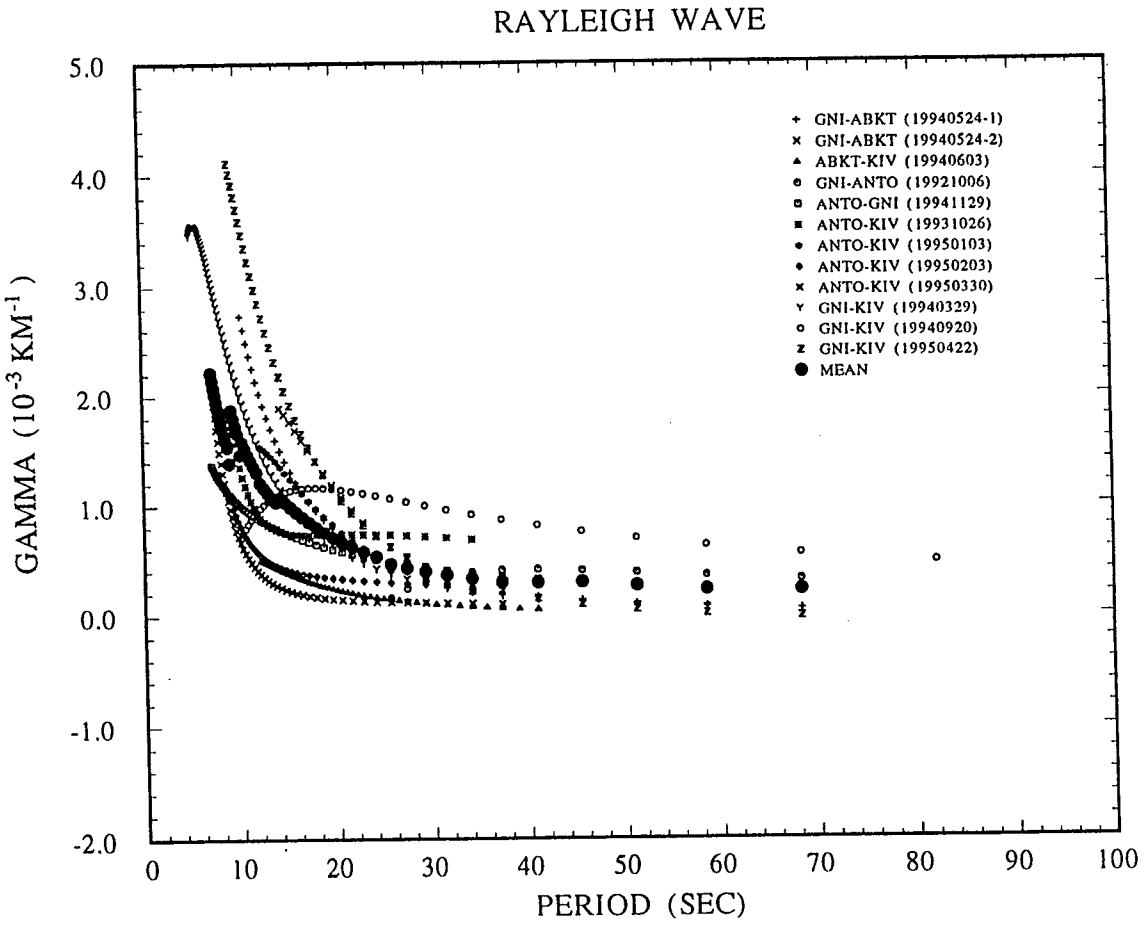

Figure 3. Inter-station attenuation coefficients for selected station pairs.

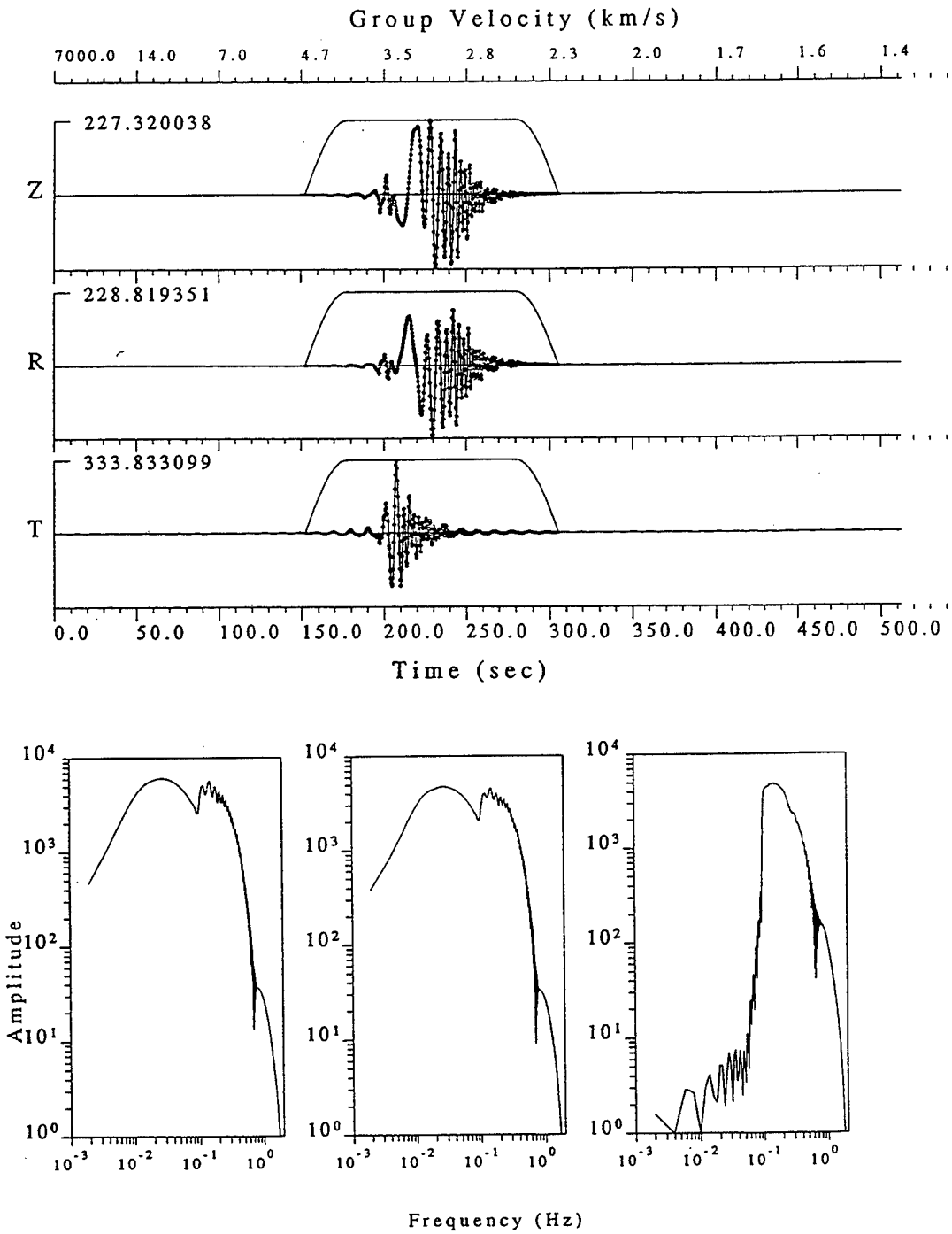

Figure 4. Top - Synthetic seismograms for fundamental and higher modes for a crustal model of the eastern United States. The window delineates the time interval over which amplitude spectra were determined. Bottom - Amplitude spectra computed for the traces above. The three traces and spectra correspond to vertical, radial, and transverse components.

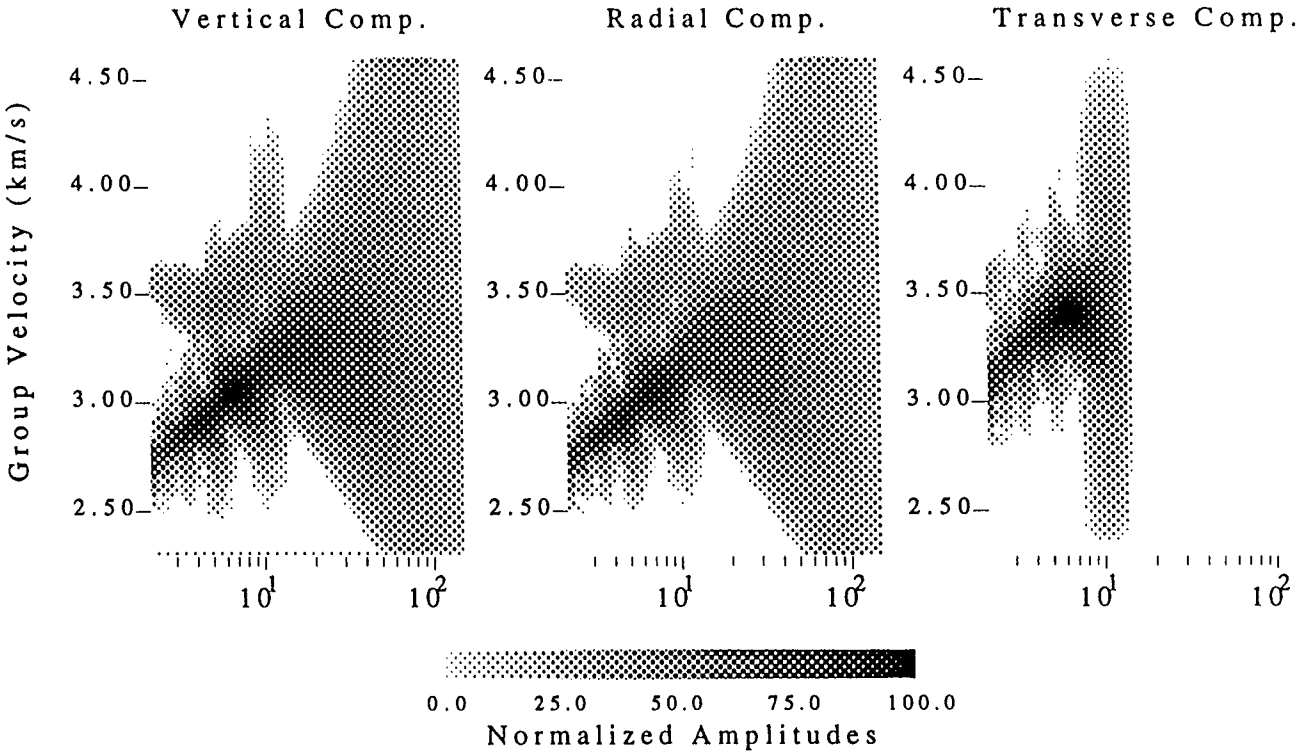

Figure 5. Contoured spectral amplitudes obtained after multiple filter analysis of the synthetic seismograms in Figure 4. The largest amplitudes correspond to the expected group velocities of fundamental-mode waves. Smaller, but still easily visible, amplitudes at group velocities near 3.5 km/s correspond to higher-mode waves.

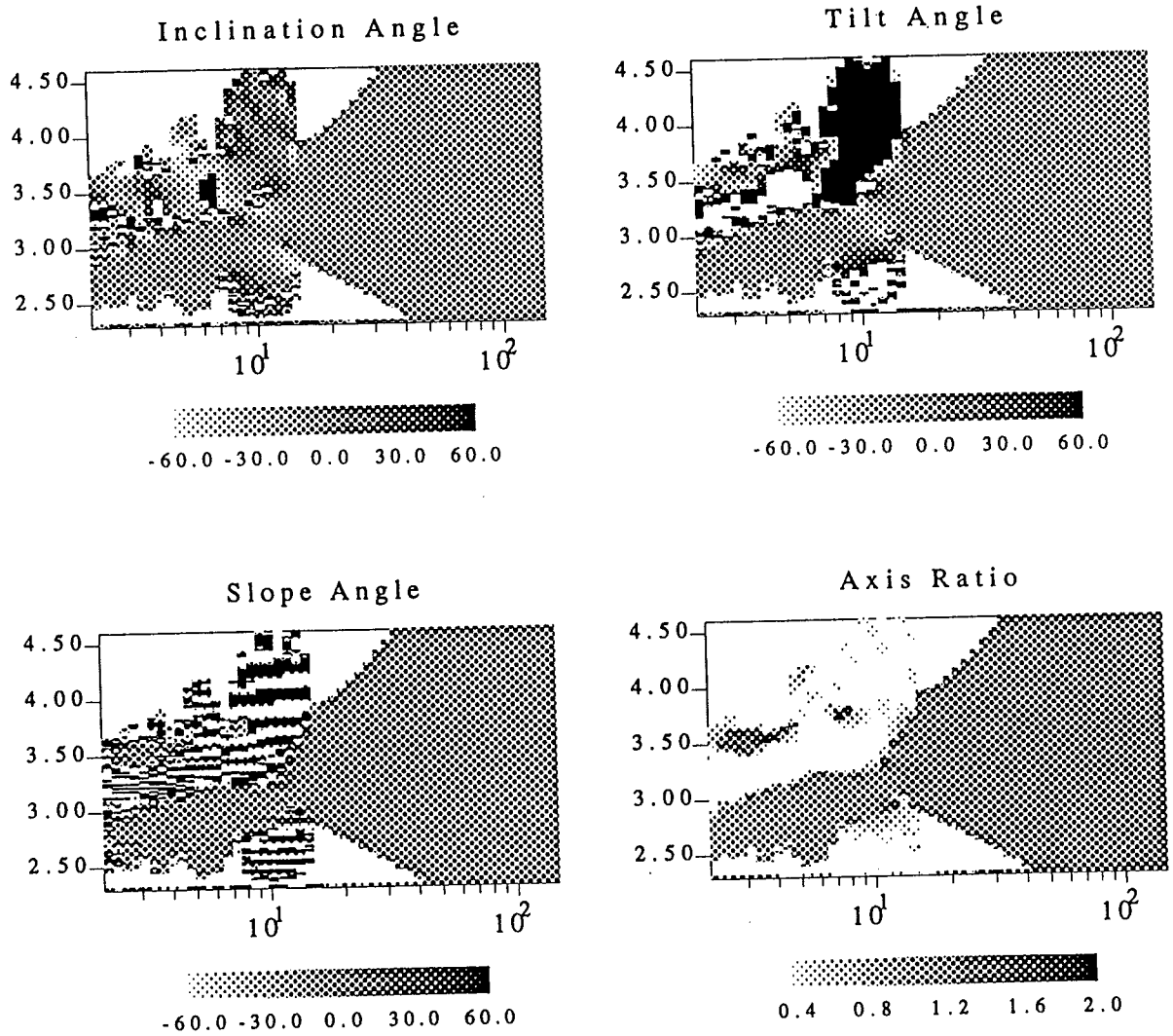

Figure 6. Polarization parameters (inclination angle, tilt angle, and slope angle) and ellipticity for the Rayleigh wave ground motion in Figure 4.

Characterization of Seismic Structure and Wave Propagation within the Tibetan Plateau

H.P. Crotwell, M.R. Powers, T.J. Owens, and G. Zandt†

Department of Geological Sciences, University of South Carolina, Columbia, SC 29208
†Department of Geosciences, University of Arizona, Tucson, AZ

AFOSR Contract No. F49620-94-1-0066
and
AFOSR AASERT Contract No. F49620-94-1-0271

ABSTRACT

Using data from the 1991-92 Tibetan Plateau Seismic Experiment deployment of broadband PASSCAL sensors, we are studying the the seismic structure of the Tibetan Plateau and the effects that this structure has on the propagation of regional seismic waves in Central Asia. Our work focusses on 3 different techniques.

We are using regional events to constrain the crust and upper mantle structure of the Tibetan Plateau. Qualitative results show that the zone of poor Sn propagation within the northern plateau is best explained by negative S velocity gradients within the uppermost mantle rather than simple attenuation. The lack of a similar effect on Pn implies the velocity gradient for P is zero or positive. This leads to a depth varying Poisson's ratio. In addition, we model other events with assumed laterally homogeneous paths to obtain quantitative information on the upper mantle within and external to the poor Sn zone.

We are using teleseismic events to characterize lateral heterogeneity in the average properties of the crust of the Tibetan Plateau. This study has documented that there is approximately 15 to 20 km of crustal thinning in the northern Tibetan Plateau relative to the southern plateau. This thinning is accompanied by an increase in Poisson's ratio, suggesting that the crust of the northern plateau is hot and partially melted.

We are developing a local magnitude scale for moderate size events in the plateau with the eventual goal of assembling a catalog of simple discriminant measures for events within the Tibetan Plateau. Richter's (1958) -log Ao correction for ML underestimates magnitudes at hypocentral distances under 200 km and tends to overestimate magnitudes at distances between 200 km and roughly 350 km to 400 km. The ML:Mo discriminant will be evaluated (and eventually compared to a regional Ms:mb discriminant) after the -log Ao for the Tibetan Plateau is determined through regression analysis.

Keywords: Tibetan Plateau, Crust and Upper Mantle Seismic Structure, ML

OBJECTIVE

One approach to calibrating areas of nonproliferation concern is the use of mobile arrays of new generation, high dynamic range, broadband digital seismic instruments. This project uses existing data to assess the utility of this approach and to develop strategies for using temporary deployments to gather data relevant to seismic monitoring concerns. We focus on regional structure and wave propagation studies of importance to understanding wave propagation in Central Asia using a large scale lithospheric profile (The 1991-92 Tibetan Plateau Broadband Seismic Experiment).

RESEARCH ACCOMPLISHED

Our efforts are broadly divided into the development of regionalized velocity structure constraints for the Tibetan Plateau (Fig. 1) and the development of magnitude scales leading to the cataloging of simple discriminant measures for events within the Tibetan plateau. We will discuss each of these aspects of our work separately.

Regional Waveform Modeling. High-frequency Sn waves do not propagate across the northern Tibetan Plateau, (Ni and Barazangi, 1983). We use broadband regional seismograms recorded during the 1991-92 Tibetan Plateau Seismic Experiment to analyze this phenomena over a much broader frequency band. The long-range goal of this study is to identify one or more causal mechanisms for the observed propagation effect and to constrain the physical state of the upper mantle beneath the Tibetan Plateau.

Previous work has shown that the efficiency of propagation is frequency dependent with longer period energy propagating throughout the entire plateau while higher frequencies are rapidly attenuated in the northern plateau, (McNamara et al., 1995). Also, through a previous modeling effort, we have shown that simple attenuation is not capable of producing the observed rapid loss of higher frequencies within the northern plateau over such short distances. In contrast, negative velocity gradients do seem capable of producing rapid reductions in the amplitude of higher frequency energy. Hence, we focus on gradients in an effort to explain this phenomenon.

North-south upper mantle variations can be illustrated with event 92.095.17.42.50. A recent source mechanism and depth estimation by Zhu and Helmberger (1996) has allowed the modeling of this event. They found this event to be below the crust at about 75 km depth. The location this event relative to our network allows an examination of the effects of propagation into the poor Sn zone on the wave shape. We model this event by modifying the M45 model of Romanowicz (1982) by adding a gradient to the uppermost mantle, between 65 and 100 km depth. The gradient was varied from -.004 km/sec/km to +.004 km/sec/km. Reflectivity synthetics were computed for the earth flattened models and compared with the data. The Pn waveform for stations within and external to the poor Sn zone both favor zero to positive gradients (Fig. 2). The Sn waveform, however, favors zero to positive gradient for station outside of the poor Sn zone, but favors negative gradients for stations within the zone (Fig. 2). The lateral heterogeneities are too great to accurately constrain the magnitude of the required gradient with our reflectivity modeling, but it appears that an S velocity gradient for the uppermost mantle within a -.002 to -.004 km/sec/km range would be sufficient.

In order to avoid the problem of lateral heterogeneity, our current modeling is utilizing other events whose paths are either wholly internal or external to the poor Sn zone. Events with paths external to the zone are relatively abundant. However, event-station pairs within the zone separated by a large enough distance to see Sn and with determined sources are rare. Recent information on lateral variations in crustal structure (Owens and Zandt, 1996; described below) suggests that the search for laterally homogeneous paths will be difficult.

Modeling near-regional seismograms in an uncalibrated area is also complicated by errors in source locations and depths derived from global catalogs. We illustrate this with initial attempts to model event 91.357.01.57.23 to WNDO (Fig. 1). The PDE depth was 33 km and the depth found by Randall et. al. (1995) was 6 km. We attempt to make use of the absolute travel time in our modeling by applying a

correction to the origin time to account for the differences between the crust and upper mantle of the Tibetan Plateau and those of the model used for the PDE location and to correct for the difference in event depth. We recalculate the origin time so that the travel time from 33 km in the PDE model to 100 km depth matched the travel time in a Tibetan Plateau model from 6 km to 104 km depth (adding 4km to account for the plateau elevation). For a vertical ray path the correction to the origin time is about 4 seconds. However, for a ray path with a takeoff angle of 30° (roughly a distance about 30°) the correction is over 5 seconds. Making the assumption that the PDE location was determined by stations within this range of takeoff angles, we choose to make the correction for a takeoff angle of 22°, which gives approximately a median correction. There are many possible flaws in this method, but it should correct the origin time to within roughly ±0.5 seconds. At short, near-regional distances, this error can still limit our ability to accurately resolve path properties.

For now, we are manually aligning the data and synthetics on the P arrival. If a better source location and origin time are found from relocation then this information may also be used. Initial results for event 91.357.01.57.23 to WNDO (a distance of 287km using the PDE location) show an average crustal velocity of 6.1 to 6.2 and thickness of 65 km. From the P minus S time and reasonable Poisson's ratios, the PDE location of this event appears to be in error by at least 13km. For a Poisson's ratio of .26 the S-P time is best fit by a distance of 274 km. This compares with a PDE distance of 287 km, which requires a Poisson's ratio of .23 to match the S-P time. This event has been relocated by McNamara et al (1995) and found to be within 10 km of the PDE location, suggesting that Poisson's ratio for this path is more likely near .26. This contrasts with the bulk crustal Poisson's ratio found by Owens and Zandt (1996) (see below), at WNDO of .29. The discrepancy may be explained by the fact that this event is shallow and so the direct S wave only samples the upper 10 to 15 km whereas the teleseismic S modeling returns bulk crustal properties.

Improvements in event location may prove to be critical for this level of modeling. We will continue to explore corrections to the PDE location as well as relocating the events using data from the portable stations and regional permanent stations. Even in the event that accurate locations are difficult to find there is still a large amount of valuable information that can be discovered from aligning on the first arrival.

Teleseismic Waveform Modeling. Analysis of teleseismic shear-coupled P-waves recorded by the 1991-92 Tibetan Plateau Broadband PASSCAL Experiment has allowed us to identify significant internal variations in both the thickness and average properties within the Tibetan Plateau (Owens and Zandt, 1996). Clear observations of three phases in the S-waveforms allow us to constrain crustal thickness, average P-velocity, and average Poisson's ratio. The phases are: *Sp,* the Moho S-to-P converted phase; *SsPmp,* a post-critical reflection from the Moho; and *SsPmsPmp,* a multiply-reflected converted phase from the Moho. These phases travel distances of 80 to more than 300 km within the crust (Fig. 3) and are thus sensitive to the average properties of the crust along their paths.

Our modeling has focussed on one remarkably simple, deep earthquake recorded by 10 of our 11 sites. Examination of the long-period displacement seismograms immediately indicates the presence of lateral variations in crustal structure within the Tibetan Plateau (Fig. 4). Comparison of some adjacent stations show remarkable long-period similarity for the *Sp* and *SsPmp* phases, and often even for the *SsPmsPmp* phase. Comparing the long-period waveforms indicates similarity of average structure of crust sampled at stations LHSA, SANG, and GANZ. ERDO and BUDO have similar seismograms that are significantly different from the southern sites. Crustal structure differences between these station groups is manifest in the moveout of the *SsPmp* phase (Fig. 4). Relative to the S-wave, *SsPmp* phases have about 4.5s of moveout between BUDO and LHSA when distance effects alone would suggest there should be only about 1s moveout. The relative time between these phases is simply the traveltime of the wide-angle Moho reflection, *Pmp* (Fig. 3). Thus, *Vp* and/or *h* are changing from north to south in

this region. However, the *Sp* phase does not moveout relative to the S-wave. This remarkable observation indicates that any changes in *Vp* and *h* are offset by changes in Poisson's ratio, v. The cummulative effect of this implied variation in crustal properties is illustrated in the observation that the moveout of *SsPmsPmp* relative to *S* between BUDO and LHSA is over 9s while simple distance effects predict less than 3s moveout.

The results of our full reflectivity modeling of these teleseismic waveforms (Randall, 1994) indicate that the average P-velocity of the crust of the Tibetan Plateau is low, ranging from 6.0 to 6.2 km/s. South of the Banggong-Nujiang suture (Fig. 1), Poisson's ratio is at or under the global average of 0.27 and the crustal thickness is over 70 km (Fig. 5). In contrast, the plateau north of the Jinsha suture has a very high Poisson's ratio (0.33) and a much thinner crust (about 55km) (Fig. 5). The central plateau has Poisson's ratio and thickness estimates that are intermediate between the northern and southern values (Fig. 5). There is evidence for a well-developed high-velocity (7.2 km/s) lower crustal layer in the southern plateau. This result and the existence of high *Pn* velocities in the south are consistent with recent models where the Indian crust underlies the southern plateau south of about 32° N. At northern plateau sites, a midcrustal shear wave low velocity zone corresponding to that identified in previous receiver function studies and a strong positive velocity gradient in the lower crust are required to match the waveforms. These observations suggest that the processes responsible for the well-known anomalous upper mantle structure in the northern plateau are also influencing the crust through thinning, heating, and partial melting.

Regional Magnitude and Discriminant Studies. In an effort to evaluate regional source discriminants for the plateau, we are developing a local magnitude scale to use in the ML:Mo discriminant (Woods et al., 1993). Following the similar work such as Bakun and Joyner (1984), Hutton and Boore (1987) and Kanamori et al. (1993), we first evaluate the station-network ML residuals using Richter's -log Ao correction and no station corrections (Richter, 1958; Lay and Wallace, 1995) for 82 regional events (1206 horizontal component records). The records used in the estimates were synthetic Wood-Anderson seismograms generated using SAC.

Ideally, plotting the residuals versus hypocentral distance (to account for depth) should yield data points scattered randomly about the zero residual line. Our plot (Fig. 6) shows that Richter's -log Ao correction tends to underestimate ML at distances less than roughly 200 km and appears to overestimate ML between 200 km and about 400 km. These findings are consistent those of other researchers. Hutton and Boore (1987) found that the Richter -log Ao produced magnitudes that were too low at distances under 50 km and too high at distances greater than 200 km (in southern California). Bakun and Joyner (1984) also noted that the Richter's correction tables underestimated ML for earthquakes closer than about 30 km in central California. We are undertaking more extensive statistical analysis of these data and regression analysis to determine a -log Ao function for the Tibetan Plateau. The analysis will also yield station corrections for the instruments deployed in the 1991-1992 PASSCAL experiment. (See Bakun and Joyner (1984), Hutton and Boore (1987), and Owens et al. (1993).)

As a preliminary measurement of the ML:Mo discriminant, magnitudes were calculated (using Richter's -log Ao) for 38 regional earthquakes that have moment tensor estimates from Randall et al. (1995). The network local magnitude was plotted against log(Mo) for each event. (Fig. 6) Three of these events (+'s in Fig. 6), located near station GANZ, occurred in an area that has been known for earthquakes with Ms:mb ratios similar to explosions (Blandford, 1977; Randall et al., 1995). Randall et al. noted that these events had mb-Mw differences around one magnitude unit. They suggested that complex fault patterns in this part of the plateau may be the cause. Future work will include the development of regional Ms and mb magnitude scales for a direct comparison of the Ms:mb and ML:Mo discriminants.

CONCLUSIONS AND RECOMMENDATIONS

Temporary deployments of broadband instruments is an attractive way to gather information needed to characterize relatively unknown areas. Our results indicate that such a portable networks are useful in estimating the bulk properties of the crust and upper mantle in the Tibetan Plateau. Previous regional travel-time studies from this experiment (McNamara et al, 1995, 1996a, 1996b) have characterized the variability of regional phase propagation throughout a large portion of the plateau. We have used teleseismic SV waveforms to add estimates of the lateral heterogeneity of crustal structure in the east-central plateau that places new constraints on the bulk properties of the crust. We are using regional waveforms to determine local magnitude scales and to assemble estimates of simple discriminants that may be useful in the regional characterization problem. Although perhaps a unusually acute problem in the Tibetan Plateau, we have also demonstrated that the large errors in at least the depths, and probably the epicenter of global locations for events in the region can limit the utility of these locations in attempts to derive structure information from near-regional stations. This suggests that the development of improved analysis methods that can utilize broadband regional waveforms propagating through relatively uncalibrated paths to constrain both the structure and location would enhance our ability to use portable networks to rapid calibrate unknown regions.

REFERENCES

Bakun, W. H. and W. B. Joyner (1984). The ML scale in central California, *Bull. Seism. Soc. Am. 74,* 1827-1843.

Blanford, R. (1977). Discrimination between earthquakes and underground explosions, *Ann. Rev. Earth Sci.,* 5, 111-122.

Hutton, L. K. and D. M. Boore (1987). The ML scale in southern California, *Bull. Seism. Soc. Am.,* 83, 330-346.

Kanamori, H., J. Mori, E. Hauksson, T. H. Heaton, L. K. Hutton, and L. M. Jones (1993). Determination of earthquake energy release and ML using TERRAscope, *Bull. Seism. Soc. Am.,* 83, 330-346.

Lay, T. and T. C. Wallace (1995). Modern Global Seismology, *Academic Press,* San Diego, California, 521pp.

McNamara, D. E., T. J. Owens, and W. R. Walter (1995). Observations of regional phase propagation across the Tibetan Plateau, *J. Geophys. Res.,* 100, 22, 215-22, 229, 1995.

McNamara, D.E., T.J. Owens, and W.R. Walter (1996a). Lg propagation in the Tibetan Plateau, *Bull. Seism. Soc. Am.,* 85, 457-469.

McNamara, D.E., W.R. Walter, T.J. Owens, and C.J. Ammon (1996b). Upper mantle velocity structure beneath the Tibetan Plateau from Pn travel time tomography, *J. Geophys. Res.,* in press.

Ni, J. and M. Barazangi (1983). High frequency seismic wave propagation beneath the Indian shield, Himalayan arc, Tibetan Plateau and surrounding regions: high uppermost mantle velocities and efficient propagation beneath Tibet, *Geophys. J. R. Astr. Soc.,* **72,** 665-689.

Owens, T.J. and G. Zandt (1996). Implications of crustal property variations on models of Tibetan Plateau evolution, *Nature,* submitted.

Owens, T. J., G. E. Randall, F. T. Wu, and R. Zeng (1993). PASSCAL instrument performance during the Tibetan Plateau passive seismic experiment, *Bull. Seism. Soc. Am.,* 83, 1959-1970.

Randall, G.E. (1994). Efficient calculation of complete differential seismograms for laterally homogeneous earth models, *Geophys. J. Int.,* 118, 245-254.

Randall, G.E., C.J. Ammon, and T.J. Owens (1995). Moment-tensor estimation using regional seismograms from portable network deployments, *Geophys. Res. Lett.,* 22, 1665-1668.

Richter, C. F. (1958). Elementary Seismology, *W. H. Freeman and Co.,* San Francisco, California, 578pp.

Romanowicz, B. A. (1993). Constraints on the structure of the Tibet Plateau from pure phase velocity and Q of surface waves, *J. Geophys. Res.,* 87, 6865-6883.

Woods, B. B., S. Kedar, D. V. Helmberger (1993). ML:Mo as a regional seismic discriminant, *Bull. Seism. Soc. Am.,* 83, 1167-1183.

Zhu, L. and D. V. Helmberger (1996). Intermediate depth earthquakes beneath the India-Tibet collision zone, *Geophys. Res. Lett.,* 23, 435-438.

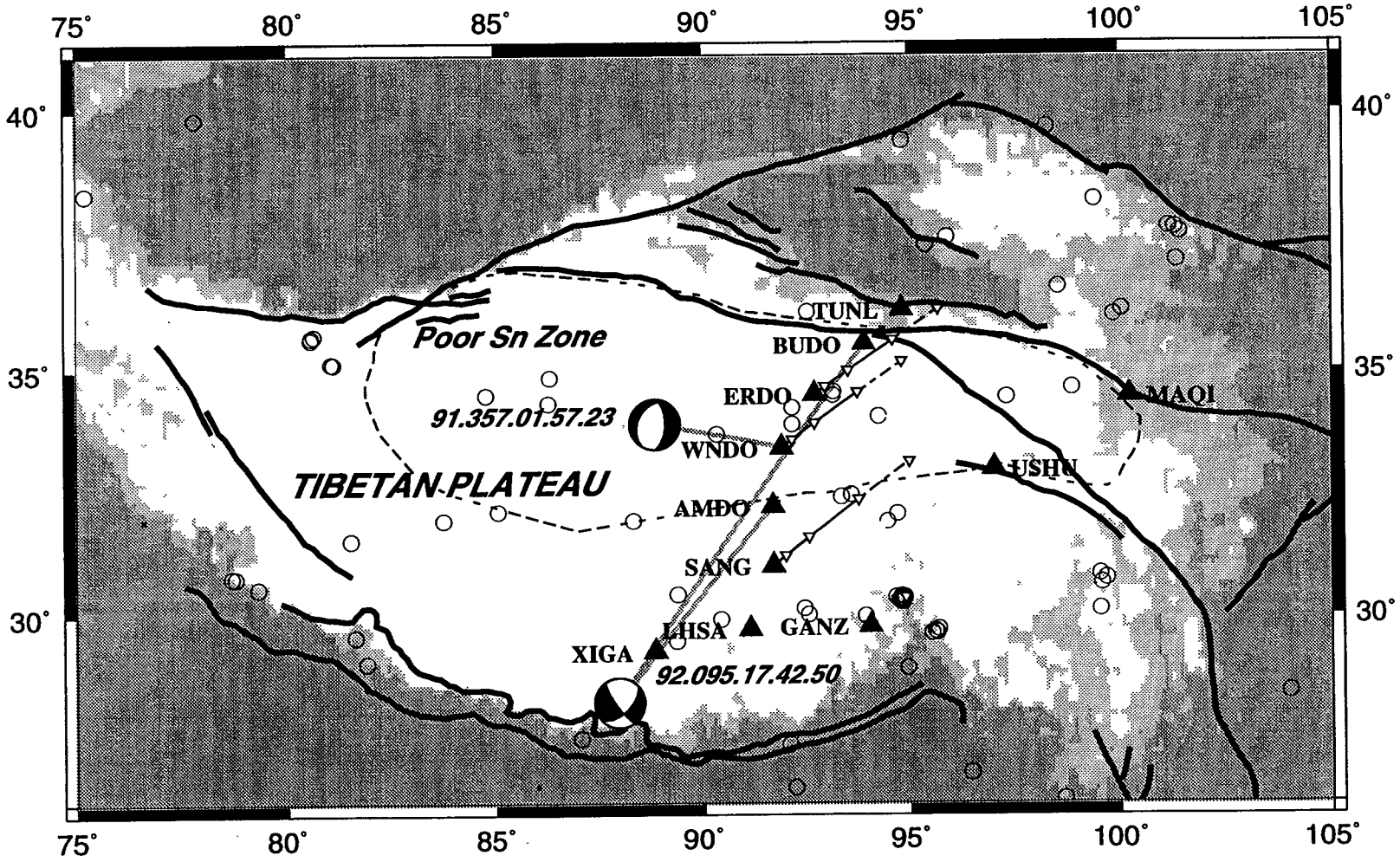

Fig 1. Map of the Tibetan Plateau showing station locations, black triangles; focal mechanisms for modelled regional events, with paths in gray; regional events, open circles; Moho sampling points for shear-coupled P-waves modeled in Fig. 5; and the zone of poor Sn propagation.

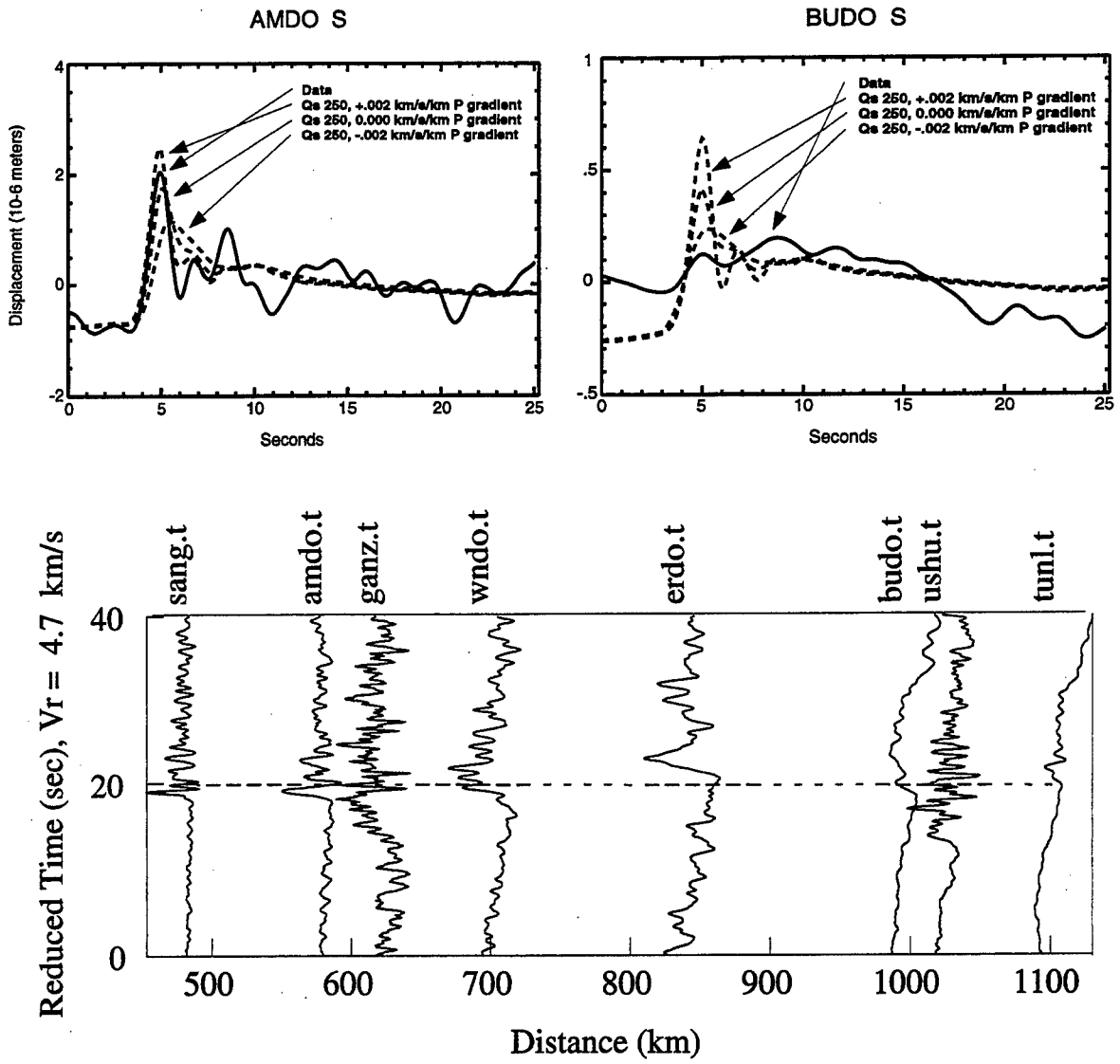

Fig 2 Comparison of three synthetic seismograms with data for the 95.095 event. The synthetics are for an earth flattened M45 model of Romanowicz(1982). The velocities were varied within the mantle lid, the layer between 65 and 100 kilometers depth. Displayed are synthetics for a positive .002 km/sec/km Vp gradient, no gradient and a negative .002 km/sec/km Vp gradient. Within each layer Vp/Vs is 1.73. Each trace is also aligned on the S arrival to make comparisons of the wave shapes easier. In addition, each trace was low pass filtered with corner at .5 Hz.

At AMDO, outside of the anomalous zone, the data favors a positive gradient. However, at BUDO, within the anomalous zone, the data shows a strong tendency toward the negative gradient model. A record section for tangential component displacement seismograms is shown centered around Sn. Note the lack of higher frequencies for the stations within the anomalous zone. Also, BUDO and USHU are at nearly the same distance but BUDO is within the zone while USHU is not.

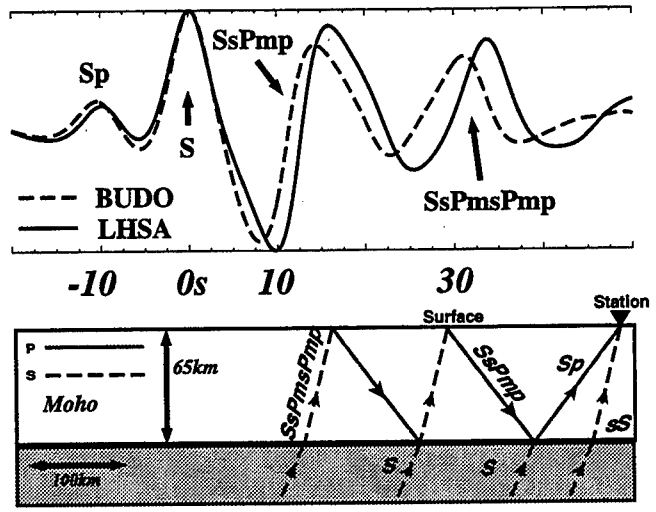

Fig. 3. The bottom frame shows ray paths of shear-coupled P-waves in the crust. Arriving from below, these phases can result in post-critical Moho reflections at distances less than about 50°. The top frame shows 10s low-pass filtered vertical component displacement seismograms for a layer (65km; Vp, 6.4 km/s; υ, 0.27) over a half-space (Vp, 8.05 km/s) for distances appropriate for BUDO (41°; dashed line) and LHSA (46°; solid line).

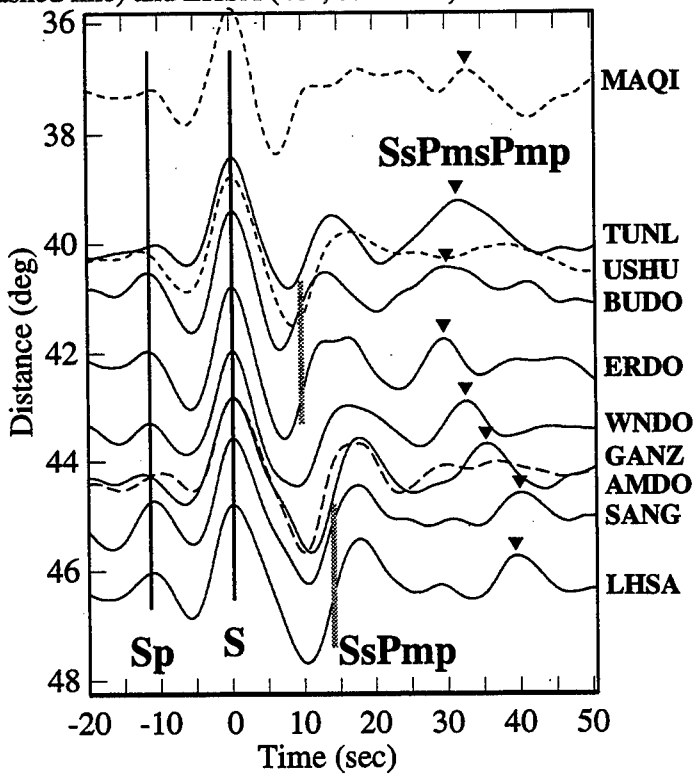

Fig. 4. Long-period Vertical component displacement seismograms for event 92.087.20.33.07. Raw data has been instrument-corrected to displacement and low-pass filtered at 10sec. Each trace has been normalized to the direct S-wave amplitude. Vertical lines mark Sp and S, thick gray lines mark zero-crossings of SsPmp and inverted triangles mark the peak of the SsPmsPmp. Dashed traces for MAQI, USHU, and GANZ indicate they are off the main line.

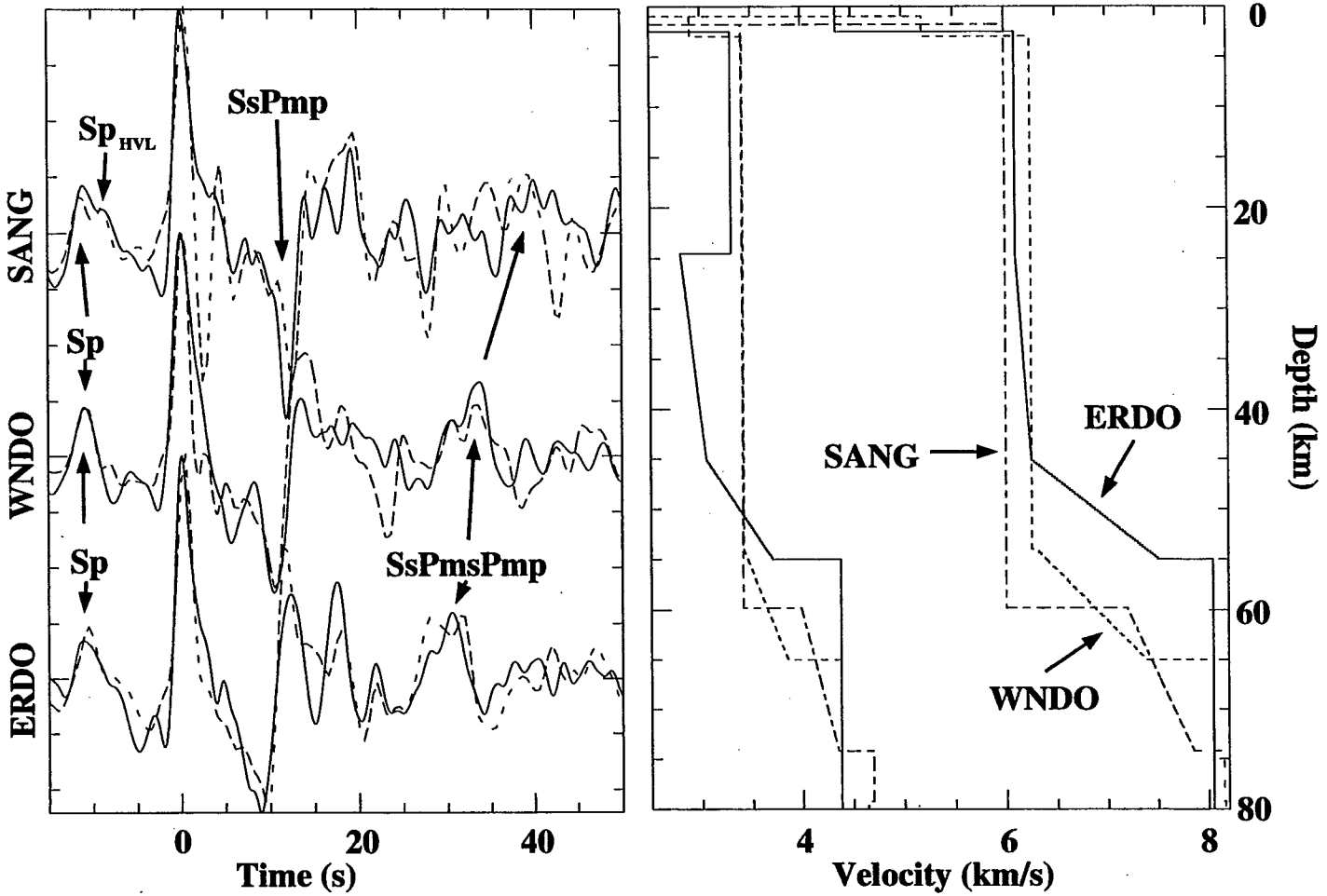

Fig. 5. Synthetic seismogram modeling results for event 92.087.20.33.07 at three sites are shown on the left with derived crustal models on the right. LEFT: Broadband vertical component seismograms (solid lines) are shown with vertical component full reflectivity synthetics (dashed). Our modeling concentrates on matching the timing and amplitude of the three labeled phases. Note the systematic decrease in the S - SsPmp time from south (SANG) to north (ERDO). RIGHT: Derived P- and S-wave velocity models for each site. All sites are characterized by nearly homogeneous P-wave velocity profiles. SANG includes an additional layer at the base of the crust whose sharp upper boundary generates the "Sp[HVL]" arrival shown in the left frame.

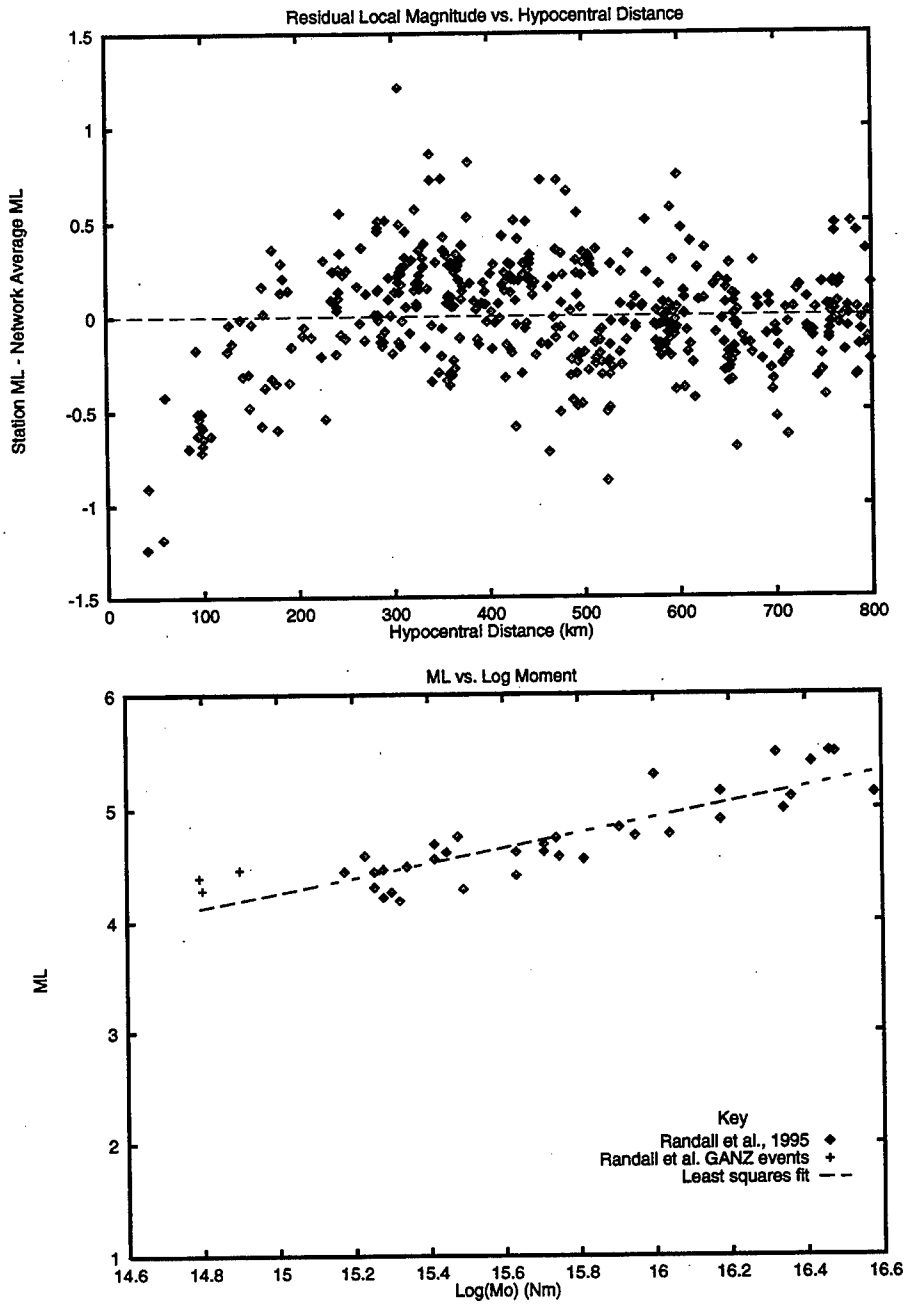

Fig. 6. TOP: Plot of station ML residuals (station ML-network ML) with Richter's -log Ao correction (Richter, 1958; Lay and Wallace, 1995). When applied to regional events recorded on the plateau, Richter's -log Ao underestimates magnitudes at hypocentral distances less than about 200 km and appears to overestimate magnitudes at distances between 200 km and about 350 km to 400 km. BOTTOM: Plot of local magnitude versus log(Mo) for events with moment tensor estimates from Randall et al. (1995). "+"'s denote earthquakes near station GANZ with abnormally high mb-Mw differences. Earthquakes in this part of the plateau often have explosion-like Ms:mb ratios (Blandford, 1977; Randall et al., 1995). The dashed line is a least squares fit: ML = -5.687 + 0.6632log(Mo).

Teleseismic P- and S-wave Attenuation under the Baikal Rift Zone and Adjacent Areas: Method, Measurements, and Interpretation

Paul M. Davis and Shangxing Gao
Department of Earth and Space Sciences, University of California, Los Angeles, CA90095
Contract No. F49620-94-1-0161
Sponsored by AFOSR

ABSTRACT

Teleseismic P- and S-wave attenuation have been measured using the data set that we gathered along a 1280 km profile traversing the Siberian platform, the Baikal rift zone (BRZ), and the Mongolian fold belt. We compared the commonly used spectral ratio method and a common spectrum method for the calculation of relative t^* using synthetic data. The comparison suggests that the common spectrum method is more stable than the spectral ratio method. We used the common spectrum method to calculate δt_p^* and δt_s^* from 37 teleseismic events. It was found that the Baikal rift zone is associated with low Q_s and Q_p, with corresponding δt_p^* of 0.2 s and δt_s^* of 0.8 s relative to the Siberia platform and the Mongolian fold belt. Under the assumption that the mean Q_p is 400 and Q_s is 200 beneath the Siberian platform, we obtain a Q_p of 130 beneath the BRZ, and a Q_s of 60 beneath the BRZ. The best fitting relation between δt_p^* and δt_s^* was found to be $\delta t_s^* = (3.15 \pm 0.18)\delta t_p^* - (0.11 \pm 0.01)$. The difference in δt_p^* and δt_s^* implies that the observed low Q in the BRZ is probably caused by intrinsic attenuation in the upper mantle rather than by scattering.

Keywords: Attenuation, Anisotropy, Baikal, Siberia, Mongolia, Continental Rift Zone, Bayesian Inversion

OBJECTIVES

The objective is to study the propagation of seismic waves in a region of large lateral heterogeneity in seismic velocity, anelasticity, and anisotropy. We used digital data that along with colleagues from the University of Wisconsin (UW), and the Institute of Earth's Crust of Russian Academy of Sciences at Irkutsk (IEC) we collected in field experiments the summers of 91 and 92 in south central Siberia and Mongolia, as well as data digitized from the regional Russian seismic network that operates in that area. Continental rifts lie in regions of some of the largest lateral heterogeneity in velocity and attenuation in the continental crust and mantle. It is therefore important for nuclear monitoring purposes to quantify how seismic waves are affected by such lateral heterogeneities so that estimates of yield and location are accurate, and source type discrimination is reliable.

RESEARCH ACCOMPLISHED

1. Introduction

In previous reports we have presented results from our ongoing study of the Baikal rift zone dealing with P wave attenuation, anisotropy, and P wave tomography (Davis and Gao, 1995). We have found the region is underlain by a low velocity zone extending from the Moho beneath the rift to depths of about 200 km and two to three hundred km wide. At almost every station SKS splitting of about 1 second has been observed with a pattern of fast directions that is variable, but shows some spatial correlation, suggesting a relation to the tectonics (Gao et al., 1994, Davis and Gao, 1995). We have reported P wave attenuation measurements along a 570 km east-west profile of seismic stations crossing lake Baikal which exhibit a relative δt_p^* of 0.1 seconds. In this report we present P wave attenuation estimates along a longer 1280 km NW-SE profile and obtain a larger contrast of 0.2 seconds. We have also calculated S wave attenuation along this profile. Characterizing the seismic properties of such a tectonic zone has relevance to CTBT in that nuclear tests in continental zones of high absorption can disguise yield. Also, explosions detonated in highly anisotropic regions may generate S waves making discrimination from earthquakes more difficult if not recognized.

2. Method: A Bayesian Approach for the Calculation of Seismic Body-wave Attenuation Factors

Most of the seismic wave attenuation studies used spectral ratio method (e.g. Teng, 1968; Solomon and Toksoz, 1970; Der and McElfresh, 1976; Taylor et al., 1986). In this method the ratio of spectra between two stations, station i and the reference station j is used to determine δt_{ij}^*, the relative attenuation factor. The spectral ratio method uses a single reference record to determine δt^*. We have performed synthetic tests that indicate that in the presence of noise the results from this method can be unstable. They are strongly affected by the spectrum of the reference record which, because it appears in the denominator, can cause infinities in the division if there are nulls in the spectrum. Thus the largest values in the fit have the greatest uncertainties and weighted methods

should be applied. The method requires careful choice of parameters such as spectral smoothing window, or where to truncate the spectrum when the signal to noise ratio is low. To overcome such problems, Halderman and Davis (1991) proposed a non-linear inversion procedure, called the "Common Spectrum method" (CS), using the routines in Bevington (1969), which makes use of a gradient search method. The CS method uses all the spectra from an event to simultaneously invert for $t*$, the receiver amplification, and a common spectrum for the event. After the seismograms have been corrected to a standard response, the spectrum recorded by the ith station from the kth event, $A_{ik}(f)$ can be expressed as

$$A_{ik}(f) = C_k(f)R_{ik}(f)\exp(-\pi t^*_{ik} f) \tag{1}$$

where f is frequency, $C_k(f)$ is the common spectrum for the event, and $R_{ik}(f)$ are the near-receiver effects which are assumed to be frequency and source-location independent.

We performed the non-linear inversions using a Bayesian approach (Jackson and Matsu'ura, 1985) to search for t^*_{ik}, R_i, and $C_k(f)$. The Bayesian approach uses some prior information such as the starting parameters and weights the data and prior data according to their *a priori* uncertainties. Data processing parameters include:

a_0 – starting guesses for $C_k(f), R_{ik}$, and t^*_{ik}. We use the mean spectrum over all the records from a given event as the starting guesses for $C_k(f)$; R_{ik} are initially set to 1; and the starting guesses for the t^*_{ik} values are taken as the values found by the spectral ratio method where the reference spectrum is the mean spectrum.

σ_0 – standard deviations of a_0. Together with a_0, the selection of σ_0 is the most important step in Bayesian inversion. It reflects the prior uncertainty of the a_0. A parameter with a larger σ_0 is more likely to be modified during the inversion than the ones with smaller σ_0.

N_{loop} – number of iterations for the inversion. We use $N_{loop} = 150$.

Note that no smoothing is performed; and no reference record is needed. We have conducted extensive tests on synthetic data of different signal to noise ratios and find that the Common Spectrum approach is significantly more accurate than the spectral ratio method and gives robust estimates for signal to noise ratios as low as 1.25 where the spectral ratio method breaks down.

3. Application to Baikal Data

We applied the common spectrum method to P wave and S wave data from Baikal. The stations analyzed were located along a 1280 km long profile traversing the Siberian platform, the BRZ, and the Mongolian fold belt; and in a 300 by 300 km cluster around the southern part of Lake Baikal (Figure 1). All the seismographs were digital and timed by the global Omega clock system. Several types of seismometers were used, most of them were three-component, short period (with free-period 0.5-2 s) sensors. The seismograms were standardized to a uniform response function with free-period 0.5 s, and damping factor 0.707.

Strong teleseismic events with direct P-wave as the first arrival were used. According to the ISC catalog, during the time of the experiment (day 180 and 265, 1992), 48 events with $m_b \geq 5.2$ occurred in the distance range of $35° - 75°$ from station 24, which was located on the southern shore of Lake Baikal. Among the 48 events, 37 are found to have sufficient P-wave signal to noise ratio on at least 10 of the stations to be used for P-wave attenuation studies, and 5 of them are found to be suitable for S-wave studies. The locations of the 37 events are shown in Figure 2. The events can roughly be divided into two groups. Events in the southern group are from a backazimuth range of 130-210°, and those in the northern group are in the range of -30-60°. The number of events in the southern and northern groups is 29 and 8 respectively. Note that all the 5 events with strong S-waves are in the southern group.

The starting values for $C_k(f)$ are taken as the mean spectrum for all the stations from event k. The *a priori* standard deviations were set at about 30% of the peak value. The starting parameters for t^*_{ik} and their standard deviations are taken as those found by the spectral ratio method. All the starting parameters for R_{ik} are taken as 1.0 with $\sigma = 0.5$. The frequency band of 0.1 - 3.0 Hz is used. Most of the energy recorded by the seismometers, which are short period sensors, is in the frequency band of 0.3 to 2.0 Hz for both P- and S-waves. In this frequency band the Q values vary slowly with period (Anderson and Given, 1982). Therefore the assumption of frequency-independent Q is close to reality.

For the calculation of both δt^*_p and δt^*_s, a time window of 12.8 s was taken starting approximately 6 s before the onset of the signal, and was tapered and Fourier transformed. A noise window of the same length was also selected before the signal window and Fourier transformed. The noise spectrum was subtracted from the signal spectrum. We found that the removal is necessary, especially for stations in the Siberian platform where a 2.09 Hz continuous seismic signal has been detected (Gao et al., 1996 in preparation).

To minimize the effects of stations contaminated by noise, a two-step procedure was used. The first step applies the method to all the stations recording a given event. The second step uses stations with misfit (reduced chi squared) smaller than a cutoff value. The misfits were normalized by the amplitude of the common spectrum and therefore a single cutoff value of the misfit is used for all the events, which is 0.05 for P-waves and 0.2 for S-waves. The reason for a larger cutoff value for S-waves is that S-wave data is nosier than P-wave data and if the same cutoff value were used, there would be only a few qualified S-wave measurements. The number of stations rejected after the first step is about 4, out of typically more than 20 stations recording the event.

4. Results and Discussion

The number of measurements for δt^*_p and δt^*_s is 596 and 82, respectively. The mean values at each station and their standard deviations are shown in Figure 3. The solid curves in Figure 3 are obtained by averaging the measurements in a window of 200 km in width and moving at 10 km each step. The peak to peak anomaly of 0.2 s for δt^*_p, and 0.8 s for δt^*_s is observed in the smoothed mean curves. The mean standard deviation for δt^*_p is 0.06± 0.03 s, and for δt^*_s is 0.14±0.08 s. The δt^*_p and δt^*_s anomalies associated with the BRZ are about 6 times the standard deviation. For δt^*_p,

the peak values are located in the area of ±200 km about Lake Baikal, for δt_s^*, the peak is located at -160 km (i.e., to the Northwest). Because all the events for δt_s^* were from the south and with an S-wave angle of incidence of about 35°, the northward shift may indicate that the depth of the center of the low-Q body is located at about 240 km.

Given that most of the lateral variation of shear wave velocities are found in the top 300 km of the Earth (e.g. Woodhouse and Dziewonski, 1984), we assume that the upper-most 300 km of the Earth beneath the array is responsible for the observed δt_p^* and δt_s^*. Under the assumption that the mean Q_p is 400 beneath the Siberian platform, the 0.2 s in δt_p^* results in a Q_p of 130 beneath the BRZ, and the 0.8 s in δt_s^* yields a Q_s of 60 beneath the BRZ if a Q_s of 200 is assumed beneath the Siberian platform.

Figure 4 shows the relation between the smoothed δt_p^* and δt_s^*. The best fitting relation is $\delta t_s^* = (3.15 \pm 0.18)\delta t_p^* - (0.11 \pm 0.01)$. The cross correlation coefficient between the two is 0.83. In comparison, similar measurements between the eastern and western United States have $\delta t_s^*/\delta t_p^*$ ranges from 2.7 to 3.4 (Der et al., 1980). In addition, using short period core phases, Kanamori (1967) found $t_s^*/t_p^* = 3.3$. This ratio indicates that the observed δt^* is the result of difference in purely intrinsic attenuation rather than difference in scattering (Walsh, 1969; Solomon and Toksoz, 1970; Richards and Menke, 1983).

CONCLUSIONS AND RECOMMENDATIONS

Using synthetic data, we tested the common spectrum method using a Bayesian non-linear inversion procedure to calculate relative attenuation factors for P- and S-waves. We found that it is more stable then the spectral ratio method. The common spectrum method was applied to the recordings from 37 teleseismic events recorded by about 60 stations in the Siberia, Lake Baikal, and Mongolia areas in the summer of 1992. The Baikal rift zone was found to be associated with a t^* of 0.2 s for P-waves and 0.8 s for S-waves relative to the Siberian platform. The best fitting relation between the smoothed δt_p^* and δt_s^* is $\delta t_s^* = (3.15 \pm 0.18)\delta t_p^* - (0.11 \pm 0.01)$. The cross correlation coefficient between the two is 0.83. This difference indicates that the observed δt^* is the result of difference in purely intrinsic attenuation rather than difference in scattering. The seismologic contrast between the Baikal rift zone and the Siberian craton is in many regards similar to that between the Basin and Range rift province and east North America.

REFERENCES

Anderson, D. L., and J. W. Given, Absorption band Q model for the Earth, *J. Geophys. Res.*, *87*, 3893-3904, 1982.

Bevington, P. R., *Data Reduction and Error Analysis for the Physical Sciences*, pp 237-239, McGraw-Hill, New York, 1969.

Davis, P.M., and S. Gao, Seismic Propagation in the Baikal Rift Zone: A Transition from a Craton to an Orogenic Zone, in *Proceedings of the 17 Annual Seismic Research Symposium on Monitoring a comprehensive Test Ban Treaty, 12-15 September, 1995*, PL-TR-95-2108,

editors James F. Lewkowicz, Jeanne M. McPhetres, and Delaine T. Reiter, pp. 99-110, 1995.

Der, Z. A., and T. W. McElfresh, The effect of attenuation on the spectra of P waves from nuclear explosions in North America, SDAC-TR-76-7, Teledyne Geotech, Alexandria, Virginia, 1976.

Der, Z. A., E. Smart, and A. Chaplin, Short-period S-wave attenuation under the United States, *Bull. Seismo. Soc. Ame., 70,* 101-125, 1980.

Gao, S., P. M. Davis, H. Liu, P. D. Slack, Yu. A. Zorin, V. V. Mordvinova, V. M. Kozhevnikov, and R. P. Meyer, Seismic Anisotropy and Mantle Flow beneath the Baikal Rift Zone, *Nature, 371,* 149-151, 1994.

Gao, S., P. M. Davis, and Yu. A. Zorin, A continuous 2.09 Hz seismic signal detected by a portable seismic network in Siberia and Mongolia, *In preparation,* 1996.

Halderman, T. P., and P. M. Davis, Q_p beneath the Rio Grande and east African rift zones, *J. Geophys. Res., 96,* 10,113-10,128, 1991.

Jackson, D. D., and M. Matsu'ura, A Bayesian approach to nonlinear inversion, *J. Geophys. Res., 90,* 581-591, 1985.

Kanamori, H., Spectrum of short-period phases in relation to attenuation in the mantle, *J. Geophys. Res., 72,* 2181-2186, 1967.

Richards, P. G., and W. Menke, The apparent attenuation of a scattering medium, *Bull. Seismol. Soc. Am., 73,* 1005-1021, 1983.

Solomon, S.C., and M.N. Toksoz, Lateral variation of attenuation of P and S waves beneath the United States, *Bull. Seismol. Soc. Am., 60,* 819-838, 1970.

Teng, T.L., Attenuation of body waves and the Q Structure of the mantle, *J. Geophys. Res., 73,* 2195-2208, 1968.

Walsh, J. B., New analysis of attenuation in partially melted rock, *J. Geophys. Res., 74,* 4333-4337, 1969

Woodhouse, J. H., and A. M. Dziewonski, Mapping the upper mantle: Three-dimensional modeling of earth structure by inversion of seismic waveforms, *J. Geophys. Res., 89,* 5953-5986, 1984.

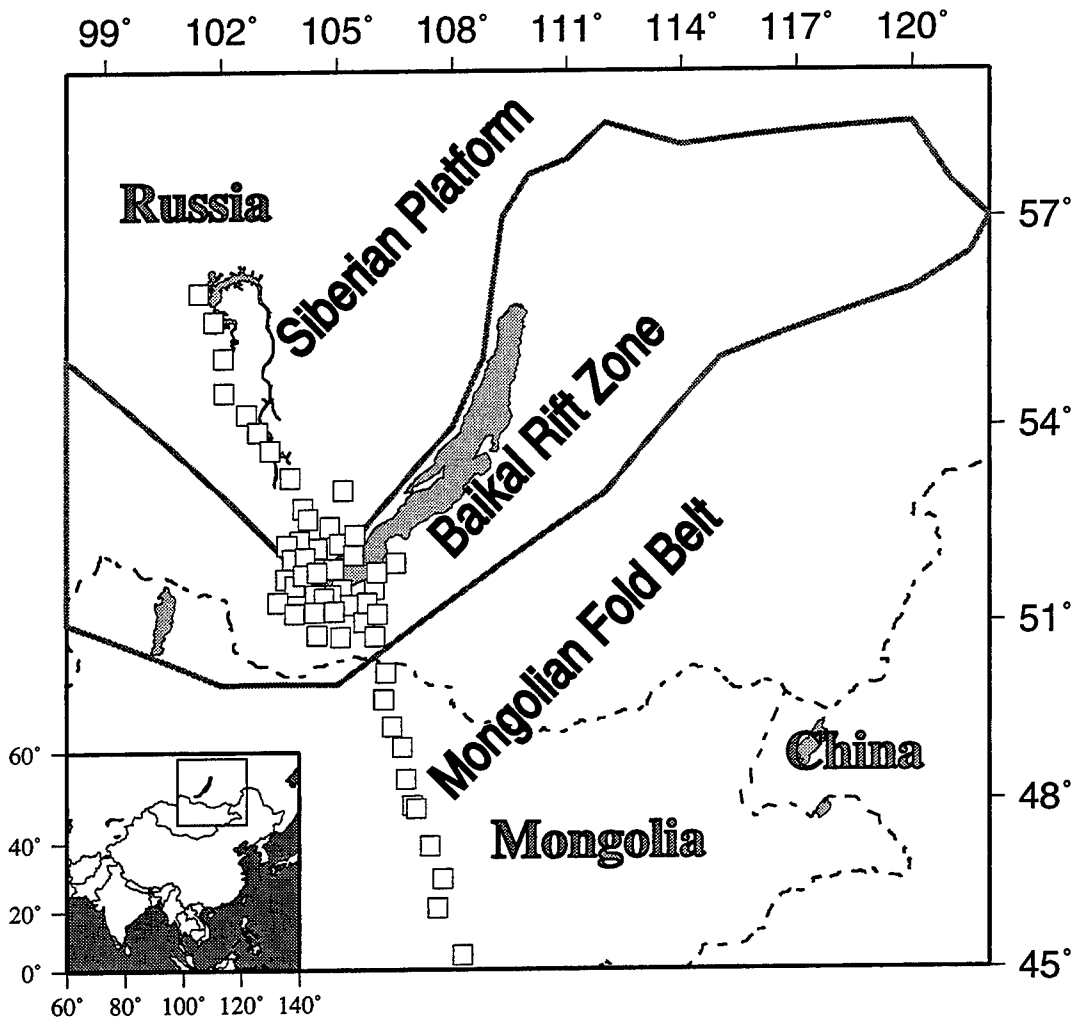

Figure 1: A Mercator projection map showing locations of stations. The lower-left inset shows coast lines and national borders of Asia and the location of the study area.

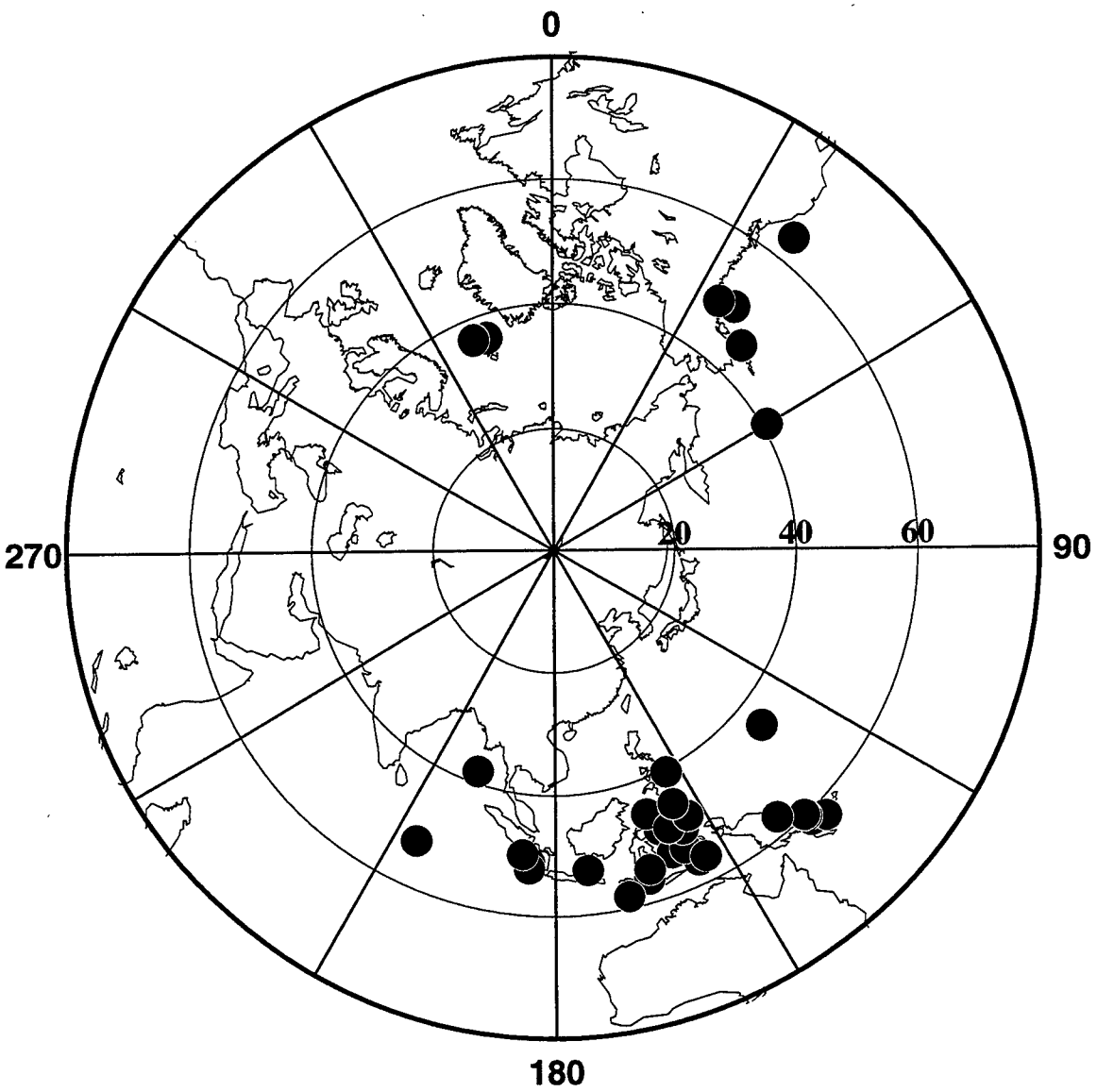

Figure 2: An azimuthal equidistant projection map showing epicenters of events, and their back-azimuths and epicentral distances to the array. The center of the map is station 24, which was on the southern shore of the Lake. The four circles represent $20°, 40°, 60°$, and $80°$ epicentral distances.

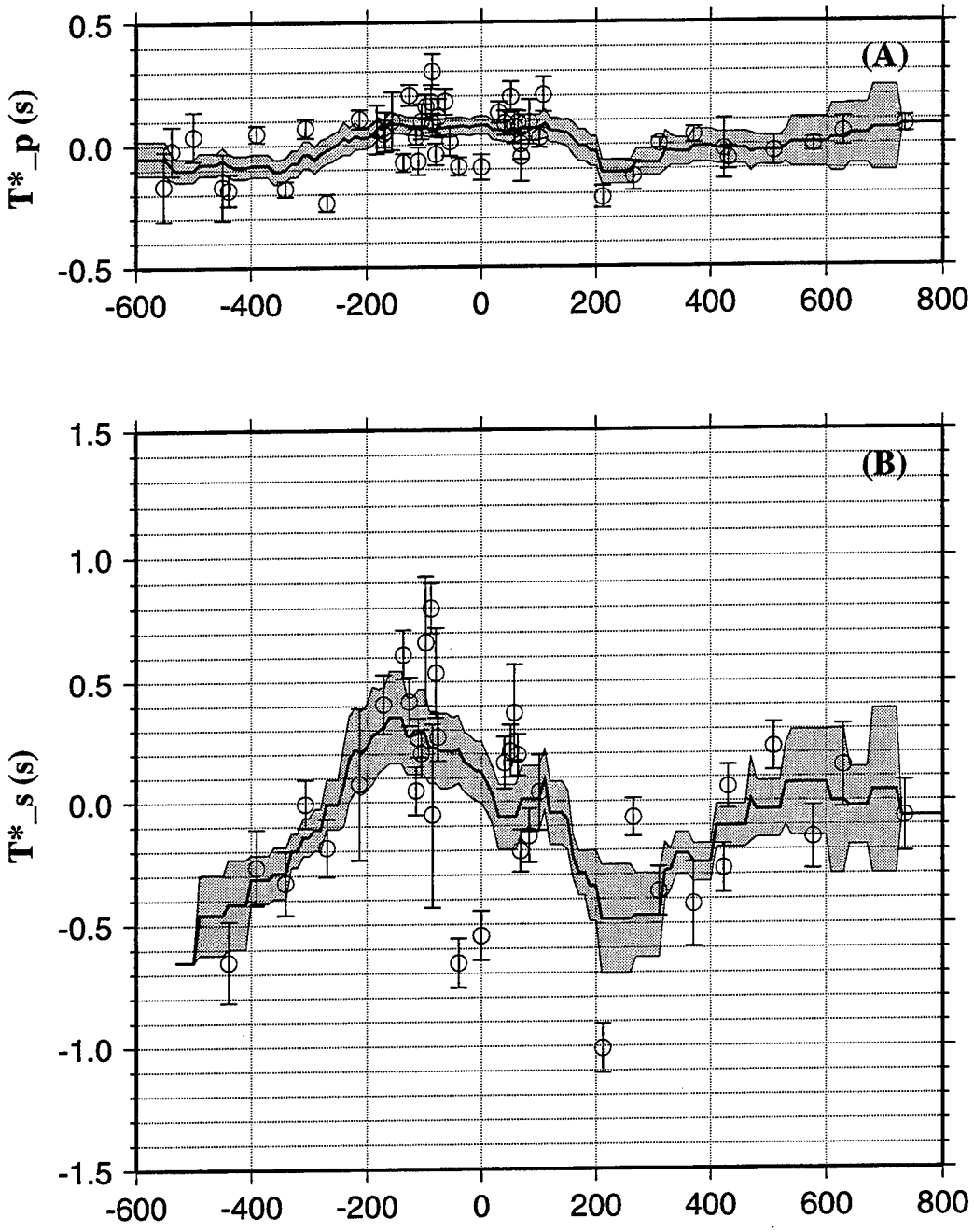

Figure 3: Results of δt^* measurements. The dots are averaged values over all the events for δt_p^* (Figure A) and δt_s^* (Figure B), and the solid lines are the results of spatial averaging in windows of 200 km wide, moving at steps of 10 km. The thickness of the shaded area is 2 times the standard error of the mean.

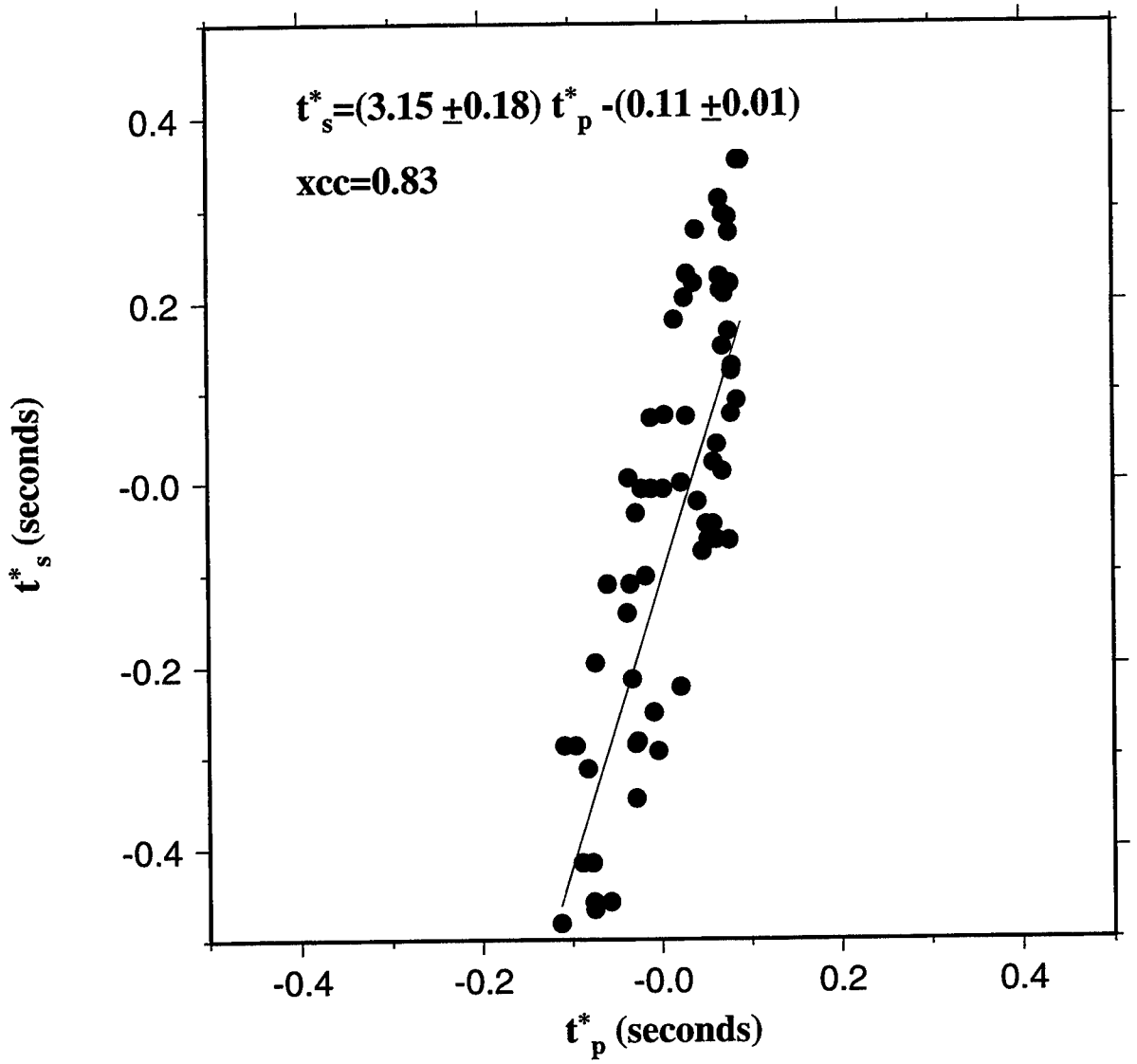

Figure 4: Relations between δt_p^* and δt_s^*. Note that the values used are from spatial averaging of the mean values (the solid curves in Figure 3). The best fitting line and the cross correlation coefficient are shown in the figure.

Development of a Lithospheric Model and Geophysical Data Base for North Africa

Diane I. Doser, G. Randy Keller, Kate C. Miller, and Steven Harder, Department of Geological Sciences, University of Texas at El Paso, El Paso, TX 79968-0555

Contract Number F19628-95-C-0104

Sponsored by DOE

ABSTRACT:

We have collected seismic, geologic, gravity and other potential field data to develop a model of the North African lithosphere via an integrated approach. We are currently modeling the gravity data along three transects across North Africa: 1) from north central Egypt across Libya to the Hoggar Uplift, 2) from central Tunisia across northern Algeria to the Atlantic coast of Morocco, 3) from north central Algeria across the Hoggar Uplift to northern Chad. These transects represent the major propagation paths between earthquakes and nuclear explosions and seismograph stations located within North Africa. The gravity models are constrained wherever possible by geologic and other geophysical information. Crustal thicknesses we have obtained for the Hoggar Uplift (38 km) agree well with preliminary results of seismological studies by other research groups. Our modeling results also suggest that the mantle anomaly under the Hoggar Uplift is relatively small (200-300 km wide, less than 60 km in vertical extent) compared to mantle anomalies associated with other hot spots and rift zones. We used these results as the basis on which to construct a preliminary map of crustal thickness. In most places away from the continental margin, the crust is about 40 km thick. Crustal thinning is associated with the Sirt Basin and the West and Central African rift system. Moderate crustal thickening is associated with the Atlas Mountains. In addition to our gravity studies, we have nearly completed collection of seismograms from Worldwide Standardized Seismograph Network (WWSSN) stations located at regional distances for magnitude > 5.0 earthquakes occurring within North Africa (between 1963 and 1988) and their associated aftershocks. We have selected these earthquake sequences for study since the mainshocks often have known focal mechanisms determined from teleseismic waveform or first motion studies and produced numerous aftershocks of varying magnitude. Using the lithospheric models obtained from the gravity modeling as first approximations of the velocity structure we will model the regional waveforms of these earthquake sequences. We have also collected delay time, travel time, and magnitude information for these sequences for further analysis.

key words: geophysical data base, North African lithosphere, gravity models, seismograms at regional distances

OBJECTIVE:

We will develop a model of North African lithosphere via an integrated analysis of seismic, potential field, and geologic data. In particular, we will construct detailed 2-D models from known earthquake source regions to key seismic monitoring stations in the region. An outgrowth of this effort will be a data base of geological and geophysical information which will be made available to the scientific community through electronic access.

RESEARCH ACCOMPLISHED:

A first step in our study of North African lithosphere was the collection of pertinent geological and geophysical information for our data base. We have digitized the locations of numerous geological features within the region including surface exposures of Precambrian rocks in the major uplifts (Hoggar, Tibesti, and Darfur), depth to Paleozoic and Mesozoic basement within the Sirt Basin of Libya, surface faults within the Sirt Basin, the location of Pan-African suture zones and Cretaceous and Cenozoic age rifts, and the boundaries of west and central African rift basins.

We have collected numerous geophysical data sets, one of the most important being gravity data between 0° and 37°N and 12°W and 40°E. These data were obtained in the form of a 5'x5' Bouguer anomaly grid from GETECH, which is associated with Leeds University. We are only free to use these data in the form of maps which are contoured at intervals of 10 mGal or greater. Gravity station locations were also provided, and the station elevations were used by GETECH to correct errors in ETOPO5. These data were merged with existing gravity data archived at UTEP, including an extensive set of gravity data for the Libya region. Figure 1 shows a Bouguer gravity map of Northern Africa generated from our existing database.

Once we had merged the GETECH data into our existing database, we selected three profiles across the region to model. These profiles represent important propagation paths between earthquakes and seismograph stations located within North Africa. Profile 1 extends from central Egypt, the site of several recent earthquakes and seismograph stations (such as HLW), across central Libya, where we have good geological and geophysical control on crustal structure (e.g. Suleiman, 1993; Nyblade et al., 1996), to the Hoggar Uplift of southern Algeria (site of station TAM, Tamanrasset, and several French nuclear tests in the early 1960's). Profile 2 extends across the Atlas Mountains from the Atlantic coast of Morocco to central Tunisia. Seismograph stations are located along this profile in Morocco, Algeria and Tunisia, and earthquakes occur throughout the region. Profile 3 extends from north central Algeria across the Atlas Mountains to the Hoggar uplift. This profile is along the propagation path between northern Algerian earthquakes and TAM. A preliminary velocity model has been obtained by McNamara et al. (1996) from regional seismograms whose waves propagate along paths that parallel Profile 3.

The preliminary density model we have obtained for Profile 1 is shown in Figure 2. The upper part of our model reflects the basin structure of Egypt, Libya and Algeria obtained from published geological and geophysical studies of these basins (e.g. Goudarzi, 1980; van der Meer and Cloetingh, 1993; Guirard and Maurin, 1992; Exxon, 1985), primarily related to their petroleum potential. Since our knowledge of the upper crust below the sedimentary basins and the lower crust is poor, we have treated these units as having uniform densities. We varied thicknesses of these units only as required to match the long wavelength features of the observed gravity data. Note that we have not attempted to match every short wavelength feature of the profile, since our knowledge of the shallow geology is incomplete. The shallow geology also should influence regional waveform propagation less than the deeper crustal structure.

Profile 1 shows a relatively uniform boundary between the upper and lower crust. There is a gradual shallowing of the crust/mantle boundary between the Hoggar Uplift (38 km) and the Egyptian coast of the Mediterranean (26 km) (Sweeney, 1995). A similar eastward shallowing of the crust/mantle boundary is observed in northern Libya (Suleiman, 1993). The crustal thickness of the Hoggar Uplift is in good agreement with the velocity model of McNamara et al. (1996) and recent receiver function studies at TAM (E. Sandoval, pers. comm., 1996).

Figure 3 shows a preliminary interpretation of Profile 3. The shallow upper crustal structure is constrained from knowledge of basin geometries and thicknesses (e.g. Schurmann, 1974; UNESCO, 1971; Lesquer et al., 1988). The Moho depth at the northern end of the profile is constrained by the results of the European Geotraverse (Ansorge et al., 1992). The crust appears to rapidly thicken beneath the Atlas Mountains, then gradually thicken to the south. A major target for effort in the near future will be to determine if the gravity low associated with the Atlas Mountains is due to a crustal root (like the Andes) or is due density variations in the crust and/or upper mantle (like the Sierra Nevada) as presently shown. Although we have not included a crustal root in our current model, one is probably present to the west of where our profile crosses the range because the negative gravity anomaly is considerably more intense. Again, the Hoggar Uplift can be modeled with a 38 km thick crust. A gravity low over the uplift suggests the presence of an upper mantle anomaly with width of 200 to 300 km and depth of 40 to 60 km. This is much smaller than observed under the Ethiopian and Kenya domes. This suggests that whatever hot spot activity is associated with this uplift has had a small effect on the lithosphere.

Figure 4 shows a preliminary map of crustal thickness based on the Bouguer gravity data. Note that the crust is generally 40 km thick away from the continental margins. There is a moderate amount of crustal thickening associated with the Atlas Mountains. Crustal thinning is associated with the Sirt Basin and the West and Central African rift system.

In related efforts, we are completing collection of seismograms from WWSSN stations located at regional distances from earthquake sequences occurring in North Africa between 1963 and 1988 (Figure 5). These sequences consist of magnitude > 5.0 mainshocks, many of which have focal mechanisms determined from teleseismic waveform modeling or first motion studies. The sequences produced numerous aftershocks of varying magnitude and we are collecting data for all events above magnitude 3.5. We have begun digitization of waveforms for the earthquakes and then will model the waveforms to validate and update the preliminary lithospheric models obtained from the gravity data. We have also collected delay time, travel time, and magnitude information from these sequences for further analysis.

CONCLUSIONS AND RECOMMENDATIONS:

We are continuing our modeling of gravity Profile 2 along the Atlas Mountains. Further 2-D filtering and analysis of the gravity data set is also planned. Modeling of regional seismic phases will continue throughout the next year. We will analyze the variations in travel times and magnitude estimates for the earthquake sequences of interest. Our final results will be a geophysical and geological data base for North Africa that will be easily accessible to the scientific community and a series of "best" lithospheric models for regions of North Africa that have been validated through waveform modeling of regional seismic phases.

REFERENCES:

Ansorge, J., D. Blundell, and St. Mueller, 1992. Europe's lithosphere-seismic structure, in A Continent Revealed: The European Geotraverse, D. Blundell, R. Freeman and St. Mueller (eds.), Cambridge University Press, 33-69.

Exxon Basin Analysis Section, 1985. Tectonic Map of the World, 1:10,000,000.

Goudarzi, G. H., 1980. Structure-Libya, in The Geology of Libya, Volume III, 879-892.

Guirard, R. and J.-C. Maurin, 1992. Early Cretaceous rifts of western and central Africa: an overview, in P.A. Ziegler (ed.), Geodynamics of Rifting, Volume II, Case History Studies on Rifts: North and South America and Africa, Tectonophysics 212, 153-168.

Lesquer, A., A. Bourmatte, and J. M. Dantria, 1988. Deep structure of the Hoggar domal uplift (central Sahara, south Algeria) from gravity, thermal and petrological data, Tectonophysics, 152, 71-87.

McNamara, D. E., W.R. Walter, C. Schultz and G. Goldstein, 1996. Regional phase propagation in Northern Africa and the Mediterranean (abstract), Seismol. Res. Lett. 67, 47.

Nyblade, A.A., I.S. Suleiman, R. Roy, B. Pursell, A.S. Suleiman, D.I. Doser, and G.R. Keller, 1996, Terrestrial heat flow in the Sirt Basin, Libya, in press, J. Geophys. Res.

Schurmann, H.M.E., 1974, The Precambrian in North Africa, E.J. Brill, Leiden, The Netherlands, 351 pp.

Suleiman, A.S., 1993. Geophysics of the rifts associated with the Sirt Basin (North Africa) and the Anadarko Basin (North America), Ph.D. Dissertation, The University of Texas at El Paso, 150 pp.

Sweeney, J.J., 1995. Preliminary maps of crustal thickness and regional seismic phases for the Middle East and North Africa, Lawrence Livermore Lab. Rept. UCRL-ID-122080, 13 pp.

UNESCO, 1971. Tectonics of Africa, UNESCO, Paris, 602 pp.

van der Meer, F., and S. Cloetingh, 1993. Intraplate stresses and the subsidence history of the Sirte Basin (Libya), Tectonophysics 226, 37-58.

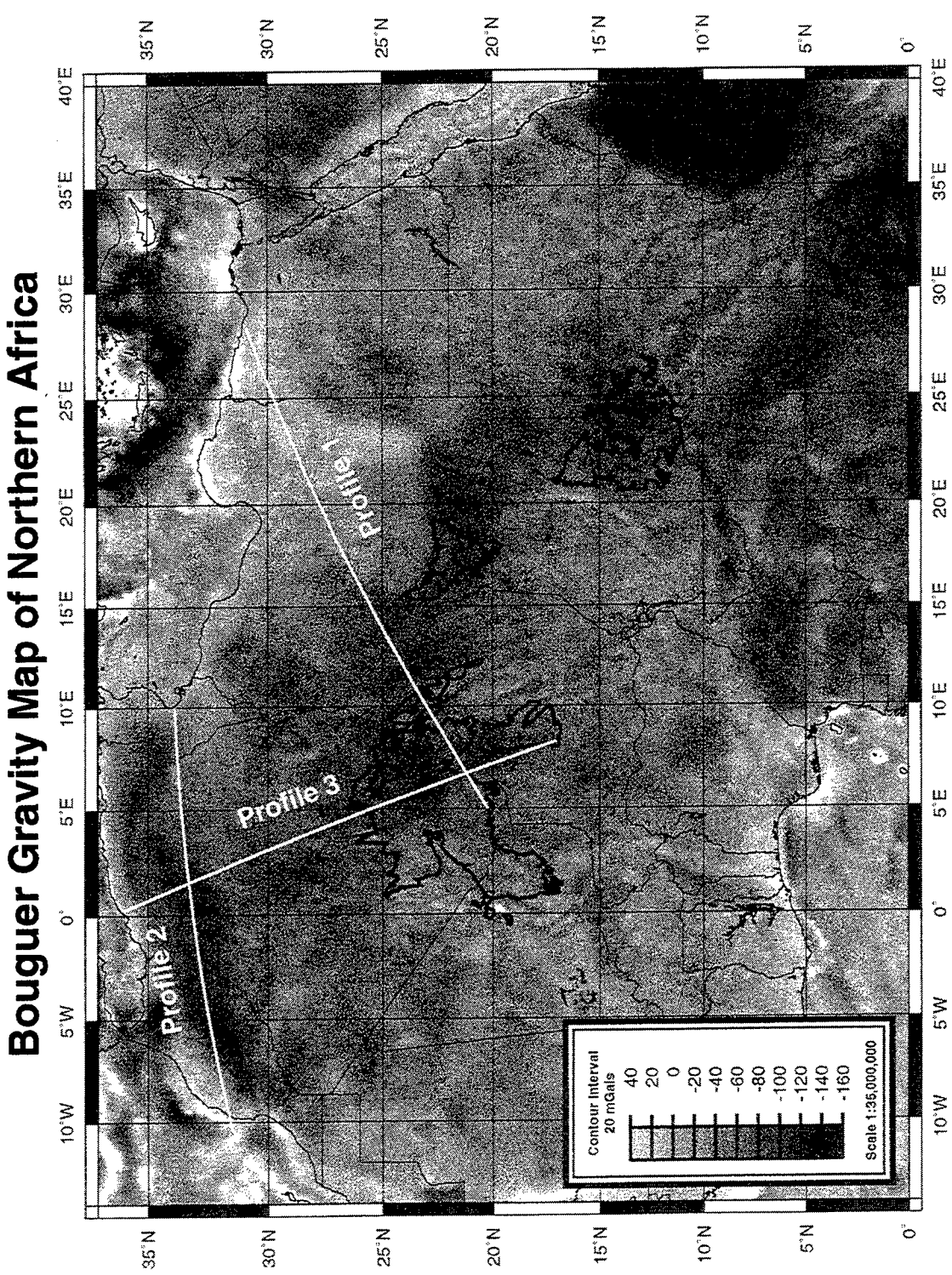
Bouguer Gravity Map of Northern Africa
Profile 1
Profile 2
Profile 3
Contour Interval
20 mGals
40
20
0
-20
-40
-60
-80
-100
-120
-140
-160
Scale 1:35,000,000
10°W
5°W
0°
5°E
10°E
15°E
20°E
25°E
30°E
35°E
40°E
35°N
30°N
25°N
20°N
15°N
10°N
5°N
0°

Figure 1

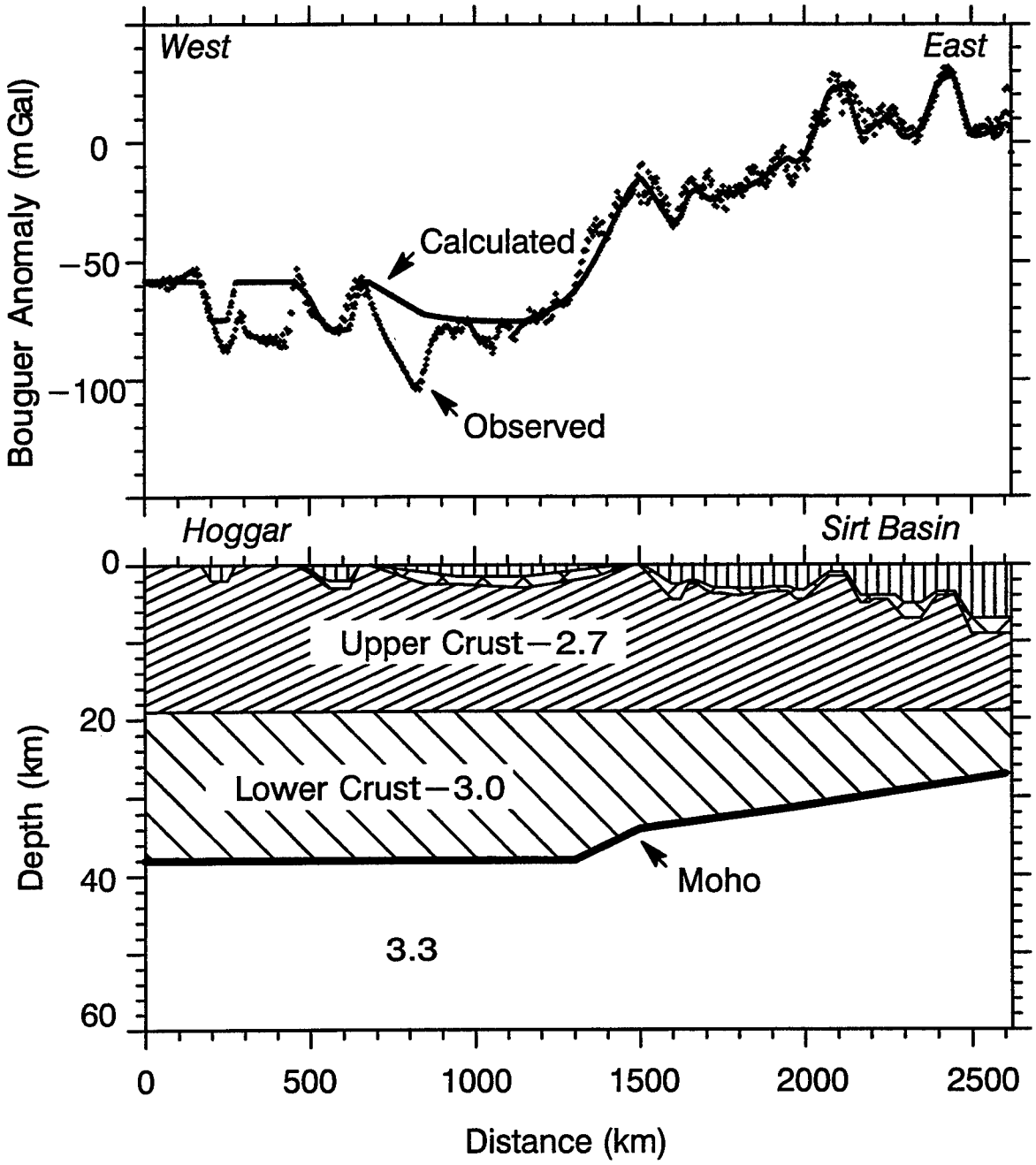

Figure 2. Preliminary lithospheric model for Profile 1 (southern Algeria to central Egypt). Numbers are densities in gm/cc. The upper two units which are not labeled are Mesozoic and Paleozoic sedimentary rocks with densities of 2.5 gm/cc and 2.6 gm/cc respectively.

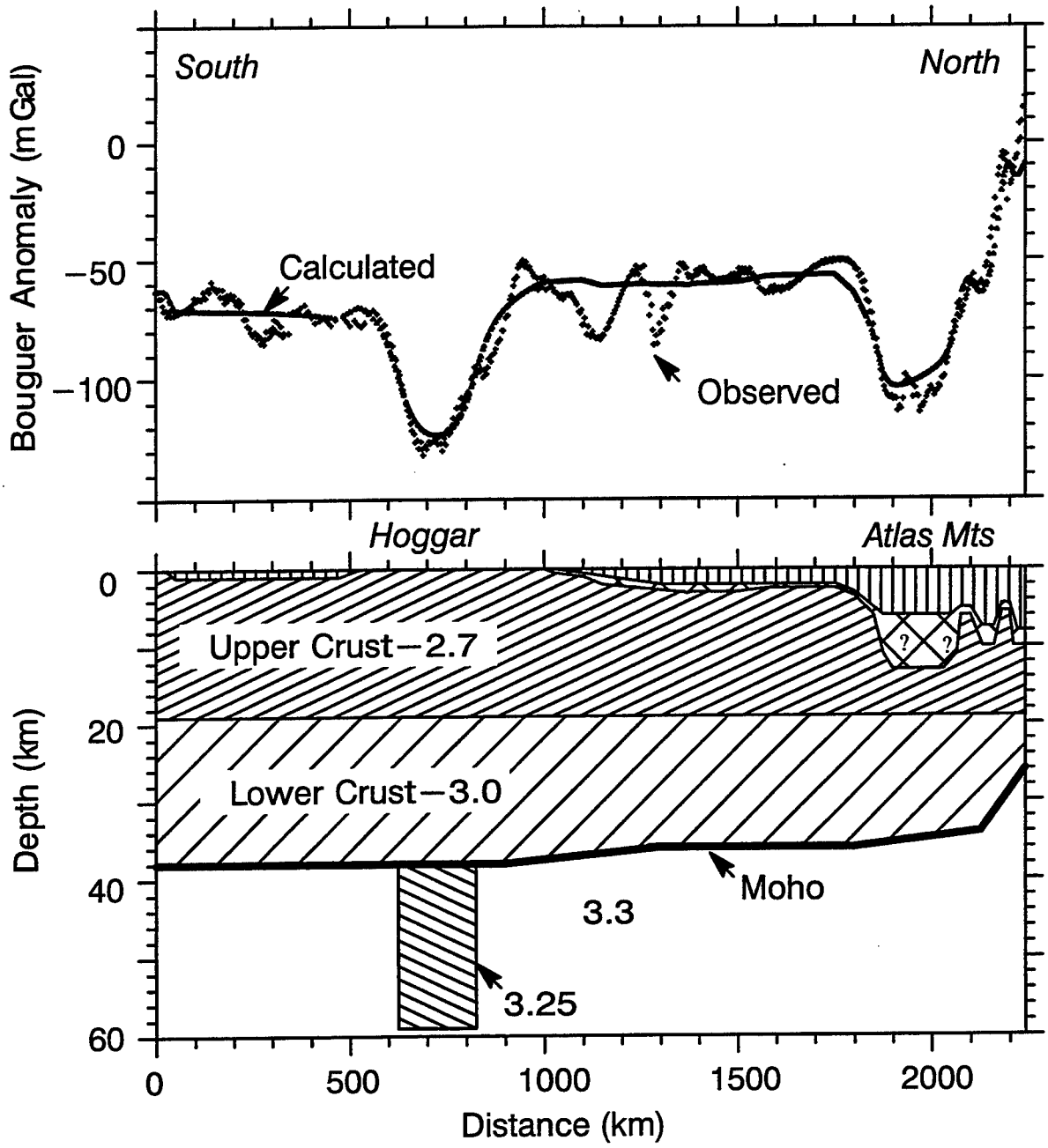

Figure 3. Preliminary lithospheric model for Profile 3 (southern Algeria to northern Algeria). Numbers are densities in gm/cc. The upper two units which are not labeled are Mesozoic and Paleozoic sedimentary rocks with densities of 2.5 gm/cc and 2.6 gm/cc respectively.

Figure 4. Preliminary map of the crustal thickness in Africa. Contour interval - 5 km.

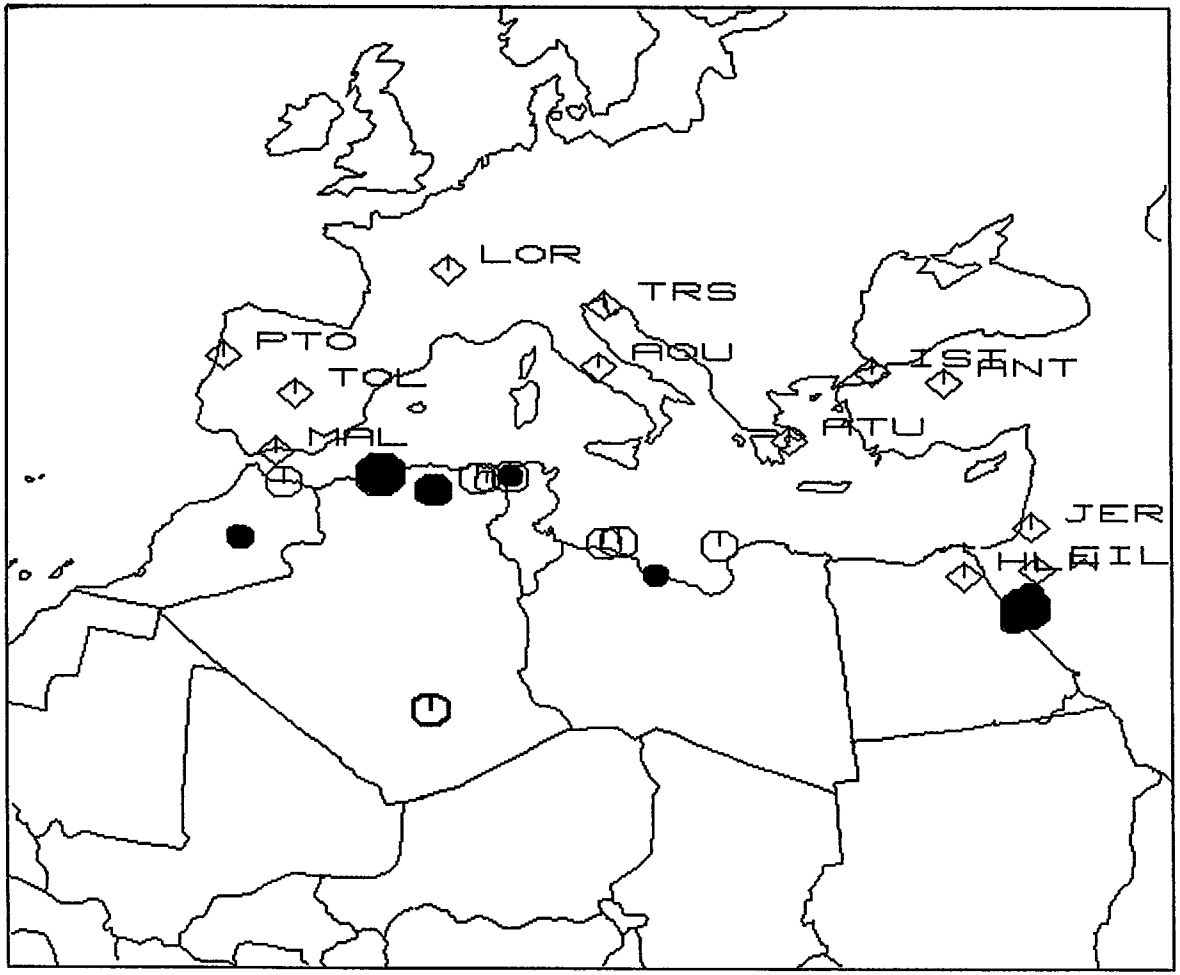

Figure 5. Earthquakes of North Africa (1963-1988) for which regional waveform data have been collected (solid dots) or will be collected (open dots). Symbol size is keyed to magnitude, largest dots are magnitude ≥ 6.0 events, smallest dots magnitude < 5.0 events. Diamonds denote WWSSN stations operating during this time period.

Seismic Regionalization in the Middle East and North Africa

F. Dowla, P. Goldstein, P. Harben, D. Harris, T. Hauk, S. Jarpe, E. Kansa, P. Lewis, D. McNamara, H. Patton, D. Rock, A. Ryall, C. Schultz, A. Smith, J. Sweeney, W. Walter, L. Wethern
(in alphabetical order)

Lawrence Livermore National Laboratory

Sponsored by U. S. Dept. of Energy, Contract W-7405-ENG-48
Comprehensive Test Ban Treaty Research and Development Program, ST482B

ABSTRACT

The U. S. DoE has undertaken seismic regionalization of the Middle East and North Africa, which entails two kinds of calibrations: point (actually path) empirical calibrations between source locations and key stations in the region, and calibrations of structure, generally through inverse methods. The calibration task is complicated by the extreme range of geophysical conditions across the study area, which span relatively simple, stable cratonic and platform regions (North Africa, Saudia Arabia) and complex tectonic provinces (subduction zones in the Mediterranean, orogenic belts in Iran, major fault zones in Turkey). Empirical calibration is feasible and probably necessary in the seismogenic regions. Calibration of the extensive aseismic regions may require model-based techniques, extrapolating regionalization results (as boundary conditions) from adjacent seismogenic regions. The relative simplicity of the aseismic regions is consistent with a modelling approach; tomographic and inverse methods are expected to play a major role.

Regionalization depends critically on the collection of waveform data from events with adequate ground truth (principally epicenter, depth, origin times and event type). Announced nuclear explosions and mining explosions are among the best calibration events (see Walter et al., this volume for methods of identifying mining explosions). However, large earthquakes with good teleseismic constraints on location, origin time and mechanism, and aftershocks with local network constraints are more readily obtained and form the bulk of our initial calibration data.

Our calibration strategy emphasizes regional phase characterization and travel-time calibration first. Travel-time curves and point corrections will be the first parameters to be delivered as part of the planned DoE Knowledge Base (KB) for data center processing pipelines. Travel-time calibrations will be followed in subsequent releases of the KB by a variety of waveform measurements (phase amplitude, group and phase velocity, back-azimuth, etc.) that require picked phase windows. Finally, tomographic and inverse methods will be applied to develop structural characterizations (e.g. surface wave dispersion, upper mantle P and S velocity) mapped on grids.

This paper presents initial results on Lg phase blockage (phase characterization), travel-time residual calibrations for six key regional stations, initial bearing and velocity calibrations at the Sonseca array, and a preview of structural inversion applied to calibration in northwest Africa.

Key Words: seismic regionalization, seismic calibration, Middle East, North Africa

This work was performed under the auspices of the U. S. Department of Energy by the LLNL under Contract W-7405-ENG-48.

OBJECTIVE

The long-term objective of our regionalization research is to provide the U. S. National Data Center (NDC) and the CTBT International Data Center (IDC) with the necessary calibrations and algorithms to improve detection, phase identification, location,and discrimination in the Middle East and North Africa. The program has three overlapping phases: data collection, phase and path characterization (measurement), and structural characterization (inversion). Our near-term objective is to provide gross characterization of phase blockage in the region, and travel-time corrections for key IMS primary and auxiliary stations in the region. The travel-time corrections are intended to improve location estimation by such algorithms as EVLOC.

The principal challenge in the Middle East and North Africa is the lack of seismic event data for calibration. Figure 1 shows the distribution of the 49,000 NEIC catalog events for the eleven years 1985-1995. In most portions of our study region this figure portrays events down to magnitude 3.5, in many regions it extends much lower. The principal feature of this figure is it's extreme heterogeneity. The region divides into seismic and aseismic areas; the seismic belts have an excess of events suitable for calibration, the aseismic areas have virtually none. Calibration can be performed empirically for the former (and is our initial focus), but must be extrapolated to the latter with some kind of model-driven approach. Not only does the distribution of seismic events pose a problem, but data collection is a formidable problem. Figure 2 shows the distribution of high-quality stations from which data are readily obtainable. The sparsity of stations is apparent when contrasted to the coverage available in the U. S., a relatively well-calibrated region of comparable size. Other stations exist in the Middle East and North Africa, but they belong to closed networks; waveform data are nearly unobtainable and bulletin data is sporadic.

RESEARCH ACCOMPLISHED

Calibration research begins with the collection of seismic waveform data. For location calibration purposes, only large events located teleseismically by a large number of stations with good azimuthal distribution are useful. Our initial focus is travel-time calibration of four proposed IMS primary stations: Sonseca (ESDC), Belbasi (BRTR), Alibek (GEYT, ABKT substitutes) and Teheran (THR, ILPA substitutes). Figure 3 summarizes the event data collected for these stations to date and the coverage that it represents. The events are largely drawn from the Harvard CMT catalog since these events are sufficiently well-constrained teleseismically to have estimates of mechanism, depth and good epicentral control. Additional large NEIC catalog events are included. We supplement the four primary regional station data with additional data from the MEDNET, GEOSCOPE and IRIS-allied networks shown in Figure 2. The total data available exceeds 16,000 individual waveforms representing 1300 events; however, the multiplicity of array channels, three-component stations and separate recording bands means that many fewer distinct source-receiver combinations are represented.

Independent information on the reliability of teleseismic locations and origin times is available on rare occasions when aftershock networks are deployed in the wake of damaging earthquakes and the results are reported. Figure 4 presents aftershock network data from the 1978 Tabas (Iran) and 1980 El Asnam (Algeria) earthquakes that demonstrates that at least 40 teleseismic observations are required to reduce location errors to around 10 kilometers. When aftershock studies coincide with periods of data availability at our primary stations, such studies provide particularly good ground truth information. We are systematically searching the literature

for these studies.

The next stage of calibration research is analysis of data quality and qualitative characterization of phase propagation and blockage throughout the region. Figure 5 displays the results of a pilot study of Lg phase blockage. Not suprisingly, Lg generally fails to propagate across the Mediterranean Sea; severe Lg attenuation appears to correlate with the length of the path in oceanic crust. This fact poses a significant problem for discrimination, and highlights the need for reliable stations on the African continent to discriminate events in north Africa. Lg propagation through the African craton appears to be especially efficient, suggesting that fewer stations may be required there for reliable monitoring than in more tectonically active regions.

The principal near-term product of the program is a knowledge base of travel-time calibrations for use in location algorithms. We are systematically picking (initially) P phases from stations in our study area to generate bulk station corrections, point corrections for specific source regions and average 1-D velocity models for each station. Travel-time residuals (from the IASP91) model for six regional stations are shown in Figure 6. The lack of discernable patterns in the residuals is consistent with the extreme complexity of the area and highlights the need for point corrections. Nearly constant bulk offsets of approximately 1.9 seconds are found across the six stations (and have been removed in the figure). Such offsets are consistent with the bias between the Jeffreys-Bullen and IASP91 travel-time models. The J-B tables were derived for the western U. S. with its slower than average crust; the IASP91 model was derived as a world average. The difference in the models maps to an origin time error expressed as a constant residual.

Once the principal phases are picked, we plan to automate measurements of phase amplitude, surface wave dispersion, back-azimuth, incidence angle and (for arrays) phase velocity. The objective is to develop corrections for these quantities to tune phase identification, association , magnitude estimation, and discrimination algorithms; these corrections will be incorporated in later releases of the DOE CTBT knowledge base. Figure 7 show the results of a pilot study for the Sonseca array which show a pronounced (northward) azimuth bias for P waves arriving from the east and a slight (fast) bias for regional P phase velocity estimates.

Calibration of the aseismic regions (the African Craton and the Arabian Shield) poses the largest regionalization challenge; the challenge is likely to be met by a series of inverse methods. Waveform modelling can be used to estimate velocity models that can, in turn, provide first-order corrections to the IASP91 travel-time curves. An example of this procedure is shown in Figure 8 for a Moroccan earthquake recorded at station TAM. This event has a Harvard CMT source mechanism (teleseismically determined). With the uncertainty of the source mechanism removed it is possible to estimate structure along the path by solving a series of forward problems (adjusting structure) to match synthetic waveforms to the observed data.

CONCLUSIONS AND RECOMMENDATIONS

The extreme geophysical variability of the Middle East and North Africa and the relative lack of seismic stations make seismic regionalization in the area a challenge. LLNL has made substantial progress in collecting what data are available and in interpreting what data we have to calibrate key regional stations. In the future, many other types of data (gravity, receiver functions, surface wave group and phase dispersion curves) and innovative methods of tomography and structural inversion will be necessary to characterize the aseismic portions of the area. In addition, the deployment of temporary stations and arrays would help acquire the data necessary for good geophysical structure determination prior to the installation of permanent stations.

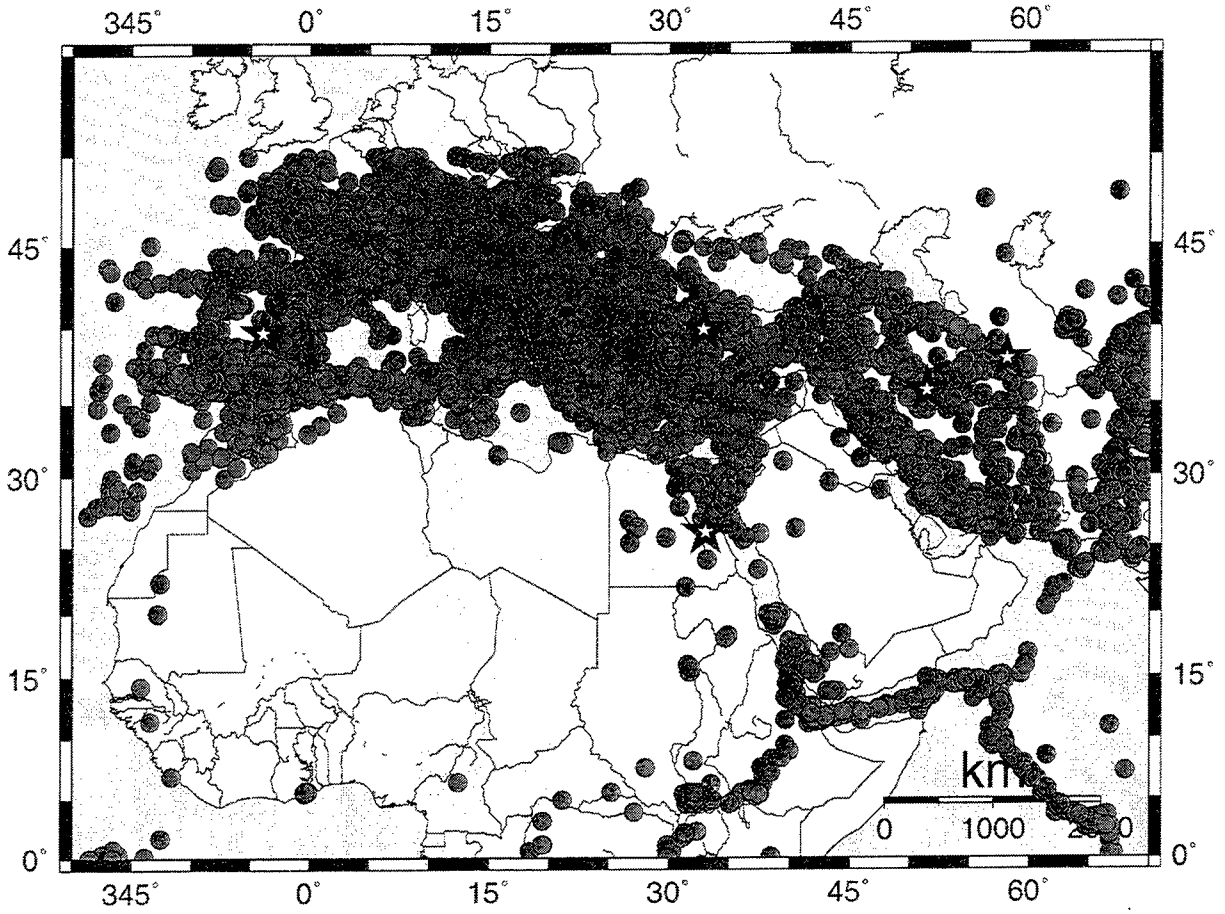

Figure 1 Much of the area to be calibrated is aseismic, especially the African Craton and the Arabian Shield. This seismicity map shows NEIC bulletin events for the period 1985-1995; the event threshold for this map varies by region, but is near 3.5 in the sparsely represented regions.

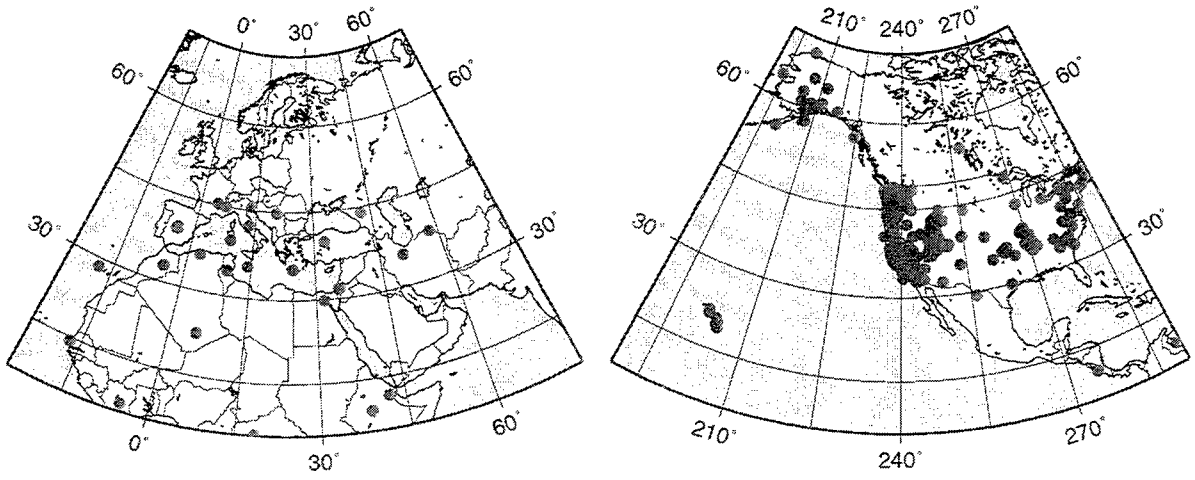

Figure 2 The Middle East and North Africa are sparsely covered with accessible seismic stations (those from which data are readily available). These maps contrast station density in our study area and the United States (a well-calibrated region of comparable size). Station up-time is frequently poor in our study area, further reducing data availability.

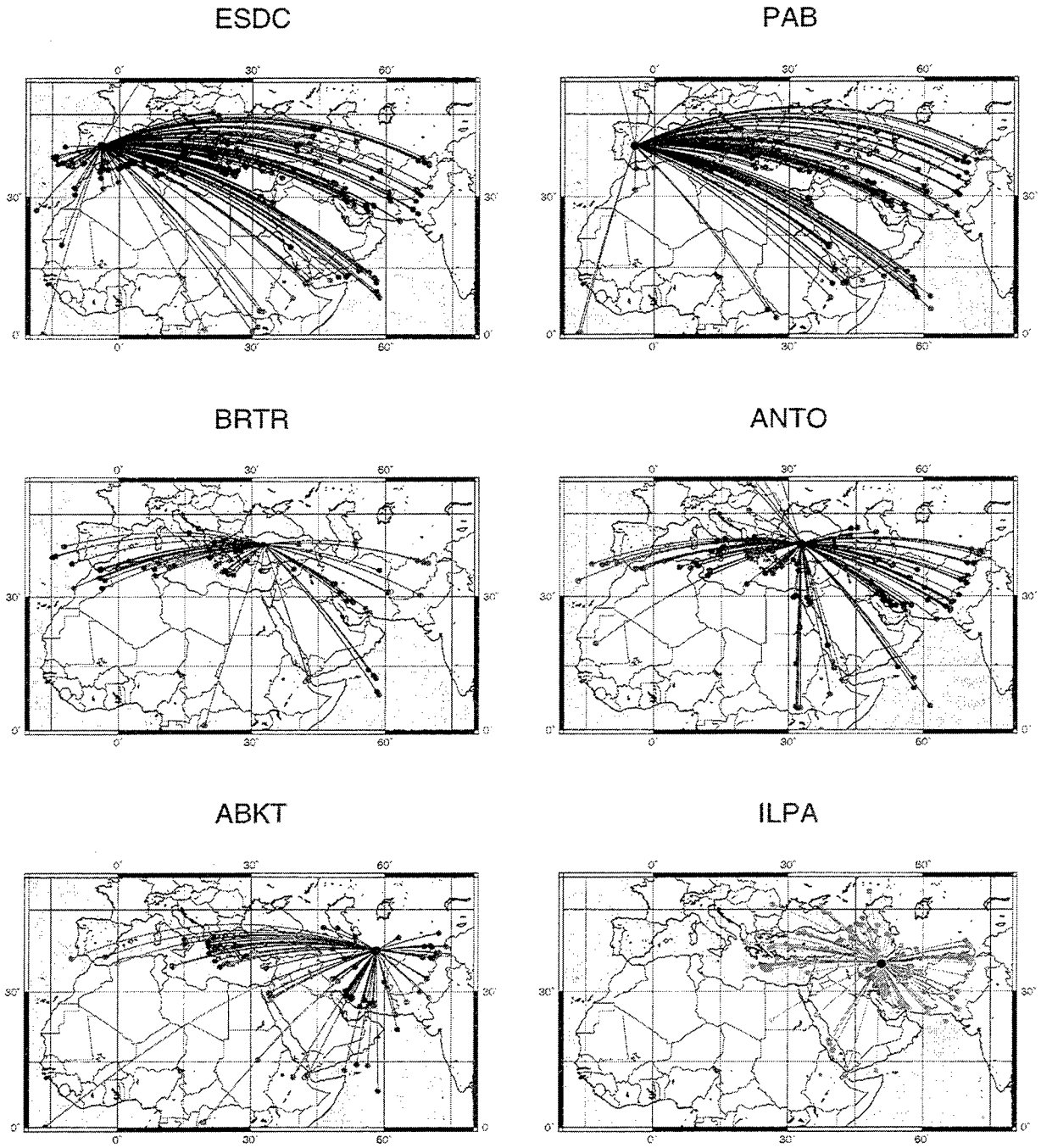

Figure 3. Paths representing waveform segments collected to date for principal IMS primary stations or their surrogates in the Middle East and North Africa. ILPA is a surrogate for THR, which is not yet on line. ANTO and PAB are nearly collocated with BRTR and ESDC, respectively, and provide additional calibration data useful for those sites. The ILPA data were organized and picked by MULTIMAX for DOE. We are also collecting data from IMS primary (GTSN) stations DBIC and BGCA, IMS auxiliary stations MDT, GNI, KIV, KEG, MBO, and AAE (surrogate for FURI), MEDNET stations GFA and MEB, GEOSCOPE station TAM, and IRIS/IDA station NIL in Pakistan.

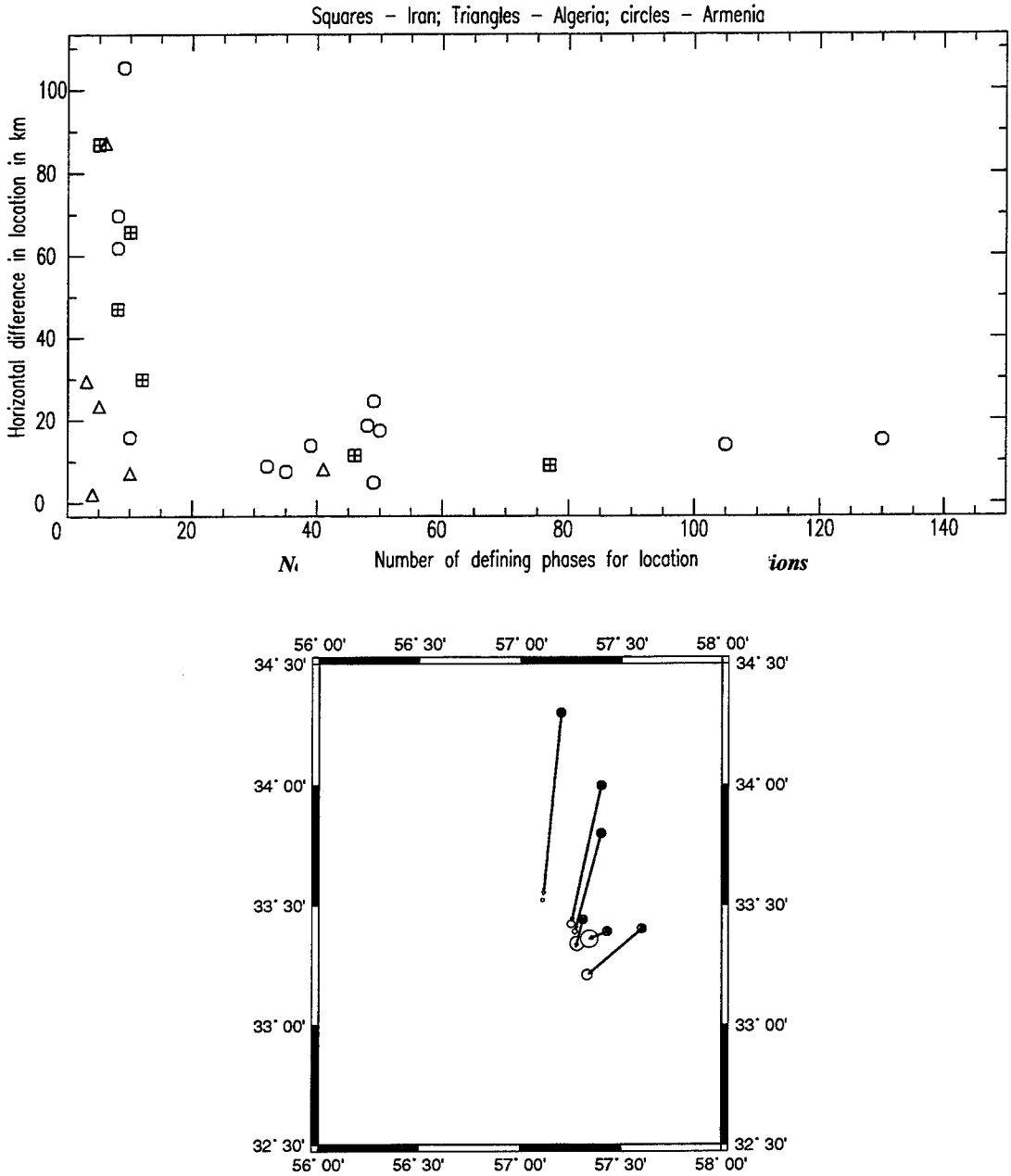

Figure 4 Large earthquakes, well-located by teleseismic networks can be used as ground-truth events for travel-time and location calibration. The top figure shows epicentral location error as a function of the number of teleseismic phases recorded for aftershocks of the 1980 El Asnam earthquake in Algeria, the 1978 Tabas earthquake in Iran, and the 1988 Spitak in Armenia. Ground truth locations for both aftershock sequences were obtained with local aftershock networks. Events large enough to be observed with 40 or more stations had epicentral errors around 10-20 kilometers. The lower figure compares the teleseismic (solid circle) and aftershock (open circle) network locations for events in the Tabas sequence. The aftershock network locations form a tighter, more linear cluster. Teleseismic locations of the larger events (largest open circles) are most accurate.

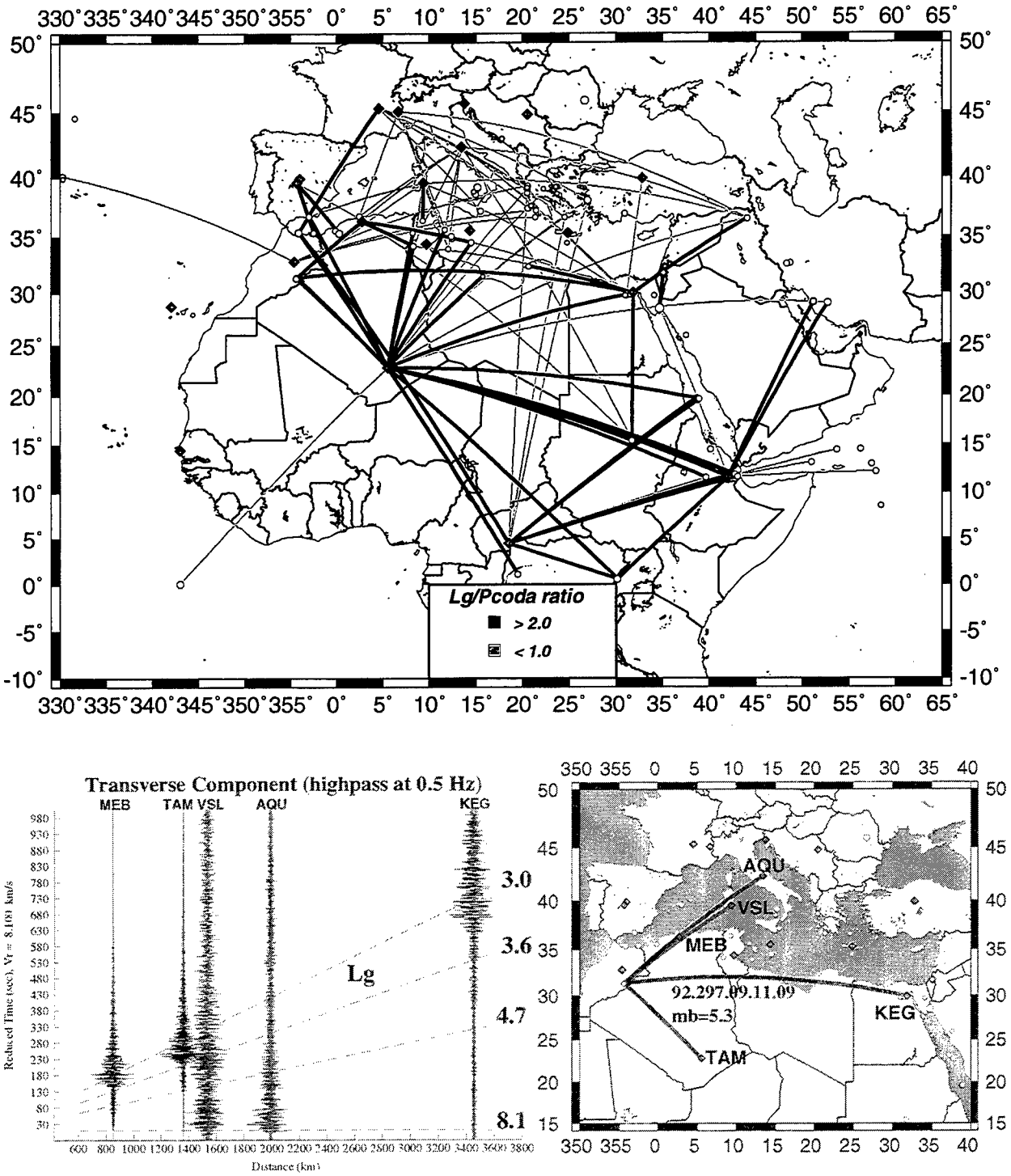

Figure 5 Phase and path characterization in our study area shows significant Lg blockage for most paths crossing the Mediterranean Sea. Consequently, application of Lg-based discriminants to events in Africa will require stations in Africa. The top figure shows paths used in the study; darker lines denote efficient Lg propagation, feinter lines poor Lg propagation. The bottom figure portrays a record section for one particular event in Morocco. Lg propagates well on the continental paths, even to 3500 km across all of North Africa. Shorter paths across the Mediterranean show less or no Lg energy depending on the length of the path through oceanic crust.

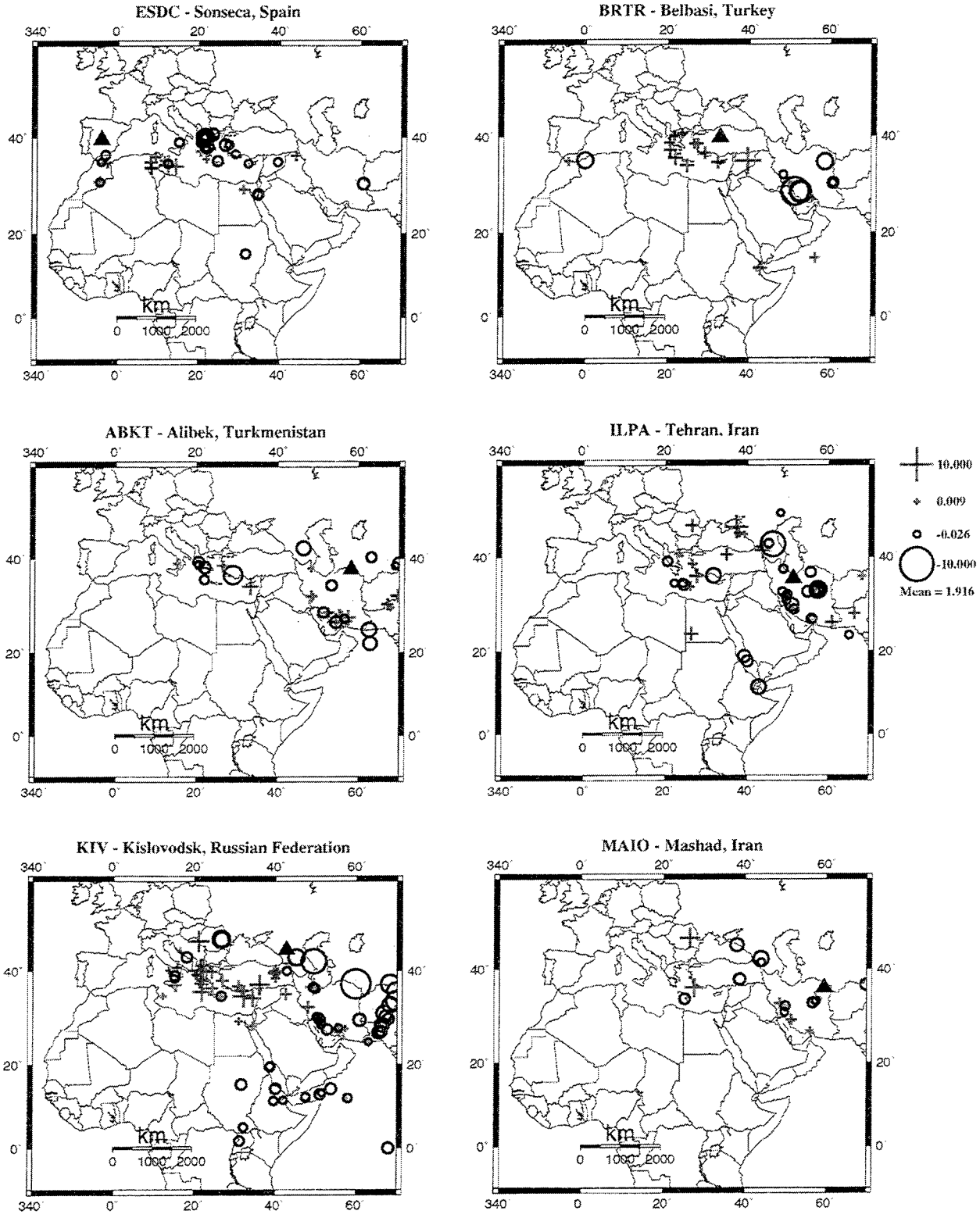

Figure 6 Initial travel-time residuals (relative to the IASP91 model) indicate the need for point travel-time corrections. Some patterns emerge: P phases from events in the Greek isles and Asia Minor arrive late to stations in their northeast, but early to Sonseca. The situation for stations due east (ILPA, Alibek and Mashad) is mixed. Bulk station corrections have been computed and removed in these figures. Data from Mashad and ILPA were organized and picked by Multimax.

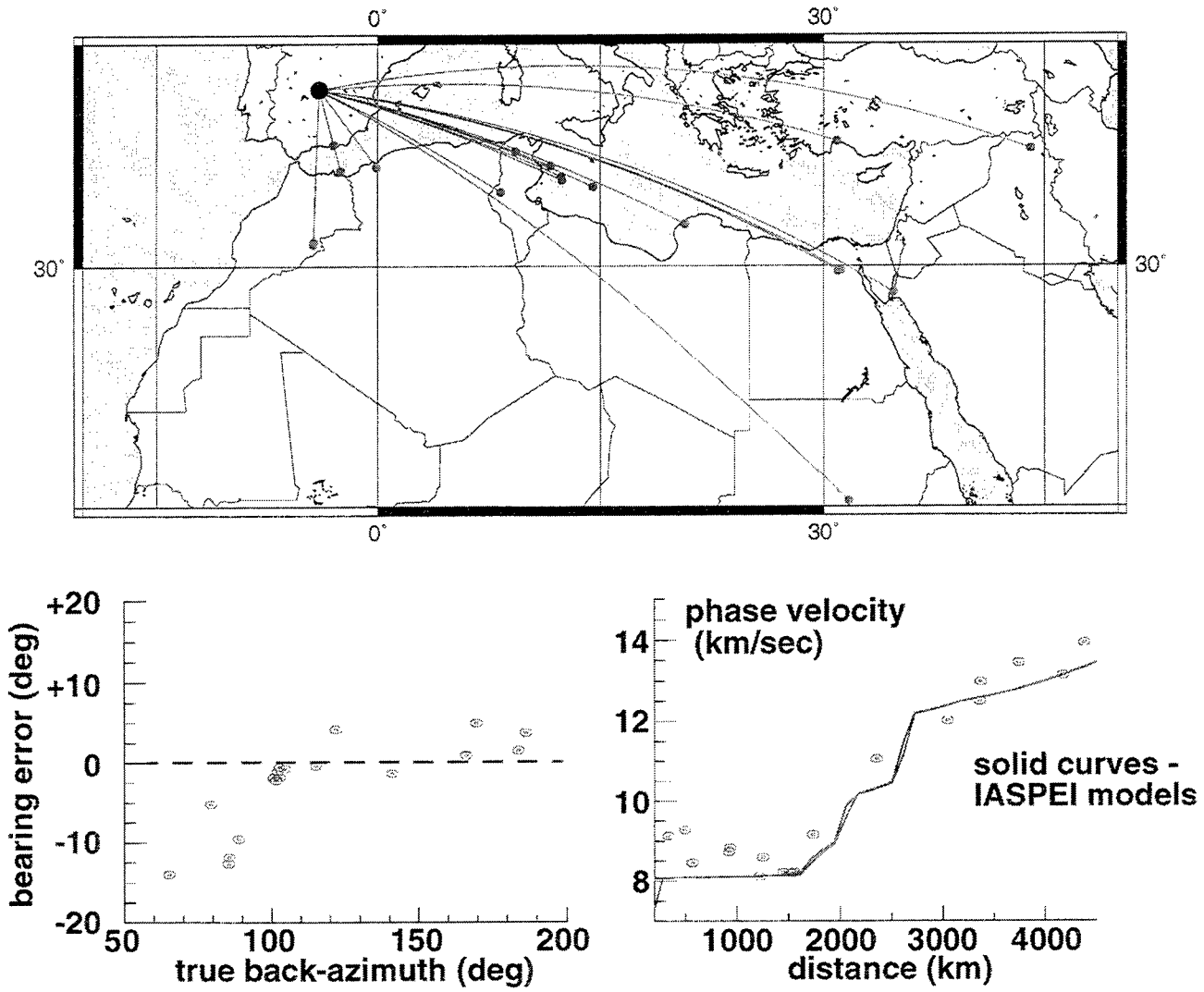

Figure 7 Initial P bearing and phase velocity measurements are the raw material from which array processing calibrations for the Sonseca array (ESDC) will be developed. We plan to automate phase amplitude, group delay, back-azimuth and incidence angle/phase velocity measurements using the picks developed in the initial waveform interpretation phase of the project. The array measurements shown here were made in the 1-3 Hz band; they show a pronounced azimuth bias for P phases arriving from the east and a slight velocity bias for regional P phases.

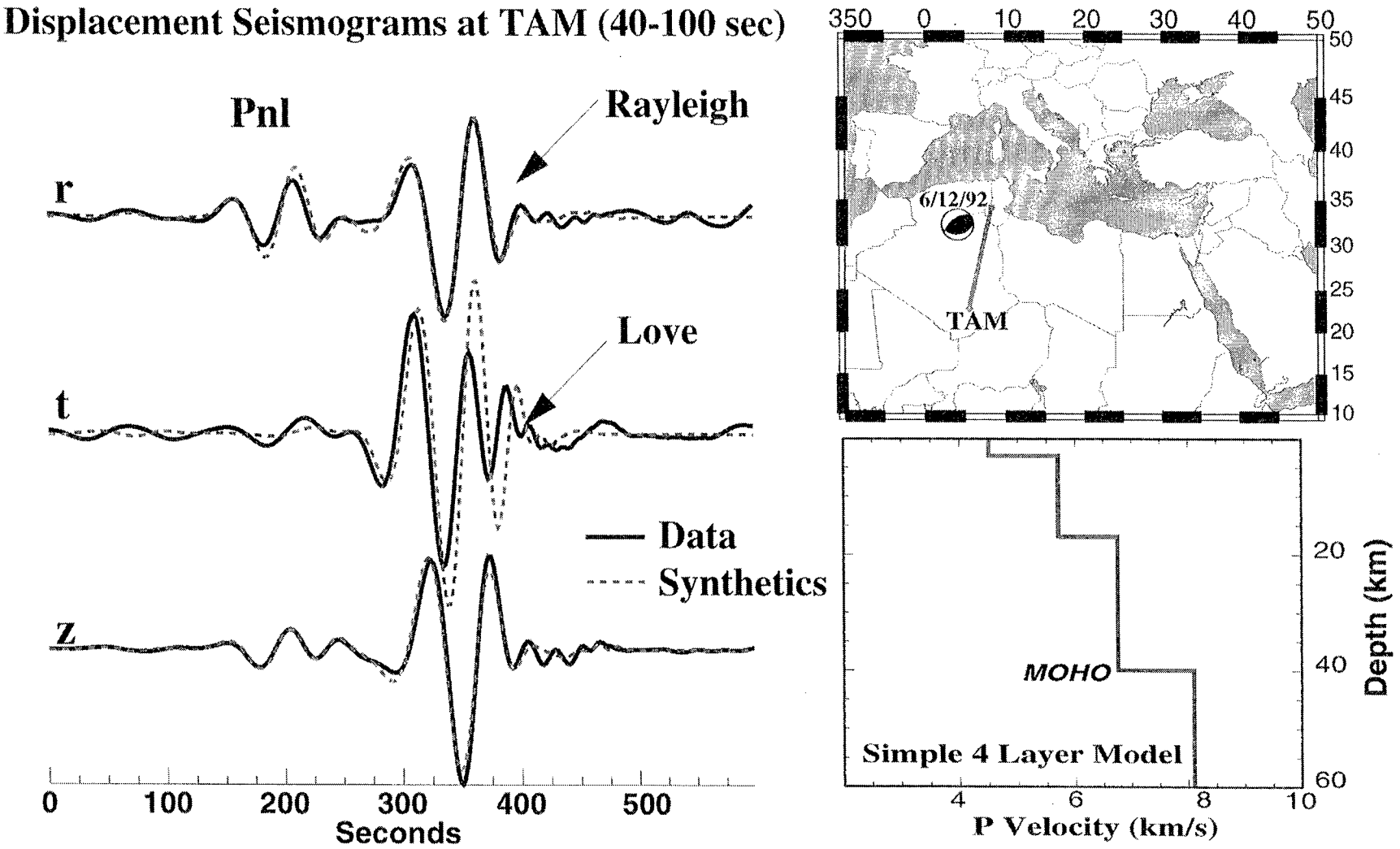

Fig. 8. Example of waveform modeling to estimate velocity structure in an aseismic region. This m_b=5.3 event in Tunisia was recorded 1288 km away at TAM. Using the independently determined Harvard CMT source mechanism, reflectivity synthetics were calculated for a series of simple velocity structures until a reasonable match between synthetics and data was obtained as shown on the left for the velocity model shown on the right. Once the velocity structure is known, waveform modeling can be used to refine mechanism, depth and location of smaller events.

Lithospheric Profiles in the Southwestern U. S.

G. Randy Keller, Kate Miller, Diane Doser, Steven Harder, and Cathy Snelson

Department of Geological Sciences, University of Texas at El Paso, El Paso, TX 79968

Grant Number F49620–92–J–0438

Sponsored by AFSOR

ABSTRACT:

As we move toward a Comprehensive Test Ban Treaty, it has become increasing clear that detailed knowledge of lithospheric structure is necessary to verification efforts. Key phases which are being used as discriminants (Pn, Pg, Lg, etc.) travel exclusively in the lithosphere and are thus much affected by its structure. However, the studies needed to acquire detailed knowledge of lithospheric structure require large explosions, recorded by hundreds of seismograph systems. In the former Soviet Union, a series of Peaceful Nuclear Explosions (PNE) were exploded to provide such data. There have been very few PNE in the U.S., and these experiments took place in the 1960's and 1970's long before there were large numbers of digital seismograph systems available to provide detailed recordings. These few PNE events do not provide detailed pictures of lithospheric structure and propagation of regional phases and thus cannot serve as effective benchmarks for comparison with other continents. Large chemical explosions can provide suitable sources for lithospheric experiments as proven by the EARLY RISE experiment in the Great Lakes region in the 1960's and the recent Non–Proliferation Experiment (NPE) at the Nevada Test Site. However, we have not had an opportunity to conduct a large–scale lithospheric experiment with modern equipment except with NTS sources. The Canadian geophysical community has organized to form LITHOPROBE which might be considered the modern prototype of a national effort to study the structure of the lithosphere. Last year we and the Rice University seismology group were able to join a LITHOPROBE experiment and record a lithospheric scale profile which extended from northwestern Canada to New Mexico. This experiment, DEEP PROBE, was the primary focus of our efforts this year, and it has shown that cost effective explosive sources can provide good information on regional phases.

OBJECTIVE:

The University of Texas at El Paso (UTEP) geophysics group as been conducting a wide variety of geophysical studies in the southwestern U. S. The objectives of this project are to use the results to investigate lithospheric structure and seismic wave propagation in the area. This year of the project has been very active with the successful completion of a major seismic field project and continued progress on our efforts to obtain a good overall view of the geophysical properties of the region. The seismic field experiment, DEEP PROBE, was ambitious and has produced a large amount of interesting data.

RESEARCH ACCOMPLISHED:

Our major field effort this year was the DEEP PROBE experiment which was undertaken in July and August in cooperation with Rice University and the Canadian LITHOPROBE project. As we move toward a Comprehensive Test Ban Treaty, it has become increasing clear that detailed knowledge of lithospheric structure is necessary to verification efforts because regional phases which are being used as discriminants (Pn, Pg, Lg, etc.) travel exclusively in the lithosphere and are thus much affected by its structure. However, the studies needed to acquire detailed knowledge of lithospheric structure require large explosions, recorded by hundreds of seismograph systems. There have been very few Peaceful Nuclear Explosions (PNE) in the U.S., and these experiments took place in the 1960's and 1970's long before there were large numbers of digital seismograph systems available to provide detailed recordings. These few PNE events do not provide detailed pictures of lithospheric structure and propagation of regional phases and thus cannot serve as effective benchmarks for comparison with other continents. Large chemical explosions can provide suitable sources for lithospheric experiments as proven by the EARLY RISE experiment in the Great Lakes region in the 1960's and the recent Non–Proliferation Experiment (NPE) at the Nevada Test Site. However, we have not had an opportunity to conduct a large–scale lithospheric experiment with modern equipment except with NTS sources.

The summer of 1995 provided us an opportunity to participate in a unique opportunity to gather seismic data at regional distances with large numbers of modern seismograph systems. The recording profile extended from Alberta, Canada to New Mexico, a distance of almost 2000 km (Figure 1). Virtually the entire US and Canadian pools of portable instruments were employed which when combined with instruments loaned to us from Europe brought the total number to about 750. Our effort focussed on the deep lithosphere employing an abandoned uranium mine in central Wyoming. Alan Levander of Rice University headed up a successful effort to obtain NSF funding to reverse the Canadian profile for the deep mantle phases. The vast variety of seismograph systems employed made merging the data into a standard format a major task which took 9 months. We have not had time to analyze the data in detail, but the initial results are very promising. The Wyoming source produced arrivals to distances of greater than 800km (Figure 2) with charges of only 6100 kg and 6800 kg. These sources were assigned Mb magnitudes in excess of 3.0 by seismic networks in the region. This very efficient shot point was loaded using liquid explosives and a pumper truck. The maximum water depth in the mine was 55 m. The lithospheric structure as revealed by regional phases appears to vary markedly across the main tectonic boundary present which is the southern margin of the Wyoming craton. Ultimately, we will compare these data to the excellent data derived from the NPE.

CONCLUSIONS AND RECOMMENDATIONS:

Initial results of the DEEP PROBE experiment show that lithospheric structure can be quite complex even in areas that are thought of as being cratonal. The effects of these complexities on regional phases can be considerable. The seismic source employed in Wyoming was very efficient and easy to load. The fact that it is still available for further studies seems like a real opportunity.

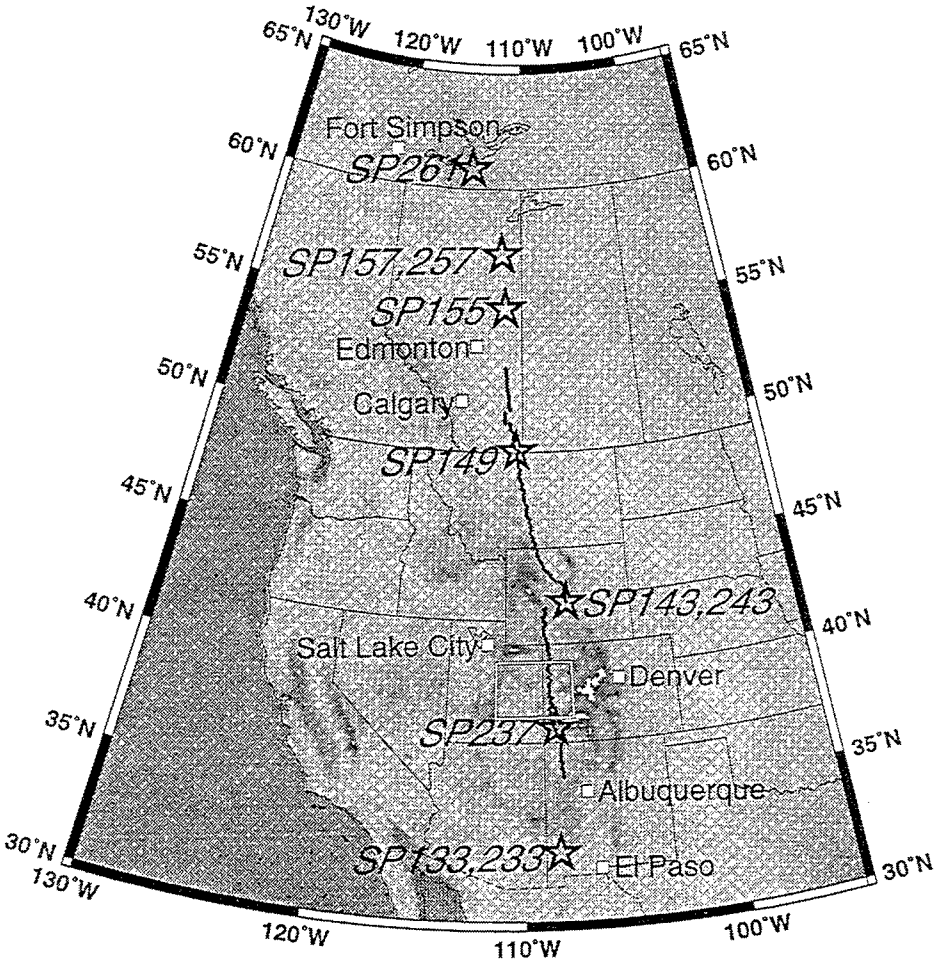

Figure 1. Index map of the DEEP PROBE experiment. Wyoming shotpoint was 143 and 243.

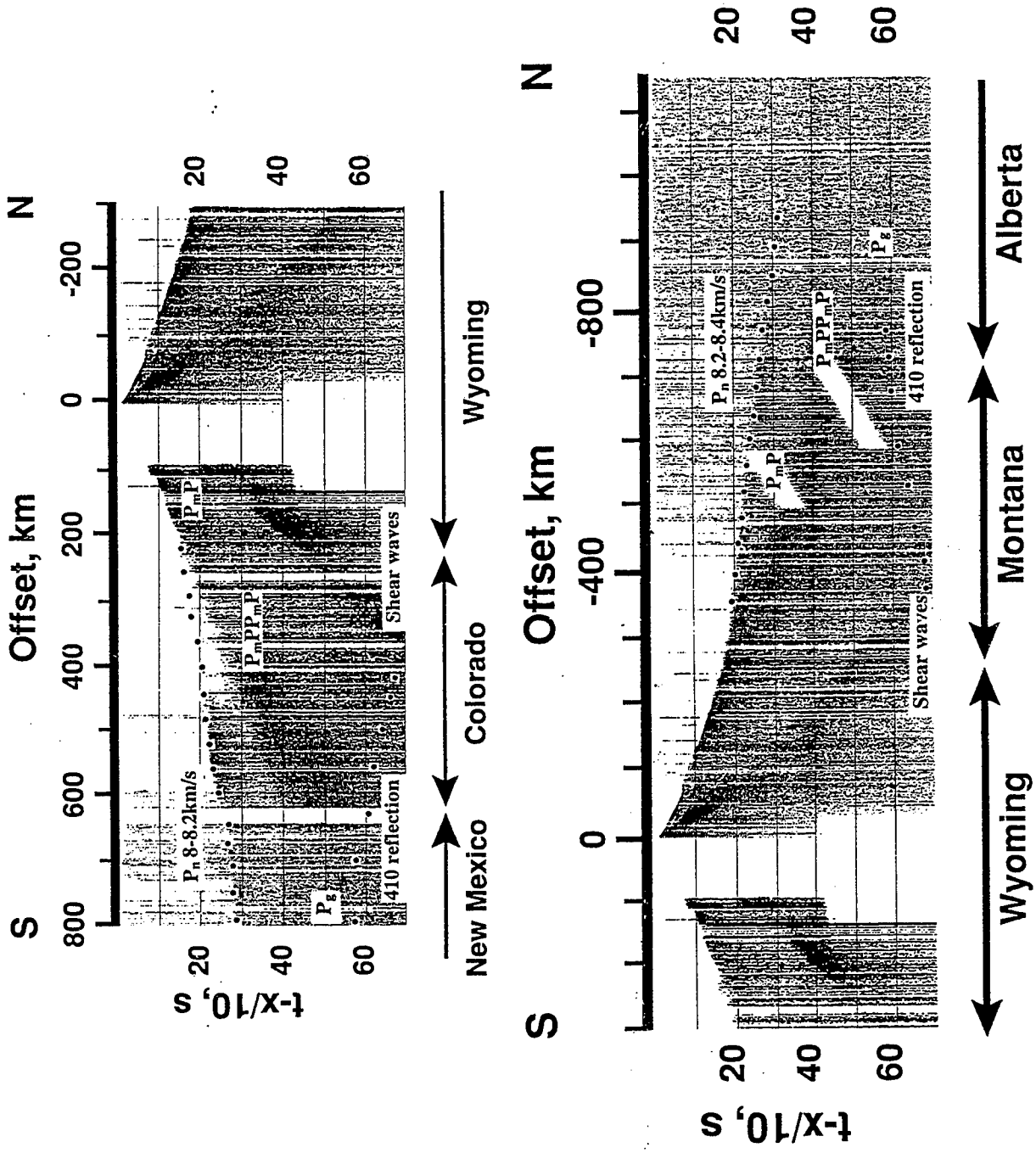

Figure 2. Record sections for the Wyoming shotpoint. Top - 143. Bottom - 243.

GROUP VELOCITY VARIATIONS ACROSS EURASIA

A.L. Levshin, M.H. Ritzwoller, S.S. Smith

Department of Physics, University of Colorado, Boulder 80309-0390
Contract Number F49620-95-1-0139
Sponsored by AFOSR

ABSTRACT

We report on the status of a systematic study of broadband Rayleigh and Love wave dispersion across Eurasia. The purpose of this study is to provide a more sharply focused model of shear velocity variations in the lithosphere with resolutions in most regions between 500 - 750 km. Group and phase velocity as well as spectral amplitude measurements have been obtained using the method described by Ritzwoller *et al.* (1995). These measurements have resulted from analyses of approximately 6,100 three-component long period seismograms from the GSN, GEOSCOPE, MEDNET, and CDSN networks following 315 events with $M_s \geq 5.0$ that occurred from 1988 through late-1995. This data set exhibits considerable redundancy, which allows for consistency tests, outlier rejection, and error estimation. We 'cluster' measurements from similar paths by combining them into a single measurement defined as the average along the 'unique path' with the estimated standard deviation among the individual measurements. The number of unique paths is period dependent, peaking at about 4,000 in number at 50 s period and falling to smaller numbers at shorter and longer periods.

Interpretation has concentrated on the group velocity measurements for two reasons: (1) they can be interpreted without knowledge of the source and (2) group velocity kernels are compressed nearer to the surface than phase velocity kernels and consequently provide better radial resolution in the crust and uppermost mantle. Group velocity maps have been constructed from 20 s period to 225 s period for Rayleigh waves and up to 150 s period for Love waves. Shown here are group velocity maps for Rayleigh and Love waves at three periods: 30 s, 50 s, and 100 s. These maps appear to provide significantly better resolution than other surface wave studies performed to date. In particular, they contain new information about large sedimentary features, lower crustal structures, Moho topography, and upper mantle structures. For example, Love wave sensitivities are compressed nearer to the surface than Rayleigh waves and the 30 s Love wave map clearly shows the large sedimentary features across Eurasia (Tarim Basin, Ganges Delta, Caspian and Black Sea Depressions, Barents Sea Depression, sediments in the Persian Gulf and Western Siberia). Rayleigh waves at 50 s period are very sensitive to Moho topography and the 50 s Rayleigh wave map exhibits striking correlation with surface topography in the Middle East and Central Asia, particularly under Tibet, the Altai Range, and the Zagros Mountains. The resolution of this study is well demonstrated by the group velocity features in the Far East.

A higher resolution regional-scale study of Central Asia with measurements made at regional networks is the subject of a companion study in this volume (Ritzwoller *et al.*, 1996).

Key Words: Eurasia, surface waves, dispersion, Rayleigh waves, Love waves, group velocity

OBJECTIVE

The purpose of this research is to provide an improved lithospheric (crust and uppermost mantle) shear velocity model for the entire Eurasian continent. The inversion is broken into two parts: (1) the estimation of period-dependent maps of the phase and group velocities of Rayleigh and Love waves across a broad period band (20 s - 250 s) and (2) the use of these maps to estimate shear velocity variations across the continent. The resolution exhibited by the resulting model will depend on path number density (lateral resolution) and the breadth of the frequency band studied (radial resolution). We report here on the first part of this research.

A more sharply focused model of lithospheric shear velocities across the continent is useful in a variety of ways. Most significantly for a CTBT, accurate high resolution structural information is needed to improve location capabilities. Location error ellipses mainly quantify ignorance concerning the structure of the crust (sedimentary thicknesses and velocities, crustal velocities and Moho topography). Studies of broadband surface wave dispersion, such as the one described here, promise much new information about crustal structures across Eurasia and will provide a more sound basis for future regional scale studies (e.g., Ritzwoller *et al.*, 1996; this volume).

RESEARCH ACCOMPLISHED

Research to date has proceeded in three steps: (1) data acquisition and dispersion measurement, (2) determination of measurement reliability, and (3) group velocity map construction. We will discuss each of these steps briefly in turn.

Data Acquisition and Processing

Long period (1 sps) waveform data from more than 450 events with $M_s \geq 5.0$ in and surrounding Eurasia from 1988 - late-1995 have been acquired from IRIS' DMC and the GEOSCOPE Data Center. These include data from the GSN, CDSN, GEOSCOPE, and Mednet networks. Of these events, 315 have been fully processed for the GSN/CDSN/Mednet data and about 190 have been processed for the GEOSCOPE stations. The locations of most of these 315 events are shown in Figure 1. At present, we have completed about 75% of the planned data processing.

By 'data processing' we mean the application of the semi-automated dispersion measurement method described by Ritzwoller *et al.* (1995). In this method, for each waveform an analyst interactively chooses the period band of measurement, defines a group velocity - frequency filter used to remove unwanted signals, and assigns a qualitative grade to the measurement (A - F). The measurement is automatically obtained on the filtered waveform. About 6,100 3-component seismograms have been processed to date yielding surface wave dispersion measurements from less than 10 s to more than 300 s period. Because the average path length is about 5,900 km, measurements less than 20 s period are rare. Significant numbers of measurements have been accumulated from 20 - 225 s for Rayleigh waves and from 20 - 150 s for Love waves.

As can be seen in Figure 2, data distribution is not uniform, but it is quite good over most of Eurasia. The main exceptions are over India and the Middle East, particularly Saudi Arabia. More southerly events are being analyzed now to help correct this problem.

Data Reliability

There are two main reasons to make the very large redundant set of measurements we are obtaining here. The first is to optimize coverage and, hence, lateral resolution. The second is to use the redundancy in the data set to estimate data uncertainties and to reject outliers. In this latter regard, we perform what we call a 'cluster analysis'. Measurements whose path-endpoints

lie within 2% of their path lengths are clustered to produce a measurement along a 'unique path'. The average velocity and standard deviation of the cluster is assigned to the unique path. An example of a cluster analysis is shown in Figure 3a. There are about 1100 Rayleigh clusters and 1000 Love clusters. As shown in Figure 3b, most clusters only possess 2 - 3 rays. The average standard deviation over all clusters, after outlier rejection, is shown in Figure 3c as a function of period. We associate this standard deviation with average measurement uncertainty (and this will be used later in Figure 7). The number of unique paths displayed as a function of period for Rayleigh and Love waves is shown in Figure 3d.

Group Velocity Maps

All dispersion measurements have been weighted by results obtained in the cluster analysis and have been used to estimate Eurasian group velocity maps. These maps represent the local group speed of a Rayleigh or Love wave propagating at a particular spatial point. Maps have been constructed for Rayleigh waves ranging between 20 - 225 s and Love waves from 20 - 150 s period. Included here are maps at 30 s, 50 s and 100 s period shown in Figures 4 - 6, respectively.

Cursory Interpretation

Group velocity maps can be interpreted directly, but only tentatively due to the complicated nature of the group velocity sensitivity kernels which can change sign with depth. Both Rayleigh and Love waves are dominantly sensitive to shear velocity, although Rayleigh waves are affected somewhat by compressional velocity as well. Generally, at a given period, Rayleigh wave sensitivity extends deeper than Love wave sensitivity and phase velocity sensitivity extends deeper than group velocity sensitivity. The eigenfunctions shown in the companion paper in this volume (Ritzwoller *et al.*, 1996; Figure 4) demonstrate the compression toward the surface as period decreases. For example, a 30 s Love wave in continental regions is trapped in the crust, insensitive to crustal thickness, but sensitive to crustal velocity variations and sedimentary thickness. Rayleigh waves at 30 s period also possess significant crustal sensitivity but are affected by Moho depth, similar to Love waves at 50 s period. Moho sensitivity maximizes for 50 s Rayleigh waves and 80 s Love waves. Rayleigh waves of 70 s period and greater penetrate into the upper mantle and provide significant information about subcrustal structures. Rayleigh waves at 200 s are sensitive down to about 400 km.

This information illuminates the maps shown in Figures 4 - 6. Space prohibits a detailed analysis, the maps are too rich in detail to discuss all their features here. We mention only a few features from these maps that characterize the types of structures that are constrained by them.

The 30 s Love wave map (most sensitive to shallow structures of the maps presented here) displays low velocity features at the major sedimentary depressions on the continent (e.g., Tarim Basin, Ganges Fan, Caspian and Black Sea Depressions, Barents Sea Depression, sediments in the Persian Gulf and Western Siberia). This map together with shorter period Rayleigh and Love wave maps will allow us resolve crustal from uppermost mantle structures in a way that longer period dispersion studies are incapable.

The 30 s Rayleigh wave samples the lithosphere similarly to the 50 s Love wave, being affected principally by crustal thickness and the integrated shear wave velocity in the crust. Their group velocity maps are consequently quite similar. The 50 s Rayleigh wave is most sensitive to crustal thickness and its group velocity map exhibits a strong correlation with surface tomography: continental roots create group velocity lows. This is particularly true in Central Asia and in the Middle East (e.g., Tibet, the Altai Range of western Mongolia, the Hindu Kush, and the Zagros Mountains in western Iran). At 100 s period, the Archaean shields reveal themselves clearly as

continental roots.

The resolving power of this study is well demonstrated by inspecting the features of the group velocity maps in the Far East. The 'island arc' chain comprising Kamchatka, Japan, the Ryukus, and Taiwan is represented as a string of low velocity features at 30 and 50 s periods for both Rayleigh and Love waves. The back arc seas are seen as high velocity regions most clearly on the 30 s maps. On the 100 s Rayleigh wave map, however, the low velocities have shifted toward the back arc, presumably revealing a hot upper mantle continent-ward of the island arc. The ability to resolve island arcs from back arc seas is characteristic of the resolution of this study, $\sim$ 500 km in many regions. Resolving power is considerably degraded in regions of large-scale structures that radically perturb ray paths, such as Tibet.

CONCLUSIONS AND RECOMMENDATIONS

This broad band surface wave dispersion study is important for three main reasons:

- Group velocity maps such as those presented here can be used to test emerging models. For example, Figure 7 presents accumulated continent-wide rms-misfit to the observed group velocity measurements of predictions from two recent global models (S12_WM13 of Su *et al.*, 1994; the combination of Crust 5.0 of Mooney *et al.*, 1996 with S16B30 of Masters *et al.*, 1996).
- A better shear wave lithospheric model under Eurasia is now being constructed. This model should prove useful to help improve location capabilities across the continent.
- This model should also form the basis for more detailed regional studies across the continent.

In the future, resolution can be improved further in three fruitful ways.

- Path corrections due to lateral refractions and multipathing should be incorporated in studying regions of large-scale significant structures (e.g., Iran, Afghanistan, Pakistan, N. India, W. China).
- Concentrated studies of shorter wave paths from regional events to regional networks should be performed in new areas (e.g., Ritzwoller *et al.*,1996 in Central Asia) where regional networks exist (e.g., Poseidon network in the Far East, GRSN in Europe, NARS in European Russia and the Ukraine, Saudi Arabian network, DoD arrays around Eurasia, PASSCAL deployments such as those in Tibet, near Baikal, and so forth).
- Multiple station studies that measure dispersion differences between stations can also be applied to yield sharper focus in regions with good regional instrumentation.

REFERENCES

Masters, G., S. Johnson, G. Laske, and H. Bolton, A shear wave model of the mantle, *Phil. Trans. Roy. Soc. Lond.*, in press, 1996.

Mooney, W.D., G. Laske, and G. Masters, CRUST 5.0: A global crustal model at 5 degrees by 5 degrees, submitted to *J. Geophys. Res.*, 1996.

Ritzwoller, M. H., A. L. Levshin, S. S. Smith, and C. S. Lee, Making accurate continental broadband surface wave measurements. *Proceedings of the 17th Seismic Research Symposium on Monitoring a Comprehensive Ban Treaty*, Phillips Laboratory, Scottsdale, AZ, 482-491, PL-TR-95-2108, Sept., 1995.

Ritzwoller, M. H., A. L. Levshin, L.I. Ratnikova, and D.M. Tremblay, High resolution group velocity variations across Central Asia, this volume, 1996.

Su, W.-J., R. L. Woodward, and A. M. Dziewonski, Degree-12 model of shear velocity heterogeneity in the mantle, *J. Geophys. Res.*, **99**, 6945-6980, 1994.

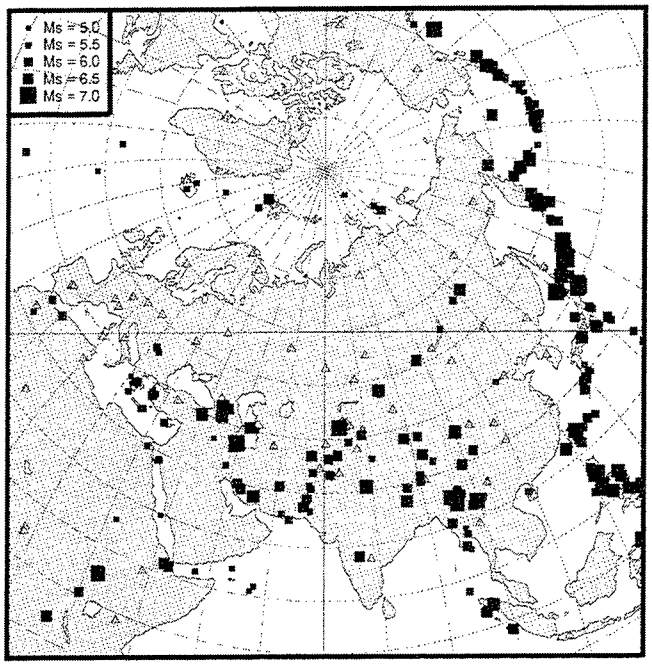

Figure 1. Distribution of sources (squares) and receivers from GSN, MEDNET, GEOSCOPE, KNET & KAZNET (triangles) used in the surface wave studies of Eurasia.

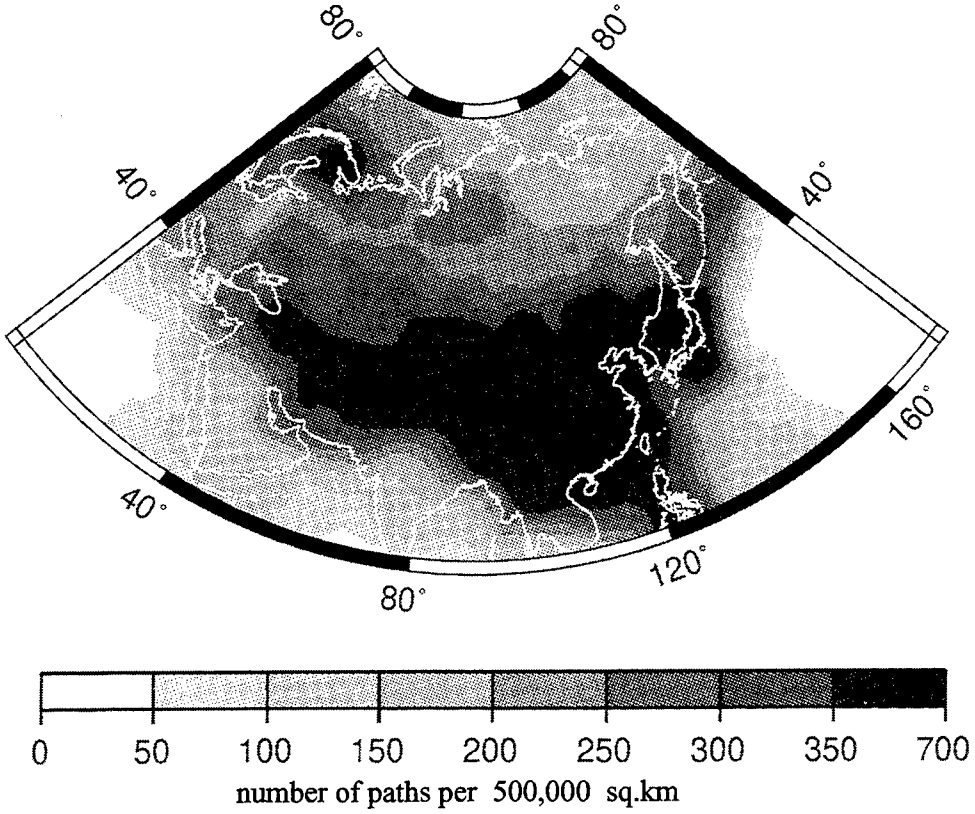

Figure 2. Density of Rayleigh wave paths crossing Eurasia, T =50 s.

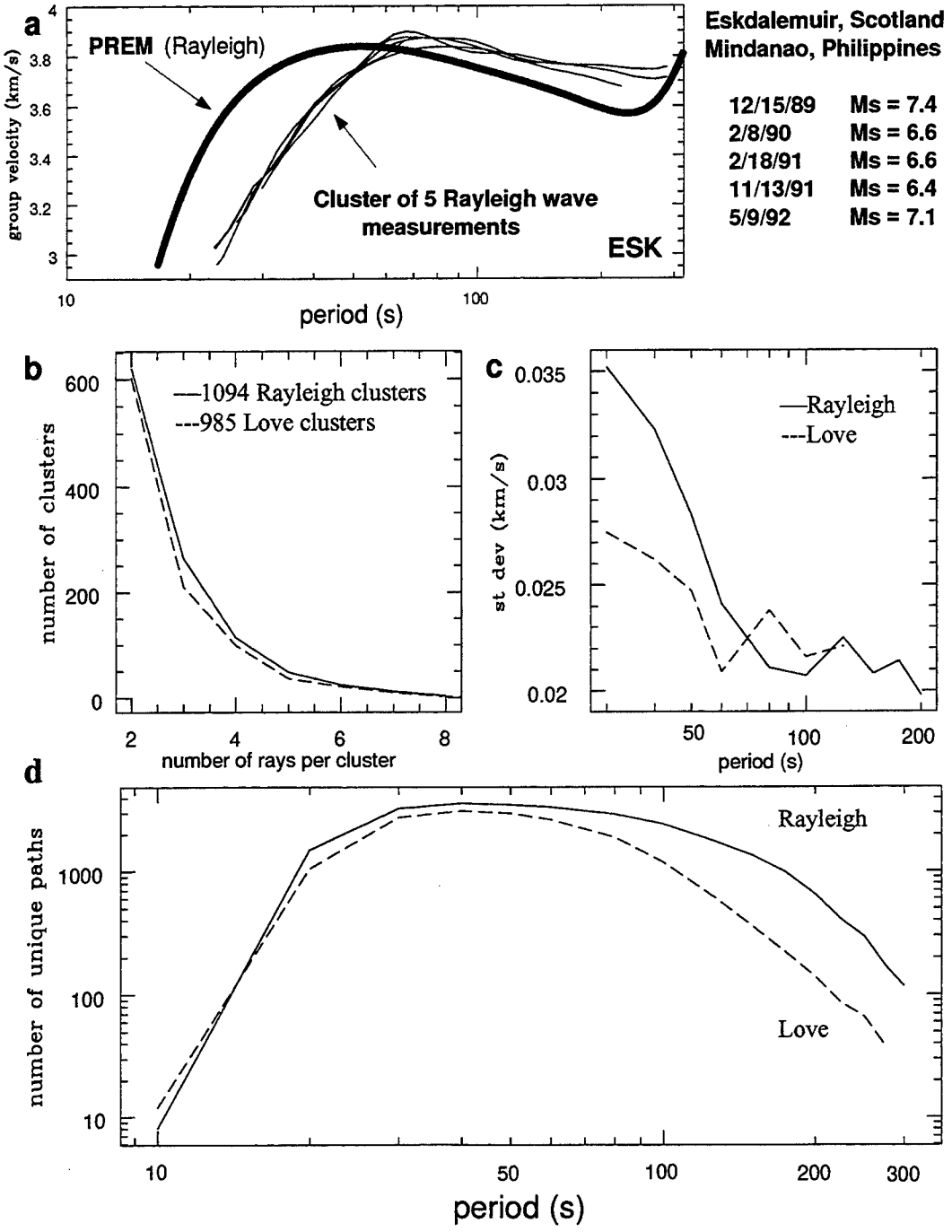

Figure 3. Cluster analysis. (a) Example of clustering for 5 events near Mindanao, Philippines, recorded at ESK, Scotland. (b)-(d) Results of cluster analysis.

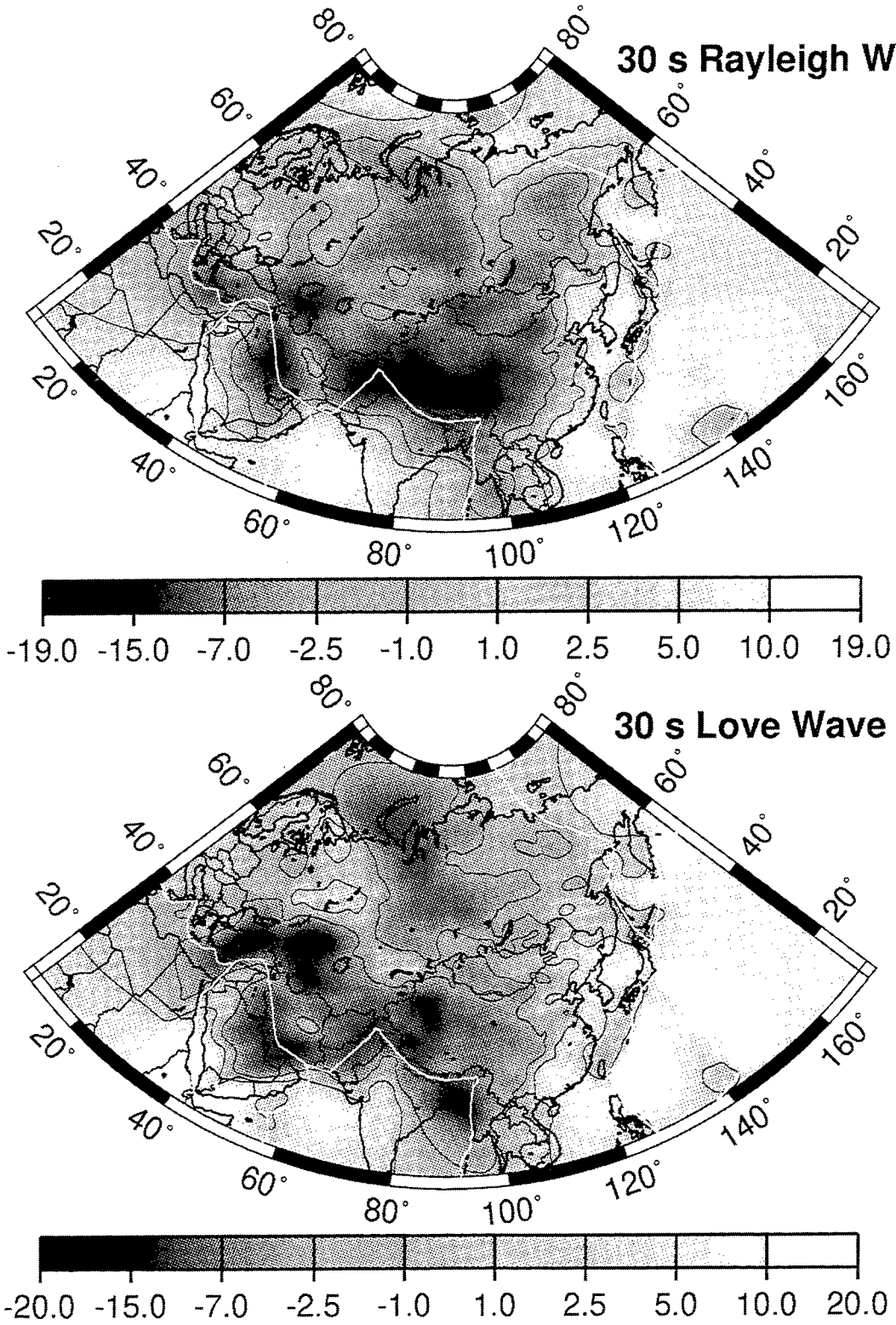

Figure 4. Rayleigh and Love wave group velocity maps at 30 s period. Units are percent deviation from the map average. The positive and negative 2.5% contours are drawn to highlight the regions of significant deviation from the map average.

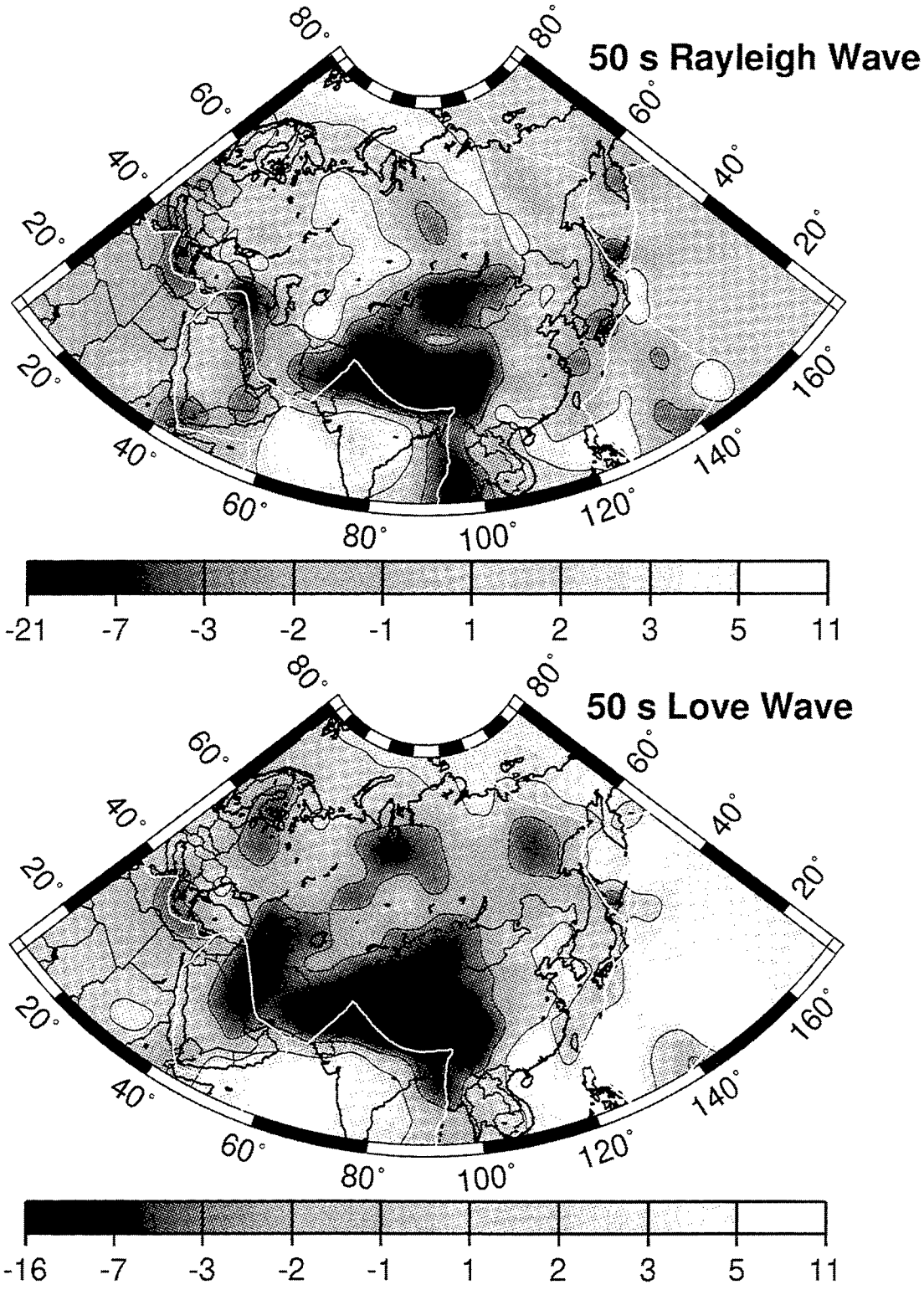

Figure 5. Rayleigh and Love wave group velocity maps at 50 s period. Units are percent deviation from the map average. The positive and negative 2.5% contours are drawn to highlight the regions of significant deviation from the map average.

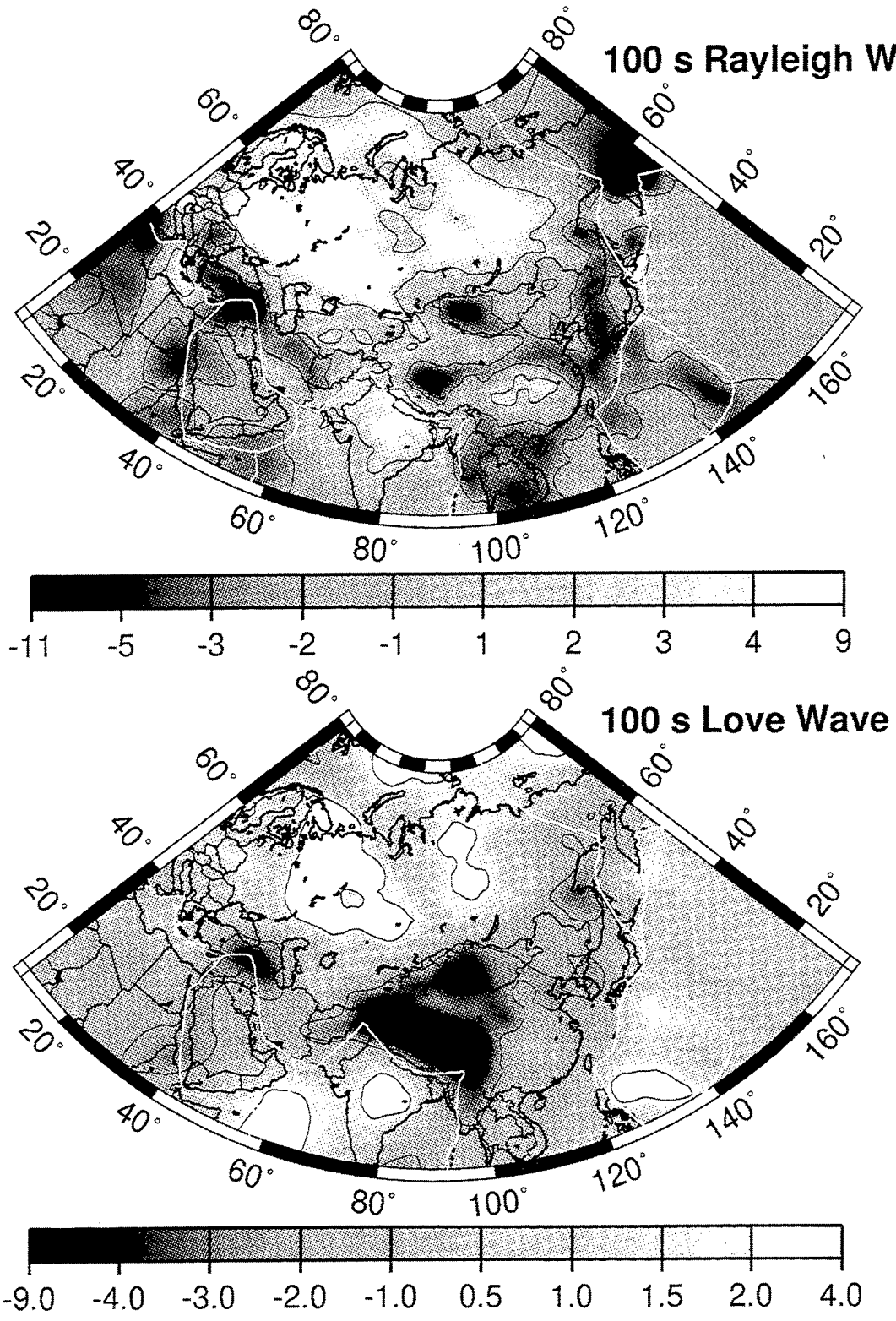

Figure 6. Rayleigh and Love wave group velocity maps at 100 s period. Units are percent deviation from the map average. The positive and negative 2% contours are drawn to highlight the regions of significant deviation from the map average.

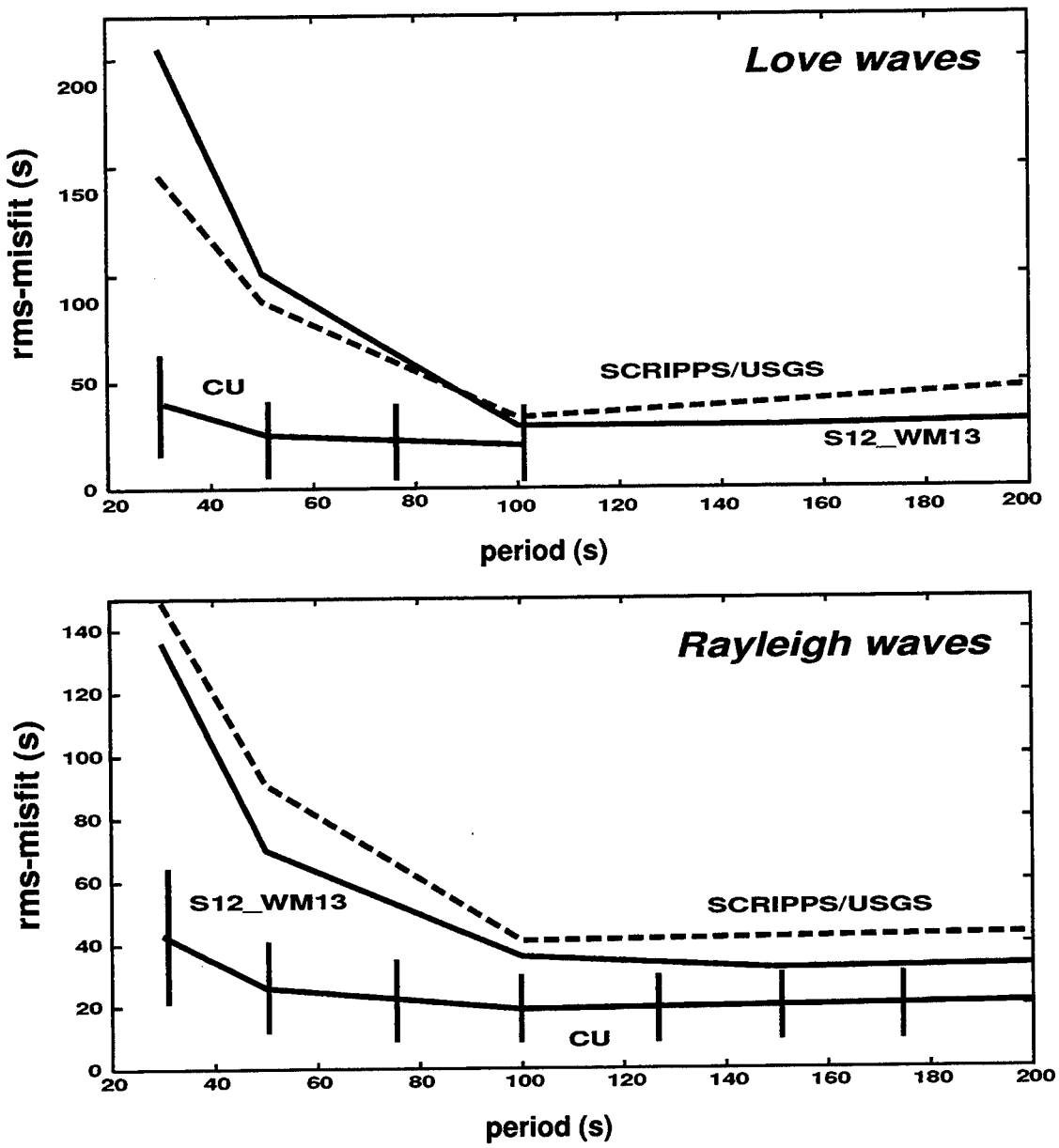

Figure 7. Total accumulated RMS-misfit over all paths between observed and predicted group times. Error bars for our measurements (CU) result from the cluster analysis and are centered at the misfit between observations and predictions from our group velocity maps. Misfit from two global models, S12_WM13 of Su *et al.* (1994) and the Scripps/USGS models S16B30/CRUST 5.0 of Mooney *et al.* (1996) and Masters *et al.* (1996), is also shown. The global models misfit the measurements significantly below about 100 s period where sensitivity is greatest to crustal structure and Moho topography.

Regional Characterization of Western China - II

G.E. Randall, H.E. Hartse, W.S. Phillips, and S.R. Taylor,
Geophysics Group EES-3, Los Alamos National Laboratory

Sponsored by the U.S. Department of Energy, Contract W-7405-ENG-36
Comprehensive Test Ban Treaty Research and Development Program, ST482A

ABSTRACT

As part of the CTBT Research and Development regional characterization effort, geological, geophysical, and seismic data are being assembled and organized for inclusion in a knowledge base for China. We have continued our analysis using data from the station WMQ of the Chinese Digital Seismic Network (CDSN) and the IRIS station AAK. We are also acquiring and analyzing data from stations that are designated as (or near a designated) primary or secondary CTBT monitoring station including MAK, KURK, NVS, TLG, NIL, LSA, TLY, ULN, HIA, MDJ, LZH, XAN, ENH, and KMI. Additional stations will be included as time permits. Regional seismograms are being analyzed to construct travel time curves, velocity models, attenuation characteristics, and to quantify regional propagation effects such as phase blockages. Using locations from the USGS Preliminary Determination of Epicenters (PDE) we have identified Pn, Pg, Sn, and Lg phases, constructed travel time curves, and estimated apparent velocities using linear regression. Amplitudes for the seismic phases have been measured using bandpassed waveforms and a series of magnitude relations have been determined for Western China. We have computed detection thresholds for the phases Pn, Pg, Sn, and Lg at WMQ for the frequency bands 1-2 Hz and 4-8 Hz out to 1200 km. Studies of path specific propagation efficiency of the seismic phases have mapped blockages and also identified a possible set of observations that can be used to identify intermediate depth (> 100 km) seismic events in the Pamir-Hindu Kush seismic zone. Chinese seismicity catalogs from the USGS and Chinese State Seismological Bureau (SSB) are being used to identify and obtain seismic data (including mine seismicity) and information for lower magnitude events. Clustering analysis has been used to identify seismicity clusters in space with origin times that are distributed during daylight hours which suggest mining operations. These clusters are being investigated with imagery to attempt to identify precise mine locations.

Key Words: regional seismic characterization, China

OBJECTIVE

We are continuing characterization of the regional excitation and propagation of seismic waves in Western China with sufficient accuracy to explain observed seismic data, and to detect, locate, and discriminate seismic events for the verification of a Comprehensive Test Ban Treaty (CTBT). Our primary source of seismic data for the initial effort has been the stations of the Chinese Digital Seismic Network (CDSN) and IRIS stations. Using seismic waveforms and event locations from the USGS PDE and Chinese seismicity catalogs, we have identified Pn, Pg, Sn, Lg, Love and Rayleigh phases and picked arrival times and amplitudes for the body waves. Analysis of these arrival times will provide travel time and travel time corrections for large well located to improve regional location. Amplitudes are analyzed to calibrate magnitude scales and for use in discrimination research.

RESEARCH ACCOMPLISHED

Seismicity Data (Natural, Explosion and Cultural combined): We have initially used the USGS Preliminary Determination of Epicenters for identifying the seismicity of Western China. For more detailed seismicity with a lower magnitude threshold we have obtained contemporary seismicity catalogs for China. We have recently seen the first results of the translation and tabulation of a more recent set of Chinese seismicity catalogs (1990-1994) for Western China which will allow us to search for waveforms for more recent events too small to be included in the PDE .

Seismic Clusters, Mines?: Figure 1 shows events that are clustered in both space and time. The spatial clustering can be indicative of natural phenomena but the requirement that the events also be clustered in time leads to a presumption of man made events. The small circled cluster on the Russian border is near a known mine. We are identifying possible mine blasts in the Chinese seismicity catalogs using cluster analysis; we searched for spatially clustered epicentral locations in the Chinese seismicity catalog from 1973 through 1989 containing magnitudes as low as 2.0. The clustering required each event to be within 10 km of a minimum of 10 other events. We then examined time-of-day (GMT) histograms of each cluster for unusual behavior. In the circled cluster, all events (over 10 years) occurred in an 8-hour time range, indicating possible, man-made origin. The cluster is within 20 km of Druzhba, a known Russian mining area. We are currently searching for overhead images to confirm and pinpoint the mine location. We will use the same cluster analysis on the more recent Chinese catalogs. Events that are confirmed as mine blasts can be used for discriminant calibration and reference waveforms.

Magnitude Scale Calibration: Figure 2a shows a magnitude scale based on linear regression of measured amplitudes for Lg phase measured at WMQ for distances ranging from about 330 km to 1000 km. Magnitude is an important, decision making parameter and we need an estimate that is tied to a broadly used magnitude scale, such as teleseismic mb. The Chinese magnitudes are unreliable, which can be seen by comparing with mb for larger (>3.8) events. Figure 2a illustrates our method using broad-band vertical Lg phase bandpassed from 1-2 Hz. We find a least-squares fit to PDE mb ($3.8<mb<6.2$) using the formula mb = log(amplitude) + a + b log(distance) for rms amplitude in nanometers/sec and distance km for events with signal-to-(pre-Pn)noise > 10. In Figure 2b we show a comparison of magnitude estimates using phases Pn, Pg, Sn, and Lg in each of 4 frequency passbands, showing the residual variance of the regression estimate. Pg, Lg and Sn

are all nearly equivalent. The percentage of observed seismic data with S/N > 10 in the 4 frequency passbands is also shown. The second figure summarizes fits for Pn, Pg, Sn and Lg, for four, octave-width, frequency bands. The best band is 1-2 Hz, best phases Sn and Lg with Pg not far behind. The mb residuals for different phases and bands are positively correlated, indicating little improvement to mb estimates are possible by combining information.

Propagation Effects: Figure: 3a shows Lg phase propagation efficiency to station AAK. The region south of AAK shows closely spaced events that show some efficient and some poor propagation of Lg to AAK. The distance range seems too short to be a structural effect. The region also includes some intermediate depth (>100km) seismicity so the problem may be a source effect, not a structural blockage of energy. The phase transmission maps are obtained by comparing the rms amplitude of the phase with the rms amplitude of a "pre-phase noise window". The noise window is generally 10-20 seconds long and sits just before the start of the actual phase window. In Figure 3b we show a seismogram comparison of an event with efficient Lg propagation to AAK with a nearby event with poor Lg propagation to AAK. Traces are short period vertical, long period vertical, and long period tangential in each case. On the left the Lg is observed on the short period vertical as well as surface waves on the long period components. On the right the Lg is not observed on the short period vertical and surface waves are not observed on either long period component. The event on the right is probably an intermediate depth event with negligible surface wave excitation, and is difficult to classify with many discriminants. Events in this region have been analyzed (Mellors et al. 1995, Pavlis and Hamburger. 1991) and the existence of intermediate depth events is well established. PDE bulletins generally list depths for many of these small events at 33 km, which is unreliable. We need to find useful ways to characterize the intermediate depth events such as the possible lack of both Rayleigh and Love waves. Propagation effects must be carefully distinguished from source effects. We are also following the results of other groups (Hearn and Ni 1996, McNamara et al. 1995, and McNamara et al. 1996) that are also characterizing regional wave propagation in Western China.

Detection Threshold Analysis: Recent work has shown the effectiveness of various regional discriminants in western China such as P_g/L_g in different frequency bands (Hartse *et al.*, 1996). Given this information, it is important to have a knowledge of detection thresholds for the different regional phases used for discrimination as a function of frequency. We have computed detection thresholds for the phases P_n, P_g, S_n, and L_g at the Chinese Digital Seismic Station (CDSN) station WMQ for the frequency bands 1-2 and 4-8 Hz. As described by Hartse *et al.*, (1996), signal and noise measurements were made for the above-mentioned regional phases from 289 presumed earthquakes recorded at WMQ. Event locations and magnitudes were obtained from both the United States Geological Survey Preliminary Determination of Epicenters (USGS/PDE) catalogs maintained at the Incorporated Research Institutions in Seismology Data Management Center (IRIS DMC) and the Chinese State Seismological Bureau (SSB) for 1988-1989. We are uncertain as to how the magnitudes in the SSB catalogs were calculated. If it is found in subsequent studies that there is a significant offset between worldwide m_b and the magnitudes from the SSB catalog, the calculated detection thresholds will be biased. The distances ranged from less than 100 to about 1200 km and magnitudes ranged from approximately 2.5 to 6.0. In this study, we use peak-to-peak measurements for P_n and RMS measurements for P_g, S_n, and L_g (Hartse, 1995). In computing signal-to-noise ratios (S/N), we use pre-P_n noise measurements (peak-to-peak for P_n S/N and RMS for P_g, S_n, and L_g S/N).

In estimating detection thresholds, we follow the basic technique outlined by Sereno and Bratt (1989). Details are given in (Taylor and Hartse, 1996). Figure 4 shows the 90% detection thresholds for earthquakes recorded at WMQ for the phases P_n, P_g, S_n, and L_g in the 1-2 and 4-8

Hz bands. At a range of 1000 km, the 90% detection threshold for the 4-8 Hz band ranges from 0.4 to 1 magnitude unit greater than the 1-2 Hz band depending on the phase. This, of course, has implications for seismic discriminants such as the P_g/L_g ratio that generally perform better at higher frequencies (e.g. Taylor, 1995; Hartse *et al.,* 1996). The S/N ratios for the P_g/L_g discriminant will be much better in the 1-2 Hz band than the 4-8 Hz band, but the discrimination performance in the 1-2 Hz band is reduced relative to the 4-8 Hz band. At a range of 1000 km we can only expect to be able to construct P_g/L_g discriminants down to a magnitude of approximately 3.5 to 3.8 at 1-2 Hz and 4.5 at 6-8 Hz.

RECOMMENDATIONS AND FUTURE PLANS

We will continue the assembly of regional information, and begin the validation of models by comparing synthetics with real data. Waveform modeling for seismic source and event depth characterization will be attempted. We will continue the collaboration with the discrimination efforts to identify propagation issues and details relevant to discrimination, obtain smaller events identified from regional seismicity catalogs, and mining related events identified from correlation of catalogs with mining. Results we be organized in a form suitable for use by AFTAC in their routine processing and special event studies.

REFERENCES

Hartse, H.E., S.R. Taylor, W.S. Phillips, and G.E. Randall, Regional event discrimination in central Asia with emphasis on western China, *Los Alamos National Laboratory, Los Alamos, NM*, LAUR-96-2002, 45pp, submitted to *Bull. Seism. Soc. Am.*, 1996.

Hearn, T.M., and J.F. Ni, Uppermost mantle structure in Southern Eurasia from Pn tomography and Sn attenuation, AFOSR Final Report, 58 p., 1996.

McNamara, D.E., T.J. Owens, and W.R. Walter, Observation of regional phase propagation across the Tibetan Plateau, *J. Geophys. Res.,* 100, 22,215-22,229, 1995

McNamara, D.E., W.R. Walter, T.J. Owens, and C.J. Ammon, Upper mantle velocity structure beneath the Tibetan Plateau from Pn travel time tomography, *J. Geophys. Res.,* in press,1996

Mellors,RJ, G.L. Pavlis, M.W. Hamburger, and HJ. Al-Shukri, Evidence for a high velocity slab associated with the Hindu Kush seismic zone, *J. Geophys. Res.*, 100, 4067-4078, 1995.

Pavlis, G.L. and M.W. Hamburger, Aftershock sequences of intermediate depth earthquakes in the Pamir-Hindu Kush seismic zone, *J. Geophys. Res.*, 96, 18107-18117, 1991.

Sereno, T.J. and S.R. Bratt, Seismic detection capability at NORESS and implications for the detection threshold of a hypothetical network in the Soviet Union, *J. Geophys. Res.*, 94, 10,397-10,414, 1989.

Taylor, S.R. and H.E Hartse, Regional phase seismic detection thresholds at WMQ, *Los Alamos National Laboratory, Los Alamos, NM*, LAUR-96-395, 7pp, 1996.

Taylor, S.R., Analysis of high-frequency P_g/L_g ratios from NTS explosions and western U.S. earthquakes, *Los Alamos National Laboratory, Los Alamos, NM*, LAUR-95-3142, submitted to *Bull. Seism. Soc. Am.*, 1995.

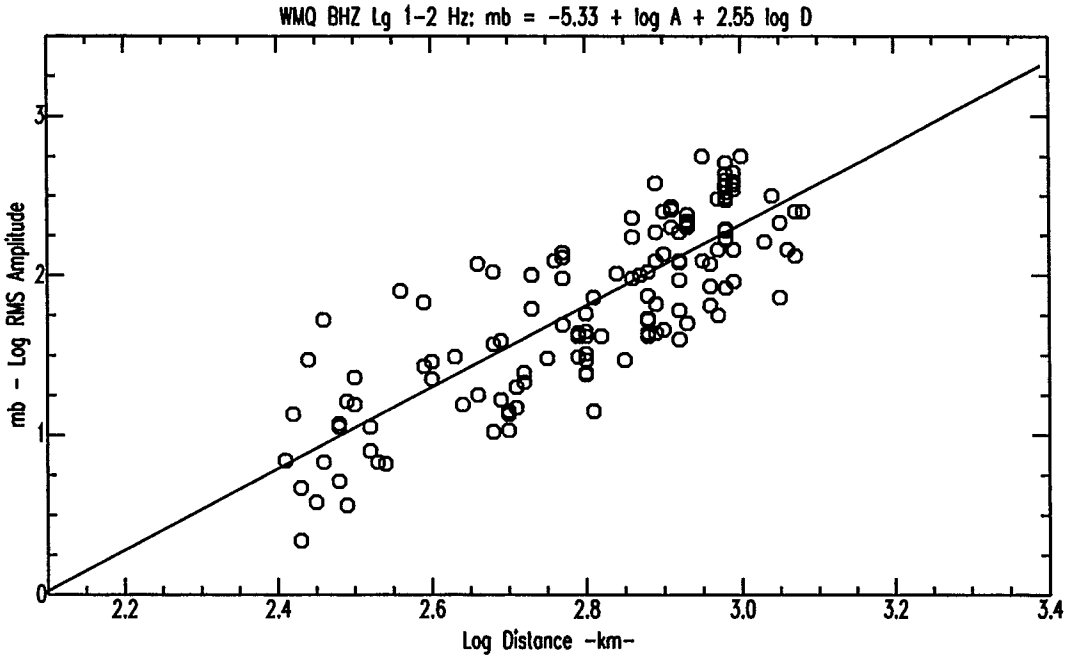

(a)

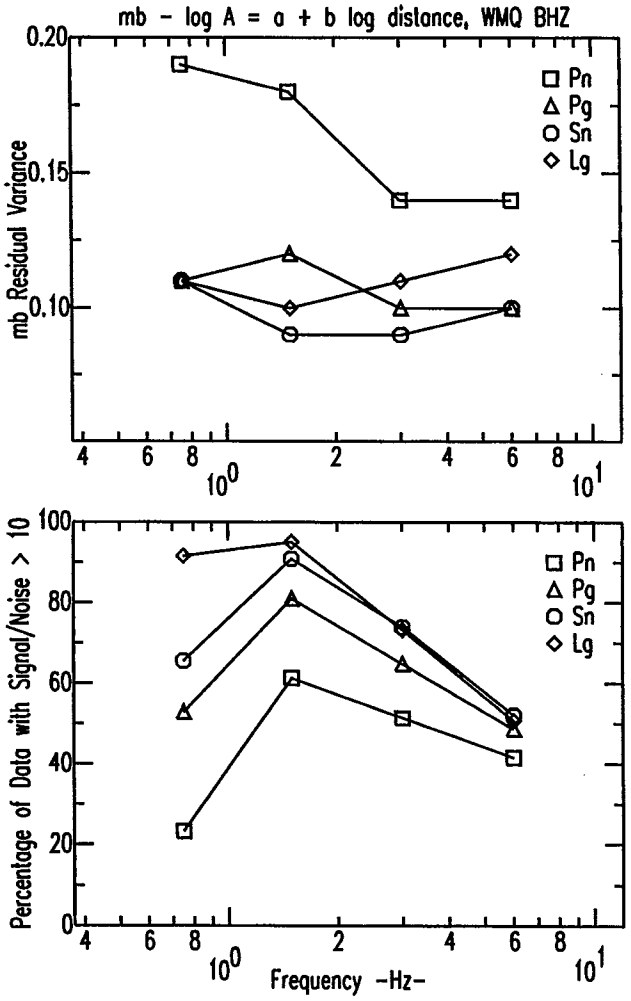

(b)

Figure 2. Results of a linear regression to calibrate a magnitude scale are shown in part a using Lg phase. In part b the results for the phases Pn, Pg, Sn, and Lg are shown for 4 passbands. Both the variance of the residual mb after claibration and the percentage of events that pass a signal to noise ratio test are shown.

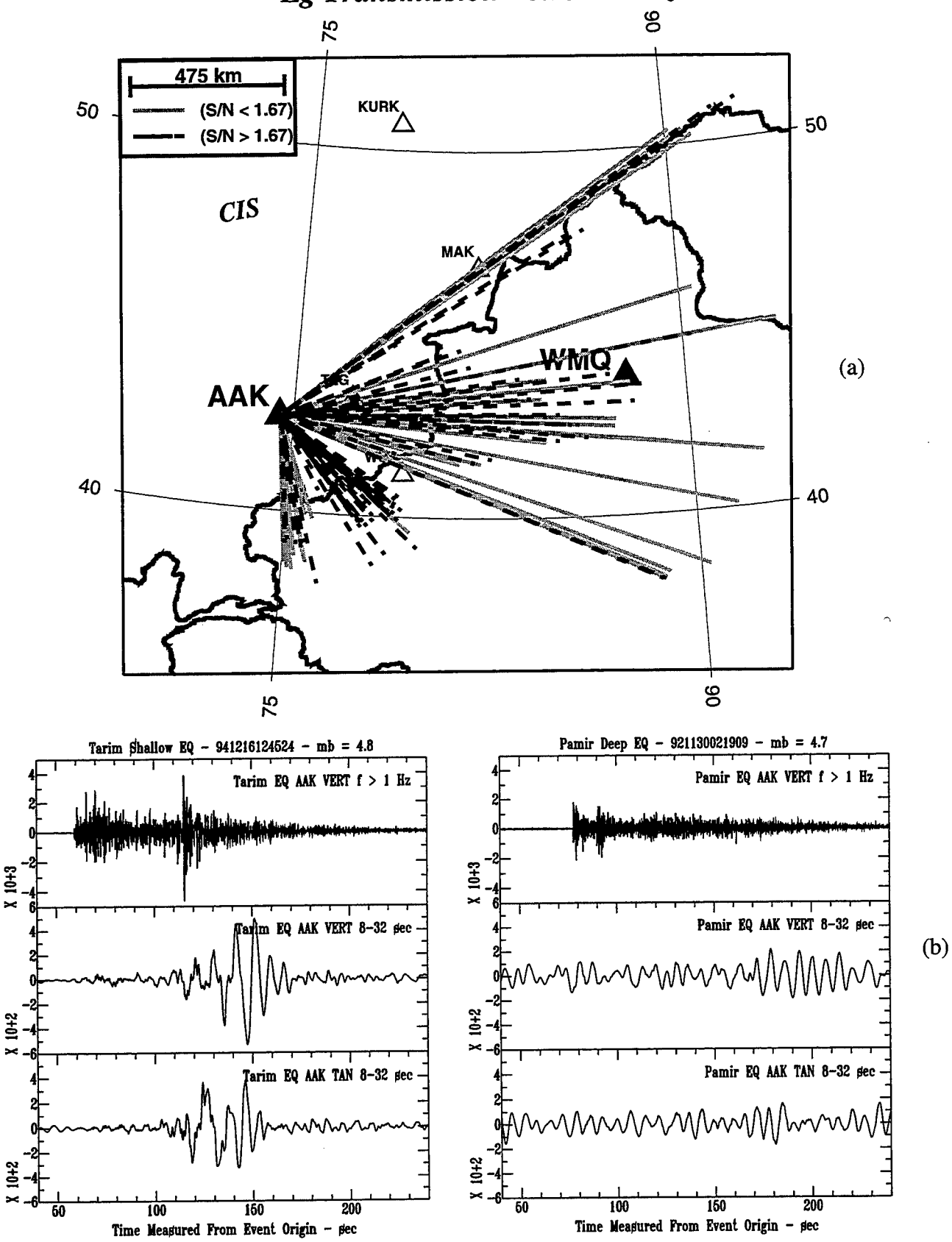

Figure 3. In part a, the map shows paths with strong and weak Lg propagation observed at station AAK. Paths to the south of AAK show both strong and weak Lg in a small region, suggesting that the change is too abrupt to be a path effect. In part b the short period vertical and long period vertical and tangential waveforms show no surface wave excitation with poor Lg, suggesting a deep source.

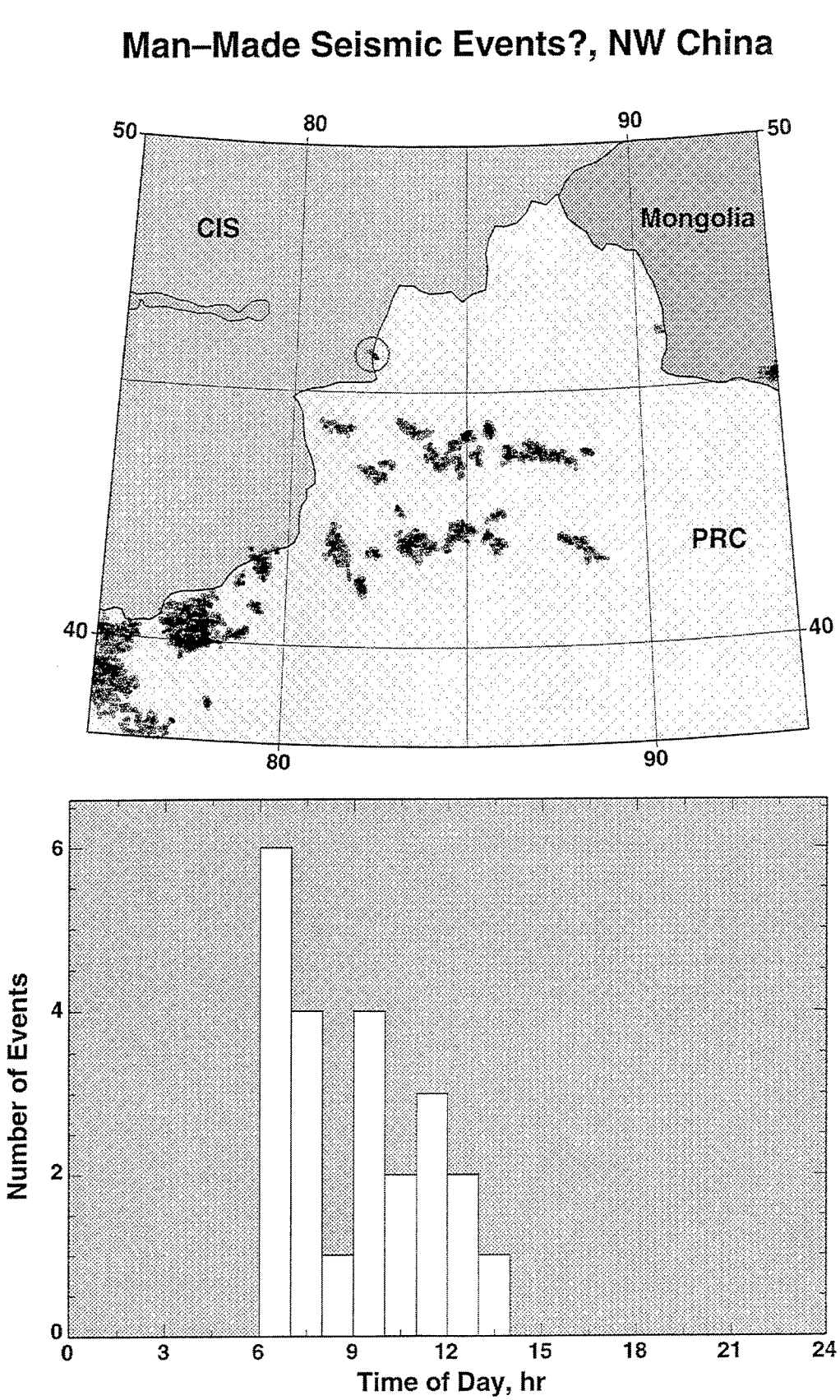

Figure 1. Map shows spatial clusters of seismicity for events from Chinese seismicity catalogs. The circled cluster on the Chinese border has a distinctive temporal clustering that suggested the events are mine blasts. We are trying to confirm this with overhead imagery and obtain a precise location.

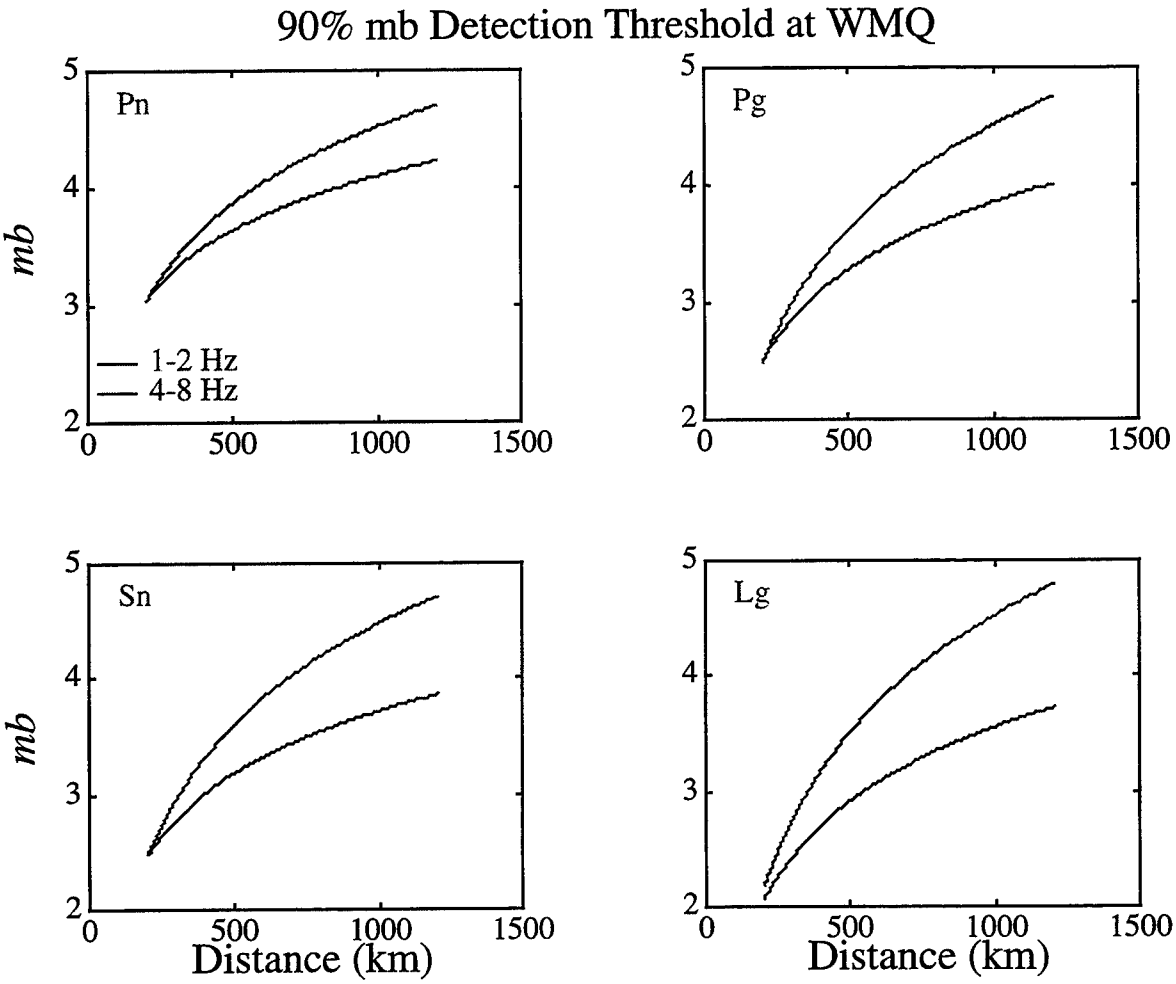

Figure 4. 90% detection thresholds for earthquakes recorded at WMQ for the phases Pn, Pg, Sn, and Lg in the 1-2 and 4-8 Hz bands.

Sn and Lg Propagation Characteristics beneath China

Richard Rapine, Thomas Hearn, Jianxin Wu, and James Ni
Department of Physics, New Mexico State University, Las Cruces, NM, 88003
Grant numbers: F19628-95-K-0009(DOE), F49620-93-1-0429 and F49620-94-1-0310 (AFOSR)
Sponsored by DOE and AFOSR

ABSTRACT

Continued mapping of Sn and Lg wave propagation efficiencies in China shows broad regions of Sn and Lg attenuation. Sn propagates efficiently across the Himalayas and the Tarim Basin, but not across most of Tibet. Other regions of Sn blockage are the Mongolian Plateau, the Baikal Rift, and the Pan-Xi Rift in southwestern China and Burma. Sn is also blocked for paths crossing the back-arc basin of the Japan Sea or the back-arc of the Ryukyu arc in the East China Sea. The association of Sn blockage with continental rifts and back-arc regions suggests that the blockage is due to the presence of partial melt in the uppermost mantle. Sn blockage in central and northern Tibet and the Mongolian Plateau probably is also due to mantle partial melt. Support for melt beneath these plateaus comes from Cenozoic volcanism in both plateaus and low Pn velocities. Lg propagates throughout most of China including the Mongolian Plateau, Baikal Rift, the continental shelf, and eastern China. Lg is blocked at the major tectonic boundaries of the Tibet Plateau as well as at the continental margin. Specific features blocking Lg are the Sea of Japan and the Himalaya Mountains. The Himalayas attenuate Lg for raypaths parallel to the mountain range, but paths perpendicular to the mountains often allow Lg to propagate through. Lg attenuation coefficients in western China are calculated for different regions using data recorded by five broadband stations of the CDSN (CHTO, LSA, LZH, KMI, WMQ). The average attenuation coefficient is 0.006 km^{-1} corresponding to a very low Q value of 150. Lg attenuation is especially strong beneath Burma and Tibet. Both regions are geothermally active and contain partial melt in the crust. While Sn is a difficult phase to use for nuclear monitoring in most of China, Lg is very useful. Even in the Tibet Plateau Lg can be monitored for short raypaths provided that stations are sited within the Plateau.

KEY WORDS: China, Sn, Lg, attenuation, Burma, Tibet.

OBJECTIVES

Regional nuclear discrimination often depends on the regional Sn and Lg waveforms; however, for many tectonic regions these waves are not present or are highly attenuated. It is therefore essential to understand the regional characteristics of these waves. In this study we map the propagation characteristics of the Sn and Lg waves in China through the visual inspection of thousands of seismograms recorded on the Chinese Digital Seismograph Network (CDSN) (Figure 1). Attenuation in the crust is further studied for western China by the direct estimation of Lg Q for raypaths to five CDSN stations.

RESEARCH ACCOMPLISHED

Sn and Lg Propagation Characteristics

For Sn and Lg propagation efficiency measurements we used only event-station paths for which good three-component waveform data were available. All data were previewed for large signal to noise ratios and all components were filtered with a two-pole, two-pass Butterworth filter with passband 0.5-5.0 Hz. The following group velocity windows were used to isolate each phase: P-wave (Pn and Pg) 8.0 km/s - 5.0 km/s; Sn 4.6 km/s - 4.1 km/s; and Lg 3.6 km/s - 3.0 km/s. Errors in some event locations and/or depths required manual picking of these windows. Sn observations were restricted to the distance range 200-2600 km and Lg observations were restricted to the distance range of 200-3000 km. Once each phase was isolated, we computed the mean and absolute maximum values for the envelope of each phase: P-wave amplitudes on the vertical component, Sn amplitudes on the transverse component, and Lg amplitudes on the vertical component. Amplitude ratios of the mean values of the Sn and Lg amplitudes to the mean P-wave amplitudes were then determined.

Amplitude ratios proved to be helpful for quantitatively assessing Lg propagation, however Sn propagation was difficult to assess purely by amplitude ratios. Thus, we subjectively ranked both Sn and Lg propagation (similar to previous studies with WWSSN and digital data, e.g. Kadinsky-Cade et al, 1981; Ni & Barazangi, 1983; Rodgers et al., 1996). We used three categories: "efficient", "inefficient" and "not observed". For Sn, "efficient" propagation means that Sn is clearly observed as a group of waves arriving with group velocity of 4.5 km/s on the transverse component seismogram as a distinct arrival above the noise. Sn/P amplitude ratios were usually greater than 1.0 for efficient Sn paths, but were sometimes as low as 0.5. "Efficient" Sn is often emergent on continental paths and impulsive on oceanic paths. "Inefficient" Sn propagation means that Sn is detectable by the analyst as an emergent arrival within the specified group velocity window, sometimes accompanied by a shift to lower frequencies. Amplitude ratios for inefficient Sn propagation are scattered between 0.5-1.0. If Sn was not distinguishable from P-wave coda, then we classified the path as Sn "not observed". Similar classifications are used for Lg propagation. "Efficient" Lg propagation means that Lg is clearly observed on vertical and transverse component seismograms with Lg/P amplitude ratios greater than 1.5. "Inefficient" Lg propagation means that Lg was observed on vertical and transverse component seismograms, but weak. Lg/P amplitude ratios for "inefficient" Lg propagation are about 1.0. Lg is classified as "not observed" when Lg/P ratios were less than 0.5.

Composite maps showing regions of efficient, inefficient, and not observed Sn and Lg wave propagation are in Figures 2. Sn propagates efficiently across the Himalayas to station LSA, Lhasa, Tibet. In contrast, Sn does not propagate through a large portion of central and northern

Tibet. Sn is observed from crustal events originating in the western Himalayas, the Pamirs, and the Tien Shan to station WMQ, Urumqui, western China. Sn paths crossing the Tarim Basin to WMQ are all efficient. A few paths from eastern Tibet to WMQ show efficient Sn propagation, but the majority of events in Tibet do not show Sn. The zone of Sn blockage in central and northern Tibet corresponds to a region of lower Pn velocity (~7.9 km/s) (Zhao and Xie, 1993; McNamara et al., 1996) and suggests that a small amount(<1%) of partial melt could exist there, possibly analogous with the mantle beneath the Turkish-Iranian Plateau or the Basin and Range Province. Neither the Baikal Rift nor the Pan-Xi Rift of Burma allow Sn propagation. Presumably, partial melt associated with rifting causes the Sn attenuation there. Most, but not all, oceanic paths also block Sn. For paths crossing the Sea of Japan or the Ryukyu back-arc of the East China Sea, mantle melt associated with back-arc spreading causes the attenuation. Blockage of Sn by the Mongolian Plateau suggests that partial melt may also exist in the uppermost mantle there.

Lg propagates efficiently for most of China except across the edges of the Tibetan Plateau and the continental margin. Regions of efficient Lg propagation include Mongolia, the Tien Shan Mountains, the Baikal Rift, and the Tarim Basin. Lg does not propagate efficiently across the Himalayas when the raypath is parallel to the mountain range; however, it is observed for shorter raypaths that originate in the Indian Shield and are perpendicular to the strike of the mountain belt. Events occurring in Burma do not propagate Lg across the Himalayas, but this may be related to the presence of the Pan-Xie Rift in Burma. Within the Tibetan Plateau, Lg is observed only for paths with distances less than about 6 degrees. We also observed that the Indus-Tangpo Suture attenuates the Lg phase. The attenuation is probably due to a partially melted middle crust that lies north of the suture (Kind et al, 1996; Zhao et al., 1996). Lg is not observed for paths crossing the continental margin, particularly those paths crossing subduction zones or the central Sea of Japan. However, many oceanic paths lie entirely on the continental shelf and the continent itself, and these paths do propagate Lg. For example, some paths in the northern Sea of Japan or paths originating near Taiwan recorded on the continent show efficient Lg propagation. Events occurring in subduction zones also show Lg propagation although some attenuation does occur. These observations add to the knowledge of world wide observations of Lg blockage at continental margins and other major tectonic boundaries.

Lg Q Estimates for Western China

Lg attenuation coefficients were measured for five broadband stations of the CDSN (CHTO, LSA, LZH, KMI, WMQ) using the statistical curve fitting method of Herrmann (1980). A each station, only selected backazimuths were used so that specific tectonic regions could be targeted. These regions are: the Tarim Basin (station WMQ), the Tsaidam Basin (station LZH), the Kunming Plateau (station KMI), the Himalaya Mountains (station LSA), and Burma (station CHTO). For analysis, the Lg waveforms were first bandpassed in the 0.5 to 5 Hz frequency range. The rms amplitudes of the data in a moving window of 55 seconds duration were then computed and the maximum of this window in the Lg group velocity window was then defined as the Lg amplitude. Theoretically, Lg amplitudes decay according to the equation

$$A(\Delta) = A_0 \exp(-\gamma\Delta) / \Delta^{1/6} \sin^{1/2} \Delta,$$

where A is the rms amplitude, Δ is the epicentral distance, A_0 is the initial amplitude, and γ is the spatial attenuation coefficient (Ewing et al., 1957). Amplitudes were first normalized to that of a magnitude 5 earthquake according to the formula

$$A = A_{obs} \exp(m_b - 5.0),$$

where A_{obs} is the observed amplitude and m_b is the reported body wave magnitude. For each event amplitude data were then used to estimate the initial amplitude, A_0, and the attenuation coefficient, γ. The attenuation coefficient is then converted to the Q value using the relation $Q = \pi f / (v \gamma)$ assuming a frequency, f, of 1 Hz and a velocity, v, of 3.5 km/s. Attenuation and Q values for each region are tabled below:

Station	Region	Component	γ (km^{-1})	Q
WMQ	Tarim Basin	vertical	0.0030 ± 0.0005	300 ± 50
	135° to 180°	radial	0.0030 ± 0.0007	300 ± 70
		tangential	0.0029 ± 0.0007	310 ± 77
LZH	Tsaidam Basin	vertical	0.0067 ± 0.0009	135 ± 18
	133° to 150°	radial	0.0067 ± 0.0006	134 ± 12
		tangential	0.0063 ± 0.0006	143 ± 14
KMI	Kunming Region	vertical	0.0067 ± 0.0005	134 ± 9
	265° to 287°	radial	0.0065 ± 0.0006	138 ± 13
		tangential	0.0074 ± 0.0006	121 ± 10
LSA	Tsangpo Suture/	vertical	0.0036 ± 0.0008	249 ± 55
	Himalayas	radial	0.0037 ± 0.0006	242 ± 39
	90° to 135°	tangential	0.0043 ± 0.0015	208 ± 72
CHTO	Burma	vertical	0.0106 ± 0.0013	85 ± 10
	210° to 343°	radial	0.0085 ± 0.0010	106 ± 12
		tangential	0.0031 ± 0.0014	289 ± 131

The average Lg attenuation coefficient for western China is 0.006 ± 0.0006 km^{-1} corresponding to a Q of 150 ± 15. This is an exceptionally low Q valued when compared to a Q of 1000 for stable continental paths or even to the Q values of around 250 found for the tectonically active Turkish Iranian Plateau (Wu et al., 1965). There is exceptionally high Lg attenuation beneath station CHTO. Paths to this station cross a hot geothermal region in Burma. There, partial melt within the crust may cause the excessive attenuation. The low Lg Q values beneath the Burma and the Kunming Plateau could similarly be related to partial melt zones that have been recently been found beneath the Tibet Plateau (Kind et al., 1996; Zhao et al., 1996).

CONCLUSIONS AND RECOMMENDATIONS

The Sn phase has difficulty propagating over much of China. This is primarily due to partial melt in the uppermost mantle in regions of rifting and extension such as the Baikal Rift, the Pan-Xi Rift , and the Sea of Japan. Sn is also attenuated beneath the Tibet and Mongolian Plateaus and we believe that this, too, is due to the presence of partial melt in the uppermost mantle. In contrast to Sn, the Lg phase propagates for most of China. Exceptions are for Lg raypaths that cross the edges of the Tibetan Plateau or the oceanic edge of the continetal shelf. This attenuation is due to large changes in the shape of the crustal waveguide at these margins. Some Lg attenuation occurs for raypaths contained within the Tibet Plateau or on the continental shelf, with these paths sometimes exhibiting Lg coda Q values as low as 100. For nuclear monitoring purposes in China, the more widely seen Lg phase is more useful than the Sn, but stations are required in Tibet

to monitor Lg there.

REFERENCES

Ewing, M., M. Jardetzky, and F. Press, *Elastic Waves in Layered Media*, McGraw-Hill, New York.

Herrmann, R., Q estimates using the coda of local earthquakes, *Bull. Seism. Soc. Am.., 70*, 447-468, 1980.

Kadinsky-Cade, K., Barazangi, M., Oliver, J. and Isacks, B., Lateral variations in high-frequency seismic wave propagation at regional distances across the Turkish and Iranian Plateaus, *J. Geophys. Res., 86*, 9377-9396, 1981.

Kind, R., J. Ni, W. Zhao, J. Wu, X. Yuan, L-S. Zhao, E. Sandvol, C. Reese, J. Nabelek, T. Hearn, Results from the INDEPTH-II passive source experiment: Mid-crustal low velocity zone beneath southern Lhasa block, Tibet, submitted to *Science*, 1996.

McNamara, D., W. Walter, T. Owens, and C. Ammon, Upper mantle velocity structure beneath the Tibetan Plateau from Pn travel time tomography, *J. Geophys. Res.*, in press, 1996.

Ni, J. and Barazangi, M., High-frequency seismic wave propagation beneath the Indian Shield, Himalayan Arc, Tibetan Plateau and the surrounding regions: High uppermost mantle velocities and efficient Sn propagation beneath Tibet, *Geophys. J. R. Astro. Soc., 72*, 665-689, 1983.

Rodgers, A., J. Ni, and T. Hearn, Pn, Sn and Lg propagation in the Middle East, submitted to the *Bulletin of the Seismological Society of America*, 1996.

Wu, J., J. Ni, and T. Hearn, Lg wave attenuation and propagation characteristics in Iran, in *Monitoring a Comprehensive Test Ban Treaty*, NATO ASI Volume, Eds., E. Husebye and A. Dainty, 655-662, Kluwer Academic Publishers, 1996.

Zhao, L-S, M. Sen, P. Stoffa, and C. Frolich, Application of very fast simulated anealing to the determination of the crustal structure beneath Tibet, Geophy. J. Int., 125, 355-370, 1996.

Zhao, L-S. and J. Xie, Lateral variations of the compressional velocity strcuture beneath the Tibetan Plateau from Pn travel-time invesrison, Geophys. J. Int., 115, 1070-1084, 1993.

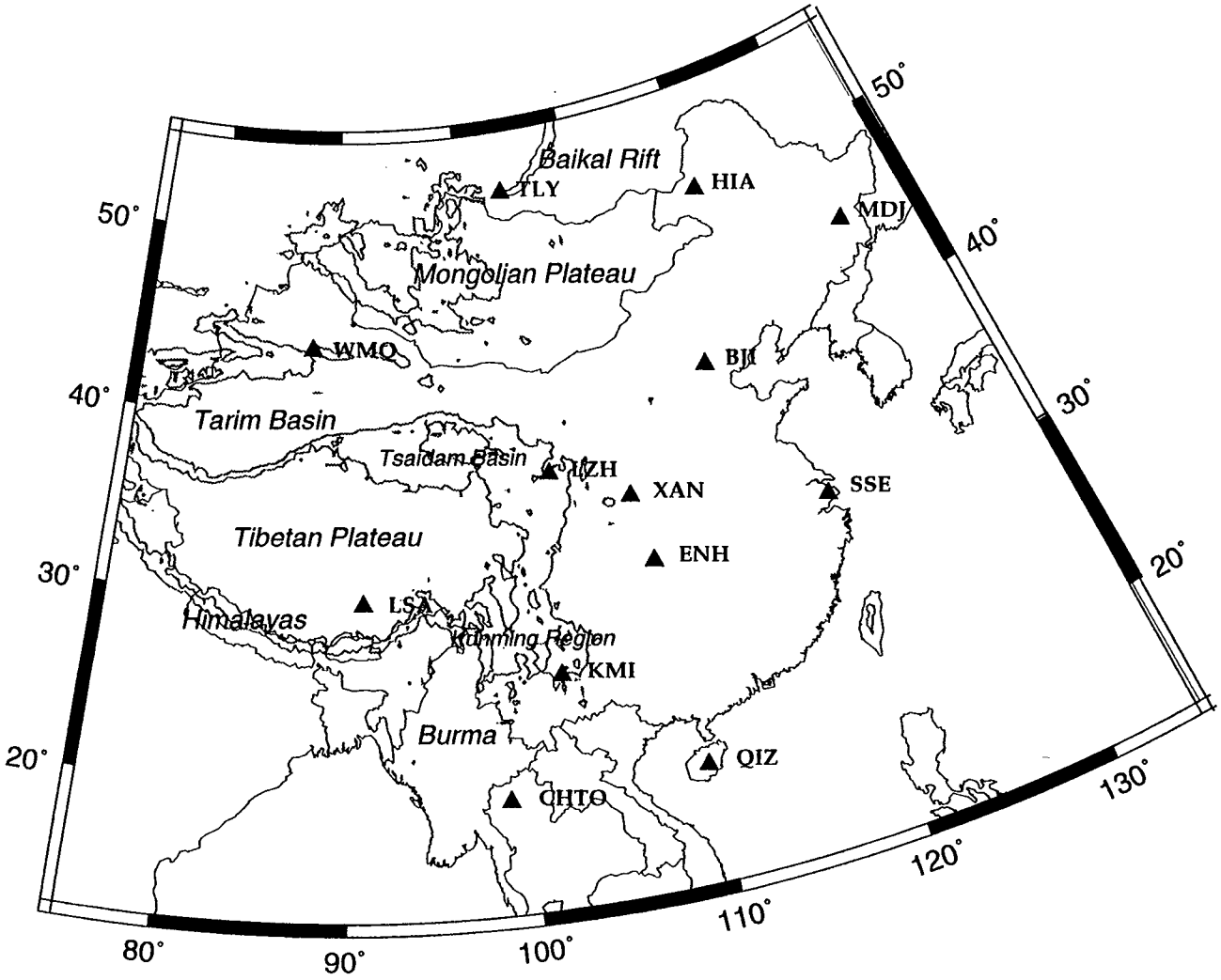

Figure 1. Simplified tectonic map of China. Dark triangles represent CDSN and GSN stations. Contour lines for 2000 and 4000 m elevations are also shown.

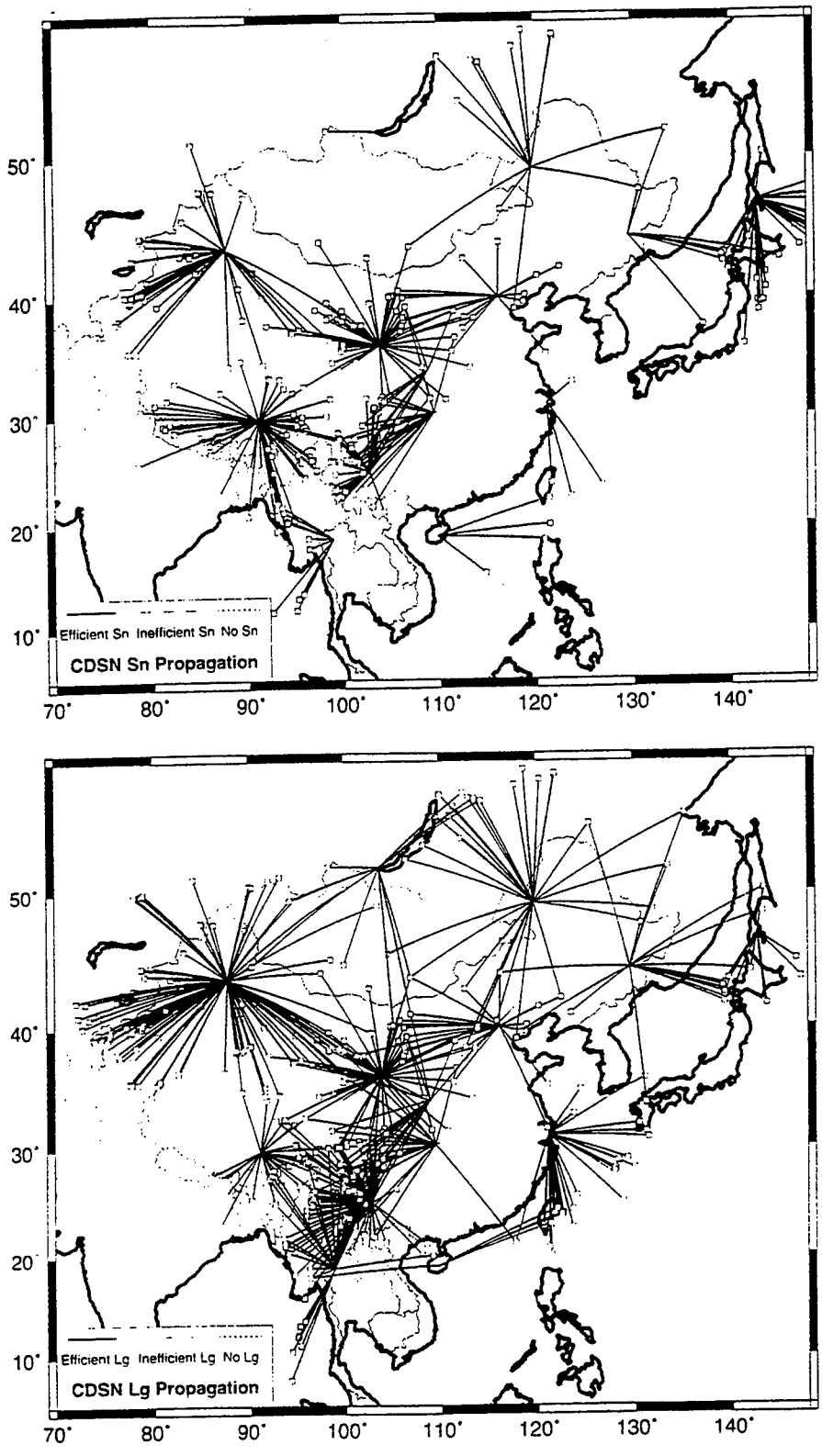

Figure 2a,b. Two summary maps of efficient Sn and Lg propagation in China. All events are between 2° and 12° from each station, have body wave magnitudes greater than 4.3 and have depths less than 50 km.

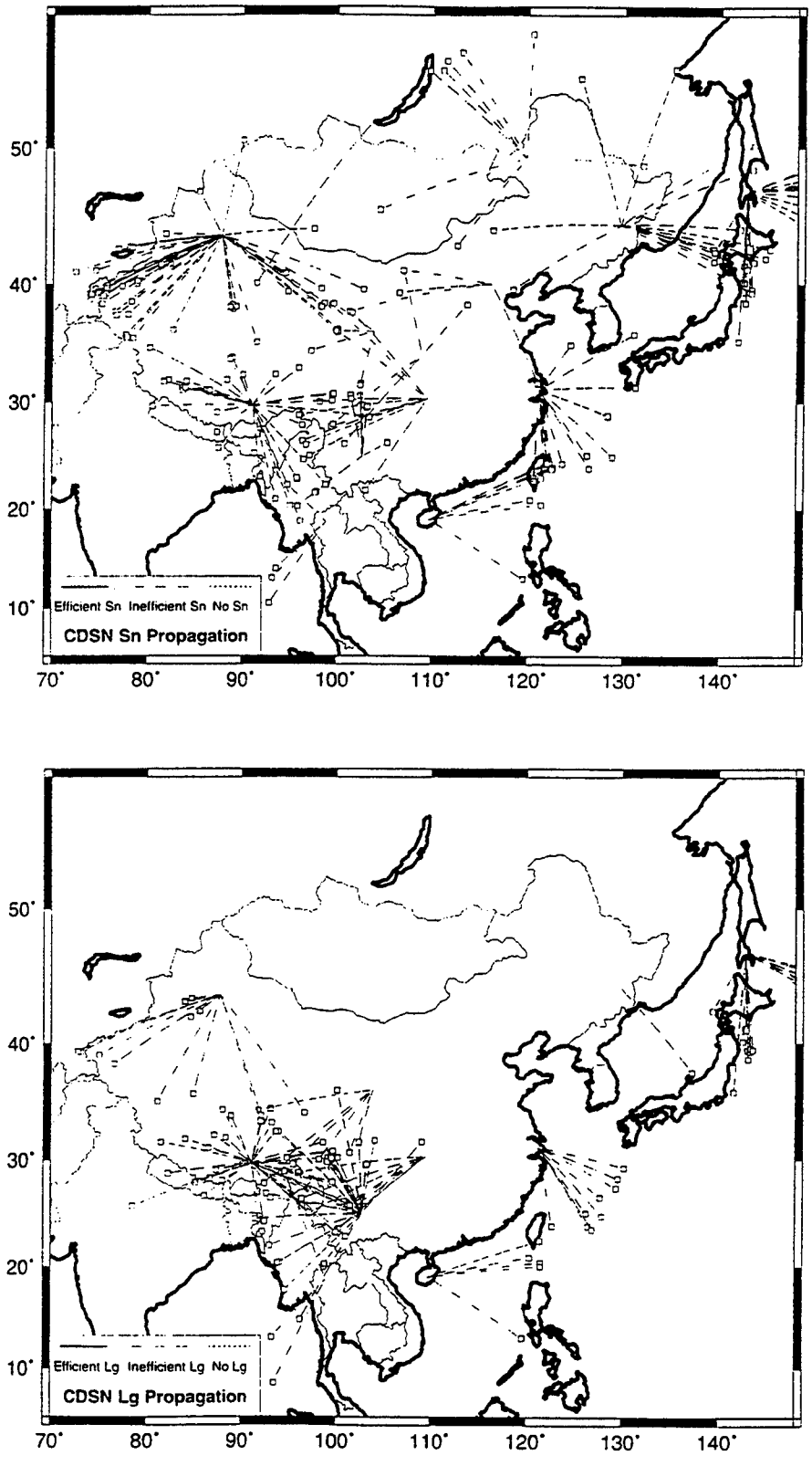

Figure 2c,d. Two summary maps showing inefficient Sn and Lg propagation in China.

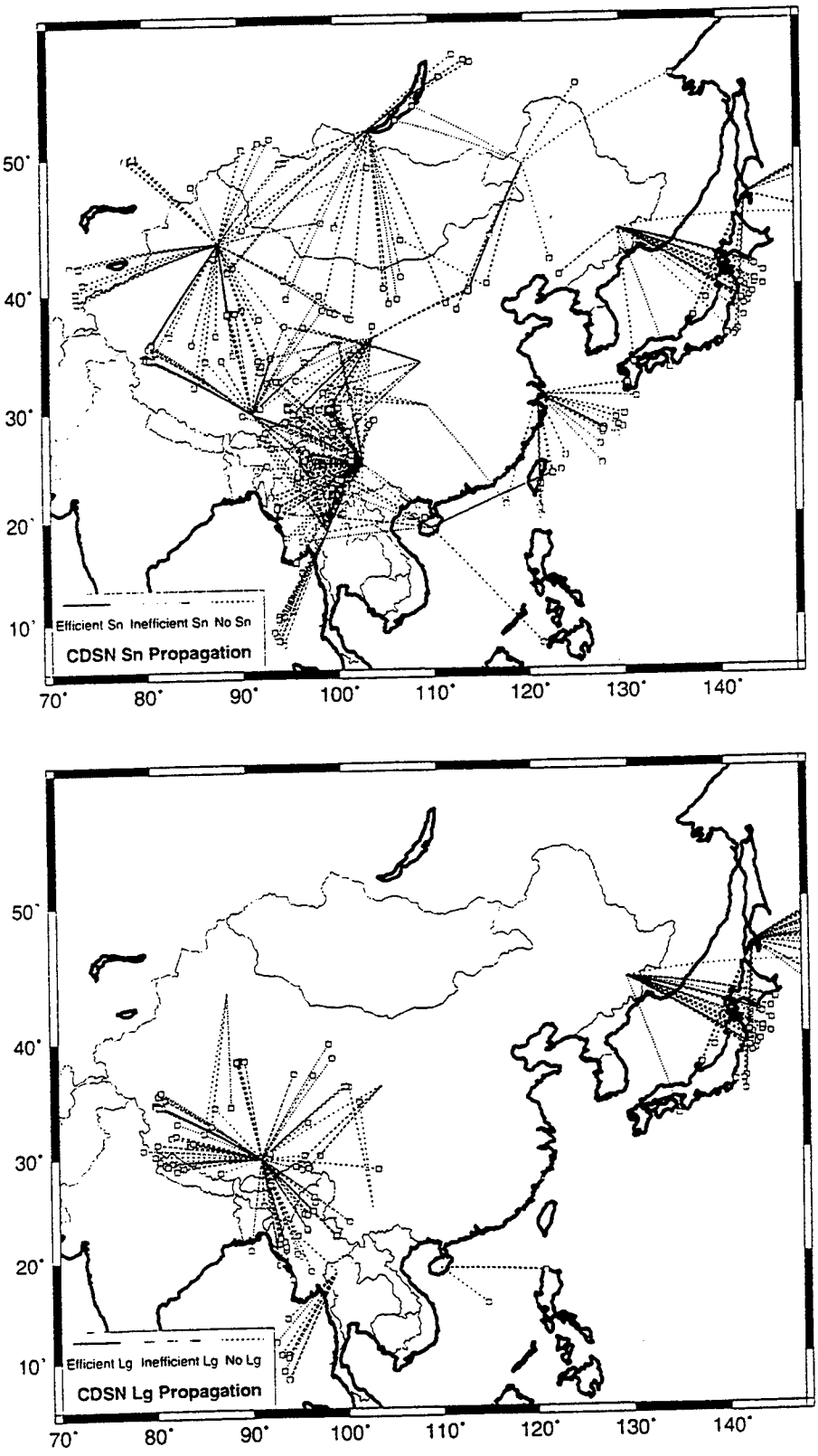

Figure 2e,f. Two summary maps showing propagation paths where Sn and Lg are not observed in China.

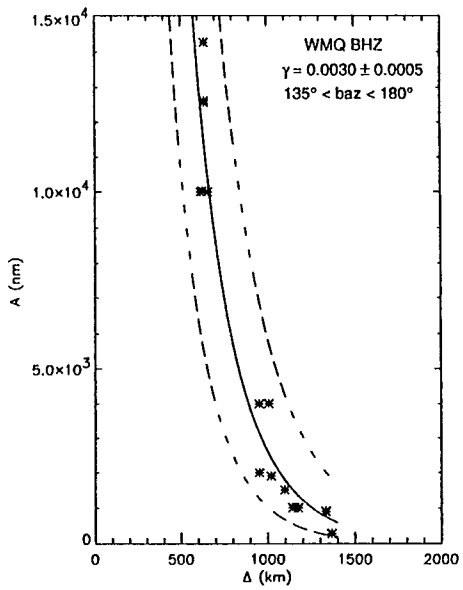

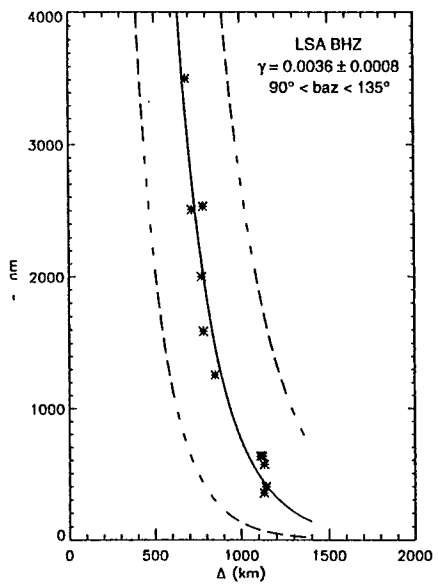

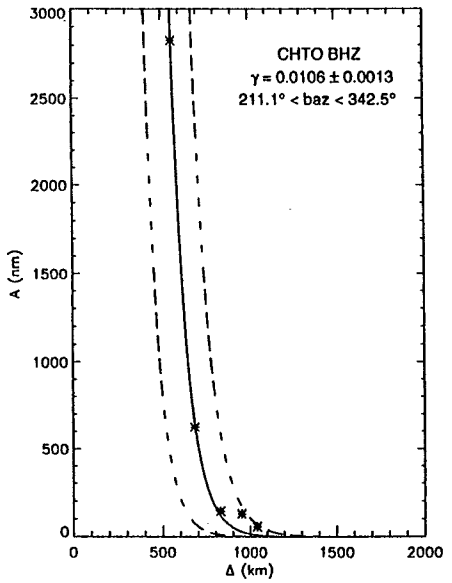

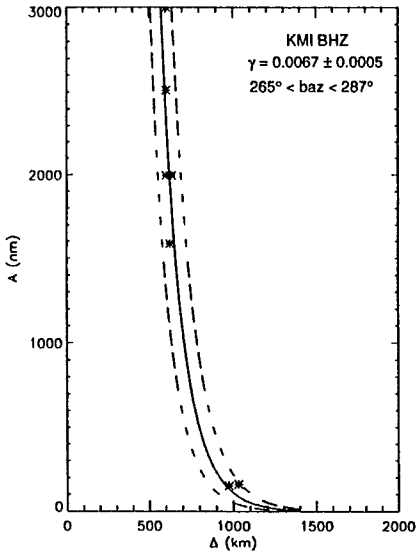

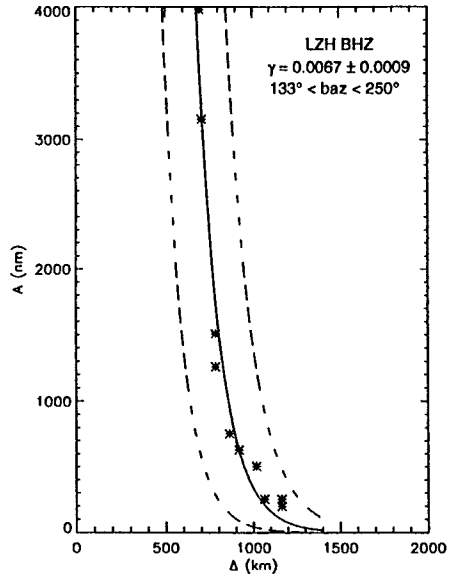

Figure 3. Best fit curves to find attenuation coefficients and Q for Lg on the vertical components of stations WMQ, LSA, CHTO, KMI and LZH.

HIGH RESOLUTION GROUP VELOCITY VARIATIONS ACROSS CENTRAL ASIA

M.H. Ritzwoller, A.L. Levshin, L.I. Ratnikova, D.M. Tremblay
Department of Physics, University of Colorado, Boulder 80309-0390
Contract Number F19628-95-C-0099
Sponsored by AFTAC

ABSTRACT

This study is a companion to another study in this volume (Levshin *et al.*, 1996). The companion study's purpose is to estimate a lithospheric shear velocity model across the entire continent of Eurasia with lateral resolutions lying between 500 - 750 km by using broadband (20 - 225 s) measurements of Rayleigh and (20 - 150 s) Love wave dispersion. The purpose of this study is to attempt to sharpen the focus further in the structurally complex regions of Central Asia (Iran, Afghanistan, Pakistan, southern republics of the FSU, and W. China) where significant off-pure-path propagation has degraded the resolution in the continent-wide study. This is accomplished in two ways. First, we use here much shorter paths which originate from smaller earthquakes ($Ms \geq 4.0$) and which have been recorded on regional arrays and networks (KNET, KAZNET, PASSCAL-Tibet, historical FSU-Mongolia) in addition to global stations (GSN/CDSN, GEOSCOPE). We have used 289 earthquakes from 1988 through late-1995 and 56 stations from these networks, all lying within 27 degrees of KNET (Kirghiz Telemetered Seismic Network). Counting all the KNET measurements for an event as a single path, the resulting data set comprises more than 1,000 paths with an average path length of 1,900 km (contrasted with the 6,000 km average path length in the companion study). Second, shorter path lengths have resulted in dispersion measurements in large numbers down to 10 s period. These shorter period measurements appear robust and provide enhanced radial crustal resolution in Central Asia.

We have constructed group velocity maps from 10 s - 60 s period for both Rayleigh and Love waves. Shown here are group velocity maps for Rayleigh and Love waves at three periods: 10 s, 20 s, and 40 s. Although there is substantial agreement with the general features of the continent-wide dispersion maps discussed in the companion study, significant improvement in resolution is apparent in Eastern Iran, Afghanistan, Pakistan, the Central Asian Republics of the FSU, and Western China. For example, the Tarim Basin in W. China appears much more sharply imaged as a low velocity feature on the short period maps (10 s, 20 s) here than in the continent-wide study. High velocities appear associated with Tibet at short periods indicating relatively high velocities near to the surface contrasted with the much lower velocities at depth. A low velocity feature is observed in Western Pakistan that appears to translate southward with depth in the crust. A linear low velocity feature is associated with the Elburz - Kopet Ranges in Northeastern Iran and Northern Afghanistan. As an indication of the resolution of the method, high near surface velocities associated with the the Pamir range (only a few degrees in diameter) are resolved in the short period maps. Other smaller amplitude features appear associated with known tectonic structures.

Key Words: Central Asia, Tarim Basin, Tibet, Iran, Afghanistan, Pakistan, Kirghizstan, Kazakhstan, surface wave dispersion, Rayleigh waves, Love waves, group velocity

OBJECTIVE

The purpose of this research is to investigate whether the resolution of lithospheric (in particular crustal) shear velocity models in the structurally complex regime of Central Asia (Iran, Afghanistan, Pakistan, southern republics of the FSU, and W. China) can be improved relative to that achieved in continent-wide studies (e.g., companion paper in this volume, Levshin *et al.*, 1996). To improve resolution, we have modified the observational protocol discussed in the continent-wide study in the ways listed below. Rayleigh and Love wave dispersion measurements are obtained:

- on a lowered period band (10 - 60 s period) which provides improved depth resolution;
- on shorter surface wave paths (average path length is less than 2,000 km contrasted with the 6,000 km average path length in the continent-wide study) which reduces uncertainties in path locations;
- from relatively small earthquakes ($M_s \geq 4.0$) more densely spaced in Central Asia than in the companion study;
- at regional networks and arrays (KNET, KAZNET, PASSCAL-Tibet, historical FSU-Mongolia) as well as global stations (GSN/CDSN, GEOSCOPE) in Central Asia.

A more sharply focused model of lithospheric shear velocities in Central Asia is useful in a variety of ways. Most significantly for a CTBT, accurate high resolution structural information is needed to improve location capabilities in the structurally complex regions of Iran, Pakistan, Afghanistan, Western China, and Northern India. Location error ellipses mainly quantify ignorance concerning the structure of the crust (sedimentary thicknesses and velocities, crustal velocities and Moho topography). Focused studies of intermediate period surface wave dispersion using regional earthquakes and seismic networks, such as the one described here, promise significantly improved crustal models on regional scales.

RESEARCH ACCOMPLISHED

As in the continent-wide study of Levshin *et al.* (1996), research to date has proceeded in three steps: (1) data acquisition and dispersion measurement, (2) determination of measurement reliability, and (3) group velocity map construction. We will discuss each of these steps briefly in turn.

Data Acquisition and Processing

The reader is referred to Ritzwoller *et al.* (1995) and Levshin *et al.* (1996) to find a discussion of the processing protocol of this study. This study differs from the continent-wide study of Levshin *et al.* (1996) by utilizing much shorter paths which originate from smaller earthquakes ($Ms \geq 4.0$) and which have been recorded on regional arrays and networks (KNET, KAZNET, PASSCAL-Tibet, historical FSU-Mongolia) in addition to global stations (GSN/CDSN, GEOSCOPE). The use of group times rather than phase times allows us to use earthquakes for which there is no detailed source information beyond a location estimate. Phase velocity measurements require moment tensor estimates. We have used 289 earthquakes (Figure 1) from 1988 through late-1995 and 56 stations (Figures 1 and 2) from these networks, all lying within 27 degrees of KNET (Kirghiz Telemetered Seismic Network). Counting all the KNET measurements for an

event as a single path, the resulting data set comprises over 1000 paths (Figure 2) with an average path length of 1900 km (contrasted with the 6000 km average path length in the companion study). This information is summarized in Table 1.

Table 1. Origin of Data (All within 27° of KNET)

Network	*Number of stations*	*Number of events*
GSN	11 (3 CDSN)	97
GEOSCOPE	2	9
KNET	11	141
KAZNET	7	30
PASSCAL (Tibet)	11	21
FSU-Mongolia	14	21
Total	56	289

Data Reliability

A 'cluster analysis' similar to that described briefly by Levshin *et al.* (1996) has been performed. The reader is referred there for a discussion. The number of 'unique paths' as a function of period is shown in Figure 3a and the path number density is displayed in Figure 3b. Path number density peaks in Kirghizstan where KNET (e.g., Vernon, 1994; Pavlis *et al.*, 1994) is located, but is also quite good in Eastern Iran, Afghanistan, Pakistan, Northernmost India, and Western China. The existence of regional networks such as KNET and KAZNET (Kazakhstan Network, Kim *et al.*, 1995) allows for detailed reliability studies across the network to be performed which are impossible using global stations alone. Figure 5 illustrates the use of regional network data, KNET here, to estimate uncertainties in dispersion measurements.

Group Velocity Maps

All dispersion measurements have been weighted by results of the cluster and reliability studies discussed above, and have then been used to estimate the Central Asian group velocity maps. These maps represent the local group speed of a Rayleigh or Love wave propagating at a particular spatial point. Maps have been constructed for Rayleigh and Love waves ranging between 10 - 60 s period. Included here are maps at 10 s, 20 s and 40 s period shown in Figures 6 - 8, respectively. The features in Central Asia that appear on the group velocity maps in the continent-wide study of Levshin *et al.* (1996) are spatially much larger and more smeared, presumably due to off-pure-path propagation that manifests itself as a reduction in resolution in structurally complex regions such as Central Asia. The features comprising the maps shown in Figures 6 - 8 appear to be better resolved than in the continent-wide study and, as discussed in the next section, are correlated with known tectonic structures.

Cursory Interpretation

Levshin *et al.* (1996) briefly discuss how to interpret group velocity maps. This information illuminates the maps shown in Figures 6 - 8 here.

The map shown here that possesses the greatest depth penetration is the 40 s Rayleigh wave map. This maps exhibits very large amplitude variations due principally to Moho topography to which the shorter period waves are relatively insensitive. The shorter period maps display a number of features that are generally consistent with the continent-wide maps of Levshin *et al.* (1996) but are apparently in sharper focus. For example, the Tarim Basin of Western China is

clearly seen as a low velocity feature on the 10 and 20 s maps. Tibet appears on these maps as a high velocity feature, to be contrasted with the longer period maps where it appears as a low velocity feature. Presumably, there are relatively high shear wave velocities in the upper crust underlying Tibet. A linear low velocity feature also shows up on the 10 and 20 s maps in Northwestern Iran and Northern Afghanistan associated with the Elburz - Kopet Ranges. The Kazakh Platform is fast on all the maps. The resolution of these maps is demonstrated by the fact that the Pamir Range (~38N, 73E) appears as a high velocity feature only a few degrees in diameter at both 10 and 20 s period.

CONCLUSIONS AND RECOMMENDATIONS

Regional scale surface wave dispersion studies, such as the study of the group velocity variability in Central Asia presented here, can be used to improve both lateral and radial resolution relative to continent-wide studies (e.g., Levshin *et al.*, 1996). This is particularly important in structurally complex regions such as Central Asia, since these regions significantly perturb wave paths propagating on continental scales (i.e., $\geq 5,000$ km). These perturbations create uncertainties about the location of wave paths that manifest themselves as regions of lowered resolution on group velocity maps and, ultimately, on continent-wide models of lithospheric velocity. Additionally, dispersion measurements on regional scales can be extended to shorter periods than continent-wide studies which provides improved radial resolution in the crust. These maps will be merged with those from the companion continent-wide study and then inverted for lithospheric shear velocity structure.

The principal recommendation that emerges from this study is that regional surface wave dispersion studies should be performed elsewhere in Eurasia, in areas of interest to CTBT monitoring that possess regional arrays or networks internal or peripheral to each area. One example is the Far East, centered on North Korea, where there is abundant well distributed seismicity and where GSN, GEOSCOPE, CDSN, POSEIDON, PASSCAL-Baikal, JNET, and DoD stations and arrays are located. The Middle East, centered on IRAN, is a similarly prime region for study, since it possesses well distributed seismicity and GSN, GEOSCOPE, Saudi Network, PASSCAL-Pakistan, and DoD stations provide fairly good peripheral coverage.

REFERENCES

Kim, W-Y., V. V. Kazakov, A. G. Vanchugov, and D. W. Simpson, Broadband and array observations at low noise sites in Kazakhstan: Opportunities for seismic monitoring of a Comprehensive Test Ban Treaty. In *Monitoring a Comprehensive Test Ban Treaty*, (editors E. S.Husebye), 1995.

Levshin, A.L., M.H. Ritzwoller, and S.S. Smith, Group velocity variations across Eurasia, this volume, 1996.

Pavlis G., H. Al-Shukri, H. Mahdi, and D. Repin, JSP arrays and networks in Central Asia, *IRIS Newsletter*, **XIII**, **2**, 10-12, 1994.

Ritzwoller, M. H., A. L. Levshin, S. S. Smith, and C. S. Lee, Making accurate continental broadband surface wave measurements. *Proceedings of the 17th Seismic Research Symposium on Monitoring and Comprehensive Ban Treaty*, Phillips Laboratory, Scottsdale, AZ, 482-491, PL-TR-95-2108, Sept. 1995.

Vernon, F., The Kyrghyz Seismic Network, *IRIS Newsletter*, **XIII**, 7-8, 1994.

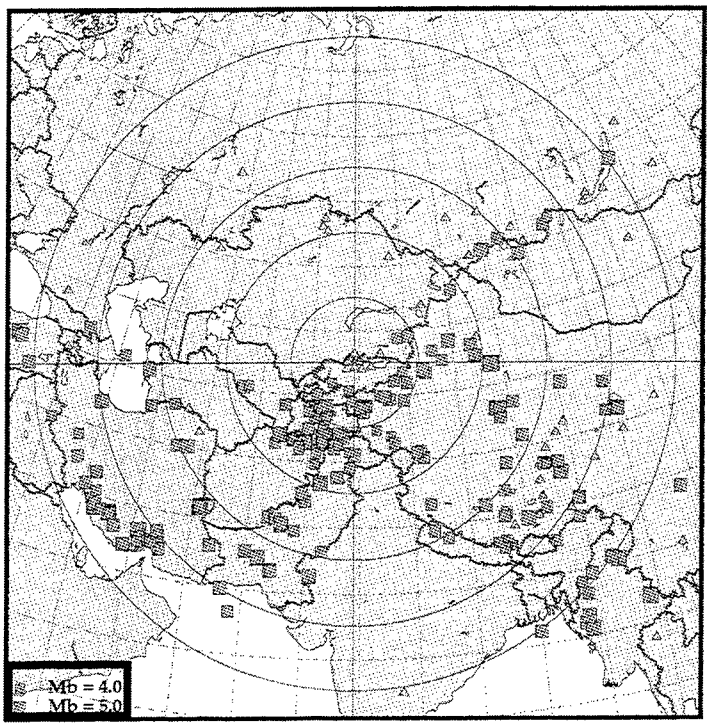

Figure 1. Distribution of sources (squares) and receivers from GSN, GEOSCOPE, KNET, KAZNET, PASSCAL & FSU networks used in the surface wave studies of Central Asia

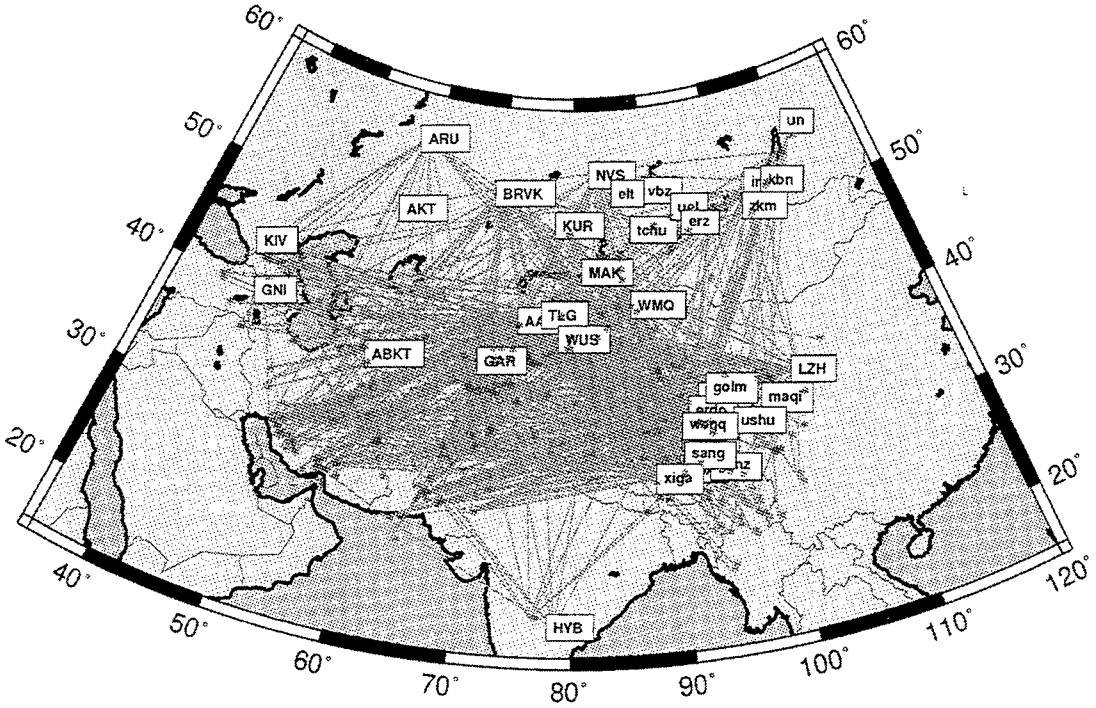

Figure 2. Source - station paths used for tomographic inversion of Central Asia group velocity data

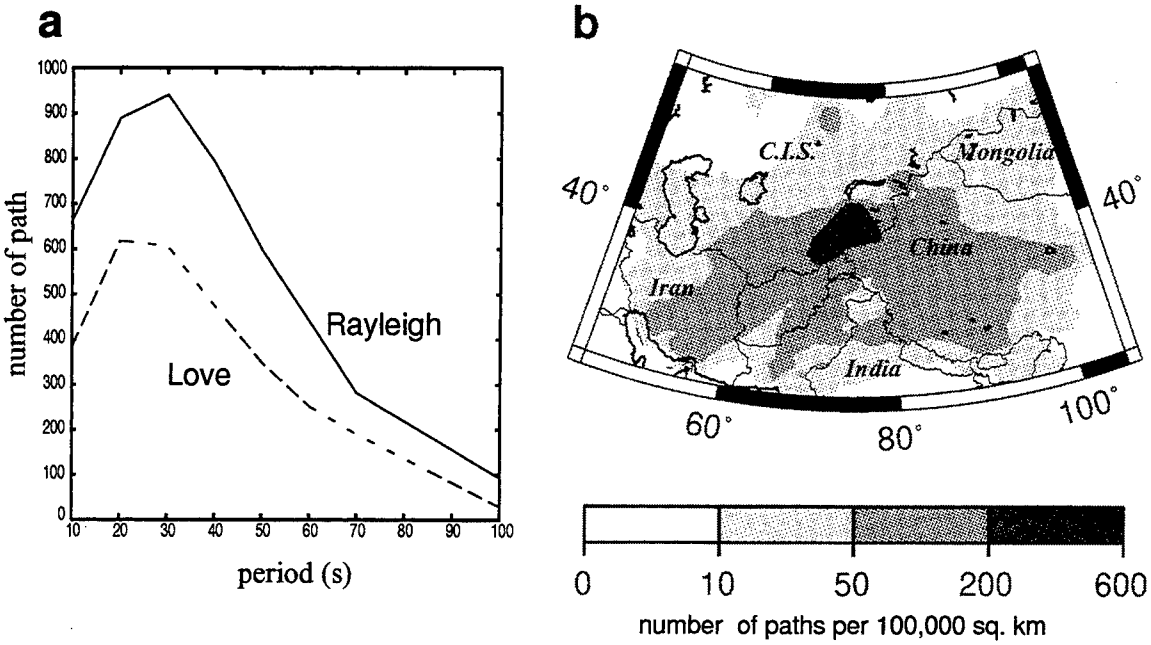

Figure 3. Number of surface wave paths as a function of period (a), and the path density for 30 s period (b).

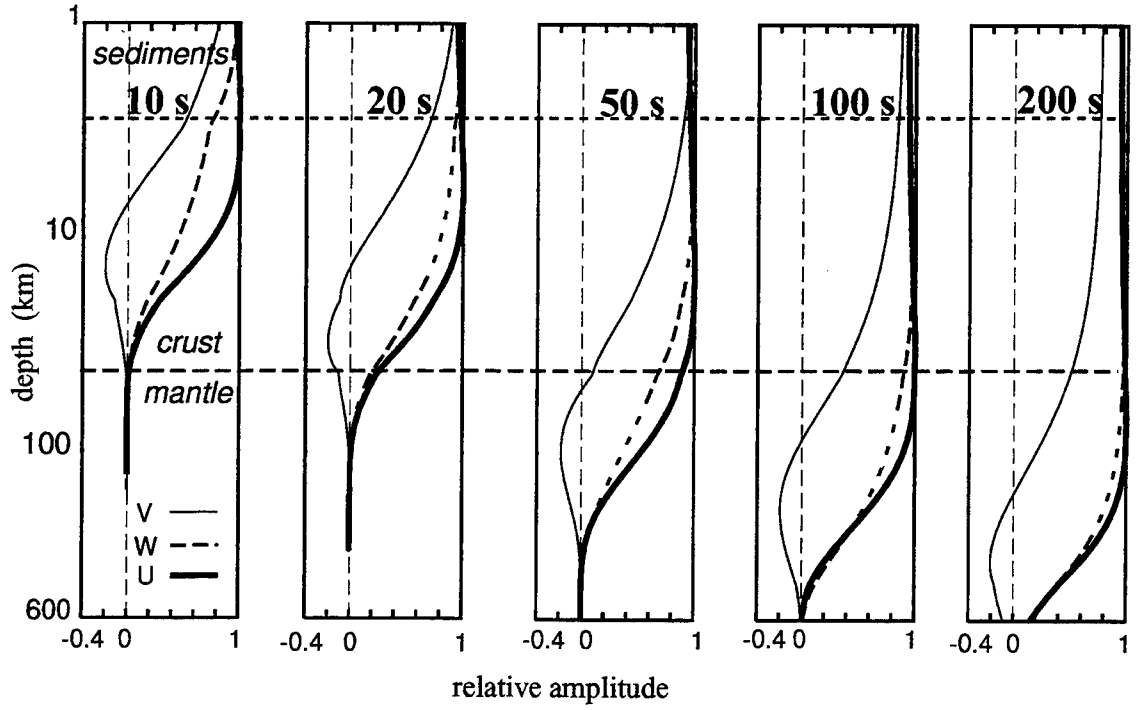

Figure 4. Eigenfunctions of Rayleigh (U, V) and Love (W) waves for different periods in the continental Earth model.

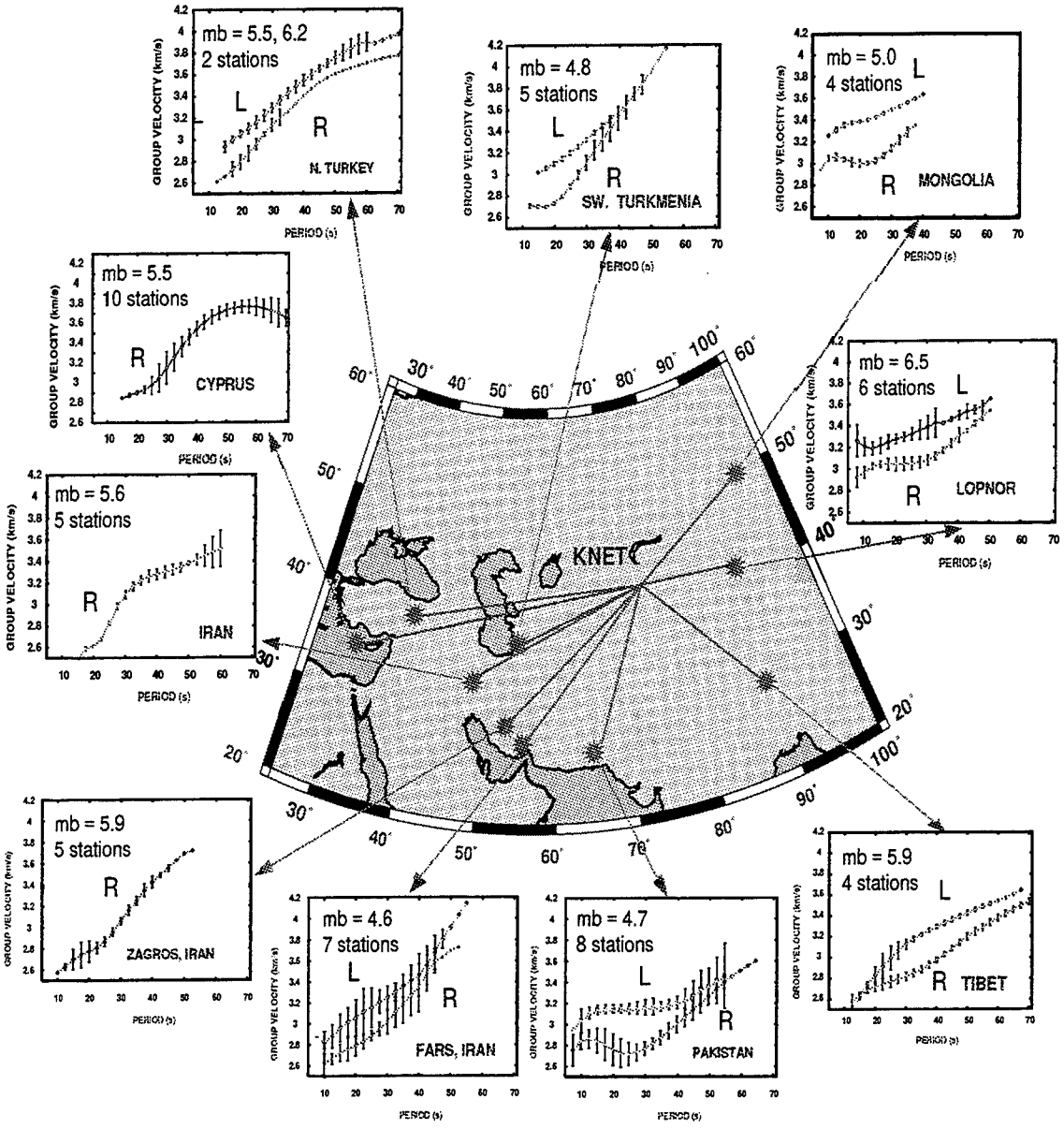

Figure 5. Group velocity variability across KNET is presented for Rayleigh (R) and Love (L) waves. One standard deviation 'error bars' are shown at periods where measurements from at least 3 stations exist, in order to represent variability observed for a variety of source regions around Central and Southern Asia.

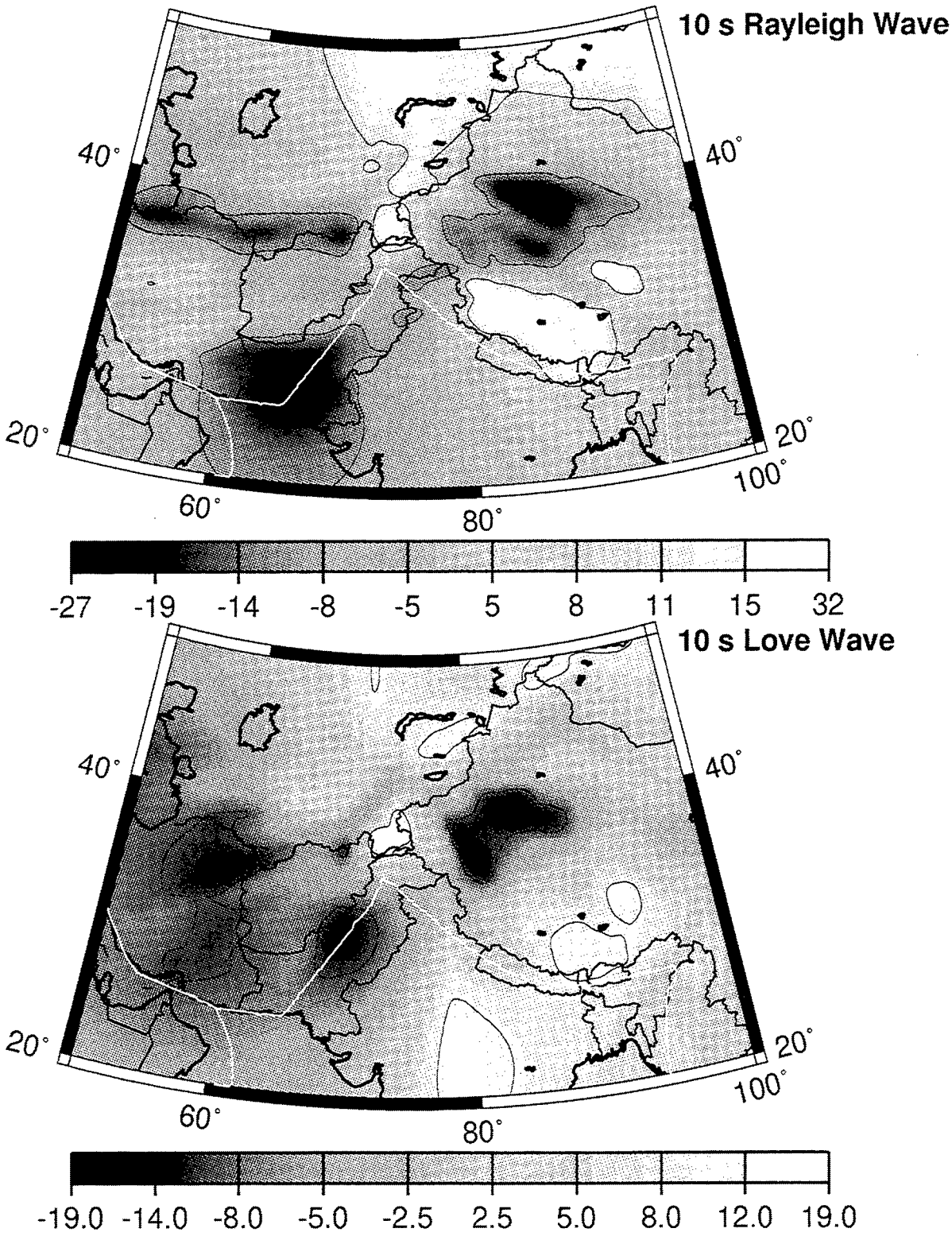

Figure 6. Rayleigh and Love wave group velocity maps at 10 s period. Units are percent deviation from the map average. The positive and negative 10% contours are drawn to highlight the regions of significant deviation from the map average.

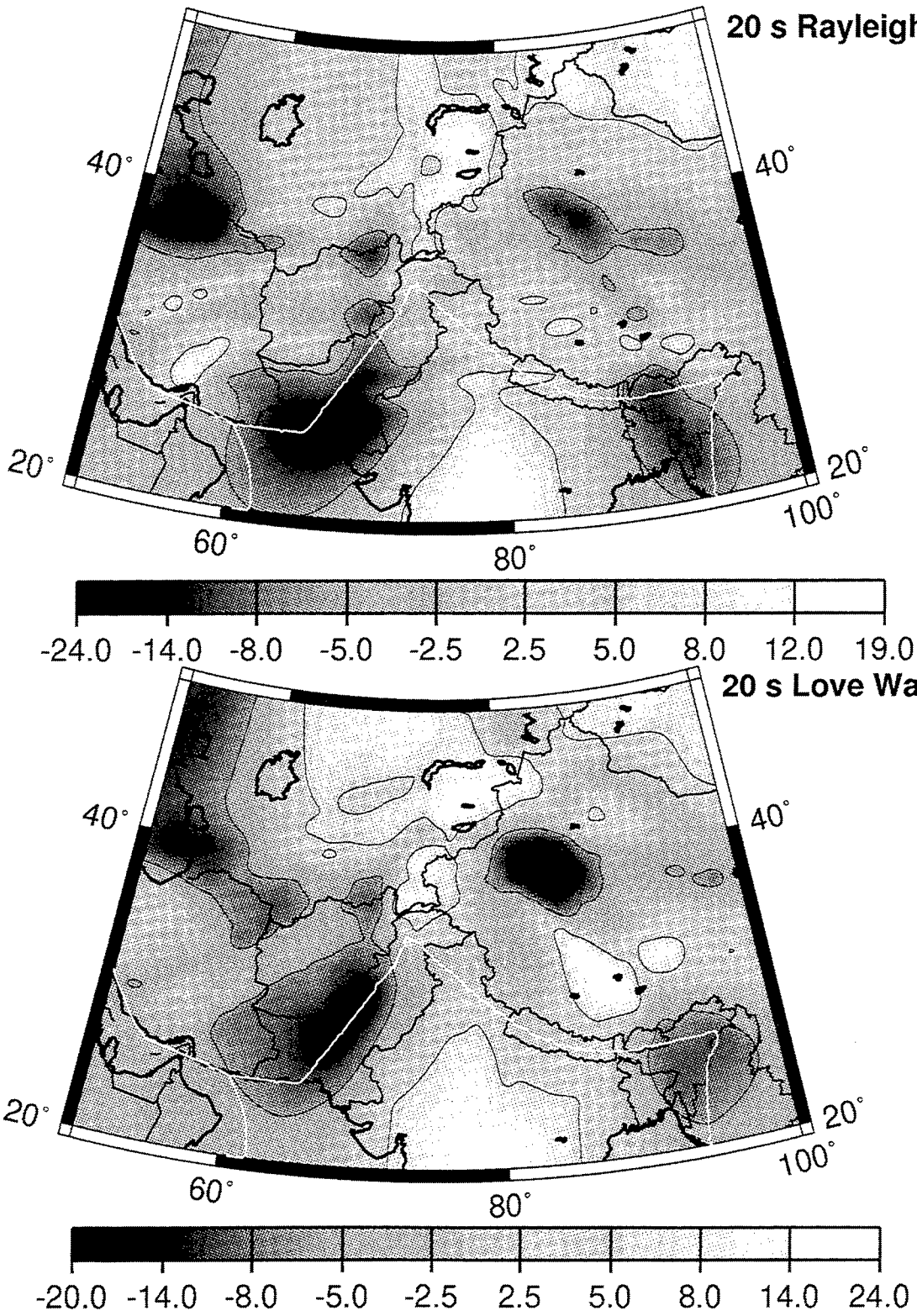

Figure 7. Rayleigh and Love wave group velocity maps at 20 s period. Units are percent deviation from the map average. The positive and negative 6% contours are drawn to highlight the regions of significant deviation from the map average.

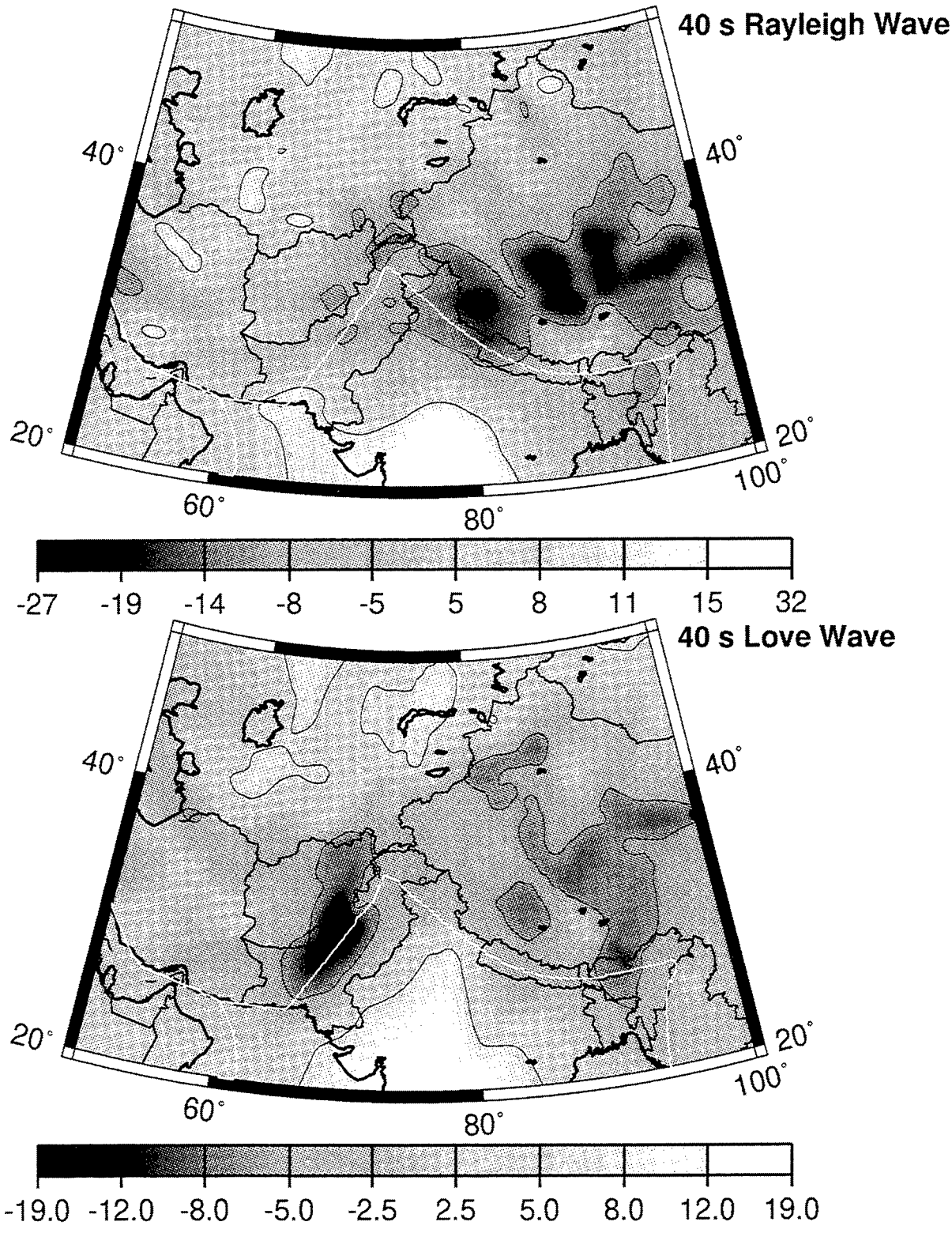

Figure 8. Rayleigh and Love wave group velocity maps at 40 s period. Units are percent deviation from the map average. The positive and negative (10%, 6%) contours are drawn on the (top, bottom) figure to highlight regions of significant deviation from the map average.

Initial Results from the Deployment of Broadband Seismometers in the Saudi Arabian Shield

Drs. F. L. Vernon, R. J. Mellors, J. Berger
IGPP, University of California at San Diego

Prof. A. M. Al-Amri
King Saud University

Dr. J. Zollweg
Boise State University

Contract No. F19628-95-K-0015
Sponsored by DOE

ABSTRACT

The preliminary results from the first six months of our field deployment of nine portable broadband stations suggest that sites in the Arabian shield are extremely quiet with ground noise near or equal to the low noise model in the frequency band from 1-10 Hz at the station RAYN. The low noise also contributes to the very low detection threshold at RAYN of events with mb = 3.5 at distances from 10 to 100 degrees. These stations appear to be among the best sites in the world for the properties of detection thresholds and ground noise levels. Seismograms from sources 10 degrees from the center of the network have very unique characteristics which can be used to identify the source regions. Zagros events have a clear Pn and Sn arrivals with an observable Lg. Shallow events from the Arabian Sea have clear P, S, and surface waves but no discernible Lg phases. From the opposite direction, aftershocks from the Gulf of Aquaba have very weak P and S waves with very strong Lg phases.

Keywords: Saudi Arabia, detection thresholds, ground noise, seismic regionalization

OBJECTIVES

This project consists of a field program in the Kingdom of Saudi Arabia to collect broadband seismic waveform data and the associated parametric data describing the sources. We currently have deployed nine portable broadband seismic stations on the Arabian Shield and plan to record over a period of about a year. Most of the regional seismic sources are in the tectonically active areas of Iran and Turkey. Other areas of seismic activity include the Red Sea Rift bordering the Shield to the southwest, the Dead Sea Transform fault zone to the north, and the Arabian Sea to the southeast.

The main research objectives of this program are:

1. to study the propagation of regional phases across the Arabian Shield over a broad band of frequencies,

2. to study the crustal structure and seismicity of the Arabian Shield,

3. to characterize potential sites for permanent seismic facility installation

RESEARCH ACCOMPLISHED

The first deployment in late 1995 consisted of 6 seismographs arranged in two linear arrays (Figure 1). One linear array consists of the stations RAYN, HALM, RANI. This profile's long axis is pointed in the direction of high seismicity in the Zagros. These earthquakes are occurring in the Arabian Plate where it is colliding with Persian Plate (Jackson and Fitch, 1981). Seismic wave ray paths along this profile from Zagros events should therefore have entirely intra-plate paths. Stations will be between 900 and 1500 km from the nearest Zagros sources. The second linear array consists of the stations AFIF, RANI, BISH, SODA. Events in the highly active area of the Afar triple junction in Africa and events in the Caucasus are also generally aligned with this alignment.

Early in the experiment the station BISH was vandalized and the station was closed. Three new stations were installed in June 1996 at TAIF, UQSK, and RIYD. These stations provide a more areal distribution that the initial deployment. The station at RAYN was converted from at portable station to a permanent GSN station in June 1996.

The array deployments will allow sampling of regional wave characteristics over a broad area, from very numerous source regions. It is reasonable to expect that ray paths traversing virtually every area of the shield will be recorded, given the high seismicity rates characteristic of most of the active areas around the shield. We expect from experience operating portable seismographs in some parts of the shield that most sites will have very low noise levels, so a variety of teleseismic signals suitable for receiver function analysis should also be obtained.

Instrumentation

Each station has a Streckeisen STS-2 broadband seismometer which has a pass band between 0.008 Hz and 50 Hz. Each seismometer is heavily insulated to protect it from the daily changes in temperature. Each sensor is attached to bedrock outcrops whenever possible.

Station	Latitude	Longitude	Elevation (Km)	Location
AFIF	23.9310	43.0400	1.1160	Afif, Saudi Arabia
BISH	19.9228	42.6901	1.3790	Bisha, Saudi Arabia
HALM	22.8454	44.3173	0.9300	Hadabat Al-Mahri, Saudi Arabia
RANI	21.3116	42.7761	1.0010	Raniyah, Saudi Arabia
RAYN	23.5220	45.5008	0.7920	Ar-Rayn, Saudi Arabia
RIYD	24.7220	46.6430	0.7170	Riyadh, Saudi Arabia
SODA	18.2921	42.3769	2.8760	Al-Soda, Saudi Arabia
TAIF	21.2810	40.3490	2.0500	Taif, Saudi Arabia
UQSK	25.7890	42.3600	0.9500	Al-Soda, Saudi Arabia

The output of the STS-2 is recorded at a sample rate of 40 sps by a 24-bit REFTEK RT72A-08 datalogger. At the station the data are stored on a 2 Gbyte SCSI disk. To take advantage of the copious amounts of sunshine available in Saudi Arabia, we use solar panels to charge car batteries. Timing to the station is provided by a local GPS clock. Data are retrieved by exchanging disks at each site during service runs. Each site is visited every four to six weeks.

Processing

The processing scheme requires several steps: raw data retrieval followed by formatting, quality control, and event association. A Sun Sparc field computer is set up in Riyadh. The data conversion to CSS 3.0 format and quality control are performed on this field computer. The data are then sent to UCSD where an automatic picking program is used to identify all arrivals. These arrivals are reviewed by an analyst. The initial event associations are based on predicted arrivals from a REB origin table using the IASPEI91 travel time tables and the actual phase picks. Any recorded events not appearing in the REB catalog are processed. The data are sectioned into an event oriented CSS 3.0 waveform database and will be distributed to interested users.

Operating at 40 samples/second continuously, each station collects 41.5 Mbytes of waveform data per day. Thus, about 250 Mbytes per day for the 6 stations will have to be processed. Assuming that there will be the equivalent of about 300 network-days of operation during the experiment, the total data produced will be on the order of 75 Gbytes.

Data

Initial processing has been started for the first six months of data. At present 367 events have been processed and are shown in lower map in Figure 2. The upper epicenter map in Figure 2 shows the 77 events within 20 degrees of the stations. Most of these events are

located in the Zagros region with the remaining concentrated as aftershocks to the 23 November 1995 Gulf of Aquaba earthquake or from events in the Arabian Sea. Each of these three source regions are approximately 10 degrees from the center of the network and have unique seismic characteristics. Events from Iran have a clear Pn and Sn arrivals with an observable Lg (Figure 3). Shallow events from the Arabian Sea have clear P, S, and surface waves but no Lg phases as demonstrated in Figure 3. From the opposite direction, aftershocks from the Gulf of Aquaba have very weak P and S waves with very strong Lg phases (Figure 4).

Signal and Noise Characteristics

The most important seismic characterizations is an estimate of its signal-to-noise properties of a particular site. The ambient noise spectra over a variety of conditions provides an estimate of the theoretical performance relative to other sites and to accepted noise models. A variety of near-site conditions affect the ambient noise including cultural activities, weather and wind patterns, local seismicity, and proximity to oceans/seas. The teleseismic and regional signal reception levels are affected more by regional structure than the site characteristics.

For each site we occupy, we will develop comprehensive estimates of the signal and noise characteristics over the seismic band from approximately 50 seconds to 15 Hz. An example of the seismic noise characteristics is shown in Figure 5. A short segment of data from each channel is shown for the station RAYN. The Low-Noise model is provided for comparison. The station at RAYN actually equals the Low-Noise model at 2 Hz.

Detection Thresholds

Following the method of Harvey, 1994, we will calculate for each station the single site magnitude detection thresholds. Using event m_b magnitudes reported in the REB, the m_b estimates from our data in the 0.8 to 3 Hertz pass band, will be corrected to produce zero mean statistics for the REB relative residuals.

Single site m_b vs. distance functions give us the raw information for determining single site detection magnitude thresholds. In a traditional analysis of single site detection magnitude thresholds one would create a map view, put events into regional bins, compute magnitude-frequency functions for each bin and set the magnitude threshold for each bin according to some roll-off criteria applied to the magnitude-frequency functions. However, this method requires more events than we are likely to have in our catalog.

The alternate method for determining single site detection magnitude thresholds which yields reasonable results from relatively small catalogs. The method is based upon using P wave signal to noise ratios observed at a given station to scale event magnitudes to equivalent threshold values for that station. This is done by adjusting the event magnitude by an amount equal to the logarithm of the ratio of the observed signal to noise level and a threshold signal to noise level representing the minimum level at which a signal would be detected. The assumption here is that the wave propagation is a linear process so that amplitudes can be scaled directly. This approach allows us to scale down large magnitude events to equivalent smaller events that would be at the detection limit for each particular source-receiver geometry.

The results of this method applied to the events shown in Figure 1b for a specified detection threshold signal to noise level of two. Figure 1b shows such a function produced from events for station RAYN where squares represent events that were in the REB and the

symbols are color coded according to event depth. We can see that the populations of shallow and deep events clearly separate as one would expect. Our preliminary results show that the mb detection threshold for the distance range of 10-100 degrees is about mb = 3.5.

CONCLUSIONS AND RECOMMENDATIONS

The preliminary results of our field deployment suggest that many of our sites in the Arabian shield are extremely quiet with ground noise near or equal to the low noise model in the frequency band from 1-10 Hz. The low noise also contributes to the very low detection threshold of events with mb >= 3.5 at distances from 10 to 100 degrees. These stations appear to be among the best sites in the world for the properties of detection thresholds and ground noise levels. Seismograms from sources 10 degrees from the center of the network have very unique characteristics which can be used to identify the source regions. Zagros events have a clear Pn and Sn arrivals with an observable Lg. Shallow events from the Arabian Sea have clear P, S, and surface waves but no discernible Lg phases. From the opposite direction, aftershocks from the Gulf of Aquaba have very weak P and S waves with very strong Lg phases.

In the future the understanding of the waveform propagation properties would be enhanced by placing stations further north in the Arabian shield areas. Based on our observations, there exist several excellent sites in the shield region of Saudi Arabia which could be used for potential seismic arrays.

Harvey, D. *IRIS News Letter* , July, 1994.

Jackson, J., and T. Fitch, Basement faulting and the focal depths of the larger earthquakes in the Zagros mountains (Iran), *Geophysical Journal of the Royal Astronomical Society*, 64 (1981), 561-586.

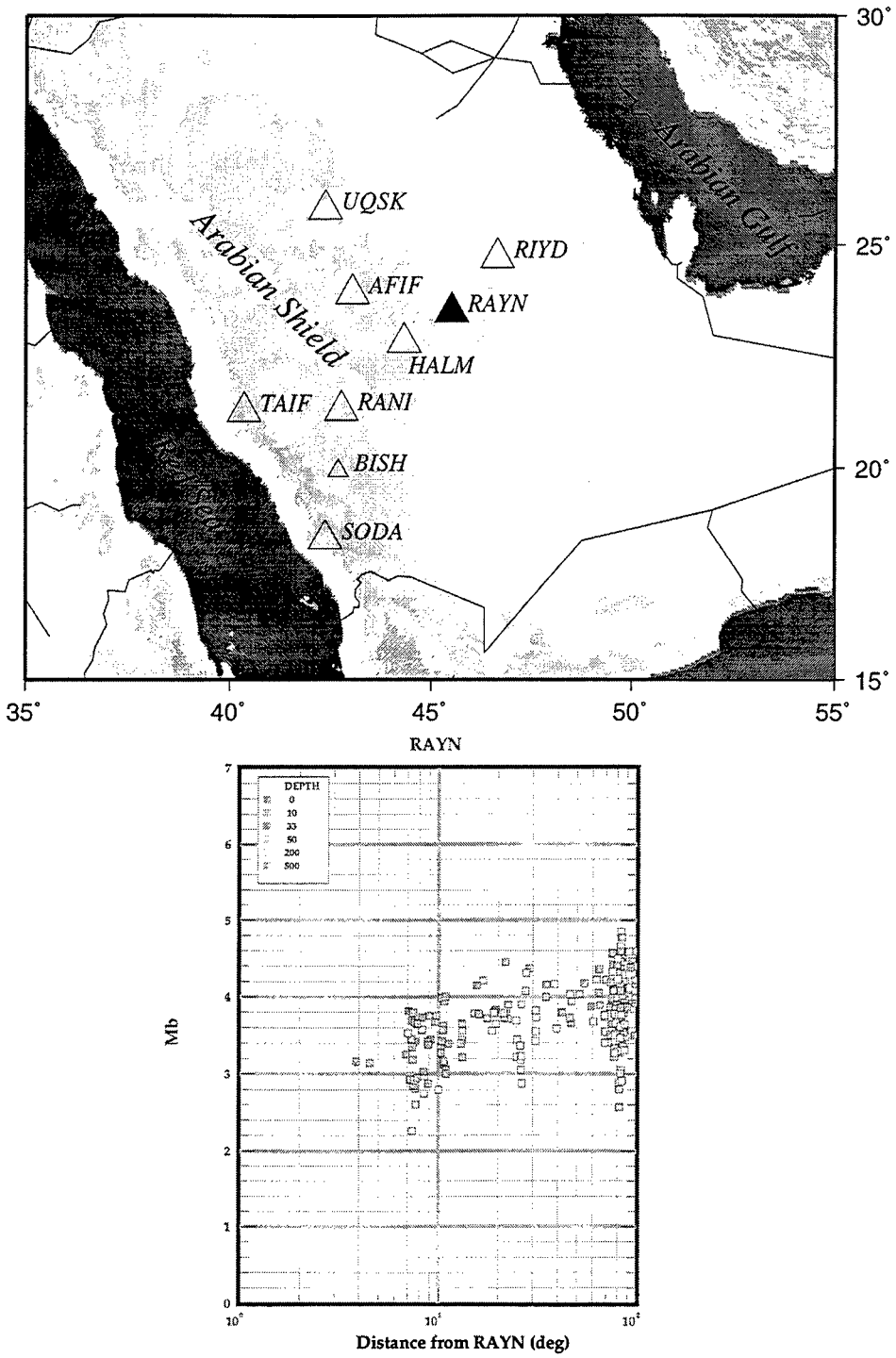

Figure 1. (**top**) Map of station deployment. Open triangles are temporary deployment and closed triangle is a permanent station. Light shading represents elevations above 1000 m, dark shading above 2000 m. (**bottom**) Magnitude/distance plot showing detection threshold for station RAYN.

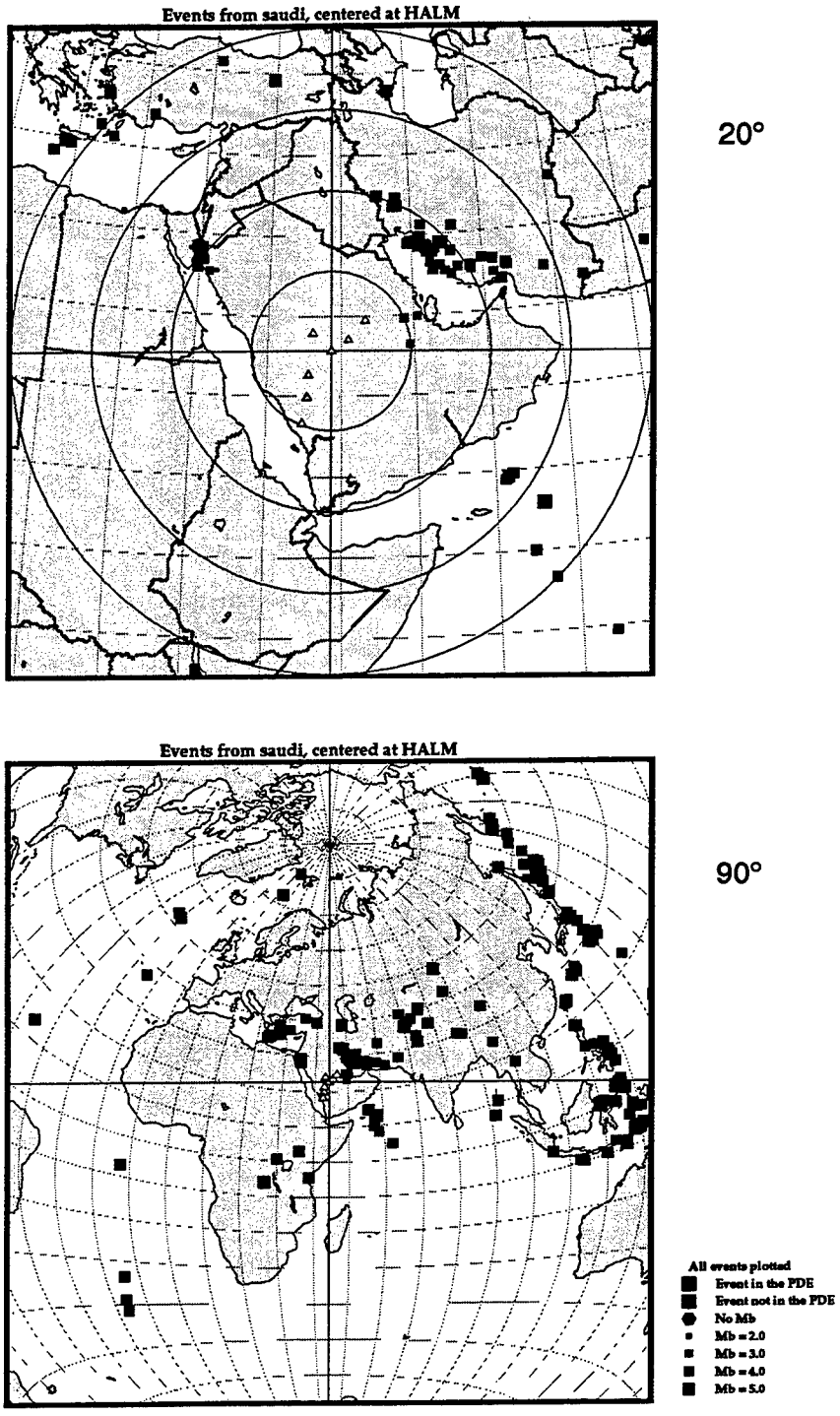

Figure 2. (Top) Map showing detected regional events for data currently processed. **(Bottom)** Regional and teleseismic events recorded by broadband deployment.

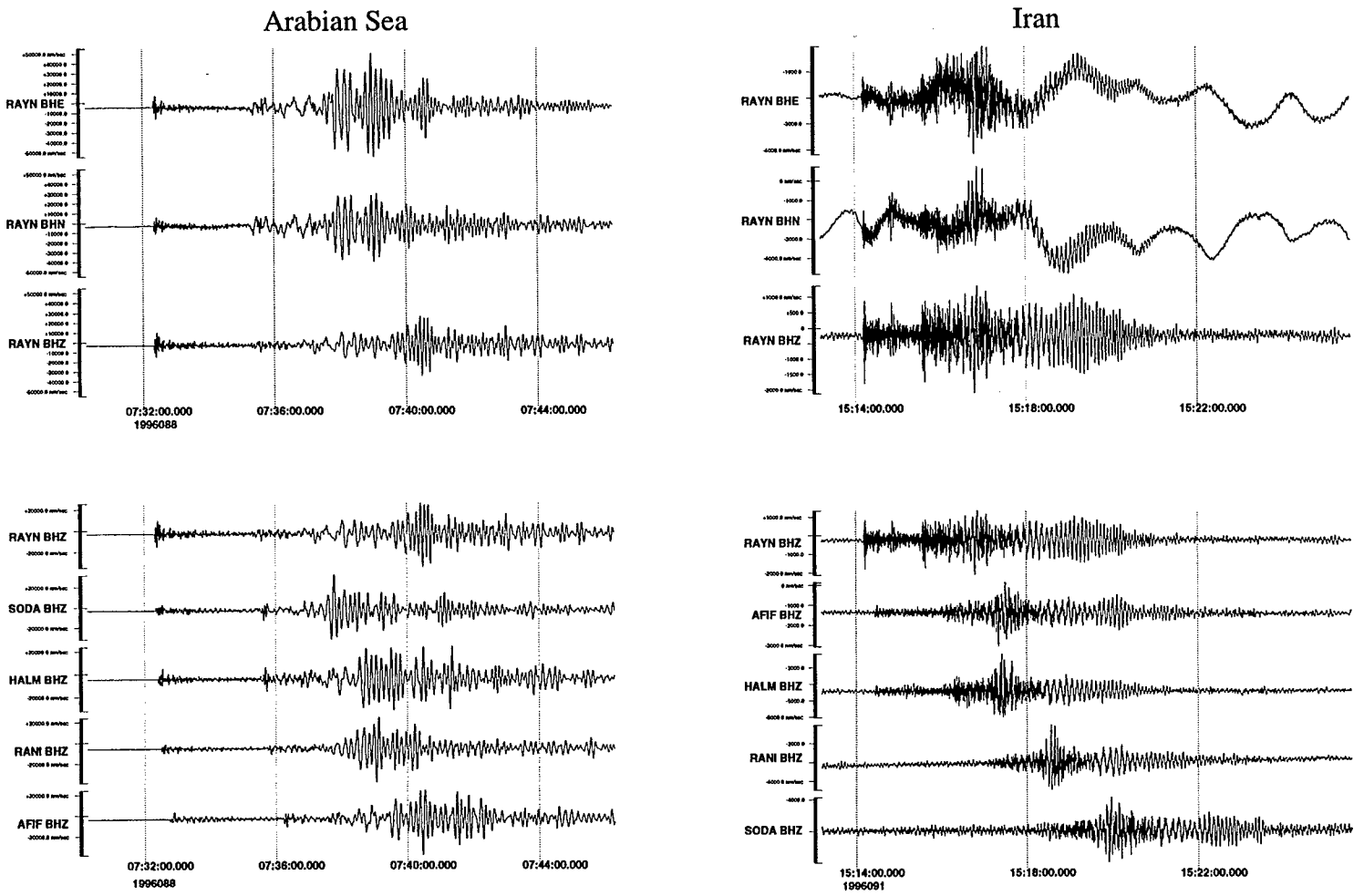

Figure 3. Two events from approximately 10° away showing vertical components for all stations (bottom) and all three components (top) for station RAYN. Note difference in regional waveforms for Mb 5.8 Arabian Sea event almost due south of network and mb 4.7 Iranian event east of network.

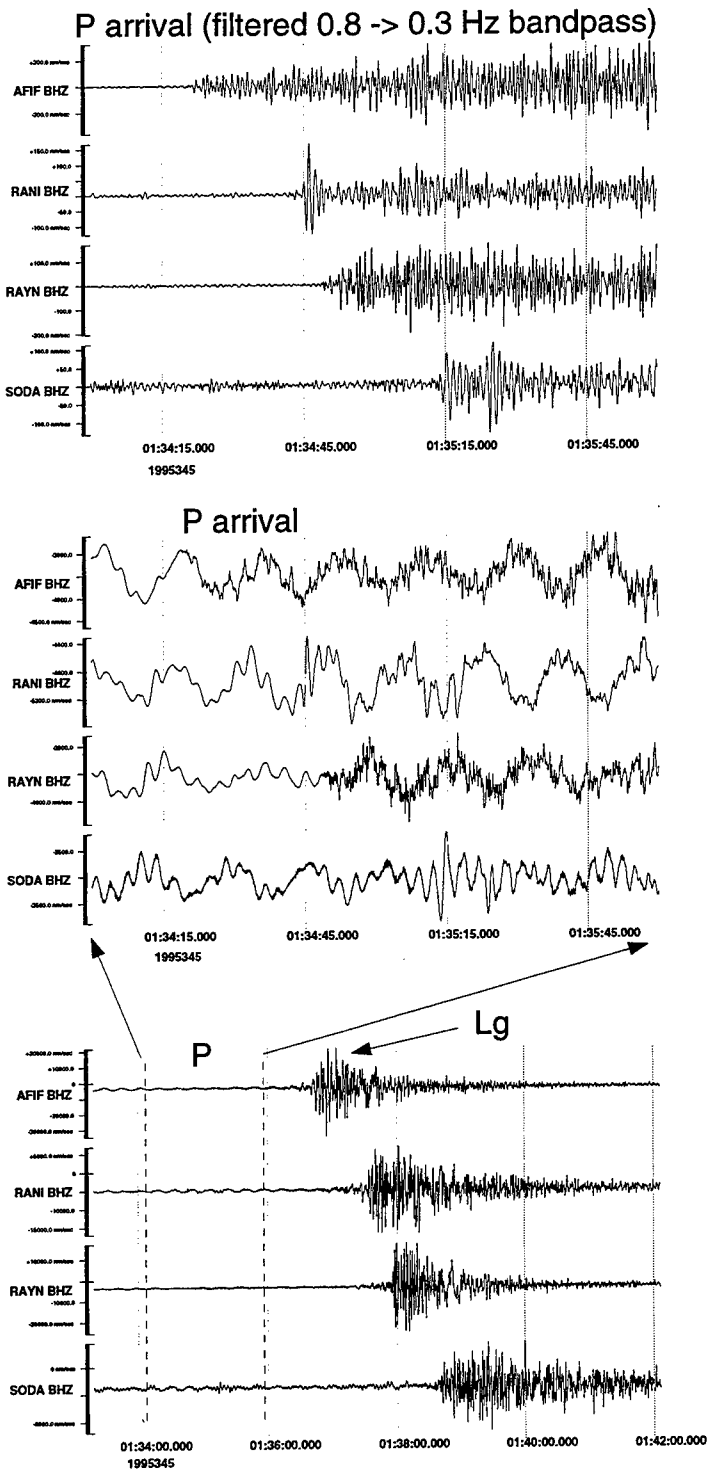

Figure 4. Mb 4.6 aftershock from the November 22 1995 Gulf of Aquaba event. Distance is approximately 8°. Note prominant Lg phase and low amplitude body phases.

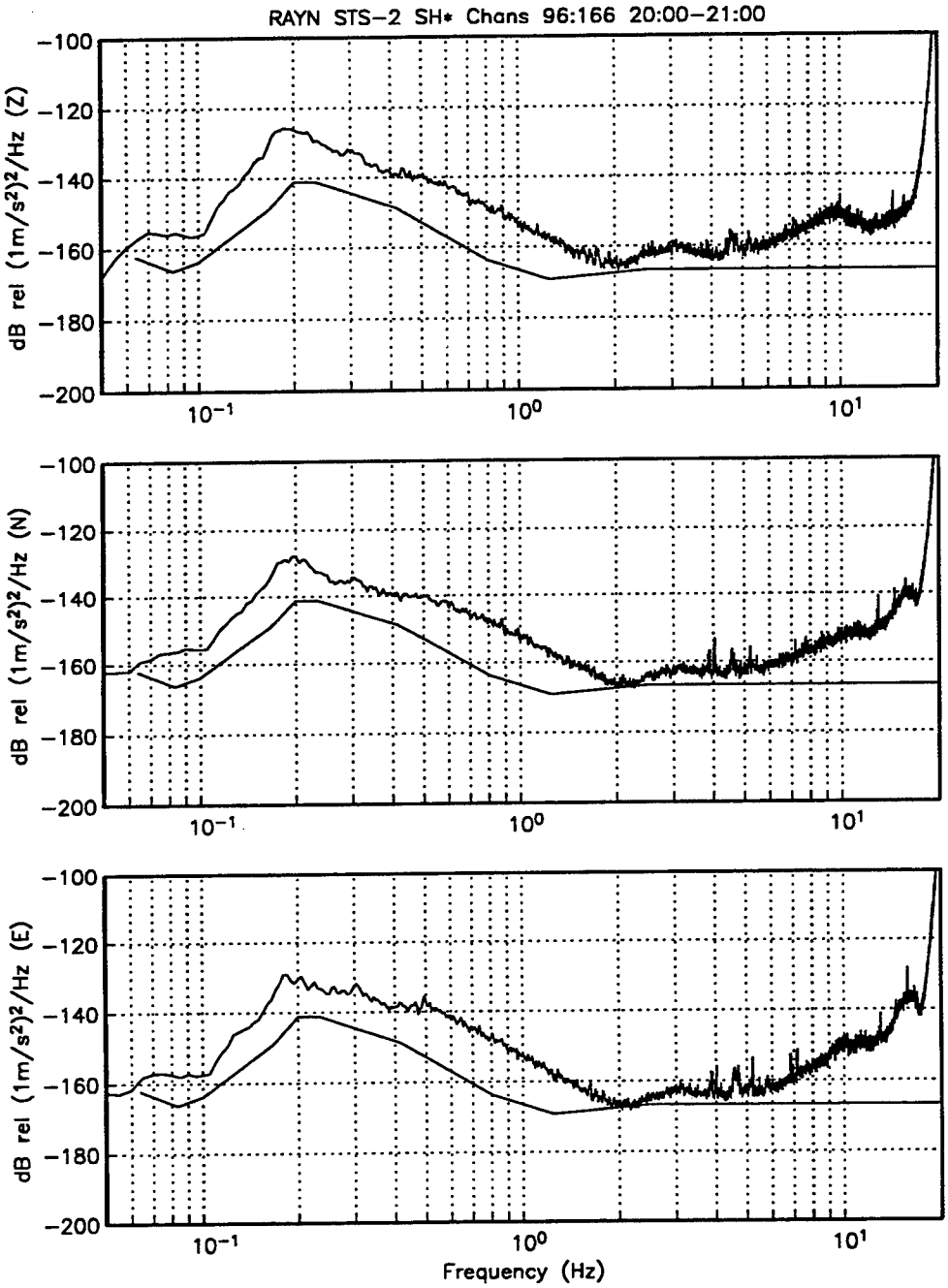

Figure 5. Acceleration power spectra for the Z, N, and E components for the station RAYN. The lower curve in each plot is the Low-Noise model.

THIS PAGE LEFT
INTENTIONALLY
BLANK.

Synthetic Seismograms at Regional Distances for May 1995 Earthquake and Explosion Sources in Western China

Fred N. App, Randy J. Bos, James R. Kamm
Los Alamos National Laboratory
Project No. ST482A
Sponsored by U. S. Department of Energy

Abstract

Waveforms recorded at several regional seismic stations at varying azimuths from explosion and earthquake sources in Western China exhibit marked variation from station to station. We have performed two-dimensional finite difference simulations of these events, using moment tensor sources and simple crustal structure models, to generate synthetic seismograms at these locations. The synthetic seismograms at three locations exhibit behavior that is qualitatively consistent with the data, while computational results at a fourth station differ from the data. We discuss these results, the assumptions of the simulations, and the limitations of this type of modeling in the context of regional seismic propagation. This report is a condensation of a Los Alamos National Laboratory, LA-UR-96-1600, with the same title.

Keywords:
synthetic seismograms
calculations/simulations
earthquake and explosion sources

Objective

This work is in direct support of U.S. and Comprehensive Test Ban Treaty (CTBT) verification goals. The research is aimed at providing the tools to minimize the frequency of false alerts (conventional explosions, mine collapses, rock bursts, or earthquakes that are mistakenly interpreted to be nuclear tests), yet provide confidence that if there were a nuclear test conducted somewhere in the world, it would be recognized as being nuclear. Whereas there are numerous seismograms from earthquakes and other conventional sources for calibrating many areas of the world, seismograms from nuclear explosions are relatively rare and from a few very localized regions. One possible way to obtain the nuclear data is through the computer generation of synthetic seismograms using realistic descriptions of the nuclear source and the more important geologic features along the path of the signal.

This is a report on the comparison of such synthetically generated seismograms with measurements in a region around Lop Nor, the Chinese Nuclear Test Site located in Western China, using a recently-developed LANL finite-difference code named AFD [1]. The study included calculations for a 15 May 1995 Lop Nor explosion and a 2 May 1995 northwest China earthquake. The objective was to evaluate the code and identify any improvements needed in order to meet requirements.

Research Accomplished

Figure 1 is a graphic with the contour of Moho depth of the region around Lop Nor superimposed on which are surface vertical velocity traces induced by the two seismic sources as recorded at several regional stations. Clockwise from the North, these stations are: TLY (ca. 1600 km NE of Lop Nor), ULN (ca. 1600 km ENE), NIL (ca. 1600 km SW), AAK (ca. 1200 km W), and BRVK (ca. 1900 km NW). Depth to Moho is but one of the elements to be taken into account in performing full waveform modeling in such a region. Other potentially important factors are location, depth and lateral extent of sedimentary basins and surface topographic features. As shown in Figure 1, there is notable variation in the recorded broadband waveforms at these various stations. To first order, an explosion is expected to have more of its energy associated with the p-wave (or *Pg*–the earlier arriving part of the signal) since the source is mostly spherical. Conversely, the earthquake energy should be primarily associated with the s-waves (or *Lg*–the later arriving signals) since the energy is released through a shearing motion. Upon inspection of the waveforms in Figure 1, it is apparent that such a clear partitioning of energy is true only along certain paths, most notably the path to Station NIL in the lower left-hand corner of the plot. At Stations AAK and BRVK the partitioning is less clear but still in evidence. At Stations TLY and ULN the explosion and earthquake are practically indistinguishable from each other. It is quite apparent that the signal undergoes substantial modification along its path; this observation demonstrates the need for numerous stations and paths for properly characterizing a given signal as being from an explosion or earthquake source. Equally important, from the

standpoint of CTBT verification needs, we need to be able to capture these same observed differences in the modeling.

A key feature to be included in the modeling is the crustal structure along each of these paths. The structure information was obtained from the Cornell Middle East / North Africa Project's online Profile maker (which also contains Eurasian data), using Lop Nor as the source location. Specifically, values for the depth-to-basement of sedimentary basins as well as for the Moho depth were obtained along each path. Approximate values for the elastic constants and attenuation factors for each material (sediment, mantle, crust) were assigned. Similarly, the values for the moment tensor coefficients and their time dependence were prescribed. Details on the input parameters used in the calculations are described in Ref. 2; the calculations were run out to simulation times of ca. 500 s.

All calculations were run with the LANL AFD anelastic finite difference code, using moment tensor sources. No detailed source physics, such as strong non-linear motion and surface spallation, was included in these calculations although that is an option in these kinds of calculations. Also, topographic effects were ignored. The simulations were run in a two-dimensional, plane-strain (Cartesian) geometry assuming a flat free surface. It is possible to run the code in either 2-D or 3-D, but the limited capabilities of current compute platforms limit regional-sized calculations to 2-D. Among the implications of these assumptions are: (1) no geometrical dispersion effects are included, (2) 3-D scattering is absent, and (3) no surface topography effects are present. The main reason these calculations were run in Cartesian as opposed to cylindrical geometry is that we have not implemented the capability to account for the 3-D moment tensor source into the coding for the cylindrical geometry equations of motion (i.e., the "2-$^1/_2$-D" approach). Due to the nature of finite difference simulations, and the memory and speed limitation of the computers available to the research team, the results are limited in frequency content to about one Hz.

Figures 2–5 are graphics containing the crustal sections of each path considered together with the computed surface vertical velocity synthetic seismograms. The crustal structure plots, in which the source location is at the left, have an expanded vertical scale relative to the horizontal scale. For this series of calculations, the same site (Lop Nor) was used for the location of both the earthquake and explosion; in reality, the earthquake was located ca. 400 km WNW of Lop Nor, in a region where there is a small depression in the Moho. In the simulations, the earthquake was centered at a depth of 33 km, and the explosion at 4 km.[1] The vertical scale of the velocities varies between the calculations and experiments, so only qualitative comparisons should be made. Additionally, all velocities have been filtered in the passband 0.2 Hz–1.0 Hz.

[1] This depth of burial (DOB) very likely exceeds the actual DOB associated with this shot. In the simulations, the source must be located several zones beneath the free surface. Therefore, the explosion source was located at a depth of 4 km, corresponding to eight computational zones, in all calculations in this series.

Figure 2 shows the results along the path to AAK, which has a relatively smooth, nearly level Moho and virtual absence of sedimentary basins. There is qualitative agreement between the data and simulation for the explosion insofar as the Lg is somewhat enhanced relative to the Pg. Similarly, although somewhat less accurately, the earthquake traces exhibit the canonical "earthquake" property of significantly enhanced Lg relative to Pg. In both simulations there is a strongly attenuated Lg coda (relative to the data), a characteristic that is evident in all simulations shown in this report.

Figure 3 presents the results along the path to NIL, which exhibits a strongly dipping Moho structure along the Tibetan suture zone, as well as a pronounced sedimentary basin. Again, there is approximate qualitative agreement between the data and simulations. The explosion synthetic shows enhanced Pg relative to Lg, although not as strongly pronounced as in the data. The earthquake synthetic shows an Lg enhancement relative to Pg that is more pronounced than in the data.

Figure 4 shows the results along the path to TLY, which has a mildly varying Moho and minor sedimentary structure. Approximate qualitative agreement between the data and simulations again obtains. In this case, both explosion and earthquake exhibit the canonical "earthquake" property of much enhanced Lg relative to Pg. In both simulations there is again a strongly attenuated Lg coda.

Figure 5 gives the results along the path to ULN, which differs only slightly in azimuth from the path to TLY (see Fig. 1) and exhibits a similar structure consisting of a mildly varying Moho and negligible sedimentary basin. In this case, however, there is notable lack of approximate qualitative agreement between the data and simulations. The waveform data for both explosion and earthquake exhibit an enhanced Pg structure (which is also evident in the broadband data shown in Fig. 1); this feature is not reproduced in the synthetics, which exhibit characteristics similar to those shown in the TLY simulations.

Conclusions and Recommendations

The computational results described above largely exhibit reasonable qualitative agreement with the data. This is a satisfying outcome, insofar as only basic path, material, and source information were used as input. Further improvement in this input, using, e.g., more refined crustal structure (stratigraphic) models and improved material property information, would very likely increase the fidelity of the results to some degree. Similarly, a more refined mesh (i.e., using a smaller computational zone size) would allow for higher frequency resolution in the calculated results.

The computational results, however, also exhibit certain limitations of this method. For example, the weak Lg coda in the simulations is likely due to the lack of scattering in the simulations. Presumably this characteristic would be improved by performing 3-D, instead of 2-D, simulations: the enhanced scattering in the 3-D case probably contributes to the Lg

coda. A more serious deficiency is shown in the comparison of the data with computations for the ULN path (see Fig. 5): the calculations do not exhibit at all the Pg structure seen in the data. There are several factors that may plausibly contribute to this discrepancy, among which are: (1) the effect of oblique 3-D subsurface structures that cannot be accounted for in the 2-D crustal "slice" simulated, (2) the crustal structure information may be inadequate or incorrect, (3) the material properties used may be inappropriate, (4) near-receiver geology and/or structure effects that were completely absent from the simulation.

Synthetics generated with the current code, even limiting the calculations to 2-D, can provide improved understanding of processes important in shaping waveforms along specific paths. An intrinsic strength of the finite difference technique is that it allows full inspection of the physical processes occurring throughout the entire stress field during the simulations. With proper qualification, the waveforms *may* be useable as crude substitute waveforms in areas for which there is no nuclear explosion data. However, in order to capture all of the salient features of a regional waveform, there is a very real need to install such improvements as topography into the code, optimize the code to minimize memory requirements and execution time, *and* implement the code onto more powerful compute platforms. As time and resources permit, we intend to develop the capability for using these simulations as an admittedly imperfect substitute for data along paths for which seismic data is either unavailable or unattainable (or both). Given such a capability, the outcome of simulations would be primarily limited by information on the geology.

References

1. J. R. Kamm, R. J. Bos & E. M. Jones, *User's Guide to AFD v. 1.0*, Los Alamos National Laboratory report LA-UR-96-853, March, 1996.

2. F. N. App, R. J. Bos & J. R. Kamm, *Synthetic Seismograms at regional Distances for May 1995 Earthquake and Explosion Sources in Western China*, Los Alamos National Laboratory report LA-UR-96-1600.

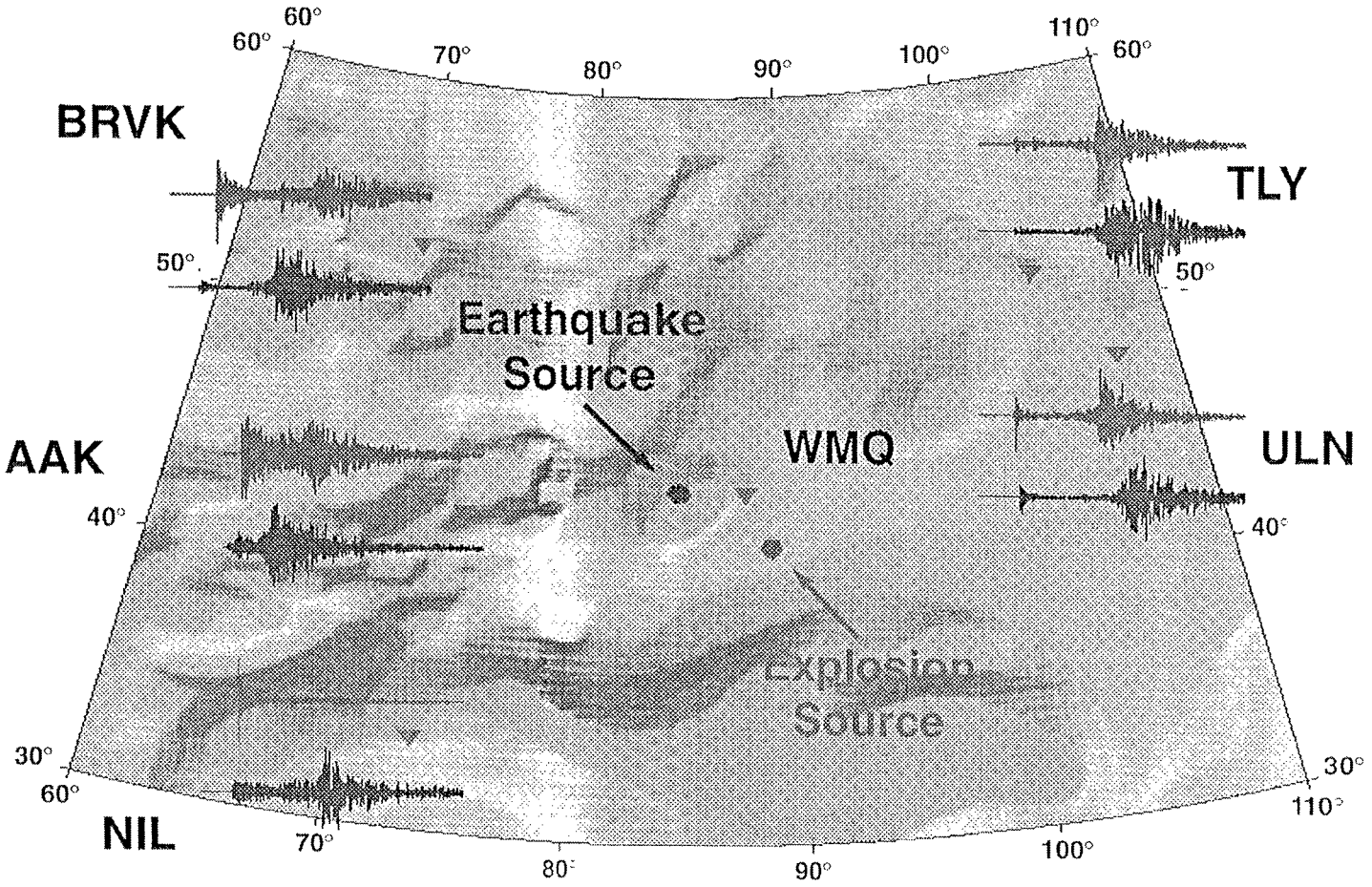

Figure 1. Contour map of Moho depth in Western China, with surface vertical velocity waveforms recorded for the 2 May 1995 magnitude 5.5 earthquake and the 15 May 1995 magnitude 6.1 explosion. The darker regions correspond to greater Moho depth. Inverted triangles denote seismic station locations, with the earthquake waveforms below those of the explosion. There is markedly varying behavior exhibited in the broadband waveforms along the different paths from these sources.

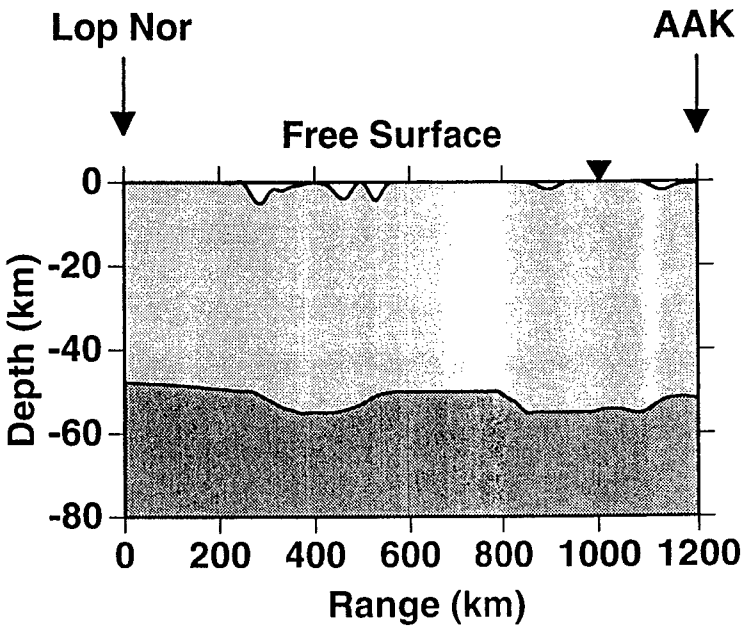

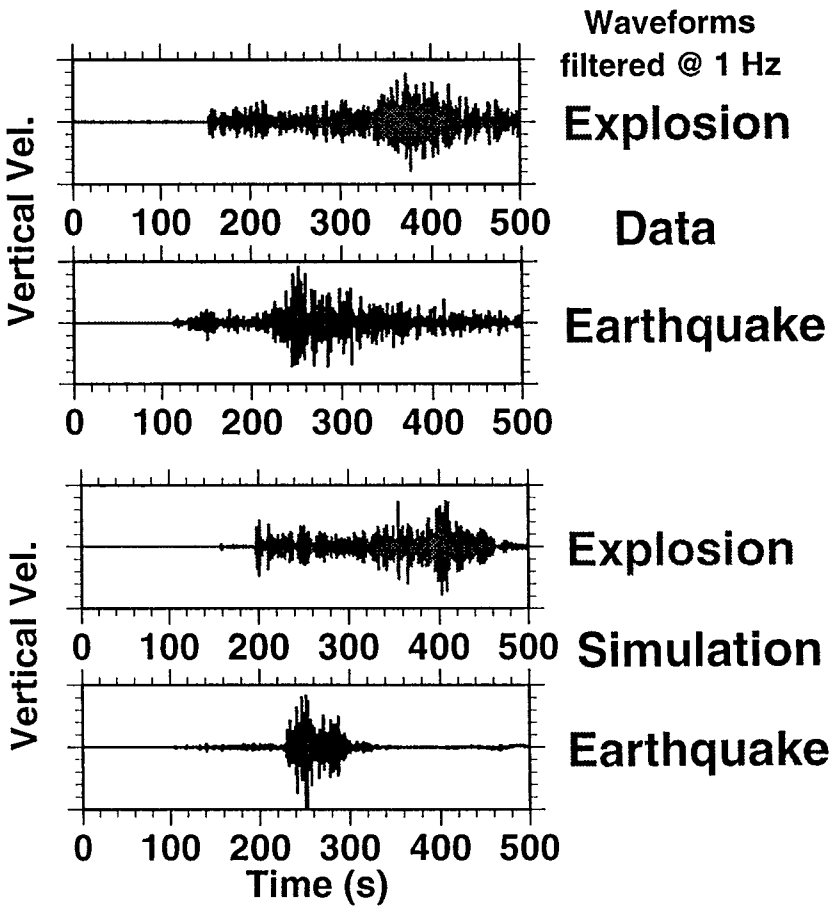

Figure 2. Crustal structure between Lop Nor and station AAK (above), located ca. 1200 km W of Lop Nor; earthquake and explosion waveforms at this station (right). There is approximate qualitative agreement between the data and simulation for both sources. The simulations exhibit a lack of Lg coda, likely due to a lack of scattering in the 2-D calculations.

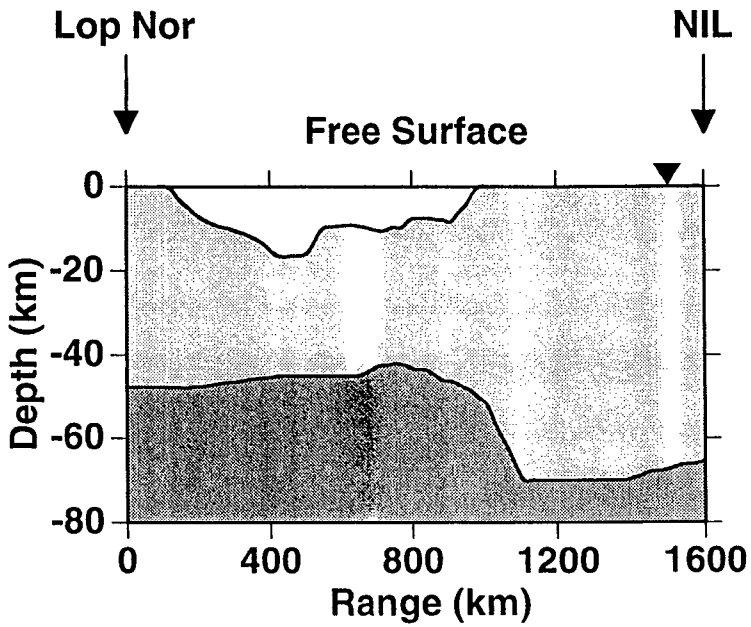

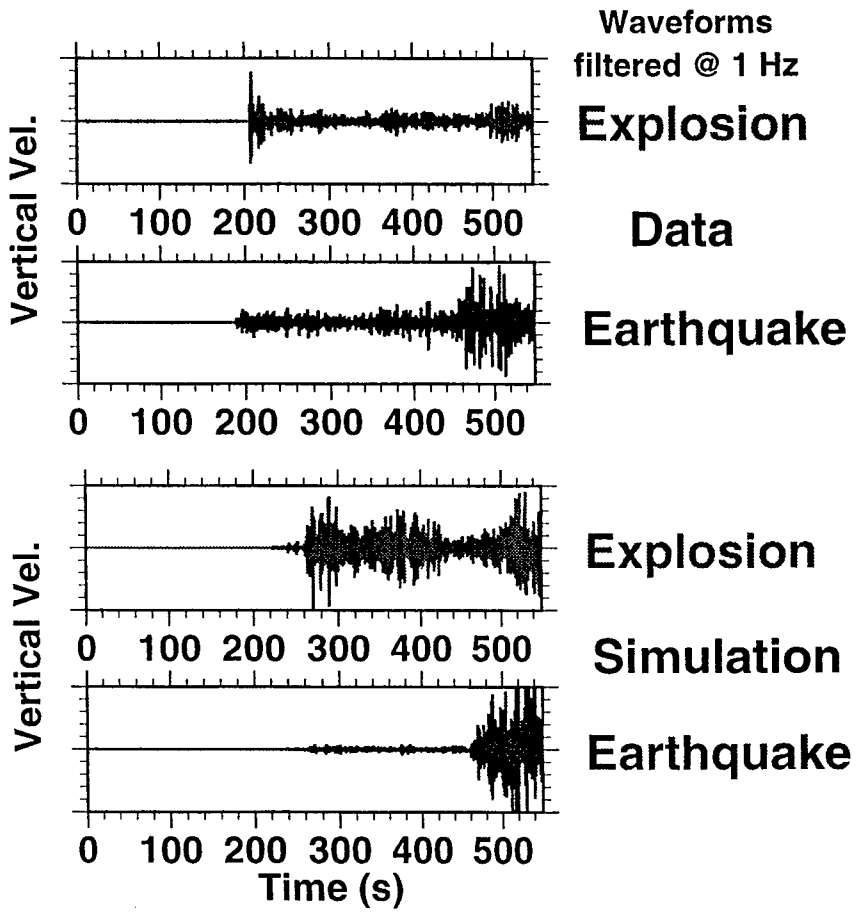

Figure 3. Crustal structure between Lop Nor and station NIL (above), located ca. 1600 km SW of Lop Nor; earthquake and explosion waveforms at this station (right). The path exhibits a strongly dipping Moho as well as a pronounced sedimentary basin. There is approximate qualitative agreement between the data and simulation for both sources.

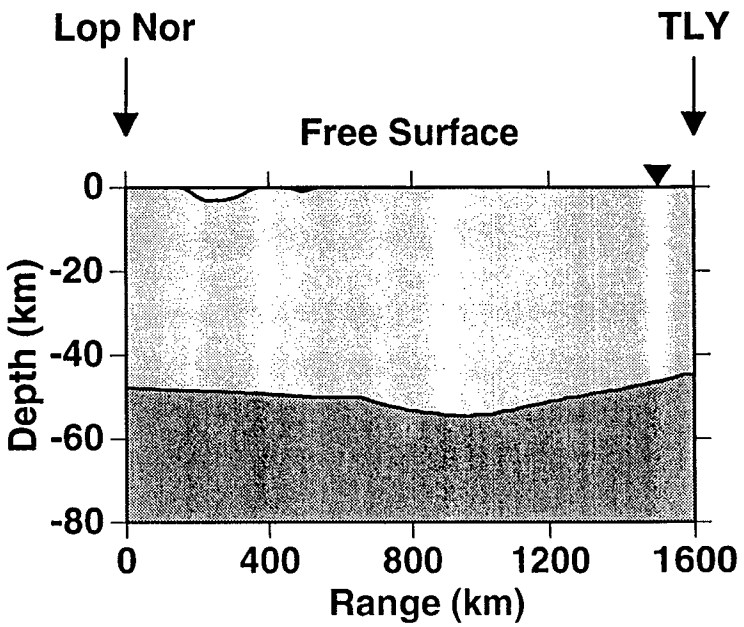

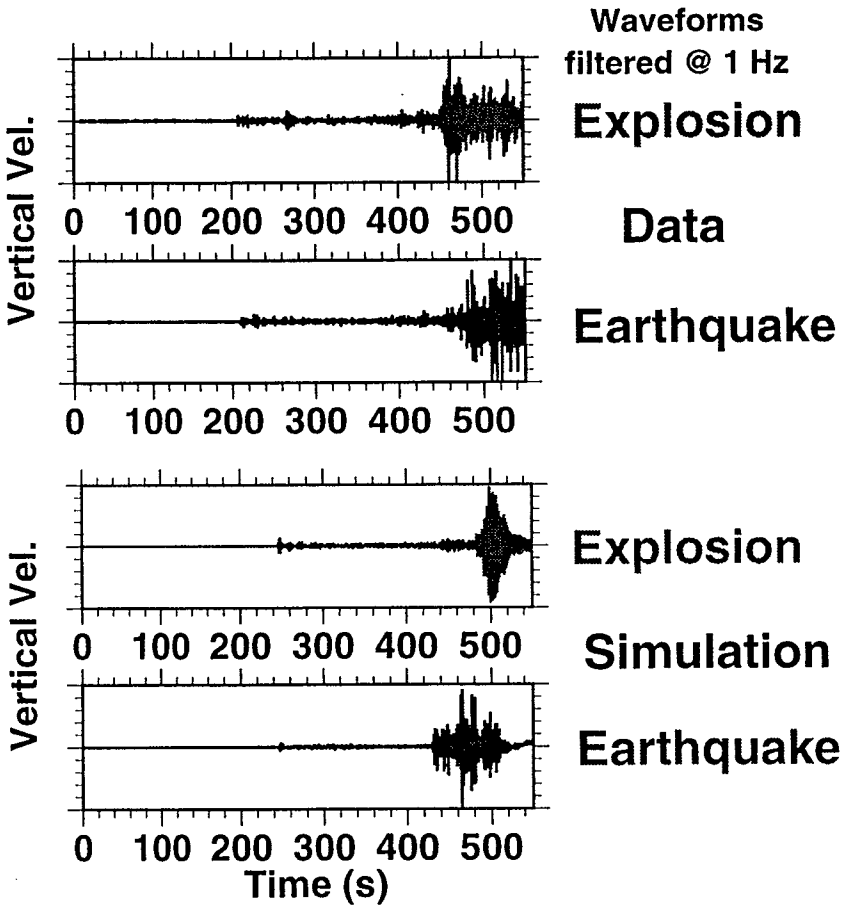

Figure 4. Crustal structure between Lop Nor and station TLY (above), located ca. 1600 km NE of Lop Nor; earthquake and explosion waveforms at this station (right). The path exhibits a mildly varying Moho and minor sedimentary basin. There is approximate qualitative agreement between the data and simulation for both sources, with the exception of the weak Lg coda in the simulations.

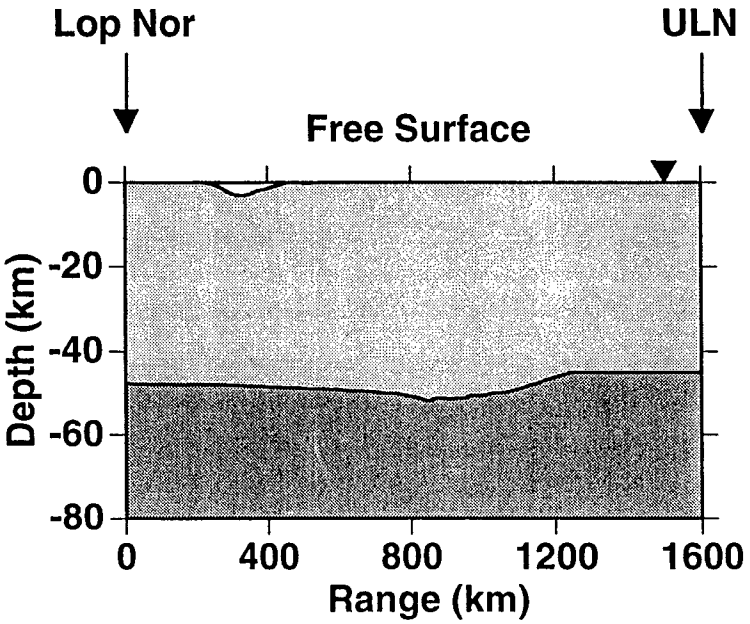

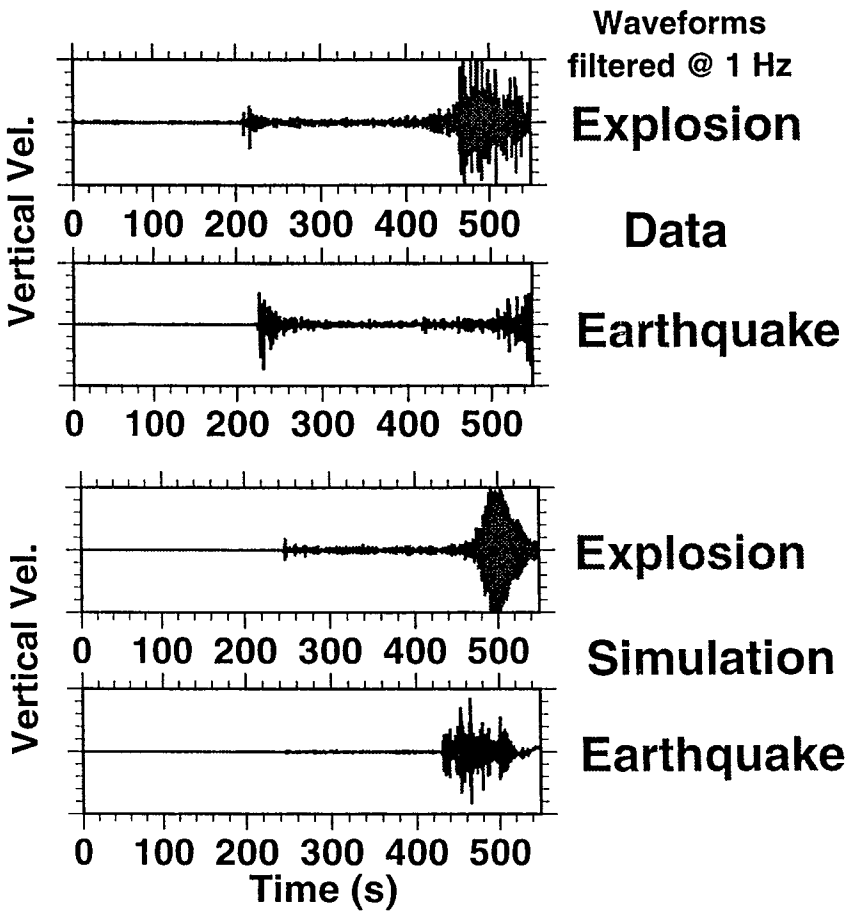

Figure 5. Crustal structure between Lop Nor and station ULN (above), located ca. 1600 km ENE of Lop Nor; earthquake and explosion waveforms at this station (right). The path is similar to that to station TLY (Fig. 4). There is notable disagreement between the data and simulation for these sources: the data for both the earthquake and explosion show a distinctive Pg that is lacking in the corresponding simulations.

3-D Seismic Wave Synthesis and Full Wavefield Inversion

C. Archambeau, J. Orrey, B. Kohl - Department of Physics, University of Colorado
Contract No. F49620-94-1-0124
Sponsored by AFOSR

ABSTRACT

This study involves the development and application of a new method for numerically modeling seismic wave fields in arbitrarily heterogeneous media. The method (GFM) is a generalization of the Fourier pseudospectral method in which a Fourier expansion set is adjoined by a finite set of functions, termed discontinuity functions, which are not infinitely differentiable with continuous derivatives like the harmonic functions. With the discontinuity function set included, the generalized Fourier method is capable of accurately representing high frequency wave fields in two- or three-dimensional media with surfaces of discontinuity. The GFM approach is formally expressed as a weighted residuals statement of momentum conservation with boundary conditions at discontinuities included. A general coordinate transformation can be used to incorporate surface topography and irregular material interfaces into models of strongly heterogeneous earth structure and to improve the resolution of small-scale wave field features. The method is both fast and accurate, allowing 2-D/3-D modeling of high frequency regional seismic wave fields in arbitrarily heterogeneous media on a work station. Systematic forward modeling, designed to investigate the effects of scattering, major structural changes and anisotropy on regional signals important in source discrimination, has been carried. In addition, a new inversion method involving the full 3-D seismic wave field, has been formulated to take advantage of the capability to compute Greens functions in general 3-D anelastic media using this forward modeling capability. The Full Wave Inversion (FWI) formulation is in the form of classical Fredholm integral equations for the components of the required corrections δU_k, $k = 1, 2, 3$, to the initial model wave field in order to match observations. Integral equations of this type can be solved using a Neumann interative series which is known to converge uniformly. This approach is used in this inverse problem and yields a system of algebraic equations to be solved for medium parameter changes at each iteration step. Successive iterations reduces differences between the observed and predicted wave field values to produce the desired, and expected, convergence. Application of this formal inversion procedure is being undertaken and is expected to be a very useful means of determining both earth structure and source properties.

Key Words: seismic modeling, sources, inversion, earth structure.

(1) Objectives

The chief objectives of this research are, ultimately, to generate methods for:

(1) Regional seismic modeling for discrimination: P_n, P_g, S_n, L_g and R_g synthesis from earthquakes and explosions in complex geologic media.

(2) Evaluation of seismic discriminants: The discrimination potential of specific discriminants and the physical basis for source identification.

(3) Determinations of detailed 3-D seismic velocity structure in selected regions where accurate discrimination of seismic events is important.

Investigations in each of these topic areas require modeling of seismic wave fields in heterogeneous three dimensional structures. Therefore, the fundamental tools to be used in the proposed investigations are numerical methods of computing seismic wave fields in complicated 3-D structures; namely a Generalized Fourier Pseudospectral Method (GFM). The GFM theory developed and applied provides complete seismograms at regional distances and accounts for anelasticity, random (small scale) and large scale strong (and discontinuous) heterogeneities in two or three dimensions, irregular topography and also general anisotropy, when necessary.

The approach taken in regional discrimination predictions is to use the GFM synthetic seismograms in a systematic study for characterization of the principal discriminatory seismic phases from areas of low seismicity. This characterization is based on predicted wave forms, amplitude spectra, dispersion, arrival times, coda length and spectra and attenuation with distance for different sources and for (appropriate) paths through complex, representative, media.

Inversion methods that make use of the ability to compute Greens functions inheterogeneous media in 3-D are also being developed in order to be able to provide the detailed earth structures required for confident source characterization and identification.

(2) Research Accomplished

2.1 Development of Generalized Fourier Pseudospectral Methods for Modeling Wave Fields in 3-D Heterogeneous Media

The analytical development of a generalized Fourier Pseudospectral Method (GFM) has been completed and a paper was submitted for publication to the Geophysical Journal International, November, 1995. (The revised manuscript, entitled, "Complete Seismic Wavefield Synthesis with a Pseudospectral Method: The Generalized Fourier Method," by J. Orrey, C. Archambeau and G. Frazier, will be resubmitted in July, 1996.)

The focus of this study has been to increase the tractable bandwidth of seismic wavefield simulations through the development of a more computationally efficient and accurate simulation method. We use efficiency to refer to a measure of both a method's storage requirements and computation time for a given problem and chosen level of accuracy. A method's efficiency for a particular simulation is therefore roughly proportional to the total required number of discrete

points in space and time. Typically, accuracy is measured in terms of solution error, such as the percentage error in phase velocity determined from a simulation. In this study, particular emphasis is placed on the accuracy of boundary condition approximations.

The central contribution of this work is to incorporate into the Fourier method boundary conditions at material discontinuities. This is achieved by combining the trigometric functions of the Fourier method with additional functions which are not, like the trigometric functions, infinitely differentiable with continuous derivatives. The additional functions, referred to as *discontinuity functions,* approximate the spatial discontinuities of the field variables, leaving a continuous remainder to be synthesized by the trigonometric functions. We refer to the resulting method as the generalized Fourier method (GFM).

The generalization of the Fourier pseudospectral method developed in this study involved supplementing the Fourier method's trigonometric basis set with discontinuity functions and using the weak Galerkin form of weighted residuals to approximate the governing equations for momentum conservation. With the particular choice of the sawtooth and quadratic discontinuity functions, accurate simulations were obtained for problems with a traction-free surface. In principle, other forms of discontinuity functions could be used in a generalization of the Fourier method, as long as they suitably handle the discontinuous portion of an approximate solution. They must be a degree higher to one another and to the Fourier basis set, and each additional function must be a degree higher in continuity than the previous one if adding the function is to improve convergence. A systematic method was developed for obtaining a set of polynomial-based discontinuity functions, up to a specific degree of continuity.

2.2 Tests and Applications of GFM Seismic Modeling

GFM predictions were compared with independent results, either analytical or these obtained from classical mode superposition in simple earth models, to test accuracy and reliability of the computational method. Figures 1 and 2 show an example of such a comparison with the normal mode representation in a simple elastic velocity model. The agreement between these results, along with similar agreement with analytical solutions (e.g., Lambs problem) provides confidence in the accuracy of this new computational method and its applicability in modeling seismic wavefields in much more complicated media.

Examples that indicate the capabilities of this modeling approach in studying the effects of typical medium complexities on seismic wave propagation illustrate the range of problems that may be addressed. Specifically, we address the effects of propagation in complex models for P, P_g, L_g, S and R_g in the regional distance range in order to test various discrimination methods involving these phases and to evaluate discriminant robustness and variability arising from common earth structure variations.

In this regard, Figures (3) and (4) illustrate the effects of increasing complexity in an earth model due to random spatial variations in the velocity values about mean values within a layered model, where the randomization is in both the vertical and lateral directions. In particular, Figure (3) shows the GFM synthetic seismograms for an explosion at 1 km depth in a 2-D, uniformly layered elastic model. Figure (4) shows the seismograms in the same model with 10% rms variability imposed on the (mean) P and S wave velocities. Clearly there are major differences, in

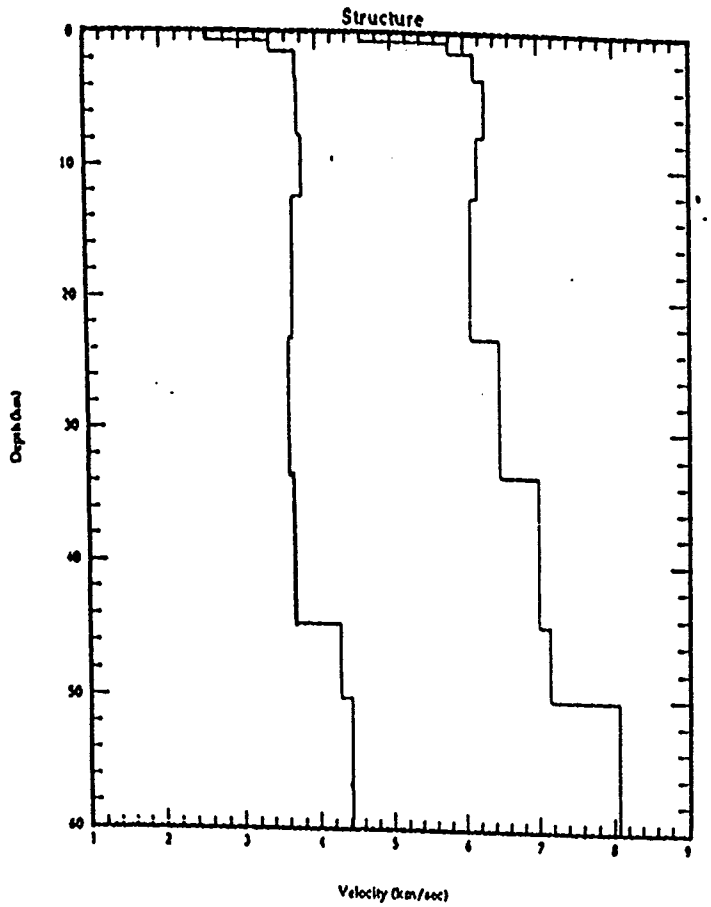

Figure (1). Structure used for Fourier-Sawtooth/Normal Mode comparison.

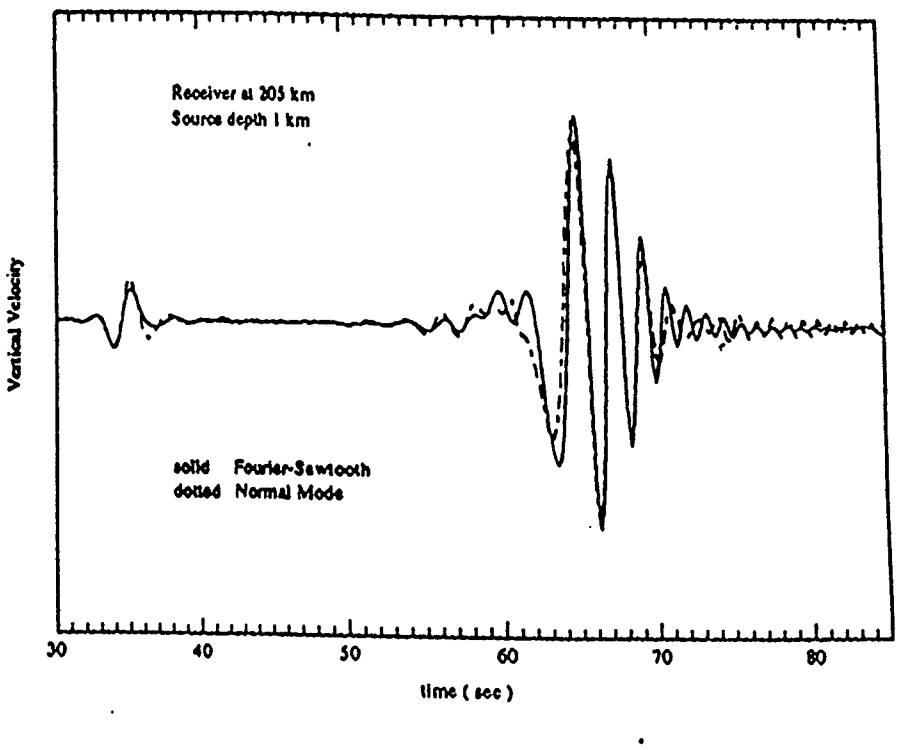

Figure (2). Time series comparison of the Fourier-Sawtooth and Normal Mode methods at a source-receiver distance of 205 km for the structure shown in Figure (1).

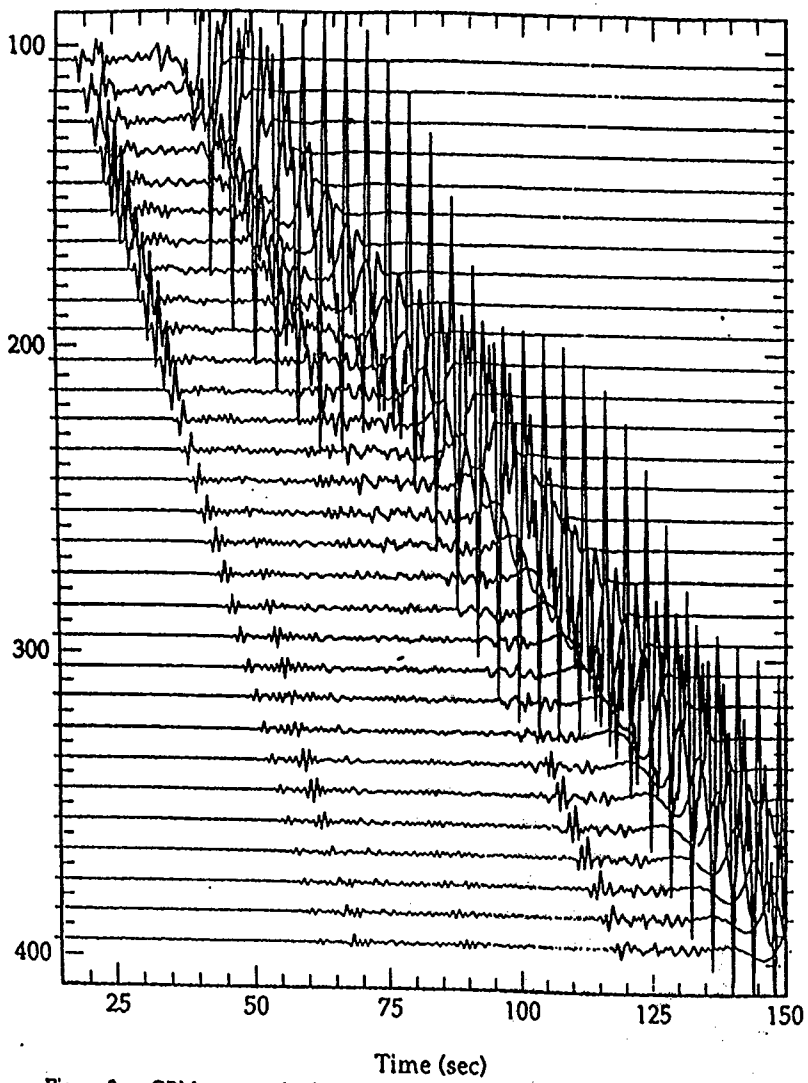

Figure 3 GPM generated seismograms at different regional distances (in kilometers) from an explosive source at 1 km depth in a simple layered half space with no anelastic attenuation.

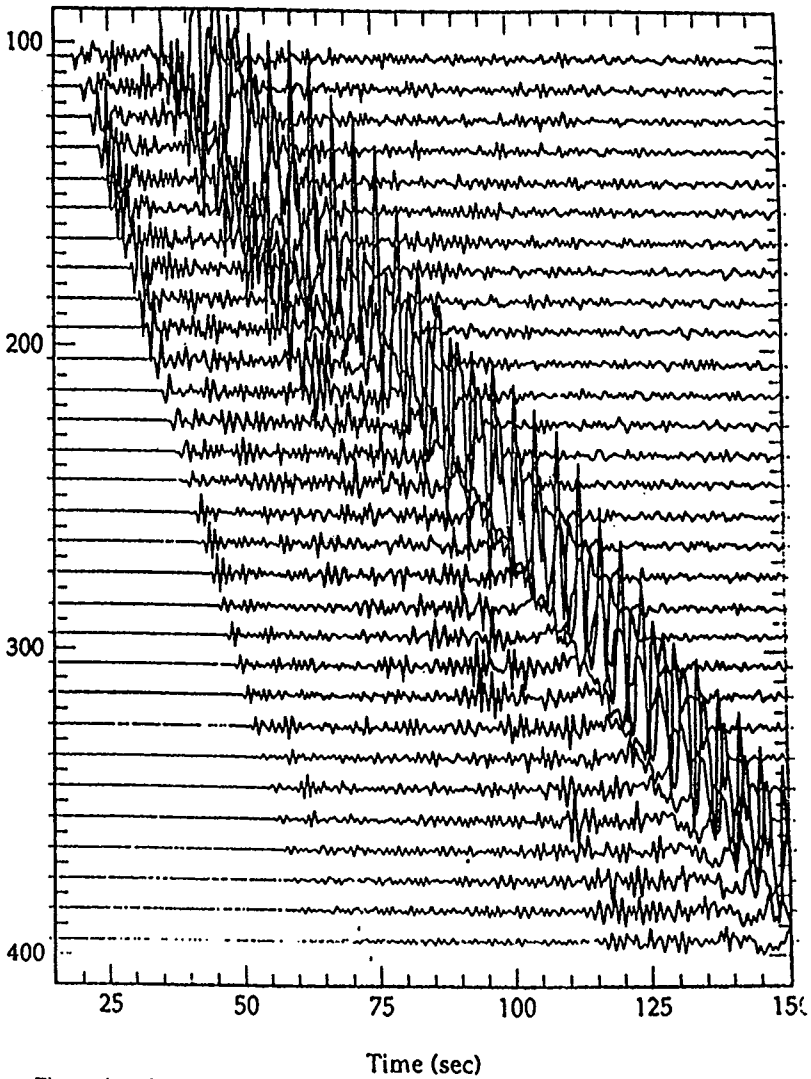

Figure 4 GPM generated seismograms at regional distances for the structure and source in Figure 3 but with 10% random fluctuations in the elastic velocities. Note the much lower levels of the R_g surface wave at larger distances and the larger amplitudes of P_g and L_g relative to the results in Figure 3, showing the transfer of energy from the fundamental mode (R_g) to the higher modes making up L_g and P_g. This effect increases as random fluctuations increase in magnitude.

that the R_g phase is reduced as a function of distance from the source and the L_g and P_g phases are considerably increased and more complex. Since this effect is generally observed, we conclude that random fluctuations are responsible for the relatively large L_g observed relative to R_g at greater distances from the source. In this case the L_g energy is largely derived from scattering from R_g, with an associated rapid attenuation of R_g with distance and a relative growth of Lg amplitudes.

Figure (5a), again with an explosion source at 1 km depth, shows the effects of vertically and laterally discontinuous changes in the randomization, where the rms percentage of randomization changes from layer to layer in depth (with decreasing fluctuations with depth) and also decreases within lateral zones at greater distances from the explosion source.

For this model, the L_g is larger and the R_g is smaller than was the case for the model results in Figure (4), which had the same average velocity values. This change is largely due to the larger fluctuations in near-surface P and S velocities for the model used for Figure (5a) compared to the structure model for Figure (4) (25% compared to 10% in the upper 1 km near the source; the source was applied at a lateral position of 30 km). These large random velocity variations, of 25% and greater, are commonly observed from well logs and can persist to depths of at least 5 km in most areas. Therefore, the structure model used in Figure (5a) is not extreme and, indeed, is probably conservative with respect to velocity fluctuations, particularly in tectonic areas. Furthermore, the synthetic seismograms in (5a) are yet closer approximations to those commonly observed, compared to those in Figure (4).

Figure (5b) shows seismograms for a simple earthquake-type source at a depth of 5 km in the same structure model used in Figure (5a). In this simulation, the short period R_g excitation is lower, relative to the explosion in (5a), in part due to its greater source depth.

Figures (6) and (7) show the effects of anelastic attenuation when compared to the simulations in Figure (5a). In particular, the structure and explosive source used for the elastic simulation in (5a) are also used for the simulations in Figures (6) and (7). However, in the latter simulations anelastic effects were included by the introduction of a space-dependent dissipation factor described by an intrinsic quality factor Q. Thus the results in Figure (5a) are for an elastic medium (infinite Q), while those in Figures (6) and (7) include different levels of dissipation.

The results in Figure (6) were produced with a depth-dependent Q factor, with a Q value of 150 near the free surface and increasing Q with depth, while those in Figure (7) are for a (low) Q value of 25 near the surface that also increases with depth. Comparing Figures (5a) and (6) shows a modest decrease in R_g and L_g due to moderate anelastic attenuation, while comparison of the results for the low Q case in Figure (7), with the elastic or moderate Q cases, shows a dramatic reduction in both the R_g and L_g energy with distance while the P waves remain relatively unaffected. We note that a low near-surface Q model will always have a rather drastic effect on the short period R_g and L_g surface wave modes and that in comparison to actual data this is not typically the case. That is, while R_g decreases rapidly with distance, L_g does not, and in fact the L_g coda tends to increase in duration and magnitude in many areas. This suggests that R_g scattering to L_g is the dominant mechanism and that results like those in Figure (6), with a moderate Q, are appropriate in the general case.

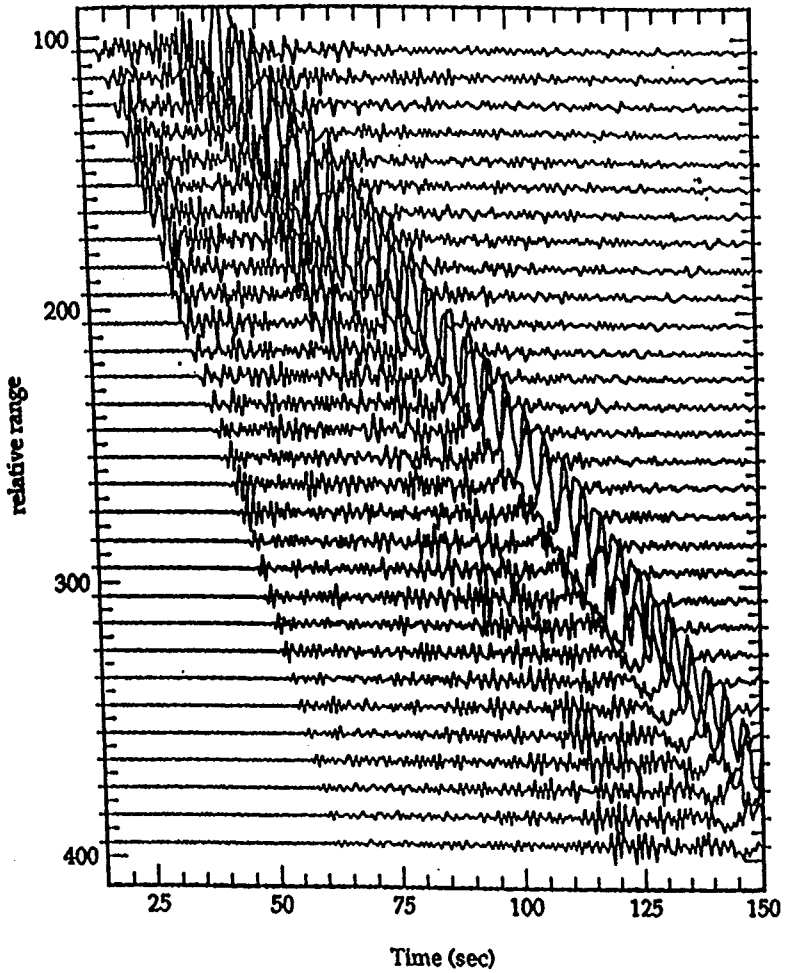

Figure (5a) GPM generated seismograms from an explosive source at 1 km depth in the layered structure with strong, random elastic velocity fluctuations and no anelastic attenuation. The strongest fluctuations are 25% rms, and the fluctuations decrease with distance from the source.

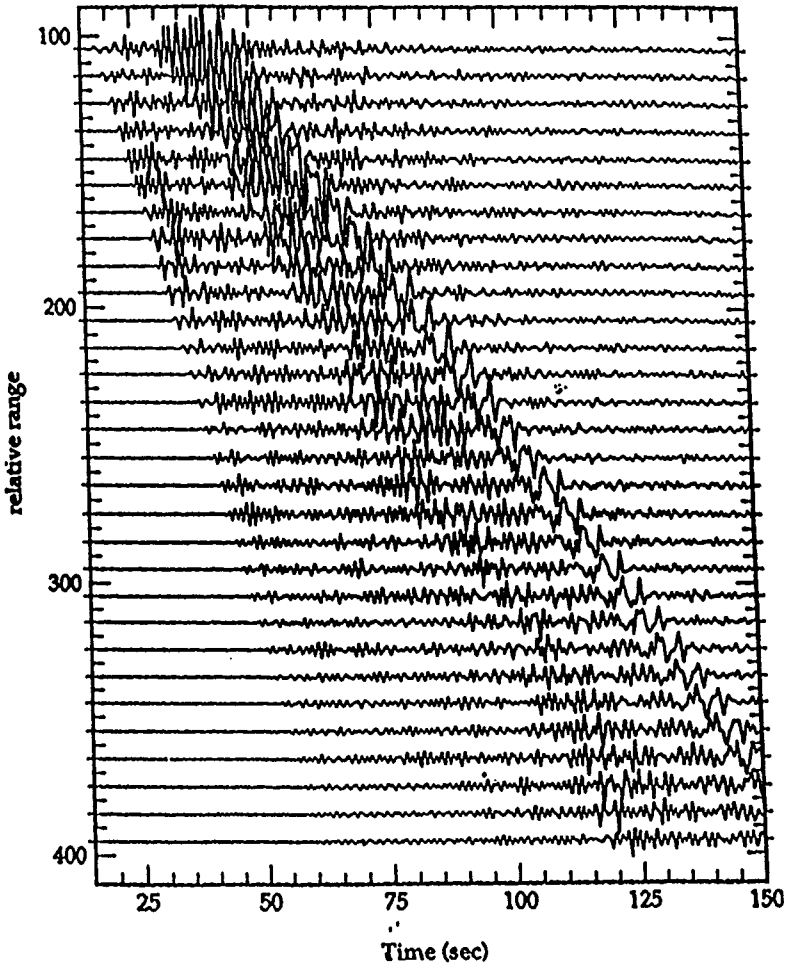

Figure (5b) GPM generated seismograms for the structure in Figure (5a) but with a double couple source at a depth of 5 km. The fault plane is oriented at 45 degrees from the vertical.

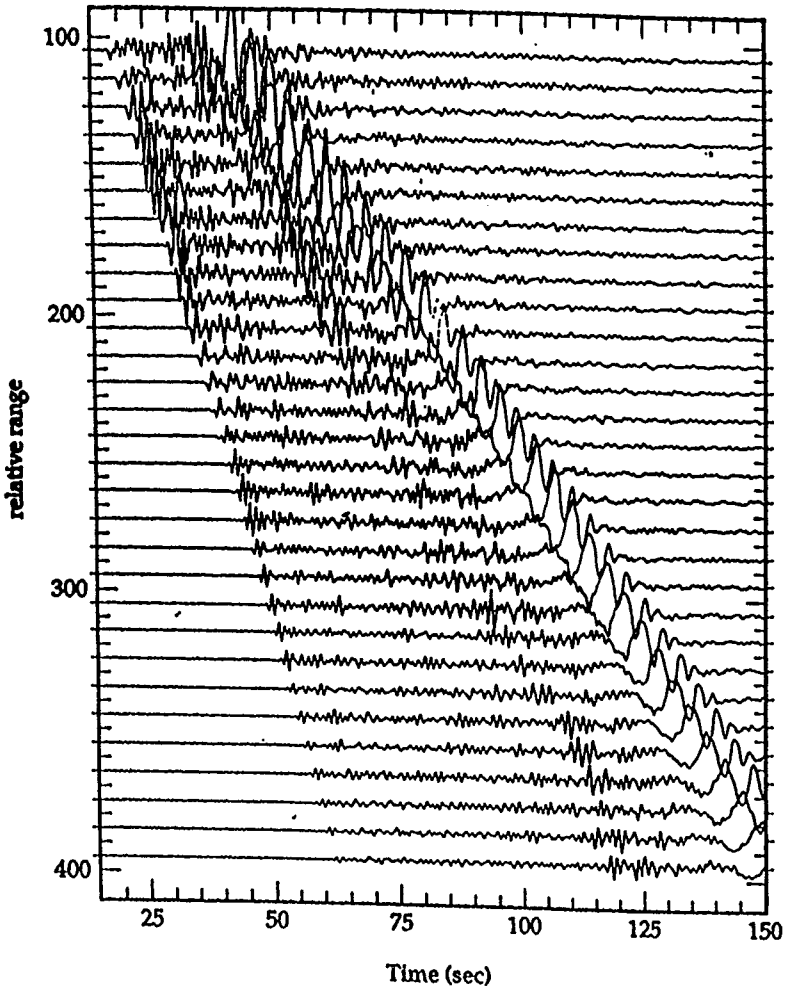

Figure (6) GPM generated seismograms from an explosive source at 1 km depth in the same structure used for the simulations of Figure (5), except this model contains anelastic dissipation effects. The Q value is depth-dependent with a minimum Q value of 150 near the free surface and increasing Q with depth.

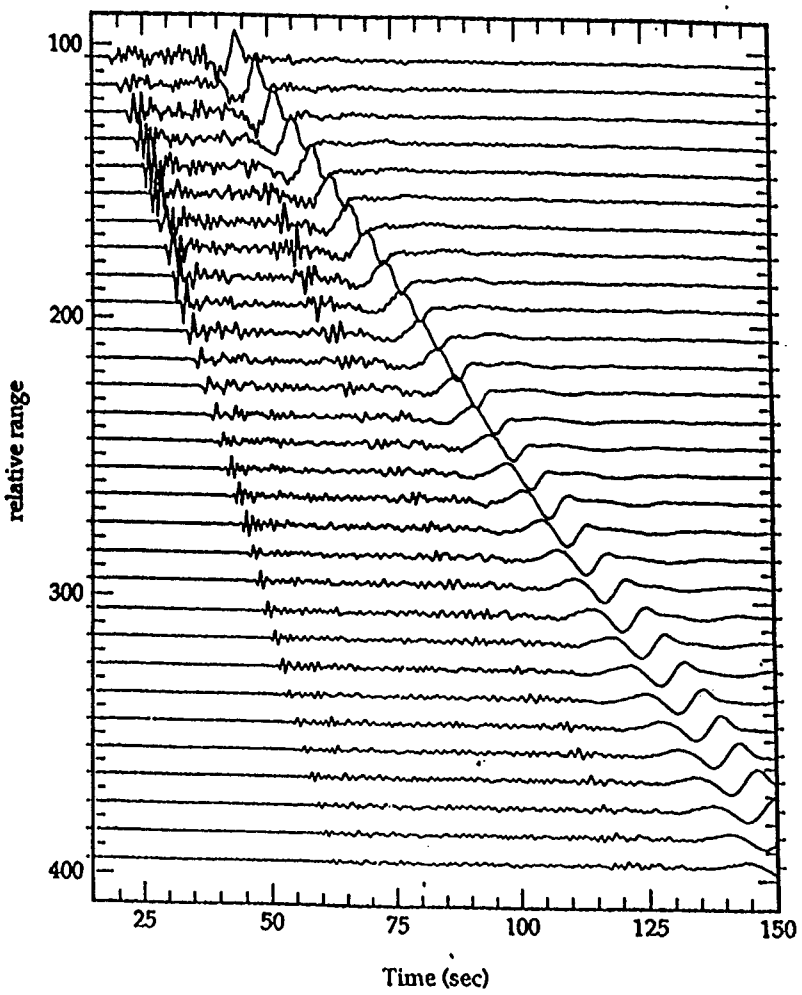

Figure (7) GPM generated seismograms from an explosive source at 1 km depth in the anelastic structure used for the simulations of Figure (6), except the structure for this simulation contains much lower Q values. The minimum Q value is 25 near the free surface.

These examples suggest the range of investigations that have been pursued as well as the similarity of the results of the numerical simulations to observed seismograms. To some extent, even with this small sampling, it is possible to infer specific effects of structure variations on the important discriminatory signals.

2.3 Development of a Full Wavefield Inversion Method

The analytical form of an inversion method for the inference of medium properties ("structure") from observations of the wavefield on the boundary, S, of a general solid medium has been developed. The approach devised can only be applied when a particular Green's function (that is, one satisfying particular boundary conditions) for the medium can be determined. Such a Green's function can, however, be obtained using the GFM modeling and involves solutions in a 3-D medium, with volume V, outer boundary S and a continuous variations of material properties in V. More specifically, the appropriate Green's function can be defined in terms of the wavefields produced by delta function point sources located successively at all receiver points on S; so that the ("two point") Green's function can be specified for receiver points on S using the reciprocity property of Green's function solutions for the (linear) operator equation. Further, to achieve the desired form that allows the inverse problem to be simply formulated, it is necessary that this Green's function satisfy a zero traction condition on S, the boundary of V. Such solutions can be obtained by GFM modeling in the most general 3-D case, so as noted earlier, the GFM modeling capability can be used to generate this special Green's function.

It is not difficult to show that if δu_η represents the difference between the observed wavefield u_η and a known wavefield ${}^{(0)}u_\eta$ for a specific structural model, then if ${}^{(0)}u_\eta$ is an approximation to u_η we have, to first order:

$$\delta u_\eta(\mathbf{x},t) = -\frac{1}{4\pi}\int_0^t dt_0 \int_V \left[{}^{(1)}L_{\alpha\gamma}\,{}^{(0)}u_\gamma(\mathbf{x}_0,t_0)\right] G_\alpha^\eta(\mathbf{x},t;\mathbf{x}_0,t_0)\,d\mathbf{x}_0 \qquad (1)$$

with

$${}^{(1)}L_{\alpha\gamma} \equiv \Delta\rho\,\delta_{\alpha\gamma}\frac{\partial^2}{\partial t^2} + \frac{\partial}{\partial x_\beta}\left[\Delta C_{\alpha\beta\gamma\lambda}\frac{\partial}{\partial x_\lambda}\right]$$

where G_α^η is the Green's function defined as above and $\Delta\rho$ and $\Delta C_{\alpha\beta\gamma\lambda}$ are the differences $[\rho - {}^{(0)}\rho]$ and $\left[C_{\alpha\beta\gamma\lambda} - {}^{(0)}C_{\alpha\beta\gamma\lambda}\right]$ respectively. Here ${}^{(0)}\rho, {}^{(0)}C_{\alpha\beta\gamma\lambda}$ are associated with ${}^{(0)}u_\eta$ and ρ, $C_{\alpha\beta\gamma\lambda}$ the "true" material property parameters, are associated with u_η, the observed field on S. Now if $\Delta\rho$ and $\Delta C_{\alpha\beta\gamma\lambda}$ are expanded as Fourier series in the spatial wavenumber $\mathbf{k}$, so that:

$$\Delta\rho(\mathbf{x}) = \sum_{\mathbf{k}} \Delta\tilde{\rho}(\mathbf{k})e^{i\mathbf{k}\cdot\mathbf{x}} \qquad (2)$$

and similarly for $\Delta C_{\alpha\beta\gamma\lambda}$, then δu_η can be represented by the algebraic system

$$\delta u_\eta = -\sum_{\mathbf{k}}\left[\Delta\tilde{\rho}\,{}^{(1)}A_\eta + \Delta\tilde{C}_{\alpha\beta\gamma\lambda}\,{}^{(2)}A_{\alpha\beta\gamma\lambda\eta}\right] \qquad (3)$$

where the "coefficients" ${}^{(1)}A_\eta, {}^{(2)}A_{\alpha\beta\gamma\lambda\eta}$ are given in terms of Green's function integrals obtained from (1), and are functions of the receiver coordinates $\mathbf{x}_R, t_R$.

Thus, inasmuch as δu_η is a time series at a receiver on S, then equation (3) expresses an algebraic relationship between the time series on each side of the equation. By treating many receiver

observations on S we create a system of such equations which can be expressed as a matrix equation. Thus, by sampling in the time domain at the receivers we can form a matrix system from (3) and then invert it for the unknown parameter coefficients $\Delta\tilde{\rho}$ and $\Delta\tilde{C}_{\alpha\beta\gamma\lambda}$. Inverse Fourier transforms, based on (2), then give the spatial representatives $\Delta\rho(\mathbf{x})$ and $\Delta C_{\alpha\beta\gamma\lambda}(\mathbf{x})$, from which we obtain $\rho(\mathbf{x})$ as ${}^{(0)}\rho(\mathbf{x}) + \Delta\rho(\mathbf{x})$ and similarly for the elastic moduli.

This brief outline illustrates some of the essential features of the results obtained. The full theoretical development involves an iteration method in which the first iterate corresponds to (3) above. The full iteration series is a Neumann series with strong convergence properties and therefore produces confidence in the final solutions; albeit at the expense of extensive computations.

Conclusions and Recommendations

A very powerful numerical modeling method has been developed that has superior accuracy, storage requirements and speed relative to all other methods tested. Most important is the accuracy and speed achievable on a moderate sized workstation, since this allows extensive modeling in 3-D for comparative studies with data. In this regard, only relatively preliminary comparisons with observations have been made and systematic studies have only begun. Therefore, further applications involving observed data, as well as prediction work, is recommended.

The formal development of a fullwave inversion method for 3-D variable media has been completed and is expected to become a basic tool for both structure and source studies. "Calibration" of structures in particular regions would be quite important for subsequent source location/identification in and near these areas. At present the computerized numerical procedure to implement the inversion method has not been completed, and this coding should be continued and tested. Testing of the method with known solutions and evaluation of its limitations is recommended for the near future, before applications with observed field data.

Quantifying the Attenuation and Blockage of Lg and Robust Statistical Estimates of Site Amplifications at SCSN stations

G. Eli Baker, J. Bernard Minster, University of California, San Diego
94-1-0204/93-1-0508
Sponsored by AFOSR

ABSTRACT

The immediate goal of this work has been to quantify the relationship between continental crustal structure and Lg propagation. A lack of appropriate observations of the effect of various structures on Lg propagation limits our ability to develop an understanding of the basis of Lg attenuation and blockage. This understanding is necessary for the transport of path corrections for Lg based discriminants. The lack of appropriate observations is due to two causes. Most studies have depended on seismic networks with station spacing much greater than the spatial scale over which Lg is seen to vary, and the amplification of most stations is unknown, so observations of amplitude can only be made relative to some other phase at the same station.

We remedy those two problems by calculating Lg site amplification factors for the southern California seismic network. (SCSN), which spans a wide range of tectonic structures, and has station spacing on the order of 20 km.

To calculate the site amplifications, we have used robust re-weighting to automatically downweight or discard dubious amplitude measurements from our very large, unwieldy data set. Because this powerful technique is likely to be useful in a broad range of geophysics problems, yet is simple to implement, we present it in some detail. The purpose of the technique is to increase the accuracy of parameter values that are estimated from data drawn from a heavy-tailed distribution. We demonstrate with synthetics how little risk there is of biasing parameter values with this technique if the errors are perfectly Gaussian, yet what significant potential for improvement in parameter values exists if the errors are heavier-tailed than Gaussian. The technique also greatly improves the accuracy of uncertainty estimates of the parameters. When applied to real data, the robust re-weighting identifies clear errors in instrument calibration tables that would otherwise have gone unnoticed, and so clearly improves the site amplifications estimated.

We present a preliminary application of site and distance corrections to Lg from regional events at different azimuths. Areas of larger and smaller Lg amplitude are spatially clustered, although the patterns vary for different events, and do not necessarily correlate with the pattern of the site amplifications themselves, suggesting that we can succesfully isolate path effects on Lg amplitudes.

We conclude that quantification of the correlation of path properties and Lg amplitude variations, on the scale at which Lg varies, is not only important to understanding Lg propagation, but is now a feasible goal.

key words: Lg, blockage, discrimination, path corrections, propagation, robust statistics, site amplification

OBJECTIVE

The long-term goal of this work is to improve discrimination capability at regional scales and so reduce the magnitude threshold for CTBT monitoring through the development of path corrections for the Lg/Pg discriminant. We have chosen to concentrate on the Lg/Pg discriminant, as it has been shown to be the most effective single high frequency regional seismic discriminant (Taylor, et. al., 1989).

Achieving this long-term goal will not only require empirical quantification of variations in Lg/Pg amplitude ratios with path properties, which should be one of the last steps of this study, but will require a solid theoretical understanding of the basis for the corrections in order to ensure their appropriate application. It is the development of the theoretical basis for path corrections that we focus on first. Attaining such understanding requires the achievement of many intermediate goals.

The attenuation and blockage of Lg has been investigated extensively via synthetic seismograms (e.g. Bouchon, 1982, Cao and Muirhead, 1992) and observational studies (Kennett, et. al., 1985, Shapiro et. al, 1996, Zhang et. al., 1994). The observational studies indicate the type of structure that affects regional propagation, but only rarely provide the spatial resolution necessary to observe details of the diminution of Lg. While synthetic studies can provide insight into the mechanisms of attenuation and blockage, there is, again, often a lack of observations at the appropriate scale with which to validate, by comparison, a study's conclusions.

There are actually two deficiencies in the observations available. One is that Lg and Pg appear to change over a very short spatial scale, on the order of 20 km (e.g. Baker and Minster, 1995, Shapiro et. al., 1996), but few networks have both sufficiently densely spaced stations and span the type of geologic structures that affect regional phase propagation. The second deficiency in observations is due to a usual lack of knowledge of the amplification of seismic station sites, which requires observations of regional phase amplitudes to be measured relative to some other phase, whose amplitude variation with propagation is likely as poorly understood as that of the phase under investigation. We note that for discrimination, a relative amplitude measurement is generally done to estimate the ratio of P to S energy at the source, but an absolute amplitude measurement would remove a major source of ambiguity in the inference of propagation effects.

To understand regional attenuation and blockage, the limitations imposed by insufficient observations must be remedied. That is the first goal of this work, which we discuss in the following section.

RESEARCH ACCOMPLISHED

Introduction: To remedy the lack of sufficiently fine scale observations, we use data from the southern California seismic network (SCSN), which has station spacing on the order of 10 km over an area approximately 500 by 300 km. Within the region spanned by the SCSN are many structures thought to affect regional wave propagation, including sedimentary basins, mountain ranges (with and without crustal roots), an active rift zone, and areas of gradually varying crustal thickness (figure 3).

To remedy the lack of absolute amplitude measurements, we have calculated Lg site amplifications for the SCSN. The theoretical basis for the use of near-receiver scattered teleseismic coda as a source of isotropic Lg-like energy, and the separation of near-receiver from near-source scattered coda, is discussed in Baker and Minster (1995). The estimation of site amplifications from coda amplitude measurements has required the application of appropriate statistical techniques. Because those techniques may be useful in a wide variety of geophysical problems, we discuss them in some detail, and then present a preliminary application of site amplifications to Lg amplitudes of regional events.

Application of robust re-weighting to site amplifications: The data used for the site amplifications are drawn from a heavy tailed distribution, contain some very large errors, and are censored, problems that are common to a wide variety of geophysical data. We present the application of a robust statistics technique that improves parameter estimation from data with the first two problems. The incorporation of censored data using maximum likelihood estimation is discussed in Baker and Minster (1996).

To estimate the site amplifications, we must also estimate event magnitudes. We write each measured amplitude as

$$A_{i,j} = E_j \cdot S_i \cdot \Gamma_{i,j} \qquad (1)$$

where S_i is the site amplification at station i, E_j is the rms amplitude of the coda over some time window for event j (for unit site amplification), and $\Gamma_{i,j}$ is a factor that accounts for random error from all possible sources. We take the natural log of (1), to obtain

$$a_{i,j} = e_j + s_i + \gamma_{i,j}. \qquad (2)$$

If $\gamma_{i,j}$ were assumed to be independent zero mean Gaussian errors with standard deviation $\sigma_{i,j}$, the least squares solution to the matrix equation for all $a_{i,j}$ would be the best solution we could find.

We weight each row of the matrix equation

$$\mathbf{M}\cdot\mathbf{e}=\mathbf{a} \qquad (3)$$

by the inverse of the standard deviation of corresponding measurement $a_{i,j}$. In (3), **M** is the forward model matrix, **e** is the parameter vector, and **a** is the data vector. We constrain the network to have no mean amplification and prevent event and station parameters from trading off by requiring that $\sum_i s_i = 0$

The large number of assumptions that are required by this model (e.g. near receiver scattering is isotropic, incoming teleseismic P-wave has constant amplitude over southern California, and instrument calibrations do not drift over time) cast doubt on the assumption that $\gamma_{i,j}$ are independent zero mean Gaussian errors. Major violations of any assumptions could lead to large outliers. Further, SCSN seismograms are often mislabeled, so some measurements may be attributed to the wrong stations, causing occasional very large errors. We estimate that as much as 1% of the data that we have used may be mislabeled in this way.

Size is one further important factor in this problem. We have recordings of 41 events on 211 stations, for a total of 4,397 on-scale amplitude measurements, 110 upper threshold measurements, and 703 lower threshold measurements. Despite the large number of measurements, some individual parameters depend on few data, so if one datum is in some way *bad*, we need a way of identifying it. Because the entire set of data in this case is too large to permit individual inspection of outliers, our means of recognizing dubious data must be automatic.

The problems of heavy-tailed distributions and egregious blunders contaminating the data are dealt with by robust statistics techniques. We use the technique of robust re-weighting, which reduces the weight applied to outlying data (which can also be viewed as increasing the estimate of $\sigma_{i,j}$ in the weighting of (3)). This effectively applies a milder penalty than is applied to these data by the least squares penalty function. Thus, such data are allowed to influence the solution but not to dominate it.

The identification and downweighting of outliers is an iterative procedure. A set of weights is determined by a reweighting function that is dependent on the misfit. The misfit is

$$\mathbf{z}_n = \mathbf{W}_n \cdot \mathbf{M} \cdot \hat{\mathbf{e}}_n - \mathbf{W}_n \cdot \mathbf{a}, \qquad (4)$$

where **M** is the forward model matrix, **a** is the data vector, $\hat{\mathbf{e}}_n$ is the estimate of the vector of log of the parameters at the n'th iteration, and $\mathbf{W}_n$ is the diagonal weight matrix that was applied at the n'th iteration. A new set of weights is calculated based on the misfit, and the least squares solution of the newly reweighted problem,

$$\mathbf{W}_n \cdot \mathbf{M} \cdot \hat{\mathbf{e}}_{n-1} = \mathbf{W}_n \cdot \mathbf{a},$$

is found. The process continues until some criterion is met.

The integrals of reweighting functions, called influence functions, are more commonly discussed in the statistics literature. The integrals of the influence functions are the penalty functions associated with the reweighted least squares inversions. A common robust reweighting penalty function and the least squares and L_1-norm penalty functions, are shown in figure 1, along with their associated influence and reweighting functions (note: the L_1-norm penalty function is shown only for comparison with the others, but has no true influence function as the weights approach infinity near zero misfit). In the upper left panel we can see the overwhelming penalty applied by the least squares criterion to data that cause moderate to large misfits. It is through that large penalty that outliers can significantly bias the least squares estimate. The L_1-norm penalty is more appropriate for data from a heavy tailed distribution (the L_1-norm solution is the maximum likelihood estimator for exponentially distributed data), although it is still very large for egregious errors. An influence function such as the Hampel 17a function, in which the influence of large outliers decreases until they are eventually completely ignored is more appropriate for data sets where occasional egregious errors are expected (see, for example, Montgomery and Peck, 1982, for more detail). Such functions are called hard redescenders. The Hampel 17a influence function is linear, like the least squares solution, for data with little misfit, constant, like the L_1-norm solution, for data with moderate misfit, and reduces the influence of data, eventually to zero, outside of that range. The robust weights for the Hampel 17a function are determined as follows:

$$\begin{aligned} w(z)&=1, && \text{for } |z|\le a \\ w(z)&=\tfrac{a}{|z|}, && \text{for } a<|z|\le b \\ w(z)&=\tfrac{a(c-|z|)}{|z|(c-b)}, && \text{for } b<|z|\le c \\ w(z)&=0, && \text{for } |z|>c \end{aligned} \qquad (5)$$

where z is the misfit from (4), normalized by its scaled median absolute deviation, s (e.g. Montgomery and Peck, 1982).

In addition to better parameter estimates, another distinct advantage of robust reweighting is that the covariance matrix becomes a much more accurate estimate of the uncertainties in the parameters. That is so because the diagonal elements of the covariance matrix, $\mathbf{C}=[(\mathbf{WM})^T(\mathbf{WM})]^{-1}$ (where W is the final weighting matrix and M is the forward modeling matrix as above) are estimates of the variance when scaled by the total misfit

$$\hat{\sigma}^2 = \frac{1}{u-v}\sum_i\sum_j [a_{i,j} - (\hat{e}_j + \hat{s}_i)]^2 .$$

The accuracy of those estimates depends on the weights being proportional to the inverses of the standard deviations.

Trade-offs between the standard least squares and the robust solutions: We have suggested that if data are not normally distributed or include some large outliers, the least squares solution could yield a poor estimate of some parameter values. If on the other hand, the errors are normally distributed, the least squares solution is the maximum likelihood solution. Any other solution, including the robust reweighted solution, would be worse, so there is a price to be paid for using robust reweighting. We illustrate with a simple synthetic example the relative extent of error we risk from using each approach.

We constructed a synthetic data set of 10 stations recording 20 events, added normally distributed random noise at 10% of the amplitude, and found the least squares and robust estimates. We repeated the experiment 100 times to accurately determine the typical error of each type of solution (Table 1). The average error of the robust estimates of magnitude are 3% worse than those of the least squares estimates, and the site amplification estimates are 3.5% worse. However, when the added noise is from the heavier-tailed exponential distribution, the least squares magnitude estimates are 12% worse than the robust estimates and the site amplification estimates are 17% worse. The difference is even greater if there are some large

outliers in the data. For a data set as above, but with a couple of measurements significantly off (one measurement is ~2.5 times too large, and one is ~2 times too small), the least squares estimates are much worse than the robust reweighted estimates. Those 2 *bad* measurements affect the estimates of 4 parameters, the 2 events involved and the 2 stations. Over 100 runs (adding different random exponential noise, but the same 2 blunders), the mean least squares estimates for those parameters were significantly worse than the robust estimates (Table 1). The difference is due to the robust weights assigned to the those parameters. In the least squares solution, all measurements are assigned equal weight. In the robust estimates, the 2 dubious data are recognized and assigned weights of about 0.36 (the mean weight for all other measurements in the final robust iteration was 0.965).

Table 1

Noise added	Mean least squares error		Mean robust solution error	
	Magnitudes	Amplifications	Magnitudes	Amplifications
Gaussian	2.57%	9.62%	2.65%	9.96%
Exponential	3.60%	13.15%	3.22%	11.23%

	Magnitudes L.S. (true)	Amplifications L.S. (true)	Magnitudes robust (true)	Amplifications robust (true)
Exponential	6.74 (6.5)	0.342 (0.300)	6.55 (6.5)	0.309 (0.300)
+2 blunders	6.33 (6.5)	0.341 (0.375)	6.52 (6.5)	0.380 (0.375)

Table 1: Differences in mean errors between the least squares (left column) and robust (right column) solutions to synthetic data with normal (top row) and exponential (second row) noise, and large outliers (bottom rows).

The effect of robust reweighting on real data: Even limiting consideration to those stations recording at least 10 events on-scale, changes in site amplifications due to robust reweighting were dramatic. 28 sites (out of 189 recording 10 or more events) had changes of 10% or greater. 13 changed by more than 20%. Examining the data that were downweighted at sites with large estimates of variance reveals the power of the robust reweighting to identify dubious data that would otherwise almost certainly go unnoticed.

We begin with a simple example, station SBK, which had the 4th largest variance and a change in site amplification from 0.51 to 0.83. Figure 2 (top left panel) shows that 7 recordings out of 29 total were given nearly zero weight, and all 7 are from the same continuous time interval (the beginning of 1992 through to the beginning of 1994). Clearly, something was different about the station during that interval. We suppose that a rough indication of the site's magnification can be obtained by the pre-event noise levels, and so compare the pre-event noise vs. the date (second row, left column) and the robust weights vs. pre-event noise (bottom row, left column). Pre-event noise levels much lower than were typical for SBK were recorded for the downweighted events. We conclude that the instrument's magnification was reduced during this time period, without the change in instrument parameters being recorded. In this case robust re-weighting has greatly improved a parameter estimate by removing dubious data. For this station, the same end might have been achieved via a careful, and lengthy, examination of pre-event noise levels vs. time for all stations (although it is only through the robust reweighting that it occurred to us to perform such a test), or by simply throwing out very large outliers. The next example is not as straightforward, and could not have been resolved by other such means.

The site amplification at LUC had by far the largest variance and the greatest change, from 0.51 to 1.02. 13 out of the 26 recordings were given robust weights of 0.3 or less, and 11 of them are from the same continuous time period (figure 2, lower right). As with SBK, it appears likely that something about the instrument response was different during that time period, but just what is less clear. The pre-event noise level was higher for the 4 events in 1990, but from then on the level remains within a roughly constant range. Something else, perhaps a change in the seismometer's response to velocities much higher than background noise levels, appears to have changed. Although we cannot identify the exact cause, the suspicious grouping of low weights

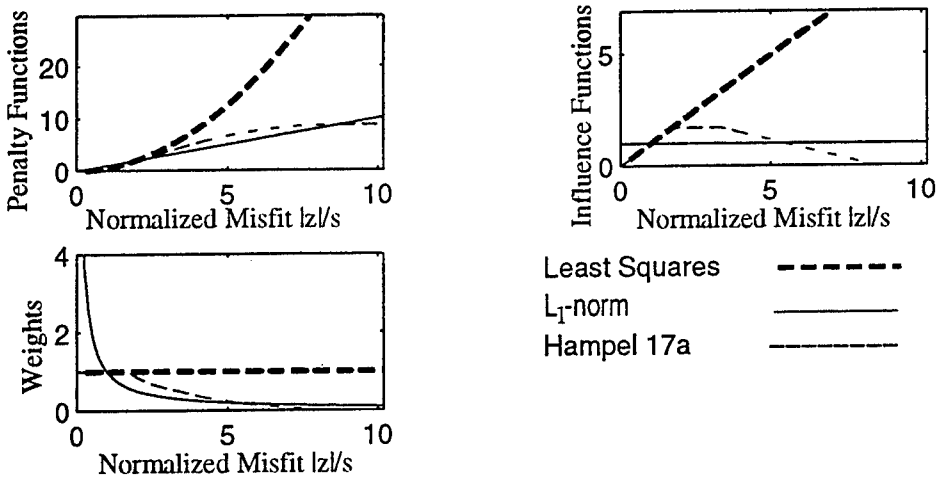

Figure 1: Penalty functions (upper left) for misfit of least squares, L_1-norm, and Hampel 17a solutions and their first and second derivatives, i.e. influence functions (upper right) and the values for robust weights (lower left). Note that the L_1-norm does not have a true influence function, as its robust weights would approach infinity near zero misfit. It is included here for comparison with the other solutions.

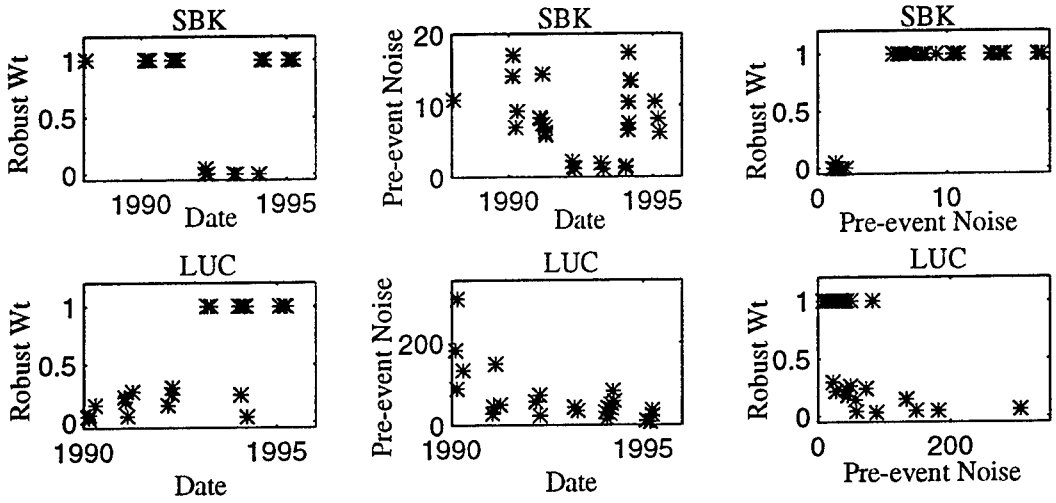

Figure 2: Robust weights vs. event dates (left column) for two of the stations most affected by robust reweighting, showing a distinct grouping of low weights within specific time periods. Pre-event noise levels vs. event dates (middle column) indicate that the magnification was likely significantly lower than was recorded in instrument parameter logs for station SBK (top row) during that time period. The robust weights are plotted vs. the pre-event noise levels in the bottom row. The correlation is perfect for SBK, but more muddled for LUC (bottom row).

with time indicates a problem with the instrument response that the robust reweighting has effectively alerted us to. Similar problems with incorrect instrument response information appear to be at the root of the changes in most other stations with high variances.

For a solution to be meaningful, it must be consistent in the face of changes to the influence function parameters (i.e. a, b, and c of (5)) and to the use of alternate influence functions. The SCSN robust solutions remained consistent throughout both types of changes.

Preliminary application of Lg site amplifications to isolate path effects on Lg amplitudes: We make a preliminary application of the site amplifications to separate site from path effects. We have simply used almost all of the site amplifications calculated and apply a distance correction by fitting a straight line to the values of site corrected Lg amplitude versus distance for just the event under consideration. For future applications, we will systematically examine the site amplifications for uncertainty and develop a distance correction from multiple events, to avoid biasing by propagation effects from a single azimuth.

The site amplifications are shown (figure 4) for comparison with plots of distance and site corrected Lg for regional events, to see whether the amplifications dominate the signal.

Figure 5 shows the distance and site corrected Lg amplitudes for a Cape Mendocino event. The amplitudes are demeaned and normalized (1 standard deviation of amplitude equals 0.25 inches) for easy visual separation of large and small amplitudes. Comparison of the gross patterns with figure 4 shows distinct differences in Lg amplitude from the pattern of site amplifications. The southern Sierra has low site amplifications but large Lg, while most of the area north of the Transverse Ranges and west of the San Andreas Fault have large site amplifications but small Lg. Lg amplitudes are medium size at the southernmost stations, but with smaller Lg in the Peninsular Ranges and larger Lg in the Imperial Valley. This variation is split along a northeast trending line, while the site amplifications in that region are sharply demarcated by northwest trending boundary.

For further comparison, we present the distance and site corrected Lg amplitudes from an event in Baja California (figure 6). The pattern of Lg variation is distinct from both the Lg site amplifications and the Cape Mendocino event.

CONCLUSIONS AND RECOMMENDATIONS

We have demonstrated with both synthetic and real data examples how robust statistics significantly improves the accuracy of magnitude and site amplification estimation. This works by reducing the influence of outliers in data drawn from heavy tailed distributions, and so should be applicable to a wide variety of geophysical problems. The robust reweighting not only automatically *throws out* very large outliers from data sets too large to permit more than spot-checking of outliers, but downweights moderate outliers so that the least squares criterion does not allow a single datum or a few data to significantly bias a solution. It also greatly increases the accuracy of uncertainty estimates for a least squares problem. Its efficiency and ease of implementation make it an attractive and sensible choice for improving geophysical parameter estimates.

Although not shown due to space constraints, application of the site amplifications and a distance correction was also made for the Pg amplitude measurements. This required the assumption that Pg and Lg site amplifications be extremely similar. Barker et. al. (1981) found no discernible difference between Lg and Pg site amplifications for a range of geologic structures. For more extensive work we recommend that this be tested for the SCSN. These preliminary plots indicate that the along path variation in Lg and Pg is very similar, and so variations in the Lg/Pg amplitude ratio are due to more subtle effects than those controlling the absolute amplitude variation. It is likely that some of the variation in the amplitude ratio is due to a relative difference in the magnitude of the effect any particular mechanism has on each phase.

We recommend that a systematic study be carried out to quantify the relationship between site and distance corrected Lg amplitudes from the SCSN and properties of path segments. Zhang et. al (1994) have provided the first systematic analysis of correlations of Lg/P amplitude ratios with various properties of the waveguide, but that study was limited to just 8 stations over much

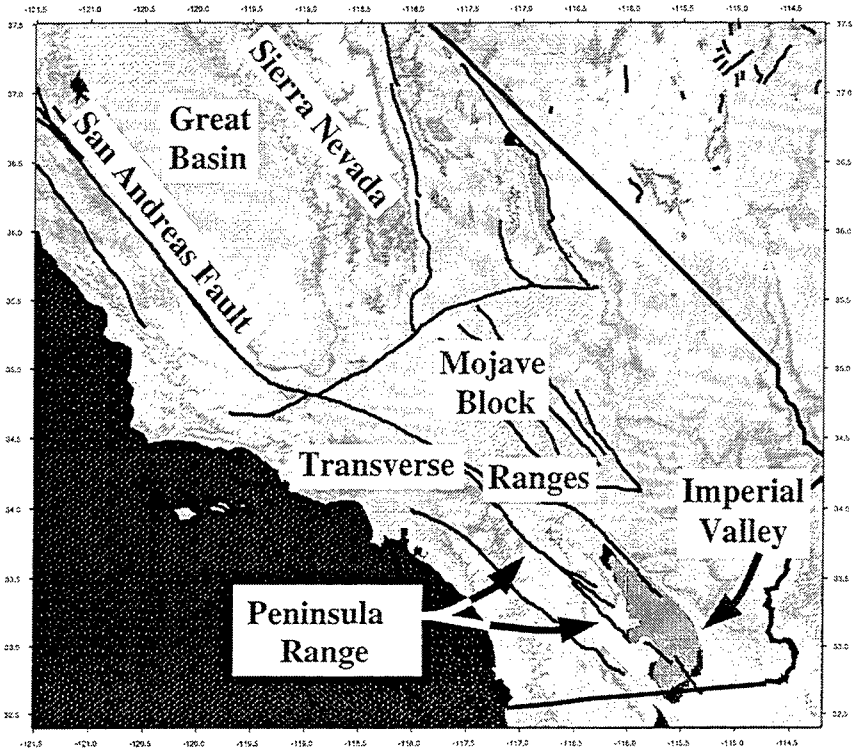

Figure 3: Major tectonic features of southern California.

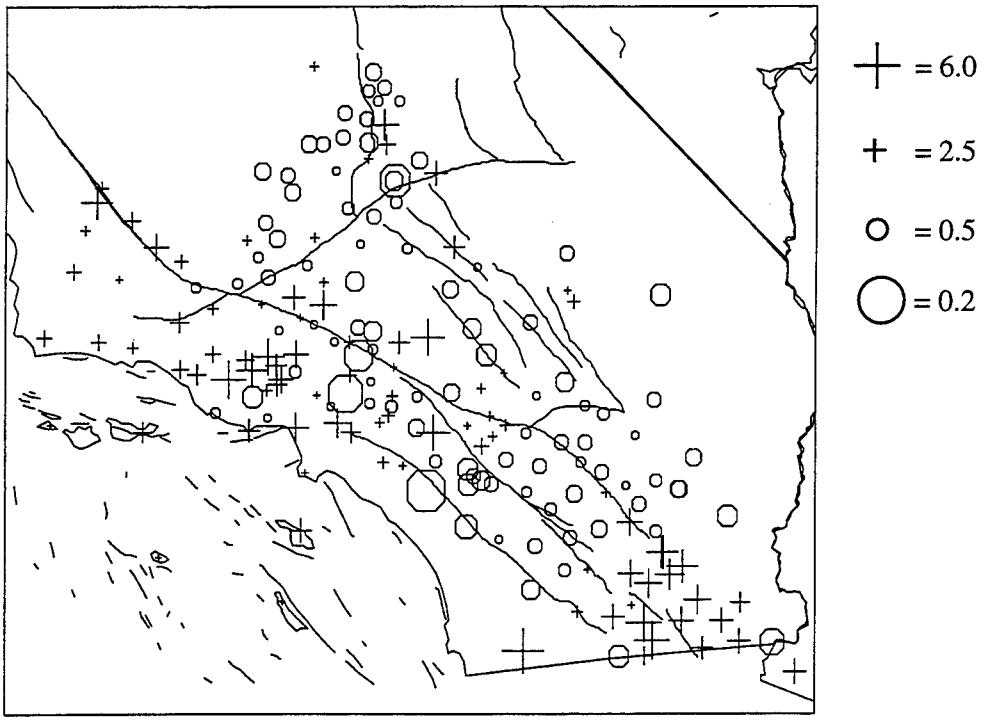

Figure 4: Lg site amplifications for the SCSN. Plusses and circles indicate sites with amplification greater and less than 1.0 respectively. Symbols are scaled by the log of the amplification. Scale values listed are in amplification.

of Eurasia, with path parameters integrated over entire path lengths ranging from 40 to 360. Using some of the same path parameters as were found to affect Lg, we recommend

1) deriving a distance correction and applying it, along with the site amplification corrections, to regional SCSN data from all possible azimuths,

2) developing an interpolation scheme for Lg amplitudes and applying it to estimate amplitude variations along azimuthal paths from the sources,

3) integrating path properties, such as those used by Zhang and Lay (1994) along each path segment between Lg amplitude estimates,

4) measuring the correlation between those path properties and Lg amplitudes.

Once the relationship between Lg amplitudes and path properties is well quantified, modeling of the observations will be warranted and offers the potential of greater insight into to mechanisms underlying the observations.

For a more complete understanding of the discriminant's variations, we must understand the changes in Pg as well as Lg. A study of Pg propagation effects, analogous to the work described above should be performed.

Finally, the correlations between all the path properties found to be relevant, and the Lg/Pg amplitude ratio, should be quantified, with the purpose of calculating path corrections. The final result should be Lg/Pg path corrections dependent on globally available geophysical parameters, with a solid understanding of their physical basis.

References:

Baker, G.E., and J.B. Minster, (1995), Lg Site Amplification Calibration for Isolation of Lg Propagation Effects, *Proceedings 17th Seismic Research Symposium*, PL-TR-95-2108, ADA 310037

Baker, G.E., and J.B. Minster, (1996), Iterative reweighting for estimation of magnitude and site amplifications from doubly censored and corrupted data, *manuscript in preparation*

Barker, B.W., Z.A. Der, and C.P. Mrazek (1981), The Effect of Crustal Structure on the Regional Phases Pg and Lg at the Nevada Test Site, *J. Geophys. Res.*, **86**, 1686-1700

Bouchon, M., (1982), The complete synthesis of seismic crustal phases at regional distances, *J. Geophys. Res.*, **82**, 1735-1741

Cao, S. and K.J. Muirhead (1993), Finite Difference Modeling of Lg Blockage, *Geophys. J. Int.*, **115**, 85-96

Kennett, B., S. Gregersen, S. Mykkeltveit, and R. Newmark, Mapping of crustal heterogeneity in the North Sea Basin via the propagation of Lg-waves, *Geophys. Jour. R. Astr. Soc.*, **83**, 299-306

Montgomery, P. and E. Peck, (1982) Introduction to linear regression analysis, *Pub. John Wiley and Sons*.

Shapiro, N., N. Bethoux, M Campillo, A. Paul, (1996) Regional seismic phases across the Ligurian Sea: Lg blockage and oceanic propagation, *Phys. Earth Plan. Int.*, 257-268

Taylor, S.R., M. Denny, E. Vergino, and R. Glaser (1989), Regional Discrimination between NTS explosions and western U.S. Earthquakes, *Bull. Seism. Soc. Am*, **79**, 1142-1176

Zhang, T.R., S. Schwartz, and T. Lay, (1994), Multivariate analysis of waveguide effects on short-period regional wave propagation in Eurasia and its application in seismic discrimination, *J.Geophys.Res.*, **99**, 21,929-21,945

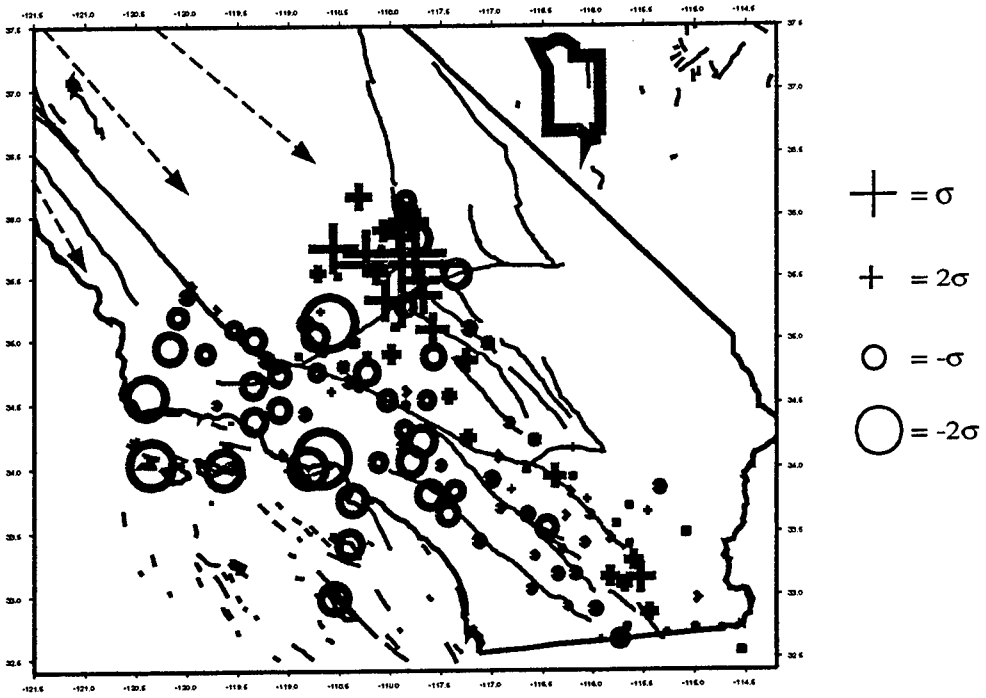

Figure 5: Site and distance corrected Lg amplitudes for a Cape Mendocino earthquake. Symbols are scaled by relative amplitude, 0.25 inches equals 2 standard deviation of the amplitudes. Plusses are large Lg and circles, small. Arrows indicate propagation direction.

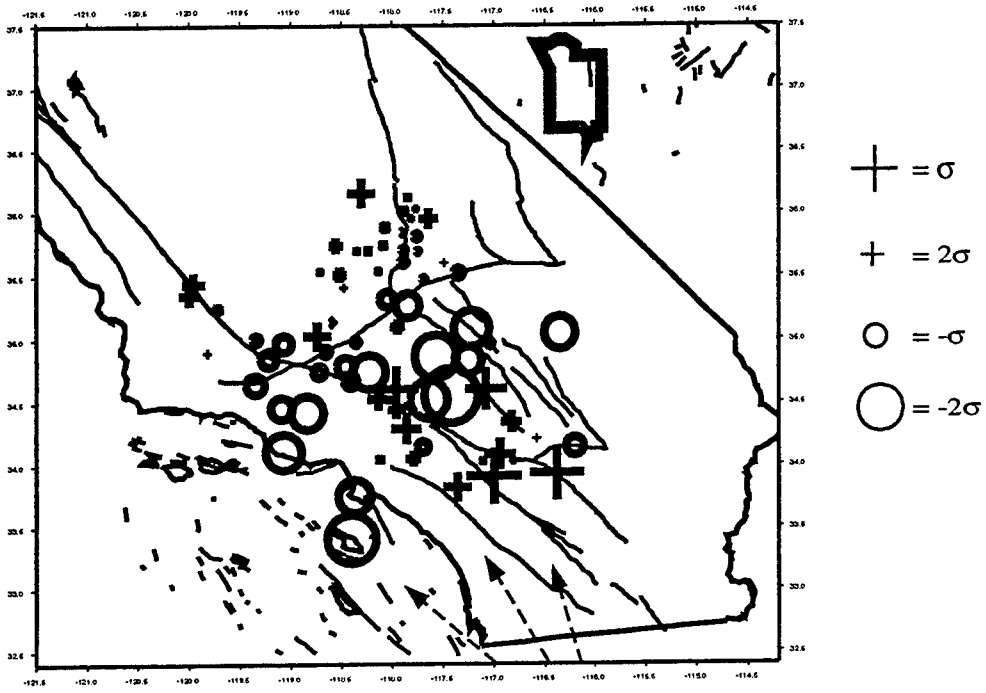

Figure 6: Site and distance corrected Lg amplitudes for a Baja California earthquake. Symbols are the same as for figure 5.

CONSTRUCTING A GENERAL RHEOLOGICAL MODEL FOR ROCK DEFORMATION

G. N. BOITNOTT
New England Research, Inc.
F49620-95-C-0019
Sponsored by: AFOSR

ABSTRACT

An experimental program is underway to develop a realistic rheology for rock deformation resulting from moderate perturbations in stress. The rheology is nonlinear and hysteretic, and is shown to cause significant deviations in strain path from those predicted by linear elasticity under stress conditions commonly assumed to lie outside the elastic radius of an explosive source. A model suitable for forward modeling of a spherically propagating compressional wave is presented.

Keywords: nonlinear rheology, rock properties, wave propagation, source function

OBJECTIVE

Interpretation of free-field waveforms to infer the source function of a seismic event is an important step in understanding the physical origin of seismic discriminants. A detailed physical understanding of the source function and the ability to forward model free-field signals from explosions is also required for assessing possible evasion scenarios of a CTBT. An experimental program is underway to develop and constrain a general rheology for rock deformation which is suitable for forward modeling of wave propagation in the moderate strain regime (nonlinear but without damage). The data confirms that significant nonlinearities exist at stress conditions typically assumed to be well outside the "elastic radius".

RESEARCH ACCOMPLISHED

Background:

Previous work on nonlinear, hysteretic rheologies has largely been based on experiments covering limited stress conditions and modes of deformation. These experiments have been important in guiding model development, having lead to an understanding of important qualitative features such as discrete memory (see *Boitnott*, [1993] ; *Guyer et al.* [1995]). Laboratory observations of the effects of nonlinearities indicate that they may be persistent even for small stress perturbations (see Johnson et al [1993]), raising questions concerning their influence on far-field waveforms and the subsequent interpretation of source functions.

In order to forward model wave propagation, explicit experiments using a much wider range of loading path are needed to test and constrain models suitable for arbitrary loading paths. We have developed and implemented an experimental protocol which provides detailed constraint of the nonlinear, hysteretic deformation of rock subject to arbitrary perturbations in axially symmetric compressive stresses. Experiments are being performed on a diverse suite of samples, including Berea Sandstone, Sierra White granite, and a variety of tuffs from N-tunnel at the Nevada Test Site (NTS). The data and resulting models will be used in forward modeling of wave propagation to assess the importance of the nonlinearities in shaping the free-field waveforms.

Experimental Protocol

In this paper, we summarize the results of some illustrative experiments on Berea sandstone, and discuss how they are used to develop and constrain a rheological model for nonlinear, hysteretic deformation during arbitrary loading protocols.

The loading history of an exemplary experiment is illustrated in Figure 1. The experiment involves a sequence of perturbations in load subject to varying boundary conditions and executed from a series of initial stress conditions. At three different starting stress conditions, the axial stress and confining pressure are controlled to produce perturbations in stresses enforcing the following boundary conditions: mean stress perturbations at constant differential stress (4 cycles of two different amplitudes), uniaxial stress perturbations (2 cycles), shear stress perturbations at constant mean stress (4 cycles of two different amplitudes), and uniaxial strain perturbations (4 cycles of two different amplitudes). Detail of one such sequence is shown in Figure 2.

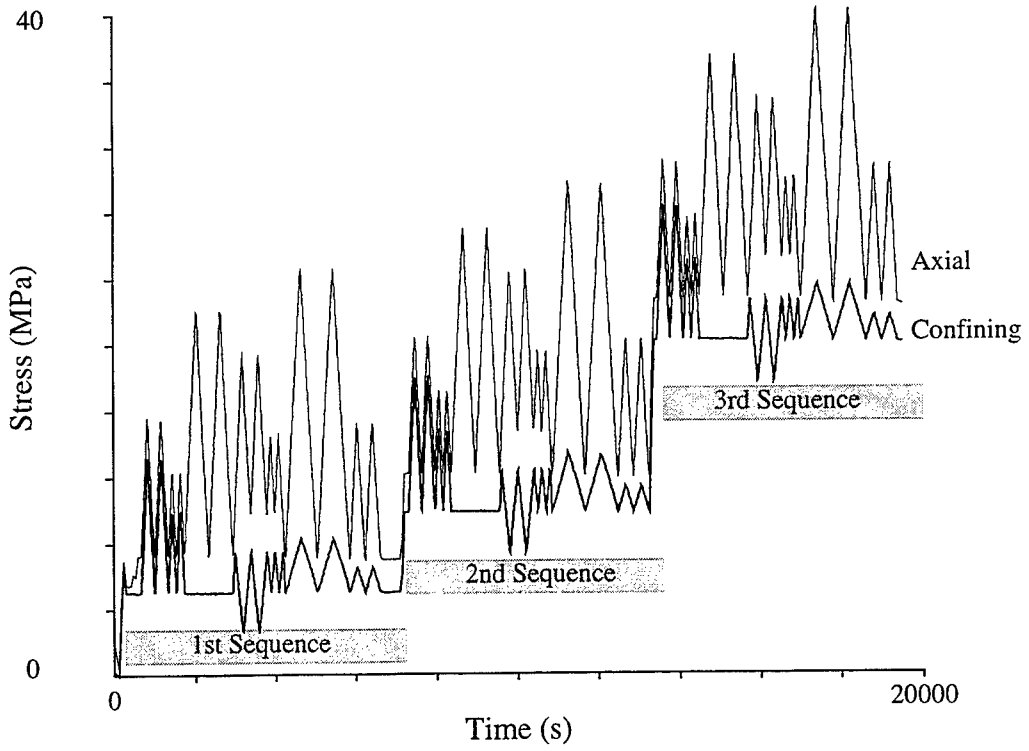

Figure 1: Loading protocol of an experiment designed to characterize the nonlinear, hysteretic rheology of rock. The protocol involves repeated execution of a sequence of loading modes, including perturbations in mean stress, uniaxial stress, shear stress, and uniaxial strain. See detail in Figure 2.

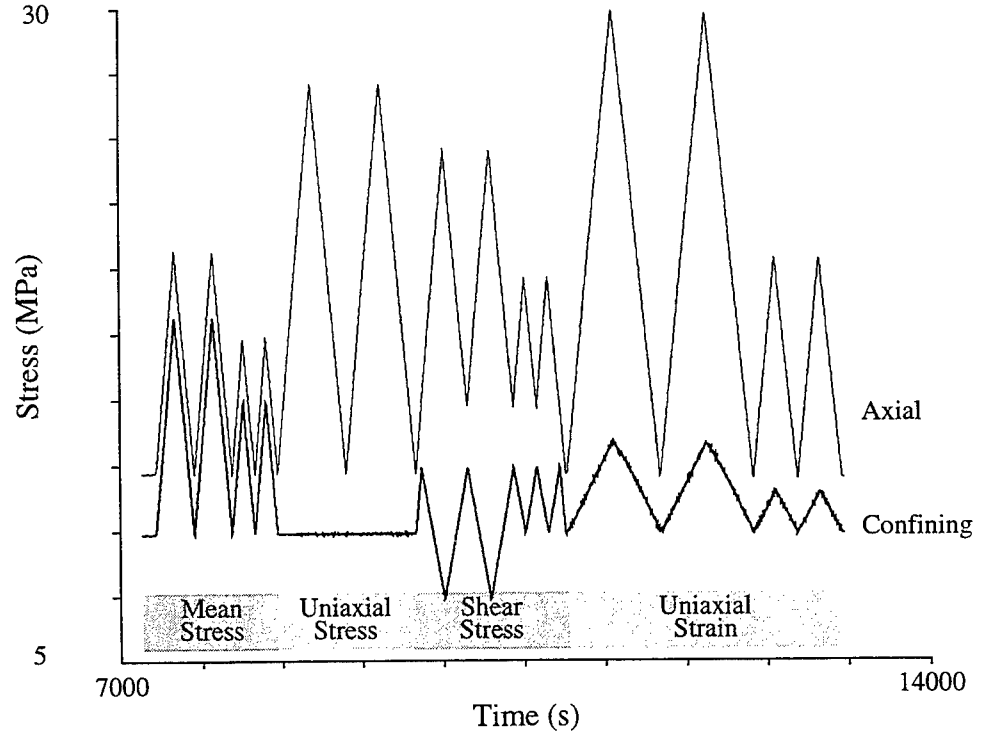

Figure 2: Detail of the loading sequence used in the experiment in Figure 1. Amplitudes of the various perturbations produce similar deviations in the shear and mean stresses.

Formulating a Model

The goal is to develop a model capable of predicting the stress-strain relationship for arbitrary loading paths in the stress space bounded by $\sigma_{11} \geq \sigma_{\theta\theta}$ (i.e. axially symmetric compressive stresses). During the experiment, the strains ε_{11} and $\varepsilon_{\theta\theta}$ are measured along with the stresses σ_{11} and $\sigma_{\theta\theta}$. Isotropy of deformation in the {23} plane is assumed (i.e. $\varepsilon_{\theta\theta} = \varepsilon_{22} = \varepsilon_{33}$).

Intuition leads us to try to formulate a rheology in terms of the mean stress (σ), the shear stress (τ), the volumetric strain (κ), and the shear strain (γ), defined as:

$$\sigma = (\sigma_{11} + 2\sigma_{\theta\theta})/3.0 \tag{1a}$$

$$\tau = (\sigma_{11} - \sigma_{\theta\theta})/2.0 \tag{1b}$$

$$\kappa = \varepsilon_{11} + 2\varepsilon_{\theta\theta} \tag{1c}$$

$$\gamma = \varepsilon_{11} - \varepsilon_{\theta\theta} \tag{1d}$$

For an isotropic, linear elastic solid, $\kappa = \sigma/K$ and $\gamma = \tau/G$, where K and G are the bulk and shear moduli, respectively. Here we will generalize the definitions of the moduli to allow for the description of nonlinear, hysteretic deformation. We define the more general bulk and shear "moduli" ($\hat{K}$ and $\hat{G}$) to be:

$$\hat{K} = \frac{\partial\sigma}{\partial\kappa} \tag{2a}$$

$$\hat{G} = \frac{\partial\tau}{\partial\gamma} \tag{2b}$$

Over a limited but significant range in mean stress perturbations, is is found that for all rock-types the data can be modeled with a simple description of $\hat{K}$ which will be referred to as the asymmetric bow-tie model (ABM). The model parameterization, and an example comparison with data, is illustrated in Figure 3. In this model, $\hat{K}$ is assumed to change linearly with mean stress for monotonic changes in mean stress. At any reversal in the direction of change of the mean stress, $\hat{K}$ reverts to a value $\hat{K}'$, which for simplicity here is modeled as a linear function of the mean stress at the reversal in loading direction. It is also observed that the deformation exhibits a memory of the stress-strain state at previous extrema in mean stress, a characteristic commonly referred to as discrete memory (see Guyer et al. [1995]). To enforce this memory we require:

$$\int_{\sigma'}^{\sigma''} \frac{\partial\sigma}{\hat{K}_1} \equiv -\int_{\sigma''}^{\sigma'} \frac{\partial\sigma}{\hat{K}_2} \tag{3}$$

where σ' and σ'' are two sequential extrema in the mean stress loading path. If we are trying to model κ for the loading path σ' -> σ'' -> σ''', we specify (or already know) $\hat{K}_1(\sigma)$ and use equation (3) to find $\hat{K}_2(\sigma)$. $\hat{K}_2$ is then used to compute κ during the loading σ'' -> σ''', and equation 3 can then be rewritten to find $\hat{K}_3$ for the next loading

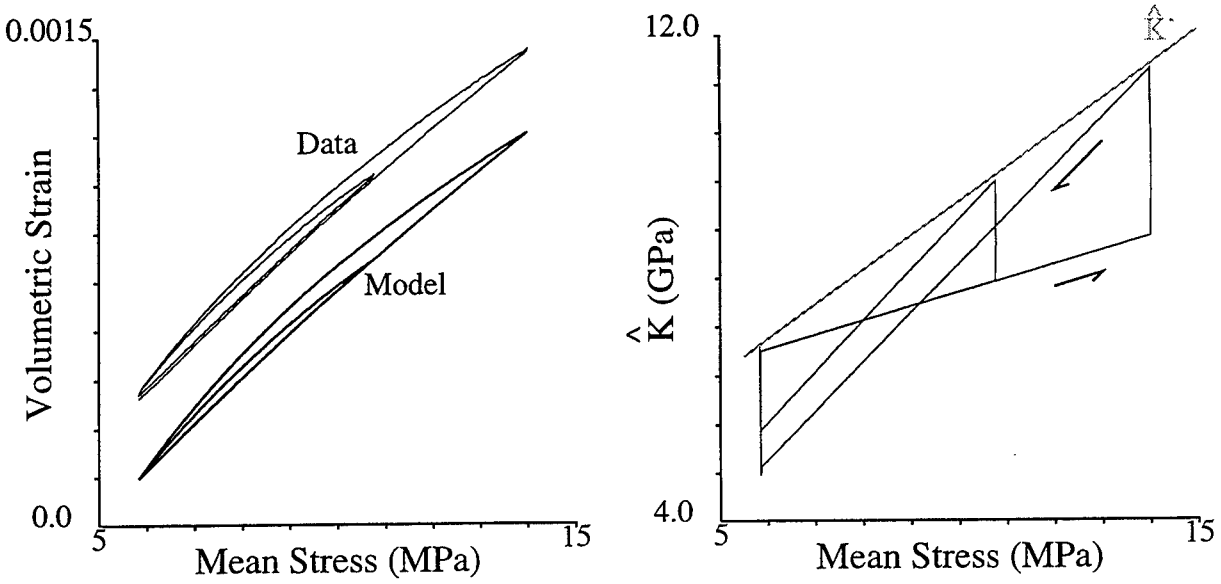

Figure 3: Comparison of stress-strain data and model predictions for a mean stress perturbation on Berea sandstone (left figure). The ABM parameterization is shown graphically in the right figure. The local modulus ($\hat{K}$) changes linearly with stress during monotonic loading and/or unloading. At each reversal in loading direction, the local modulus reverts to a value of $\hat{K}'$, which is again a linear function of stress. The model is constrained by equation 3 to enforce discrete memory.

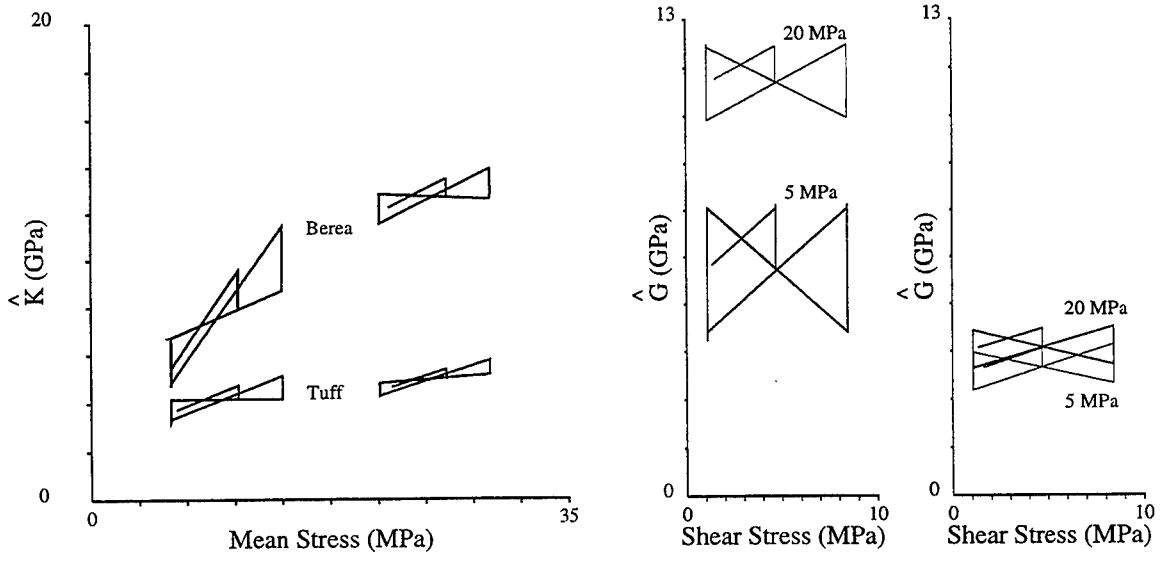

Figure 4: Model results for Berea sandstone and NTS tuff illustrating the dependence of model parameters on mean stress. Models results for mean stress perturbations are shown in the left figure (for a detailed example see Figure 3). Fits are to data from the mean stress perturbations during the 1st and 3rd sequence in Figure 1. The other figures (center -> Berea; right -> Tuff) illustrate the inferred shear rheology, again for the 1st and 3rd sequence in Figure 1. While the ABM holds for moderate perturbations in stress, large perturbations require a functionally more complex parameterization. This is particularly true for Berea sandstone, which exhibits a large mean stress dependence.

leg. With prior specification of the functional form of $\hat{K}$, the necessary model parameters are constrained by the memory enforced by equation (3). For the case of the ABM, there are three free parameters, two describing the mean stress dependence on $\hat{K}'$, and one describing $\partial\hat{K}/\partial\sigma$ during the current loading leg.

For the case of shear stress changes at constant mean stress, it is found that the same parameterization appears to describe $\hat{G}$ (now in terms of γ and τ). Thus the ABM parameterization appears to describe the hysteresis in both the volumetric and shear strains (at constant shear and mean stress, respectively). This is found to be true for each of the rock-types tested.

Figure 4 illustrates the results of model fits to data from Berea sandstone and N-tunnel tuff. By comparing results from different initial mean stresses, it is clear that the model parameters describing $\hat{K}$ and $\hat{G}$ are dependent on the initial mean stress This dependence is much stronger and functionally more complex for a rock like Berea sandstone compared to tuff. These observations illustrate that for large perturbations in σ, the data require a functionally more complicated parameterization, with $\hat{K}'$ and $\hat{G}'$ being described by nonlinear functions of σ. Accordingly, large amplitude perturbations also require $\partial\hat{K}/\partial\sigma$ and $\partial\hat{G}/\partial\tau$ during monotonic loading and/or unloading to be described by nonlinear functions as well (e.g. see the previous work on Young's modulus: *Boitnott* [1993]). We should also expect that $\hat{K}$ and $\hat{G}$ may be dependent on τ (over and above the dependency of $\hat{G}'$ on τ), and thus similar complexity should arise for large shear perturbations. Despite this complexity, over limited but rather large changes in σ and τ, the ABM appears to provide a good approximation of the deformation from shear and mean stress perturbations in variety of rocks and covering a wide range of stress conditions.

Mixed-Mode Loading Paths

Unfortunately, the data indicate that, in general, it is not sufficient to superimpose the rheologies discussed above for $\hat{K}$ and $\hat{G}$ to describe deformation during arbitrary (mixed-mode) loading paths. While under some conditions, and for some rock types, a simple decoupled model may be appropriate, in general additional effects are commonly observed. Figure 5 plots the volumetric strain as a function of the mean stress for Berea sandstone during the 2nd perturbation sequence (as shown in Figures 1 and 2). Here we see that for the mixed mode cases (i.e. uniaxial stress and uniaxial strain), $\hat{K}$ (as determined from the mean stress perturbations, is not sufficient to model the volumetric strain during other modes of deformation.

We do however note some pattern to the stress-strain behavior shown in Figure 5. In Figure 5, it can be seen that the shear stress perturbation (at constant mean stress) causes an appreciable decrease in volumetric strain (i.e. a dilation). Accordingly, the uniaxial-stress and uniaxial-strain perturbations produce less volumetric strain (per unit change in mean stress) than is observed during the pure mean stress cycles. This suggests that a "coupling" term is required to handle volumetric strain resulting from changes in shear-stress. Similarly for the shear strain (not shown), there is again evidence of coupling in the sense that the shear stress - shear strain relationship is not fully described by $\hat{G}$ when σ is changing. Here again, a coupling term is required to handle the effects of mean stress changes on the shear rheology.

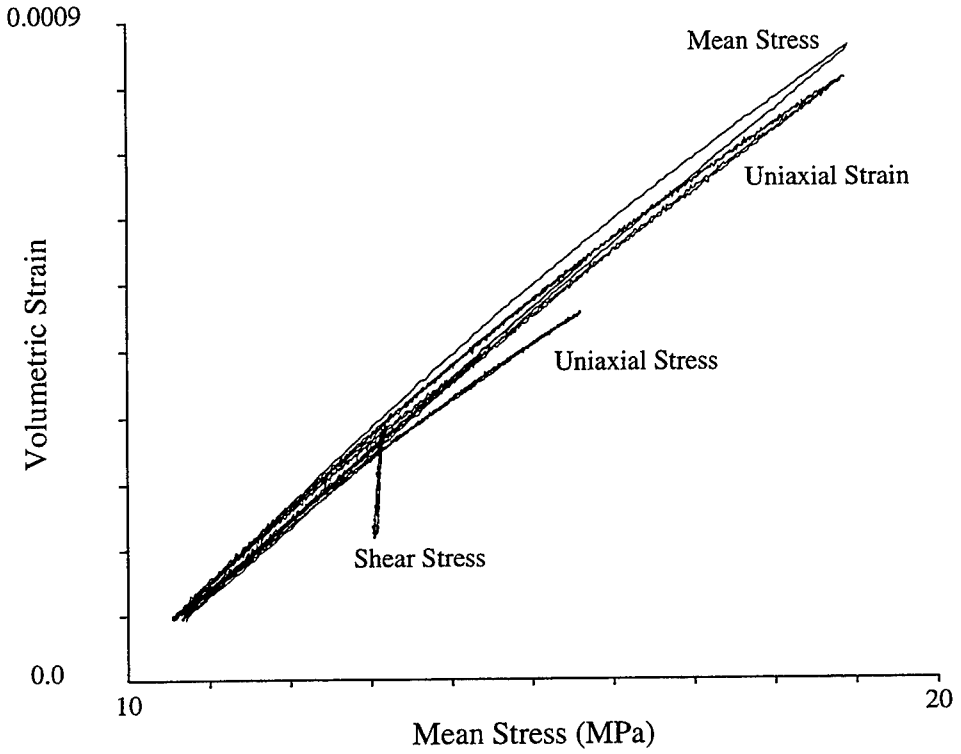

Figure 5: Volumetric strain versus mean stress for Berea during the second loading sequence (see Figures 1 and 2). Note that the shear stress produces a significant dilation.

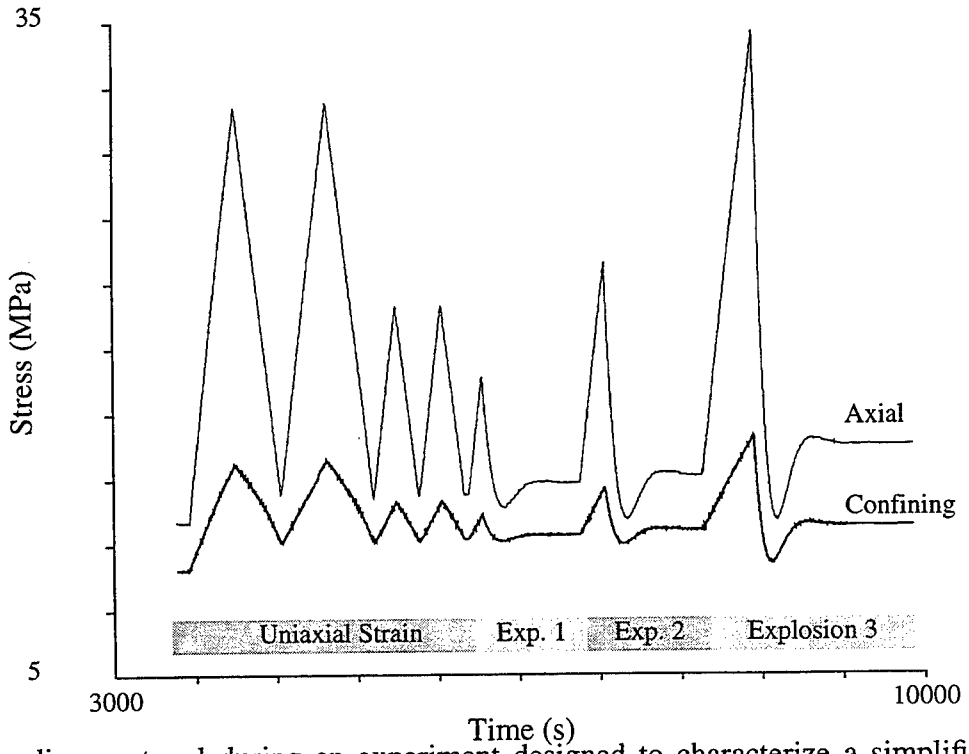

Figure 6: Loading protocol during an experiment designed to characterize a simplified rheology for the case of a spherically propagating compressional wave. Uniaxial strain perturbations are followed by three "explosion like" loading paths of increasing amplitude.

The coupling terms appear to be a strong function of rock type, and for Berea appear to become less significant as the initial mean stress increases. It is likely that they result at least in part from stress induced anisotropy in mechanical properties in response to differential loads. While the nature of these coupling terms is still poorly characterized, preliminary modeling efforts indicate that these effects can be incorporated into a general rheology based on the ABM without the addition of a significant number of additional parameters. In some cases, the coupling terms appear relatively elastic (i.e. univalued functions of stress state), and thus their incorporation into a hysteretic rheology such as the ABM may require only a superposition upon the ABM described above.

The Explosion Loading Path

Despite the apparent complexity introduced by the coupling terms, we find that a related but simpler rheology can be formulated which is applicable to the case of compressional wave propagation from an explosive source. Figure 6 illustrates the loading protocol of an experiment designed to characterize deformation during loading paths which mimic (quasi-statically) the stress path expected as a result of an underground explosion. The loading paths are constructed to follow that predicted for a Heaviside step function in radial stress at a spherical cavity in a linear elastic material. The resulting explosion loading path involves a uniaxial strain loading followed by a mixed-mode unloading which follows a damped oscillation about a final stress state. The unloading path is a function of the range and the effective elastic constants of the material. In the experiment illustrated in Figure 6, we have performed four cycles of uniaxial strain loading, followed by three successive explosion loading paths with increasing amplitude (representing decreasing range).

Figure 7 illustrates the stress-strain relationship during this experiment, deconvolved into stresses and strains as defined in equations 1[a,b,c,d]. Here we see that the deformation is well behaved (although nonlinear and hysteretic), without noticeable complications by the coupling terms (as was seen in Figure 5). In fact, the data can be modeled fairly well using a uncoupled ABM for both $\hat{K}$ and $\hat{G}$, where $\hat{K}$ and $\hat{G}$ are constrained by the uniaxial strain data. In effect, this short-cut groups the coupling terms discussed previousing into the ABM description of $\hat{K}$ and $\hat{G}$, and is thus valid only for loading paths for which the coupling terms themselves are functionally consistent with the ABM. The explosion loading path examined here appears to be such a path, and thus this simplified model is appropriate for the problem of the spherically propagating compressional wave for an explosion-like source.

This experiment provides a example of the consequences of such a rheology, as illustrated in Figure 8. Here we compare the measured strain path with the strain path predicted by a linear elastic rheology (for the identical stress path). The elastic constants used for the linear elastic predictions are constrained to enforce the uniaxial strain loading leg during the early stages of the loading path. The measured strain path upon unloading is noticeably different from that of the linear elastic model. Such differences are readily noted even for conditions which would typically be considered well outside the elastic radius.

The implications of these differences are not well known at this point. However, qualitatively one can reason that if the measured strains were used to infer a stress

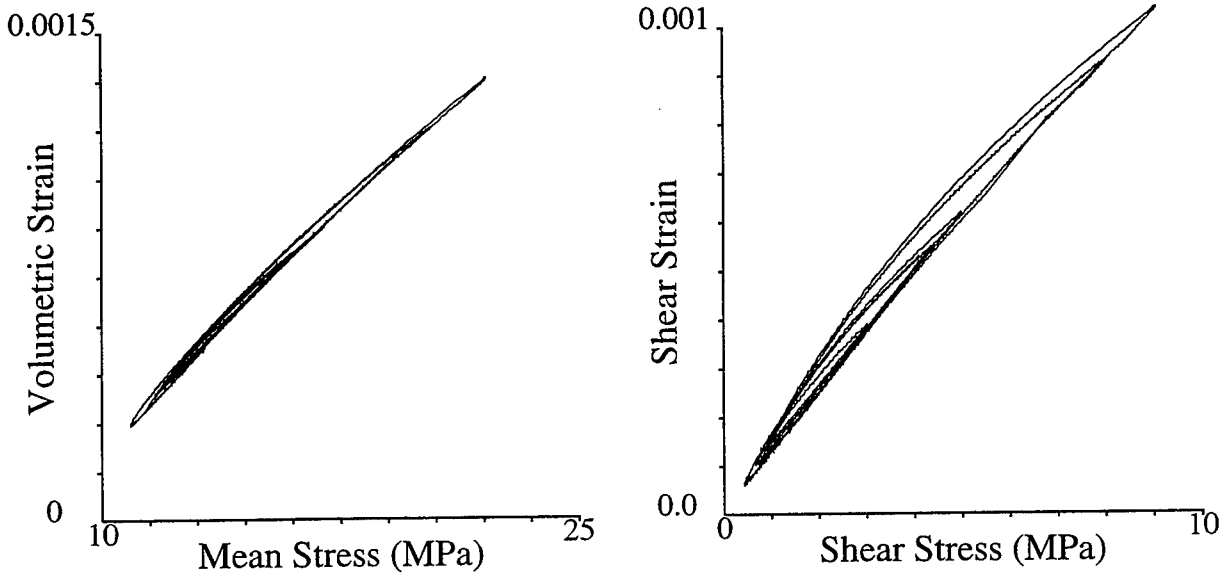

Figure 7: Volumetric strain versus mean stress and shear strain versus shear stress for Berea sandstone during the loading protocol in Figure 6. Note the well behaved nature of the hysteresis and nonlinearity, exhibiting the characteristic shape and "nested loop" behavior of the ABM.

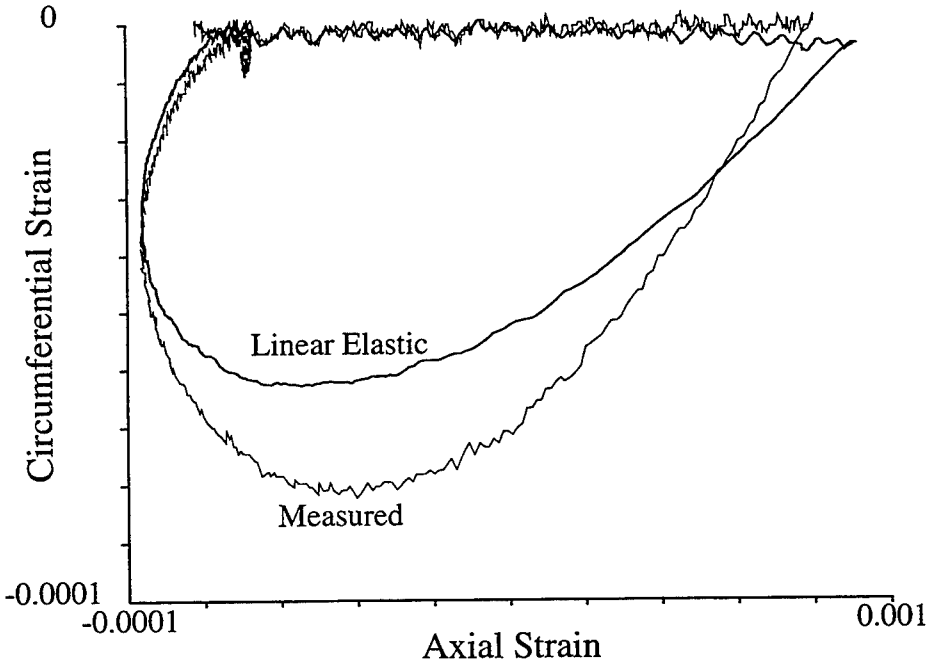

Figure 8: Strain path measured during the 3rd "explosion" as shown in Figure 6. The prediction for a linear elastic solid (with elastic constants constrained to fit the uniaxial strain loading), is shown for comparison. While qualitatively similar, systematic differences arise from the nonlinearity and hysteresis which may have a significant effect on wave propagation and/or the interpretation of a source function.

path (using a linear elastic model), the inferred stress path would be different from the actual stress path. Thus, if back-propagated to the source, the error would result in an incorrect (unphysical) source function. In addition to this contamination of an observation at a particular range, the rheology will also have effects on the propagation of the compressional wave itself, further distorting a source function derived through inappropriate use of a linear elastic model.

CONCLUSIONS AND RECOMMENDATIONS

An experimental protocol has been developed and implemented to constrain the nonlinear, hysteretic deformation of rock in the moderate strain regime. The data clearly illustrates gross nonlinearities even at stress conditions which might typically be considered outside the elastic radius of a seismic event. The resulting nonlinear and hysteretic rheology is developed to a point where forward modeling of compressional wave propagation can be performed.

The implications of this rheology on interpretations of free-field seismic signals should be studied in the context of a number of problems relevant to a CTBT. The rheology should be used to assess the importance of the nonlinearities on shaping the far-field seismic signal (i.e. spectral distortion and attenuation). Forward models should also be used to address issues in the context of traditional analysis techniques, such as what is an appropriate value for the elastic radius and how is it dependent on rock-type, depth of burial, and yield. The use of forward models should shed considerable light on the physical origin of a number of features characterizing commonly assumed source functions, such as overshoot, roll-off, and steady state value.

REFERENCES

Boitnott, G. N., Fundamental observations concerning hysteresis in the deformation of intact and jointed rock with applications to nonlinear attenuation in the near source region, *in* Proceedings of the Numerical Modeling for Underground Test Monitoring Symposium, Durango, Colorado, LA-UR-93-3839, p.121-134, 1993.

Guyer, R. A., K. R. McCall, and G. N. Boitnott, Hysteresis, discrete memory, and nonlinear wave propagation in rock: a new paradigm, Phys. Rev. Lett., v. 74, p. 3491, 1995.

Johnson, P. A. K. R. McCall, and J. D. Meegan, Experimental and theoretical studies of spectral alteration in ultrasonic waves resulting from nonlinear elastic response in rock, *in* Proceedings of the Numerical Modeling for Underground Test Monitoring Symposium, Durango, Colorado, LA-UR-93-3839, p.107-120, 1993.

Lg BLOCKAGE AND SCATTERING AT CNET AND KNET

Vernon F. Cormier and Tom Anderson
Department of Geology and Geophysics
University of Connecticut
Storrs, CT 06269-2045
F49620-94-1-0059
Sponsored by AFOSR

ABSTRACT

The effects of 3-D heterogeneity on Lg is investigated using both deterministic and statistical models of crustal structure. Variations in the efficiency of Lg propagation to the KNET and CNET arrays agree well with predictions deduced from ray trajectories of multiple SmS computed in deterministic models of crustal thickness in these regions. Complete regional seismograms are synthesized by the locked-mode method in plane layered models with the effects of scattering small scale heterogeneities included by the Born approximation. Experiments with varying random distributions of small scale scatterers demonstrate that scattering close to the source and receiver is more important than scattering mid-way along the crustal waveguide in lengthening Lg coda and equalizing energy on all components of motion.

Key words: Seismic wave propagation, Lg, scattering, crustal structure

Moho gradients and Lg efficiency have been described by us in experiments with Moho topography at KNET. Recent ray studies indicate Lg efficiency is correlated with paths crossing strong gradients in Moho topography at CNET. We conclude that Moho topography is a dominant factor in the efficiency of Lg propagation at both the CNET and KNET arrays. Although an option for sedimentary basins have been incorporated in our ray tracing codes, we have yet not investigated their effects on Lg propagation in these regions.

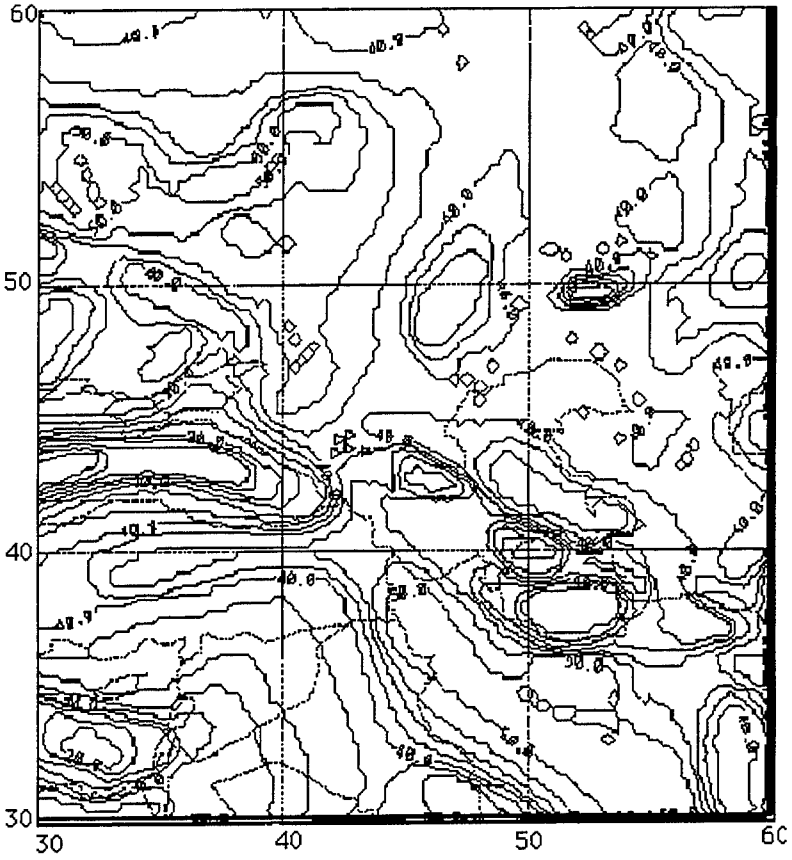

Figure 1. Moho topography in the vicinity of CNET (filled black circle) from Fielding et al. (1993).

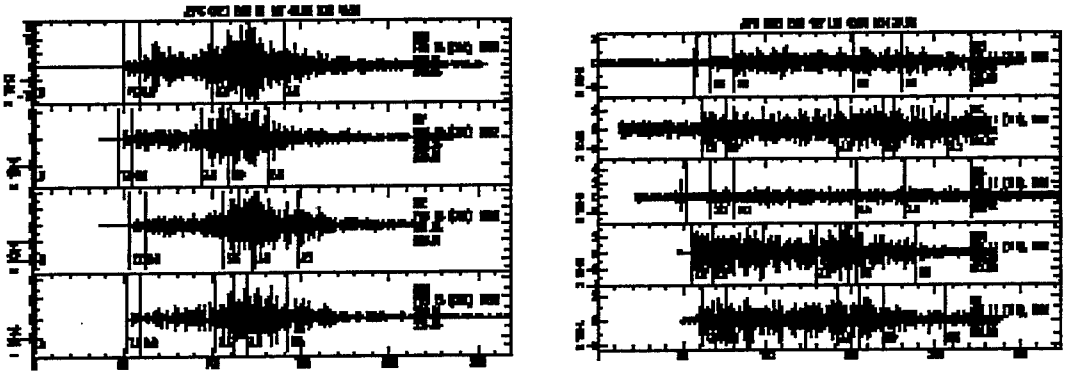

Figure 2. Example of efficient Lg propagation from an event to the east of KNET (left) and inefficient Lg propagation from an event to the west and southwest of KNET (right).

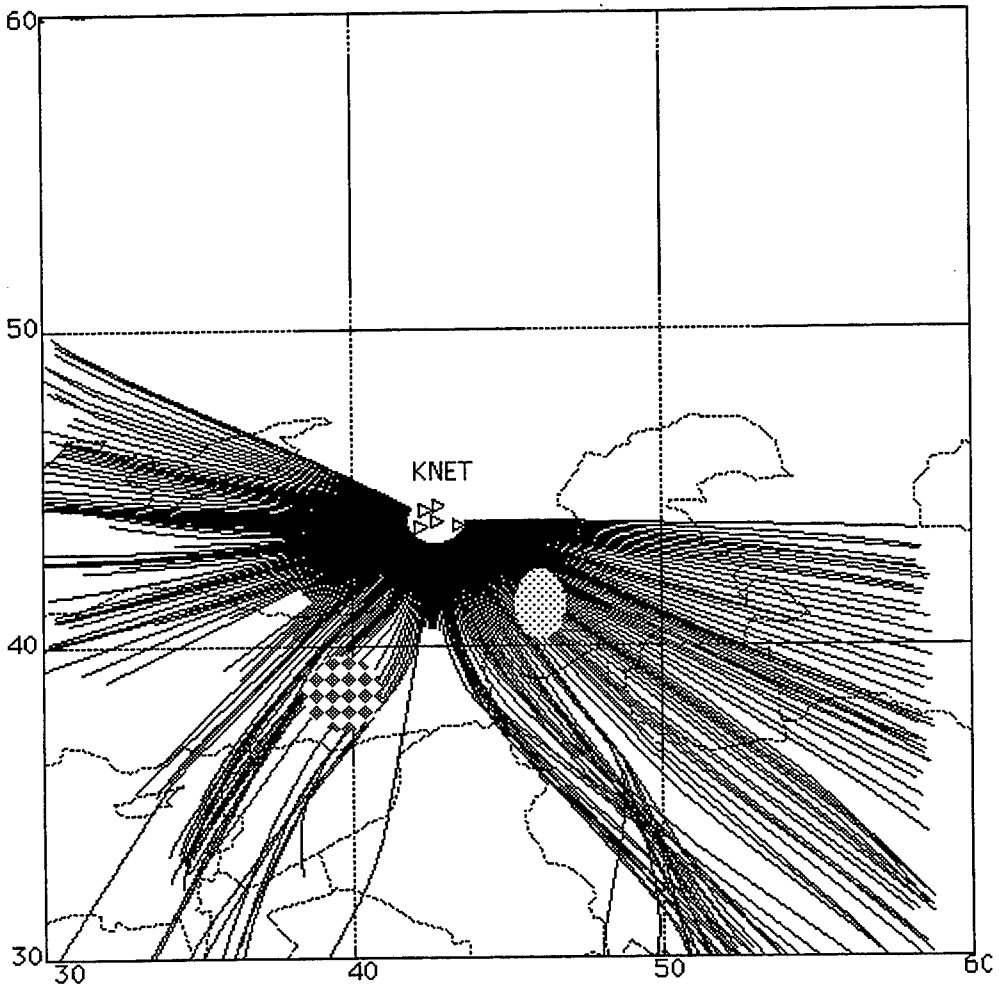

Figure 3. Lg ray paths (vertical projections of SmS turning and reflection points connected for starting azimuth) from KNET. Events having inefficient Lg propagation are in the checkered region to the southwest. Events having strong Lg are in the shaded region to the west.

Small Scale Structure. Although ray models of Lg are useful in qualitatively predicting gross features of blockage by large scale crustal transitions, the effects of smaller scale heterogeneity are more difficult to include. Indeed, the assumptions of the ray method break down when the scale length of the medium (measured by quantities like the ratio of velocity to magnitude of the spatial gradient of velocity) approaches the scale length of heterogeneity (measured by the a linear spatial dimension of the heterogeneity or radius of curvature of a rough boundary). Paradoxically, the most important effects of small scale heterogeneity can still be accurately included in the ray method by the Rayleigh-Born approximation to scattering when the scale length of the heterogeneity is much smaller than the wavelength (e.g., Wu and Aki, 1985).

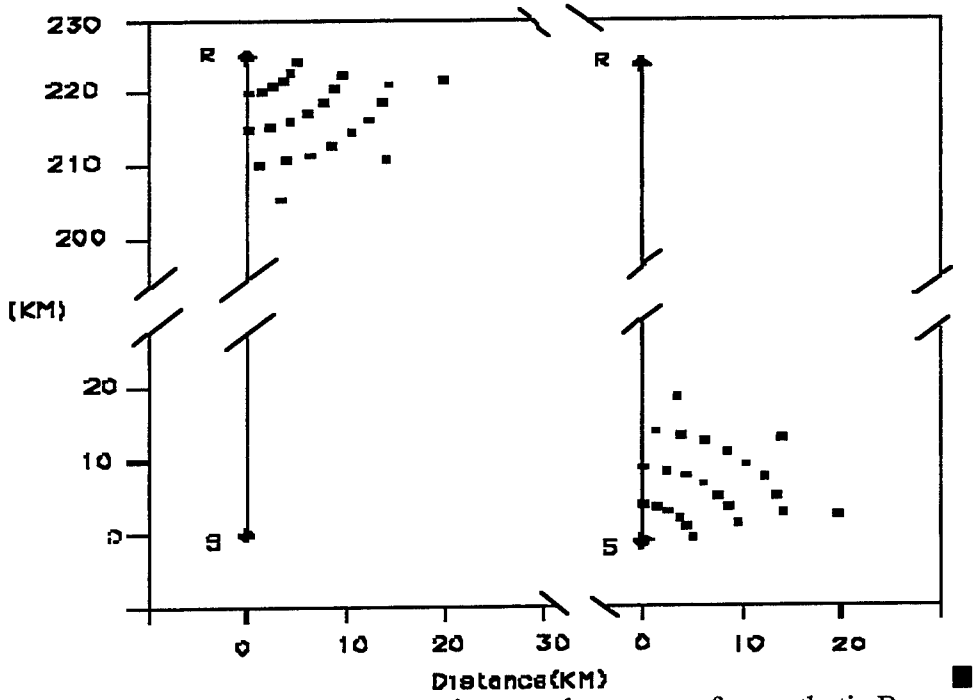

Figure 4a. Geometry of source, receiver, and scatterers for synthetic Born scattering experiments for the effect of near-source or near-receiver scattering. Depths of scatterers are randomly placed between 5 to 10 km. Perturbations in λ, μ, and ρ are 10%, 9%, and 8% , respectively. Radius of scatterers is 7.5 km.

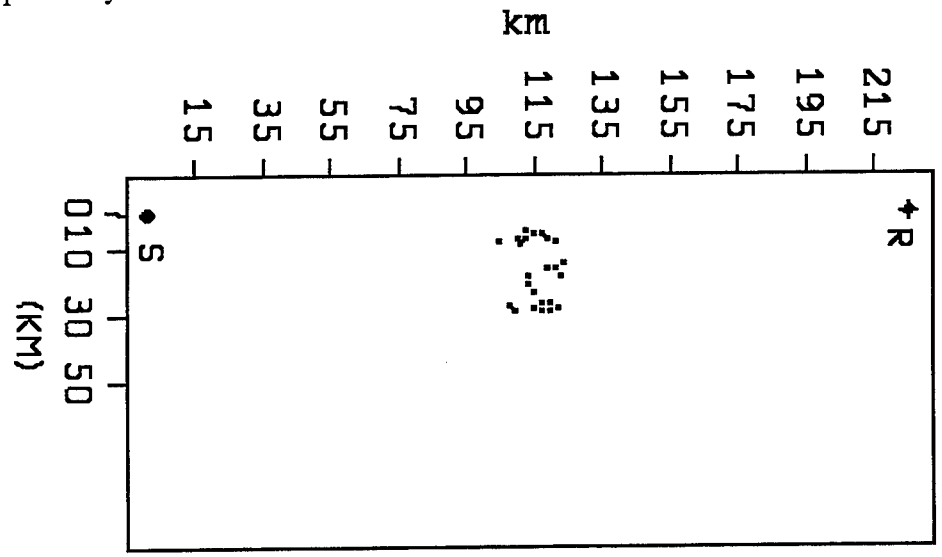

Figure 4b. Geometry of source, receiver, and scatterers for synthetic Born scattering experiments for the effects of scattering mid-way between source and receiver.

Since realistic phase complexity is difficult to achieve in a ray method without either or both fine scale layering and large numbers of scatterers, we have chosen to initially investigate the effects of fine scale heterogeneity in plane-layered, laterally homogeneous structures, using the locked mode method (Cormier et al, 1991) and the Rayleigh-Born approximation. A fundamental problem on which we are first focusing is an answer to

the question: where in crust and upper mantle is it important to have an accurate statistical description of small scale heterogeneity to describe the complexity of various regional phases. To answer this question we have begin some experiments on the effects of different distributions of scatterers. The dimensions of the scatterers (7.5 km radius) were chosen to be large under the usual assumptions of Rayleigh scattering to insure large effects. The errors associated with wavelength approaching the dimensions of the scatterers, however, are expected to be on the order of 10-30% in amplitude (e.g., Cormier, 1995). In future experiments, we plan to investigate the effects of heterogeneities well within the Rayleigh scattering domain.

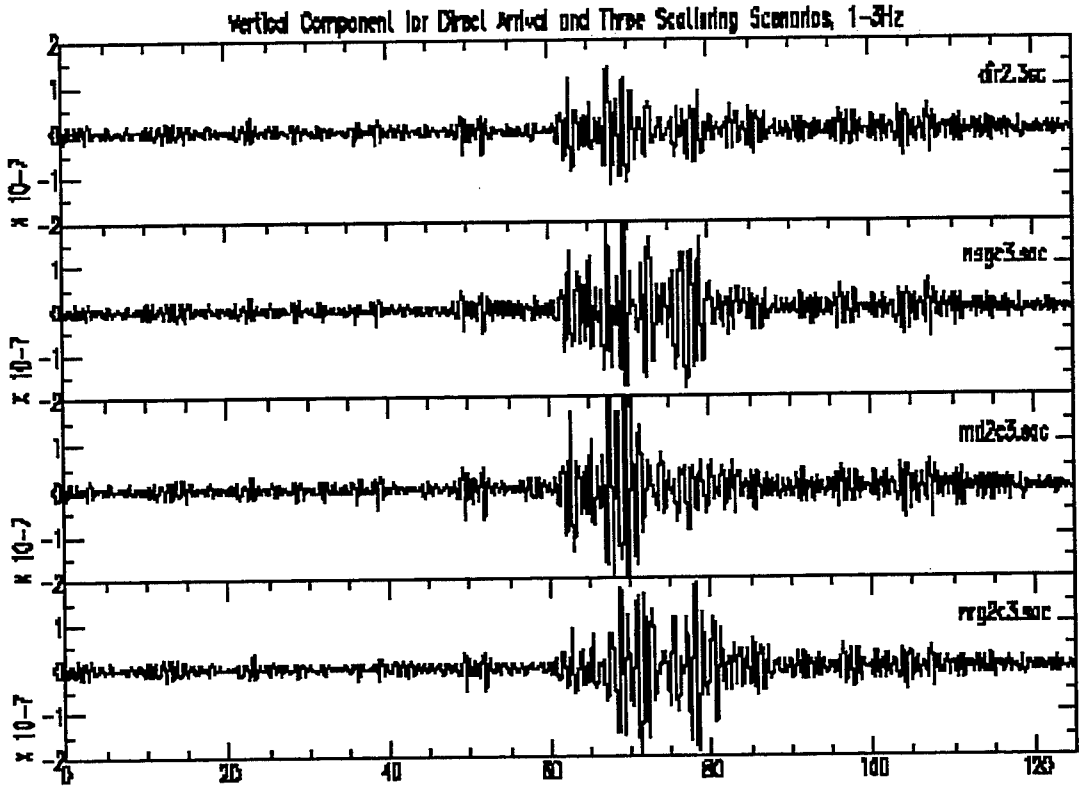

Figure 5. Vertical component displacement (band passed 1-3 Hz) synthesized for a vertical point force at the surface (delta function source-time function) by locked mode summation in a plane layered elastic and anelastic structure for the KNET region. Seismograms ordered from the top to bottom are for no scatterers, scatterers near the receiver, scatterers mid-way between source and receiver, and scatterers near the source.

Figures 4a and 4b show the geometry of source, receiver, and scatterers we have considered. Figure 5 shows the effects of these scatterers on complete regional seismograms. For scatterers in the crustal waveguide, we conclude that near source and near receiver scattering is most important in lengthening the Lg coda and equalizing the energy on components of motion. To simulate these characteristics of a seismogram, it is less important to accurately describe the statistics of scatterers mid-way along the crustal waveguide between source and receiver.

CONCLUSIONS AND RECOMMENDATIONS

A viewpoint is taken that the effects crustal heterogeneity can be best predicted by separating the effects of large scale (10 km and greater) from those of small scale (less than 10 km heterogeneity). The most important effects of large scale structure, including strong Lg attenuation and blockage, can be estimated from deterministic crustal models determined from regional refraction and deep seismic reflection surveys, surficial topography, and gravity. Strong lateral gradients in crustal thickness, for example, have been shown to be associated with Lg blockage at CNET and KNET.

Although it is impossible to ever accurately know the smaller scale structure in a given region, the effect of the statistics of the smaller scale structure on regional phases can be easily investigated using simple single scattering approximations and, eventually, numerical solutions of the elastic equation of motion in 3-D heterogeneous media. Scattering statistics close to the source and receiver are shown to be much more important in controlling Lg complexity than detailed knowledge of scattering statistics all along the crustal waveguide. An understanding of the effects of these statistics and their variation as a function of large scale crustal structure and tectonic setting, together with the gross effects of phase blockage of large scale structure, will form an important knowledge base for the transportability of seismic methods of detection, discrimination and yield estimation.

REFERENCES

Cerveny, V., The application of ray tracing to the propagation of shear waves in complex media, in *Seismic Exploration* pp. 1-124, Treitel and Helbig, Vol. on Seismic Shear Waves, G. Dohr, ed., Geophysical Press, 1985.

Cormier, V.F., B. Mandal and D. Harvey, Incorporation of velocity gradients in the synthesis of complete seismograms by the locked mode method, *Bull. Seism. Soc. Am.*, *81*, 897-930, 1991.

Cormier, V.F., and T. Anderson, Regional variations in Lg observed and synthesized at the CNET and KNET arrays, (abstract), *Seismological Research Letters, 66*, 28, 1995.

Cormier, V.F., (1995). Time domain modeling of PKIKP precursors for constraints on the heterogeneity in the lowermost mantle, *Geophys. J. Int.*, 121, 725-736.

Fielding, E., M. Barazangi, and B. Isacks, A network-accessible geological and geophysical database for Eurasia, North Africa, and the Middle East, *Proceedings 15th Annual Seismic Research Symposium*, AFOSR/DARPA, 1993, PL-TR-93-2160, ADA271458

Wu, R.S., and K. Aki, Scattering characteristics of elastic waves by an elastic heterogeneity, *Geophysics, 50,* 582-595, 1985.

Modeling of Regional Wave Propagation Phenomena in the Middle East and North Africa and New Analysis Capabilities in SAC2000

Peter Goldstein, Craig Schultz, Shawn Larsen, and Lee Minner
Geophysics and Global Security, Lawrence Livermore National Laboratory

Work sponsored by the U.S. Department of Energy, Contract No. W-7405-Eng-48
Comprehensive Test Ban Treaty Research and Development Program, ST482B

ABSTRACT

As part of our efforts to regionalize the Middle East and North Africa and to develop new techniques for automated data processing and special event analysis, we are developing and using our modeling capability and implementing new capabilities in SAC2000. Accurate computer simulations of regional seismic signals from sources in relatively aseismic areas are needed to help monitor a Comprehensive Test Ban Treaty. Such simulations can provide a range of plausible seismic parameters and provide constraints on both source location and source type. Predictions provided by such simulations may be critical for event identification when limited amounts of seismic or other data are available. We are developing finite-difference, reflectivity, and hybrid techniques that can accurately simulate regional seismic signals at high frequencies. We are using these techniques to test a variety of hypotheses and thus explain observations of regional wave propagation phenomena such as L_g blockage. We are also using these techniques to help identify and explain regional phase characteristics in the Middle East and North Africa.

Significant developments in SAC2000 include: new mapping capabilities via an interface to the Generic Mapping Tools (GMT) program, direct access to user-defined functions and subroutines via an external command interface, enhanced travel-time analysis capabilities, color spectrograms and binary sonograms, on-line documentation, and documentation via our Web page (http://www-ep.es.llnl.gov/tvp/sac.html). Successful applications of the SAC2000 capabilities include the following: investigation of regional travel-time variability at stations in the Middle East and North Africa, development and testing of a robust coda magnitude-estimation technique, and development and testing of a broadband regional discriminant based on slopes of *P*- to *S*-wave spectral ratios.

KEY WORDS: Middle East, North Africa, SAC2000, regional wave propagation

COMPUTER SIMULATION OF REGIONAL SEISMIC SIGNALS

Testing Hypotheses to Explain L_g *Blockage*

Monitoring a Comprehensive Test Ban Treaty will require discrimination and identification of small-magnitude events in many regions where there is very little seismicity and associated empirical observations of seismic discrimination parameters. Without such observations, it could be very difficult to identify seismic events. Accurate numerical simulations can improve a monitoring agency's ability to correctly identify such events by helping to constrain the range of seismic parameters that would be expected for a particular seismic event.

Motivated by the common use of L_g in seismic discriminants and the absence or significant reduction of L_g amplitudes in many regions including the Middle East and North Africa (e.g., Shapiro et al., 1996; McNamara et al., 1996), we are testing a variety of hypotheses to explain the blockage of L_g including: (1) reduction in L_g amplitudes due to attenuation in thick sedimentary basins; (2) reduction in L_g amplitudes due to backscattering and conversion in areas of reduced crustal thickness; (3) conversion to S_n or scattered energy in regions where there are rapidly varying boundaries; and (4) scattering and conversion of L_g due to heterogeneities.

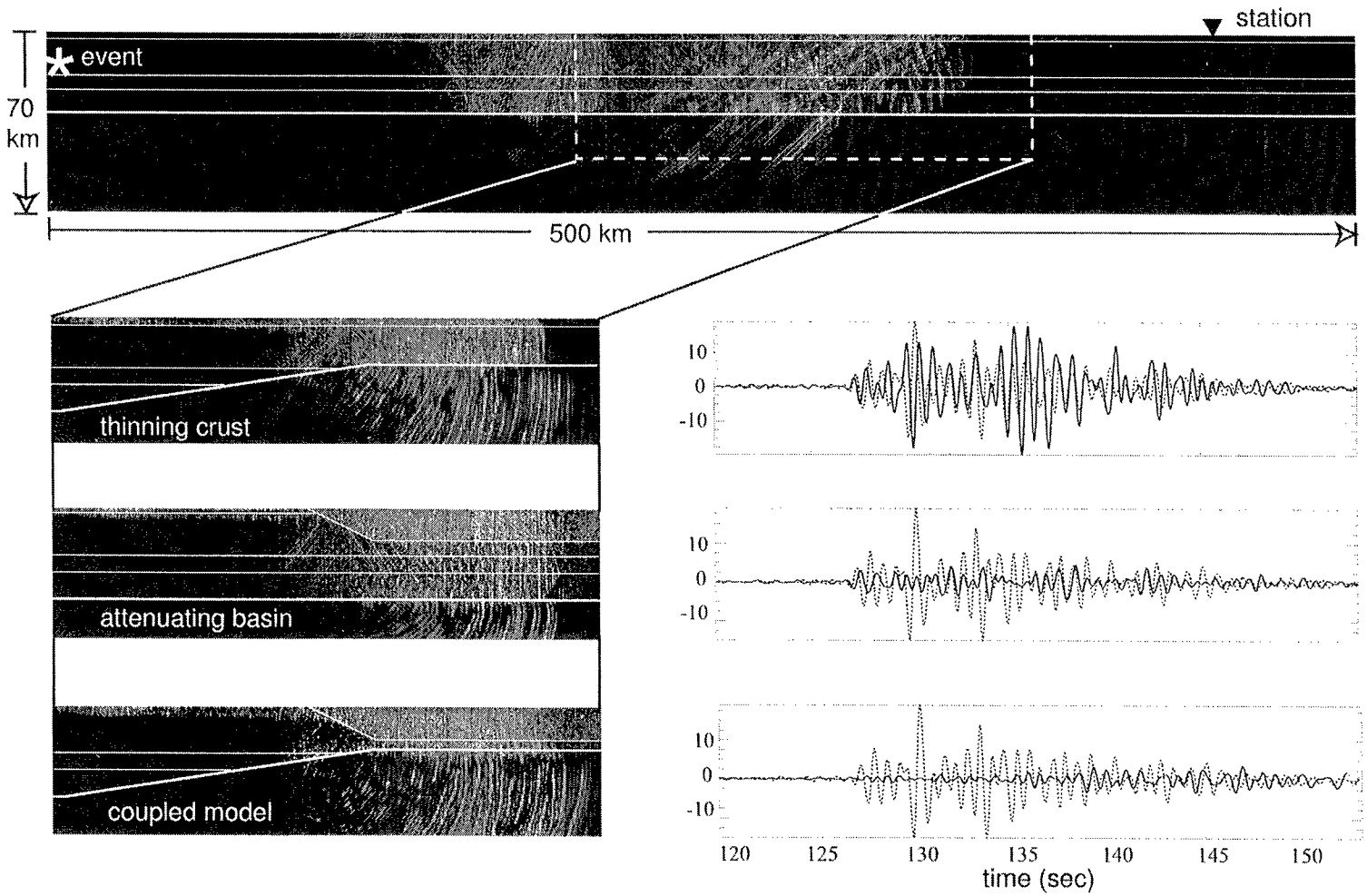

Figure 1. Comparison of finite-difference L_g synthetics for 1- and 2-D models. A sample snapshot of ground motion in the 1-D model is shown at the top. Sample snapshots of ground motion in 2-D models with a thinning crust, attenuating basin, and a combination of a thinning crust and attenuating basin are shown on the lower left with their corresponding synthetic ground motions on the lower right. The snapshots for the 2-D models are subsets of the full model's cross-section in the area indicated by the dashed line in the top cross-section. Synthetic ground motions for the 2-D models (solid lines) overlay the synthetic for the 1-D model (dashed line). The source and reciever locations are indicated in the upper panel by the star and inverted triangle, respectively. These synthetics suggest that a thick sedimentary basin can be particulary effective in blocking L_g, and that crustal thinning is less important but can contribute when coupled with a thick basin.

Previous studies have addressed a number of these issues. For example, Kennett (1986) used ray diagrams to illustrate Ewing's (1957) hypothesis that crustal thinning would allow initially trapped L_g energy to radiate out of the crust. Zhang and Lay (1995) showed that a lack of low-frequency L_g along oceanic paths can be explained by the inability of the thin oceanic waveguide to propagate higher modes. Shapiro et al., (1996) found that low-frequency L_g will convert to S_n in regions where the crust thins, and that shallow, high-attenuation, low-velocity sediments can significantly reduce L_g.

Our results thus far indicate that thick sedimentary basins are particularly effective at attenuating higher frequency (~2-Hz) L_g amplitudes, especially when combined with a reduced crustal thickness, because more of the L_g path length is in the highly attenuative sedimentary basin (Figure 1). For reasonably smooth transitions from a thick to thin crust, we found relatively little reduction in L_g amplitudes. However, some conversion from L_g to S_n occurs in the transition region from thicker to thinner crust. Our observations suggest that crustal thinning enhances the effect of the thick sedimentary basin because L_g is channeled into and propagates a greater distance in the more attenuative sedimentary layers.

Simulating the 1992 (m_b = 5.9) Cairo, Egypt, Earthquake

We are also developing the capability to model regional signals with improved speed and accuracy. Many of the necessary tools are already available, and we are implementing them on selected problems. For example, we used our finite-difference model to simulate the signals observed at a station in Ankara, Turkey, from the moderate-sized (m_b = 5.9), October 12, 1992, Cairo, Egypt, earthquake. The region modeled crosses the eastern part of the Mediterranean Sea and has large lateral variations in structure. A comparison of simulations for a flat-layer model and a two-dimensional finite-difference model (Figure 2) with data indicates the importance of such capabilities. Simulations of regional wave propagation in laterally varying media give a better fit to the energy distribution, relative phase amplitudes, and frequency content. Additional simulations indicate that the thick sedimentary basin controls the evolution of most of the regional seismic signals. Variations in crustal thickness account for relatively small differences in the seismic waveforms. The presence or absence of the Mediterranean Sea does not seem to be significant.

SAC2000: A TOOL FOR SPECIAL-EVENT ANALYSIS AND DEVELOPMENT OF AUTOMATED DATA-PROCESSING ROUTINES

Special-event analysis and implementation of an automated data-processing system for monitoring a Comprehensive Test Ban Treaty will require accurate, robust, and efficient data-processing and analysis techniques. The development of such techniques usually involves a detailed testing phase using large data sets that are well calibrated , i.e., with detailed descriptions of event locations and types. We are producing and using the tools that are needed to develop and test such techniques. Our principal tool is SAC2000 (Goldstein and Minner, 1995, 1996). SAC2000 is a signal-processing and seismic-analysis software package that has evolved from the Seismic Analysis Code (SAC) that was developed by the Treaty Verification Program at Lawrence Livermore National Laboratory during the 1980s. SAC and SAC2000 are used throughout the world by more than 300 institutions ranging from universities and government agencies to private companies and contractors. SAC2000's capabilities range from making relatively simple signal measurements, such as travel times and amplitudes, to more complex analyses using macros to estimate magnitudes and discriminant parameters, and to perform high-resolution spectral and array analyses.

Much of our work is focused on enhancing SAC2000's capabilities for mapping and for travel-time, array, and spectral analysis (Figure 3) so that research and development of monitoring techniques can proceed efficiently. For example, we implemented image plotting and processing tools along with high-resolution spectrogram and sonogram techniques because they were needed for the research and development of quarry-blast monitoring techniques (e.g., Figure 3e). AFTAC has used SAC2000's spectrogram and sonogram capabilities as part of its research on mining-

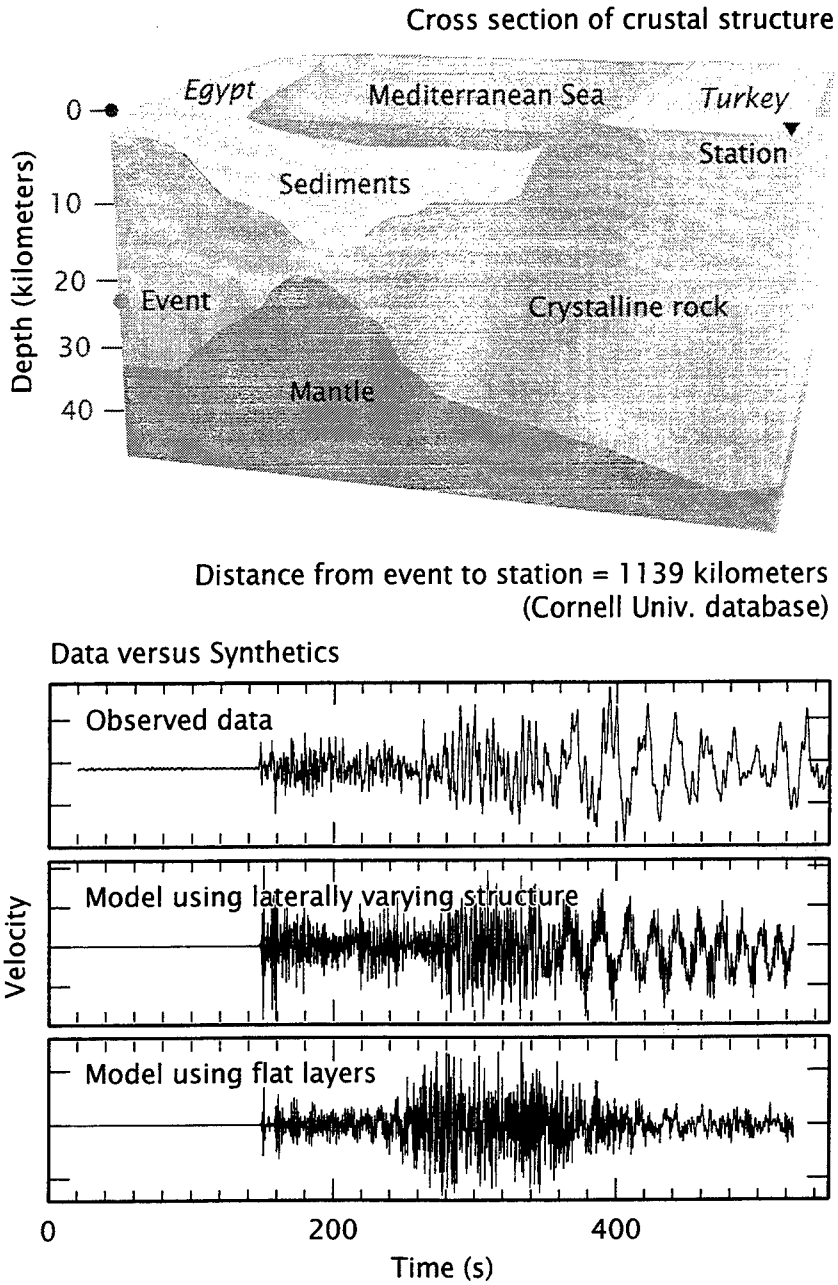

Figure 2. Cross section of the Middle East showing the travel path of a seismic signal; comparison of observed data with a reflectivity (flat-layer) model and a finite-difference (laterally varying) model.

related seismic signals. We have also added important data-access capabilities needed by AFTAC and the monitoring community, and we are configuring a more efficient and user-friendly interface.

A number of our research and development efforts focus on developing new automated data-processing techniques. For example, we developed and delivered to AFTAC robust algorithms to estimate coda magnitude (a highly stable moment- and magnitude-estimation technique, Figure 4; Mayeda and Walter, 1996) and measure slopes of *P*- to *S*-wave spectral ratios (a promising new discriminant, Figure 5; Goldstein, 1995).

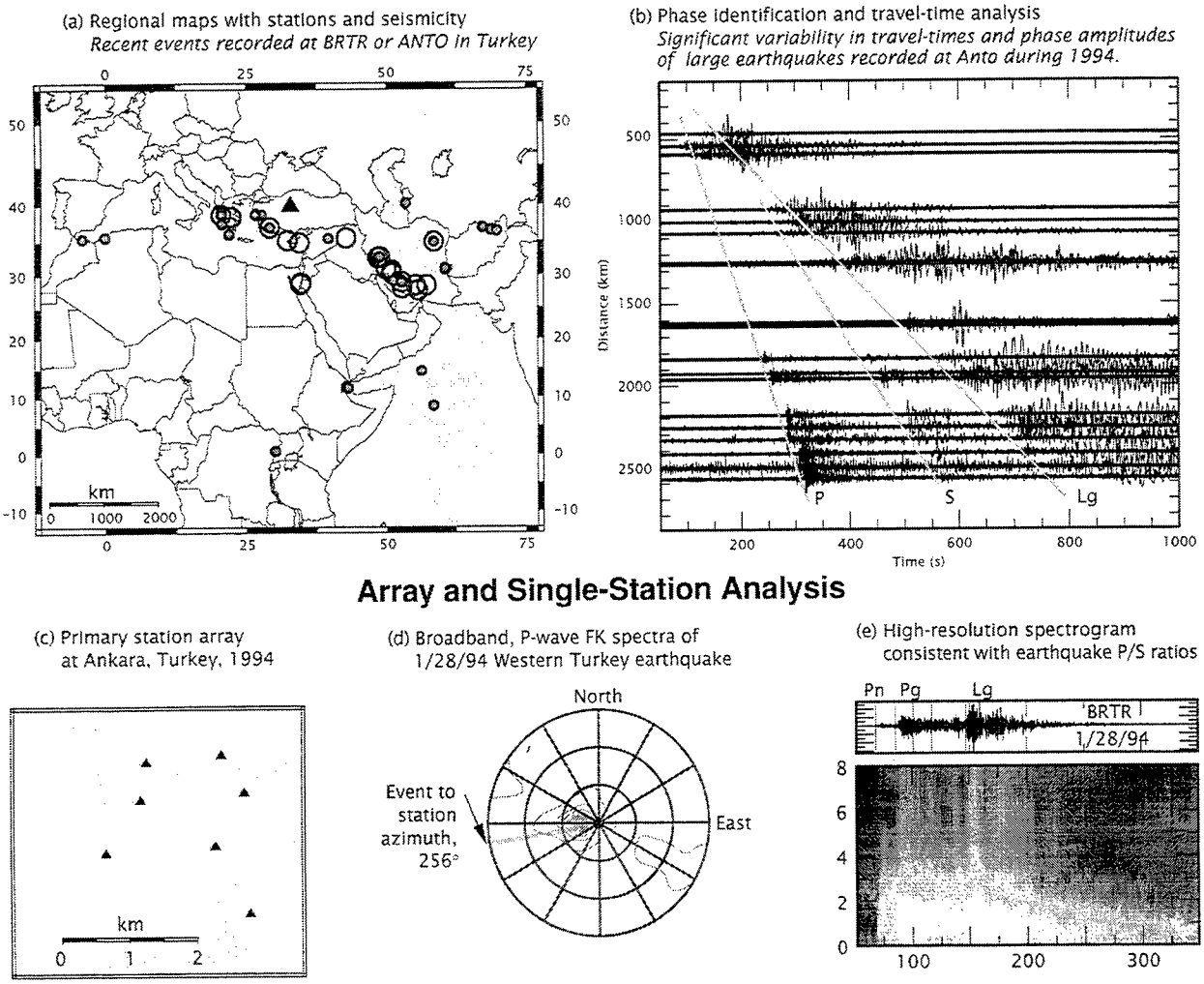

Figure 3. SAC2000's enhanced mapping, travel-time modeling, array analysis, and spectrogram capabilities are useful for analyzing special events and developing new monitoring techniques. SAC2000 can be used to generate local and regional maps (a and c), plot seismic data in record-section format with travel-time curves (b), estimate frequency-wavenumber (FK) spectra of individual phases (d), and compute high-resolution spectrograms of individual traces (e).

CONCLUSIONS

We are developing the modeling and analysis capabilities and knowledge needed for special event analysis and improved automated CTBT monitoring. For example, we have utilized our wave propagation modeling capabilities to test a variety of hypotheses to explain observations of L_g blockage. Preliminary findings suggest that thick sedimentary basins are particularly effective at attenuating L_g, especially when combined with crustal thinning, because a greater portion of the L_g propagation path length is in the highly attenuative sediments. Crustal thinning alone did not produce significant reduction in high-frequency L_g amplitudes but did enhance S_n, as suggested by Shapiro et al. (1996).

We have developed a number of enhancements to SAC2000 that are useful for special event analysis and for developing and testing automated data processing algorithms. Examples include new mapmaking capabilities, direct access to user defined subroutines, and high resolution spectrogram and binary sonogram capabilities. Examples of recent successful uses of SAC2000 include the development of robust coda magnitude-estimation techniques and of a broadband regional seismic discriminant based on slopes of *P*- to *S*-wave spectral ratios.

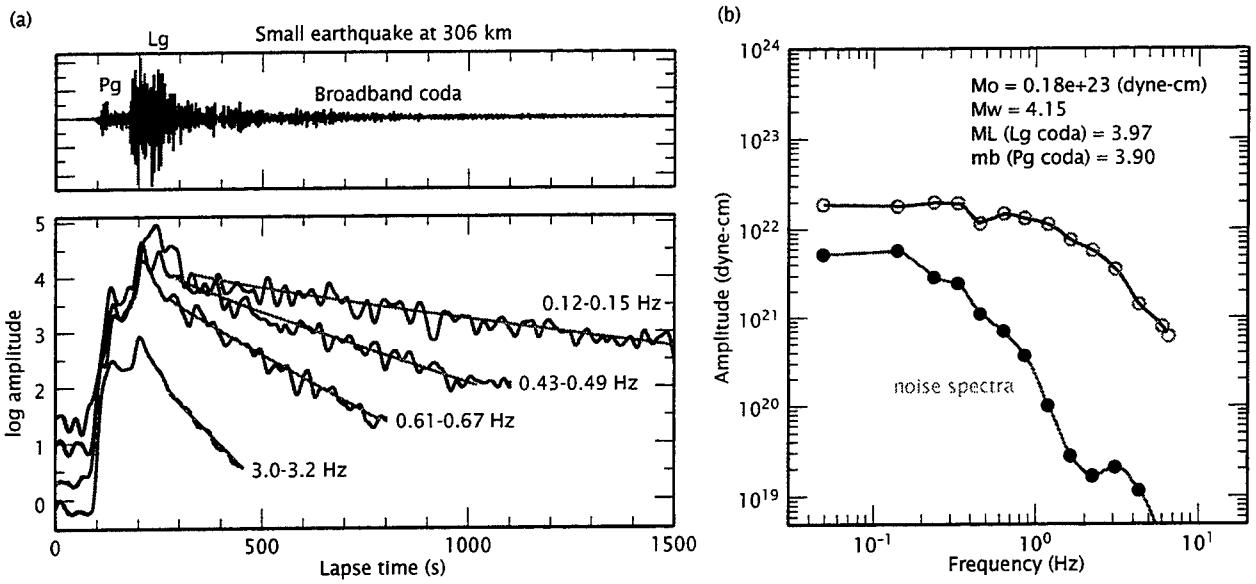

Figure 4. Narrowband coda envelopes (a) can be used to estimate moment rate spectra and seismic moment magnitude (b).

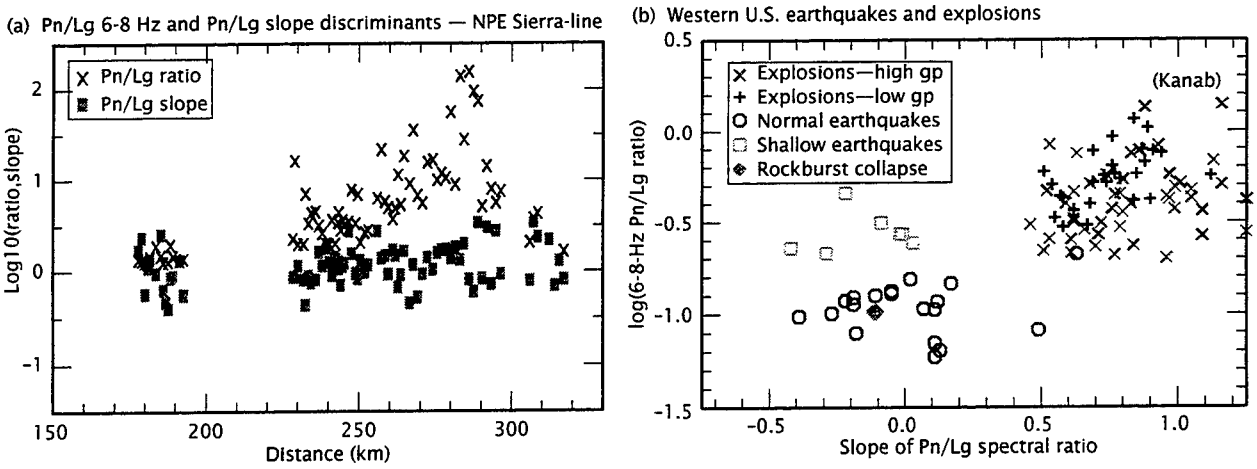

Figure 5. Ratios of *P*- and *S*-wave amplitude spectra can be used to discriminate earthquakes and explosions. Slopes of *P*- to *S*-wave spectral ratios have been shown to have less variability with distance than conventional narrowband *P*- to *S*-wave spectral ratios (a). The slope and amplitude of *P*- to *S*-wave spectral ratios can be combined to improve discriminations performance (b).

REFERENCES

Ewing, M., W. S. Jardetsky, and F. Press, "Elastic waves in layered media," McGraw–Hill, New York (1957).

Goldstein, P., "Slopes of *P*- to *S*-Wave Spectral Ratios: A Broadband Regional Seismic Discriminant and a Physical Model," *Geophys. Res. Lett.* **22**, 3147–3150 (1995).

Goldstein, P., and L. Minner, "SAC2000: Seismic Signal Processing and Analysis Tools for the 21st Century," *Seism. Res. Lett.* **67**, 39 (1996).

Goldstein, P., and L. Minner, *A Status Report on the Development of SAC2000: A New Seismic Analysis Code*, Lawrence Livermore National Laboratory, Livermore, CA, UCRL-ID-121523 (1995).

Kennett, B. L. N., "L_g waves and structural boundaries," *Bull. Seis. Soc. Am.*, **76**, 1133–1141 (1986).

Mayeda, K. M., and W. R. Walter, "Source Parameters of Western U.S. Earthquakes: Moment, Energy, Stress Drop and Source Spectra from Regional Coda Envelopes," *J. Geophys. Res.* **101**, 11,195–11,208 (1996).

McNamara, D., W. R. Walter, C. S. Schultz, and P. Goldstein, "Regional Phase Propagation in North Africa and the Mediterranean," *Seism. Res. Lett.* **67**, 47 (1996).

Shapiro, N., N. Bethoux, M. Campillo, and A. Paul, "Regional Seismic Phases Across the Ligurian Sea: L_g Blockage and Oceanic Propagation," *Phys. Earth Planet. Interiors*, **93**, 257–268 (1996).

Zhang, T.R., and T. Lay, "Why the L_g phase does not traverse oceanic crust," *Bull. Seis. Soc. Am.*, **85**, 1665–1678 (1995).

WAVE PROPAGATION IN A COMPLEX CRUST - CTBT IMPLICATIONS

Eystein S. Husebye and Bent O. Ruud
Institute of Solid Earth Physics, University of Bergen, Norway
Grant No. F49620-94-1-0278
Sponsored by AFOSR

ABSTRACT

A major CTBT monitoring issue is that of detecting and locating events at local and regional distance ranges using local seismograph network observations. We have developed a scheme for doing so in an automatic manner taking advantage of the excellent SNRs of short period recordings and processing robustness of envelope signals. When tested on local mining explosions our scheme gave more accurate locations as compared to those in the local bulletins.

Much efforts have been spent on expanding to 3D models and streamlining our finite difference (FD) wavefield simulation scheme. 3D FD modeling of topography wavefield responses in the NORESS array siting area have been successful; we are able to reconstruct P-to-Rg scattering with a 'secondary' source in the Bronkeberget hills. Using the 2D FD variant we have also simulated Lg-blockage across the North Sea graben structures. Partial blockage of Lg is caused by crustal thinning as expected but on the other hand this factor is insufficient for explaining the observational records at hand. In the extreme, the crystalline part of the crustal model was only 5 km thick and besides subjected to a RMS velocity perturbations of 8% beneath the graben area, still the Lg amplitude reduction amounted to only 12 dB. To ensure blockage of the extent seen in North Sea earthquake recordings, a low Q-value of 100 (at 2 Hz) have to be introduced in the graben crust. An apparently ignored aspect of North Sea Lg observations is that when Lg is weak the associated Sn-phase most often is strong with an extended coda and visa versa. This implies that when the crustal waveguide is distorted Lg-waves leak into the upper mantle and 'return' to the free surface as Sn-waves. These phenomena, not restricted to graben structures only, make it problematic to properly separate crustal waveguide distortions, attenuation and upper mantle path effects.

Most of our crustal structure knowledge stem from long range seismic profiling surveys. Puzzling features here are that the crust is modeled as an aggregate of many, homogeneous layers and that the ray synthetics have little semblance with real recordings. We have investigated this problem by computing 2D FD synthetics for original Baltic Shield crustal models and also for the same models subjected to 3% RMS velocity perturbations. ProMAX software was used for processing and mapping the synthetics in the x–t and p–tau domains. Our conclusions here are that overly detailed crustal models have no obvious counterpart in the observational data. Analysts appear to pick secondary phases in the 100–300 km distance range where PmP (Moho) and coda waves are dominant. Our preference is for crustal gradient models subjected to small scale stochastic velocity perturbations of the order of 2–4%.

Keywords: CTBT monitoring, automatic event location, 2D and 3D FD synthetics, scattering, Lg-blockage, $Lg - Sn$ coupling, crustal profiling, deterministic versus stochastic modeling.

OBJECTIVES

- Foster a better understanding of seismic wave propagation in complex media.
- Principal analysis tools are 2-D and 3-D finite difference (FD) synthetics for models also including surface topography.
- Corroborating synthetics through analysis of array and network data.
- Use 'synthetic' knowledge in design of event classification schemes.
- Seismic network performance and real time location of local events.
- Principal objective: contribute to more efficient CTBT monitoring capabilities at local and regional distance ranges.

RESEARCH ACCOMPLISHED

In the following summaries are given for different research tasks accomplished.

NATO ASI symposium & book on CTBT monitoring

Our NATO ASI Symposium in Alvor, Portugal 23 Jan–1 Feb, 1995 on CTBT monitoring was rated a great success. The final outcome of this undertaking was the book: E.S. Husebye and A.M. Dainty (eds): Monitoring a Comprehensive Test Ban Treaty, Kluwer Academic Publ., Doordrecht, The Netherlands, pp 836, 1995. The book contains contributions from many scholars on most CTBT issues albeit with emphases on seismic monitoring. More than 100 key lecturers and students attended the symposium including 10 scientists and nuclear physicists from the former Soviet Union.

Automatic *Pn* and *Lg* magnitude estimation

Local magnitude and moment of a seismic event can be estimated in near real time by means of signal detector parameters being defined as *rms* trace estimates. The advantage of such a signal detector is accurate prediction of maximum signal amplitude via random vibration theory. Using source theory, we have computed geometrical spreading and attenuation correction curves for different frequency ranges using P and Lg propagation parameters as published in the scientific literature.

Real time noise and signal amplitude estimates are important in many context of monitoring seismology; the essential feature being joint use of time and amplitude information. For example, seismic network performance can conveniently be estimated in near real time; facilitating threshold monitoring of seismic surveillance, improved phase association , automatic magnitude and moment estimation and routine extraction of seismic source discriminant like the P/Lg amplitude ratio. Details on this study is given by Mendi and Husebye (1995).

Local event location in an automatic manner

A Comprehensive Test Ban Treaty would hopefully be approved by U.N. member states in 1996. This Treaty would exclude any kind of nuclear tests so the seismic monitoring focus is shifted from teleseismic to local/regional distance ranges. In these ranges the typical high-frequency signals vary unpredictably even between closely spaced stations so efficient automatic monitoring schemes are lacking. A solution to this problem that is real time event detection and location as described by Ryzhikov *et al.* (1996). Design principles are tied to transforming high-frequency complex signal waveforms to low-frequency simple signals and anchored on wave propagation theory for stratified media (Kennett, 1983). Testing the new method on mining events from S. Norway our epicenter determinations were far better than those derived by the analyst (bulletins).

Ray tracing versus 2D FD synthetics in analysis of profiling records

Knowledge of the structure and petrology of the continental crust is of fundamental importance in understanding crustal generation and evolution. The principal geophysical tool for achieving this has been and still is long-range seismic refraction and wide-angle profiling surveys In the past crustal profiling models were usually presented in terms of a stack of essentially horizontal, homogeneous layers which more recently have generally been discarded in favour of more geological reasonable gradient models including velocity perturbations. There is also strong seismic evidence disfavouring extensive crustal layering models; seismic reflection surveys have identified imprints of Precambrian tectonic events also at Moho depths in shield areas but not refraction profiling style crustal layering. We may in fact argue in favour of discrete crustal layering models namely that refraction profiling resolution only permits mapping of bulk crustal properties and hence, in this regard, layered models are adequate. The geological justification here is the general subdivision in a strong upper sialic crust and a relative ductile lower basaltic crust.

In this study we explore the adequacy of detailed crustal modeling based on long range seismic refraction and wide-angle surveys. The real issues at hand are to what extent deterministic structure models are appropriate and likewise whether ray synthetics are a convenient tool in analysis of such data. Our approach to these problems were to compute 2D FD (finite difference) synthetics for published crustal models within the Baltic shield (Kola and FENNOLORA); we used both the original deterministic ones and their randomizations introduced through von Karman functions of order 0.3 and 3.0% RMS velocity fluctuations.

In Fig. 1 the SW segment of the FENNOLORA profile is shown: A) original trace display and phase pickings, B) ray synthetics for the final crustal model shown in C). The striking features here are the mismatch between the field recordings and the ray synthetics and the apparent element of randomness in picking secondary arrivals in the 100–300 km distance range.

The synthetic wavefields, here restricted to 190 km, are shown in Fig. 2 for the 3% RMS velocity model shown in Fig. 1c. The displayed 2D FD synthetics imply that intercrustal reflections at critical angles and beyond should be most clearly observable in the distance range 50-120 km (crustal thickness ca 35-40 km). For distances exceeding 100 km the wavefields are dominated by the classical phases like Pg, Pn and the strong PmP (Moho) and its extended coda and in this regard appears similar to the original field recordings in Fig. 2a. On the other hand, the multitude of phase pickings in Fig. 2a are not easily reconciled with the quite realistic 2D FD

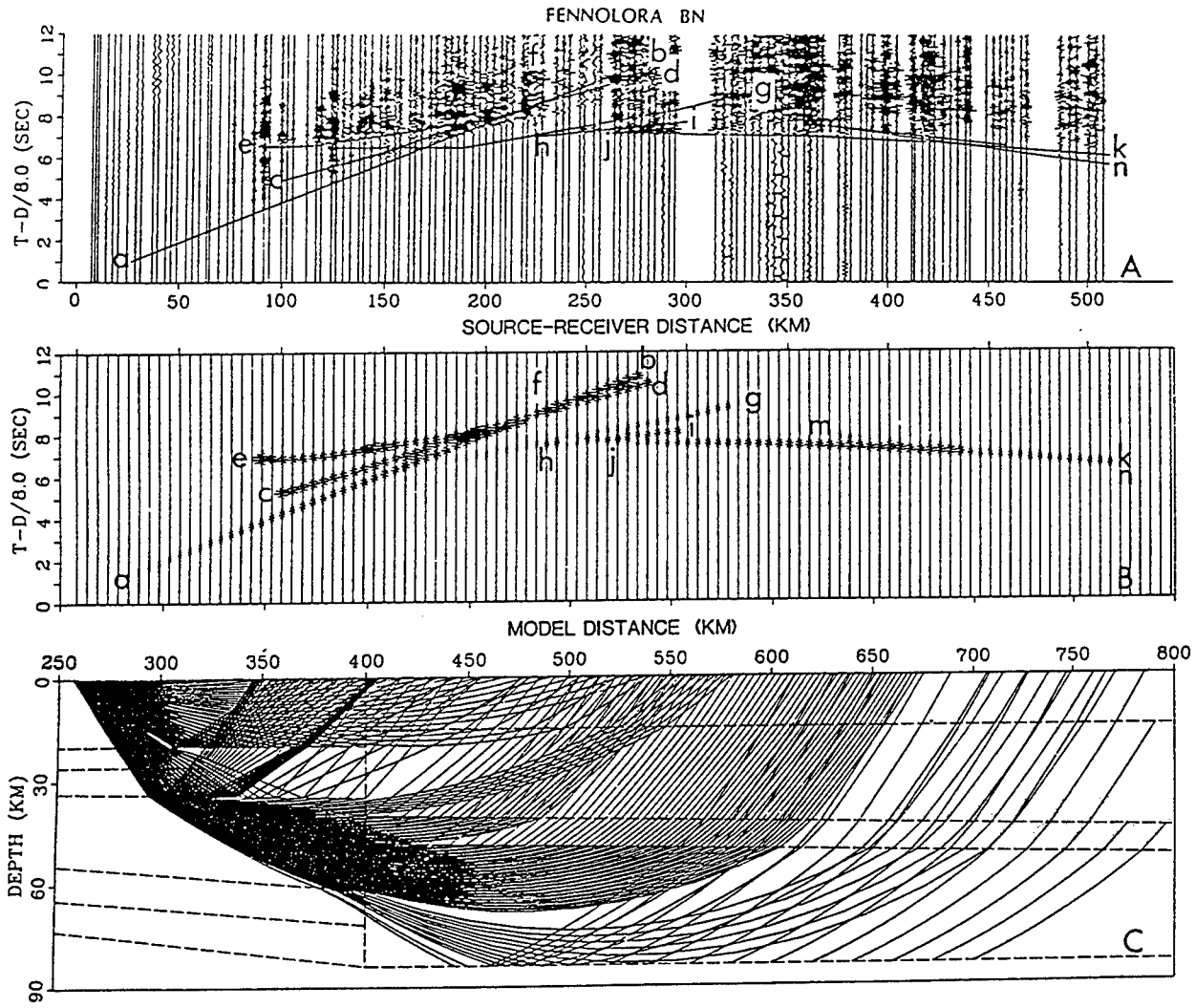

Figure 1: a) The FENNOLORA BN record section (z-comp.). Amplitudes are enhanced proportional to the source receiver distance, normalised at 100 km. b) Synthetic seismogram for the a) distance range. c) crust and upper mantle model with rays originating at the a) shotpoint – distance scale is shifted 250 km (figures from Clowes *et al.*, 1987).

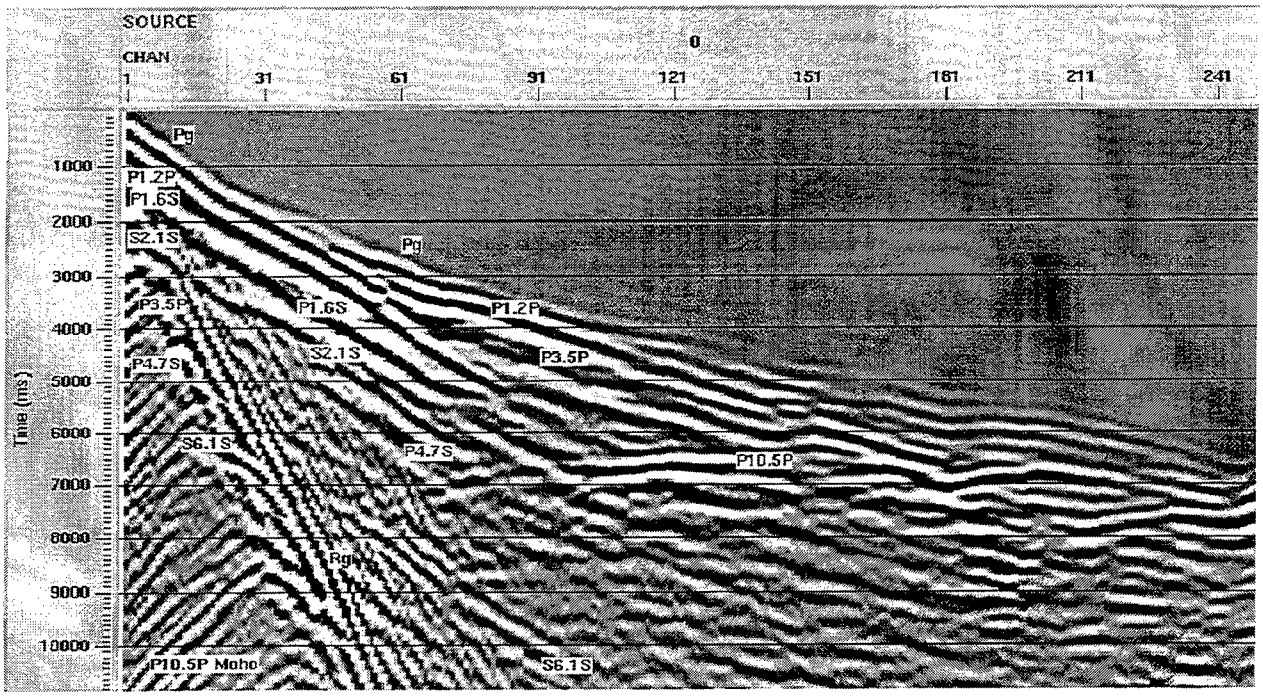

Figure 2: 2D FD synthetics for the 3% velocity perturbed FENNOLORA crustal model using the ProMAX VD display option. Horizontal scaling unit is sensor no; the spacing is 0.8 km. Of the intercrustal PmP reflections only the PmP (Moho) appears observable beyond ca. 100 km. Beyond this distance the first arriving Pg- and Pn-phases plus P10.5P Moho reflection dominate. PmP and PmS indexing are as follow: P1.2P, P1.6S and S2.1S are from a reflector at 3.12 km depth. P3.5P, P4.7S and S6.1S are from a reflector at 10.14 km. P10.5P is the strong Moho reflection.

synthetics which incorporate coda wave excitation. For the perturbed model synthetics many of the 'weaker' crustal layers are not observable seismically albeit clearly seen in the unperturbed model synthetics (not shown) at distances less than 100 km. In contrast, the subjective analyst phase pickings are mainly in the 100-300 km distance range and this in combination with ray tracing synthetics being dissimilar to real records, appear to explain the endproduct of overly detailed, deterministic crustal models here rated partly fictive. These are strong words, but in the Mårdalen *et al.* (1996) paper extensive references are given to recent scattering and stochastic crustal modeling works and also to recent deep seismic reflection surveys in the Baltic and Skagerrak Seas. The common denominator for these studies are that the crustal velocity distribution is not discontinuous (stepwise) but continuous (gradients) subject to RMS velocity perturbations of a few percent. The latter kind of crustal models are a prerequisite for calculating realistic synthetic wavefield in 2- and 3-dimensions including strong coda wave excitation.

Lg-blockage across North Sea grabens

The North Sea *Lg*-blockage for wave paths across the crustal graben structures is a well-established observational fact (Fig. 3). Analysis of such observations implies that *Lg*-blockage takes place in graben areas associated with sedimentary basin formation and crustal thinning. These intriguing observations have triggered many theoretical studies aimed at highlighting specific *Lg* loss mechanisms albeit so far with only moderate success. With the latter statement is meant that the claimed *Lg*-blockage is far less than that actually observed; in Fig. 3 the *Lg*-wave train is nearly completely wiped out at several recording stations. A reason for this mismatch may be that most theoretical modeling schemes do not incorporate intrinsic attenuation effects until very recently.

Our approach to this problem is to simulate seismic wavefield propagation through the crustal waveguide using 2D finite difference (FD) techniques. Currently, our FD schemes do not account for intrinsic attenuation. From oil exploration works in the North Sea the graben structures are known in detail which enabled us to use realistic crustal models in our *Lg* synthetics. In the most extreme model tested, the crystalline crust thickness beneath the graben amounted to only 5 km while the overlying sedimentary pile is nearly 10 km thick. At the base of the crust the Moho is elevated nearly 10 km the graben area. This model has similarities to the oceanic crustal waveguide where total *Lg*-blockage is claimed for path lengths exceeding 100 km. In another experiment, the crystalline crust in the graben area was subjected to 8% RMS velocity perturbations.

Synthetic wavefields for realistic North Sea graben structures are displayed in Fig. 4 in a series of snapshots at 10 sec intervals. Clearly, the dominant structural *Lg* loss mechanisms are *Lg*-to-*Rg* conversions (scattering) in the sediments and *S*-wave leakage out of the crustal waveguide and into the upper mantle. Part of these upper mantle *S*-waves return to the crust and appears as *Sn* coda. Observationally, as illustrated in Fig. 3 strong *Sn*-phases of long duration are often associated with weak *Lg* phases and vice versa.

Our synthetics produced *Lg* amplitude decay amounting at most to 6-10 dB, depending on the model (Fig. 5), while observational data imply blockage amounting to 15-20 dB. The latter is equivalent to *Pn*-*Lg* magnitude difference of nearly one magnitude unit. The main outcome of this study is therefore that *Lg*-wave propagation is very, very robust and that a likely, dominant blockage effect is associated with intrinsic attenuation. In other words, Q values of the order of

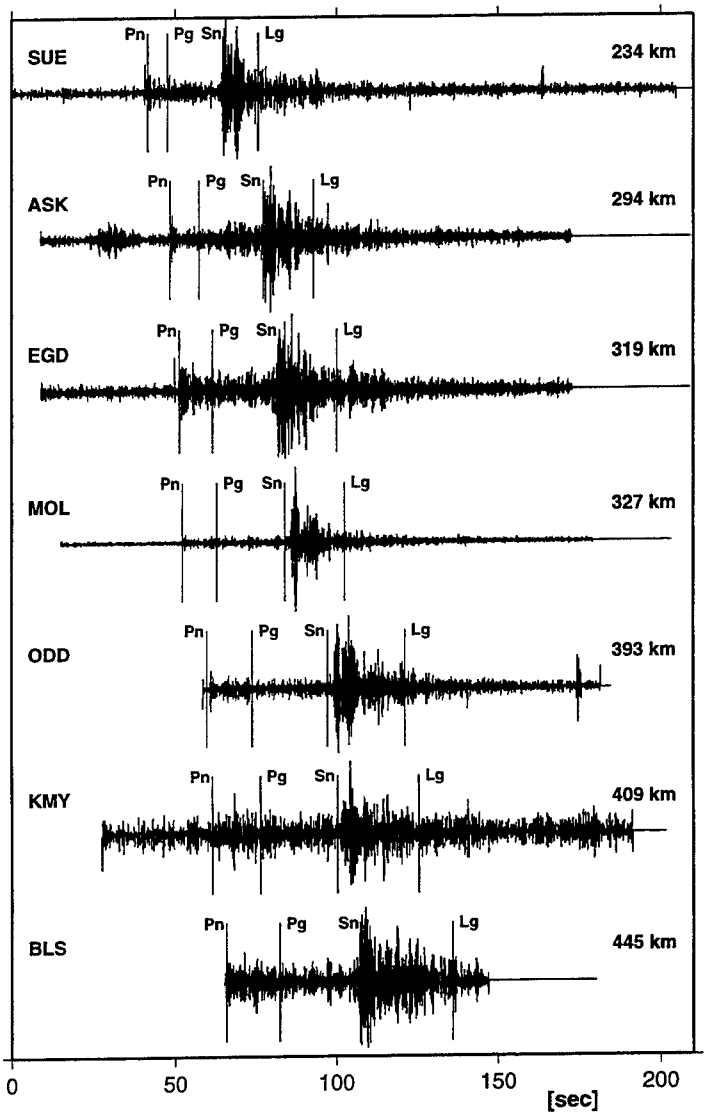

Figure 3: Seismic recordings from a northern North Sea earthquake on 21/04/1995. Outstanding seismogram features are strong Sn phases of long durations followed by weak Lg phases. Apparently, the graben blockage cause Lg wave energy leaking as S-waves into the upper mantle and subsequently re-appearing in the crust as part of the Sn coda. Pn and Lg magnitudes are measured to 2.0 and 1.6, respectively.

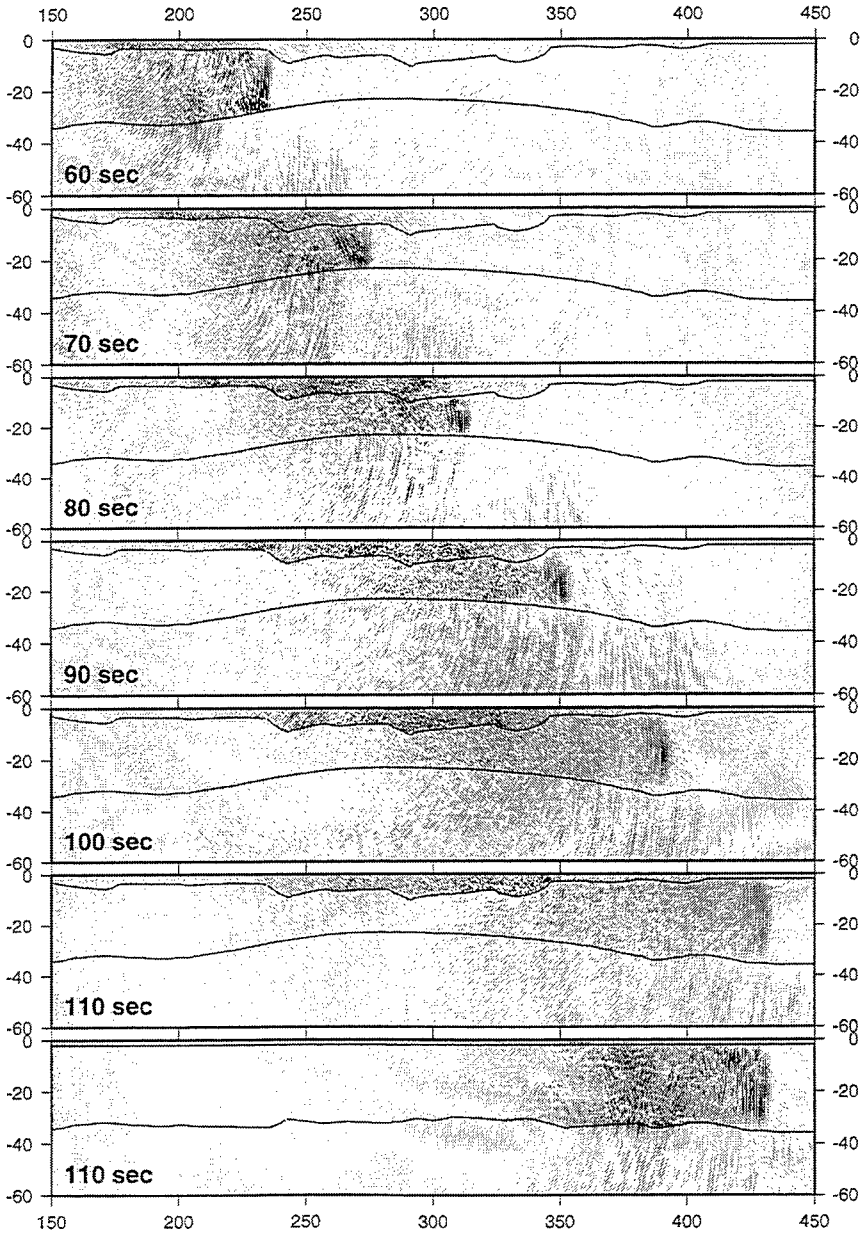

Figure 4: A series of snapshots illustrating wave propagation through a typical graben area. The horizontal axis gives the distance from the source (in km) and the vertical axis gives the depth from the surface (in km). The Moho and the sediment/crust interfaces are shown as solid lines. The lower most snapshot is shown for comparison with a reference model (no graben structure).

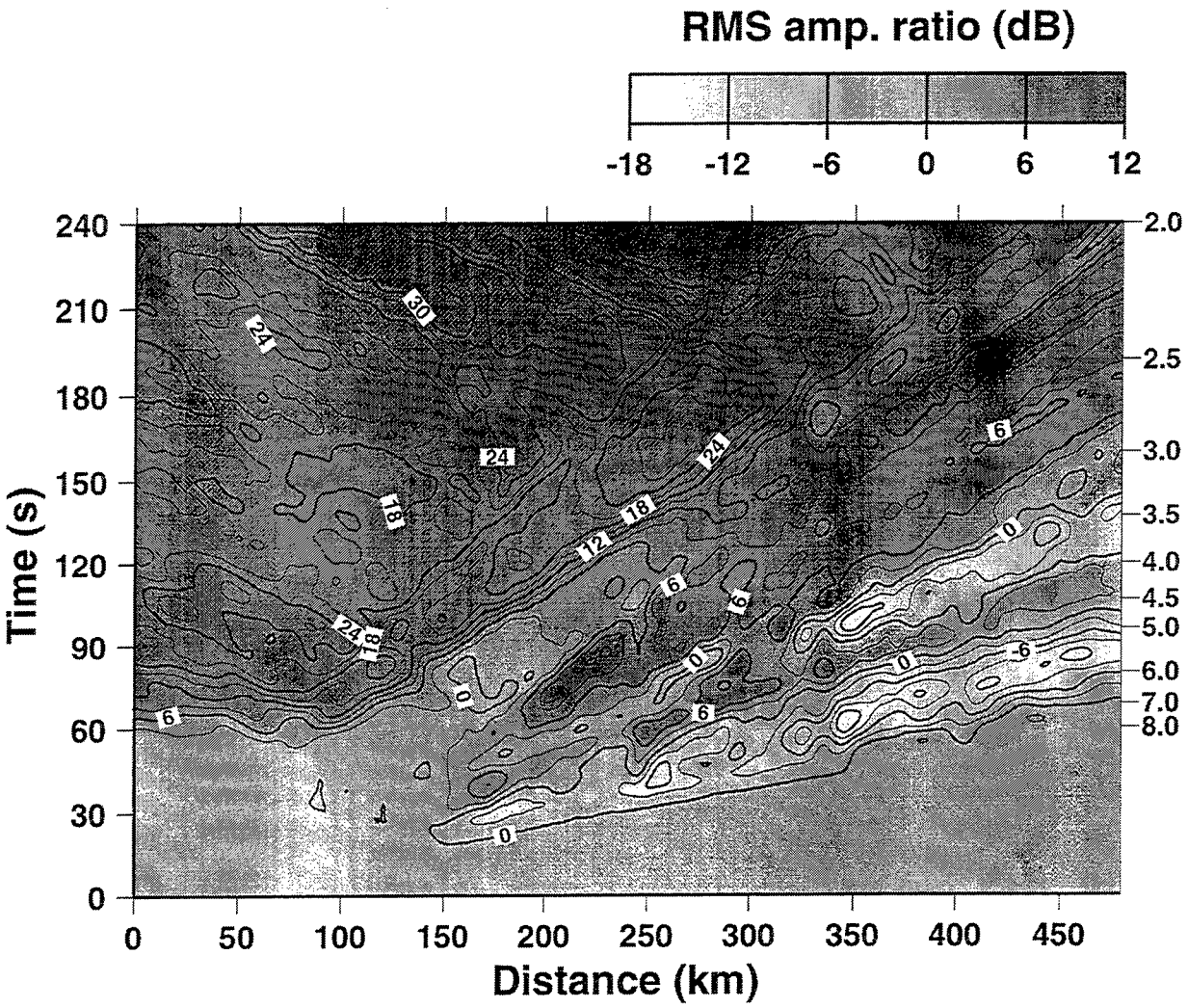

Figure 5: Relative RMS amplitudes for the two models in Fig. 4. RMS amplitudes were computed for each sensor at the surface (1 km spacing) with a 2 sec long moving time window. On the right vertical axis the group velocities are given in km/s. Typical *Lg* group velocities are in the interval 3.2 to 3.9 km/s. The light shading implies amplitude losses (blockage) which in this case seldom exceed 6 dB for the most effectively blocked *Lg* waves and 12 dB for *Pg*. The strong surface wave amplification in the later part of the synthetics is due to the fact that the reference model (no sedimentary basins or crustal thinning) is practically void of scattered *Rg* waves.

100 at 2 Hz for a path length of minimum 100 km, is needed for the synthetics to conform to observations. The latter explanation is not necessarily unique since the amount of *Lg* leakage into the mantle is not accurately known. Details on our *Lg*-blockage study is given in a forthcoming paper by Mendi *et al.* (1996).

CONCLUSIONS AND RECOMMENDATIONS

In the reporting period work efforts have been focussed on generating realistic seismic wavefield synthetics in 2D and 3D using finite difference techniques. Such analysis tools add a new dimension to understanding wave propagation in complex media like the crust. Illustrative examples are given in terms of *Lg* blockage across North Sea grabens (Mendi *et al.*, 1996), *P*-to-*Rg* scattering from 3D topography (Hestholm and Ruud, 1996) and the relative merits of long range seismic refraction surveys (Mårdalen *et al.*, 1996). Essentially, the structural concept of the crust (high frequency waves) should be in terms of velocity gradient models subject to randomized velocity perturbations of a few (2–4) percent. Such models easily explain coda wave excitation, a dominant seismogram feature, and also occasionally large phase amplitude variations with no need to invoke in an ad hoc manner major crustal discontinuities.

The currently envisaged International Monitoring System (IMS) as part of a likely CTBT is not efficient for small events say below magnitude 3.5. These are most easily detected and identified by local seismograph networks which are often unable to do so due to lack of adequate analysing scheme for automatically detecting and locating small event. Likewise, source discrimination parameters have to be extracted routinely and also aimed at being more site and source specific. Population of events scattered over hundreds of kilometers are not likely to constitute an adequate basis for efficient source identification. Our future research efforts would be focussed on these problems: automatic event locations and extraction of discrimination parameters.

References

Clowes, R.M., E. Gens-Lenartowicz, M. Demartin and S. Saxov (1987). Lithospheric structure in southern Sweden – results from FENNOLORA, *Tectonophysics*, **142**, 1–14.

Hestholm, S. abd B.O. Ruud (1996). 3-D finite difference elastic wave modeling including surface topography, m/s submitted for publication.

Mendi, C.D. and E.S. Husebye (1995). Near real time estimation of seismic magnitude and moment via *P* and *Lg* phases. In: R.Console and A. Nikolaev (eds.), *Earthquakes induced by underground explosions*, NATO ASI Series 2, Springer-Verlag, Berlin, Germany.

Mendi, C.D., B.O. Ruud and E.S. Husebye (1996). The North Sea *Lg*-blockage puzzle, m/s submitted for publication.

Mårdalen, T.V, E.S. Husebye and B.O. Ruud (1996). Facts and fiction in derived crustal model from seismic refraction profiling, m/s in preparation.

Kennett, B.L.N. (1983). *Seismic Wave Propagation in Stratified Media*, Cambridge University Press, Cambridge, UK, 342 pp.

Ryzhikov, G.A., Biryulina, M.S. and Husebye, E.S., 1996. A novel approach to Automatic Monitoring of Regional Seismic Events, *IRIS Newsletters*, Vol. XV, 12–14.

WAVEGUIDE EFFECTS OF LARGE-SCALE STRUCTURAL VARIATION, ANELASTIC ATTENUATION, AND RANDOM HETEROGENEITY ON SV Lg PROPAGATION: A FINITE-DIFFERENCE MODELING STUDY

Rong-Song Jih
Phillips Laboratory (GPE), Hanscom AFB, MA 01731-3010

Sponsored by AFTAC under Project Authorization T/0121

ABSTRACT

Many empirical studies have found evidence that abrupt thinning of the crust can weaken the L_g phase, and that contained sedimentary basins or mountain ranges on the path can completely or partially block the phase. Theoretical (modeling) studies can provide insights for better understanding and interpretations of the physical mechanisms involved. This study attempts to quantitatively predict the waveguide effects using extensive two-dimensional linear elastic (P–SV) finite-difference [LFD] calculations. Miscellaneous waveguide effects are analyzed and compared, both qualitatively and quantitatively, through visualization and spectral analysis. A pure L_g wave packet is injected into a stratified portion of the grid as the reference initial condition to trigger all LFD calculations for a suite of heterogeneous crustal structures. An obvious advantage of this approach is that the effects due to different types of heterogeneity on L_g phase can be isolated and evaluated easily. Each model contains a laterally heterogeneous crust superimposed on the homogeneous mantle. The heterogeneities examined include large-scale lateral structural variations in the crustal waveguide (such as Moho uplift, crustal thickening, rugged free-surface topography, embedded thick sedimentary layers, *etc.*), anelasticity, and small-scale random heterogeneity.

The LFD results demonstrate that indeed both abrupt changes in the Moho topography and a thick contained sedimentary layer can cause L_g blockage primarily through strong L_g-to-S_n conversions (with actually different physical mechanisms). Alluvial basin structures cause strong reverberations as well as very strong L_g-to-R_g conversions. If the principle of seismic reciprocity is invoked, R_g-to-L_g conversion could be an important mechanism of L_g excitation for certain structures. Unlike the case of R_g waves, a moderate free-surface topography alone does not seem to affect L_g propagation as much as do other types of heterogeneity. Anelasticity and small-scale random heterogeneity can also explain the L_g blockage. An RMS velocity variation of 8 percent in the whole crust is equivalent to a $Q_0(L_g)$ of about 270, which would be sufficient to reduce the peak amplitude of 1Hz L_g waves by 30 percent for every 100 km it traverses. However, LFD calculations also indicate that these mechanisms exhibit some systematic differences in the couplings of L_g into other phases. Thus, identifying the actual mechanism responsible for the blockage along a specific path is possible.

Key Words: Seismic wave propagation, SV Lg phase, finite-difference method, phase blockage, anelastic attenuation, random heterogeneity, topography, path correction.

OBJECTIVE

The long-term objective of this project is to improve the fundamental understanding of seismic wave excitation and propagation. The full potential of linear finite-difference [LFD] method and other techniques shall be exploited in modeling various seismological problems directly related to a CTBT monitoring.

RESEARCH ACCOMPLISHED

The importance of understanding crustal waveguide effects on L_g waves has motivated many modeling studies of blockage in recent years.[1] Some of these studies suggest that the observed blockage is not straightforward to simulate, and that the unmodeled small-scale random heterogeneity is required to account for the blockage, on top of the large-scale structural (that is, geometrical) variation of the waveguide. Although either low Q or large velocity variation can be invoked to explain the L_g blockage of many paths, we might be able to narrow down the possible mechanisms with some additional diagnostic information. For instance, if a pronounced L_g -to-S_n conversion is observed along with the L_g blockage, then it is likely that the blocking mechanism is not due to low Q. This paper concludes a numerical modeling study initiated two years ago (Jih, 1994). A model-based correction procedure is presented, followed by a summary of results based on LFD calculations. The details can be found in Jih (1996b).

One the major challenges in monitoring a Comprehensive Test Ban Treaty [CTBT] is discriminating small events at regional distances. Various forms of compressional/shear (P/S) ratios have been proposed and extensively tested as candidate discriminants. In tackling such problems, a better amplitude (or, equivalently, magnitude) scale of the regional phase of interest, with respective path effects carefully accounted for, is definitely useful or sometimes even necessary. Along this line of thought, Jih *et al.* (1995) (and also Jih and Lynnes, 1993) suggest a simple, convenient magnitude scale for L_g :

$$m_{L_g} = 4.0272 - \text{Bias} + \log A(\Delta) + \frac{1}{3}\log(\Delta(\text{km})) + \frac{1}{2}\log\left[\sin\left(\frac{\Delta(\text{km})}{111.1(\text{km/deg})}\right)\right] + \frac{\gamma(\Delta - 10\text{km})}{\ln(10)}, \qquad [1]$$

$$\text{where } \gamma = \frac{\pi \cdot f}{Q \cdot U}, \quad Q(f) = Q_0 \cdot f^{\zeta},$$

Δ is the epicentral distance in km and $A(\Delta)$ is the observed raw L_g amplitude measured in the time domain in μm [microns] at the epicentral distance of Δ km. Or, equivalently,

$$\hat{A}_{L_g} = A(\Delta) \cdot 10^{4.0272 - \text{Bias}} \cdot (\Delta(\text{km}))^{\frac{1}{3}} \cdot \left[\sin\left(\frac{\Delta(\text{km})}{111.1(\text{km/deg})}\right)\right]^{\frac{1}{2}} \cdot e^{\gamma(\Delta - 10\text{km})}. \qquad [2]$$

The "Bias" term in Eqs. (1) and (2) is meant to account for the different L_g excitation (relative to m_b). It is set to zero for the Eastern U.S. Thus a seismic source with 1-sec L_g amplitude of 110 μm at 10 km (extrapolated) epicentral distance would correspond to a m_{L_g} of 4.0272 + 2.0414 + 0.3333 - 1.4019 + 0.0000 = 5.000, which has been suggested to be appropriate for both Eastern North America and Semipalatinsk. That is to say, a seismic source in these two regions with m_b 5.0 would have a m_{L_g} approximately the same. Jih *et al.* (1995) suggest use of 0.34 and 0.26 m.u. for the "Bias", respectively, for Pahute Mesa and Novaya Zemlya explosions. For earthquakes in the Iranian Plateau, Nuttli (1980)

[1] See Jih (1996b) or Reiter and Jih (1996) for a brief overview of modeling studies by others.

suggested a bias value of 0.39 m.u., which includes both the bias due to regional tectonics as well the $L_g - m_b$ bias due to source type. In a situation where some geometrical blockage occurs along the path, that is, there is a major structural variation along the path, it may be possible to further refine Eq. (1). As an example, the $\gamma(\Delta\text{-}10\text{km})/\ln(10)$ term for the path from Novaya Zemlya to KEV can be broken down into $\gamma_1 \cdot (\Delta_1\text{-}10\text{km})/\ln(10) + \gamma_2 \cdot \Delta_2/\ln(10)$, where $\gamma_2 = 0.0052$ (that is, Q_0=185; see the model 0D in Table 2, page 19, Jih, 1996b), Δ_2 is the lateral span of the Terrigenous Sediments,[2] and γ_1 is the average L_g attenuation along the great-circle path excluding the sedimentary segment. Obviously it is necessary to acquire relevant geological and geophysical information along the path before applying this model-based correction.

Major observations made with LFD calculations are summarized in the following:

Early L_g: The Moho uplift, which is common in models of the "A" and "F" series, breaks down the L_g waveguide and causes L_g-to-S_n coupling at the ascending interface (Figure 1). When the converted S_n waves encounter the descending Moho of these models, some energy penetrates the interface again, either as a leg of S_n or as converted L_g. The Moho uplift in "F"-series models is not as dramatic as in "A"-series models. Nevertheless, both the L_g-to-S_n and possibly S_n-to-L_g conversions are still apparent (Figure 1). The early L_g observed for paths from Novaya Zemlya to Scandinavia can be explained with this mechanism. The fact that L_g can be excited at continental margins from oceanic S_n conversion has long been observed and reported.

Late L_g and longer coda waves: The sedimentary layer, which is present in all "C"-series models and some of "D" and "F" models, is the apparent cause of late L_g arrivals. For models 0Db, 0Fb and 0Fc, the uppermost soft layer causes strong reverberations as well as a very strong L_g-to-R_g conversion (Figure 2). By seismic reciprocity, there should be some structures that would cause strong R_g-to-L_g conversion. Part of this issue has been addressed in Jih (1995, 1996a). Regarding the coda decay rate, intrinsic attenuation and scattering (particularly, that by random heterogeneity) appear to have different effects. Increased scattering attenuation causes more energy to be distributed into the coda from the direct phase with increasing time (Figures 3 and 4). On the other hand, increased intrinsic attenuation entails a greater loss of elastic energy with time from both the coda and the direct wave. This observation can be verified by comparing synthetic seismograms in Figures 61 and 67 of Jih (1996b).

S_n excitation and S_n/L_g ratios: Except for models 00, 2, 2a, 3, 3a, 0C, 0Ca, and 0Cb, all other models in Jih (1996b) excite significant S_n waves through the L_g-to-S_n conversion. A thick sedimentary layer by itself does not necessarily cause strong L_g-to-S_n conversion. Models of the "C"-series are such examples (see pages 29-32 of Jih, 1996b). However, if the thick sediment layer is contained, such as in models of "D" series, then some S_n waves can be generated at the pinched interface. Models with irregular Moho topography generate S_n with a different mechanism, as discussed above. Most models excite converted S_n waves in the forward direction. Hoever, models 0A and 0B of Jih (1996b) also excite some S_n in the backward direction. The extremely large S_n/L_g ratio associated with models 0E, 0Ea, and 0Ec (all with a thickened crust) offers an excellent demonstration for the observation Ruzaikin *et al.* (1977) made.

---

[2] See Gramberg (1988), Clarke and Rachlin (1990), and Baumgardt (1991) for a detailed review on the geology of this path.

Topographic relief: Models with a mild free-surface topography alone (for example, models 2 and 3) generate a relatively weak L_g-to-S_n conversion comparable to that of "C" models (Figure 5). Comparing the synthetics in Figures 55 and 58 of Jih (1996b), it appears that the transmitted L_g wave trains of models with mild mountainous topography are very similar to those of the reference model 00. In fact, these mountainous models and models with weak random heterogeneity as well as anelastic models would stand out among all models in that the checkerboard-like interference pattern of the original L_g wave train is (somewhat) retained (see Figures 45, 49, 59, and 62 of Jih, 1996b). This is very different from the case of R_g for which the rugged free-surface topography is shown to be a strong scatterer (Jih, 1993ab, 1995).

Lg to Pg conversion: All models of the "F" series exhibit significant L_g-to-P_g conversion. The peak horizontal amplitude on trace No. 25 ranges from 10 to 15 percent of that of the original L_g wave train (Figure 2). To a lesser extent, models of "C" and "D" series as well as models 0A and 0Ba also generate the same conversion.

Coupling to teleseismic phases: For mountainous models, L_g-to-S is twice as strong as L_g-to-P. For the "A" and "B" series of models, as well as the random media, these two mechanisms are about equally strong. For anelastic models and "C"-type models, L_g-to-S is weaker than the L_g-to-P, whereas models of the "D", "E", and "F" series show the opposite trend (See Table 2 of Jih, 1996).

Lg blockage: Both abrupt changes in the Moho topography and a thick contained sedimentary layer can cause strong L_g-to-S_n conversions. The physical mechanisms underlying the conversion are different for these two structures, however. The early L_g observed for paths from Novaya Zemlya island to Scandinavia is illustrated with LFD calculations. Alluvial basin structures cause strong reverberations as well as very strong L_g-to-R_g conversions. Valley structures with large depth to width ratios and large velocity contrast with the substrate support very large amplitude lateral resonance modes. If we invoke the principle of seismic reciprocity, R_g-to-L_g conversion could be an important mechanism of L_g excitation for certain structures. Recent observational study by Patton and Taylor (1995) suggests that this is the case, at least for Yucca Flat explosions.

Other than major structural discontinuities in the crustal waveguide, both anelasticity and small-scale random heterogeneity can also contribute to the so-called "L_g blockage". For instance, an RMS velocity variation of 8 percent in the whole crust is equivalent to a $Q_0(L_g)$ of about 270, which would be sufficient to reduce the peak amplitude of 1Hz L_g waves by 30 percent for every 100 km they traverse. The classical example of an L_g-blocking path between Novaya Zemlya and northern Scandinavia has a $Q_0(L_g)$ about 252 and could be modeled with an RMS velocity variation of 8 percent alone.

CONCLUSIONS AND RECOMMENDATIONS

An accurate prediction of the regional phases in areas of high proliferation concern requires a decent understanding of the attenuation and scattering mechanisms along the propagation paths. Synthetic data have been of great benefit in gaining physical insight into discriminants, and may be the only means of evaluating evasion scenarios. Synthetic seismograms are particularly useful for regions where earthquake or explosion data are not available. There is no doubt that both geometrical blockage (due to large-scale lateral structural variation), intrinsic attenuation, and small-scale random heterogeneity in the crust affect L_g propagation. But it is often very difficult to separate these effects observationally. Again, numerical modeling could be the only means to quantitatively identify the respective roles played by these factors.

In this study, the two-dimensional LFD method has been used to model the propagation and scattering of L_g waves in a suite of crustal models, including rough interfaces, rugged free-surface topography, and embedded thick sedimentary layers. Two non-standard techniques have been specifically developed for this study: [1] a pure L_g wave packet (for triggering LFD calculations), and [2] a crude, causal attenuation operator (see Jih, 1996a). The pure L_g wave packet is injected into a stratified portion of the grid as the reference initial condition to trigger all LFD calculations. This is a natural extension of Jih's (1993ab) work on R_g to L_g problems. In addition to those commonly recognized advantages of LFD method, another obvious advantage of this approach is that the effect due to different types of heterogeneity on the seismic phase of interest can be isolated and evaluated easily. The other tool tested in this study is a new attenuation operator suitable for time-domain numerical calculations. As a crude approximation, it applies to a moderate band within which it gives a nearly frequency-independent γ, as expected. The most notable advantage is its simplicity to implement. Furthermore, it is a causal operator which, at least conceptually, is more realistic. Overall it appears to perform reasonably well.

Unlike R_g waves, L_g propagation is not affected by a moderate free-surface topography alone as much as other types of heterogeneity. Topographic relief has been shown to be a very strong scatterer for the R_g phase (Jih, 1993ab, 1995). This is because R_g energy is confined in the uppermost layer. The energy of L_g is evenly distributed in the crust, and the surface topography variations are generally small relative to the crustal thickness. Thus it may be expected that the topographic variations alone should have relatively weaker influence on L_g propagation, as compared to R_g. This is illustrated with models 2 and 3 of this study (Figure 5). However, the topography may reflect the crustal thickness through isostasy. It has been suggested that S_n/L_g ratios may be correlated to some roughness measures of the paths, based on a limited number of observations. LFD appears to be the ideal tool to test the existence of any correlation between some roughness measure and the propagation characteristics of regional phases, as demonstrated with the very few mountainous models tested in this study. Similar statistical analysis should also be conducted to examine the effects of water column, random Moho topography, and irregular intra-crustal interfaces, as well as the combination of all these factors.

REFERENCES

Baumgardt, D. R. (1991). *High frequency array studies of long range L_g propagation and the causes of L_g blockage and attenuation in the Eurasian continental craton,* Report PL-TR-91-2059(I), Phillips Laboratory, Hanscom Air Force base, MA (ADA236984).

Clarke, J. W. and J. Rachlin (1990). *Geology of the Barents Sea Structural Basin,* U.S. Geological Survey Open-File Report, July 1990. Military Geology Project, Reston, VA.

Gramberg, I. S. (1988). *The Barents Shelf Plate* (in Russian), Volume 196, Nedra, Leningrad.

Jih, R.-S. (1993a). *Directional excitation of R_g due to ripple-fired explosions: a 2-dimensional finite-difference calculation,* in *Proceedings of Numerical Modeling for Underground Nuclear Test Monitoring Symposium* (S. Taylor and J. Kamm, eds.), *Los Alsmos National Laboratory Report No. LAUR-93-3839.*

Jih, R.-S. (1993b). *Statistical characterization of rugged propagation paths with application to Rg scattering study,* Report TGAL-93-07, Teledyne Geotech, Alexandria, VA (ADA275237).

Jih, R.-S. (1994). *Numerical modeling of crustal phase propagation in irregular waveguides,* in *Proceedings of 16th PL/AFOSR Seismic Research Symposium* (7-9 Sept 1994, Thornwood, NY; J. Cipar, J.

Lewkowicz, and J. McPhetres, eds.), Report PL-TR-94-2217, Phillips Laboratory, Hanscom AFB, MA, pp. 173-181 (ADA284667).

Jih, R.-S. (1995). *Numerical investigation of relative contributions of R_g scattering and incomplete dissipation to L_g excitation,* in *Proceedings of 17th PL/AFTAC/DoE/AFOSR Seismic Research Symposium* (12-15 Sept 1995, Scottsdale, AZ; J. Lewkowicz, J. McPhetres, and D. Reiter, eds.), Report PL-TR-95-2108, Phillips Laboratory, Hanscom AFB, MA, pp. 401-410.

Jih, R.-S. (1996a). *A simple, causal method to incorporate approximate anelastic attenuation into finite-difference calculations,* Report PL-TR-96-2015, Phillips Laboratory, Hanscom AFB, MA.

Jih, R.-S. (1996b). *Waveguide effects of large-scale structural variation, anelastic attenuation, and random heterogeneity on SV Lg propagation: a finite-difference modeling study,* Report PL-TR-96-2016, Phillips Laboratory, Hanscom AFB, MA.

Jih, R.-S. and C. S. Lynnes (1993). *Studies of regional phase propagation in Eurasia.* Report PL-TR-93-2003 (=TGAL-93-01), Phillips Laboratory, Hanscom AFB, MA (ADA262801).

Jih, R.-S., R. R. Baumstark, and R. A. Wagner (1995). *Simultaneous inversion of event m_{L_g} and path attenuation coefficient with application to a transportable L_g magnitude scale,* in *Proceedings of 17th PL/AFTAC/DoE/AFOSR Seismic Research Symposium* (12-15 Sept 1995, Scottsdale, AZ; J. Lewkowicz, J. McPhetres, and D. Reiter, eds.), Report PL-TR-95-2108, Phillips Laboratory, Hanscom AFB, MA, pp. 411-419.

Nuttli, O. W. (1980). The excitation and attenuation of seismic crustal phases in Iran, *Bull. Seism. Soc. Am.,* **70,** 469-485.

Patton, H. J. and S. R. Taylor (1995). Analysis of L_g spectral ratios from NTS explosions: implications for the source mechanisms of spall and the generation of L_g waves, *Bull. Seism. Soc. Am.,* **85,** 220-236.

Reiter, D. T. and R.-S. Jih (1996). *Report on phase blockage phenomenology session, SSA 91st annual meeting, 2 April 1996, St. Louis, Missouri,* Report PL-TR-96-2105, Phillips Laboratory, Hanscom AFB, MA.

Ruzaikin, A. I., I. L. Nersesov, V. I. Khalturin, and P. Molnar (1977). Propagation of L_g and lateral variation in crustal structure in Asia, *J. Geophys. Res.,* **82,** 307-316.

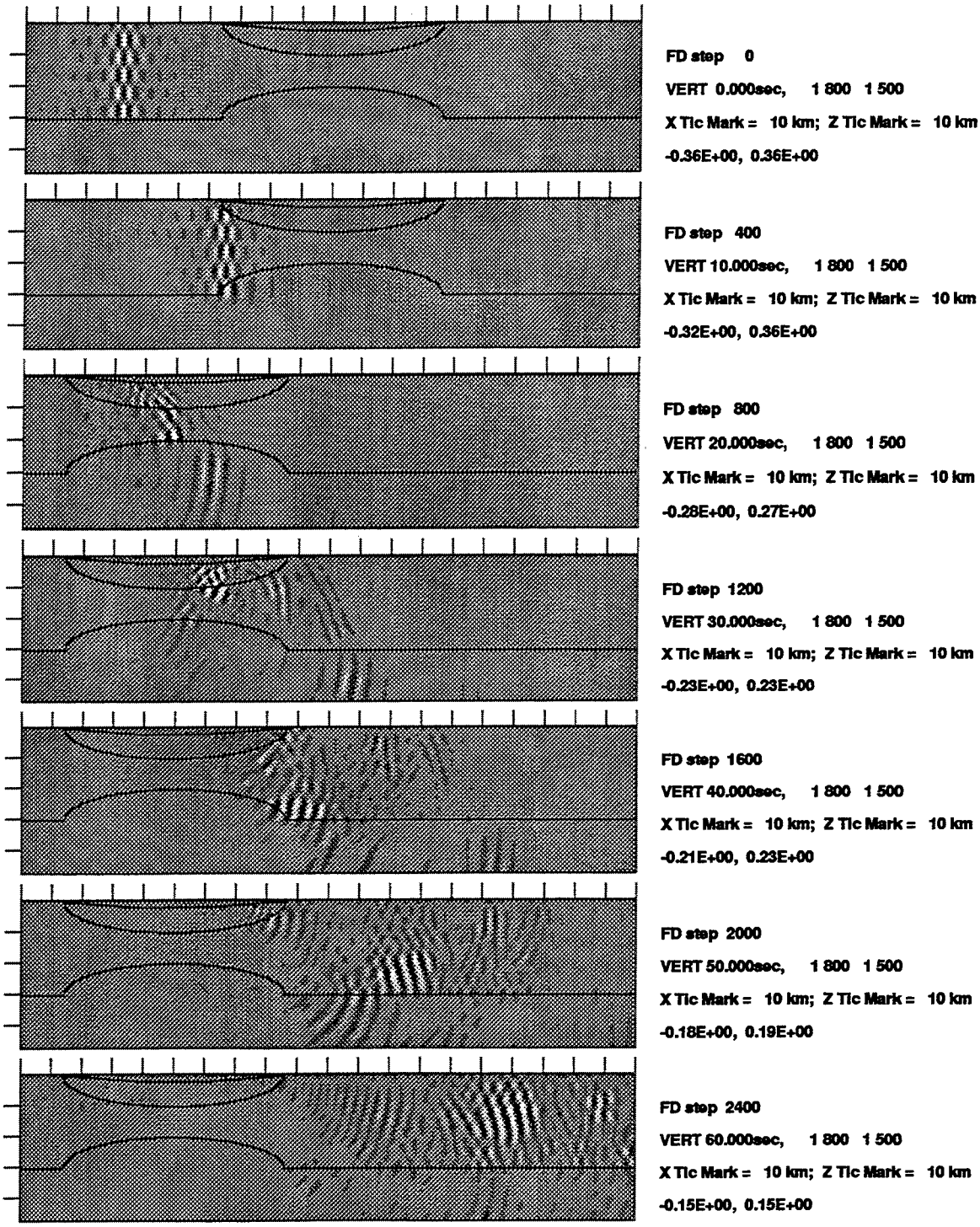

LFD Simulation of Lg Propagation: Model 0Fc

Figure 1. The vertical-component snapshots of L_g wave propagation in model 0Fc, which has two sedimentary layers and a Moho uplift. The basin edge acts like a secondary point source. A prominent SmS-mode of propagation is quite clear at 50 and 60 seconds. The visibility of this phase is distance-dependent, however.

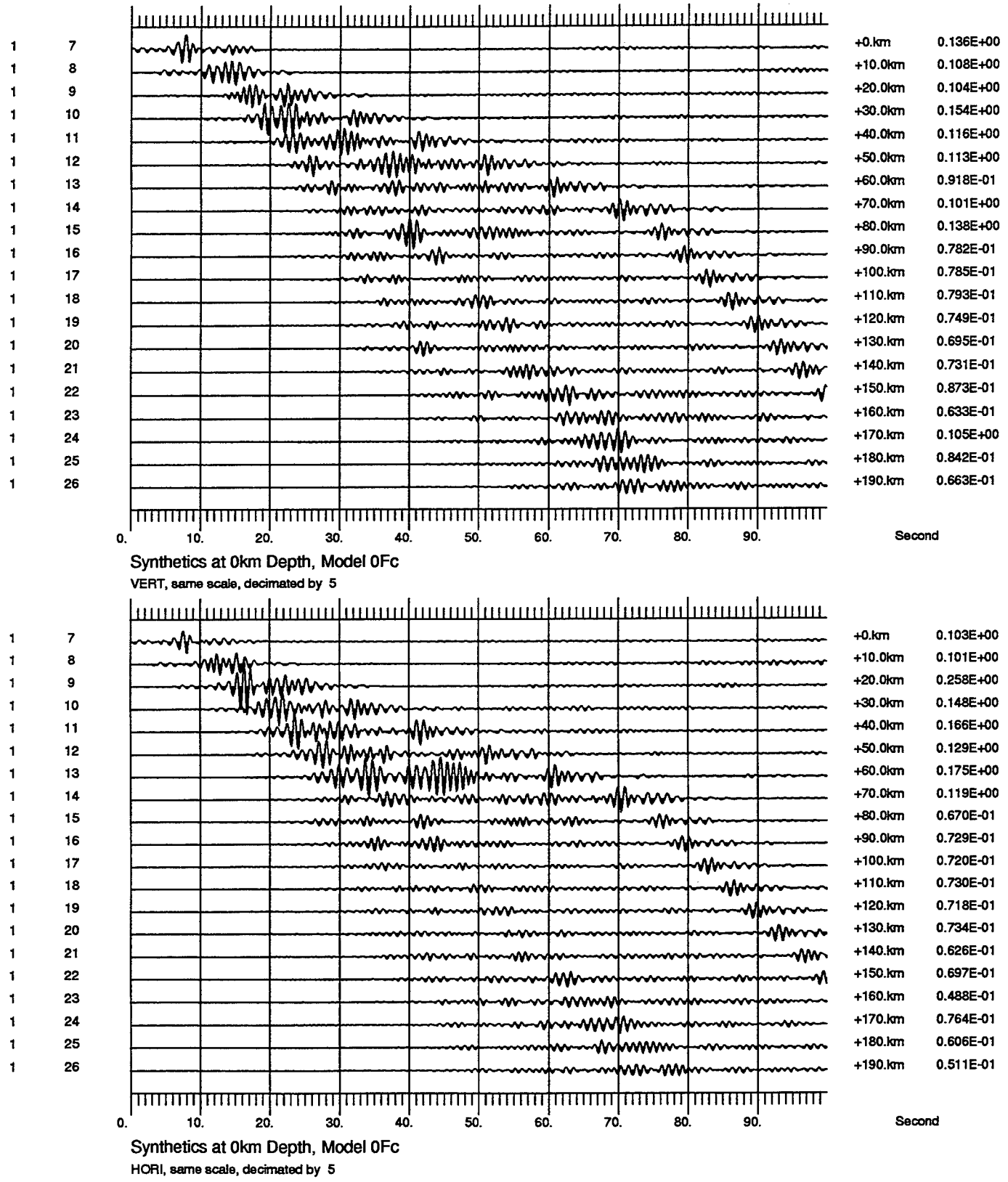

Figure 2. Seismic sections of model 0Fc, which has a Moho uplift and two sedimentary layers. The most prominent phase before R_g is the SmS radiated from the basin edge, which can be seen at certain receivers, depending on the distance (see traces No. 21 through 26).

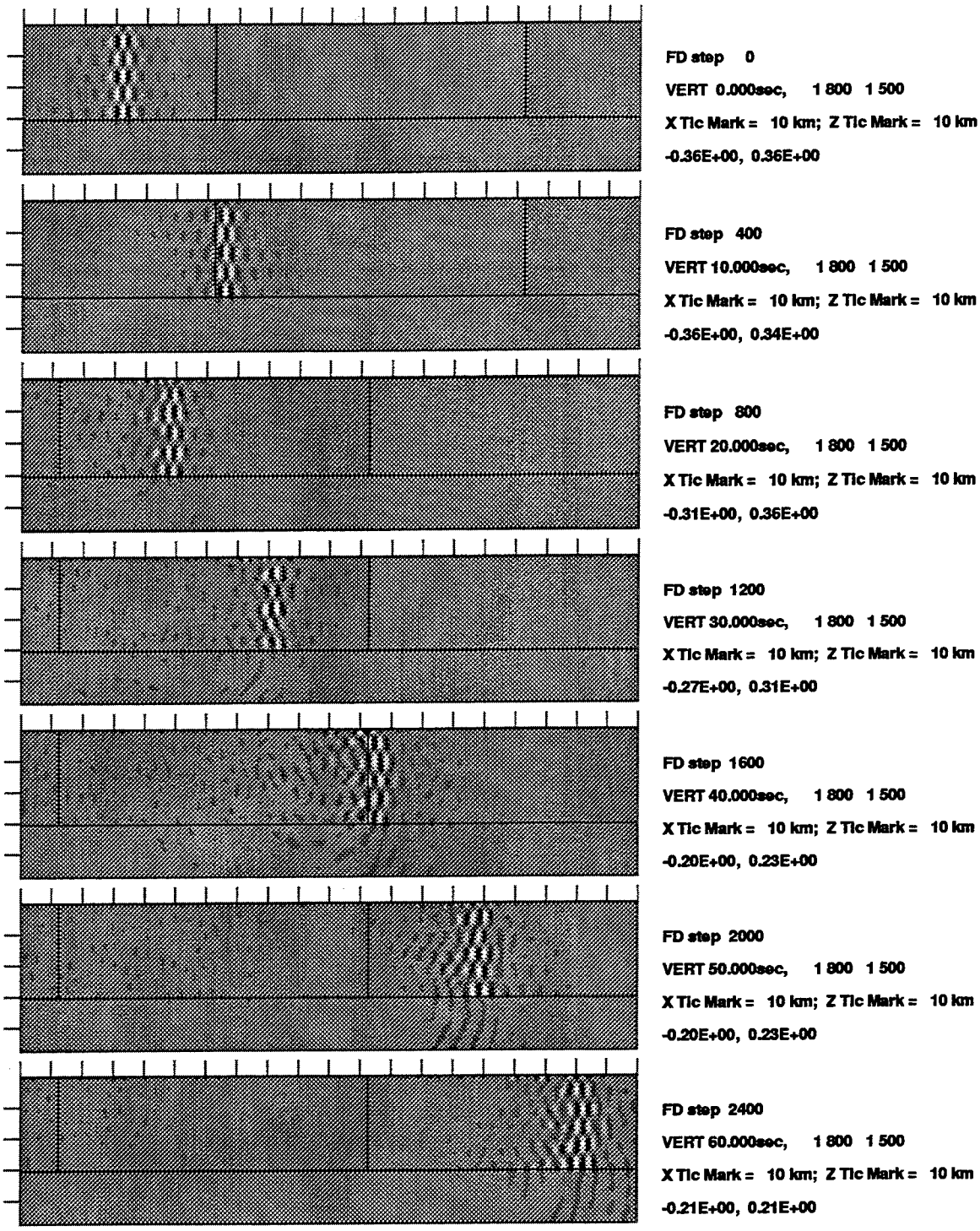

LFD Simulation of Lg Propagation: Model 0Y,10%

Figure 3. The vertical-component snapshots of L_g wave propagation in a single-layer model with a heterogeneous portion 100 km long and 30 km thick embedded in it. The self-similar random heterogeneity in this sandwiched portion has an RMS velocity fluctuation of 10 percent and a scale length of 1 km.

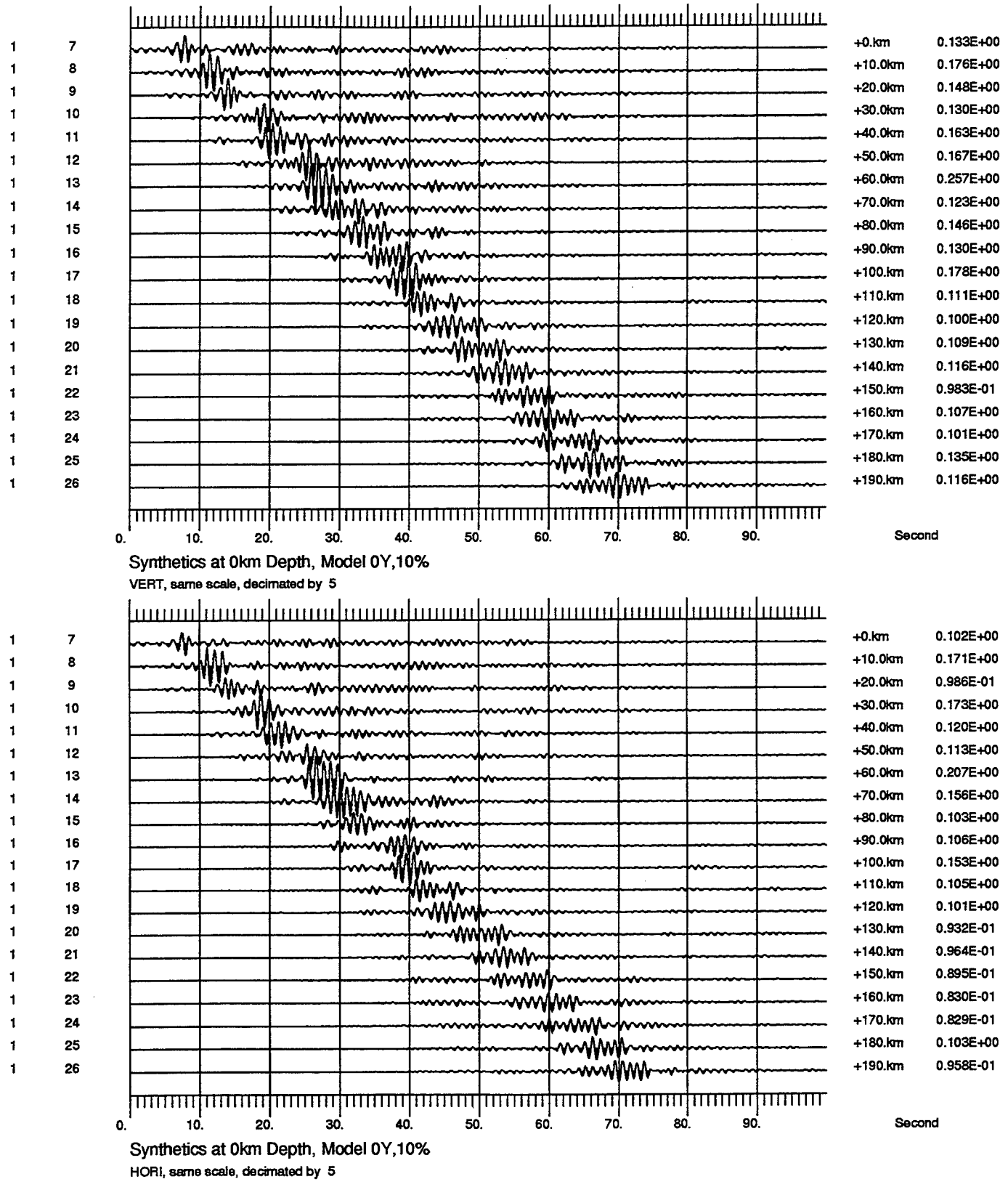

Figure 4. Seismic sections of the model 0Y,10%. This model has 10 percent velocity variation in an embedded heterogeneous volume which is 100 km long and 30 km thick.

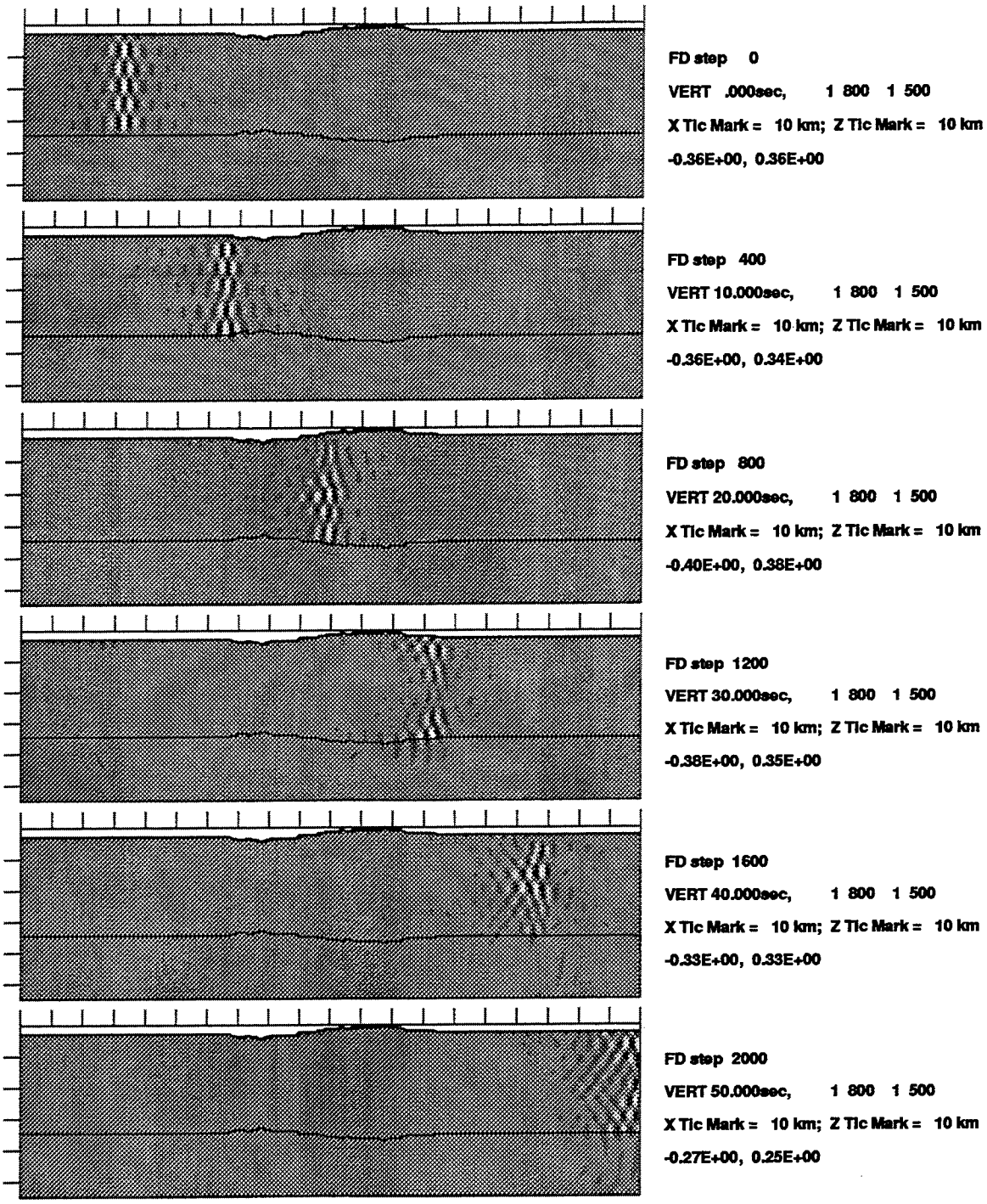

Figure 5. The vertical-component snapshots of L_g wave propagation of model 2a, in which the Moho is fully compensated. The elevation change of this topographic profile is relatively small compared to the thickness of the homogeneous crust, and hence the transmission of L_g is still fairly efficient.

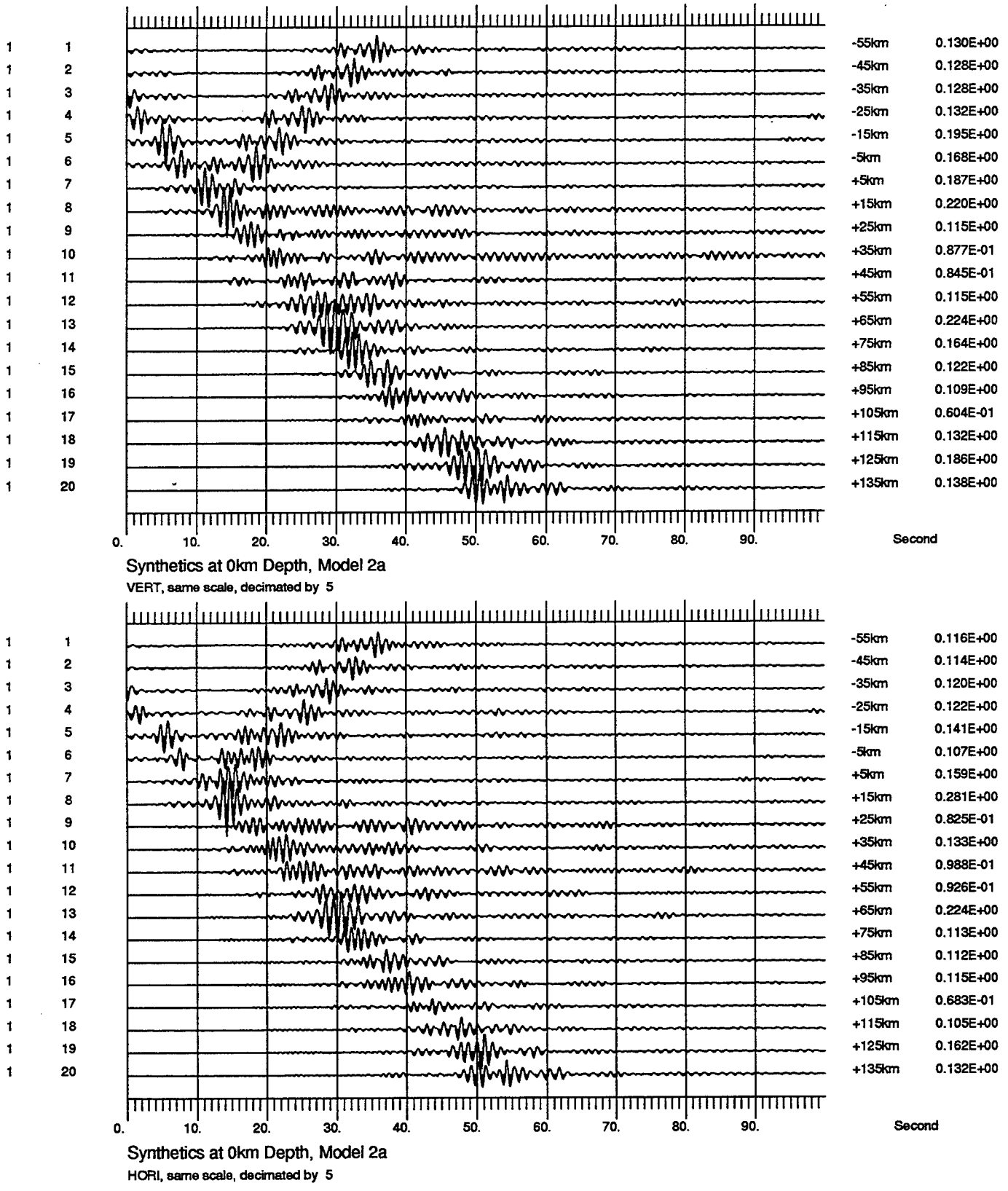

Figure 6. Seismic sections of model 2a, which has a moderate free-surface topography and a fully compensated Moho. The scattering effects of topography on L_g are not as strong as those due to large-scale structural discontinuities.

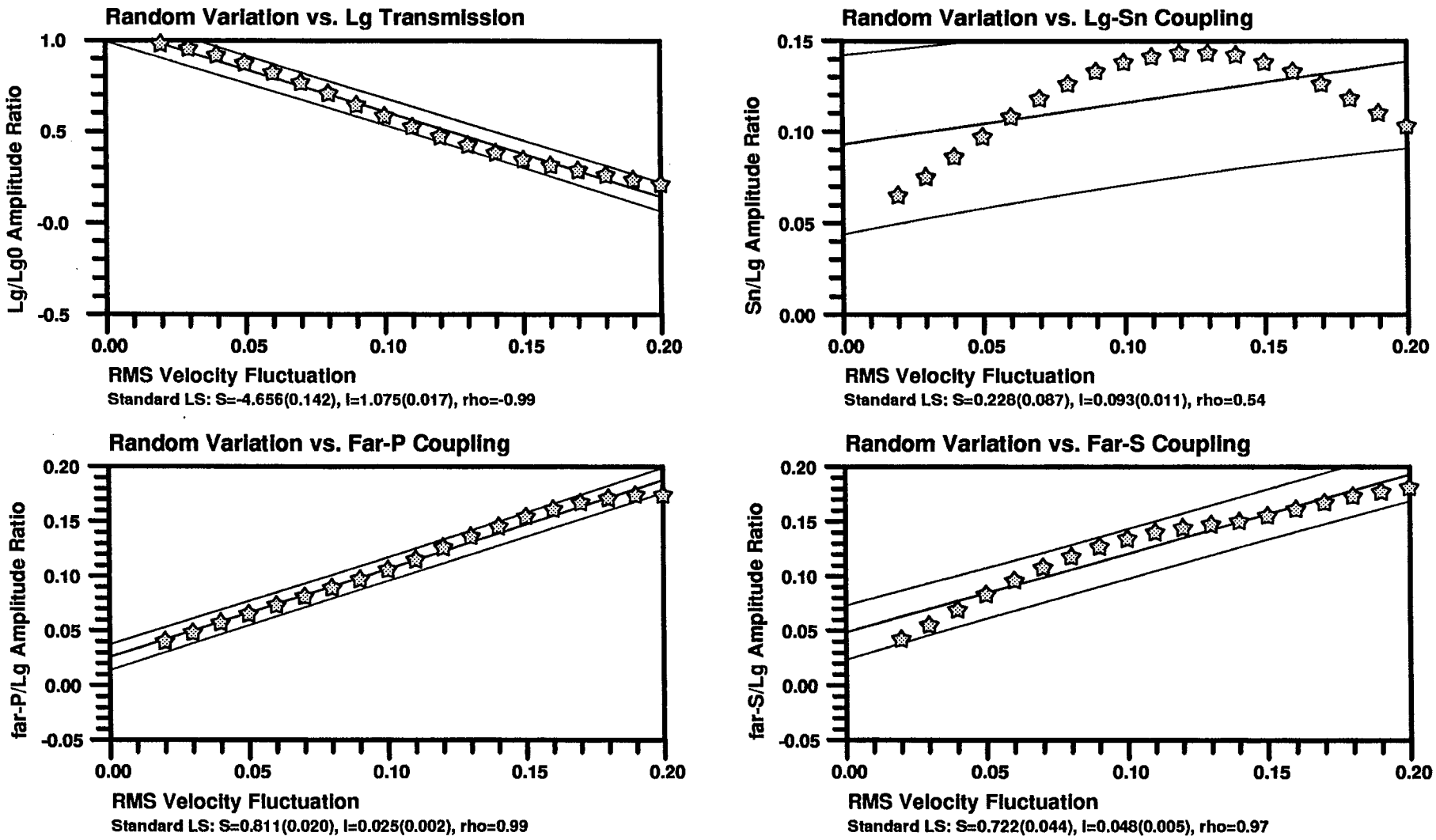

Figure 7. Regressing the L_g transmission coefficient (top left), S_n/L_g amplitude ratio (top right), far–P/L_g amplitude ratio (bottom left), and far–S/L_g amplitude ratio (bottom right). As the model becomes more heterogeneous (that is, has a larger RMS velocity variation), the L_g-to-S_n coupling as well as the coupling to teleseismic phases become more prominent.

THE EFFECT OF DAMAGE ON EXPLOSION GENERATED ELASTIC WAVES

Lane R. Johnson

Center for Computational Seismology, Lawrence Berkeley Laboratory,
and Seismographic Station, University of California,
Berkeley, California 94720

Contract No. F49620-94-1-0197
Sponsored by AFOSR

ABSTRACT

In the study of physical processes involved in the generation and propagation of seismic waves at near and regional distances, it is important to acquire an understanding of what happens in the region of high stresses immediately surrounding the explosion. In the present study the question of whether the elastic waves propagating outward from the explosion can cause secondary cracking of the media is investigated. Also considered is whether this secondary cracking can generate additional elastic waves. The problem is approached by making use of methods developed for damage mechanics in brittle solids. Preliminary calculations are performed for the chemical explosion detonated as part of the Non-Proliferation Experiment. The stress field surrounding the explosion is generated using the equivalent elastic method. While the results are preliminary, they suggest that significant damage can be generated in an extensive region surrounding an explosive source.

OBJECTIVE

The general objective of this research effort is the detection and discrimination of underground explosions through the study of radiated seismic waves. Particular emphasis is on the study of physical processes in the source region through the development of improved models for the generation and propagation of elastic waves. Such models are tested by the collection and analysis of broad-band seismic data at near and regional distances. The present paper reports on one phase of the research effort which is concerned with the reliability of source parameters which are inferred from the analysis of waveform data. The near-source seismic data from the Non Proliferation Experiment (NPE) provide an opportunity to check one aspect of this general problem.

RESEARCH ACCOMPLISHED

Introduction

The region of non-linear processes which surrounds an explosive source is still a subject of considerable interest. Computer codes have been developed for modeling this region, but they are fairly complicated, involving hydrodynamic effects, shock waves, and non-linear equations of state. Because of the basic numerical approach which is followed in these codes, they do not readily provide insight into questions about which parameters are playing critical roles in determining the characteristics of radiated elastic waves. This have motivated an investigation of alternative more analytical methods of modeling this region immediately surrounding an explosive source.

The basic objective of the research described in this report is to determine if the secondary cracking predicted by damage mechanics can have a significant effect upon the elastic waves generated by an explosive source. Several different aspects of this problem have to be considered. The first involves the matter of whether the stresses generated by an explosive source are sufficient to displace and extend preexisting microcracks. The nucleation and propagation of cracks due to applied stresses will be referred to as damage, so the task is to determine the extent and characteristics of the damage zone. If this damage zone can be shown to exist, then it is of interest to investigate the properties of the secondary elastic waves which are generated by motion on the microcracks. Here it is necessary to consider the cumulative effect of motion on a large number of oriented microcracks distributed throughout the damage zone surrounding the explosion. Finally, there remains the matter of permanent changes in material properties caused by the damage and whether these changes are sufficient in magnitude to be detected by post-shot investigations.

In order to test the potential effect of damage on realistic explosive sources, preliminary calculations have been performed for the chemical explosion detonated as part of the Non-Proliferation Experiment (NPE) in September, 1993. This 1 kiloton explosion provides a convenient test case because of the large amount of waveform data which was recorded near the explosion.

Stress field surrounding an explosion

The primary ingredient necessary for the investigation of damage surrounding an explosion is knowledge of the stress field generated by the explosion. In this study that stress field has been generated using the equivalent elastic method (Johnson, 1993). While this is approximate approach that does not incorporate all of the physics contained

in complete equation-of-state approaches, it does provide a very efficient method of estimating the basic characteristics of elastic waves radiated by an explosion. The use of the equivalent elastic concept allows analytical solutions developed for linear problems to be employed, thus providing a relatively simple algorithm that can be used to explore a wide variety of features associated with the explosion process.

Calculations employing the equivalent elastic method were used to simulate the elastic waves generated by the NPE explosion. The source properties such as cavity size and amount of explosive are very well known for this event so the initial conditions for the calculations contain little uncertainty. Furthermore, there was a large amount of data recorded during this experiment, including the recordings of free-field motions at approximately 20 different sites. These recordings were used to check the calculations by comparing observed and calculated radial velocities out to horizontal distances of over 500 meters. The agreement was good with respect to maximum velocity and approximate with respect to waveform shape. On the basis of these comparisons it is assumed that the stress field generated by the equivalent elastic method also provides a reasonably accurate approximation to the actual stresses that were present during the NPE.

Damage mechanics

The concept of damage used in this study is that described by Ashby and Sammis (1990). In that paper the conditions under which an initial crack can be extended under axisymmetric loading are derived. The dimensionless damage is defined as

$$D \equiv \frac{4}{3}\pi(\alpha a)^3 N_v$$

where α is a geometric term (typically 0.7), $2a$ is the dimension of the crack, and N_v is the number of cracks per unit volume. Then, given the initial damage D_o and the major and minor stresses, σ_1 and σ_3, the condition under which the damage will be extended by growth of the crack surface is derived. The amount of crack growth is obtained as that required to reduce the stress intensity at the crack tip to the fracture toughness of the medium. The result is a fairly complicated cubic equation that must be solved for the final damage value, but the solution is easily obtained by numerical methods.

The basic procedure followed in this study is to use the equivalent elastic method to generate the stress field in the entire region surrounding an explosion. At each point in space the radial and tangential stresses are generated as a function of time and these are used to calculate whether additional damage has occurred. The net result is the determination of damage as a function of time and distance in the region of high stresses surrounding the explosion.

Damage as a source of secondary elastic waves

One of the more interesting aspects of the possibility that damage may be generated by the elastic waves propagating outward from an explosion is the the potential for the microcracks to act as secondary sources of elastic waves. The damage of Ashby and Sammis (1990) is modeled as an initial crack which is extended by wing cracks. This can be represented as the combination of two separate source moment tensors, a shear dislocation on the initial crack and a tensile opening on the wing crack, and the elastic waves excited by such sources are easily generated. However, in the present case it is necessary to sum up the effects of all the damage the occurs in the region surrounding the source. Thus it is necessary to evaluate an integral over the entire damage zone, taking

into account the amount of damage, orientation of the cracks, and time history of the motion on the cracks at each point in this zone. Such integrals can be obtained by numerical methods.

During the initial stage in these calculations, it has been assumed that the initial microcracks are uniformly distributed and randomly oriented in the medium surrounding the explosion. This leads to a considerable simplification in the integration over the damage zone. However, in principle the problem where the initial microcracks have a preferred orientation can also be solved, which should lead to asymmetric radiation of elastic waves from the damage zone. This extension of the results in now under investigation.

Permanent changes in material properties

Damage represents a permanent change in material properties, and the amount and orientation of microcracks are known to have an important effect upon macroscopic elastic constants. A variety of effective media theories are available for the estimation of any changes in material properties caused by the damage and these are being applied to the damage estimates.

Preliminary results

Much of the effort so far in this project has been devoted to formulating the approach and developing the necessary computer programs. Some preliminary results have been obtained for the NPE explosion. Significant damage is found to extend out to a distance of about 50 meters from the explosion, which is almost 10 source radii. The total moment estimated for this damage zone is $2 \cdot 10^{20}$ dyne-cm, which is about 10% of the moment for the NPE explosion. However, the seismic waves generated by this moment of the damage zone are diminished because of the interference caused by the random orientation of the microcracks, particularly for S waves. Detailed calculations of this effect are now underway, as is the estimation of permanent changes in material properties.

CONCLUSIONS AND RECOMMENDATIONS

This investigation of the effect of damage mechanics upon the elastic waves generated by an explosion has opened up a series of interesting problems concerning with the region of high stresses surrounding an explosion. While the results are preliminary, it seems clear that meaningful calculation of this type are possible and that some of the effects may be significant. Considerable more work is needed, but the potential application of the results seem to warrant continuation. Some of the features which need further study are the effect of depth of burial, the effect of pre-stress such as tectonic stress, the effect of orientation of initial cracking, and the detonation of an explosion in a region which has already been damaged by a previous explosion.

References

Ashby, M. F., and C. G. Sammis, The damage mechanics of brittle solids in compression, Pure and Appl. Geophys., 133, 489-521, 1990.

Johnson, L. R., Wave propagation near explosive sources, PL-TR-93-2118, Phillips Laboratory, 22 pp., 1993., ADA270102.

HIGH FREQUENCY PROPAGATION OF CRUSTAL WAVES

H. Keers, K. Vogfjörd, G. Nolet, F. A. Dahlen
Department of Geosciences, Princeton University, Princeton NJ 08544
Contract No. F49620-94-1-0077
Sponsored by AFOSR

ABSTRACT

This report discusses both theoretical and observational aspects of asymptotic crustal wave propagation.

Crustal models (both 2D and 3D) are conveniently expressed using undulating interfaces. This makes it necessary to develop special ray tracing algorithms (both for the kinematic and dynamic ray tracing). These algorithms and the chaotic properties of rays traveling through these models are discussed briefly.

One consequence of the chaotic ray behavior is the large number of caustics that are generated. This makes it necessary to use Maslov theory to compute synthetics, rather than geometrical ray theory. It is shown in this report how to compute the correct Maslov phase and amplitude using the method of stationary phase.

One of the major obstacles in computing Maslov synthetics has been the presence of spurious arrivals caused by pseudo-caustics. Using the method of stationary phase these pseudo-caustics are shown to disappear if one uses 2D Maslov integrals. An algorithm is presented that efficiently computes 2D Maslov integrals. Previously Maslov synthetics were plagued by the effect of the endpoints of the integration. This endpoint effect is removed by a simple change of variables.

The Maslov synthetics can be used to justify the use of ray density plots as energy plots. The ray density plots are used to study array data from the NPE at the Nevada test site. Lg waves, propagating in the direction of the southern Sierra Nevada range, disappear in the epicentral distance range of 250 km - 350 km. It is shown how the theoretical modeling of Lg can be used to put constraints on the crustal structure of sourthern California.

Keywords: crustal waves, chaotic rays, Maslov synthetics, energy plots, array data

OBJECTIVES

The first goal of this project is to develop reliable and efficient methods to compute synthetic seismograms through 2D and 3D heterogeneous crustal models, using asymptotic methods. The second goal of this project is to apply these methods to study crustal wave propagation (with special emphasis on Lg) using array data. Both of these aspects are discussed in this report.

RESEARCH ACCOMPLISHED

Kinematic Ray Tracing Through 3D Multilayered Media

We briefly describe raytracing in 3D layered media with undulating interfaces separated by homogeneous layers. Two aspects are important: first one needs to trace rays from one interface to the next interface. Secondly all multiples generated need to be traced. Here, for the sake of conciseness, we only consider the first aspect of the algorithm; for more details see Keers et al. (1996b).

The interfaces are described by the equation $z = h_p + f_p(x, y)$ and, as before, the pth layer is right below the pth interface. We choose the coordinate system as shown in figure 1.

Consider a ray impinging upon the pth interface from above. The unit vector pointing in the direction of the ray is $\mathbf{i_n} = (\cos\alpha_n, \cos\beta_n, \cos\gamma_n)$ (see figure 1). This vector is assumed to be known. The unit normal to the pth interface at $(x_n, y_n, h_p + f_p(x_n, y_n))$ is denoted by $\mathbf{n} = (n_1, n_2, n_3)$. From figure 2 it can be seen that $\mathbf{r}_n = 2(\mathbf{i}_n \cdot \mathbf{n})\mathbf{n} - \mathbf{i}_n$, where $\mathbf{r}_n$ is the unit vector pointing in the direction of the reflected ray. The derivation of $\mathbf{t}_n$ is a bit more involved. From figure 2 we see that

$$\mathbf{t}_n - (\mathbf{t}_n \cdot \mathbf{n})\mathbf{n} = c(\mathbf{i}_n - (\mathbf{i}_n \cdot \mathbf{n})\mathbf{n}), \tag{1}$$

for some $c < 0$. We compute c by taking the inner product of (1) with $\mathbf{i}_n$ and $\mathbf{t}_n$ respectively. We find

$$\mathbf{t}_n = (\mathbf{t}_n \cdot \mathbf{n})\mathbf{n} + \mathbf{t}_n - (\mathbf{t}_n \cdot \mathbf{n})\mathbf{n} = -\left(\frac{\alpha_{p+1}}{\alpha_p}\right)\mathbf{i}_n + \left(\left(\frac{\alpha_{p+1}}{\alpha_p}\right)(\mathbf{i}_n \cdot \mathbf{n}) - \cos\psi\right)\mathbf{n}. \tag{2}$$

Here ψ is found with Snell's law. These results enable us to derive the raytracing equations. If a ray goes up then direction vector is denoted by $\mathbf{u}_n^p$. If the ray goes down then the direction vector is $\mathbf{d}_n^p$. It can be shown that

$$h_p + f_p(x_n^p, y_n^p) + \left(\frac{u_{n,z}^p}{u_{n,x}^p}\right)(x_{n+1}^{p-1} - x_n^p) = h_{p-1} + f_{p-1}(x_{n+1}^{p-1}, y_n^p + \left(\frac{u_{n,y}^p}{u_{n,x}^p}\right)(x_{n+1}^{p-1} - x_n^p)) \tag{3}$$

which is an implicit equation for x_{n+1}^{p-1},and

$$y_n^p + \left(\frac{u_{n,y}^p}{u_{n,x}^p}\right)(x_{n+1}^{p-1} - x_n^p) = y_{n+1}^{p-1}. \tag{4}$$

The reflection vector $\mathbf{d}_{n+1}^{p-1}$ and the transmission vector $\mathbf{u}_{n+1}^{p-1}$ are found using the formulas given above and the correct choice of orientation of $\mathbf{n}$. In vector notation:

$$\mathbf{i}_{n+1}^{p-1} = -\mathbf{u}_n^p \tag{5}$$

$$\mathbf{d}_{n+1}^{p-1} = 2(\mathbf{u}_n^p \cdot \mathbf{n})\mathbf{n} + \mathbf{u}_n^p \tag{6}$$

$$\mathbf{u}_{n+1}^{p-1} = \left(\frac{\alpha_{p-2}}{\alpha_{p-1}}\right)\mathbf{u}_n^p + \left(\left(\frac{\alpha_{p-2}}{\alpha_{p-1}}\right)(\mathbf{u}_n^p \cdot \mathbf{n}) - [1 - \left(\frac{\alpha_{p-2}}{\alpha_{p-1}}\right)^2 (1 - (\mathbf{u}_n^p \cdot \mathbf{n})^2)]^{1/2}\right)\mathbf{n}. \tag{7}$$

Similar formulas can be derived for the downgoing ray (Keers et al, 1996b).

Dynamic Ray Tracing

We now proceed to derive the partial derivatives of the kinematic ray equations. It is clear that in 3D media the parameters that give the ray positions are: x_n, y_n and $\mathbf{d}_n$ (the superscripts p and $p-1$ are deleted from now on). All the other parameters are found from these. In particular we shall be interested in the dependence of these parameters on the initial take-off angle θ_0. These are necessary in establishing the degree of chaoticity using Lyapunov exponents and the computation of synthetics with Maslov integrals (see the next two sections). In 3D media $\mathbf{d}_n$ has three components and for the computation of the Maslov amplitude we also need the dependence of x_n, y_n and $\mathbf{d}_n$ on the initial azimuth δ_0. The differentation can be computed by perturbing the ray equations with the appropriate parameter (e.g. δx_n) and then derive expressions of the form

$$\frac{\delta x_n}{\delta x_{n+1}} \tag{8}$$

Taking the limit gives the required partial derivative. For brevity we only give some of the partial derivatives. Note that, whenever possible, use should be made of the vector notation. As in the case of the kinematic ray tracing this considerably reduces the algebraic effort. One finds

$$\frac{\partial x_{n+1}}{\partial x_n} = \left(r_1 - \frac{\partial f_{p-1}}{\partial y_{n+1}}\frac{\partial y_{n+1}}{\partial x_n}\right) / \left(r_1 - \frac{\partial f_p}{\partial x_n} + \frac{\partial f_{p-1}}{\partial y_{n+1}}\frac{\partial y_{n+1}}{\partial x_n}\right), \tag{9}$$

etc. where

$$r_1 = \frac{r_{n,z}}{r_{n,x}}, \tag{10}$$

$$r_2 = \frac{r_{n,y}}{r_{n,x}}. \tag{11}$$

$$\frac{\partial d_{n+1}}{\partial x_n} = 2[(\mathbf{u}_n \cdot \partial_{x_n}\mathbf{n})\mathbf{n} + (\mathbf{u}_n \cdot \mathbf{n})\partial_{x_n}\mathbf{n}], \tag{12}$$

etc. Similar partial derivatives are derived for the upgoing ray.

Chaotic Ray Behavior and Lyapunov Exponents

We showed previously (Keers et al., 1996a) that a small change in the take off angle gives rise to a large change in the epicentral distance. This chaotic behavior can be quantified using the concept of Lyapunov exponents. The idea is to measure the separation d between two points in phase space that are initially together. Note that two points in phase space are close together only if they are

at almost the same position in coordinate space and if, in addition to that, the slownesses of the rays emanating from these points are almost the same as well.

If the ray tracing system is chaotic then, by definition, the separation rate of the two points in phase space is exponential. In other words there is a constant $l > 0$ such that

$$e^{nl} = d(n), \tag{13}$$

In order to illustrate this we use the 2D version for a one layered model of the kinematic and dynamic ray equations derived above. After scaling x with the thickness of the crust one can define $M(\theta_n, x_n) = (\theta_{n+1}, x_{n+1})$ and

$$D(\theta_n, x_n) = \begin{pmatrix} \frac{\partial \theta_{n+1}}{\partial \theta_n} & \frac{\partial \theta_{n+1}}{\partial x_n} \\ \frac{\partial x_{n+1}}{\partial \theta_n} & \frac{\partial x_{n+1}}{\partial x_n} \end{pmatrix} \tag{14}$$

Let $y_n = (\theta_n, x_n)$ and $\delta y_n = (\delta\theta_n, \delta x_n)$.If $\delta\theta_n$ and δx_0 are small then y_0 and $y_0 + \delta y_0$ are close together. After one iteration we have $y_1 = M(y_0)$. Since $\mid \delta y_0 \mid$ is very small $M(y_0 + \delta y_0)$ may be approximated by $M(y_0) + D(y_0)\delta y_0 = y_1 + D(y_0)\delta y_0$. Therefore $\delta y_1 \approx D(y_0)\delta y_0$. More generally $\delta y_n = D(y_{n-1})\delta y_{n-1} = D^n(y_0)\delta y_0$, where $D^n(y_0) = D(y_{n-1})D(y_{n-2}) \cdot D(y_0)$. The distance between y_0 and $y_0 + \delta y_0$ after n iterations can therefore be approximated by $\mid \delta y_n \mid = \mid D^n(y_0)\delta y_0 \mid$. The rate of divergence l between y_0 and y_0 and $y_0 + \delta y_0$ is therefore given by

$$e^{nl} = \frac{\mid \delta y_n \mid}{\mid \delta y_0 \mid} \tag{15}$$

In principle l depends on y_0, δy_0 and n: $l = l(y_0, \delta y_0, n)$. However l can be shown to be independent of the initial conditions, and to converge to a constant as $n \to \infty$. Therefore it is useful to define the Lyapunov exponent l_L:

$$l_L(\theta_0, x_0) = \lim_{n \to \infty} \frac{1}{n} \frac{D^n(y_0)\delta y_0}{\mid \delta y_0 \mid} \tag{16}$$

When explicitly computing the Lyapunov exponents we use the method of Benettin et al. (1980). Choose $(\delta\theta_0, \delta x_0)$ arbitrary and rescale $(\delta\theta_n, \delta x_n)$ every p iterations by dividing by its magnitude. In this way numerical overflow is avoided. If we do this q times and denote the resulting scaling factors by $s_i (i = 1, \cdots, q)$ then

$$l_L \approx \frac{1}{qp} \sum_{i=1}^{l} \ln s_i \,. \tag{17}$$

In practice we choose $p = 10$ and $q = 100$. Figure 3b shows the results of the computation of 9 Lyapunov exponents. The corresponding solutions of the rays in phase space are shown in figure 3b. The Lyapunov exponents of all the rays converge to a certain value. In fact, since they converge relatively rapidly, we could have taken $q = 50$. The most chaotic ray in figure 3b with an initial take-off angle of 70°, has a Lyapunov exponent of 0.8. This means that rays that are initially 100 m apart, after ten reflections from the Moho are almost 300 km apart; this strongly chaotic behavior results in a large degree of multipathing and many caustics. When computing synthetics it therefore is necessary to use an algorithm that easily can handle these phenomena. The major candidate for this is Maslov theory.

Maslov Theory and Pseudo-caustics

An acoustic wavefield u excited by a point source at x_0 at time 0 satisfies

$$\nabla^2 u(\mathrm{x},t) - \frac{1}{c^2(\mathrm{x})}\frac{\partial^2}{\partial t^2}u(\mathrm{x},t) = \delta(\mathrm{x}-\mathrm{x}_0)\delta(t) \tag{18}$$

If we define the Fourier transform as

$$\hat{f}(\omega) = \int_{-\infty}^{\infty} f(t)e^{-i\omega t}dt \tag{19}$$

then the wave equation can be transformed to the frequency domain and we have

$$\nabla^2 \hat{u}(\mathrm{x},\omega) + k^2(\mathrm{x})\hat{u}(\mathrm{x},\omega) = \delta(\mathrm{x}-\mathrm{x}_0) \tag{20}$$

Here $k = \omega/c$. In Maslov theory one looks for solutions of the form

$$\hat{u}(\mathrm{x},\omega) = \int \mathcal{A}(\mathrm{x},q)e^{i\omega\mathcal{T}(\mathrm{x},q)}dq \tag{21}$$

and

$$\hat{u}(\mathrm{x},\omega) = \int\int \mathcal{A}(\mathrm{x},q_1,q_2)e^{i\omega\mathcal{T}(\mathrm{x},q_1,q_2)}dq_1 dq_2 \tag{22}$$

Whenever both asymptotic ray theory (ART) and one of the Maslov integrals are valid then the ART solution can be obtained from the Maslov integrals by applying the method of stationary phase. One advantage of this is, that the Maslov amplitude can easily be found. Application of the method of stationary phase to the 1D Maslov integral gives the expression for $\mathcal{A}$. If we take q to be the initial take-off angle ϕ_0, then the wavefield becomes

$$\hat{u}(\mathrm{x},\omega) = \oint \mathcal{A}e^{i\omega\mathcal{T}}d\phi_0 \tag{23}$$

This has the advantage that the integration is over a closed circle. The usual boundary points therefore don't exist, and there are no spurious arrivals in the integral. Also the application of a taper at the boundaries becomes superfluous. The stationary phase method gives $\mathcal{A}$ again. Also in this case the we may take $(q_1,q_2) = (\phi_0,\theta_0)$, in which case the integral reduces to

$$\hat{u}(\mathrm{x},\omega) = \oint \mathcal{A}(\mathrm{x},\phi_0,\theta_0)e^{i\omega\mathcal{T}(\mathrm{x},\phi_0,\theta_0)}d\phi_0 d\theta_0 \tag{24}$$

It is worthwile to have a closer look at the singularities of the asymptotic wavefield expressions. Classical ray theory breaks down at points where $J = 0$ (J is the Jacobian from coordinate space to ray coordinates). Similarly the Maslov integrands are singular at points where $\mathcal{J} = 0$ (here $\mathcal{J}$ is the Jacobian from mixed phase space to ray coordinates). These points form pseudo-caustics. In the case of a 1D integral these points also correspond to stationary points. In the 2D integral the pseudo-caustics are given by

$$|\mathcal{J}| = 0 \tag{25}$$

However, stationary points are given by,

$$\frac{\partial p_1}{\partial q_1}(x-X)+\frac{\partial p_2}{\partial q_1}(y-Y)=0, \tag{26}$$

$$\frac{\partial p_1}{\partial q_2}(x-X)+\frac{\partial p_2}{\partial q_2}(y-Y)=0. \tag{27}$$

A singularity in the Maslov integral then would only be prominent whenever we have simultaneously a pseudo-caustic and a stationary point. Therefore pseudo-caustics are less troublesome in 2D integral expressions than in 1D integral expressions.

In the time domain we get the following expression for the Maslov wavefield

$$u(\mathrm{x},t)=\frac{1}{4\pi}\mathrm{Re}[\Delta(t)*\sum_{t=\mathcal{T}}\mathcal{A}\left(\frac{\partial\mathcal{T}}{\partial q}\right)^{-1}] \tag{28}$$

where $\Delta(t)=\delta(t)-i/\pi t$ is the analytic delta function. In the 1D case the integration is done similarly to the WKBJ evaluation of wavefields in 1D media following Chapman et al. (1988). In the 2D case we either are integrating over a plane or a sphere, as discussed previously. This requires a slight adaptation of the integration algorithm (subroutine THETAC (Chapman et al., 1988). The integration domain is triangulated (Delaunay triangulation for example) and a suitable taper is chosen in the case that the integration domain is plane. The Delaunay triangulation has the useful property that the 3 gridpoints closest to each point in a triangle form the triangle. The best linear approximation to a function at a point in the triangle that uses the gridpoints, is therefore given by the average of the values of that function on the three vertices of the triangle.

Ray Density Plots and Lg Propagation in California

The Maslov method can also be used to justify the use of ray density plots as energy plots. Energy plots are useful for studying the crustal wavetrain as a whole. Figure 4 shows vertical component data from the Non Proliferation Experiment (NPE) at the Nevada Test Site. All data are highpassed at 2 s. Traveltime curves of PmP and SmS are shown as well as traveltime curves of other dominant crustal multiples. The source and station locations are shown in figure 5. We concentrate in this report on Lg. Using a three layered crustal model ray density plots are obtained for different models. In the case the model is flat the different multiples can be readily identified (figure 6a). However from the data it can be seen that Lg, while still strong at 270 km, quickly reduces in amplitude and is almost invisible in several records at distances larger than 300 km. More realistic models include crustal thickening under the Sierra Nevada and bumps in the midcrustal interfaces. The resulting ray density plot for a 10 km amplitude and 150 km wavelength bump is shown in figure 6b. If, in addition to these undulations, variations in the midcrustal interfaces are added (figure 6c) then Lg disappears at the required epicentral distance. Using the ray density plots it is possible to constrain the heterogeneity of the Moho between the NTS and the receivers. It was found that the bump in the Moho has its maximum just slightly to the east of the center of the Sierra Nevada. This result is rather independent of the strength of the heterogeneities in the midcrust. Figure 6d shows the ray density plots for a model like that in figure 6c, but with additional random undulations of the

midcrustal interface with an amplitude of 2 km and and a dominant wavelength of 100 km. The random structure has the effect to even out some prominent arrivals still present in figure 6c. Since the data do not show such arrivals, we prefer the last model.

CONCLUSIONS AND RECOMMENDATIONS

We show in this report how to compute ray paths through 2D and 3D layered crustal structures. These crustal models generate chaotic rays, the effect of which is to create many caustics and a high degree of multipathing. Using Maslov theory synthetics can be computed; the effect of pseudo-caustics was shown to disappear if 2D Maslov integrals are used. Maslov amplitudes are computed using dynamic ray tracing and the method of stationary phase.

The theory was applied to study Lg propagation in southern California. Array data from the NPE at the Nevada Test Site showed that Lg disappears at epicentral distances between 250 km and 350 km. By using ray density plots it was shown what crustal structure is needed in order to show this behavior.

The algorithm presented here concerns acoustic wave propagation. In order to study crustal waveforms in general, and not only Lg, it is necessary to extend the algorithm to include P-S and S-P conversion. This would also make it possible to study the change of P/Lg amplitude ratios. The use of ray density plots as energy plots should be justified using synthetics. An excellent method is provided by the Maslov algorithm presented in this paper. This algorithm also makes it possible to study effects of 3D heterogeneity. However this requires the existence of high quality array data.

REFERENCES

Benettin, G., Galagni, L., Giorgilli, A. and Strelcyn, J.-M., 1980. Lyapunov characteristic exponents for smooth dynamical systems and for Hamiltonian systems: a method for computing all of them. Part 2: numerical application, *Meccanica*, **15**, 21.

Chapman, C. H., Jen-Yi, C. and Lyness, D. G., 1988. The WKBJ Seismogram Algorithm, in *Seismological Algorithms*, Doornbos G. (ed.), *Academic Press*, 47-74.

Keers, H., Nolet G., and Dahlen F. A., 1996a. Ray Theoretical Analysis of Lg, *Bull. Seism. Soc. Am.*, **86**, 726-736.

Keers, H., Dahlen F. A., and Nolet G., 1996b. Chaotic Ray Behavior in Seismology, *Geoph. Journal. Int.*, submitted.

Keers, H., and Chapman C. H., 1996. Maslov Theory and Pseudo-caustics, in preparation.

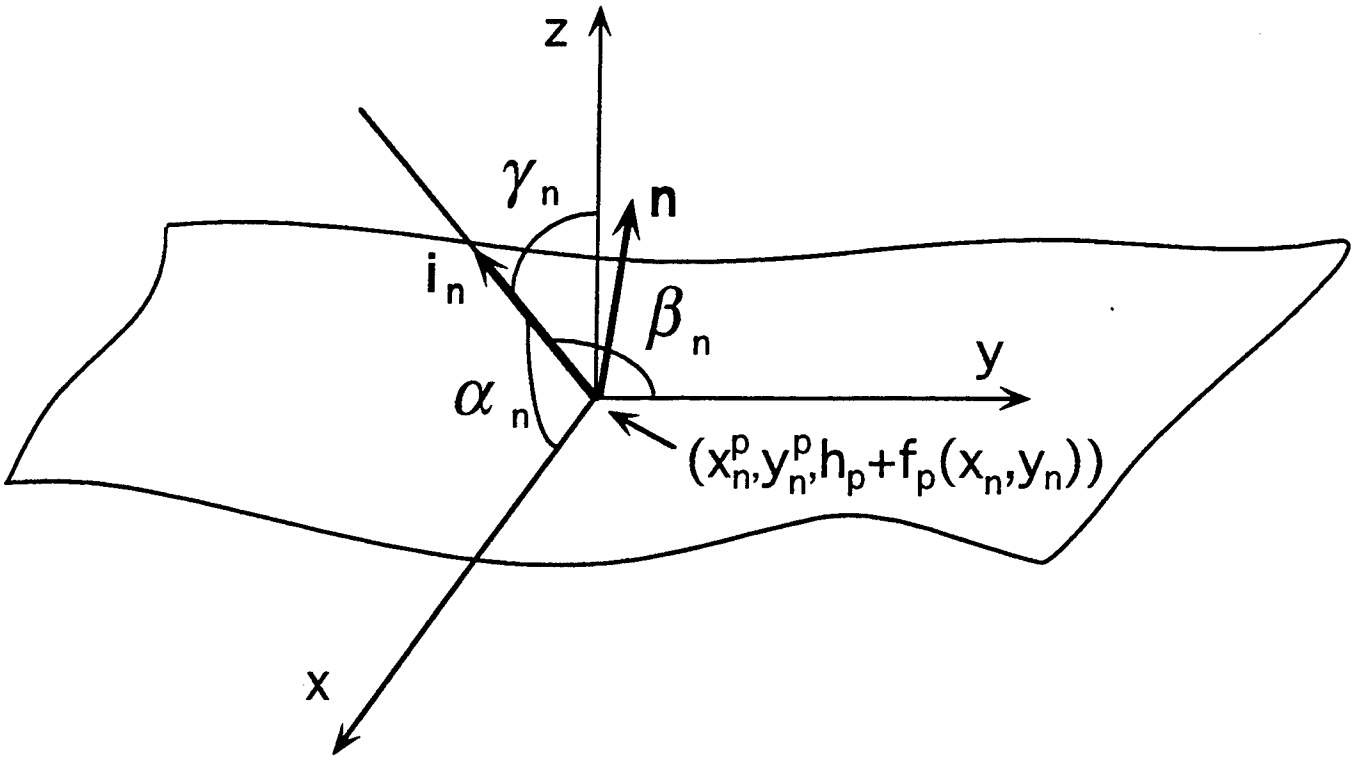

Figure 1. Definitions of ray tracing parameters used in the derivation of the kinematic ray equations.

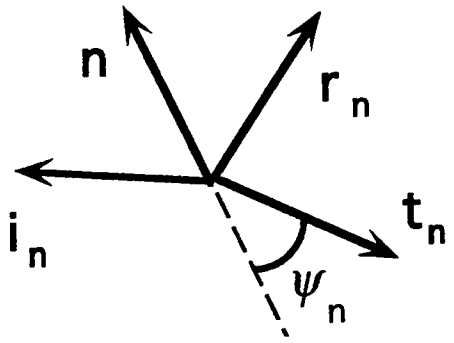

Figure 2. Definitions of the unit vectors and angle used in the kinematic ray equations.

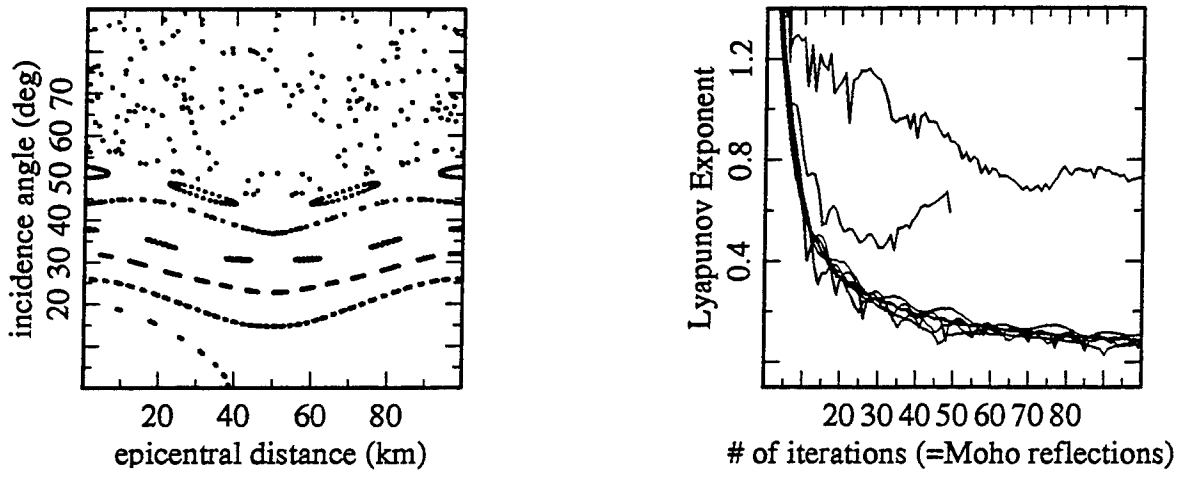

Figure 3. Phase space plots (left) and Lyapunov exponents (right) for 9 rays.

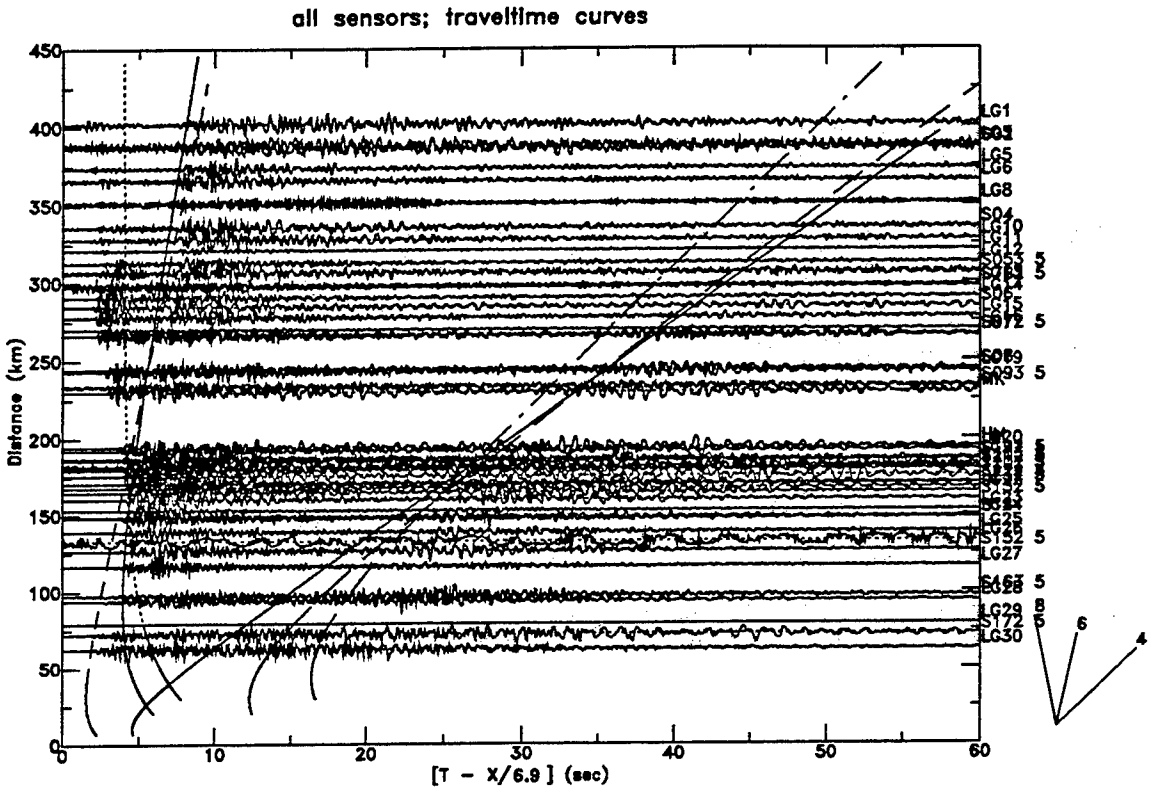

Figure 4. NPE data from the Nevada Test Site. The reduction velocity is 6.9 km/s. Traveltimes of PmP, SmS and midcrustal multiples are shown. Lg arrives after SmS.

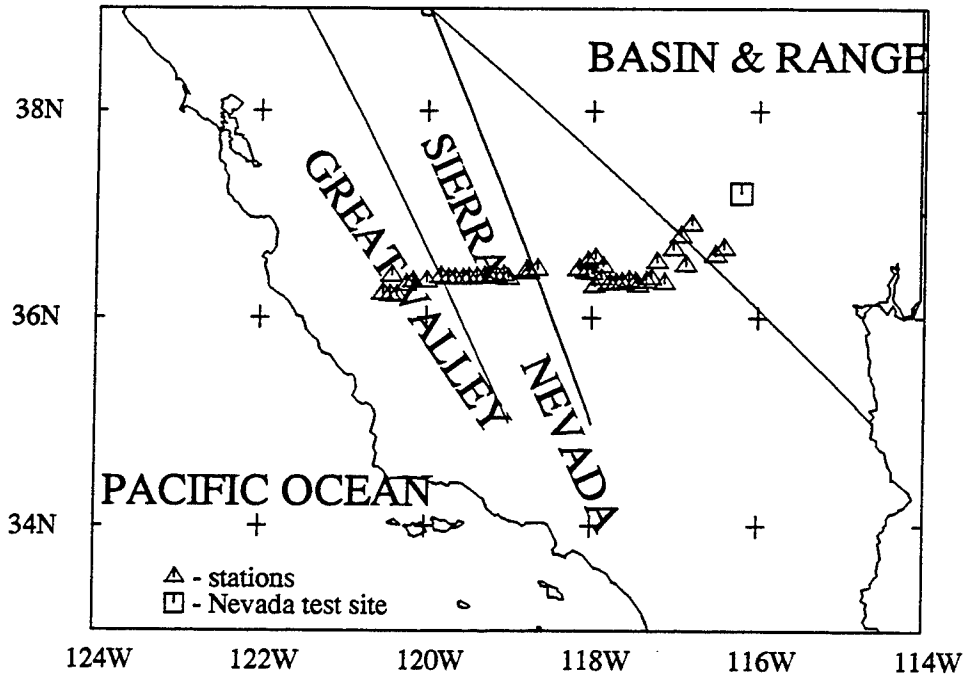

Figure 5. Source and station locations for the data shown in figure 4. Also indicated are the major tectonic provinces of the area.

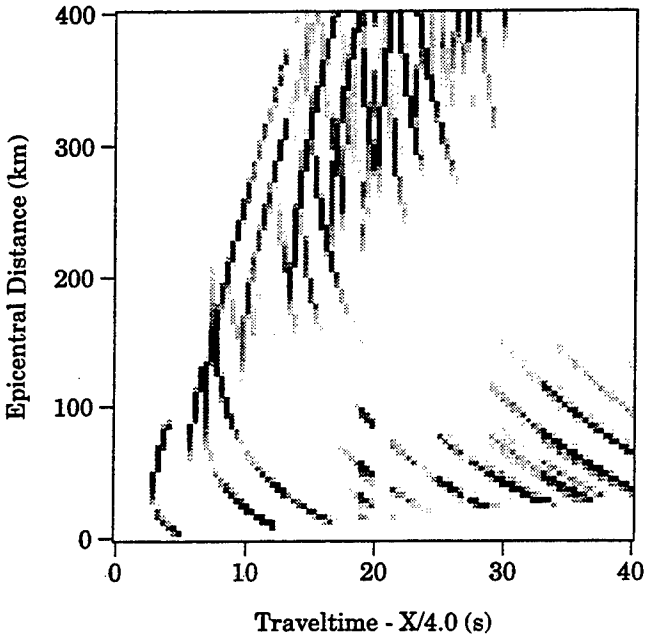

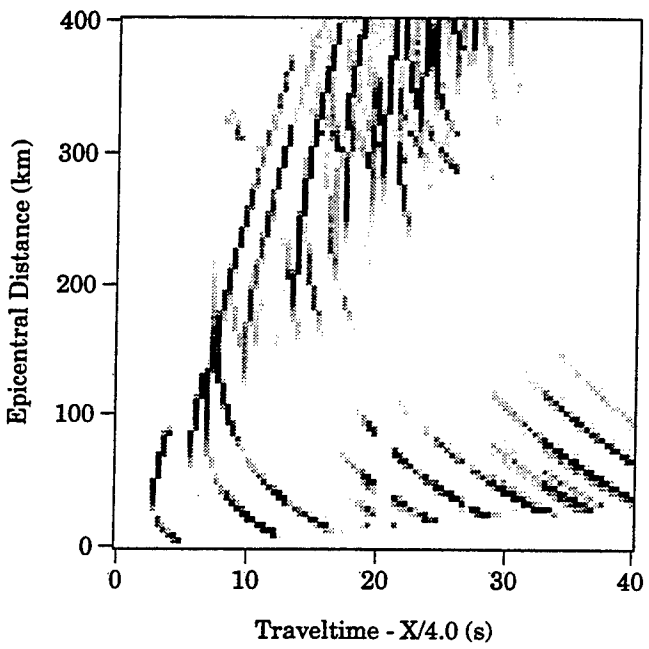

Figure 6a (left) and figure 6b (right). Ray density plots of Lg. The model corresponding to figure 6a is flat, the model corresponding to figure 6b has a bump in the Moho of 10 km and a wavelength of 100 km.

Figure 6c (left) and figure 6d (right). Same as figure 6b, with undulations of the midcrustal interfaces added (figure 6c) and random undulations (figure 6d).

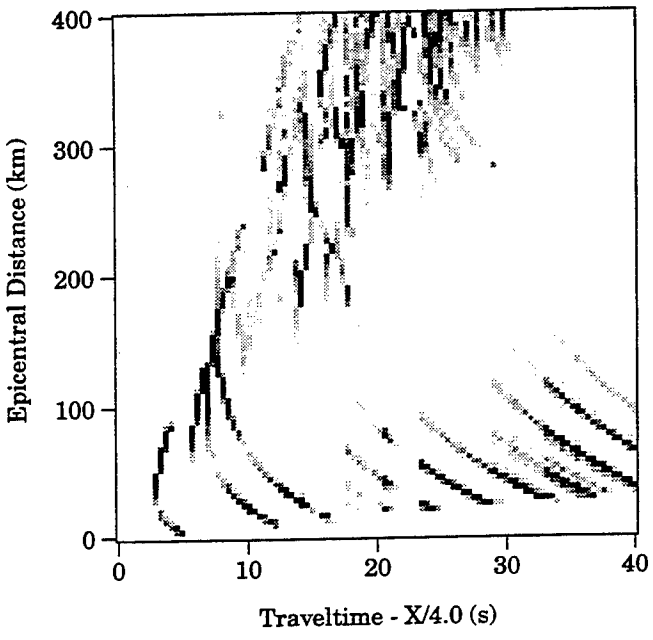

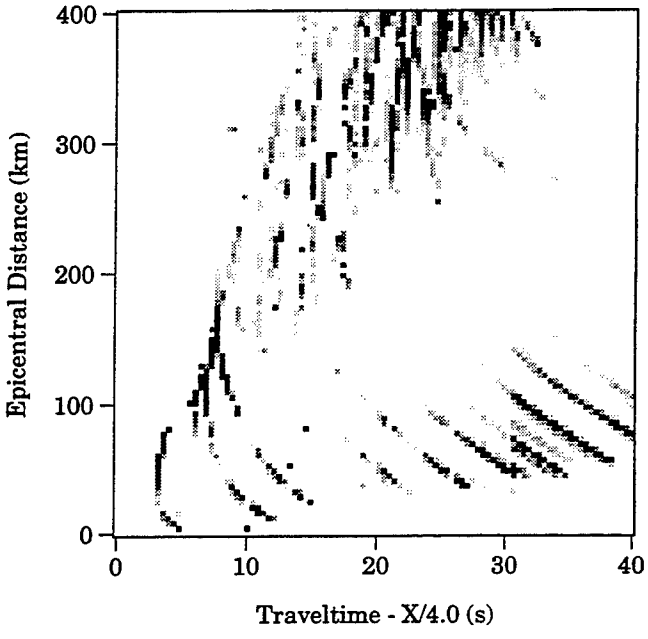

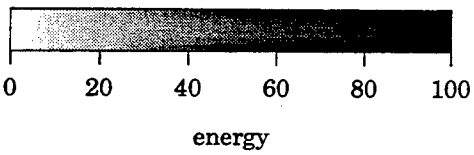

CALIBRATION OF REGIONAL WAVE DISCRIMINANTS IN DIVERSE GEOLOGICAL ENVIRONMENTS: TOPOGRAPHIC CORRELATIONS

Thorne Lay
University of California, Santa Cruz
Contract #F49620-94-1-0247
Sponsored by AFOSR

ABSTRACT

One of the major obstacles to utilizing regional seismic phases in nuclear test treaty monitoring is the sensitivity of these signals to highly variable crustal structure. Crustal structure influences the energy partitioning in the regional seismic wavefield and can produce important effects such as blockage of phases that are used for discriminants, negating their value for certain paths. The research effort supported in this contract involves several studies of the effects of irregular crustal waveguide structure on regional phases, with the intent of developing an understanding of the role played by both surface topography and other waveguide structures in shaping the regional wavefield.

A study has been completed on the influence of crustal thickness on regional phase excitation and propagation, which provides a clear understanding of why low frequency Lg phases (P-SV) fail to propagate through oceanic crust. The essential mechanism is not the shape of the continental/oceanic waveguide transition, but instead is the lack of stable low frequency Rayleigh wave overtones in very thin crustal structures. The thickness of the crust controls the number of modes in a given frequency range, and while there are still many modes at higher frequencies, these are vulnerable to strong attenuation in shallow sediments, so even high frequency Lg tends to be suppressed in oceanic environments. Using finite difference modeling, the effects of laterally varying waveguide thickness have been explored, with a 100-km segment of oceanic structure being sufficient to effectively block low frequency Lg.

Surface topographic roughness along the propagation path has been shown to have significant correlations with Pg/Lg ratios for earthquake recordings in the Western U.S.. Motivated by observation of topographic influences on Sn and Lg phases in Eurasia, the recent work demonstrates that high frequency (1-6 Hz) Pg/Lg ratios can be corrected for empirical topographic influences. The effect is comparable to that of geometric spreading, and corrections based on correlations of Pg/Lg measurements with distance and topographic roughness can reduce the variance of the log Pg/Lg discriminant by 22-25% in the 2-4 Hz band. Log Pn/Lg and individual phase spectral ratios have stronger distance dependence and little dependence on surface roughness compared to Pg/Lg.

Surface topography plays an important role in high frequency array analysis as well, as has been demonstrated in a recently completed study of the 1-20 Hz wavefield from dynamite explosions recorded by a dense short-period array (15 m station spacing). The dipping surface and dipping near-surface layers beneath this array are responsible for 45-50° back azimuth rotations, and the regional surface topography appears to be the source of significant scattered coda arriving at the array.

Numerical modeling of laterally varying waveguide structures is also being conducted under this grant, and preliminary calculations of simple structures with laterally varying crustal thickness indicate that observed variations of Sn/Lg energy partitioning in Eurasia may be largely the result of lateral variations in average crustal thickness from the source regions to the receivers.

Objective This research is directed at improving the performance of regional wave discriminants used for identifying clandestine nuclear tests by developing empirical and, potentially, theoretical wave propagation corrections for Pg/Lg and Pn/Lg ratios, as well as for Sn and Lg amplitudes. It will hopefully provide fundamental advances in our understanding of the regional wavefield that is used in CTBT monitoring. The basic idea is that by establishing the influence of large-scale crustal waveguide structure on the amplitude ratios of regional phases, the scatter in those ratios can be reduced, thereby enhancing the discriminant performance. We have empirically explored the influence of irregularities in the crustal waveguide such as surface topography, bathymetry characteristics, Moho depth, sedimentary basin depth, and Lg attenuation. Numerical modeling is being pursued to quantify some of the observed behavior.

Research Accomplished We have been working on five research projects supported by this contract and an associated AASERT award. Three of the studies have been completed and are published or in press. Two of the studies are on-going, and will be completed by the end of the contract period (through April 30, 1997).

The influence of crustal thickness on the propagation efficiency of Lg phases was the primary focus of our first research effort. This study is now published as Zhang and Lay (1995). It has long been observed that conventional Lg (0.2-2 Hz) only propagates efficiently in continental crust. Many studies have explored whether the effects of propagation across the ocean-continental margin is responsible for a disappearance of Lg, but there were some early observations within strictly oceanic paths that suggest that Lg does not propagate even within a uniform oceanic crustal layer. Based on our earlier work, supported by prior ARPA and AFOSR grants, which established that there is significant correlation between regional phase amplitude ratios and minimum crustal thickness along some propagation paths (Zhang and Lay, 1994a,b; Zhang et al., 1994) we conducted numerical studies of the role of crustal thickness on Lg propagation. We used normal mode and finite difference methods to analyze simple crustal models, finding that the number of Rayleigh wave overtones in the 0-2 Hz range decreases rapidly as crustal thickness reduces to less than 10 km. For a 32-km thick crust (Figure 1a), the group velocity minima (or Airy phases) concentrate within a narrow group velocity range between 3 and 3.5 km/s. The Lg phase develops by constructive interference among these higher modes. For the 6-km thick crust there are only a small number of modes in the same frequency range (Figure 1d), and the corresponding synthetic waveforms show almost no energy in the conventional Lg group velocity window. The calculations reported in this study indicate that the lack of Lg signals for oceanic paths is primarily a gross structural effect, intrinsic to the thin crustal waveguide. Two-dimensional models indicate that a 100-km long segment of oceanic crust can reduce Lg amplitudes significantly, whereas a 50-km long segment does not, and this effect occurs without a water layer. An area for future research is to examine higher frequency Lg signals in purely oceanic environments to establish whether these signals survive the strong attenuation effects of the shallow sedimentary layer to provide any observable signal of potential use for CTBT monitoring applications where paths with oceanic segments must be considered (e.g. for North Korea).

A study of surface topography influences on the regional discriminant Pg/Lg was conducted in a study by Zhang et al. (1996). This project involved analysis of broadband recordings from the Lawrence Livermore National Laboratory NTS seismic network, for earthquakes in the western U.S.. This study demonstrates that characterizing some of the path variability by the readily-measured surface topographic roughness along each path allows reduction of the scatter in some regional discriminants. Pg/Lg and Pn/Lg ratios, and Pg, Pn, and Lg low frequency/high frequency spectral ratios for 80 earthquakes in the

western U.S. were analyzed. While all of the regional phase discriminants display distance dependence, log Pg/Lg is also found to be significantly correlated with surface roughness (Figure 2). The correlation is emphasized when the product of distance and roughness is used as an independent variable, and the data in the frequency range 1-6 Hz have the strongest trends. Corrections based on the correlations with distance and roughness can reduce the variance of the log Pg/Lg discriminant by 22-25% in the 2-4 Hz band. Log Pn/Lg and individual phase spectral ratios have stronger distance dependence than log Pg/Lg, but the correlation with surface roughness is weak for those data. It appears that coupling of the Pg and Lg energy which reverberates in the crust accounts for the sensitivity to the gross waveguide properties that are manifested in the surface roughness parameterization. The results support the concept of pursuing path corrections beyond purely range-dependent trends.

Surface topography also has strong influence on very local observations, even when these involve array measurements. Xu et al. (1996) have studied signals from a rectangular (4 x 5) array of short-period three-component seismometers with 15 m spacing, which was deployed to record several explosions detonated around the Santa Cruz Mountains. The array was located at a site where an earlier study had recorded frequency-dependent polarized site resonances for aftershocks of the 1989 Loma Prieta earthquake. The site is on a hillside believed to be a landslide structure, with the near-surface consisting of poorly sorted sediments and weather rocks with dipping subsurface layers. The primary objective was to explore the site effects in this complex three-dimensional soft rock environment which has substantial local topography. The direct P waves from four nearby (15-20 km) explosions at easterly azimuths from the array show counter-clockwise arrival azimuth anomalies of 30-50°. These deflections are attributed to the presence of one or more dipping velocity contrasts immediately below the array, with dips of from 10-30° and dip directions toward the south. One such boundary may correspond to the landslide slip surface, and the presence of dipping velocity contrasts underlying the site is probably responsible for some of the observed directional site resonance. A slowness vector analysis demonstrates that arrivals early in the P coda have similar azimuthal anomalies, while later scattered arrivals come from many azimuths. Particle motions indicate that the more coherent arrivals in the coda are comprised of scattered P waves and Rayleigh waves, probably associated with scattering from the rough topography in the region. The coda displays greater spatial coherency along the hill strike than down the slope, consistent with a wedge-shaped landslide. The overall wavefield spatial coherence, $C(f,\Delta x)$, decreases with increasing frequency, f, and spatial offset, Δx, and on average can be well represented by $C(f, \Delta x) = \exp(-cf\Delta x)$, with $c = 0.6$ km^{-1}Hz^{-1}. This behavior is comparable to that found for previously studied hard rock locations.

Another study which is now underway, to be partially supported by this contract and then to be completed under a mini-grant from LLNL-IGPP involves analysis of regional phase behavior in the western U.S., extending the study of Zhang et al. (1996). In this work, researcher Julie Zaslow is examining NTS explosion and Little Skull Mountain earthquake signals at larger distances than the LLNL NTS network to assess how well the promising discriminants developed using the latter stations hold up at larger distances. An additional aspect of this work will be an exploration of the effects of focal mechanism and source depth on the frequency dependent discriminants being used for CTBT monitoring. The goal is to understand the contribution to the variance in the data from source effects and to design procedures to reduce the scatter that are independent of knowledge of the source type.

The fifth project being performed under this contract involves numerical modeling of regional phases in laterally varying waveguides, with postdoctoral researcher Guangwei

Fan being involved. This work is using the finite difference programs described in Xie and Lay (1994), to compute regional distance synthetics for two-dimensional models out to distances of 1000 km. While the synthetics are only for frequencies less than 1 Hz, many of the observations made by Zhang and Lay (1994a,b) can be addressed. Figure 4 shows some time slices for regional distances for a crustal model with a laterally thickening crust, from 50 km thick near the source to 65 km thick at a distance of 900 km. The crust begins to thicken 250 km from the source, which is a CLVD-type source 2 km deep. Corresponding waveforms are shown in Figure 5, and the results of measuring various ratios of regional phases for three different crustal models are shown in Figure 6. The models involve a structure that thins to 35 km, one that is constant in crustal thickness of 50 km, and one that thickens to 65 km along the path. While the modeling is still in a fairly preliminary stage, the results show some distance dependent variations between the models which may provide an explanation for the highly efficient coupling between Sn and Lg phases observed by Zhang and Lay (1994a). The results will be updated at the 1996 meeting.

Conclusions and Recommendations

Observational and numerical applications reinforce the importance of varying crustal structure on regional phase energy partitioning. For CTBT monitoring efforts, calibration of regional behavior, and determination of correction procedures based on regional correlations with regional and geological properties are needed to enable widespread application of regional discriminants with high confidence. Ongoing efforts are being made by our group (under a PL/DOE grant) to apply empirical calibration to the Middle East and Western China. Quantitative modeling efforts should be sustained to provide a sound physical basis for using empirical discriminant corrections.

References:

Xie, X.-B., and T. Lay (1994). The excitation of explosion Lg: a finite-difference investigation, *Bull. Seism. Soc. Am.*, 84, 324-342.

Xu, Z., S. Y. Schwartz, and T. Lay (1996). Seismic wavefield observations at a dense, small aperture array located on a landslide in the Santa Cruz Mountains, California, *Bull. Seism. Soc. Am.*, in press.

Zhang, T., and T. Lay (1994a). Analysis of short-period regional phase path effects associated with topography in Eurasia, *Bull. Seism. Soc. Am.*, 84, 119-132.

Zhang, T., and T. Lay (1994b). Effects of crustal structure under the Barents and Kara Seas on short-period regional wave propagation for Novaya Zemlya explosions: Empirical relations, *Bull. Seism. Soc. Am.*, 84, 1132-1147.

Zhang, T., S. Y. Schwartz, and T. Lay (1994). Multivariate analysis of waveguide effects on short-period regional wave propagation in Eurasia and its application in seismic discrimination, *J. Geophys. Res.*, 99, 21929-21945.

Zhang, T., and T. Lay (1995). Why the Lg phase does not traverse oceanic crust, *Bull. Seism. Soc. Am.*, 85, 1665-1678.

Zhang, T., T. Lay, S. Schwartz, and W. R. Walter (1996). Variation of regional seismic discriminants with surface topographic roughness in the Western United States, *Bull. Seism. Soc. Am.*, in press.

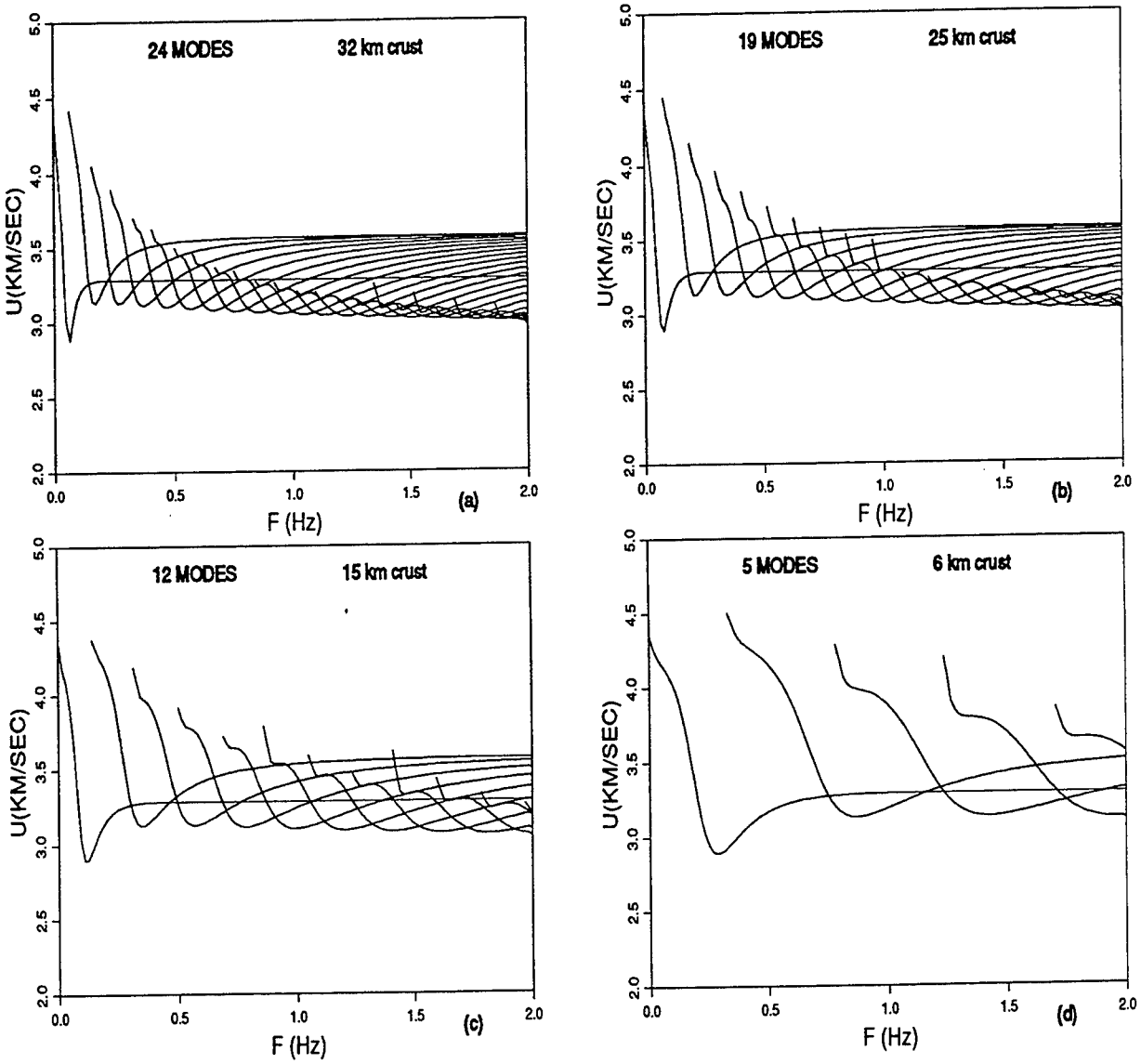

Figure 1. Group velocity curves for Rayleigh waves in layer over a halfspace models with crustal thickness of (a) 32 km, (b) 25 km, (c) 15 km, and (d) 6 km. The number of overtones present in the 0-2Hz band decreases dramatically as the crust becomes thinner than 10 km. This eliminates the constructive interference that gives rise to the Lg phase. From Zhang and Lay (1995).

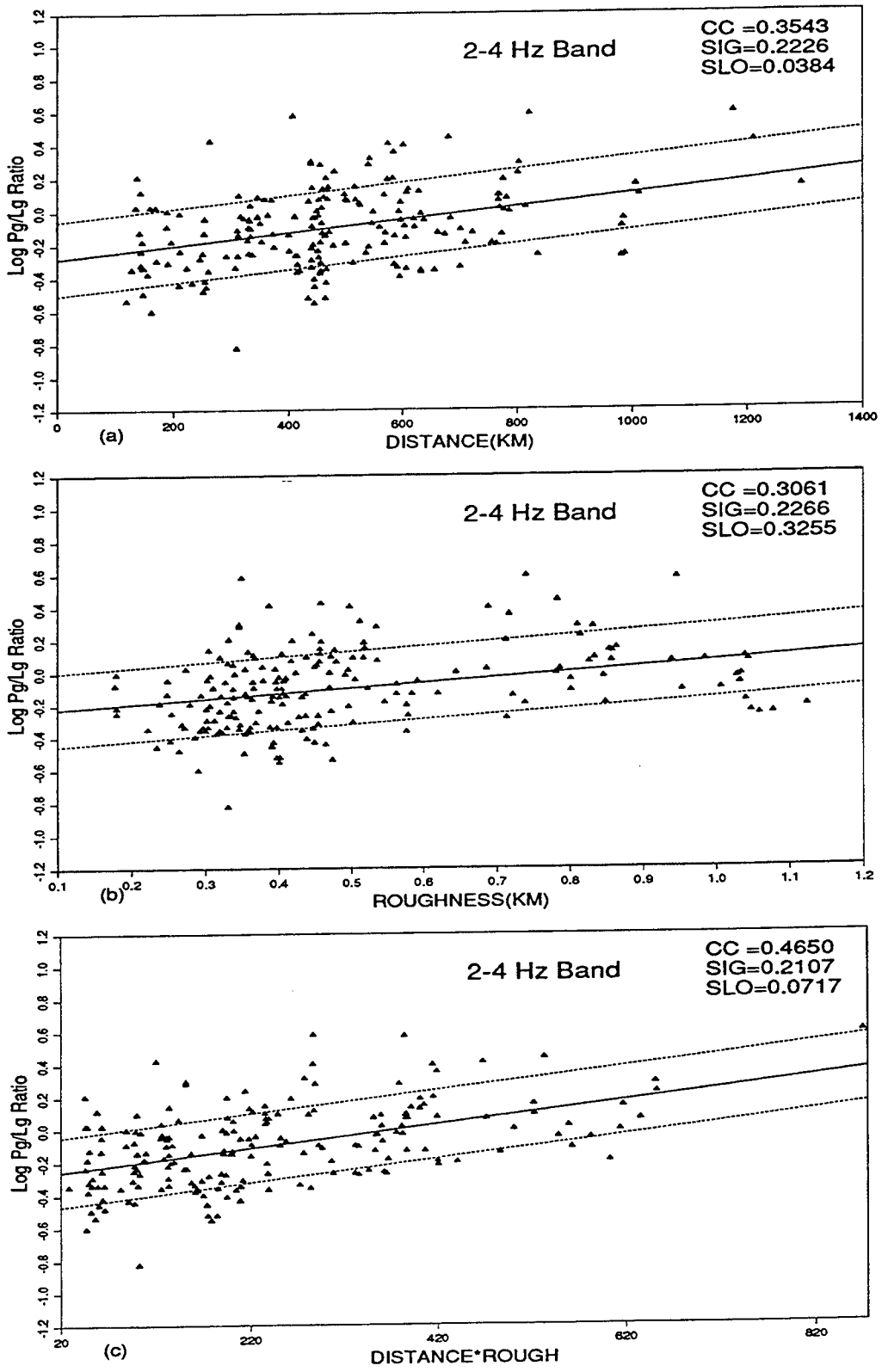

Figure 2. Log (Pg/Lg) ratios from Western U.S. earthquakes as a function of (a) distance, (b) rms topographic roughness on the path, and (c) distance x roughness for the frequency band 2-4 Hz. The trends are similar for distance and rms roughness, but these variables are almost uncorrelated. As a result, the combined variable involving their product gives the best correlation and best variance reduction. From Zhang et al. (1996).

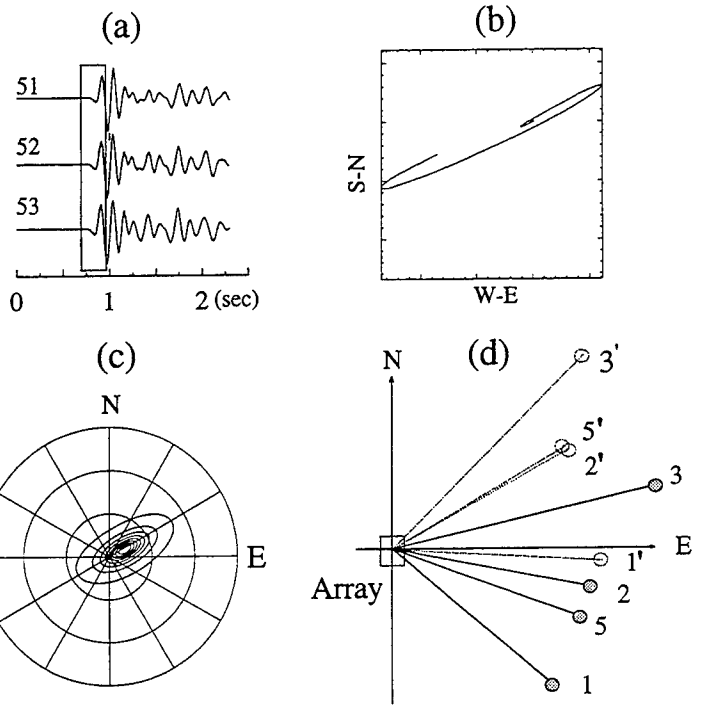

Figure 3. Procedures used to estimate the backazimuth for initial P waves recorded by a dense short-period array in the Santa Cruz mountains. (a) A few vertical component seismograms for one of the 4 explosions, illustrating the time window used for frequency-wavenumber (f-k) analysis. A very short, highly coherent interval is used. (b) Horizontal particle motion for one station indicating the initial nearly linear motion that is used to define the apparent backazimuth at each station. (c) Broadband f-k analysis of the direct P wave power spectrum for shot #2 in the window shown in (a). A maximum likelihood method is used, with the spectrum contoured in the wavenumber doamin. The peak contour indicates the northeasterly backazimuth. (d) Summary of estimated (open circles) and actual (filled circles) backazimuths for the four shots. The average estimates from the particle motion and f-k methods are shown. Biases of 30-50° are found for all four events, with systematic counterclockwise rotations. From Xu et al. (1996).

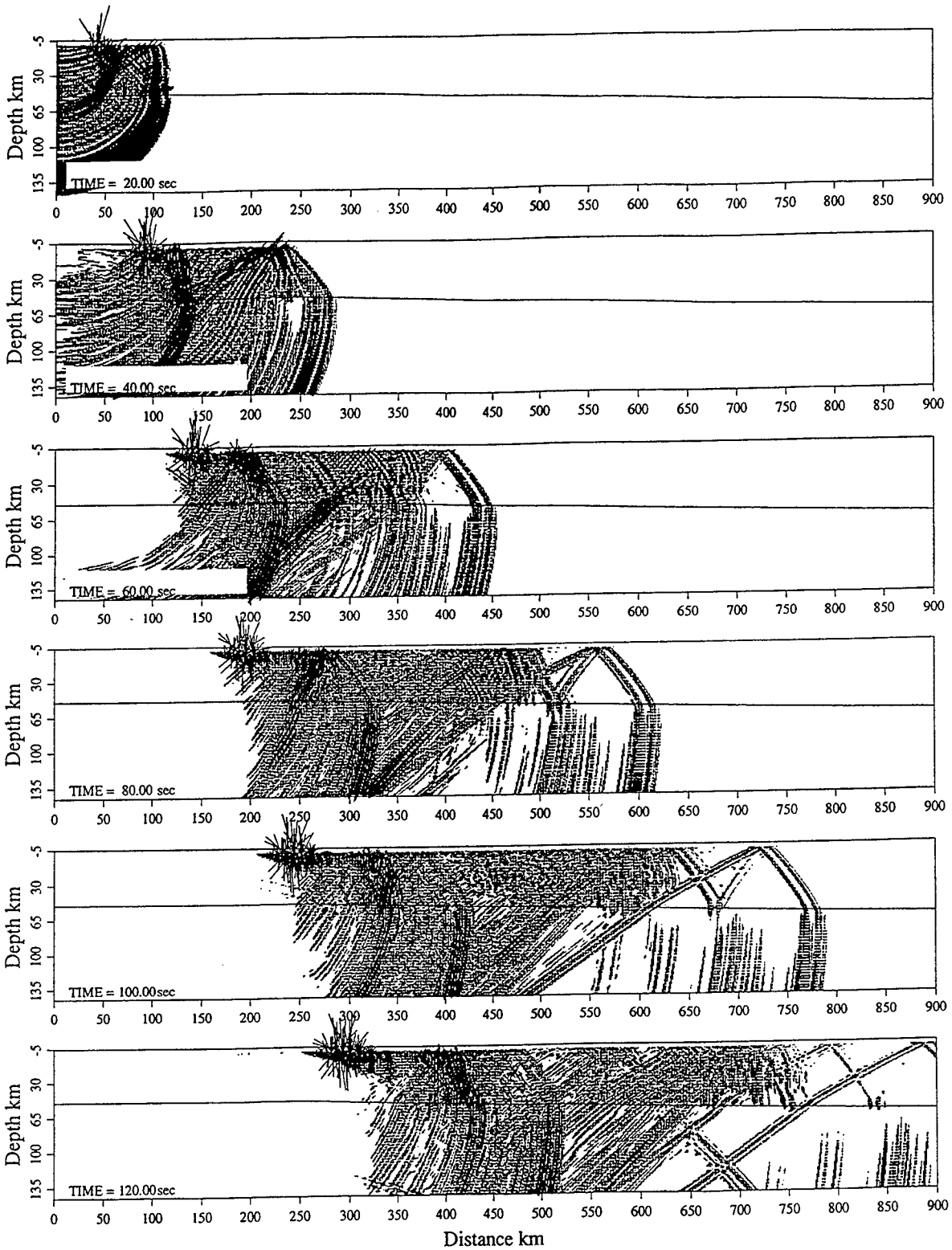

Figure 4. Time slices in a two-dimensional finite difference calculation for a model with a laterally varying crustal model. The model has a simple layered structure in the crust, with the source being 2 km deep, and having a spall-source mechanism. The crust near the source is uniform out to a distance of 250 km, where the depth to the Moho begins to increase slowly to a maximum depth of 65 km at a range of 1000 km. The slow crustal thickening can be seen in the evolving Pn and Pg wavefields.

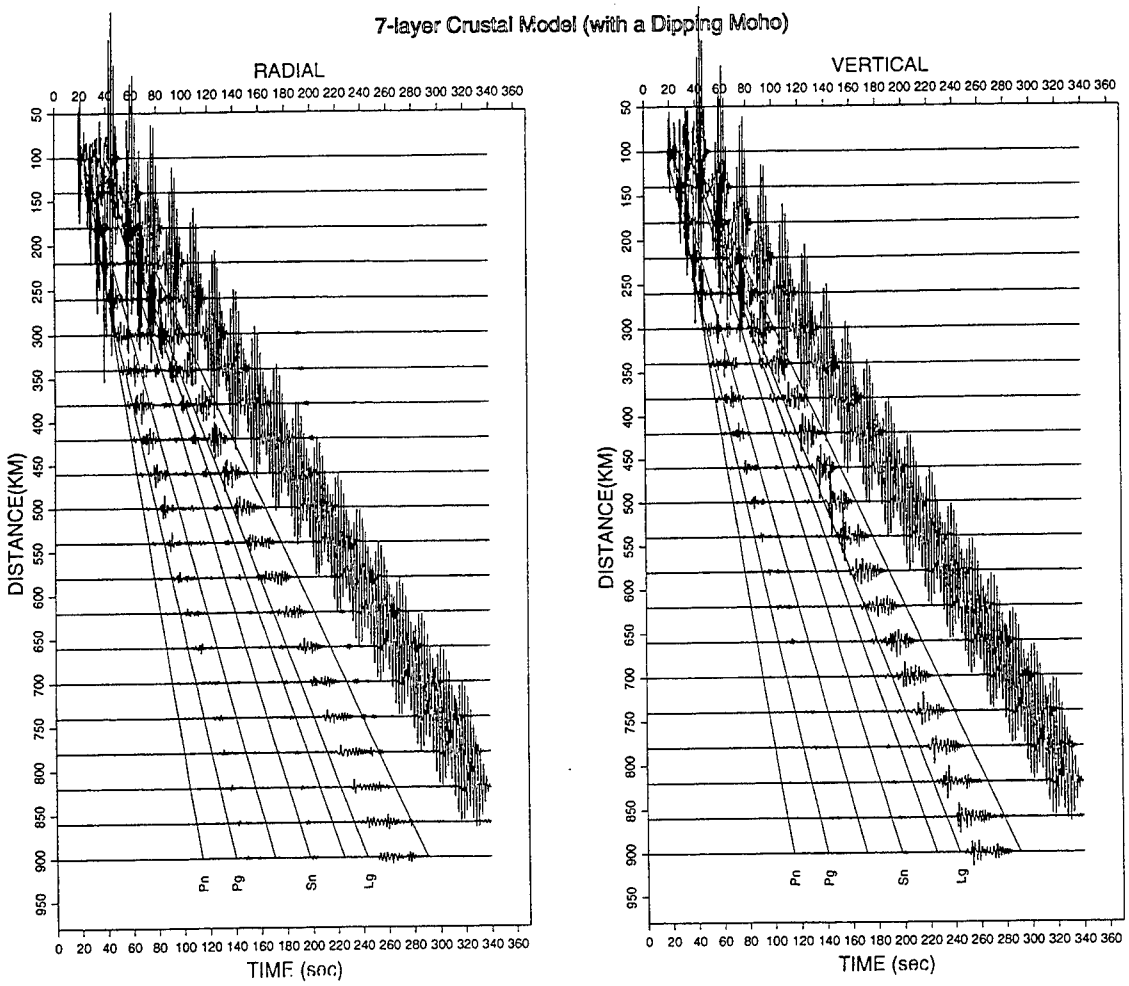

Figure 5. Seismograms for the calculations in Figure 4, showing the well-defined seismic phases excited in this crustal model. The Lg phase is efficiently generated by the spall source and is well above noise level out to large distances. The windows shown are used for calculating rms amplitudes for each phase.

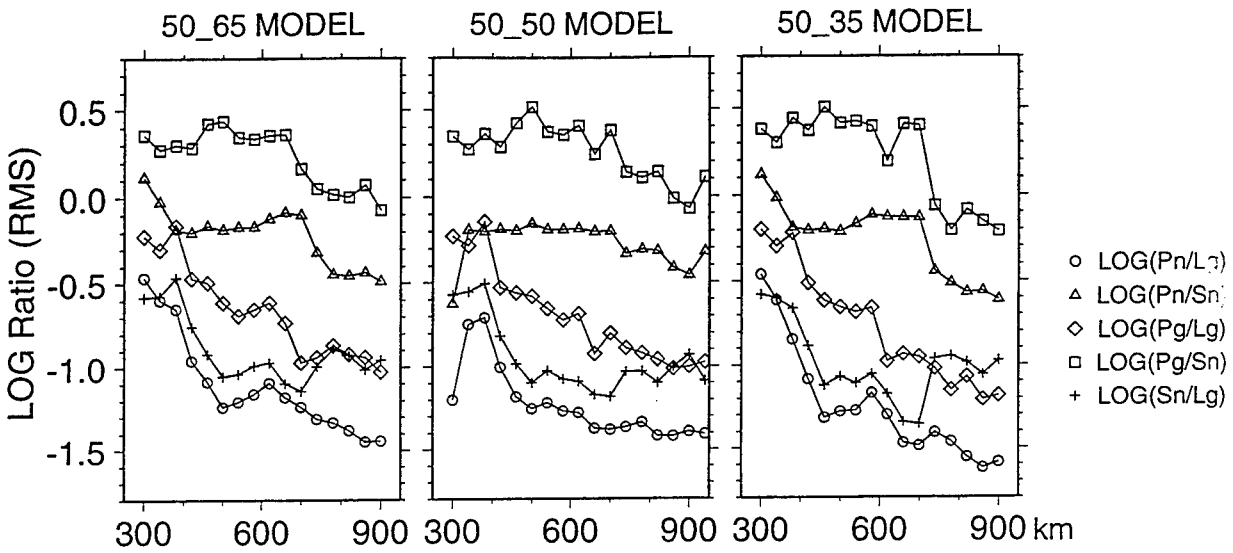

Figure 6. Log rms amplitude ratios for various regional phases from the synthetics in Figure 5 (for a linearly thickening crustal model) and similar synthetics for models with a constant 50 km thick crust and a thinning crust which thins to 35 km. Note the subtle differences in the range-dependence of the ratios and in the relative behavior between the three models. Such variations are being explored in an attempt to understand the strong energy partitioning observed by Zhang and Lay (1994a).

Calculation of Synthetic Seismograms Using PVM on a Network of Workstations

Keith L. McLaughlin and Boris Shkoller
S-CUBED Division of Maxwell Laboratories
POB 1620 La Jolla CA 92038
619-587-8436, FAX 619-755-0474, scatter@scubed.com
Contract F19628-95-C-0207
Sponsored by DOE

ABSTRACT

Over the last year two major tasks have been accomplished. 1) An X-Windows MOTIF graphical user interface was developed on the SUN computer platform to facilitate preparation of wavenumber integration calculations of synthetic seismograms in layered media. Several changes were made to the original wavenumber integration program to accommodate fluid layers, optimize performance, and enhance portability. 2) A parallel version of the program was developed to run on a heterogeneous network of workstations.

The original wavenumber integration program was broken into a master program and a slave program. The master program breaks the task of synthetic seismogram calculation into independent tasks (frequency by frequency) and apportions the tasks to multiple slave programs running on a heterogeneous network of computers. These programs have been ported to SUN OS4, SUN Solaris, HP, SGI, and DEC-Alpha workstations using the Parallel Virtual Machine (PVM) message passing software. The master program and slave program each work on all five platforms. The master/slave PVM program has been tested using both local and wide area networks of workstations using as many as five different platforms at a time and as many as 40 separate CPU's.

The master program performs load balancing by a simple algorithm. As each slave finishes a task, it is given a new task. The response time of each slave is monitored and the average response time and number of tasks completed are tabulated. Once all tasks have been assigned to slaves, the master program will send duplicate unfinished tasks to the fastest machines on the network that have completed all of their previous tasks. When all tasks are completed the master program closes the synthetic seismogram file and exits. The Green's function synthetics are written in CSS 3.0 format and can be read with several standard programs including SAC. Benchmark runs to properly measure the speedup on the heterogeneous PVM network are difficult to compare since network loads are not repeatable, however, near linear speed up over the use of a single CPU is apparent when the relative speeds of the diverse set of CPU's are taken into account.

Keywords: wavenumber integration, PVM, parallel computing, synthetic seismograms

OBJECTIVES

Provide more accurate and efficient means to compute, store, and retrieve synthetic seismograms for reference layered Earth structures and examine limitations of using layered Earth structures to model principal features of regional seismograms in the presence of lateral heterogeneity.

RESEARCH ACCOMPLISHED

Work in the first year of the contract focused on providing a portable and convenient means to run wavenumber integration synthetic calculations using a heterogeneous network of workstations. A beta version of the graphical user interface and parallel software is completed and in the final testing phase.

CONCLUSIONS AND RECOMMENDATIONS

Wavenumber integration is an excellent candidate for parallel implementation. PVM has proved to be a simple and efficient method for this implementation on the S-CUBED network. We have demonstrated that synthetics can be computed efficiently using a heterogeneous network of computers with minimal overhead. PVM has proved to be a simple and efficient method for parallel implementation. Future plans call for porting the program to other workstations as platforms become available. A body of synthetic seismograms for reference structures must now be assembled.

L_g Propagation across Northern Eurasia Recorded by Profile "Quartz"

Igor Morozov, Elena Morozova, Yuri Ganchin, and Scott Smithson

Department of Geology and Geophysics, University of Wyoming, PO Box 3006, Laramie, WY, 82071-3006.

Grant F49620-94-1-0134, Sponsored by AFOSR

ABSTRACT

We examine kinematic and dynamic characteristics of L_g phases recorded along the ultra-long Deep Seismic Sounding profile (DSS) "Quartz". The use of DSS profiles provides us with unique opportunities to study large-scale propagation effects of various seismic phases, and especially L_g, across geological and tectonic boundaries. Three industrial nuclear explosions were detonated during the acquisition of "Quartz" data in different tectonic and geological environments. Recorded within a continuous range of offsets 0-3200 km, and in overall along 3850 km-long profile, these seismic data provide unique and valuable information for the calibration of seismic discriminants.

Examination of the nuclear explosion records show L_g at offset ranges 300-1200 km. In contrast, mantle P-wave phases are observed within the entire offset range, and S_n can be traced up to 2500 km. L_g is strongly attenuated under the sedimentary basins, and is characterized by group velocities near 3.5 km/sec. In the Baltic Shield area, L_g is significantly stronger and has higher velocity of 3.75 km/sec.

This study demonstrates that Russian DSS data provide valuable information for the analysis of the propagation of L_g and other phases for their use in CTBT applications.

Key words: Baltic Shield, Deep Seismic Sounding, L_g propagation, Northern Eurasia.

INTRODUCTION

Profile "Quartz" (Murmansk-Kizil profile) acquired in 1984-87 is a part of the unique Deep Seismic Sounding (DSS) program carried out in the USSR during the past 25-30 years. The profile spans 3950 km from northwestern Russia to central Asia, crossing six major tectonic provinces (e.g., Zonenshain et al., 1990). 3 nuclear explosions (PNEs) were recorded by over 330 3-component instruments spaced at 10-16 km. The PNE data provided an unparalleled insight into the structure of the mantle down to 600-800 km (e.g., Ryaboy, 1989; Egorkin and Mikhaltsev, 1990; Mechie et al.,1993; Ryberg et al, 1995). The potential of the data for the analysis of crustal-guided phases, however, has not been examined before.

During 1993-1995, all analog records of "Quartz" data were digitized up to 600 sec lengths. Acquisition geometry and data parameters, and interpretation of major seismic phases were given by Mechie et al. (1993) and Morozova et al. (1994); a detailed overview of Soviet DSS program can be found in Ryaboy (1989). Crustal models derived from the "Quartz" data were developed by the center GEON, Moscow (L. Solodilov, personal communication). An alternative, more suitable for the purposes of L_g modeling, tomographic crustal model, and the corresponding resolution analysis, were proposed in our recent report (Morozov et al., 1995). In this paper, we discuss the application of this data to the observation of L_g propagation.

Modeling of the propagation of crustal-guided phases requires a detailed knowledge of the crustal structure of the region. Along with the analysis of "Quartz" data, we briefly present new wide-angle data acquired in August 1995 across the northeastern boundary of the Baltic Shield.

Ultra-long densely spaced DSS profiles acquired during the past 25-30 years in the Soviet Union using nuclear and chemical explosions provide unique opportunities to study wave propagation through complex lithospheric structures. With the typical listening time over 300-400 sec, and using 3-component instruments, these data may serve as an valuable source of calibration of seismic discriminants. Understanding of the process of the propagation of crustal-guided seismic phases, especially L_g, is recognized as one of the major clues to seismic calibration and CTBT monitoring.

OBJECTIVES

In this report, analysis of Lg phases observed in "Quartz" data pursues the following major objectives:

- Analysis of kinematic characteristics of L_g, providing information on the nature of L_g in several tectonic provinces crossed by the profile.
- Amplitude information will provide insight into the mechanism of L_g blockage. Amplitude ratios of regional phases provide potential seismic discriminants.
- Modeling of seismic wave propagation across laterally variable geological structures; to study the effects of the crustal P- and S- wave velocity structure on L_g wave propagation.

- As an integrating result, a contribution to the calibration of regional seismic event discriminants.

RESEARCH ACCOMPLISHED

L_g phases in "Quartz" records

Examination of the PNE records shows that S_n and L_g phases are generally very diffuse and hard to pick, and have long 20-40 s codas (due to space limitations, we show in Figure 1 first 400 sec of the records only from the southern PNE, characterized by the highest quality data). The phases exhibit certain variability, especially among the horizontal components. However, instantaneous amplitude plots, low-pass filtered below 1 Hz (Figures 2-4) enable easy observation of many important features of these phases. These features can be summarized as follows:

- Travel time picks result in Lg propagation velocities ranging from 3.5 km/sec in the sedimentary basins to 3.75 km/s in the Baltic Shield.
- L_g generated by a PNE is weaker then S_n in all 3 shot gathers. with an exception of the northernmost part of the gather 123, where L_g propagates across the Baltic Shield.
- The above observation is especially true for shot 323, detonated in the crystalline rocks of Altai. In shot gather 323, strong S_n can be observed at distances near 3000 km, whereas L_g can be traced only to 1300 km. The latter is, however, the largest recorded distance of L_g propagation, but clearly its amplitude at 1100 km offset is still lower then L_g amplitude at the Baltic Shield from shot 123 at the same offset. We attribute this differences to higher energy and frequency of shot 323 and, on the other hand, to the seismic attenuation in the West Siberian Basin.
- Although some records of shot 123 corresponding to the Ural region have been truncated within the L_g coda (Figures 1 and 3), closer examination of these records and comparison to the records from shot 213 from the eastern side of the Urals, and also the absence of L_g at offsets exceeding 1000 km indicate that L_g is probably more strongly attenuated in the Pre-Ural depression.

1995 wide-angle experiment in the Baltic Shield - Barents Sea Platform transition zone

As a part of research efforts directed at the analysis of L_g blockage in Barents Sea area, AFOSR supported the participation of the University of Wyoming in a wide-angle offshore-onshore experiment on the north-eastern shelf of the Barents Sea, along the international geotraverse EU-3 (Chekunov et al., 1993). A schematic summary of seismic sections along this geotraverse (Figure 5) shows a gap over an interval of about 100 km. The newly obtained data will fill this gap, providing important information on the structure of the ocean-continent transition.

The pilot investigations along parts of 200 km sea- and 100 km surface profile Kola Superdeep-Liinahamary-Barents sea were carried out in August 1995. Seismic signals from

marine 90-liter air gun sources were recorded at 5 surface sites using REFTEK seismographs. The moving marine source spacing had average values of 250 and 460 m.

The Moho reflection (P_mP) could be traced with the largest certainty (Figure 6). The P_mP wave group is traced for the offset range 70-290 km. We estimate crustal thickness in the marine-land transition zone of 38-40 km, slightly decreasing towards the sea (Figure 5).

CONCLUSIONS AND RECOMMENDATIONS

Analysis of the data from the ultra-long range DSS profile "Quartz" shows that although the data acquisition targeted the deep mantle structure, obtained data provide information on the propagation characteristics of regional phases, especially S_n and L_g. L_g was identified at ranges below 1200 km, and shows distinctive variations of its propagation characteristics while propagating in the crystalline crust or in sedimentary basins. The recorded amplitude of L_g is significantly lower within the parts of the profile crossing sedimentary basins. Pre-Ural Depression appears to cause especially strong attenuation of L_g.

Modeling of the propagation of regional phases along the "Quartz" traverse will reveal the mechanism of observed L_g attenuation under the sedimentary basins and Urals. Major components of this ongoing work are:

- refraction/reflection tomographic inversion of the crustal and uppermost mantle velocity structure along the southern part of the profile, and corresponding resolution analysis and interpretation;
- refinement of crustal velocity structure using reflected arrivals;
- inversion and modeling of the Barents shelf continental transition zone using the newly acquired wide angle data, and marine CDP data provided by Russian colleagues;
- ray-tracing and finite-difference modeling of L_g propagation and quantitative amplitude analysis of "Quartz" PNE records.

These efforts will provide a better understanding of the mechanisms resulting in the variability of L_g propagation across the boundaries of various geological structures. Such understanding, in turn, is necessary to accomplish the goal of development of invariant seismic discriminants.

REFERENCES

Chekunov, A.V., Starostenko, V.I., Krasovsky, S.S., Sharov, N.V., Zagorodny, V.G., 1993, Euro - 3 (EU-3). Geophysical Jornal, 15, no 2, p. 3-32 (in Russian).

Egorkin, V. A., and Mikhaltsev, 1990, The result of seismic investigations along geotraverses, *in:* Fuchs, K., Kozlovsky, Y. A., Krivtsov, A. I., and Zoback, M. D. (Eds.), Super Deep Continental Drilling and Deep Geophysical Sounding, Springer Verlag, Berlin Heidelberg New York, 11-119.

Mechie, J., Egorkin, A. V., Fuchs, K., Ryberg, T., Solodilov, L. and Wenzel, F., 1993. P-wave mantle velocity structure beneath northern Eurasia from long-range recordings along the profile Quartz: Phys. of the Earth and Plan. Int., 79, 269-286.

Morozov, I., Schueller, W., Morozova, E., and Smithson, S., 1995, Two-dimensional crustal and upper-mantle velocity models from profile "Quartz", Russia, *in*: Proc. of the 17th PL/DARPA Seismic Research Symposium. (Eds. Lewkowicz, J. F., McPhetres, J. M., Reiter, D. T.): Scottsdale, AZ, Aug. 1995. **PL-TR-95-2108, ADA 310037**

Morozova, E. A., Morozov, I. B., Smithson, S. B., Shatzman, J. C., and Solodilov, L. N., 1994, Studies of P_n, S_n and L_g wave propagation across major crustal structures using PNEs. *in*: Proc. of the 16th PL/DARPA Seismic Research Symposium. (Eds. Lewkowicz, J. F., McPhetres, J. M.): Thornwood, Sept. 1994, **PL-TR-94-2217, ADA284667**

Ryberg, T., Fuchs, K., Egorkin, V. A., and Solodilov, L., 1995, Observation of high-frequency teleseismic P_n waves on the long-range profile QUARTZ across Northern Eurasia, J. Geophys. Res., 100, 18151-19165.

Ryaboy, V., 1989, Upper mantle structure studies by explosion seismology in the USSR, Delphic Assoc., Inc., Falls Church, VA.

Zonenshain, L. P., Kuzmin, M. I., and Natapov, L. M., 1990. Geology of the USSR: A Plate-Tectonic synthesis. In: B.M. Page (Ed.), Am. Geophys. Union Geodynamics Ser., 21; 242 pp.

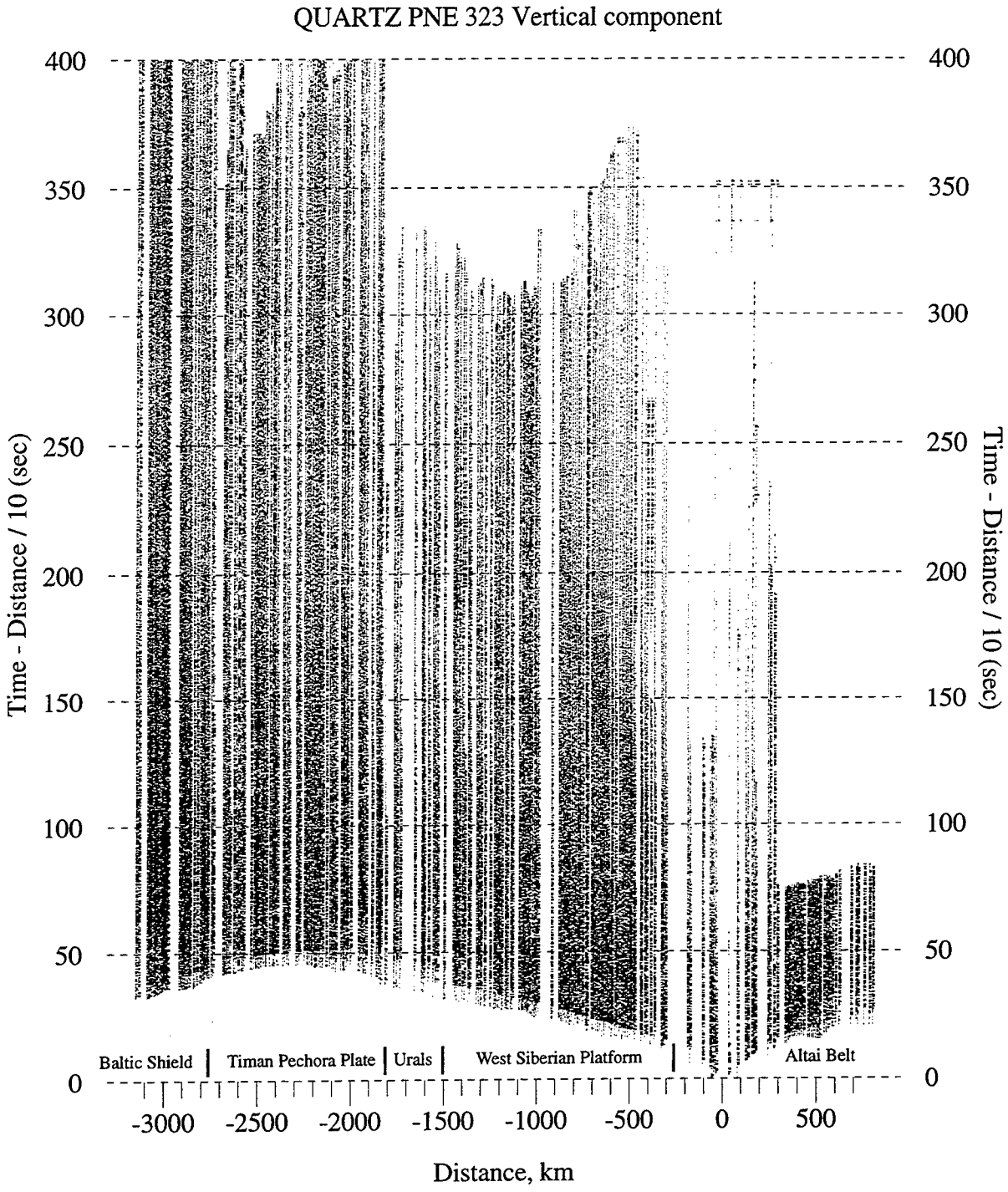

Figure 1. Transverse component shot gather from shot point 323 (southern PNE). Reduction velocity is 10 km/sec. Main tectonic structures are indicated.

Note the prominent mantle refracted wave Sn. Lg is following Sn and can be seen within 0-1200 km offset range. First 60 sec of records contain a multitude of continious P-wave phases.

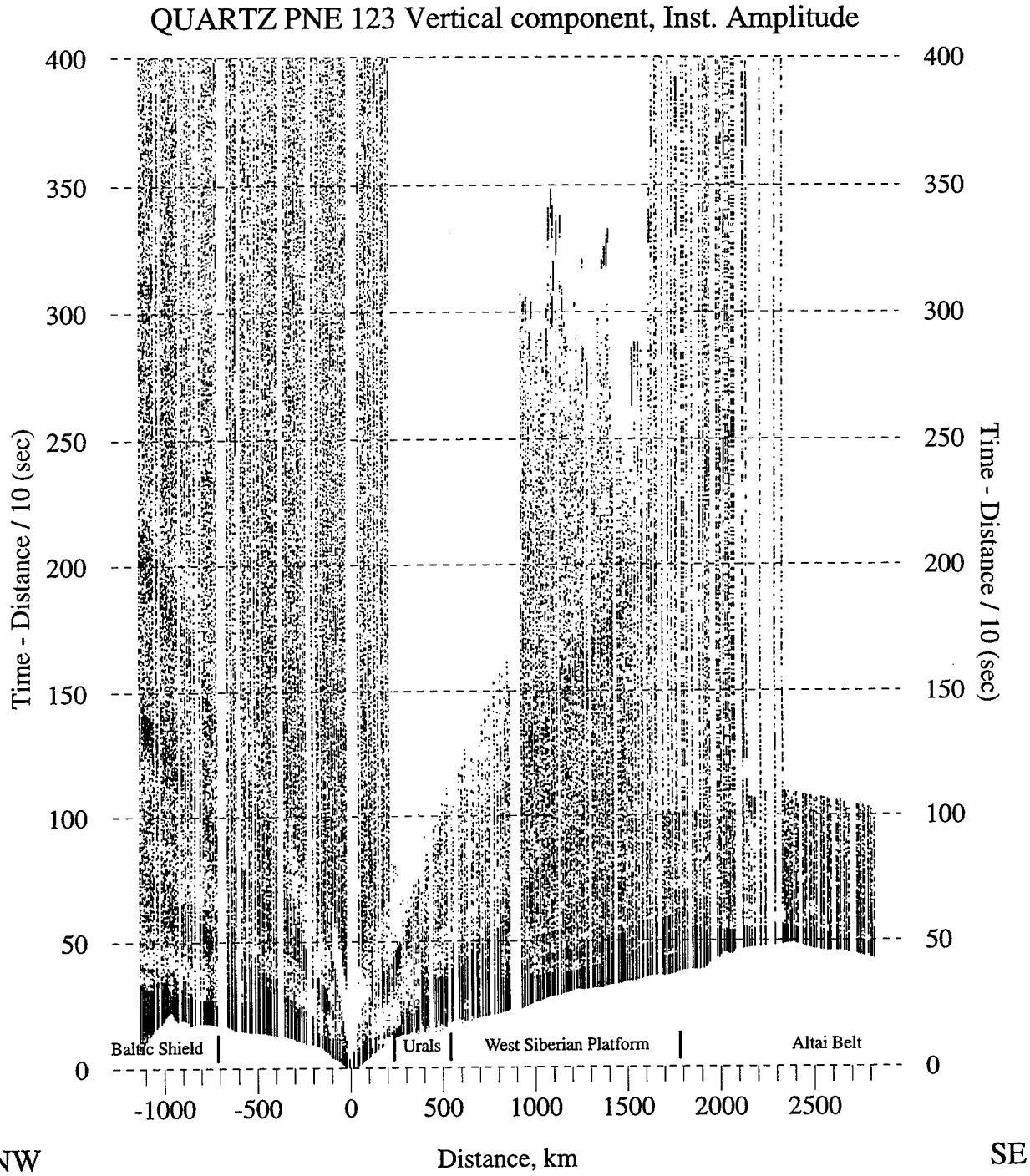

Figure 2. Filtered below 1 Hz instantaneous amplitude of vertical component record from shot point 123 (northern PNE). Reduction velocity is 10 km/sec. Note that Pg, Sn and Sg phases become easily observable.

Lg (arriving at 1200 km offset at about 200 sec reduced travel time) is very prominent in the Baltic Shield (NW end of the gather). To the SE, Lg can be traced only to the eaqstern flank of Ural Mountains (Pre-Ural Depression). However, Sn arrival is clear up to 2200 km to the SE (250 sec reduced travel time at this offset), where the data quality becomes poor.

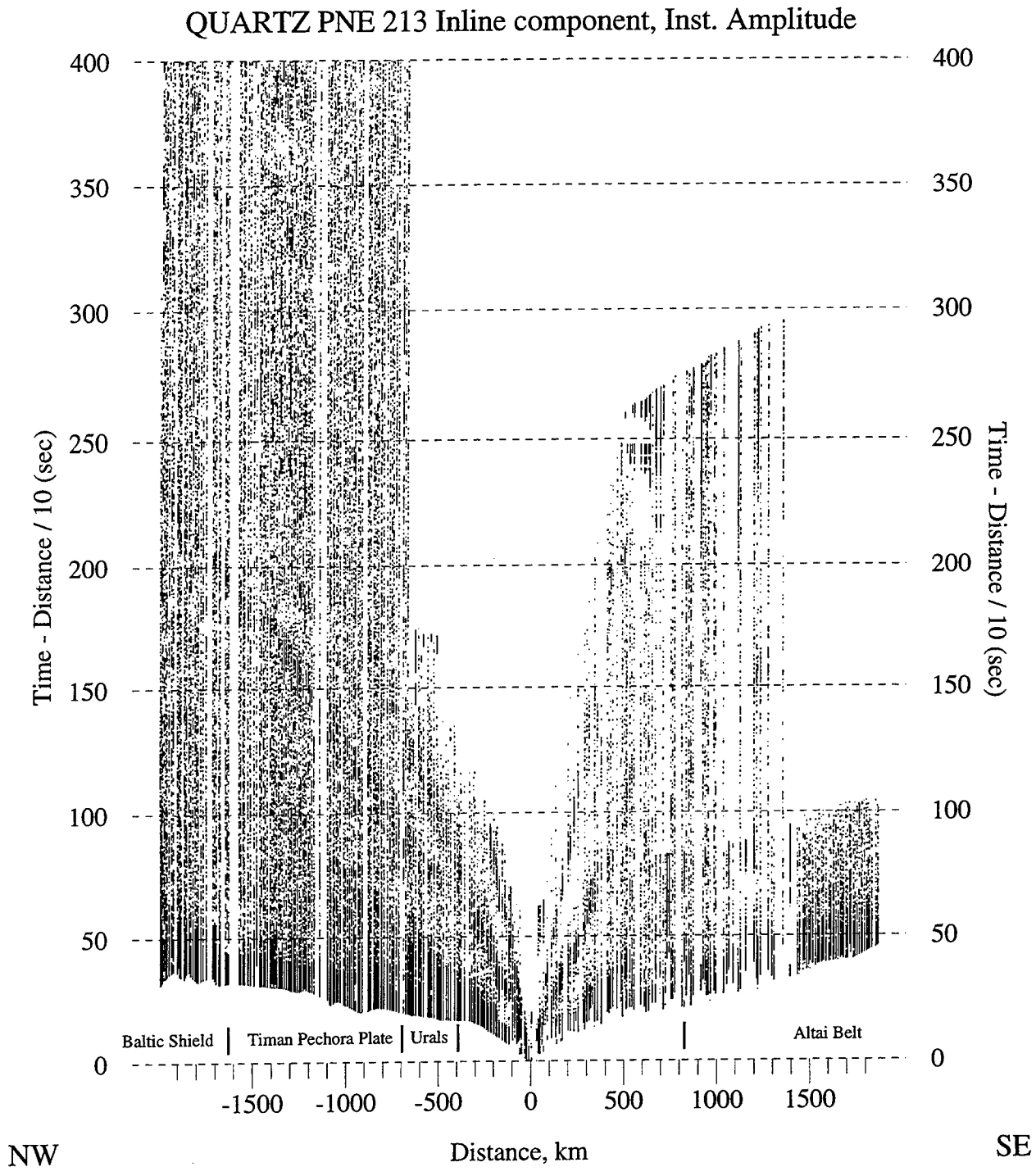

Figure 3. Filtered below 1 Hz instantaneous amplitude of vertical component record from shot point 213 middle PNE, detonated in the Yarsom depression, West Siberian Basin). Reduction velocity is 10 km/sec.

Part of the traces are truncated in the SE part of the gather, resulting in poorer data quality. However, Sn can be traced to 2000 km offset to the NW, while Lg dies out after passing the Urals. Pg is also much less pronounced than in the Baltic Shield (Figure 2).

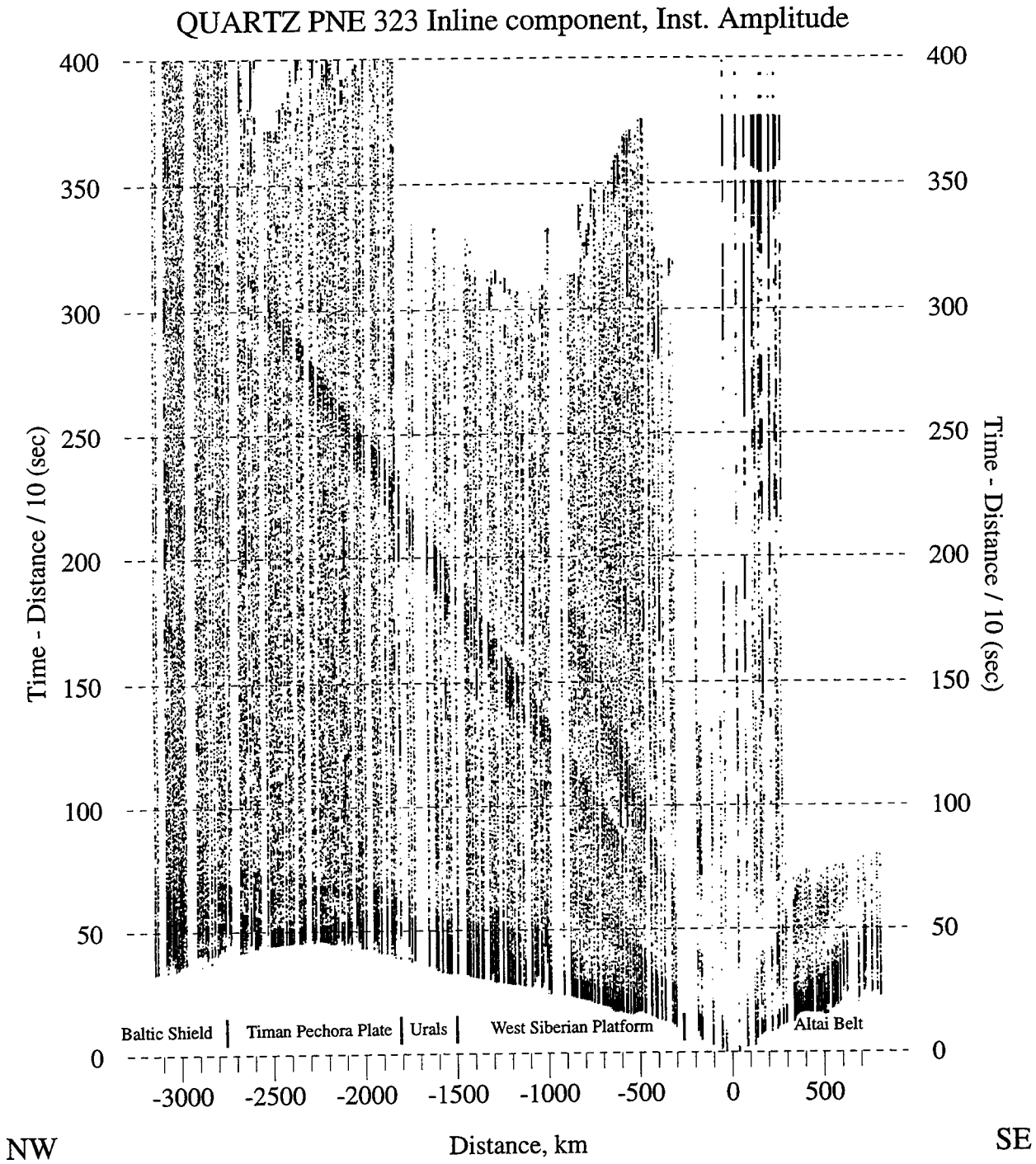

Figure 4. Filtered below 1 Hz instantaneous amplitude of vertical component record from shot point 323 (southern PNE). Reduction velocity is 10 km/sec.

The explosion was detonated in crystalline rocks of Altai Mountains, resulting in higher frequency and quality seismic data. Sn is remarkably strong, especially on the horizontal component records (see also Figure 1). Lg and Pg, however, are strongly attenuated within the West Siberian Basin, at propagation distances below 1000 km, and disappear approaching the Urals.

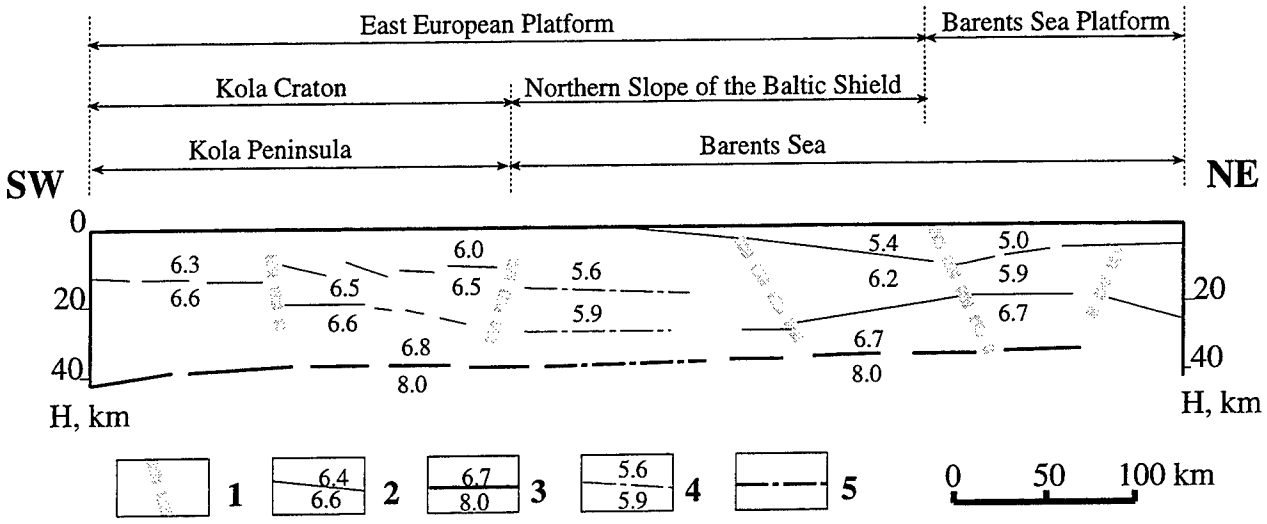

Figure 5. Seismic section of the earth's crust along the EU-3 geotraverse (modified from Chekunov et al., 1993). 1 - main fault zones; 2 - crustal reflecting boundaries with velocity values above and below; 3 - Moho reflecting boundaries with interval velocity values; 4 - crustal boundaries with average velocity values above the reflectors determined in 1995 pilot wide-angle study, and 5- Moho determined in the same study.

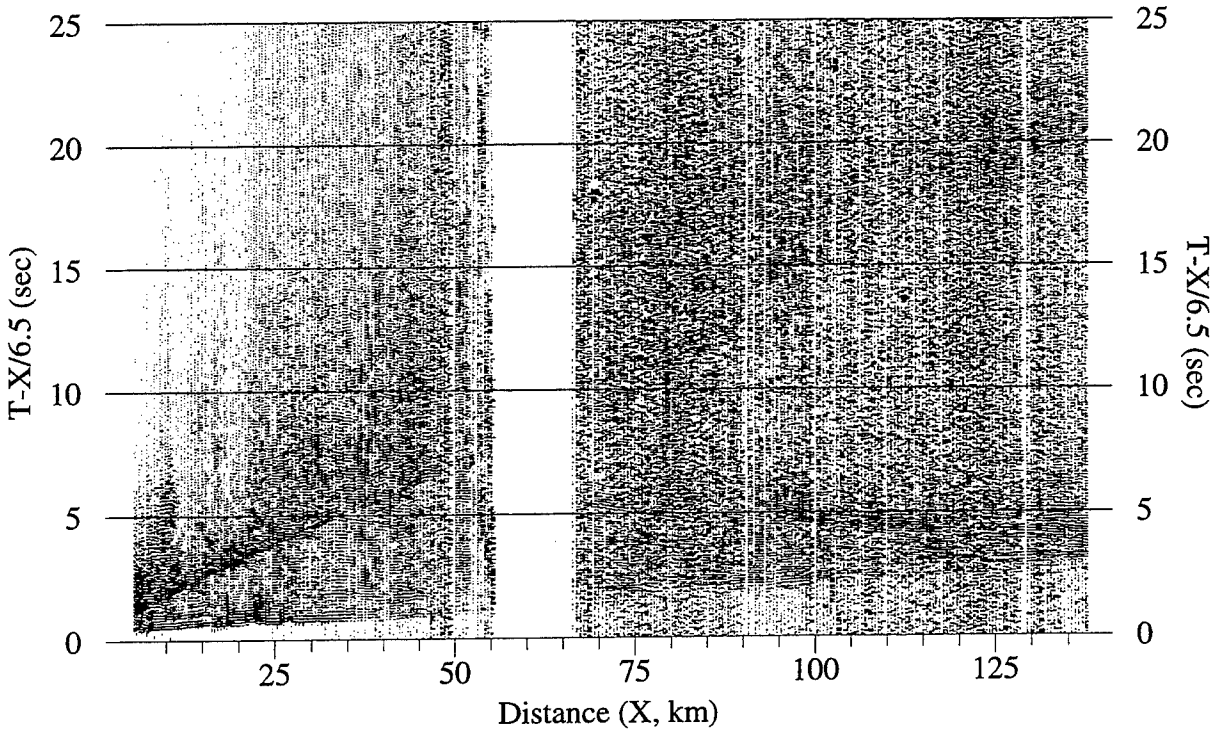

Figure 6. One of wide angle receiver gather acquired during the 1995 wide-angle experiment on the Barents Sea shelf. Crustal P- and S-wave refractions and Moho reflections, and some intracrastal reflections can be seen. These reflections were used to deleniate horizons shown in Figure 5.

IRREGULAR-GRID MODELING OF REGIONAL WAVE PROPAGATION

B. Nolte, R. L. Gibson, Jr., and M. N. Toksöz
Earth Resources Laboratory, MIT
Contract No. F19628-95-C-0091.
Sponsored by AFTAC

ABSTRACT

We present a method for the modeling of wave propagation in crustal models containing irregular topography, Moho or other interfaces. We parameterize the input model on an irregular triangular grid which is constructed as a Delaunay mesh. Particle velocity is computed on the vertices of this mesh, whereas stress is computed on a dual mesh which is obtained via Dirichlet tessellation. We express the momentum equation in integral form, and use a finite-volume (FV) approximation for its solution. The constitutive relation is approximated with finite difference (FD). The FV method has the advantage over FD techniques that grid points can be positioned on interfaces so that interfaces in a model can be represented more accurately and surface topography can be included in the model. Moreover, the grid spacing can vary throughout the model, which saves computation time, thus making the program well suited for the modeling of regional wave propagation.

Keywords: Finite difference, finite volume, irregular grid, regional wave propagation

OBJECTIVES

The task of reliably discriminating between nuclear explosions and earthquakes or mining events requires knowledge of the propagation effects for any area under investigation. Accurate full-waveform modeling capabilities for regional distances are therefore of vital importance for the monitoring of the CTBT. At regional distances (from roughly 150–2,000 km) the dominant observed signals are the P_g and L_g waves (e.g., Campillo, 1987). It is therefore of particular importance to numerically model the effect of complex geological structures on the propagation of these waves, especially the often observed blocking that occurs when they cross geological boundaries, such as grabens or mountain ranges (Ruzaikin et al., 1977; Kennett et al., 1985; Campillo et al., 1993).

Our current work is the development of a modeling program suitable to this task. Our goal, once the testing and optimization of the code is completed, is to model regional wave propagation in the Tornquist-Teisseyre Zone in Poland, an area where regional-wave blocking has been observed (Schweitzer, 1995).

Finite-difference (FD) methods are often employed for full-wavefield modeling in heterogeneous media (e.g. Vidale & Helmberger, 1988; Xie & Lay, 1994). However they have several drawbacks. For a given frequency the number of grid points needed to avoid numerical dispersion is a function of the wave speed; the lower the wave speed the more grid points are needed. Therefore, when performing FD modeling, one is usually forced to spatially oversample the model in most regions, which can lead to high computation times. Moreover, interfaces in a model have to be approximated by discrete steps in the grid. Therefore, if some part of the model has a detailed structure, the accurate representation of this structure may force dense grid spacing on the entire model. Finally, the modeling of surface topography can be problematic unless it is sufficiently smooth (Hestholm & Ruud, 1994).

For these reasons, we developed a method that allows the grid to be irregular and thus does not suffer from any of these disadvantages. It is based on a discrete approximation of the integral form of the wave equation, the FV approximation (e.g., Vinokur, 1988). Previously, FV has been applied to elastic wave propagation by Dormy and Tarantola (1995). While their algorithm uses FV to update both velocity and stress, our method uses FV only to update velocity, making it easier to implement absorbing boundary conditions. It also allows for easy coupling of the method to FD, which may be desirable as we will see later. Our algorithm is similar to that of Lee et al. (1994) for the modeling of electromagnetic wave propagation.

RESEARCH ACCOMPLISHED

So far we have developed both serial and parallel versions of the modeling code, and have implemented the latter on the nCUBE2 parallel computer of the Earth Resources Laboratory, using the Message Passing Interface (MPI). We are currently in a phase of testing and further optimizing the code. In addition, we have started to develop programs for the parameterization of input models on irregular grids. This work is still in progress.

Theory

Consider 2-D elastic wave propagation in the plane $y = 0$. For SH waves the momentum equation can be written in integral form as:

$$\iint_A dA\,\rho\frac{\partial v_y}{\partial t} = \oint_{\partial A} ds\,\sigma_{yn}. \tag{1}$$

Here v_y is the y-component of particle velocity, σ_{yn} is the y-component of stress on a surface element with normal $\hat{n}$, and ρ is the mass density. A is an area element with boundary ∂A.

For P/SV waves the equations are:

$$\begin{aligned}\iint_A dA\,\rho\frac{\partial v_x}{\partial t} &= \oint_{\partial A} ds\,(\sigma_{nn}\cos\phi - \sigma_{nt}\sin\phi)\\ \iint_A dA\,\rho\frac{\partial v_z}{\partial t} &= \oint_{\partial A} ds\,(\sigma_{nn}\sin\phi + \sigma_{nt}\cos\phi).\end{aligned} \tag{2}$$

In Eqs. (2) ϕ is defined as the angle between the x-axis and the surface normal $\hat{n}$, measured counterclockwise from x.

The constitutive relations for the SH case can be written as

$$\frac{\partial\sigma_{ny}}{\partial t} = \mu\frac{\partial v_y}{\partial n}, \tag{3}$$

and for the P/SV case as

$$\begin{aligned}\frac{\partial\sigma_{nn}}{\partial t} &= (\lambda+2\mu)(\frac{\partial v_x}{\partial n}\cos\phi + \frac{\partial v_z}{\partial n}\sin\phi)\\ \frac{\partial\sigma_{nt}}{\partial t} &= \mu(-\frac{\partial v_x}{\partial n}\sin\phi + \frac{\partial v_z}{\partial n}\cos\phi).\end{aligned} \tag{4}$$

Here λ and μ are the Lamé parameters.

Delaunay and Dirichlet Tessellations

For the spatial discretization of equations (1)–(4) we use Delaunay and Dirichlet tessellations (Fig. 1). They are defined as follows (e.g., Miller & Wang, 1994). Let Ω be a 2-D domain on which the variables in Eqs. (1)–(4) are defined. Let T be a partitioning of Ω by triangular elements and let $X = \{x_i\}$ denote the set of all vertices of T. Then T is a Delaunay mesh if, for any element of T, the circumcircle (the circle containing the three points of the triangle) of the element contains no other vertices in X (Delaunay, 1934). The Delaunay mesh is represented by solid lines in Fig. 1. The Dirichlet tessellation D corresponding to the Delaunay mesh T is defined by $D = \{d_i\}$ where

$$d_i = \{x \in \Omega : |x - x_i| < |x - x_j|, x_j \in X, j \neq i\}$$

for all $x_i \in X$. In other words, d_i describes the region that is closer to the Delaunay vertex x_i than to any other Delaunay vertex. The boundary ∂d_i of d_i is called the Voronoi polygon and is

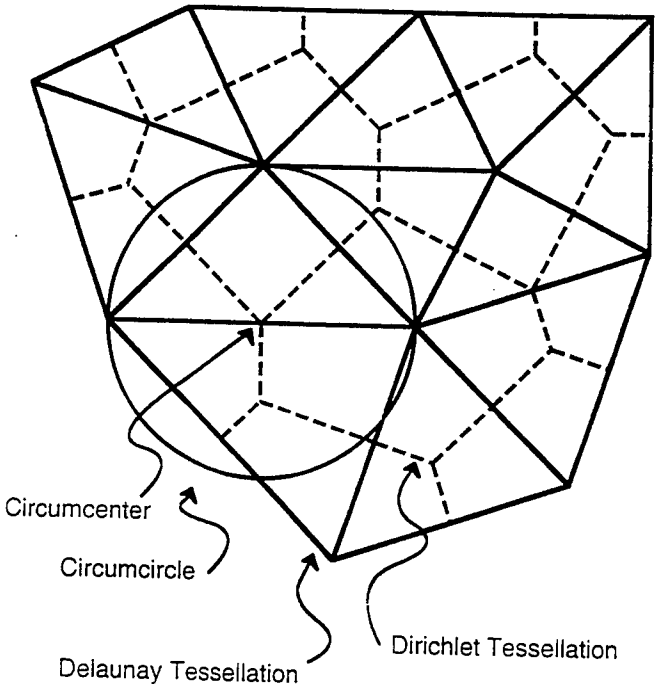

Figure 1: Delaunay mesh (solid) and Dirichlet tessellation (dashed). Also shown is a circumcircle of a Delaunay element having a vertex of a Voronoi polygon as its center.

obtained by connecting the circumcenters (the centers of the circumcircles) of the elements of T which have x_i in common. Voronoi polygons are shown as dashed lines in Fig. 1. Also shown is a circumcircle of a Delaunay element which can be seen to have its center at a Voronoi vertex. The Voronoi polygon has the important property that it consists of the perpendicular bisectors of the edges of the Delaunay triangles.

Discrete Equations

For the discretization of Eqs. (1)–(4) we use the indexing illustrated in Fig. 2. Velocities are updated on the vertices of the Delaunay grid while stresses are updated at the points where the Voronoi polygon intersects the Delaunay grid, i.e. halfway between the Delaunay vertices. The material properties ρ and μ are assumed to be constant within each Delaunay element. This is different from FD methods where the material properties are defined at the grid points. Equation (1) is then approximated as

$$\left(\sum_{k=1}^{N_k} A_{[j,k]}\rho_{[j,k]}\right)\frac{v_j^m - v_j^{m-1}}{\Delta t} = \sum_{k=1}^{N_k} \sigma_{[j,k]}^{m-1/2} l_{[j,k]}. \tag{5}$$

Here N_k is the number of neighbors of point j which is also the number of sides of the Voronoi polygon. $A_{[j,k]}$ is the area element indicated in Fig. 2, v_j^m is the y-component of the particle velocity at point j at the m-th time step, $l_{[j,k]}$ is the length of the line element on the Voronoi polygon between the velocity points k and j, and $\sigma_{[j,k]}$ is the normal stress on this line element.

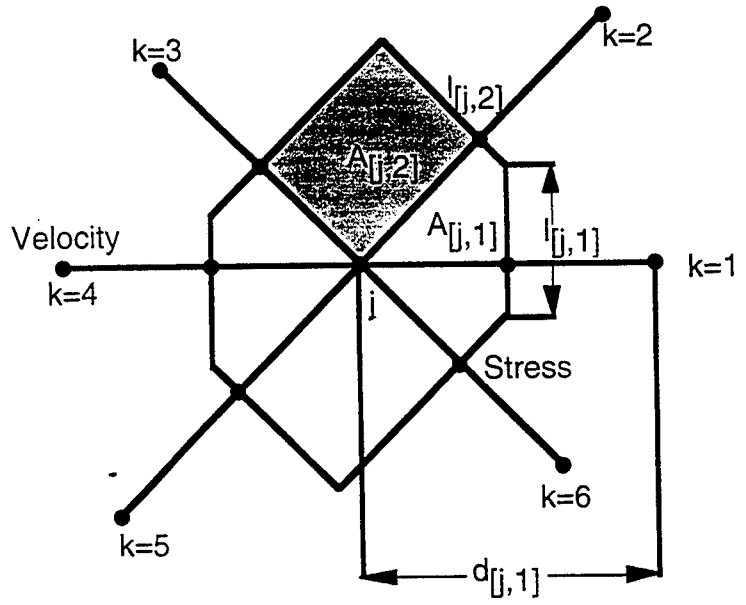

Figure 2: Indexing used for the computations. The particle velocities are defined at the Delaunay vertices (circles) and the stresses at the points marked by triangles. In order to update particle velocities the stresses are summed over the corresponding Voronoi polygons.

From Eq. (3) we obtain a discrete approximation for $\tau = \sigma_{ny}/\mu$:

$$\frac{\tau_{[j,k]}^{m+1/2} - \tau_{[j,k]}^{m-1/2}}{\Delta t} = \frac{v_k^m - v_j^m}{d_{[j,k]}} \tag{6}$$

Here, $d_{[j,k]}$ is the distance between the Delaunay vertices k and j. Note that the velocity is updated at time steps $m, m+1, m+2, \ldots$ while the stress is updated at time steps $m+1/2, m+3/2, \ldots$

In Eqs. (5) and (6) we have made use of the fact that $d_{[j,k]}$ is perpendicular to $l_{[j,k]}$ which is guaranteed by the properties of the Delaunay and Dirichlet tessellations described above. This means that Eq. (6) always computes the stress normal to the line element $l_{[j,k]}$, which is what we desire. From Eqs. (5) and (6) we obtain our final equations for the updating of velocity and stress:

$$v_j^m = v_j^{m-1} + \left(\frac{\Delta t}{\sum_{k=1}^{N_k} A_{[j,k]} \rho_{[j,k]}} \right) \sum_{k=1}^{N_k} l_{[j,k]} \mu_{[j,k]} \tau_{[j,k]}^{m-1/2} \tag{7}$$

$$\tau_{[j,k]}^{m+1/2} = \tau_{[j,k]}^{m-1/2} + \Delta t \frac{v_k^m - v_j^m}{d_{[j,k]}}. \tag{8}$$

For the P/SV case we obtain analogously (with $\eta = \sigma_{nn}/(\lambda + 2\mu)$ and $\xi = \sigma_{nt}/\mu$):

$$v_{xj}^m = v_{xj}^{m-1} + \left(\frac{\Delta t}{\sum_{k=1}^{N_k} A_{[j,k]} \rho_{[j,k]}} \right) \sum_{k=1}^{N_k} l_{[j,k]} [(\lambda_{[j,k]} + 2\mu_{[j,k]}) \eta_{[j,k]}^{m-1/2} \cos\phi - \mu_{[j,k]} \xi_{[j,k]}^{m-1/2} \sin\phi]$$

$$v_{zj}^{m} = v_{zj}^{m-1} + \left(\frac{\Delta t}{\sum_{k=1}^{N_k} A_{[j,k]}\rho_{[j,k]}}\right) \sum_{k=1}^{N_k} l_{[j,k]}[(\lambda_{[j,k]} + 2\mu_{[j,k]})\eta_{[j,k]}^{m-1/2} \sin\phi + \mu_{[j,k]}\xi_{[j,k]}^{m-1/2} \cos\phi] \quad (9)$$

and

$$\eta_{[j,k]}^{m+1/2} = \eta_{[j,k]}^{m-1/2} + \frac{\Delta t}{d_{[j,k]}}[(v_{xk}^{m} - v_{xj}^{m})\cos\phi + (v_{zk}^{m} - v_{zj}^{m})\sin\phi]$$

$$\xi_{[j,k]}^{m+1/2} = \xi_{[j,k]}^{m-1/2} + \frac{\Delta t}{d_{[j,k]}}[-(v_{xk}^{m} - v_{xj}^{m})\sin\phi + (v_{zk}^{m} - v_{zj}^{m})\cos\phi]. \quad (10)$$

Boundaries

The free-surface boundary condition can be easily satisfied by Eqs. (7) and (9). These equations can be directly applied to updating the particle velocity on the free surface. The condition there is that the stress vanishes. Therefore instead of summing the stress over a closed curve in Eqs. (7) and (9), as in the interior of the region, the stress is summed over an open curve at the free surface. Note that there is no need for the surface to be flat. Thus, surface topography can be included in the model.

At all other boundaries we implement absorbing boundary conditions. This is done in the same way as in standard FD schemes. We use Higdon's (1987) boundary condition, which is of the form

$$\prod_{j=1}^{p}(\cos\theta_i \frac{\partial}{\partial t} - \alpha\frac{\partial}{\partial x_k})v = 0 \quad (11)$$

where i is the order of the boundary condition, θ_i is the incident angle of maximum absorption, α is the wave speed and x_k is $+x/-x/+z$ for the right/left/bottom boundary. The derivatives w.r.t. x and z have to be computed from the derivatives w.r.t. n. The absorbing boundary conditions are only applied to velocity. The stress is updated as before (Eqs. (8) and (10)).

Parallel Implementation

As mentioned above, we have implemented the algorithm in parallel using MPI. An efficient parallel implementation of our method is more difficult than of standard FD. An optimal grid decomposition is considerably more complicated because for irregular grids the position of an element in the array of grid points bears no direct relation to the location of that grid point, i.e., neighboring points in the model are not offset in a systematic fashion in the array. In our current implementation we have therefore subdivided the grid in such a way that each node communicates with at most two other nodes (see Fig. 3). We distribute stress and velocity points approximately equally among different nodes in such a way that each node has on one of its boundaries all the stress points required to update its own velocity points, while on the other boundaries it has all the velocity points required to update its own stress points. Thus, at each boundary between two nodes, one of the nodes needs to receive velocities only, while the other needs to receive stress points only (see Fig. 3).

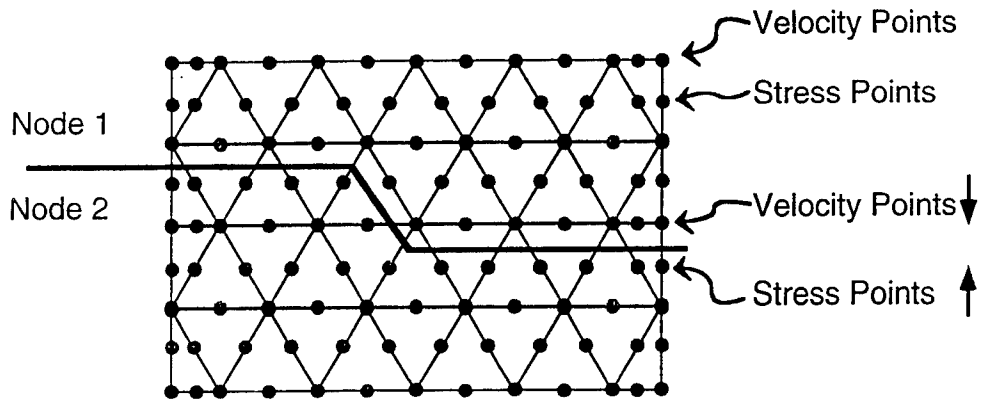

Figure 3: Parallel implementation of the algorithm. Node 1 is sending velocity points to and receiving stress points from node 2 and vice versa.

Numerical Example

We test our method on the two-layer crustal model shown at the top of Fig. 4. The only interface present is the Moho. This represents a strongly simplified model of the Tornquist-Teisseyre Zone. The velocities and densities of the lower crust and upper mantle are based on Guterch et al. (1986), and data for the Moho topography were obtained from the Cornell Middle East/North Africa Project Online Profile Maker (http://www.geo.cornell.edu/geology/me_na/main.html). Figure 4 shows a series of snapshots of the total amplitudes of the waves propagating in this model. The source was a horizontal point force exciting horizontally propagating P-waves. The snapshots and Moho profile are plotted with a vertical exaggeration of 2.5.

CONCLUSIONS AND RECOMMENDATIONS

The FV method is an attractive alternative to FD that allows the model to be parameterized on an irregular grid. The flexibility in positioning the grid points allows using fewer grid points than required by FD to obtain accurate results. There are, however, some drawbacks. First, as mentioned above, the parallelization is more difficult. Then, our method, like any method that uses irregular grids, requires some computer memory to store the grid geometry making the total memory requirement higher than that of FD methods. A possible way to take advantage of the strong points of both methods would be the coupling of FV and FD. FV could be used at depth regions where structure is present, whereas FD could be used in homogeneous depth regions and in regions with velocity gradients. FV might be particularly useful for the near-surface part of the model because of its potential to model surface topography. The coupling of FV and FD is

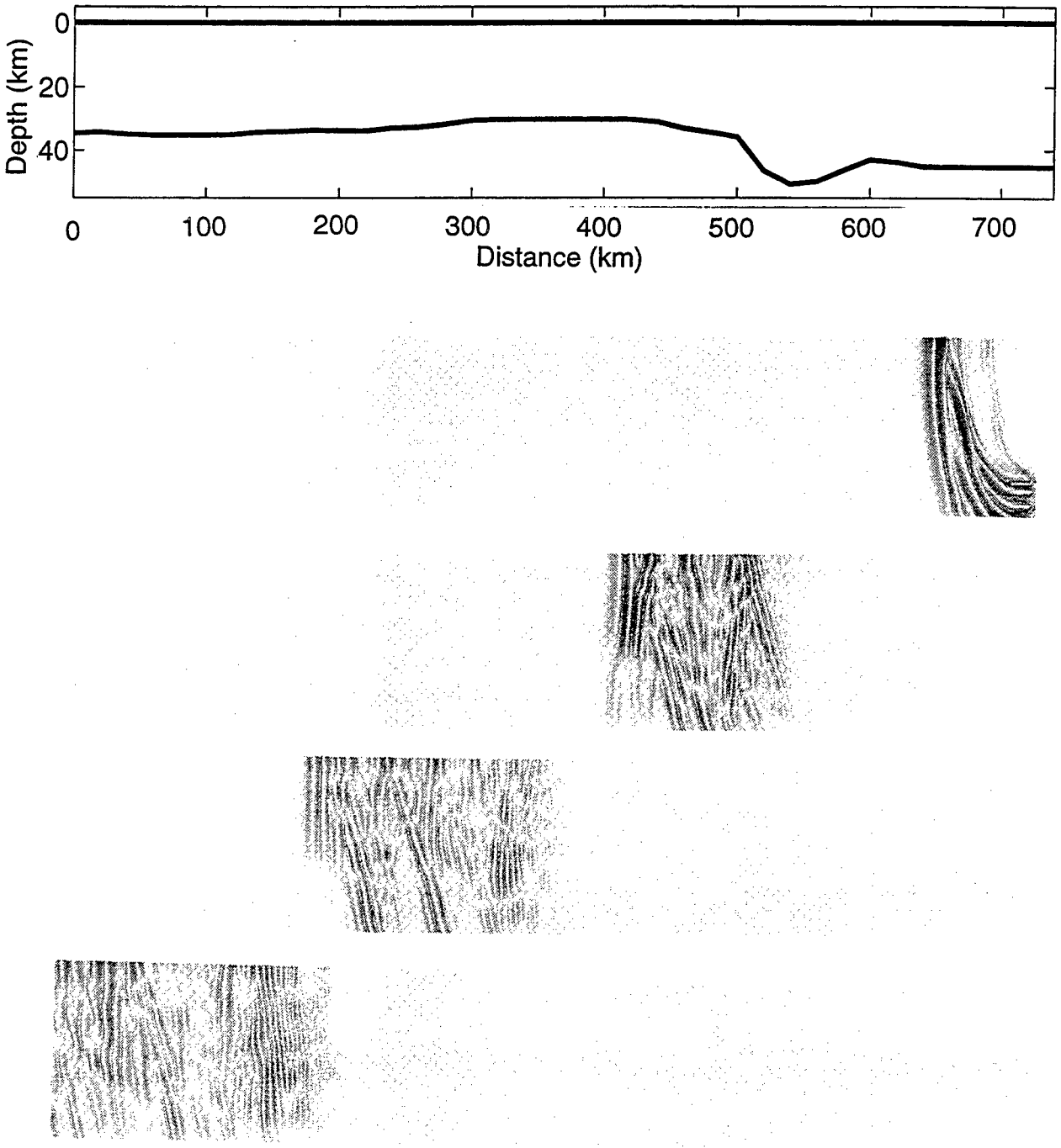

Figure 4: Moho Topography (top) and snapshots of the total amplitude at 12 s, 48 s, 84 s, and 120 s. The elastic parameters are $\alpha = 7.2$ km/s, $\beta = 4.3$ km/s, $\rho = 3.3$ g/cm^3 for the crust and $\alpha = 8.3$ km/s, $\beta = 4.5$ km/s, $\rho = 3.5$ g/cm^3 for the mantle.

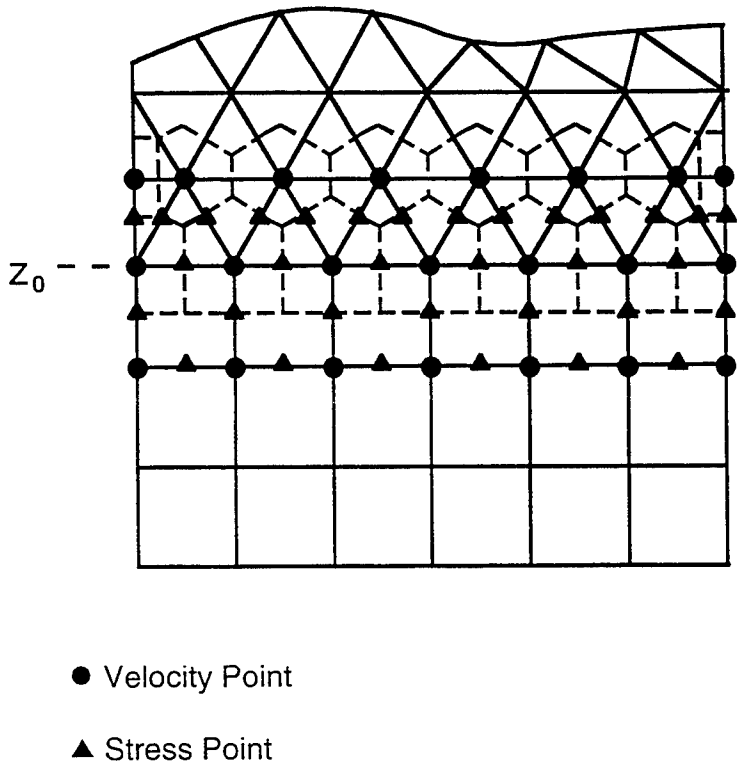

Figure 5: Possible coupling of FV and FD. In this figure FV is used only for the near-surface part of the model ($z \leq z_0$). At greater depth FD is used.

illustrated in Fig. 5. In this sketch FV is used to update velocity points at depths z_0 and above, and FD is used to update velocity points at depths below z_0. We plan to implement this coupling.

A different problem is the computation of the irregular grid itself. In particular, one has to take care that the velocity points are positioned in such a way that each interface in the model is aligned with the edge of a Delaunay triangle. We are currently developing such model parameterization algorithms.

Planned future work also includes a more efficient parallelization of the algorithm. Our current parallelization technique is not optimal because the fact that each node communicates with at most two other nodes results in a high communication-to-computation ratio. We plan to change this in a future version of the code.

We also plan to extend our method to 3-D. In 3-D the velocity grid will be tetrahedral instead of triangular and the summations in Eqs. (7) and (9) will be over volumes instead of areas and areas instead of lines.

On the application side we plan to perform extensive modeling of regional wave propagation across the the Tornquist-Teisseyre Zone using data obtained at the German Experimental Seismic System (GERESS) (Harjes, 1990). The models of Guterch et al. (1986) and Schweitzer (1995) will serve as a starting point for this project.

REFERENCES

Campillo, M., 1987. L_g wave propagation in laterally varying crust and the distribution of the apparent quality factor in Central France, *J. Geophys. Res., 92*, 12604–12614.

Campillo, M., Feignier, B., Bouchon, M., and Bethoux, N., 1993. Attenuation of crustal waves across the Alpine range, *J. Geophys. Res., 98*, 1987–1996.

Delaunay, B. N., 1934, Sur la sphere vide, *Bull. Acad. Science, USSR VII: Class. Sci. Math.*, 793–800.

Dormy, E. and Tarantola, A., 1995, Numerical simulation of elastic wave propagation using a finite-volume method, *J. Geophys. Res., 100*, 2123–2133.

Guterch, A., Grad, M., Materzok, R. and Perchuc, E., 1986. Deep structure of the earth's crust in the contact zone of the palaeozoic and precambrian platforms in Poland (Tornquist-Teisseyre Zone), *Tectonophysics, 128*, 251–279.

Harjes, H.-P., 1990. Design and siting of a new regional seismic array in Central Europe, *Bull. Seis. Soc. Am., 80*, 1801–1817.

Hestholm, S. and Ruud, B., 1994. 2D finite-difference elastic wave modelling including surface topography, *Geophys. Prosp., 42*, 371–390.

Higdon,, R. L., 1987, Numerical absorbing boundary conditions for the wave equation, *Math. Comp., 49*, 65–90.

Kennett, B. L. N., Gregersen, S., Mykkeltveit, S. and Newmark, A., 1985. Mapping of crustal heterogeneity in the North Sea basin via the propagation of L_g waves. *Geophys. J. R. ast. Soc, 83*, 299–306.

Lee, C. F., McCartin, B. J., Shin, R. T., and Kong, J. A., 1994. A triangular-grid finite-difference time-domain method for electromagnetic scattering problems, *J. Electromagnetic Waves and Applications, 8*, 449–470.

Miller, J. H. and Wang, S., 1994. An exponentially fitted finite volume method for the numerical solution of 2-D unsteady incompressible flow problems, *J. Comp. Phys., 115*, 56–64.

Ruzaikin, A. I., Neresov, I. L., Khalturin, V. I., and Molnar, P., 1977. Propagation of L_g and lateral variations of crustal structure in Asia. *J. Geoph. Res., 82*, 307–316.

Schweitzer, J., 1995. Blockage of regional seismic waves by the Teisseyre-Tornquist zone. *Geophys. J. Int., 123*, 260–276.

Vidale, J. E. and Helmberger, D., 1988. Elastic finite-difference modeling of the 1971 San Fernando, California earthquake, *Bull. Seis. Soc. Amer., 78*, 122–144.

Vinokur, M., 1988. An analysis of finite-difference and finite-volume formulations of conservation laws, *J. Comp. Phys, 81*, 1–52.

Xie, X.-B. and Lay, T., 1994. The excitation of L_g waves by explosions: a finite-difference investigation, *Bull. Seis. Soc. Amer., 84*, 324–342.

The Effects of Seismic Anisotropy on Regional Seismic Wave Propagation

PI: Jeffrey Park
Co-Workers: Vadim Levin & Liqiang Su
Department of Geology and Geophysics, Box 208109
Yale University, New Haven, CT 06520-8109
Contract: F49620-94-1-0043
Sponsored by AFOSR

ABSTRACT

We have examined the effect of seismic anisotropy on the scattering of surface and body waves in actively-deforming continental regions, many of which occur in areas of nonproliferation concern. We have concentrated on three topics in the past year: 1) we developed a flat-layered surface wave synthetic seismogram code to study the effect of crust and upper-mantle anisotropy on synthetic seismograms, 2) we adapted this synthetic code to compute the effect of crustal anisotropy on the generation of body-wave coda, and 3) we applied wavelet-based signal processing methods to estimate the polarization of coherent seismic energy across the Terrascope broadband seismic array in Southern California. Most previous studies have posited a horizontal or vertical axis of symmetry for seismic anisotropy, but our 1-D layered code can incorporate a tilted axis of symmetry, which enhances Love-Rayleigh coupling and scattering effects. An explosive source in a crust with plausible anisotropy is predicted by this code to 'radiate' Love waves that mimic a secondary thrust mechanism. Using the 1-D anisotropic code, P-to-SH converted waves on the transverse component of the P-coda can be modelled either by trial-and-error forward modelling, or via a genetic-algorithm model search. P-coda data from seismic stations in Eurasia can be modelled, at least partially, by these anisotropic reverberation effects. The wavelet-based method for detecting frequency-dependent polarization in Terrascope data finds a strong refraction of intermediate-period surface waves along the "big-bend" portion of the San Andreas Fault. Coupled-mode waveform modelling suggests that an upper-mantle anisotropic structure, consistent with shear-wave splitting measurements, is a more likely cause of this refraction than are variations in isotropic seismic velocities. This highlights the potential influence of anisotropic variations on back-azimuth anomalies that hamper the accuracy of source locations.

Keywords: seismic anisotropy, surface waves, P-coda reverberation, wavelets, array methods, surface-wave polarization.

OBJECTIVES

We wish to determine the effect of seismic anisotropy, within the crust and uppermost mantle, on surface waves with periods between 10 and 30 seconds. In particular, we wish to characterize the scattering caused by lateral variations in anisotropy in regions of past and present lithospheric deformation. This path-dependent scattering can distort seismic waveforms, and make more difficult the discrimination of explosions from earthquakes. We plan to identify regions of the Earth where scattering associated with lithospheric anisotropy is important. Data from regional networks and arrays located in Eurasia and the US will also be used in experiments to extract 'scattered' waveforms from the principal Love and Rayleigh wavepackets. In addition to standard stacking/beamforming techniques, we will develop a frequency-dependent variant of the MUSIC algorithm to identify coherent surface waves that traverse an array. We plan to test, in selected areas, whether anisotropy inferred from the 'splitting' of 1-20 second shear waves is sufficient to explain observed Love to Rayleigh scattering.

RESEARCH ACCOMPLISHED

In last year's symposium paper, we anticipated submitting manuscripts for publication in three areas: (1) on the array-version of the multiple-wavelet transform, with application to regional network data; (2) on the hybridization of Love and Rayleigh waves in 1-D anisotropic structures; (3) on the effect of receiver-side 1-D anisotropy, with an arbitrary symmetry axis, on upgoing body waves. Manuscripts on these three topics have been submitted to journals - (1) is being revised after review; (2) is due for publication this summer, and (3) was submitted at the start of June. In addition to these papers, we are 1) incorporating lateral anisotropic structure into the Love-Rayleigh surface wave coupling problem by means of a simplified path-integral approximation, and 2) looking at the azimuthal dependence of P-SH converted phases in data from global seismic stations in Eurasia. The first project has thusfar found theoretical justification for several empirical rules-of-thumb for Love-Rayleigh coupling. The second project has found good evidence that a 1-D anisotropic crust may explain some puzzling features in the coda of steeply-incident P waves.

We have developed synthetic-seismogram codes for crustal surface waves in 1-D anisotropic media, with an axis of symmetry that can be chosen independently in each layer. A modification of this code was used to examine the behavior of teleseismic body waves that propagate upward through an anisotropic crustal structure. Enhanced coupling between P-SV and the SH particle motion occurs for waves that have either a significant non-vertical incidence, or else impact anisotropy with a tilted axis of symmetry Previous investigations used symmetry axes that were either vertical or horizontal. However, a tilted axis of symmetry is plausible in the uppermost crust and perhaps near the Moho, where thrusting and extension involves a combination of vertical and horizontal deformation.

Surface Wave Applications: Surface waves confined to the Earth's crustal waveguide typically exhibit strong scattering effects, most notably where explosive sources generate large amplitudes on the transverse component. Since such scattering does not occur for surface waves in a laterally homogeneous isotropic earth model, efforts at modeling have examined the effects of 3-D structure

and anisotropy. Large-amplitude small-scale structure seems required if attention is restricted to 3-D isotropic models, and methods based on phase-screens (Wu, 1994; Fisk & McCartor, 1993) and finite difference (Levander & Hollinger, 1992) have been applied, typically using a stochastically-generated velocity model. The justification for this approach is the large amount of small-scale variation in rock composition and properties evident in outcrop (Goff et al 1994). However, elastic anisotropy can also generate significant scattering. Large amounts of elastic anisotropy (> 20%) are evident in many crustal minerals e.g. hornblendes and micas (Babuska & Cara, 1991), to which must be added the velocity anisotropy associated with aligned cracks within rocks (Crampin, 1984), and the directional effects of small-scale compositional layering on wave speed (Backus, 1962).

We have developed and implemented a reflectivity-based algorithm to calculate surface wave motion in a layered anisotropic structure, in which the anisotropy can be expressed as a deviation from isotropy with a particular axis of symmetry, or a linear combination of such deviations. In some cases where both upgoing (and/or both downgoing) quasi-shear plane wave are evanescent within a layer, their particle motion vectors can become nearly parallel, leading to numerical instability. This can sabotage automatic rootfinding algorithms for the surface-wave dispersion curves. We developed an alternate solution for propagating waves within the layer, which removes this instability in these exceptional cases.

Because the dispersion characteristics of higher-mode Love and Rayleigh surface wave are quite similar, they can suffer strong coupling in a layered anisotropic structure. With plausible levels of crustal anisotropy, Rayleigh-dominant surface wave overtones can exhibit SH-amplitudes at the surface that are 15-25% of total displacement. The SH-waveforms are typically not coherent with P-SV motion, and so appear as a scattered wave, not a polarization anomaly (Figure 1). Because these overtones, which combine to form the L_g phase, are composed of multiply reflected S waves trapped in the full crust, the precise location of anisotropy with depth has only a modest influence on the strength of Love-Rayleigh 'scattering.' Fundamental-mode Love and Rayleigh waves have strongly different dispersion behavior, and so are more weakly coupled.

Synthetic seismograms for crustal models demonstrate that significant Love-to-Rayleigh and Rayleigh-to-Love "scattering" can occur in the absence of lateral variation in seismic properties. This scattering depends on the azimuth relative to the axis of symmetry $\hat{\mathbf{w}}$, suffering polarity reversals that resemble the effect of a spurious addition to the source mechanism (Figure 2). Surface waves from explosive sources in an anisotropic crust will appear to have a component of 'tectonic release,' with fault and auxilary planes parallel and perpendicular to the anisotropic axis of symmetry.

Body Wave Applications: The occurrence of P-to-SH conversion is common in teleseismic P waves, and has been observed in a variety of tectonic environments. Two explanations, besides misaligned seismometers, are typically offered: a) ray divergence from the great circle path due to velocity heterogeneities (e.g., *Visser & Paullsen* 1993, *Hu* 1993) and b) the presence of inclined interfaces beneath the receiver (e.g., *Owens & Crosson* 1988, *Zhu et al.* 1995). Our modeling suggests an alternative explanation in terms of flat-layered anisotropy. If all velocity discontinuities in a medium are horizontal, their cumulative effect on an upgoing seismic wave may be represented by a "transmission response," readily calculated for any number of interfaces using reflectivity techniques. We use this approach to compute 3-component synthetic seismograms in a 1-D anisotropic

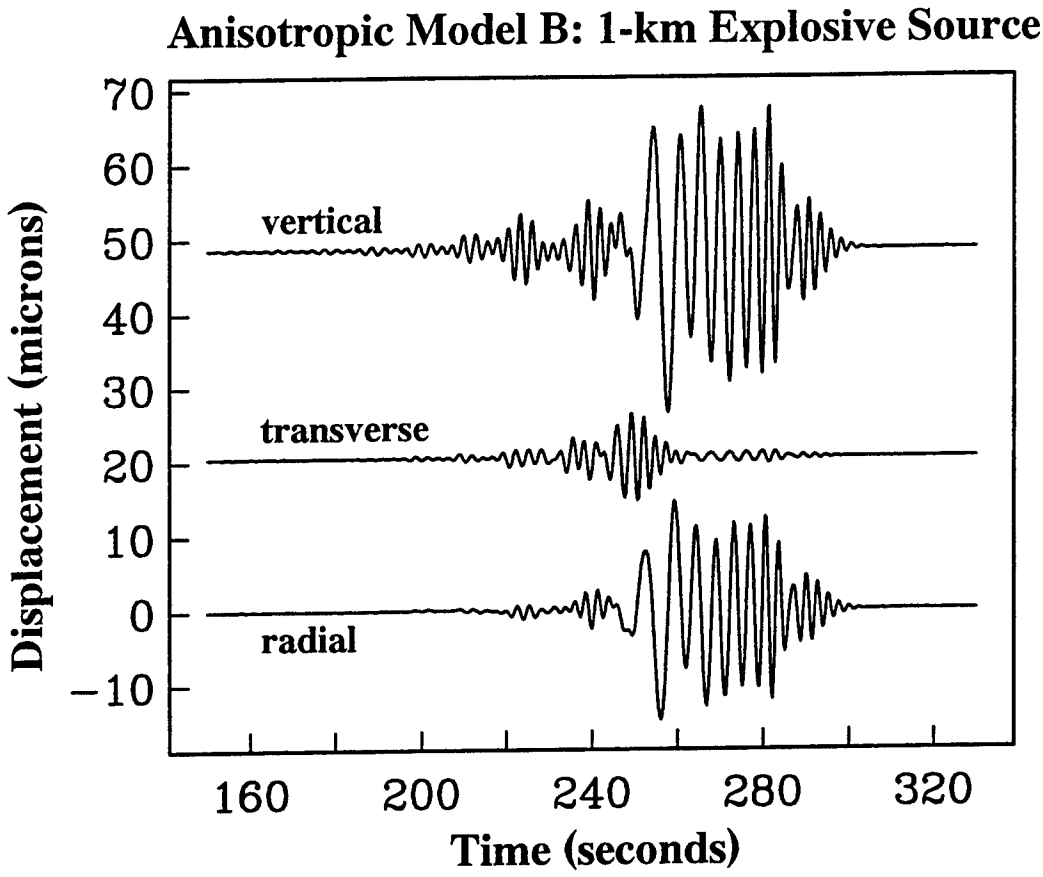

Figure 1. Surface-wave particle motion for anisotropic crust with 4% and 2% peak-to-peak variation in P- and S-velocity, respectively, in the upper and middle crust, with axis of symmetry at 45° strike to the propagation direction, and tilted 30° above the horizontal in the upper 4 km. The station is 800 km from an explosive source at 1 km depth, for which the nominal Love-wave radiation is zero. Note the particle motion on the transverse component, which comprises both a "scattered" Love-wave and the expression of a tilted Rayleigh ellipse.

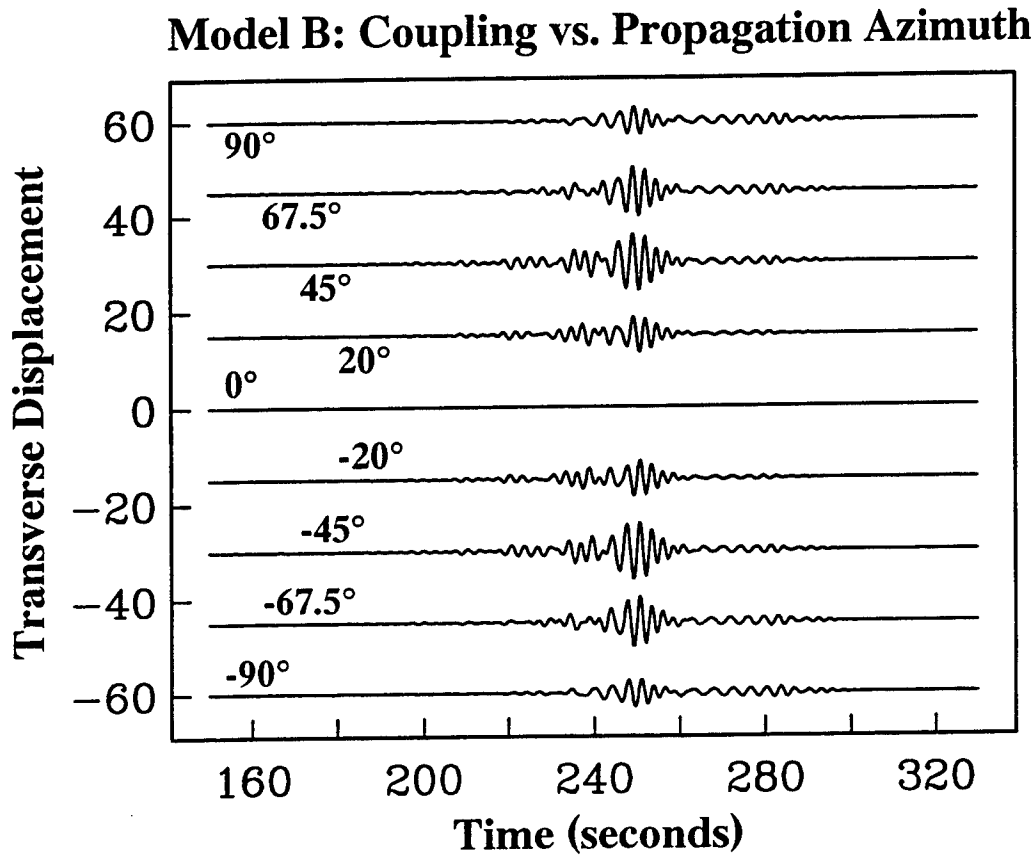

Figure 2. Transverse-component particle motion for the same anisotropic crustal model for an explosive source at 1 km depth, at a range of propagation azimuths, ranging from −90° to 90° relative to the projection of $\vec{w}$ on the horizontal plane. Note the azimuthal variation of the "scattered" Love wave amplitude, which resembles that of a thrust earthquake.

layered medium. A compressional wave in an anisotropic velocity structure suffers conversion to both SV- and SH-polarized shear waves, unless the axis of symmetry is everywhere vertical or the wave travels parallel to all symmetry axes.

The P-to-SV conversion forms the basis of the widely used "receiver function" technique. The P-to-SH conversion occurs at interfaces where one or both layers are anisotropic. A tilted axis of symmetry and a dipping interface in isotropic media produce similar amplitudes of both direct (P) and converted (Ps) phases. The relative timing of the P and Ps phases is the main discriminant between anisotropy and a tilted interface. For equivalent transverse-component amplitudes, the tilted interface has larger azimuthal variation (typically 0.5-1.0 second) in the $P - Ps$ differential arrival time. Seismic anisotropy with a tilted symmetry axis leads to complex synthetic seismograms in velocity models composed of just a few flat homogeneous layers. It is possible therefore to model observations of P codas with prominent transverse components with relatively simple 1-D velocity structures (Figure 3).

Using a genetic algorithm search technique, we estimated the potential for nonuniqueness in the interpretation of such data. Synthetic inversion tests argue that anisotropy near large velocity jumps can be detected with some confidence, but that a single P coda can be fit adequately by models with quite different isotropic velocity profiles. Joint analysis of observations from different azimuths may be necessary to constrain the anisotropic symmetry-axis adequately.

With this in mind, we compiled P-coda data sets from selected Eurasian stations of the Global Seismographic Network (GSN) that cover broad ranges of back-azimuth. The polarity of a P-to-SH converted phase should exhibit $\sin(\phi - \phi_o)$ dependence, where ϕ is back azimuth, and ϕ_o is the azimuth of the anisotropic symmetry axis (or else the strike of a dipping interface). Although we restrict the data set to deep earthquakes, free of near-source reverberations, source complexities make direct comparison of seismic waveforms difficult. Instead, we deconvolve the source using the time-domain receiver-function technique used by Sheehan et al (1995), which can combine data from multiple events in narrow ranges of back-azimuth. At several stations (e.g. ARU, YSS, YAK in eastern Russia) pulses in the transverse-component receiver function show polarity reversals with back-azimuth, strongly suggesting that they are generated by either anisotropy or significantly tilted crustal interfaces (Figure 4). Although modelling of this data remains to be done, we note that a similar azimuthal sweep in P-codas from Tibet was interpreted by Zhu et al (1995) to require an interface tilt of 25° and a 20% velocity inversion. (Only amplitudes were modelled, not P-Ps differential travel times.) In such a context, anisotropies of 5-15% in the upper crust may seem less implausible.

Array Polarization Studies: We applied a multiple-station seismic analysis method, based on Slepian wavelets (Lilly and Park, 1995), to 20–200 sec surface wave data from the Terrascope regional network in Southern California. Unlike conventional stacking techniques, this method uses a singular-value-decomposition (SVD) to allow for differing polarization behavior among stations, and can be used to detect amplitude and polarization anomalies *within* a seismic array or regional network. Multiwavelet polarization analysis detects weak amplitude anomalies, but strong polarization anomalies, within the aperture of Terrascope. The singular values of the SVD show that array-correlated Rayleigh and Love waves are retrieved well. For events in the western and southwest Pacific, surface wave observations at inland stations suffer significant 'refraction' relative

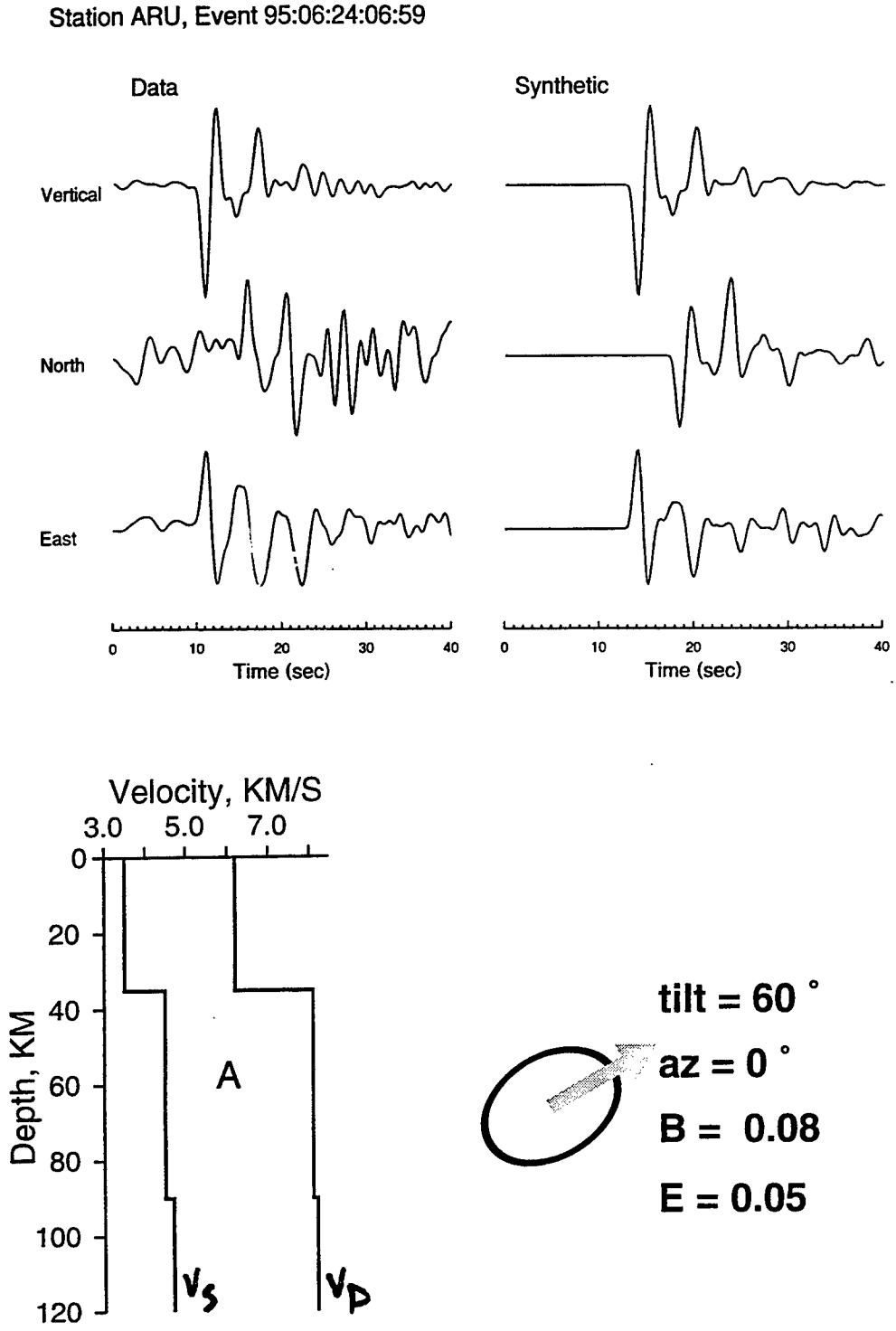

Figure 3. Example of forward modeling the P-coda using a simple anisotropic structure. Observed seismogram at ARU (Arti, Russia) for the 24 June 1995 earthquake, at 390 km depth, in the New Ireland region. Data is shown by left traces, synthetics by right traces. Scaling of traces is relative. The timing and approximate waveform of the converted phase on the transverse component is matched by a 50-km thick layer in the uppermost mantle with 8% and 5% peak-to-peak variations in P- and S-velocity, respectively, with an axis of symmetry inclined 60° from the vertical, with roughly north-south strike.

Figure 4. Sweep of back-azimuth (130°–210°) for radial- and transverse-component receiver functions for station YAK (Yakutia, Russia). Each trace is processed from the P-coda of a single deep earthquake. Scaling is absolute. Note, especially in the first 5 seconds, how the radial-comp receiver function varies little with azimuth. For the transverse component, note how the first 3 seconds of the receiver-functions at 200° back-azimuth switch the polarity of the traces at 130° azimuth. Composite receiver functions derived from groups of records confirm this polarity reversal, with near-zero response near 170° back-azimuth. Shallow anisotropy with a north-south azis of symmetry could explain such behavior. Note also the polarity reversal on the transverse component at 6.5 seconds, suggesting P-to-SH conversion at a deeper interface.

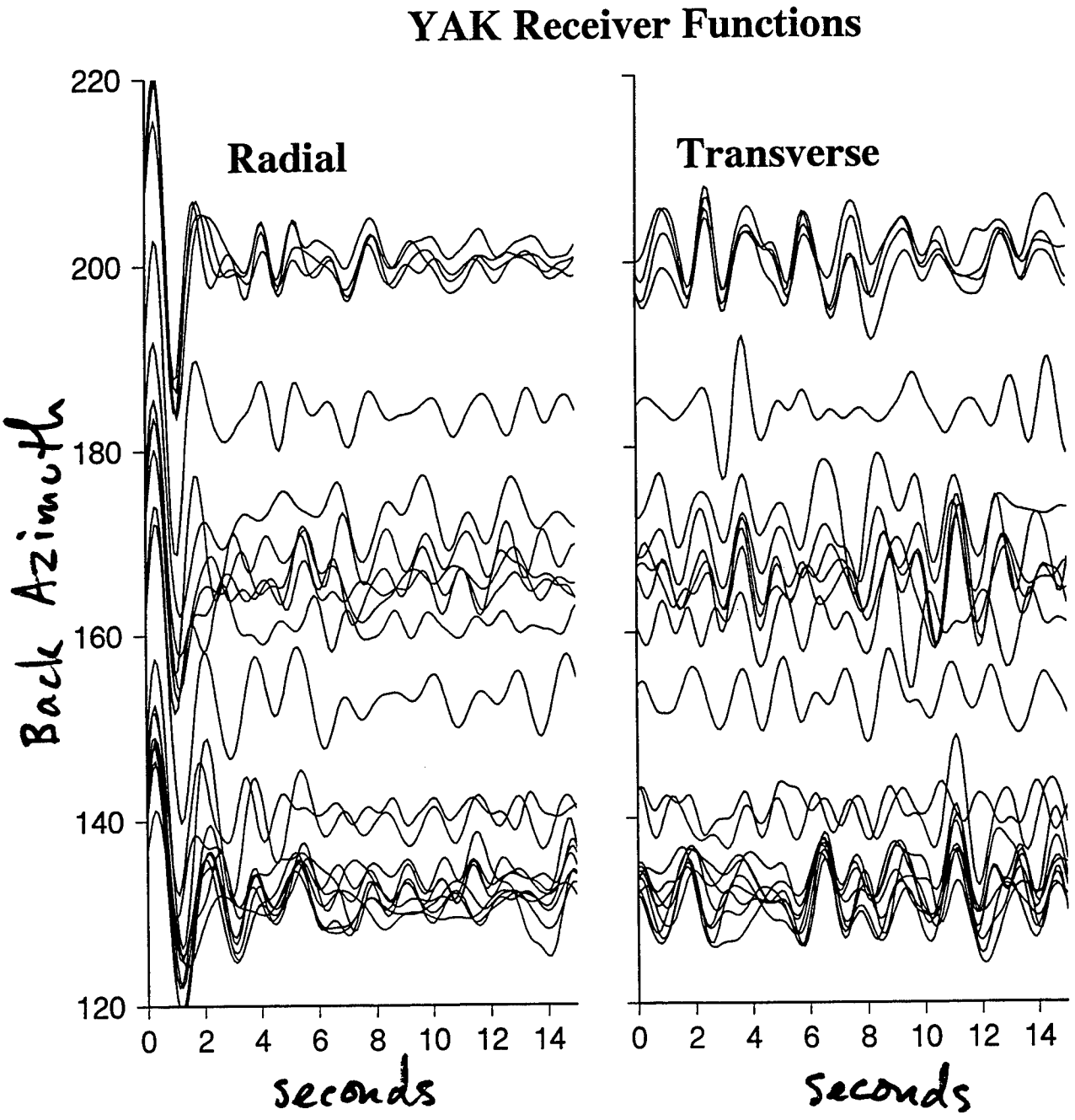

to the great-circle path, while the coastal stations suffer little polarization anomaly.

In order to interpret the array-polarization estimates of surface waves, we computed synthetic seismograms using coupled free oscillations for idealized isotropic and anisotropic models of the uppermost mantle beneath Southern California. The fast mantle root of the Transverse Ranges has been inferred from body-wave traveltime inversion (Humphreys and Clayton, 1990; Revenaugh, 1995) to express regional compression related to the "big bend" of the San Andreas Fault in southern California. Its high-velocity mantle root has been modelled by Humphreys and Hager (1990) as a small-scale convection feature in the upper mantle. In the same region, Liu et al (1995) reported strong SKS splitting with an east-west fast axis. For an anisotropic model, we prescribed 6% P wave and 4% S wave anisotropy in the block with an east-west fast axis, an orientation consistent with both shear-wave splitting and regional compression. Although we set an unreasonably high S wave velocity perturbation of 20% for the isotropic model, it fails to explain the observed polarization anomalies, especially when compared with the more modest perturbations of the anisotropic model. The waveform comparison suggests that anisotropy is an important influence on the surface wave propagation direction, and that Terrascope particle-motion deflections confirm the existence of upper-mantle anisotropy beneath southern California.

The following papers have been supported by this contract thusfar:

Yu, Y., J. Park & Wu, F., 1995. Mantle anisotropy beneath the Tibetan Plateau: evidence from long-period surface waves, *Phys. Earth and Planet. Int.*, , *87*, 231–246.

Lees, J., and J. Park, 1995. Multiple-taper spectral analysis: A standalone C-subroutine, *Computers and Geosciences, 21,* 199–236.

Park, J., 1995. Seismic wave propagation studies in the US: 1991-1994, US National Report to the IUGG, *Reviews of Geophysics Supplement, 33*, 335–340.

Lilly, J. and J. Park, 1995. Multiwavelet spectral and polarization analysis of seismic records. *Geophys. J. Int., 122*, 1001–1021.

Park, J., 1996. Surface waves in layered anisotropic structures, *Geophys. J. Int.* in press.

Su, L., and J. Park, 1996. Asymptotic path integral synthetics using the strong Born approximation, *Geophys. J. Int.*, in review.

Su, L., and J. Park, 1996. Multiwavelet spectrum and polarization analysis of Terrascope network data *Bull. Seism. Soc. Amer.*, in review.

Levin V. and J. Park, 1996. $P - SH$ conversions in a flat-layered medium with anisotropy of arbitrary orientation *Geophys. J. Int.*, in review.

CONCLUSIONS AND RECOMMENDATIONS

Conclusions: Synthetic seismograms for anisotropic crustal models demonstrate that significant Love-to-Rayleigh and Rayleigh-to-Love "scattering" can occur in the absence of lateral variation in seismic properties. This scattering depends on the angle between wave-propagation and the axis of symmetry $\hat{\mathbf{w}}$, and can cause Love-Rayleigh scattering to resemble a spurious addition to the source mechanism. This effect could masquerade as 'tectonic release' in some settings.

Synthetic seismograms show that a simple volume of modestly anisotropic rock can cause significant surface wave refraction and polarization anomalies in the 20-100 sec range, more efficiently

than an isotropic velocity gradient. Array-polarization analysis of Terrascope data suggests a significant anisotropy in the mantle beneath southern California, consistent with the direction inferred from shear-wave splitting in and around the Transverse Ranges. This result suggests that crustal anisotropy may cause significant arrival-azimuth deviations in surface waves.

Codas of steeply incident P waves with prominent transverse components can be modelled with relatively simple 1-D velocity structures. The $P-SH$ conversion occurs at interfaces where one or both layers are anisotropic. A tilted axis of symmetry and a dipping interface in isotropic media produce similar amplitudes of both direct (P) and converted (Ps) phases, leaving the relative timing of the P and Ps phases as the main discriminant. Polarity reversals with back-azimuth are evident in the transverse-component "transmission response" of several Eurasian GSN stations, strongly favoring either anisotropy or tilted ($> 15°$) interfaces in the crust.

Recommendations: Rayleigh-Love 'scattering,' significant in a 1-D anisotropic crust, will be larger if the anisotropy varies laterally, e.g. across a mountain range and/or crustal suture. Therefore we plan to extend the above theory to develop path-integral mode-branch coupling approximations. The goal would be a practical synthetic seismogram code. Preliminary results confirm the empirical "speed bump" model of Love-Rayleigh coupling, in which the largest polarization disturbances occur when the axis of symmetry is angled $\pm 45°$ to the source-receiver path. The full 1-D layered anisotropy code can be used to ground-truth perturbative approaches to generating synthetic seismograms.

The polarization deflections in Terrascope data that we attribute to regional anisotropy may be important in actively deforming regions in Eurasia and other regions of nonproliferation concern. Therefore, network data from Kirghizstan, the CDSN, and PASSCAL data from Baikal region should be examined for these effects. Examining data from a smaller-aperture array, to examine polarization effects at higher frequency, would also be desirable.

We have demonstrated the potential impact of P-to-SH conversion by 1-D anisotropy in the crust, but further work must be done to put this knowledge can be of practical use. To this end, we would like to extend our genetic-algorithm codes to perform "computer-assisted forward modelling" of P codas from many back-azimuths at a single station. Deconvolving crustal reverberations with a receiver-function code seems a promising way to equalize source effects in this effort. We expect some ambiguity between anisotropy and tilted interfaces, but constraints from local geology and tectonics should resolve many cases. Combining information from P-coda and network-polarization may reveal a common source for waveform distortion and deflection in data from earthquakes and explosions.

In the next 12 months, we anticipate submittal of three or four manuscripts: 1) outlining a method to generate fast coupled-mode surface wave seismograms in laterally-variable anisotropic crustal models; 2) applying the wavelet-based array-polarizaton technique to a Eurasian region; 3) a survey of P-coda reverberation effects for Eurasian stations, relating them to regional tectonics; 4) development of a receiver-function inversion technique that incorporates back-azimuth variability.

REFERENCES (aside from papers listed above)

Babuska, V., & Cara, M., 1991. *Seismic Anisotropy in the Earth*, Kluwer Academic, Dordrecht.

Backus, G. E., 1962. Long-wave elastic anisotropy produced by horizontal layering, *J. Geophys. Res.*, *67*, 4427–4440.

Chen, X., 1993. A systematic and efficient method of computing normal modes for multilayered halfspace, *Geophys. J. Int.*, *115*, 391–409.

Crampin, S., 1984. Effective elastic constants for wave propagation through cracked solids, *Geophys. J. Roy. astron. Soc.*, *76*, 135–145.

Fisk, M. D., & McCartor, G. D., 1993. Fluctuation analysis of elastic waves in random media via phase screen simulations, *J. Geophys. Res.*, *98*, 685–698.

Goff, J. A., Hollinger, K., & Levander, A., 1994. Modal fields: A new method for characterization of random seismic velocity heterogeneity, *Geophys. Res. Letts.*, *21*, 493–496.

Hu, G., 1993. Lower crustal and Moho structures beneath Beijing, China from formal inversion of single station measurements of teleseismic *P*-wave polarization anomalies, *EOS*, *74*, 426.

Humphreys, E. D., and R. W. Clayton, 1990. Tomographic image of the Southern California mantle, *J. Geophys. Res.*, *95*, 19725–19746.

Humphreys, E. D., and B. H. Hager, 1990. A kinematic model for the late Cenozoic development of Southern California crust and upper mantle, *J. Geophys. Res.*, *95*, 19747–19762.

Langston, C. A., 1977. The effect of planar dipping structure on source and receiver responses for constant ray parameter, *Bull. Seism. Soc. Am.*, *67*, 1029–1050.

Levander, A. R., & Hollinger, K., 1992. Small-scale heterogeneity and large-scale velocity structure of the continental crust, *J. Geophys. Res.*, *97*, 8797–8804.

Liu, H., P. M. Davis, and S. Gao, 1995. SKS splitting beneath Southern California, *Geophys. Res. Letts.*, *22*, 767–770.

Owens, T. J. & Crosson R. S., 1988. Shallow structure effects on broad-band teleseismic *P* waveforms, *Bull. Seism. Soc. Am.*, *77*, 96-108.

Revenaugh, J., 1995. A scattered-wave image of subduction beneath the Transverse Ranges, *Science, 268*, 1888–1892.

Sambridge, M., and Drijkoningen, G., 1992. Genetic algorithms in seismic waveform inversion, *Geophys. J. Int.*, *109*, 323–342.

Sen, M. K., and Stoffa, P. L., 1992. Rapid sampling of model space using genetic algorithms: Examples from seismic and waveform inversions, *Geophys. J. Int.*, *108*, 281–292.

Sheehan, A. F., Abers, G. A., Jones, C. H., and A. L. Lerner-Lam, 1995. Crustal thickness variations across the Colorado Rocky Mountains from teleseismic receiver functions, *J. Geophys. Res.*, *100*, 20391-20404.

Visser, J., & Paullsen, H., 1993. The crustal structure from teleseismic *P*-wave coda–II. Application to data of the NARS array in western Europe and comparison with deep seismic sounding data, *Geophys. J. Int.*, , *112*, 26–38.

Wu, R.-S., 1994. Wide-angle elastic wave one-way propagation in heterogeneous media and an elastic wave complex screen method, *J. Geophys. Res.*, *99*, 751–766.

Zhu, L., Owens, T. J. & Randall G. E., 1995. Lateral variation in crustal structure of North Tibetan Plateau inferred from teleseismic receiver functions, *Bull. Seism. Soc. Am.*, *85*, 1531–1540.

NEAR-SURFACE EFFECTS ON HIGH-FREQUENCY SEISMIC WAVES OBSERVATIONS FROM DENSE, THREE-COMPONENT SEISMIC ARRAYS

Gary L. Pavlis, Dimitri Repin, and Stanley Radzevicius,
Department of Geological Sciences, Indiana University, Bloomington, IN

Frank Vernon, Scripps Institute of Oceanography,
IGPP, University of California, San Diego, La Jolla, CA

F49620-94-1-0039 and F49620-94-1-0037
Sponsored by AFOSR

ABSTRACT

We examine data from two dense, three-component seismic array experiments to understand the affects of near-surface weathered material on high-frequency seismic waves: (1) the 1990 Pinyon Flats, array experiment, and (2) the IRIS Joint Seismic Program experimental array deployment in Turkmenistan (1993-1994). We examined these data using two novel tools. First we utilized a three-dimensional visualization method to examine the spatial variations in particle motion across each array. Variable filtering allowed us to examine the effect of frequency on particle motions. In both arrays particle motions are wildly variable for both P and S waves on scales on the order of 10s of meters, but the Pinyon Flats site is noticeably worse. P wave particle motions skew systematically across the array in swirling patterns. S particle motions show strong deviations out of the radial-transverse plane defined by phase velocity measurements. This suggests the bulk elastic properties of the near-surface at Pinyon may be anisotropic due to irregular weathering along joints in the granite. At the Turkmenistan site, which is characterized by mudstone bedrock, we see less dramatic variability of particle motions. The largest effects we observe at this site are amplification of horizontal motions on stations located on hillsides. The second approach we used was a statistical one based on multitaper spectral estimates. We calculated 24,243 P and 24,118 S spectra from the Pinyon Flats data, and 31,580 P and 30,384 S spectra from the Turkmenistan data. We then formed spectral ratios for each event-channel combination relative to an array median. These spectral ratios are a measure of local site effects. We then averaged all the spectral ratios from each station to determine an average site effect. We find clear evidence for statistically significant variabilities in spectra across the aperture of both of these arrays. To examine the large amount of information contained in even the averages of these spectral ratios we utilize another three-dimensional visualization technique that displays the spectral ratio results at each frequency as a three-component "jack" figure and/or transparent spheres. In this way we find clear evidence for systematic variability of site response on scale as short as 20 m. We hypothesize that both sets of results can be explained by irregular elastic properties in the near-surface introduced by the universal tendency for rocks to preferentially weather along existing fracture surfaces. This heterogeneity yields a range of complex phenomena including anisotropy, scattering of body waves to surface waves, and complex resonance modes.

Keywords: site effects, high-frequency wave propagation, visualization, arrays

OBJECTIVES

It has been known since the earliest work on seismic arrays in the 1960s that something in the near surface profoundly affects the propagation of high-frequency seismic waves. It is now well established that this "something" is the near-surface weathered layer. It is not widely appreciated, however, that the weathered layer is the most dramatic velocity contrast on the entire planet. It is not unusual for the shear wave velocities of soil to be less than the sound speed in air. Almost everywhere the shear velocity of soil is 10% or less of the P wave velocity of the underlying bedrock. Furthermore, except in unusual circumstances (e.g. glacial deposits on top of ice-polished bedrock found in places like NORSAR) the weathered layer is outrageously heterogeneous. This occurs because the geologic processes responsible for weathering accentuate initial rock heterogeneity in two basic ways: (1) weathering is universally strongest along rock fractures, especially those that are favorably oriented to provide a drainage pathway for water; and (2) we all learned in freshman geology that some minerals are more stable than others, and this leads to differential weathering that depends upon bedrock lithology.

The weathered layer has profound affects on what we measure on seismograms. Where it's influence becomes important is site dependent, but generally one can only assume the weathered layer has no affect on seismic observations when the propagation time of an S wave through the weathered zone is small compared to the period. Almost everywhere this transition probably occurs somewhere in the range of 0.5 to 10 Hz, which is directly in the middle of the main frequency band of importance for regional phases. Thus, understanding how seismic waves interact with the weathered layer and how this interaction affects seismic measurements is of extreme importance for understanding how regional phases propagate and what we can and cannot quantify from seismic measurements.

In this paper we present some observational results that provide important new insights on the nature of how seismic waves interact with the weathered layer. We find evidence for variability of the seismic wavefield on remarkably short distance scales that can only be explained by heterogeneity in the upper tens of meters of the crust.

RESEARCH ACCOMPLISHED

Introduction. Four principles limit the class of data we could use in this study.

(1) In order to investigate physical phenomena associated with the weathered layer, useful data come only from experiments with sensors spaced at intervals of the thickness of the weathered layer or less.
(2) In nuclear monitoring at regional distances, "high frequency" is approximately defined as the 0.5 - 20 Hz band.
(3) We wanted to focus on sites that geologically were characterized by soil that is the end product of *in situ* weathering, not a depositional process (e.g. stream beds, loess, or glacial deposits), since this environment characterizes nearly all "hard rock sites".
(4) We focus on three-component recordings to allow us to study details of the ground motion that are not possible with single component data.

Items 1 and 2 are almost mutually exclusive, because the dominant wavelength of most regional phases are on the order of 1-10 km. Thus, arrays like NORESS have a nominal spacing of the order 100 m, which is not consistent with requirement 1. The frequency band also excludes nearly all existing seismic reflection data, where recording below 10 Hz, let alone with triaxial sensors, is nearly unheard of. Two unique data sets were,

however, recently collected as part of the IRIS Joint Seismic Program that satisfy all of these requirement: the 1990 Pinyon Flats high frequency array experiment (Owens et al., 1991; Al-Shukri *et al.*, 1995; Vernon *et al.*, 1996); and an experimental array deployed in Turkmenistan from August, 1993, to November, 1994 (Pavlis *et al.*, 1994 or Al-Shukri *et al.*, 1995).

Both of these experiments recorded a significant number of high frequency seismic events (frequencies as high as 100 Hz) on an array of three-component sensors spaced at intervals of from 1 to 100 m. The Pinyon Flat experiment used a 6×6 grid of 2 Hz sensors spaced at 7 m intervals (Figure 1). The Turkmenistan array used groups of twelve, 4.5 Hz, triaxial geophones deployed in linear subarrays with a nominal spacing of 4 m between sensors. These were deployed in a star pattern (Figure 3) with four linear segments defining the diagonals and bisectors of a 600×600 m area. Along the bisectors the geophones formed a continuous line of sensors with a nominal spacing of 4 m and 50 m between groups. That is, the output of each seismic station is an average of 12 sensors that average ground motion over a 50 m linear section of the ground.

Particle Motion Analysis. We examined a number of events from both of these data sets using a 3-D visualization scheme introduced by Pavlis *et al.* (1990) and refined by Anderson (1993) and Repin and Pavlis (1996). Particle motion diagrams that are projections on the radial-vertical or transverse-radial plane are a standard analysis technique. Here we plot the same information as a three-dimensional object. In an array, however, we also have many other stations located within one wavelength of each other. We draw the particle motion diagrams in three space at a grossly amplified scale centered at points corresponding to the location in space of each seismic station. The result shows us how particle motions vary spatially across the aperture of the array. The entire sequence is displayed as an animation that we playfully refer to as "dancing worms". This imagery comes from the fact that we draw the particle motion over a fixed time interval. Motion occurs as we move forward in time through the seismic signal and continuously change the time window we display in three dimensions. This aspect of the analysis cannot be presented in this report because we are restricted by the medium to black and white, still images.

Figures 1, 2, and 3 show a sample of results applied to a P and S waveform from local events recorded by these two arrays. In all cases we first scaled each signal by calibration constants to ground velocity and then integrated the signals to yield a record of ground displacement. We also time shifted the signals to compensate for propagation times across the array using different velocities to study P and S signals. Finally, we then studied the effect of the wavelength of the incoming signal on the results by applying various bandpass filters to the data before displaying them.

A great deal is lost in the translation to a black and white, flat sheet of paper, but we assert the following are significant observations that come from this analysis:

1. In all cases, the particle motions we see vary a great deal on remarkably short distance scales. These variations are clearly real and not generated by random noise or instrumentation problems because they change smoothly across the array.

2. The results are highly frequency dependent. At Pinyon Flats, particle motions become noticeably less variable below around 5 Hz while at the Turkmenistan site this transition seems to be slightly higher for a comparable scale length.

3. Particle motions are almost always skewed drastically from that expected for propagation in a homogeneous medium. Figure 1 shows a swirling motion commonly seen in

the particle motions of the first cycle of the P wave of events recorded at Pinyon Flats. Figure 2 shows that S wave particle motions are equally variable, but even in the lower frequency band the particle motions are all skewed at a high angle out of the transverse plane. These results suggest the shear elastic properties of the weathered layer at Pinyon Flats may be anisotropic since this is precisely the behavior expected in an anisotropic medium.

4. The Turkmenistan data are consistently less variable than the Pinyon Flats data. This may be partly a result of the averaging affect of the geophone strings, but we suggest this is not the dominate factor for one reason. The Turkmenistan array also had nine STS-2 sensors installed in vaults at the center and ends of each of the linear segments seen in Figure 3. These nine sensors form a 3×3 grid of stations with a spacing of 300 m, which is about the same as the full aperture of the Pinyon Flats array. The particle motions seen on these stations are variable at high frequencies, but not nearly as much as at Pinyon Flats. At Pinyon Flats stations at that spacing commonly would show no relation to each other whatsoever.

Spectral Analysis. A quantitative measure of the frequency dependence of the phenomena seen in the particle motion is obtained from a parallel spectral study we have conducted. We made these calculations according the following procedure:

1. We defined time windows around P and S wave records of local and regional events. For both data sets this was defined as 0.25 s before the onset time to 1.0 s after the measured onset time.

2. We calculated power spectra for each component from each measured P and S phase using the multitaper spectral method of Thomson (1982) as implemented by Vernon (1989). We also calculated the total power spectrum for each station as the sum of the power spectra of all three components. We calculated spectra for P, S, and a 5 s noise window preceding the P wave. For the Pinyon Flats data this yielded 24,243 and 24,118 spectral estimates for P and S respectively. For the subset of the Turkmenistan data we examined this yielded 31,580 P and 30,384 S spectra.

3. For each event-phase combination (P, S, and noise segments) we calculated the average spectrum for that event as the median of all the individual spectral measurements at each frequency.

4. For each spectral measurement we calculated a spectral ratio relative to the appropriate array median calculated in step 3.

5. We assembled all the spectral ratios for all P and S measurements for each station-channel combination. To avoid bias introduced by events with low signal-to-noise ratio, we only included spectral ratios for which the parent median array spectrum had a signal-to-noise ratio exceeding 5. Note this was done seperately for each frequency and each spectral ratio. We summarized the statistics of the resulting distributions in terms of the total range, the median, interquartiles of the distribution, and the number of estimates at each frequency that satisfied the signal-to-noise criteria.

6. We examined the results using two methods. First, we made plots of the spectral ratio statistics for each station-channel-phase combination. This type of plot helped us ascertain the statistical significance of our results. The four inch thick stack of paper this approach yields is, however, not very easy to look through, let alone present in a concise fashion. Consequently, we developed a new three-dimensional visualization technique. This again looses a great deal in the translation to a black and white sheet of paper, but Figure 4 illustrates the concept. For a given phase (e.g. Figure 4 is for P waves) we draw a three-

dimensional "jack figure" at the location of each station in the array. The lengths of the arms of each of these "jacks" is scaled by the logarithm of the median spectral ratio for the appropriate component (e.g. the vertical component results is drawn as a vertical line segment.). We distinguish positive (site amplification) values from negative values by using different colors that depend upon the sign (upper portion of Figure 4). The lower portion of Figure 4 shows the other part of this analysis. The total power spectrum ratios (sum of power spectra on all three components) is drawn as a transparent sphere whose radius is scaled to the spectral ratio and similarly colored depending on the sign of the spectral ratio. The transparency is impossible to present on a black and white figure, so Figure 4 shows the spheres alone in a black and white format. In the actual visualization display the spheres are displayed simultaneously with the jack figures. The actual display is an animation. We vary the frequency and redraw the display for each frequency. We can step through the frequency axis or run through the whole range as an animation.

In a recent paper Alshukri *et al.* (1995) showed there were large fluctuations in spectral amplitudes measured from both of these arrays. The analysis we present here clarifies the spatial scale of these fluctuations and how much the results vary from event to event. From analysis we have done to date we make the following observations.

1. Both sites show statistically significant variability at all frequencies above 4 Hz (the lowest resolved frequency with the time window we have used here). These changes occur smoothly across the array indicating we are not seeing random fluctuations, but a real variability in site response.

2. The Pinyon experiment simultaneously recorded two triaxial sensors in 150 m and 300 m deep boreholes. Spectral ratios from these stations demonstrate that all the surface stations are affected by a site amplification above 5 Hz that often exceeds a factor of 10.

3. In general the results are more stable spatially than might be thought based on the interquartile distances. That is, consistent patterns are commonly seen across the array for frequencies at which median spectral ratios are less than interquartile distances at most, if not all, stations. This suggests that a significant fraction of the observed fluctuations in amplitude may be azimuthally dependent. Work is in progress to examine the azimuthal dependence of the spectral estimates by working with more restricted subsets of these data.

3. More variability occurs in the Pinyon Flats data at drastically shorter distance scales than those found in the Turkmenistan data. For these data the most dramatic amplitude anomalies correlate with topography. We see clear evidence at one station for a transfer of energy from the verticals to the horizontal components. This station has a string of geophones traversing the face of a very steep hill suggesting the free face of the hill is responsible for this transfer of energy. In contrast, at Pinyon Flats the whole array sits on a featureless surface of weathered granodiorite.

Interpretation. We hypothesize that all our results can be explained by irregular elastic properties in the near-surface introduced by the universal tendency for rocks to preferentially weather along existing fracture surfaces. It is intuitively clear that this should generate a range of complex phenomena that depend upon the scale of the seismic wavefield, which clearly equates with a frequency dependence. The skewed particle motions can be explained by irregular elastic parameters that lead to local variability in strain on distance scales shorter than one wavelength. This further introduces rapidly variable site effects because the local displacement field is amplified in areas with low elastic moduli compared to areas of intact rock where the material remains relatively stiff. In addition, bulk elastic

properties at longer periods may become effectively anisotropic. This should not be surprising in a fractured media with a preferred orientation of fractures. In this situation we should really expect anisotropic elastic properties. Finally, some of what we are seeing may be a result of complex near-surface resonance modes. The site amplification (Figure 4) and swirling P motions seen in the Pinyon Flats results may result from excitation of near-surface resonance modes of weathered rock pinnacles surrounded by partially weathered rock. We speculate that the Turkmenistan data is less variable than the Pinyon Flats data because of differences in rock type and weathering. Pinyon Flats is characterized by deeply weathered granite while the Turkmenistan site has mudstone bedrock. The former is heavily fractured and it is well established that weathering in granites preferentially occurs along such fractures (e.g. Bloom, 1991). The later is fractured, but mudstone does not undergo extensive chemical weathering at the surface because clay minerals are more stable. Thus, the observed lower variability of seismic wavefields at that site may be a reflection of the more homogeneous weathered layer that results.

CONCLUSIONS AND RECOMMENDATIONS:

The near-surface weathered zone is of more importance to shaping observed seismic signals than most people probably recognize. Earlier recognition of some aspects of the phenomena we have observed led to the standard practice of placing short-period array stations in boreholes. This works, but this is an expensive solution that may not be viable at some sites where new arrays might be installed for monitoring a CTBT. It is our view that there is little question that array performance at frequencies higher than about 10 Hz is almost everywhere limited by near-surface effects. Further fundamental research is needed to better understand the nature of how seismic waves interact with the complex heterogeneity at the earth's surface. Improved understanding of the basic phenomena would fold into the practical problem of site of high-frequency arrays on hard rock sites.

REFERENCES:

Al-Shukri, H.J., G. L. Pavlis, and F. L. Vernon III, Site effect observations from broadband arrays, *Bulletin of the Seismological Society of America, 85*, 1758-1769, 1995.

Anderson, P.N., Animated visualization techniques for three-component seismic array data, PhD Dissertation thesis, Indiana University, 1993.

Bloom, A.L., *Geomorphology: A systematic analysis of late Cenozoic landforms*, Prentice-Hall, Englewood Cliffs, New Jersey, 1991.

Owens, T.J., P. N. Anderson, and D. E. McNamara, Data Report for the 1990 Pinyon Flat high-frequency array experiment, An IRIS Eurasian seismic studies program passive array experiment, IRIS Data Management Center, 1991.

Pavlis, G.L., P. N. Anderson, Visualization techniques for seismic array data, *Geophysics: The Leading Edge of Exploration, 9*, 26-29, 1990.

Pavlis, G.L., H. Alshukri, H. Mahdi, D. Repin, and F. Vernon, JSP arrays and networks in central Asia, *IRIS Newsletter, 13*, 9-12, 1994.

Repin, D. G. and G. L. Pavlis, Three-dimensional visualization of seismic array data, *Seism. Res. Lett., 67*, 52, 1996.

Thomson, D.J., Spectrum estimation and harmonic analysis, *I.E.E.E. Proc., 70*, 1055-1096, 1982.

Vernon, F.L., Analysis of data recorded on the ANZA seismic network, Ph.D. dissertation thesis, University of California, San Diego, 1989.

Vernon, F.L., G. L. Pavlis, T. J. Owens, D. E. McNamara, and P. N. Anderson, Near-surface scattering effects observed with a high-frequency phased array at Pinyon Flats, California, *Bulletin of the Seismological Society of America, in press*, 1996.

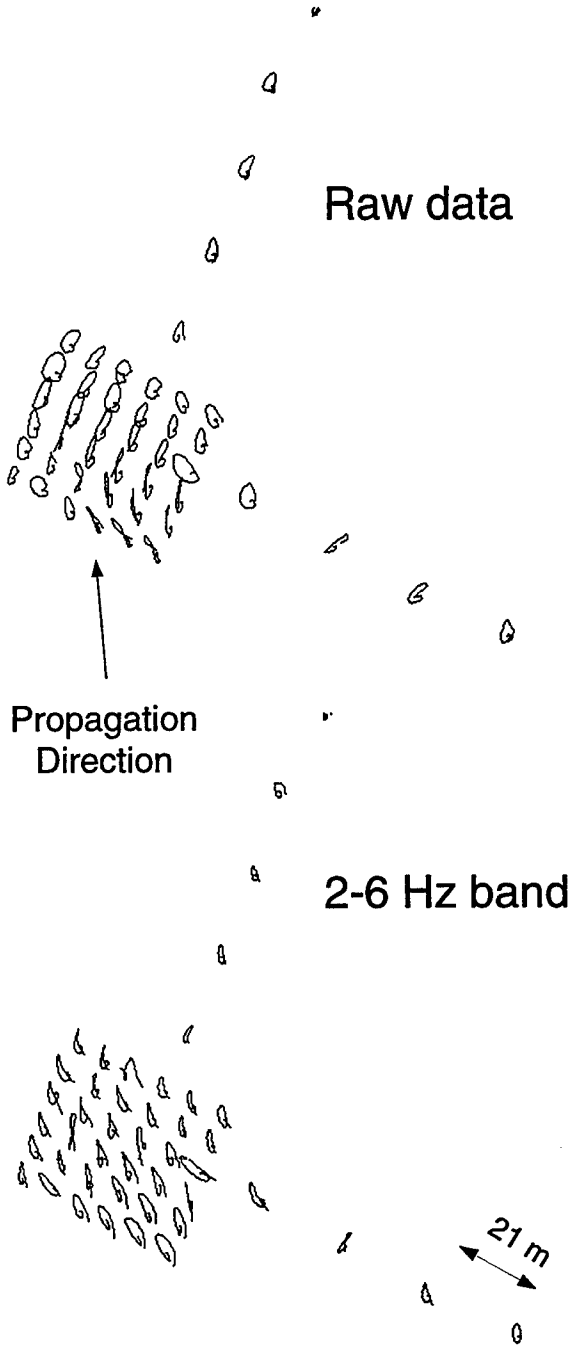

Figure 1. Three-dimensional particle motion results for P wave recorded by Pinyon Flats, California, high-frequency array experiment. Results shown are for an event recorded on May 14, 1990. Both parts of this figure are projections from the same point in space located above the surface of the earth and southwest of the array. Hence the scale is the same on both figures. The upper portion displays the raw data with only dc shifts removed while the lower portion of the figure shows the same data bandpass filtered between 2 and 6 Hz.

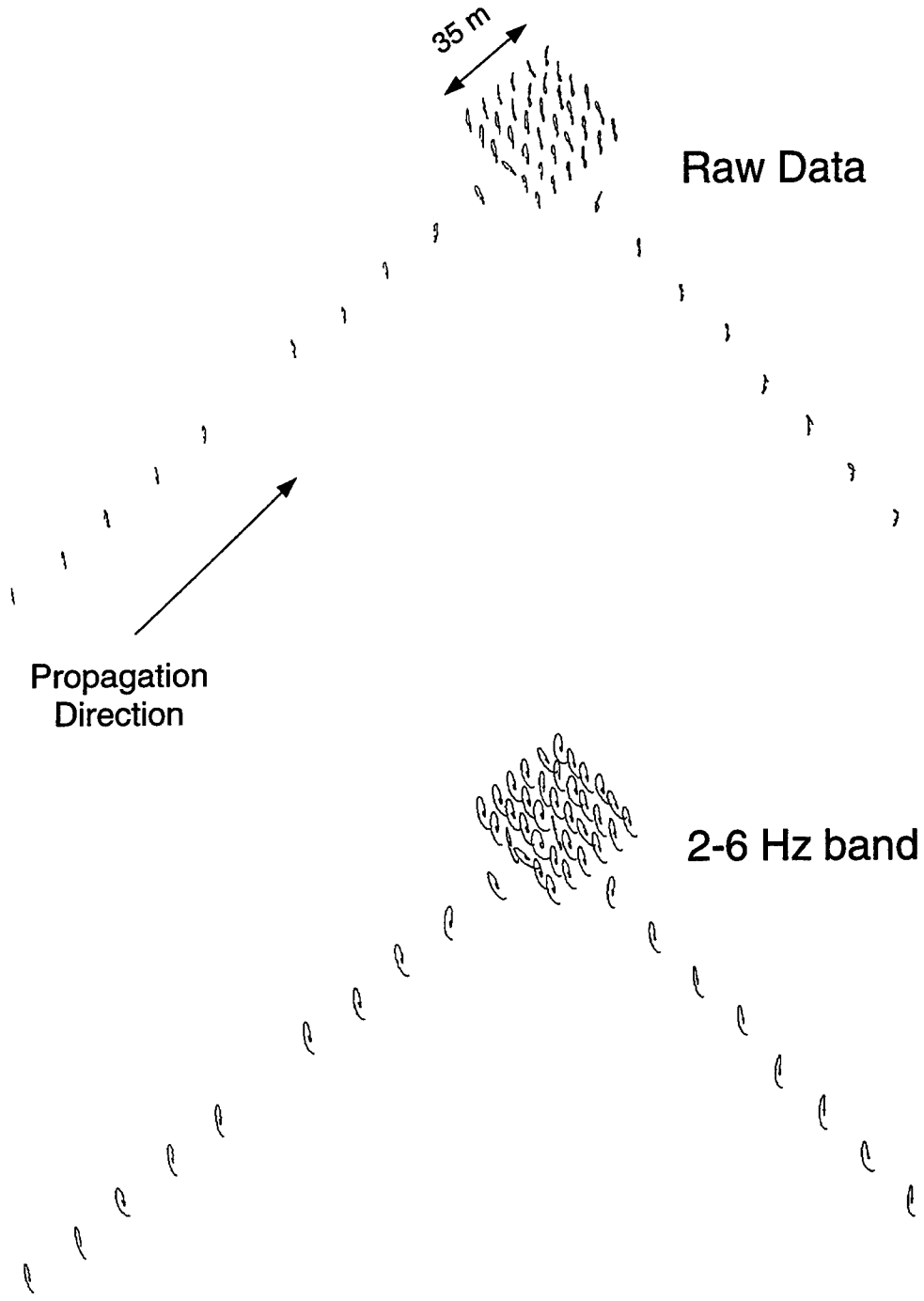

Figure 2. S wave particle motions for Pinyon Flats, California, high-frequency array data. Results shown are exactly as in Figure 1 except these data are for a time window centered on the first cycle of the S wave from an event recorded on May 24, 1990, that occurred nearly straight south of the array. The viewpoint here is above and southwest of the array.

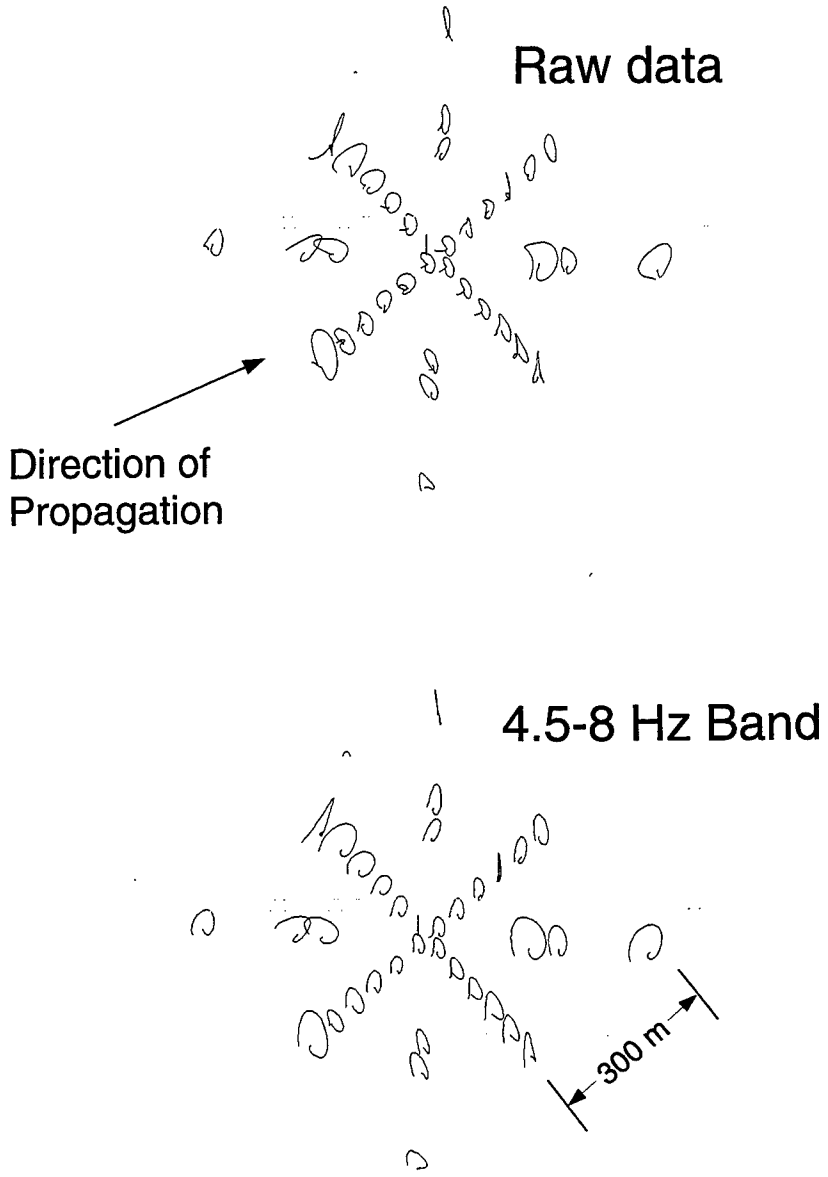

Figure 3. S wave particle motions for Geyokcha array data. Viewpoint for this figure is straight above the array center. S waves at this site are nearly purely horizontally polarized. Results shown are for an event recorded on April 5, 1994. We display only data from stations utilizing 4.5 Hz geophone strings.

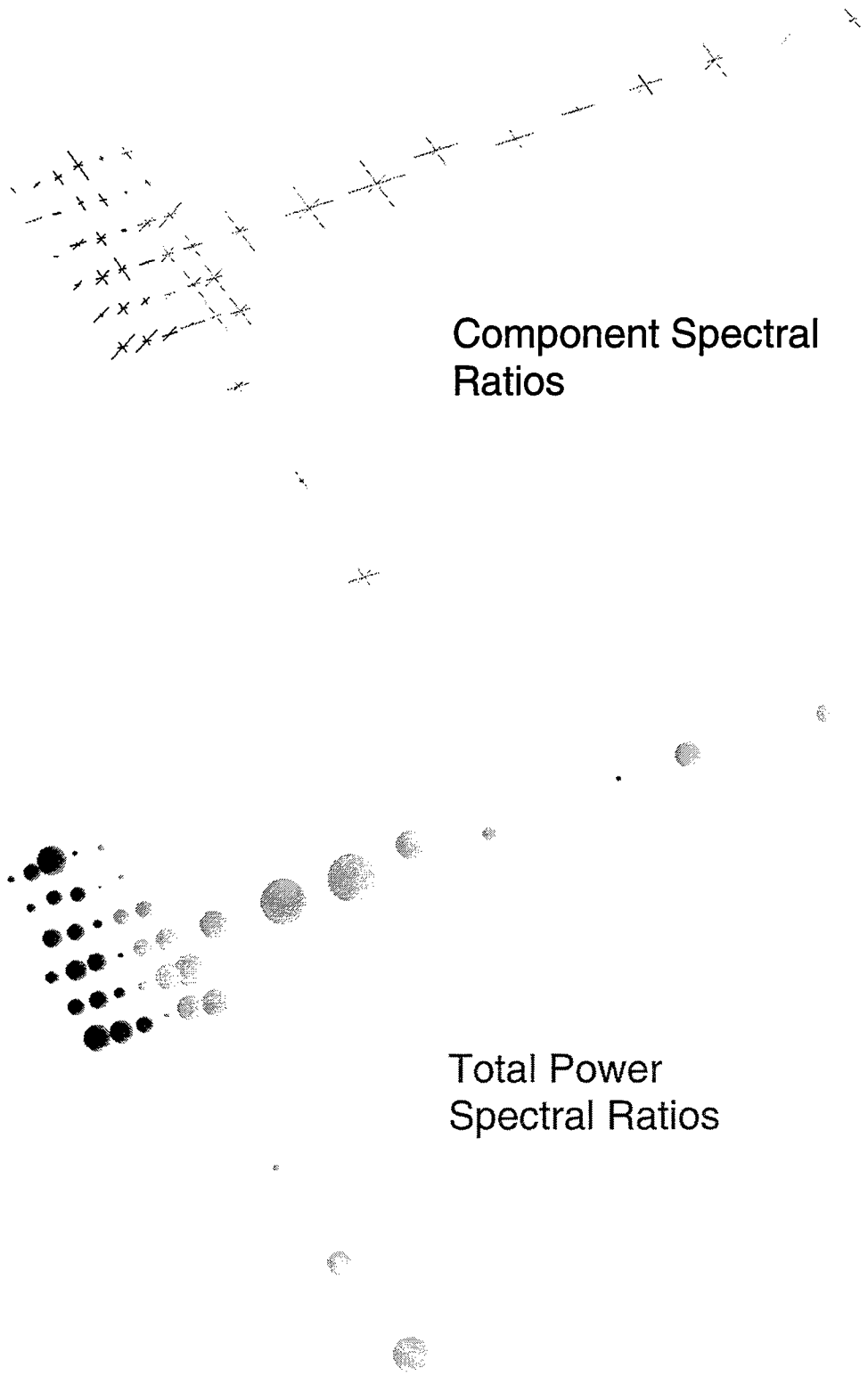

Figure 4. Array spectral ratio visualization still image. Figures show the spatial distribution of variations in spectral power at 8.79 Hz. Black objects are positive (site amplification) and grey objects are negative (low amplitudes). Each arm of "jacks" in the upper figure points along a sensor component direction. North is parallel to the line of objects running from the upper left to lower right.

A PSEUDO-SPECTRAL SCHEME FOR VISCOELASTIC SEISMIC MODELING

James C. Schatzman, University of Wyoming, Department of Mathematics

Grants Nos. F49620-94-1-0134 and F49620-94-1-0408
Sponsored by AFOSR

ABSTRACT

It is universally acknowledged that major crustal features such as deep sedimentary basins and an uplifted moho can alter the propagation characteristics of the crustal waveguide. Computer modeling of crustal propagation characterists for CTBT applications places great demands on the numerical algorithms. Adequate computer simulation requires highly accurate and efficient software. Traditional technique such as ray-tracing and finite difference algorithms do not provide the necessary performance. Pseudo-spectral algorithms can provide the necessary performance, but several difficulties of the usual implementations of these algorithms must be overcome:

- It is very difficult to implement the free-surface boundary condition with Fourier methods.
- Chebyshev polynomial and other polynomial methods suffer from restrictive stability constraints.

Our approach has been to use a mixed Fourier-Chebyshev algorithm together with a stabilization procedure using coordinate transformations. The result is a software package for 2-D visco-elastic wave modeling in an irregularly shaped (crustal) region that is highly accurate and reasonably efficient. A future version of the software will perform full 3-D visco-elastic wave modeling.

Objective It is universally acknowledged that major crustal features such as deep sedimentary basins and an uplifted moho can alter the propagation characteristics of the crustal waveguide. Especially important for Comprehensive Test Ban Treaty applications is the dramatic change of amplitude of the L_g and P_g phases relative to the other phases. Major crustal features have been observed to drastically attenuate or obliterate the L_g and/or P_g phases. This has a major impact on signal analysis methods that rely on the relative amplitude of the different phases for test/earthquake discrimination.

For some scenarios, it may be that the suppression of L_g and P_g is so severe that no useful information can be obtained from these phases. However, in cases where the attenuation is not so severe, the problem is one of calibration. Given knowledge of propagation characteristics between the source and receiver, measurements may be calibrated for the propagation effects. To do this requires accurate knowledge of propagation effects.

It is not generally the case that sufficient controlled experimental data are available to adequately characterize the crustal propagation characteristics. Instead, this may be accomplished by computer simulation. Accurate computer simulation in turn requires adequate geophysical models for the crust; such models are more readily available than nuclear test and earthquake data.

Anelasticity and anisotropy of the earth play important roles in wave propagation, especially when waves travel long distances. Finite difference and finite element methods suffer from inaccuracies in the form of numerical dispersion and attenuation that make it difficult to simulate wave propagation over hundreds to thousands of wavelengths. The pseudospectral method exhibits very striking features of very low grid density and high efficiency, compared to the standard Cartesian discrete methods. The goal here is to simulate wave propagation in a region of about 2,000 km in azimuth and 100-200 km in depth; source frequencies are 0.5-10 Hz. Since wavelengths range from 120-4,000 meters, this represents propagation of about 500-20,000 wavelengths. Most FD or FE schemes either exhibit excessive numerical artifacts or are very inefficient for such problems.

Due to space limitations, we describe only the isotropic 2-D formulation. However, the anisotropic 3-D case is a straightforward extension and a detailed analysis is available from the authors.

Research Accomplished A workable mathematical formulation has been devised for the visco-elastic problem. According to Voigt's model, for an isotropic-elastic medium the stress-strain relation is

$$\sigma_{ii} = \overline{\lambda}\Delta + 2\overline{\mu}\varepsilon_{ii}, \quad i = 1,2,3, \tag{1}$$

$$\sigma_{ij} = \overline{\mu}\varepsilon_{ij}, \quad i \neq j, \ i,j = 1,2,3, \tag{2}$$

where $\overline{\lambda} = \lambda + \lambda' \frac{\partial}{\partial t}$ and $\overline{\mu} = \mu + \mu' \frac{\partial}{\partial t}$. It is beyond the scope of this paper to include a derivation, but we find that λ' and μ' are related to the Q for P- and S-wave propagation by

$$Q_p = \frac{\sqrt{(\lambda + 2\mu)^2 + k^2(\lambda' + 2\mu')^2 v_p^2} + \lambda + 2\mu}{2(\lambda' + 2\mu')kv_p}. \tag{3}$$

$$Q_s = \frac{\sqrt{\mu^2 + k^2\mu'^2 v_s^2} + \mu}{2\mu' k v_s}. \tag{4}$$

and

$$\mu' = \frac{4\mu Q_s}{kv_s(4Q_s^2 - 1)} \tag{5}$$

$$\lambda' = \frac{4(\lambda + 2\mu)Q_p}{kv_p(4Q_p^2 - 1)} - 2\mu' \tag{6}$$

We see that in this model, Q_p and Q_s are not constant but are functions of wavenumber. The viscoelastic equations of motion are

$$\rho\frac{\partial^2 u_i}{\partial t^2} = \frac{\partial}{\partial x_i}[(\overline{\lambda} + \overline{\mu})\theta] + \nabla \cdot (\overline{\mu}\nabla u_i) + f_i, \ i = 1,2,3, \tag{7}$$

where $\mathbf{f} = (f_1, f_2, f_3)^T$ is the applied force.

If in a region the medium is partially homogeneous (μ and μ' are constants), then in this region we have

$$\rho\frac{\partial^2 \theta}{\partial t^2} = (\overline{\lambda} + 2\overline{\mu})\Delta\theta, \tag{8}$$

and

$$\rho\frac{\partial^2 \boldsymbol{\omega}}{\partial t^2} = \overline{\mu}\Delta\boldsymbol{\omega}. \tag{9}$$

where $\theta = \nabla \cdot \mathbf{u}$ and $\boldsymbol{\omega} = \nabla \times \mathbf{u}$. Thus we see that even in viscoelastic media the dilation wave equation is similar to a "pure" P-wave equation and the rotational wave equations coincides in form with the "pure" S-wave equation.

To obtain a rectangular geometry for a problem with an irregular top and bottom (due to surface topography and curvature of the earth) we employ a transformation from (x_1, x_3) to (x_1, η), where $\eta = \eta(x_1, x_3)$ (Fig. 1). The equations of motion then become

$$\frac{\partial u_1}{\partial t} = v_1, \tag{10}$$

$$\frac{\partial u_3}{\partial t} = v_3, \tag{11}$$

$$\rho\frac{\partial v_1}{\partial t} = \left(\frac{\partial}{\partial x_1} + \eta_{x_1}\frac{\partial}{\partial \eta}\right)\left[\left(\lambda+\mu\right)\left(\frac{\partial u_1}{\partial x_1} + \eta_{x_1}\frac{\partial u_1}{\partial \eta} + \eta_{x_3}\frac{\partial u_3}{\partial \eta}\right)\right]$$

$$+\left(\frac{\partial}{\partial x_1} + \eta_{x_1}\frac{\partial}{\partial \eta}\right)\left[\mu\left(\frac{\partial u_1}{\partial x_1} + \eta_{x_1}\frac{\partial u_1}{\partial \eta}\right)\right] + \left(\eta_{x_3}\frac{\partial}{\partial \eta}\right)\left[\mu\left(\eta_{x_3}\frac{\partial u_1}{\partial \eta}\right)\right]$$

$$+\left(\frac{\partial}{\partial x_1} + \eta_{x_1}\frac{\partial}{\partial \eta}\right)\left[\left(\lambda'+\mu'\right)\left(\frac{\partial v_1}{\partial x_1} + \eta_{x_1}\frac{\partial v_1}{\partial \eta} + \eta_{x_3}\frac{\partial v_3}{\partial \eta}\right)\right]$$

$$+\left(\frac{\partial}{\partial x_1} + \eta_{x_1}\frac{\partial}{\partial \eta}\right)\left[\mu'\left(\frac{\partial v_1}{\partial x_1} + \eta_{x_1}\frac{\partial v_1}{\partial \eta}\right)\right] + \left(\eta_{x_3}\frac{\partial}{\partial \eta}\right)\left[\mu'\left(\eta_{x_3}\frac{\partial v_1}{\partial \eta}\right)\right] + f_1 \tag{12}$$

$$\rho\frac{\partial v_3}{\partial t} = \left(\eta_{x_3}\frac{\partial}{\partial \eta}\right)\left[\left(\lambda+\mu\right)\left(\frac{\partial u_1}{\partial x_1} + \eta_{x_1}\frac{\partial u_1}{\partial \eta} + \eta_{x_3}\frac{\partial u_3}{\partial \eta}\right)\right]$$

$$+\left(\frac{\partial}{\partial x_1} + \eta_{x_1}\frac{\partial}{\partial \eta}\right)\left[\mu\left(\frac{\partial u_3}{\partial x_1} + \eta_{x_1}\frac{\partial u_3}{\partial \eta}\right)\right] + \left(\eta_{x_3}\frac{\partial}{\partial \eta}\right)\left[\mu\left(\eta_{x_3}\frac{\partial u_3}{\partial \eta}\right)\right]$$

$$+\left(\eta_{x_3}\frac{\partial}{\partial \eta}\right)\left[\left(\lambda'+\mu'\right)\left(\frac{\partial v_1}{\partial x_1} + \eta_{x_1}\frac{\partial v_1}{\partial \eta} + \eta_{x_3}\frac{\partial v_3}{\partial \eta}\right)\right]$$

$$+\left(\frac{\partial}{\partial x_1} + \eta_{x_1}\frac{\partial}{\partial \eta}\right)\left[\mu'\left(\frac{\partial v_3}{\partial x_1} + \eta_{x_1}\frac{\partial v_3}{\partial \eta}\right)\right] + \left(\eta_{x_3}\frac{\partial}{\partial \eta}\right)\left[\mu'\left(\eta_{x_3}\frac{\partial v_3}{\partial \eta}\right)\right] + f_3 \tag{13}$$

The free surface boundary conditions at the top become:

$$(\lambda+2\mu)\left(\eta_{x_3}\frac{\partial u_3}{\partial \eta}\right) + \lambda\left(\frac{\partial u_1}{\partial x_1} + \eta_{x_1}\frac{\partial u_1}{\partial \eta}\right) + (\lambda'+2\mu')\left(\eta_{x_3}\frac{\partial v_3}{\partial \eta}\right) + \lambda'\left(\frac{\partial v_1}{\partial x_1} + \eta_{x_1}\frac{\partial v_1}{\partial \eta}\right) = 0 \tag{14}$$

$$\mu\left(\eta_{x_3}\frac{\partial u_1}{\partial \eta}+\frac{\partial u_3}{\partial x_1}+\eta_{x_1}\frac{\partial u_3}{\partial \eta}\right)+\mu'\left(\eta_{x_3}\frac{\partial v_1}{\partial \eta}+\frac{\partial v_3}{\partial x_1}+\eta_{x_1}\frac{\partial v_3}{\partial \eta}\right)=0 \qquad (15)$$

The radiation boundary conditions at the bottom take the form

$$\alpha_1+\cos\phi\left(\frac{\partial u_1}{\partial x_1}+\eta_{x_1}\frac{\partial u_1}{\partial \eta}\right)+\sin\phi\left(\eta_{x_3}\frac{\partial u_1}{\partial \eta}\right)+\frac{v_1}{v}=0, \qquad (16)$$

$$\alpha(x_1,x_3)u_3+\cos\phi(x_1,x_3)\left(\frac{\partial u_3}{\partial x_1}+\eta_{x_1}\frac{\partial u_3}{\partial \eta}\right)+\sin\phi(x_1,x_3)\left(\eta_{x_3}\frac{\partial u_3}{\partial \eta}\right)+\frac{v_3}{v(x_1,x_3)}=0. \qquad (17)$$

These equations are to be approximated through collocation and quadrature (we use fourth order Runge-Kutta). The solutions are represented as 2-D discrete Fourier-Chebyshev transforms in (x_1,η). Differentiations with respect to x_1 and η are carried out in the usual way. The η derivatives of u_1, u_3, v_1 and v_1 result in four unknowns per k_x value: the $4N_x$ highest Chebyshev modes are lost in the differentiation process. In principal, these are to be determined by the $4N_x$ top and bottom boundary conditions. Due to the higher derivatives in the equations of motion, there are actually a total of $14N_x$ unknown highest Chebyshev modes. The highest modes are updated according to the $4N_x$ top and bottom boundary conditions.

The strategy adopted for choosing the mapping function η is to flatten the surface and major contours. "Major contours" are those interfaces, typically the basement and moho, that are continuous across the section. Fig. 1 shows one of a set of "deep sedimentary basin" models that are being tested. Once the "major contours" are identified, the average travel time between the contours is computed (p-waves have been used so far), and constant values of η are assigned to the major contours so that the differences in η are proportional to the travel time. In this way, increments of constant $\Delta\eta$ correspond roughly to equal increments of travel time. This is done so as to improve the stability properties of the time integration.

As described so far, the algorithm would not perform well because of restrictive stability constraints (the time step would have to be impractically small). We have studied stability of Runge-Kutta for this problem. Kosloff and Tal-Ezer (1993) have pointed out that coordinate transformations can be used to stabilize explicit time-stepping methods using Chebyshev polynomials. However, they fail to observe that their coordinate transformations can give excessive local truncation error. Figure 2 demonstrates that the α parameter in their arcsine coordinate map:

$$x=\frac{\sin^{-1}(\alpha\xi)}{\sin^{-1}\alpha}; \qquad \frac{d\xi}{dx}=\frac{\sin^{-1}(\alpha)}{\alpha}\sqrt{1-(\alpha\xi)^2} \qquad (18)$$

must be chosen carefully, balancing stability and truncation error in order to obtain satisfactory results.

Preliminary calculations indicate that it is practical to simulate wave propagation for 2-D models of about 2,000 by 200 km. Such simulations require several days of compuation on a SGI Power Challenge (300 MFlops).

We are in the process of quantifying the effects of particular types of crustal features on regional waveforms. Features under study include deep sedimentary basins (as in Fig. 1), moho uplift and lateral variation in surface features. Fig. 2 shows a surface seismogram resulting from the geophysical model (Fig. 1).

Recommendations and Future Plans Other authors have performed simulations for particular models (e.g., Jih (1994) uses a finite difference method); there is not yet completed a comprehensive and quantitative study of the effects of crustal features. Our plan is to use a series of models, for example the deep sedimentary basin models, varying the size and elastic parameters of the basin, to determine how the effects of such basins on crustal wave propagation, such as attenuation of L_g, depend on the parameters of the basin. Additionally, we will study the effects of moho uplift, combined basin and uplift, and surface topographical roughness and other surface features.

One weakness of this method is that, because of its 2-D nature, amplitudes and decay times are not correct, and relative amplitudes of differing phases are not readily obtainable. Although the method described in this paper can readily be applied to the 3-D problem, it is apparent that elastic wavefield computations in a region of 2,000 by 2,000 by 200 km are not practical with any computer available to the authors. However, two acceleration techniques may be employed when solving the problem of wave propagation between two points (source and receiver):

1. Model only a narrow channel between the source and receiver (see Fig. 3). Use absorbing boundary conditions on the lateral boundaries to avoid reflections or wrap-around.
2. Use smaller tracking grids that follows the major wave fronts. A full simulation would then require several runs, each to capture the modes with essentially different paths, but each run would be much quicker than a global computation.

CONCLUSIONS AND RECOMMENDATIONS

This project, being relatively new, has focused to date on the development of the computer algorithms that are so crucial for accurate characterization of crustal prop-

agation characteristics. As the algorithm development is now complete, additional work will focus of applying the computer algorithms to the geophysical problems of interest.

1. Bayliss, A., Jordan, K. E., Lemesurier, B. J. and Turkel, E., 1986, A fourth-order accurate finite-difference scheme for the computation of elastic waves: *Bulletin of the Seismological Society of America*, **76**, pp. 1115–1132.
2. Carcione, J. M., 1992, Modeling anelastic singular surface waves in the earth: *Geophysics*, **57**, pp. 781–792.
3. Carcione, J. M., Kosloff, D. and Kosloff, R., 1988, Wave propagation simulation in an elastic anisotropic (transversely isotropic) solid: *Q. J. Mech. Appl. Math.*, **41**, pp. 319–415.
4. Carcione, J. M., Kosloff, D., Behle, A. and Serian, G., 1992, A spectral scheme for wave propagation simulation in 3-D elastic-anisotropic media: *Geophysics*, **57**, pp. 1593–1607.
5. Fan, Z. and Teng, Y., 1988, Numerical simulations of viscoelastic waves: *Acta Geophysica Sinica*, **31**, pp. 198–209.
6. Fornberg, B., 1988, The pseudospectural method: Accurate representation of interfaces in elastic wave calculations: *Geophysics*, **53**, pp. 625–637.
7. Fornberg, B., 1987, The pseudospectrul method: Comparisons with finite difference for the elastic wave equation: *Geophysics*, **52**, pp. 483–501.
8. Fornberg, B. and Sloan, D. M., 1994, A review of pseudospectral methods for solving partial differential equations: *Acta Numerica*, pp. 203–267.
9. Gottlieb, D., Gunzburger, M. and Turkel, E., 1982, On numerical boundary treatment of hyperbolic systems for finite difference and finite element methods: *SIAM Journal of Numerical Analysis*, **19**, pp. 671–682.
10. **R.-S. Jih, 1994,** Numerical Modeling of Crustal Phase Propagation in Irregular Waveguides, 16th PL/AFOSR Seismic Symposium, pp. 173-81. *
11. Kindelan, M., Kamel, A. and Sguazzero, P., 1990, On the construction and efficiency of staggered numerical differentiators for the wave equation: *Geophysics*, **55**, pp. 107–110.
12. Kosloff, D., Kessler, D., Filho, A. Q., Tessmer, E., Behle, A. and Strahilevitz, R., 1990, Solution of the equations of dynamic elasticity by a Chebychev spectral method: *Geophysics*, **55**, pp.734–748.
13. Kosloff, D. and Tal-Ezer, P., 1993, A Modified Chebyshev Pseuspectral Method with an $O(N^{-1})$ Time Step Restriction, **104**, 457-69.
14. Nielsen, P., Flemming, I, Berg, P. and Skovgaard O., 1994, Using the pseudospectrual technique on curved grids for 2D acoustic forward modeling: *Geophysical Prospecting*, **42**, pp. 321–341.
15. Sheriff, R. E., and Geldart, L. P., 1982, *Exploration Seismology*, Vol. 1:*History, Theory and Data Acquisition*, Cambridge, Cambridge University Press.
16. Sheriff, R. E. and Geldart, L. P., 1983, *Exploration Seismology*, Vol. 2: *Data-processing and Interpretation*, Cambridge, Cambridge University Press.
17. Tessmer, E. and Kosloff, D., 1994, 3-D elastic modeling with surface topography by a Chebyshev spectral method: *Geophysics*, **59**, pp. 464–473.
18. Tessmer, E., Kosloff, D. and Behle, A., 1992, Elastic wave propagation simulation in the presence of surface topography: *Geophysical Journal International*, **108**, pp. 620–632.

* PL-TR-94-2217, ADA284667

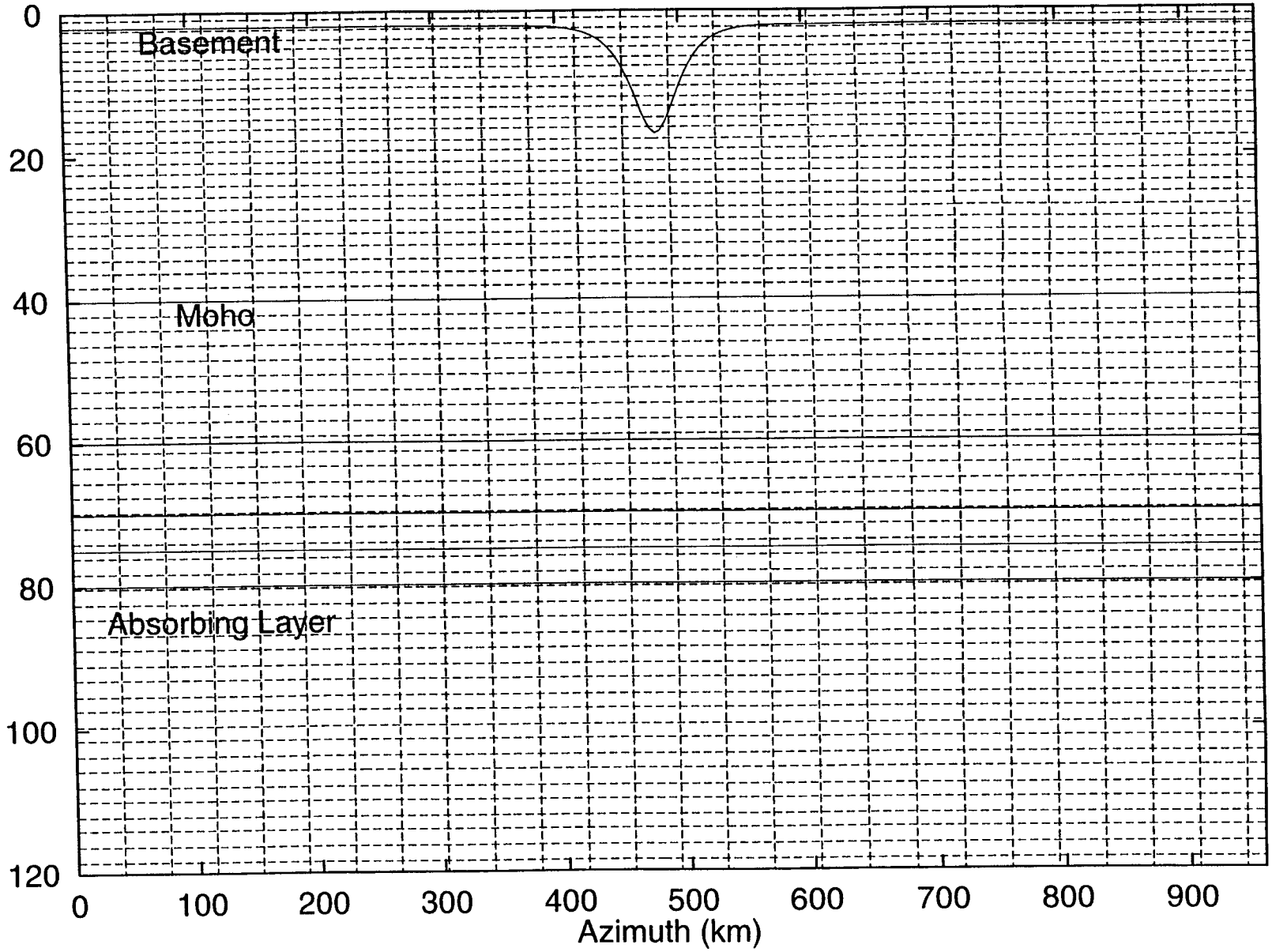

Figure 1. Grid showing subset of (x,eta) contours.

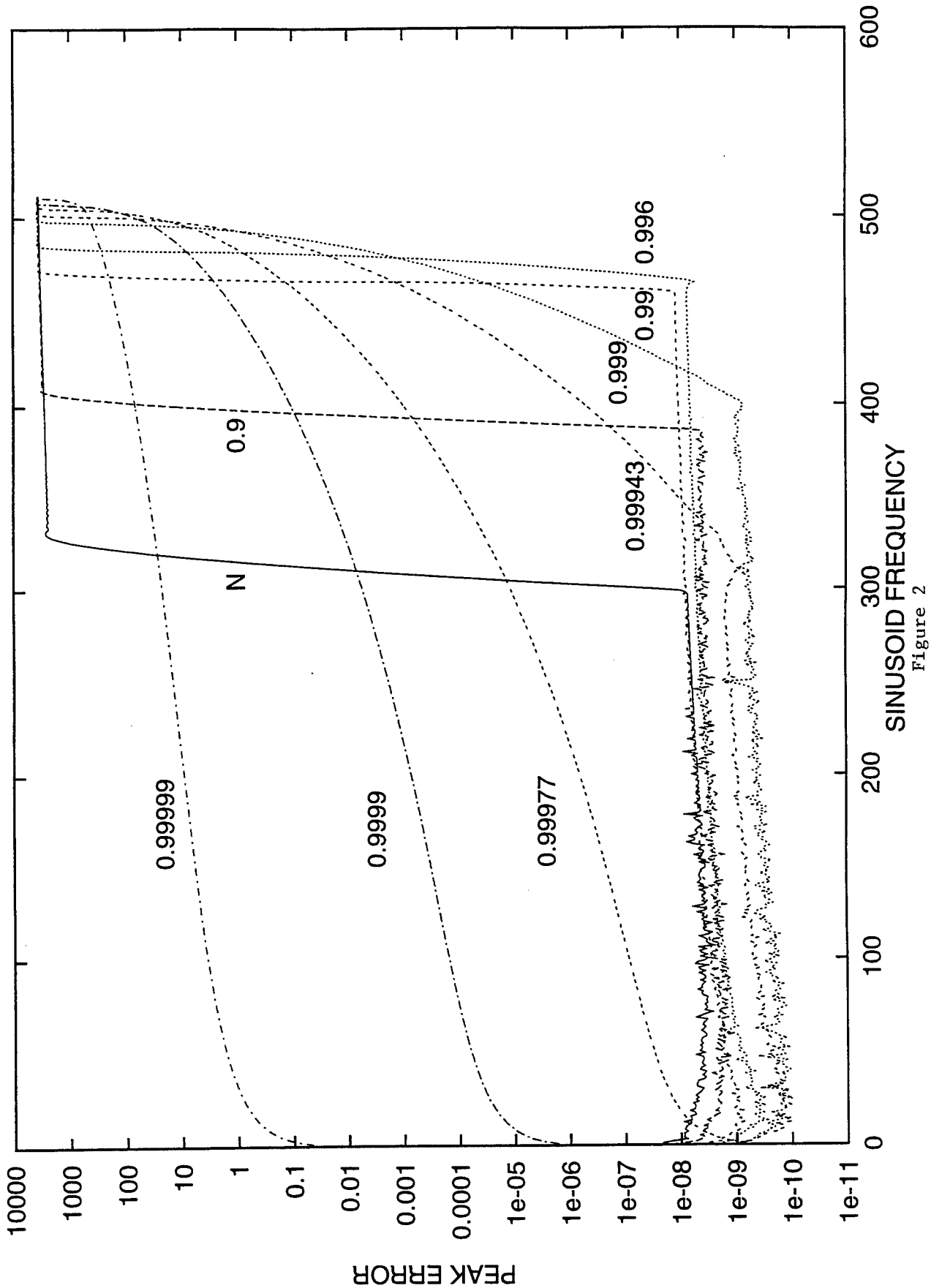
PEAK ERROR
SINUSOID FREQUENCY
10000
1000
100
10
1
0.1
0.01
0.001
0.0001
1e-05
1e-06
1e-07
1e-08
1e-09
1e-10
1e-11
0
100
200
300
400
500
600
0.99999
0.9999
0.99977
N
0.9
0.99943
0.999
0.99
0.996

Figure 2

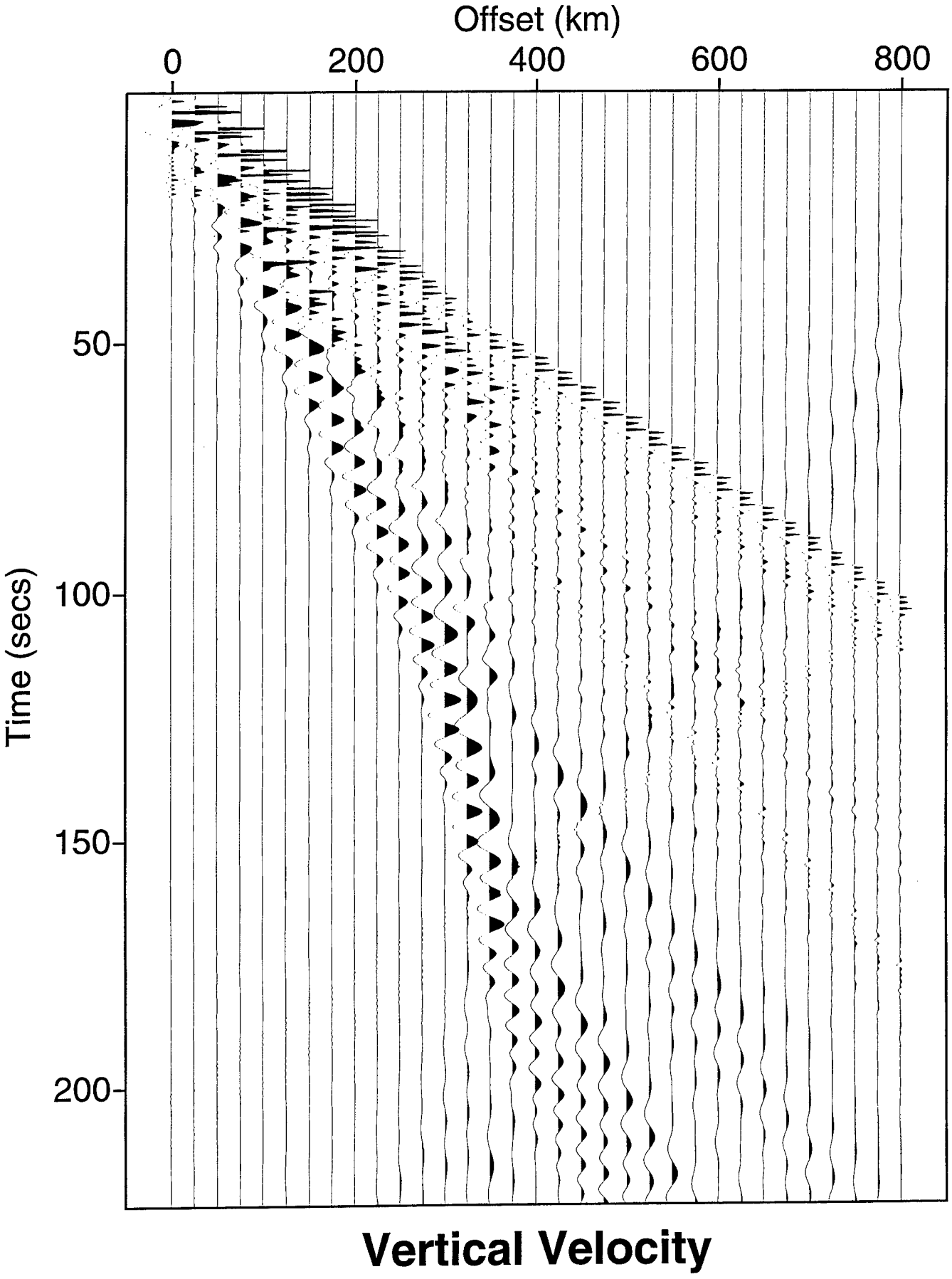
Offset (km)
0
200
400
600
800
Time (secs)
50
100
150
200
Vertical Velocity

Figure 3

A Subspace Processing Approach for Three-Component Seismic Array Data

Gregory S. Wagner

Physics Department

University of Colorado

AFOSR Grant F49620-94-1-0066

Abstract

In this paper I outline a processing approach for three-component seismic array data. Three-component seismic array (*3C*A) data analysis schemes appeal to vector space methods that have long been the mainstay of multivariate statistical analysis [*Pearson*, 1901; *Hotelling*, 1933; *Bartlett*, 1947; *Luenberger*, 1969; *Lawley and Maxwell*, 1971; *Mardia et al.*, 1979]. There are currently two popular approaches for the analysis of *3C*A data. The first is a factor analysis (*FA*) approach that entails a search for signals that satisfy simultaneously the wavefront and polarization characteristics for a very specific, idealized signal (*i.e.* wavetype, polarization, incidence angle, bearing, apparent velocity) [*Esmersoy et al.*, 1985]. This search would be particularly time consuming for cases with superimposed signals with different wavetypes and propagation directions. The second existing *3C*A analysis approach entails performing principal component (*PC*) polarization analysis of the covariance matrix that is the ensemble average of the covariance matrices from the individual three-component sensors across the array [*Jurkevics*, 1988]. This approach does not take full advantage of the spatial sampling provided by an array and leaves the numerous problems and ambiguities inherent in *PC* analysis of single-site three-component seismic data unresolved.

My three-component array processing scheme involves a succession of principal component analysis, factor analysis, and principal component analysis. The initial *PC* analysis is conducted in an effort to separate the coherent and random components of the wavefield into orthogonal subspaces. The ensuing *FA* is employed to isolate coherent superimposed arrivals and noise, and estimate the propagation direction and apparent velocity of the coherent signals. The final *PC* analysis provides estimates of the coherent signals' polarization characteristics. This *3C*A processing scheme is similar to that proposed by *Schmidt* [1979] for electromagnetic wave propagation, but incorporates several adaptations required by the nature of the seismic wavefield (*i.e.* three-dimensional as opposed to two-dimensional polarization subspace) and facilitated by the nature of seismic sensors (*i.e.* three mutually orthogonal components). For both the electromagnetic and elastic cases, this processing scheme represents an effort to conduct *PC* polarization analysis on isolated signals whose propagation directions and apparent velocities are estimated *a priori* using high-resolution wavefront analysis.

key words: seismic array, polarization, statistical signal processing

• Objectives

Much of what we know about earth structure and source processes has been inferred from seismic waveform data. Accurate waveform and signal parameter estimates are crucial to the success of any study using waveform modeling or inversion to infer subsurface structure and/or source parameters. Three-component seismic array (*3CA*) data provide a spatially unaliased, multidimensional sampling of the seismic wavefield and the potential for unprecedented signal parameter and waveform estimates. Our ability to realize the full potential of *3CA* data is contingent on our ability to develop processing schemes that allow us to fully utilize the abundance of information provided by these unique data.

The objective of my research is to develop processing schemes that will allow us to exploit and fully utilize the wealth of information provided by *3CA* data, and to use *3CA* data to address several issues of relevance for monitoring a *CTBT*. In particular, *(i)* to improve event detection and the signal-to-noise ratio for broadband data, *(ii)* to improve our understanding of the excitation and propagation of regional seismic phases , and *(iii)* to study regional wave propagation and scattering in realistic 3-D structures.

• Research Accomplished

The data vector for a two sensor (f_i, $i = 1,2$), three-component seismic array can be written as

$$\mathbf{f}^T(\omega) = \left[f_{1_Z}(\omega), f_{2_Z}(\omega), f_{1_{NS}}(\omega), f_{2_{NS}}(\omega), f_{1_{EW}}(\omega), f_{2_{EW}}(\omega) \right], \tag{1}$$

where ω is frequency, the Z,NS,EW subscripts denote the vertical, north-south and east-west components of motion, respectively, and ^{T} denotes transpose. The sample covariance matrix is the expected value of the outer product of the data vector

$$\mathbf{R}(\omega) = \mathcal{E}\left[\mathbf{f}(\omega)\, \mathbf{f}^\dagger(\omega) \right], \tag{2}$$

where $\mathcal{E}[\bullet]$ represents the expected value operator, † denotes conjugate transpose, and the $\mathbf{f}(\omega)$ are assumed to have zero mean. In practice, the expected value operator implies smoothing over ω. Without smoothing, the product $\mathbf{f}(\omega)\mathbf{f}^\dagger(\omega)$ is a matrix with rank 1; the matrix whose columns are multiples of $\mathbf{f}(\omega)$.

An alternative formulation for $\mathbf{R}(\omega)$ is provided by recognizing the fact that the $f_i(\omega)$ $(i = 1_Z, 1_{NS}, 1_{EW}, \ldots, N_Z, N_{NS}, N_{EW}$ where N is the number of three-component sensors) are themselves vectors whose elements are the ω components. The $\mathbf{f}(\omega)$ data vector can also, therefore, be viewed as the matrix $\mathbf{F}(\omega)$ whose rows are the $\mathbf{f}_i^T(\omega)$ vectors. Using this formulation, the estimate of the sample covariance matrix is

$$\mathbf{R}(\omega) = \frac{2}{L}\, \mathbf{F}(\omega)\, \mathbf{F}^\dagger(\omega)$$

$$= \frac{2}{L} \begin{bmatrix} \mathbf{f}_{1_Z}^T(\omega) \\ \vdots \\ \mathbf{f}_{N_{EW}}^T(\omega) \end{bmatrix} \begin{bmatrix} \mathbf{f}_{1_Z}^*(\omega) & \cdots & \mathbf{f}_{N_{EW}}^*(\omega) \end{bmatrix}, \tag{3}$$

where * denotes complex conjugate and the $\mathbf{f}_i(\omega)$ are L-element ω-vectors centered at the frequency of interest. Note that I have neglected the negative frequency components and doubled the estimate in Equation 3; by doing so I have computed the sample covariance matrix for the complex analytic signal [*Means*, 1972]. Using this formulation, element $R_{mn}(\omega)$ of the sample covariance matrix is

the inner product of the m-th and n-th data channels, where $m,n = 1,\ldots,3N$. The $3N \times 3N$ sample covariance matrix is Hermitian and plays the role analogous to that of the auto-covariance function in univariate (*i.e.* time series) analysis. Embedded in $\mathbf{R}(\omega)$ are the relative sensor-wise propagation-induced phase shifts, and component-wise amplitude and phase relations.

The initial *PC* analysis of $\mathbf{R}(\omega)$ facilitates an approximate separation of the coherent and incoherent components of the wavefield into orthogonal subspaces. The *PC* analysis/eigen-decomposition of $\mathbf{R}(\omega)$ is simply a coordinate transformation to an orthogonal basis in which $\mathbf{R}(\omega)$ is reduced to a diagonal matrix. In this "natural" coordinate system, the sample covariance matrix can be written in terms of its eigenvalues, $\lambda_i(\omega)$, and eigenvectors, $\mathbf{u}_i(\omega)$, as [*Golub and Van Loan*, 1989]

$$\mathbf{R}(\omega) \;=\; \sum_{i=1}^{3N} \lambda_i(\omega)\;\mathbf{u}_i(\omega)\;\mathbf{u}_i^{\dagger}(\omega) \;=\; \mathbf{U}(\omega)\;\mathbf{\Lambda}(\omega)\;\mathbf{U}^{\dagger}(\omega)\;, \qquad (4)$$

where the eigenvectors form the columns of $\mathbf{U}(\omega)$, and $\mathbf{\Lambda}(\omega)$ is the diagonal matrix whose ii-th element is $\lambda_i(\omega)$. The eigenvectors are assumed to be normalized and the eigenvalues ordered in decreasing magnitude.

Signal subspace processing schemes assume that the number of signals is known or can be determined by examining the magnitudes of the eigenvalues of $\mathbf{R}(\omega)$ [*Owsley*, 1978][†]. This being the case, the eigenspace can be partitioned into orthogonal "signal" (plus noise) and "noise" subspaces spanned by subsets of the eigenvectors. Following this misleading nomenclature—note that because *PC* analysis is strictly variance-oriented, there is no guarantee that the separation into common and unique factors is complete—an estimate of the signal covariance matrix is provided by

$$\mathbf{R}_{\mathcal{S}}(\omega) \;=\; \sum_{i=1}^{N_{\mathcal{S}}} \lambda_i(\omega)\;\mathbf{u}_i(\omega)\;\mathbf{u}_i^{\dagger}(\omega) \;=\; \mathbf{U}_{\mathcal{S}}(\omega)\;\mathbf{\Lambda}_{\mathcal{S}}(\omega)\;\mathbf{U}_{\mathcal{S}}^{\dagger}(\omega)\;, \qquad (5)$$

where $N_{\mathcal{S}}$ is the dimension of the signal subspace. The signal subspace is spanned by the $\mathbf{u}_i(\omega)$, $i = 1,...,N_{\mathcal{S}}$; the columns of $\mathbf{U}_{\mathcal{S}}(\omega)$ Likewise, an estimate of the noise covariance matrix is provided by

$$\mathbf{R}_{\mathcal{N}}(\omega) \;=\; \sum_{i=N_{\mathcal{S}}+1}^{3N} \lambda_i(\omega)\;\mathbf{u}_i(\omega)\;\mathbf{u}_i^{\dagger}(\omega) \;=\; \mathbf{U}_{\mathcal{N}}(\omega)\;\mathbf{\Lambda}_{\mathcal{N}}(\omega)\;\mathbf{U}_{\mathcal{N}}^{\dagger}(\omega)\;. \qquad (6)$$

The noise subspace—the signal subspace's orthogonal-complement—is spanned by the $\mathbf{u}_i(\omega)$, $i = N_{\mathcal{S}}+1,...,3N$; the columns of $\mathbf{U}_{\mathcal{N}}(\omega)$

The second step in my *3CA* processing scheme entails *FA* to isolate coherent signals and estimate their propagation direction and apparent propagation velocity. It is important to recognize the fact that "the compounding of a number of observable variables into one or a few factors [*i.e. PC* analysis] was not meant to yield again an observable variable, and could not be expected to do so. All we could expect to get in this way was a hypothetical variable which might or might not correlate with something in nature" [*Bartlett*, 1947]. The basis/geometry provided by the *PC* decomposition is not necessarily true in the sense that the individual $\mathbf{u}_i(\omega)$ parameterize the mode vectors of the individual superimposed signals, it is merely convenient in the sense that it allows us to account for the largest portion of the *total variance* with as few parameters as possible. In conventional beamforming (*BF*), the individual signal mode vectors are identified by locating maxima in the Hermitian form

$$P(\theta,\omega,c) \;=\; \mathbf{e}^{\dagger}(\theta,\omega,c)\;\mathbf{R}(\omega)\;\mathbf{e}(\theta,\omega,c)\;, \qquad (7)$$

[†] The dimension of the signal subspace is typically estimated using one of the numerous flavors of the sphericity test [*Bartlett*, 1947; *Lawley and Maxwell*, 1971; *Mardia et al.*, 1979; *Forster and Vezzosi*, 1987].

where the steering vectors, $\mathbf{e}(\theta,\omega,c)$, parameterize the propagation induced sensor-wise phase shifts for an ideal signal. Instead of employing a conventional *BF* approach, I compute high-resolution estimates by conducting this *FA* not in the vector space spanned by the columns of $\mathbf{R}(\omega)$ or $\mathbf{U}_S(\omega)$, but in the subspace spanned by the columns of $\mathbf{U}_N(\omega)$. Both sharper bearing estimates and improved resolution of multiple signals are provided by identifying those modes that are orthogonal or nearly orthogonal to the noise subspace as opposed to identifying those modes that correspond to maxima in the signal subspace's Hermitian form [*Bienvenu and Kopp*, 1983]. A simple analogy to this orthogonal-complement null-steering idea is as follows. Suppose that $\cos(\theta-\phi)$ provides an estimate of the array beam power for a signal traveling in directions ϕ (for $\phi-90° < \theta < \phi+90°$). For superimposed signals traveling in direction ϕ and ψ, the beam power would be (see Figure 1)

$$P_S(\theta) \;=\; \cos(\theta-\phi) \;+\; \cos(\theta-\psi) \;. \tag{8}$$

Instead of attempting to estimating ϕ and ψ by looking for maxima in Equation 8 we could, alternatively, adopt the orthogonal-complement null-steering idea and estimate ϕ and ψ by looking for maxima in

$$P_N(\theta) \;=\; \frac{1}{\sin(\theta-\phi)} \;+\; \frac{1}{\sin(\theta-\psi)} \;. \tag{9}$$

The orthogonal-complement null-steering approach provides much sharper bearing estimates and improved resolution of closely spaced, superimposed signals. Note, however, that the amplitude of the peaks in the null-spectrum do not provide a measure of the signals' power, they merely provide high-resolution estimates of ϕ and ψ.

For a single-component array, the $\mathbf{e}(\theta,\omega,c)$ are computed using a simple application of the shift theorem, where a shift of τ in the time domain corresponds to multiplication by $\exp(j\omega\tau)$ in the frequency domain ($j=\sqrt{-1}$). The propagation-induced time delay experienced by sensor i for a plane wave traveling in direction θ with apparent propagation velocity c is given by $\tau_i(\theta)=r_i(\theta)/c$, where $r_i(\theta)$ is sensor i's radial offset from some reference point. For an N sensor single-component array, the steering vector used to search θ for a plane wave with frequency ω and apparent propagation velocity c would be

$$\mathbf{e}^T(\theta,\omega,c) \;=\; \Big[\, \exp(j\, r_1(\theta)\,\omega/c),\; \ldots\;,\; \exp(j\, r_N(\theta)\,\omega/c) \,\Big]. \tag{10}$$

For a three-component seismic array, one might presume that the steering vectors would need to parameterize both the sensor-wise propagation-induced phase shifts and the component-wise amplitude and phase relations for the assumed signal [*Esmersoy et al.*, 1985]. Again, parameterizing the steering vectors in this manner implies *FA* for signals that satisfy simultaneously the wavefront and polarization characteristics for a very specific idealized signal.

The approach I adopt circumvents the computational drawbacks inherent in the *FA* approach proposed by *Esmersoy et al.* [1985], and resolves the ambiguities inherent in the *PC* analysis approach proposed by *Jurkevics* [1988]. I conduct *PC* polarization analysis of the covariance matrix computed by projecting three specific, mutually orthogonal steering vectors onto the noise subspace. For the two sensor scenario in Equation 1, the three steering vectors are

$$\mathbf{e}_Z^T(\theta,\omega,c) \;=\; \Big[\, \exp(j\, r_1(\theta)\,\omega/c),\; \exp(j\, r_2(\theta)\,\omega/c),\; 0,\; 0,\; 0,\; 0 \,\Big] \tag{11}$$

$$\mathbf{e}_{NS}^T(\theta,\omega,c) \;=\; \Big[\, 0,\; 0,\; \exp(j\, r_1(\theta)\,\omega/c),\; \exp(j\, r_2(\theta)\,\omega/c),\; 0,\; 0 \,\Big] \tag{12}$$

$$\mathbf{e}_{\mathrm{EW}}^{T}(\theta,\omega,c) \;=\; \Big[\; 0,\; 0,\; 0,\; 0,\; \exp(j\, r_1(\theta)\,\omega/c),\; \exp(j\, r_2(\theta)\,\omega/c) \;\Big] . \tag{13}$$

These vectors parameterize the propagation-induced phase shift information for purely Z,NS,EW linearly-polarized signals. The location of the N non-zero elements in each of the $\mathbf{e}_i(\theta,\omega,c)$ is determined by the arrangement of the Z,NS,EW components in the data vector (Equation 1). The polarization analysis covariance matrix computed using an enhanced minimum-variance (*EMV*) spectral estimate [*Owsley*, 1985] is

$$\mathbf{C}_{\mathrm{EMV}}(\theta,\omega,c) \;=\; \mathbf{E}^{\dagger}(\theta,\omega,c)\;\; \mathbf{U}_{\mathcal{N}}(\omega)\;\; \mathbf{\Lambda}_{\mathcal{N}}^{-1}(\omega)\;\; \mathbf{U}_{\mathcal{N}}^{\dagger}(\omega)\;\; \mathbf{E}(\theta,\omega,c)\;\;, \tag{14}$$

where $\mathbf{\Lambda}_{\mathcal{N}}^{-1}(\omega)$ is the diagonal matrix whose ii-th element is $1/\lambda_i(\omega)$, and

$$\mathbf{E}(\theta,\omega,c) = \Big[\; \mathbf{e}_{\mathrm{Z}}(\theta,\omega,c),\; \mathbf{e}_{\mathrm{NS}}(\theta,\omega,c),\; \mathbf{e}_{\mathrm{EW}}(\theta,\omega,c) \;\Big] \;\;. \tag{15}$$

The magnitude of the *EMV* spectrum is the inverse of the minimum eigenvalue, $\tilde{\lambda}_3(\theta,\omega,c)$, of $\mathbf{C}_{\mathrm{EMV}}(\theta,\omega,c)$. The associated eigenvector, $\mathbf{p}_3(\theta,\omega,c)$, is in general complex and parameterizes the component-wise amplitude and phase relations (*i.e.* the signal's polarization characteristics). The wavetype can be inferred based on θ,c and the particle motion polarization parameterized by $\mathbf{p}_3(\theta,\omega,c)$. The complete $3N$-element mode vector is

$$\mathbf{e}(\theta,\omega,c,\mathbf{p}_3) \;=\; \mathbf{E}(\theta,\omega,c)\;\; \mathbf{p}_3(\theta,\omega,c)\;\;. \tag{16}$$

This basic approach can be incorporated into other array processing schemes. For example, the magnitude of the *MUSIC* null-spectrum [*Schmidt*, 1979], and the minimum-variance distortionless response (*MVDR*) spectrum [*Owsley*, 1985] are $1/\tilde{\lambda}_3(\theta,\omega,c)$ for

$$\mathbf{C}_{\mathrm{MUSIC}}(\theta,\omega,c) \;=\; \mathbf{E}^{\dagger}(\theta,\omega,c)\;\; \mathbf{U}_{\mathcal{N}}(\omega)\;\; \mathbf{U}_{\mathcal{N}}^{\dagger}(\omega)\;\; \mathbf{E}(\theta,\omega,c) \tag{17}$$

and

$$\mathbf{C}_{\mathrm{MVDR}}(\theta,\omega,c) \;=\; \mathbf{E}^{\dagger}(\theta,\omega,c)\;\; \mathbf{R}^{-1}(\omega)\;\; \mathbf{E}(\theta,\omega,c), \tag{18}$$

where $\mathbf{R}^{-1}(\omega)$ is the inverse of $\mathbf{R}(\omega)$. The magnitude of the spectra for conventional/Bartlett (*BF*) and signal subspace (SS) beamforming (SS) is the largest eigenvalue, $\tilde{\lambda}_1(\theta,\omega,c)$, of

$$\mathbf{C}_{\mathrm{BF}}(\theta,\omega,c) \;=\; \mathbf{E}^{\dagger}(\theta,\omega,c)\;\; \mathbf{R}(\omega)\;\; \mathbf{E}(\theta,\omega,c) \tag{19}$$

and

$$\mathbf{C}_{\mathrm{SS}}(\theta,\omega,c) \;=\; \mathbf{E}^{\dagger}(\theta,\omega,c)\;\; \mathbf{U}_{\mathcal{S}}(\omega)\;\; \mathbf{\Lambda}_{\mathcal{S}}(\omega)\;\; \mathbf{U}_{\mathcal{S}}^{\dagger}(\omega)\;\; \mathbf{E}(\theta,\omega,c)\;, \tag{20}$$

respectively. Waveform estimates can be computed by "stacking" the data using

$$\hat{x}(\theta,\omega,c,\mathbf{p}_3) \;=\; \mathbf{e}^{\dagger}(\theta,\omega,c,\mathbf{p}_3)\;\; \mathbf{f}(\omega) \tag{21}$$

or, similarly, by projecting the $\mathbf{e}(\theta,\omega,c,\mathbf{p}_3)$ onto the signal subspace [*Wagner*, 1994] or, alternatively, by using the $\mathbf{e}(\theta,\omega,c,\mathbf{p}_3)$ to compute the *MVDR* weight vector [*Owsley*, 1985]

$$\mathbf{a}(\theta,\omega,c,\mathbf{p}_3) \;=\; \frac{\mathbf{R}^{-1}(\omega)\;\; \mathbf{e}(\theta,\omega,c,\mathbf{p}_3)}{\mathbf{e}^{\dagger}(\theta,\omega,c,\mathbf{p}_3)\;\; \mathbf{R}^{-1}(\omega)\;\; \mathbf{e}(\theta,\omega,c,\mathbf{p}_3)}\;\;, \tag{22}$$

and waveform estimate

$$\hat{x}(\theta,\omega,c,\mathbf{p}_3) \;=\; \mathbf{a}^{\dagger}(\theta,\omega,c,\mathbf{p}_3)\;\; \mathbf{f}(\omega)\;\;. \tag{23}$$

- *Data analysis example*

In this section I compare the parameter estimates realized using single-site three-component (*3C*), vertical-component array (*ZA*), and three-component array (*3CA*) data. The synthetic data used for this demonstration consist of simultaneously arriving, linearly-polarized *P* and *SH* body waves (longitudinal and transverse particle motions, respectively) and a Rayleigh surface-wave (retrograde circular particle motion) superimposed on spatially and temporally white noise. Signal parameters are listed in Table 1; examples of the waveform data are shown in Figure 2. The array consisted of five sensors arranged in a circular geometry with a radius of 320 meters. The synthetic data were analized using broadband single-site *PC* polarization analysis [*Means*, 1972] and broadband three-component array analysis [*Wagner*, 1995]. For the *3C* data, *PC* analysis is performed using both the real and complex analytic signals; use of the complex analytic signal allows us to account for elliptically polarized particle motion [*Means*, 1972].

In Figure 3 I show the direction-of-arrival spectra computed for ten simulations using *EMV*, *MUSIC*, *MVDR* and SS estimates for both three-component and vertical-component array data. At the top of Table 2 I list the estimated bearings, wavenumbers, and polarization analysis eigenvalue-eigenvector pairs corresponding to the peaks in the *EMV* spectrum. For the *EMV* estimate, the particle motion polarization is parameterized by the eigenvector associated with the minimum eigenvalue. At the bottom of Table 2 I list the eigenvalue-eigenvector pairs from single-site *PC* analysis of the real and complex analytic signals as *PC* and *PC**, respectively. For the *3C* data, an estimate of the mode vector for the largest coherent signal is provided, ideally, by the eigenvector associated with the largest eigenvalue.

It is important to note that in and of themselves, the eigenvectors obtained from *PC* polarization analysis provide little if any useful information. The eigenvectors can be used to infer the signal's wavetype only if its propagation direction is known *a priori* or, alternatively, used to infer the signal's propagation direction only if its wavetype is known *a priori*. The main advantage of a *3CA* is simply that these data allow us to estimate a signal's propagation direction and apparent propagation velocity as well as its particle motion polarization characteristics. *3C* data provide only particle motion polarization information which can be reliably interpreted only with additional information that may not always be available. The information provided by the *3CA* data allowed us to resolve and accurately estimate the propagation direction and polarization characteristics for each of the three signals in the synthetic data. Analysis using the *3C* synthetic data was not capable of resolving the three signals or properly estimating the polarization characteristics of any one signal.

- **Conclusions**

I have outlined a statistical array processing approach for three-component seismic array data that involves a succession of principal component analysis, factor analysis, and principal component analysis. The initial *PC* analysis is conducted in an effort to separate the coherent and random components of the wavefield into orthogonal subspaces. The ensuing *FA* allows us to isolate superimposed signals and noise and estimate the coherent signals' propagation direction and apparent propagation velocity. The final *PC* analysis provides estimates of the signals' polarization characteristics. This processing scheme provides a relatively simple and computationally efficient approach for the analysis of *3CA* data that allows us to exploit and fully utilize the abundance of information provided by these unique data.

• References

Bartlett, M. S., Multivariate Analysis (with discussion), *J. Roy. Stat. Soc.*, **9**(2), 176–197, 1947.

Bienvenu, B., and L. Kopp, Optimality of high resolution array processing using the eigensystem approach, *IEEE Trans. Acoust., Speech, Signal Processing*, **31**(5), 1235–1248, 1983.

Esmersoy, L., V. F. Cormier, and M. N. Toksöz, Three component array processing, in *The VELA program: A twenty-five year review of basic research*, edited by A. Kerr, pp. 565–578, Executive Graphics Services, Arlington, VA, 1985.

Forster, P. and G. Vezzosi, Application of spheroidal sequences to array processing, *Proc. IEEE Int. Conf. on Acoustic, Speech and Signal Proc.*, 2268–2271, 1987.

Golub, G. H., and C. F. Van Loan, *Matrix Computations*, The John Hopkins University Press, Baltimore, MD, 1989.

Hotelling, H., Analysis of a complex of statistical variables into principal components, *J. Edu. Psych.*, **24**, 417–441, 1933.

Jurkevics, A., Polarization analysis of three-component array data, *Bull. Seism. Soc. Am.*, **78**(5), 1725–1743, 1988.

Lawley, D. N. and A. E. Maxwell, *Factor Analysis as a Statistical Method*, Elsevier, New York, 1971.

Luenberger, D. G., *Optimization by Vector Space Methods*, John Wiley & Sons, New York, 1969.

Mardia, K. V., J. T. Kent, and J. M. Bibby, *Multivariate Analysis*, Academic Press, New York, 1979.

Means, J. D., Use of the three-dimensional covariance matrix in analyzing the polarization properties of plane waves, *J. Geophys. Res.*, **77**(28), 5551–5559, 1972.

Owsley, N. L., Adaptive data orthogonalization, *Proc. IEEE Int. Conf. Acoust., Speech, Signal Processing*, 109–112, 1978.

Owsley, N. L., Sonar array processing, in *Array Signal Processing*, edited by S. Haykin, pp. 115–193, Prentice–Hall, Englewood Cliffs, NJ, 1985.

Pearson, K., On lines and planes of closet fit to systems of points in space, *Phil. Mag.*, **2**, 559-572, 1901.

Schmidt, R. O., Multiple emitter location and signal parameter estimation, *Proc. of the RADC Spectrum Estimation Workshop*, 243–258, 1979.

Wagner, G. S., Analysis of multidimensional JSP data, *IRIS Newsletter* (summer), 13–16, 1994.

Wagner, G. S. and T. J. Owens, Broadband eigen-analysis for three-component seismic array data, *IEEE Trans. on Signal Processing*, **43**(7), 1738–1741, 1995.

wavetype	peak ω	bearing	incidence angle	SNR
P	23 Hz	140°	38.6°	4
SH	12 Hz	135°	32.3°	4
Rayleigh	4.25 Hz	130°	circ. polar.	4

Table 1: Signal parameters for the synthetic simulation. The medium is a Poisson solid with a P velocity of 5.0 km/sec. The Rayleigh wave has retrograde circular particle motion and a velocity of 0.92 times the S velocity. See Figure 2 for examples of the synthetic waveform data.

θ	k	$\tilde{\lambda}$	p_{Z} (rl,im)	p_{N} (rl,im)	p_{E} (rl,im)
129.6°	1.59	0.08	-0.03, 0.72	0.39, 0.07	-0.57, 0.0
		2.81	-0.05,-0.06	-0.74,-0.23	-0.62, 0.0
		4.99	-0.09, 0.68	-0.44,-0.19	0.54, 0.0
135.2°	2.18	0.08	-0.13, 0.06	-0.70, 0.03	-0.69, 0.0
		1.52	0.54, 0.46	0.45,-0.15	-0.52, 0.0
		4.49	0.39, 0.57	-0.52,-0.12	0.49, 0.0
139.8°	2.87	0.06	0.76, 0.02	0.49,-0.04	-0.42, 0.0
		3.32	0.00, 0.02	-0.64, 0.02	-0.76, 0.0
		4.98	0.65, 0.05	-0.58,-0.01	0.49, 0.0
	PC	11.98	0.75	-0.67	0.01
		9.48	0.23	0.27	0.94
		6.34	0.62	0.69	-0.36
	PC^*	10.20	0.74, 0.0	0.29, 0.38	-0.08,-0.47
		6.00	-0.09, 0.0	0.64, 0.42	0.34, 0.53
		3.73	-0.67, 0.0	0.24, 0.35	-0.14,-0.59

Table 2: Bearings (θ), wavenumbers (k, cycles/km) and the polarization analysis eigenvalues ($\tilde{\lambda}$) and components of the associated eigenvectors (real and imaginary parts) for the signals corresponding to the peaks in Figure 3. PC and PC^* in the lower part of the table are the eigenvalue-eigenvector pairs from single-site PC polarization analysis of the real and complex analytic signals, respectively.

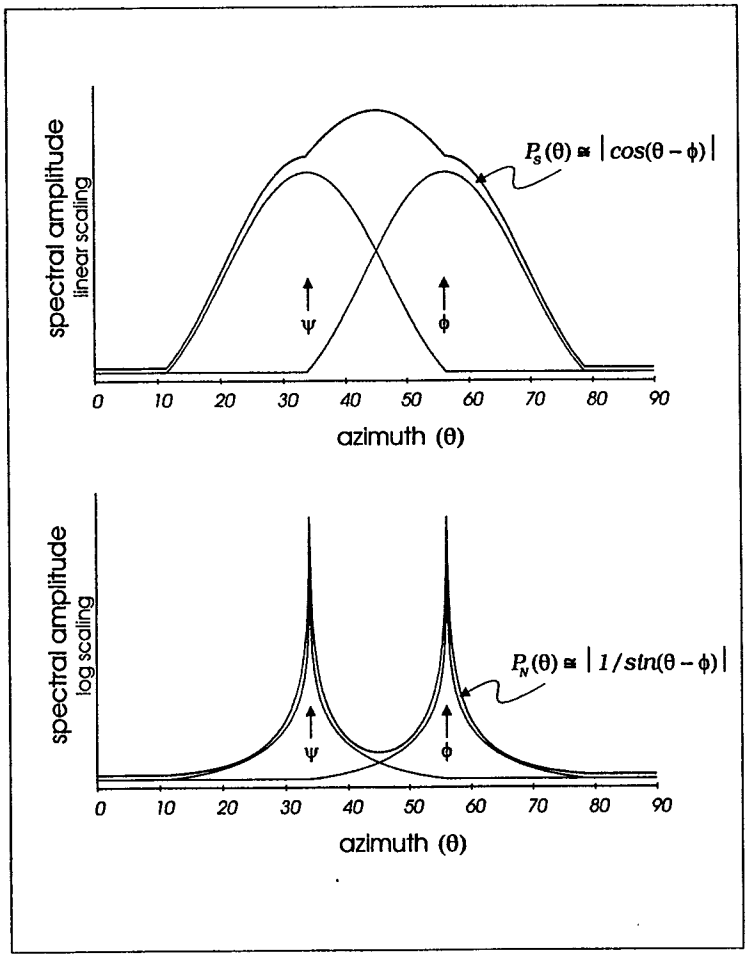

Figure 1: Cartoon depicting the improved resolution realized using orthogonal-complement factor analysis/null-steering.

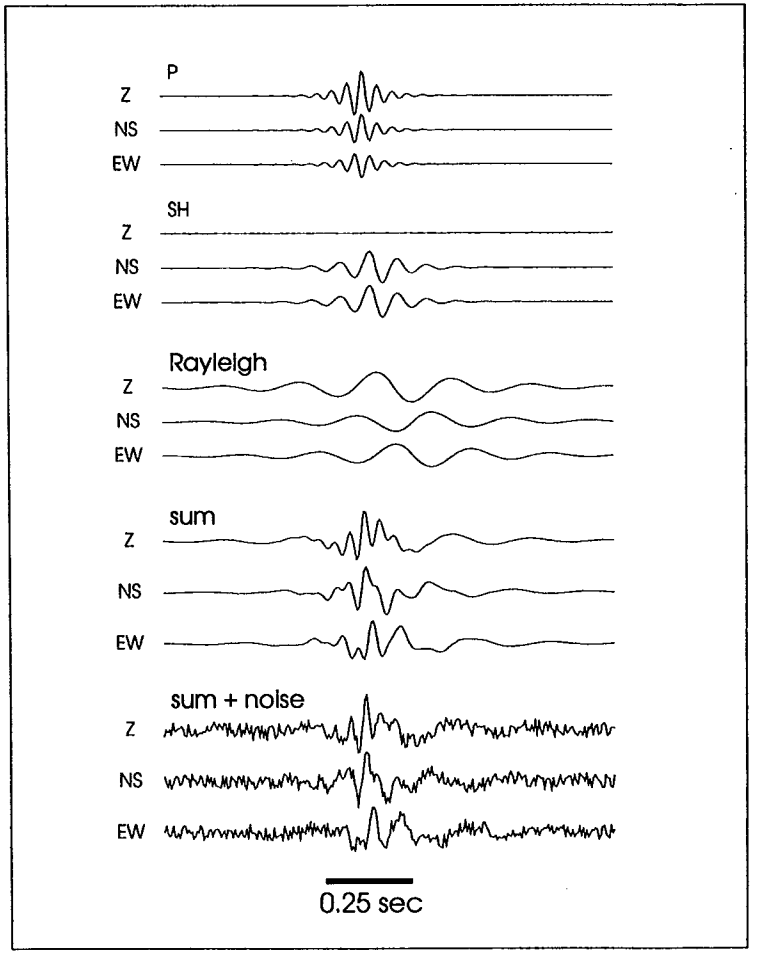

Figure 2: Examples of the synthetic waveform data used in the simulation. See Table 1 for input signal parameters

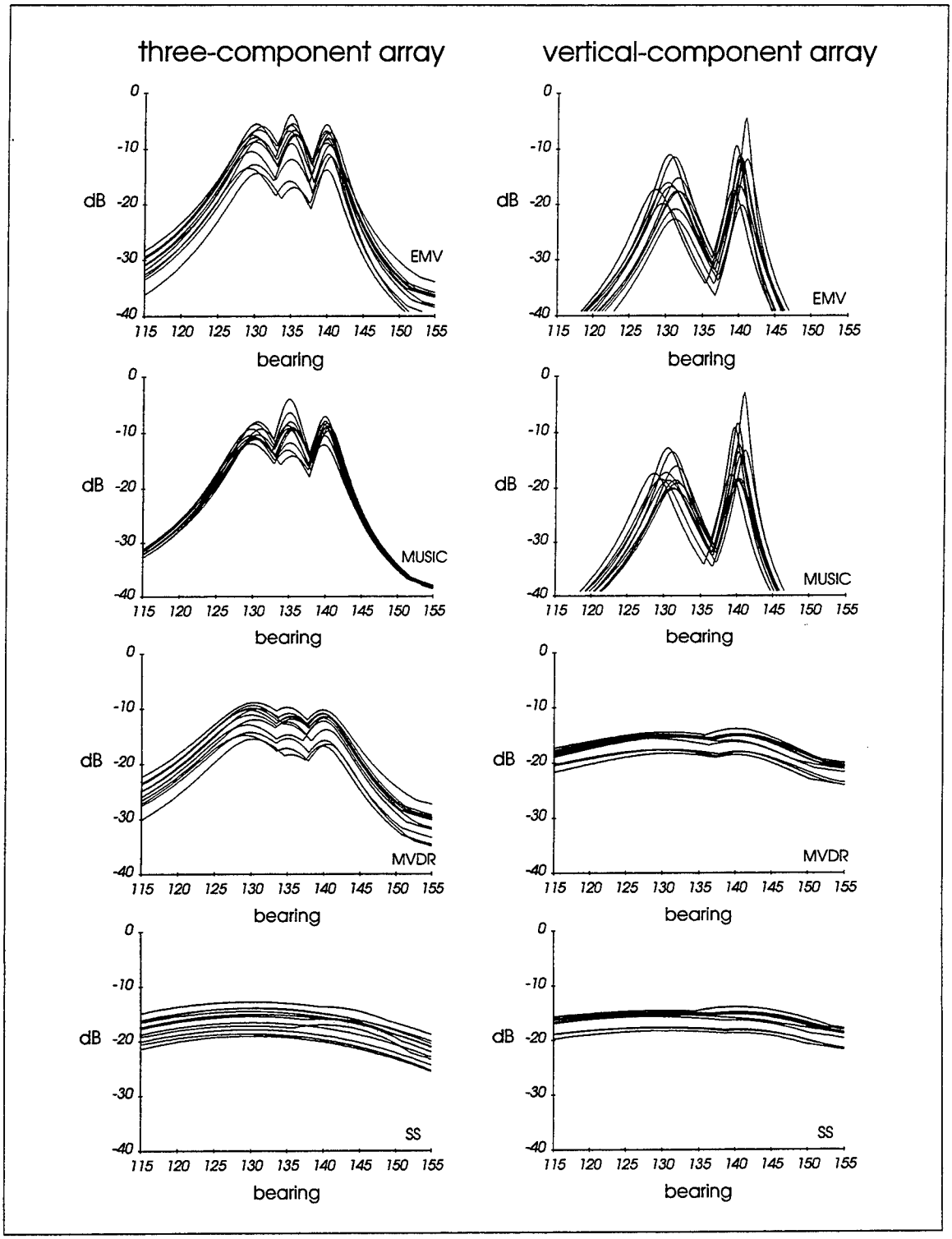

Figure 3: Direction-of-arrival spectra for ten simulations computed using EMV, MUSIC, MVDR and SS algorithms for three-component and vertical-component array data. See Table 1 for input signal parameters, Figure 2 for examples of the waverform data, and Table 2 for signal parameter estiamtes.

MODELING THE EFFECTS OF SURFACE TOPOGRAPHY ON LG WAVE PROPAGATION BY A HYBRID METHOD

Ru-Shan Wu, Xiaofei Chen, and Thorne Lay
University of California, Santa Cruz
Sponsored by
U.S. DEPARTMENT OF ENERGY
Office of Nonproliferation and National Security
Office of Research and Development
ST486
Issued by the Phillips Laboratory
under Contract No. F19628-95-K-0016

ABSTRACT

The object of this research is to study the effects of surface topography, near-surface (sedimentary) structure and the associated small-scale heterogeneities on regional wave propagation which is critical for both discrimination and yield estimation in monitoring a Comprehensive Test Ban Treaty and the current Nuclear Non-Proliferation Treaty. We aim at developing a hybrid method which couples our recently developed fast screen propagator theory and methods (Wu, 1994, Wu and Xie, 1994; Wu and Huang, 1995) with a modified Boundary Integral Equation (BIE) method to treat the influences of both volume heterogeneities and irregular interfaces, including the influence of surface topography.

This report summarizes the effort in theoretical and computer code development during the first ten months of the project. In order to treat Lg wave propagation and scattering in complex crustal waveguides with arbitrary surface topography and irregular interfaces, we adopt Chen's GGRTM (Global Generalized Reflection/Transmission Matrix) method as the major element in our hybrid method. As the first step, we test the method and the connection with the one-way wave method for the two-dimensional SH case. Chen's theory has been modified for this purpose and the connection formulas have been derived and numerically tested. The excellent agreement between seismograms for direct propagation and propagation using the connection formulas proves the correctness of the theory and the feasibility of the methodology.

Keywords: Topography effects, Lg waves, Hybrid modeling method, Boundary integral equation.

OBJECTIVES

The object of this research is to study the effects of surface topography, near-surface (sedimentary) structure and the associated small-scale heterogeneities on regional wave propagation which is critical for both discrimination and yield estimation in monitoring a Comprehensive Test Ban Treaty and the current Nuclear Non-Proliferation Treaty. We aim at developing a hybrid method which couple our recently developed fast screen propagator theory and methods (Wu, 1994, Wu and Xie, 1994; Wu and Huang, 1995) with a modified Boundary Integral Equation (BIE) method to treat the influences of both volume heterogeneities and irregular interfaces, including the influence of surface topography. We will apply one-way type surface element interactions to achieve great reduction in 3D modeling computations.

RESEARCH ACCOMPLISHED

This report summarizes the effort in theoretical and computer code development during the first ten months of the project. In order to treat Lg wave propagation and scattering in complex crustal waveguides with arbitrary surface topography and irregular interfaces, we adopt Chen's GGRTM (Global Generalized Reflection/Transmission Matrix) method as the major element in our hybrid method. As the first step, we test the method and the connection with the one-way wave method for the two-dimensional SH case. Chen's theory has been modified for this purpose and the connection formulas have been derived and numerically tested. The excellent agreement between seismograms for direct propagation and the propagation using the connection formulas proves the correctness of the theory and the feasibility of the methodology.

Introduction

In the past, boundary integral equation (BIE) or boundary element (BE) methods have been extensively used to study the effects of topography or sedimentary basin structures on seismic motions on the surface. It has been also used to study Lg blockage problem with limited success. Blockage is assumed to be caused by coastlines, mountains and sudden change of crustal thickness. However, numerical simulations of blockage by large-scale crustal structures have not succeeded in matching the observations (Campillo et al., 1993; Gibson and Campillo, 1994). Most simulations are either for surface topography or for irregular structure under a half space (sedimentary layer) due to the restriction of computational complexity. However, the combination of both surface-topography and sedimentary structure may have more dramatic influence. Irregular surface and low-velocity layer can both trap part of the Lg energy into the surface layer and scatter the Lg wave out of the crustal waveguide. Existing methods are also not capable of simulating the combined effects of both large-scale structure and the associated small-

scale heterogeneities. Irregular topography and near-surface structure are the manifestation of past and/or present tectonic processes which often produce crustal heterogeneities at different scales. The effects from the small-scale (wavelength-scale) heterogeneities must be taken into consideration in modeling blockage and other Lg propagation, scattering and attenuation phenomena.

We are in the process of developing a new hybrid numerical method by combining BIE methods and the generalized screen (phase-screen, wide-angle screen, elastic complex-screen, etc.) one-way wave method (Wu, 1994, 1996; Wu and Xie, 1994; Wu and Huang, 1995). The discretization of BIE can be done by integration of the Green's function along small elements of the boundary (e.g. Sanches-Sesma and Campillo, 1991), or by using the discrete wave number representation of the Green's function (Bouchon, 1985; Campillo and Bouchon, 1985; Chen, 1990, 1995, 1996). In the latter approach, the singularity problem of the Green's function is avoided by using truncated series. The wavenumber domain BIE has another advantage which is that it can be easily extended to the case of multilayered media with irregular interfaces. In Bouchon et al. (1989), propagator matrices are used to relate equivalent force distributions on neighboring interfaces. Chen (1990, 1995, 1996) related the fields at neighboring layers by global reflection/transmission coefficients and then derived the global generalized R/T coefficients to relate observations and sources. In these methods, the dimensionality of the linear system to solve are independent of the number of layers involved. the computation time increases only linearly with the number of interfaces. Due to its superior properties, we adopt Chen's GGRTM (Global Generalized Reflection/Transmission Matrix) method as the major element in our hybrid method.

Because of the matrix operation involved, the wavenumber domain BIE has some difficulty in the applications for problems of Lg wave propagation and scattering. When the ratio of model dimension to wavelength is too large, the computation time and memory requirement become formidable. This problem can be circumvented through two approaches. One is to propagate the waves by other fast algorithms in the smoothly varying part or homogeneous part of the waveguide and input the regional waves into the roughly irregular part by a connection formula. Then the local interaction and evolution of the regional waves can be studied by the accurate BIE method. The other is to make some approximation, such as the Rayleigh ansatz, to the BIE method to speed up the computation. We will test the first approach in this study, and leave the second approach for future research. Besides, the Aki-Larner method fails for interfaces with steep slopes (Axilrod and Ferguson, 1990). On the other hand, for many problems of Lg propagation, such as topography effects, the influence can be localized to a rather small spatial extent. Therefore, we can inject the Lg waves to the local crustal structure, and examine the topographic effects on Lg waves by expensive but accurate BIE methods. This approach has

been adopted by Regan and Harkrider (1989a,b), to connect the field calculated by propagation matrix to a region to be calculated by finite element algorithm. In this study regional field calculated by other methods such as reflectivity method, is injected into model space as vertically distributed sources. In the following the general scheme of the hybrid method will be given . Numerical test of the connection formula is followed to demonstrate the validity of the methodology.

The GGRTM (global generalized reflection/transmission metrix) method

This method can be viewed as an extension of the reflectivity method for horizontally layered case to an irregularly layered case, and it has been demonstrated to be an accurate and effective method to simulate seismic waves in laterally varying layered media (Chen, 1991, 1995, 1996). For example, for the scattering problem due to a semi-circular canyon (shown in figure 1), GGRTM can provide very accurate results. Figure 2 and 3 show the comparisons of the results (solid lines) computed by GGRTM with the analytical solutions of Trifunac (dotted lines) for various normalized frequencies, showing excellent agreement between them. It is known that in this semi-circular canyon topography model, there are two sharp edges (with infinite derivatives) at x=±a , and many other methods, for instance, Aki-Larner method, T-matrix method and high-frequency asymptotic method , fail to provide correct solution.

Connection formulation

Assume domain II is the model space we are interested in and the field in domain I is easy to calculated by other less expensive methods. According to the representation theorem, wave-fields inside domain II can be expressed as

$$u^{II}(\mathbf{x},\omega) = \int_0^{+\infty} \left\{ \tau^I(\mathbf{x}') + u^I(\mathbf{x}')\mu(z')\frac{\partial}{\partial x'} \right\} G^{II}(\mathbf{x},\mathbf{x}')dz' \qquad (1)$$

Where u^I and τ^I are the displacement and traction fields on the vertical boundary surface dividing domain I and II, and can be calculated using methods valid in domain I, μ is the shear rigidity, and G^{II} is the Green's function in domain II which will be calculated by GGRTM.

Algorithm of computing synthetic Lg waves

Having the connection formulation, we can use GGRTM to compute synthetic Lg waves. The step by step procedure of applying GGRTM to computing a synthetic seismogram in a general irregularly layered medium can be summarized as follows.

Step 1

Calculate the interface matrices for each interface, $\mathbf{Q}_{\downarrow\uparrow}^{(j)}$, $\mathbf{Q}_{\uparrow\downarrow}^{(j)}$, $\mathbf{Q}_{\uparrow\uparrow}^{(j)}$, $\mathbf{Q}_{\downarrow\downarrow}^{(j)}$, $\mathbf{P}_{\uparrow\uparrow}^{(j)}$, $\mathbf{P}_{\downarrow\downarrow}^{(j)}$, $\mathbf{P}_{\uparrow\downarrow}^{(j)}$, $\mathbf{P}_{\downarrow\uparrow}^{(j)}$; for j=1,2, ..., N}, by carrying out the integrals over each interface. These interface matrices contain the structural information of the media and are defined as (Chen, 1990)

$$\left(\mathbf{Q}_{\downarrow\uparrow}^{(j)}\right)_n = \frac{-1}{2\nu_n^{(j)}L}\int_{-L/2}^{L/2}\left\{\dot{\xi}^{(j-1)}(x)k_n + \nu_n^{(j)}\right\}\exp[i\Xi_{\downarrow\uparrow}^{(j)}(x,n,m)]dx, \tag{2a}$$

$$\left(\mathbf{Q}_{\downarrow\downarrow}^{(j)}\right)_n = \frac{-1}{2\nu_n^{(j)}L}\int_{-L/2}^{L/2}\left\{\dot{\xi}^{(j-1)}(x)k_n - \nu_n^{(j)}\right\}\exp[i\Xi_{\downarrow\downarrow}^{(j)}(x,n,m)]dx, \tag{2b}$$

$$\left(\mathbf{Q}_{\uparrow\downarrow}^{(j)}\right)_n = \frac{-1}{2\nu_n^{(j)}L}\int_{-L/2}^{L/2}\left\{\dot{\xi}^{(j)}(x)k_n - \nu_n^{(j)}\right\}\exp[i\Xi_{\uparrow\downarrow}^{(j)}(x,n,m)]dx; \tag{2c}$$

$$\left(\mathbf{Q}_{\uparrow\uparrow}^{(j)}\right)_n = \frac{-1}{2\nu_n^{(j)}L}\int_{-L/2}^{L/2}\left\{\dot{\xi}^{(j)}(x)k_n + \nu_n^{(j)}\right\}\exp[i\Xi_{\uparrow\uparrow}^{(j)}(x,n,m)]dx, \tag{2d}$$

$$\left(\mathbf{P}_{\downarrow\uparrow}^{(j)}\right)_n = \frac{-\nu_m^{(j)}}{2\nu_n^{(j)}L}\int_{-L/2}^{L/2}\left\{1+[\dot{\xi}^{(j-1)}(x)]^2\right\}^{1/2}\exp[i\Xi_{\downarrow\uparrow}^{(j)}(x,n,m)]dx, \tag{2e}$$

$$\left(\mathbf{P}_{\downarrow\downarrow}^{(j)}\right)_n = \frac{-\nu_m^{(j)}}{2\nu_n^{(j)}L}\int_{-L/2}^{L/2}\left\{1+[\dot{\xi}^{(j-1)}(x)]^2\right\}^{1/2}\exp[i\Xi_{\downarrow\downarrow}^{(j)}(x,n,m)]dx, \tag{2f}$$

$$\left(\mathbf{P}_{\uparrow\downarrow}^{(j)}\right)_n = \frac{-\mu^{(j+1)}\nu_m^{(j+1)}}{2\mu^{(j)}\nu_n^{(j)}L}\int_{-L/2}^{L/2}\left\{1+[\dot{\xi}^{(j)}(x)]^2\right\}^{1/2}\exp[i\Xi_{\uparrow\downarrow}^{(j)}(x,n,m)]dx, \tag{2g}$$

and

$$\left(\mathbf{P}_{\uparrow\uparrow}^{(j)}\right)_n = \frac{-\mu^{(j+1)}\nu_m^{(j+1)}}{2\mu^{(j)}\nu_n^{(j)}L}\int_{-L/2}^{L/2}\left\{1+[\dot{\xi}^{(j)}(x)]^2\right\}^{1/2}\exp[i\Xi_{\uparrow\uparrow}^{(j)}(x,n,m)]dx, \tag{2h}$$

where $\xi^{(j)}(x)$ is the height of the topography for the jth interface, and

$$k_n = 2\pi n / L,\quad \nu_n^{(j)} = \sqrt{(\omega/\beta^{(j)})^2 - (k_n)^2}\,,\ \text{and}\ \mathrm{Im}\left\{\nu_n^{(j)}\right\} \geq 0,$$

$$\Xi_{\uparrow\uparrow}^{(j)}(x,n,m) = (k_m - k_n)x + \nu_n^{(j)}[\xi^{(j)}(x) - \xi_{\min}^{(j)}] + \nu_m^{(j+1)}\left|\Delta\xi^{(j)}(x)\right|,$$

,

$$\Xi_{\downarrow\uparrow}^{(j)}(x,n,m) = (k_m - k_n)x + v_n^{(j)}[\xi^{(j-1)}(x) - \xi_{\min}^{(j-1)}] + v_m^{(j)}\left|\Delta\xi^{(j-1)}(x)\right|,$$

and

$$\Xi_{\downarrow\downarrow}^{(j)}(x,n,m) = (k_m - k_n)x - v_n^{(j)}[\xi^{(j-1)}(x) - \xi_{\max}^{(j-1)}] + v_m^{(j)}\left|\Delta\xi^{(j-1)}(x)\right|;$$

for j = 1, 2, ..., N.

Where $\Delta\xi^{(j)}(x) = \xi^{(j)}(x) - z^{(j)}$.

Step 2

Calculate the global modified reflection and/or transmission matrices, { $\mathbf{R}_{\downarrow\uparrow}^{(j)}$, $\mathbf{T}_{\uparrow\uparrow}^{(j)}$, $\mathbf{T}_{\downarrow\downarrow}^{(j)}$, $\mathbf{R}_{\uparrow\downarrow}^{(j)}$}, from the interface matrices using the following formulas:

$$\begin{bmatrix} \mathbf{R}_{\downarrow\uparrow}^{(j)} & \mathbf{T}_{\uparrow\uparrow}^{(j)} \\ \mathbf{T}_{\downarrow\downarrow}^{(j)} & \mathbf{R}_{\uparrow\downarrow}^{(j)} \end{bmatrix} = \begin{bmatrix} \mathbf{Q}_{\uparrow\uparrow}^{(j)} & \mathbf{P}_{\uparrow\uparrow}^{(j)} \\ -\mathbf{Q}_{\downarrow\downarrow}^{(j+1)} & -\mathbf{P}_{\downarrow\downarrow}^{(j+1)} \end{bmatrix} \begin{bmatrix} -\mathbf{Q}_{\uparrow\downarrow}^{(j)} & -\mathbf{P}_{\uparrow\downarrow}^{(j)} \\ \mathbf{Q}_{\downarrow\uparrow}^{(j+1)} & \mathbf{P}_{\downarrow\uparrow}^{(j+1)} \end{bmatrix}^{-1} \begin{bmatrix} \mathbf{E}_{\max}^{(j)} & \\ & \mathbf{E}_{\min}^{(j+1)} \end{bmatrix}, \tag{3}$$

and

$$\mathbf{R}_{\uparrow\downarrow}^{(o)} = -\mathbf{Q}_{\downarrow\downarrow}^{(1)}\left(\mathbf{Q}_{\downarrow\uparrow}^{(1)}\right)^{-1}\mathbf{E}_{\min}^{(1)}, \tag{3a}$$

where, $\mathbf{E}_{\min}^{(j)}$ and $\mathbf{E}_{\max}^{(j)}$ are diagonal matrices given by

$$\mathbf{E}_{\min}^{(j)} = diagonal\left\{\exp[iv_n^{(j)}(\xi_{\min}^{(j)} - \xi_{\min}^{(j-1)})];\ n = 0,\pm1,\pm2,...\right\},$$

and

$$\mathbf{E}_{\max}^{(j)} = diagonal\left\{\exp[iv_n^{(j)}(\xi_{\max}^{(j)} - \xi_{\max}^{(j-1)})];\ n = 0,\pm1,\pm2,...\right\}.$$

These global modified reflection and/or transmission matrices describe the reflection and/or transmission effects due to single interface regardless of the influences from other existing interfaces.

Step 3

Compute the global generalized reflection and/or transmission matrices, $\hat{\mathbf{T}}_{\uparrow\uparrow}^{(j)}$, $\hat{\mathbf{R}}_{\downarrow\uparrow}^{(j)}$, $\hat{\mathbf{T}}_{\downarrow\downarrow}^{(j)}$, and $\hat{\mathbf{R}}_{\uparrow\downarrow}^{(j)}$, from the global modified reflection and/or transmission matrices through following recursive formulas:

$$\begin{cases} \hat{\mathbf{R}}_{\uparrow\downarrow}^{(o)} = \mathbf{R}_{\uparrow\downarrow}^{(o)} \\ \hat{\mathbf{T}}_{\uparrow\uparrow}^{(j)} = [\mathbf{I} - \hat{\mathbf{R}}_{\downarrow\uparrow}^{(j)}\hat{\mathbf{R}}_{\uparrow\downarrow}^{(j-1)}]^{-1}\mathbf{T}_{\uparrow\uparrow}^{(j)}, & \text{for j=1, 2, ..., N;} \\ \hat{\mathbf{R}}_{\downarrow\uparrow}^{(j)} = \mathbf{R}_{\downarrow\uparrow}^{(j)} + \mathbf{T}_{\downarrow\downarrow}^{(j)}\hat{\mathbf{R}}_{\uparrow\downarrow}^{(j-1)}\hat{\mathbf{T}}_{\uparrow\uparrow}^{(j)} \end{cases} \tag{4}$$

and

$$\begin{cases} \hat{\mathbf{R}}_{\downarrow\uparrow}^{(N+1)} = 0 \\ \hat{\mathbf{T}}_{\downarrow\downarrow}^{(j)} = [\mathbf{I} - \hat{\mathbf{R}}_{\uparrow\downarrow}^{(j)} \hat{\mathbf{R}}_{\downarrow\uparrow}^{(j+1)}]^{-1} \mathbf{T}_{\downarrow\downarrow}^{(j)}, \quad \text{for j=N, N-1, ..., 2, 1.} \\ \hat{\mathbf{R}}_{\uparrow\downarrow}^{(j)} = \mathbf{R}_{\uparrow\downarrow}^{(j)} + \mathbf{T}_{\uparrow\uparrow}^{(j)} \hat{\mathbf{R}}_{\downarrow\uparrow}^{(j+1)} \hat{\mathbf{T}}_{\downarrow\downarrow}^{(j)} \end{cases} \tag{5}$$

These global generalized reflection and /or transmission matrices represent the total reflection and/or transmissions due to the multi-irregular layers.

Step 4

Compute the expansion coefficients of displacement spectra at free surface, $z = \xi^{(0)}(x)$, by using the formula

$$\underline{\alpha}^{(o)} = \left(\mathbf{Q}_{\downarrow\uparrow}^{(1)}\right)^{-1} \mathbf{E}_{\min}^{(1)} \left\{ \hat{\mathbf{s}}_{\uparrow}^{(1)} + \hat{\mathbf{T}}_{\uparrow\uparrow}^{(1)} \hat{\mathbf{s}}_{\uparrow}^{(2)} + \hat{\mathbf{T}}_{\uparrow\uparrow}^{(1)} \hat{\mathbf{T}}_{\uparrow\uparrow}^{(2)} \hat{\mathbf{s}}_{\uparrow}^{(3)} + \ldots + \hat{\mathbf{T}}_{\uparrow\uparrow}^{(1)} \hat{\mathbf{T}}_{\uparrow\uparrow}^{(2)} \ldots \hat{\mathbf{T}}_{\uparrow\uparrow}^{(N)} \hat{\mathbf{s}}_{\uparrow}^{(N+1)} \right\}, \tag{6}$$

where $\hat{\mathbf{s}}_{\uparrow}^{(j)}$ is the equivalent source term for the jth layer derived by the representation theorem and

$$\hat{\mathbf{s}}_{\uparrow}^{(j)} = \left\{ \mathbf{I} - \hat{\mathbf{R}}_{\uparrow\downarrow}^{(j-1)} \hat{\mathbf{R}}_{\downarrow\uparrow}^{(j)} \right\}^{-1} \left(\mathbf{s}_{\uparrow}^{(j)} + \hat{\mathbf{R}}_{\downarrow\uparrow}^{(j)} \mathbf{s}_{\downarrow}^{(j)} \right) \tag{6a}$$

$$\left(\mathbf{s}_{\uparrow}^{(j)}\right)_n = \frac{i}{2 v_n^{(s)} L} \int_{-L/2}^{L/2} dx \int_{\xi^{(j-1)}(x)}^{\xi^{(j)}(x)} f^{(j)}(x,z) \exp[-ik_n x + i v_n^{(j)} (z - \xi_{\min}^{(j)})] dz, , \tag{6b}$$

$$\left(\mathbf{s}_{\downarrow}^{(j)}\right)_n = \frac{i}{2 v_n^{(j)} L} \int_{-L/2}^{L/2} dx \int_{\xi^{(j-1)}(x)}^{\xi^{(j)}(x)} f^{(j)}(x,z) \exp[-ik_n x - i v_n^{(j)} (z - \xi_{\max}^{(j-1)})] dz, \tag{6c}$$

for j =1, 2, ..., N, N+1;

and

$$f^{(j)}(x,z) = \left\{ \tau^{(j)}(x,z) + \mu^{(j)} u^{(j)}(x,z) \frac{\partial}{\partial x} \right\} . \tag{6d}$$

Step 5

Calculate the displacement spectra at the free surface by using the following formula:

$$W^{(o)}[x, \xi^{(o)}(x), \omega] = \sum_{m=-M}^{M} \alpha_m^{(o)} \exp\left\{ ik_m + i v_m^{(1)} \left| \Delta \xi^{(o)}(x) \right| \right\}. \tag{7}$$

Taking the Fourier transform on the above frequency domain solution, we can finally obtain the time domain solution, i.e., the synthetic seismogram.

Numerical Test and Preliminary results

To test the validity of our hybrid method, we consider a trivial case: laterally homogeneous layered case. This problem can be fully solved by reflectivity method. To test our algorithm, we use our hybrid method to solve this problem, then compare this solution with that of the reflectivity method. The test model is a single layer crustal model. The velocities and densities for the crust and mantle are 3.5km/sec, 2.8km/sec, 4.5km/sec and 3.2 g / cm^3, respectively. The thickness of the crust is 32km, seismic source is buried at z_s=2km and x_s=0.0. Receiver is placed at z_0=0.0 and x_0=250km. The connection boundary is located at x=150km. The synthetic seismogram of GGRTM is shown in figure 4b, the synthetic seismogram of reflectivity method is plotted in figure 4a. Comparison of these two seismograms shows an excellent agreement between the hybrid method and the reflectivity method, confirming the validity of the connection scheme for our hybrid method.

The computer code for calculating general irregular media case is under development at this stage, and expected to be finished soon. We will then calculate synthetic Lg waves propagating through an arbitrary irregular layered medium to study the influence of surface topography and interface irregularities.

CONCLUSIONS AND RECOMMENDATIONS

We have derived the connection formulas for our hybrid scheme and its validity has been proved by numerical tests. The algorithm for seismogram synthesis in arbitrarily irregular layered media is under development. We will also study the approximation involved in the so -called Rayleigh ansatz method, or the Aki-Larner method (A-L method). A-L method is a wavenumber domain implemented and approximated BIE method. It is much faster than the strict BIE method and therefore can simulate more realistic 3D topography and interface problems. Horike et al. (1990) has applied the method to non-axisymmetric 3D surface structure problems. We will test the accuracy and speed of AL method by comparing it with the strict BIE method (such as Chen's GGRTM method) and incorporate the approximation into our hybrid method.

References

Aki, K and K. Larner, 1970, Surface motion of a layered medium having an irregular interface due to incident plane SH waves, *J. Geophys.. Res., 75,* 934-954.

Baumgardt, D.R., 1990, Investigation of teleseismic Lg blockage and scattering using regional arrays, *Bull. Seismol. Soc. Am., 80*, 2261-2281.

Bouchon, M., 1981, A simple method to calculate Green's functions for elastic layered media, *Bull. Seismol. Soc. Am., 71*, 959-971.

Bouchon, M. and K. Aki, 1977, Near-field of a seismic source in a layered medium with irregular interface, *J. R. Astron. Soc., 50,* 669-684.

Bouchon, M., M. Campillo and S. Gaffet, 1989, A boundary integral equation-discrete wavenumber representation method to study wave propagation in multilayered media having irregular interfaces, *Geophysics, 54*, 1134-1140.

Campillo, M. B. Feignier, M. Bouchon and N. Bethoux, 1993, Attenuation of crustal waves across the Alpine range, *J. Geophys. Res., 98*, 1987-1996.

Chazalon, A., Campllio, M., Gibson, Jr, R.L., and Carreno, E., 1993, Crustal wave propagation anomaly across the Pyrenean range: comparison between observations and numerical simulations, *J. Geophys. Res., 115*, 829-838.

Chen, X.F., 1990, Seismogram synthesis for multi-layered media with irregular interfaces by the global generalized reflection/transmission matrices method - Part I. Theory of 2-D SH case, *Bull. Seismol. Soc. Am., 80*, 1694-1724.

Chen, X.F., 1995, Seismogram synthesis for multi-layered media with irregular interfaces by the global generalized reflection/transmission matrices method - Part II. Applications of 2-D SH case, *Bull. Seismol. Soc. Am., 85*, 1094-1106.

Chen, X.F., 1996, Seismogram synthesis for multi-layered media with irregular interfaces by the global generalized reflection/transmission matrices method - Part III. Theory of 2D P-SV case, *Bull. Seismol. Soc. Am., 86*, 389-405.

Gibson, R.L. and Camplillo, M., 1994, Numerical simulation of high- and low-frequency Lg-wave propagation, *Geophys. J. Int., 119*, 47-56.

Horike, M., H. Uebayashi and Y. Takeuchi, 1990 Seismic response in three-dimensional sedimentary basin due to plane S wave incidence, *J. Phys. Earth, 38*, 261-284.

Regan, J., and Harkrider, D.G., 1989, Numerical modeling of SH Lg waves in and near continental margins, *Geohys. J. R. astr. Soc., 98*, 107-130.

Sanchez-Sesma, F.J., and M. Campillo, 1991, Diffraction of P, SV and Rayleigh waves by topographic features: a boundary integral formulation, *Bull. Seis. Soc. Am., 81,* 2234-2253.

Wu, R.S., 1994. Wide-angle elastic wave one-way propagation in heterogeneous media and an elastic wave complex-screen method, *J. Geophys. Res., 99*, 751-766.

Wu, R.S., 1996, Synthetic seismograms in heterogeneous media by one-return approximation, *Pure and Applied Geophys.*, in press.

Wu, R.-S., and Huang, L.-J., 1995, Reflected wave modeling in heterogeneous acoustic media using the de Wolf approximation: in S. Hassanzadeh (Ed.), *Mathematical Methods in Geophysical Imaging~III, SPIE Proceedings Series, 2571, 176-186.*

Wu, R.S. and X.B., Xie, 1994, Multi-screen backpropagator for fast 3D elastic prestack migration, in S. Hassanzadeh (Ed.), *Mathematical Methods in Geophysical imaging II,* S*PIE Proceedings Series, 2301,* 181-193.

Xie, X.B. and T. Lay, 1994, The excitation of explosion Lg, a finite-difference investigation, *Bull. Seismol. Soc. Am.,, 84,* 324-342..

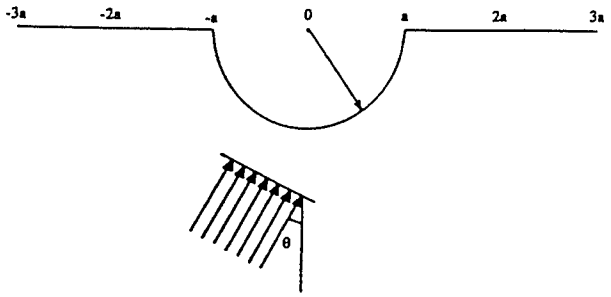

Figure 1. The configuration of the scattering problem due to a semi-circular canyon and an incident plane wave, where a is the radius of the canyon, and θ is the angle of incident wave.

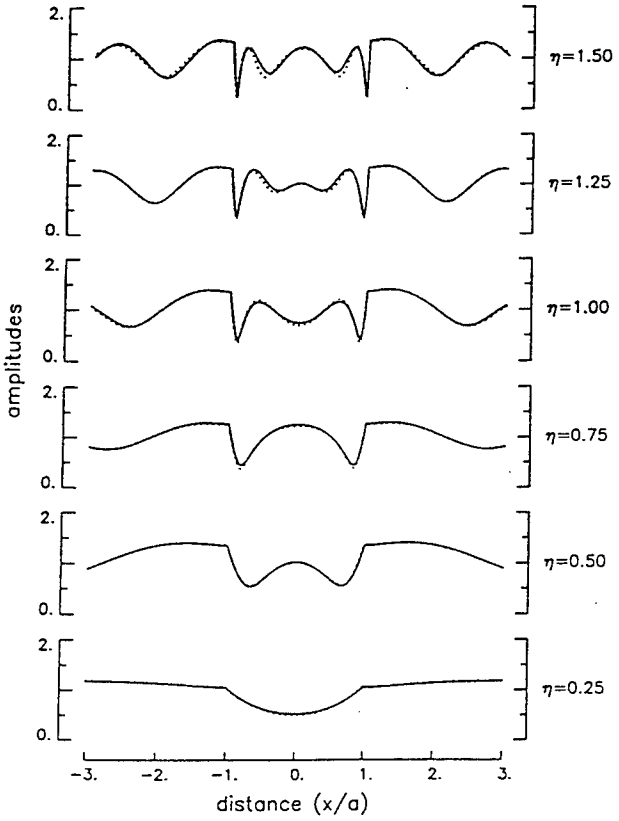

Figure 2. The frequency responses of a semi-circular canyon to vertical incident SH wave for various normalized frequencies η, which is defined by $2a/\lambda$, where a is the radius of a semi-circular canyon and λ is the wavelength of the incident wave. Here, we used a = 1 km, L = 40 km, V = 2 km/sec, and $\omega_l = \pi V/L$. The solid lines denote our results and the dotted lines denote the exact solutions (Trifunac, 1973).

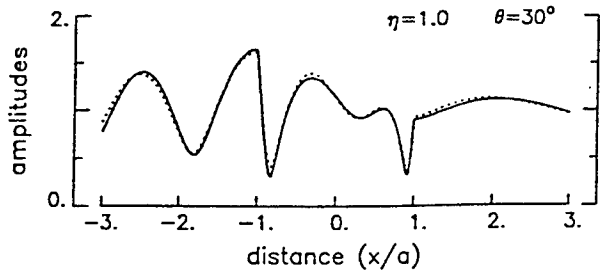

Figure 3. The same response as Figure 3, but for 30° incidence and η = 1.0.

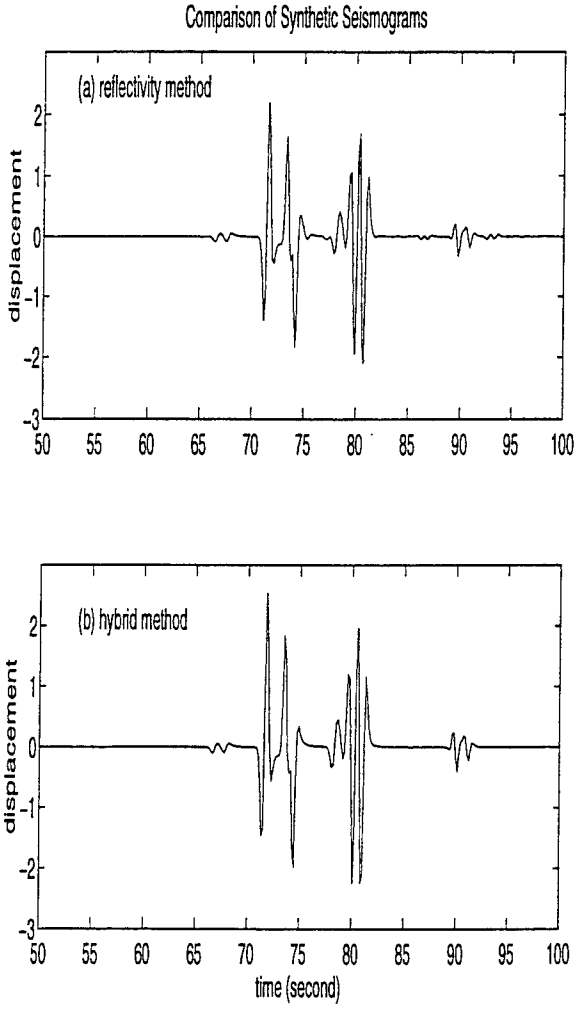

Figure 4: Comparison of synthetic seismigrams computed by the reflectivity method and our hybrid method.

Synthetic Seismograms in Heterogeneous Crustal Waveguides Using Screen Propagators

Ru-Shan Wu, Shengwen Jin and Xiao-Bi Xie
University of California, Santa Cruz
Contract No. F49620-95-1-0028
Sponsored by AFOSR

ABSTRACT

The object of this project is aimed at development and application of a new 3D wave propagation and modeling method in complex heterogeneous media using one-way wave approximation to study many outstanding problems of regional wave propagation in the context of nuclear test monitoring. The great advantages of one-way propagation methods are the fast speed of computation, often by several orders of magnitudes faster than finite difference and finite element methods, and the huge saving in internal memory. The major effort for the new project will be to solve the problems of backscattering calculation and free-surface/Moho reflections so that the one-way wave theory and method can be applied to the regional waveguide environment. This year's effort is concentrated in free-surface/Moho reflection simulations in the framework of one-way wave propagation. Due to the complexity of the problem, as the first step we solved the 2D SH wave problem. The theoretical foundation has been laid and numerical tests were conducted. Comparison with finite difference at short distance showed excellent agreement. Synthetic seismograms for the Flora-Asnes crustal model in the NORSAR area is generated by this method as an example. It is seen that the half-space phase-screen propagator is fast and stable, and can be used to calculate synthetic seismograms efficiently in regional distances with complex crustal structures.

Keywords: seismic waves, heterogeneous crustal waveguide, Lg waves, one-way waves.

OBJECTIVES

The new task for monitoring a Comprehensive Test Ban Treaty and the current Nuclear Non-Proliferation Treaty presents a great challenge to the existing modeling methods using regional phases. The study of path effects of complex structure and heterogeneities on the excitation and propagation of regional phases in different areas remains critical for both the discrimination and yield estimation for low-yield nuclear test monitoring. The object of this project is aimed at development and application of a new 3D wave propagation and modeling method in complex heterogeneous crustal waveguides using the one-way wave approximation to study many outstanding problems of regional wave propagation in the context of nuclear test monitoring. The great advantages of one-way propagation methods are the fast speed of computation, often by several orders of magnitudes faster than finite difference and finite element methods, and the huge saving in internal memory. The new project will take the advantages of the recent progress in elastic one-way wave propagation theory (Wu, 1994; Wu and Xie, 1994) and continue to develop the theory and method for the purpose of regional wave synthetic seismograms. The major effort for the new project will be to solve the problems of backscattering calculation and free-surface/Moho reflections so that the one-way wave theory and method can be applied to the regional waveguide environment. Then the influence of upper and lower crustal small-scale heterogeneities to Lg propagation and attenuation, and other path effects will be examined by numerical simulations using the new method. The development of the theoretical model will be combined with analysis of the Eurasian regional phase observations to extract quantitative information from regional phases.

RESEARCH ACCOMPLISHED

During the first year of the project, significant progress had been made on the calculation of backscattered waves using the De Wolf approximation, i.e. the multiple forescattering-single backscattering approximation. This year's effort was concentrated in free-surface/Moho reflection simulations in the framework of one-way wave propagation. Due to the complexity of the problem, as the first step we solved the 2D SH wave problem. The theoretical foundation was laid and numerical tests were conducted. It is found that the half-space phase-screen propagator is fast and stable, and can be used to calculate synthetic seismograms efficiently for regional distances with complex crustal structures.

The modeling effort for backscattered waves was continued in a small scale. The work accomplished in this aspect has resulted in two publications (Wu and Huang, 1995 and Wu, 1996).

In the following, we report the progress in the SH wave modeling in heterogeneous crustal waveguides.

Introduction

In the past ten years, substantial progress has been made in modeling regional wave propagation in simplified structures and understanding the influence of large geophysical features to the propagation (e.g. Bouchon et al., 1985; Kennett, 1989, 1990; Baumgardt, 1990; Campillo, 1990; Campillo et al., 1993; etc.). However, modeling techniques for real 3D heterogeneous media rather

than smoothly varying layered media are much needed to test and study many observations and hypothesises. Sudden changes of crustal thickness, strong lateral variation and irregular 3D heterogeneities are among the problems requiring new modeling methods. As pointed out by Campillo et al. (1993), the Lg amplitude was reduced more than 10 times for paths passing through an anomalous zone on the east of Alpine range, while the modeling results using existing method (including the effect of known large-scale lateral structural variation) only account for 20 - 30 % of the amplitude reduction. Other mechanisms such as the scattering and attenuation by small-scale heterogeneities must be taken into account, which again call for new modeling methods. We propose to develop a fast new numerical method using elastic wave one-way propagation algorithm. In the crustal waveguide environment, major wave energy is carried by forward propagating waves, including forward scattered waves, and therefore the neglection of backscattered waves in the modeling will not change the main features of regional phases in most cases. By neglecting backscattering in the theory, the method becomes a forward marching algorithm in which the next step propagation depends only on the present values of wavefield in a transverse cross-section and the heterogeneities between the two cross-sections. The saving of computing time and storage is enormous and makes it a very competent method for large 3D elastic wave propagation problems. As the first step, in this paper we treat the two-dimensional SH problem for heterogeneous crustal waveguide. We first derive the wide-angle screen formulas for one-way SH waves in a half space. Then a phase-screen algorithm is obtained under the small-angle forward scattering approximation. The treatment of the Moho discontinuity is also discussed. Numerical examples are then given to demonstrate the feasibility of te approach.

General wide-angle formulation

First we derive the wide-angle screen formula for the 2D SH wave one-way propagation in an elastic half space. In this case, only the y-component of the displacement field u exist. The equation of motion can be written as

$$-\omega^2\rho(\mathbf{r})u(\mathbf{r}) = \frac{\partial}{\partial x}[\mu(\mathbf{r})\frac{\partial}{\partial x}u] + \frac{\partial}{\partial z}[\mu(\mathbf{r})\frac{\partial}{\partial z}u] \tag{1}$$

where ω is the frequency, $\mathbf{r} = (x, z)$ is a 2D position vector, ρ is the density, and μ is the shear rigidity. We decompose the parameters of the elastic medium and the total wave field into

$$\begin{aligned} \rho &= \rho_0 + \delta\rho \quad \mu = \mu_0 + \delta\mu \\ u &= u^0 + U \end{aligned} \tag{2}$$

where ρ_0 and μ_0 are the parameters of the background medium, $\delta\rho$ and $\delta\mu$ are the corresponding perturbations, u^0 is the primary field and U is the scattered field. Then the SH wave equation can be rewritten as

$$(\nabla^2 + k^2)u(\mathbf{r}) = -k^2F(\mathbf{r})u(\mathbf{r}) \,, \tag{3}$$

where $k = \omega/v$ is the wavenumber in the background medium and v is the background S wave velocity defined by

$$v = \sqrt{\mu_0/\rho_0} \tag{4}$$

In the right hand side of (3), $F(\mathbf{r})$ is a perturbation operator

$$F(\mathbf{r}) = \varepsilon_\rho(\mathbf{r}) + \frac{1}{k^2}\nabla \cdot \varepsilon_\mu \nabla \,, \tag{5}$$

with

$$\varepsilon_\rho(\mathbf{r}) = \frac{\delta\rho(\mathbf{r})}{\rho_0}, \quad \varepsilon_\mu(\mathbf{r}) = \frac{\delta\mu(\mathbf{r})}{\mu_0} \,. \tag{6}$$

Under the forward-scattering approximation, or more generally the multiple-forescattering-single-backscattering (MFSB) (Wu and Huang, 1995; Wu, 1996) the total field and Green's function under the integration in above equation can be replaced by their forward-scattering approximated counterparts, and the field can be calculated by a one-way marching algorithm along the x-direction using a dual domain technique. We will derived in the following the dual domain expressions of the marching algorithm for the heterogeneous half-space case.

For each step of the marching algorithm under the forward-scattering approximation, the total field at x_1 is calculated as the sum of the primary field which is the field free-propagated in the half-space from x' to x_1, and the scattered field caused by the heterogeneities in the thin-slab between $x'$and x_1. The thickness of the slab should be taken thin enough to ensure the validity of the local Born approximation. Under this condition, the Green's function can be approximated by the homogeneous half-space Green's function. The latter can be obtained by the image method. Transforming the equations into wavenumber domain and performing some algebra result in

$$\begin{aligned}
U(x_1, K_z) &= U_\rho(x_1, K_z) + U_\mu(x_1, K_z) \\
U_\rho(x_1, K_z) &= ik \int_{x'}^{x_1} dx e^{i\gamma(x_1 - x)} \mathcal{C}[\frac{k}{\gamma}\varepsilon_\rho(z) u_0(z)] \\
U_\mu(x_1, K_z) &= ik \int_{x'}^{x_1} dx e^{i\gamma(x_1 - x)} \left\{ \mathcal{C}[\varepsilon_\mu(z)\bar{\partial}_x u_0(z)] - i\mathcal{S}[\frac{K_z}{\gamma}\varepsilon_\mu(z)\bar{\partial}_z u_0(z)] \right\}
\end{aligned} \tag{7}$$

where

$$\gamma = \sqrt{k^2 - K_z^2} \,, \tag{8}$$

is the propagating wavenumber, and

$$\bar{\partial}_x = \frac{1}{ik}\frac{\partial}{\partial x}, \quad \bar{\partial}_z = \frac{1}{ik}\frac{\partial}{\partial z} \tag{9}$$

are dimensionless partial derivatives. In the above equations, $\mathcal{C}[f(z)]$ and $\mathcal{S}[f(z)]$ are the cosine and sine transforms, defined by

$$\begin{aligned}
\mathcal{C}[f(z)] &= \int_0^\infty dz 2\cos(K_z z) f(z) \\
\mathcal{S}[f(z)] &= \int_0^\infty dz 2\sin(K_z z) f(z)
\end{aligned} \tag{10}$$

for forward transforms, and

$$\begin{aligned}
\mathcal{C}^{-1}[f(K_z)] &= \frac{1}{2\pi}\int_0^\infty dK_z 2\cos(K_z z) f(K_z) \\
\mathcal{S}^{-1}[f(K_z)] &= \frac{1}{2\pi}\int_0^\infty dK_z 2\sin(K_z z) f(K_z)
\end{aligned} \tag{11}$$

for inverse transforms.

In Eq. (7), u_0, $\bar{\partial}_x u_0$ and $\bar{\partial}_z u_0$ can be calculated by

$$\begin{aligned} u_0(x,z) &= \frac{1}{2\pi}\int_{-\infty}^{\infty} dK_z' e^{iK_z' z} e^{i\gamma'(x-x')} u_0(x', K_z') \\ &= \mathcal{C}^{-1}[e^{i\gamma'(x-x')} u_0(x', K_z')] \end{aligned} \tag{12}$$

and

$$\begin{aligned} \bar{\partial}_x u_0(x,z) &= \mathcal{C}^{-1}[e^{i\gamma'(x-x')}\frac{\gamma'}{k} u_0(x', K_z')] \\ \bar{\partial}_z u_0(x,z) &= i\mathcal{S}^{-1}[e^{i\gamma'(x-x')}\frac{K_z'}{k} u_0(x', K_z')] \end{aligned} \tag{13}$$

Eq. (7), (12) and (13) are the dual-domain expressions of the wide-angle screen propagator for half-space SH problems.

Small angle approximation and the phase-screen propagator

When the energy of crustal guided waves are carried mainly by small-angle waves (with respect to the horizontal direction), the small angle approximations can be invoked to simplify the theory and calculations. Substitute (12) and (13) into (7) and make the small-angle approximation, resulting in

$$\begin{aligned} U(x_1, K_z) &= U_\rho(x_1, K_z) + U_\mu(x_1, K_z) \\ &= ike^{i\gamma(x_1-x')}\frac{1}{2\pi}\int_0^\infty dK_z' 2\cos(K_z' z)\int_0^\infty dz 2\cos(K_z z) \\ &\quad \int_{x'}^{x_1} dx e^{i(\gamma-\gamma')(x-x')}\left[(\frac{k}{\gamma})\varepsilon_\rho(z) - (\frac{\gamma'}{k})\varepsilon_\mu(z)\right] u_0(x', K_z') \\ &\approx ike^{i\gamma(x_1-x')}\mathcal{C}\left[2S_s(z) u_0(x', z)\right] \end{aligned} \tag{14}$$

where

$$\begin{aligned} 2S_s(z) &= \int_{x'}^{x_1} dx[\varepsilon_\rho(x,z) - \varepsilon_\mu(x,z)] \\ &\approx 2\Delta x \bar{\varepsilon}_s(z) \end{aligned} \tag{15}$$

where $\bar{\varepsilon}_s(z)$ is the average S-wave slowness perturbation over the thin-slab at depth z, $\Delta x = (x_1 - x')$ is the thin-slab thickness, and S_s is the corresponding slowness screen for the half-space thin-slab. Eq. (14) is the screen approximation of the half-space SH problem. Summing up the primary and scattered fields and invoking the Rytov transform result in the dual-domain expression of phase-screen propagator for this case

$$\begin{aligned} u(x_1, K_z) &= u_0(x_1, K_z) + U(x_1, K_z) \\ &= e^{i\gamma(x_1-x')}\int_0^\infty dz 2\cos(K_z z)[1 + ik2S_s(z)] u_0(x', z) \\ &\approx e^{i\gamma(x_1-x')}\mathcal{C}\left[e^{2ikS_s(z)} u_0(x', z)\right] \end{aligned} \tag{16}$$

where $e^{2ikS_s(z)}$ is the phase delay operator.

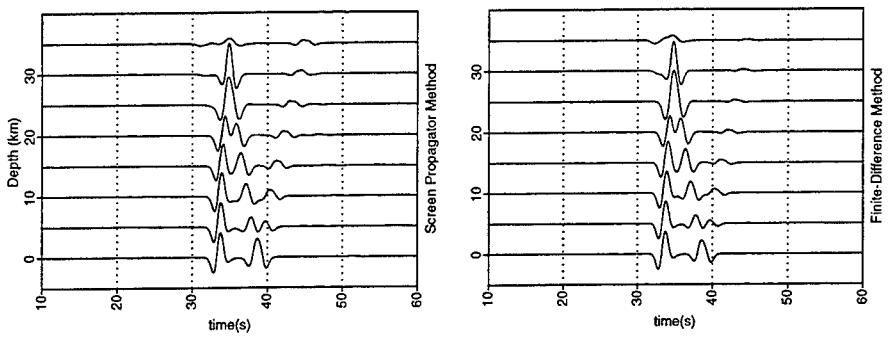

Figure 1: Comparison of synthetic seismograms along a vertical profile at an epicenter distance of $100km$ generated by the half-space phase screen method (left) and the finite difference method (right). The source is at a depth of 2 km and the model is a homogeneous crust over a half space.

Treatment of the Moho discontinuity

The Moho discontinuity can be treated in two ways. One is to put the impedance boundary conditions in the formulation, the other is to treat the parameter changes as perturbations and therefore be incorporated into the screen interaction. The former has the advantage of computational efficiency. The latter has the flexibility of handling irregular interfaces. In this paper, we adopt the latter approach and check the validity of perturbation approach for the Moho discontinuity by a finite difference algorithm.

Numerical Simulations

In this section we test the phase-screen algorithm for regional wave propagation. First we test the method by comparing synthetic seismograms generated by this method with those generated by a finite difference algorithm (Xie and Lay, 1994). For the finite-difference method, a fourth-order elastic SH-wave code is used to calculate the synthetic seismograms. The spatial sampling interval is 0.25 km and the time interval is 0.025 second. For the screen method, the spatial sampling interval is 0.25 km in vertical direction and the screen interval is 1.0 km. A Gaussian derivative is used as the source time function for both methods. Because of the computational intensity of the finite difference method, we did the comparison at short propagation distances. Fig. 1 shows the synthetic seismograms along a vertical profile at an epicenter distance of 100 km generated by the two methods. The source is located at a depth of 2 km. The model is a homogeneous 32 km thick crust with a S wave velocity of 3.5 km/s over a half space ($v_s = 4.5\ km/s$). The upper panel is from screen propagator method and the lower panel is from the finite-difference method. Excellent agreement can be seen.

Fig. 2 shows the snap shots at 10, 30 and 60 *sec.* (from top to bottom). The source is located at the top-right corner at depth 2 km and the wave is propagated to the left. The development of head wave and mantle wave, multiple reflections between the free surface and the Moho for crustal waves and head waves can been seen clearly.

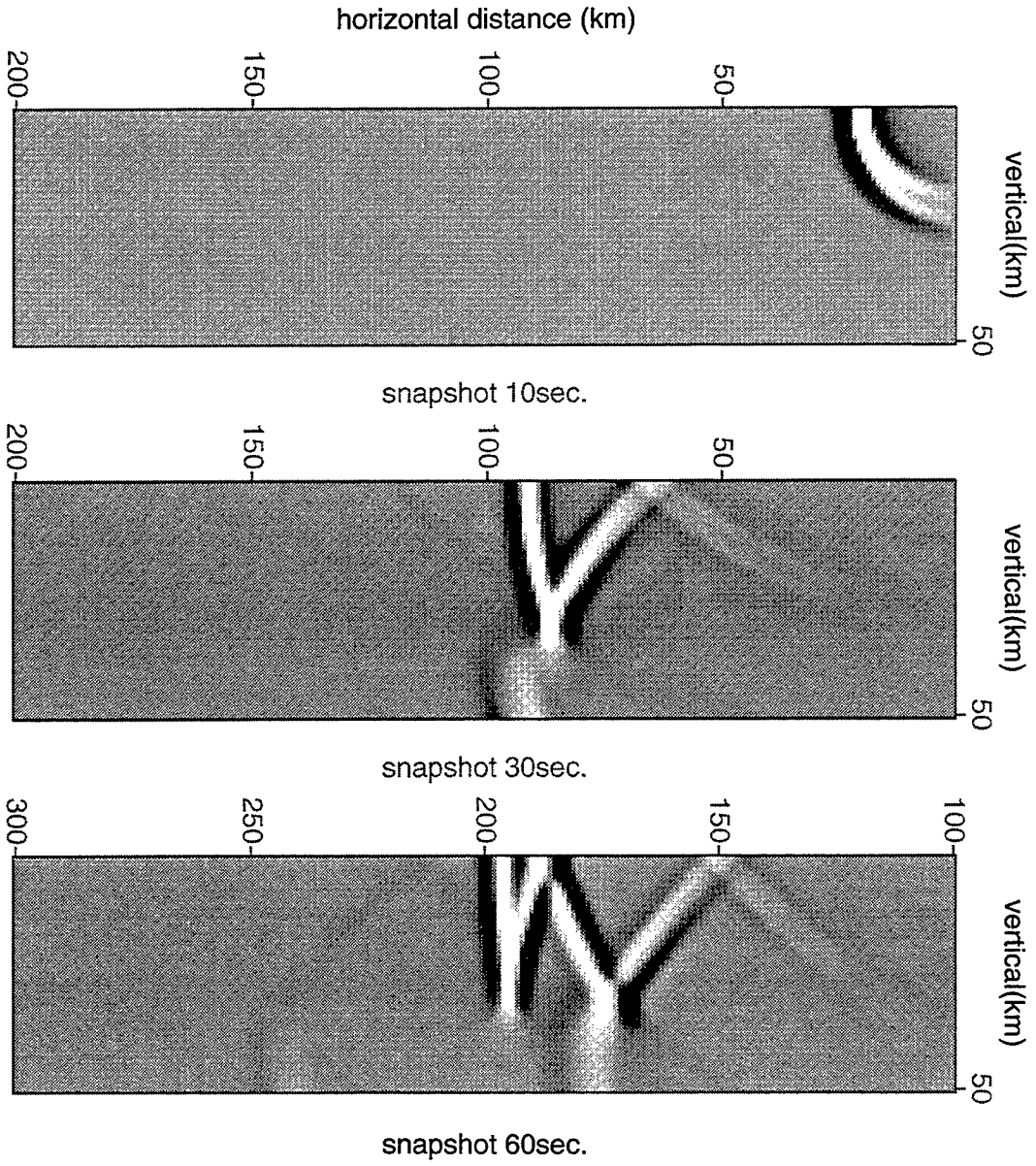

Figure 2: Snap shots at 10, 30 *and*60*sec.* (from top to bottom). The source is located at the top-right corner at depth $2km$ and the wave is propagated to the left.

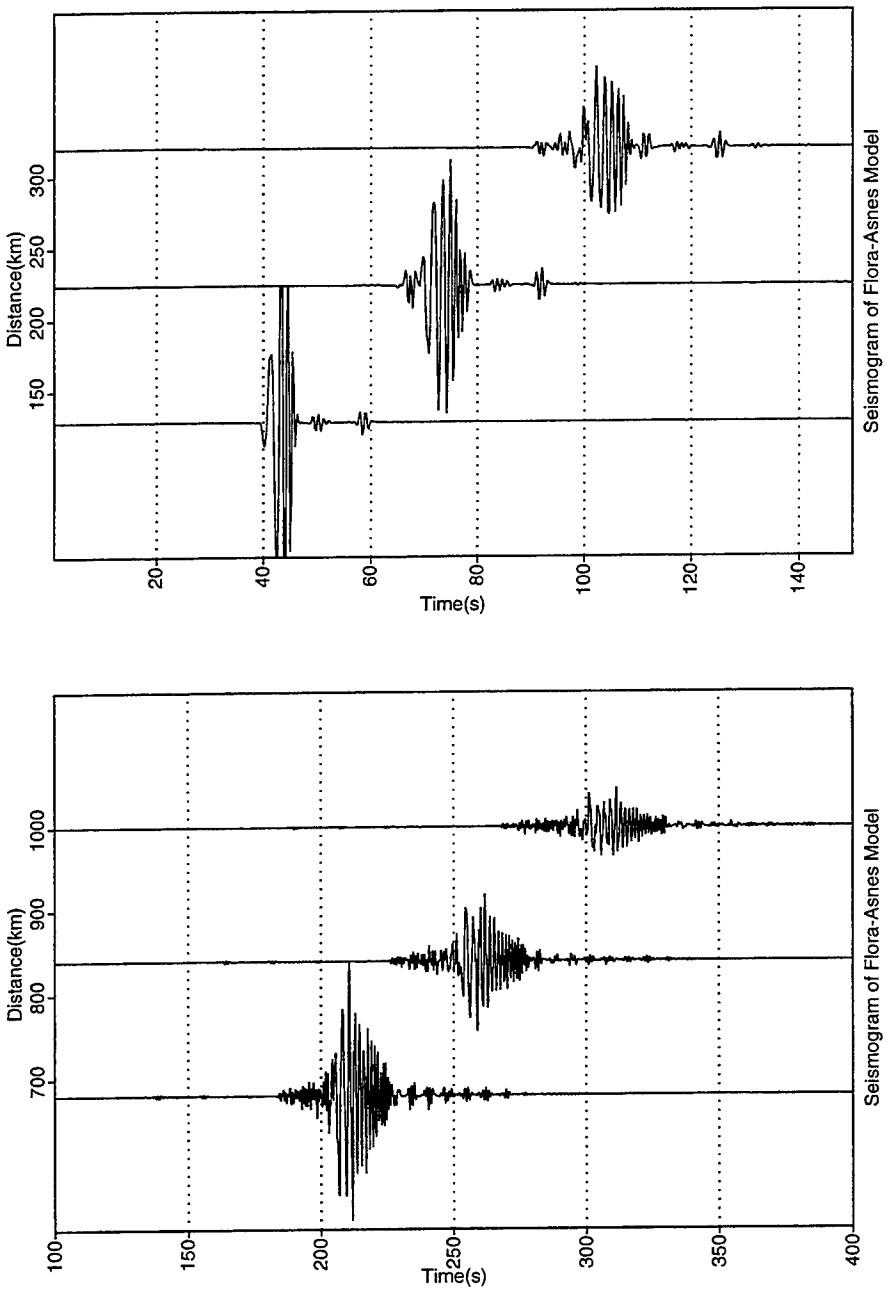

Figure 3: synthetic seismograms for the Flora-Asnes crust model in the NORSAR region. The parameters for this model are listed in Table 3.

Fig. 3 shows the synthetic seismograms for the Flora-Asnes crust model in the NORSAR region. The parameters for this model are listed in Table 3. The model has a low velocity layer in top 1 km and a velocity discontinuity at depth 15 km. The receivers are on the surface. A Ricker wavelet is used for this simulation with $f_0 = 1\ Hz$. Shown in the upper panel are at short distances (up to 350 km), on the lower panel are for long distances (up to 1000 km). In this case the Lg group is formed by multiple reflections by the Moho and the crustal discontinuities. With the capability of the method in modeling complex crustal structure and small scale heterogeneities, synthetic seismograms can be generated for more realistic crustal models.

Table 1: Flora-Asnes crust model

thickness (km)	V_s (km/s)	ρ (g/cm^3)
1.00	3.00	2.60
14.00	3.46	2.80
22.00	3.76	3.00
infinity	4.65	3.30

CONCLUSIONS AND RECOMMENDATIONS

We have made significant progress in modeling backscattering and 2D guided one-way wave modeling for SH regional wave problems. The use of half-space phase-screen propagator has made the seismogram synthesis in the regional distances (more than one thousand kilometers) very efficient. The rapid change of crustal structures and small scale heterogeneities in the crust can be easily handled. This demonstrates the advantages and feasibility of the generalized screen propagator approach in modeling regional waves. In order to further explore and take the full advantage of the method, we recommend the following:

1. Further develop the half-space screen propagators for the case of P-SV and full 3D elastic waves.

2. Incorporate the smoothly irregular surface topography into the theory and method so that the fast method can simulate guided wave propagation with irregular surface and interface topographies.

3. Conduct extensive comparisons with other methods, such as wavenumber integration, finite difference, boundary element and boundary integral equation methods, to asses the accuracy and speed of the method for different crustal environments.

References

Baumgardt, D.R., 1990, Investigation of teleseismic Lg blockage and scattering using regional arrays, *Bull. Seismol. Soc. Am.*, **80**, 2261-2281.

Bouchon, M., et al., 1985, Theoretical modeling of Lg wave attenuation, in The VELA program; A twenty-five year reveiw of basic research.

Campillo, M., 1990, Propagation and attenuation characteristics of the crustal phase Lg, *Pure and Appl. Geophys.*, **132**, 1-19.

Campillo, M. B. Feignier, M. Bouchon and N. Bethoux, 1993, Attenuation of crustal waves across the Alpine range, *J. Geophys. Res.,* **98**, 1987-1996.

Kennet, B.L.N., 1989, Lg-wave propagation in heterogeneous media, *Bull. Seismol. Soc. Am.,* **79**, 860-872.

Kennet, B.L.N., 1990, Guided wave attenuation in laterally varying media, *Geophys. J. Int. ,* **100**, 415-422.

Lanston, C.A., 1991, Wave propagation theory and synthetic seismograms, *Rev of Geophys.*, **29**, 662-670.

Stoffa, P.L., Fokkema J.T., Freire, R.M.D., and Kessinger, W.P., 1990. Split-step Fourier migration, *Geophysics*, **55**, 410-421.

Thomson, D.J. and Chapman, N.R., 1983. A wide-angle split-step algorithm for the parabolic equation, *J. Acoust. Soc. Am.*, **74**, 1848-1854.

Wu, R.S., 1994. Wide-angle elastic wave one-way propagation in heterogeneous media and an elastic wave complex-screen method, *J. Geophys. Res.*, **99**, 751-766.

Wu, R.S., 1996, Synthetic seismograms in heterogeneous media by one-return approximation, to appear in: *Pure and Applied Geophysics.*

Wu, R.-S., and Huang, L.-J., 1995, Reflected wave modeling in heterogeneous acoustic media using the de Wolf approximation: *in* S. Hassanzadeh (Ed.), *Mathematical Methods in Geophysical Imaging III*, SPIE Proceedings Series, **2571**, 176-186.

Wu, R.S. and X.B., Xie, 1994, Multi-screen backpropagator for fast 3D elastic prestack migration, *in* S. Hassanzadeh (Ed.), *Mathematical Methods in Geophysical Imaging II*, SPIE Proceedings Series, **2301**, 181-193.

Xie, X.B. and T. Lay, 1994, The excitation of explosion Lg, a finite-difference investigation, *Bull. Seismol. Soc. Am.,*, **84**, 324-342..

Two-dimensional nonlinear wave propagation in an endochronic material

Heming Xu[1], Steven M. Day[2], and Jean-Bernard H. Minster[1]

[1] Institute of Geophysics and Planetary Physics
Scripps Institution of Oceanography
University of California, San Diego
La Jolla, CA, 92093-0225

[2] San Diego State University
Department of Geological Sciences
5178 College Avenue
San Diego CA 92182

Sponsored by AFOSR under contracts No. F49620-94-1-0204 F49620-94-1-0205

Abstract

We have further developed a constitutive model applicable to rock in the intermediate strain regime, i.e., approximately 10^{-6} to 10^{-3}, where nonlinear losses, pulse distortion, and harmonic distortions have been documented in the laboratory. This model has been fit to a set laboratory data on Berea sandstone, obtained by Dr. *G. Boitnott* of New England Research, Inc. The main generalizations we report are (1) the inclusion of nonlinear hysteresis for both hydrostatic compression and for shear deformation and (2) the development of a capablity to study nonlinear wave propagation in two-dimensions. As in the one dimensional case, we find that nonlinear propagation from a mono-chromatic source excites odd harmonics of the source frequency, and that interaction of two monochromatic wavefields leads to energy transfer to other bands corresponding to various combinations of the two source frequencies

Keywords: Nonlinear wave propagation, hysteresis, endochronic constitutive model, Prony expansions, harmonic distortion

Objectives

Wave propagation in linear elastic materials is so well understood that elastic problems can be used to validate the numerical codes necessary to simulate nonlinear propagation. Nonlinear *elastic* waves have recently been studied both in laboratory experiments and in numerical simulations (e.g. McCall 1994). Nonlinearity at intermediate strain levels has been well documented because there is now a rather large body of experimental data demonstrating departures from linearity. This has led us to argue that nonlinearity should be taken into consideration in the vicinity of the source, particularly in the case of a contained explosion. Our main objective is to apply a new endochronic rheological model to simulate the behavior of rocks at intermediate strain levels, as observed in the lab, and to conduct validated simulations of nonlinear wave propagation in such materials. Pseudo-triaxial experiments performed by Dr. G. Boitnott in New England Research are used to constrain the rheological model. We show below that hysteresis loops observed in such experiments can be well approximated with an endochronic rheology. Our two-dimensional wave propagation simulations use the pseudo-spectral method (Kosloff,1984) and are validated against analytical solutions

Research accomplished

1. Endochronic constitutive formalism

The endochronic formalism incorporates the fact that the behavior of materials depends not only on the current strain state but on the entire strain history as well. This formalism requires specification of kernel functions and definition and evaluation of the *intrinsic* time scale z. As defined by Valanis and Read (1982), the equations include:

$$\mathbf{S} = \int_0^z \rho(z - z') \frac{\partial \mathbf{e}^p}{\partial z'} dz'$$

$$d\mathbf{S} = \mu(d\mathbf{e} - d\mathbf{e}^p)$$

for the deviatoric stress tensor $\mathbf{S}$, strain tensor $\mathbf{e}$ and plastic strain tensor $\mathbf{e}^p$; here μ is a modulus. Also

$$\sigma_{kk} = \int_0^z K(z - z') \frac{\partial \varepsilon_{kk}^p}{\partial z'} dz'$$

$$d\sigma_{kk} = k(d\varepsilon_{kk} - d\varepsilon_{kk}^p)$$

for volumetric stress σ_{kk}, volumetric strain ε_{kk}, and volumetric plastic strain ε_{kk}^p. k is bulk modulus.

If the kernel functions are given, then, given the increment of the strain tensor, the corresponding increment of stress tensor can be calculated from the above equations. If the kernel functions are weakly singular, of the form $z^{-\alpha}$, then the constitutive functionals imply that the initial loading/unloading will occur along the elastic slope in the stress-strain plane (Valanis and Read, 1982). The kernel functions are usually expanded into a

Dirichlet series to permit convenient evaluation of the integrals in the constitutive equations, that is:

$$\rho(z)=\sum_{r=1}^{n}A_r e^{-\alpha_r z};K(z)=\sum_{r=1}^{n}B_r e^{-\beta_r z}$$

Enough terms should be used to provide an adequate approximation to the weakly singular kernels. Then we get

$$d\mathbf{S}=\rho(0)d\mathbf{e}^{\mathbf{p}}+\mathbf{h}(z)dz$$

$$\text{where } \mathbf{h}(z)=\int_0^z \hat{\rho}(z-z')\frac{\partial \mathbf{e}^{\mathbf{p}}}{\partial z'}dz';\ \hat{\rho}(z)=d\rho/dz$$

$$d\sigma_{kk}=K(0)d\varepsilon_{kk}^{p}+g(z)dz;$$

$$\text{where } g(z)=\int_0^z \hat{K}(z-z')\frac{\partial \varepsilon_{kk}^{p}}{\partial z'}dz';\ \hat{K}(z)=dK/dz$$

The dz is defined as the length of the plastic strain path increment, and provides coupling between the deviatoric and volumetric strain tensors:

$$|dz|^2=c_1\left\|d\mathbf{e}^{\mathbf{p}}\right\|^2+c_2\left\|d\varepsilon_{kk}^{p}\right\|^2$$

where c1 and c2 are constants.

Given the increment of strain tensor, through a little algebra, we may get

$$(dz)^2\left[A\|\mathbf{h}\|^2+Bg^2-1\right]-2(dz)\left[A\mu\|\mathbf{h}d\mathbf{e}\|+Bkd\varepsilon_{kk}g\right]+A\mu^2\|d\mathbf{e}\|^2+Bk^2(d\varepsilon_{kk})^2=0$$

where

$$A=\frac{c_1}{(\mu+\rho(0))^2};\ B=\frac{c_2}{(k+K(0))^2}$$

And the **h** and g will be updated as following

$$\mathbf{h}=\sum_{r=1}^{n}\mathbf{h}_r;\ \mathbf{h}_r(z+\Delta z)=\mathbf{h}_r(z)e^{-\alpha_r\Delta z}-A_r\left[1-e^{-\alpha_r\Delta z}\right]\frac{\partial \mathbf{e}^{\mathbf{p}}}{\partial z};$$

$$g=\sum_{r=1}^{n}g_r;\ g_r(z+\Delta z)=g_r(z)e^{-\beta_r\Delta z}-B_r\left[1-e^{-\beta_r\Delta z}\right]\frac{\partial \varepsilon_{kk}^{p}}{\partial z}$$

Using the above scheme, it is quite convenient to construct the complicated strain-stress relationship for endochronic materials.

2. Experimental data and numerical endochronic simulations

The experiments used in this study were performed at New England Research, Inc. by Dr. Boitnott et al. Cylindrical Berea sandstone samples were subjected to axial and confining

stress histories using a servo-controlled apparatus. In this way, the samples were cycled through a series of loading and unloading histories at predefined loading rates. The resulting hysteresis loops are typically plotted with axial and radial strains versus axial stress and confining pressure, respectively. For example, Figure 1a shows the axial stress versus axial and radial strains at constant confining pressure. Volumetric stress versus strain is shown in Fig. 1b in a case where the axial stress and confining pressure were varied to as to provide a hydrostatic load. These loops illustrate the fact that Berea sandstone is not a perfectly linear elastic medium and that its behavior at large strains levels is in fact dominated by some nonlinear mechanisms.

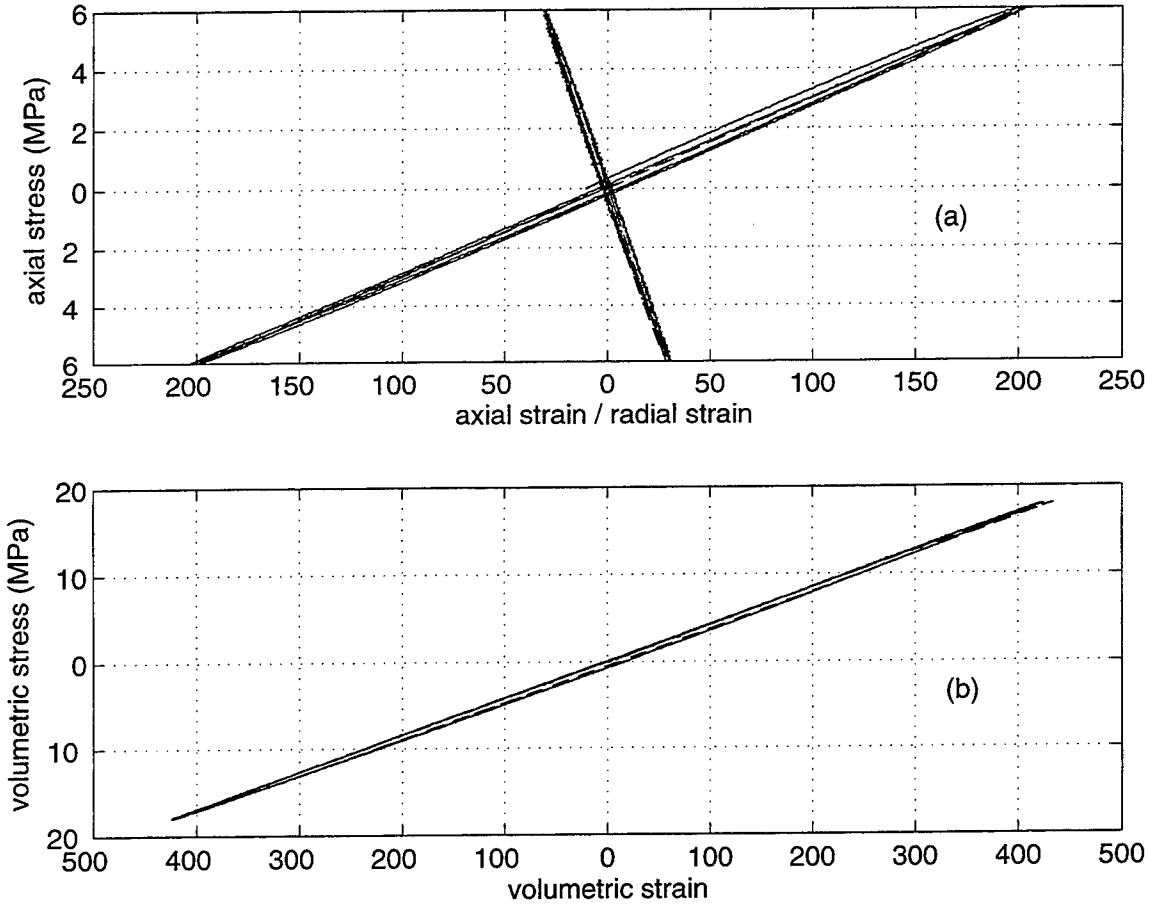

Fig.1 (a) Axial stress versus axial and radial strains at constant confining pressure.
(b) Pressure versus volumetric strain for hydrostatic loading conditions.

We model such hysteresis loops using the endochronic constitutive law. The parameters K and μ are derived independently from analysis of hysteresis loops under hydrostatic loads and shear loads, respectively. The resulting parameters and coefficients are then applied to compute the hysteresis loops for different loading paths. This provides the means to verify that possible nonlinear interactions between the different moduli can be ignored at this level of approximation. We then use Prony expansions to approximate the power law kernel functions (We have shown in the past that the selection of $\alpha = 0.5$ yields a linear relationship of Q^{-1} with strain amplitude, a common observation for rocks

under low confining pressure). Figures 1a-b also show calculated hysteresis superimposed on the observed ones. The match is quite satisfactory.

3. Numerical wave propagation

Nonlinearity will distort a propagating wave, more significantly at the larger strain amplitudes. We have examined such distortions through the following numerical simulations.

2-D wave propagations in purely linear elastic materials

The 2-D elastic wave propagation in linear elastic materials is calculated with the Fourier method. The approximation of spatial derivatives in the Fourier method is infinitely accurate for band-limited periodic functions with cutoff spatial wavenumbers which are smaller that the cutoff wavenumbers of the mesh (e.g. Kosloff et al; Daudt et al). A larger computational domain (256x256 grids) is used to avoid the unphysical wave interactions that result from the use of periodic boundary conditions. A low CFL number is used in order to suppress numerical dispersion.

In the calculations shown here, the homogeneous medium has a P velocity of 4 km/s and S velocity of 2.6 km/s. The time step is 1 ms, and the spatial step is 20 m. The source is a center of dilatation. The solutions are validated in the elastic case by comparison with the analytical solution and proved to be fully consistent and accurate.

2-D wave propagations and harmonic generations in endochronic model

The wave propagation problem for an endochronic material is posed using the same elastic moduli as above and endochronic plastic strain tensor is introduced. For lower excitation amplitudes the elastic wave and endochronic wave are found to propagate at exactly the same wave speed and with the same radiation pattern. This constitutes further validation, since the rheology should be quasi-elastic in the limit of low strain.

But at higher strain levels the linear elastic and nonlinear endochronic solutions become distinctly different.

1) The elastic waves propagate with smaller attenuation (due to geometrical spreading) than the endochronic waves because of the energy loss due to hysteresis loops.
2) The monochromatic elastic waves emanate from the source and remain monochromatic, but the endochronic waves generated by a monochromatic source propagate as multi-chromatic waves and various harmonic components evolve with distance.
3) As in the one-dimensional case, the harmonic amplitudes are nonlinearly dependent on the excitation amplitude.
4) Interactions between two waves of different frequencies excite other frequencies which are combinations of two source frequencies.

Some of these features are illustrated in the following plots. The harmonic generation and propagation have been observed in many experiments.

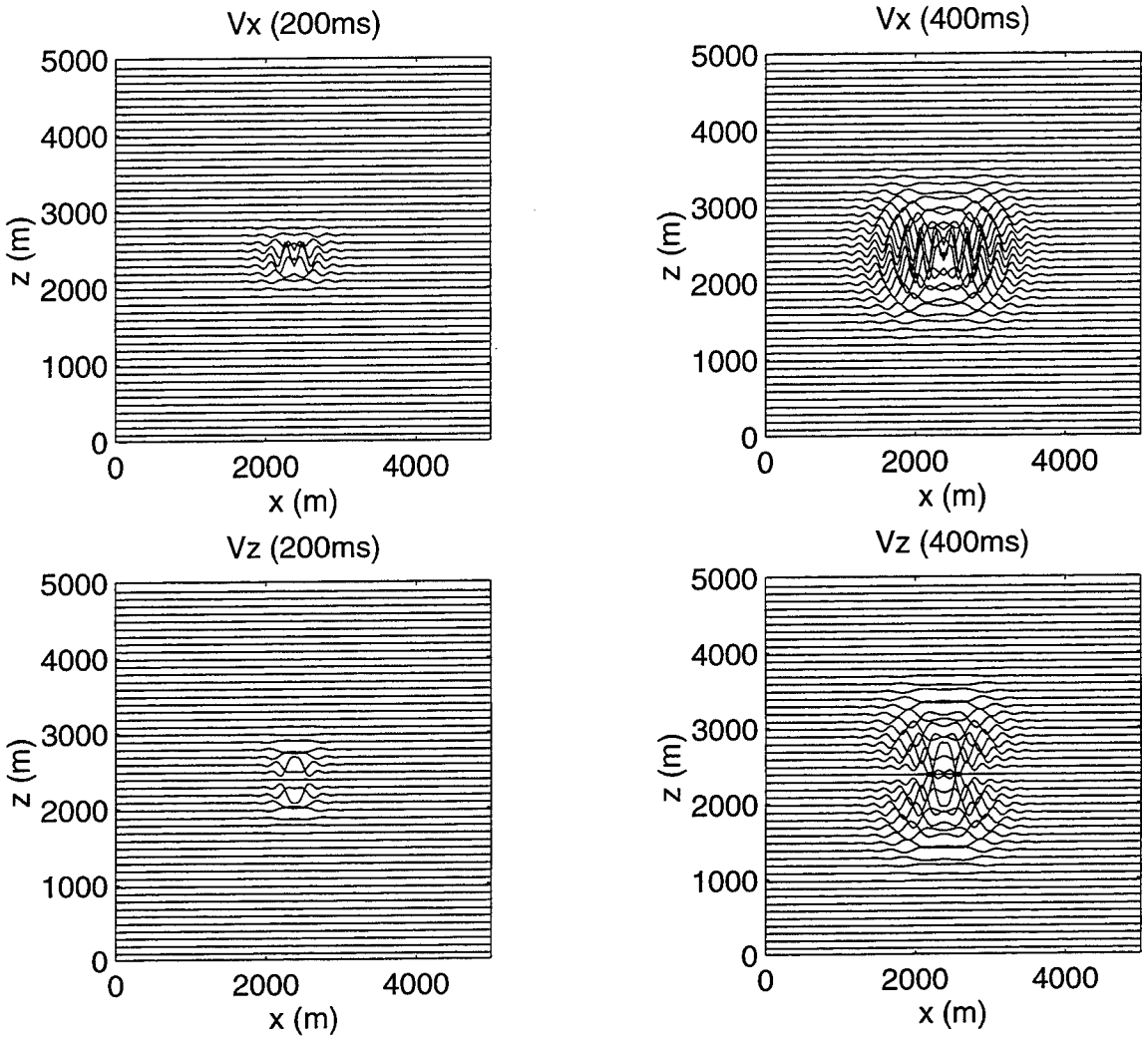

Figure 2: Snapshots of velocity wave field generated by a center of dilatation, at two successive times. The top frames depict the x-component of the velocity field, and the bottom ones show the z-component. The good quality of symmetry of these plots indicate that absorbing boundary conditions along all four boundaries do not introduce undue distortions. The rheology is nonlinear endochronic and selected to matfch quasistatic laboratory experiments on Berea sandstone (Courtesy Dr. G. Boitnott, NER, Inc.) Note that distortions caused by nonlinearity are very difficult to detect in these plots. Spectral analysis (see Figure 3) does evidence such distortions, however.

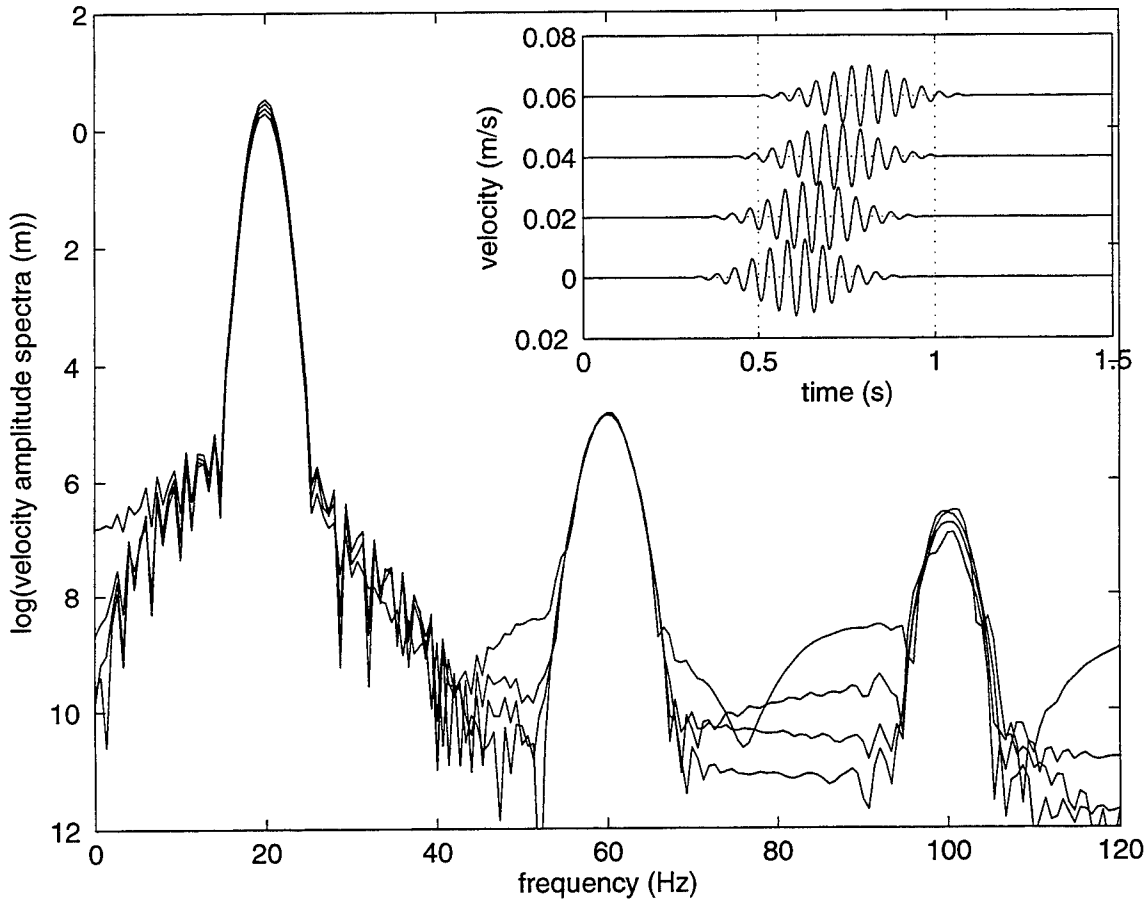

Figure 3: Radial velocity histories at 6 to 10 wavelengths from the source in the calculation shown in Figure 2. Note the development of harmonics of the basic source frequency in the successive spectra, indicative of nonlinear propagation effects.

Conclusions

1) We have generalized our analysis of nonlinear wave propagation in an endochronic solid to permit simulations of wave progagation in two dimensions. The results are consistent with earlier results we had obtained in one-dimension, and are in agreement with laboratory results, and with previous results based on perturbation methods.

2) The endochronic model can produce a close match to laboratory data for nonlinear hysteresis in rock. Simple singular kernels function and their approximations by Prony series have proved to be adequate to fit the data collected in hysteretic cycling experiments on Berea sandstone.

3) The integration scheme we use for evaluating the constitutive equation appears efficient and accurate, even with an approximate kernel, over the frequency band we have explored. The quality of the fit to laboratory data is practically independent on the strain increment for reasonable values, indicating that the scheme is stable. On the other hand the use of the Frourier technique for calculating spatial derivatives is computationally intensive. Nevertheless, in a situation where the "correct" answer is not known *a priori*, the added accuracy is well worth it.

References

McCall K.R., Theoretical study of nonlinear elastic wave propagation, *J. Geophys. Res.*, **99**,2591-2600,1994.

McCall, K. R., and R.A. Guyer, Equation of state and wave propagation in hysteretic nonlinear elastic materials, *J. Geophys. Res.*, **99**, 23887, 1994.

Valanis, K. and H. Read, A new endochronic plasticity model for soils, *S-CUBED Report SSS-R-80-4292*, San Diego , California,1982.

Bor-Shouh Huang, A program for two-dimensional seismic wave propagation by the pseudo-spectrum method, *Computers and Geosciences*,**18**,289-307,1992.

B.C.Reynolds, Boundary conditions for the numerical solution of wave propagation problems, *Geophysics*,**43**,1099-1110,1978.

Daudt, C.R., L.W. Braile,R.L.Nowack,and C.S. Chiang, A comparison of finite difference and Fourier method calculations of synthetic seismograms, Bull. Seismol. Soc. Amer., 79,1210-1230,1989

Kosloff, D., Reshef, M. and Loewenthal, D., Elastic wave calculations by the Fourier method, Bull. Seismol. Soc. Amer., 74,3,875-891, 1984

Elastic and Anelastic Structure Beneath Eurasia

Göran Ekström, Adam M. Dziewonski, Gideon P. Smith and Wei-jia Su

Department of Earth and Planetary Sciences
Harvard University
Cambridge, MA 02138

Contract No. F49620-92-J-0392
Sponsored by AFOSR

Abstract

We are collecting and analyzing large and diverse datasets of seismic waveforms, absolute and relative body wave travel times, and surface wave phase velocities and amplitudes. Our primary objective is to map the variations of elastic mantle properties beneath Eurasia over horizontal lengthscales of approximately 1000–1500 km and vertical lengthscales of 50–100 km in the upper mantle.

In order to characterize and properly account for the highly heterogeneous velocity structure associated with the crust and uppermost mantle, we have made several tens of thousands of measurements of intermediate period surface wave dispersion, and have developed global maps of phase velocity for Love and Rayleigh waves in the period range 35–150 s. The new maps, expanded in spherical harmonics up to degree 40, provide up to 96% reduction of the variance observed in the phase measurements, and, at short periods, show a very strong correlation with the thickness of the crust and the surface geology. The new dataset of surface wave dispersion, which provides excellent constraints on crustal and lithospheric structure, is being combined with previously collected data in the finalization of our new 3-D whole mantle model. In comparison with previous Harvard mantle models, such as S12WM13, we have increased the horizontal resolution by expanding the global structure up to spherical harmonic degree $l = 20$, and we have adopted a radial parameterization which gives better vertical resolution in the upper mantle.

The new model shows many of the same features seen in previous tomographic images, but with significantly sharper definition, in particular in the upper mantle. Lithospheric roots beneath the stable continental interiors are the most prominent feature in the uppermost mantle. A surprising and complicating result of our study is that when P/SV- and SH-sensitive data are inverted separately, differences in the resulting models are apparent in the middle of the upper mantle (200-300 km). The suggestion is that anisotropy may be a significant contributor to lateral heterogeneity, particularly beneath the oceans.

We have started efforts to validate our models, and to explore their utility in event location, through the prediction of *Pn* travel times. In some regions we obtain relatively good agreement between the observed residual and the *Pn* travel time predicted from the *P* and *S* model S&P12WM13 (expanded only to l=12). In other regions the agreement is poor, probably indicating limited resolution of the structure in the uppermost mantle.

Objective

We are adapting the seismic tomographic techniques developed in global scale studies to the regional scale problem of mapping the elastic and anelastic material properties beneath Eurasia. The main objective of this research is to obtain a tomographic seismic velocity model for the structure beneath Eurasia with a horizontal resolution corresponding to at least $l = 20$, consistent with the widest possible range of seismological observations.

Use of tomographic models of the mantle in the calculation of teleseismic travel times have been shown to result in improved teleseismic event locations (*Smith and Ekström*, 1996). These models are therefore relevant to the global monitoring of a Comprehensive Test Ban Treaty, in particular for obtaining better locations for events in previously uncalibrated regions. In addition, the improved ability to model dispersed intermediate-period surface waves makes it possible to perform more efficient filtering and stacking and, as a consequence, to achieve both a lower surface wave detection threshold, and to obtain better surface wave magnitudes. The advance in our ability to model surface waves can therefore benefit both the detection and discrimination tasks of a monitoring program.

Research Accomplished

In previous reports (1993, 1994, 1995) we have presented preliminary results of our higher resolution upper mantle model S20U7L5. We have also shown the improvement of teleseismic event locations using heterogeneous mantle models. In this report we discuss (1) some final results for the surface wave dispersion characterization at intermediate periods; (2) new indications for anisotropy in the upper mantle which have become apparent as we finalize the model S20U7L5, and; (3) some preliminary modeling of *Pn* residuals using global tomographic models.

Surface Wave Dispersion

Due to their sensitivity to the elastic structure of the crust and the top of the mantle, measurements of intermediate-period surface wave dispersion are ideal for imaging the shallowest portions of the Earth. The main difficulty in obtaining dispersion measurements from teleseismically observed surface waves at periods less than about 100 s is that variations in phase velocities are sufficiently big to cause path variations of several cycles in phase, and isolated residual phase measurements $[-\pi, \pi]$ at a single period are therefore ambiguous in multiples of 2π. For minor arc observations, phase measurements at periods longer than 100 s can, however, be associated with a total cycle count. If a continuous dispersion curve can be anchored at long periods, the total phase perturbation can then be inferred without ambiguity.

In order to obtain the complete broadband dispersion, we have developed a method we call *iterative frequency band expansion.* We initially determine the dispersion parameters in a narrow frequency range centered around 100 s, and then, in several iterations, increase the higher frequency end of the total frequency range. In each iteration, the dispersion parameters are adjusted to minimize the residual dispersion between an observed and a model surface wave using the downhill simplex method of *Nelder and Mead* (1965). Once a misfit between the two wavegroups is minimized for a given frequency range, the range is expanded to include higher frequencies. Because of the smoothness of the dispersion curve, a prediction can be made for frequencies slightly higher than the ones included in the previous iteration. This ensures that the phase difference between model seismogram and observed

seismogram always remains small, so that gradient methods continue to work in the next iteration.

This method of analysis has been systematically applied to digital seismograms from the IRIS/USGS, IRIS/IDA, GEOSCOPE, CDSN, GTSN, and MEDNET networks, using earthquake sources for the period January 1989–September 1995. Analysis was attempted for all earthquakes during this time period with $M_W \geq 5.5$. We use the moment tensors and centroid locations in the Harvard CMT catalog to calculate the source excitation. Only shallow earthquakes ($h < 50$ km) were included, in order to maximize the excitation of surface waves. In addition, we only consider paths in the distance range $25° \leq \Delta \leq 150°$, in order to avoid problems of separation of the fundamental mode at short distances and close to the antipode.

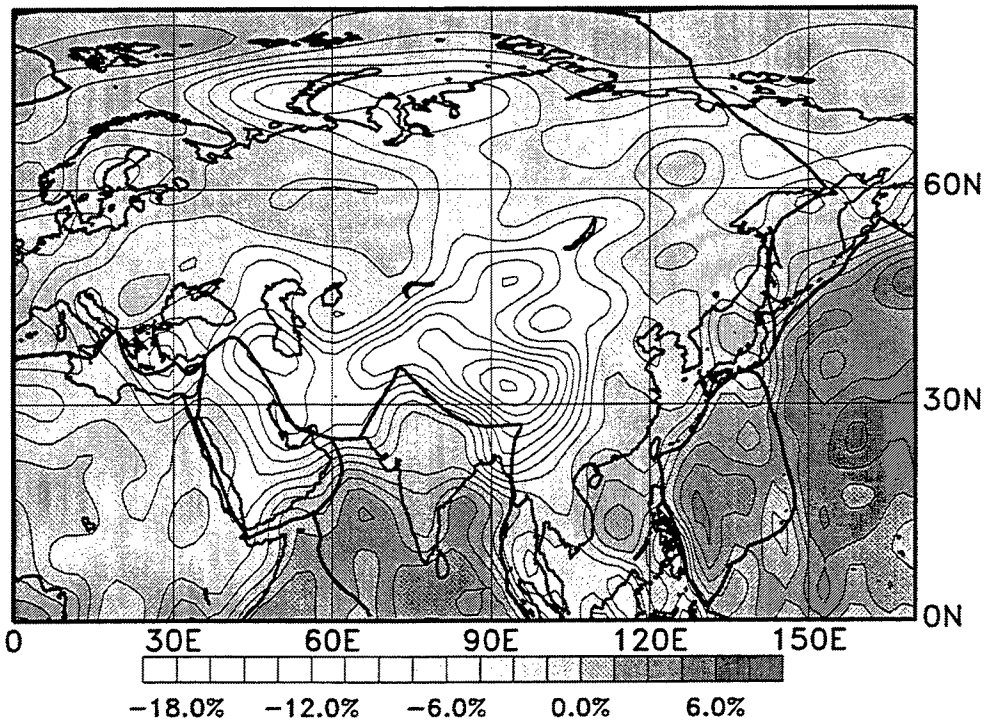

Figure 1: Map shows the phase velocity variations of 35 s Love waves for Eurasia. Note the strong correlation between slow velocities and thick and low-velocity crust.

More than 128,000 station-receiver paths were analyzed. Approximately 37,000 high-quality measurements for Rayleigh waves at 50 s resulted from the analysis, while at 35 s, the number was somewhat smaller — 28,000. Fewer good measurements were obtained for Love waves, in part due to the higher noise levels on horizontal components. In the analysis of the measurements, the dispersion curves were converted to phase anomalies $\delta\Phi$ at the discrete periods 150, 100, 75, 60, 50, 45, 40, 37, and 35 s. Observational uncertainties of the measurements were determined from statistical analysis of repeated measurements for similar paths.

The phase anomalies were next inverted for the model coefficients of global phase velocity maps expanded in spherical harmonics. The predicted phase anomaly between a source at

(θ_S, ϕ_S) and a receiver at (θ_R, ϕ_R) is written in terms of real spherical harmonics

$$\delta\Phi = -\frac{\omega}{c_0} \int_{(\theta_S,\phi_S)}^{(\theta_R,\phi_R)} \sum_{l=0}^{L} \sum_{m=0}^{m=l} (A_{lm} \cos m\phi + B_{lm} \sin m\phi) p_l^m(\theta) ds, \qquad (1)$$

where A_{lm}, B_{lm} are the model coefficients, L is the maximum angular degree of the expansion, and p_l^m are the Legendre polynomials. The coefficients A_{lm}, B_{lm} are determined by damped least-squares inversion. The result of these inversions are global phase velocity maps (*Ekström et al.*, 1996). The model coefficients can be obtained in electronic form via anonymous ftp to `saf.harvard.edu`, by retrieving the files in `pub/ETL-JGR-96`.

The resulting maps explain 80–96% of the variance in Love wave phase anomalies, and between 70–90% of the Rayleigh wave data. The lowest variance reduction is obtained for the longest periods. Figure 1 shows the phase velocity map for Eurasia and Love waves at 35 s period. Clearly, a very large portion of the signal is associated (as expected) with the contrast between oceanic and continental crust and lithosphere. Within Eurasia, very large variations are seen which reflect both the total thickness of the crust (as beneath western Tibet), tectonic activity (the Alpine-Himalayan belt in general) and very thick sedimentary basins (Arctic ocean shelf, southern Caspian sea). Resolution experiments indicate that these features are well resolved. It is interesting to note that when compared with phase velocity predictions from the recent global crustal model CRUST-5.0 (*Mooney et al.*, 1995), there are some areas which show very large similarities, and other areas (in particular sedimentary basins) which do not. The correlation between the observed phase velocity map and that predicted by *Mooney et al.*'s model is approximately 0.80 for Love waves at 35 s.

A degree 20 model of the Mantle

The surface wave data described above are being used in conjunction with previous seismological datasets to derive a higher resolution 3-D model of the Earth's mantle. Preliminary results have been presented at various meetings (*Ekström and Dziewonski*, 1994; 1995; *Dziewonski et al.*, 1996), and we are in the final stages of finalizing the model S20U7L5 (spherical harmonic degree 20, degree 7 in the upper mantle and degree 5 in the lower mantle).

The parameterization and inversion approach are similar to those used for earlier Harvard mantle models, such as S12WM13 (Su *et al.*, 1993), with the following notable differences:

- We use a split parameterization for the mantle, and parameterize the radial variations in the upper mantle in terms of Chebyshev polynomials of degree 0–7. For the lower mantle we use Chebyshev polynomials of degree 0–5.
- The spherical harmonic expansion is extended from degree 12 to degree 20.
- The data are corrected for crustal structure using a new compilation of crustal thicknesses and velocities by *Mooney et al.* (1995). This is in contrast to previous models which were only corrected for average continental and oceanic crustal structure.

Several types of data with sensitivity to velocity variations in different parts of the mantle are included. So far, the following data have been incorporated in the derivation of the new model

- Absolute and differential travel times measured from waveform data (S, SS, ScS, $SS-S$, $ScS-S$, $S-SKS$).

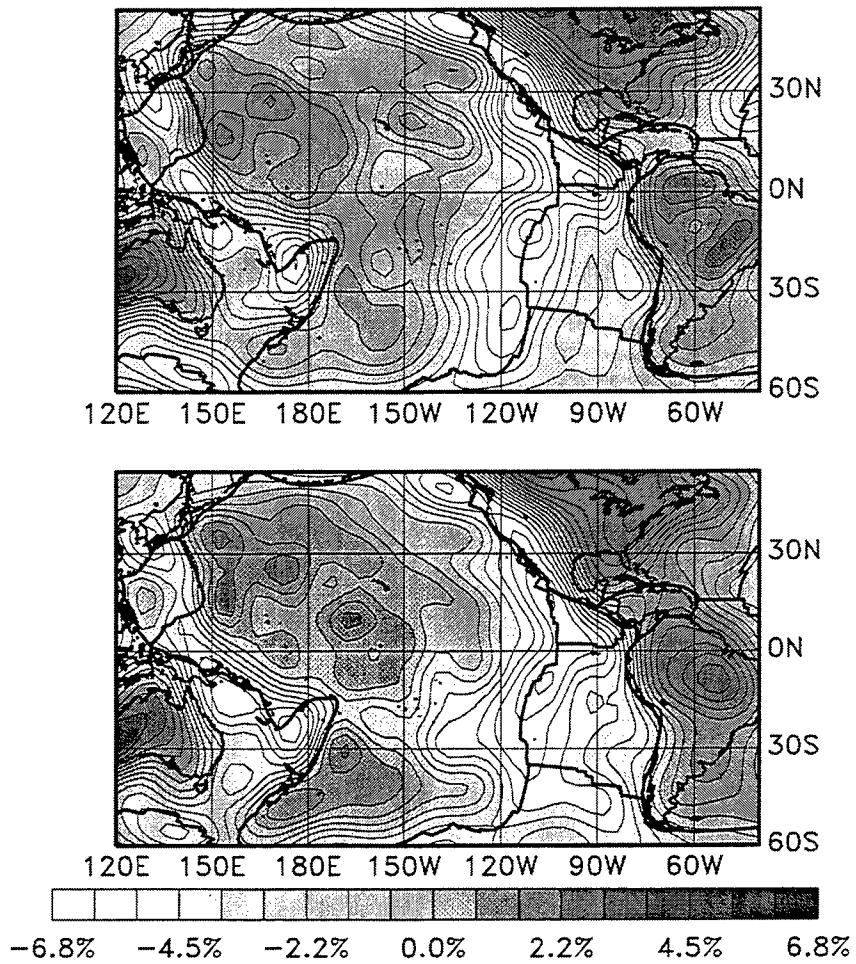

Figure 2: Maps show the S velocity variations at 100 km depth beneath the Pacific and adjacent areas. The top panel shows the S-velocity variations recovered from primarily P/SV-sensitive data, and the bottom panel for SH-sensitive data. There is strong similarity between the two maps in most regions.

- Long-period body and mantle waveforms from earthquakes recorded on the Global Seismic Network.
- Very long-period mantle waveforms from large earthquakes recorded on the Global Seismic Network.
- Intermediate period dispersion measurements of Rayleigh and Love waves (described above).

The new model S20U7L5 shows many of the same features seen in previous tomographic images, but with significantly sharper definition. On a global scale, the fast velocities beneath stable continental interiors are the most prominent anomalies in the top 300 km of the mantle. The very high velocities beneath the stable interior of West Africa continue even deeper. The new model also shows that the slow velocity anomalies associated with ridges continue to great depth, in particular in the Indian Ocean. The Red Sea rift shows slow velocities

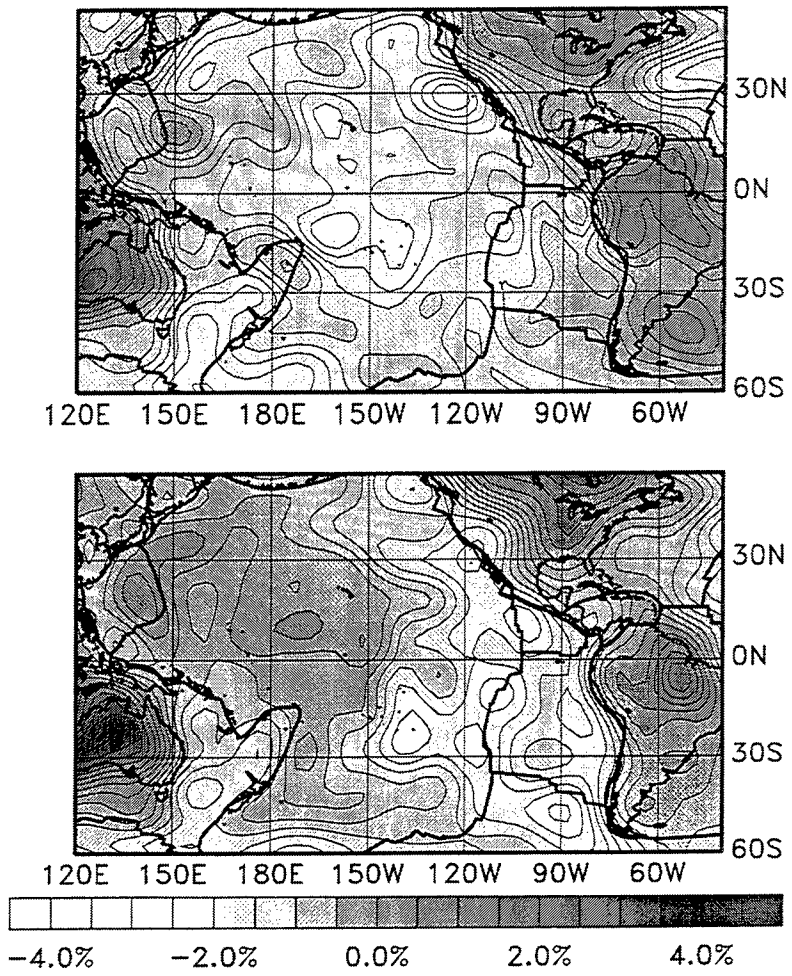

Figure 3: Maps show the S velocity variations at 200 km depth beneath the Pacific and adjacent areas obtained from separate inversions of P/SV and SH sensitive data. Note the slow velocities in the central Pacific seen in the top (P/SV) map, but absent in the bottom (SH) map. Also, the East Pacific Rise remains a slow feature at this depth for SH data, but not for P/SV data.

extending down to 400 km. Below 250 km slow features not directly associated with surface tectonics predominate, in particular in the center of the Pacific Ocean.

In order to investigate the compatibility of the various datasets, we have performed several inversions using subsets of the full dataset. In particular, we have separated the data which are primarily sensitive to SH-type structure from those which primarily sense P/SV-type structure, by considering separately observations made from transversely polarized seismograms and those made on vertical and radial seismograms. The somewhat surprising result is that there are regions and depth ranges where we obtain distinctly different patterns in the separate inversions. In Figure 2 we show a comparison of the structures at 100 km depth beneath the Pacific as imaged using the two sets of data. While there are differences between the two maps, overall there is fairly close agreement. Mostly we see the fast roots beneath the continents, and the signature of the hot and cooling lithosphere in the oceans. At 200 km (Figure 3), however, the slow velocity in the central Pacific seen in the P/SV map (as well

as in many previous models) is not seen in the SH map, which instead shows consistently fast velocities in the same region. The SH map also shows slower velocities at this depth associated with the East Pacific Rise, while the P/SV map does not.

There are different possible explanations for this result. The most straightforward reason could be that this is the effects of varying levels of transverse anisotropy in the asthenosphere. A second possibility is that azimuthal anisotropy in the oceanic lithosphere and/or asthenosphere gets mapped, through the ray coverage, into different apparent velocity structures for Love and Rayleigh waves. A third possibility is that we have overestimated the resolving power of the different datasets, and that the observed patterns are spurious. Based on the robustness of the results (established through additional experiments), we do not believe the third explanation is likely, and we are currently exploring the need for including specific considerations of anisotropy in future modeling efforts.

Our current objective remains to determine a good compromise model for S-velocity heterogeneity in the mantle, linked with a description of the likely level of anisotropy in the mantle and its possible biasing influence on our model.

Modeling of Regional Phases

The limited distribution of sources and the sparse (in a global sense) distribution of receivers set a limit on our ability to simply keep increasing the resolution of our global models. To obtain good global resolution on the scale of 500 km or less will probably be very difficult, if not impossible, for some time to come. It is possible though to obtain high resolution models of a number of regions, both large and small, that are well sampled. To obtain the best possible coverage in a given region, one would ideally use sources and receivers that are both within and outside the region of interest. Proper treatment of such a combination of data would require a hybrid parameterization (*Fukao et al.*, 1992).

As a preliminary step in such an investigation we have been examining how well our current 3-D mantle models may be used to explain trends in regional data in different regions. In Figure 4 we show the *Pn* raypath coverage for events reported by the ISC for northeastern North America. This region was chosen to test our model in an area where we predict large anomalies based on the model S&P12WM13 (*Su and Dziewonski*, 1993) and have a good path coverage using data from the ISC.

Figure 5 shows the observed and calculated *Pn* residuals for this region. The *Pn* travel time was calculated using the average *P* velocity at the top of the mantle in the model S&P12WM13. Despite some scatter a correlation between the residuals found for these regional phases and those derived from our global model can be seen. In particular, the level of heterogeneity appears to be well matched. A second region for which we performed this experiment was southern Eurasia. This region has many fewer stations reporting to the ISC. Figure 6 shows the ISC residuals and the predicted residuals. In this case there is no apparent correlation. This may be for one of several reasons: there is some evidence that earthquakes in this region are poorly located; our model in this region may not be so well constrained due to lack of data coverage; structure in this region may be more complex than the resolution of our current model allows; or the correlation may be obscured due to the smaller range of predicted anomalies.

Despite being based wholly on teleseismic data, our current global models appear to provide fairly good estimates of uppermost mantle velocities beneath regions such as northeastern North America. The experiment also suggests that beneath areas such as Eurasia regional phases may need to be included to adequately model the uppermost mantle structure. How-

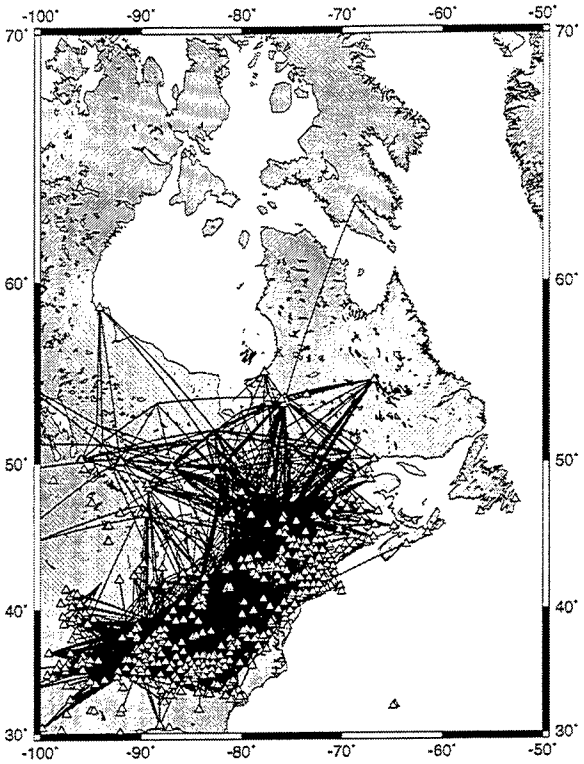

Figure 4: Map showing ray coverage for *Pn* observations in northeastern U.S., reported in the ISC.

ever, such an analysis will require careful relocation of the seismicity before utilizing the travel times. With the inclusion of regional data, parameterization in terms of spherical harmonics is a poor choice since by definition they have a uniform resolution everywhere. In future work, we will instead move towards hybrid parameterizations with variable resolution, to be able to include and subsequently to better model observations corresponding to both regional and teleseismic distances.

Conclusions and Recommendations

By combining a large number of diverse seismological observations, we have made progress towards obtaining higher resolution tomographic images of the regional scale elastic structure globally and beneath Eurasia. The shallowest part of the mantle is effectively constrained and imaged using intermediate period surface waves. Both global and regional scale heterogeneity in the mantle has been shown to bias seismically derived event locations. In some regions, our current tomographic models can predict the gross residual patterns seen in regional phase data. It appears likely that further improvements in locations can be achieved by correcting for better known elastic heterogeneity in the Earth's mantle.

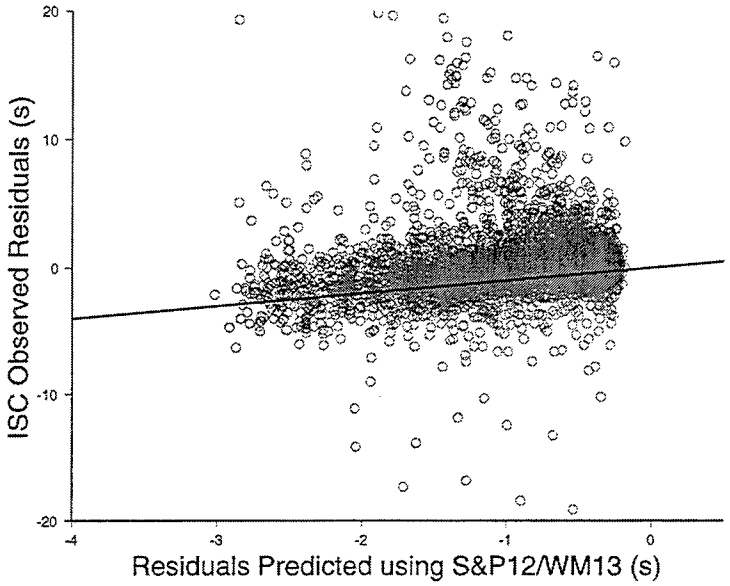

Figure 5: Observed residuals for *Pn* compared with predictions from S&P12WM13 for paths in northeastern U.S.

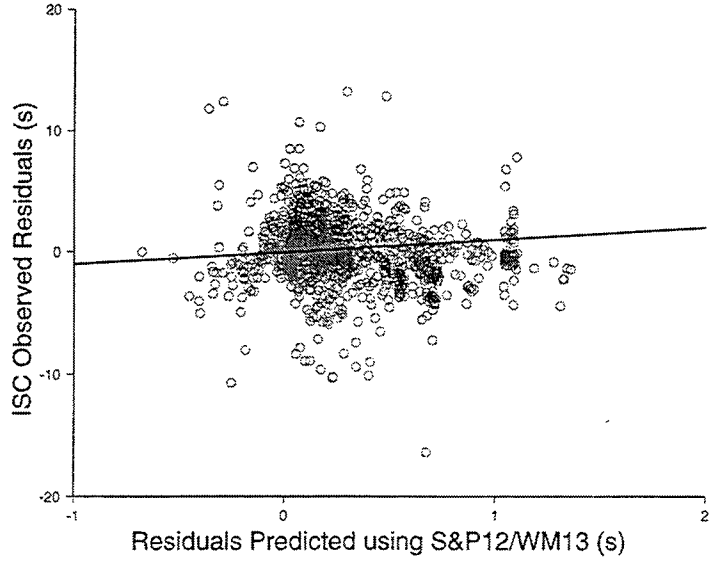

Figure 6: Observed residuals for *Pn* compared with predictions from S&P12WM13 for paths in southern Eurasia.

References

Dziewonski, A. M., G. Ekström, and X.–F. Liu, Structure and the top and the bottom of the mantle, in *Proceedings of NATO Advanced Study Institute "Monitoring a Comprehensive Test Ban Treaty" Alvor, Portugal, Jan., 1995*, 521–550, 1996.

Ekström, G., and A. M. Dziewonski, Higher resolution upper mantle S velocity structure (abstract), 75, *EOS, Trans. Am. Geophys. Soc.*, *475*, 1994, .

Ekström, G., and A. M. Dziewonski, Improved models of upper mantle S velocity structure (abstract), 76, *EOS, Trans. Am. Geophys. Soc.*, *421*, 1995, .

Ekström, G., J. Tromp, and E. W. Larson, Measurements and global models of surface wave propagation, *J. Geophys. Res.*, submitted, 1996.

Fukao, Y., M. Obayashi, H. Inoue, and M. Nenbai, Subducting slabs in the mantle transition zone, *J. Geophys. Res.*, *97*, 4809–4822, 1992.

Mooney, W. D., G. Laske, and G. Masters, A new global crustal model at 5x5 degrees: CRUST-5.0, *EOS, Trans. Am. Geophys. Soc.*, *76*, 421, 1995.

Nelder, J. A. and R. Mead, 1965. A simplex method for function minimization, *Computer Journal*, *7*, 308–313, 1965.

Su, W.-J. and A. M. Dziewonski, Joint 3-D inversion for P- and S-velocity in the mantle (abstract), *EOS, Trans. Am. Geophys. Un.*, **74**, 556, 1993.

Su, W.-J., R. L. Woodward and A. M. Dziewonski, Degree-12 Model of Shear Velocity Heterogeneity in the Mantle, *J. Geophys. Res.*, **99**, 6945–6980, 1993.

Simulating Crustal Heterogeneity Fields from Stochastic Models: A Performance Evaluation

John A. Goff[1] and Alan Levander[2]

[1]University of Texas Institute for Geophysics
[2]Rice University

AFOSR Grant F49620-94-1-0100

Abstract

Our AFOSR-sponsored research contains two primary elements: (1) investigation of the stochastic properties of random crustal heterogeneity and establishing appropriate statistical models, and (2) investigation of the response of observed seismic wavefields to heterogeneity described by such models. A critical link between these two efforts is the simulation of a crustal heterogeneity field based on the stochastic model; these constitute the input for finite difference calculations of wavefield response to heterogeneous fields.

Field simulation techniques enjoy a diverse and substantial body of literature, based primarily in the oil and mineral exploration sciences. However, evidently lacking from the published record is any critical evaluation of the relative merits, drawbacks, and performance of the various methods available. In past work we have relied on Fourier methods, considering them to be fast, accurate, and simple in implementation. Simulations performed in the oil industry, used primarily to investigate flow through heterogeneous permeability fields, dominantly use "sequential Gaussian simulation" (SGS) techniques. The primary advantage of this method is a unified methodology for generating the simulation and for incorporating prior constraints or conditions. Commercially available software are available for implementing SGS which are highly optimized for performance. The Fourier method can also incorporate conditioning information, but in a separate modeling step which adds computation time.

In this paper we compare Fourier and SGS techniques in a synthetic (but realistic) conditional simulation experiment. The SGS component of the experiment was conducted courtesy of J. Jennings of the University of Texas Bureau of Economic Geology using the commercially available ISATIS software. Despite the optimized commercial SGS code, the Fourier method ran approximately an order of magnitude faster on a slower computer. The Fourier method was also far simpler to implement, as the SGS code requires user input to several parameters which control the level of compromises which must be instituted in order to make the code run in a reasonable time frame. An incorrect choice of such parameters can have a drastic detrimental effect on the simulation. A posteriori investigation of the statistical properties of the simulated fields reveal problems with both methods. The SGS fields are *less* correlated at fine scale than allowed for by the statistical model. This is likely a result of some of the necessary compromises, mentioned above, which limit the amount of surrounding conditioning information that are used in simulating each grid node. Fourier-generated fields are *more* correlated at fine scales than they should be, especially in the along-strike direction of an anisotropic field. This is an aliasing effect, where much of the high-wavenumber power is emplaced at the edge of the simulated field rather than distributed throughout. We are currently contemplating anti-aliasing algorithms to reduce this effect.

Key Words: conditional simulation, Fourier simulation, sequential Gaussian simulation, stochastic modeling, crustal heterogeneity

Objectives

Our AFOSR-sponsored research contains two primary elements: (1) investigation of the stochastic properties of random crustal heterogeneity and establishing appropriate statistical models, and (2) investigation of the response of observed seismic wavefields to heterogeneity described by such models. Relevance to the Comprehensive Test Ban Treaty comes from our increased understanding of seismic wave propagation and scattering Q within the crust.

A critical link between these two efforts is the simulation of a crustal heterogeneity field based on the stochastic model; these constitute the input for finite difference calculations of wavefield response to heterogeneous fields. The primary objective of this paper is to make a critical assessment of two methods for generating simulations: Fourier transformation and sequential Gaussian simulation (SGS). Both methods enjoy wide use in the literature, but have not (to our knowledge) heretofore been compared or rigorously assessed with respect to their ability to perform as advertised.

Research Accomplished

Background

A wide body of literature exists on the subject of unconditioned and conditioned simulations. Below we provide a brief outline of the two most prominent methods: Fourier transformation and SGS. Comprehensive presentations of these methods and reference lists are provided in Deutsch and Journel (1992) and Christakos (1992).

Fourier Transform Simulation

An unconditioned Gaussian-distributed simulation $Z_u(\mathbf{x})$, with second-order statistical model expressed as the amplitude spectrum $A(\mathbf{u})$, can be generated by discrete Fourier transform (DFT) via:

$$Z_u(\mathbf{x}) = DFT\{A(\mathbf{u})\exp[i2\pi\phi(\mathbf{u})]\},$$

where $\mathbf{x}$ and $\mathbf{u}$ are discretized on an m by n grid, and ϕ, the phase value, is a uniformly distributed random number sampled on [0,1). Hermetian symmetry is enforced on the product of amplitude and phase spectra.

In many applications, we may wish to generate a simulation conditioned on prior field values at a subset of grid location: $\hat{Z}(\mathbf{x}_i)$, $i \in 1,2,...,N$. This can be accomplished with the following algorithm:

Step 1: Perform smooth interpolation of $\hat{Z}(\mathbf{x}_i) \rightarrow Z_i(\mathbf{x})$. Use Kriging, which is determined by: $Z_i(\mathbf{x}) = E[Z(\mathbf{x})|\hat{Z}(\mathbf{x}_i), i \in 1,2,..,N]$, where $E[a|b]$ is the expected value of a conditioned on b as specified by the second-order statistical model.

Step 2: Compute unconditioned simulation $Z_u(\mathbf{x})$ via Fourier method described above.

Step 3: Sample $Z_u(\mathbf{x})$ at locations $(\mathbf{x}_i)$, $i \in 1,2,...,N$ and perform smooth interpolation $Z_{ui}(\mathbf{x})$ as in step 1.

Step 4: Conditional simulation $Z_c(\mathbf{x}) = Z_u(\mathbf{x}) - Z_{ui}(\mathbf{x}) + Z_i(\mathbf{x})$

Sequential Gaussian Simulation

Assume grid geometry and conditioning values as described above. The SGS algorithm, conditioned ($N \neq 0$) or otherwise ($N = 0$) proceeds as follows (here, $E[a|b]$ is the expected value, and $Var[a|b]$ the variance of a conditioned on b as specified by the second-order statistical model):

Step 1: Compute $E[Z(\mathbf{x}_{N+1})|\hat{Z}(\mathbf{x}_i), i \in 1,..,N]$, $Var[Z(\mathbf{x}_{N+1})|\hat{Z}(\mathbf{x}_i), i \in 1,..,N]$. Then choose a value for $Z^*(\mathbf{x}_{N+1})$ from the Gaussian PDF defined by this conditional mean and variance.

Step 2: Compute $E[Z(\mathbf{x}_{N+2})|\hat{Z}(\mathbf{x}_i), i \in 1,..,N+1]$, $Var[Z(\mathbf{x}_{N+2})|\hat{Z}(\mathbf{x}_i), i \in 1,..,N+1]$. Then choose a value for $Z^*(\mathbf{x}_{N+2})$ from the Gaussian PDF defined by this conditional mean and variance.

•
•

Step mn - N: Compute $E[Z(\mathbf{x}_{mn})|\hat{Z}(\mathbf{x}_i), i \in 1,.,mn-1]$, $Var[Z(\mathbf{x}_{mn})|\hat{Z}(\mathbf{x}_i), i \in 1,..,mn-1]$. Then choose a value for $Z^*(\mathbf{x}_{mn})$ from the Gaussian PDF defined by this conditional mean and variance.

The sequence of grid indices chosen in the above algorithm is arbitrary, providing that all grid nodes are simulated.

The primary drawback to the SGS algorithm is that at each step a covariance matrix is computed with column and row dimension equal to the number of conditioning values, and furthermore this matrix must be inverted. Even for relatively small grids such a computation can become prohibitive as the grid becomes filled out and the number of conditions approaches the total number of grid points. Hence, in actual application, SGS algorithms must limit in some manner the number of conditions applied at each step. There are no set rules for applying such limitations.

Non-Gaussian Simulations

Unconditional non-Gaussian simulations can be created by first generating a Gaussian simulation, then mapping the Gaussian probability distribution onto the desired distribution. Some examples from this PI include simulation of keeled sea ice (Goff, 1995), and binary lithologic heterogeneity (Goff and Levander, 1996). Conditioned non-Gaussian simulations can be generated if the conditioning information can be "reverse" mapped onto Gaussian-distributed space (a "normal scores" transformation). The procedures described above for generating a conditional Gaussian simulation can then be applied, and the result forwarded mapped into the "real world" distribution. For continuous non-Gaussian distributions, such as those used to describe sea ice, the forward mapping is one-to-one and onto, so the reverse mapping is unique and readily obtainable. However, for discrete distributions, such as those used for lithologic heterogeneity, the reverse mapping is non-unique. Theoretically that presents no problem, as one mapping is as good as another as long it satisfies the conditioning criteria and the spatial statistics. Nevertheless, picking one reverse mapping among the infinite possible represents a significant and (to our knowledge) unsolved theoretical challenge.

Synthetic Gaussian Experiment

We have formulated a simple synthetic experiment to directly compare the Fourier and SGS methods of conditional simulation. The geometry of the experiment is demonstrated in Figure 1. We begin with an unconditioned simulation (a "master" grid) generated by Fourier transformation from known statistics (Figure 2): a simple fractal model (power law amplitude spectrum), with anisotropic ratio of 5:1 (long axis in horizontal direction), sampled on a 1000 by 1000 grid. We sample the unconditioned simulation on both left and right edges to establish a priori constraints, and generate conditioned simulations using both Fourier and SGS methods. The master grid therefore represents "reality", and comparison with the simulations provides an assessment of performance.

The Fourier simulation was run on a Sun IPX workstation. The SGS simulation was conducted using the ISATIS commercial software on an SGI computer (SGS runs were performed courtesy of J. Jennings at the University of Texas Bureau of Economic Geology). The Fourier simulation was performed within a span of ~10 minutes, whereas the SGS simulation took approximately 1.5-2 hours.

Figure 3 displays step 2 of the Fourier algorithm: a smooth, Kriged interpolation of the conditioning data. Figure 4 displays the final Fourier conditional simulation. Note that right and left sides are identical to the "master" grid in Figure 2, while the interiors of these two grids deviate from one another (as they should). The general visual comparison of roughness characteristics is satisfactory.

Figure 5 shows an example of an SGS conditional simulation in which the conditioning limitations are clearly too severe. This demonstrates the danger of rote application of SGS. A far superior SGS conditional simulation is shown in Figure 6, as visually satisfactory in comparison to the master grid (Figure 2) as the Fourier simulation (Figure 4).

We seek, of course, a more rigorous assessment criterion than "visually satisfactory" (though the power of that criterion should not be underestimated, as Figure 5 demonstrates). We do so by examining the a posteriori statistical properties of the simulated fields. There are several ways to do so which will test the adherence of the simulated field to the desired statistical model. The simplest in our view is the power spectrum, in particular the average profile power spectrum in both the row (along-strike) and column (cross-strike) directions. Averaging the profile spectrum from all rows or all columns greatly reduces the uncertainty inherently associated with the power spectrum, especially at higher wavenumbers where redundancy is greater. Prior to computing the power spectrum, we subtract the mean and taper the ends (Hanning taper) of each row or column profile.

The average column and row power spectra of the master grid, Fourier simulation, and SGS simulation are presented in Figures 7, 8, and 9, respectively, along with the model spectra for the column and row directions. The column power spectrum for the master grid (Figure 7a) is a nearly perfect match to the respective model spectrum. This observation is very important as it implies that our starting conditions for the conditional simulations, the left and right edges of the master grid, are truly samples from the statistical model. However, the average row spectrum for the master grid (Figure 7b) deviates from the model spectrum: the high wavenumber portion of the observed spectrum is significantly less than expected, implying a smoother or more correlated morphology at smaller scales in the row direction than desired. The reason for this discrepancy is demonstrated for 1-D in Figure 10 (though the problem only becomes significant for the along-strike direction of a 2-D grid): in performing the inverse Fourier transform of the complex spectrum, a portion of the high-wavenumber power is realized as the step-function which exists at the edge of the space-domain field rather than distributed uniformly across the

field as it should. Hence, when the edges of the profile are tapered, as they must be to prevent step-function power from leaking into the power spectrum, this power is lost.

The column and row spectra for the Fourier simulation (Figure 8) are identical to those of the master grid. Although, as expected, this indicates the same aliasing problem associated with unconditional Fourier simulation as described above, it also demonstrates that the conditioning algorithm has not adversely affected the field statistics.

The column and row spectra for the SGS simulation (Figure 9) indicate a different sort of mismatch with the model spectrum: observed in both row and column directions, the high wavenumber portions of the spectrum are significantly greater than expected, indicating a rougher or less correlated morphology at smaller scales. We believe this is caused by the constraints in conditioning information necessary to make the SGS algorithm practical, which necessarily reduces the correlation among grid points.

Conclusions and Recommendations

The Fourier method for generating simulations from a statistical model is superior to SGS in at least two aspects: speed and ease of implementation: the Fourier method ran ~10 times faster on a slower computer, and did not require user manipulation of "compromise" parameters to ensure a satisfactory run. Both methods, however, displayed discrepancies at high wavenumber with respect to the model which each is expected to emulate: the Fourier simulation was smoother (in strike direction only) and the SGS simulation rougher (in all directions) at high wavenumbers than the statistical model. We believe that the SGS discrepancy is inherent to the compromises which are necessary to make the SGS algorithm practical. The Fourier discrepancy is likely attributable to an aliasing problem: in the inverse transform from the wavenumber domain, a significant amount of high-wavenumber power is realized as the step function at the edges of the space-domain field rather than distributed throughout as it should.

The SGS discrepancy probably cannot be narrowed significantly without an unrealistic increase in computation time. The Fourier discrepancy, however, might be improved by an antialiasing algorithm which enforces a tapered edge of the space domain image (simply insuring that a large enough simulation is generated so that the edges can be avoided in the desired sample). This will be investigated in the coming months. If such an algorithm were practicable, the Fourier simulation method would be considered superior in all respects. We also intend to investigate methods for generating conditioned binary simulations using the Fourier method.

References

Christakos, G., *Random Field Models in Earth Sciences*, Academic Press, San Diego, 1992.

Goff, J. A., Quantitative analysis of sea ice draft 1. Methods for stochastic modeling, *J. Geophys. Res.*, *100*, 6993-7004, 1995.

Goff, J. A., and A. Levander, Incorporating "sinuous connectivity" into stochastic models of crustal heterogeneity: Examples from the Lewisian gneiss complex, Scotland, the Franciscan formation, California, and the Hafafit gneiss complex, Egypt, *J. Geophys. Res.*, *101*, 8489-8501, 1996.

Deutsch, C. V., and A. G. Journel, *GSLIB Geostatistical Software Library and User's Guide*, Oxford University Press, New York, 1992.

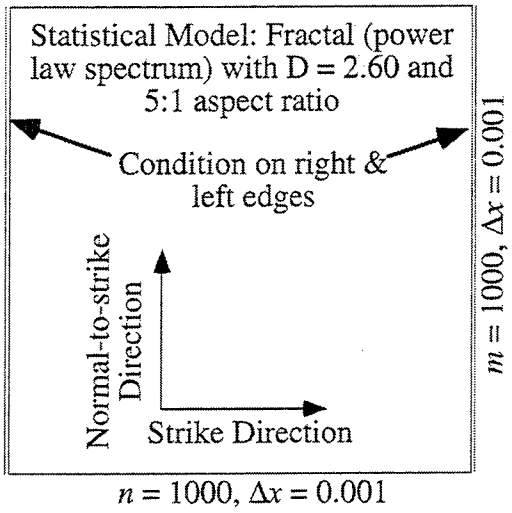

Figure 1: Geometry for conditional simulation experiment.

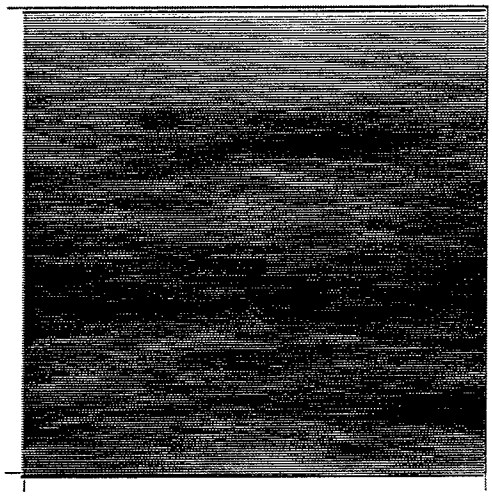

Figure 2: "Master" grid for conditional simulation experiment: an unconditional Fourier simulation of the statistical model.

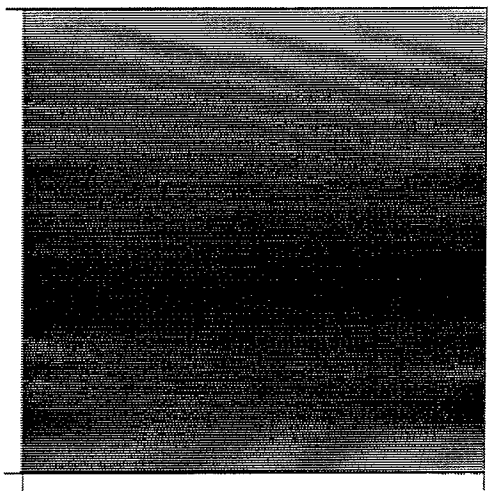

Figure 3: Step 2 in the conditioned Fourier simulation: a Kriging interpolation of the conditioning information (left and right edges of master grid shown in Figure 2).

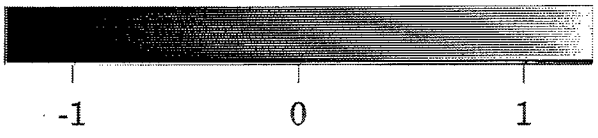

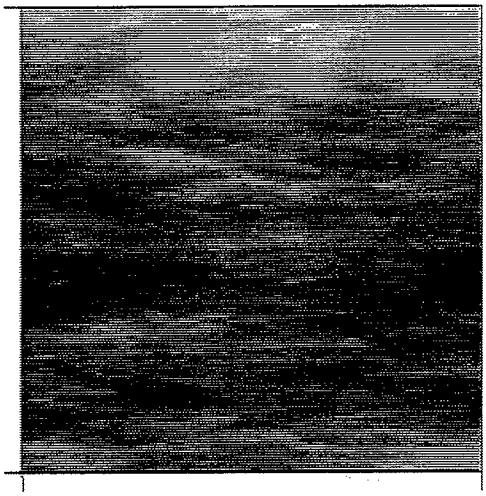

Figure 4: Complete Fourier conditional simulation.

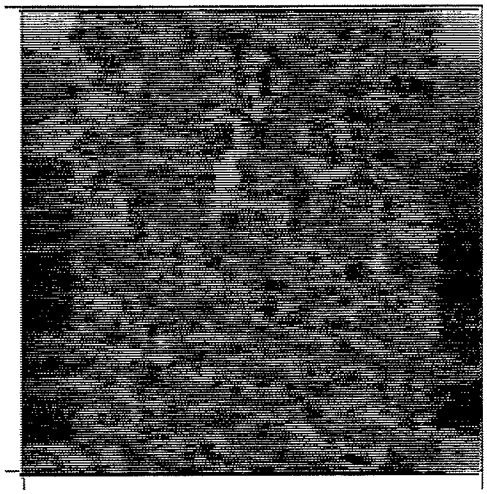

Figure 5: Complete SGS conditional simulation with a poor choice of "compromise" parameters.

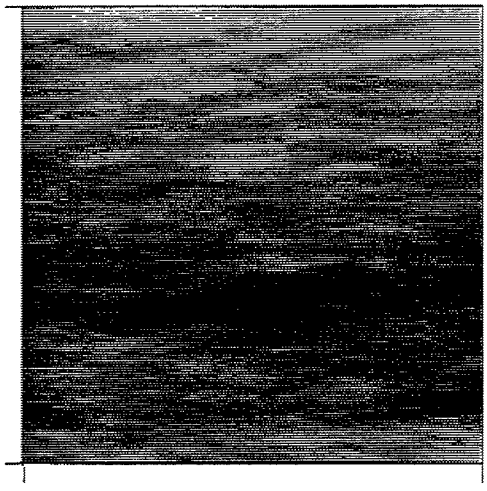

Figure 6: Complete SGS conditional simulation that perhaps represents the best balance of computer efficiency and realism.

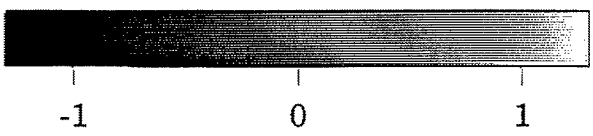

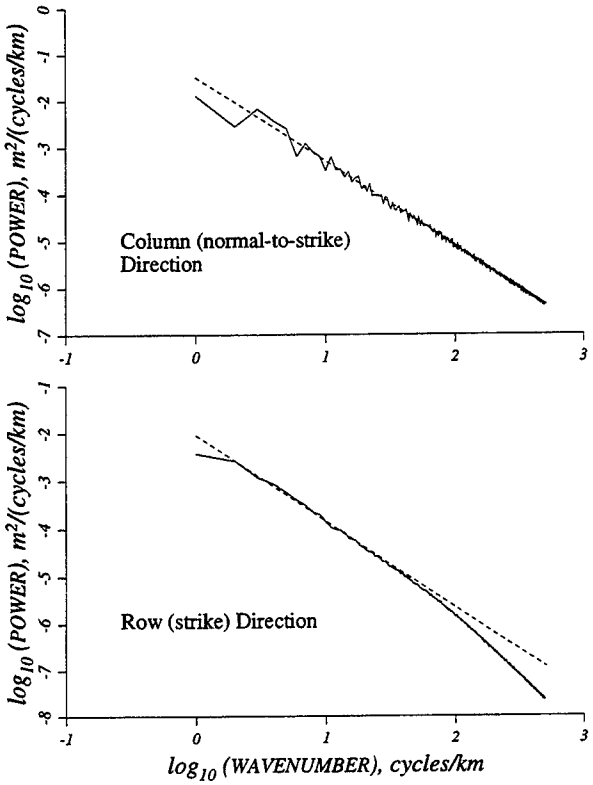

Figure 7: Average column and row power spectra for master grid (Fig 2). Solid = observed, dashed = model.

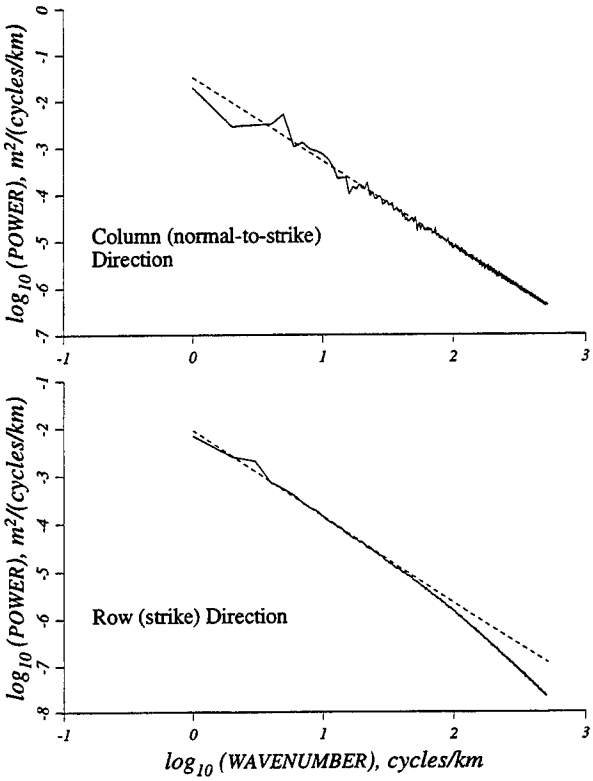

Figure 8: Average column and row power spectra for Fourier simulation grid (Fig. 4). Solid = observed, dashed = model.

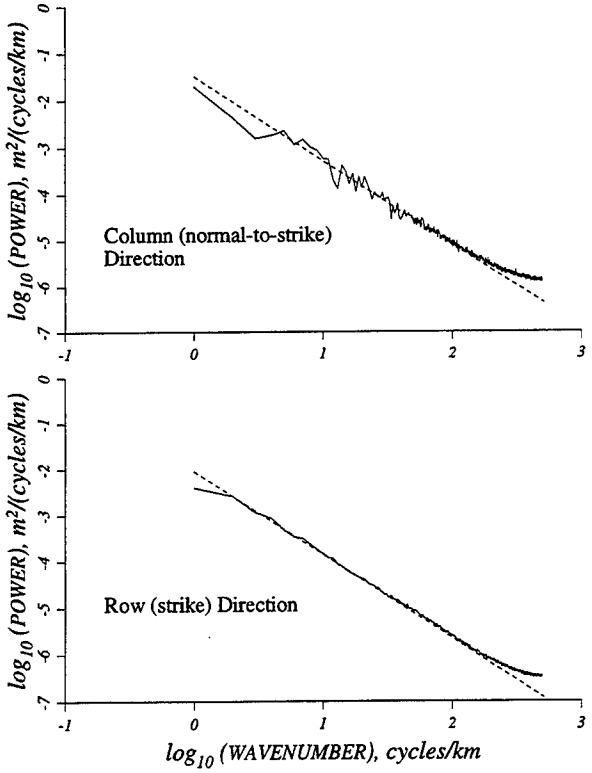

Figure 9: Average column and row power spectra for SGS simulation (Fig. 6). Solid = observed, dashed = model.

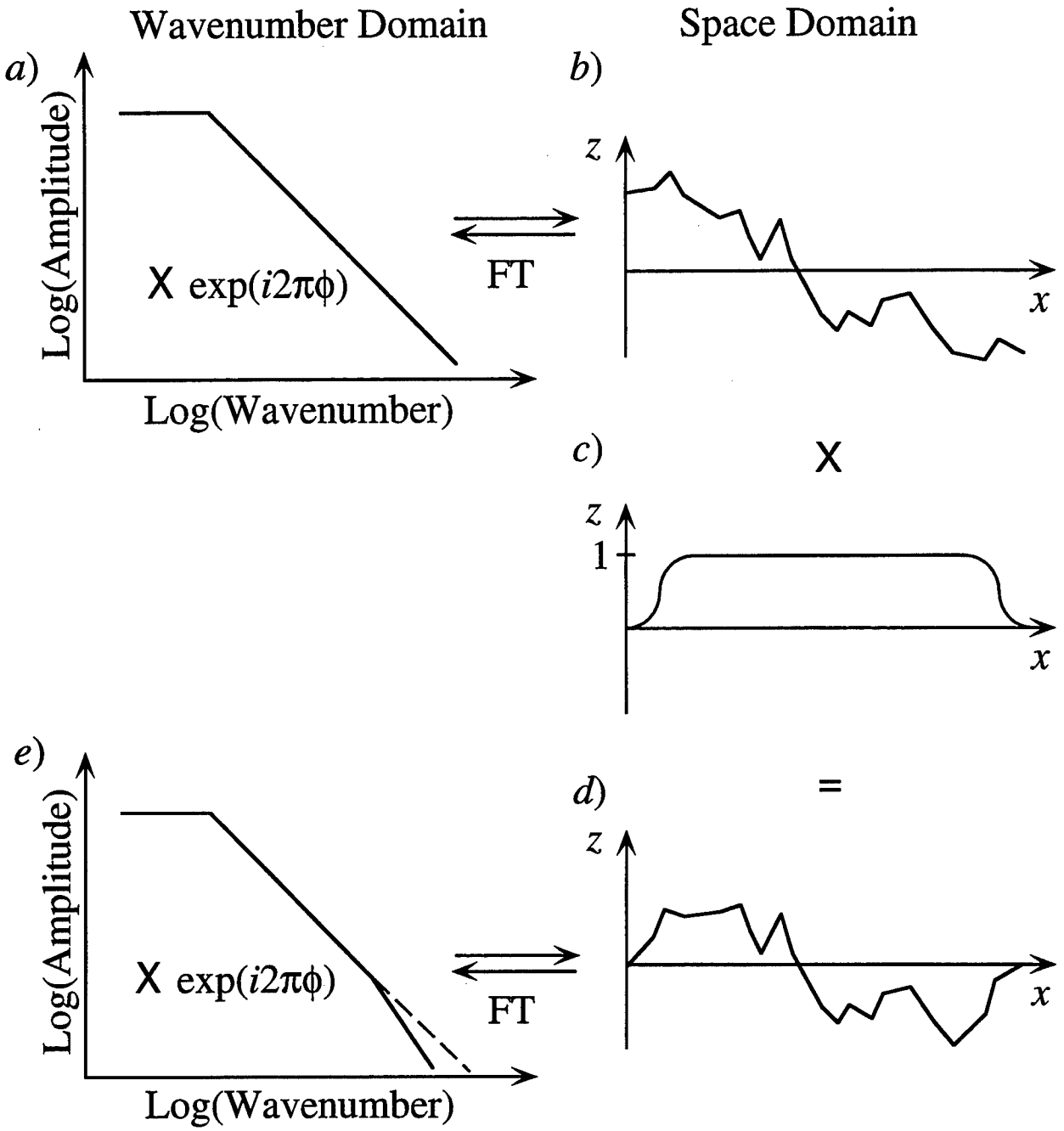

Figure 10: Illustration of aliasing problems associated with Fourier simulation. (*a*) Simulation begins with an amplitude spectrum multiplied by a random phase spectrum. (*b*) Fourier transformation yields a space-domain field (simulation). (*a*) and (*b*) are Fourier pairs, including step function at edge of space-domain field where much of high wavenumber power is placed. In the normal course of estimating the spectral properties of (*b*), a tapering function (*c*) is applied, yielding space domain image (*d*) with no step function at edges. This operation removes much of the high wavenumber power that had existed at the edges of (*b*), so that the amplitude of the Fourier transform of (*d*), (*e*), is reduced in high wavenumber amplitude relative to model spectrum (*a*).

STUDY OF LOW FREQUENCY Lg FROM EXPLOSIONS AT NEVADA, KAZAKH, LOP NOR, AND AZGIR TEST SITES

Indra N. Gupta and Tian-Run Zhang
Multimax, Inc.
1441 McCormick Drive, Largo, Maryland 20774
Contract No. F19628-95-C-0176
Sponsored by DOE

ABSTRACT

An understanding of the mechanism of generation of Lg from underground nuclear explosions is essential for seismic monitoring and source discrimination at regional distances. Earlier studies have suggested that near-source scattering of explosion-generated Rg into S is responsible for the low-frequency Lg from nuclear explosions at both NTS and Kazakh test sites. A recent analysis of regional data from NTS explosions has indicated that the source of Rg waves must have a strong CLVD component and the prominent low-frequency spectral null in the observed Lg is due to Rg from a CLVD source. An objective of this research is to investigate the spectral nulls and other characteristics of the low-frequency Lg from explosions at various test sites so that the scattering mechanism and its potential for obtaining useful source information can be fully exploited. The dependence of spectral nulls on shot depths and other source parameters is first investigated by analyzing Lg from a large number of Yucca Flats (NTS) explosions, with known ground truth, recorded at several broadband stations. Methods of analysis include narrow bandpass filtering, network-averaging, spectral ratios, and comparison of results with those from synthetics. Most Lg spectra indicate prominent nulls that are in remarkably good agreement with those expected from Rg due to a CLVD source at about one-third the shot depth.

Low-frequency Lg from nuclear explosions at Kazakh, Lop Nor, and Azgir test sites are analyzed by using regional data from mostly broadband stations, including WMQ, BRV, and stations belonging to the NRDC, KNET and the ILPA array. The observed spectral nulls, although generally not as strong as for the NTS shots, are in most cases distinct and identifiable, especially if data from several broadband stations are available. The null frequencies appear to depend strongly on shot depth and local velocity structure and a comparison with theory provides useful source information, including shot depth with an accuracy not possible by other methods. An effective CLVD source is present not only for Lg from NTS explosions but also for explosions from other test sites in significantly different geological environments. By providing an improved understanding of Lg from explosions and its usefulness for obtaining source information, these results make important contribution to seismic monitoring of the Comprehensive Test Ban Treaty.

Key Words:
Lg, regional phases, scattering of Rg, source discrimination, seismic monitoring, NTS, Kazakh, Lop Nor, Azgir, CTBT

OBJECTIVE

A clear understanding of the broadband characteristics of regional phases and their dependence on various near-source parameters must be obtained if successful techniques developed in one region are to be used in other locations. Several recent studies have provided new insight into the generation of Lg from explosions. Scattering of explosion-generated Rg near the source appears to be responsible for the low-frequency Lg from nuclear explosions at both NTS and Kazakh test sites (Gupta *et al.*, 1991; 1992). This mechanism has been supported by the analysis of regional data from several Yucca Flats (NTS) explosions by Patton and Taylor (1995) who further indicated that the prominent low-frequency spectral null in Lg is due to Rg from a CLVD source. The null in the Rg spectrum is due to the centroid depth of the CLVD source so that an analysis of the low-frequency Lg may be useful for estimating source depth if one can establish a relationship between the centroid depth of the CLVD source and the explosion depth. Modeling of the observed Lg with the help of synthetics may also provide other source and near-source information. Rg is stronger for shallow sources such as mining explosions and rockbursts than for deeper sources such as earthquakes. The main objective of this research is to investigate broadband characteristics of regional phases, especially Lg, under various tectonic settings. This will contribute to monitoring of a CTBT by providing a physical basis for regional discriminants, essential for improving their reliability and transportability from one region to another.

RESEARCH ACCOMPLISHED

Nevada Test Site (NTS) Shots

The dependence of spectral nulls on shot depths is investigated by analyzing Lg from 22 Yucca Flats explosions recorded well at the four broadband stations (MNV, KNB, LAC, and ELK) of the Lawrence Livermore National Lab's network. Using 51.2 sec long Lg windows, multitapered spectra were obtained for each of the four stations and the network-averaged spectra were used to determine the spectral null frequencies. Results from 8 shots are shown in Figure 1 which clearly indicates an increase in the null frequency with increased shot depth for data from one station (Figure 1a) as well as from the average of all four (Figure 1b). As expected, spectral nulls in the network-averaged spectra, corrected for attenuation by using Lg(Q) values in Patton (1988), are considerably more distinct and reliable than those from a single station. The increase in null frequency with shot depth is at first small but much larger for shallower depths.

For a homogeneous semi-infinite medium, the CLVD spectral null frequency occurs approximately at V/(16 h) where V is the P-wave velocity and h is depth of the CLVD source (Poisson's ratio of 0.25 is assumed) so that the null frequency is inversely proportional to source depth and directly proportional to medium velocity. In order to understand the observed variation with depth of the Yucca Flats explosions, the wavenumber integration technique was used for generating the Rg synthetics for vertically oriented CLVD sources at various depths. The crustal velocity model of Patton and Taylor (1995) was used; the source was assumed to be an impulse, and the epicentral distance was 20 km. Figure 2 shows the spectra of Rg for various

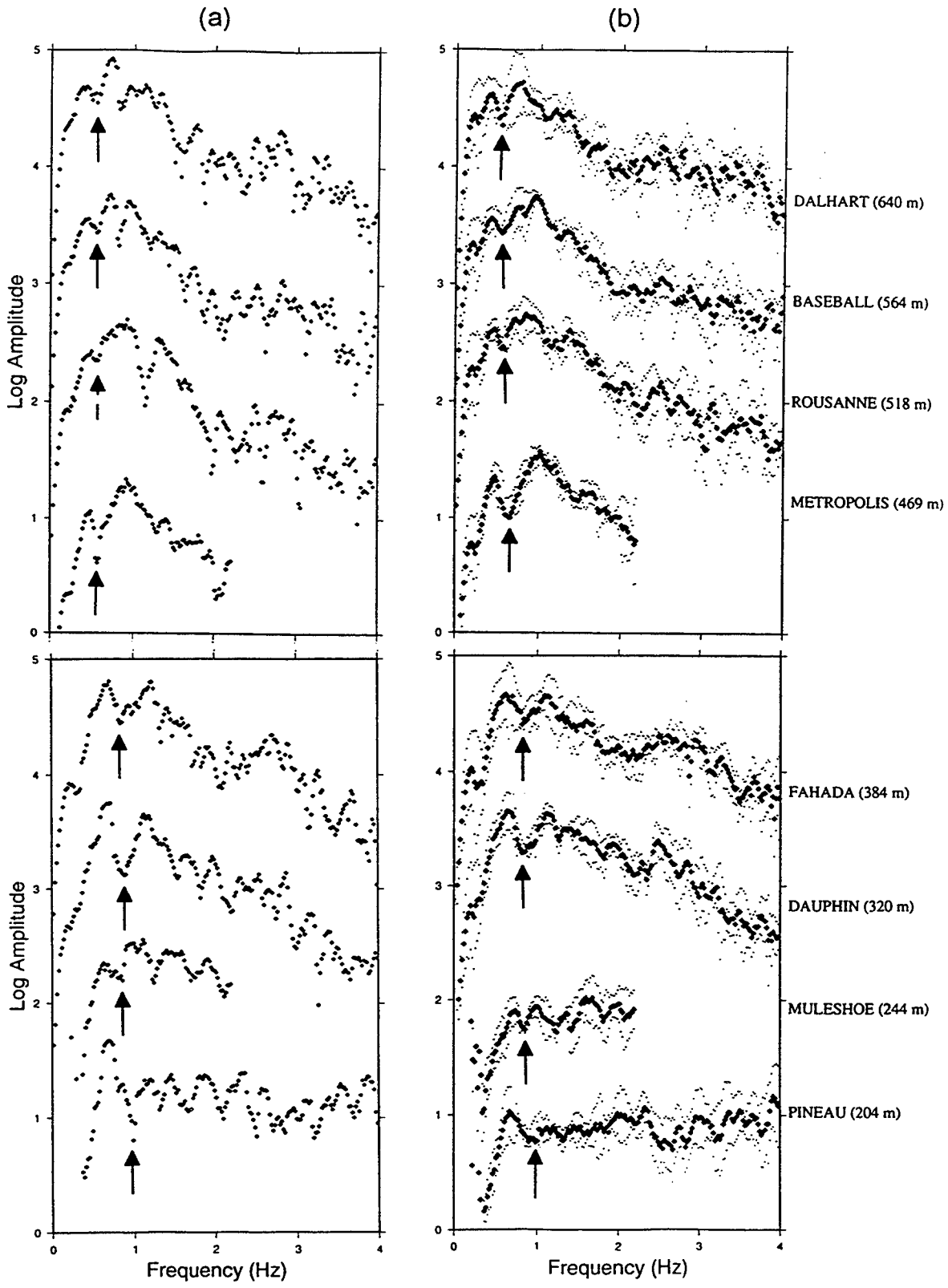

Figure 1. Spectra of Lg for 8 explosions at Yucca Flats with shot depths as indicated, based on (a) data from a single station, MNV, and (b) network averaged over all four stations. The null frequencies (indicated by arrows) are larger for shallower shots.

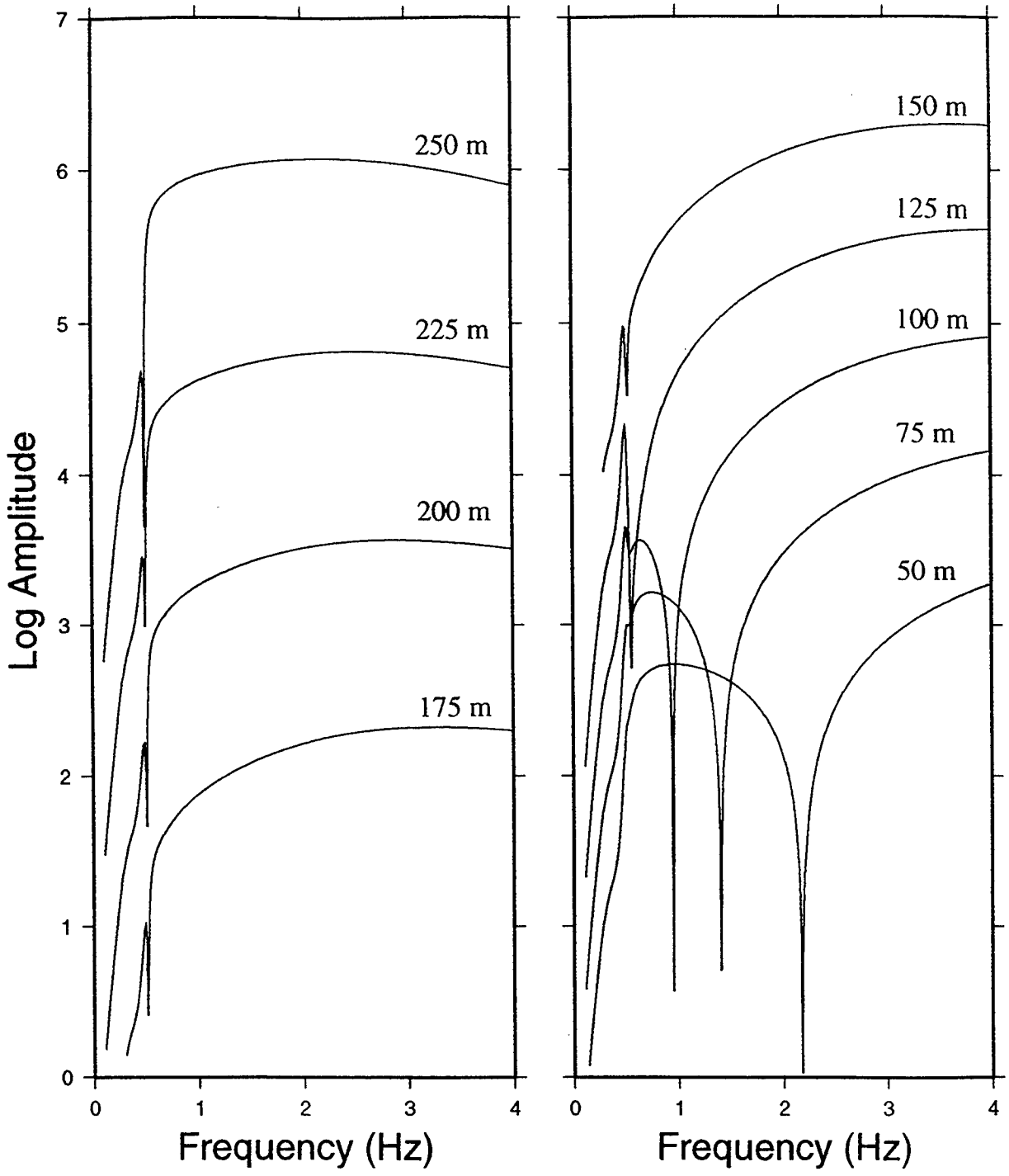

Figure 2. Spectra of Rg synthetics for CLVD source at various depths for crustal velocity model of Yucca Flats used by Patton and Taylor (1995). The increase in the null frequency with source depth is similar to that in Figure 1.

depths of the CLVD source. It is interesting to note that the increase in the null frequency is slow at first but becomes much larger for shallower depths, remarkably similar to the observed variation in Figure 1. Use of the frequency nulls in Figure 2 to estimate depth of the CLVD source for the observed null frequencies of 22 Yucca Flats shots indicated the CLVD source for each explosion at about one-third the shot depth (Gupta and Zhang, 1996).

Spectral Nulls in Lg from Kazakh Explosions

Regional data from the Soviet underground nuclear explosion of the Joint Verification Experiment (JVE, 14 September 1988, m_b = 6.03) are available at the three Natural Resources Defense Council (NRDC) stations, KSU, KKL, and BAY at epicentral distances of about 160, 255, and 255 km, respectively. Narrow bandpass filtering of these regional data indicated a spectral null in Lg at a period of about 0.7 sec, implying that an effective CLVD source is present not only for explosions at Yucca Flats but also at the East Kazakh test site with completely different crustal structure and tectonics (Alexander *et al.*, 1995; Gupta and Salzberg, 1995).

Regional data from the JVE and several other East Kazakh nuclear explosions are also available at the broadband stations, WMQ (CDSN network) and BRV (Borovoye, Northern Kazakhstan) at distances of about 700 and 950 km, respectively from the Kazakh Test Site (KTS). Spectral ratios of Lg from the JVE and the much smaller explosion of 12 March 1987, 87071 (m_b = 5.31), both recorded at WMQ (vertical component) so that path effects are minimized, are shown in Figure 3(a) for Lg windows of 76.8, 51.2, and 25.6 sec. Each of the three plots shows a spectral null at about 1.4 Hz which corresponds to the null at period of 0.7 sec observed in the NRDC regional data. Furthermore, the plots suggest a maximum at frequency of about 1.8 Hz which may be due to the shallower CLVD source associated with Lg from the smaller explosion, 87071. Spectral ratios of Lg from the explosion of 3 April 1987 (87093), with m_b = 6.12 (somewhat larger and presumably deeper than the JVE) and the smaller explosion 87071, shown in Figure 3(b), also indicate a spectral null at frequency of about 1.1 Hz, likely to be due to the CLVD source associated with the larger explosion 87093. Spectra of Lg (51.2 sec long windows) from 7 explosions from the southwest region of KTS, recorded at WMQ and arranged in order of decreasing m_b, with Q correction from Xie *et al.* (1996), are shown in Figure 3(c); these also suggest a systematic increase in the Lg null frequency with decreasing m_b which should be associated with decreasing shot depth, and therefore decreasing depth of the CLVD source. Similar results were obtained from the rather limited BRV data for several explosions. All these results suggest that shot depth is important in defining the spectral null in Lg and a determination of the spectral nulls in Lg and comparison with theory should be useful for determination of shot depths and other source and near-source characteristics.

Chinese Tests at Lop Nor

There is increased interest in nuclear explosions at the Lop Nor test site because, in contrast with the U.S., Russian, and French nuclear test sites, this test site is still being used.

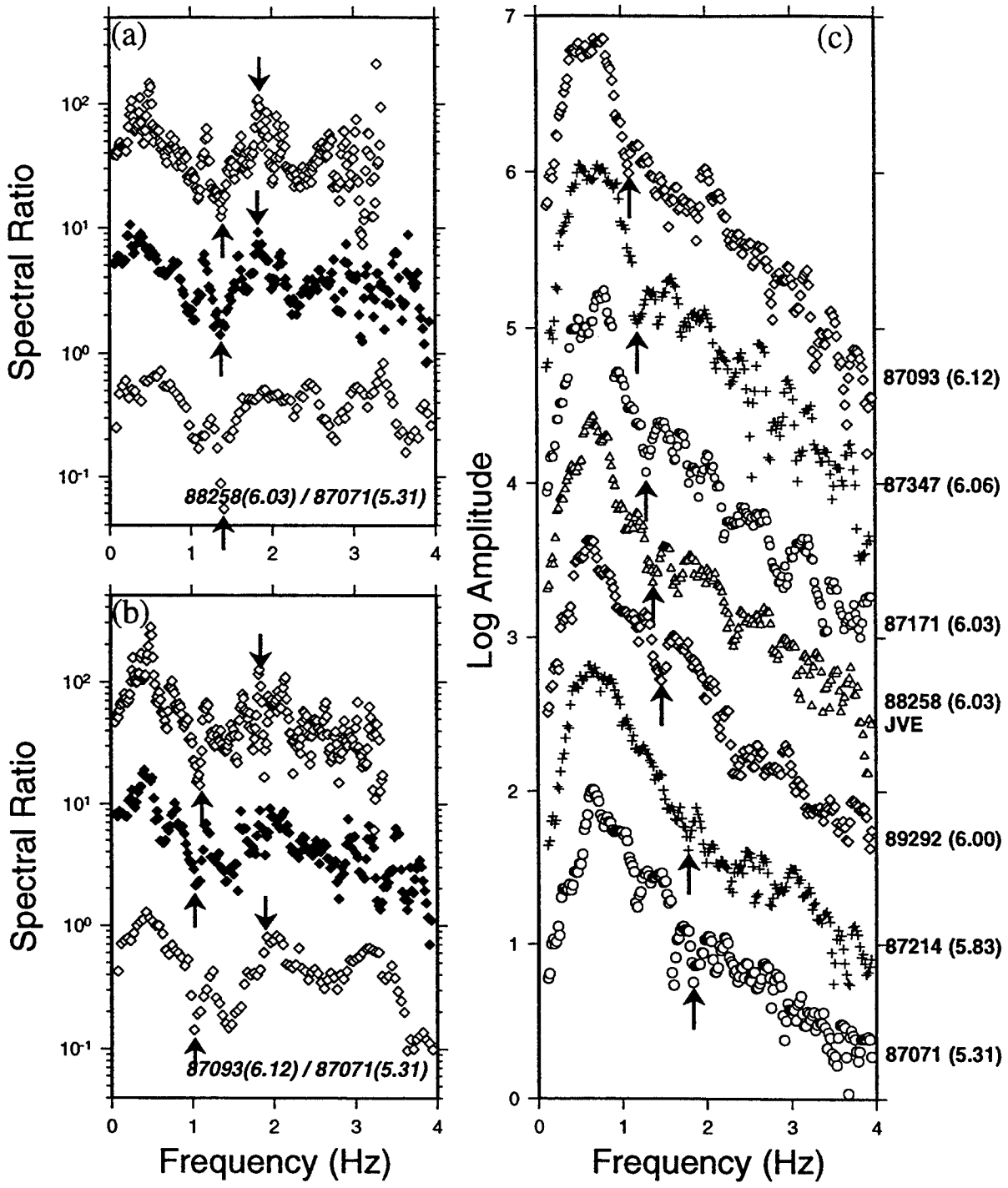

Figure 3. Lg spectral ratios for Kazakh shots recorded at WMQ (a) 88258(JVE)/87071 and (b) 87093/87071 for window lengths of 76.8 sec (top), 51.2 sec (middle), and 25.6 sec (bottom). Each of the three plots in (a) shows a spectral minimum at about 1.4 Hz and a maximum at about 1.9 Hz; plots in (b) indicate a spectral minimum at about 1.1 Hz. (c) Spectra of Lg for 7 Kazakh explosions suggesting a systematic increase in null frequency with decreasing m_b.

Analysis of Lg from several Lop Nor shots recorded at stations belonging to the Kyrghizstan Network (KNET) showed distinct low-frequency nulls at most stations. Results from vertical-component broadband data from the KNET station, AAK for 5 shots are shown in Figure 4. The individual spectra, with Q correction from Xie *et al.* (1996) (Figure 4a), and the spectral ratios (Figure 4b) indicate the same distinct spectral nulls and a general increase in frequency with decrease in magnitude. Moreover, the null frequencies are similar to those for Kazakh shots (Figure 3) for shots with similar magnitudes.

Matzko (1994) provided a detailed description of the geological structure and rock types at the test site. According to him, the largest shot of 21 May 1992 was emplaced in a shaft over 900 m deep and had a yield of about 1 megaton. Furthermore, the nuclear shots are fired in either vertically drilled shafts or horizontal tunnels but there is hard rock coupling in both areas and the Lop Nor test site is, in several respects, more similar to the KTS than the NTS. This provides a possible explanation for the similarity of the observed Lg null frequencies at KTS (Figure 3) and Lop Nor test site (Figure 4).

Azgir PNE At ILPA Array

Regional data from the salt shot (PNE) of 18 December 1978 (m_b = 5.9) at Azgir (north of the Caspian Sea) are available at the ILPA array (Figure 5); see www.multimax.com/~gtdb. The vertical-component waveforms at two locations, IR1 and IR7 show considerably less energy in Lg than in Sn. A possible reason for the diminished Lg is the presence of mostly oceanic path through the Caspian Sea. Spectra of Lg and Sn windows, each 51.2 sec long and starting at velocities of 3.5 and 4.3 km/sec, respectively, are also shown in Figure 5. Not only the Lg spectra but also the Sn spectra indicate a prominent spectral null at frequency of about 1.1 Hz. It appears therefore that the source of the low frequency energy in the large Sn phase is the same as in Lg and the low-frequency energy in both phases originated from the near-source scattering of Rg into S.

CONCLUSIONS AND RECOMMENDATIONS

Our study of Lg from four distinct test sites indicates that near-source scattering of explosion-generated Rg is an important contributor to the low-frequency Lg from explosions at not only NTS but also in other regions of the world. Good agreement between observation and theory suggests the effective CLVD source to be at about one-third the shot depth. Broadband data can be effectively used to determine the observed spectral nulls. Dependence of the Lg spectral nulls on shot depth and local velocity structure provides a method for determining source parameters by comparing theory with observation. Preliminary results also indicate that the near-source scattering of Rg may also make significant contribution to other S phases, such as Sn.

It is recommended that the broadband characteristics of not only Lg but also other phases (especially Sn and Pg) be investigated under various geological settings so that the role of near-source scattering of explosion-generated Rg is clearly understood and exploited for deriving source and near-source information. Representative sets of seismic data covering a

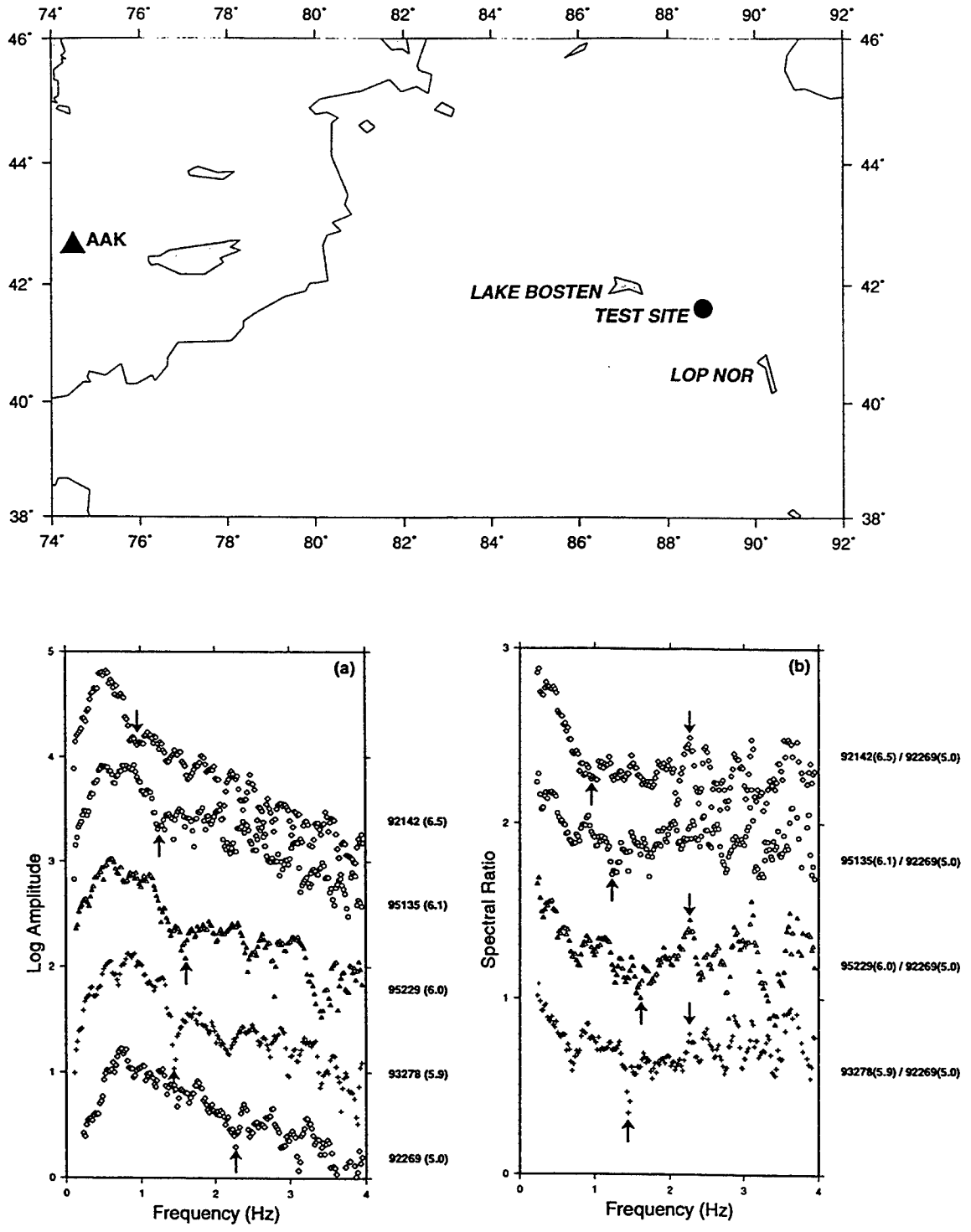

Figure 4. Results from 5 Lop Nor shots recorded at AAK. Both (a) spectra of Lg and (b) spectral ratios indicate the same spectral nulls (indicated by arrows) and a general increase in null frequency with decrease in m_b.

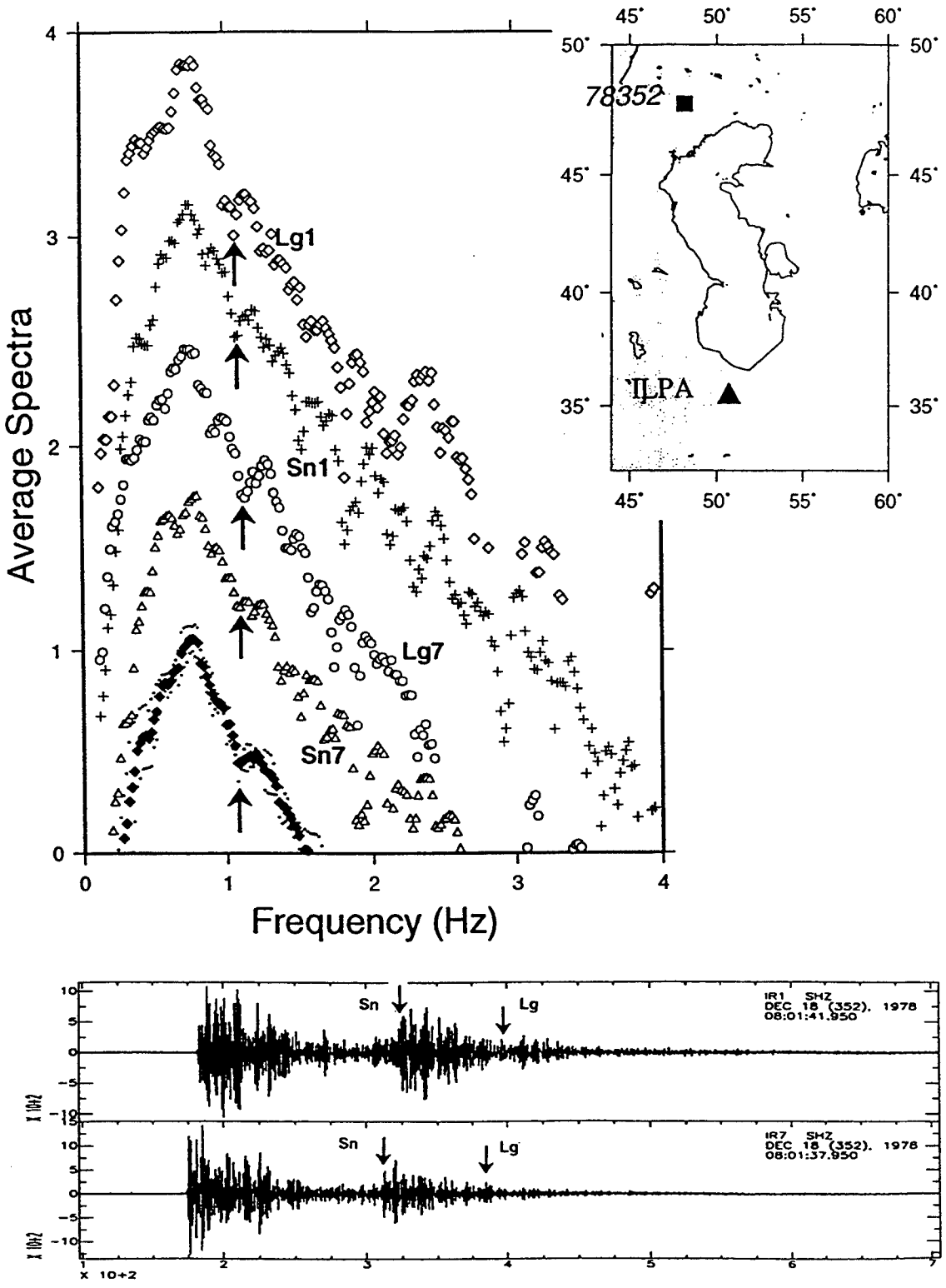

Figure 5. Waveforms and spectra of Lg and Sn from the Azgir PNE (78352) recorded at two ILPA sensors. The four spectra and their average indicate a distinct null at about 1.1 Hz, perhaps due to near-source scattering of explosion-generated Rg into S.

wide range of known near-source parameters should be analyzed to understand the generation of both low and high frequency Lg and other regional phases. A comparison of the observations with synthetic seismograms (including finite-difference calculations) should be carried out so that the generation and propagation of regional phases are better understood. These studies will improve the seismic monitoring capability of regional phases by improving their reliability and transportability from one region to another.

References:

Alexander, S. S., R. C. Hsu, S. L. Karl, I. N. Gupta, and D. H. Salzberg (1995). New techniques for estimating source depth and other diagnostic source characteristics of shallow events from regional observations of P, Lg, and Rg signals, *in* Proceedings of the 17th Annual Seismic Research Symposium on Monitoring a Comprehensive Test Ban Treaty, 12-15 September 1995, *PL-TR-95-2108*, 821-830.

Gupta, I. N., W. W. Chan, and R. A. Wagner (1992). A comparison of regional phases from underground nuclear explosions at East Kazakh and Nevada test sites, *Bull. Seism. Soc. Am.* 82, 352-382.

Gupta, I. N., C. S. Lynnes, and R. A. Wagner (1991). Studies of near-source and near-receiver scattering and low-frequency Lg from East Kazakh and NTS explosions, *PL-TR-91-2287*, Phillips Laboratory, Hanscom Air Force Base, Massachusetts, ADA248046

Gupta, I. N. and D. H. Salzberg (1995). Observations of spectral nulls in Lg from underground explosions at the Nevada and Kazakh test sites, *EOS* 76, no. 17, S205.

Gupta, I. N. and T. R. Zhang (1996). Mechanism of generation of low-frequency Lg from NTS explosions - observations and interpretation, *Seismol. Res. Lett.* 67 (2), 40.

Matzko, J. R. (1994). Geology of the Chinese nuclear test site near Lop Nor, Xinjiang Uygur Autonomous Region, China, *Engineering Geology* 36, 173-181.

Patton, H. J. (1988). Application of Nuttli's method to estimate yield of Nevada Test Site explosions recorded on Lawrence Livermore National Laboratory's digital seismic system, *Bull. Seism. Soc. Am.* 78, 1759-1772.

Patton, H. J. and S. R. Taylor (1995). Analysis of Lg spectral ratios from NTS explosions: implications for the source mechanisms of spall and the generation of Lg waves, *Bull. Seism. Soc. Am.* 85, 220-236.

Xie, J., L. Cong, and B. J. Mitchell (1996). Spectral characteristics of the excitation and propagation of Lg from underground nuclear explosions in central Asia, *J. Geophys. Res.* 101, 5813-5822.

Source and Structure Parameters From the Urals Event of 5 January 1995 Using Rayleigh Waves From Russian and Kazak Broadband Stations

Danny J. Harvey, Physics Department, University of Colorado
Contract no. F49620-94-1-0109
Sponsored by AFOSR

ABSTRACT

We show the results of applying full waveform inversion to the determination of source parameters of the presumed mine collapse event near the Ural mountains on 5 January 1995. Data from four IRIS broadband stations that were close to the event (< 10°) were used in the inversion. In this study we made use of the fundamental Rayleigh wave along with P wave first motion at the closest station. We used a method which simultaneously inverts for both structure and source parameters using laterally homogeneous structure. We conducted the inversions individually for each station and for center of compression/dilatation and dipolar source types. The results show agreement between real and synthetic waveforms at all four stations. Dipolar sources are compressional at all four stations and P wave first motion was consistent with observed motion at the closest station. Center of compression/dilatation sources are dilatational at all four stations and P wave first motion was inconsistent with observed motion at the closest station. These results indicate a dipolar, compressional source type which is consistent with a mine collapse. Quantitative moment estimates varied by a factor of five between pre-Urals depression and Siberian/Kazak shield propagation paths. We interpret these variations as being due to three dimensional propagation effects which were not modeled in this study. Our results indicate that an inversion using the fundamental mode Rayleigh wave can be adequate for determining basic source type. Accurate determination of quantitative source properties, such as moment, probably requires more complex 3-D modeling than was used in this study. Future studies will concentrate on extending the present technique to include 3-D structure effects.

KEYWORDS:
inversion source mine surface-wave

1. Objective

Our objective was to make use of full waveform inversion to determine detailed source and structure parameters using an event that is highly relevant to nuclear monitoring. The Urals event of 5 January 1995 represents a class of events that will be important in the upcoming Comprehensive Test Ban Treaty. This event occurred in a region of mining activity and low natural seismicity. Its reported magnitude (REB Mb = 4.4) was high enough to indicate a very large chemical explosion, a small nuclear explosion, a moderate size earthquake, or a large mine collapse. Given the low natural seismicity in the region, the most likely source types were explosion or collapse. Our ability to quickly and reliably discriminate between these two source types is obviously an important ability for monitoring a Comprehensive Test Ban Treaty. We decided to apply the techniques we have developed previously to this event, as a test of overall capabilities. Our source-structure inversion technique uses a simple laterally homogeneous representation of the structure. In order to speed up and simplify the inversion, we decided to primarily use the fundamental Rayleigh wave. One of our objectives was to see if this simple inversion technique could yield the information we would need to discriminate the subject event.

2. Research Accomplished

2.1 Inversion Procedure

The inversion method we have developed is described in Harvey, 1995. Our method allows for full waveform inversion of 3-component data to yield simultaneous source and structure parameters. We use a mode base forward modeling technique that uses the lateral homogeneous structure assumption. Our inversion method is quick and accurate and is only limited by the applicability of a laterally homogeneous structure, although this is a severe limitation in some cases.

2.2 Data and Observations

We used seismic data recorded by the IRIS Global Seismographic Network station at Arti, Russia (ARU), which was the closest station to the event, and seismic data recorded by three IRIS Joint Seismic Program stations in Kazakstan, Aktyubinsk (AKT), Zerenda (ZRN) and Borovoye (BRVK), which were part of the JSP Kazak Network. All four stations used broadband 3-component instruments with a Streckeisen STS-1 at ARU and Streckeisen STS-2 instruments at AKT, ZRN and BRVK. A map with the event and stations is shown in Figure 1. In this figure the event is centered at the crosshairs and the concentric circles are at distance increments of five degrees. Station distances are ARU = 3.3°, AKT = 9.1°, ZRN = 9.5°, BRVK = 10.0°.

The data from these four stations can be seen in Figure 2, after bandpass filtering from 0.1 to 0.5 Hz. These data have been time aligned so that the first predicted P-wave arrival is aligned to the event origin time. We can clearly see Rayleigh waves in all of these data, although there

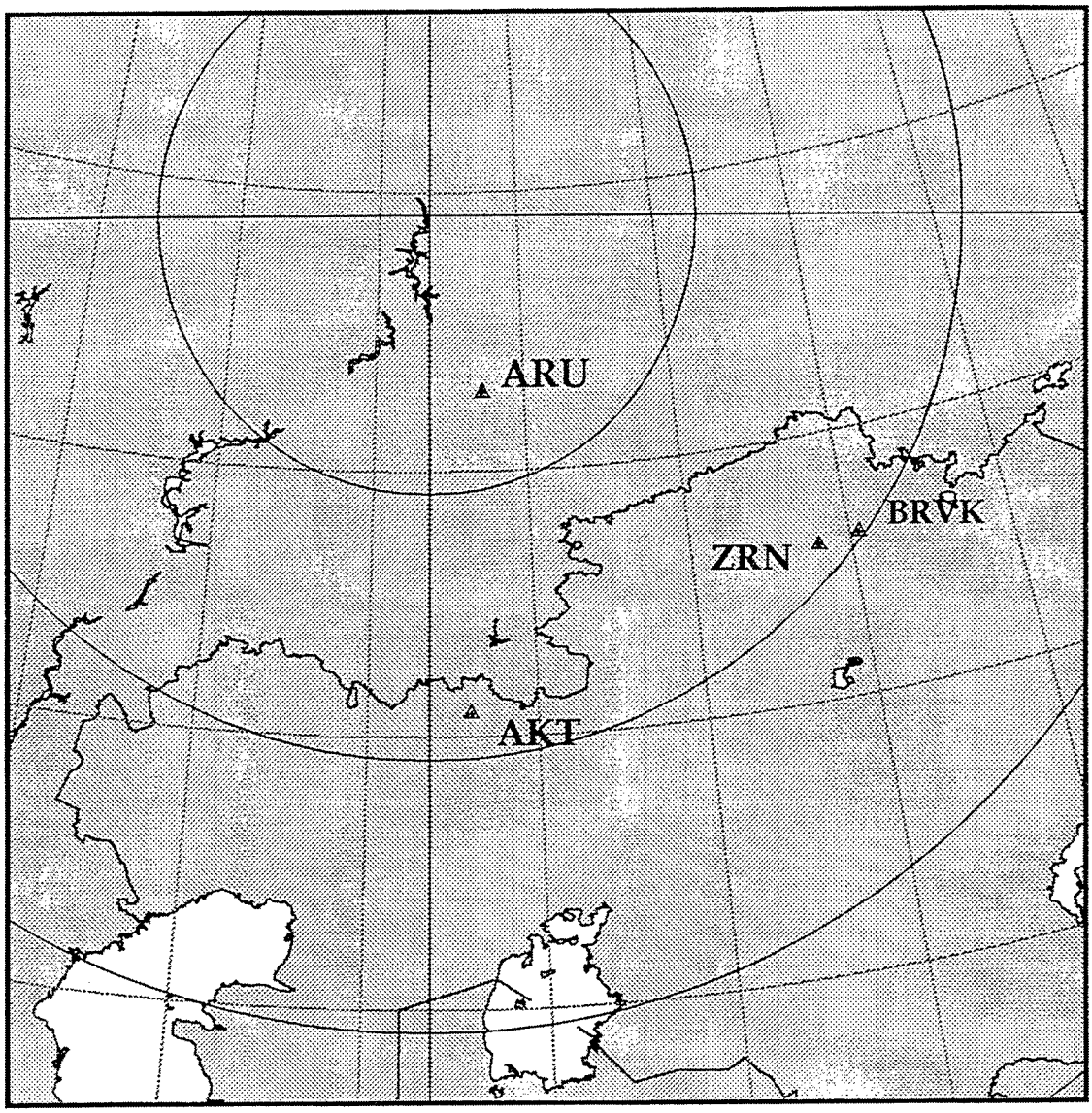

Figure 1. Event of 5 Januray 1995

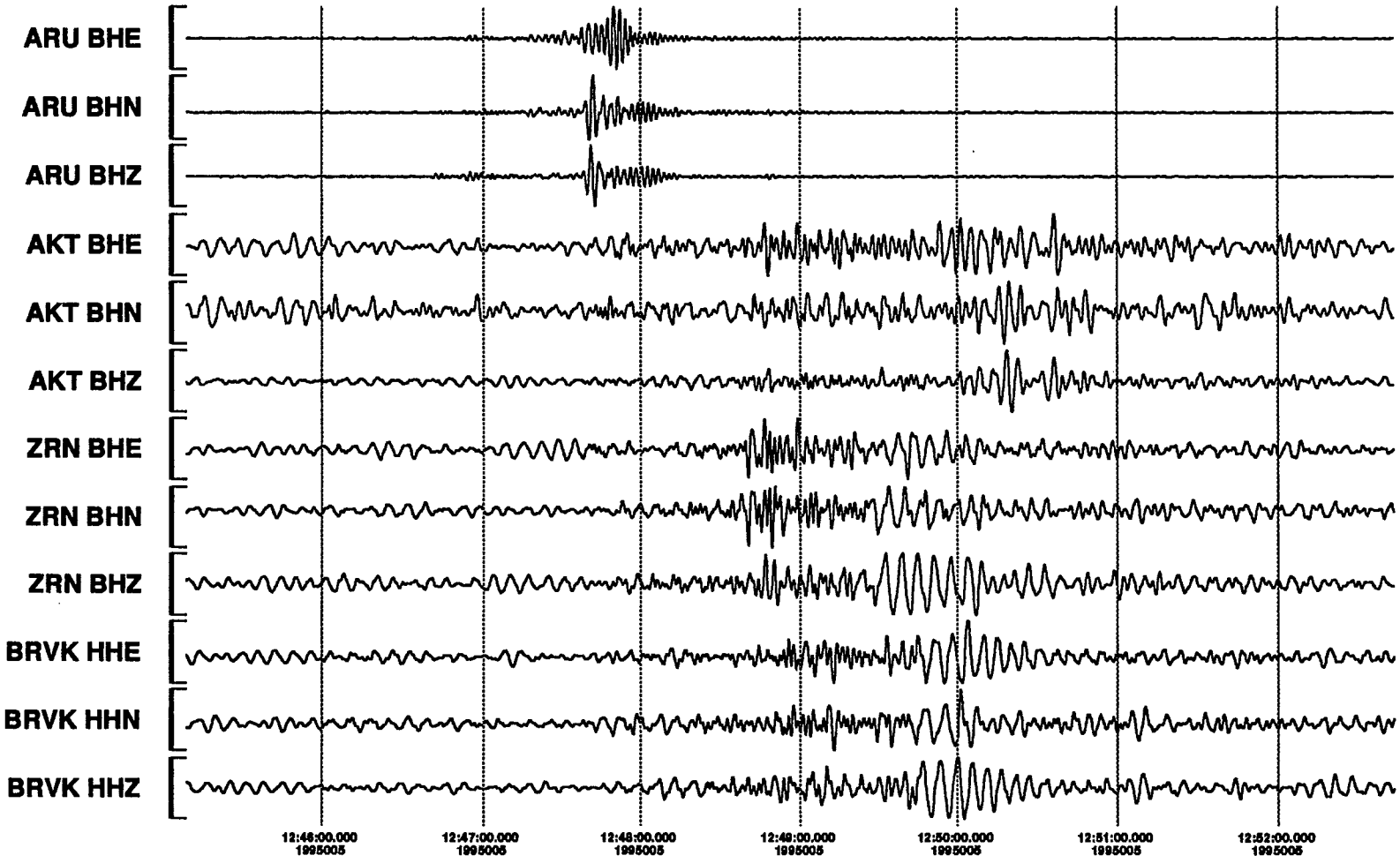

Filter: 0.1-0.5 BP, Amp: Auto

JSPC dbpick: urals rsec.ps danny Thu Jun 27 15:33:49 1996

Fig 2. Data recorded from Urals event of 5 January 1995

are considerable variations in group velocities and in the waveform characteristics. The stations ARU and AKT are roughly on the same azimuth from the event, approximately due south, and both of these stations lie near the western flanks of the Ural mountains. The propagation paths to these stations lie along the boundary of the Ural mountains and the pre-Ural trough, a thick sedimentary basin to the west of the mountains. The stations ZRN and BRVK are roughly at the same azimuth from the event, approximately southeast, and both of these stations are on the Kazak shield. The propagation paths to these stations go primarily through the Siberian and Kazak shields. We can see in Figure 2 a similarity in the Rayleigh waves for ARU and AKT and in the Rayleigh waves for ZRN and BRVK . We can also see that strong differences exist between the Urals-path Rayleigh waves and the shield-path Rayleigh waves which is indicative of relatively large structure differences between the two paths.

We observed a lack of Love surface wave energy at all of the stations, with the possible exception of AKT which shows an apparent late arriving Love wave. There is transverse energy at most of the stations, but it usually comes in at the same time as the Rayleigh wave, leading us to speculate that this transverse energy is scattered from the Rayleigh wave as opposed to source generated. We also noted apparent Rayleigh wave multi-pathing at AKT with a later arriving surface wave-like bundle of energy. The most noticeable scattering effects associated with the surface waves seem to be in the ARU and AKT data, which makes sense considering the lateral structural variations in the vicinity of these two stations.

2.3 Inversion Results

We started with two structure models obtained from Anatoli Levshin that were considered to be typical of Urals paths and Siberian/Kazak paths. We then perturbed these models to match the observed group velocity-frequency dispersion properties at the four stations to produce starting structure models for each station. Our first major decision was to decide whether to do one inversion using all four stations with different structures and the same source, or to do four separate inversions at each station. We decided to do four separate inversions, reasoning that if we got agreement in the source parameters we would be happy and if not we could go on to the simultaneous inversion. Doing the four stations separately also gave us flexibility in fixing the overall source size which could be strongly effected by scattering differences between the different propagation paths.

We also decided to do the inversions twice at each station; once with the source constrained to be a pure center of compression/dilatation and again with the source constrained to be a pure vertical dipole. These sources produce no transverse terms, so we only used radial and vertical components in the inversions. A center of compression source would indicate an explosion and a compressional dipole source would indicate a mine collapse. The observed first P-wave motion at ARU was up, which is consistent with either an explosion or a compressional dipole, not an implosion or a dilatational dipole.

The results of the inversions for the Urals path stations, ARU and AKT, are shown in Figure 3. In this figure for each station are two panels; the left panel showing observed and synthetic seismograms and the right panel showing the resulting structure. The seismogram panel is further broken into four sub-panels, from top to bottom showing respectively The radial and vertical components for the dipolar inversion and the radial and vertical components for the explosion/implosion inversion. The moment value for each inversion is printed with a + value indicating a compressional source and a - value indicating a dilatational source.

We can see good agreement between observed and synthetic waveforms at ARU for both dipolar and explosion/implosion sources. The dipolar solution is compressional, consistent with the P-wave first motion and the explosion/implosion solution is dilatational, inconsistent with the P-wave first motion. We would conclude from these results that the source is most likely compressional dipolar, indicating a mine collapse instead of an explosion. The agreement between observed and synthetic seismograms is not so good at AKT in part due to the relatively high level of noise at AKT. As with ARU, we get compressional dipolar and dilatational explosion/implosion solutions at AKT. We also get remarkable good agreement between the source moments at ARU and AKT.

We show the inversion results for the Siberian-Kazak shield path stations, ZRN and BRVK, in Figure 4. As with ARU and AKT, we get good agreement between observed and synthetic waveforms and we get consistent compressional dipolar and dilatational explosion/implosion solutions at ZRN and BRVK. We get good agreement between the source moments at ZRN and BRVK, although the moments from the Siberian-Kazak shield path stations are about five times larger than the moments from the Urals path stations. We started off with essentially elastic structure models and we attempted to adjust anelastic attenuation parameters for the Urals path stations to reduce these differences. However, we found that we could not reconcile the moment differences with realistic Q values. We speculate that lateral structure variations along the Urals paths are defocusing, refracting or scattering away surface wave energy.

3. Conclusions and Recommendations

We have shown how full waveform inversion can be used to help in the determination of the source type for a typical event that could cause concern in monitoring a Comprehensive Test Ban Treaty. We were able to determine that the Urals event of 5 January 1995 was most likely a mine collapse instead of an underground explosion.

However, the accuracy and robustness of our method has yet to be determined. We have shown in this study that there can be large variations in quantative source parameter estimates, presumably due to propagation effects. In the next phase of our research we hope to be able to include the effects of lateral structure variations which will make it possible to model the characteristics that we see in the data. We also suspect that there could be large tradeoffs in structure

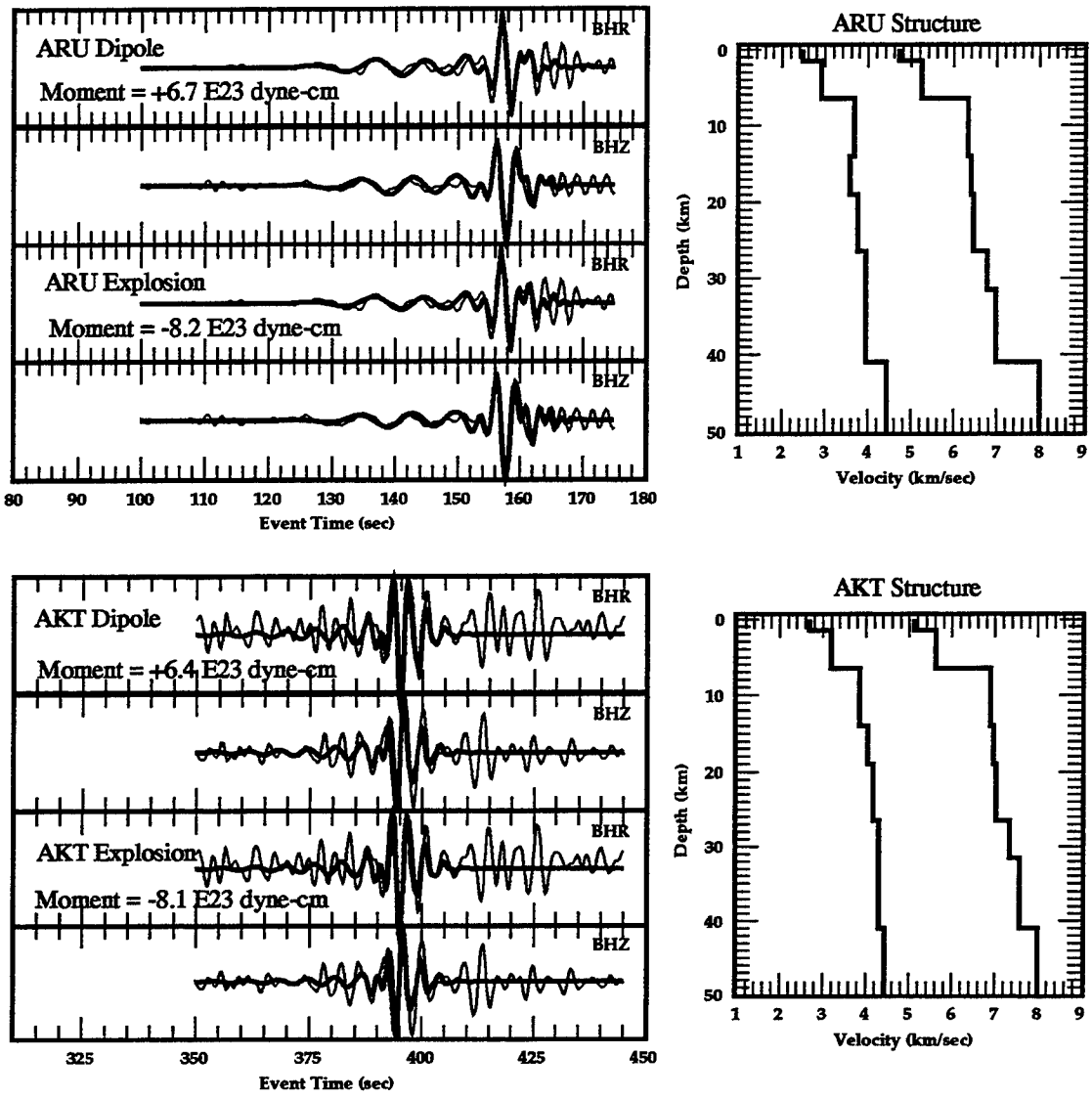

Figure 3. Inversion results for Urals path stations ARU and AKT

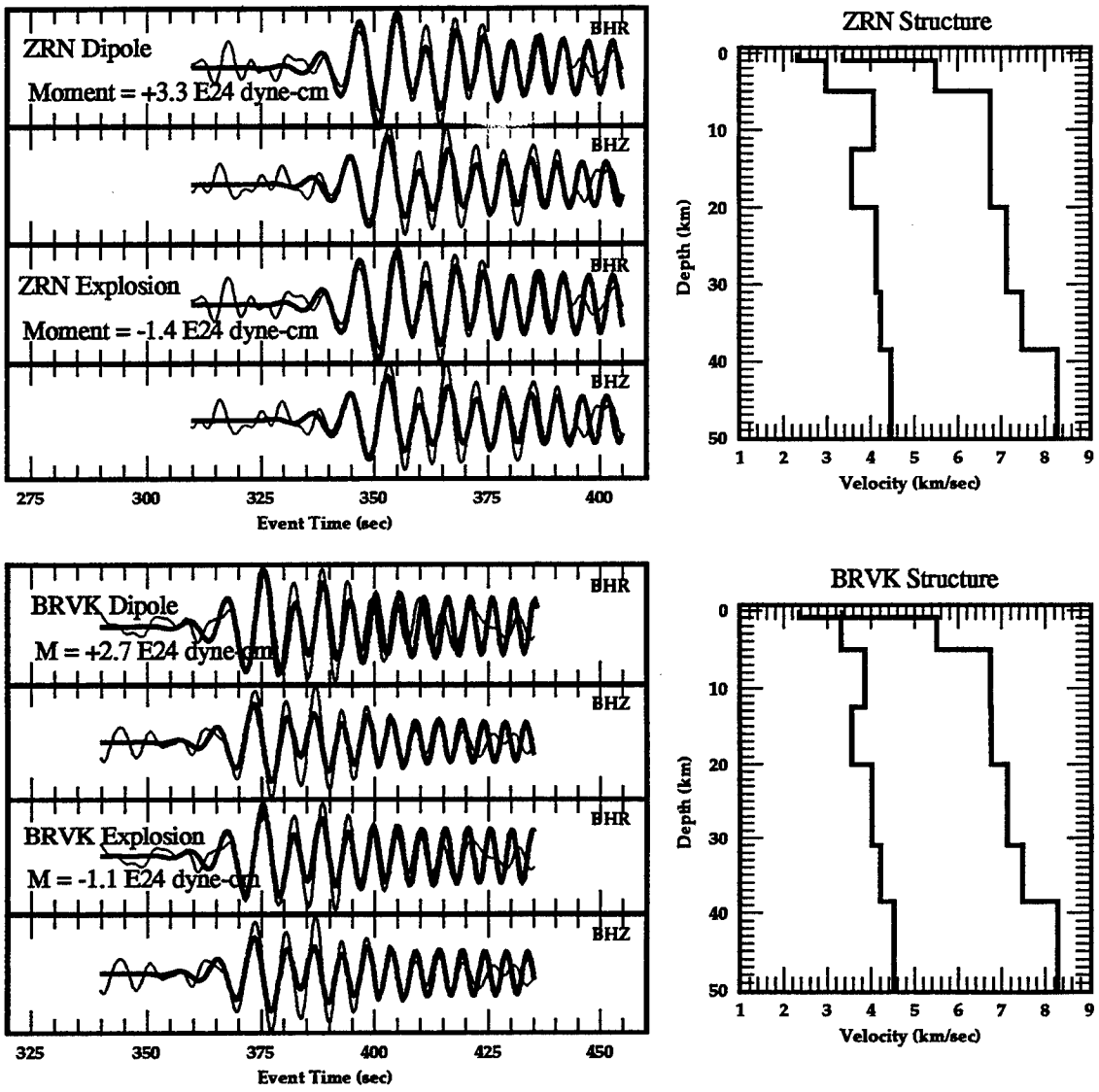

Figure 4. Inversion results for Siberian/Kazak path stations ZRN and BRVK

and source parameter esrtimates. This needs to be systematically checked by griding out a large number of starting model parameters or by employing something like simulated annealing to find all of the performance function local minima.

REFERENCES

Harvey, D., 1995, Simultaneous inversion for detailed source and structure parameters using quarry blast data recorded in Eastern Kazakhstan, Proceedings of the 17th annual seismic research symposium on monitoring a comprehensive test ban treaty, PL-TR-95-2108, ed. Lewkowicz, McPhetres, Reiter, pp 636-646.

PROGRESS IN WAVEFORM INVERSION

Robert B. Herrmann and Tao-Ming Chang, Saint Louis University
Contract F19628-95-K-0019
Sponsored by DOE
AFOSR Grant No. F49620-93-1-0276
Sponsored by AFOSR

ABSTRACT

We apply two surface-wave waveform inversion algorithms: the method of generalized seismological data functionals, GSDF, (Gee and Jordan, 1992) and linear waveform inversion (Gomberg and Masters, 1988) to the April 14, 1995 Texas earthquake (30.26 °N 103.33°W, 00:32:55UT) to see the capabilities of each algorithm. The source depth of the Texas event is 23 km, with strike, dip, rake angles of 114°, 64°, -101°, respectively with $\mathbf{M}_w$ = 5.6. The G&J inversion results, applied by using an earth flattening transformation, indicate that anisotropy is a major character for continental mantle, and this phenomenon may exist as deep as 400 km. The Rayleigh wave waveform envelope shape is an excellent indicator for the Q values around the crust_mantle boundary. For those short epicentral distance stations, the waveform can be matched at period short as 10 sec, while most stations synthetic can be easily fit seismogram down to 20 sec. Application of the G&M technique with a simple crustal model easily fits waveforms down to 4 sec with good agreement event to 2 sec, but inverted models are not unique.

Key words: waveform inversion, earth structure

OBJECTIVE

The objective of this work is to develop robust techniques to define earth structure from the direct inversion of broadband waveform data, and then to apply these techniques to an area of interest, the Arabian Plate and surrounding regions, which will commence in September.

RESEARCH ACCOMPLISHED

Station Distribution and Source

The current data set consists of 49 broadband stations from IRIS, the Canadian National Seismological Data Center (CNSDC), the USGS and UNAM. Initial published estimates of focal mechanism and source depth were revised by applying a grid search over fault motion parameters and source depth to spectral amplitudes in the 5 - 60 sec period range. The $pP - P$ times observed at distances greater than 33° supported the source depth of 23 km obtained by the grid search.

With the source parameters fixed, the techniques of generalized seismological data functionals, GDSF (Gee and Jordan, 1992) and linear least squares inversion, LSQ (Gomberg and Masters, 1988) were applied to each three component time history to invert for earth structure.

GSDF

The concept for GSDF is very simple: parameterize waveform components in terms of time delays with respect to synthetics generated for a reference model. The time delays can be a phase lag, a group delay, a Q dependent time delay or a time delay associated with slightly different frequency content in the signal. Conceptually, the time delays should be more more easily mapped into modifications of the structural model than other measures, such as dispersion or spatial attenuation, and in addition could be combined with arrival times of specific body wave arrivals in a joint inversion. The difficulty in implementing GSDF is in defining the approximately linear relationship between any of the time delays and structural perturbations. The advantage is that the initial model could be grossly incorrect, and yet converge to a model that provides an acceptable fit.

The starting earth model consists of a simple layered crustal model grafted onto PREM, with a presumed Moho at a 40 km depth. It was found that it was not possible to match both the SH and P-SV time histories using a single isotropic velocity model. This may indicate the need for anisotropy or the imperfections of the earth flattening approximation used in the waveform synthesis. Since we were interested primarily in the inversion algorithm and did not have an available code for transversely anisotropic media, we used separate isotropic models for the P-SV and SH wavefields. P-SV data were inverted using fixed Poisson ratios of 0.25 for 0-40 km, 0.28 for 40-200 km, and those of PREM for deeper structure. Sh data were used to estimate th initial V_S and Q_S^{-1} models.

Figure 1 shows the GSDF fit to the three component time histories at ANMO, a distance of 596 km from the earthquake. The observed and synthetic time histories are band pass filtered between 0.010 and 0.050 Hz. The transverse, T, component is well fit in amplitude and phase while the Z and R time histories are fit in terms of phase but not amplitude.

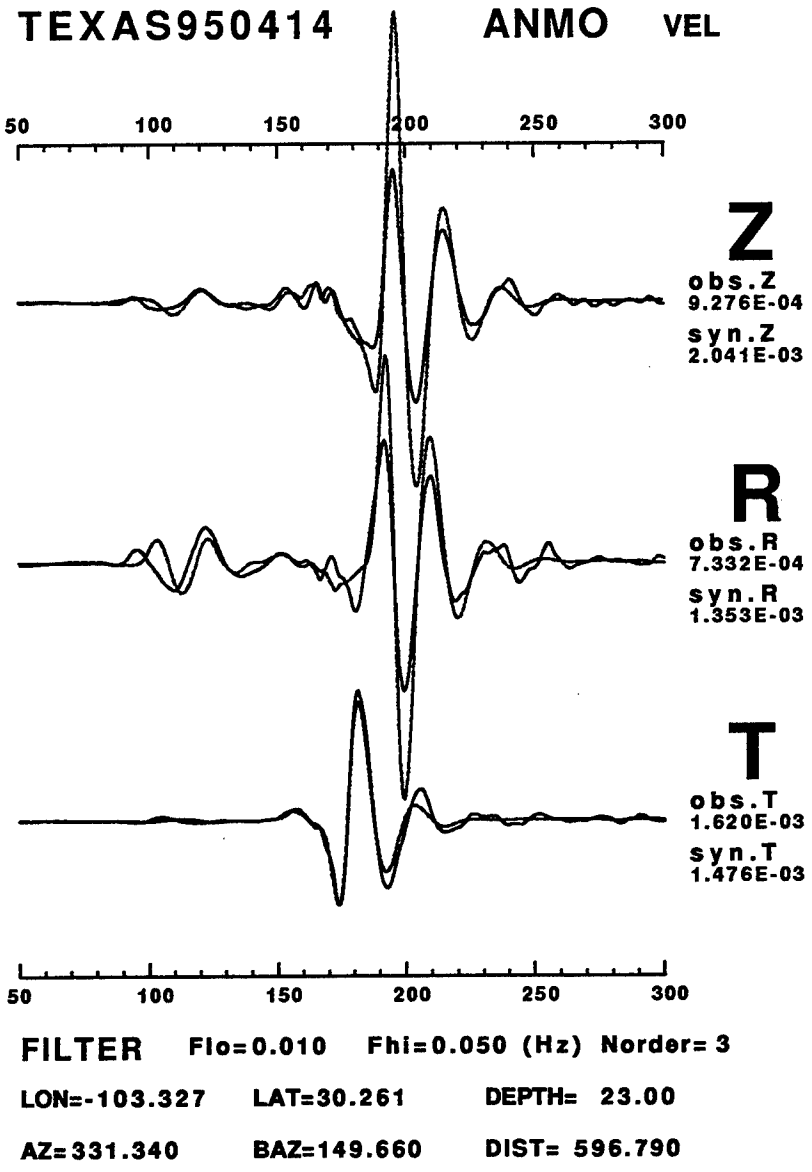

Figure 1. Comparison of observed (solid) and synthetic (dotted) three component time histories for ANMO. Units are filtered ground velocity in (cm/sec).

In many cases the locked mode approximation can model the PP, S and SS phases. The arrival times of the body wave phases could be an additional constraint on the present model.

Least Squares Inversion

The Gomberg and Masters (1988) technique requires the computation of partials of the time histories with respect to medium parameter changes. As noted in our earlier work, there is a conceptual problem in approaching our inversion in that we expect changes in the velocity model to be related to changes in arrival times. The partial derivative kernels so computed are really for infinitesimal changes in

model parameters, and thus seem to indicate the effect of medium changes on layer reflectivity rather than on arrival times. If an initial model is significantly away from the true solution, then a null space of partial derivatives are expected to account for the residual seismograms. Only be starting at low frequencies will the filtered residuals and filtered partial derivatives overlap.

The linear inversion technique was set up as a shell script with various controls on inversion parameters and filter frequencies. To test the uniqueness of the model, two different starting model extremes were used: that of a linear gradient (Nmodl.orig) and of a simple wholespace (NNmodl.orig) which are shown in Figure 2. The result of 109 iterations for each starting model are compared in Figure 3 to the GSDF models 18Sh and 26SV.

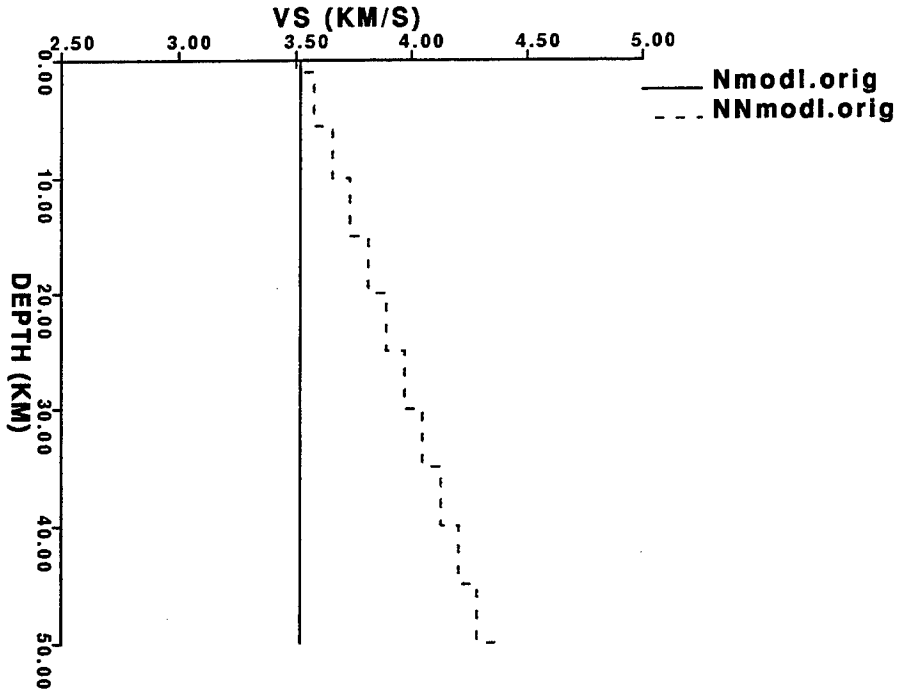

Figure 2. Initial starting models for testing the linear inversion method. One model approximates a halfspace, and the other a linear gradient.

Figures 4 and 5 compare the observed and synthetic time histories at ANMO for the Nmodl and NNmodl models. The NNmodl fits amplitudes very well, especially for the first three cycles of the SH and for the fundamental model Rayleigh wave with a single isotropic model. The Nmodl over predicts the fundamental model Rayleigh wave amplitudes but fits some of the later SH arrivals. In an smoothed sense, both models are similar to a depth of 30 km.

Other Techniques

If a direct waveform fit, and some non-linear measure of the waveform, such as the envelope at different filter frequencies is used, then numerical techniques such as steepest descent, conjugate gradient or genetic algorithm can be used. The

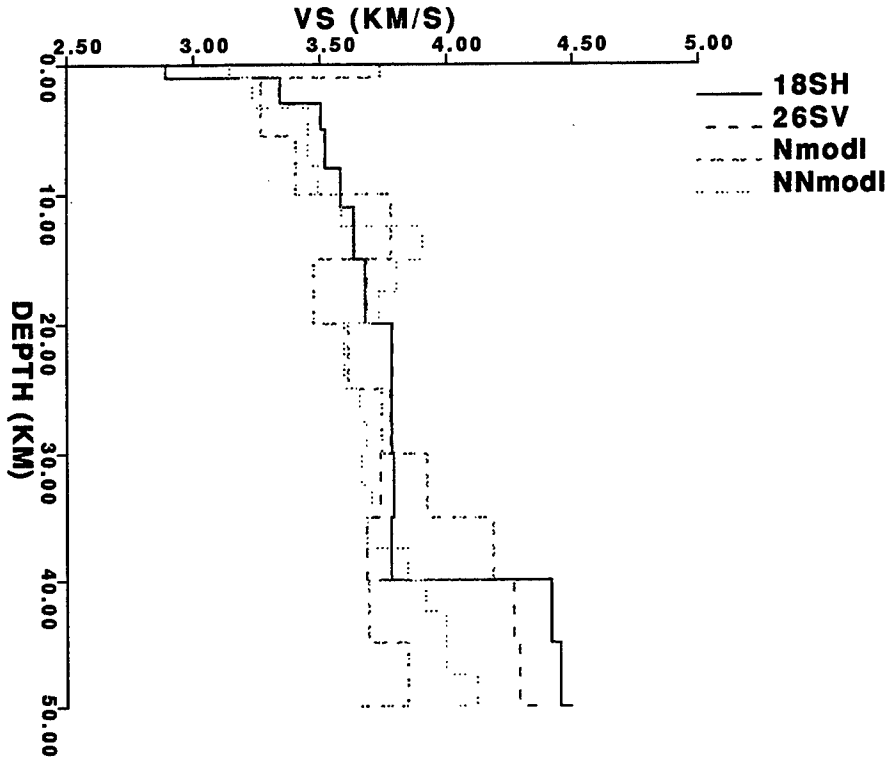

Figure 3. Comparison of the final models from linear inversion: Nmodl (initially a halfspace), NNmodl (initially a gradient), 18SH (GSDF for SH), and 26SV (GSDF for P-SV).

genetic algorithm technique is of interest since a suite of models providing a prescribed goodness of fit can be obtained. This suite would provide some indications of the uniqueness of the resultant model. Unfortunately, the number of models tested must be few given the computational time required for just one forward synthetic.

Summary

The Texas earthquake of April 14, 1995 is a good one to use to study earth structure and the usefulness of waveform inversion programs to provide *unique* earth structure because

- it was well recorded,
- the source depth is well constrained,
- the focal mechanism is fairly determined, and
- the seismic moment is constrained by long period surface waves,

thus reducing the influence of these major factors on the time histories

- The waveform inversion programs using both GSDF and linear waveform inversion theory can successfully match the surface wave waveform.

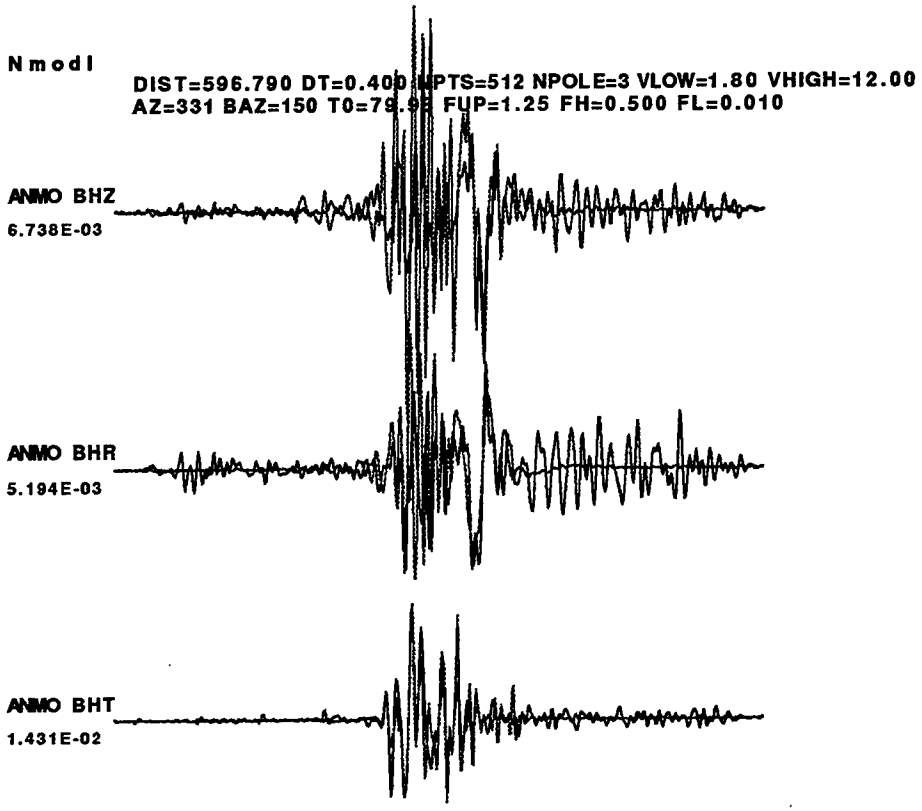

Figure 4. Comparison of three component observed and synthetic time histories at ANMO for the final Nmodl model. Time histories are bandpass filtered ground velocity (cm/sec) 0.01 - 0.50 Hz range. The synthetics only model the S-wave field.

- The anisotropy phenomenon seems to be a common character for the continental mantle region. The anisotropic zone may appears as deep as 400 km.
- From the waveform envelope shapes for different frequency ranges, it is possible to add one more constraint on the Q behavior across the crust and mantle boundary for the north America continent. The Q values may have a very sharp contrast across crust_mantle boundary.

Pushing waveform matches to complete seismograms and to high frequencies is an interesting computational challenge, both in development of inversion strategies and of efficient algorithms. We are making progress toward understanding the limits of applying simple 1-D earth models to real data.

CONCLUSIONS AND RECOMMENDATIONS

• Pushing the high frequency limits of waveform inversion is still being tested. Two fundamentally different techniques have been implemented: direct linear waveform inversion and generalized seismological data functionals. While neither technique is outstanding at high frequencies ($\approx$ 0.5 Hz), the linear inversion seems to work better at high frequencies.

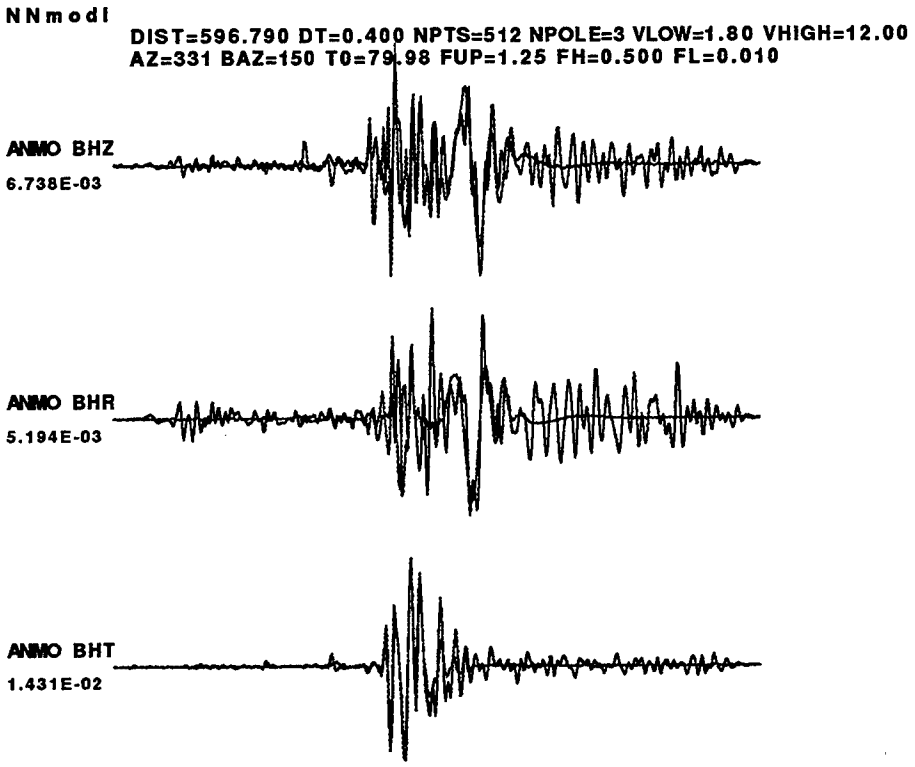

Figure 5. Comparison of three component observed and synthetic time histories at ANMO for the final NNmodl model. Time histories are bandpass filtered ground velocity (cm/sec) 0.01 - 0.50 Hz range. The synthetics only model the S-wave field.

• Algorithm testing requires the use of well known calibration events. At present the Texas earthquake of April 14, 1995 and the Missouri earthquake of September 26, 1990 have been used with varying results. An earth model that consists of 60 km of crustal and upper mantle layering over a halfspace seems adequate for describing both the P, SV and SH wavefields out to distances of 500 km in simple structure. Attempting to model time histories at larger distances by a locked mode approximation and an earth flattening transformation yields good fits at long periods, but also requires different isotropic model for the P-SV and SH wave fields in the upper mantle. We are uncertain whether anisotropy is required or whether this is an artifact of the earth-flattening approximation.

• A detailed analysis using both inversion techniques of the ANMO recording of the April 14, 1995 Texas earthquake yields some similarities in earth models. Although the models fit high frequency Lg waveforms to the same degree, the consequences of these models for location have not been ascertained.

• The concept of using a robust program for definition of earth structure still requires more work before this task is realized. A testing procedure for model uniqueness must be developed.

VARIABILITY OF THE $M_I - Y$ and $\psi_\infty - Y$ RELATIONS

Robert B. Herrmann, Saint Louis University
Contract F19628-95-K-0005
Sponsored by DOE

ABSTRACT

Variability in the relation of yields of small explosions to seismological source parameters is investigated by studying the short-period, fundamental mode Rayleigh waves recorded at a 0 - 200 km distance range from point and spatially distributed chemical explosions. The data set includes long linear array and single station observations. Surface-wave time histories are analyzed for source and propagation path parameters. Since the source medium is not well known, observed variability in the empirical moment - yield relation may be indicative of scatter to be expected in a test ban treaty monitoring effort when only a few observations along an uncalibrated path exist. Our source parameter estimates and their variability are consistent with those determined from a larger data set. Observations indicate that the isotropic moment, M_I and ψ_∞ are related to yield, Y, as

$$M_I(dyne-cm)=1.06\,x\,10^{18}Y(tons) \quad \psi_\infty(m^3)=0.385Y(tons)$$

Key words: isotropic moment, yield, chemical explosion, nuclear explosion

OBJECTIVE

The purpose is to learn how to characterize the attenuation of regional seismic phases in different environments. The goal is to develop a well understood methodology that can be routinely applied by DOE contractors to define the attenuation to distances of 1000 km. This effort is important as a step at quantifying seismic source sizes and as an essential component of other efforts to develop distance invariant discriminants.

RESEARCH ACCOMPLISHED

Experiments

We estimated M_I and shallow earth structure from an analysis of short period Rayleigh waves generated by shallow explosions in three distinct regions: the northeastern United States, the central United States, and in northern Italy. The shallow velocity structures affecting the Rayleigh wave are metamorphosed paleozoic, glacial till covered paleozoic and quaternary alluvium, respectively, for the three regions. Thus the data sets form a strong test on the relation between M_I and Y.

The results for each data set were summarized in Table 1. Within each data set there are more than one estimate of M_I or ψ_∞. The individual estimates are averaged in a logarithmic sense. If an individual estimate of a parameter is x_i, then the logarithmic mean of N observations is defined as

$$\bar{x} = 10^{\mu}$$

where

$$\mu = \frac{1}{N} \sum \log x_i .$$

The standard error in logarithmic space is defined as

$$\sigma = \left[\sum (\log x_i - \mu)^2 / (N-1) \right]^{1/2},$$

which corresponds to a multiplicative error $ERR_x = 10^{\sigma}$. Finally, the standard error of the mean value of the logarithms is

$$\sigma_\mu = \sigma / N^{1/2},$$

which corresponds to a multiplicative error in $\bar{x}$ of $ERR_{\bar{x}} = 10^{\sigma_\mu}$. The choice of logarithm space for averaging is based on modeling the observed time histories $o(t)$ in terms of the synthetic Green's functions $g(t)$ by the relation $o(t) = \bar{x} g(t)$. Note that σ indicates the scatter of individual observations and σ_μ indicates the scatter is the estimate of the mean.

Since it was assumed that both M_I and ψ_∞ will be directly proportional to yield Y, the estimates of these parameters are normalized by yield in Figures 1 and 2 (solid symbols) to highlight the variability of the estimates. The error estimates of Table 1 are not plotted, though, for clarity. The yields used for the chemical explosions are the actual amounts used and were provided by the shooters. Since there was insufficient information available on the exact type of chemical used, no

attempt was made to use an equivalent energy yield for comparison to nuclear yields. In addition, little was known about the depth of burial, degree of containment or material properties to apply the detailed analysis of Denny and Johnson (1991).

Denny and Johnson (1991) note that to a first order approximation, M_I and ψ_∞ are linear functions of yield Y. This is supported by our data set, which covers 4 orders of yield.

Of the events studied, the Ferrara shot of 0.01 tons is lower than expected in terms of yield normalized moment, but fits better in terms of ψ_∞. This is not unexpected because of the very low P-wave velocity of the shot medium.

Source Parameter Variability

The data set of 24 source parameter estimates of this study is augmented by other estimates available in public and classified literature. Table 1 combines our 24 events to a tabulation of 104 events compiled by M. Denny (personal communication, 1996). This tabulation indicates whether the event is a single chemical, C, a multishot commercial mining, D or a nuclear explosion, N. The yields are given for announced events, while the yield normalized M_I and ψ_∞ are given for unreleased events.

The additional values of M_I and ψ_∞ with announced yields are also plotted in Figures 1 and 2 as open symbols. These data demonstrate that our estimates from short-period Rayleigh waves agree well with an independent data set. The yield normalized M_I exhibit significantly larger scatter than the yield normalized ψ_∞ for the very small chemical explosions and for the nuclear event Fisher (Y = 13,400 tons). This further that ψ_∞ may be a better estimator of yield since the effects of low velocity source material are reduced.

To study the variability of estimates, we computed μ, σ, and σ_μ from the M_I/Y and ψ_∞/Y entries of Table 1. The residuals of the logarithms are plotted as histograms in Figure 3. Histograms were made for the complete data sets, for the nuclear explosion and chemical explosion data sets. In addition the total number of observations N and σ are used to draw Gaussian distributions on the histograms. With the exception of the nuclear data set, it is obvious from the histograms for M_I that the complete data set and chemical data set are not fit as well by a Gaussian distribution. On the other hand the ψ_∞ data set is better fit.

To test whether a Gaussian distribution is adequate, we followed Guenther (1966). Let o_i be the observed and p_i the predicted number of observations in k histogram intervals, then the hypothesis that the distribution is normal can be rejected with a significance level α if

$$\chi'^2_{k-3} = \sum_{i=1}^{k} \frac{(o_i - p_i)^2}{p_i} > \chi'^2_{k-3;1-\alpha}$$

The 3 in $k-3$ arises since the normalization factor, μ and σ are estimates. The histograms in Figure 3 have 31 bins. We compared the sum of observed and predicted values in bins 1, 5, 9 ... to those of bins 2, 6, 10 ..., 3, 7, 11, ... and 4, 8, 12, ... to have $k = 4$, and to have the p_i about the same within each group. Table 2 shows the results of the test. We conclude that the distribution of residuals for the complete

Table 1.
Source Parameters From Short-Period Rayleigh Waves

ID	Y (T)	M_I (dyne-cm)	$ERR\,M_I$	$ERR\,\overline{M_I}$	ψ_∞ (m^3)	$ERR\,\psi_\infty$	$ERR\,\overline{\psi_\infty}$	Ref
Distributed Chemical Source								
111891	14.56	6.010^{19}	2.82	1.59	19.0	2.59	1.53	Hutchenson (1994)
111991	13.23	2.710^{19}	3.31	1.70	8.9	3.09	1.65	Hutchenson (1994)
112191	29.44	1.7510^{20}	1.96	1.29	55.1	1.74	1.23	Hutchenson (1994)
090892	49.89	1.9910^{20}	2.85	1.39	73.2	2.89	1.39	Hutchenson (1994)
091192	64.62	1.6410^{20}	3.22	1.44	60.3	3.27	1.45	Hutchenson (1994)
Point Chemical Source								
Ferrara	0.01	6.810^{15}	1.02		0.016	1.02		Malagnini *et al* (1996)
10279	1.25	7.010^{18}	1.45	1.24	0.98	1.47	1.25	Hutchenson (1994)
SP4-POS	1.0	1.410^{18}		1.06	0.20		1.06	Al-Eqabi (1994)
SP6-POS	1.0	2.210^{18}		1.07	0.38		1.07	Al-Eqabi (1994)
SP6-NEG	1.0	1.710^{18}		1.05	0.27		1.05	Al-Eqabi (1994)
SP3B-POS	1.0	3.610^{18}		1.10	0.54		1.10	Al-Eqabi (1994)
SP3A-NEG	1.0	1.610^{18}		1.07	0.20		1.07	Al-Eqabi (1994)
SP1-POS	1.0	1.810^{18}		1.08	0.29		1.08	Al-Eqabi (1994)
SP1-NEG	1.0	1.510^{18}		1.10	0.22		1.10	Al-Eqabi (1994)
SPC2-NEG	0.5	1.010^{18}		1.08	0.14		1.08	Al-Eqabi (1994)
SP13-NEG	1.0	1.510^{18}		1.08	0.28		1.08	Al-Eqabi (1994)
SP4A-POS	1.0	2.010^{18}		1.15	0.23		1.15	Al-Eqabi (1994)
SP15-POS	1.0	2.010^{18}		1.10	0.24		1.10	Al-Eqabi (1994)
SP17-NEG	1.0	5.110^{18}		1.10	0.64		1.10	Al-Eqabi (1994)
SP19-NEG	1.0	2.410^{18}		1.09	0.45		1.09	Al-Eqabi (1994)
SP19-POS	1.0	1.710^{18}		1.08	0.28		1.08	Al-Eqabi (1994)
SP20-POS	1.0	2.210^{18}		1.05	0.30		1.05	Al-Eqabi (1994)
SP23-NEG	1.0	4.710^{18}		1.09	0.65		1.09	Al-Eqabi (1994)
SP26-NEG	1.0	3.610^{18}		1.12	0.47		1.12	Al-Eqabi (1994)

EVID: Event identification used in the primary references
Mean M_I and ψ_∞ are obtained by taking the anti-logarithm of their logarithmic averages. $ERR\,M_I$ and $ERR\,\psi_\infty$ are multiplicative factors obtained as 10^{σ}, where σ is the standard deviation of their logarithms.
$ERR\,\overline{M_I}$ and $ERR\,\overline{\psi_\infty}$ are multiplicative factors obtained by the relation 10^{σ_μ}, where σ_μ is the standard deviation of the mean of their logarithms.

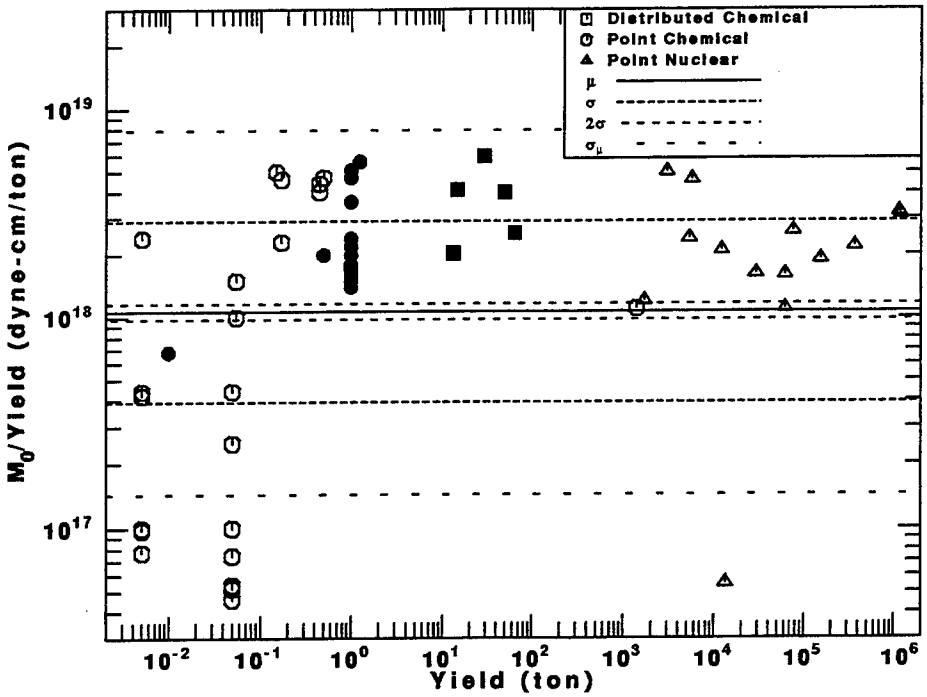

Figure 1. Yield normalized isotropic moment vs yield. The data of Table 1 are indicated by solid symbols.

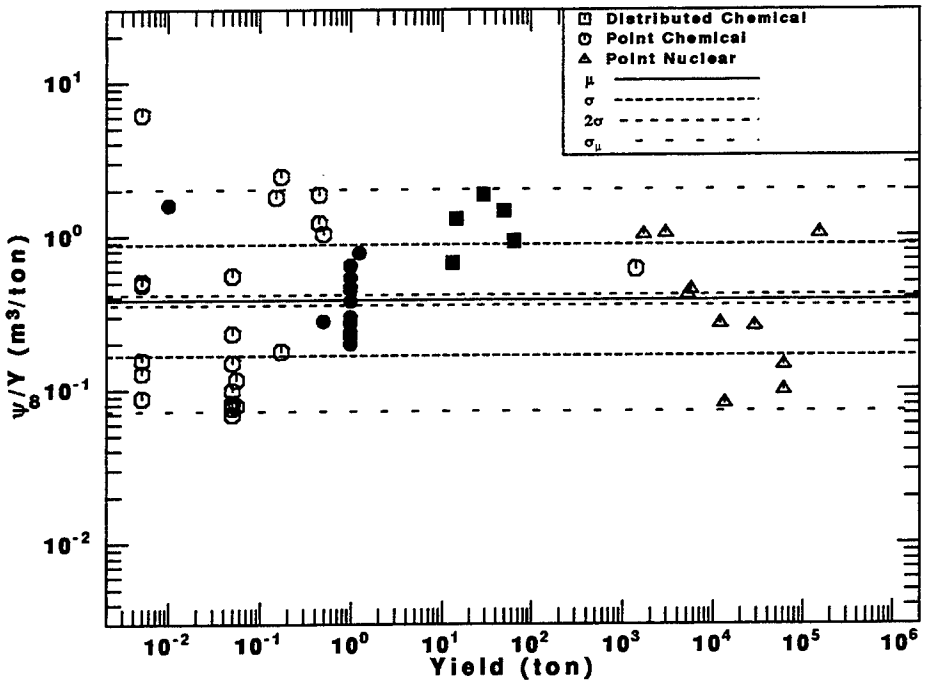

Figure 2. Yield normalized ψ_∞ vs yield. The data of Table 1 are indicated by solid symbols. Additional data from Denny (personal communiciton) are show as open symbols. Mean estimates and error bounds are based on the complete data set consisting of Table 1 and the data from Denny (personal communication).

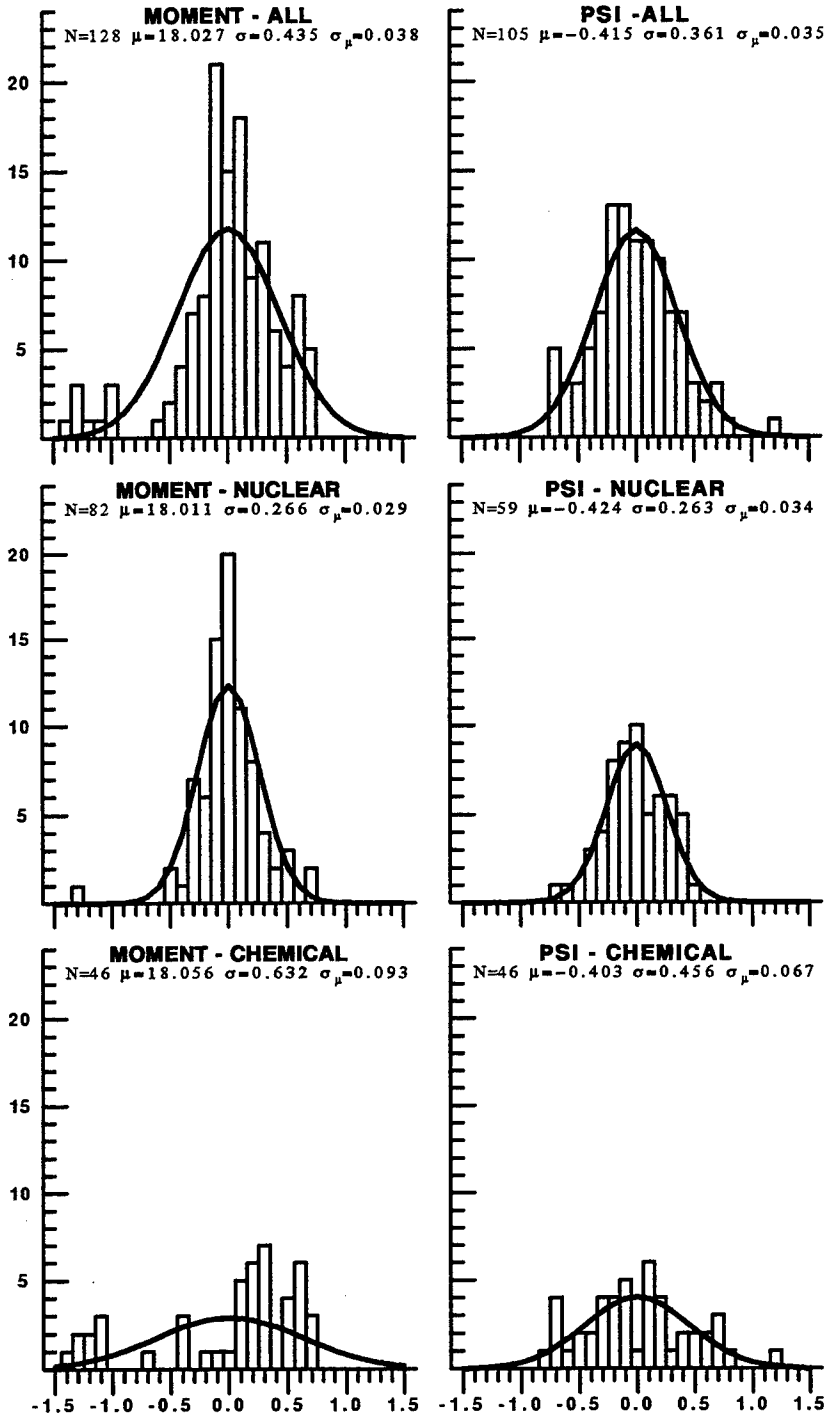

Figure 3. Histograms of deviations logarithms of the Table 2 data set of M_I/Y and ψ_∞/Y from logarithmic means. N is the number of observations, μ is the logarithmic mean, σ is the standard deviation, and σ_μ is the standard deviation of the mean. The Gaussian normal distribution is plotted using σ. The figures are for the M_I and ψ_∞ for the complete data set, and for the nuclear and chemical event subsets.

M_I data set is not Gaussian at a 95% confidence level. For the M_I and ψ_∞ data sets, the three estimates of μ are within one σ_μ of each other respectively.

Table 2.
Test of Normal Distribution at 95% level ($\alpha = 0.05$)

Data Set	χ'^2_{k-3}		$\chi'^2_{k-3;1-\alpha}$	Action
M_I - all data	4.49	>	3.84	Reject
M_I - nuclear	2.97	<	3.84	Do not reject
M_I - chemical	3.49	<	3.84	Do not reject
ψ_∞ - all data	0.18	<	3.84	Do not reject
ψ_∞ - nuclear	1.67	<	3.84	Do not reject
ψ_∞ - chemical	2.86	<	3.84	Do not reject

CONCLUSIONS AND RECOMMENDATIONS

- Analysis of short-period Rayleigh waves for velocity and attenuation model can also lead to consistent estimates of M_I and ψ_∞.
- The residual distribution for ψ_∞/Y is quite similar for the combined data set and the nucluear and chemical subsets.
- The M_I/Y residual distribution is not Gaussian for the combined data set.
- The statistics of the combined data set permit bounds on yield estimates based on a small number of observations of M_I or ψ_∞.

Regional Upper-Mantle Structures and their Interpretation in terms of Small-Scale, Anisotropic Heterogeneities

THOMAS H. JORDAN, JAMES B. GAHERTY, MAMORU KATO*, AND OLAV VAN GENABEEK

Department of Earth, Atmospheric and Planetary Sciences
Massachusetts Institute of Technology, Cambridge, MA 02139

**Present Address: Department of Geophysics, Kyoto University, Kyoto, Japan*

AFOSR Grant F49620-95-1-0051

Abstract

We have derived crustal and upper-mantle models from self-consistent, three-component data sets along corridors spanning Australia (AU3), the central Pacific Ocean (PA5), and the northern part of the Philippine Sea (PHB3). The locations and impedance contrasts of all discontinuities were directly constrained by path-averaged reflectivity profiles derived from stacking *ScS* reverberation data, and the velocity gradients and radial anisotropy were tied down by an extensive set of frequency-dependent travel times measured from surface waves, body waves, and guided waves of various polarizations, including *S*, *sS*, *SS*, *sSS*, *SSS*, *Sa*, R_1, and G_1. The attenuation structures were determined from a combination of *ScS*-reverberation and surface-wave amplitude data. The data for each corridor were jointly inverted with a complementary set of mineralogical constraints for a complete radially-anisotropic, frequency-dependent parameterization. At high frequencies, these structures provide a significantly better match to the observed seismograms than path averages constructed from global tomographic models.

All three regional models are transversely isotropic, and observations at various azimuths indicate that this symmetry is a good approximation at the frequencies (< 50 mHz) and distances (35°-55°) employed in their construction. In the case of the continental upper mantle, we interpret this anisotropy in terms of a stochastic model for small-scale, anisotropic heterogeneity, where the local anisotropy is a constant hexagonal tensor $\hat{\mathbf{C}}$ rotated to an axis of symmetry $\hat{\mathbf{s}}(\mathbf{x})$ that varies both laterally and with depth. Our stochastic model for $\hat{\mathbf{s}}$ is described by a characteristic horizontal wavenumber k and three dimensionless numbers: an aspect ratio of the anisotropy, ξ, an aspect ratio of the heterogeneity, η, and a fractal dimension, D. We estimate these stochastic parameters for the continental upper mantle by matching the polarization anisotropy in our regional model AU3, the statistics of vertical *S*-wave splitting parameters in Silver's [1996] recent compilation, and various petrological estimates of $\hat{\mathbf{C}}$. The aspect ratio of the anisotropy, ξ, must be greater than 2 to satisfy the AU3 anisotropy, which implies that $\hat{\mathbf{s}}$ deviates from the horizontal with an rms angle that is less than 30°. Our best estimate, $\xi = 4.0$, corresponds to an rms angle of 14°. The aspect ratio of the heterogeneity, η, is less well constrained, although the observations of coherently split, vertically propagating *S* waves suggest that it cannot be too large. Assuming a fractal dimension of D = 3.2, we estimate the horizontal correlation length, k, to be about 1000 km, from which we infer $\eta < 10$. Because stochastic models of this type are likely to play a crucial role in the simulation of high-frequency wave propagation at regional distances, further observational work is recommended to test these models and reduce the uncertainties in their parameters.

Key words: Anisotropy, heterogeneity, upper mantle, regional structure, scattering theory.

Objectives

The technologies of nuclear-monitoring seismology are built in part on studies of wave propagation at regional distances (< 2000 km). One poorly understood aspect of regional propagation is the forward scattering of high-frequency signals by small inhomogeneities. The objectives of this research are threefold: (1) to formulate parameterized stochastic models of small-scale heterogeneity that are suitable for assessing scattering effects at regional distances, (2) to constrain the model parameters using broadband seismic data, and (3) to assess the implications of these models for regional wave propagation related to nuclear monitoring.

Research Accomplishments

Regional Upper-Mantle Models.

One of our primary research accomplishments has been the development of a new generation of regional models that satisfy larger and richer sets of seismic observations. These models have the following attributes:

- The models were derived as path averages along relatively short (35°-55°) corridors between deep-focus source regions and high-performance seismic stations. The corridors were chosen for high data density and tectonic homogeneity.
- High-resolution, self-consistent data sets were obtained by applying a uniform methodology to three components of ground motion from earthquakes with well-determined source parameters. The observational procedures employed spherical-earth synthetic seismograms computed by complete mode summation, and the Fréchet kernels used in the inversions accounted for frequency-dependent diffractions and other wave-propagation effects, including the interference from other seismic phases [Gee and Jordan, 1992].
- The vertical travel times to, and *SV* impedance contrasts across, all discontinuities in the models were directly constrained by path-averaged reflectivity profiles derived from stacking *ScS* reverberation data [Revenaugh and Jordan, 1991]. The stacking procedure was able to detect and measure impedance variations as small as 1%.
- Velocity gradients and anisotropy were constrained from an extensive set of frequency-dependent travel times measured from surface waves, body waves, and guided waves of all polarizations. The observed seismic phases included *S*, *sS*, *SS*, *sSS*, *SSS*, *Sa*, R_1, and G_1.
- The attenuation structure along each corridor was determined from a combination of *ScS*-reverberation and surface-wave amplitude data.
- The data were jointly inverted with a complementary set of mineralogical constraints for a complete radially-anisotropic, frequency-dependent parameterization. Various inversion experiments were performed to test for the depth extent of the anisotropy.

We have thus far completed the inversions for corridors traversing Australia [Gaherty and Jordan, 1995], the central Pacific Ocean [Gaherty et al., 1996], and the northern part of the Philippine Sea [Kato and Jordan, in prep., 1996]. The final models, designated AU3, PA5, and PHB3, respectively, are listed in Tables 1-3 and their *S*-wave structures are displayed in Figure 1.

In Figure 2, we show comparable path averages for the global tomographic model S12_WM13 of Su et al. [1994]. Some of the features are similar to those in Figure 1. For example, the

Australian path is fast above 350 km, the lid in the Philippine Sea is slow, and magnitude of the shear-wave anisotropy in the uppermost mantle reaches about 4%. However, the global tomographic model does not capture a number of the important features of upper-mantle structure. In particular, the mantle discontinuities in S12_WM13 are at fixed depths, the mantle anisotropy does not vary with depth, and the shear-speed values and gradients are similar for all three paths. Our high-resolution models show substantial variations in the discontinuity depths and amplitudes, in the maximum depth of the anisotropy, and in the shear-speed gradients, especially between 100 and 400 km. Moreover, S12_WM13 has a large jump in v_S across a Lehmann (L) discontinuity at 220 km (inherited from its radial reference model, PREM), whereas the isotropic shear speeds at this depth are essentially continuous in our models.

We have investigated the L discontinuity in some detail, and our preferred explanation associates this feature with an abrupt transition from an anisotropic layer to a more isotropic region below this layer [Revenaugh and Jordan, 1991; Gaherty and Jordan, 1995]. This transition is particularly evident in stable continental regions, where it is seen by long-period *SV* waves as a velocity increase [Revenaugh and Jordan, 1991] and by long-period *SH* waves as a velocity decrease [Grand and Helmberger, 1984]. In the continents above L, the temperatures have evidently remained cold enough to freeze-in the small-scale anisotropic structures and tectonic fabrics generated in episodes of orogenic compression associated with tectospheric stabilization [Jordan, 1988; Silver and Chan, 1991]. Below L, such structures were either never generated, perhaps because L coincides with a transition from dislocation to diffusion creep [Karato, 1992], or were annealed out subsequent to their formation. These hypotheses about subcontinental structure have considerable bearing on a diverse set of geological and geodynamical problems, ranging from formation of the cratons to kimberlite vulcanism [Gaherty and Jordan, 1995].

A second feature of scientific interest is the structure of the lid beneath the oceanic regions. In the central Pacific, the lid is thin (56 km) and has high seismic velocities ($\overline{v}_S$ = 4.75 km/s), whereas in the Philippine Sea, it is thicker (72 km) with lower velocities ($\overline{v}_S$ = 4.48 km/s). Since the area sampled in the Philippine Sea is younger than in the Pacific, the difference in the depth to the lid-LVZ boundary (G discontinuity) requires a compositional control. We favor the scenario where the depth of G in older oceanic regions is set by the depth of melting during the production of the overlying oceanic crust. As discussed by Hirth and Kohlstedt [1996], the water content in olivine increases rapidly below the zone of residual harzburgite, causing an abrupt drop in viscosity [Karato and Wu, 1993]. The increase in water will also decrease the seismic velocities [Karato, 1995], so that G may mark the fossilized lower boundary of the melt separation zone. This hypothesis implies that the depth of melting in the northern part of Philippine Sea was greater than in the central Pacific. This hypothesis agrees the observed differences in crustal thickness: 11.5 km for PHB3 vs. 6.8 km for PA5 [Gaherty et al., 1995].

Figure 3 displays representative seismograms for paths in the three corridors, and it compares these observations with synthetics calculated for the path-averaged models in Figures 1 and 2. At low frequencies (left panels), both our regional models and those derived by the global tomography match the observations, but at higher frequencies (right panels), the latter show substantial discrepancies. The regional models thus provide an improved capability for calculating the effects of wave propagation through the upper mantle, which will be useful in the verification of the CTBT.

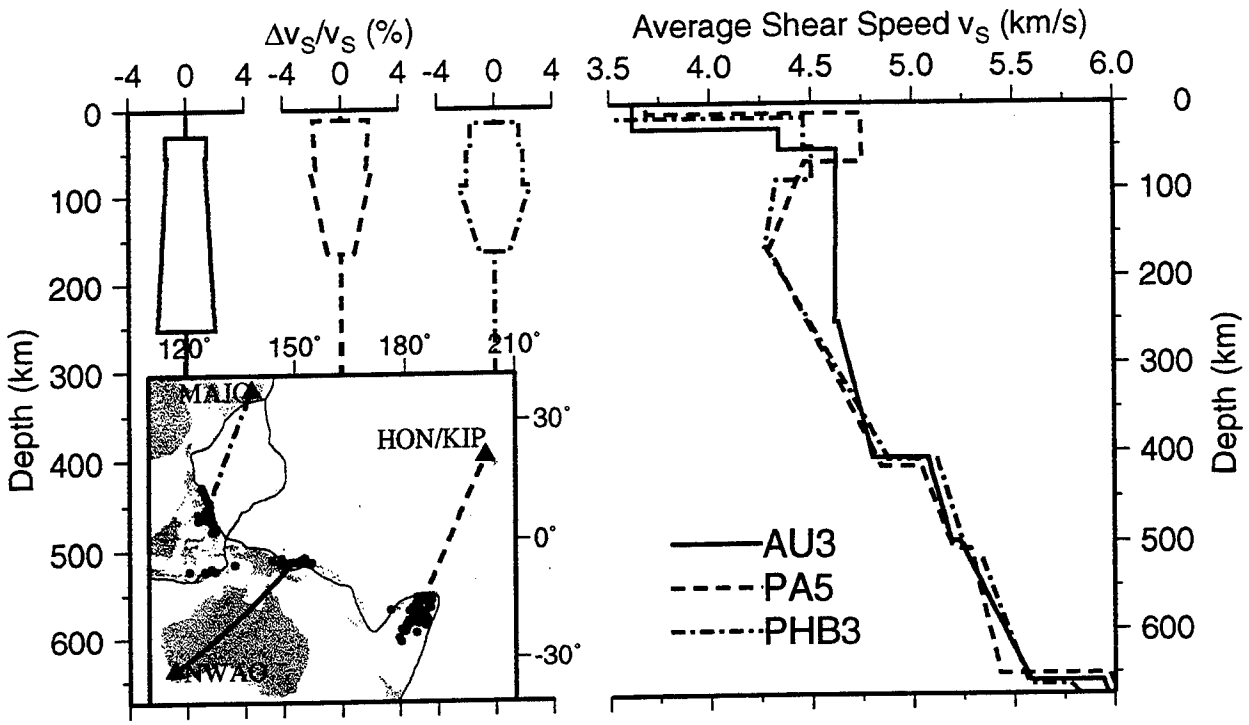

Figure 1. Comparison of shear-wave structures for the three regional models obtained in this study (Tables 1-3). The mean shear speeds for AU3 (solid line), PA5 (dashed line), and PHB3 (dash-dotted line) are plotted in the right panel, and the anisotropic variations about these means, in percent, are plotted in the left panels. The inset map shows the seismic corridors for each of these models, including the stations (triangles) and earthquakes (dots) used in the data processing.

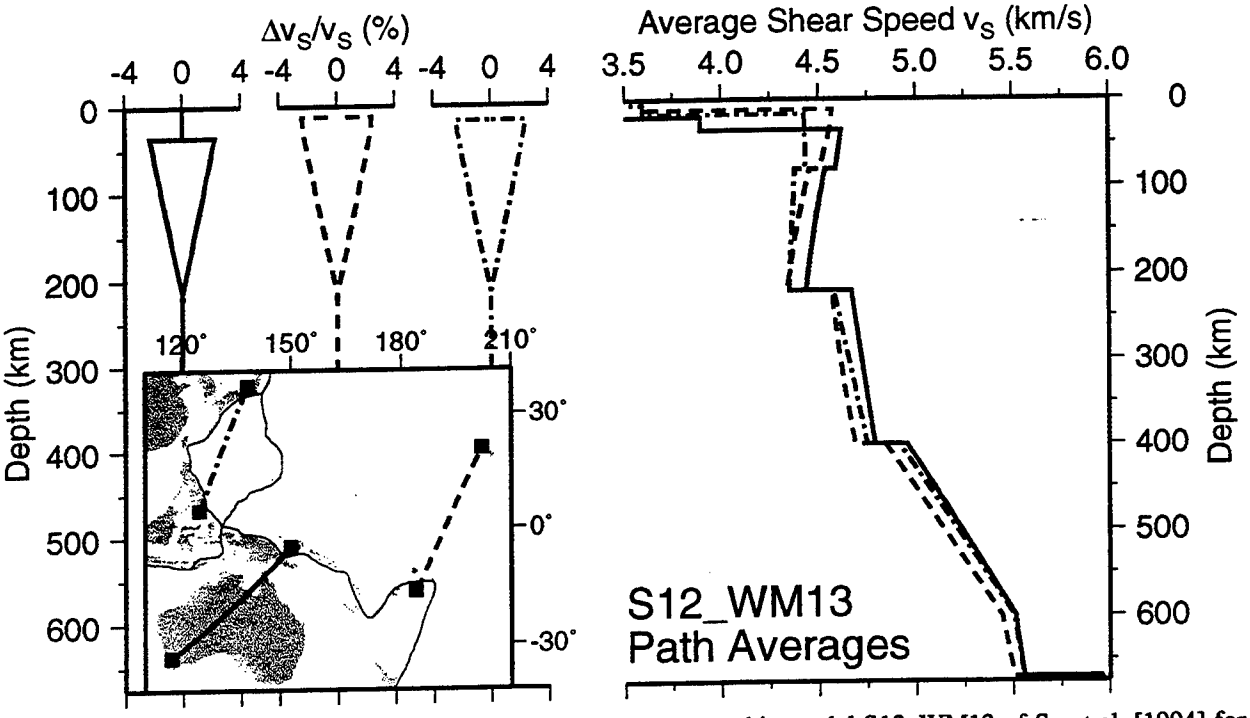

Figure 2. Shear-wave structures obtained from the global tomographic model S12_WM13 of Su et al. [1994] for the seismic corridors corresponding to the AU3 (solid line), PA5 (dashed line), and PHB3 (dash-dotted line) regional models. These structures were obtained by averaging S12_WM13 along the paths shown on the inset map.

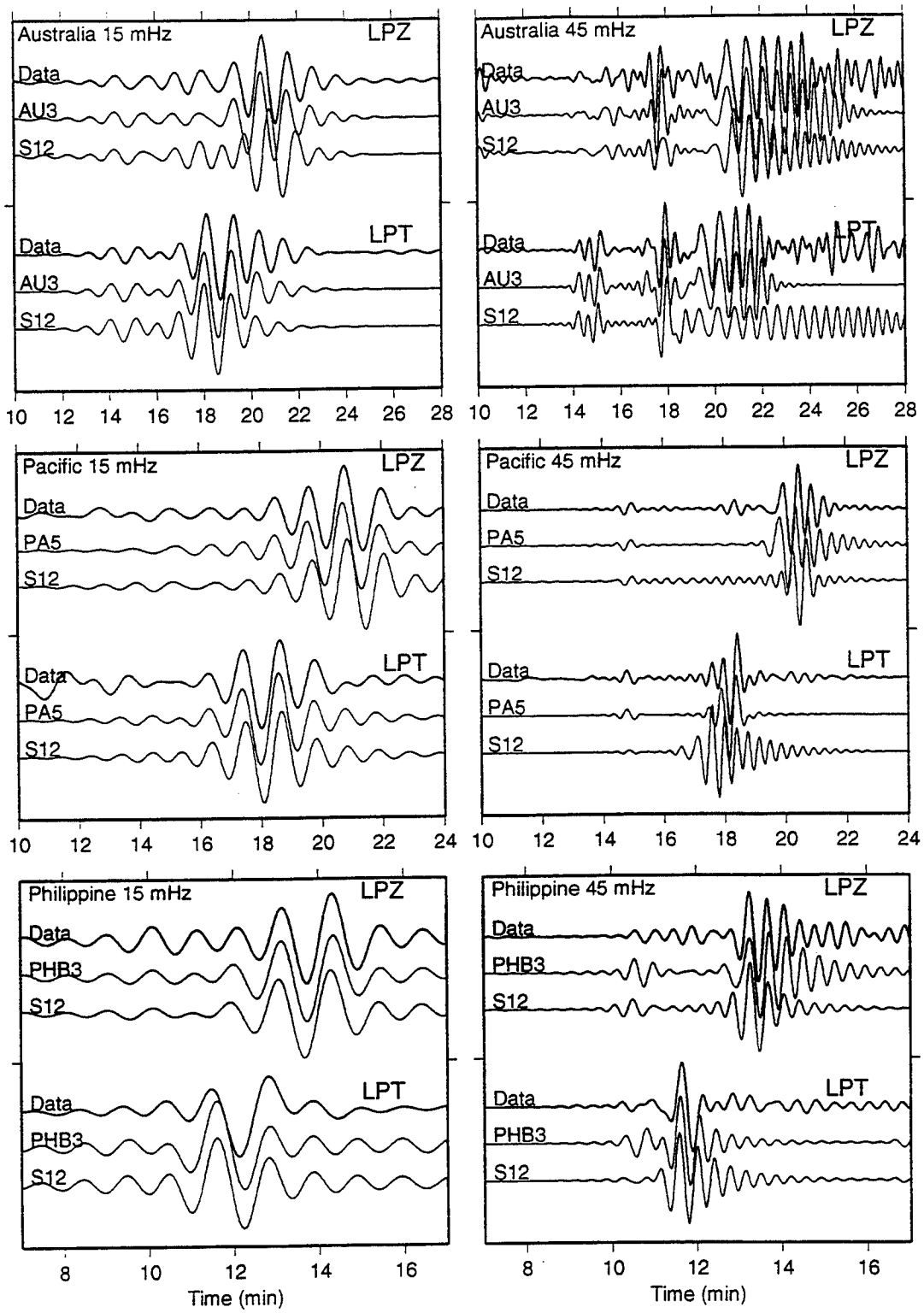

Figure 3. Comparison of observed seismograms (labeled Data) with synthetics computed from the regional models of Figure 1 (labeled AU3, PA5, and PHB3) and the path-averaged tomographic models of Figure 2 (labeled S12). The seismograms are from shallow-focus events recorded at the seismic stations indicated on the inset map in Figure 1. They have been low-pass filtered with corners at 15 mHz (left panels) and 45 mHz (right panels). Both sets of models provide good fits to the former, but the regional models are considerably better at matching the latter.

Stochastic Modeling of Small-Scale Heterogeneity in the Upper Mantle.

We have observed polarization anisotropy as the splitting of surface, guided, and shear body waves in all of the regions discussed above; however, an analysis of these same waves shows no obvious azimuthal anisotropy. This is expected if the local orientation of olivine crystals in the upper mantle is incoherent on the scale of the path lengths used in these studies ($\Delta = 35°–55°$). We have therefore represented the splitting in terms of radially anisotropic, but transversely isotropic, elasticity (Tables 1-3).

In the current phase of our research program, we are focusing on the interpretation of this polarization anisotropy, as well as observations of azimuthal splitting from vertically propagating shear waves [e.g., Silver, 1996], in terms of small-scale, anisotropic heterogeneity. We have formulated stochastic models that specify upper-mantle inhomogeneities as samples of Gaussian random fields with self-affine (fractal) scaling at high wavenumbers, and we have derived expressions relating the parameters of these models to various types of seismic observations [Jordan and Gaherty, 1995a,b]. Solving these forward problems has allowed us to set up quantitative inverse problems for the parameters of the stochastic distributions. Some preliminary estimates are presented below.

We consider a medium governed by a fourth-order elasticity tensor $\mathbf{C}(\mathbf{x})$ that is a function of three-dimensional position vector $\mathbf{x}$. Theoretical calculations [Estey and Douglas, 1986] and measurements on kimberlite xenoliths [Mainprice and Silver, 1993; Christensen, 1994] indicate that the elasticity of upper-mantle peridotites has quasi-hexagonal symmetry on the hand-sample scale. Therefore, it is reasonable to approximate $\mathbf{C}(\mathbf{x})$ as a hexagonal tensor field with a local axis of symmetry given by a unit vector $\hat{\mathbf{s}}(\mathbf{x})$. In petrological terms, $\hat{\mathbf{s}}(\mathbf{x})$ is largely determined by the local average orientation of the *a*-axis of olivine, which is aligned by mantle deformation [Estey and Douglas, 1986]. We therefore restrict the tensor field to be a functional of a Gaussian random vector field $\mathbf{s}(\mathbf{x}) = s\ \hat{\mathbf{s}}(\mathbf{x})$: $\mathbf{C}(\mathbf{x}) = \mathbf{C}(\mathbf{s}(\mathbf{x}))$. The functional relationship is specified by requiring the anisotropic perturbation to the elastic parameters to be proportional to the vector length $s = |\mathbf{s}(\mathbf{x})|$ raised to some power $n \geq 0$, called the strength exponent [Jordan and Gaherty, 1995a]. For the case $n = 0$, adopted in the calculations presented here, $\mathbf{C}(\mathbf{x})$ is a constant tensor $\hat{\mathbf{C}}$ rotated to an axis of symmetry $\hat{\mathbf{s}}(\mathbf{x})$. Because it is hexagonal, $\hat{\mathbf{C}}$ has five independent (positive) components, which we denote (a, b, c, f, m).

The vector field is assumed to have zero mean, $\langle \mathbf{s}(\mathbf{x}) \rangle = 0$, and an autocovariance tensor $\boldsymbol{C}_{\mathbf{ss}}$ that is transversely isotropic. In the simple Gaussian model proposed by Jordan and Gaherty [1995a], this autocovariance tensor is described by a characteristic horizontal wavenumber k, which has dimensions of $length^{-1}$, and three dimensionless numbers: an aspect ratio of the anisotropy, $0 \leq \xi < \infty$, an aspect ratio of the heterogeneity, $0 \leq \eta < \infty$, and a fractal dimension, $3 \leq D < 4$. Since the autocovariance tensor of a zero-mean, Gaussian random field determines its higher moments, the entire stochastic model is therefore specified by ten nonnegative scalars.

We have solved a series forward problems that related the parameters of this stochastic model to seismological observables, and by applying these theories to existing data, we have determined some preliminary values for the stochastic parameters:

Voigt Averages. We have derived closed-form expressions for the Voigt average, $\overline{C}_{ijkl} = \langle C_{ijkl} \rangle$ [Jordan and Gaherty, 1995a]. This one-point average depends only on $\hat{\mathbf{C}}$, n, and ξ. It should be noted that, while the vector field $\mathbf{s}(\mathbf{x})$ is Gaussian, the tensor field $\mathbf{C}(\mathbf{x})$ is not, so that

even simple Voigt averaging is mathematically complex. In solving such forward problems, we have found the Maxwell-multipole representation of fourth-order elasticity tensors developed by Backus [1970] to be very valuable, because the tensor problem is thereby reduced to averaging over scalar fields of harmonic polynomials.

Higher-Order Effective-Media Theories. We have derived a Born approximation for the effective elasticity tensor $\tilde{C}_{ijkl} = \langle \sigma_{ij} \rangle \langle \varepsilon_{kl} \rangle^{-1}$ in the low-frequency limit ($\omega \to 0$) using a self-consistent theory based on the Lippman-Schwinger scattering equation [Jordan and Gaherty, 1995a]. Explicit results have been obtained using the Backus harmonic decomposition in the limit $\xi \to \infty$, where the orientation vector $\hat{\mathbf{s}}(\mathbf{x})$ is everywhere horizontal [van Genabeek and Jordan, in prep., 1996]. In this case, symmetries reduce the problem from a system of 81 equations to 7. Because this theory is easily generalized to finite ω, we are investigating its application to higher frequency seismological observations.

For comparison, we have obtained analytical expressions for $\tilde{C}_{ijkl}$ in the limits $\omega \to 0$, $\xi \to \infty$, $\eta \to \infty$ using a generalization of Backus's [1962] averaging method. The latter limit applies to a stochastic laminate, where the horizontal correlation length k is large compared to the vertical correlation length. A comparison of these results with the Voigt average shows that the effective medium for low-frequency wave propagation is only weakly dependent on the parameters η and D. Hence, using estimates of the local anisotropy tensor $\hat{\mathbf{C}}$ derived from petrological samples and models, we can employ the Voigt theory to estimate the aspect ratio of the anisotropy ξ from the seismic models.

Figure 4 shows the results for model AU3 in the case $n = 0$. If we take the local anisotropy to be the perfectly oriented pyrolite of Estey and Douglas [1986], we infer ξ = 2-3, which implies that the root-mean-square (rms) angular deviation of $\hat{\mathbf{s}}$ from the horizontal is 18°-26°. This value is probably an upper bound, since the magnitude of $\hat{\mathbf{C}}$ calculated by this method is higher than the local anisotropy observed in most mantle xenoliths [Mainprice and Silver, 1993; Christensen, 1994]. An estimate of $\hat{\mathbf{C}}$ more in line with the xenoliths comes from the Hidaka dunite [Kawasaki and Kon'no, 1984], which yields $\xi \approx 4$, corresponding to an rms angle of only 14°.

Vertical Shear-Wave Splitting. We have derived an propagator-matrix theory for the scattering of vertically propagating shear waves of frequency $\omega << \bar{v}_S k$ in a layer where the orientation field $\hat{\mathbf{s}}(\mathbf{x})$ is approximately horizontal ($\xi >> 1$), and we have applied this theory to investigate the effects of scattering on the apparent splitting parameters derived from the observations of *SKS* and other teleseismic shear waves [Jordan and Gaherty, 1995b]. We have shown that the scattering introduced by vertical variations in $\hat{\mathbf{s}}$ ($\eta > 0$) in a layer of thickness D is strong if $\eta k D >> 1$. The successful recovery of apparent splitting parameters by Silver and Chan [1991] and others (see review by Silver [1996]) therefore implies that $\eta k D \sim 1$.

This inference allows us to estimate the horizontal correlation length k from the splitting observations (Figure 5). Let $\tilde{\psi}(x) = \tilde{\phi} - \tilde{\phi}'$ be the difference in the apparent splitting angles $\tilde{\phi}$ and $\tilde{\phi}'$ observed at two stations separated by a horizontal distance x. If each observation is contaminated by an error with an angular standard deviation of ε and errors at different stations are uncorrelated, then we can derive an expression for the rms angular difference $\tilde{\psi}_{\text{rms}}(x) \equiv \arccos\langle \cos^2 \tilde{\psi}(x) \rangle^{1/2}$ that is a function of k, D, and ε. The limiting values are $\tilde{\psi}_{\text{rms}}(0) = \sqrt{2}\,\varepsilon$ and $\tilde{\psi}_{\text{rms}}(\infty) = 45°$. Assuming a fractal dimension of D = 3.2, we obtain estimates of $\varepsilon \approx 14°$ and $k \approx 1000$ km from the data plotted in Figure 5.

Table 1. Model AU3*

z km	ρ Mg/m^3	v_{SV} km/s	v_{SH} km/s	v_{PV} km/s	v_{PH} km/s	η
0.0	2.85	3.62	3.62	6.05	6.05	1.00
30.0	2.85	3.62	3.62	6.05	6.05	1.00
30.0	3.30	4.28	4.40	8.00	8.15	0.90
54.0	3.30	4.28	4.40	8.00	8.15	0.90
54.0	3.40	4.56	4.68	8.23	8.52	0.90
252.0	3.44	4.52	4.70	8.28	8.61	0.90
252.0	3.45	4.63	4.63	8.45	8.45	1.00
406.0	3.58	4.80	4.80	8.88	8.88	1.00
406.0	3.69	5.07	5.07	9.31	9.31	1.00
499.0	3.85	5.19	5.19	9.64	9.64	1.00
499.0	3.88	5.23	5.23	9.67	9.67	1.00
659.0	4.00	5.58	5.58	10.21	10.21	1.00
659.0	4.21	5.94	5.94	10.72	10.72	1.00
861.0	4.50	6.28	6.28	11.21	11.21	1.00

Table 2. Model PA5*

z km	ρ Mg/m^3	v_{SV} km/s	v_{SH} km/s	v_{PV} km/s	v_{PH} km/s	η
0.0	1.03	0.00	0.00	1.50	1.50	1.00
5.0	1.03	0.00	0.00	1.50	1.50	1.00
5.0	1.50	0.92	0.92	2.01	2.01	1.00
5.2	1.50	0.92	0.92	2.01	2.01	1.00
5.2	3.03	3.68	3.68	5.93	5.93	1.00
12.0	3.03	3.68	3.68	5.93	5.93	1.00
12.0	3.34	4.65	4.84	8.04	8.27	0.90
68.0	3.38	4.67	4.83	8.06	8.30	0.90
68.0	3.35	4.37	4.56	7.88	8.05	0.90
166.0	3.41	4.26	4.34	8.04	8.09	1.00
166.0	3.42	4.29	4.29	8.06	8.06	1.00
415.0	3.58	4.84	4.84	8.92	8.93	1.00
415.0	3.71	5.04	5.04	9.29	9.29	1.00
507.0	3.85	5.20	5.20	9.64	9.64	1.00
507.0	3.88	5.28	5.28	9.71	9.71	1.00
651.0	4.02	5.43	5.43	10.11	10.11	1.00
651.0	4.29	5.97	5.97	10.76	10.76	1.00
791.0	4.46	6.23	6.23	11.08	11.08	1.00
791.0	4.46	6.23	6.23	11.08	11.08	1.00
801.0	4.46	6.24	6.24	11.10	11.10	1.00

Table 3. Model PHB3*

z km	ρ Mg/m^3	v_{SV} km/s	v_{SH} km/s	v_{PV} km/s	v_{PH} km/s	η
0.0	1.03	0.00	0.00	1.50	1.50	1.00
5.4	1.03	0.00	0.00	1.50	1.50	1.00
5.4	1.50	0.92	0.92	2.10	2.10	1.00
5.5	1.50	0.92	0.92	2.10	2.10	1.00
5.5	2.83	3.48	3.48	6.27	6.27	1.00
16.9	2.83	3.48	3.48	6.27	6.27	1.00
16.9	3.28	4.39	4.54	7.91	8.02	0.91
51.0	3.28	4.39	4.54	7.91	8.02	0.91
51.0	3.35	4.41	4.59	8.00	8.14	0.91
89.3	3.35	4.41	4.59	8.00	8.14	0.91
89.3	3.35	4.22	4.43	7.89	8.05	0.91
165.5	3.35	4.23	4.31	7.99	8.07	0.94
165.5	3.35	4.27	4.27	8.03	8.03	1.00
407.7	3.87	5.27	5.27	9.76	9.76	1.00
407.7	3.76	5.12	5.12	9.36	9.36	1.00
520.4	3.87	5.27	5.27	9.76	9.76	1.00
520.4	3.88	5.34	5.34	9.77	9.77	1.00
664.0	4.02	5.57	5.57	10.22	10.22	1.00
664.0	4.35	5.78	5.78	10.66	10.66	1.00
761.3	4.42	6.16	6.16	10.94	10.94	1.00
761.3	4.44	6.19	6.19	11.02	11.02	1.00
771.0	4.44	6.22	6.22	11.05	11.05	1.00

* Models are calculated at a reference frequency of 35 mHz, linearly interpolated between depths, and identical to PREM below last depth listed.

Table 4. Stochastic Parameters

Symbol	Description	Plausible Range	Model STAT1
n	Strength exponent	0 – 2†	0
k	Horizontal correlation length	500-2000 km	1000 km
ξ	Anisotropy aspect ratio	2 – 6	4.0
η	Heterogeneity aspect ratio	1 – 10†	1.0
D	Fractal dimension	3.1 – 3.5†	3.2

† Range poorly constrained by available data.

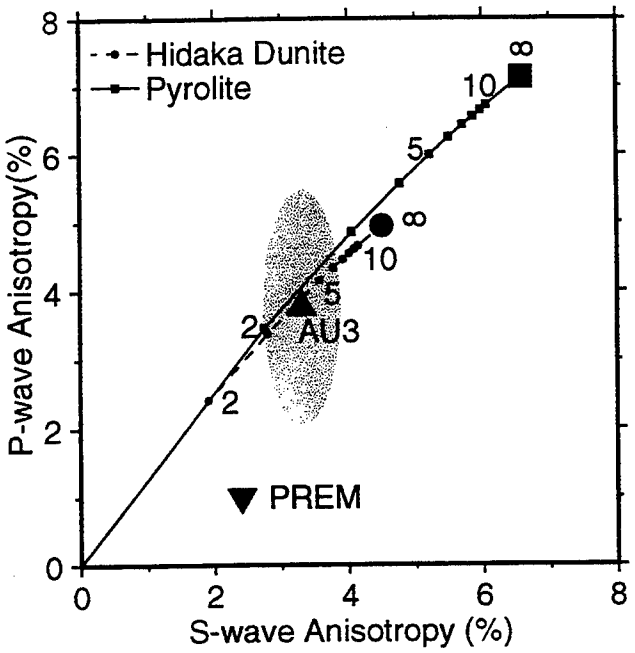

Figure 4. Plot of the *P*-wave anisotropy, $(v_{PH} - v_{PV}) / v_{PV}$, versus the *S*-wave anisotropy, $(v_{SH} - v_{SV}) / v_{SV}$. The triangle with the 95% confidence ellipse is the upper-mantle average from model AU3, and the inverted triangle is a similar average for PREM. The filled square is the value calculated by Voigt averaging the hexagonally symmetric pyrolite model of Estey and Douglas [1986] assuming complete crystallographic alignment in the horizontal plane ($\xi = \infty$), and the filled circle is a similar average for the Hidaka dunite of Kawasaki and Kon'no [1984]. The lines are the loci of the Voigt averages with a strength exponent $n = 0$ for decreasing values of the anisotropy aspect ratio ξ, showing how the apparent anisotropy decreases as the local orientation becomes statistically more isotropic. This calculation suggests that the value of ξ appropriate for the Australian upper mantle is in the range 2-6.

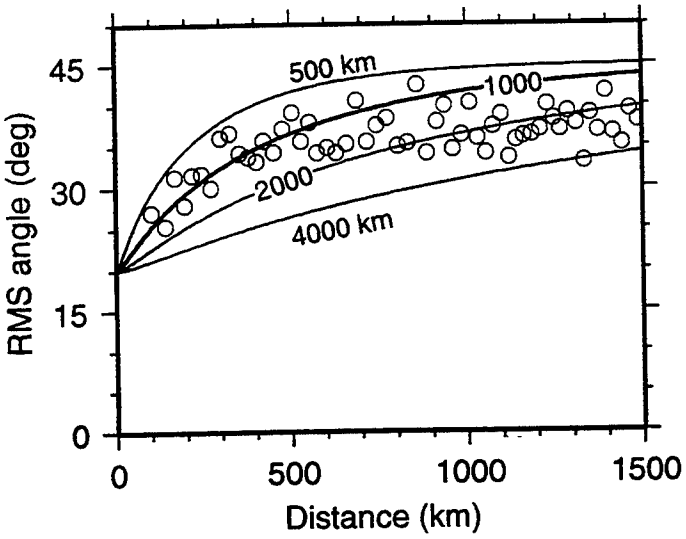

Figure 5. Plot of the rms angular difference $\tilde{\psi}_{rms}(x)$, which is a measure of the decorrelation in the apparent splitting directions for vertical *S* waves recorded at a horizontal distance x. Points are estimates constructed from the continental data set of Silver [1996] by averaging $\cos^2(\tilde{\phi} - \tilde{\phi}')$ in distance bins containing 75 samples. Lines are theoretical values for D = 3.2 and k = 500, 1000, 2000, 4000 km. At short separations, the data are best fit by a model with a horizontal correlation distance of k = 1000 km. This model underestimates the correlations in the splitting orientations at large distances (x > 1000 km), which may reflect the large-scale structure of the continents.

Conclusions and Recommendations

We have derived a new set of regional models for the upper mantle in which the discontinuity and radial-anisotropy structures are well constrained by path-averaged data (Tables 1-3). At high frequencies, these structures provide a significantly better match to the observed seismograms than path averages constructed from global tomographic models. All three regional models are transversely isotropic, and observations at various azimuths indicate that this symmetry is a good approximation at the frequencies (< 50 mHz) and distances (35°-55°) employed here. In the case of the continental upper mantle, we interpret this anisotropy in terms of a stochastic model for small-scale, anisotropic heterogeneity, where the local anisotropy is a constant hexagonal tensor $\hat{\mathbf{C}}$ rotated to an axis of symmetry $\hat{\mathbf{s}}(\mathbf{x})$ that varies both laterally and with depth.

Table 4 summarizes the estimates of the stochastic parameters derived from our regional model AU3, Silver's [1996] compilation of vertical S-wave splitting azimuths, and various petrological estimates of $\hat{\mathbf{C}}$. Because some of the parameters are not yet well constrained by seismological data, we give values for both a "plausible range" and a specific model, STAT1. To match the polarization anisotropy of AU3 requires that $\xi > 2$, which means that $\hat{\mathbf{s}}$ deviates from the horizontal with an rms angle < 30°. Our best estimate, $\xi = 4.0$, corresponds to an rms angle of only 14°. The value of η is less well constrained, although the *SKS* splitting observations imply that it cannot be too large. Assuming a fractal dimension of D = 3.2, we estimate $k \approx 1000$ km, from which we infer $\eta < 10$. Because stochastic models like STAT1 are likely to play a crucial role in the simulation of high-frequency wave propagation at regional distances, we recommend that additional observations be collected to test these models and reduce the uncertainties in their parameters.

References

Backus, G.E., Long-wave elastic anisotropy produced by horizontal layering, *J. Geophys. Res., 67*, 4427-440, 1962.

Backus, G.E., A geometrical picture of anisotropic elastic tensors, *Rev. Geophys. Space Phys., 8*, 633-71, 1970.

Chernov, L.A., *Wave Propagation in a Random Medium*, McGraw-Hill, New York, 1960.

Christensen, N.I., Seismic properties of mantle xenoliths: clues to the interpretation of deep seismic observations beneath the kimberlite province of Yakutsia, unpublished manuscript, January, 1994.

Estey, L.H., and B.J. Douglas, Upper-mantle anisotropy: a preliminary model, *J.Geophys. Res.,91*, 11393-406, 1986.

Gaherty, J.B., and T.H. Jordan, Lehmann discontinuity as the base of an anisotropic layer beneath continents, *Science, 268*, 1468-71, 1995.

Gaherty, J.B., T.H. Jordan, and L.S. Gee, Seismic structure of the upper mantle in a central Pacific corridor, *J. Geophys. Res.*, in press, 1996.

Gee, L.S., and T.H. Jordan, Generalized seismological data functionals, *Geophys. J. Int., 111*, 363-90, 1992.

Grand, S.P., and D.V. Helmberger, Upper mantle shear structure of North America, *Geophys. J.R. Astr. Soc., 89*, 11465-75, 1984.

Goff, J., and T.H. Jordan, Stochastic modeling of seafloor morphology: inversion of Sea Beam data for second-order statistics, *J. Geophys. Res., 93*, 13589-608, 1988.

Karato, S., On the Lehmann discontinuity, *Geophys. Res. Lett., 19*, 2255-8, 1992.

Kawasaki, I., and F. Kon'no, Azimuthal anisotropy of surface waves and the possible type of the seismic anisotropy due to the preferred orientation of olivine beneath the Pacific Ocean, *J. Phys. Earth, 32*, 229-44, 1984.

Jordan, T.H., Structure and formation of the continental tectosphere, *J. Petrology, Lithosphere Issue*, 11-37, 1988.

Jordan, T.H., and J.B. Gaherty, Polarization anisotropy and small-scale structure of the continental upper mantle, *Proceedings of the 16th Annual Seismic Research Symposium*, PL-TR-94-2217, Phillips Laboratory, Massachusetts, pp. 189-95, 1994.

Jordan, T.H., and J.B. Gaherty, Stochastic modeling of small-scale, anisotropic structures in the upper mantle, *Proceedings of the 17th Annual Seismic Research Symposium*, PL-TR-95-2108, Phillips Laboratory, Massachusetts, pp. 433-51, 1995a.

Jordan, T.H., and J.B. Gaherty, Vertical shear-wave splitting in a heterogeneous, anisotropic medium, *Eos, 76*, F414, 1995b.

Mainprice, D., and P. Silver, Interpretation of SKS waves using samples from the subcontinental lithosphere, *Phys. Earth Planet. Inter., 78*, 257-80, 1993.

Revenaugh, J.R. and T.H. Jordan, Mantle layering from *ScS* reverberations, 3, The upper mantle, *J. Geophys. Res., 96*, 19,781-810, 1991.

Silver, P.G., Seismic anisotropy beneath the continents, *Annu. Rev. Earth Planet Sci., 24*, 385-432, 1996.

Silver, P.G. and W.W. Chan, Shear-wave splitting and subcontinental mantle deformation, *J. Geophys. Res., 96*, 16,429-54, 1991.

Su, W.-J., R.L. Woodward, and A.M. Dziewonski, Degree 12 model of shear velocity heterogeneity in the mantle, *J. Geophys. Res., 99*, 6945-80, 1991.

SEISMIC WAVE PROPAGATION IN SOUTHERN AND CENTRAL AFRICA

Charles A. Langston, Andrew A. Nyblade, and Ming Zhao
Department of Geosciences
Pennsylvania State University
University Park, PA 16802

Grant No. F49620-94-1-0031
Sponsored by Air Force Office of Scientific Research

ABSTRACT

Crustal and mantle structure within southern Africa have been investigated using regional waveform modeling. Pnl phases have been modeled to estimate crustal thickness, average velocity, and upper mantle P wave velocity within the Proterozoic mobile belts located around the Tanzania and Kalahari cratons. Crustal thickness and average velocity determined from Pl waveforms agree with previous refraction profile results in southern Africa. The Pn to Pl amplitude data require small or no upper mantle P wave velocity gradients for paths within the mobile belts. This simple uppermost mantle structure suggests that the process which compensates for the relatively high topography within the African Superswell is located below typical continental lithosphere.

Transition zone structure of the upper mantle is being investigated using data from GSN and IRIS/PASSCAL stations of the Tanzania Broadband Experiment. A moderate earthquake in South Africa produced spectacular recordings of triplicated body waves in the range of 18 to 26 degrees. Teleseismic modeling of the earthquake to infer source depth and mechanism yielded surprising differences in the actual depth (1 km) and inferred depth previously reported in the literature (12 km). This points out the problems that remain for regional seismic verification in relatively unknown areas even when high quality broadband data is available. We are using the source parameters inferred from the teleseismic and local data to model the upper mantle triplications seen across Tanzania. A notable aspect of the triplication data is the apparent strength and longevity of the 400 km discontinuity reflection travel-time branch out to 27 degrees distance.

keywords: regional body waves, Pnl, crustal structure, mantle P wave velocity structure, source parameters, southern Africa, mantle gradients, upper mantle triplications

OBJECTIVE

Study of regional waveforms from small seismic events is mandated by issues surrounding the Comprehensive Test Ban Treaty (CTBT). Detection and discrimination of small events will have to be accomplished using local or regional distance waveforms since these events will be difficult to be observed at teleseismic distance. Thus, it is essential that the characteristics of regional wave propagation in remote continental regions be known in order to infer source parameters which can be used to discriminate between naturally occurring earthquakes and possible clandestine explosions.

In this work, we study local and regional waveforms for events in southern Africa. We are interested in characterizing the nature of wave propagation in this area generally underlain by Proterozoic and Archean crystalline crust. Because of the influence of the East African Rift Zone and occurrence of the proposed African Superswell (Nyblade and Robinson, 1994), upper mantle structure may be significantly different than structure in other, well known parts of the world. Upper mantle structure affects the long range regional propagation of P and S waves and will affect the fundamental character of the seismic signature needed for inferring source parameters. Our work is concerned with modeling both crustal and mantle structure in this region and then using this knowledge to infer source parameters from naturally occurring events. Source parameters of interest in the CTBT context are source depth and focal mechanism, since these can be used in discrimination studies to support or refute the hypothesis that an event is actually a clandestine explosion.

RESEARCH ACCOMPLISHED

Pnl Waveform Modeling

Broadband Pnl waves have been studied for determining crustal structure and uppermost mantle structure in Proterozoic terrains in southern Africa. The results of this study have been recently published (Nyblade et al, 1996), so they will not be described in detail here. The general result was concerned with inferring the P wave upper mantle velocity gradient by using Pn to Pl amplitude ratios and waveforms. It was found that the uppermost mantle in Proterozoic terrains associated with the African Superswell could be explained by structure with little to no positive or negative velocity gradient with depth.

The Pl wave was also used to infer average crustal structure through a grid search of velocity models and resulting Pl waveforms. Waveforms were computed and compared to the data Pl wave using a cross correlation measure of fit. A starting crustal structure was perturbed systematically in the grid search and Pnl waves computed using a wavenumber integration method. The grid search was an effective way to invert for structure since the resulting correlation factors could be used to examine the tradeoff between the crustal parameters of average crustal velocity, Poisson's ratio, and crustal thickness. A similar grid search was used to infer upper mantle velocity structure by modeling a simple parameterization based on piecewise continuous velocity gradients.

Source Parameter Inversion

One of the main purposes for studying the effect of structure on wave propagation is to subsequently use the known wave propagation to invert for source parameters. Source parameters of interest to the CTBT include source depth, source mechanism, and source time function. Each is one piece of information that can be used to discriminate earthquakes from explosions. Events which are inferred to be located deeper than a few kilometers would naturally preclude man-made explosion sources because of the technical difficulties of emplacing explosions at those depths. Source mechanism can subsequently be used to exclude the possibility of explosive sources at shallow depths if

there are well-developed nodal planes in the P wave radiation pattern or if clear dilatational arrivals are observed at many stations. Source time function can be used as a secondary indicator of the type of source since relatively low-frequency, long-duration source time functions would not be plausibly expected for small explosions. Inferring all of these parameters relies on knowledge of the nature of wave propagation through local and regional earth structure.

As a case in point, we are examining a moderate earthquake which occurred in the center of the Kalahari craton in South Africa (Oct. 30, 1994), Figure 1. This mb 5.7 event was initially studied by Fan and Wallace (1995) using two local broadband seismographic stations. They performed moment tensor inversion using the three-component data and determined the focal mechanism and depth. The mechanism was pure normal faulting on north-south fault planes, dipping 14 degrees to the east or 76 degrees to the west. Source depth was inferred to be 12 km. We are interested in this event since it produced spectacular recordings of upper mantle triplications across the Tanzania Array (see below). Depth, mechanism and time function are essential parameters needed in modeling the upper mantle triplication data.

However when using these previously determined source parameters in creating synthetic seismograms, it was quickly seen that the source depth of the event was grossly over-estimated which, in turn, produced inappropriate teleseismic waveforms. Fan and Wallace (1995) showed credible waveform fits for the local data so we collected all available teleseismic data to investigate depth, mechanism and time function parameters in an independent study.

Figure 2 shows the results of a grid search focal mechanism study of all available P, SV, and SH first motions. The data come mostly from teleseismic distances but also include the local waveforms at LBTB and BOSA used by Fan and Wallace (1995). The mechanism is not particularly sensitive to source depth for this data set and shows a result similar to Fan and Wallace's (1995) result, except that the dips of the possible fault planes are now reversed for these normal faults.

However, the most important parameter to affect teleseismic waveforms is source depth. Figure 3 shows that the observed teleseismic P waveforms are impulsive and two-sided. Direct P and the surface reflections pP and sP undergo destructive interference early in the waveform to produce an explosion-like waveform (except for the dilatational polarities). This waveform can be effectively modeled using a point source at only 1 km depth with a symmetric time function approximately 1 sec in duration (Figure 3).

This result was quite surprising since 1 km depth can produce significantly different local waveforms than from a 12 km depth source. Langston (1987; 1994) showed that a common characteristic of local/regional P waveforms was the occurrence of sPmP phases which tend to be as large or larger than direct P or PmP phases. In fact, sPmP can be used to constrain source depth quite well even from data recorded at a single station. A synthetic study of this problem showed that Fan and Wallace's (1995) result was obtained by finding a local minimum in the inversion where their focal mechanism produced a nodal sPmP phase. Indeed, a careful look of the P waveform at BOSA station shows the first motion to be clearly dilatational with the bulk of the P arrival being compressional, and under the interpretation presented here, composed of sPmP. BOSA is just at the cross-over distance of Pn and PmP with Pn arriving first by a second. Figure 4 shows the fit between observed and synthetic waveforms at BOSA station for the mechanism and source depth inferred from the teleseismic data. Synthetic waveforms were computed using wavenumber integration for a plane layered crust over mantle.

Overall, the source mechanism is not significantly different between the two modeling attempts. Both yield a normal fault mechanism for north-south nodal planes. The preponderance of dilatational arrivals observed from the event would preclude it being interpreted as an explosion. However, a strong impulsive source at 1 km depth is very interesting in terms of the CTBT and it would have to undergo closer scrutiny in other circumstances. It is also significant that this event occurred near the gold mining

district in South Africa which may make it yet more provocative as a possible underground explosion. The lesson gained from this exercise is that interpretation of broadband waveforms must be done with all available data and with great attention to detail, as in the case of using the observed dilatational arrival of Pn in the focal mechanism inversion.

Upper Mantle Triplications within Africa

The original purpose of modeling the source of the South African event was to obtain source parameters useful for computing synthetic seismograms between 16 and 27 degrees. This event occurred during the deployment of an IRIS/PASSCAL experiment in Tanzania, East Africa. Figure 1 shows the location of the stations which cross the Tanzanian craton between the branches of the East African Rift Zone. Figure 5 shows displacement P waveforms recorded by the array displayed in a time-distance record section.

We are currently using these data to infer structure near the 430 km and 670 km upper mantle discontinuities. The data clearly show triplications associated with the two discontinuities. Arrival times for direct P are fast, relative to the IASPEI 91 model, for waves turning near 400 km and normal for waves turning under 670 km. Of particular note in these data is the large arrival associated with reflection from the 430 km discontinuity. This reflection is quite large and clear, relative to direct P, even at 27 degrees (station LONG on Figure 5). The consistency and amplitude of this phase suggests a structure similar to that inferred by King and Calcagnile (1976) for western Russia where the 430 km discontinuity is large with little P wave velocity gradient just above it. Ryberg et al (1996) also show data from the Deep Seismic Sounding "Quartz" profile in northern Eurasia which display similar high amplitude reflections from the 430 km discontinuity. We are modeling these data with travel time and waveform matching techniques to investigate this deeper structure compared to our first studies of the uppermost mantle using Pnl phases.

CONCLUSIONS AND RECOMMENDATIONS

There are vast continental areas where little is known of local and regional wave propagation effects, southern and central Africa being a prime example. These areas must be explored from a seismological point of view to gain the necessary knowledge of structure effects in wave propagation to be able to infer source parameters from small sources there.

Pnl waveforms from earthquakes in southern/central Africa are proving to be a useful reconnaissance tool for inferring average crustal structure and the nature of mantle velocity gradients in the uppermost mantle. Proterozoic crustal terrains are characterized by smaller positive mantle gradients, if any, compared to Archean terrains (Nyblade et al, 1996; Clouser and Langston, 1990) and remain consistent with heat flow models of old lithosphere in the area (Ballard and Pollack, 1987). Our Pnl results also suggest that little lithospheric erosion has occurred under southern Africa by upwelling asthenosphere and that compensation for the topography under the African Superswell must be occurring at relatively large depths in the upper mantle.

Inversion of regional broadband waveforms is a function of both knowledge of local crustal structure and careful consideration of all available data. Determination of detailed source parameters from the Oct. 30, 1994, South African earthquake became unambiguous when teleseismic data were added to the problem. The event proved to be very shallow and, hence, suspicious from a CTBT point of view. More detailed work is needed to investigate crustal and upper mantle structure in the area to more fully understand the local/regional waveform. Based on this study and past studies of

broadband regional waveforms (Langston, 1994;1995), more work on regional wave propagation is needed in most areas of the world.

Upper mantle triplications in southern Africa suggest unique structure at depth, particularly associated with the 430 km discontinuity. Structure of the upper mantle is important from a tectonic viewpoint where it is related to large scale mechanisms of uplift of the African Superswell and from a practical, wave propagation viewpoint, where it plays an important role in shaping the near-teleseismic waveform. Such studies are becoming possible as Africa becomes the site of more broadband GSN stations and the focus of a number of special passive seismic experiments.

References

Ballard, S., and H. N. Pollack (1987). Diversion of heat by Archean cratons: a model for southern Africa, *Earth Planet. Sci. Lett. 85*, 253-264.

Clouser, R.H., and C.A. Langston (1990). Upper mantle structure of southern Africa from Pnl waves, *Jour. Geophys. Res., 95,* 17,403-17415.

Fan, G., and T. Wallace (1995). Focal mechanism of a recent event in South Africa: A study using a sparse very broadband network, Seism. Res. Lett., 66, 13-18.

King, D.W., and G. Calcagnile (1976). P-wave velocity in the upper mantle beneath Fennoscandia and western Russia, *Geophys. J. R. astr. Soc., 46*, 407.

Langston, C.A. (1987). Depth of faulting during the 1968 Meckering, Australia, earthquake sequence determined from waveform analysis of local seismograms, *Jour. Geophys. Res., 92*, 11, 561-11,574.

Langston, C.A. (1994). An integrated study of crustal structure and regional wave propagation for southeastern Missouri, *Bull. Seism. Soc. Am., 84*, 105-118.

Langston, C.A. (1995). Anatomy of regional phases and source characterization of the Soviet Joint Verification Experiment, underground nuclear explosion, *Bull. Seism. Soc. Am., 85*, 1416-1431.

Nyblade, A.A., and S.W. Robinson (1994). The African superswell, *Geophys. Res. Lett., 21*, 765-768.

Nyblade, A.A., K. S. Vogfjord, and C.A. Langston (1996). P wave velocity of Proterozoic upper mantle beneath central and southern Africa, *Jour. Geophys. Res., 101*, 11,159-11,171.

Ryberg, T., F. Wenzel, J. Mechie, A. Egorkin, K. Fuchs, and L. Solodilov (1996). Two-dimensional velocity structure beneath northern Eurasia derived from the super long-range seismic profile Quartz, *Bull. Seism. Soc. Am., 86*, 857-867.

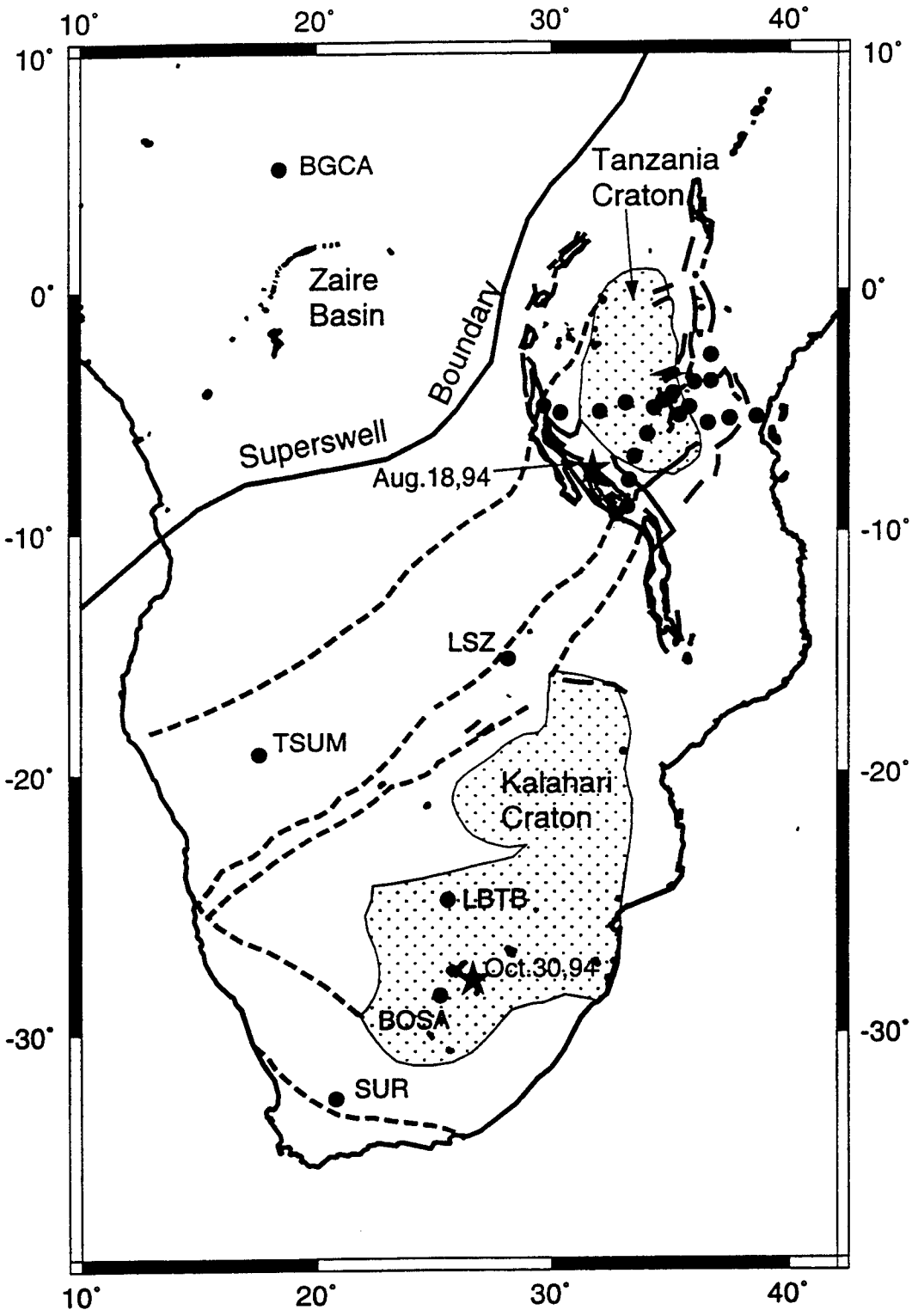

Figure 1 - Map of southern Africa showing the locations of seismic stations (filled circles) and the Oct. 30, 1994, event in South Africa. Also shown are the boundaries of the Tanzania and Kalahari cratons (stippled areas), boundaries of major Proterozoic mobile belts (dashed lines), and the boundary of the African Superswell (solid line).

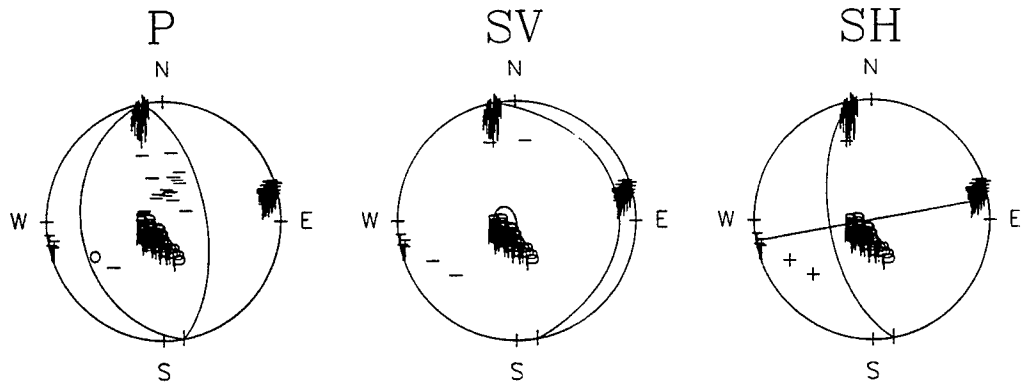

Figure 2 - Grid test results for the focal mechanism of the 30 October 1994 event. Teleseismic and local P, SV, and SH first motions were compared to theoretical double couple radiation patterns in 2.5 degree intervals in the orientation angles. The cluster of "P" (pressure), "I" (Intermediate), and "T" (tension) axes show the allowable variation in double couple orientation. First motion data are shown by "-" and "+". The lower hemisphere of the focal sphere is displayed.

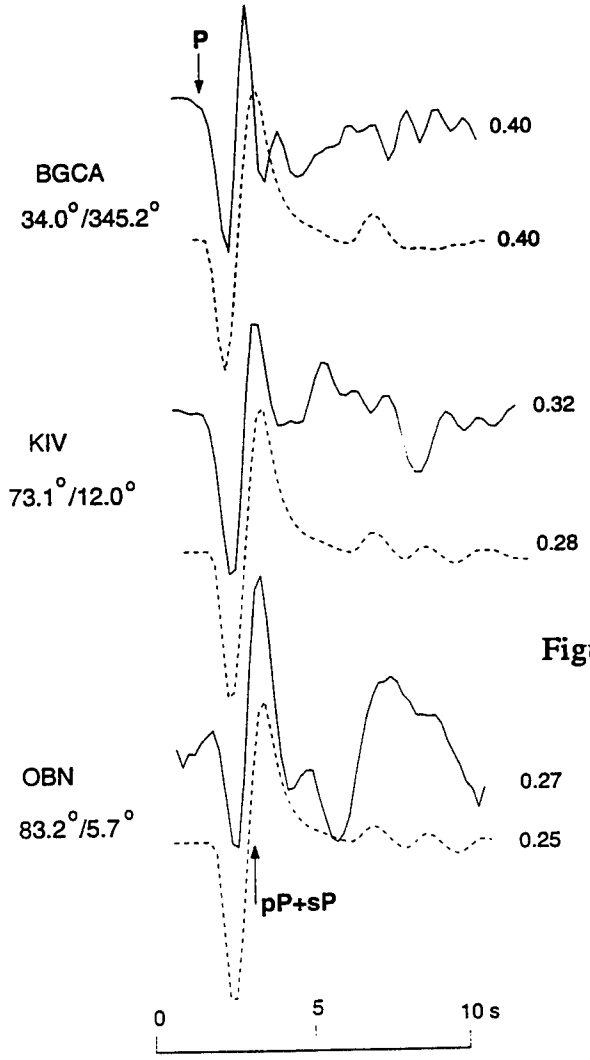

Figure 3 - Three teleseismic P waveforms from the 30 October 1994 event. Data are shown by solid lines and synthetics by dashed lines. The 1 km source depth produces extreme interference between direct arrivals and the near-source surface reflections.

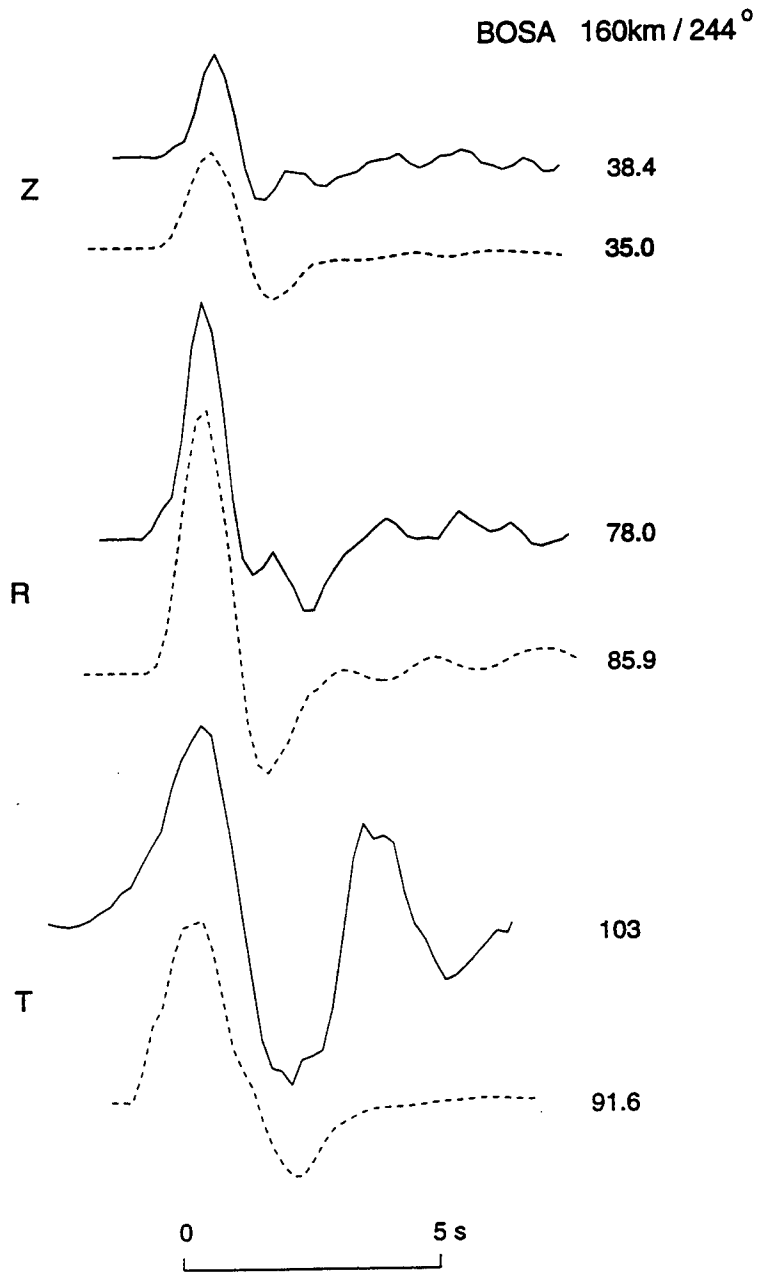

Figure 4 - Observed (solid lines) and synthetic (dashed lines) displacement seismograms at the local station BOSA for the 30 October 1994 event.

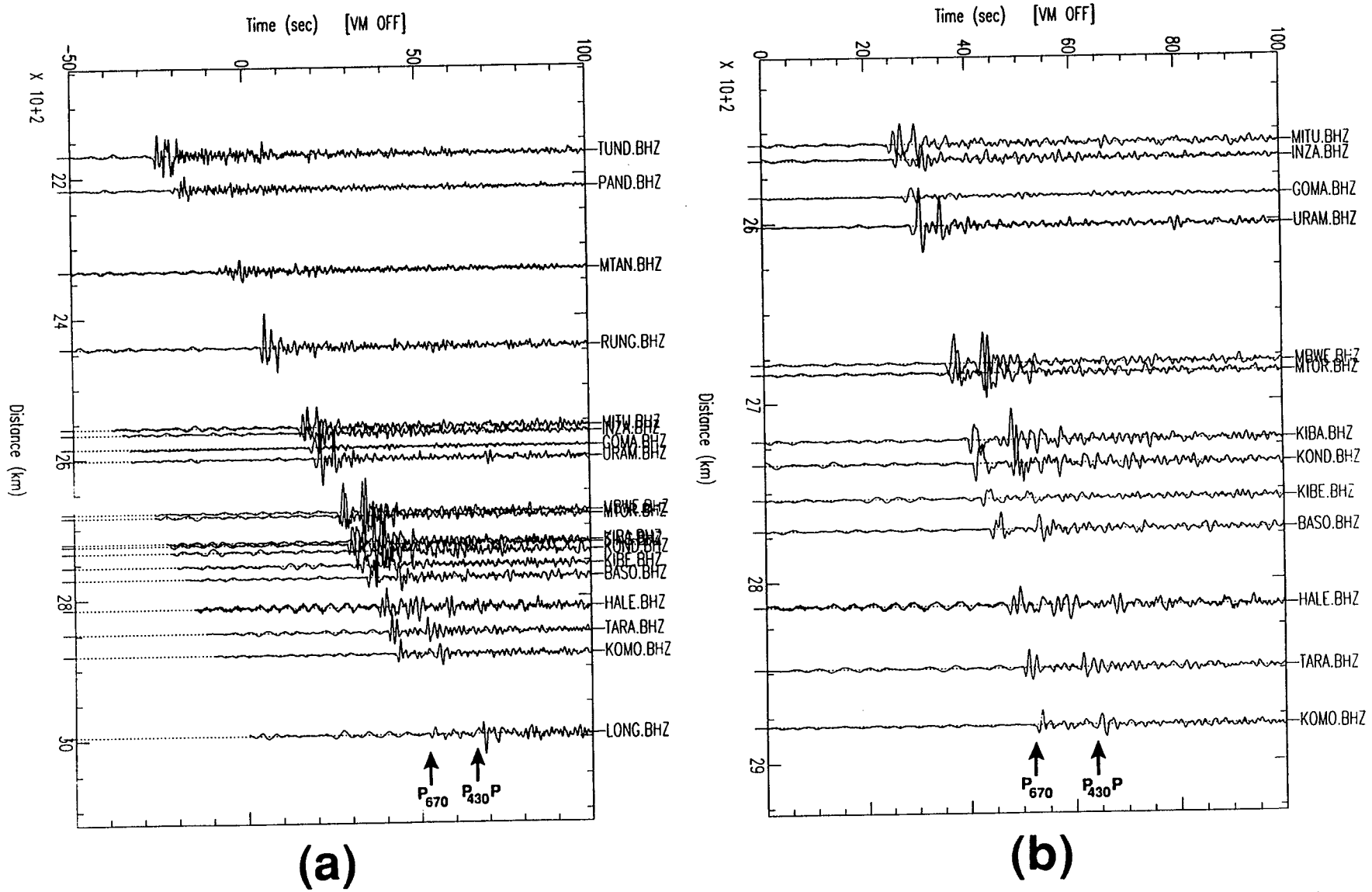

Figure 5 - Displacement waveforms recorded by the Tanzania Array from the 30 October 1994 earthquake. (a) shows the entire profile and (b) diplays the high-density area near the center of the profile. Note the prominent arrival branch from the 430 km discontinuity which continues out to 27 degrees (arrows). The Tanzania profile starts with the arrival bottoming above the 430 km discontinuity and ends with the turning ray from below the 670 km discontinuity.

ESTIMATION OF FINE-SCALE CRUSTAL HETEROGENEITY FROM SEISMIC EXPLORATION DATA WITH APPLICATIONS TO THE BASIN AND RANGE

A. LEVANDER, S. PULLAMMANAPPALLIL, S.P. LARKIN, L.M. LA FLAME,
RICE UNIVERSITY

J.A. GOFF
UNIVERSITY OF TEXAS INSTITUTE FOR GEOPHYSICS

CONTRACT NUMBER : F49620-94-1-0100
SPONSORED BY AFOSR

ABSTRACT : Fine scale velocity heterogeneity in the Earth's crust and upper mantle can modulate the response of wavefields transmitting through and backscattering from it, if the characteristic scales of the heterogeneity and the wavelengths in the illuminating field are comparable. Crustal seismic reflection data show surprisingly complicated crustal columns in a wide variety of geologic provinces. Much of the complexity observed in both seismic reflection sections and in large-aperture wide-angle reflection/refraction records can be synthetically reproduced using stochastic models of the Earth's crust superimposed upon deterministic, smoothly varying velocity models developed from refraction analysis. The stochastic models are developed from statistical analysis of geologic/petrophysical maps of exposures of upper, middle and lower crust. Here we report on a method we have developed to estimate the lateral scale lengths of crustal heterogeneity directly from seismic reflection data. We assume that the stochastic component of the velocity field can be described as a self-affine medium with a von Kármán autocorrelation function. The lateral characteristic length and the Hurst number can be estimated in the horizontal wavenumber-time (k_X-t) domain using a Monte Carlo optimization scheme to fit the observed spectra to a 1-D von Kármán function. The basic reflection dataset can be sorted into a number of different types of gathers, some of which are more suitable for heterogeneity estimates than others. Our synthetic tests show that the best datasets for estimation of lateral scales are common-offset sections and the CMP stacked and the CMP migrated sections. We have applied the k_X-t measurement to vibrator and explosion seismic reflection data from the Basin and Range province to estimate the lateral scales in the crustal column. Data acquired with the different source types in the same location produce similar estimates for lateral scale and Hurst number. We have estimated the lateral scale on an entire COCORP vibrator reflection section and found good agreement between measured scale length and the seismic reflection image.

Keywords : Estimation of seismic velocity heterogeneity, stochastic models, Basin and Range.

OBJECTIVE : Fine scale velocity heterogeneity in the Earth's crust and upper mantle can modulate the response of wavefields passing through it and backscattering from it if the characteristic scales of the heterogeneity and the wavelengths in the illuminating field are comparable. The now global seismic reflection database shows that the entire crust can be surprisingly complicated in geologic terranes as diverse as Phanerozoic mountains belts and the Precambrian cratons. Much of the heterogeneity observed in the seismic reflection sections ranges from the sub-kilometer scale to the few tens of kilometers scale length laterally, and to the few kilometer to sub-kilometer length vertically. These scales can severely affect seismic wavefields in the 0.5-30Hz band. Our objective is to produce geologically reasonable seismic velocity models of the crust, including the fine-scale heterogeneity using available geologic, petrophysical, and seismic evidence. These models can be used to determine the effects of crustal heterogeneity on regional distance wave propagation.

In the past we have constructed seismic velocity heterogeneity models for the crust using stochastic parameters estimated from geologic maps of exposed upper, middle, and lower crustal rocks. These crustal cross-sections produce synthetic seismograms which qualitatively match field observations. Here we are interested in the inverse problem, estimating the statistical parameters directly from seismic exploration data.

RESEARCH ACCOMPLISHED : Analyses of many geologic/petrophysical maps of exposed crustal rocks have shown that the fine-scale velocity structures can be described as two-dimensional self-affine media which can be specified by the 2-D von Kármán autocovariance function and a velocity probability density function, i.e., if the velocity field V(x,z) consists of a smoothly varying function $V_O(x,z)$, and a rapidly varying function $\delta V(x,z)$ then

$$V(x,z) = V_o(x,z) + \delta V(x,z) \qquad (1)$$

where $V_O(x,z)$ is the long wavelength "average" velocity field measured by the conventional seismic refraction experiment (which we assume lacks first order discontinuities) and the vertical derivative of $\delta V(x,z)$ is the heterogeneity imaged in the conventional seismic reflection experiment. $\delta V(x,z)$ can be modeled using the 2-D von Kármán function and an appropriate velocity probability density function (Holliger and Levander, 1992; Holliger et al., 1993; Levander et al., 1994). The 2-D von Kármán function requires 3 parameters, the horizontal and vertical characteristic scales a_X and a_Z, and the Hurst number, ν, which is related to the fractal dimension, D, by $D=E+1-\nu$, where E is the Euclidean dimension (Goff and Jordan, 1988). The fundamental seismic reflection model of the subsurface is the Primary Reflectivity Sequence or PRS (Claerbout, 1985; Gibson and Levander 1990). This representation of the subsurface is a primaries only, vertical incidence reflection seismogram which is constructed from the vertical reflection coefficient series convolved with the seismic wavelet, but is unfortunately not a physically realizable image of the subsurface. The goal of much of seismic reflection data processing is to approximate the PRS. The reflection coefficient sequence, and therefore the PRS, retains the same lateral structure as the seismic velocity model from which it is derived, whereas the vertical structure of the reflection coefficient sequence is the vertical derivative of the underlying velocity model. The vertical structure of the PRS is further modulated by the seismic wavelet. We restrict the discussion to two dimensional cases, with x the lateral coordinate and z the vertical coordinate. If R(x,z) is the reflection coefficient sequence in depth then :

$$\begin{aligned} R(x,z) &= \frac{d}{dz}\delta V(x,z) \\ R(x,t) &= R(x,t = z/V_o(x,z)) \\ P(x,t) &= W(t) * R(x,t) \end{aligned} \qquad (2\text{-}4)$$

where R(x,t) is the reflection coefficient sequence mapped to time, P(x,t) is the PRS, and W(t) is the seismic wavelet. Fourier transforming the above relations over the lateral coordinate show that the lateral spectra of the PRS and the velocity model are the same:

$$P(k_x,t) = W(t)*\frac{dt}{dz}\frac{d}{dt}\delta V(k_x,t) \qquad (5)$$

Here we wish to estimate a_X and ν from the lateral spectrum of some gather of seismic data, $S(k_X,t)$, using the seismic data as a proxy for $P(k_X,t)$. Estimation of a_Z is more complicated, as it requires knowledge of the seismic wavelet W(t), a notoriously difficult problem in land data, as well as implies an integration of the reflectivity series. We assume that the lateral power spectrum of the seismic data is identical to that of the PRS, and that the lateral spectrum of the PRS is described by the 1-D von Kármán power spectrum

$$S(k_x,t) \sim P(k_x,t) \qquad (6)$$

$$P(k_x,t) = \frac{\Gamma(2\nu)a_x}{2^{2(\nu-1)}\Gamma^2(\nu)(1+k_x^2a_x^2)^{\nu+1/2}}G(t) \qquad (7)$$

where G(t) contains the time dependence in the PRS. From this expression a_X and ν are estimated using a Monte Carlo based process called simulated annealing which minimizes the difference between the mean squared observed and calculated spectral values (Bohachevsky et al., 1986; Rothman, 1985). Equation (7) assumes a continuous random field, but suitable mappings exist to transform a_X and ν to values appropriate for the discrete random fields frequently found in the crust (Goff et al., 1994). In practice the spectral estimates are averaged over time windows in the data:

$$S(k_x,t_o) \sim \int_{t_0-\Delta t}^{t_o+\Delta t} dt \frac{\Gamma(2\nu)a_x}{2^{2(\nu-1)}\Gamma^2(\nu)(1+k_x^2a_x^2)^{\nu+1/2}}G(t) \qquad (8)$$

We first conducted a series of synthetic tests to determine which types of gathers produce the most reliable measurements of a_X and ν, by generating three synthetic seismic reflection experiments over three stochastic velocity models in which we changed the lateral characteristic scale, a_X, from 200m to 1000m to 2000m, and left the vertical scale constant at 200m. The stochastic target zone consisted of a binary 1:1 self-affine medium with velocities of 6.0 km/s and 6.3 km/s. The numerical experiment geometry is shown in Figure 1. The source spectrum was centered at 27Hz, with a bandwidth from 12-60Hz, corresponding to wavelengths of 500-100m. The finite-difference grid spacing was 20m. We then processed the data to form the commonly analyzed data gathers (NMO corrected common shot gathers, common offset gathers, CMP sections, and migrated CMP sections) for estimation of a_X and ν. We also verified that analysis of velocity model and the PRS for each model did indeed reproduce the lateral power spectrum of the 1-D von Kármán function. The results are summarized in Pullammanappallil and Levander (1996). First we note that the smallest lateral scale, 200m, was not well estimated even from the PRS. The most important result is that for the two larger characteristic scales (1000m and 2000m), common offset and CMP stacked and migrated sections can be used to estimate the both the characteristic scale within 25% and the Hurst number within 25%. Whether the shorter characteristic scale (200m) is not well estimated because the medium is isotropic, or because the bandwidth of the illuminating field overlaps this scale is not clear. Additional, less complete, numerical experiments

suggest that both the anisotropy of the medium, and the wavelength to scale length ratios play a role.

We applied this analysis tool to seismic reflection data from the Basin and Range province. Vertical incidence seismic data from the northern Basin and Range Province are often characterized by a transparent upper crust, a highly reflective midcrust, a slightly less reflective lower crust, and a strong reflection from the Moho transition which is up to a second in thickness. The COCORP 40°N transect - Nevada Line 2 is part of a vibrator-source seismic survey crossing the northern Basin and Range Province which has been processed and interpreted previously (Klemperer et al., 1986; Allmendinger et al., 1987: Hauge et al., 1987) We have recently reprocessed this line at Rice (La Flame et al, 1995). These data are interesting because they are nearly coincident with a joint vertical-incidence to wide-angle reflection/refraction explosive-source experiment (the PASSCAL Basin and Range Experiment) conducted in the same area in 1986.

Interpretations of these two datasets previously produced somewhat contradictory models of the crust in the Basin and Range. One COCORP CMP section is a single fold near-trace CMP section, which shows a pair of bright reflectors at the base of the crust, whereas the stacked CMP stacked section shows a broad zone of reflectors from 9.5-10.5s two-way-time (TWT), as opposed to two distinct bands of reflectivity. Neither of the earlier vibrator CMP stacked sections showed the bright or continuous middle crustal reflectivity which is apparent in a short-offset densely recorded dynamite shot from the PASSCAL Basin and Range experiment. Reprocessing the vibrator data, and paying greater attention to surface related noise phenomena, produced an image that is more consistent with the patterns seen in the limited explosion data (Figures 2 and 3). This suggests that we can reprocess the entire COCORP Basin and Range dataset to estimate crustal fabric at the regional scale, a task which we have undertaken.

We applied the k_X-t analysis to the middle crustal reflections in both the explosion and vibrator reflection data from roughly the same location (Figure 2a). The 4.0-6.5s reflective zone produces $a_X = 250\pm30$m and $\nu = 0.4$ (D=2.8) from the vibrator data and $a_X = 240\pm50$m and $\nu = 0.6$ (D=2.7) from the explosion data (Figure 2b). We thus get very similar estimates for a_X and ν from two very different datasets that sample the same region of the crust, demonstrating that the parameter estimation is reliable and is independent of source type. (Similar measurements on white fields produced $a_X = 31$m, equivalent to the trace spacing). Since these two datasets are not exactly coincident, this also suggests that we are making reliable measurements on middle crustal reflections that have propagated through a "transparent" upper crust, although it fails to tell us how the transparent crust is influencing our measure of a_X and ν.

Lastly we applied the k_X-t analysis in windows of 200 common midpoints (~10km) which overlap by half the window length to the entire middle and lower crustal image of Nevada-Line 2. The a_X values resulting from this analysis were gridded and are plotted as a contour map over the seismic section (Figure 3). The fractal dimension was nearly constant at 2.7-2.8 for the entire section. We note that the lower crust and Moho show the longest correlation scales, the transparent zone between the lower and middle crust the shortest scales, and the middle crust intermediate scales. The estimated scale lengths correspond well to the reflectivity patterns observed in the data. (Here we admit that our estimation technique applied to large datasets and the gridding are still rather primitive, and that some of the features in the contour map result from data truncations). We feel that we have developed a means of quantifying and displaying one measure of statistical heterogeneity in seismic reflection data which appears to be compatible with the reflection image, and which can be used to develop regional scale stochastic models.

Figure 4a displays a deterministic-stochastic velocity model for the northern Basin and Range. The transparent upper crust is modeled as felsic intrusions into a gneissic basement terrane. The horizontal and vertical characteristic scales for the upper crustal zone are 963 m and 817 m respectively, with a fractal dimension of 2.5, and a binary probability density function (pdf) of 67% fast (avg 6.0 km/s) and 33% slow (avg 5.7 km/s). These statistics were obtained from outcrop maps within the Chocolate Mountains of southeastern California. (Maps of this area show the effects of upper crustal Mesozoic plutonism, see Larkin et al., 1996). Seismic velocities are

taken from laboratory measurements of rocks with similar compositions and are consistent with the bulk velocities determined from upper crustal refractions.

High heat flow and volcanism in the Basin and Range indicate that mafic intrusions are likely to exist at several levels in the crustal column. These intrusions provide the impedance contrasts that produce high amplitude reflections. Rheological arguments suggest that these intrusions can have different orientations depending on the depth of emplacement, with horizontal intrusions preferring weak rheological boundaries, such as at the brittle/ductile transition and at the crust/mantle boundary (Parsons et al., 1992; Holliger and Levander, 1994). For these reasons we have developed a stochastic model of velocity heterogeneity consisting of either horizontally or vertically elongated high velocity bodies within a more felsic background. The zones having elongated horizontal bodies within the midcrust and at the Moho produce the observed high amplitude reflectivity. The mid and lower crust consists of dikes and sills with characteristic scales of 100 m and 300 m depending on orientation, a fractal dimension of 2.7, and a binary pdf of 25% fast (avg 6.8 km/s) and 75% slow (avg 6.5 km/s). The fractal dimension is consistent with that measured from outcrop maps of the Ivrea Zone in northern Italy, an area believed to expose extended and intruded lower crust similar to that in the Basin and Range (Holliger et al., 1993). Though we presently have no seismic constraints on the percentage of intrusives in the crust, we have chosen a a relatively small proportion of mafic intrusives to emphasize the importance of orientation in producing reflectivity. Average crustal velocities and gradients were obtained by averaging the results of previous refraction interpretations (e.g., Holbrook, 1991).

The velocity model described above was used to generate 2-D visco-elastic finite-difference synthetic seismic sections (Robertsson et al., 1993). For the vertical incidence simulations, the models were 20 by 36km with 20m grid spacing. The source pulse had an 18Hz center frequency. For the wide-angle simulations, the models were 210 by 36km with 60m grid spacing. The source had a 5Hz center frequency. The near-surface was modeled as a series of 2-D layered sedimentary basins. Average velocity within the near surface layer was 3.1 km/s with a gradient of 0.8 km/s/km and a Q of 50. Velocities were determined from travel time analysis; Q was determined from spectral ratios of the near-offset first arrival. Sedimentary layers were modeled as fractal bodies with horizontal and vertical characteristic scales of 6000m and 60m, respectively, a fractal dimension of 2.5 (the smoothest possible binary fractal fabric), and a binary pdf of 50-50% high and low velocities with velocity contrasts of 0.4 km/s. The results of the simulations are shown in Figures 4b and 4c. Compare Figure 2a showing a shot record (SP4B) from the 1986 PASSCAL seismic experiment, and Figure 4b showing the near-vertical incidence synthetic. Both show a reflective midcrust and a 1.0s thick Moho transition zone. No bulk change in velocity occurs at the onset of the reflective midcrust. A synthetic wide-angle record is shown in Figure 4c, and compares well with the large-aperture field data (not shown). A significant fraction of the energy in the record is the result of crustal scattering and basin reverberation.

CONCLUSIONS AND RECOMMENDATIONS : The k_X-t analysis provides stable measurements of the lateral characteristic scale and the fractal dimension of some stochastic media which are accurate to ±25% when applied to the CMP stacked section, the CMP migrated section, and common offset sections. At this point it is unclear whether the validity of the measurement is controlled by the anisotropy of the medium or the wavelength to characteristic scale ratio or both. The k_X-t analysis applied to the entire COCORP Nevada-Line2 CMP section produces a contour map of a_X which shows the largest characteristic scales associated with the zones of brightest reflectivity, and the shortest scales associated with the weakest reflectivity, in agreement with our expectations of the source of the reflectivity. We have therefore developed a seismic attribute map of an important statistical parameter of a stochastic medium. Our ability to estimate seismic velocity fabric from seismic data directly permits utilization of the vast global seismic reflection/refraction database to quantitatively classify the Earth's crust according to heterogeneity type.

The seismic modeling shows that a large fraction of the seismic wavefield observed in conventional seismic refraction profiles can be reproduced by scattering from wavelength scale seismic velocity heterogeneity. Moho reflections are modulated by 1) wavelength-scale fluctuations

on the transmission path, 2) heterogeneity near the Moho reflection point, and 3) reverberation in heterogeneous near-surface layers. The next issues to be resolved are the influence of complex overburden on statistical measurements made on signals from deeper targets, and the conditions under which the measurements are valid. Lastly we plan to model regional propagation (to ~2000 km) in realistic stochastic models of the crust, using the Basin and Range models as a starting point.

REFERENCES :

Allmendinger, R.W., Hauge, T.A.,Hauser, E.C.,Potter, C.J.,Klemperer, S.L.,Nelson, K.D., Knuepfer, P., and Oliver, J., Overview of the COCORP 40°N Transect, western U.S.A.: The fabric of an orogenic belt. *Geol. Soc. Am. Bulletin, 98*, 308-319, 1987.

Bohachevsky, I.O., M.E. Johnson, and M.L. Stein, Generalized simulated annealing for function optimization, *Technometrics, 28*, 209-217, 1986.

Claerbout, J.F., *Imaging the Earth's Interior*, Blackwell Scientific Publishers, Oxford, 1985.

B.S. Gibson and A.R. Levander, Apparent layering in CMP stacked images of two-dimensionally heterogeneous targets, *Geophysics, 55*, 1466-1477, 1990.

Goff, J.A., and T.H. Jordan, Stochastic modeling of safloor morphology: inversion of Sea Bsam data for second order statistics, *J. Geophys. Res., 93*, 13,589-13,608, 1988.

Goff, J.A., K. Holliger, and A. Levander, Modal fields: A new method for characterization of random seismic velocity heterogeneity, *Geophys. Res. Letters, 21*, 493-496, 1994.

Hauge, T.A., Allmendinger, R.W., Caruso, C., Hauser, E.C., Klemperer, S.L., Opdyke, S., Potter, C.J., Sanford, W., Brown, L., Kaufman, S., Oliver, J., Crustal structure of western Nevada from COCORP deep seismic reflection data. *Geol. Soc. Am. Bulletin, 98*, 320-329, 1987.

Holbrook, W.S., The crustal structure of the northwestern Basin and Range province, Nevada, from wide-angle seismic data. *J. Geophys. Res., 95*, 21,843 - 21,869, 1991.

Holliger, K., and A. R. Levander, A stochastic view of the lower crust based on the Ivrea Zone, *Geophys. Res. Lett., 19*, 1153-1156, 1992.

Holliger, K., A. Levander, and J. A. Goff, Stochastic modeling of the reflective lowercrust: petrophysical and geological evidence from the Ivrea Zone (northern Italy), *J. Geophys. Res., 98*, 11967-11980, 1993.

Holliger, K., and A. Levander, Lower crustal reflectivity modeled by rheological controls on mafic intrusions, *Geology, 22*, 367-370, 1994.

Klemperer, S.L., Hauge, T.A., Hauser, E.C., Oliver, J.E., and Potter, C.J., The Moho in the Northern Basin and Range Province, Nevada, along the COCORP 40°N Seismic Reflection Transect. *Geol. Soc. Am. Bulletin,* v. 97, 603-618, 1986.

La Flame, L.M., S.P. Larkin, and A. Levander, 1995, Crustal heterogeneity in the northern Basin and Range from PASSCAL and COCORP seismic data, *EOS, 76*, F400.

Larkin, S.P., A. Levander, D. Okaya, and J.A. Goff, The RISC seismic experiment: A deterministic and stochastic velocity model for the Salton Trough/Basin and Range transitiojn zone and constraints on magmatism during rifting, submitted to *J. Geophys. Res.*, 1996.

Levander, A., R. W. Hobbs, S. K. Smith, R. W. England, D. B. Snyder, and K. Holliger, The crust as a heterogeneous "optical" medium, or "crocodiles in the mist",*Tectonophysics, 232*, 281-287, 1993.

Parsons, T., Sleep, N.H., and Thompson, G.A., The role of magma overpressure in suppressing earthquakes and topography: Implications for understanding extending crust, *Tectonics, 11*, 1348-1356, 1992.

Pullammanappallil, S., and A. Levander, Estimation of crustal stochastic parameters from seismic exploration data, submitted to *J. Geophys. Res.* , 1996.

Rothman, D.H., Non-linear inversion, statistical mechanics, and residual statics estimation, *Geophysics, 50*, 2792-2807, 1985.

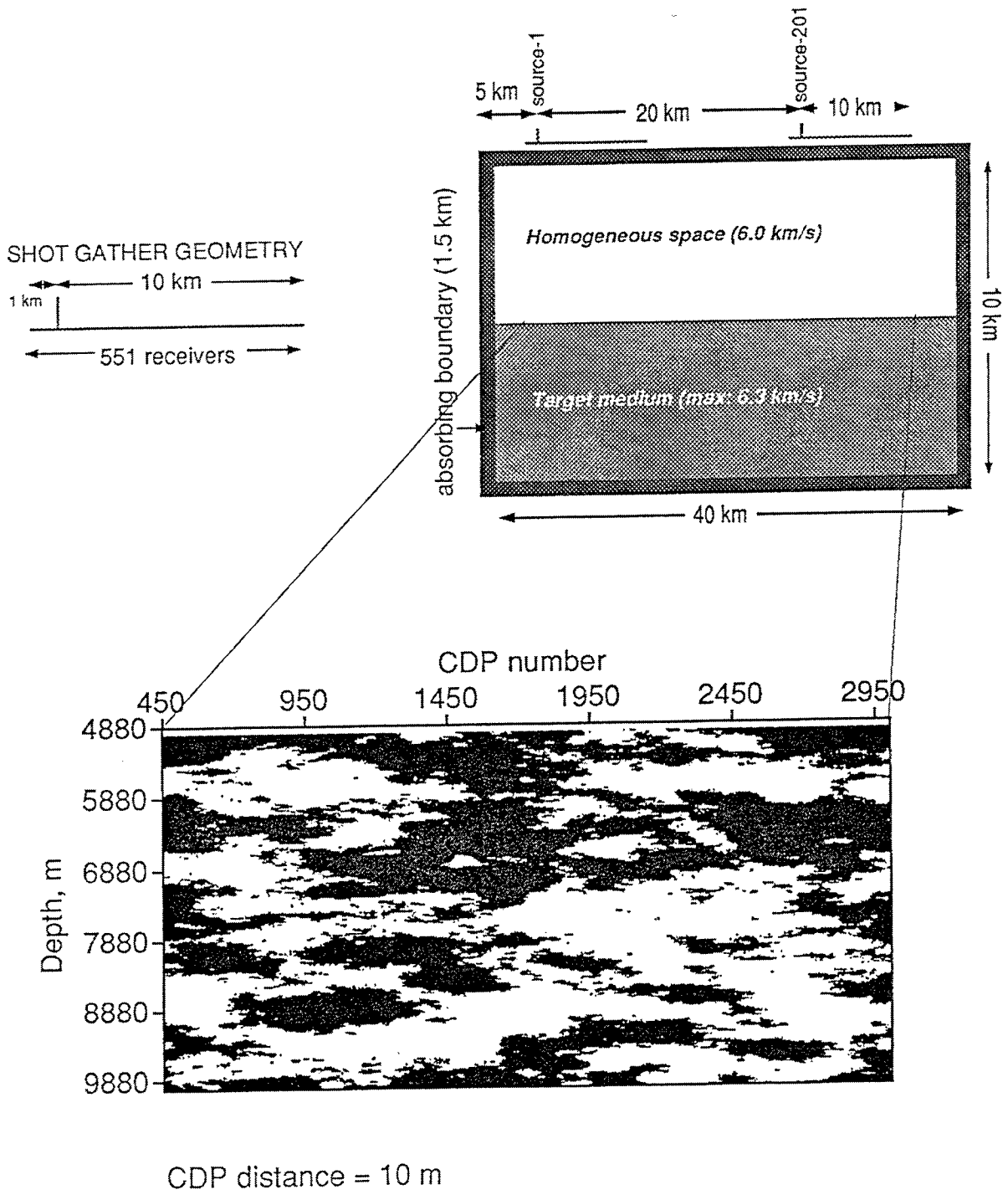

FIGURE 1 : 1a (Top) Schematic illustration of finite-difference model used for numerical experiments to measure lateral characteristic scale (right), and recording geometry used for data processing (left). 1b (Bottom) Realization of a_X=2000, a_Z=200, ν=0.3, 1:1 binary stochastic medium used in one numerical experiment. Black represents 6.3 km/s, white 6.0 km/s.

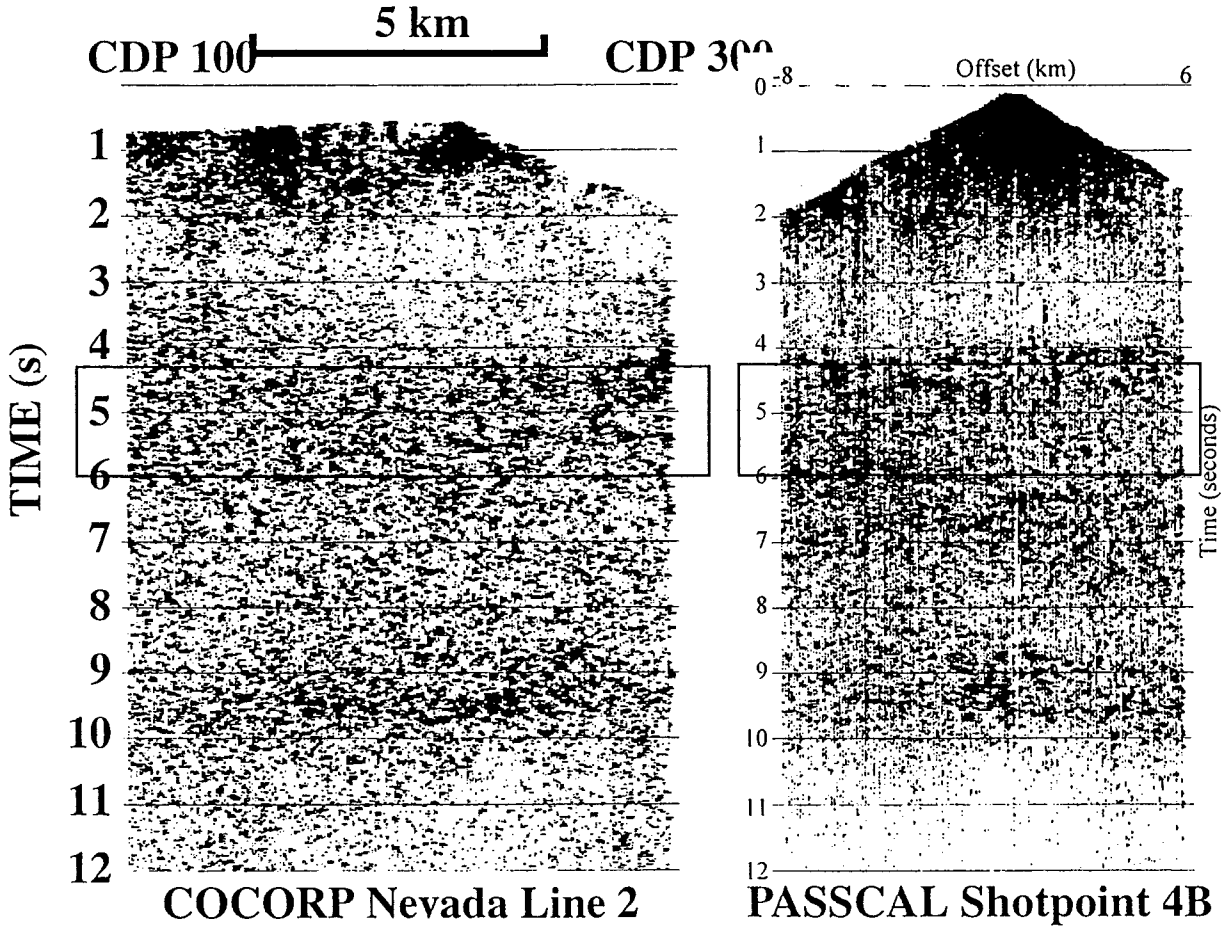

FIGURE 2: 2a (Left) Part of COCORP Nevada Line 2 CMP stacked section used to test lateral characteristic scale estimation. Middle crustal reflectivity extends from ~4.0-7.0s two-way-time, the Moho transition zone is from ~8.5-9.5s twt. Box shows analysis window in middle crustal reflectivity. 2b (Right) Nearly coincident PASSCAL SP 4B dynamite record used to test lateral characteristic scale estimation. Box shows analysis window in middle crustal reflectivity. Note that the sections are plotted at slightly different horizontal scales. Estimates of a_x and ν from the two datasets were nearly identical.

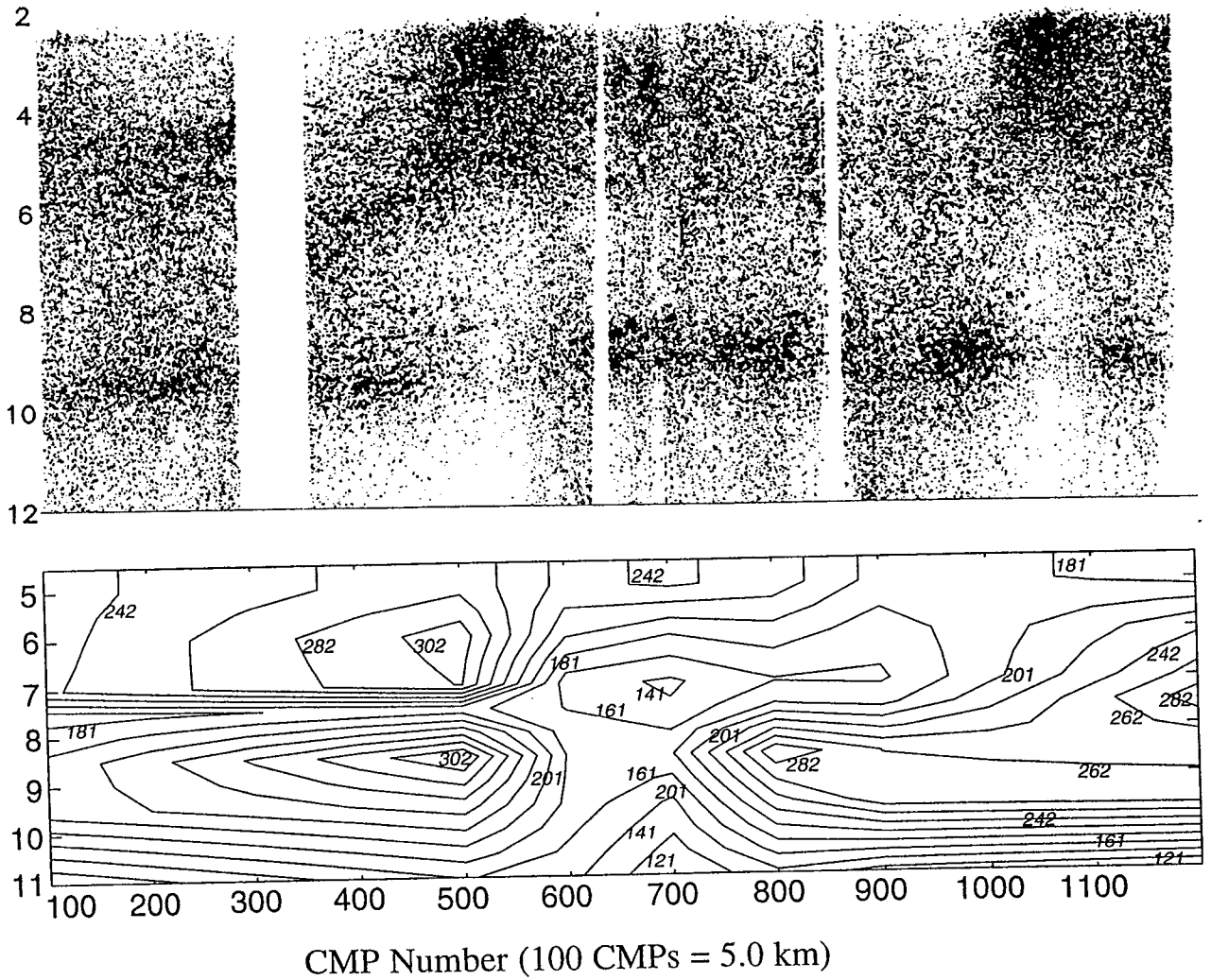

FIGURE 3 : 3a (Top) Entire COCORP Nevada Line 2 CMP stacked section from 2-12s two-way-time. The section extends approximately 55 km. Figure 2a is the leftmost part of this section. 3b (Bottom) Contour plot of a_x measurements made across entire section from 4-12s twt. The two displays are plotted at the same scale. Note that large a_x values correspond to the Moho transition and the middle crustal reflectivity. The small a_x values in the Moho transition zone near CMP 700 are from the no-data zones in the section.

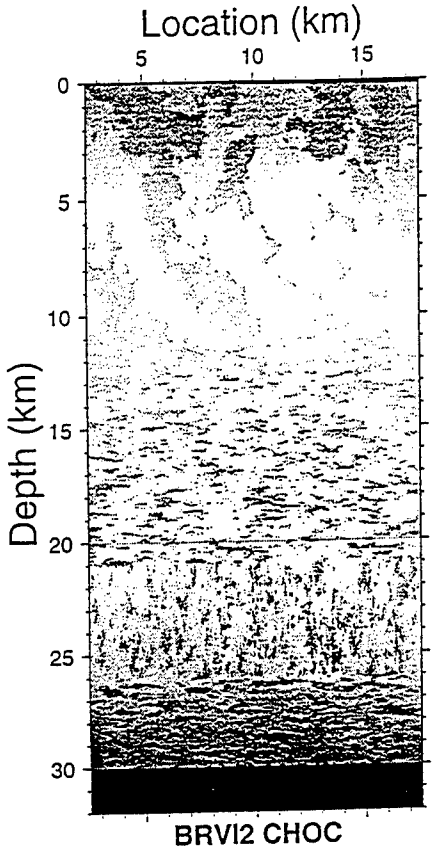

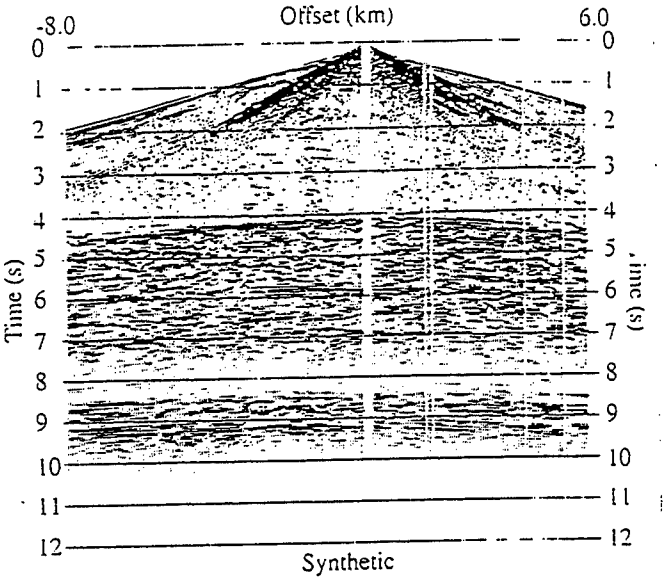

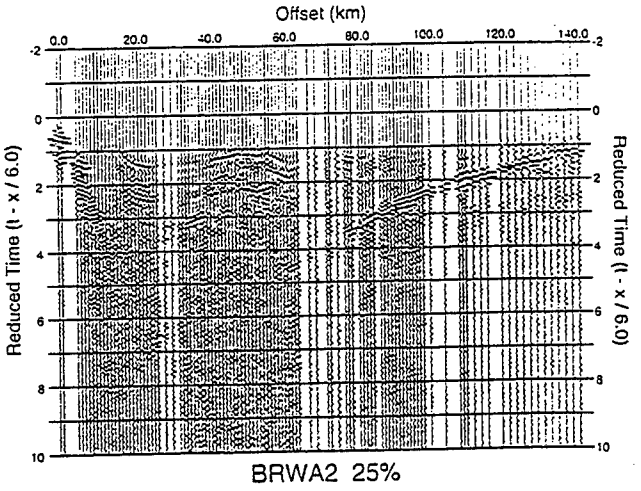

FIGURE 4 : 4a (Top left) Stochastic velocity model for northern Basin and Range derived from a_x measurements and inferred from geologic data. The deterministic velocity field is roughly the average of that derived from numerous refraction analyses of large-aperture data. 4b (Top right) Near vertical incidence synthetic shot record from the stochastic model. Compare to Figure 2b. 4c (Bottom right) Large-aperture synthetic shot record from deterministic-stochastic model.

Crustal Structure and Attenuation in Southern Tibet

James Ni, Chris Reese, and Jianxin Wu
Department of Physics, New Mexico State University
Las Cruces, NM 88003-0001

Lian-She Zhao
Institute for Geophysics, The University of Texas at Austin
8701 N MoPac Expressway, Austin TX 78759-8397

F49620-94-1-0310 and F19628-95-K-0009
Sponsored by AFOSR and DOE

ABSTRACT

High quality earthquake data collected by the INDEPTH-II Passive-Source Experiment show that there is a substantial south to north variation in the velocity structure of the crust beneath southern Tibet. North of the Yarlung-Zangbo suture, beneath the southern Lhasa block, a mid-crustal low velocity zone is revealed by Rayleigh wave phase velocities and modeling of the radial component of teleseismic P-waveforms. Conversely, to the south beneath the Tethyan Himalaya, no low velocity zone is observed. The existence of the mid-crustal low velocity zone in the north implies the existence of a partially molten, effectively fluid mid-crustal layer beneath the northern Yadong-Gulu rift and possibly much of the southern Tibet.

The attenuation characteristics of the crust beneath southern Tibet is determined from analysis of S-wave coda recorded at the INDEPTH-II broadband stations. A method for determinng Qc is developed which utilizes the coda spectrogram observed at a single station. The average S-wave coda quality factor for the southern Tibet is $Q_c(f) = (156 \pm 61)(f/f_0)^{1.11\pm0.19}$. The shear wave extinction mechanisms for the crust beneath the southern Tibetan plateau and the Tethyan and High Himalaya are dominated by intrinsic attenuation and scattering attenuation respectively. Additionally, the results are consistent with other measurements of Q_c in continental collisional environments which typically exhibit low values of Q_c at one Hertz and a strong dependence on frequency.

Keywords: Tibet, crustal structure, low velocity zone, attenuation.

OBJECTIVES

The Tibetan Plateau is the most spectacular result of the collision between the northward moving Indian continental lithosphere and the southern margin of Asia that began in the late Eocene (Molnar, 1988). Although much has been learned about the crustal and mantle velocity structure, mantle discontinuities, thermal and electrical properties, and surface manifestation of this collision zone, there is not an unified consensus on the answers to the dynamic processes and particularly on how the Tibetan crust gets thickened and to what extent the Indian shield and its continental margin underthrust beneath southern Tibet. Detailed information on the crustal and mantle structure of Tibet are still lacking and obtaining such infomation is crucial to further our understanding of the evolution of the Tibetan Plateau.

Most previous studies on the crustal and mantle sturcture of Tibet are from staions located outside of the Tibetan Plateau. Surface wave studies indicate that long-period Rayleigh wave dispersion data are consistent with a 70 km thick crust with low average shear wave velocity of about 3.5 km/s (e.g. Romanowicz, 1982; Jobert et al., 1985; Brandon and Romanowicz, 1986). Models presented in these studies suggest a possible low velocity zone in the crust. Chun and McEvilly (1986) found very low Rayleigh wave group velocities in the period range from 25 to 40 s and indicated that a prominent mid-crustal low velocity channel overlying a higher velocity lower crust in southern Tibet is required to fit the surface wave data. The discovery of the mid-crustal low velocity zone is significant because it not only gives clues to the thermal mechanical properties of the Tibetan crust, but also is fundamental to the understaning of the Neogene evolution of the Himalayas and Tibet. Although the seismic data indicate the existence of a low crustal velocity zone in southern Tibet, neither the location of the transition from a two-layered Himalayan crust to one with a low velocity channel nor the areal extent of the low velocity is well established. The INDEPTH-II broadband data offer a detailed picture of the south to north variations in crustal and mantle velocity structure beneath southern Tibet.

The coda waves of local earthquakes are an efficient tool for studying average crustal attenuation characteristics. In southern Tibet, Q_c at 1 Hz has been estimated to be about 100 to 200 (Jin and Aki, 1987). The INDEPTH-II broadband data are particularly suited for the determination of the crustal attenuation as a function of frequency. The purpose of the study was to constrain the nature of the coda wave attenuation mechanism in southern Tibet and quantify average crustal attenuation properties in terms of a frequency dependent coda quality factor.

RESEARCH ACCOMPLISHED

The 1994 INDEPTH-II Passive-Source Experiment yielded high-quality earthquake data with which to analyze the interaction between the Indian and Eurasian plates. A 15-station

passive recording array was deployed, extending from the High Himalaya to approximately 150 km north of the Zangbo suture (Figure 1). Nine of the stations were equipped with broadband Guralp CMG-3T seismometers with a usable frequency range of 0.01 Hz to 30 Hz; the remaining six stations were equipped with Mark Products 1 Hz L-4 seismometers. Each station had one data stream which continuously recorded 24 bit data at 50 samples per second. From May to October, 1994, approximately 200 earthquakes were recorded. Using these data we have examined the velocity structure of the crust beneath the INDEPTH-II survey by two independent methods: surface wave dispersion and P-waveform modeling.

Surface wave dispersion data were analyzed for a pair of stations north of the Zangbo suture. Pure-path long-period Rayleigh wave phase velocity dispersion data for a path north of the suture were obtained from seismograms recorded at station pair BB05-BB14 from the September 1, 1994, northern California earthquake. Two-station techniques were used to isolate the phase velocities of fundamental mode Rayleigh waves in the period range of 20-60 seconds (Figure 2). The California earthquake which originated from 103 degrees away and traveled along a mostly continental path is well dispersed. We infer that lateral variations within Tibet do not significantly affect the pure-path phase velocity calculations, because the observed particle motion of Rayleigh waves from the California earthquake has a back azimuth similar to that computed from the stations and earthquake location (Wu et. al., 1995).

The two-station phase velocity dispersion of the fundamental mode Rayleigh wave was computed using the programs developed by Robert Herrmann of St. Louis University. In the data analysis we first extracted the group velocity dispersion curve of the fundamental mode by applying a Gabor Transform to the recorded Rayleigh wavetrain. The fundamental mode Rayleigh waveforms were isolated from the recorded Rayleigh waves by applying a phase match filter. Once the fundamental mode waveforms at each station were obtained, we inverted for an initial earth model using interstation group velocities. A time domain cross correlation technique was then used to refine the phase velocities. We then inverted for a new earth model from the refined phases velocities. After four to five iterations the phase velocities can no longer be improved. We also tried to obtain the fundamental mode Love waves but were unsuccessful due to contamination by core phases. The error in the phase velocity is mainly contained in the computed interstation phase spectra and can be estimated by the same method used for calculating phase error of a frequency response function. In our study, the maximum and minimum phase velocity errors were found to be around 0.1 km/s and 0.01 km/s, respectively.

By minimizing the error between the observed and calculated phase velocities with an iterative least square method, we obtained a best fitting model for the crust between BB05 and BB14 (Figure 2). This model shows a 70 km thick crust overlying an upper mantle with a very fast shear-wave velocity of about 4.9 km/s. The crust is characterized by a low average shear-wave velocity of about 3.45 km/s (5.9-6.0 km/s in P wave), a 20 km thick mid-crustal low velocity zone of 3.0 to 3.1 km/s, and a high velocity lower crust. We note that 10 years

ago Chun and McEvilly, (1986) found very low Rayleigh group velocities in the period range from 23 to 40 s and indicated that a prominent mid-crustal low velocity channel overlying a higher shear velocity lower crust in the southern Tibet is required to fit the group velocity data. Jobert et al., (1985) inverted pure-path Rayleigh wave phase velocities for shear-wave velocity models in the suture region from data obtained by the Sino-French southern Tibet experiment in 1982. Their preferred model has an upper crust with an average velocity of 3.2 km/s, a possible crustal low velocity zone and a lower crust with a steep velocity gradient.

In a second examination of the crustal velocity structure, P-waveform modeling was undertaken using the method of Zhao and Frohlich, (1996) (SORVEC) in which a radial-component seismogram is calculated from vertical-component observations. This can then be compared iteratively with a large number of model-generated synthetic radial-component seismograms using a very fast simulated annealing method.

The INDEPTH-II array produced teleseismic recordings of sufficient quality from fourteen earthquakes with back azimuths between 45° to 157° and one with a back azimuth of 247°. The back azimuth coverage is not ideal. For each earthquake-station pair, the inversion was carried out on the recorded body waves and optimum four-layer and five-layer velocity models were obtained. All the available vertical- and radial-component waveform data for each station were merged into a single inversion, and an average model for each station was calculated (Figure 3).

The models for the stations north of the suture exhibit a distinct low velocity zone with a top at about 20 km depth. In general, the upper crust velocity is well constrained with an uncertainty of about $\pm$ 0.2 km/sec for shear-wave velocity. The uncertainty is somewhat larger at greater depths. The depth of the Moho is not tightly constrained, but clearly lies between 65 km and 80 km. South of the suture, beneath the Tethyan Himalaya, the modeling yields an average crustal thickness of about 70 km, and shows no mid-crustal low velocity zone. The velocity increases gradually with depth in the upper crust and more rapidly in the deep crust, with the lower crustal velocity gradient similar to that observed to the north (Figure 3).

A method for determining Q_c was developed which utilizes the coda spectrogram observed at a single station. The method utilizes the weak-single scattering expression of Aki and Chouet, (1975) for the coda power decay at long lapse times. The functional form for the coda quality factor is specified as $Q_c(f) = \alpha(f/f_0)^b$. At a particular station the coda power spectrogram $P(f,t)$ is calculated for a time window beginning at some lapse time $t > t_S$ where t_S the lapse time corresponding to the arrival of the S-wave. In practice the lapse time t is taken to be twice t_S. The coda quality factor $Q_c(f)$ is assumed to be independent of time throughout the time window. The model paramters (α, b) are estimated by minimizing the error surface in parameter space. The error function is taken to be the F-norm of the difference between the model coda power as a function of time and the observed coda spectrogram. The minimization algorithm employs a simplex search method that does not require any error function derivative information. Although no systematic grid search is

performed, convergence is robust with respect to perturbations from the starting model.

The frequency window used in this study was chosen on the basis of sufficient coda signal to pre-event noise ratio. The analysis of this ratio led to an important observation concerning the nature of seismic wave extinction in southern Tibet. An example of the coda signal spectra and pre-event noise spectra is shown for two events in Figure 4a. For lapse times of around 200 sec at station BB05, frequencies above 4 Hz in the coda signal are completely attenuated below the noise floor. This coda and noise spectra signature is typical of coda waves sampling the crust beneath southern Tibetan plateau north of the suture. On the other hand, Figure 4a also shows the coda and noise spectra for an event which samples mostly Himalayan crust. These spectra indicate that even at long lapse times the coda signal is well above the noise floor over the entire usable frequency band. In this sense, Figure 4a demonstrates that north of the suture intrinsic attenuation is the dominant coda attenuation mechanism while in the Tethyan and High Himalaya the scattering effect is important due to weak absorption.

An example of the inversion for the model parameters is shown in Figure 4b. The coda spectrogram and the model solution are plotted together. Such a calculation is performed for each station-event pair in the data set. Disregarding the difference in attenuation mechanism across the suture, the average coda quality factor for a six earthquake data set is

$$Q_c(f) = (156 \pm 61)(f/f_0)^{1.11\pm.19},\ 1 < (f/f_0) < 4. \tag{1}$$

This result is consistent with the calculations of Jin and Aki, (1987) who calculate Q_c at 1 Hz and plot contours of Q_c for mainland China. For southern Tibet, the authors report results in the range $100 < Q_c < 200$. A correlation between seismically active regions and low Q_c is also inferred (Aki, 1989). Constraining the differences in model parameters across the suture is difficult for this small data set. For events mainly sampling the crust in the southern Tibetan plateau, the average value of α is 135 while for the one piece of data sampling Himalyan crust, $\alpha \sim 250$.

This intrinsic attenuation of shear waves with frequencies above 4 Hz. beneath southern Tibet is consistent with various independent geophysical observations including reflection profiles, receiver functions, and magneto-telluric surveys which all indicate the existence of partial melt of a few percent in a mid-crustal layer at about 20-35 km. depth. On the other hand, the observed long duration of high frequency coda waves south of the suture indicates that in the Tethyan and High Himalaya, intrinsic attenuation is negligible and that the scattering mechanism is dominant. Thus, the suture can be interpreted as marking a seismic wave extinction mechanism boundary. A quantitative separation of intrinsic and scattering attenuation in this collisional environment is beyond the scope of this study.

CONCLUSIONS AND RECOMMENDATIONS

In summary, Rayleigh wave phase velocity dispersion, and P-waveform modeling give consistent, independent views of the velocity structure of the crust beneath the INDEPTH-II survey. North of the Zangbo suture there is a distinct low velocity zone in the crust, which dies out at the suture or a short distance north of the suture. The crust that lies within and north of the suture has a very low average shear-wave velocity of about 3.45 km/s. Our finding is consistent with the results of Zhao at al. (1996). The mid-crustal low velocity zone is also consistent with the Bouguer gravity data which indicate without a doubt that the middle Tibetan crust must be mushy (Jin et al, 1994). It is weak enough to decouple folding in the crust from that in the upper mantle. The attenuation of shear waves with frequencies above 4 Hz observed in local earthquake coda spectra indicates that absorption is the dominant attenuation mechanism in the crust beneath the southern Tibetan plateau north of the suture. The Moho, while not tightly constrained in these analyses, lies between 70 and 80 km depth along the length of the survey. As seismic velocity characteristically increases downward in crystalline continental crust, we infer that the low velocity zone north of the suture marks a partial melt zone developed within the middle crust of the Lhasa block. The prominent bright spots imaged on the INDEPTH-II CMP profiles coincide within resolution with the top of the mid-crustal low velocity zone delineated by the earthquake data, supporting their inference that this feature may represent an evolving intrusive boundary at the top of the partial melt zone. This mid-crustal low velocity zone has important implications for how the Himalaya and Tibetan plateau as a whole has evolved. The Neogene evolution of the Himalaya and mountains to the southeast of the Tibetan plateau can be viewed as the southward and eastward extrusion of the fluid middle crust underlying southern Tibet.

REFERENCES

Aki, K. and B. Chouet, Origin of Coda Waves: Source, Attenuation, and Scattering Effects, *J. Geophys. Res.* **80**, 3322-3342 (1975).

Aki, K., Deterministic and Stochastic Approaches in Seismogram Analysis, In *Observatory Seismology.* (ed. Litehiser, J.) (University of California Press, Berkeley 1989) pp, 257-265 (1989).

Brandon, G.B. and B.A. Romanowicz, A "No-Lid" zone in the central Chan-Thang platform of Tibet: evidence from pure path phase velocity of long period Rayleigh wave, *J. Geophys. Res.*, **91**, 6547-6564 (1986).

Chun, K. and T. V. McEvilly, Crustal structure in Tibet: High seismic velocity in the lower crust, *J. Geophys. Res.*, **91**, 10405-10411 (1986).

Jin, A. and K. Aki, Spatial correlation of coda Q with the long-term seismicity in China: Implication to the eastern and central U.S. long-term seismicity., Presented at the annual meeting of the Seismological Society of America, Santa Barbara, California, March 24-27, 1987.
Jin, Y., M. K. McNutt and Y. Zhu, Evidence from gravity and topography data for folding of Tibet, *Nature*, **371**, 669-674 (1994).
Jobert, N., B. Journet, G. Jobert, A. Hirn, and S. K. Zhong, Deep structure of southern Tibet inferred from the dispersion of Rayleigh wave through a long-period seismic network, *Nature*, **313**, 386-388 (1985).
Molnar, P., A review of geophysical constraints on the deep structure of the Tibetan Plateau, the Himalaya and the Karakoram, and their tectonic implications, *Trans. R. Soc. Lond.*, **A327**, 33-88 (1988).
Reese, C. and J. Ni, Attenuation of coda waves in southern Tibet, *Geophys. Res. Lett.*, submitted (1996).
Romanowicz, B. A., Constraints on the structure of the Tibet plateau from pure path phase velocities of Love and Rayleigh waves, *J. Geophys. Res.*, **87**, 6865-6883 (1982).
Wu, J. and J. Ni et al., *EOS, Transactions*, **76**, F392 (1995).
Zhao, L. S. and C. Frohlich, Teleseismic body-waveforms and receiver structures beneath seismic stations, *Geophy. J. Int.*, **124**, 525-549 (1996).
Zhao, L. S., M. K. Sen, P. Stoffa and C. Frohlich, Application of very fast simulated annealing to the determination of the crustal structure beneath Tibet, *Geophy. J. Int.*, **125**, 355-370 (1996).

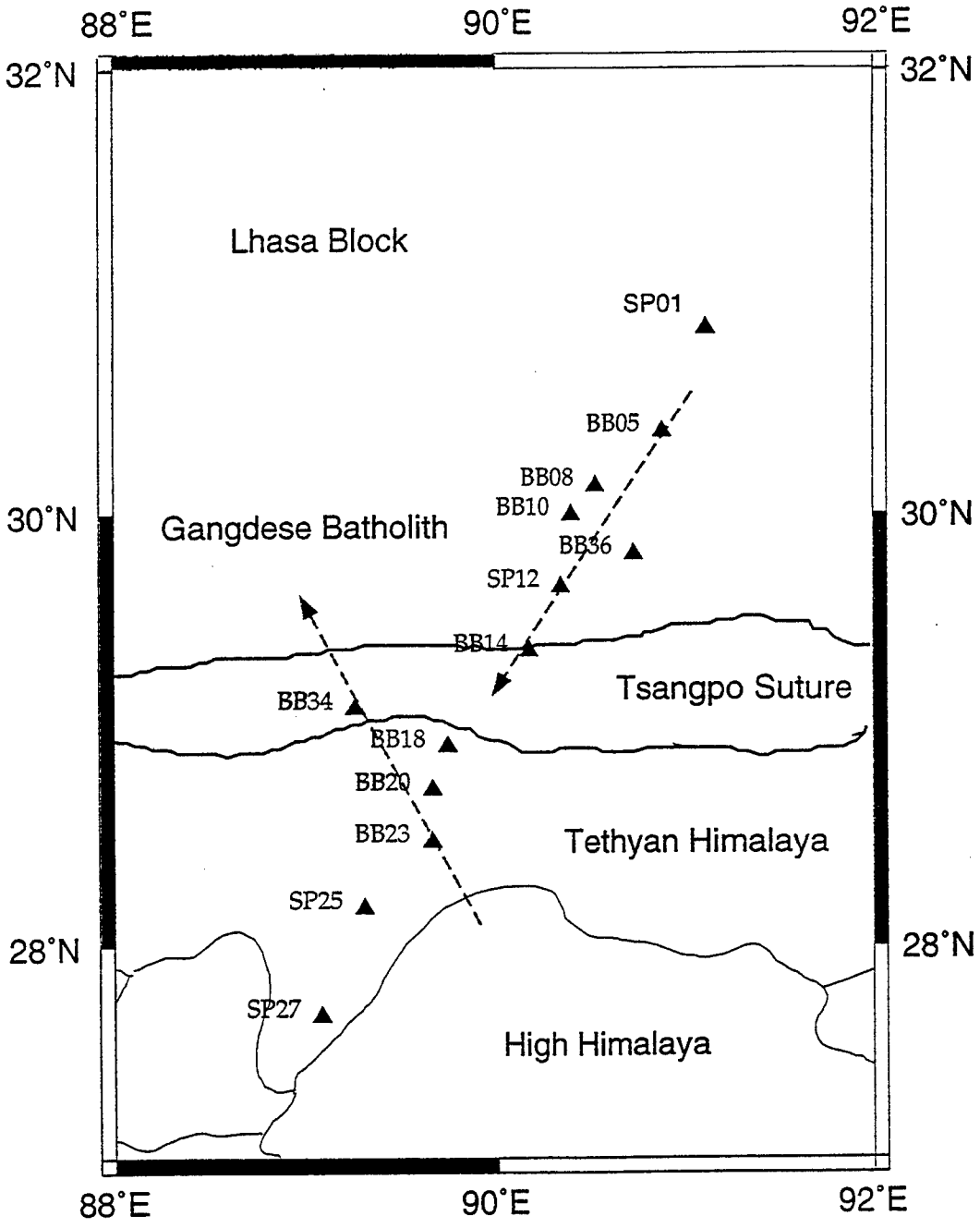

Figure 1. A map showing the INDEPTH-II array and simplified tectonic regions.

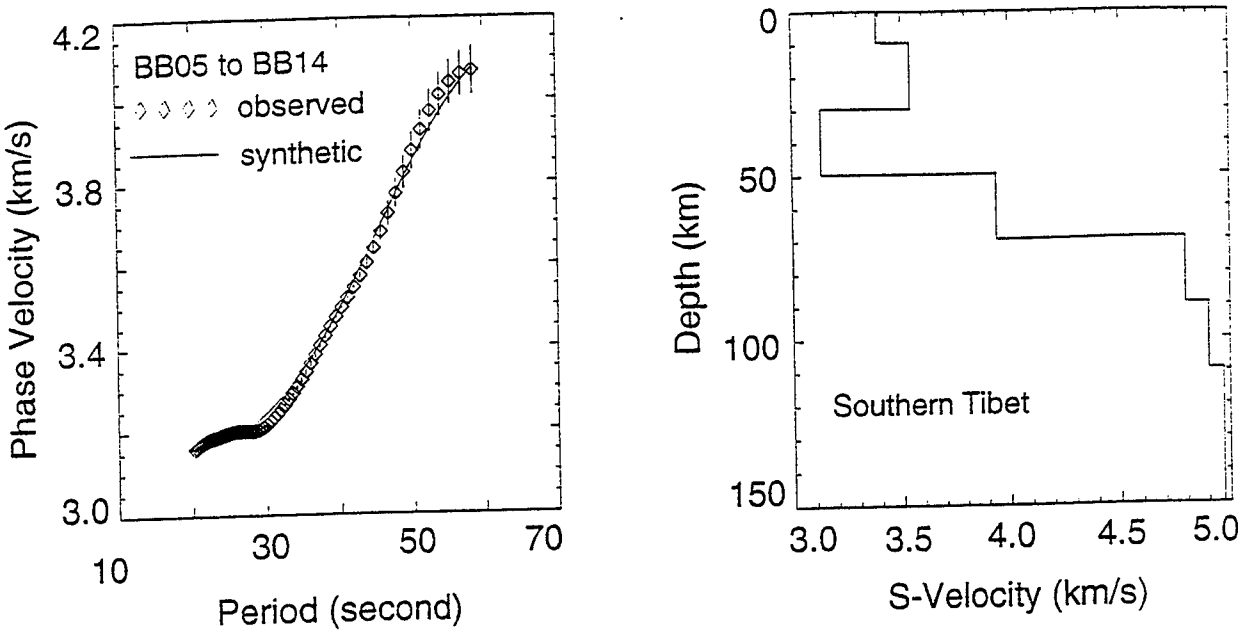

Figure 2. The fit between the observed and calculated phase velocities for the southern Tibetan Plateau are shown on the left. The vertical bars in the phase velocity plots represent errors. The best-fit model from the least squares inversion are shown on the right of the figure.

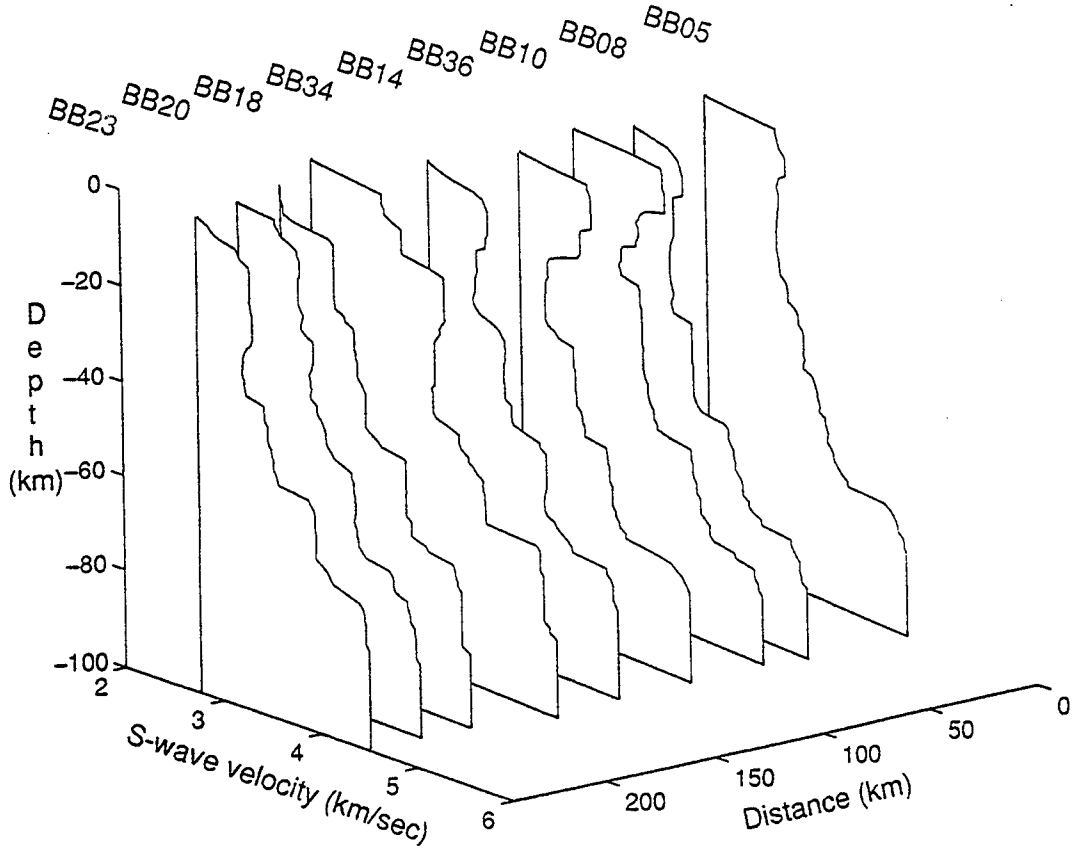

Figure 3. Cross-section summarizing main features of crustal shear-wave velocity along the profile from P-waveform modeling.

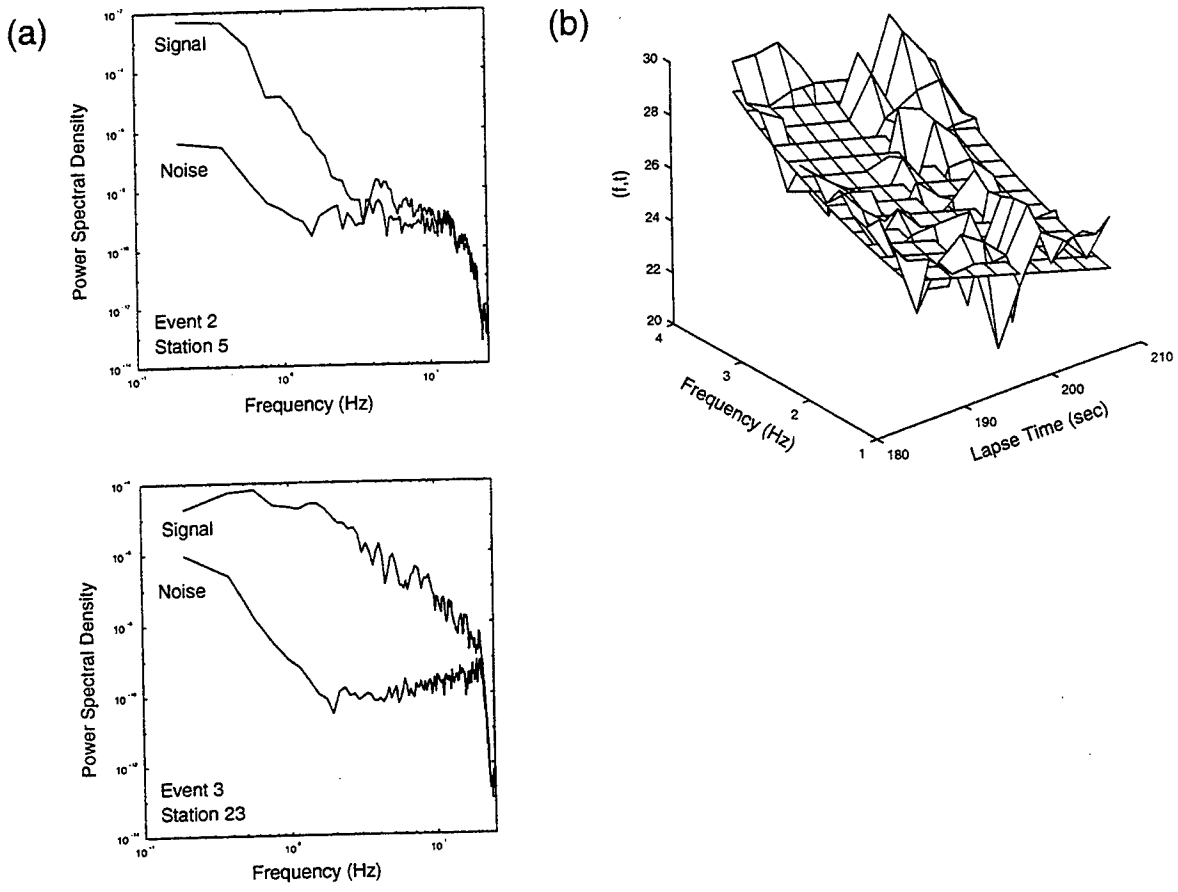

Figure 4. (a) An example of typical signal to noise ratios for stations 5 and 23. The power spectral density of the pre-event noise and the coda signal in the appropriate lapse time window are plotted together. (b) An example of the inversion for the model parameters. The model coda spectrogram and observed data are plotted together.

Structure of the Crust and Upper Mantle in the South Caspian Basin and Surrounding Region

Keith Priestley and Steve Mangino
University of Cambridge
Contract No. F19628-95-K-0017
Sponsored by DOE

ABSTRACT

This paper reports progress on determination of the crust and upper mantle velocity structure of the south Caspian basin and the central Iranian plateau using seismograms recorded on the Caspian Seismic Network operated by the University of Cambridge in the region surrounding the south Caspian basin, the Iranian Long Period Array, and the GDSN seismographs at Alibek in Turkmenistan and Mashad in Iran. We have analyzed teleseismic P–wave delay times, back azimuth anomalies, and P–wave receiver functions to determine the crustal velocity structure beneath four Caspian Seismic Network stations and Alibek, and used these results plus published DSS results to construct a cross section of the crust for the region extending from the Kura Depression to the eastern Kopet Dag Mountains. This shows thick sediments beneath the Kura Depression ($\sim$ 8 km thick), and anomalously thick sediments (15–20 km thick) but no "granitic" crust beneath the south Caspian basin. Normal continental crust underlies the Kopet Dag Mountains. Observed phase velocities across the south Caspian basin are extremely low showing the effect of the low velocity sediments; intermediate period surface waves show a large decrease in amplitude as a result of the high sediment attenuation. Analyses of surface waves from regional events in Iran show the average velocity of the crust beneath the central Iranian plateau is anomalously low compared to similar elevated regions such as the Basin and Range.

Keywords: South Caspian Basin, Central Iranian Plateau, Seismic Structure

OBJECTIVES

The Middle East is a region of intense crustal deformation that is accommodating the 30 mm/yr convergence between the Eurasian and Arabian plates. This deformation is manifested as a broad zone of seismicity extending from the Aegean, through Turkey, the Caucasus, and Iran. Within the south Caspian/Iran region there is a high rate of dispersed seismicity; there are also several regions such as the south Caspian basin and central Iranian plateau within which seismicity is relatively low (Fig. 1). Analyses of earthquake focal mechanisms show that the south Caspian basin is under compression on its northern, western and southern boundaries [Priestley, Baker & Jackson, 1994], and that the central plateau is moving northward and rotating clockwise as a semi–rigid block [Jackson & McKenzie, 1984; Baker, Jackson & Priestley, 1994]. In addition to the dispersed seismicity, there are many active mining operations in Iran, some of which are thought to have blasting events greater than 100 metric tons of ammonium nitrate – fuel oil (ANFO). Tectonic processes in this region have produced a highly disrupted and attenuating crust which results in complex regional seismograms. The detection and discrimination of small–to–moderate magnitude seismic events in such an environment is challenging. In the absence of a distributed set of known events, the characterization of regional seismic phases and the retrieval of source parameters for small–to–moderate size seismic events from regional data requires accurate models of the crust and upper mantle velocity structure. Velocity models have been proposed for the Middle East region but current monitoring objectives require a re-evaluation and refinement of these models. The objectives of our research contract are to improve understanding of (1) the crust and upper mantle velocity structure, (2) the amplitude and frequency characteristics of regional seismic phases Pn, Pg, Sn, and Lg, and (3) the source characteristics of moderate size seismic events in the region surrounding and to the south of the Caspian Sea. During this first year of our contract, we have focused on the first of these tasks.

RESEARCH ACCOMPLISHED

The Caspian Seismic Network: A major restriction on improving seismic discrimination capabilities in the Middle East has been the scarcity of seismic data recorded within the region. In mid–1993 we installed five, three–component broadband digital seismographs around the south Caspian Sea in the republics of Turkmenistan and Azerbaijan (Fig. 1) which we will refer to as the Caspian Seismic Network (CSN). The original sites were Baku (BAK) and Lenkoran (LNK) in Azerbaijan and Krasnovodsk (KRV), Nebit Dag (NBD), and Kyzil Atrek (KAT) in Turkmenistan. A sixth site at Dana Tag (DTA) in Turkmenistan was added in late 1993. Because of noise problems and power outages at station BAK, the instruments were moved to Shemaha (SHE) in June, 1994 (Fig. 1). As a result of the escalation of local warfare in Azerbaijan, the stations LNK and SHE were removed in March 1995, and a fifth Turkmenistan station installed at Kara Kala (KAR) in June, 1995 (Fig. 1). Data at each site are recorded on a Refraction Technology 72a-02 data logger that is equipped with either Omega or GPS timing. Stations KRV, DTA, KAT and LNK have Guralp CMG-3T sensors and stations BAK and SHE have Geotech SL-210/220 long period sensors. The station NBD initially had a Guralp CMG-3T sensor but this was replaced with a Geotech SL-210/220 long

period sensor when the DTA station was installed. All stations record data continuously at 10 samples per second and some have had at times a triggered data stream at 50 samples per second. For several months when the LNK station was difficult to reach, the sampling rate was reduced to 5 samples per second. Instruments are calibrated with a pulse of known current at intervals and have been calibrated once with a pseudo–random binary input. We have encountered numerous problems working in this environment, the most serious being the intermittent warfare and power.

Seismic Structure of the South Caspian Basin: The velocity structure of the Earth's crust and upper mantle is most accurately determined through active controlled source seismic experiments. For various reasons, such experiments are difficult in the Caspian region. An alternate approach to controlled source experiments are passive source experiments using earthquake recordings. Although the exact location and origin time are not known, passive source experiments have certain advantages over active seismic experiments. For example, shear wave velocity structure is more difficult to determine in controlled source experiments, but much easier to determine in passive experiments. We have analyzed recordings of teleseismic body–waves to determine the crust and upper mantle velocity structure beneath several of the CSN stations and recordings of regional and teleseismic surface waves to examine the crust and upper mantle velocity structure across the south Caspian basin.

We have analyzed teleseismic P–wave delay times, back azimuth anomalies, and P–wave receiver functions to determine the crustal velocity structure beneath four CSN stations and the IRIS station at Alibek (ABKT – Fig. 1). Although seismic receiver functions are most sensitive to the crustal shear wave velocity, our results are reported in terms of compressional wave velocity (Fig. 2) for easier comparison with the published Deep Seismic Sounding (DSS) results. Although these models represent only five estimates of the velocity structure across a complex region, most of the main structural features of the area can be observed in these models.

The stations KRV, NBD, and ABKT all lie along the trend of the Apserhron Sill – Kopet Dag Mountains and the crustal velocity models beneath these stations are generally similar but differ in some details. The receiver function analysis shows a gradational Moho extending over 3 to 4 km depth range beneath all three sites. The crust thickens from $\sim$ 46 km beneath ABKT in the eastern Kopet Dag, to $\sim$ 48 km beneath NBD in the west Turkmenistan Depression, to $\sim$ 52 km beneath KRV on the Krasnovodsk Plateau on the eastern shore of the Caspian Sea. The shallow structure is somewhat variable with basement velocities reaching 6 km/sec at $\sim$ 8 km depth beneath ABKT, 3 km beneath NBD, and 7 km depth beneath KRV. The lower crustal velocities are similar beneath ABKT and KRV; however, there is a slight velocity reversal in the lower crust beneath KRV. The average crustal velocity beneath NBD is lower than that beneath ABKT or KRV.

The crustal structure beneath the stations KAT and LNK along the southern periphery of the south Caspian basin is very different from that along the northern periphery. Beneath station KAT in the western Turkmenian Lowland, the crust is only about 31 km thick but has a gradational Moho similar to that seen in the north. The velocity of the crust is abnormally low compared to the average continental crust. The sedimentary section (velocities from 3 to 4.8 km/sec) extends to about 10 km depth. Between this depth and the Moho the average crustal P–wave velocity is $\sim$ 6 km/sec. Receiver function data for station LNK on the western side of the Caspian are equally well–fit with either a gradational Moho extending from 32 to 38 km depth or with a sharp Moho at $\sim$ 35 km depth. The sedimentary section beneath LNK is $\sim$ 6 km thick and there is an

anomalously thin section of upper crustal material (velocities 5.8 to 6.4 km/sec). Between about 13 km depth and the Moho the LNK receiver function data can be adequately fit with a crust of uniform velocity 7.1 km/sec. The velocity of this layer is consistent with ultra–mafic rocks. Similar observations from DSS studies across the central part of the south Caspian basin have been been interpreted as evidence for a remnant of oceanic crust or metamorphosed lowermost crustal rock. The thick sedimentary layer observed at KAT and LNK has a strong effect on the behavior of the P–to–S converted phases and on the P–wave travel time residuals.

Figure 3 shows a cross–sectional model of the crust for the region extending from the Kura Depression to the eastern Kopet Dag Mountains. This model has been constructed by combining the receiver function results for data from LNK, KAT, and ABKT with the results from 14 DSS studies across the south Caspian basin and surrounding region. In this figure the complexities of the DSS crustal models have been simplified so that the crust is divided into three layers based on the P wave velocity. These layers are defined as: (1) sediments and consolidated sediments (velocities < 4.8 km/sec), "granitic" (velocities between 4.8 km/sec and 6.3 km/sec) and "basaltic" (velocities between 6.4 km/sec and 7.3 km/sec). These terms correspond to the earlier Russian terminology and it is important to note that these terms are used to denote a velocity range and not a specific rock composition, i.e., "basaltic" does not imply that the rock is actually basalt, only that its velocity is consistent with measured velocities of ultra–mafic rocks.

Beneath the eastern Kopet Dag the crust is typical of the continents, $\sim$ 45 km thick and composed of a 2–3 km thick sedimentary section, a 18–22 km thick "granitic" crust, and a 20–25 km thick "basaltic" crust. Beneath the Kura Depression the crust is as much as 55 km thick consisting of a $\sim$ 8 km thick sedimentary section, a $\sim$ 40 km thick lower crust, but a thin 6–8 km thick "granitic" crust. Over a short distance near the west Caspian Sea coast the crust thins significantly and is as little as 30 km thick beneath the south Caspian basin and west Turkmenian Lowlands. From the data we have it is impossible to tell whether the crust thins abruptly beneath the eastern boundary of the west Turkmenian Lowlands or more gradually beneath the Kopet Dag. Beneath the south Caspian basin the sediments are as thick as 15–20 kilometers, and the "granitic crust" becomes extremely thin and probably disappears.

Analysis of the CSN surface wave data for paths across the south Caspian basin is incomplete at present. Figure 4 compares fundamental mode Rayleigh wave phase velocity curves measured for the south Caspian basin, with those observed in two other regions of thick sediments – the Bay of Bengal [Brune & Singh, 1986] and the Barent Sea [Levshin & Berteussen, 1979]. The two station (KAT–LNK, KAT–KRV) intermediate period phase velocity curve was determined using a constrained least–squares algorithm [Gomberg, Priestley, Masters & Brune, 1988] from the teleseismic waveforms. The short period portion of the phase velocity curve was determined from regional events on the periphery of the basin using the single station method [Brune, Nafe, & Oliver, 1960]. The effect of the anomalously thick sediment of the south Caspian basin can be seen in the low phase velocities.

It has long been known that the south Caspian basin blocks the propagation of the regional seismic phase Lg. One of the new observations from the CSN is the effect of the south Caspian basin on the propagation of intermediate period fundamental mode surface waves. The top pairs of seismograms in Figure 5 show broadband vertical component seismograms, the middle pair show the waveforms high–passed at 22 mHz, and the bottom pair show the waveforms low–passed at 22

mHz. All waveforms are plotted on the same time scale and both traces of each pair are plotted on the same amplitude scale. A well–developed fundamental mode surface waveform enters the basin but the intermediate frequency surface waves are largely missing from the surface wave train emerging from the basin only 450 km away. The low frequency surface waves are not significantly affected; however, both eastward and westward propagating surface waves are affected in the same manner.

Finite difference synthetic seismograms were computed for a 2–D model simplified from Figure 3, to gain insight into the features which lead to the anomalous surface wave propagation. Figure 6 is a record section of vertical component synthetic seismograms in the 33 to 100 mHz frequency band spaced at 50 km intervals across the model. The source is at a distance of 3300 km from the model edge. As the wave train passes into the basin [upper "basin boundary" arrow] there is a significant increase in amplitude due to the impedance mismatch between the high velocity rocks outside the basin and the low velocity sediment within the basin. There are also small amplitude converted body waves in the basin and reflected surface waves in the crystalline crust [arrows]. As the wave train propagates through the basin the waveform is spread out in time due to the increased dispersion, and reduced in amplitude due to attenuation. As the wave train passes out of the basin [lower "basin boundary" arrow] there is a reduction in amplitude of the surface wave train and a second reflected surface wave [late arrow]. From the preliminary 2–D tests made thus far, the dominant factors influencing the surface wave amplitudes are the high attenuation and low velocity of the sediments.

Seismic Structure of the Iranian Plateau: Asudeh (1982) analyzed travel time data from earthquakes and fundamental mode phase velocity dispersion curves and determined a crust and upper mantle velocity model for the central Iranian plateau. We computed locked–mode synthetic seismograms using the Asudeh velocity model for several earthquakes for which centroid moment tensor (CMT) solutions have been determined by Harvard. Even after altering the source mechanisms and focal depths over an reasonable range, we found little resemblance between the synthetic and observed seismograms at LNK, KAT, ABKT, and MAIO. We next altered the velocity structure until more acceptable fits were obtained. The Fundamental mode Rayleigh wave phase velocity curve for this model closely matches the observed phase velocity curves of Asudeh (1982). Like the Asudeh velocity model, our preliminary earth model (Table 1) has an extremely slow average crustal velocity.

Table 1. Preliminary Surface Wave Velocity Models

South Caspian Basin		Central Iranian Plateau	
Thickness (km)	S-wave velocity (km/sec)	Thickness (km)	S-wave velocity (km/sec)
1.0	0.00	1.4	1.85
7.5	2.02	5.0	3.15
7.5	2.31	20.0	3.35
10.0	3.93	14.0	3.55
20.0	3.93	36.0	4.35
50.0	4.74	40.0	4.45
100.0	4.40	80.0	4.35
	4.68		4.70

CONCLUSIONS AND RECOMMENDATIONS

The surface wave velocity models in Table 1 are preliminary and need to be completed. From the tests made thus far, the cause of the anomalous intermediate surface wave propagation across the south Caspian basin is the extremely thick and highly attenuating sediments. This is most likely also the cause of the Lg blockage but this needs to be verified with finite difference synthetic calculations. To better determine the velocity model for the crust and upper mantle of the central Iranian plateau and to assess the variability of the structure within Iran, we are now inverting the the surface wave data from the regional earthquakes for velocity structure using a differential seismogram technique. For this method the synthetic seismogram is represented as a sum of locked-mode traveling waves in a layered medium. This representation allows the modeling of slowly varying heterogeneity. The difference between the observed and synthetic seismograms is related to perturbations of starting model parameters and is used to determine directly the model of the Earth structure. Once the work on the velocity model for the central Iranian plateau is complete we will examine the amplitude and frequency characteristics of regional seismic phases Pn, Pg, Sn, and Lg and the source characteristics of moderate size seismic events in the region surrounding and to the south of the Caspian Sea.

References

Asudeh, I., Seismic structure of Iran from surface and body wave data, *Geophys. J. Roy. Astron. Soc.*, **71**, 715–730, 1982.

Ammon, C.J, G.E. Randall & G. Zandt, On the nonuniqueness of receiver function inversions, *J. Geophys. Res.*, **95**, 15303–15318, 1990.

Baker, C., J. Jackson, & K.F. Priestley, Earthquakes on the Kazerun line in the Zagros Mountains of Iran: strike-slip faulting within a fold-and-thrust belt, *Geophys. J. Int.*, **115**, 41-61, 1993.

Brune, J.N., J. Nafe, & J. Oliver, A simplified method for the analysis and synthesis of dispersed wave trains, *J. Geophys. Res.*, **65**, 287–304, 1960.

Brune, J.N., & D.D. Singh, Continent–like Crustal thickness beneath the Bay of Bengal sediments, *Bull. Seism. Soc. Am.*, **76**, 191–203, 1986.

Gomberg, J.S., K.F. Priestley, T.G. Masters, & J.N. Brune, The Structure of the Crust and Upper Mantle of Northern Mexico, *Geophys. J. Roy. Astron. Soc.*, **94**, 1–20, 1988.

Jackson, J. & D. McKenzie, Active tectonics of the Alpine–Himalayan Belt between western Turkey and Pakistan, *Geophys. J. Roy. Astron. Soc.*, **77**, 185–264, 1984.

Levshin, A, & K.A. Berteussen, Anomalous propagation of surface waves in the Barent Sea as inferred from NORSAR recordings, *Geophys. J. Roy. Astron. Soc.*, **56**, 97–118, 1979.

Priestley, K.F., C. Baker, & J. Jackson, Implications of earthquake focal mechanism data for the active tectonics of the south Caspian basin and surrounding regions, *Geophys. J. Int.*, **118**, 111–141, 1994.

Acknowledgements: The operation of the Caspian Seismic Network was funded by an AFOSR grant through Phillips Laboratory, an EOARD AFOSR grant, and an INTAS grant. We would like to thank Drs. J. Cipar and K. Kadinsky–Cade for critically reading this manuscript and making a number of helpful suggestions.

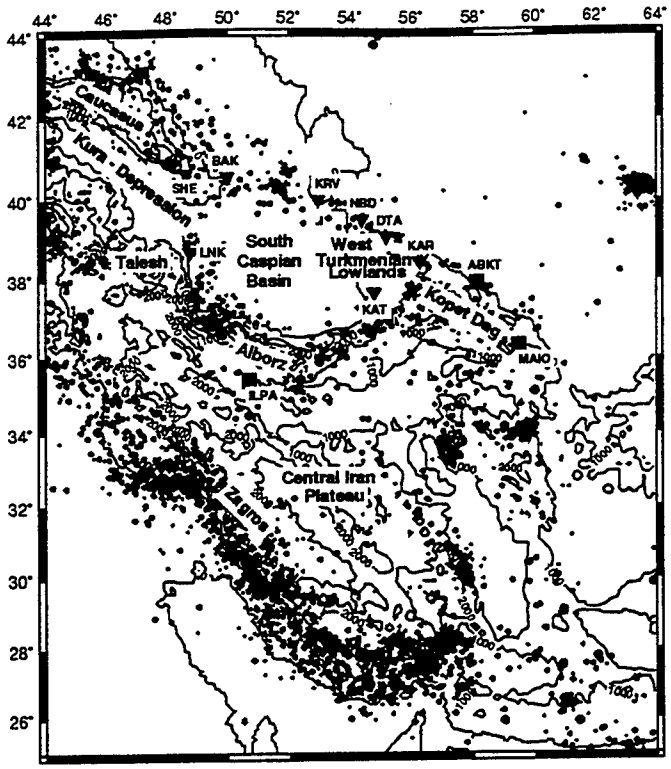

Figure 1: Topographic map of the south Caspian Basin and central Iranian plateau. The variation in elevation ranges from 30 m below sea level around the Caspian Sea to more than 2 km in the bordering mountains. The contour interval is 1000 m, the solid black triangles indicate the location of the seismograph stations that were installed and the solid square shows the location of IRIS station ABKT, the SRO station MAIO, and the Iranian Long Period Array (ILPA).

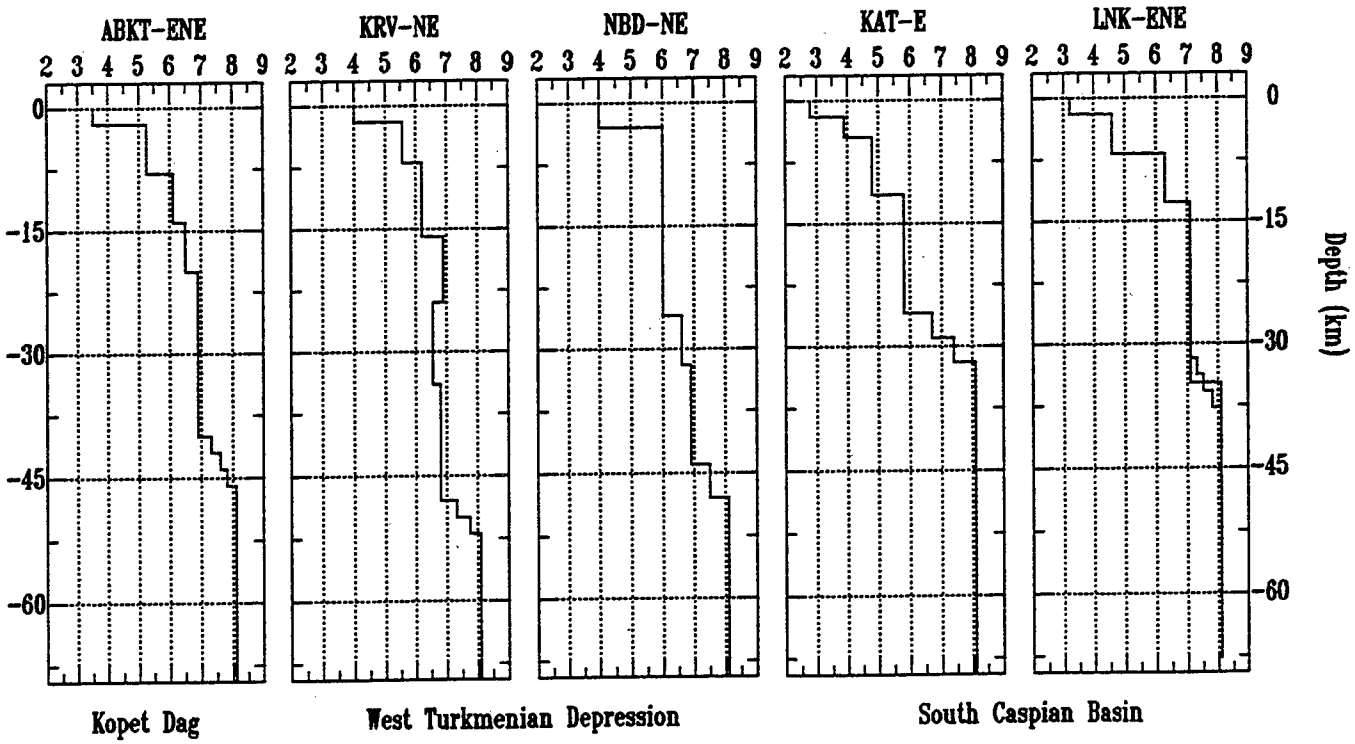

Figure 2: Crustal velocity models derived from the analysis of the receiver function data from the CSN and station ABKT. The receiver function data were first inverted using the routine of Ammon, Randall & Zandt [1990], then the simplest model was found by forward modelling only those features which were felt to be significant in the data.

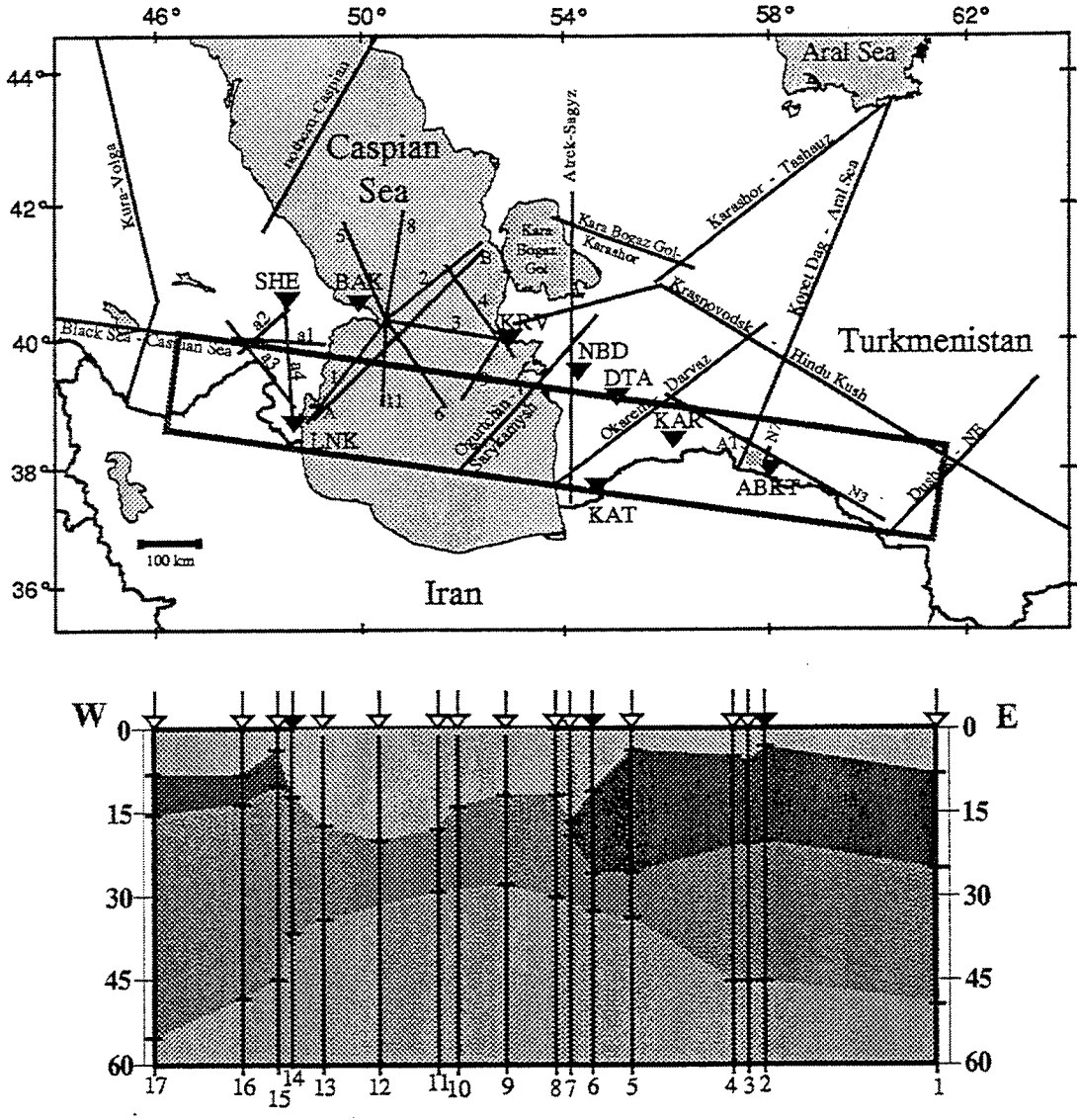

Figure 3: Composite DSS and receiver function cross section for the area beneath the box across the south Caspian Basin and surrounding region. Three principal crustal layers are characterized by average P wave velocities that correspond to: sediments and consolidated sediments (upper light gray) (Vp less than 4.8 km/s), "granitic" (dark gray) (Vp between 4.8 and 6.3 km/s), "basaltic" (light gray) (Vp between 6.4 and less than 8.0 km/s), and upper-mantle (medium grey) (Vp $\geq$ 8.0 km/s). Control numbers 1-17 correspond to the following DSS (open arrows) and receiver function results (solid arrows): (1) Dushak-NE, (2) station ABKT, (3) ATS, (4) Kopet Dag-Aral Sea, (5) Okarem-Darvaz, (6) Station KAT, (7) Atrek-Sagyz, (8) Okarem-Darvaz, (9) Ogurtchin-Sarykamysh, (10) number (9, (11) number (6, (12) number (11, (13) number (1), (14) Station LNK, (15) (a4), (16) (a3) and (17) Black Sea-Caspian Sea.

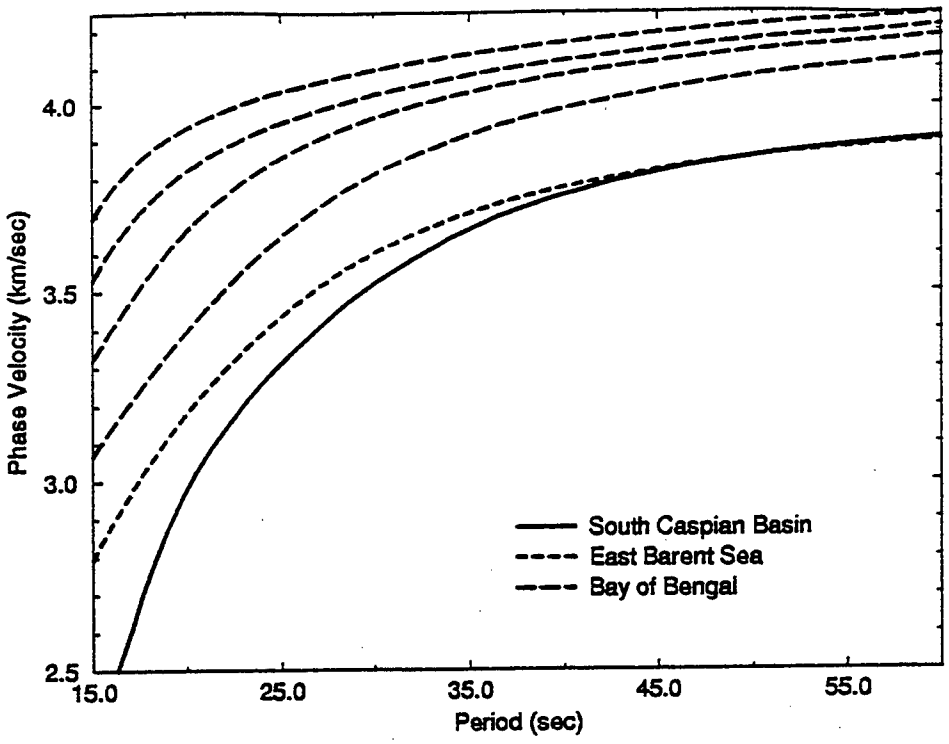

Figure 4: Comparison of fundamental mode Rayleigh wave phase velocity curves for the south Caspian basin with those observed for the Bay of Bengal and the Barent Sea.

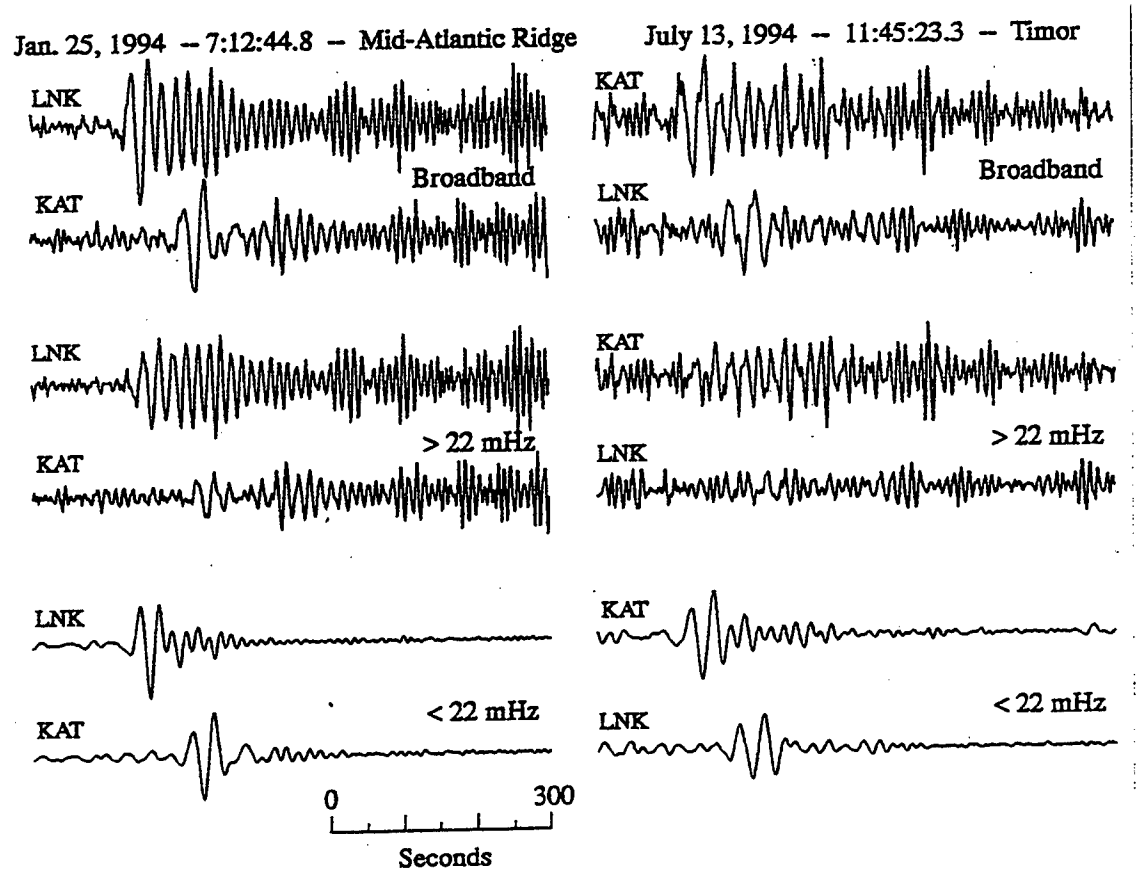

Figure 5: Comparison of broadband and bandpass filtered seismograms for W–E (left) and E–W (right) propagation between LNK and KAT across the south Caspian basin.

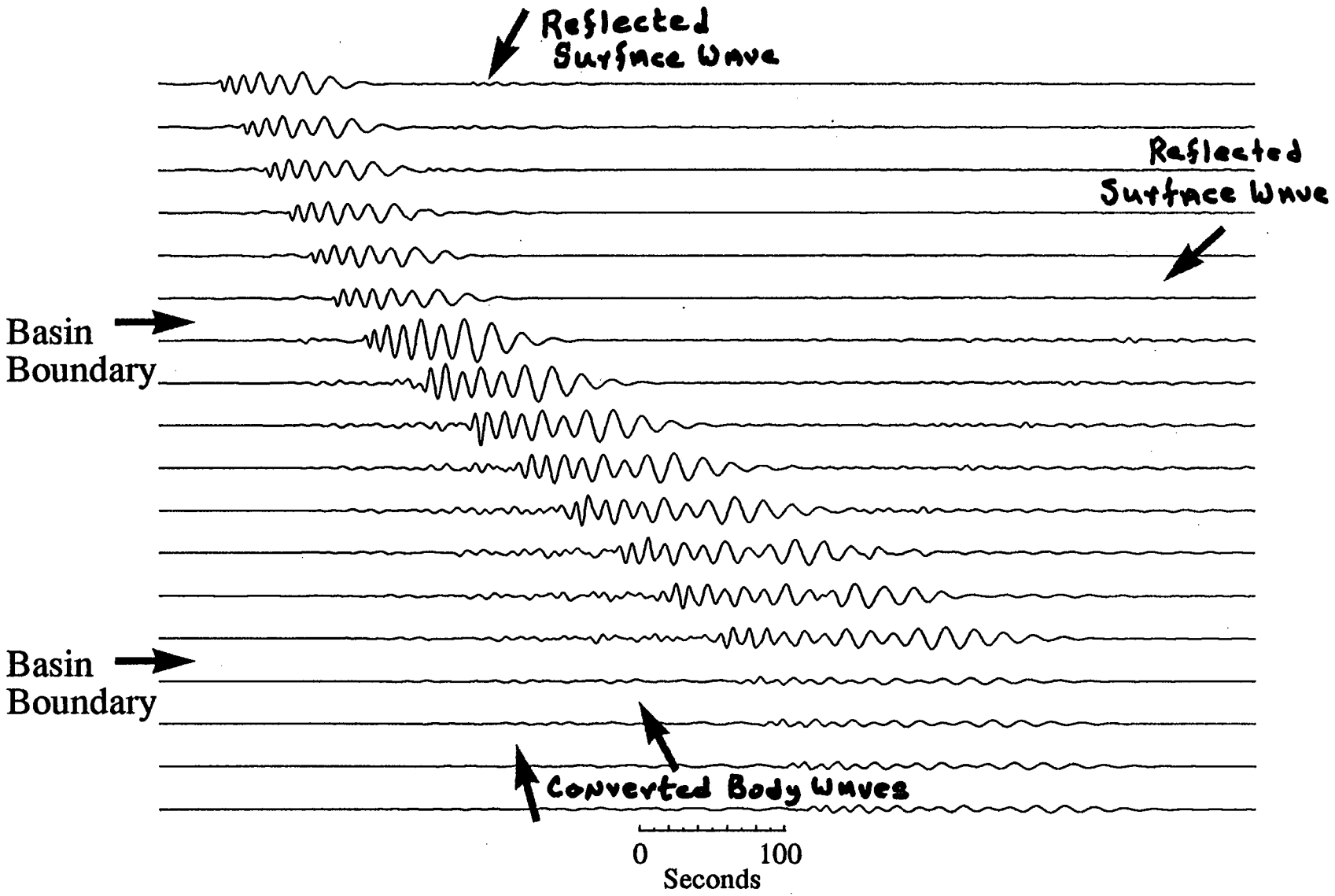

Figure 6: Finite difference synthetic seismogram record section for a simplified 2-D model of the south Caspian basin. The synthetics are coumputed at 50 km intervals.

ASIAN LITHOSPHERIC STRUCTURE FROM WAVEFORM MODELLING: REGIONAL Pnl AND COMPLETE WAVEFORMS, P and PP TRIPLICATIONS

Arthur Rodgers and Susan Schwartz
Institute of Tectonics, University of California, Santa Cruz, CA, 95064
Contract # F49620-94-1-0050
Sponsored by AFOSR

ABSTRACT

We inferred pure-path one-dimensional seismic velocity structure of the crust and uppermost mantle in Asia by modelling observed broadband waveforms. Many velocity structures were investigated in a grid-search scheme using reflectivity synthetics. We modelled a variety of seismic phases: for regional events we modelled Pnl or the complete waveform (Pnl, Sn and the surface waves); triplicated P and S (PP and SS) were modelled for distances in the range 15°-27° (30°-55°). Objective measures of model performance were used to understand the sensitivity of the data to structure and determine the best-fitting model for each path. The travel time residual of the first arriving P-wave was determined by cross-correlating the data and synthetic. Waveform misfit was determined with the rms difference and linear correlation between the filtered and windowed data and synthetic.

Previous work on P and PP triplication distances (15°-55°) found great variability in lithospheric structures within the Asian continent. Shields (e.g., Indian Shield, Angara Craton) generally have high Pn velocities and thick, fast mantle lids. Tectonically active regions (e.g., northern Tibet, Western China) have lower Pn velocities, thinner lids and weaker velocity gradients. Platforms (e.g., Kazahk, North China & Yangtze Platforms) have intermediate Pn velocities and lids.

Recent efforts have focused on regional waveforms (3°-15°) in order to isolate velocity structures associated with specific tectonic/geologic regions within Asia. Regional Pnl and complete waveforms for paths in southern Tibet revealed an extremely thick, low velocity crust (70 km, 5.9-6.1 km/s, respectively) and variations in mantle lid velocities. The mantle lid beneath the southern Lhasa Terrane is shield-like (Pn velocity 8.20-8.25 km/s, lid thickness 80-140 km, positive velocity gradient 0.0015-0.0025 s^{-1}). Relative Pn travel time residuals require an abrupt decrease in the mantle velocities beneath the northern Lhasa Terrane or Banggong-Nujiang Suture.

Key words: Asia, regionalization, crust and upper mantle structure

OBJECTIVE

The objective of this research is to determine one-dimensional crustal and upper mantle structures for the Asian continent. Seismic event discrimination methods, such as those relevant to CTBT monitoring, are strongly dependent on the structure of the crust and upper mantle. Thus, the transportability of discriminants is affected by regional differences in crustal and upper mantle structures, particularly the nature of the mantle lid and low velocity zone (e.g., Beckers, Schwartz and Lay, 1993). Observed waveforms in the distance range 3° to 55° are highly sensitive to the seismic velocity structure of the crust and uppermost mantle (the lid). Recent deployments of IRIS-GSN, IRIS-PASSCAL, CDSN and GEOSCOPE instrumentation in Asia and efforts by the IRIS-DMC to make these data available now make it possible to gather high-quality, modern data at these critical distances for many regions that were previously unsampled by historical data (e.g., WWSSN, SRO).

RESEARCH ACCOMPLISHED

1. Data and Modelling Strategy

Broadband three-component recordings of crustal events occurring within the Asian continent were extracted from IRIS-FARM and IRIS-PASSCAL products. We searched for moderately large (M_W = 5.5-6.8) events with known mechanisms and simple source-time functions. Instrument deconvolved displacement seismograms were previewed and judged for source simplicity and good signal-to-noise. The source parameters (i.e., event depth, focal mechanism and source-time duration) were evaluated and possibly adjusted by modelling broadband waveforms of teleseismic P using WKBJ synthetics.

We modelled the observed waveforms for those events with well constrained source parameters. Synthetics were computed using the reflectivity method. It has been shown (Schwartz and Lay, 1993) that reflectivity is superior to ray-based methods for synthesizing the surface reflected PP phase, which consists of interfering multiple reflections and conversions (e.g., whispering gallery waves).

A grid search scheme was used to infer the pure-path average velocity structure. Reflectivity synthetics for many models of crustal and mantle structures were computed in a systematic way. Objective measures of model performance were used to understand the sensitivity of the data to structure and to determine the best-fitting model(s). The travel time residual of the first-arriving P-wave was found by cross-correlating the windowed data and synthetic. Waveform misfit was determined by the scaled rms-difference of a longer time window (e.g., including regional Pnl, Sn and/or surface waves, triplicated P or PP).

2. Regional Pnl Waveforms

Pnl is the long-period P-SV response of the Earth to shallow seismic excitation. It consists of Pn, the first-arriving mantle phase and PL, a shear-coupled P-wave. The travel time of Pn is sensitive to the velocity, velocity gradient and thickness of the mantle lid. PL is sensitive to the thickness and P- and S-wave velocities of the crust. Pn and PL have roughly independent sensitivities to the average velocities of the mantle and crust (Holt and Wallace, 1990) .

A regional event recorded by the 1991-1992 IRIS-PASSCAL Tibetan Plateau Experiment (Owens et al., 1993) allows excellent pure-path sampling of southern Tibet (Figure 1). This event excited high signal-to-noise Pnl records. Data and synthetics for the best-fitting models are shown in Figure 2. Using an appropriate average mantle model for southern Tibet, we investigated average crustal models by varying the crustal thickness (66-78 km, 2 km increment) and crustal velocity (5.8-6.3 km/s, 0.1 km/s increment). Contours of constant rms difference for each data and model are shown in Figure 3. Note that there is a trade-off between the thickness and velocity in a direction that preserves the vertical travel time through the crust. The data are consistently well fit by models with low crustal velocities (5.9-6.1 km/s), with the northern paths slightly faster. Lower velocities and thicknesses for stations GANZ and USHU (at far-regional distances) probably result from poorly modelled

triplication arrivals due to inappropriate mantle lid structure. These stations are better fit by thicker, high velocity lids. Mantle lid structure was inferred by holding the crustal thickness and velocity to their best-fitting values and varying the mantle lid Pn velocity, mantle lid thickness and velocity gradient. Mantle parameters were estimated by fitting the Pn arrival time. We varied the Pn velocity (8.10-8.25 km/s, 0.05 km/s increment), lid thickness (60-140 km, 20 km increment) and lid velocity gradient (0.001-0.003 s^{-1}, increment 0.0005 s^{-1}). Figure 4 shows contours of constant Pn travel time residual and rms differences for the mantle lid parameters considered. Trade-offs between the Pn travel time and the mantle lid parameters make it difficult to uniquely determine all three of these parameters. Nonetheless, an abrupt decrease in the mantle lid velocities are required to fit the Pn travel times for paths traversing the northern Lhasa Terrane and/or Banggong-Nujiang Suture. Results for mantle structure indicate that a thick, positive velocity gradient lid underlies a region of southern Tibet previously inferred to have fast Pn velocities (McNamara et al., 1995).

3. Complete Regional Waveforms

Regional complete waveforms consist of Pnl, Sn and the surface waves. Compared to Pnl, these data have greater sensitivity to crustal thickness and P- and S-wave velocities due to the surface waves. Figure 5 shows the paths for an event on the Tibetan Plateau that was recorded by several permanent stations at regional distances. Figure 6 shows the observed vertical component displacement seismograms for this event and the best-fitting synthetics. The shorter paths (LSA, LZH and KMI) can be well modelled by one-dimensional models in the filter band 0.01-0.1 Hz. Results for the path to LSA confirm the low crustal velocities (6.0 km/s) and fast mantle lid velocities (Pn velocity 8.20 km/s, thick, positive velocity gradient) inferred from the Pnl waveforms considered above. Note that the surface waves for these paths are remarkably well fit at relatively short periods. Average crustal velocities for paths to LZH, ENH and XAN are slightly higher (6.1-6.3 km/s). Waveforms for longer paths (XAN and HYB) are difficult to fit at shorter periods, presumably due to along path heterogeneity. Nonetheless, these data are reasonably well fit by a one-dimensional model when filtered from 100-20 seconds.

4. P and PP Triplications

Our previous work (Rodgers and Schwartz, 1995) concentrated on modelling P and PP triplication waveforms. We have applied our grid search strategy to a limited number of paths. Figure 7 shows the locations of paths studied for an event in the Hindu Kush. The observed vertical displacement seismograms, best-fitting synthetics and models for P and PP triplication distances for this event are shown in Figure 8. Data and synthetics were filtered in the passband 0.01-0.1 Hz. Results reveal differences in crustal thickness, Pn velocity, mantle lid thickness and gradient. In particular, the best-fitting model for the path to HYB reveals a thick lid with a positive lid gradient, while the path to CHTO requires faster lid velocities. Paths to LSA and ENH are best-fit by models with thick (70 km) crusts and thinner mantle lids.

CONCLUSIONS AND RECOMMENDATIONS

Our preliminary results for the regionalization of Asia (Rodgers and Schwartz, 1995) indicated that large areas can be characterized by single average regional upper mantle velocity models. The regions correspond fairly well with the known provinces of surface tectonics. The average regional models differ significantly in the uppermost 200 km and will affect event discrimination techniques. Recently, we have found that much better fits can be achieved by modelling regional waveforms, providing higher confidence in velocity model estimates. Further modelling of regional data will improve resolution of velocity heterogeneity within the Asian continent.

References

Beckers, J., Schwartz, S. and Lay, T., 1993. Analysis of the effects of Eurasian crustal and upper mantle structure on regional phases using broadband seismic data, PL-TR-93-2131, Final Report for the Philips Laboratory, Hanscom Air Force Base, MA, ADA272446

Beckers, J., Schwartz, S. and Lay, T., 1994. The velocity structure of the crust and upper mantle under China from broad-band P and PP waveform analysis, *Geophys. J. Int.*, **119**, 574-594.

Holt, W. and Wallace, T., 1990. Crustal thickness and upper mantle velocities in the Tibetan Plateau region from the inversion of regional Pnl waveforms: evidence for a thick upper mantle lid beneath southern Tibet, *J. Geophys. Res.*, **95**, 12,499-12,525.

McNamara, D., Walter, W., Owen, T. and Ammon, C., 1995. Upper mantle velocity structure beneath the Tibetan Plateau from Pn travel time tomography, *LLNL-UCID*.

Owens, T., Randall, G., McNamara, D. and Wu, F., 1993. 1991-92 Tibetan Plateau Passive-source seismic experiment, PASSCAL Data Report 93-005, *IRIS-DMC*, Seattle, WA.

Rodgers, A. and Schwartz, S., 1995. Proceedings of the 17th Annual Seismic Research Symposium on Monitoring a Comprehensive Test Ban Treaty, Philips Laboratory PL-TR-95-2108.

Schwartz, S. and Lay, T., 1993. Complete PP-waveform modelling for determining crust and upper mantle structure, *J. Geophys. Res.*, **112**, 210-224.

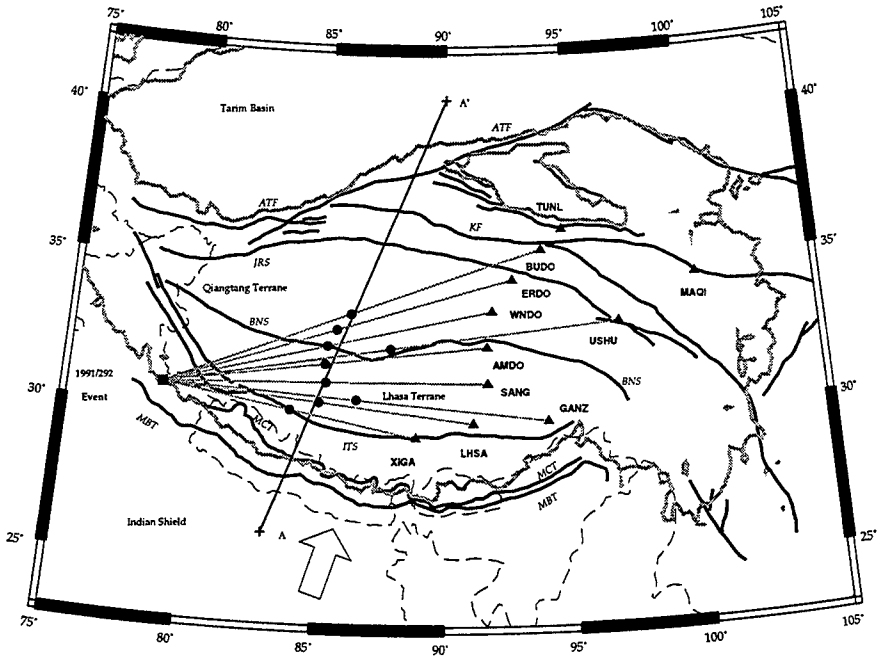

Figure 1. Major geographic and tectonic features of the Tibetan Plateau (faults and sutures are shown as thick black lines, 3.0 km elevation contours are shown as thick grey lines). Also shown are the locations of the 1992/292 event studied (square), stations (triangles) and ray plaths (thin grey lines). Midpoints of the ray paths (circles) lie along the line AA', roughly parallel to the direction of convergence between India and Asia (large arrow).

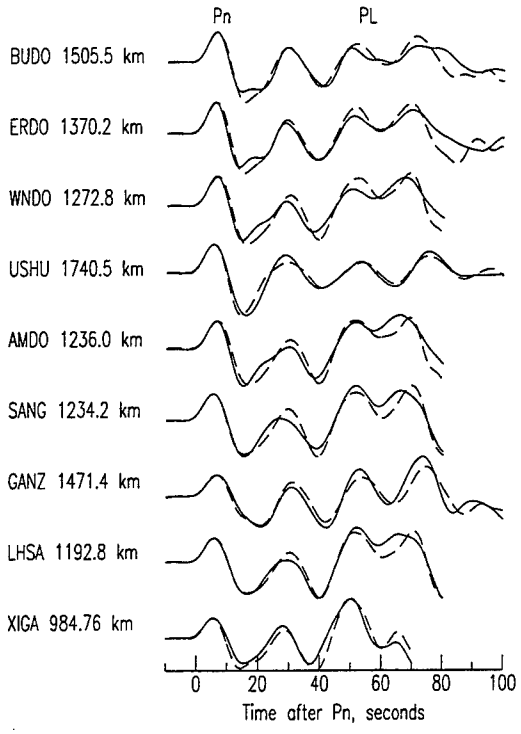

Figure 2. Instrument deconvolved vertical displacement seismograms (solid) and synthetics for best-fitting models (dashed). Pn and PL phases are labelled. Also shown are the station and distance.

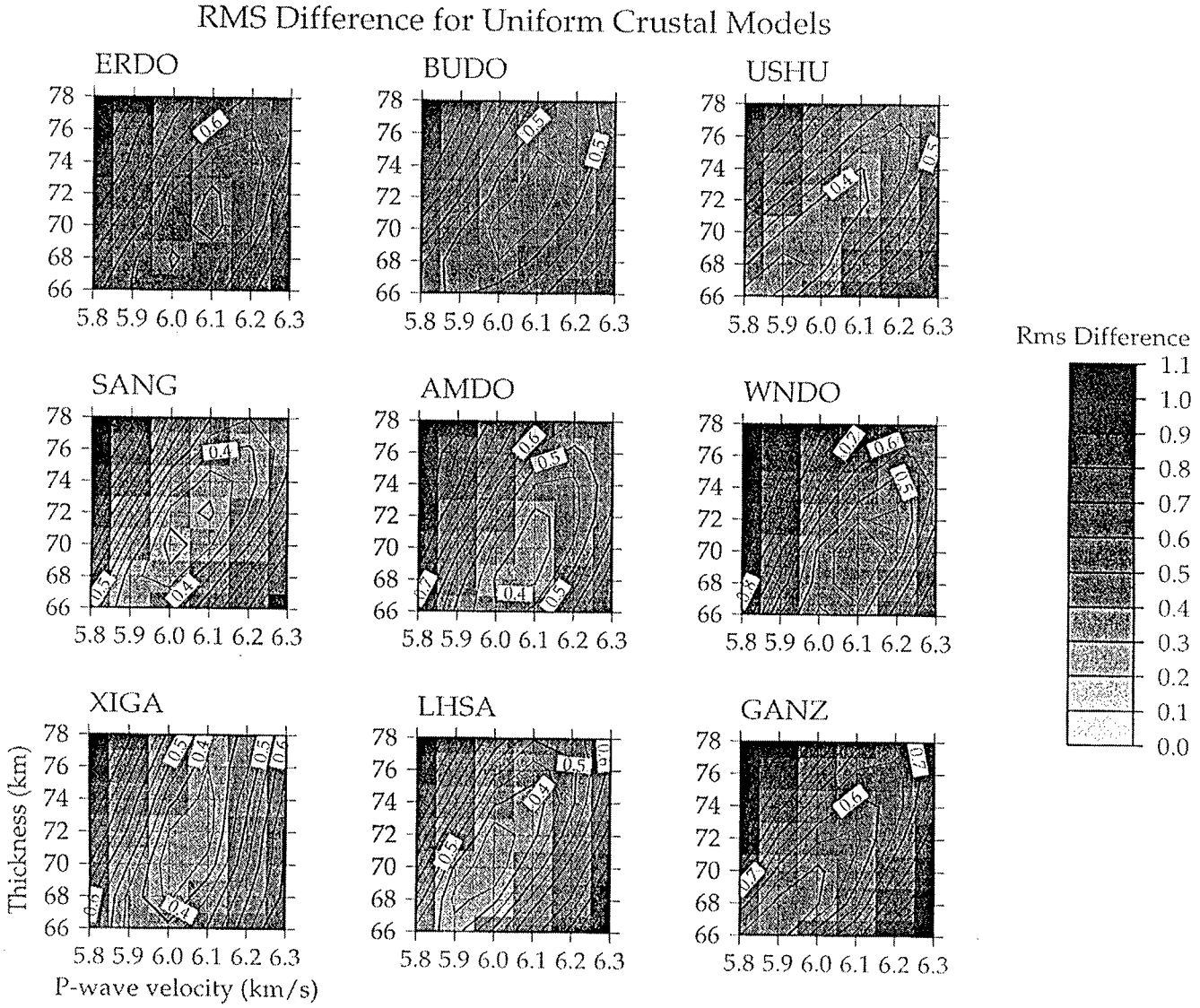

Figure 3. Contours of constant rms difference for the crustal thicknesses and velocities considered in our grid search. Crustal Poisson's ratio (0.25) and mantle lid parameters (Pn velocity 8.15 km/s, thickness 80 km, gradient 0.002 1/s were held constant for each model. Note that best-fitting models (minimum rms difference) are found for low crustal P-wave velocities of 5.9-6.1 km/s and crustal thicknesses of about 70 km.

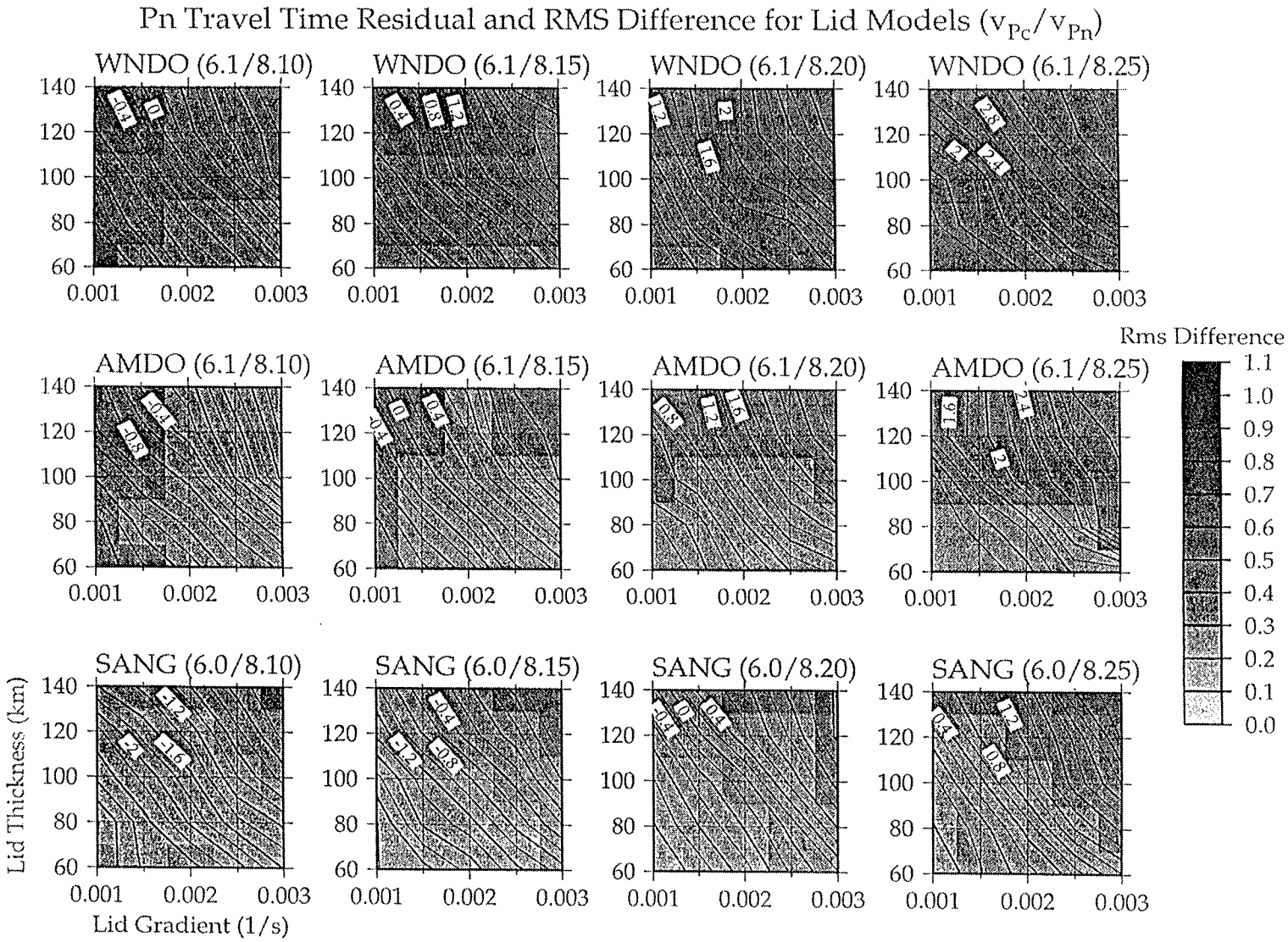

Figure 4. Contours of constant Pn travel time residual and rms difference for the lid parameters considered in our grid search for the stations SANG, AMDO and WNDO. Crustal thickness was held at 70 km. The crustal P-wave velocity and Pn velocity are given in parenthesis above each panel. Note that the three lid parameters trade-off, but that significant variations between each station are required to fit the Pn arrival times.

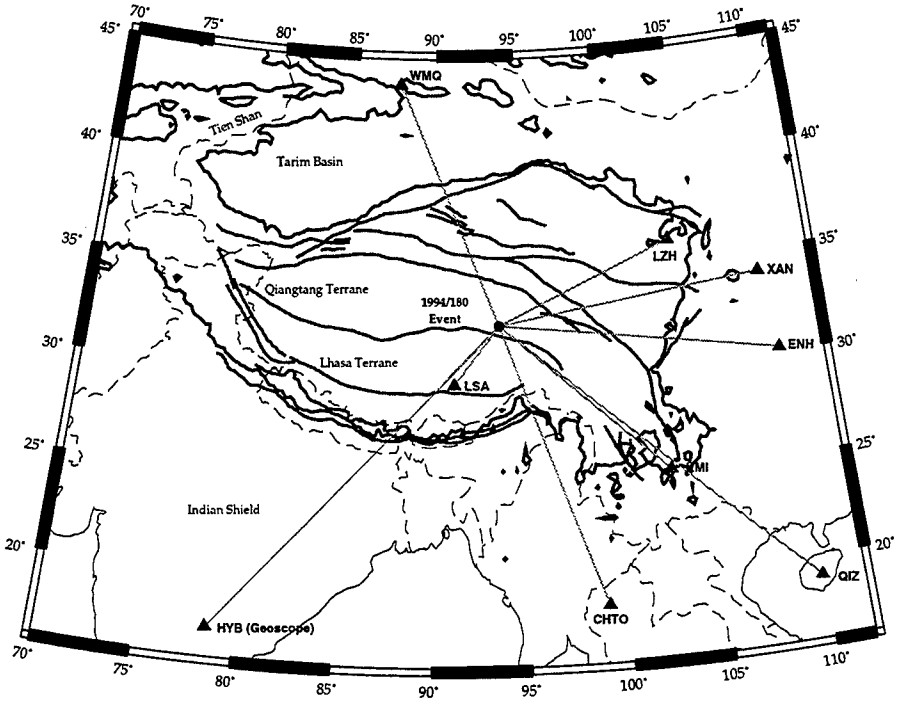

Figure 5. Locations of the event (circle), stations (triangles) and ray paths for the 1994/180 Tibetan Plateau event. Several permanent stations recorded broadband waveforms for this event at regional distances.

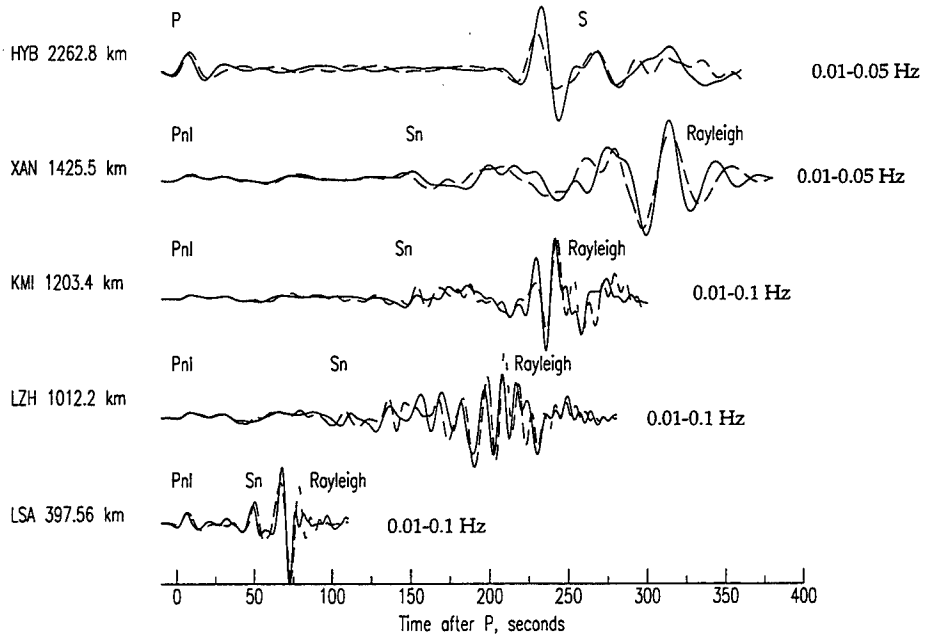

Figure 6. Observed vertical component seismograms and synthetics for the best-fitting models. Major phases are labelled and the station, distance and filter band are shown.

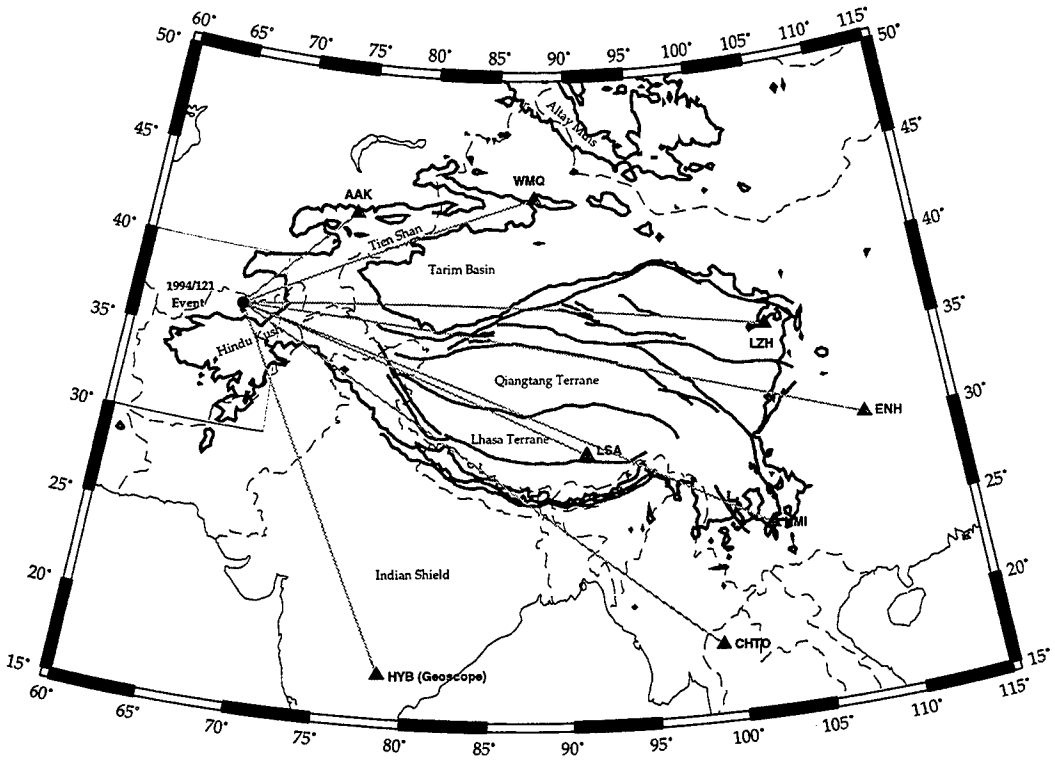

Figure 7. Locations of the event (circle), stations (triangles) and ray paths for the 1994/121 Hindu Kush event studied.

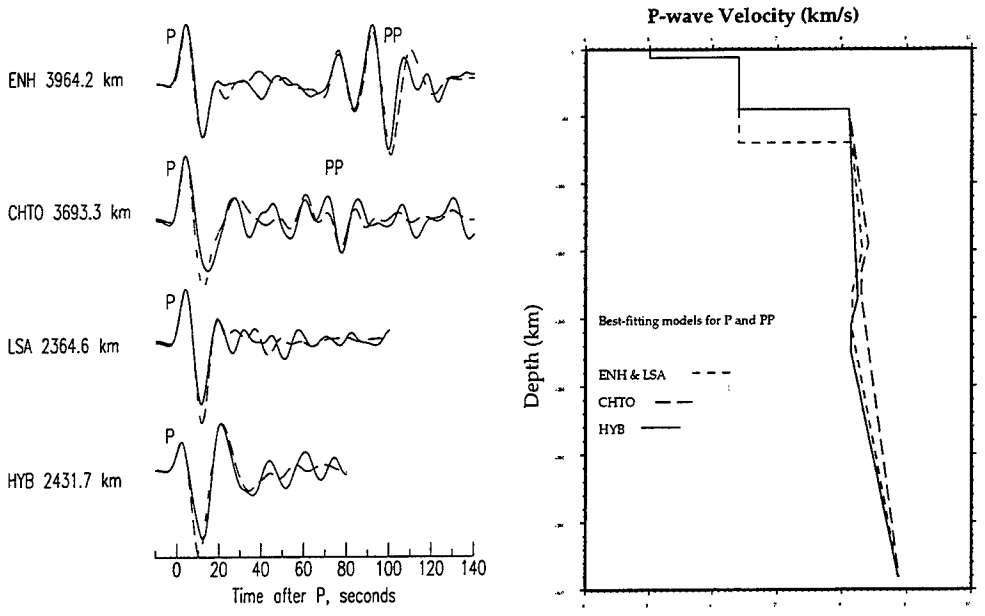

Figure 8. (left) Triplicated P and PP waveforms (solid) and synthetics for the best-fitting models (dashed). (right) The best-fitting models reveal differences in crustal thickness, lid thickness and velocity gradient.

EXCITATION AND PROPAGATION OF Pn IN CENTRAL ASIA

Jiakang Xie
Lamont-Doherty Earth Observatory, Columbia University
Route 9W, Palisades, NY 10964
Contract No. F19628-95-K-0013
Sponsored by DOE

ABSTRACT

We have made several attempts to improve the methodology to better estimate source and path spectral parameters using Pn. The non-linear spectral inverse method of Xie (1993) was modified to further reduce effects of deviations of sources, paths and sites from idealized models used in the inversion. We also attempted to estimate the Pn geometrical spreading term in reasonable 1D structures. Synthetic calculations of Pn propagation in central Asia were conducted using various recently published 1D velocity models. The results typically show that a Δ^{α} model, with α ranging between -1.3 to -1.5, is roughly valid, but one should expect localized deviation of Pn amplitude from that model by at least a factor of 2.

We have collected more than one hundred Pn spectra from broad-band seismic stations in central Asia. Pn amplitude across the Kyrghistan network (KNET) from sources located in and around the Lop Nor Test Site is found to be highly unstable. Despite the small aperture of the KNET (~ 2 °), the time domain Pn amplitude varies by as much as a factor of 19. Spectral analysis reveals that the amplitude variation primarily occurs at low frequencies (~ 1hz). Due to the pronounced topographic variation near the stations, frequency-dependent polarization analysis yields little information on the origin of the amplitude variation. Analysis of Pn propagating through the network in different directions, on the other hand, suggests that the amplitude variation is not due to a systematic variation in site responses. The more likely cause of the amplitude variations is deep-seated 3D structural complications, such as a topographic variation at the Moho.

Pn amplitudes at KNET stations from some Northern Xinjiang earthquakes are much weaker than from the nearby Lop Nor explosions, making Pn/Lg ratio an effective discriminant between these particular earthquakes and underground nuclear explosions. The weak Pn amplitude from these earthquakes are likely caused by a null in the Pn radiation pattern of the earthquakes involved, whose mechanisms are likely dominated by an east-west strike slip motion. Therefore, it is misleading to extrapolate the low Pn/Lg amplitude ratio to earthquakes with other source-station configurations. For the earthquakes that occurred in southern Tien Shan, for example, observed Pn amplitudes at the KNET stations are typically quite high. This is consistent with higher Pn radiation patterns predicted for focal mechanisms that are predominantly reverse slip, which is typical for seismicity in southern Tien Shan.

Research so far demonstrates that the Pn amplitude in central Asia are affected significantly by 3D structural complications and source radiation patterns. Any attempt to utilize Pn in discriminating explosions from earthquakes, or in characterizing source/path properties, must account for these complications. An extensive analysis is underway to compare the stability of spectral inversion using Pn alone with that jointly using Pn and Pn coda, which is expected to be more stable than Pn.

KEY WORDS: Pn, Q, source parameters, explosion discrimination, Central Asia

OBJECTIVE

Recently we have developed and applied a nonlinear inverse method to simultaneously estimate the seismic moment (M_0), corner frequency (f_c) and path-variable Q_0 and η (Q at 1 hz and its power-law frequency dependence, respectively) using the Lg spectra from both explosions and earthquakes. The main objective of this research is to extend that method to analyze Pn spectra from both explosions and earthquakes. The analysis should yield Pn source M_0, f_c, and path Q_0, η values. These values will advance our fundamental understanding on how the excitation and propagation of Pn differ from those of Lg. By comparing the $M_0 \sim f_c$ scalings derived using Pn from explosions and earthquakes with those derived using Lg, we will investigate if, when and why the Pn/Lg ratio works as an discriminant between explosions and earthquakes.

The proposed research is composed of several tasks. The first is to develop a relatively reliable and robust method to measure the source M_0, f_c, and path Q_0, η values using the Pn phase. This task is difficult due to the effects of source radiation pattern and 3D path structural complexities in the Pn spectra. The second task is to analyze, with the method developed, Pn spectra from many events to obtain their M_0 and f_c values, as well as the Pn Q_0 and η values for various regions such as central Asia and middle-east. The third task is to compare the $M_0 \sim f_c$ scalings for earthquakes and explosions, derived using Pn, with those derived using Lg, to obtain the differences in those scalings.

This research provides important input to the implementation of a new Comprehensive Test Ban Treaty, since Pn/Lg amplitude ratio is on one of the most promising discriminants between explosions and earthquakes.

RESEARCH ACCOMPLISHED

Over the past ten months, we have made several accomplishments, which are summarized in the following paragraphs.

Modification of the inverse algorithm

We have modified the non-linear inverse algorithm for simultaneous determination of source M_0, f_c, and path Q_0, η values using the Lg spectra, and extended the method to the inversion of the Pn spectra. The modified method is more robust in that it is more tolerant of the effects of spectral fluctuations at one or more stations that have high path Q values and are close to the source. Previously, spectral fluctuations of this kind may result in numerical instabilities at localized frequencies when the double-logarithm (equation (18) of Xie, 1993) was applied to the Lg spectra. When such instabilities occurred, the corresponding M_0 and f_c values were rejected as a reasonable set of solution. In the modified program, such a fluctuation is handeled by a iterative non-linear algorithm that estimates the Q_0 and η values without taking the logarithm twice. This modification is important for Pn, which is more subjected to the instability since it has a shorter travel time resulting from both a faster group velocity and narrower distance range (less than about 12°).

Another modification to the algorithm is made such that when two-station paths are available, the algorithm takes the Q_0 and η values measured between the two-stations as a constraint in the simultaneous M_0, f_c and path Q_0 and η inversion. The use of this constraint in the inversion can reduce effects of the source radiation patterns and the deviation of source spectra from the idealized (*e.g.*, omega-square) model.

Synthetic study of Pn geometrical spreading

One of the most uncertain factors in determining the Q and source spectral parameters using Pn is its geometrical spreading term (GST) (*e.g.*, Sereno *et al.*, 1988; Sereno & Given 1990; Zhu *et al.*, 1991). Sereno *et al.* and Zhu *et al.* suggested that the best GST for Scandinavia and Canada are approximately Δ^{α}, with α being approximately -1.3. We have estimated the GST with synthetic Pn seismograms for central Asia, using a frequency-wave number integration algorithm (Saikia, 1994) and some recently published velocity models for the area. As an example, Fig. 1 shows the decay of synthetic Pn amplitude spectra between 0.2 and 2.0 hz, calculated using model M1 of Roecker *et al.* (1993) for northern Tien Shan. Following Sereno & Given (1990), we applied the earth flattening correction. In this particular example, parameterizing the GST by a constant α result in an estimate of α of -1.4 ± 0.2. This parameterization, however, clearly oversimplifies the detailed distance variation of Pn amplitude spectra, and one should expect a deviation from $\Delta^{-1.4}$ by at least a factor of 2. Considering that the real structure varies three dimensionally, an attempt to obtain a more precise GST is not practical. Thus we plan to use an α of -1.3 throughout this research.

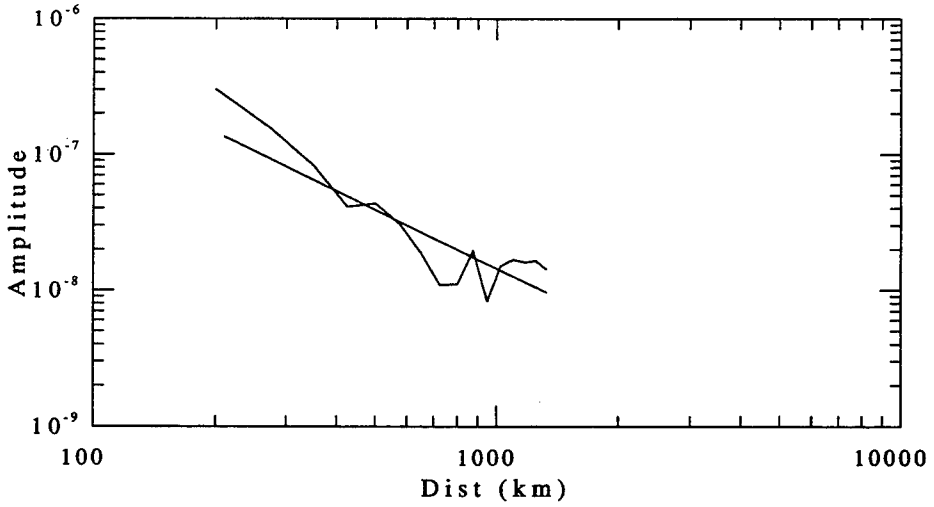

Fig. 1. Decay of synthetic Pn amplitude spectra averaged over 0.2 to 2.0 hz, calculated using model M1 of Roecker *et al.* (1993) with infinite Q values. The straight line is the linear-regression fit of the decay, with a slope of -1.4 ± 0.2.

Drastic Pn amplitude variations across the KNET

We have collected more than one hundred Pn spectra recorded at 16 broad-band IRIS, Kyrghistan network (KNET), Kazakhstan Network (KZN) and CDSN stations, from three underground nuclear explosions and 14 earthquakes in central Asia. A wealth of information have been gained on the characteristics of excitation and propagation of Pn in central Asia. As has been noted by several authors before, time domain Pn amplitudes from Lop Nor explosions vary drastically across the KNET stations. As an example, Figure 2 shows the record section from the Oct. 7, 1994 Lop Nor explosion, which is located to the east of the KNET stations (Fig. 4). The Pn amplitude varies by a factor of about 19 across the KNET, despite the relative small span (~ 2°) of the network. Figure 3 shows the corresponding amplitude spectra of Pn, obtained using a window with an effective length of 4.5 s. The amplitude variation primarily occur at low (~ 1hz) frequencies. For instance, the 1 hz amplitude is a factor of 27 higher at station KBK than at AML.

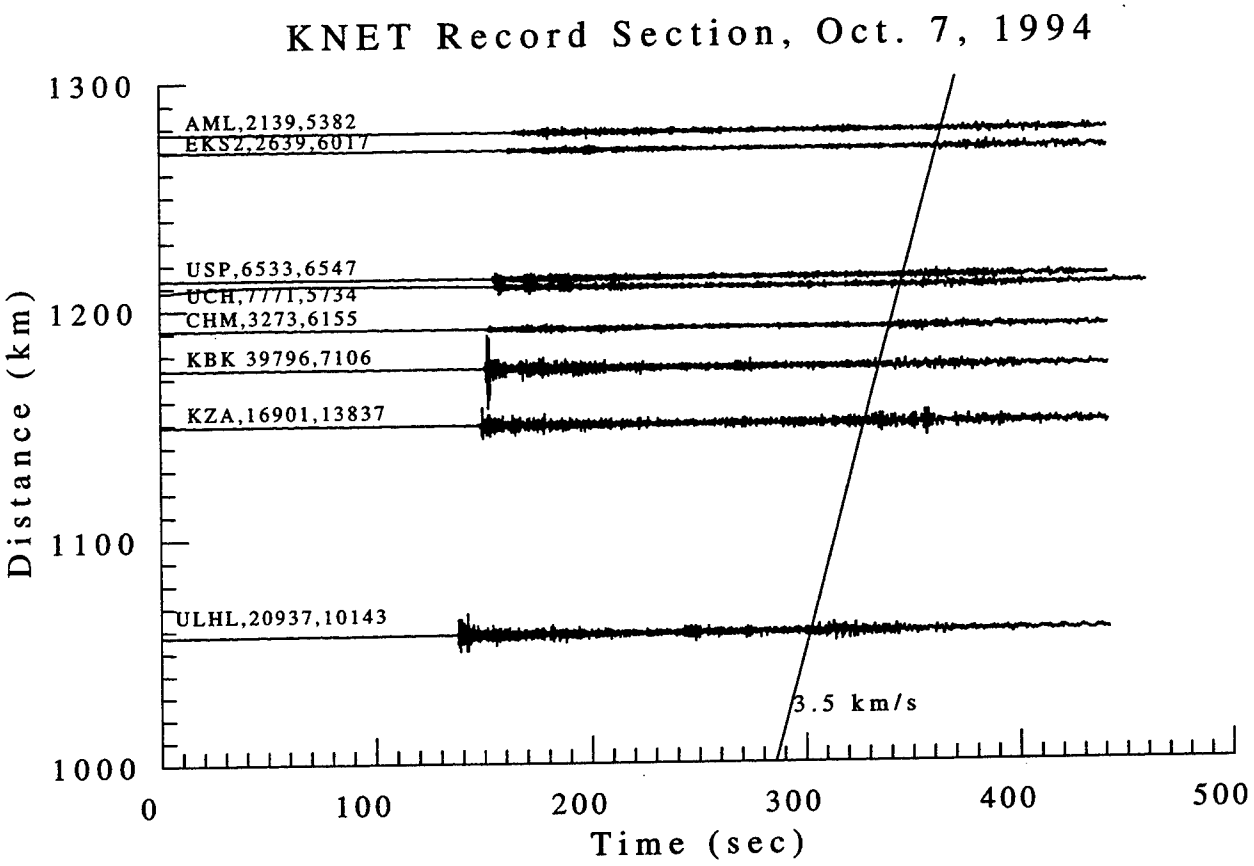

Fig. 2. Record section showing seismograms from the Oct. 7, 1994 Lop Nor explosion, at the KNET stations. The first arrival is the Pn phase. The time corresponding to a group velocity of 3.5 km/s (typical of Lg) is marked by a straight line. The traces are normalized by a common factor. Station name and peak Pn and Lg amplitudes are indicated near each trace. Note that at KBK, the amplitude is 12 times of that at a nearby station (CHM), and 19 times of that at station AML.

Various attempts have been made to explore the origin of this amplitude variation. We studied frequency-dependent polarization of Pn across KNET from Lop Nor explosions, but found that the polarization is strongly affected by the topography near individual stations, thus is not very useful in inferring the origin of the amplitude variation. We studied Pn amplitude across KNET from earthquakes in southern Tien Shan, and found that the pattern of Pn amplitude variation differs from that of Lop Nor explosions. Fig. 5 shows a record section from a southern Tien Shan earthquake. In Fig. 5, Pn amplitudes at stations KBK and AML are low and high, respectively, opposite to the trend observed in Fig. 2. Therefore, a systematic site response is ruled out as the cause of the amplitude variation. We also analyzed Pn from earthquakes in northern Xinjiang, west of Lake Bosten Hu (Fig. 4). Fig. 6 shows the record section for one of such earthquakes. Generally, Pn is very weak across the KNET, but the pattern of amplitude variation is similar to that found from Lop Nor explosions: Pn amplitude reaches its maximum at stations KBK and KZA and drops to a minimum at more distant stations. This suggests that some 3D velocity anomaly along the east-west oriented paths is responsible for the amplitude variation. Fig. 7 shows a synthetic Pn ray pattern through model M1 (last section). This ray pattern is stable since the structure is 1D. The observed large amplitude variation must be associated with an

unstable ray pattern, and the easiest way to introduce such a unstable pattern is to introduce a 3D topography to the Moho, where the most drastic ray bending occurs in the absence of 3D complications. The degree of deviation from the layered 1D structure, necessary to cause unstable ray patterns, is minimum if the deviation occurred as such a 3D topographic variation near the bending point of Pn ray at Moho. The 3D Moho topography may be associated with the drastic variations in surface topography and geology from Lake Issyk-kul to the mountains in the west (Fig. 4).

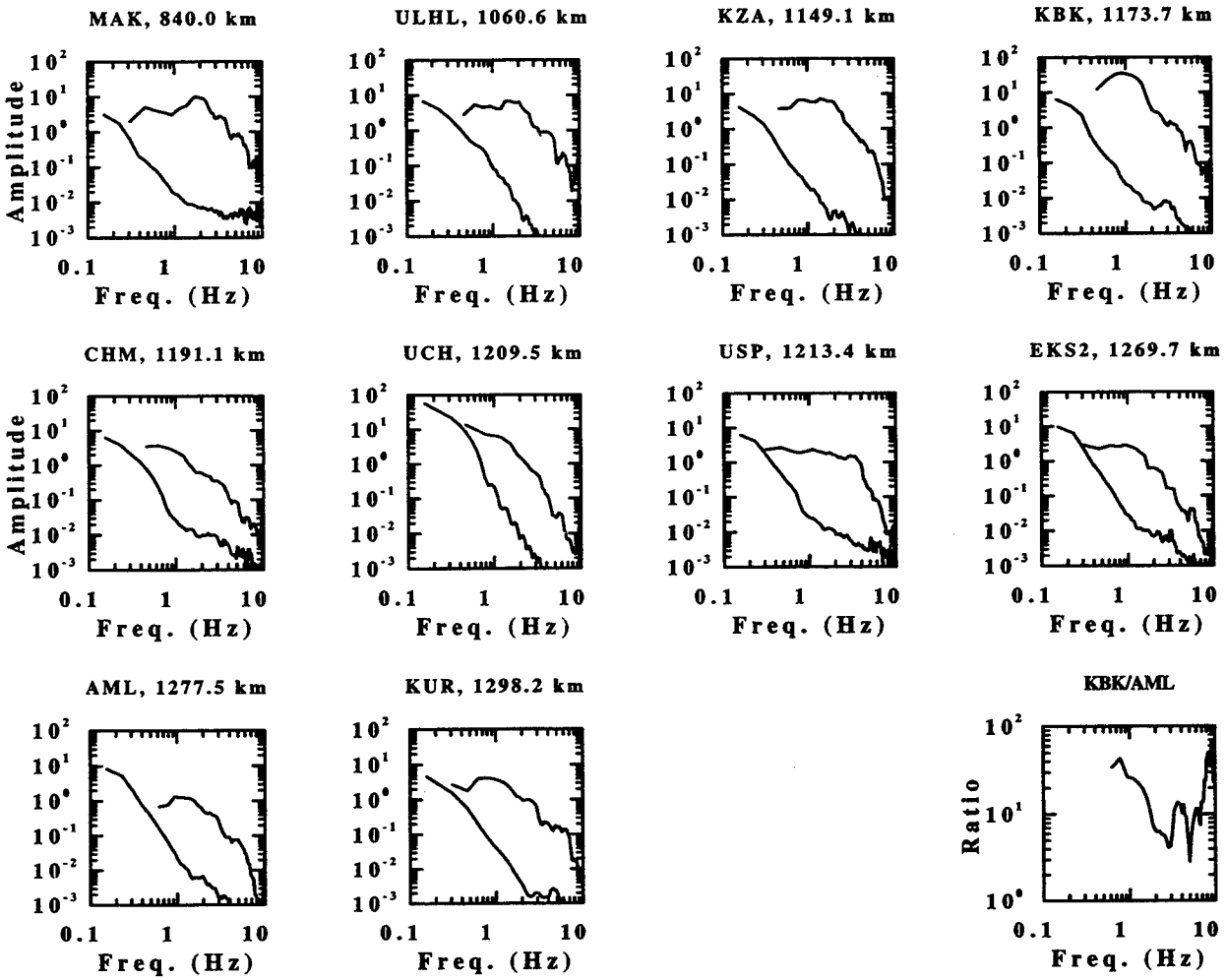

Fig. 3. Pn and noise spectra from the Oct. 7, 1994 Lop Nor explosion, calculated for ten KNET and KZN stations (all but the lower right panels), with an effective window length of 4.5 s. The lower right panel is the spectral ratio of KBK/AML. Note the wide range of the amplitudes at 1 Hz for various stations, and the factor of 27 at 1 Hz in the KBK/AML spectral ratio.

Pn/Lg ratio as a discriminant?

Comparing Figs. 2 and 6, one would be tempted to draw an easy conclusion that the Pn/Lg amplitude ratio works well as a discriminant between explosions and earthquakes. However, this conclusion is premature. The reason for the low Pn amplitudes in Fig. 6 is likely caused by a null in the source-to-Pn radiation pattern since the earthquakes occurred east of Lake Bosten Hu, where earthquakes sources are typically characterized by an east-west strike-slip motion (Center

for Analysis and Prediction, 1991). The earthquakes from southern Tien Shan generate stronger Pn signals across KNET (Fig. 5), suggesting that the Pn/Lg ratio from earthquakes is significantly affected by the focal mechanism. Therefore, any attempt to use Pn/Lg amplitude ratio as a discriminant must account for the instabilities of the Pn amplitude (and to a less extend, Lg amplitude) caused by 3D velocity complications, as well as the source-to-Pn radiation pattern. We are currently analyzing Pn from more earthquakes to quantify these instabilities.

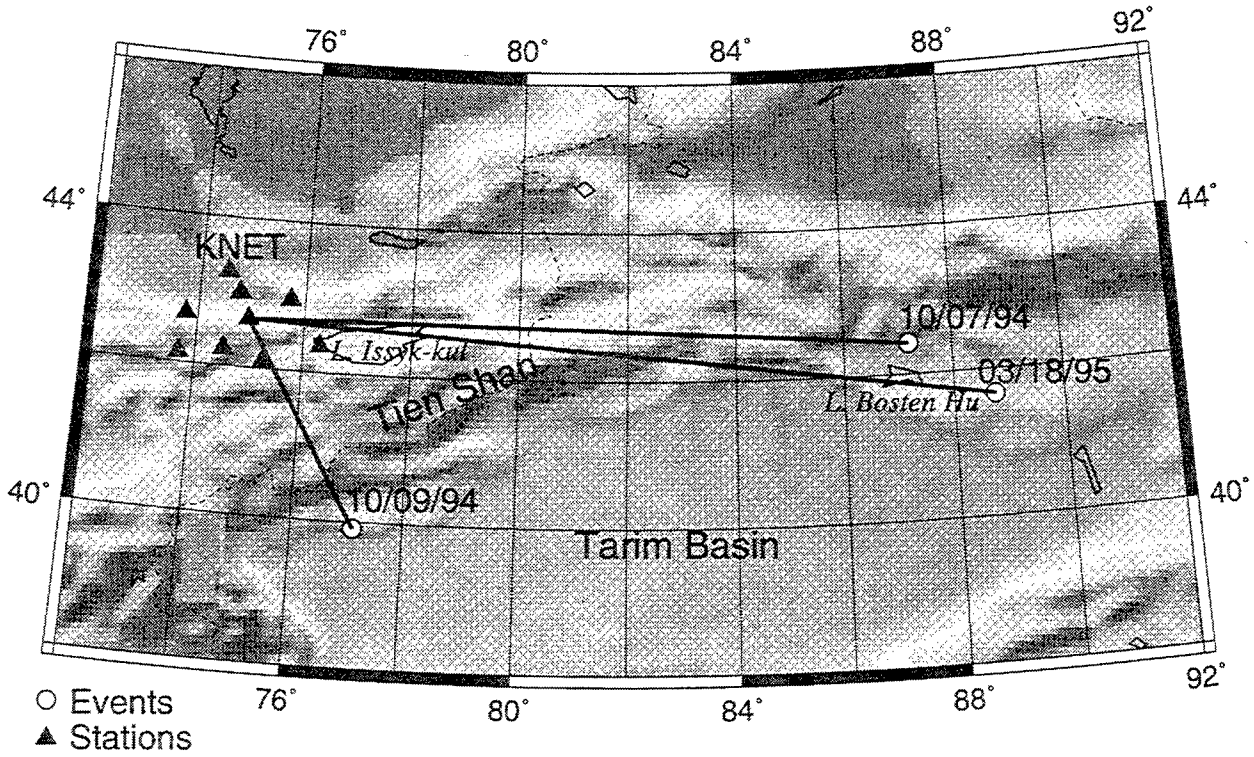

Fig. 4. Map showing locations of a Lop Nor explosion (event 10/07/94), an earthquake in northern Xin Jiang (east of Lake Bosten Hu; 03/18/95), and an earthquake in southern Tien Shan (10/09/94). Pn from these three events are presented in this paper as examples. Paths to a representative KNET station (station KBK) are plotted.

Measurement of Pn M_0, f_c *and path Q*

In a preliminary analysis, we measured the source and path spectral parameters using Pn from the Oct. 7, 1994 Lop Nor explosion, with the modified algorithm mentioned in a previous section, and the modified Mueller-Murphy source model (Sereno *et al.*, 1988). Station KBK is not used due to the abnormal large amplitude (Figs. 2 and 3). The resulting M_0 and f_c values are 1.5×10^{23} dyne-cm and 1.6 Hz, respectively. For comparison, a previous inversion using Lg (Xie *et al.*, 1996) has resulted in an M_0 of 5.5×10^{22} dyne-cm, and an f_c of 0.8 Hz. The averaged Pn Q_0 and η values are 379 and 0.7, respectively, for the nine paths connecting the Lop Nor and stations MAK, ULHL, KZA, CHM, UCH, USP, EKS, AML, KUR. All but the first of these stations belong to the KNET. The lowest and highest Q_0 values are 204 (to station AML) and 573 (to station KZA). Currently, results for more events are being obtained with more reliable means, described in the next section.

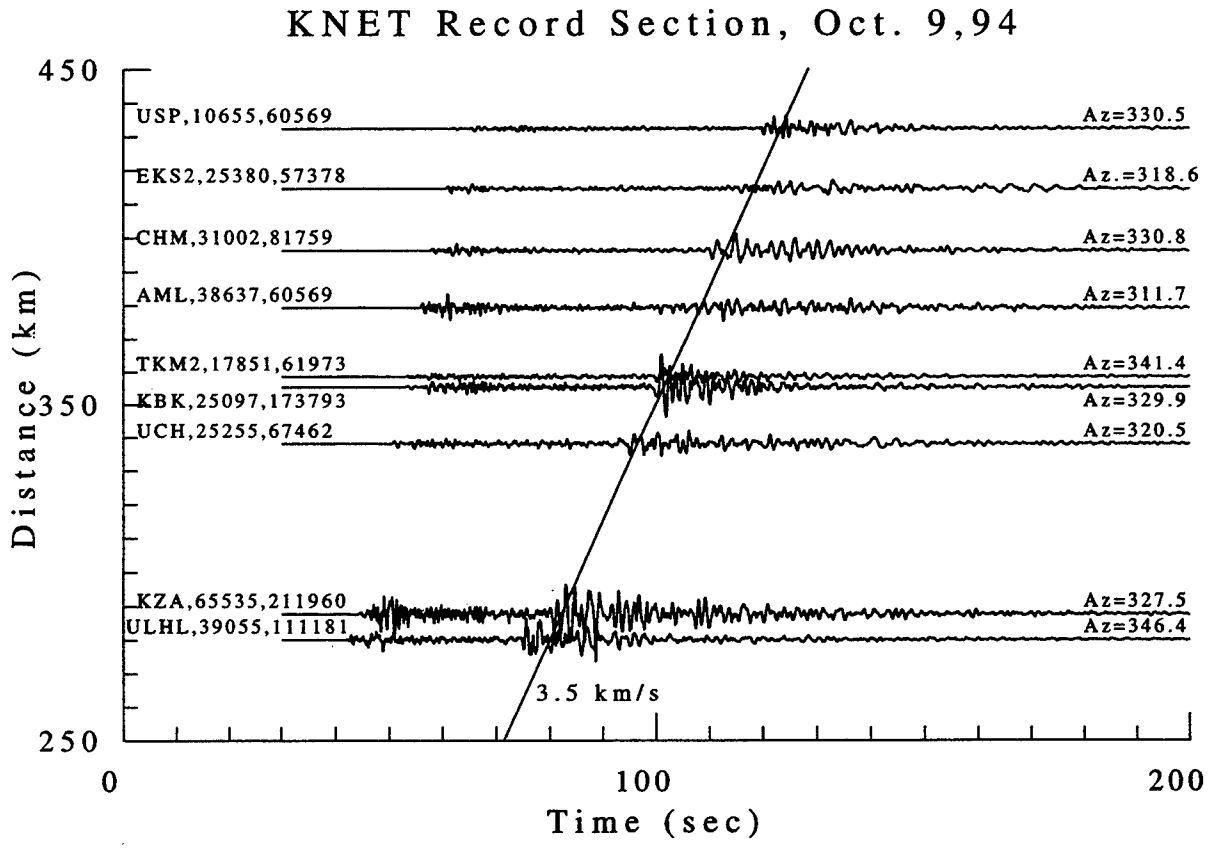

Fig. 5. Record section showing seismograms from the Oct. 9, 1994 southern Tien Shan earthquake. The first arrival is the Pn phase. Plotted in the same manner as in Fig. 2. Note that the Pn amplitude at KBK is lower than at AML.

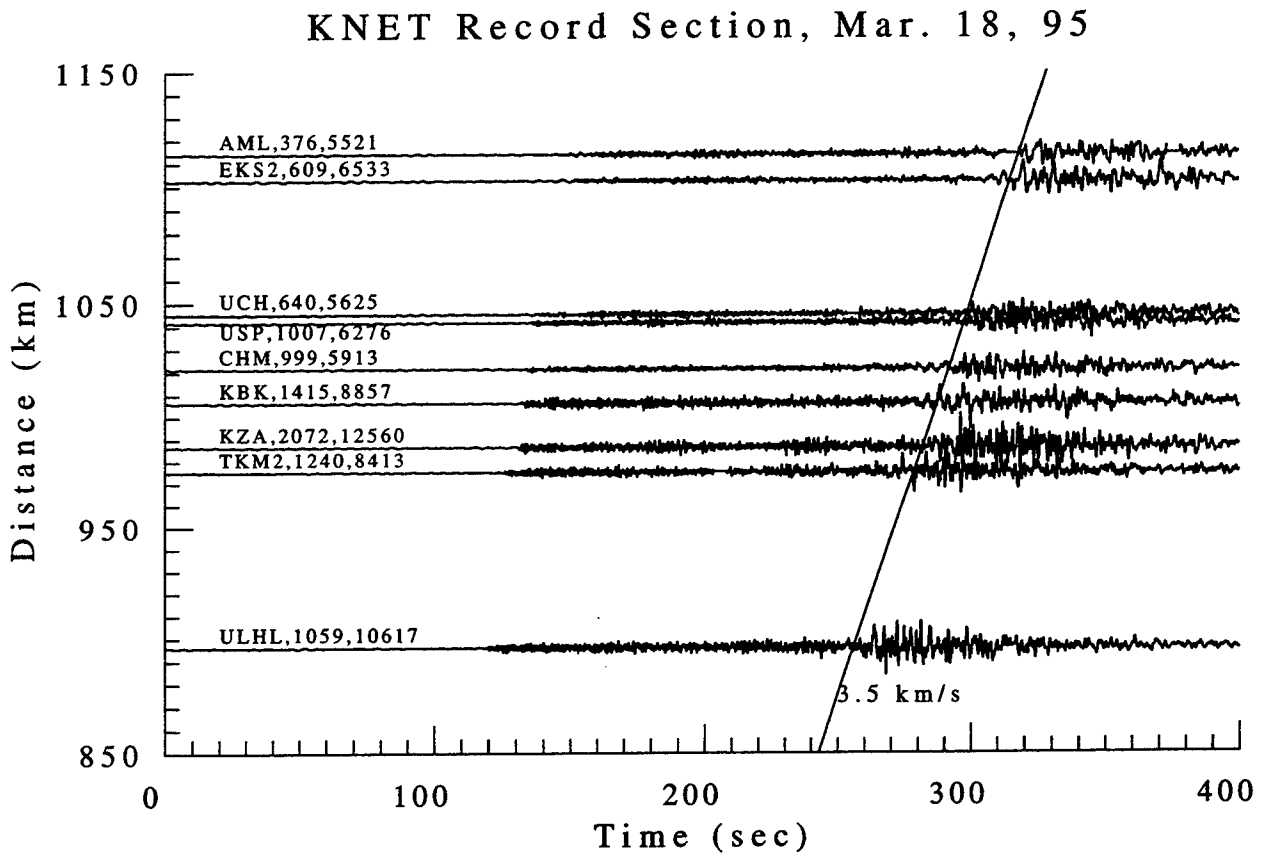

Fig. 6. Record section showing seismograms from the March 18, 1995 Northern Xin Jiang earthquake. The first arrival is the Pn phase. Plotted in the same manner as in Figs. 2 and 5.

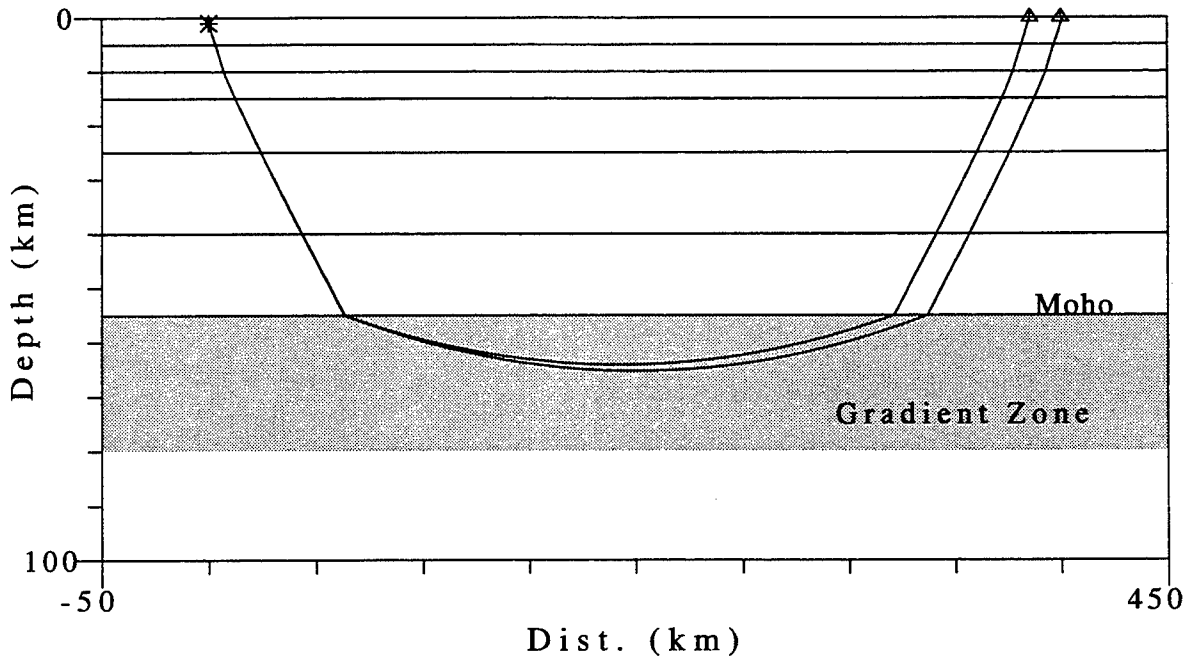

Fig. 7. Pn ray pattern for a shallow source (star) in a 1D structure, which is slightly modified from model M1 of Roeker *et al.* (1993) by introducing a zone of a larger velocity gradient (~ 0.009 s^{-1}) below Moho. The ray pattern only serves for a schematic purpose since the velocity gradient used is likely larger than the average value in central Asia.

CONCLUSIONS AND RECOMMENDATIONS

Much of the first ten months of this research has been devoted to software development, data collection and processing, and synthetic studies of the Pn propagation. Several important findings have been made on the characteristics of Pn excitation and propagation in central Asia. These include:

(1) Pn geometrical spreading estimated using synthetics in 1D structures for central Asia suggests that it agrees roughly with a trend of $\Delta^{-1.3}$, although the localized fluctuation is quite significant (by a factor of 2 or more) from that trend.

(2) The observed Pn amplitude varies drastically (by a factor of up to 20 to 30) across KNET from Lop Nor explosions and Northern Xinjiang earthquakes, which are located to the east of the stations. This amplitude variation primarily occurs at lower (~ 1 hz) frequencies, and does not correlate with the amplitude variation across KNET from events in the south. The most likely cause of the amplitude variation is a short wavelength variation in the Moho topography near the bending point of Pn raypath.

(3) Pn/Lg amplitude ratio also appears to be highly dependent on the source-to-Pn radiation pattern. This ratio can be used efficiently to identify earthquakes when the station is located at the Pn radiation null. For other source-station configurations, however, the validity and/or efficiency of the ratio as a discriminant between explosions and earthquakes need further investigation.

(4) Preliminary inversion of a well-recorded Lop Nor explosion suggests that the M_0 and f_c values derived using Pn are both higher than those derived using Lg. Inversion of Pn spectra from many more events, with an improved method, is underway.

Research conducted so far suggests that any attempts to use Pn/Lg amplitude ratio as a discriminant, or to invert for source/path spectral parameters must take into account the Pn amplitude variations caused by effects of 3D velocity complications and the source radiation pattern. Since both effects are supposed to be reduced when Pn coda is used, we have already implemented an algorithm to invert for M_0, f_c, path Q_0 and η using the entire wavetrain that includes Pn and Pn coda, received *prior* to Pg. We will compare the stability of the results using Pn alone with those using the averaged spectra of Pn and Pn coda. Since almost all necessary software development has been achieved, the next 14 months of the research will be mainly devoted to data processing, inversion and interpretation.

By collecting Pn records at KNET stations from more Northern Xinjiang earthquakes, particularly those earthquakes whose focal mechanisms differ from the typical east-west strike slip, we will continue to explore the cause for the large Pn amplitude variation across the KNET for the east-west oriented paths. In particular, the existence of any 3D Moho topography and its link to the topographic/geological variation from Lake Issyk-kul to Northern Tien Shan will be investigated.

References

Center for Analysis and Prediction, 1991. *Focal Mechanism Map of China and Adjacent Areas*, Chinese Science and Technology Publisher, Beijing, China.

Roecker, S.W., T.M. Sabitova, L.P. Vinnik, Y.A. Burmakov, M.I. Golyanov, R. Mamatkanova, and L. Munirova, 1993. Three-dimensional elastic wave structure of the western and central Tien Shan, *J. Geophys. Res.*, **98**, 15,779-15,795.

Saikia, C.K., 1994. Modified frequency-wave number algorithm for regional seismograms using Filson's quadrature: modeling of Lg waves in eastern North America, *Geophys. J. Int.*, **118**, 142-158.

Sereno, T.J., S.R. Bratt and T.C. Bache, 1988. Simultaneous inversion of regional wave spectra for attenuation and seismic moment in Scandinavia, *J. Geophys. Res.*, **93**, 2019-2036.

Sereno, T.J. and J. W. Given, 1990. Pn attenuation for a spherically symmetric Earth model, *Geophys. Res. Lett.*, **17**, 1141-1144.

Xie, J. 1993. Simultaneous inversion of source spectra and path Q using Lg with applications to three Semipalatinsk explosions, *Bull. Seism. Soc. Am.*, **83**, 1547-1562.

Xie, J., L. Cong & B.J. Mitchell, 1996. Spectral characteristics of the excitation and propagation of Lg from underground nuclear explosions in Central Asia, *J. Geophys. Res.*, **101**, 5813-5822.

Zhu, T.F., K.Y. Chun & G.F. West, 1991. Geometrical spreading and Q of Pn waves: An investigative study in eastern Canada. *Bull. Seism. Soc. Am.*, **81**, 882-896.

Source Characterization Using Simplified Waveforms: Tests on Earthquakes and Nuclear Explosions in Xinjiang, China

Jiajun Zhang
Institute of Tectonics, University of California, Santa Cruz, CA 95064

Contract No: F49620-94-1-0315
Sponsored by AFOSR

ABSTRACT

Complete seismic waveforms with periods longer than 30 s recorded at teleseismic and regional distances are used to determine the location, depth, and focal mechanisms of several earthquakes and underground nuclear explosions in the Lop Nor area, Xinjiang, China. An algorithm called the Earth simplifying transformation (EST) is applied to the primary-event data to remove propagation effects of Earth's lateral and radial heterogeneities that are not predicted by a given Earth model. The procedure involves frequency domain division of each pair of observed and synthetic waveforms for several auxiliary events, in the vicinity of the primary event, with the synthetics being computed for a standard Earth model using a well-constrained focal mechanism for each auxiliary event. The frequency dependent deconvolution filters obtained for the auxiliary events are interpolated to obtain the predicted deconvolution filter for the primary event using a modified Lagrange polynomial. The predicted deconvolution filter is then convolved with corresponding signals for the primary event.

The waveforms obtained from the EST algorithm are noise-desensitized by separately determining the envelope and instantaneous phase using corresponding deconvolution filters. The EST waveforms are then used to determine the centroid location, depth, time and focal mechanism of the primary event by centroid-moment-tensor (CMT) inversion. For the September 7, 1994 earthquake, which has a m_b magnitude of 5.1, our analysis yields a centroid depth of 13 km, significantly shallower than the 33 km depth reported from PDE and from the Harvard CMT catalogue. Our analysis suggests that the centroid depth of the May 21, 1992 nuclear explosion is about 10 km; and the centroid depth of the October 5, 1993 nuclear explosion is about 5 km shallower than that of the May 21, 1992 explosion.

The EST algorithm may provide high resolution in analysis of source properties of small earthquakes and explosions that occurred in the Lop Nor area with, say, m_b magnitudes less than 4. To this end, it is necessary to apply the algorithm to regional waveforms recorded at station WMQ and to develop the crustal model for paths from auxiliary events to the station for the computation of synthetic seismograms for waves with periods as short as a few seconds. The synthetic waveforms for the auxiliary events will allow us to obtain high-resolution deconvolution filters for the determination of location, depth, and focal mechanism of small earthquakes and explosions.

Key words: source parameters, regional seismograms, nuclear test monitoring

OBJECTIVE

The objective of this study is to develop and apply new methods for high-resolution characterization of source properties of explosions and earthquakes, including location, depth, mechanism, magnitude, and source-time functions. Our analysis involves complete waveform data, with emphasis being on short-period regional waves and on small earthquakes and explosions. The high-resolution characterization of these source properties will improve the regional monitoring and discrimination capability under a CTBT as well as basic seismological knowledge on global and regional seismicity and on source processes involved in explosions and earthquakes.

RESEARCH ACCOMPLISHED

Our progress in the past year includes mainly the following developments: (1) extending the single-auxiliary-event Earth Simplifying Transformation (EST) algorithm for source characterization proposed last year to multiple-auxiliary-events EST algorithm; (2) developing a noise-desensitizing deconvolution technique for reducing amplitude fluctuation due to deconvolution; (3) computing short-period regional waveforms using several reflectivity methods to explore the possibility of improving resolution by including crustal model determination in the EST algorithm.

Development (3) is directed at improving the results from inversions of EST waveforms, but it is not much different from many Earth's structure studies documented elsewhere and thus is not discussed in details in this report. We will focus on (1) and (2), which involve a new data processing algorithm. This algorithm is referred to as the Earth simplifying transformation (EST), which allows us to simplify observed waveforms by reducing the effects of the complexity of the Earth's structure, including both lateral and radial heterogeneities. The simplified waveforms are used in a waveform inversion technique to determine hypocentral locations and moment tensors of earthquakes or explosions.

Method. Following Gilbert and Dziewonski [1975], the spectrum of a component of ground motion excited by a point source at angular frequency ω for a given Earth model may be given by

$$u_k'(\mathbf{x}, \mathbf{x}_j', \omega) = \sum_{i=1}^{6} \psi_{ki}(\mathbf{x}, \mathbf{x}_j', \omega) f_i'(\mathbf{x}_j', \omega). \quad (1)$$

where u_k' is the k-th record in a set of seismograms, with the receiver at position $\mathbf{x}$ and the source at $\mathbf{x}_j'$; ψ_{ki} are excitation kernels, and f_i' represent six independent components of the moment-rate tensor. In the following discussion ω is ignored for expression simplicity. The question that we shall address in this study is as follows. Given a set of seismograms at common stations from an event at $\mathbf{x}_p$ (the primary event) and from N events at $\mathbf{x}_1'$, ... , $\mathbf{x}_N'$ (auxiliary events), which are located in the proximity of $\mathbf{x}_p$, along with synthetics for the auxiliary events, u_k', computed for a given Earth model, is it possible to determine hypocenter position ($\mathbf{x}_p$) and moment-rate tensor (f_i) of the primary event?

Taking into account our imperfect knowledge of Earth's structure and background noise, the spectra of observed ground motion for the auxiliary events may be expressed as

$$U_k'(\mathbf{x}, \mathbf{x}_j') = u_k'(\mathbf{x}, \mathbf{x}_j')\,\alpha_k'(\mathbf{x}, \mathbf{x}_j') + \varepsilon'(\mathbf{x}, \mathbf{x}_j') \qquad (j = 1,...,N), \tag{2}$$

where α' represents effects of the deviation of the Earth's structure from the Earth model. In this analysis we ignore the noise terms (ε) and search for functions α_k' (hereafter referred to as the observed transfer function) by solving the following equations:

$$\alpha_k'(\mathbf{x}, \mathbf{x}_j') = U_k'(\mathbf{x}, \mathbf{x}_j') \,/\, u_k'(\mathbf{x}, \mathbf{x}_j') \qquad (j = 1,...,N). \tag{3}$$

Since α' are not uniquely constrained by equations (3) and the auxiliary events span a region with very small volume around the hypocenter of the primary event near the Earth's surface, we will determine $\alpha'(\mathbf{x}, \mathbf{x}')$ for each station $\mathbf{x}$ using a polynomial of degree N-1 modified from the Lagrange interpolation formula [Dahlquist and Björck, 1974], which are bounded for any $\mathbf{x}'$. The coefficients of the polynomials are determined using (3) from data and synthetics for the auxiliary events. Then we may compute $\alpha'(\mathbf{x}, \mathbf{x}')$ for any $\mathbf{x}'$, say, the assumed position of the primary event, $\mathbf{x}_p$. This results in $\alpha'(\mathbf{x}, \mathbf{x}_p)$ (hereafter is referred to as the predicted transfer function).

Using the value of $\alpha'(\mathbf{x}, \mathbf{x}_p)$ and the observed spectra for the primary event, $U_k(\mathbf{x}, \mathbf{x}_p)$, we define the following transformation

$$u_k^P(\mathbf{x}, \mathbf{x}_p) = U_k(\mathbf{x}, \mathbf{x}_p) \,/\, \alpha_k'(\mathbf{x}, \mathbf{x}_p). \tag{4}$$

which is referred to as the Earth simplifying transformation (EST). Following the notation used in (1) and (2) the observed spectra for the primary event can be written as

$$U_k(\mathbf{x}, \mathbf{x}_p) = u_k(\mathbf{x}, \mathbf{x}_p)\,\alpha_k(\mathbf{x}, \mathbf{x}_p), \tag{5}$$

where the theoretical spectra are given by

$$u_k(\mathbf{x}, \mathbf{x}_p) = \sum_{i=1}^{6} \psi_{ki}(\mathbf{x}, \mathbf{x}_p)\, f_i(\mathbf{x}_p). \tag{6}$$

In general, α are slowly varying functions of the source position and the moment-rate tensor. Therefore we assume

$$\alpha_k(\mathbf{x}, \mathbf{x}_p) = \alpha_k'(\mathbf{x}, \mathbf{x}_p). \tag{7}$$

The accuracy of this assumption is influenced by the proximity of the events, the frequency content of the data, and our choice of the theory for the calculation of the synthetics, accounting our imperfect knowledge of Earth's structure and of excitation and propagation of seismic waves. Then it follows from (4) to (7) that

$$u_k^P(\mathbf{x}) = \sum_{i=1}^{6} \psi_{ki}(\mathbf{x}, \mathbf{x}_p)\, f_i(\mathbf{x}_p). \tag{8}$$

which is correct to first-order in terms of α's Taylor series expansion and will be used to determine the hypocentral position ($\mathbf{x}_p$) and moment-rate tensor (f_i) of the primary event. For simplicity of analysis, we adopt a frequently used assumption: f_i are considered to be independent of frequency except for a common correction for an assumed duration of the source, and are regarded as the moment tensor. We use an iterative procedure to determine the hypocentral depth, location, centroid time, and source moment-tensor; in each iteration, first we solve equations (8) for the moment-tensor, then we calculate partial derivatives of seismograms and determine the perturbation of the depth, location, and centroid time using residual seismograms.

In comparison with conventional algorithms, in which the moment tensor of an event is directly determined from data for the primary event itself, the EST algorithm described above requires additional data from auxiliary events, which must be located at close distances to the primary event and must have known moment tensors. However, the algorithm allows us to make use of seismic waves, in particular short-period surface waves, that may be affected by the complexity of the Earth's structure, including both lateral and radial heterogeneities. Clearly, errors in auxiliary-event moment-tensors will project into the primary-event solution, so good independent constraints on moment tensors of auxiliary events are critical. It is preferred to chose a set of auxiliary events larger than the primary event, since larger events usually have better signal-to-noise ratio than smaller events, and the source mechanisms of larger events can be better constrained using waveforms recorded by global seismic networks.

Note that for the EST algorithm involving only one auxiliary event the EST waveform (u_k^P) depends linearly on the moment tensor (f_i') of the auxiliary event. This removes the sensitivity of the centroid location and depth obtained from inversions of EST waveforms to the assumed focal mechanism of the auxiliary event. Suppose a linear transformation is applied to synthetics for the auxiliary event (u_k'), so that the synthetics will correspond to moment tensor $g_i'(\mathbf{x}')$ with $g_i'(\mathbf{x}') = f_i'(\mathbf{x}')\, d_i$, ($i$ = 1, ..., 6) instead of $f_i'(\mathbf{x}')$ as in (1). Then the EST waveforms may be written as

$$u_k^P(\mathbf{x}) = \sum_{i=1}^{6} \psi_{ki}(\mathbf{x}, \mathbf{x}_p)\, g_i(\mathbf{x}_p), \tag{9}$$

where $g_i(\mathbf{x}_p) = f_i(\mathbf{x}_p)\, d_i$, ($i$ = 1, ..., 6). It follows that the centroidal parameters for the primary event determined from EST waveforms (9) are essentially the same as those from EST waveforms (8), with their differences being due to noise in data and errors in assumption (7), that is, errors in the predicted transfer function. Ideally, the centroidal parameters determined from the EST algorithm are independent of the focal mechanism which is used in the calculation of the synthetics for the auxiliary event.

Therefore, using well determined centroidal parameters of the auxiliary event which is located in the close proximity of the primary event, the centroidal parameters of the primary event can be determined without using *a priori* focal mechanism for the auxiliary event. We utilize the stability of centroidal solution from inversions of EST waveforms in the experiments to determine the apparent depth of the October 5, 1993 explosion relative to that of the May 21, 1992 explosion. Our analysis suggests that the 1992 and 1993 explosions have centroid depths of about 10 and 5 km, respectively.

Tests. We carried out a series of experiments on the determination of source parameters of earthquakes and nuclear explosions in the Lop Nor area (Table 1, Figure 1). Figure 2a shows short-period regional waveforms recorded at station WMQ from two earthquakes that occurred on the Lop Nor test site (event A, m_b 4; event B, m_b 4.6) and the May 2, 1995 earthquake (event III, m_b 5.5) located to the west of the station (Figure 1).

The crustal structure model for the path between WMQ and the test site obtained by Gao and Richards [1994] was used to compute the synthetic seismograms for the May 2, 1995 earthquake using the source mechanism from the Harvard CMT catalogue (Figure 2). The synthetics were computed using a wavenumber-frequency integration algorithm

[Saikia, 1994]. Several other reflectivity methods were also used, which gave essentially the same synthetic waveforms.

Figure 2a shows that the synthetics match the observerd waveforms for the vertical and transverse component qualitatively. The similarity between observed waveforms for events A and III suggests that it is possible to use a layered crustal structure model in the EST algorithm in analysis of regional waves with periods as short as a few seconds for data recorded at WMQ from events at various azimuths.

Comparison between observed waveforms indicates that event B has more complex waveforms than for event A and III. A close examination of the records suggests that the original time of event B reported from PDE may correspond to the arrival from an earlier, much smaller event, and this small event is followed by a larger event after about 10 s into the record. Figure 2b shows vertical records for the two earthquakes on the test site. Since records for small earthquakes often show energy from multiple events, it is often difficult to identify the first arrival from an event. Therefore, it is important to use waveform inversion techniques in the determination of origin time, location, and depth of small earthquakes and explosions.

Figure 3 shows displacement waveforms for two stations at teleseismic distances from several earthquakes, bandpass filtered between 20 and 30 mHz, along with synthetics computed using the PREM model [Dziewonski and Anderson, 1981]. Various experiments were carried out in this study to stablize the result of deconvolution. To reduce the amplitude fluctuation of EST waveforms, we use a procedure to determine separately the envelope and instantaneous phase of the EST waveform, which are referred to as the envelop transformation and phase transformation.

Figure 3 shows the EST waveforms obtained with the envelope transformation and those without the transformation. The synthetics for the 1994 earthquake (event IV) fit the EST waveforms with the transformation much better than for EST waveforms without the transformation. For all the events used in this study, variance reductions in inversions of EST waveforms with the envelop transformation are much larger than for inversions of EST waveforms without the transformation.

Figure 4 shows vertical and radial components of EST waveforms for the 1994 earthquake for various stations, along with the synthetics computed for the Harvard CMT solution and for the solution obtained from inversions of EST waveforms (hereafter are referred to as the CMT synthetics and EST synthetics, respectively). The CMT solution has a depth of 33 km, which is the same as the hypocentral depth reported from PDE. In general, for the transverse component the differences between the CMT synthetics and EST synthetics are much smaller than for the vertical and radial components, reflecting that the transverse component is less sensitive to the variation of source depth or focal mechanisms.

Figure 4 shows that differences between CMT synthetics and EST synthetics become greater at larger epicentral distances. High-mode surface waves are more strongly excited for the CMT synthetics than for the EST synthetics, reflecting their sensitivity to the source depth. Teleseismic waveforms may provide important information on the depth of the source because of better separation of high-mode and fundamental-mode surface waves. However, for the data set used here teleseismic waveforms are often not usable

because of their small SNR, in particular, for the radial component at SNZO (Figure 4).

CONCLUSIONS AND RECOMMENDATIONS:

The EST waveforms provide superior resolution power in the source characterization than original waveforms. This method works better for stations at close distances from the source. It is desirable to extend this procedure to analysis of regional waves with periods as short as a few seconds by including the crustal structure determination for the auxiliary events. This extension will reduce the threshold of the determination of the location, depth, and focal mechanisms of small earthquakes and explosions that occurred in remote regions.

REFERENCES

Dahlquist, G., and Å. Björck, *Numerical Methods*, Prentice-Hall, Englewood Cliffs, New Jersey, 1974.

Dziewonski, A. M., and D. L. Anderson, Preliminary reference Earth model, *Phys. Earth Planet. Int., 25*, 297-356, 1981.

Gao, L., and P. G. Richards, Studies of earthquakes on and near the Lop Nor, China, nuclear test site, *Proceedings of The 16th Annual Seismic Research Symposium*, 106-112, Phillips Laboratory, Hanscom, 1994, PL-TR-94-2217, ADA284667

Gilbert, F. and Dziewonski, A.M., 1975. An application of normal mode theory to the retrieval of structure parameters and source mechanisms from seismic spectra. *Philos. Trans. R. Soc. London, Ser. A.*, 278, 187-269.

Hu, F., J. Hu, M. Bai, S. Chen, D. Zhou, and J. Liu, Seismotectonics of Xinjiang Uygur Autonomous Region, in *Lithospheric Dynamics Atlas of China*, edited by Editorial Board for Lithospheric Dynamics Atlas of China, State Seismological Bureau, pp. 57, China Cartographic Publishing House, Beijing, 1989.

Saikia, C. K., Modified frequency-wavenumber algorithm for regional seismograms using Filon's quadrature–modeling of Lg waves in North America, *Geophys. J. Int., 118*, 142-158, 1994.

Table 1. Hypocentral Parameters of Events Used in This Study †

Event	Date	Time	m_b	Depth km	Lat °N	Long °E
I	91/08/19	06:05:51.3	5.5	30	46.944	85.302
II	93/10/02	08:42:32.7	6.2	14	38.190	88.663
III	95/05/02	11:48:11.6	5.5	33	43.776	84.660
IV	94/09/07	13:56:25.2	5.1	33	38.491	90.345
V	95/03/18	18:02:36.6	5.2	22	42.422	87.199
VI	92/05/21	04:59:57.5	6.5		41.604	88.813
VII	93/10/05	01:59:56.5	5.9		41.647	88.681
A	95/08/02	11:59:44.0	4.0	10	41.688	88.572
B	94/12/26	16:58:46.1	4.6	10	41.594	88.833

† Hypocentral parameters are from PDE monthly listings. Events VI and VII are underground nuclear explosions at the Lop Nor test site; other events are earthquakes. Earthquakes I to III are used as auxiliary events for the analysis of source parameters of other events.

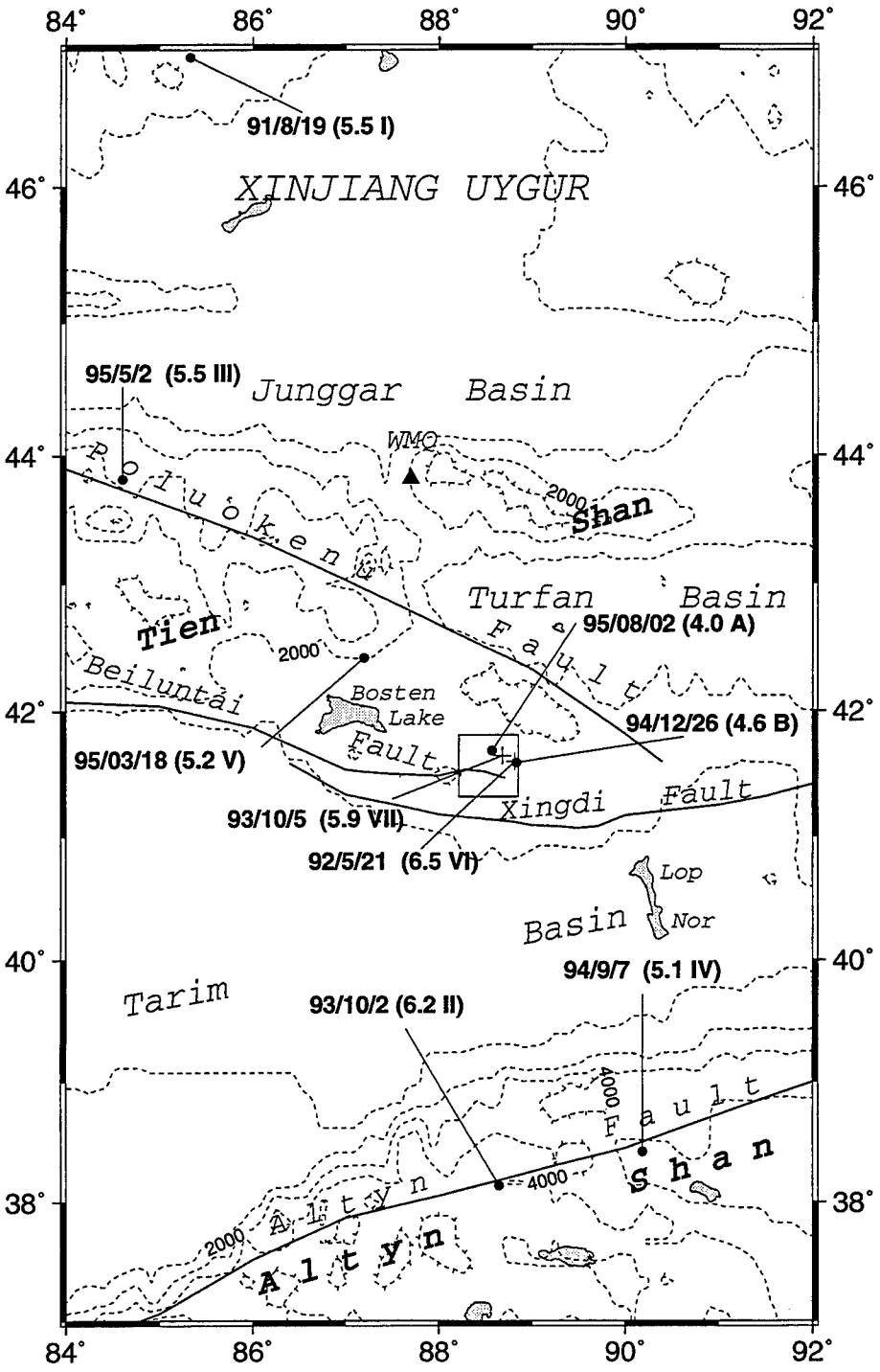

Fig. 1. Map showing the Lop Nor, China, underground test site (box) and locations of nuclear explosions (crosses) and earthquakes (solid circles) used in this study. Body-wave magnitude m_b and event numbers listed in Table 1 are shown in the paratheses for each event. Station location for WMQ is shown with the solid triangle. Active faults in the area are from Hu et al. [1989].

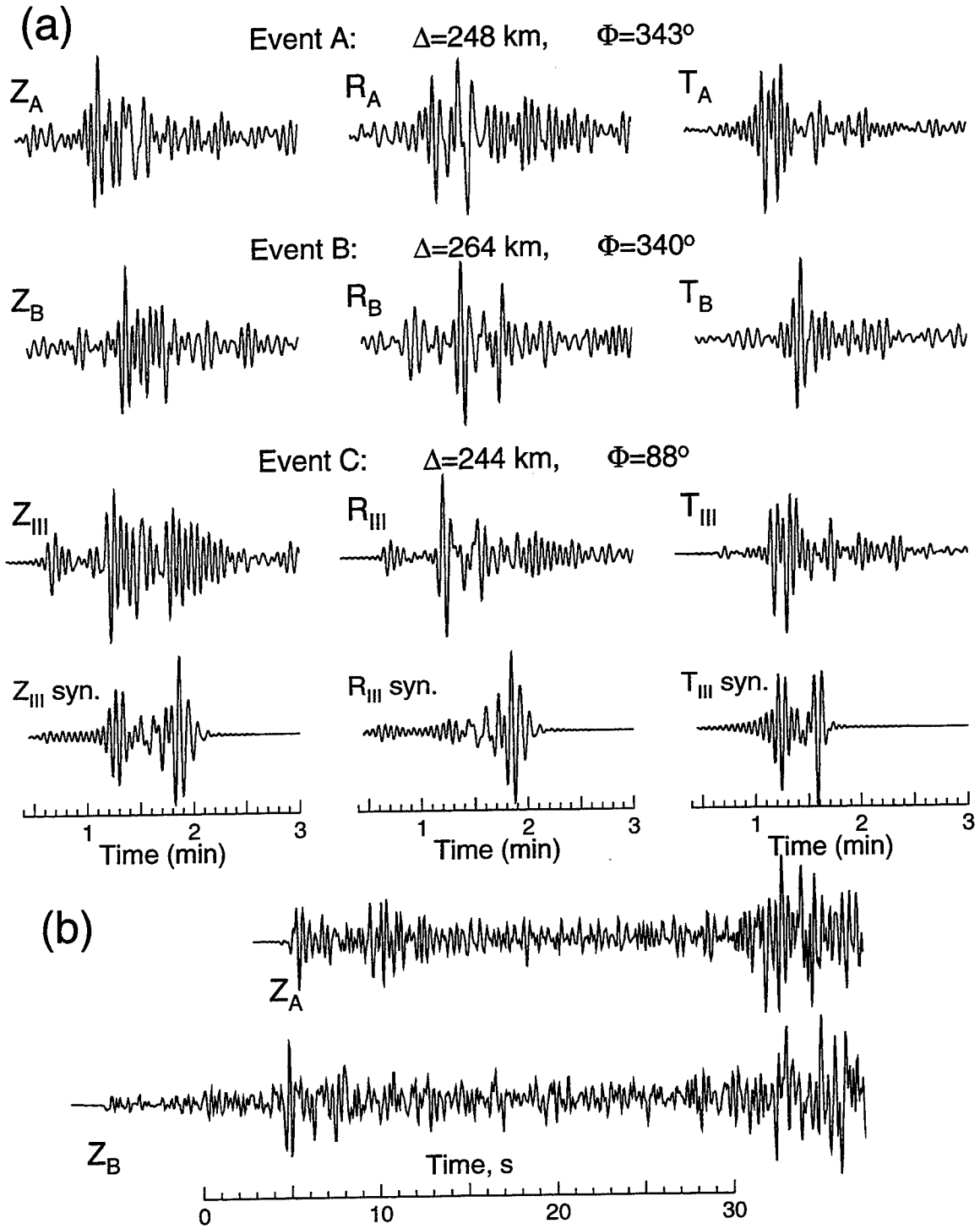

Fig. 2. (a) Regional broadband seismograms and synthetics (low-pass filtered at corner frequency 0.3 Hz) for station WMQ. Symbols with subscripts indicate vertical (Z), radial (R), and transverse (T) components for the events listed in Table 1 (subscript identifies the event). Time is measured from the origin time of the corresponding event. Synthetics were computed using a wavenumber-frequency integration algorithm [Saikia, 1994] and convolved with the instrument response. (b) Vertical-component broadband seismograms recorded at WMQ for the two earthquakes on the Lop Nor test site. Start times for the records are adjusted for waveform comparison.

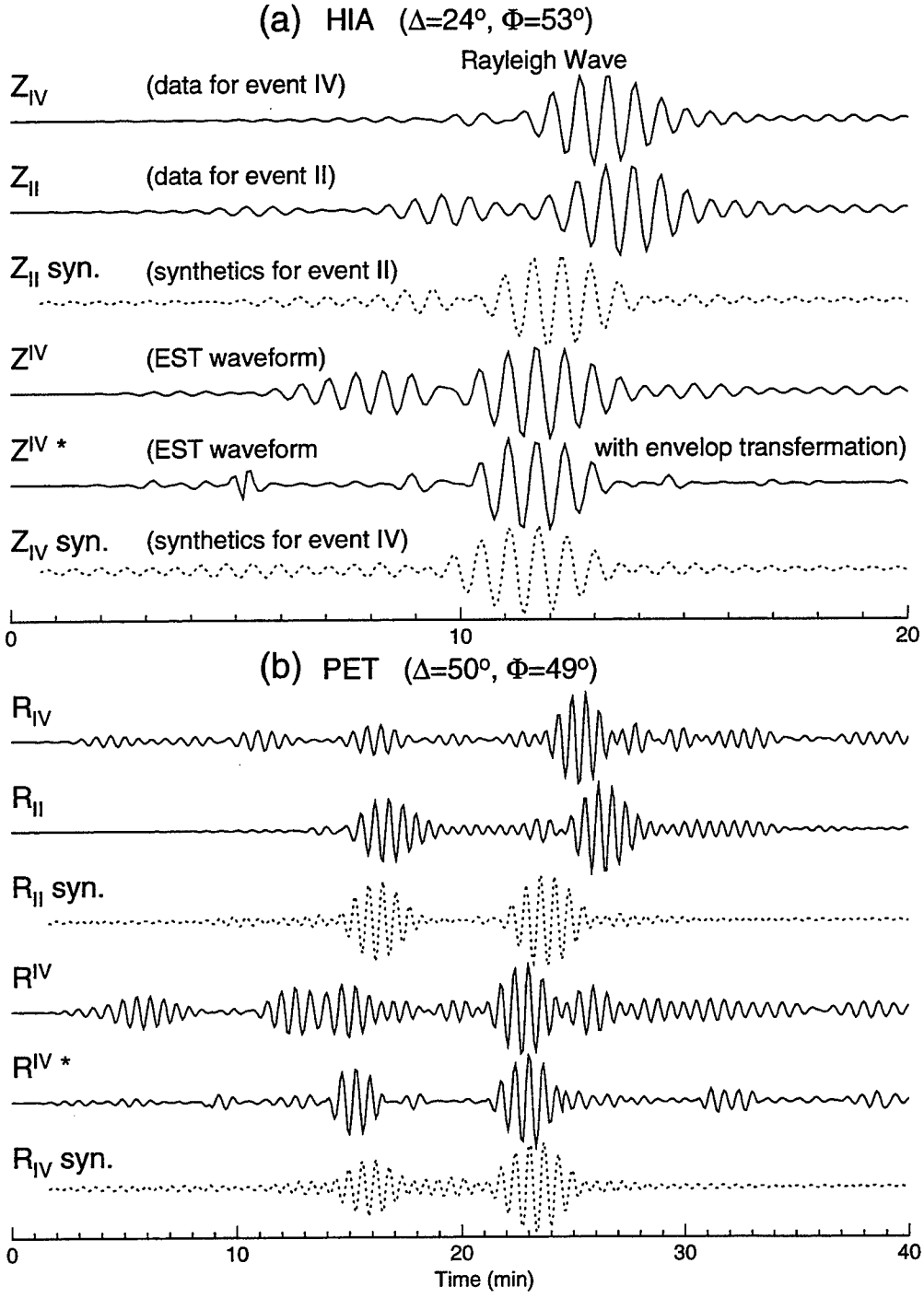

Fig. 3. Data and synthetics for stations HIA (Hailar, China) and PET (Petropavlovsk, Russia). Dotted lines indicate synthetics for event II computed using the Harvard CMT solution and synthetics for event IV using the moment-tensor solution obtained in this study. EST waveforms for event IV with event II as the auxiliary event are obtained without the envelop transformation (Z^{IV} and R^{IV}) and with the transformation (Z^{IV}* and R^{IV}*). Amplitude is arbitrarily set to show waveform coherence. Time is measured from the origin time of the corresponding event.

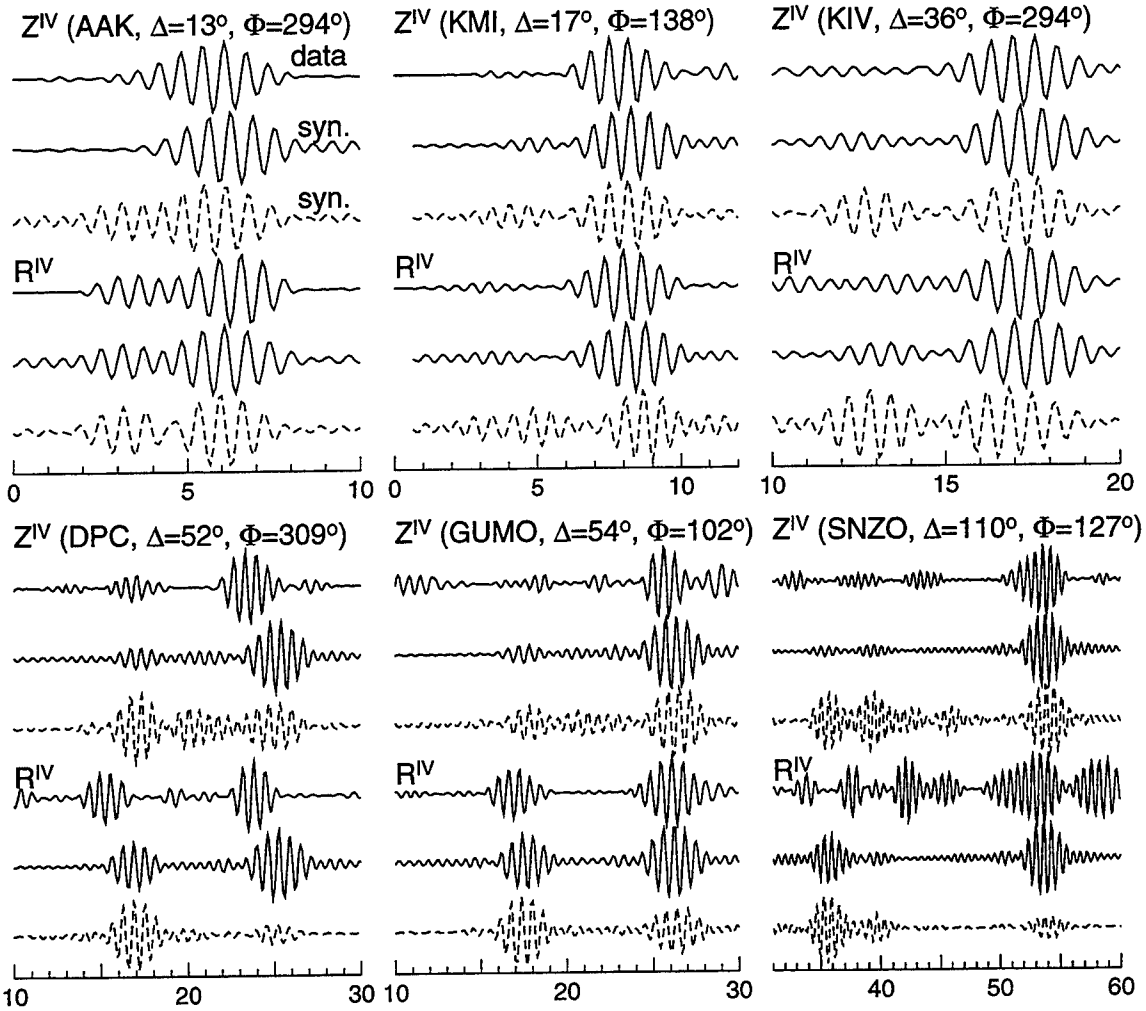

Fig. 4. Vertical (Z^{IV}) and radial (R^{IV}) components of EST waveforms (first trace for each component) and synthetics for the September 7, 1994 earthquake. The synthetics (second trace for each component) are computed using the moment-tensor solution obtained in this study, which has a depth of 13 km. Dashed lines show synthetics for the Harvard CMT solution, which has a centroid depth of 33 km.

Crustal and Upper Mantle Structure of the Tibetan Plateau

Lupei Zhu and Donald V. Helmberger
California Institute of Technology
Contract No. F19628-95-C-0096

July 8, 1996

Abstract

Our present efforts involve developing discrimination techniques for explosions and earthquakes occurring in southwestern U.S. and the transportability of these methods to the extended Tibetan Plateau regions. Nearly 400 events with $M_L \geq 3.5$ recorded by broadband instruments in Southern California (SC) provide with a variety of mechanisms and depths. This data set serves as a test bed in deriving new techniques for extracting source information from regional data. Our recent modeling attempts indicate that whole seismograms can be used in source estimation by applying a "cut and paste" approach. We start with a set of Green's functions from a standard Southern California model. The beginning P-wave portion is removed and aligned to the corresponding observation and similarly for the SV and Rayleigh wave portion. The best fitting source model denoted by strike, rake, dip, and M_0 is then obtained by least-squared waveform modeling determined by a direct grid search. The procedure is repeated over a range of depths and the best overall fit determined, see Zhao and Helmberger (1994). This method has been improved by changing the misfit normalization to better utilize absolute amplitude by Zhu and Helmberger (1996). The new method has become sufficiently stable to automate and is now servicing the TERRAscope datastream. It takes a few minutes to estimate source parameters for an individual event. In batch model, it takes a few days to run through the complete TERRAscope data achieve and test the influence of a new crustal model on mechanisms, depths, etc. Applications of this procedure to SC data and Tibet will be presented. However, because deep events, Zhu and Helmberger (1996), occur beneath various parts of the plateau, the upper mantle structure becomes important. Preliminary results of modeling upper-mantle triplication data reveal rapid variation as suggested by multi-bounce data, Rodgers and Schwartz (1995).

1 OBJECTIVE

In order to lower the magnitude threshold of CTBT monitoring, it is inevitable to rely on regional waveform records for discrimination. At regional distances, the propagation of seismic waves is strongly affected by the crustal and upper mantle structure. So the success of transporting established discriminants to a new area depends on our knowledge about the regional structure.

This paper continues and extends our previous work on the crustal structure of Tibet plateau and surrounding regions. On the basis of 1D crustal structure derived from receiver functions and regional broadband waveforms, we add several events in Pamir and Hindu Kush recorded by Tibet stations at upper-mantle distances. These records are used to constrain the upper mantle structure beneath the plateau. We have also developed a rapid source estimation technique which can process real-time waveform data automatically for source parameters. The performance of this technique using southern California TERRAscope data demonstrates its promptness and robustness. It is quite feasible to install it on some permanent IRIS stations for a fast and routinely based monitoring in the Tibet and surrounding regions.

2 RESEARCH ACCOMPLISHED

2.1 Rapid automatic source estimation technique

We have improved the "cut and paste" (CAP) source estimation technique developed by Zhao and Helmberger (1994) by redefining the waveform misfit error (Zhu and Helmberger, 1996b):

$$e = \| \left(\frac{r}{r_0}\right)^p \| \cdot \| f - u \|, \tag{1}$$

here f and u are observed waveform and synthetics respectively, p is a scaling factor to give the record at distance r the same weight as that at reference distance r_0. By removing the normalization in the origin CAP method, the amplitude information in the data can be better utilized to constrain the focal mechanisms and depths. It is shown that the modified method increases the stability and resolution of inversion.

Because there is essentially no manual intervention required for this technique, it can be fully automated. We have implemented it using data from the southern California TERRAscope network. As soon as a regional event larger than 3.5 occurred, preliminary event location is used to trigger the code to estimate the source mechanism using the real-time waveform data. Usually it takes about 3 min on a SUN-SPARC 10 workstation for the code to complete a 10 deg spacing grid search while fixing the source depth. If needed, the best focal depth can be determined through an additional iteration in a range of depths.

2.2 Application to southern California TERRAscope data

As a performance test, our new source estimation technique has been applied to all available regional events of $M_L \geq 3.5$ recorded by southern California TERRAscope network since 1990. A total of 335 focal mechanism solutions are obtained. Although a large number of

them are aftershocks of the 1992 Landers and 1994 Northridge earthquakes, the data set still gives a good sampling of active source regions in southern California.

The p-value in (1) is calibrated according to the actual amplitude attenuation in the studying area. Figure 1 shows the misfit error as function of distance range for the southern Californian events. By least-square-fitting, we have estimated the amplitude decays with distance; they are $r^{1.13}$ for Pnl, $r^{0.55}$ for Love waves, $r^{0.74}$ for Rayleigh waves. These values are close to the theoretical values assuming geometrical spreading, i.e., 1 for body wave and 0.5 for surface waves.

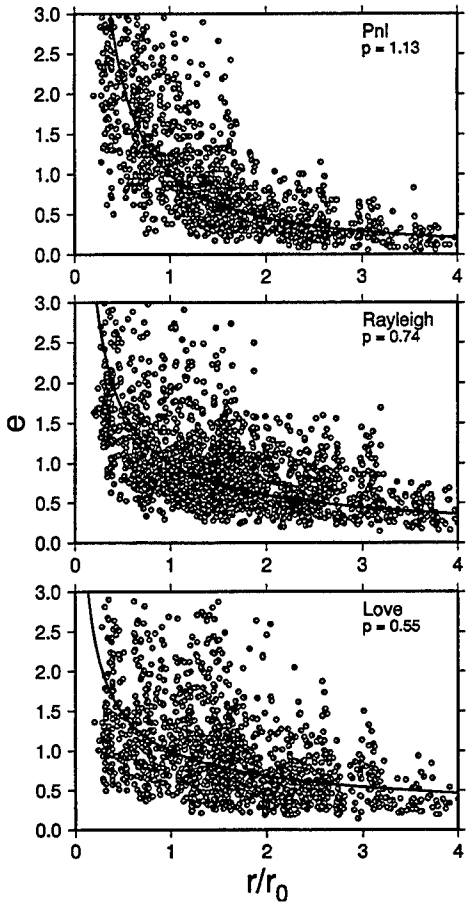

Figure 1: Misfit errors of different portions of seismograms of 335 southern California events. True amplitude waveforms are used in the inversion. We chose $r_0 = 100$ km as reference distance. The solid lines are $(\frac{r_0}{r})^p$ where the p values are determined from a least-square fit.

Fig.2 shows the histograms of the Southern California Seismological Network (SCSN) catalog depths and waveform inversion depths for the 335 events included in this study. The catalog depths are determined from the P arrival times as recorded by the southern California short-period network. Large uncertainty exists for these routinely determined depths, mostly caused by trade-off between depth and origin time and some cases sparse station distribution. Because our new technique preserves the amplitude information, focal depths are better constrained. The depth distribution obtained from waveform inversion shows a strong peak at about 12 km with few events occurring above 5 km and below 20 km.

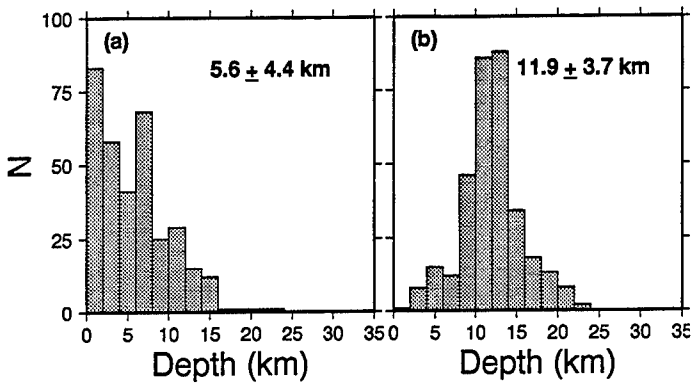

Figure 2: Histograms of depth distribution in southern California, a) SCSN catalog depths; b) waveform inverted depths. The numbers in the figure are the average focal depths and the standard deviation.

This seems quite compatible with the expected seismogenic zone for a tectonically active region as southern California.

Some of the shallowest events occurring in Fig.2 were studied in depth by Song and Helmberger (1996). They found that events occurring in the San Fernando Basin ($h < 3.5$ km) contain considerable scattered phases with energy moments, M_E/M_0 ratios, as high as found for NTS events, Zhao and Helmberger (1996). This result suggests that the shallow earth structure, top 3 to 4 kms, is primarily responsible for the differences in regional characteristics with source type playing a secondary role except for the initial P-wave. Fortunately, shallow earthquakes, also, tend to be low stress-drop with weak P_n's and, thus, discrimination is still possible, see Woods and Helmberger (1996).

2.3 1D crustal structure of the Tibetan Plateau and lateral variation

In previous work (Zhu et. al., 1993; Zhu and Helmberger, 1995), we have derived a 1-D crustal model for the Tibetan Plateau using both teleseismic receiver functions and broadband regional waveforms. The model consists of a main crustal layer of 60 km thick with a 4 km thick layer on top of it. The average crustal shear velocity is very low (3.5 km/s) with a higher crustal Vp/Vs ratio.

This model works quite well in modeling the broadband regional waveforms in the period range of 100 sec to 5 sec. We have determined focal depths and source mechanisms of about 50 Tibetan events as recorded during the 1991-1992 PASSCAL experiment. Our results confirmed the shallow seismicity in the plateau. But we also found three intermediate depth events under the Himalaya and Indus-Zangbo suture zone (Zhu and Helmberger, 1996a).

Although we were able to model regional waveforms below 1 Hz with a simple 1D model, we have also observed large amplitude variations at high frequency. One of possible sources of these variations is the local scattering near the receiver site. This is very important at the shorter periods and we need help from other investigators to do this right. However, one possible approach is to treat the receiver as a separate operator and introduce a separate structure at the receiver. Figure 3 displays such a procedure, Wen et al (1996). We can

propagate the wave field analytically up to near the receiver and introduce a local 3D structure where finite-difference is used. Since finite-differencing does not need to propagate far, this becomes a viable approach. The method would allow us to model some of the obvious shifts in radial vs. vertical Rayleigh waves and their strange amplitude ratios. We could also use this technique to account for high frequency energy enhancement at particular stations that is commonly observed.

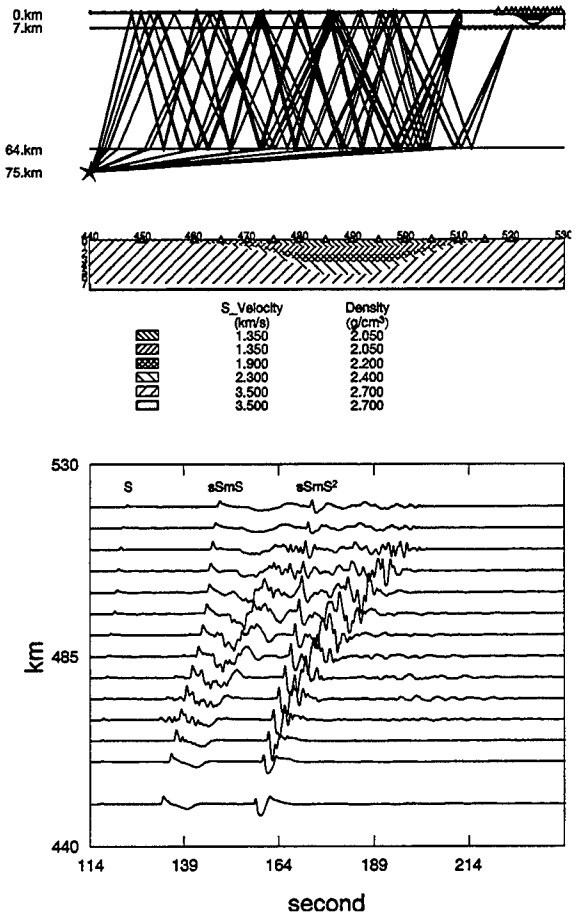

Figure 3: Modeling local scattering at receiver site for one of subcrustal events in Tibet (upper panel). A small basin structure is introduced beneath station SANG (middle panel). The computed SH motions are displayed in the bottom.

2.4 Upper mantle structure beneath the Tibetan Plateau

In addition to about 50 regional events of magnitude larger than 4, the Tibet 1991-1992 PASSCAL experiment also recorded numerous large events in the surrounding areas (Figure 4). The distance ranges from these events to the experiment stations are between 15 to 25 degrees and most of events have Harvard CMT solutions. So they can be used to resolve upper mantle structure beneath the plateau. In particular, the paths from events in Pamir-Hindu Kush lie totally within the plateau. So we can eliminate possible contamination of waveforms as they are propagating cross major tectonic boundaries.

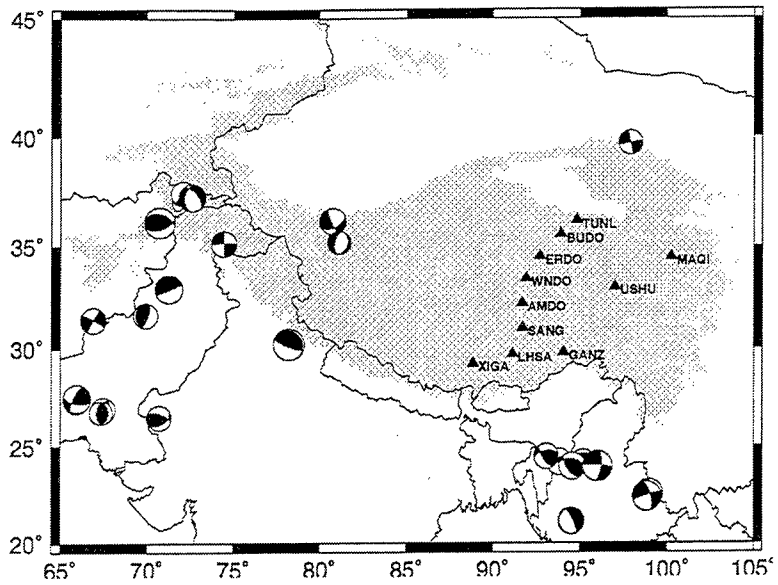

Figure 4: Location of broadband stations of the 1991-1992 Tibet PASSCAL experiment. Shading indicates elevation above 3 km. Focal spheres are Harvard CMT solutions of large earthquakes in Tibet and surrounding regions recorded by the experiment.

To model the observed waveforms, we did forward calculation of synthetics using various upper mantle velocity models, including PREM (Dziewonski and Anderson, 1981), SNA and TNA (Grand and Helmberger, 1984), and TIP (Zhao et. al., 1991). These models are shown in Figure 5. SNA and TNA are for shield-like and tectonic active upper-mantle structures under the north America respectively. TIP was derived from $S - SS$ waveforms cross the Tibet plateau. Both generalized ray (GRT) and frequency-wavenumber (FK) integration methods are used to compute the Greens' functions for these models. We have developed a new FK code based on the formalisms of Wang and Herrmann (1980) and a implement by Saikia (1994). It can calculate very efficiently the full responses of double-couple/explosion source at distances ranging from tens of kilometers to thousands of kilometers. The GRT code is used to isolate individual phase and help to make necessary modification of the model.

Figure 6 shows the synthetics of different models and their comparisons with observed waveforms for one of Hindu Kush events. Out of the four upper mantle models, PREM and TIP fit the SH waveforms at stations in central and southern Tibet. But for the northernmost path to TUNL SNA is more appropriate. Note this path is very close the Tarim Basin in the north which is believed lying on top of old Precambrian shield (Zhao et. al., 1991). The waveform fits for $P - SV$ are not as good as SH, although synthetics of model PREM and TIP show some promising features. These discrepancies serve as a starting point for our present efforts.

3 CONCLUSION AND RECOMMENDATIONS

We have developed a rapid automatic source estimation technique which can be used to obtained focal mechanisms and depths within minutes after an event is detected. By com-

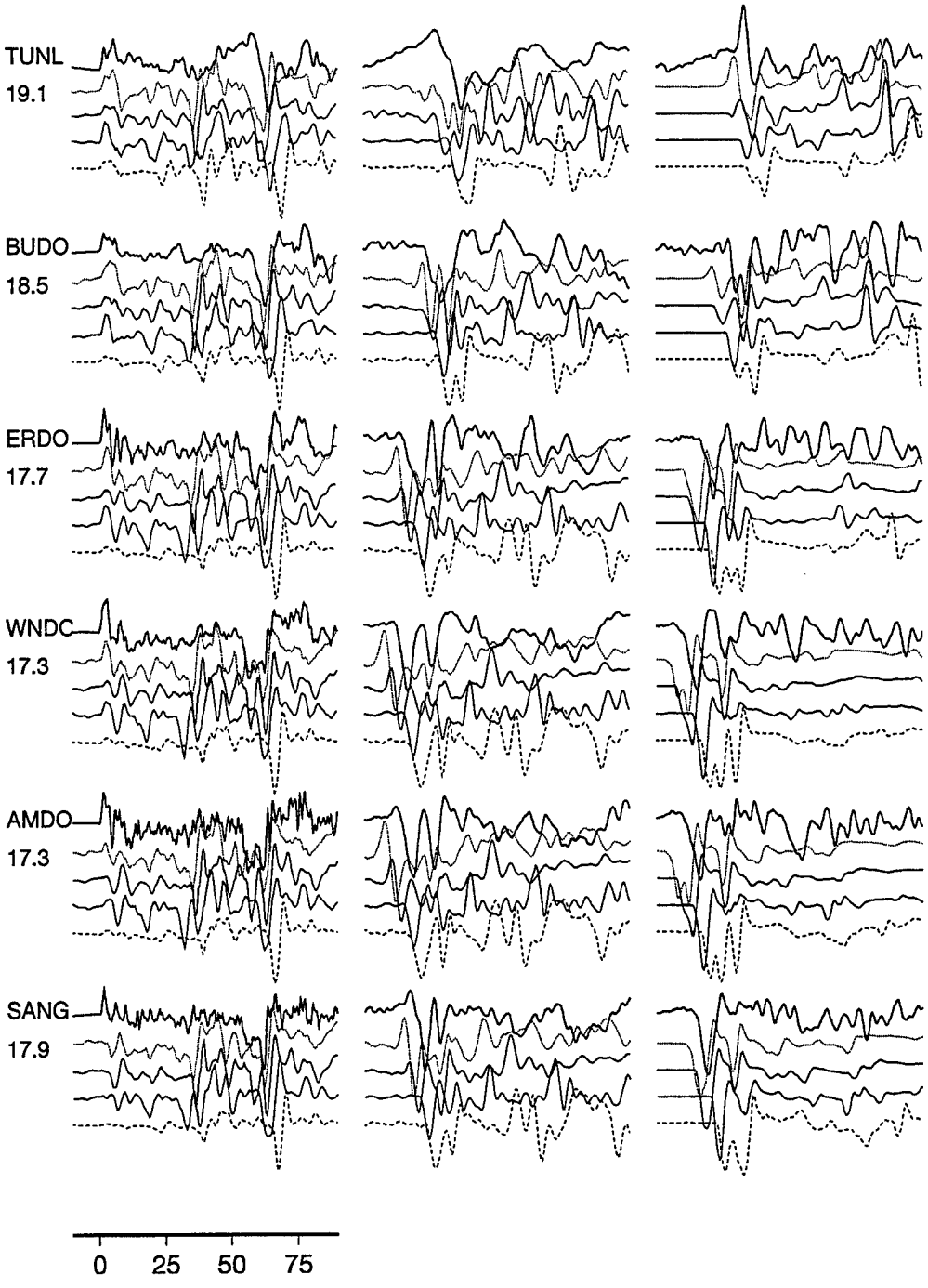

Figure 6: Vertical P (left column), vertical SV (middle column), and tangential SH waves (right column) of a Hindu Kush event (depth of 200 km) and corresponding synthetics for upper mantle (below the data trace, from top to bottom) SNA, TIP, PREM, and TNA. The numbers below station names are distance ranges in degrees.

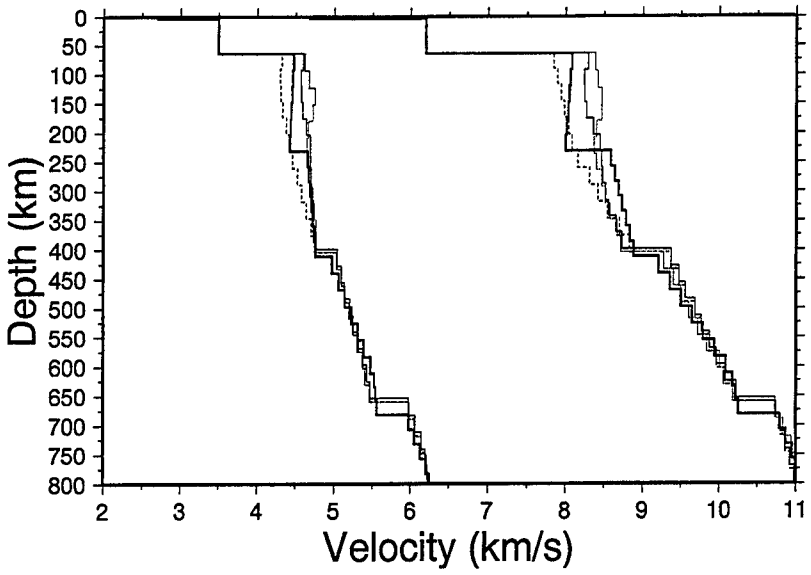

Figure 5: Several upper mantle velocity structures; PREM (heavy solid line), TIP (solid line), SNA (dotted line), and TNA (dashed line).

bining it with single station event detection algorithm, it is possible to establish a routinely based event detection and discrimination technique using one or two permanent broadband stations.

In order to model the high frequency amplitude variation, a local 3D structure near the receiver site is introduced. The wave propagation outside the local structure is computed using best 1D regional velocity model while finite-difference method is used inside the local structure. So the site responses of CTBT monitoring stations can be calibrated by this method.

Broadband waveforms of Hindu Kush earthquakes recorded at Tibet stations were used to resolve the upper mantle structure beneath the plateau. Preliminary results show that the northernmost path can be modeled by a shield-like upper mantle velocity structure. PREM and TIP models are good at fitting the SH waveforms at stations in central and southern Tibet. However, there are large discrepancies between observed $P - SV$ waveforms with synthetics. We will continue to work on this data set for a better upper mantle velocity structure beneath the Tibetan Plateau.

4 references

Dziewonski, A.M. and D.L. Anderson, 1981, Preliminary reference earth model, Phys. Earth Plant. Int., 25, 297-356.

Grand, S.P. and D.V. Helmberger, 1984, Upper mantle shear structure of North America, Geophys. J. R. astr. Soc., 76, 399-438.

Rodgers, A. and S. Schwartz, 1995, Asian upper mantle P-wave velocity structure from the analysis of broadband waveforms, Plateau, Proc. of 17th Annual Seismic Research Symposium, Scottsdale, Arizona, 677-683. PL-TR-95-2108, ADA 310037

Saikia, C.K, 1994, Modified frequency-wavenumber algorithm for regional seismograms using Filon-quadrature method - modeling of Lg waves in eastern North-America, Geophys. J. Int. 118, 142-158.

Song, X.J. and D.V. Helmberger, 1996, The northridge aftershocks, a source study with TERRAscope data, submitted to Geophys. J. Int..

Wang, C.Y. and R.B. Herrmann, 1980, A numerical study of P, SV, and SH-wave generation in a plane layered medium, BSSA 70, 1015-1036.

Wen, L., C. Scrivner, and D.V. Helmberger, 1996, Hybrid method and its application to Los Angeles Basin (in preparation).

Woods, B.B. and D.V. Helmberger, 1996, Regional seismic discriminants using wavetrain energy ratios, BSSA (in press).

Zhao, L., D.V. Helmberger and D.G. Harkrider, 1991, Shear-velocity structure of the crust and upper mantle beneath the Tibetan Plateau and southeastern China, Geophys. J. Int. 105, 713-730.

Zhao, L. and D.V. Helmberger, 1994, Source estimation from broadband regional seismograms, BSSA 84, 91-104.

Zhao, L. and D.V. Helmberger, 1996, Regional moments, energy levels, and a new discriminant, PAGEOPH 146, 281-304.

Zhu, L., R.S. Zeng, F.T. Wu, T.J. Owens, and G.E. Randall, 1993, Preliminary study of crust-upper mantle structure of the Tibetan Plateau by using broadband teleseismic body waveforms, Acta Seism. Sinica 6, 305-315.

Zhu, L and D.V. Helmberger, 1995, Focal mechanism determination and propagation characteristics of high-frequency S-waves on the Tibetan Plateau, Proc. of 17th Annual Seismic Research Symposium, Scottsdale, Arizona, 702-710. PL-TR-95-2108, ADA 310037

Zhu, L. and D.V. Helmberger, 1996a, Intermediate Depth Earthquakes beneath the India-Tibet Collision Zone, submitted to Geophys. Res. Lett.

Zhu, L. and D.V. Helmberger, 1996b, Advancement in source estimation techniques using broadband regional seismograms, BSSA (in press).

THIS PAGE LEFT
INTENTIONALLY
BLANK.

SHEAR WAVE GENERATION FROM CONTAINED EXPLOSIONS

Thomas J. Ahrens and Cangli Liu, California Institute of Technology
Contract No. F19628-95-C-0115
Sponsored by AFTAC and Phillips Laboratory

ABSTRACT

The usefulness of the amplitude ratio of seismic phases such as L_g/P, as well as the ratio of magnitudes (e.g. M_b/M_s) to discriminate explosions from earthquakes depends, in part, on the efficiency of shear wave production from seismic sources. We are studying shear wave generation at the source, initially from explosions within limestone blocks. Initially the samples are subjected to hydrostatic stress. However, we will be able to also simulate tectonic strain energy release in future experiments. Using a 1.6 m long, 0.8 m diameter sample subjected to an ambient pressure of up to 1 MPa, with a centrally placed explosive source, we propose to study the amplitude of shear wave generation of stress-wave induced radial cracking in symmetric and asymmetric cavities. In unstressed rock, this shear wave production is expected to be controlled in part by the natural anisotropy of the rock (e.g. bedding). We expect to measure the S/P ratio from tamped explosions using (0.2 to 2 gram charges). Later tests will be conducted in partially decoupled asymmetric cavities, and the resultant shear wave radiation pattern will be compared to previous detailed finite element calculations of P and S wave radiation versus frequency and angle for elliptical cavities of aspect ratios in the range of 1:3 to 1:10 conducted by Glenn et al. [1985].

To measure both P and S wave particle motion, we are using strain gauge arrays and are able to record 8 channels with a 500 MHz bandwidth. Initial test results have just been attained and it is expected that data for symmetric and asymmetric cavities will be available by the time of the Conference that will allow comparison to theoretical models.

2. OBJECTIVES

We are conducting small-scale explosive experiments to test discrimination theories of shear wave generation from explosions in symmetric and asymmetric cavities in rocks. Small PETN charges are detonated in symmetric and asymmetric cavities, within meter-sized samples of limestone, shale, and other rock types. We constructed an apparatus (Figs. 1-3) to measure shear wave generation both from the asymmetric stresses imposed on the explosion cavity walls by the detonation, as well as from the cracking of the rock. We also expect to develop a theoretical model of these effects. We expect to apply Brune's (U. Nevada) and L. Glenn's (LLNL) model of stresses from such cavities to test discrimination algorithms.

We have developed sealing methods for conducting the tests under ~1 MPa of water pressure, as shown in Fig. 1. Initially rock samples of Bedford limestone are being employed.

3. RESEARCH ACCOMPLISHED

We have completed construction and check out of the experimental assembly shown in Figs. 1-3. An initial experiment was fired with 0.24 grams of PETN explosive in a 13.14 cm^3 volume cavity. The quasistatic calculated pressure for the explosive products (in the cavity) is 2.0 MPa.

All 8 channels of strain gauge data (from type CEA-06-125UT-120 strain gauges) produced adequate data. These are summarized in Fig. 4.

It is expected that additional data from shots from a series of asymmetric cavities will be available in September 1996 to provide tests of theories of shear wave generation. Later experiments will be conducted so as to (1) overdrive (permanently deform) cavities, and induced shear waves from shear failure, and (2) release "tectonic" stress imposed from our test specimens.

4. CONCLUSIONS

Experiments and analyses are underway. Preliminary results look promising and initial results from shear wave generating experiments will be presented at the Symposium.

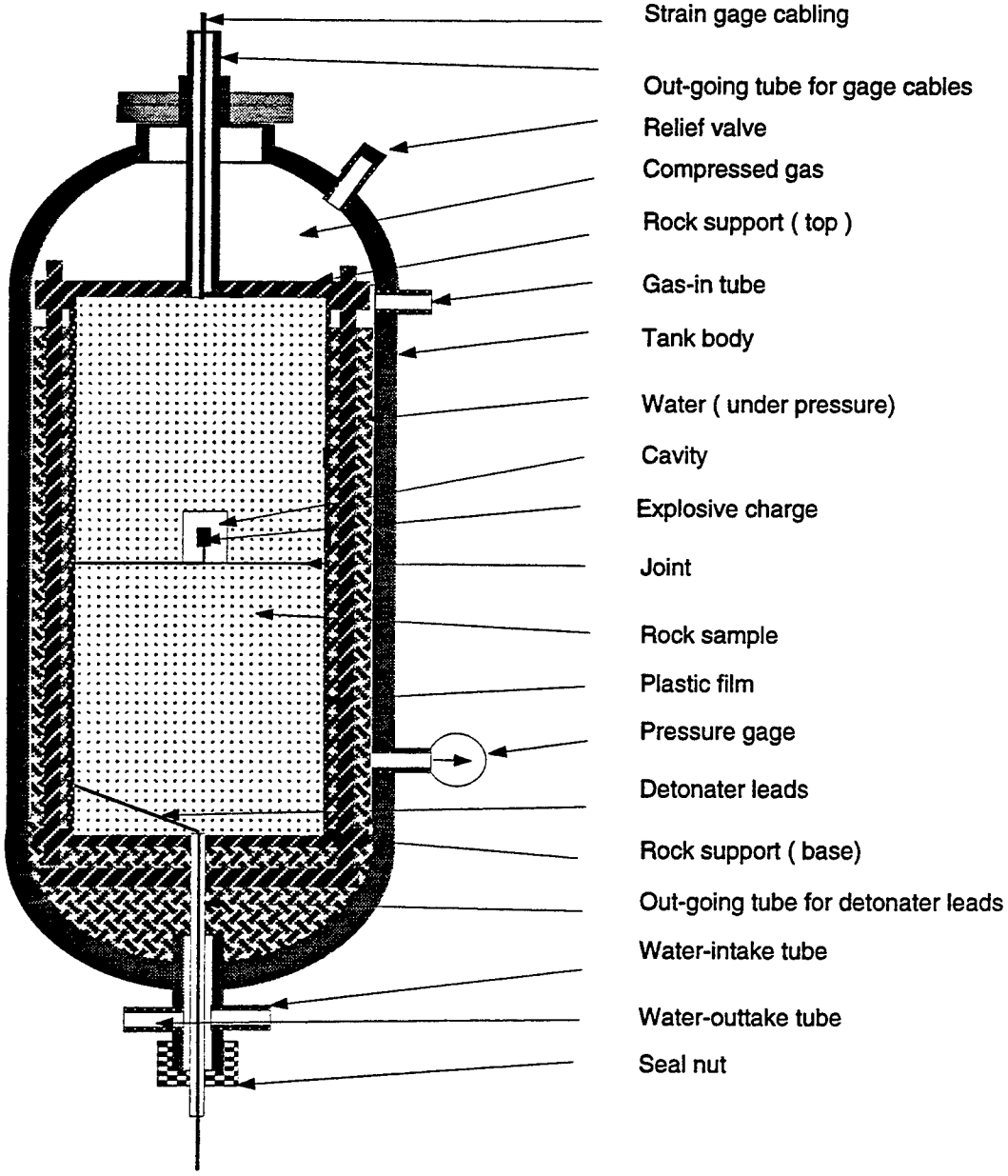

Fig.1 Mechanical configuration of test chamber to study shear wave generation in rocks

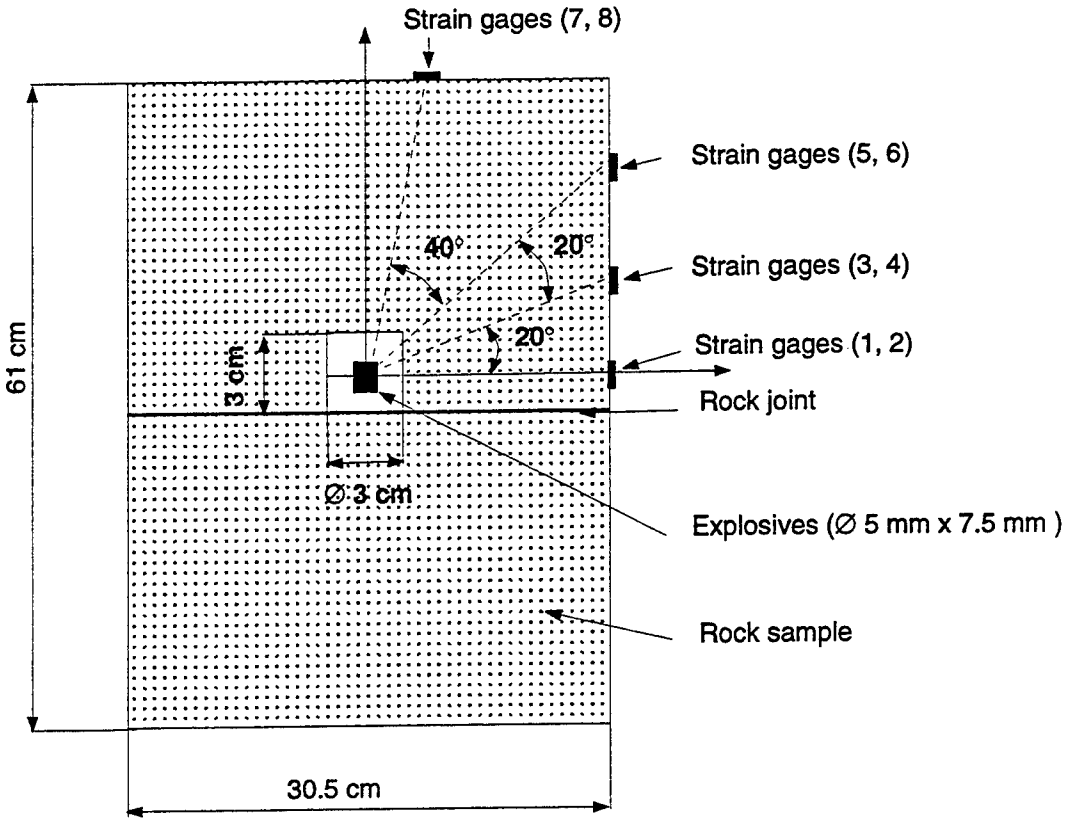

Fig.2 (A) Layout of rock sample, strain gages and explosive charge

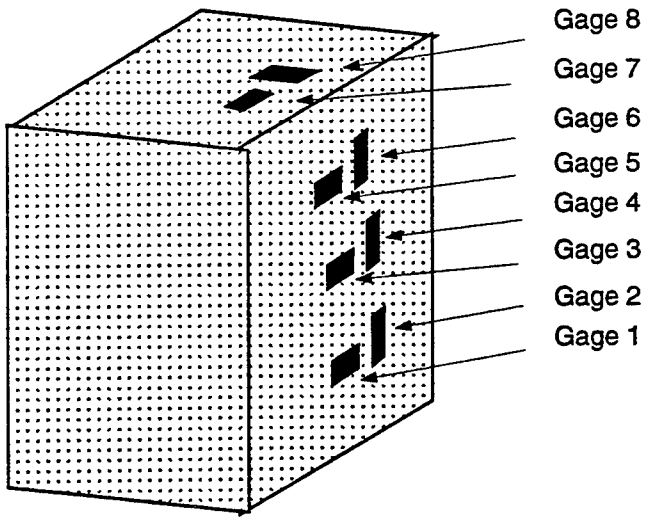

Fig.2 (B) Sketch of polarization directions of strain gages

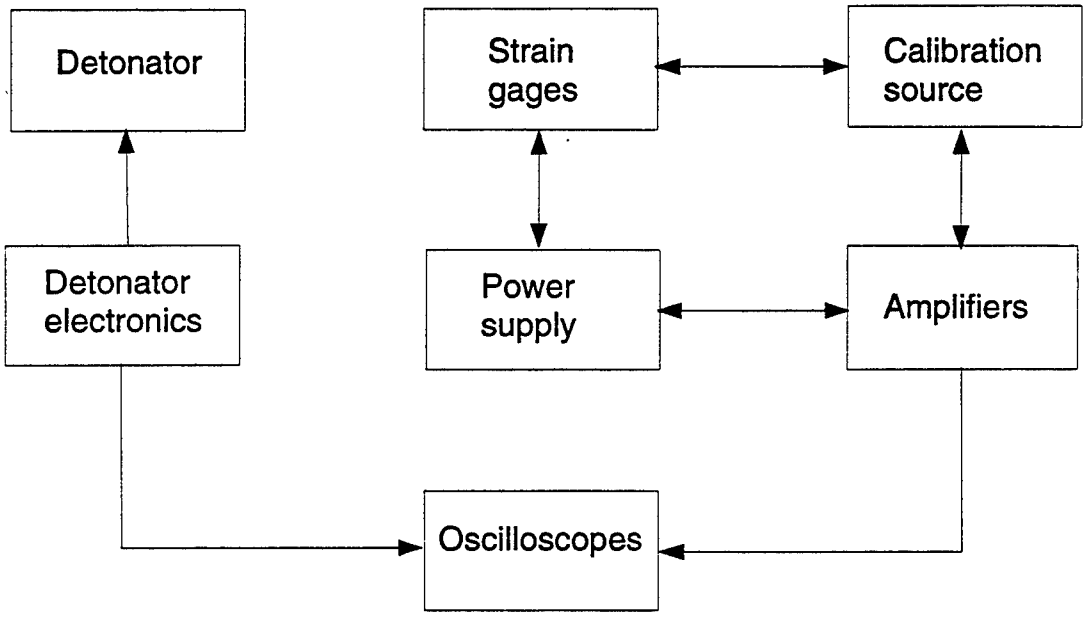

Fig.3 Block diagram of shear wave generation experiments

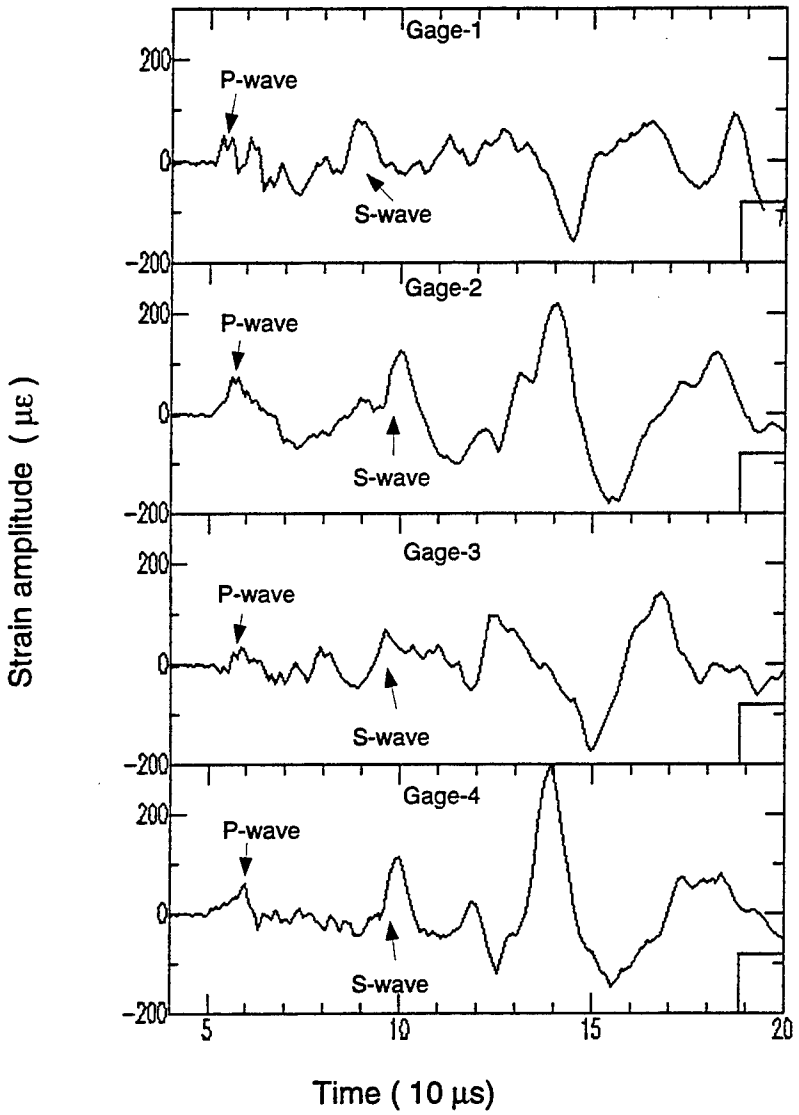

Fig.4 (a) Recording of strain versus time from gages 1 - 4, Shot #1

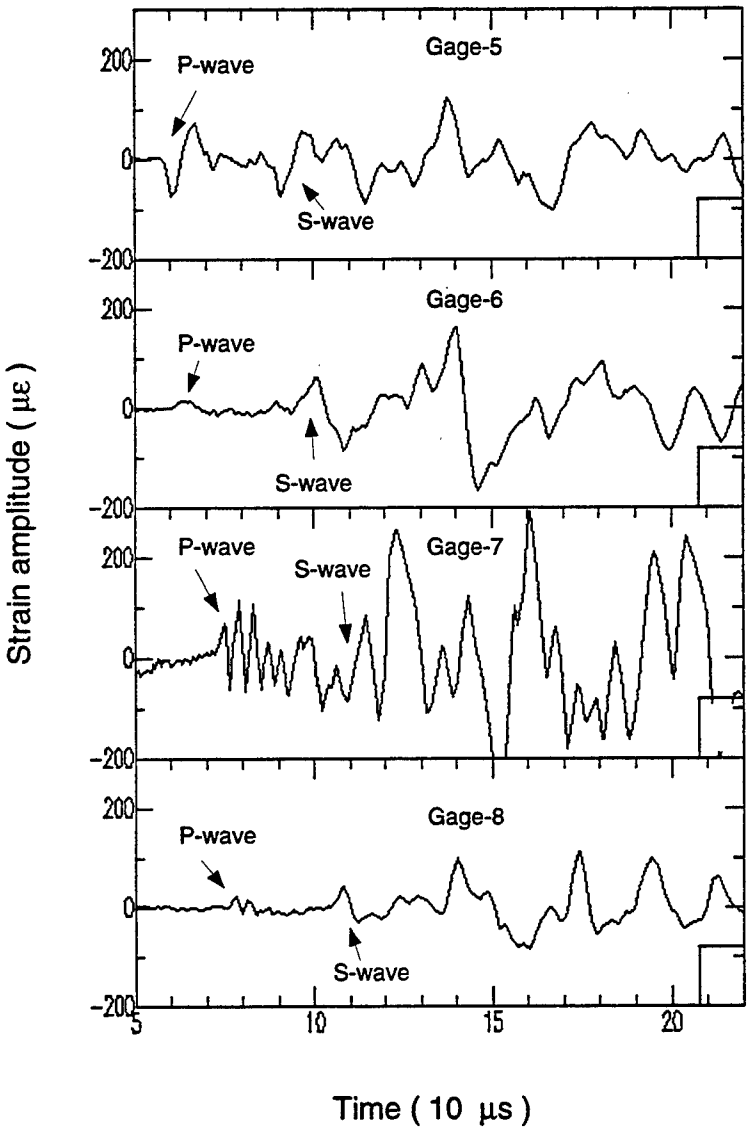

Fig.4 (b) Gages 5 - 8

PERFORMANCE OF SEISMIC DISCRIMINATION FRAMEWORKS

D.N. Anderson K.K. Anderson D.N. Hagedorn K.T. Higbee
N.E. Miller T. Redgate A.C. Rohay
Statistics Group — Pacific Northwest National Laboratory

Sponsored by U.S. Department of Energy, Contract DE-AC06-76RLO 1830
Comprehensive Test Ban Treaty Research and Development Program, ST482C

Abstract

The performance of eight statistical discrimination methods, as applied to regional seismic data, are documented. The ground-truth data used in this study has some of the characteristics that might typify training data in future regions of interest under a CTBT. The discriminants used in this study were calculated with a fully automated approach in which phases were identified with an approximate velocity model rather than with human analyst interaction. A small number (seven) of seismic stations in the distance range 200–800 km, at both quiet and noisy locations, were used in the study. All of these properties are indicative of the ground-truth data that might need to be initially used in a future region of interest. The cross-validated misclassification rates for the eight methods ranged from 10% to 14%. Based on overall misclassification, there is no appreciable difference between the performance of the eight discrimination frameworks. Anderson et al. (1996) illustrates that CART best satisfies many other important requirements of CTBT discrimination such as: interpretable decision boundaries, handling of missing values, allowing of both discrete and continuous data. We recommend that the CTBT discrimination framework be based on CART in conjunction with several of the other methods such as logistic, KNN, and VRDA (which has LDA and QDA as special cases). These methods can be used both in an automated setting and for in-depth analyst event review. These statistical discrimination methods can also be applied to other technologies that will be included in a CTBT monitoring capability.

Key Words: CTBT, discrimination, seismic

Objective

The statistical discrimination research for FY96 at Pacific Northwest National Laboratory (PNNL) included a technical review of eight statistical discrimination frameworks. The review criteria was based, in general, on the capability of a discrimination framework to:

1. effectively contribute to a decision process,
2. be interpreted in terms of seismic theory,
3. accurately predict the source of seismic activity (statistical rigor).

Anderson et al. (1996) extensively reviews the first two criteria which are extremely important. In Michie et al. (1994) we read

> ... It is important also, that human operators believe the system. An oft-quoted example is the Three-Mile Island case, where the automatic devices correctly recommended a shutdown, but this recommendation was not acted upon by the human operators who did not believe that the recommendation was well founded.
> ...

The statistical discrimination frameworks that were reviewed represent a wide range of possible approaches. The eight frameworks are:

- **Linear discriminant analysis (LDA)** — Assumes normality and equal covariance matrices. Produces linear decision region boundaries.
- **Quadratic discriminant analysis (QDA)** — Assumes normality. Produces quadratic decision region boundaries.
- **Variably regularized discriminant analysis (VRDA)** — Assumes normality. Generalizes both LDA and QDA (with both as special cases). Produces quadratic decision region boundaries.
- **Flexible discriminant analysis (FDA)** — A generalization of LDA which uses non-parametric regression techniques in place of least squares regression.
- **Logistic discrimination** — Based on modeling the log-odds in favor of a group as a linear combination of discriminants (which may include powers and interactions). Logistic regression is used in estimating the decision region boundaries.
- **K-th nearest neighbor (KNN) discrimination** — Non-parametric method where the decision region is determined by examining the nearest K training data points. Decision region boundaries are often highly irregular.
- **Kernel discrimination** — Non-parametric method that estimates the density for each group and determines the decision region boundaries based on the ratio of the densities in a local region.

- **Classification and regression trees (CART)** — Non-parametric method that produces decision region boundaries by recursively partitioning the region so as to best separate the groups. Decision region boundaries are easily interpretted.

Research Accomplished

For the eight frameworks listed above, a detailed assessment of seismic interpretability and effective contribution to a CTBT decision process is given in Anderson et al. (1996). In summary, that report indicates that no one framework is superior in all settings. However, the CART method appears to satisfy many important aspects of the general review criteria noted above. In this paper, the discrimination accuracy (statistical rigor) of these eight frameworks is evaluated.

The data used in this evaluation included 80 earthquakes and 20 explosions recorded on the Nevada Test Site (NTS) by seven regional IRIS stations. The stations are Columbia, CA; Goldstone, CA; Pinyon Flats, CA; Tucson, AZ; Albuquerque, NM; Pasadena CA; and Isadora, CA. Energy measurements for the P_g and L_g phases across a suite of frequency bands (0.5–1, 1–2, 2–4, 4–6, 6–8, 4–8, 1–3, 3–6, and 3–9 Hz) were taken from raw waveforms with Seismic Analysis Code (SAC) algorithms. These measurements were calculated with a fully automated approach — i.e., phases were identified without intervention by or interaction with a human analyst. A preliminary, "best-guess" velocity model was used to identify phases. Earthquake locations and origin times from the NEIC were used, and velocities of 6.1 and 3.6 km/s were used to predict the beginning of the P_g and L_g phases. These locations are observed to have depth and epicentral errors on the order of 10–20 km relative to precise local array locations. These properties are similar to data that might need to be used initially in a region of future interest. For example, automatically identifying P_n onsets requires a more precise location and depth estimate than might be initially available in a new region of interest. After removing events with incomplete data, the ground-truth data set consisted of 71 earthquakes and 19 explosions.

For each event, the P_g and L_g energy measurements from the seven stations were combined into a seismic magnitude discriminant given by:

$$mb_{P_g} - mb_{L_g}(\omega_l, \omega_u) \;=\; \log \prod_{i=1}^{7} \left(\frac{RMS\ P_{g_i}(\omega_l, \omega_u)}{RMS\ L_{g_i}(\omega_l, \omega_u)} \right)^{1/7}$$

The frequency bands (ω_l, ω_u) examined were: (0.5, 1), (1, 2), (2, 4), (4, 6), (6, 8), (4, 8), (1, 3), (3, 6), (3, 9). The discriminants $mb_{P_g} - mb_{L_g}(0.5, 1)$, $mb_{P_g} - mb_{L_g}(2, 4)$, and $mb_{P_g} - mb_{L_g}(4, 6)$ were chosen to evaluate the eight frameworks based on an all possible subsets analysis that indicated that these three discriminants together were better than any of the other subsets of discriminants. A total of ten analyses were conducted on each classification framework. The data were randomly partitioned into ten groups, preserving (as best as possible) the proportion of earthquakes and explosions in each group. One group has one explosion and eight earthquakes while the remaining nine groups have two explosions and

seven earthquakes. The ten analyses performed for each classification method correspond to these ten random partitions of the data. Each partition, in turn, is held out (or set aside) while the remaining 90% of the data is used to pick algorithm parameters and train the classification methods. The 10% hold out data is then used to evaluate the performance of the classification method. The results of this experiment are summarized in the tables (known as confusion matrices) shown in Figure 1.

Conclusions

Based on overall misclassification, there is no appreciable difference between the performance of the eight discrimination frameworks. Anderson et al. (1996) illustrates that CART best satisfies many other important requirements of CTBT discrimination such as: interpretable decision boundaries, handling of missing values, allowing of both discrete and continuous data. We recommend that the CTBT discrimination framework be based on CART in conjunction with several of the other methods such as logistic, KNN, and VRDA (which has LDA and QDA as special cases). These methods can be used both in an automated setting and for in-depth analyst event review.

Figure 2 summarizes the overall misclassification rates from Figure 1. The results in Figure 2 and Figure 1 are based on equal prior probabilities and equal misclassification costs for both explosions and earthquakes. Due to using equal misclassification costs the conditional probability of misclassifying an explosion ranges from 5% to 32% and the conditional probability of misclassifying an earthquake ranges from 6% to 15%. Obviously, a 32% misclassification rate for explosions is unacceptable for a CTBT. This misclassification rate can easily be lowered (at the expense of the earthquake misclassification rate) by incorporating appropriate costs into each of the discrimination frameworks. Since CTBT regional training data will likely contain few ground-truth explosions, the resolution of the estimate of the misclassification rate for explosions will be coarse. In our study it can only be estimated in increments of $1/19 \approx 5\%$. See Anderson et al. (1996) for an intuitive discussion of the decision theory approach to discrimination. As a last note, this study gives an indication of the performance that might be expected from an automated discrimination algorithm when the ground-truth data (training data) possess the characteristics of the data used in this study.

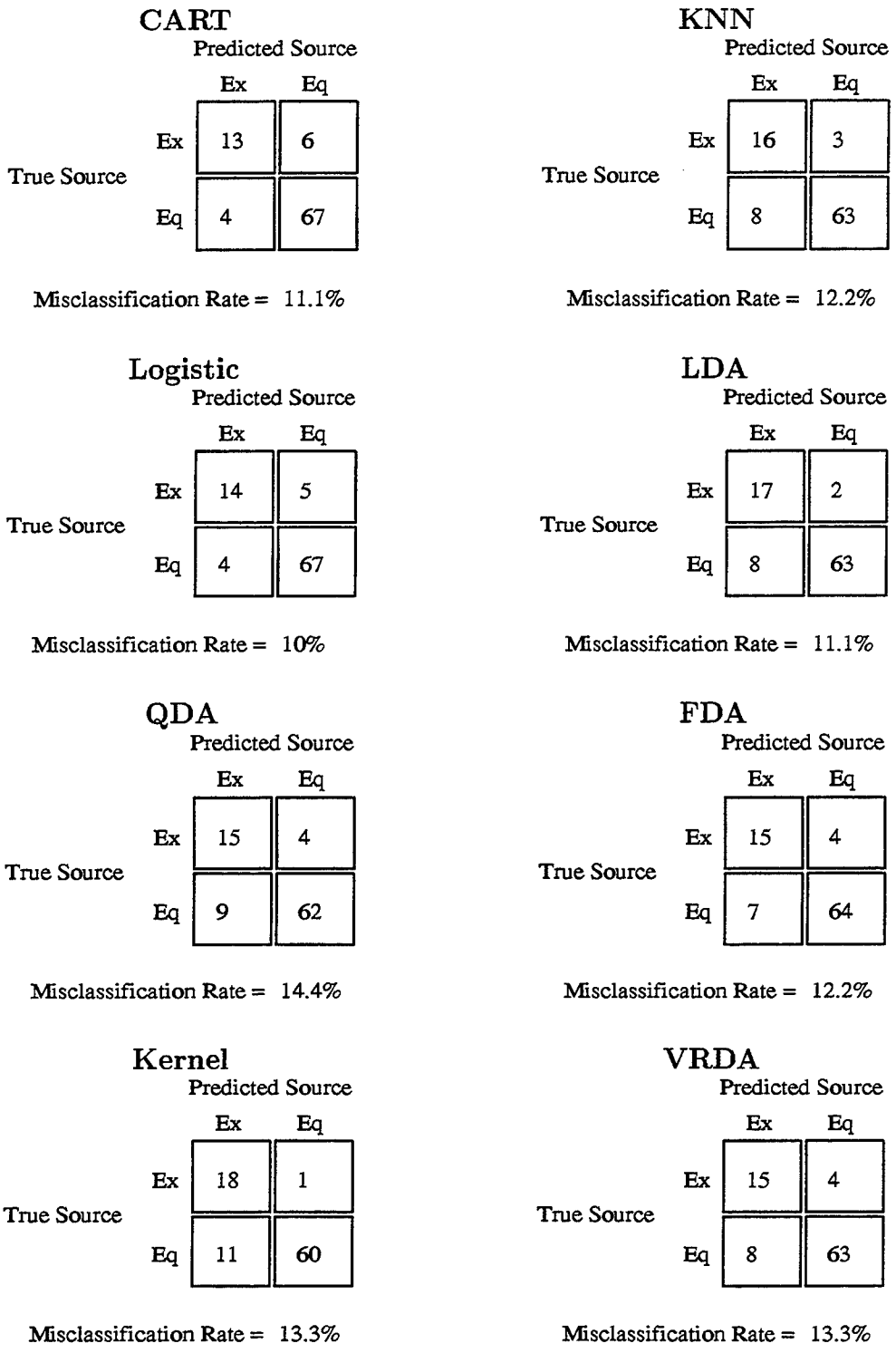

Figure 1: Confusion Matrices and Cross-Validated Overall Misclassification Rates for Eight Discrimination Frameworks. Ex = Explosion, Eq = Earthquake.

Framework	Pr(Misclassification)
Logistic	10%
CART	11%
LDA	11%
KNN	12%
FDA	12%
Kernel	13%
VRDA	13%
QDA	14%

Figure 2: Estimated Overall Misclassification Probabilities for Eight Discrimination Frameworks

References

Anderson, D. N., Hagedorn, D. N., Higbee, K. T., Miller, N. E., Redgate, T., and Rohay, A. C. (1996). Statistical classification methods applied to seismic discrimination. Technical Report PNNL-11192, Pacific Northwest National Laboratory, Richland, WA.

Michie, D., Spiegelhalter, D. J., and Taylor, C. C., editors (1994). *Machine Learning, Neural and Statistical Classification.* Ellis Horwood, New York, NY.

Advanced Systems for Assessing the Performance of Regional Networks

T.G. Barker, K.L. McLaughlin and J.L. Stevens
Contract F19628-95-C-0111
Sponsored by DOE

ABSTRACT

The goal of this research is to formulate and apply techniques for making statistical descriptions of the performance of the tasks of detecting, locating and identifying seismic sources. These methods are to be applied to existing seismic networks and identification procedures, or to modifications. The program to be used is called Xnice, for X windows version of Network Identification Capability Evaluation.

We find that detection levels based on both regional and teleseismic phases computed by Xnice agree well with those computed by NetSim. The Xnice simulations predict that Lg/P spectral ratios would be effective discriminants while Lg spectral ratio would not, in accordance with observations. The simulations also indicate that Ml:Mo would be effective, but we have no observations at this time to test this.

Simulations done world-wide using events in the Events Bulletin for 1993 to 1996 from the prototype IDC (Alpha stations alone) show that network magnitudes computed using arithmetic means of station values have a positive bias of several tenths of a magnitude unit for small magnitudes (<3). Network magnitudes found using maximum likelihood estimates do not have this bias.

The results of Middle East/North Africa simulations will be shown at the meeting as a poster presentation and as a computer demonstration.

Keywords: seismology, seismic discrimination, earthquakes, Monte-Carlo simulations

OBJECTIVES

The goal of this research is to formulate and apply techniques for making statistical descriptions of the performance of the tasks of detecting, locating and identifying seismic sources. These methods are to be applied to existing seismic networks and identification procedures, or to modifications. The program to be used is called Xnice, for X windows version of Network Identification Capability Evaluation.

RESEARCH ACCOMPLISHED

Accomplishments on this project have been in three areas: (1) calibration and validation studies for central Europe, (2) studies of the efficacy of the maximum likelihood estimator of network magnitude, (3) data synthesis and preparation for Middle East simulations and (4) enhancements to the usability and robust performance of Xnice.

CONCLUSIONS AND RECOMMENDATIONS

We find that detection levels based on both regional and teleseismic phases computed by Xnice agree well with those computed by NetSim. The Xnice simulations predict that Lg/P spectral ratios would be effective discriminants while Lg spectral ratio would not, in accordance with observations. The simulations also indicate that Ml:Mo would be effective, but we have no observations at this time to test this.

Simulations done world-wide using events in the Events Bulletin for 1993 to 1996 from the prototype IDC (Alpha stations alone) show that network magnitudes computed using arithmetic means of station values have a positive bias of several tenths of a magnitude unit for small magnitudes (<3). Network magnitudes found using maximum likelihood estimates do not have this bias.

Network Simulations

Central Europe

The primary objective of simulations in Central Europe was to compare the calculated detection levels with the NetSim program (Sereno, 1990) and compare calculated identification performance with observations in a region where the propagation and source parameters are well known. We find that detection levels based on both regional and teleseismic phases computed by Xnice agree well with those computed by NetSim. The Xnice simulations predict that Lg/P spectral ratios would be effective discriminants while Lg spectral ratio would not, in accordance with observations. The simulations also indicate that Ml:Mo would be effective, but we have no observations at this time to test this.

Middle East and North Africa

We have synthesized available earth structure, wave propagation, source property and identification performance data for the Middle East and North Africa in a form usable by Xnice. At the time of this writing, we are incorporating data from recently made requests for earth structure and source descriptions from investigators working on this area. The results will be shown at the meeting as a poster and as a computer demonstration.

Maximum Likelihood Estimate Studies

Maximum Likelihood Estimates of Teleseismic mb
for the GSETT-3 Primary (Alpha) Network

1. Introduction

The maximum likelihood estimates of magnitude (Ringdal, 1976) was developed to improve measures of signal amplitudes when are below detection levels in some or all of the network As pointed out by Von Seggern and Rivers (1978), values of mb derived from arithmetic mean tend to have a positive bias, which may be eliminated by the use of maximum likelihood estimates. In the following, we simulate a suite of earthquakes recorded at the GSETT-3 Alpha network, and compare the mb's computed using the two methods with true values.

2. Simulations

The simulations described here use the Xnice program, described in detail in Barker, 1996. In the following, we specify parameters specific to this problem and refer the reader to that document for methods, models and other parameters.

2.1. Source Properties

So that a realistic geographic distribution of events is simulated, we extracted event locations from the Late Events Bulletin for 1993 to 1996 from the prototype IDC. This included about 20,000 events. Seismic moments were then distribution followed the rule

$$\log N_{cum} = 2.85 - \log M_0,$$
$$\log M_0 \geq 15,$$

where N_{cum} is the cumulative number of events with moment $\geq M_0$ (note that in Xnice a moment distribution is specified, rather than a magnitude). The stress drop were governed by log-normal distribution with a mean of 10 MPa (100 bars) and standard deviation of 5 Mpa.

2.2. Propagation Parameters

Amplitude tables are from the Vieth and Claussen tables. Random errors in log amplitude of teleseismic P due to propagation followed a log-normal distribution with zero mean and 0.28 log-units standard deviation.

2.3. GSETT-3 Primary Station Network

The 41 stations used in this simulation, their location and mean log noise amplitude (microns) at 1 Hz are given the following table:

Station	Latitude	Longitude	Noise
AKT	50.434	58.018	-3.147
ARA0	69.535	25.506	-2.156
ASAR	-23.666	133.905	-2.774
BDFB	-15.633	-48.000	-2.899
BGCA	5.176	18.424	-3.349
BJT	40.018	116.168	-3.064
BOSA	-28.613	25.416	-2.726
CMAR	18.824	98.947	-2.920
CPUP	-26.331	-57.329	-2.919
DBIC	6.670	-4.856	-3.147
ESDC	39.675	-3.965	-2.751
FIA0	61.444	26.079	-2.488
GEC0	48.836	13.704	-3.147
HFS0	60.134	13.696	-2.814
KBZ	43.950	42.683	-3.147
LBNH	44.240	-71.930	-2.375
LOR	47.268	3.859	-2.618
LPAZ	-16.288	-68.131	-3.552
MAW	-67.604	62.871	-2.303
MBC	76.242	-119.360	-3.347
MIAR	34.546	-93.573	-2.868
MJAR	36.542	138.207	-2.891
NAO	61.040	11.215	-2.450
NPO	64.771	-146.886	-2.007
NRI	69.400	88.000	-3.179
PDAR	42.780	-109.560	-3.315
PDY	59.600	112.500	-3.073
PFCA	33.610	-116.460	-3.005
PLCA	-40.731	-70.550	-2.955
SCHQ	54.817	-66.783	-2.735
SPITS	78.180	16.370	-1.583
STKA	-31.882	141.592	-2.813
TXAR	29.334	-103.667	-3.243
ULM	50.250	-95.875	-3.015
VNDA	-77.519	161.846	-2.780
WALA	49.056	-113.911	-2.983
WHY	60.695	-134.967	-2.840
WOOL	-31.073	121.678	-2.919
WRA	-19.944	134.341	-3.020
YKA	62.493	-114.605	-3.433
ZAL	53.940	84.805	-3.463

The GSETT-3 Primary network of stations has a wide range of short-period noise levels ranging from a high of -1.6 (0.025 microns) to low values of -3.5 (0.003 miscrons).

2.4. Results

Figure 1 shows the locations of stations (triangles) and events (circles) used in the simulations. In Figure 2, we have plotted arithmetic mean mb's (m_b^{am}) versus $\log M_0$. Only those events which meet the GSE detection criteria are included. Also plotted in this figure is the ensemble average of the values of mb within 0.125 of the plotted $\log M_0$ (the averages are indicated by x's). A third set of values on the figure are the values of mb when there is no propagation variation or ground noise and no statistical variation in the stress drop. We refer to these values as the "true" values. The curvature is due to the change in corner frequency with moment. We see that m_b^{am} exceed the true values by about 0.5 at the lowest magnitudes and approach the true value at higher mb. Figure 3 shows a comparable plot for maximum likelihood estimated mb (m_b^{mle}). The values of m_b^{mle} are quite close to the true values across the magnitude range. m_b^{am} and m_b^{mle} are plotted against each other in Figure 4, which shows that the m_b^{am} exceed the m_b^{mle}, in agreement with Von Seggern and Rivers (1978).

The incremental number of events versus m_b^{mle} and m_b^{am} are shown in Figure 5. In each case the values are normalized by the total number of events detected. The peak number of events for m_b^{mle} occurs at a lower value than m_b^{am}, indicating an apparent lower detection threshold for m_b^{mle}. The cumulative numbers (number with values greater than mb) are shown in Figure 6. Also shown on this figure are the true values. The slope of the m_b^{mle} distribution at high magnitudes (from which a "b value" would be measured) has about the same value as the slope of the true values, while the m_b^{am} distribution has a greater slope. Note that the slope is greater than one (the slope of the log moment distribution above) due to corner frequency effects.

These results indicate that replacement of m_b^{am} with m_b^{mle} as the network mb values in future bulletins will reduce magnitude bias at low magnitudes and decrease the slope of the cumulative distribution of events versus mb in accordance with conventional wisdom.

Figure 1. GS3_5a network and epicenters

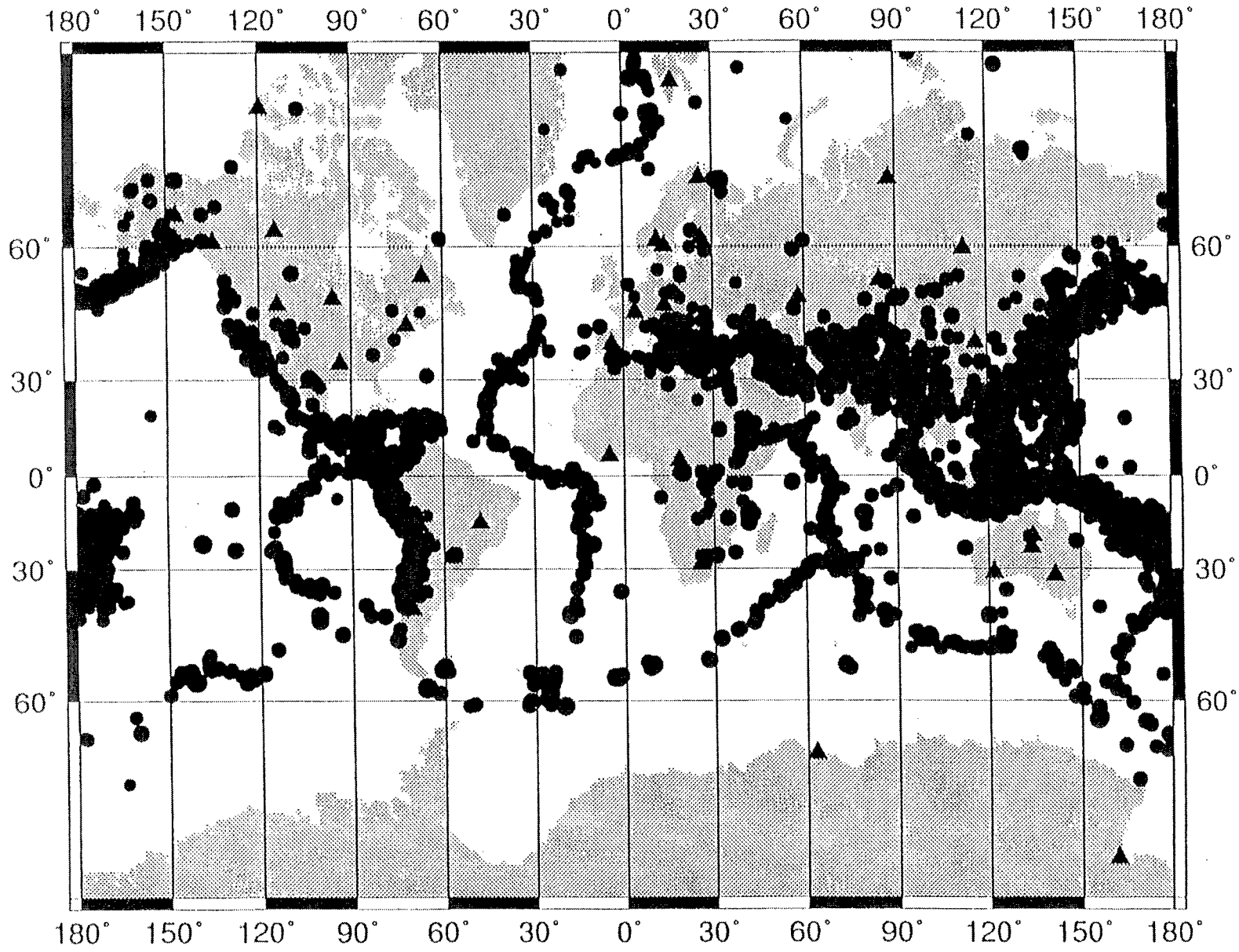

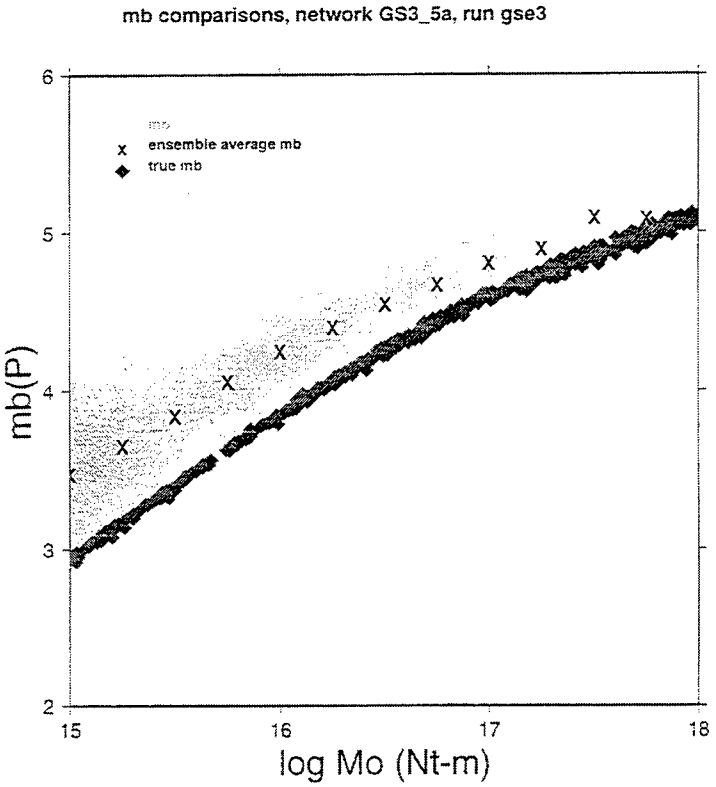

Figure 2. Arithmetic mean mb (circles), ensemble average mb (x) and true mb (diamonds) are plotted verus log moment.

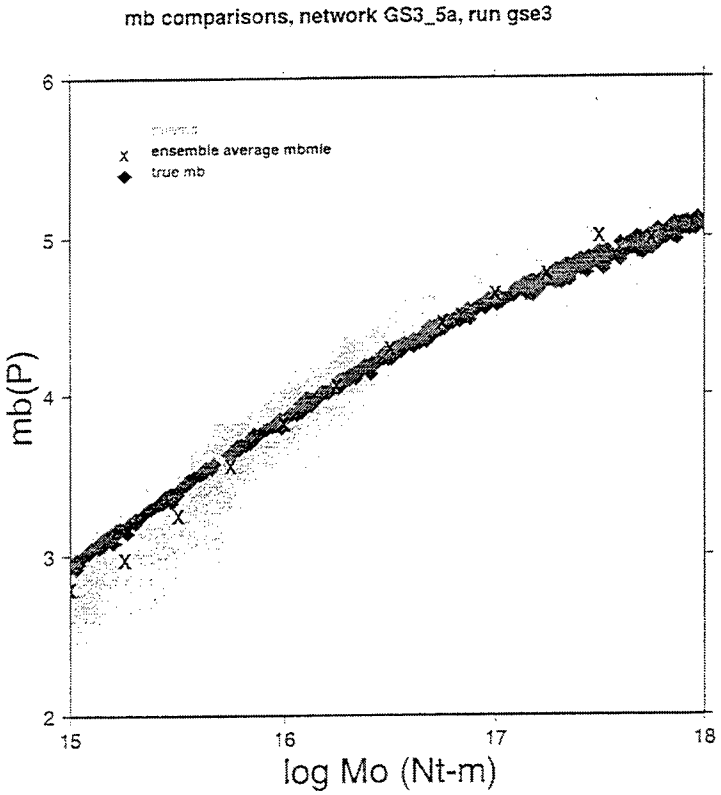

Figure 3. Maximum likelihood estimate mb (circles), ensemble average mlemb (x) and true mb (diamonds) are plotted verus log moment.

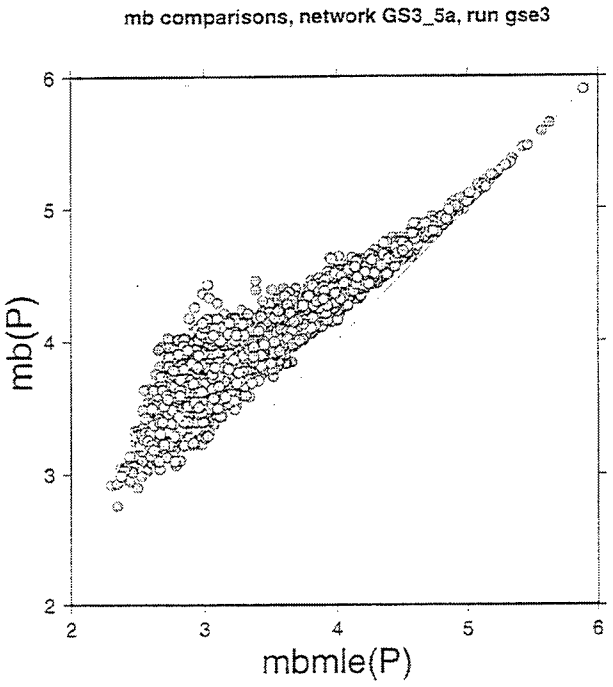

Figure 4. Arithmetic mean mb versus mle mb

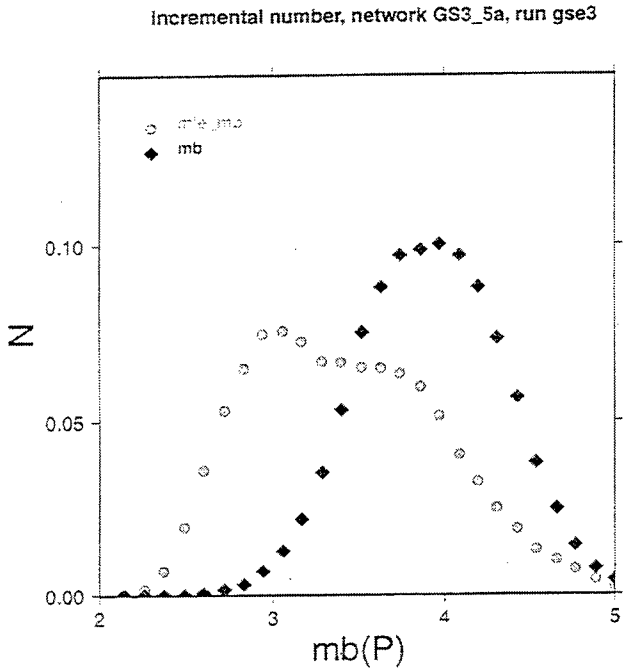

Figure 5. Incremental number of events are plotted versus arithmetic mean mb (diamonds) and mle mb (circles).

3. References

Barker, T.G. (1996), "Xnice: A System for Assessing Network Identification Performance", S-Cubed Scientific Report No.2 to Phillips Laboratory, SSS-FR-95-15215 , PL-TR-96-2087

Ringdal, F. (1976), "Maximum Likelihood Estimation of Seismic Magnitude", *Bull. Seism. Soc. Am.*, **66**(3), 789-802.

Sereno, T.J. (1990), "NetSim: A computer Program for simulating the Detection and Location Capability of Regional Seismic Networks", Science Applications International Corporation Technical Report to DARPA, SAIC 90/1163.

Von Seggern D. and D.W. Rivers (1978), "Comments on the use of Truncated Distribution Theory for Improved Magnitude Estimation", *Bull. Seism. Soc. Am.*, **68**(5), 1543-1546.

CHARACTERIZATION OF REGIONAL-PHASE PROPAGATION AND SEISMIC DISCRIMINANTS FOR THE MIDDLE EAST

Douglas R. Baumgardt, ENSCO, Inc.

F19628-95-C-0203
Sponsored by DOE

ABSTRACT

To support low-magnitude, seismic-event identification for the verification of Comprehensive Test Ban and Non-Proliferation Treaties, the characteristics of regional phase propagation and regional discriminants have been investigated for events and propagation-paths in Israel, Jordan, Lebanon, Syria, Egypt, Iran and Iraq. Mostly earthquake recordings have been studied at stations in the Middle East, including Iranian Long Period Array (ILPA) and various stations in the Mednet and IRIS, with the goal of relating regional characterization of events in the Middle East to discrimination in the region. Pg and Lg propagation blockages have been noted for paths crossing the Levantine Basin of the Eastern Mediterranean and the Southern Caspian Basin north of Iran. However, efficient propagation of Lg has been observed for propagation paths which do not cross sedimentary basins, including earthquake in the Gulf Of Aqaba and Ethiopia recorded at KEG. Sn phases tend to be strong for the Lg blockage paths, such as earthquakes along the Dead Sea Transform whose paths cross the Levantine basin, but are weak when Lg is not blocked, such as the Gulf of Aqaba. Examples of attenuated Sn have been observed for the Red Sea region and may be due to high attenuation in the mantle in this region.

GIS geological and geophysical databases have been used to analyze propagation paths and look for explanations for strong Sn and Lg attenuation. Lg blockage in the Levantine basin may be caused by pinchouts in the granitic layer. The lack of Sn waves for paths along the western margin of the Red Sea may be correlated with high heatflow in the region.

KEG spectra and cepstra of Gulf of Aqaba events reveal a subtle modulation in the Pn and Pg spectra, but not the Lg spectra, consistent with multiple phases of delay time of 0.3 seconds. This effect may be caused by acoustic water reverberations. Delay time of 0.3 seconds would indicate an approximate water depth of 228 meters.

To address discrimination issues in the Middle East, amplitude ratio discriminants have been applied to earthquakes along the Dead Sea Transform, the Gulf of Aqaba, along the Red Sea, and in the Zagros Mountains of Iran. Because there are no known explosions in these regions, the discriminants are being compared to like paths in other regions outside the Middle Eastern countries. Pn/Sn and Pn/Lg ratios are interchangeable as discriminant features and usually can discriminate Middle Eastern earthquakes from mine blasts and nuclear explosions in other regions of Eurasia. Future studies should address the regional tectonic effects on regional discriminants to support intra-regional comparisons with explosions outside the Middle East, since it is unlikely the calibration explosions will be forthcoming within the Middle East. Such studies may also support future sitings of stations to avoid Lg blockage paths.

Keywords: Discrimination, Middle East, regional phases, Lg blockages, Sn attenuation, underwater reverberations

OBJECTIVES

Understanding regional phase propagation and discriminants for seismic events in the Middle East poses a major challenge to developing the capability for monitoring the Comprehensive Test Ban and Non Proliferation Treaties. Seismic monitoring of events in this region is complicated two difficulties: (1) The extreme geologic and tectonic complexity of regional propagation paths in the region needs to be understood and calibrated in order to use seismic waveform features for discrimination. (2) Although earthquakes occur in abundance in the tectonic belts of the Middle East, discrimination studies in this region are necessarily limited by the paucity of known explosive sources in the region.

Our approach to the first problem has been to assemble a database of seismic events, consisting mostly of earthquakes, for the key countries of interest (Egypt, Jordan, Israel, Iran, Iraq) and to investigate the characteristics of regional phase propagation in the region. Of key interest in this study is variation of excitation of high-frequency regional shear waves, principally Sn and Lg, relative to regional P (Pn, Pg). Where variations and anomalies are found, we have tried to interpret them in terms of geological characteristics of the propagation path. Of particular interest has been the observation of the blockage of Lg, a key regional phase for a number of different discriminants.

To address the second problem, seismic waveform-feature discriminants have been extracted, using the Intelligent Seismic Event Identification System (ISEIS) (Baumgardt et al, 1991), for presumed earthquakes recorded at stations in the Middle East. As much as possible, we try to compare them with known or presumed explosions in the region. However, because only limited numbers of such events, in particular, nuclear explosions, are available for the region, we compare the earthquake features with known explosions in other regions which have been collected in the ISEIS database.

RESEARCH ACCOMPLISHED

Data Sources

A comprehensive investigation of regional phase propagation and discrimination analysis for key countries of the Middle East has begun with primary focus on Israel, Jordan, Egypt, Iran, and Iraq. An Oracle database of seismic waveforms has been collected from the following data sources:

(1) Iranian Long-Period Array (ILPA) - This array operated during the 1970s and included broadband borehole KS36000 seismometers. A database assembled by Lori Grant of Multimax, and analyzed by Flori Ryall, has been imported into the ISEIS database. Our initial focus has been on seismic events in the Caspian region, in particular, propagation paths which cross known Lg blockage region of the South Caspian Basin (Baumgardt, 1996). The characteristics of other paths within and around Iran are also being investigated.

(2) Single station data from Mednet and IRIS Stations - The key Mednet station of interest has been Kottamya, Egypt (KEG) because of its proximity to the planned location of the LUXESS array in Northern Egypt. This station is in an advantageous location to record events in many different regions of interest in the Middle East.

Lg Propagation Barriers in the Levant

Amplitude ratios of regional P (Pn, Pg) to region S (Sn, Lg) have proven effective for discriminating earthquakes and explosions, both conventional and nuclear. However, the

discriminant has had variable application in different regions because of apparent regional phase barriers, particularly to Lg, but in certain regions, Sn phases are not always observed. Similarly, Pn and Pg may have variable amplitudes due to propagation path barriers, although these have been less evident.

Baumgardt (1996) has shown, using ILPA observations, that the Lg barriers in the Southern Caspian Basin may be caused by the presence a sedimentary basin which interrupts the granitic-layer waveguide for Lg. Similar effects have been observed in the Barents Basin (Baumgardt, 1990) and other basins in the Russian platform (Baumgardt, 1991). Similar Lg blockages have been observed at KEG in Egypt for earthquakes occurring along the Dead Sea Transform of Israel, Lebanon, and Syria. Figure 1 shows a map of propagation paths from a number of earthquakes along the transform to KEG. The waveforms are shown as a record section in Figure 2.

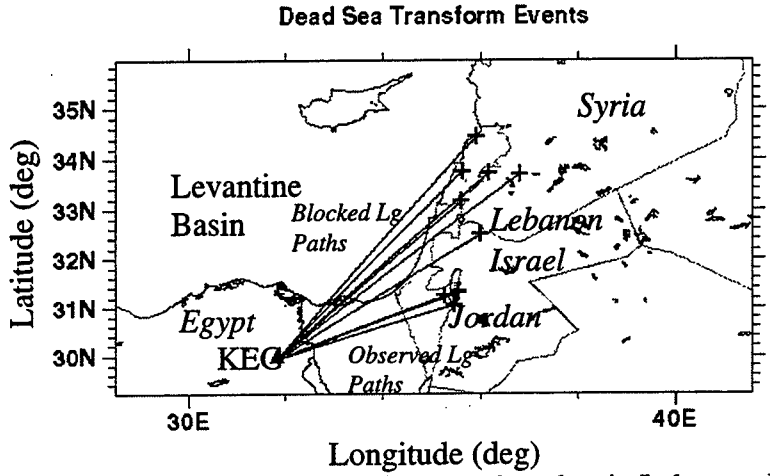

Figure 1: Map showing propagation paths from earthquakes in Lebanon, Israel, Jordan, and Syria recorded at KEG.

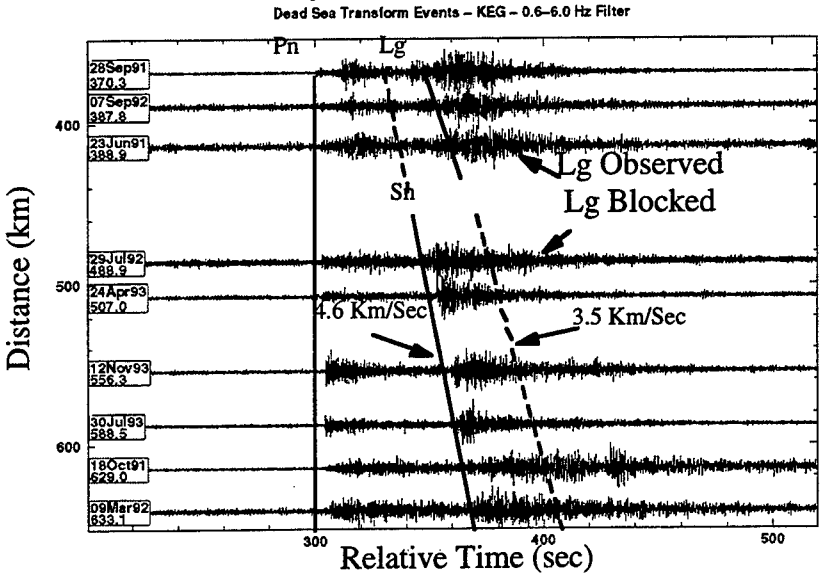

Figure 2: Record section plot of the waveforms shown in the map in Figure 1.

The record section shows a sudden disappearance of Lg beginning at a distance of about 400 km. As shown in Figure 1, the blocked-Lg propagation paths cross the eastern Mediterranean Sea.

A contrasting situation exists for events in the Gulf of Aqaba and Suez, shown in Figure 3. Figure 4 shows the record section of these paths which exhibit strong Lg waves.

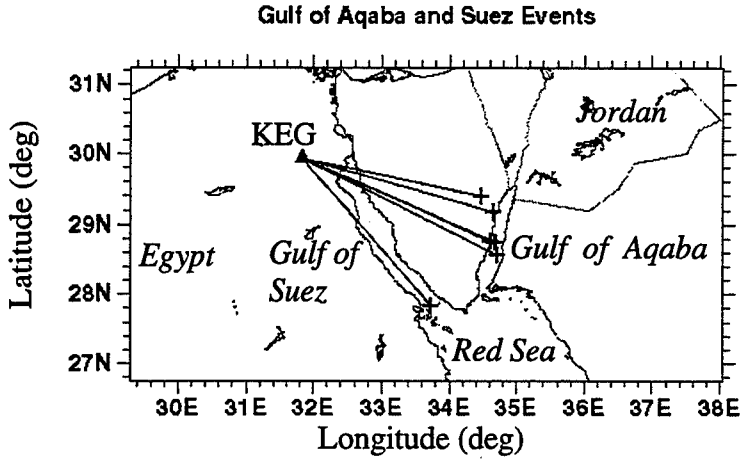

Figure 3: Propagation paths for selected events in the Gulf of Aqaba and Suez to KEG.

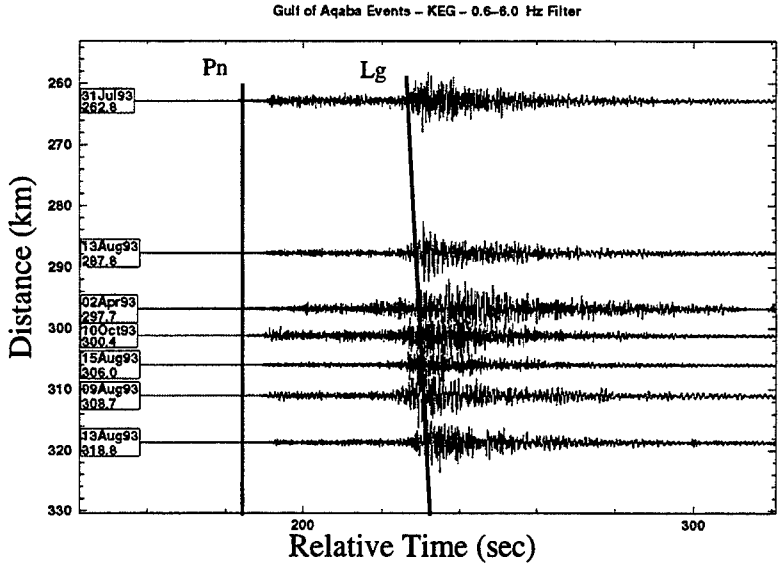

Figure 4: Waveforms for Gulf of Aqaba and Suez events recorded at KEG.

Sn phases tend to be strong for the Lg blockage paths, such as earthquakes along the Dead Sea Transform beyond 400 km from KEG shown in Figure 2, whose paths cross the Levantine basin. At the shorter distances, where Lg can be observed, no Sn waves were recorded. Sn waves are also missing in Figure 4 for the paths from the Gulf of Aqaba events to the south. A similar result was obtained for blockages in the South Caspian Basin (Baumgardt, 1996). Where Lg is blocked, strong Sn waves were observed. However, for paths where strong Lg (and Pg) phases were observed, only weak Lg phases were observed.

Figure 5 shows paths from events to the south at distances up to 2000 km. Figure 6 shows a KEG record section for these paths.

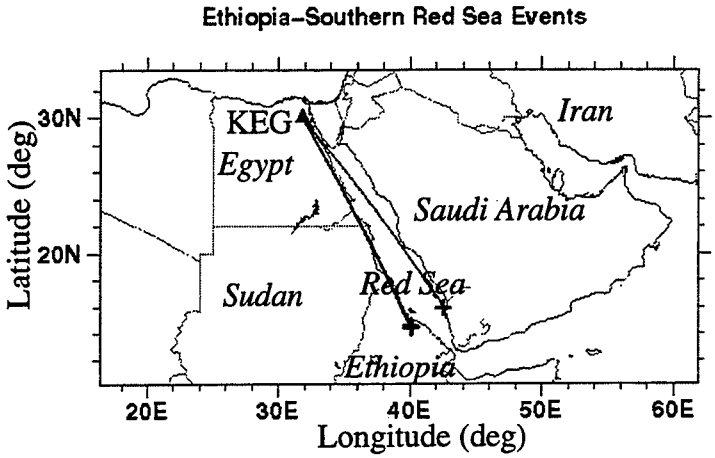

Figure 5: Map showing propagation paths to KEG from events in the southern Red Sea region.

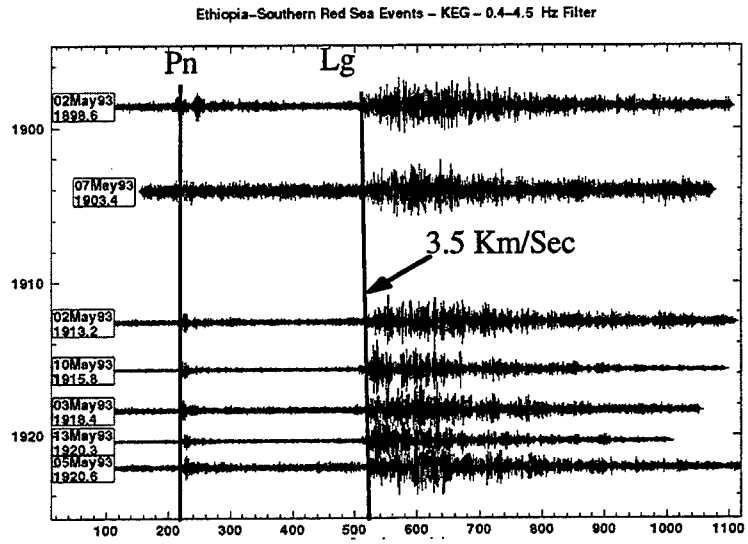

Figure 6: Record section of the waveforms, aligned to Pn, for the paths from the southern Red Sea region shown in Figure 7.

These paths show very strong Lg excitation, although they are very low frequency. Evidently the path along the western edge of the Red Sea is very efficient for Lg propagation. However, as in the paths farther north, there is no apparent Sn phase for these paths.

Geophysical and Geological Interpretations of Regional-Phase Propagation Paths

The apparent explanation for the Lg blockage in the Levant can be seen in Figures 7 and 8, which compare the sediment basement and Moho depths for the different propagation paths, obtained from the Eurasia and ME-NA GIS databases at Cornell (Fielding et al, 1993; Barazangi, et al, 1995). The dashed lines indicate the propagation paths from the north and the solid lines indicate the paths from the south to KEG.

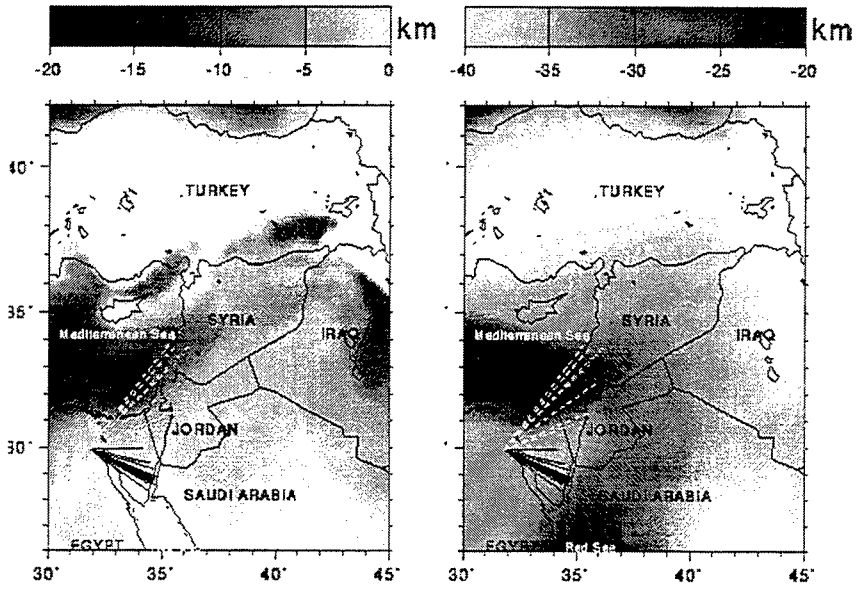

(a) (b)

Figure 5: Comparison of the crustal structure for the propagation paths from the Dead Sea Transform (white dashed lines) and Gulf of Aqaba (solid black lines) to KEG. (a) Depth to basement, (b) Moho depths.

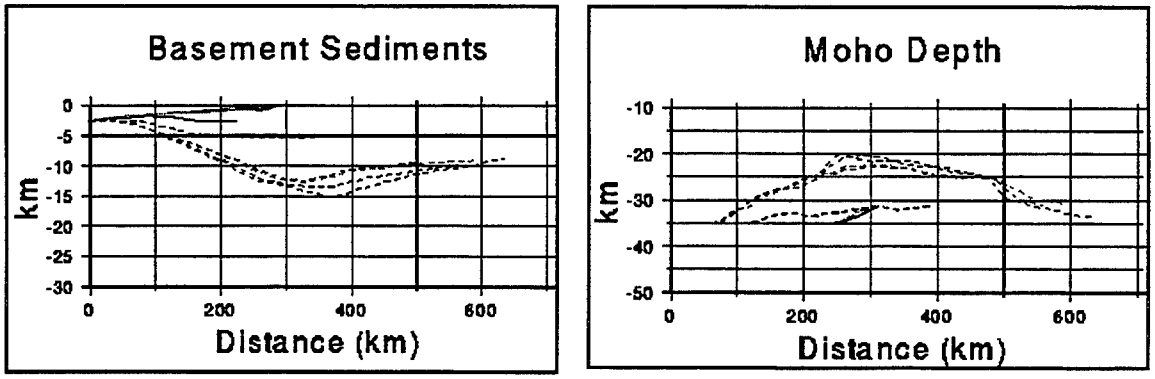

(a) (b)

Figure 6: Comparison of crustal cross-sections for the paths in Figure 5 for paths from the Dead Sea Transform (dashed lines) and the Gulf of Aqaba (solid lines) to KEG. (a) Depth to basement, (b) Moho depths.

These plots show a clear pinchout of the granitic layer, where the sediments thicken by 15 km and the Moho thins by nearly the same amount. These two effect together result in a breakdown in the Lg propagation across the Levant and cause the Lg blockage. For the paths from the Gulf of Aqaba events, which cross the Sinai Peninsula and Northern Arabian desert, there are virtually no sediments and the Moho depth is relatively constant at about 35 km. Thus, Lg propagates efficiently in this region.

In order to further explore other geophysical explanations for unusual Sn and Lg attenuation, a gridded heatflow database for the Middle East, using the GMT Nearneighbor function (Wessel and Smith, 1995) is being generated from the global heatflow data of Pollack et al (1993). Figure 7(a) shows the part of this database for the Dead Sea, Sinai, and Red Sea regions. Presumably, strong seismic attenuation may be related to regions of

high heatflow. To check this, heatflow cross sections for the propagation paths from the Dead Sea Transform and Gulf of Aqaba regions are plotted in Figure 7(b) and for the longer Red Sea paths in Figure 7(c).

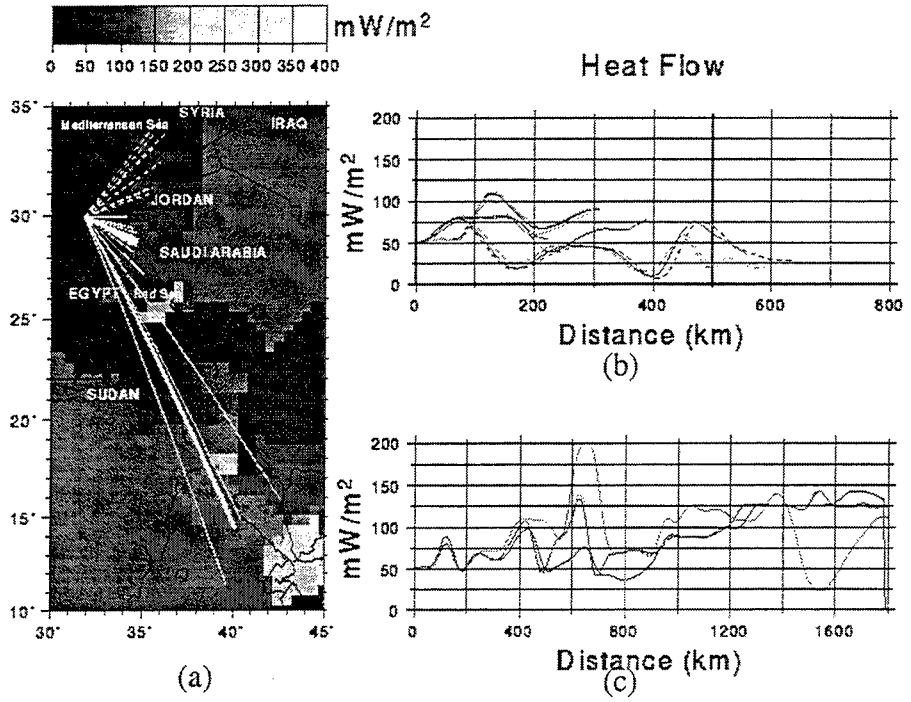

Figure 7: Gridded heatflow database for the Middle East from the global heatflow database of Pollack et al (1993). (a) Gray-level contour map, (b) heatflow cross sections for the northern paths KEG, (c) heatflow cross sections for the southern paths.

Figure 7 shows the most of the paths from the Dead sea Transform region in the north have lower heatflows, usually less than 50 mW/m^2, whereas paths from the Gulf of Aqaba are higher than 50 mW/m^2. Paths from the southern Red Sea have highly variable heat flows which reflects the coarseness of the original heatflow point database itself. However, on average, the heatflow is higher along the southern propagation paths compared to those to the north. High heatflows in this region appear to be related to the fact that the Red Sea may be an incipient spreading center, and there may be upwelling of hot material from the mantle, particularly in the center part of the Red Sea.

High heatflow does not appear to correlate with Lg blockage in the Middle East. However, it may partly cause the low frequencies of the phases to the south and the strong Sn attenuation along the Red Sea region even when Lg propagates efficiently. Because Sn primarily propagates in the mantle, whereas Lg propagates in the crust, we might expect greater Sn attenuation near spreading centers.

Water Reverberations in the Gulf Of Aqaba

The earthquakes in the Gulf of Aqaba, in addition to producing strong Lg waves, have an interesting pattern associated with their spectra. Figure 8 shows two spectra computed for the Pn, Pg and Lg phases recorded at KEG for two events in the Gulf of Aqaba.

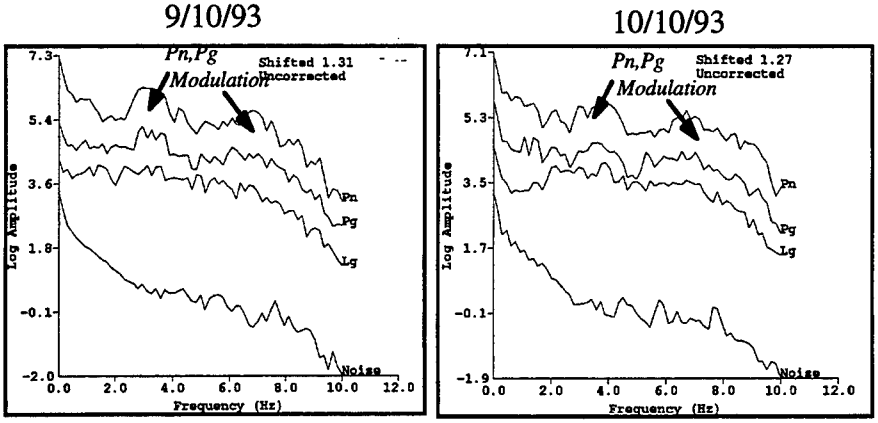

Figure 8: Spectra for the regional phases Pn, Pg, and Lg, and noise recorded at KEG for two events in the Gulf of Aqaba. Spectra have been shifted for display purposes.

Both these spectra produce a weak modulation, as indicated, which is the same for Pn and Pg but weaker or non-existent in Lg. Using the ISEIS Multiple Event Recognition System (MERSY), designed for detecting multiple events like ripple fire, the cepstra have been computed and are plotted in Figure 9.

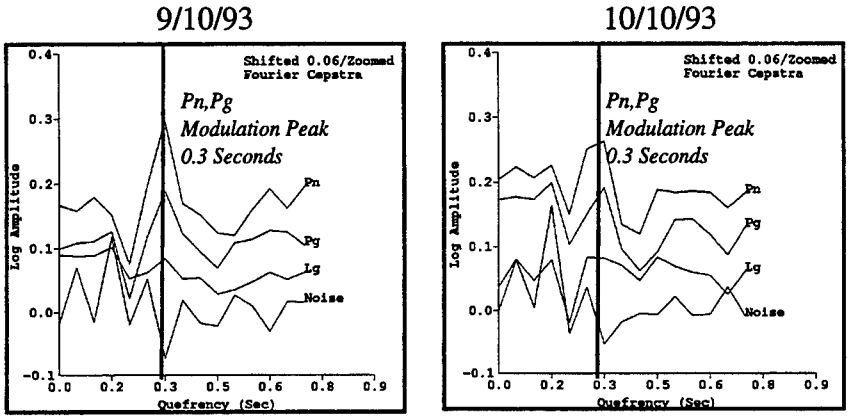

Figure 9: Cepstra computed from the spectra in Figure 8, shown the strong modulation peak in Pn and Pg, but not in Lg and noise. Cepstra shifted for display purposes.

The plots show a consistent cepstral peak at about 0.3 seconds. The fact that this peak only appears in Pn and Pg, but not Lg, suggests that it may be a reverberation and not due to source multiplicity. Since these events occur beneath the Gulf of Aqaba, these reverberations may be due to water column reflections. This result shows how to use multiple-phase cepstra to distinguish near surface reverberations from multiple events, i.e., look for consistent cepstral peaks which appear in regional P phases but not in regional S phases, like Lg. A similar approach may be useful for identifying depth-phase reverberations in the crust for estimation of event depth.

Discriminant Analysis of Middle East Earthquakes

Because there are few known explosions in the Middle East, discriminant features for earthquakes in the Middle East are being compared with similar features extracted for

explosions in other parts of the world. The ISEIS database stores all discriminant features which have been previously computed, and these features can be called up and compared with features computed for new events in other regions. As an example, Figure 10 shows examples of "incoherent beam" or RMS amplitude envelopes computed for one of the Gulf of Aqaba earthquakes.

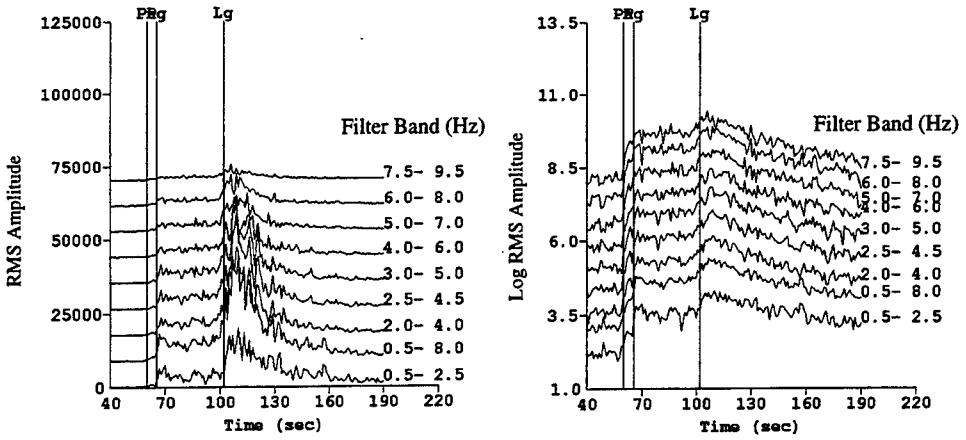

Figure 10: Incoherent beam plots showing phase picks used for multi-frequency amplitude ratio analysis. (a) Unlogged RMS. (b) Logged RMS.

In this example, incoherent beams computed on bandpass filtered waveforms are used to compute Pn/Lg and Pg/Lg amplitude ratios in all bands. Plots of the ratios, versus distance, are shown in Figure 11, measurements for earthquakes recorded at KEG from the Zagros Mountains of Iran.

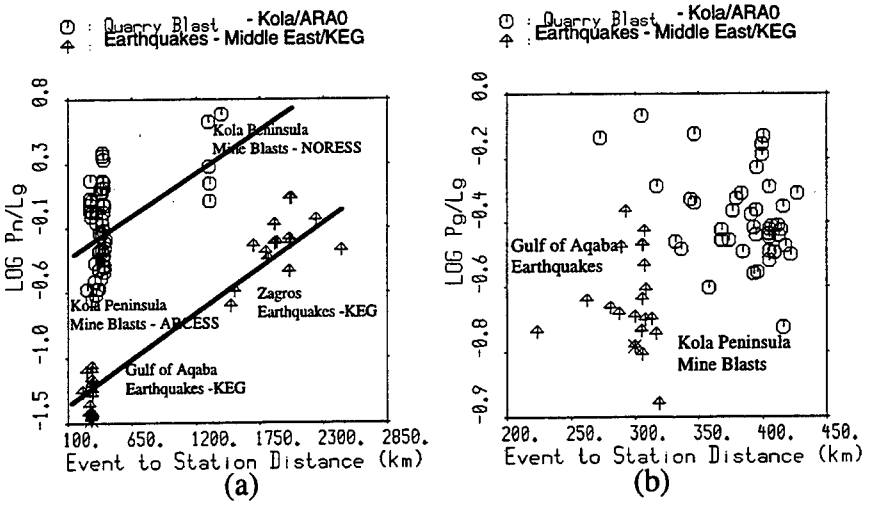

Figure 11: ISEIS analysis of regional amplitude ratios, in the 4 to 6 Hz band, comparing Middle East earthquakes recorded at KEG with Scandinavian blasts recorded at NORESS and ARCESS. (a) Pn/Lg ratios. (b) Pg/Lg ratios.

Figure 11(a) shows that earthquakes in the Middle East discriminate from blasts on the Kola Peninsula, although a clear distance dependence in the Pn/Lg ratio is evident. However, Figure 11 (b) shows that the discrimination is less distinct for Pg/Lg ratios.

CONCLUSIONS AND RECOMMENDATIONS

This paper summarizes work in progress in the study of discrimination problems in the Middle East. We have identified Lg blockages in the Levant which appear to be caused by granitic layer perturbations in the Levantine sedimentary basin of the western Mediterranean Sea. Lg propagates efficiently in the Sinai and Arabian deserts, although Sn is strongly attenuated. Sn appears to be attenuated in the Red Sea region, perhaps due to high attenuation in the mantle do to upwelling beneath the Red Sea spreading center. For the paths we have studied, we find that where Lg is blocked, Sn is observed. Pn/Sn and Pn/Lg amplitude ratios can be used interchangeably as discriminants if one or the other of the phases is blocked.

We believe that information from GIS databases, such as those being assembled at Cornell, will be useful for interpreting and calibrating propagation paths which cross complex and varying tectonic regions. To solve the problem of missing explosions in the Middle East, we recommend comparing with discriminants measured for other regions. This method, combined with the GIS canonical correlation scheme suggested by Baumgardt and Der (1994), can be used to evaluate waveform feature discriminants even when events of different types are not available for the same region.

REFERENCES

Barazangi, M. D. Seber, M. Vallve, and B. Isacks (1995). A geological and geophysical information system for Eurasia, the Middle East, and North Africa, Final Report, PL-TR-95-2168, Cornell University, Ithaca, NY , ADA305455

Baumgardt, D.R. (1990). Investigation of teleseismic *Lg* blockage and scattering using regional arrays, *Bull. Seism. Soc. Am.*, **80**, 2261-2281.

Baumgardt, D.R. (1991). High frequency array studies of long range *Lg* propagation and the causes of *Lg* blockage and attenuation of the Eurasian continental craton, PL-TR-91-2059(II), 21 March 1991. ADA236984

Baumgardt, D.R. (1996). Lg propagation-path barriers in the Eurasian continental craton - possible shallow crust explanations, Presentation at 91st Annual Meeting, Seismological Society of America, Abstract in *Seismological Research Letters*, p. 31.

Baumgardt, D.R. and Z. Der (1994). Investigation of the transportability of the *P/S* ratio discriminant to different tectonic regions, Scientific Report No. 1, *PL-TR-94-2299*, ENSCO, Inc., Springfield, VA, ADA292944

Baumgardt, D.R., S. Carter, M. Maxson, J. Carney, K. Ziegler, and N. Matson (1991). Design and development of the intelligent event identification system, *PL-TR-91-22298(I)*, Final Report, Volumes I, II, and III, ENSCO, Inc., Springfield, VA. ADA248381

Fielding, E.J., B.L. Isacks, and M. Barazangi (1992). A geological and geophysical information system for Eurasia, *Technical Report No. 2*, Cornell University, Ithaca, New York.

Pollack, H.N., S.J. Hurter, and J.R. Johnson (1993). Heat flow from the earth's interior: analysis of the global data set, *Rev. of Geophys.*, **31**, 267-280.

Wessel, P. and W.H.F. Smith (1995). The Generic Mapping Tools (BMT) version 3.0, Technical Reference and Cookbook, SOEST/NOAA.

The Physical Basis for the L_g/P Discriminant

T. J. Bennett, K. L. McLaughlin, and M. E. Marshall
Maxwell Laboratories, Inc., S-CUBED Division
11800 Sunrise Valley Dr., Suite 1212
Reston, Virginia 22091
Contract No. F 19628-95-C-0107
Sponsored by AFTAC

Abstract

The Comprehensive Test Ban Treaty (CTBT) will require detection and identification of small seismic events and the consequent increased reliance on regional seismic monitoring. Reliable regional discrimination has proven to be an elusive goal, but over the years discriminant measures based on the relative amplitudes of L_g and P regional phases have shown great promise for distinguishing between nuclear explosions and other source types in some regions. This research program is aimed at improving fundamental understanding of the physical basis for L_g/P ratios as regional discriminants. Such physical understanding is expected to lead to more reliable regional discrimination and should also enable extending this regional discrimination capability into uncalibrated regions. To help reach our research objectives, we have been using available data to characterize the behavior of L_g/P ratios as a function of frequency for various source types. This characterization provides the basis for comparison to theoretical modeling studies which predict the behavior of the L_g/P ratio for different source types and propagation environments.

During the initial phase of this research, the focus of our empirical studies has been to assemble the representative regional database of high-quality digital data from NTS, Shagan River, and Novaya Zemlya nuclear tests and PNE explosions from the former Soviet Union, as well as earthquakes, non-nuclear blasts, and rockbursts from several regions at comparable distances. We currently have available a fairly large waveform database and have begun to systematically compute frequency-dependent L_g/P ratios. Preliminary results indicate that in many regions the behavior of the L_g/P ratios appears to be consistent with prior experience in which ratios were lower for nuclear explosions than for other source types with largest differences at high frequencies. For these computations we have been experimenting with some alternative spectral estimation schemes to identify more reliable L_g/P discriminant measures and to determine robust features in the regional signal behavior. The theoretical part of this program has focused on setting-up various modeling schemes for representative earth models and investigating model factors which affect the relative L_g and regional P phase amplitudes. We have analyzed a scattering mechanism for R_g-to-L_g conversion from shallow explosion sources for three models (viz. Gutenberg earth, NTS, and East Kazakh test site). The predictions indicate approximately the same relative amplitude between the near-field R_g and the far-field L_g for all three models which agrees with empirical evidence of consistency in L_g generation from nuclear explosion sources in a variety of tectonic environments.

Key Words: Seismic, Discrimination, Regional, Explosion, Earthquake, Mechanism

Objective

Recent interest in a CTBT has stimulated a desire to detect and identify much smaller seismic events. Furthermore, concern for possible proliferation of nuclear weapons into countries where nuclear weapons testing was not previously at issue requires extending seismic capabilities into new geographic regions. To reach these goals at magnitude levels of interest will require utilization of regional seismic signals. Unfortunately, implementation of effective regional discriminants has proven to be elusive due to the complexity of regional signals and incomplete physical understanding of their dependence on regional propagation and excitation. The objective of this research program is to improve fundamental understanding of the L_g/P ratio regional discriminant, which over the years has proven to be one of the most promising and enduring measures at regional stations for distinguishing between explosions and earthquakes. This research program includes an empirical element to review and formalize the salient features of the L_g/P measure for distinct tectonic environments and different source types and a theoretical element to explain the observed features in terms of source mechanism, source size, depth, and propagation path influences on the regional signals.

Research Accomplished

Empirical Studies

In the empirical element of this research project, we have been reviewing digital waveform data from regional recordings of nuclear explosion tests, earthquakes, non-nuclear explosions, and rockbursts, which we had available from prior research efforts, and collecting additional supplemental regional signals measurements from some regions. We currently have high quality regional waveform samples with good signal-to-noise levels for each of the seismic source types from several regions of interest. The nuclear explosion sample includes events from NTS recorded at both near and far regional distances, events from the former Soviet test sites in East Kazakhstan and at Novaya Zemlya recorded mainly at far regional distances, and events from the Chinese test site at Lop Nor recorded mainly at far regional distances. In addition we have recently supplemented the nuclear explosion regional recordings with PNE tests from throughout the former Soviet Union recorded at the Borovoye station over a range of near to far regional distances. In addition to collecting this database, we have been reviewing experience with L_g/P ratio measurements. Based on that experience we have developed a working hypothesis for the behavior of the L_g/P ratios, as a function of frequency, from various source types. We have been checking that hypothesis against measurements derived from several of the waveforms. Besides these data collection efforts, we have been testing some alternative methods of making the spectral measurements used to determine the L_g/P ratio frequency dependence.

The original development of the L_g/P ratio as a regional discriminant was strongly influenced by observations at regional distances from nuclear explosions at NTS and earthquakes in the surrounding region of the western U.S. (Blandford, 1981). These data continue to represent some of the best controlled samples for testing regional discriminants, since we have there in fairly close proximity nuclear explosions and earthquakes with known source properties. We, therefore, have focused some of our initial efforts at L_g/P characterization on a review of these data. For this region our principal database includes regional observations at the former VELA array stations at TFO, UBO, and BMO and a sample of selected events from the LLNL array stations surrounding NTS. These are primarily at nearer regional distances (less than about 800 km). Figure 1 shows the LLNL array station locations and a sample of ten NTS nuclear explosions and eight earthquakes in the vicinity of NTS. We have performed traditional bandpass filter analyses (cf. Bennett et al., 1995) on the vertical-component records from these events at the various array stations and used the peak measurements from the appropriate group velocity windows to estimate the L_g/P ratios for each filter output. Figure 2 shows a comparison of the average L_g/P ratios measured at station KNB, plotted at the filter center frequencies, for the NTS nuclear explosions and nearby earthquakes. The L_g/P ratios start off at fairly similar levels at low frequencies, but the

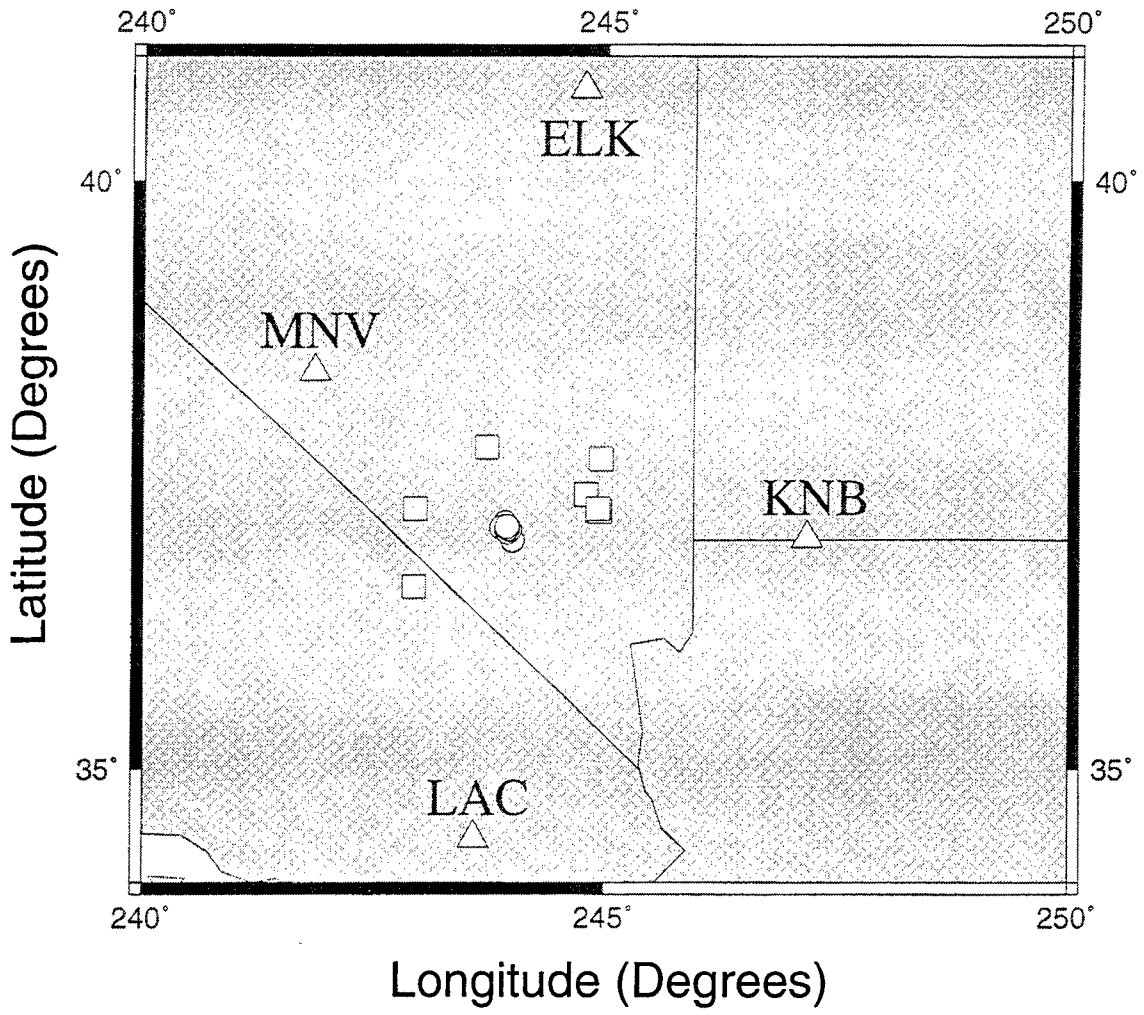

Figure 1. Map showing the location of NTS nuclear explosion and nearby earthquake sample relative to the LLNL network stations.

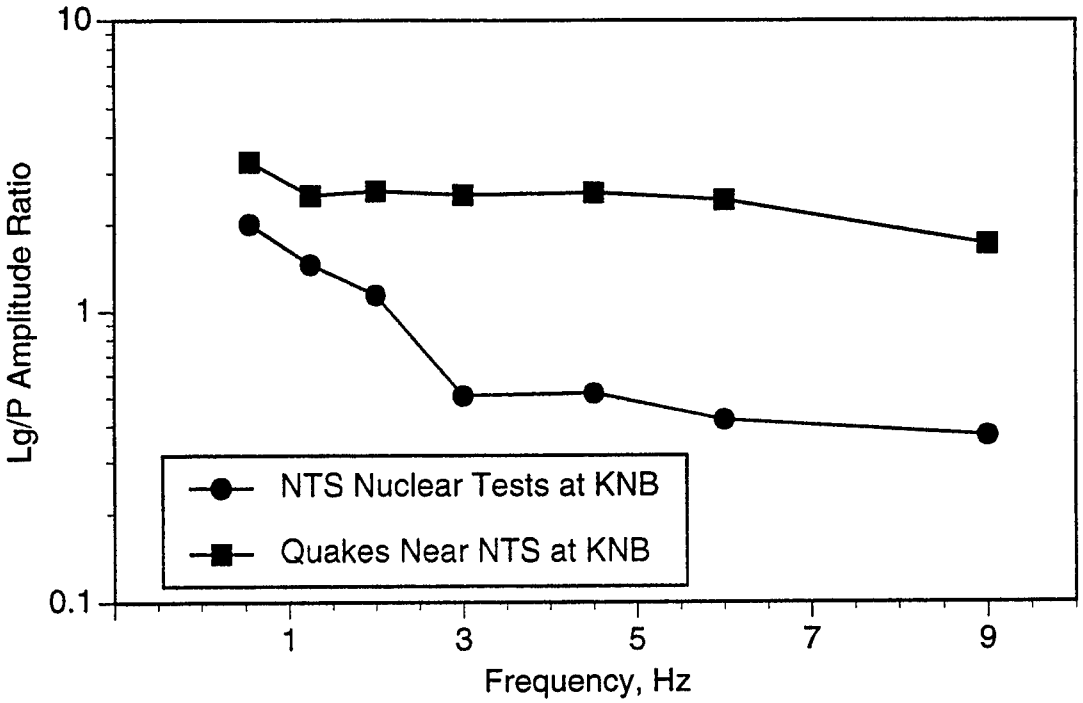

Figure 2. Comparison of average Lg/P amplitude ratios as a function of frequency at station KNB for NTS nuclear tests and nearby earthquakes.

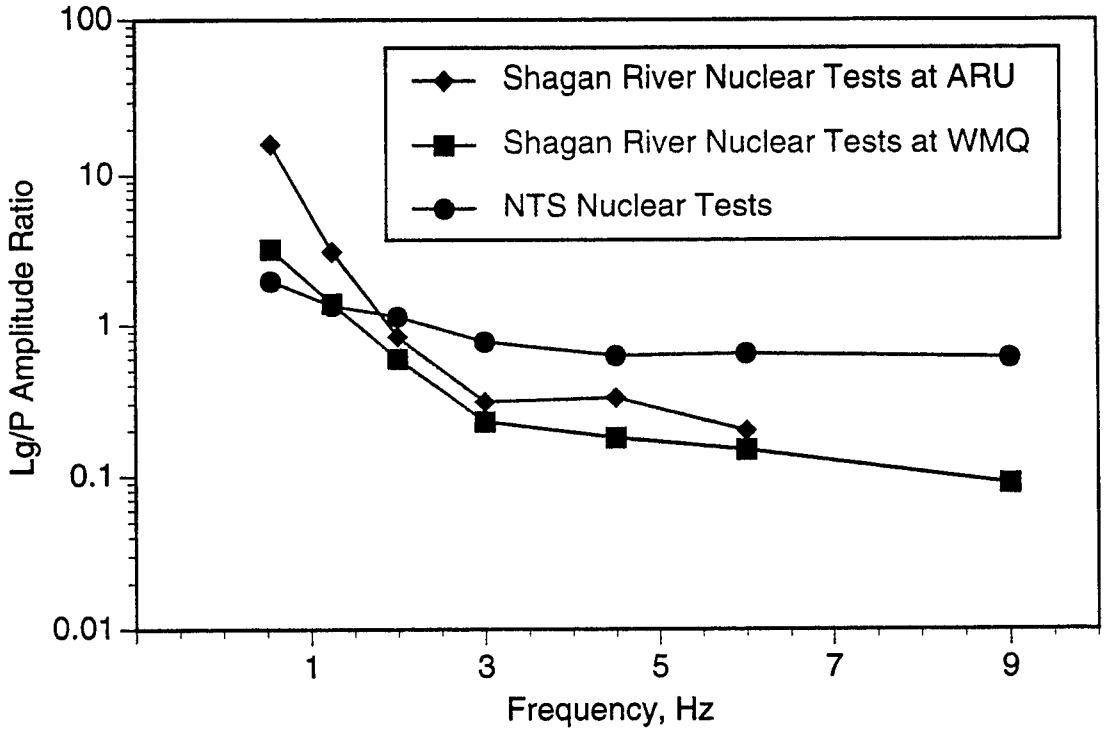

Figure 3. Comparison of average Lg/P ratios as a function of frequency for nuclear explosions at NTS and Shagan River.

earthquake ratios remain fairly high (well above one) across the entire frequency band while the ratios for the nuclear explosions tend to drop off more rapidly and remain low at high frequencies. This general behavior is consistent with our past experience for the L_g/P ratios in this and other regions (cf. Bennett et al., 1992).

Figure 3 shows L_g/P ratios as a function of frequency for nuclear explosion tests at NTS and the former Soviet test site at Shagan River. For NTS in this case we have plotted the average L_g/P ratios, determined as described above, for the ten NTS nuclear explosion tests averaged over all four LLNL stations. The plots for the CDSN station WMQ and for the IRIS station ARU are averages for ten Shagan River nuclear explosions recorded at somewhat larger regional distances. The spectral dependence of L_g/P for the average NTS observations is similar to that described above in Figure 2 for the single station KNB; in general the average L_g/P ratio for the NTS nuclear explosions falls below one at frequencies above about 2 Hz. The L_g/P ratios for the Shagan River nuclear tests tend to start off at higher values at low frequencies but fall off more rapidly at high frequencies and appear to be fairly consistent between the two stations. One cause for the more rapid decrease in the L_g/P ratio could be propagation differences and the larger distance of the Shagan River observations.

We show in Figure 4 some comparisons of two alternative procedures for estimating spectral dependence of the L_g/P ratios. The comparisons are for the NTS nuclear test GORBEA and the nearby 05/12/82 earthquake The solid symbols correspond to the traditional bandpass filter analyses described above; the corresponding filters are fairly broad and have considerable overlap. We have also applied a second filtering scheme using narrow Gaussian filters which are evenly spaced over the frequency range and overlap only slightly. This latter scheme is believed to provide spectral estimates more like those obtained from Fourier analysis, and we are continuing to test its applicability. The L_g/P ratios for the narrow Gaussian filters seem to be more variable with frequency but still show differences between the explosion and the earthquake consistent with out past experience. We see in the L_g/P ratio plots that the traditional broad filters tend to provide a smoother dependence which could be associated with spectral leaking due to the relatively large filter overlap. We are continuing to test these filtering schemes in an effort to find more robust and reliable L_g/P ratio measures.

Theoretical Studies

The early model studies conducted in conjunction with this project have involved a variety of preliminary tests with simple sources and non-specific structures. As information on velocity structure and attenuation appropriate to specific regions of interest is being collected, we are beginning to incorporate that into the models. Initially we have considered the non-specific Gutenberg earth model and more site-specific models representative of NTS and the former Soviet test site in East Kazakhstan. Using these models we have conducted some preliminary analyses of the influence of scattering on L_g signals. It is well known that mechanisms for trapping explosion compressional-wave energy as L_g in the crustal waveguide are generally inefficient. To explain the relatively consistent observation of L_g signals from pure explosion sources, it has been suggested by Patton and Taylor (1995) and others (e.g. Jih and McLaughlin, 1988; Gupta et al., 1991; Xie and Lay, 1994) that scattering of short-period Rayleigh waves may be a significant source of L_g from shallow explosions. This mechanism is looked upon as a likely source because short-period Rayleigh waves have been found to correlate with explosion yield, and it might be inferred that such a scattering mechanism would produce L_g also correlated with yield, as indicated by observations from explosions in many regions.

We have made some theoretical estimates of the maximum L_g that could occur from this scattering mechanism assuming that (1) all of the R_g scatters into P-SV L_g, and (2) seismic energy is conserved. This analysis leads to an upper bound on the L_g amplitude that can be produced by the R_g to L_g scattering mechanism. The analysis is performed using energy integrals for the R_g and L_g modes. Figure 5 shows the values of the energy integrals, calculated at a frequency of 1 Hz, for the first ten modes in three earth structures: (1) a Gutenberg earth model, (2) a model for

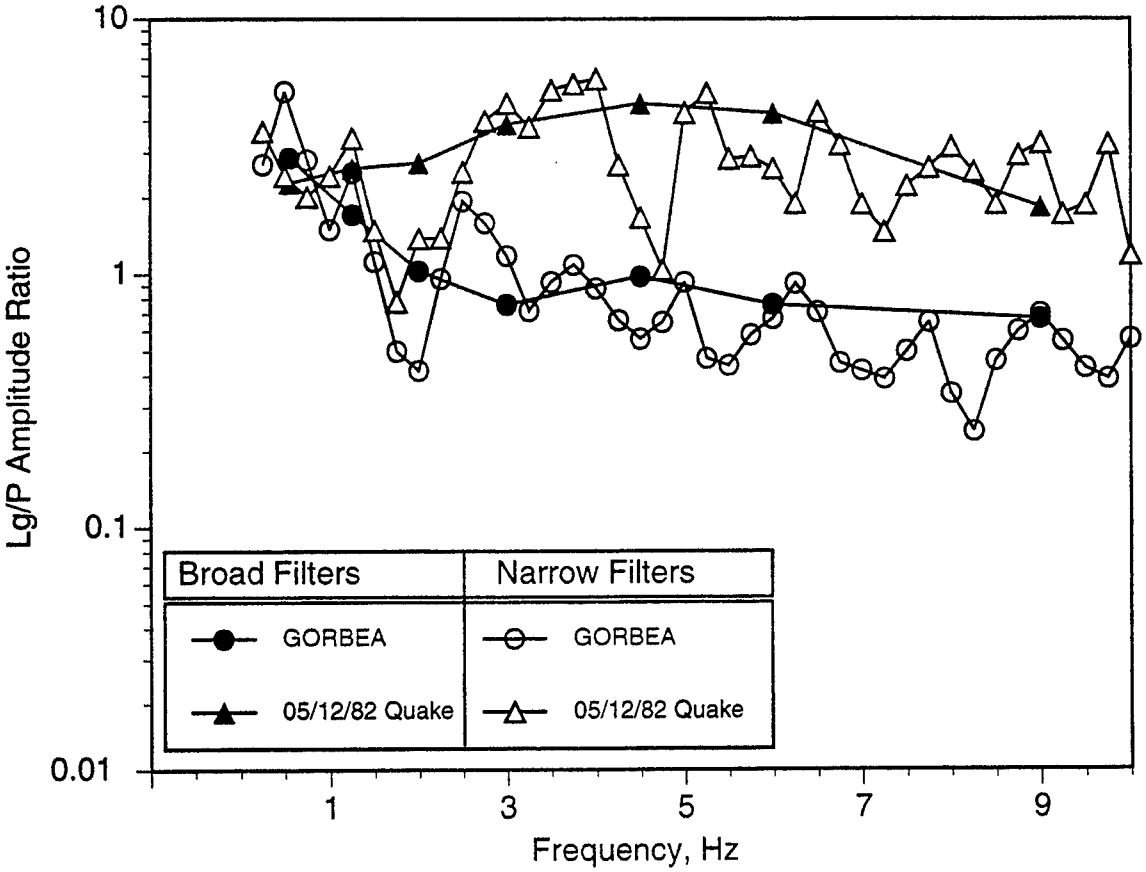

Figure 4. Comparison of Lg/P spectral estimates at station KNB for broad traditional bandpass filters and narrow Gaussian filters for nuclear test Gorbea and 05/12/82 earthquake.

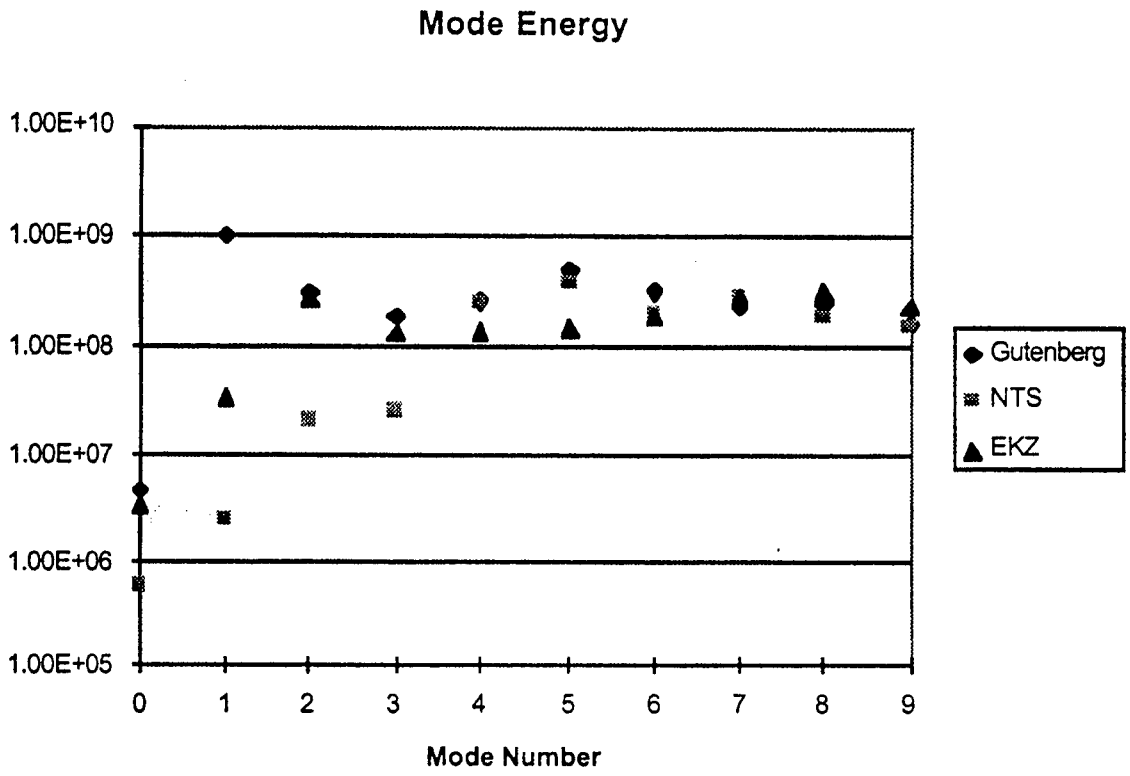

Figure 5. Energy in each mode for three different earth models.

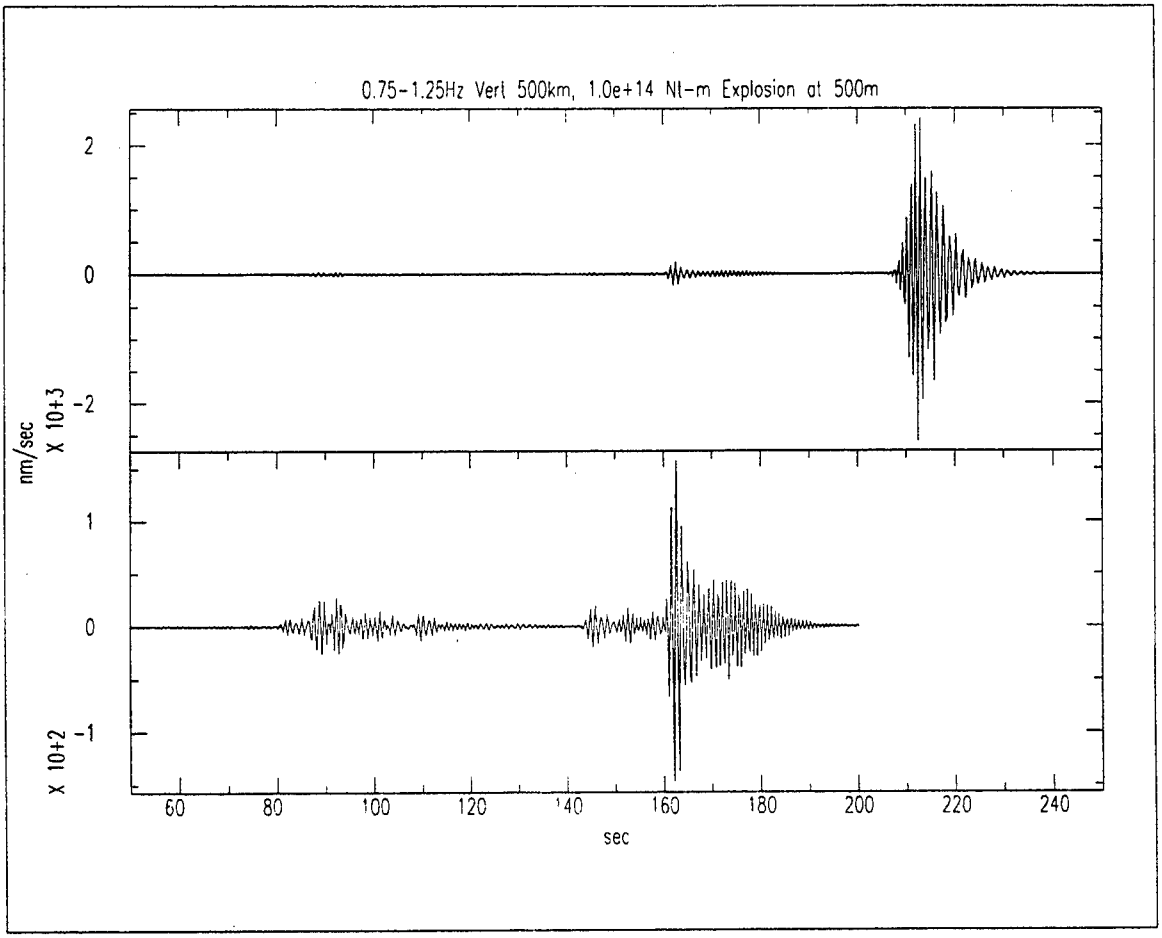

Figure 6. Vertical component synthetic seismogram (0.75 - 1.25 Hz) at a distance of 500 km from a point explosion source at a depth of 500 m in the EKZ model. The upper panel shows the complete synthetic seismogram. The lower panel shows the P and Lg waveforms at a higher magnification.

NTS, and (3) a model for the former Soviet test site in East Kazakhstan. It should be noted that, for mode numbers greater than three, the energy integrals are nearly constant for each model. The energy in these modes is distributed throughout the crust. For an energy equipartition model (assuming energy is equally partitioned among all higher modes), the computed scattering ratios are fairly consistent at about 15 % between the different earth models. Scattering ratios vary from about 6 % to 50 % for other scattering models (assuming the same amplitude for all modes or alternatively assuming that all R_g energy transfers to the L_g mode with the minimum energy. The equipartition model is attractive in that it predicts that the L_g amplitudes will be approximately the same fraction of the Rg amplitude for all three models.

As an example of the use of these bounds on P-SV L_g from R_g scattering we estimated the spectral amplitude ratios of L_g/P for the three models at a distance of 500 km at 1 Hz. Figure 6 shows a synthetic vertical-component velocity seismogram bandpassed between 0.75 and 1.25 Hz for an explosion point source at a depth of 500 meters. From this seismogram the spectral amplitudes of P, L_g, and R_g were measured and tabulated. For the East Kazakh model we get a ratio of about eight at 1 Hz. For comparison the L_g/P ratios for the point source explosion is three. If 100 % of the explosion R_g is converted to P-SV L_g, the L_g spectral amplitude would nearly double. The results for the three models assuming equipartition of modal energy indicate that L_g generated by R_g to L_g scattering would range from 120 % to 640 % of the direct L_g. We are continuing to investigate this behavior for other source types and models.

Conclusions and Recommendations

Under the empirical element of this research, we have collected a large representative database of regional seismic signals from nuclear tests, earthquakes, non-nuclear blasts, and rockbursts in a variety of propagation environments. We have reviewed the behavior of the L_g/P observations and their dependence on frequency from many of these events and have found that they tend to be consistent with the experience that L_g/P ratios are larger for earthquakes and rockbursts than for nuclear explosions. The differences tend to be larger at higher frequencies. We are continuing to investigate procedures to improve estimates of the spectra of regional phase signals for use in defining more robust measures of L_g/P ratios for use in discrimination.

In our theoretical studies we have investigated upper bounds on the mechanism of R_g to L_g conversion using simple modal energy integrals assuming only (1) all R_g energy is converted to P-SV higher modes and (2) all seismic energy is conserved. These upper bounds may be lowered if we consider the additional conversion of R_g and P-SV modes to SH modes or P and S energy that leaks out of the crustal waveguide, or intrinsic attenuation of R_g. Three earth structures considered thus far all predict approximately the same relative amplitude between the near-field R_g and the far-field L_g.

References

Bennett, T. J., A. K. Campanella, J. F. Scheimer, and J. R. Murphy (1992). "Demonstration of Regional Discrimination of Eurasian Seismic Events Using Observations at Soviet IRIS and CDSN Stations," PL-TR-92-2090, ADA253275

Bennett, T. J., B. W. Barker, M. E. Marshall, and J. R. Murphy (1995). "Detection and I dentification of Small Regional Seismic Events," PL-TR-95-2125, ADA305536

Blandford, R. R. (1981). "Seismic Discrimination Problems at Regional Distances," in *Identification of Seismic Sources - Earthquake or Underground Explosion*, D. Reidel Publishing Co.

Gupta, I. N., T. W. McElfresh, and R. W. Wagner (1991). "Near-Source Scattering of Rayleigh to P in Teleseismic Arrivals from Pahute Mesa NTS Shots," in *Explosion Source Phenomenology*, AGU Monograph 65, pp. 151 - 159.

Jih, R.-S., and K. L. McLaughlin (1988). "Investigation of Explosion Generated SV Lg Waves in 2-D Heterogeneous Crustal Models by Finite Difference Method," AFGL-TR-88-0025.

Patton, H. J., and S. R. Taylor (1995). "Analysis of Lg Spectral Ratios from NTS Explosions: Implications for the Source Mechanisms of Spall and the Generation of Lg Waves," *Bull. Seism. Soc. Am.*, 85, pp. 220 -236.

Xie, X.-B., T. Lay (1994). "The Excitation of Lg Waves by Explosions: A Finite-Difference Investigation," *Bull. Seism. Soc. Am.*, 84, pp. 324 - 342.

Transportability of Regional Phase Spectral Ratio Discriminants

T. J. Bennett, M. E. Marshall, B. W. Barker, and J. R. Murphy
Maxwell Laboratories, Inc., S-CUBED Division
11800 Sunrise Valley Dr., Suite 1212
Reston, Virginia 22091
Contract No. F 19628-95-C-0108
Sponsored by AFTAC

Abstract

This research program is intended to provide a thorough assessment of the transportability of regional phase spectral ratios as discriminants between underground nuclear explosions and other source types. Although L_g spectral ratios appeared to offer considerable promise for distinguishing between nuclear explosions and nearby earthquakes based on experience from the vicinity of the Nevada Test Site, attempts to extend this spectral ratio discriminant into other geographic regions (e.g. the vicinity of the Semipalatinsk/Shagan River test site) have not always proven to be successful. One of the main obstacles to demonstrating the value of regional phase spectral ratios as discriminants has been difficulty in finding events of different source types with similar magnitudes and like propagation paths to enable direct comparisons of spectral ratio measurements. In addition, attempts to provide theoretical bases for understanding differences in regional phase signals from different source types have proven to be of only limited success. Improving understanding of the influences of source and propagation effects on potential regional phase discriminants will be critical to implementing such procedures in uncalibrated areas under a Comprehensive Test Ban Treaty (CTBT).

Under this research program we have been collecting the database of high-quality digital data from underground nuclear explosions and earthquakes for sources in the western U.S. and Eurasia. We have separated the database into nearer regional signals (ranges less than about 800 km) and farther regional signals. Nearer regional signals provided the principal basis for the original proposed spectral ratio discriminants, and our initial analyses have focused on reassessment of some of these observations and investigation of alternate schemes for quantifying spectral differences. Our analyses confirm earlier findings that L_g and P_g signals from earthquakes appear to be enriched in high frequencies relative to nearby nuclear explosion tests. However, we find that regional phase spectral differences seem to be reduced when theoretical scaling techniques are used to make the explosion and earthquake samples more similar in magnitude. We also see some differences in spectral separation for alternative measurement schemes and plan to seek more robust spectral measurement methods. In addition, we have been looking at results of regional phase attenuation studies for various regions to help identify appropriate procedures to correct spectral ratio measurements for propagation effects.

Key Words: Seismic, Discrimination, Regional, Calibration, Explosion, Earthquake.

Objective

Since the status of regional seismic discrimination was reviewed by Blandford (1981) and Pomeroy et al. (1982), considerable progress has been made in understanding the effects of seismic source mechanisms on regional phase excitation and the influences of geologic structure on regional phase propagation. However, many problems remain with regard to determining how potential regional discriminants will perform in uncalibrated regions, as would be required in the context of a CTBT. This research project is focused on a particular class of regional discriminants, viz. those associated with frequency differences in the signals from different source types. In particular, regional phase spectral ratios involve exploitation and parameterization of differences in the relative spectral shape, or frequency content, of regional phase signals from different source types. The principal objectives of this research program are to develop more complete understanding of the influences of source excitation and propagation on the transportability of regional phase spectral ratio discriminants and to define criteria for application of spectral ratio discrimination methods in uncalibrated areas. We anticipate that, by applying appropriate corrections for source and propagation effects, we will be able to more reliably discern source-dependent differences in the regional phase spectral ratios which should be transportable into different, uncalibrated monitoring environments.

Research Accomplished

Our investigation of the transportability of regional phase spectral ratio discriminants encompasses a broad range of issues including availability of data, parameterization of spectral differences between source types, and analysis of source size and propagation effects on observed spectral differences. With regard to data availability, the original development of regional phase spectral ratios as discriminants (cf. Ryall, 1970; Murphy and Bennett, 1982; Bennett and Murphy, 1986; Taylor et al., 1988, 1989) was based primarily on analysis of near-regional (ranges less than about 800 km) signals from NTS nuclear explosions and earthquakes in the western U.S. These data still provide the best controlled sample for comparing regional phase signals from nuclear explosions and nearby earthquakes, and we decided to focus our initial studies on additional careful analyses of some of these data. At greater regional distances (ranges greater than 800 km) waveform data have also been collected from nuclear explosions in several different source areas including former Soviet test sites in East Kazakhstan and Novaya Zemlya, the Chinese test site at Lop Nor, and PNE sites throughout the former Soviet Union, as well as more distant recordings of NTS nuclear explosions. For use in developing empirical comparisons with these latter events, regional waveforms have also been collected for earthquakes in the surrounding regions at comparable epicentral distances and, in many cases, at the same recording stations. In all cases the available database includes high-quality digital data with good signal-to-noise levels. Because of the history and nature of nuclear explosion testing, the relevant digital database is extremely limited; and it seems unlikely that nuclear testing, if any, in the future will provide much to assist with calibration of regional discrimination capabilities for many source regions of interest under a CTBT. We must rely, then, on the available data to aid in inferring the behavior of regional phase spectral ratios as discriminants in these uncalibrated areas. To assist with this inference process, we are seeking to identify more robust measures of regional phase spectral ratios and to determine their dependence on source size and propagation conditions.

In our initial analyses we have focused on five NTS nuclear explosions and five nearby earthquakes recorded by the four LLNL stations surrounding NTS. Epicentral distances for the nuclear tests were between 230 km and 410 km, and distances for the earthquakes were between 180 km and 490 km. Magnitudes for the explosions were between 4.1 m_b and 5.7 m_b (4.2 M_L to 5.5 M_L), and magnitudes for the earthquakes were between 3.5 M_L and 4.2 M_L (most earthquakes had no reported m_b's). Figure 1 shows one of our traditional bandpass filter analyses applied to the nuclear test GORBEA recorded at station KNB (R = 294 km). The filters in this case are fairly broad and have considerable overlap (cf. Bennett et al., 1995). The records

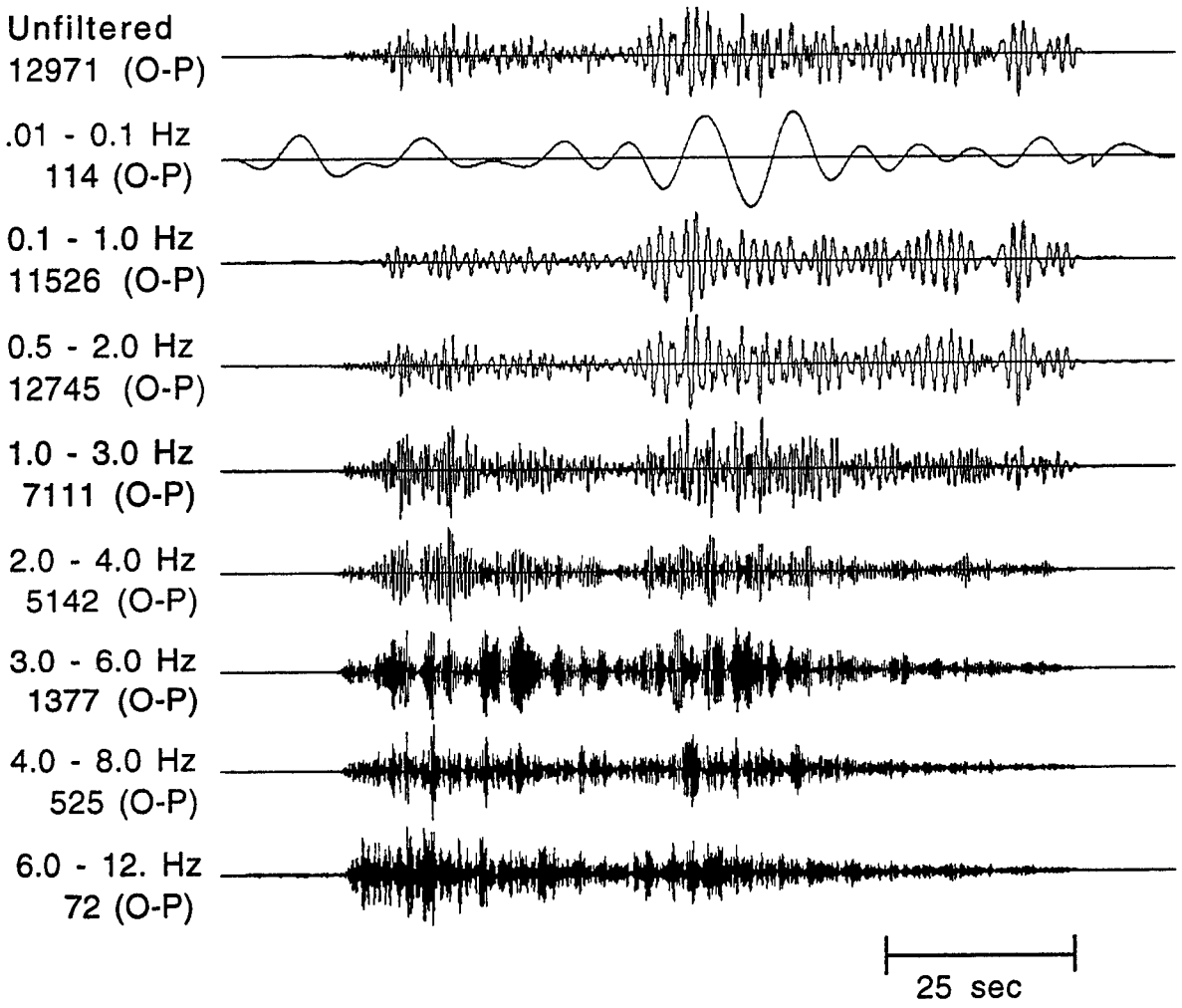

Figure 1. Traditional bandpass filter analysis of NTS explosion GORBEA recorded at station KNB.

show a rather clear but emergent P_n phase followed a few seconds later by a stronger P_g phase. Much later is a stronger L_g phase characterized by a somewhat longer-period signal. At a slightly later time, a long-period Rayleigh wave signal is also apparent for the lowest frequency passband. These features are typical of the bandpass filter output for both NTS explosions and nearby earthquakes recorded at the LLNL stations, and the signal-to-noise levels shown are fairly representative.

In these analyses we have used the bandpass filter output to obtain estimates of the relative spectral content of the regional phase signals. Maximum amplitudes in the appropriate group velocity windows were measured and used as estimates of the spectral amplitude for each frequency band. Figure 2 shows the L_g spectral amplitudes, normalized to the value at 0.55 Hz (center frequency), for the five nuclear tests and five earthquakes recorded at station KNB. The data show some scatter but generally agree with past observations that the earthquake L_g signals appear to be enriched in high frequencies relative to low frequencies compared to the nuclear tests. Figure 3 shows the average L_g spectra at KNB for the two different source types. The average L_g spectral levels are completely separated between the unscaled NTS nuclear tests and the nearby earthquakes, at the $\pm$ 1 σ level, for all frequencies above the normalization frequency. As noted, this result is not surprising and simply confirms that the bandpass filter spectral estimates are in agreement with our prior findings, which had been based on Fourier analysis of the L_g group velocity window.

To further test this potential discriminant measure, we have made some preliminary analyses of the influences of source size, recording station, alternative phase type, and alternative measures of spectral content. The NTS explosions used in Figure 2 are somewhat larger in magnitude than the earthquakes used for comparison; the average M_L difference is 1.25 magnitude units. To test the effects of source size on the spectra, we used Mueller-Murphy source scaling (cf. Mueller and Murphy, 1971) to scale the explosion records down to the average magnitude level of the earthquakes. As we have shown in prior reports (cf. Bennett et al., 1995; Murphy et al., 1996), the effect of this down scaling is to enhance high frequencies relative to low; and, thus, this operation would be expected to reduce the separation seen in Figure 3 between the unscaled explosions and the earthquakes. After scaling the records we performed the same bandpass filter analyses and re-estimated the relative L_g spectra. The scaling reduces the separation between the average spectra for the two source types, as can be seen in Figure 3; but the data remain separated at the $\pm$ 1 σ level at all frequencies above the normalization frequency.

The results obtained for an additional recording station are less satisfactory. Figure 4 shows average L_g spectra determined in the same way for the same five nuclear tests and a slightly different sample of earthquakes at LLNL station MNV. We again find that the L_g signals for the earthquakes on average appear to be relatively richer in high frequencies than for the unscaled nuclear tests. However, the separation is not as great and there is more scatter; so that there is overlap between the two source types at the $\pm$ 1 σ level. Furthermore, when we apply the scaling procedures to the nuclear tests at MNV and recompute the L_g spectral estimates, the values for the scaled NTS nuclear tests and nearby earthquakes nearly coincide. The decreased capability of the discriminant at this station will be investigated further. For the earthquakes the observed reduction in relative spectral levels at MNV versus KNB could be explained as a combination of radiation patterns and propagation effects, while the increase in relative spectral levels for the explosions seems more likely to be a propagation effect.

We also computed P_g spectral estimates at station KNB for the same event sample. The average P_g spectra developed from the bandpass filter analysis are shown in Figure 5. The average earthquake P_g spectrum appears to be relatively richer in high frequencies than for the NTS nuclear explosions. There is fairly large scatter in the measurements, and we find separation at the $\pm$ 1 σ level between the two source types only at the two highest frequencies, viz. 6 Hz and 9 Hz. The separation between the average P_g spectra is greatly reduced for the

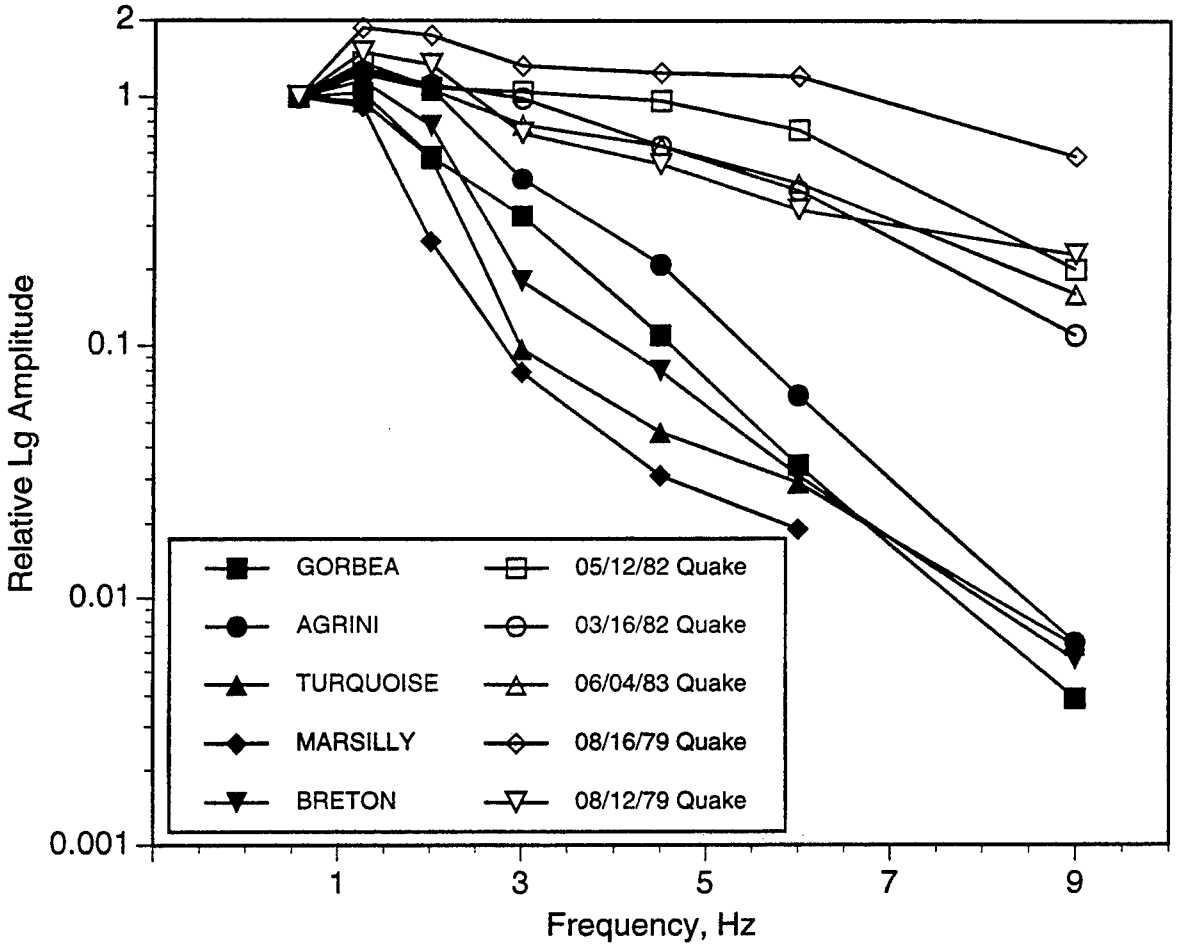

Figure 2. Relative Lg spectral estimates obtained for NTS nuclear tests and nearby earthquakes from traditional bandpass filter analyses of records at station KNB.

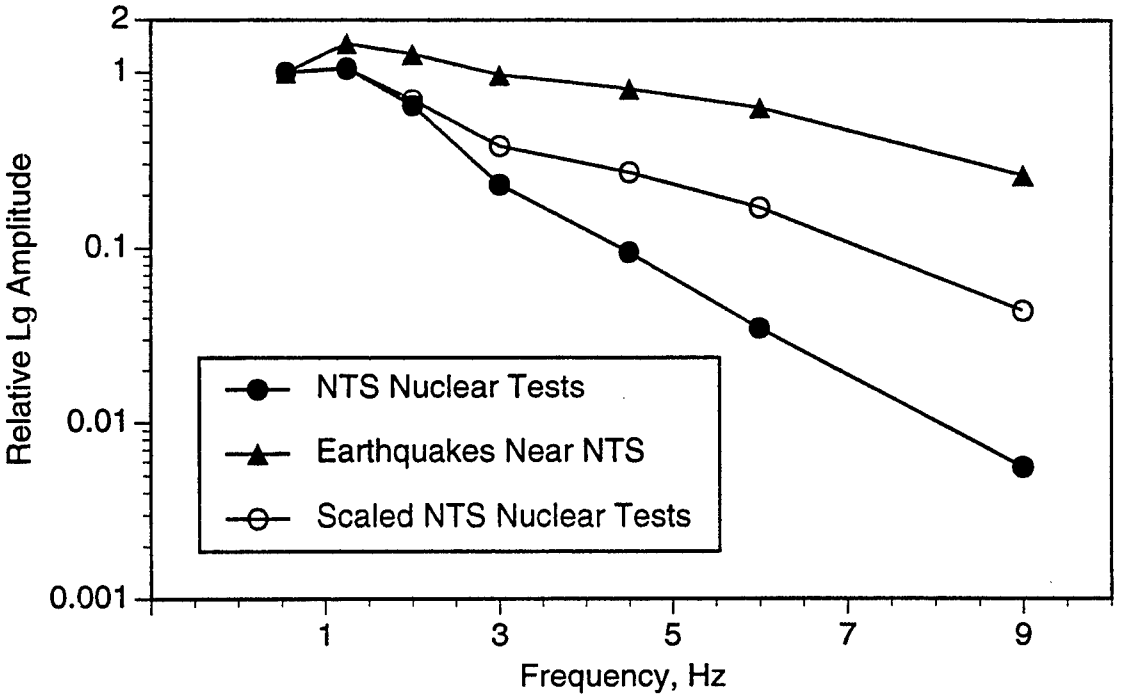

Figure 3. Comparison of average Lg spectral estimates at station KNB for 5 NTS nuclear tests, 5 nearby earthquakes, and 5 scaled NTS nuclear tests.

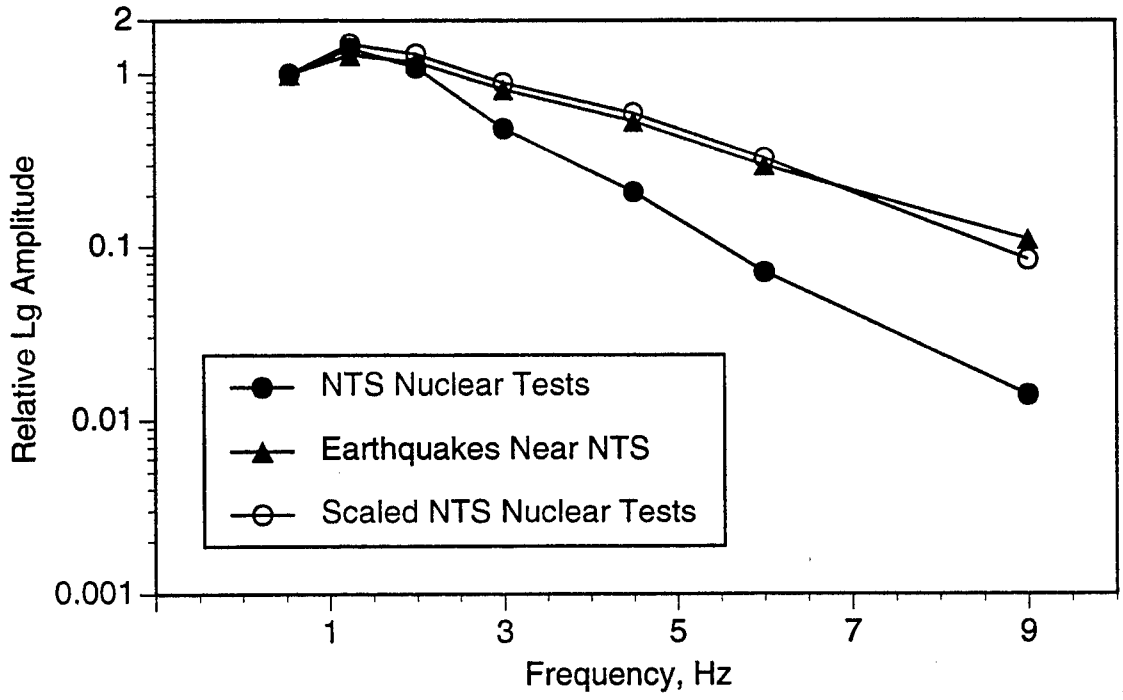

Figure 4. Comparison of average Lg spectral estimates at station MNV for 5 NTS nuclear tests, 5 nearby earthquakes, and 5 scaled NTS nuclear tests.

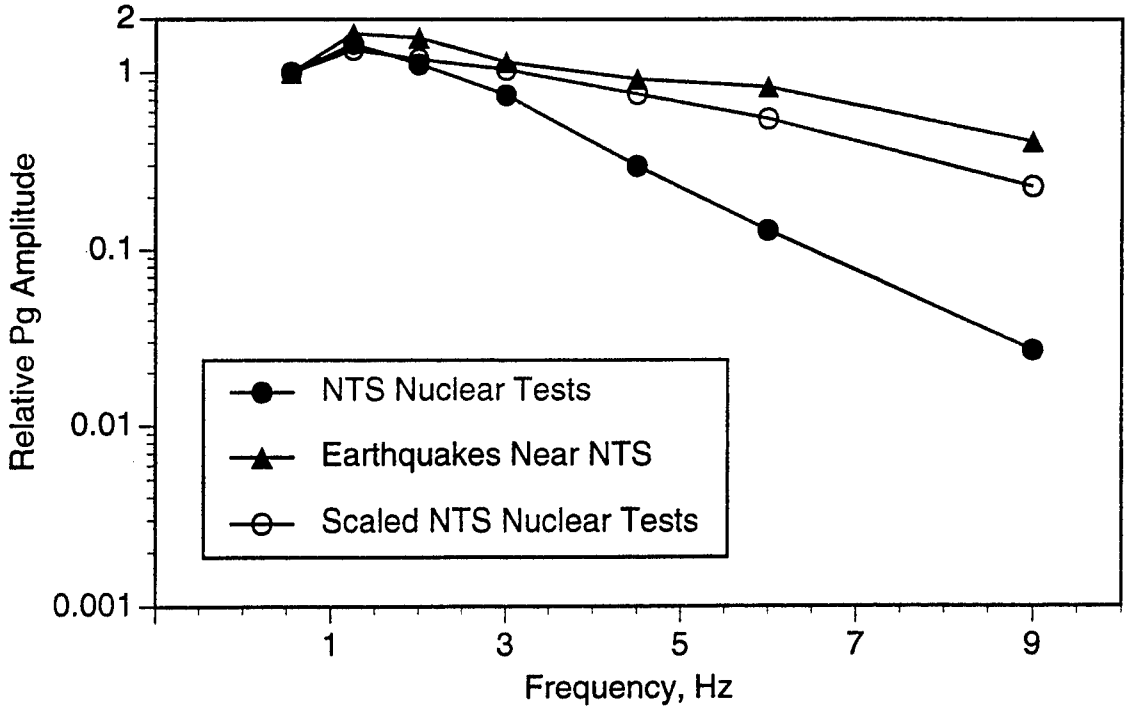

Figure 5. Comparison of average Pg spectral estimates at station KNB for 5 NTS nuclear tests, 5 nearby earthquakes, and 5 scaled NTS nuclear tests.

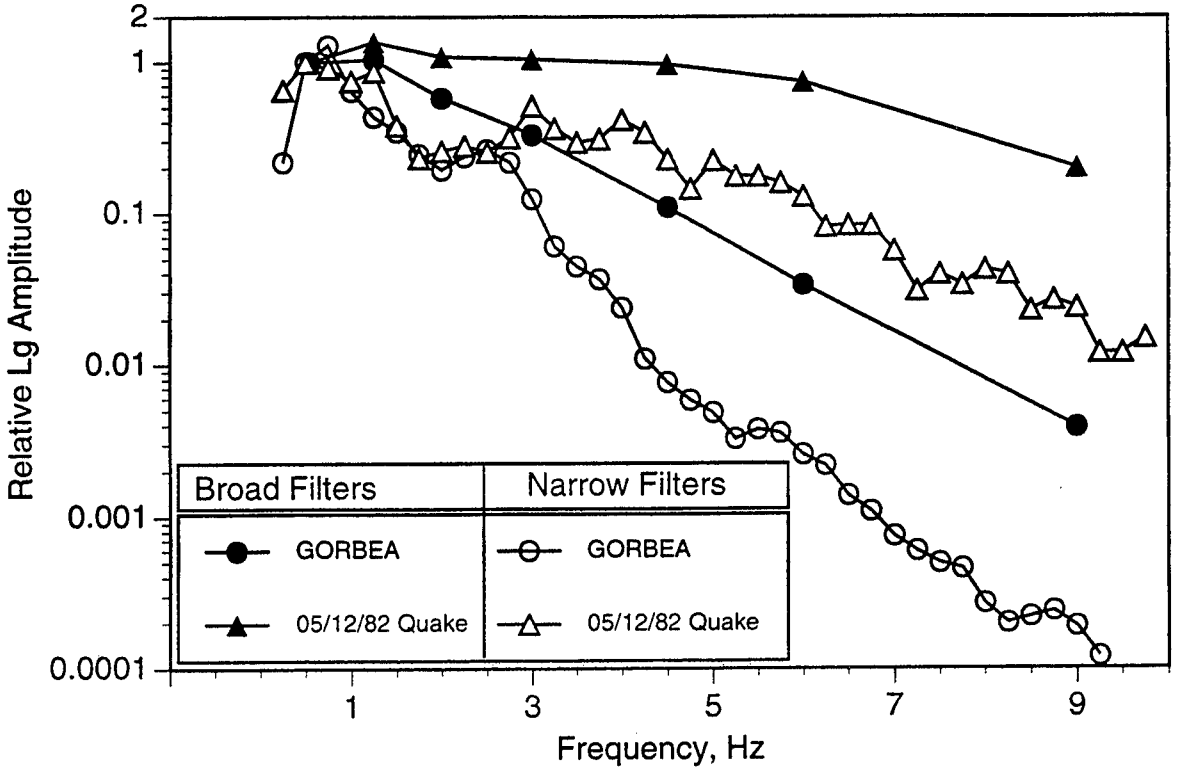

Figure 6. Comparison of Lg spectral estimates at station KNB for broad traditional bandpass filters and narrow Gaussian filters for nuclear test Gorbea and 05/12/82 earthquake.

nuclear explosions scaled down to the average earthquake magnitude, and we find no significant differences. It seems clear from these results and those above that scaling effects could be important when comparing regional phase spectral ratios for events of different magnitudes.

Finally, as part of this research project, we have been exploring some alternative measures of the regional phase spectral ratios in an effort to identify more robust and/or simpler measurement schemes. As part of this effort, we have utilized a different set of bandpass filters for which the filters are narrow Gaussian filters with slight overlap and center frequencies evenly spaced between 0.25 Hz and 10 Hz. The spectral estimates are again obtained for the regional phases from a measure of the amplitudes of the filter outputs in the appropriate group velocity windows. In addition to simple maximum amplitude measures of the output, we have been evaluating RMS measure of signal strength. Figure 6 shows a comparison of the L_g spectral estimates for a sample NTS nuclear test (viz. GORBEA) and a nearby earthquake (viz. 05/12/82 Quake) measured at station KNB for the traditional bandpass filter scheme, as in Figure 1 above, and for an RMS measurement from the narrow Gaussian filter output. Over the band from 0.5 Hz to about 2.5 Hz, the Gaussian filter output shows little difference in L_g spectra between the NTS explosions and the earthquakes; while the older scheme did show some differences in this band. Above 2.5 Hz both methods show substantial differences in the L_g spectral levels between the two source types with somewhat greater separation for the Gaussian filters versus the broader bandpass filters. Additional testing of these and other filter and measurement schemes will be applied to larger samples of data and a variety of regional phases to identify procedures which produce the largest and most consistent separation between different source types. These results will be used to develop and recommend appropriate regional phase spectral ratio discriminants for future application.

As this work continues we will be extending our investigations to regional phase measurements at greater distances, including observations from the Eurasian explosion and earthquake sample. At these larger distances propagation effects are expected to have greater influences on regional phase spectral measurements, particularly for regions where earthquake and explosion sources are not co-located. For these observations corrections to the regional phase spectral ratios should be made to account for attenuation differences. To help determine appropriate attenuation corrections, we have been reviewing published reports on regional phase propagation conditions for various regions of interest. We plan to compare these published results with behavior of regional phase spectra from our database to establish an empirical attenuation model which can be used to evaluate appropriate adjustments to the regional phase spectral ratios.

Conclusions and Recommendations

Our initial results from analyses of nearer regional signals for nuclear explosions and nearby earthquakes confirms previous findings that L_g and P_g regional phases appear to be enriched in high frequencies for earthquakes compared to NTS nuclear explosions. However, when the explosion signals are scaled down to be more nearly equal in magnitude to the earthquakes, we see a reduction in the spectral separation for the two source types. Additional work is needed to determine the more general significance of such scaling on observed regional phase spectral ratio differences. We have conducted some preliminary work to identify more robust and simpler schemes for quantifying spectral ratios and have found some differences in the results between alternative procedures. Additional studies will be useful to identify optimal measurement techniques for regional phase spectral ratios. We have collected information on the influences of propagation on regional phase spectra for various regions of interest, and we will be using that information to help establish an appropriate attenuation model for application to the available database.

References

Bennett, T. J., and J. R. Murphy (1986). "Analysis of Seismic Discrimination Capabilities Using Regional Data from Western United States Events," *Bull. Seism. Soc. Am.*, 76, pp. 1069 - 1086.

Bennett, T. J., B. W. Barker, M. E. Marshall, and J. R. Murphy (1995). "Detection and Identification of Small Regional Seismic Events," PL-TR-95-2125, ADA305536

Blandford, R. R. (1981). "Seismic Discrimination Problems at Regional Distances," in *Identification of Seismic Sources - Earthquake or Underground Explosion*, D. Reidel Publishing Co.

Murphy, J. R., and T. J. Bennett (1982). "A Discrimination Analysis of Short-Period Regional Seismic Data Recorded at Tonto Forest Observatory," *Bull. Seism. Soc. Am.*, 72, pp. 1351 - 1366.

Pomeroy, P. W., W. J. Best, and T. V. McEvilly (1982). "Test Ban Treaty Verification with Regional Data - A Review," *Bull. Seism. Soc. Am.*, 72, pp. S89 - S129.

Ryall, A. (1970). "Seismic Identification at Short Distances," in *Copies of Papers Presented at Wood's Hole Conference on Seismic Discrimination*, 2, DARPA, Arlington, VA.

Taylor, S. R., N. W. Sherman, and M. D. Denny (1988). "Spectral Discrimination Between NTS Explosions and Western United States Earthquakes at Regional Distances," *Bull. Seism. Soc. Am.*, 78, pp. 1563 - 1579.

Taylor, S. R., M. D. Denny, E. S. Vergino, and R. E. Glaser (1989). "Regional Discrimination Between NTS Explosions and Western U. S. Earthquakes," *Bull. Seism. Soc. Am.*, 78, pp. 1142 -1176.

Regional Seismic Discrimination in Central Asia With Emphasis on Western China

Hans E. Hartse, Steven R. Taylor, W. Scott Phillips, and George E. Randall
Geophysics Group - EES-3, Los Alamos National Lab

Sponsored by U.S. Department of Energy, Contract W-7405-ENG-36
Comprehensive Test Ban Treaty Research and Development Program, ST482A

ABSTRACT

In support of an anticipated Comprehensive Test Ban Treaty, we have started to evaluate regional seismic event discrimination capabilities for central Asia, emphasizing western China. We have measured noise and seismic phase amplitudes of over 250 earthquakes and 18 underground nuclear explosions recorded at the broadband, digital station WMQ in western China and over 100 earthquakes and 5 nuclear explosions at station AAK in Kyrgyzstan. The explosions are from the Kazakh Test Site (KTS) and Lop Nor, China. The earthquakes are mostly from northwest China. Event magnitudes (m_b) range between 2.5 and 6.5 and maximum event-station distance is about 1700 km. Using these measurements we formed phase, spectral, cross-spectral, short-period/long-period, and long-period ratios to test many possible event discriminants. All ratios were corrected for distance effects before forming ratio-versus-magnitude discrimination plots.

The most consistent discriminants for separating earthquakes from explosions are a high-frequency ($f > 4\,Hz$) P/S ratio versus m_b and a short-period P ($f > 1\,Hz$) - to - long-period Rayleigh-wave ($0.05\,Hz < f < 0.1\,Hz$) ratio versus m_b. For the short-period P/S ratio, separation between earthquakes and explosions increases as frequency increases. P_n, P_g, and S_n spectral ratios ($3–6\,Hz$ / $0.75–1.5\,Hz$) and P ($3–6\,Hz$) / S ($0.75–1.5\,Hz$) cross-spectral ratios also separate most earthquakes from the explosions. In contrast to the western United States, the L_g spectral ratio does not separate earthquakes and nuclear explosions in central Asia. We believe this observation is related to the source effects of hard-rock geology and a near-surface water table for the Asian test sites. P spectral ratios may prove to be useful discriminants in cases where path effects block L_g propagation, making the P_g/L_g ratio unavailable. The cross-spectral ratios, involving high-frequency P and low-frequency L_g, may also prove useful as smaller explosions recorded at greater distances can be evaluated compared to the high-frequency P/L_g ratio. The KTS explosions separate from earthquakes when an R/L (Rayleigh-wave/Love-wave) ratio is formed. The large Lop Nor explosions do not separate from the earthquakes when the R/L ratio is formed, possibly indicating strong tectonic release is associated with explosions at the Lop Nor test site. However, because we have examined only one path at a single station for these explosions, source-radiation pattern may be influencing this observation. For station AAK, the short-period spectral and cross-spectral ratios identify a few earthquakes (not recorded at WMQ) from the north Pamir region that plot with the Lop Nor explosions. The waveforms from these earthquakes lack surface waves and a distinct L_g phase. These events, which we interpret as having mantle source depths, do separate from the explosions on high-frequency P/S discrimination plots.

Key Words: seismic discrimination, China

OBJECTIVE

As part of the Comprehensive Test Ban Treaty (CTBT) research and development program, we have been evaluating regional seismic discriminants for central Asia, emphasizing western China. We have obtained waveforms recorded with the Chinese Digital Seismic Network (CDSN) station WMQ and the Kyrgyz Network (KNET) station AAK (Figure 1). Besides recording local and regional earthquakes, WMQ recorded several nuclear explosions in 1988 and 1989 from the former Soviet Union test site in Kazakhstan (KTS). AAK was installed in 1990, after testing ended at KTS, but the station has recorded regional seismicity and underground nuclear explosions from the Chinese test site at Lop Nor since 1991.

Our primary goal has been to evaluate many combinations of phases, frequency bands, and types of measurements for their potential as seismic discriminants. Hence, using seismograms from WMQ and AAK, we measured RMS, peak-to-peak, and peak-envelope amplitudes for the phases P_n, P_g, S_n, L_g, L (Love waves), and R (Rayleigh waves) over many frequency bands. We tested five general classes of seismic discriminants: (1) short-period phase ratios, such as P_g (3–6 Hz) / L_g (3–6 Hz) (both phases measured in the same frequency band); (2) short-period spectral ratios, such as L_g (0.75–1.5 Hz) / L_g (3–6 Hz); (3) short-period cross-spectral ratios, such as P_g (0.75–1.5 Hz) / L_g (3–6 Hz); (4) short-period to long-period ratios, such as P_g (0.75–1.5 Hz) / L (8–16 s); and (5) long-period Rayleigh-wave to Love-wave ratios, such as R (8–16 s) / L (8–16 s). We found that all five classes of these discriminants are useful for separating earthquakes from explosions in central Asia, provided the right combinations of frequency bands and phases are selected. For details that are not covered in this summary, see *Hartse et al.* (1996).

REASEARCH ACCOMPLISHED

Seismic Stations and Data

We obtained all seismograms from the IRIS Data Management Center (DMC). WMQ (Figure 1) was upgraded to a CDSN station in 1986, and digital data is available from 1988 to the present. Digital data from KNET station AAK is available from 1990 to the present. For both stations, we requested data recorded with three-component, broadband (BH) seismometers (20 sps). We requested waveforms at both stations by using the United States Geologic Survey PDE catalogs maintained at the IRIS DMC as a guide. These are global catalogs, and for central Asia they include only those events with $m_b \approx 4.0$ and greater. We requested all PDE events between latitudes 55°N and 38°N and longitudes 100°E and 75°E (Figure 1). To request records from smaller events (down to $m_b \approx 2.5$), we used local Chinese catalogs, available for the 1970's and 1980's (Gao and Richards, 1994). With these "PRC" catalogs we were limited to data requests for the years 1988 and 1989 as WMQ data is not available prior to 1988.

Nuclear explosions from Lop Nor have been recorded at station AAK (about 1200 km west of the test site) since 1992. However, due to station down time, both Lop Nor explosions from 1994 were not recorded with the broadband components. Seismograms of only one Lop Nor nuclear test recorded at WMQ are available at the IRIS DMC. However, 17 nuclear explosions from KTS (≈ 950 km northwest of WMQ) were recorded in 1988 and 1989. We processed a total of 256 suspected earthquakes and 18 nuclear explosions recorded at WMQ. Magnitudes (m_b) range between 2.5 and 6.1 for the earthquakes and between 4.5 and 6.1 for the explosions. The maximum event-station distance is 1205 km. For AAK, we processed 101 earthquakes and 5 nuclear explosions. Magnitudes range between 3.7 and 6.1 for the earthquakes and 5.0 and 6.5 for the explosions. The maximum event-station distance is 1704 km.

Event Processing

Event processing involved (1) converting SEED-format waveform data to SAC files, (2) picking body wave phases (when possible), (3) correcting records for instrument response

(final units are ground velocity in m/s), (4) bandpass filtering, (5) making RMS, peak-to-peak, and peak-envelope amplitude measurements, (6) correcting for distance (path) effects, and (7) plotting phase ratios versus event magnitude to test discriminants. Measurements were made on vertical component seismograms, except for L, for which we rotated the horizontal components to obtain transverse record. When clearly visible, we hand picked body wave phases (P_n, S_n, P_g, and L_g) from the three-component BH records. We estimated velocities for the body wave phases from traveltime - distance plots, and then defined "data window" velocities that surround the body wave velocities. For surface wave processing, we visually examined many Love-wave and Rayleigh-wave arrivals, and then selected velocities that defined measurement windows surrounding the peak-to-peak maximums of L and R. For each phase measurement we also made a pre-P_n noise measurement.

Figure 2 shows sample waveforms of the Lop Nor nuclear explosion recorded at WMQ (BHZ component) and a nearby earthquake. The unfiltered (*top*) traces show the first arrival (P_n), and the two lower seismograms show bandpass-filtered seismograms with P_g and L_g measurement windows marked. For each window, we measured ($\log_{10}$) RMS amplitude, the maximum peak-to-peak amplitude, and the peak-envelope amplitude.

We computed distance corrections by linear regression of earthquake ratios on the logarithm (base 10) of distance, and applied the corrections to both earthquake and explosion ratios. For each regression we used earthquake ratios formed with signal measurements at least 10 times greater than pre-P_n noise levels. When actually applying the regression results and forming the discrimination plots, we used ratios of earthquakes and explosions formed with signal measurements at least twice the pre-P_n noise level. We used the reported PDE m_b magnitudes and, for the small earthquakes, the Chinese local magnitudes (M_L).

Discrimination

We tested many combinations of phases and frequency bands as event discriminants. Here, we qualitatively class discriminants as good, fair, or poor. We will report on quantitative discriminant performance in a later paper. Below, are some examples of discrimination ratios that separate earthquakes from explosions, and also some examples that are known to work in the western United States, but are poor discriminants in central Asia. All ratios have been corrected for a distance effect, as described in the previous section, and all measurements used to form ratios have signal that is at least twice the pre-P_n noise level.

Short-Period Discriminants

Phase ratios. Many short-period regional discriminants that exploit a P/S ratio have been discussed in the literature (*cf.* Pomeroy *et al.*, 1982). Figure 3 shows examples of the P_g/L_g ratio versus m_b. We show two bands with center frequencies of 1.125 and 4.5 Hz. The 0.75-1.5 Hz P_g/L_g ratio fails to separate the explosions and earthquakes. However, as frequency increases, the explosion and earthquake separation increases substantially. For frequency bands above 3 to 4 Hz, the explosions and earthquakes can be separated with P_g/L_g, P_n/L_g, and P_n/S_n ratios.

These high-frequency ($f > \approx 4$ Hz) P/S ratios work for northwest-southeast paths from KTS to WMQ, a distance of about 950 km. Considering the similarity of the source-area geology at KTS and Lop Nor (*i.e.* hard rock sites, Matzko (1994)), we anticipate that these ratios will work for reversed paths from the Lop Nor area into Kazakhstan. The primary drawback of this discriminant is that it depends on high frequencies for both P and S. For explosions, S_n and L_g are low-amplitude phases, and for passbands above ≈ 4 Hz, an m_b of nearly 5.0 is required before signal exceeds noise at recording distances of ≈ 1000 km.

Spectral Ratios. Spectral discriminants have been successfully applied to relatively small events ($3.0 < m_b < 4.8$) from the western United States. Taylor *et al.* (1988) used the L_g (1–2 Hz) / L_g (6–8 Hz) ratio, Bennett and Murphy (1986) used the L_g (0.5–1 Hz) / L_g (2–4 Hz) ratio, Hartse *et al.* (1995) used the coda (0.5–1 Hz) / (2–4 Hz) ratio, and Walter

et al. (1995) used P_n, P_g, L_g and L_g coda ratios to separate nuclear explosions from earthquakes. Figure 4 shows that some spectral discriminants do separate earthquakes and explosions in central Asia, but the L_g spectral discriminant does not. The western U.S. studies generally examined small explosions ($m_b < 4.8$) that were detonated above the water table. Most explosions from Lop Nor are thought to be detonated below the water table (Matzko, 1994). As discussed by Taylor and Denny (1991), Patton and Taylor (1995), and Walter *et al.* (1995), the amount of gas-filled porosity near the explosion appears to control the performance of the L_g spectral-ratio discriminant. In the western United States, L_g-waves from explosions are deficient in high frequency energy relative to earthquakes. For the KTS and Lop Nor explosions, the P_n, P_g, and S_n phases have a high-frequency enhancement relative to regional earthquakes of similar magnitudes.

The P_n, P_g, and S_n ratios for the 3-6/0.75-1.5 Hz bands all separate explosions from earthquakes. Taylor and Denny (1991) and Taylor and Marshall (1991) have noted that a high-frequency to low-frequency ratio of P waves recorded at teleseismic distances separates Kazakh nuclear explosions from Asian earthquakes. Arora and Basu (1984) noted a similar relationship for Lop Nor explosions and western China earthquakes recorded in southern India. Figure 4 shows that these relationships can also be observed at regional distances, at least for explosions down to $m_b \approx 4.5$.

Cross-Spectral Ratios. The spectral ratios of Figure 4 imply that the P energy generated by Lop Nor and KTS explosions is rich in high frequencies ($f > 4$ Hz) relative to regional earthquakes. At the same time Figure 2 suggests that the explosions have relatively less L_g energy than the earthquakes. Hence, a P phase with $f > \approx 4$ Hz in ratio with an S phase of any short-period band should be a good discriminant.

Figure 5 shows examples of the cross-spectral discriminants that we tested. The high-frequency P to low-frequency S ratios have an important advantage over the high-frequency phase ratios (Figure 3). Because event separation can be obtained using S in frequency bands near 1 Hz, the lower magnitude explosions, which have S_n and L_g energy levels above background noise, can be included in the discrimination plots. Hence, these cross-spectral ratio discriminants can be applied to smaller explosions and out to greater distances than the high-frequency phase ratios. For example, the cross-spectral plot of Figure 5a includes an $m_b = 4.6$ KTS explosion that was dropped from the 3-6 Hz P_g/L_g phase-ratio plot of Figure 3a due to a low signal-to-noise ratio.

Short-Period/Long-Period Ratios. We tested P/R and P/L ratios for several bands. As our study of central Asia progresses, we will develop regional m_b and M_S magnitude scales, enabling us to present the P_n/R ratio in its more common form, the $m_b : M_s$ discriminant. The $m_b : M_s$ discriminant has been successfully applied at regional distances in the western United States by Taylor *et al.* (1989). We measured peak-to-peak and peak-envelope velocity amplitudes from broadband records to test this discriminant. Peak-envelope measurements show less scatter than the peak-to-peak measurements.

Figure 6 shows examples of short-period / long-period discrimination plots. The P_n $(0.75\text{–}1.5\,Hz)$ / R $(8\text{–}16\,s)$ ratio, provides good separation between earthquakes and explosions. As in the case of phase ratios and cross-spectral ratios, raising the P_n band to 3-6 Hz improves event separation when ratios are formed with R. We tested a P_n $(0.75\text{–}1.5\,Hz)$ / L $(8\text{–}16\,s)$ ratio, which separates explosions and earthquakes, but requires a large explosion before L can be measured above the noise. Although we do not show examples here, the P_g/R, P_n/L, and P_g/L ratios are all improved by measuring higher frequency body waves. The primary drawback of the short-period / long-period discriminant is the weak surface waves generated by the explosions. Most explosions we processed are recorded at more than 950 km. With closer recording distances and signal enhancement through array processing, the short-period / long-period discriminants may become more useful for separating smaller events.

Long-Period Ratios. We do not show examples of long-period ratios in this summary, however, we tested long-period R/L discriminants, and found that the 6-12 s and 8-16 s periods show the best separation and least scatter. The R/L discriminant was mentioned by Pomeroy *et al.* (1982), but has not been widely tested or applied. The primary drawback is that the weak L of the explosions often fail to exceed noise levels. The Kazakh explosions had to be large ($m_b > 5.0$) to generate L that was above the noise at WMQ. Further, the Lop Nor explosions recorded at AAK do not clearly separate from earthquakes. We suspect that tectonic release associated with the large Chinese explosions may be affecting this discriminant.

Sub-Crustal Earthquakes. The PDE catalog lists the depths of several Pamir earthquakes (recorded at AAK) as 33 km. However, we suspect that at least four of these earthquakes are deep (mantle source) because the seismograms lack a clear L_g and have weak surface waves. We identify these events with a separate symbol on the discrimination plots shown in Figures 3-6 (right-hand columns). These suspected deep earthquakes merge with the explosions on the spectral, and cross-spectral discrimination plots (Figures 4 and 5). However, they do separate from the explosions on the high-frequency P_g/L_g discrimination plot (Figure 3). We will be studying deep events from the Pamir and Hindu-Kush in the future, paying particular attention to depth phases.

RECOMMENDATIONS AND FUTURE PLANS

We have measured noise and phase amplitudes of over 250 earthquakes and 18 underground nuclear explosions recorded at the broadband, digital station WMQ in western China and over 100 earthquakes and 5 nuclear explosions at station AAK in Kyrgyzstan. Event magnitudes (m_b) range between 2.5 and 6.5 and maximum event-station distance is about 1700 km. Using these measurements we formed phase, spectral, cross-spectral, short-period/long-period, and long-period ratios to test many possible event discriminants. All ratios were corrected for distance effects before plotting ratio-versus-magnitude discrimination plots.

The most consistent discriminants for separating earthquakes from explosions are a high-frequency ($f \gtrsim 4\,Hz$) P/S ratio versus m_b and a short-period P ($f \gtrsim 1\,Hz$) to long-period Rayleigh-wave ($0.05 < f < 0.1$) ratio versus m_b. The short-period P/S ratio was even successful at separating several apparently deep earthquakes from the North Pamir region of far western China, which merge with explosions on spectral and cross-spectral discrimination plots.

P_n, P_g, and S_n spectral ratios ($\approx 3\text{–}6\,Hz$ / $0.75\text{–}1.5\,Hz$) and P ($\approx 3\text{–}6\,Hz$) / S ($\approx 0.75\text{–}1.5\,Hz$) cross-spectral ratios also separate most earthquakes from the explosions. The KTS explosions separate from earthquakes when an R/L ratio is formed. However, the large Lop Nor explosions do not separate from the earthquakes when the R/L ratio is formed, indicating strong tectonic release may be associated with explosions at the Lop Nor test site.

We plan to continue this study by collecting and analyzing waveform data from other Asian seismic stations. Future studies will include detailed analysis of the suspected deep Pamir earthquakes, development of regional magnitude scales, and efforts to incorporate small ($2.0 < m_b < 3.5$) chemical explosions into our event discrimination plots. Because we evaluate several different discriminants, we will develop multivariate techniques that combine measurements and quantitatively assess discrimination performance.

Acknowledgements

Brian Stump provided a thoughtful review of this manuscript. We thank the staff at the IRIS Data Management Center for prompt replies to our data requests. The GMT mapping software (Wessel and Smith, 1991) was used to construct Figure 1. This work is in support of the DOE Comprehensive Test Ban Treaty Research and Development Program, ST482A, and was performed at Los Alamos National Lab under the auspices of the United States Department of Energy, Contract Number W-7405-ENG-36.

References

Arora, S. K. and T. K. Basu (1984). A source discrimination study of a Chinese seismic event of May 4, 1983, *Tectonophysics*, **109**, 241-251.

Bennett, T. and J. Murphy (1986). Analysis of seismic discrimination using regional data from western United States events, *Bull. Seis. Soc. Am.*, **76**, 1069-1086.

Gao, L. and P. G. Richards (1994). Studies of earthquakes on and near the Lop Nor, China, nuclear test site, *Proceedings of the 16th Annual DARPA/AF Seismic Research Symposium*, 106-112. PL-TR-94-2217, ADA284667

Hartse, H. E., W. S. Phillips, M. C. Fehler, and L. S. House (1995). Single-station spectral discrimination using coda waves,, *Bull. Seis. Soc. Am.*, **85**, 1464-1474.

Hartse, H. E., S. R. Taylor, W. S. Phillips, and G. E. Randall (1996). Single-station spectral discrimination using coda waves,, *Bull. Seis. Soc. Am.*, **86**, submitted.

Matzko, J. R. (1994). Geology of the Chinese nuclear test site near Lop Nor, Xinjiang Uygur Autonomous Region, China, *Engineering Geololgy*, **36**, 173-181.

Patton, H. J. and S. R. Taylor (1995). Analysis of *Lg* spectral ratios from NTS explosions: Implications for the source mechanism of spall and the generation of *Lg* waves, *Bull. Seism. Soc. Am.*, **85**, 220-236.

Pomeroy, P. W., J. B. Best, and T. V. McEvilly (1982). Test ban treaty verification with regional data - a review, *Bull. Seis. Soc. Am.*, **72**, S89-S129.

Taylor, S. R. and M. D. Denny (1991). An analysis of spectral differences between Nevada Test Site and Shagan River nuclear explosions, *J. Geophys. Res.*, **96**, 6237-6245.

Taylor, S. R. and P. D. Marshall (1991). Spectral discrimination between Soviet explosions and earthquakes using short-period array data, *Geophy. J. Int.*, **106**, 265-273.

Taylor, S. R., N. W. Sherman, and M. D. Denny (1988). Spectral discrimination between NTS explosions and western United States earthquakes at regional distances, *Bull. Seis. Soc. Am.*, **78**, 1563-1579.

Taylor, S. R., M. D. Denny, E. S. Vergino, and R. E. Glaser (1989). Regional discrimination between NTS explosions and western U.S. earthquakes, *Bull. Seis. Soc. Am.*, **79**, 1142-1176.

Walter, W. R., K. M. Mayeda, and H. J. Patton (1995). Phase and spectral ratio discrimination between NTS earthquakes and explosions. Part I: Empirical Observations, *Bull. Seism. Soc. Am.*, **85**, 1050-1067.

Wessel, P. and W. H. F. Smith (1991). Free software helps map and display data, *EOS Trans. AGU*, **72**, 441.

Figure 1. Study area map showing, shaded topography, nuclear explosion and test site locations, natural seismicity, and seismic stations. We used seismic data recorded at stations WMQ and AAK in this study.

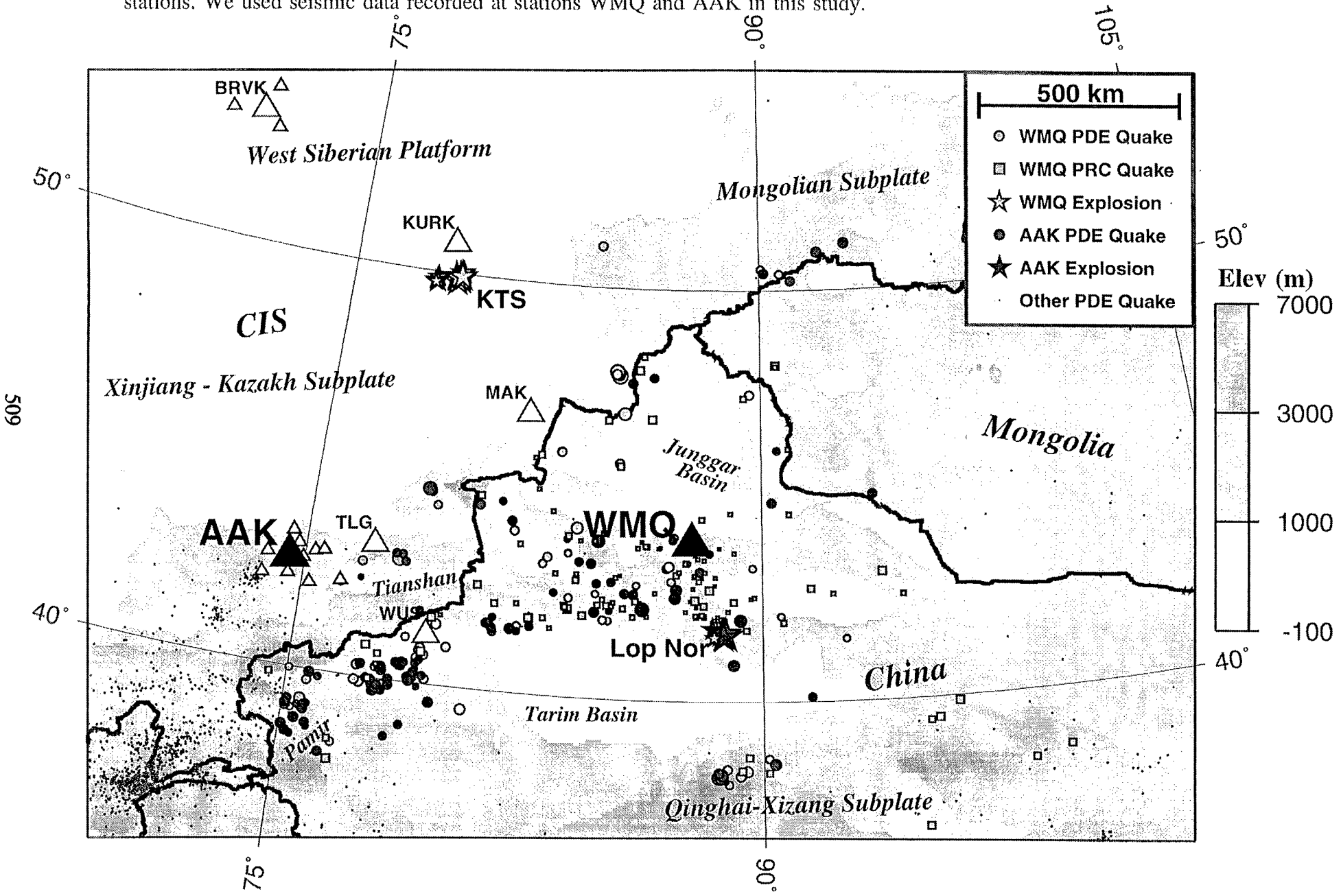

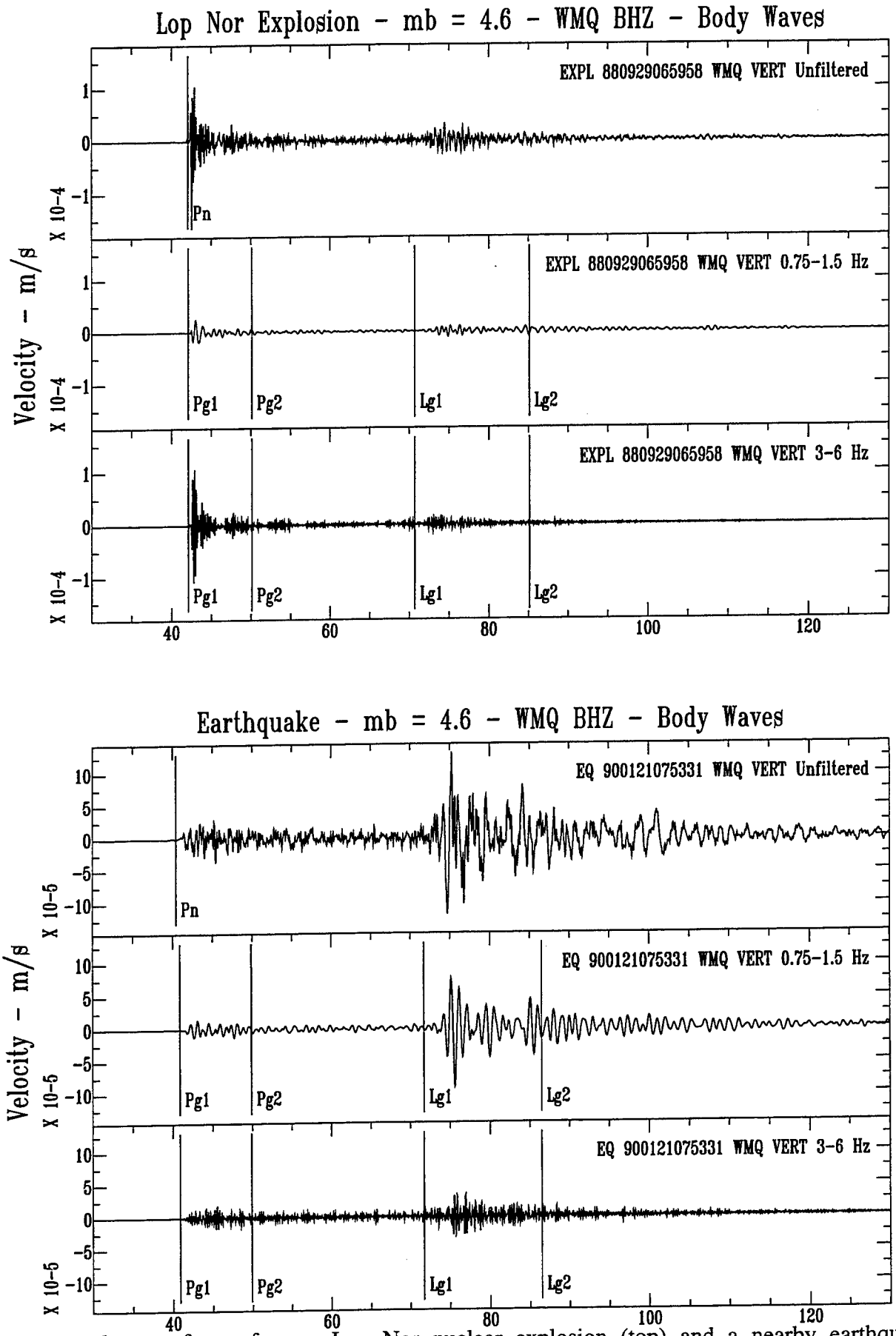

Figure 2. Sample waveforms from a Lop Nor nuclear explosion (top) and a nearby earthquake recorded at station WMQ. Event-station distance for both events is about 250 km. Note that P for the explosion is enhanced in 3-6 Hz energy relative to the earthquake. L_g for the explosion is deficient in frequencies above $\approx 1\,Hz$ relative to the earthquake.

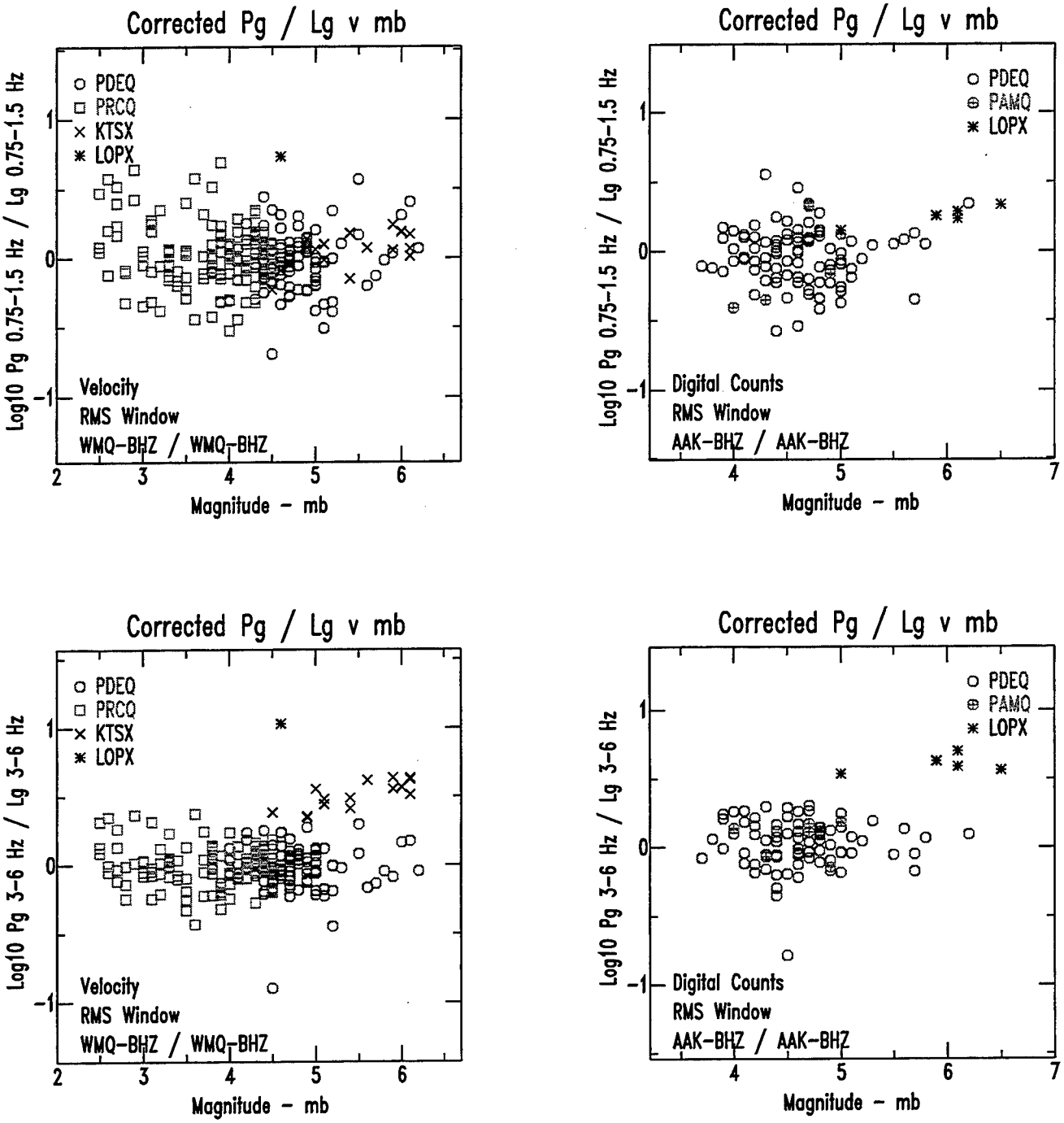

Figure 3. Phase ratio P_g/L_g discrimination plots for stations WMQ (left) and AAK. Center frequencies are 1.125 Hz and 4.5 Hz. As frequency increases, separation between earthquakes and explosions also increases.

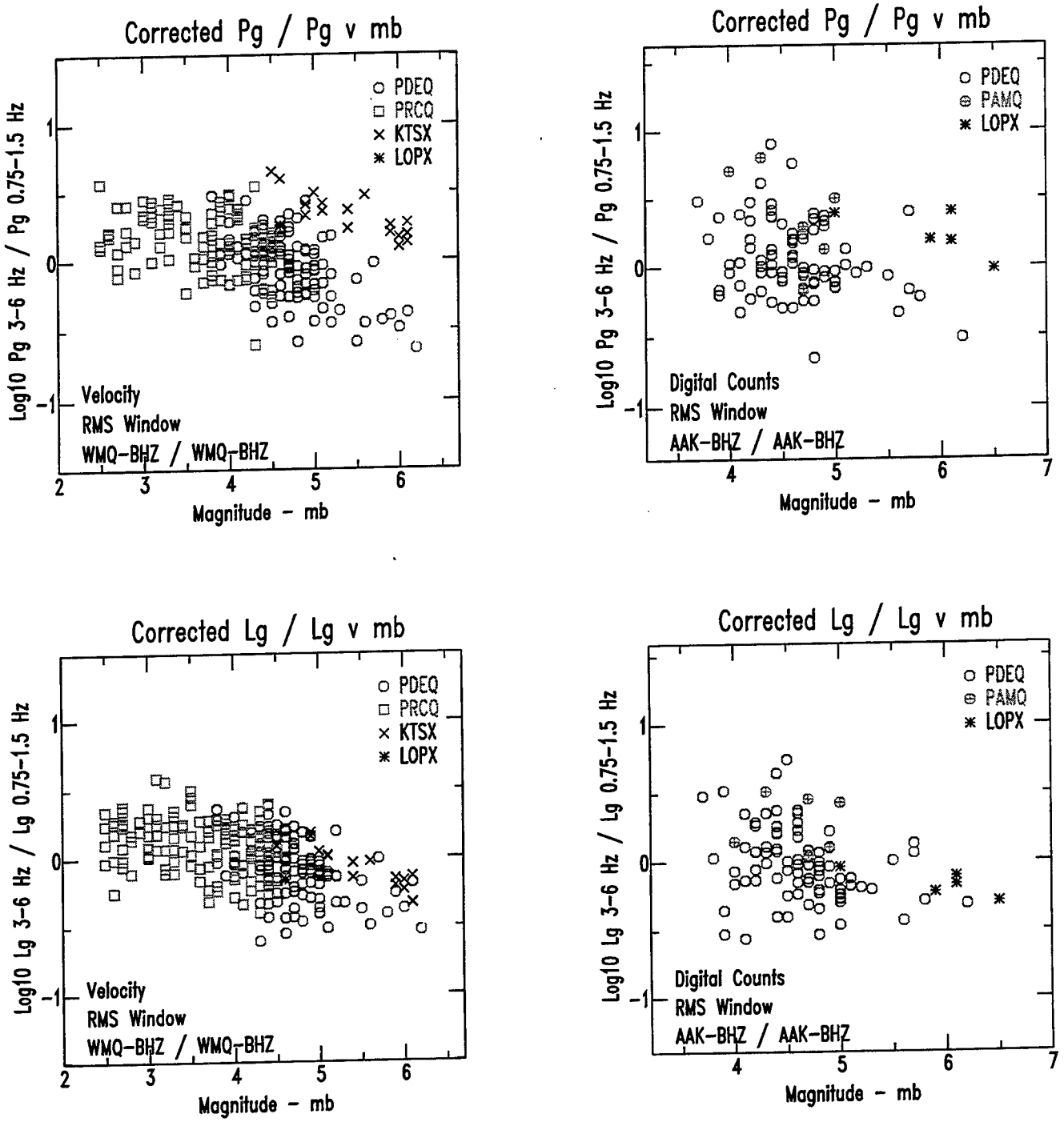

Figure 4. Spectral ratio discrimination plots for stations WMQ (left) and AAK. In contrast to the western United States, the L_g spectral ratio (bottom) performs poorly in central Asia. Some of the suspected sub-crustal earthquakes from the Pamir uplift (PAMQ) merge with the explosions at AAK (top left).

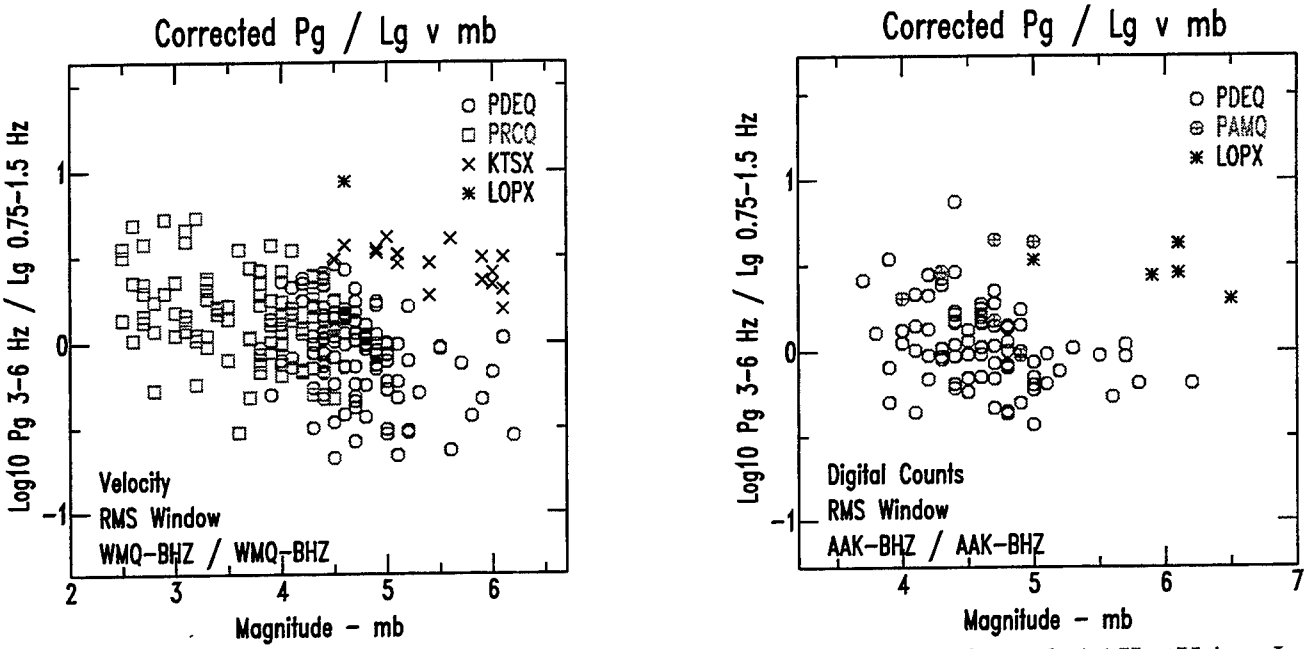

Figure 5. Cross-spectral ratio discrimination plots for stations WMQ (left) and AAK. Using L_g measured at around 1 *Hz* allows us to evaluate smaller explosions compared to using L_g measured at around 4 *Hz* (see Figure 3). Some of the suspected sub-crustal earthquakes from the Pamir uplift (PAMQ) merge with the explosions at AAK (left).

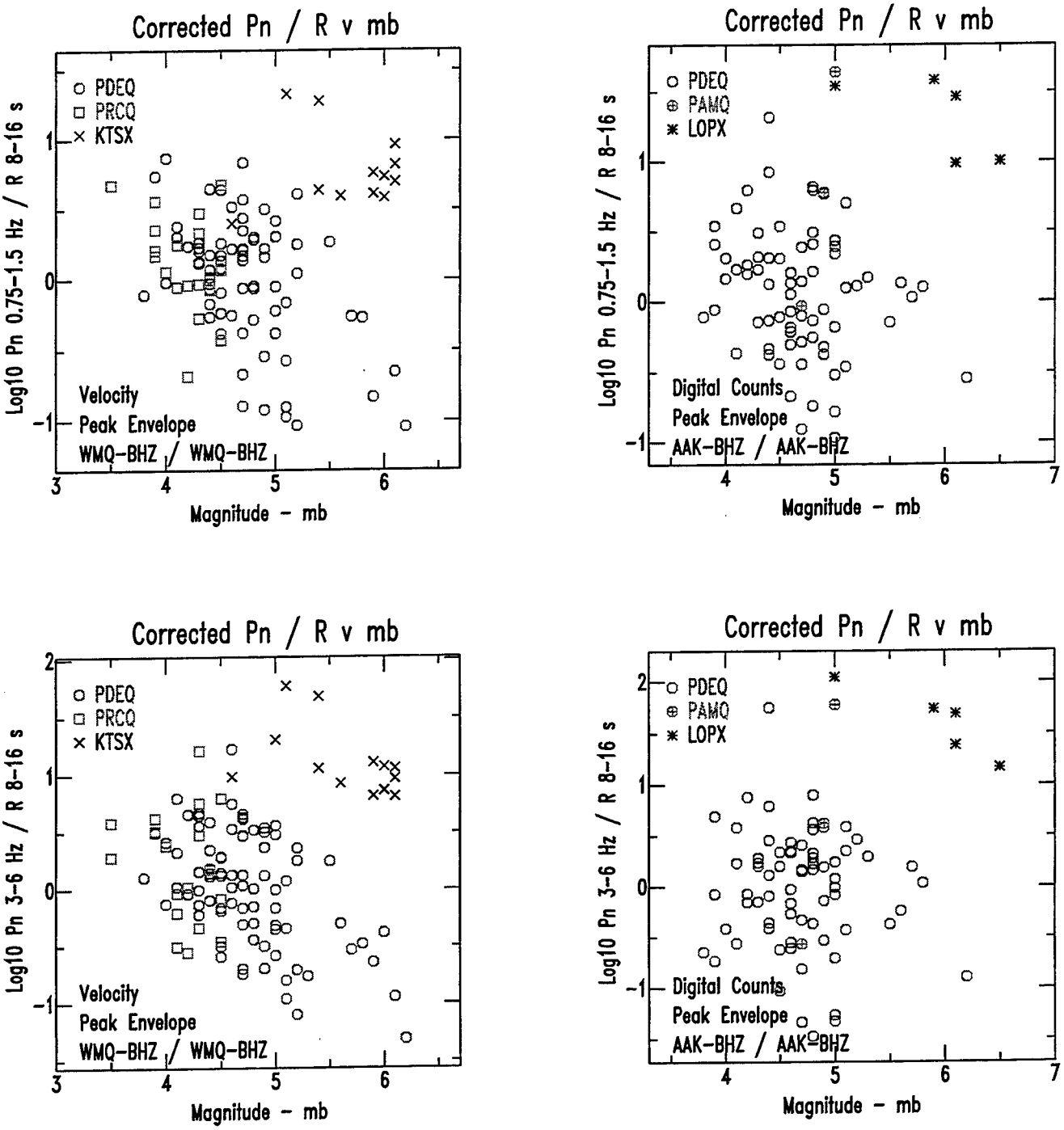

Figure 6. Short-period / long-period discrimination plots for stations WMQ (left) and AAK. Here we show P_n in ratio with R, but P_n in ratio with L also performs well. As P_n frequency increases, separation increases.

Experiments in Regional Monitoring of Small Seismo/Acoustic Events

Michael A.H. Hedlin, Frank L. Vernon, J.-Bernard Minster & John A. Orcutt
IGPP, Scripps Institution of Oceanography, University of California, San Diego

Sponsored by the Air Force Technical Applications Center
Directorate of Nuclear Treaty Monitoring
Issued by the Phillips Laboratory under Contract No.
F19628-95-K-0012

ABSTRACT

The CTBT negotiations have endowed small seismo/acoustic events (m_b ~ 2.5) with a much greater significance than they have had in the past and have increased the need for automated regional discrimination. We have been contracted by AFTAC to develop a small event discriminant that uses time-frequency expansions of seismic coda to discriminate ripple-fired mining explosions from single explosions and earthquakes. The Automated Time-Frequency Discriminant (ATFD) which we have developed will use data collected by single stations, arrays or regional networks.

During the past year we have tested the ATFD on data collected in central Asia, Europe and North America. We have found the discriminant to be robust, with misclassification probabilities, estimated with multivariate statistics, ranging from 0.5 to 3.5 percent. The method is easily adapted to any kind of regional seismic data.

To improve the ATFD we have analyzed wavelet expansions of coda, begun to look at discriminants based on hybrid (seismo/acoustic) data and will shortly collect data to help us address the issue of outliers. These data will be collected this summer in Wyoming and will consist of broadband seismic, acoustic and infrasound recordings of ground truthed mining explosions in the Black Thunder coal mine. We will also be looking for ionospheric perturbations with a network of continuous GPS receivers.

An initial version of our ATFD has been given to David Jepsen at the IDC and is currently being incorporated into their Detection Feature Extraction (DFX) software package.

Keywords: comprehensive test ban treaty (CTBT), time-frequency expansion, wavelets, automated discrimination, multivariate statistics, coda cepstrum, ripple-firing.

OBJECTIVE

Our overall objective is to create a robust discriminant which can be applied to regional seismic data and used to distinguish large numbers of ripple-fired mining explosions from small nuclear explosions and earthquakes as part of a monitored Comprehensive nuclear Test Ban Treaty (CTBT). In specific, we have the following objectives:

- ***Test existing discrimination software.***
  - Use data collected by single stations, arrays, regional single or 3-Component networks.
  - Examine near to far regional recordings of single explosions, quarry blasts and earthquakes recorded by broadband or short period instrumentations
  - Compare with other techniques.

- ***Software development.***
  - use wavelet based expansion techniques.
  - examine hybrid (seismic and acoustic) monitoring.
  - improve our understanding of the interaction of wavefields produced by ripple-fired events. To what extent can the regionally recorded wavefields be explained with linear superposition? Explain time and component independence.
  - improve our understanding of outliers.

- ***Low-frequency discrimination.***
  - determine if ripple-fired explosions generate unique signals at low-frequencies.

- ***Software distribution.***

RESEARCH ACCOMPLISHED

The automatic time-frequency discriminant. The rationale behind our Automated Time-Frequency Discriminant (ATFD), which is designed to distinguish ripple-fired mining explosions from single explosions and earthquakes, has been described in earlier papers (*e.g. Hedlin et al., 1989; Hedlin et al., 1990; Hedlin et al., 1995*) and so only a brief review will be given here. The ATFD expands waveforms (onsets and coda) into time-frequency sonograms. These sonograms are converted into binary form (*Hedlin et al., 1989*) to enhance small scale features. Binary displays derived from ripple-fired events are often banded indicating long lived spectral scallops likely caused by source finiteness or multiplicity (*Hedlin et al., 1989; 1990*). When present, the banded patterns tend to be independent of the recording direction (*Hedlin et al., 1989; 1995*). Binary sonograms derived from non ripple-fired events tend to exhibit little, if any, organization in time, frequency or between recording components.

The ATFD estimates the time-independence of the binary patterns by calculating the serial correlation at all frequencies along the time axis. Independence from recording direction is judged by cross-correlation. The "bandedness" is estimated by calculating the coda cepstrum (*Hedlin et al., 1990; 1995*) and taking the extreme value which is independent of time. These individual parameters are merged into a single discrimination score with the aid of multivariate statistics (*Seber, 1984*).

Global test of the ATFD. We have used a wide variety of datasets to test the utility of the ATFD. Specifically, we have tested the adaptability of the algorithm to various styles of seismic deployment (*incl.* single 3-Component stations, single- and 3-Component networks and arrays) varying seismic instrumentation (*incl.* short period and broadband), different geologic settings and mining customs. In the past year we have analyzed the following datasets (Figure 1):

1) single explosions and quarry blasts recorded by a sparse 3-Component network (NRDC) deployed on a high Q crust in Kazakhstan. The events occurred within 300 km of the stations.

2&3) earthquakes and quarry blasts recorded by a dense 3-Component network (KNET) deployed in a thrust belt (in Kyrgyzstan). We have analyzed two clusters of earthquakes and contrasted them with two sets of quarry blasts which occurred at the same mine.

4) recordings of quarry blasts and earthquakes made by the NORESS small aperture array in southern Norway. These events occurred within 7.5° of the array (Figure 2).

5) recordings of quarry blasts and earthquakes made by GERESS. These recordings were obtained from the European Ground Truth Database and were contributed by J. Wuster.

6) recordings of quarry blasts (in the Newmont Gold Mine) and earthquakes made by a single 3-Component station (ELK) located near Carlin, NV. These data were provided by LLNL.

To illustrate the technique we show the results of the analysis of dataset #4 (collected by NORESS; shown in Figures 2 and 3). The upper two and lower left panels of Figure 3 show the raw output from the ATFD. These panels show how well the two event types (earthquakes and quarry blasts) are separated by the metrics applied to the time-frequency expansions. The means by which these parameters are calculated are listed in the figure caption. The lower right panel shows the linear discriminant scores obtained by a multivariate analysis of the raw parameters. The misclassification probability of this dataset is 3.6%.

The results of the other studies are summerized in Figure 4 where we show the misclassification probabilities in datasets 2 through 6. By necessity we have paid the closest attention to the problem of discriminating quarry blasts from earthquakes. However, the most challenging problem involves the discrimination of single and multiple explosions. Althouth we haven't analyzed a large number of single explosions (3 recorded by the NRDC network in Kazakhstan; dataset # 1) it appears that the ATFD is effective at separating these event types (see *Hedlin et al. ,1995* for details). To further address this problem we will examine the single explosions recorded during the 1995 Black Thunder experiment (*Stump et al., 1995).*

Outliers and Hybrid monitoring: The Black Thunder seismo/acoustic experiment. To improve the science of small-event discrimination we need to understand better why some events are misclassified and we need to explore better data collection and processing techniques. To investigate the physical relationship between the ripple-fired source and regionally recorded seismic and acoustic wavefields we have formed a collaboration with Brian Stump, Craig Pearson and Rod Whitaker at LANL. The primary result of this collaboration is an experiment which will occur in July and August of this year. As part of this experiment Brian Stump and Craig Pearson from LANL will deploy video equipment,

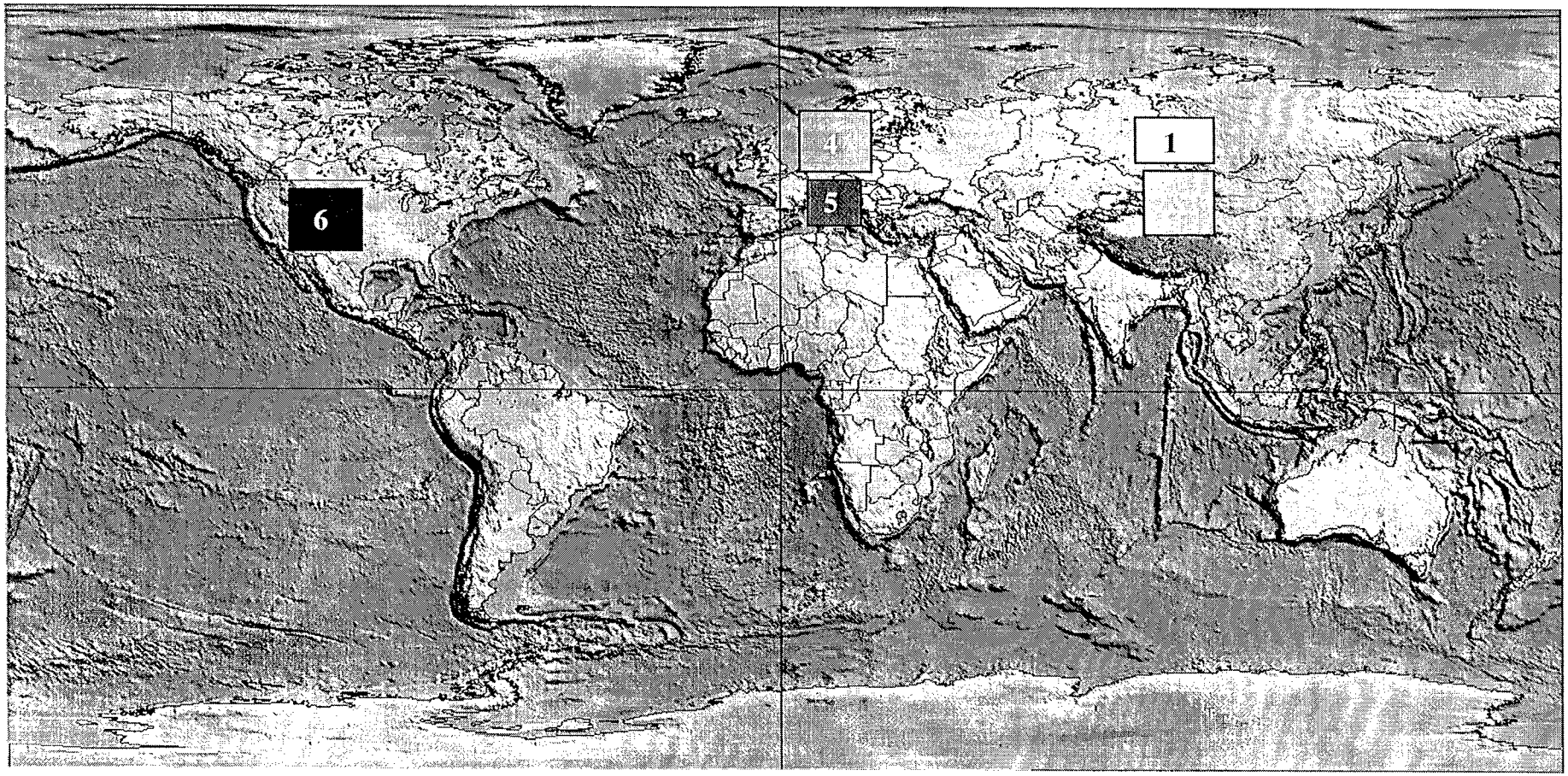

Figure 1 Locations of the datasets analyzed in the past year

Etopo5 basemap courtesy of
http://www.geo.cornell.edu/geology/
mc_na/dataset_info/new_etopo5.html

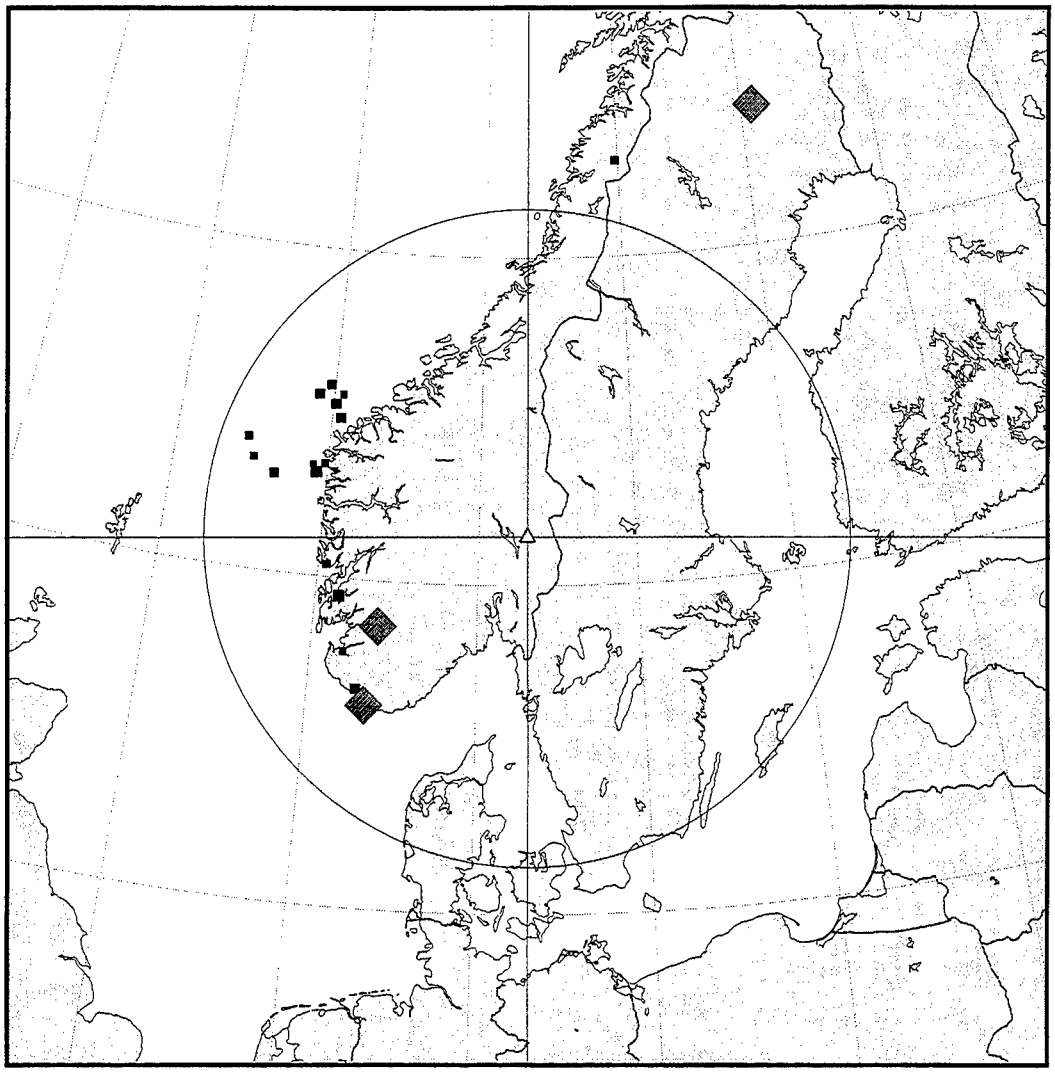

Figure 2 Dataset number 4. Collected by the NORESS small aperture array. This dataset contains recordings of 26 quarry blasts (from 3 mines including Blasjo and Titania) and 16 earthquakes. The events range from 2.7 to 7.5° from the array and have magnitudes of 1.6 to 3.0. A preliminary analysis of these events is presented in *Hedlin et al. (1990).*

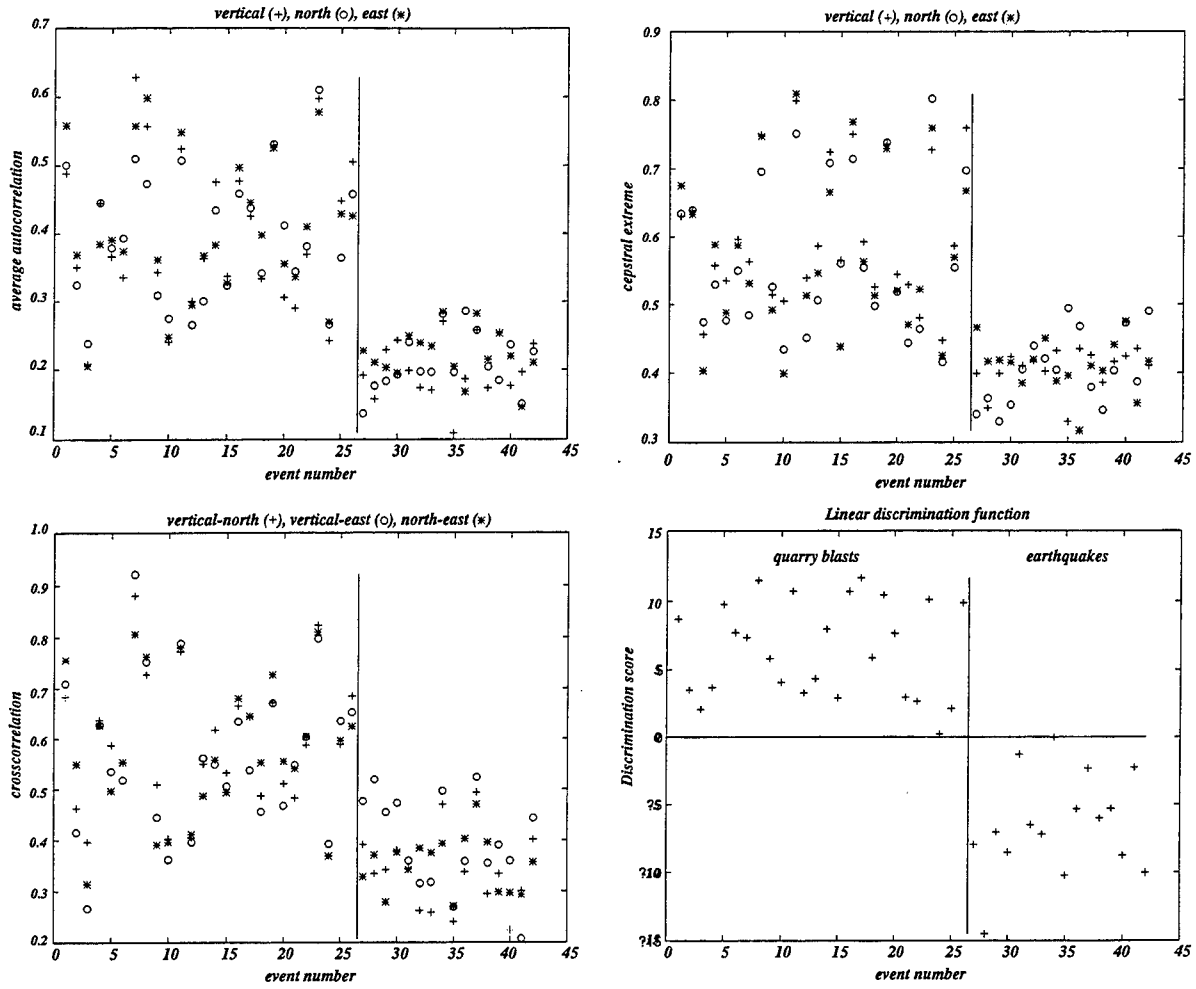

Figure 3 The four panels in this figure show the output of the ATFD applied to NORESS recordings of the events displayed in Figure 2. Events 1 through 26 are quarry blasts, 27 through 42 are earthquakes. The top left panel shows the average autocorrelation of all frequencies in the binary sonograms. A value of 1.0 means that all frequencies at all stations are invariant wrt time (they have either +1 or -1 at all times). The different symbols refer to different recording components. The top right panel shows the extreme values of the two-dimensional coda cepstra (see *Hedlin et al., 1989; 1995*) for an explanation of the coda cepstrum. A binary sonogram which is periodic in frequency and independent of time would have an extreme value of 1.0. These symbols represent the average of all stations in NORESS. The lower left panel shows the average cross-correlations between the 3 pairs of binary sonograms computed using the four 3-Component stations in NORESS (typically A0, C2, C4 and C7). The lower right panel shows the linear discriminant scores.

accelerometers and acoustic gauges inside the Black Thunder coal mine in Wyoming. A team from UCSD will deploy a regional network of broadband seismometers, pressure gauges and infrasound receivers (Figure 5). The network will include five 3-Component broadband seismic stations (STS2's) sampling continuously at 100 sps. Four of the stations will be located 200 km from the mine. The fifth station will be deployed 100 km from the mine on the same azimuth as one of the outer stations. This temporary network will add to permanent seismic deployments that include the 3-Component GSETT3 beta station RSSD and the array at Pinedale. Three pressure gauges will be deployed at the stations located 200 km to the north, south and west of the mine. Paired with the pressure gauge at the western site will be a small infrasound array consisting of 3 infrasound receivers in a triangle 100 m on a side.

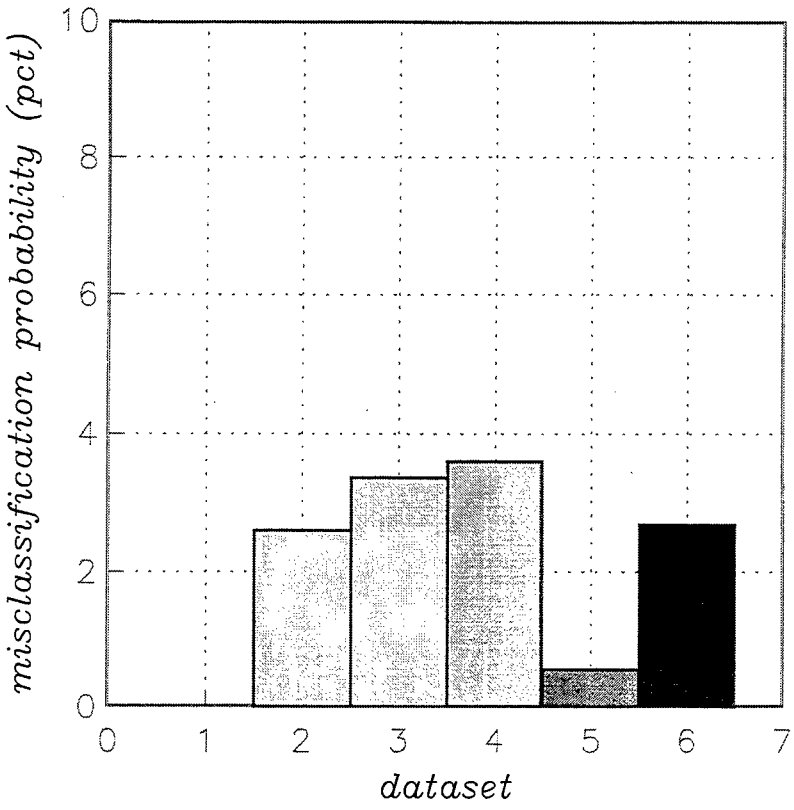

Figure 4 Misclassification probabilities in the datasets described in Figure 1 and in the RESEARCH ACCOMPLISHED section. Dataset 1 contains recordings of quarry blasts and just 3 single-explosions and is not summarized statistically. Dataset 4 is discussed in detail in the text.

In part we will be pairing the acoustic and infrasound equipment to assess the signal to noise gain that the infrasound receivers (loaned to us by Rod Whitaker) will give us. The acoustic and seismic equipment will be co-located to allow us to assess the value of a seismo/acoustic station. The acoustic instrumentation should be located within the first acoustic convergence zone and we expect the signals from the mine will be relatively strong to the west due to refraction in the mid-atmosphere. All acoustic signals will be digitized at 40 sps.

A second team from UCSD will deploy 3 continuous GPS receivers to detect ionospheric perturbations that result from the pressure front that emanates from the mine and is not ducted between the mid-atmosphere and the ground but propagates into the ionosphere. The current plan has 2 receivers located near to each other at a range of 50 km to the southwest of the mine. A third receiver will be deployed on the same azimuth but at a range of 200 km (Figure 5).

In addition to this near-regional equipment we have made arrangements with Bob Ellis and Michael Bostock (both at the University of British Columbia) to collect far-regional recordings of the mine blasts at 700 km (using an array of 7 seismic sensors in Saskatchewan, Canada) and at 2000 km (using an array of seismic sensors located in the Northwest Territories, Canada).

We expect that this instrumentation will record three significant (cast) explosions. On or about July 24 there will be a shot involving ~8 million pounds of explosives. We expect two smaller shots (3 to 4 million pound range) to occur on Aug 1 and Aug 15. The data from this experiment will allow us to test the utility of pressure gauges and an infrasound array to detect acoustic emissions from a surface mine and estimate the back azimuth to the source. We will also be testing the utility of the hybrid seismo/acoustic monitoring station and have an opportunity to address the issue of outliers. The video data that Brian and Craig collect will enable us to model the regional waveforms and should allow us to test linear superposition. Permanent stations and the temporary deployments in Canada will give us some idea about the range to which signals from ripple-fired blasts can propagate.

WY96 Regional Deployment

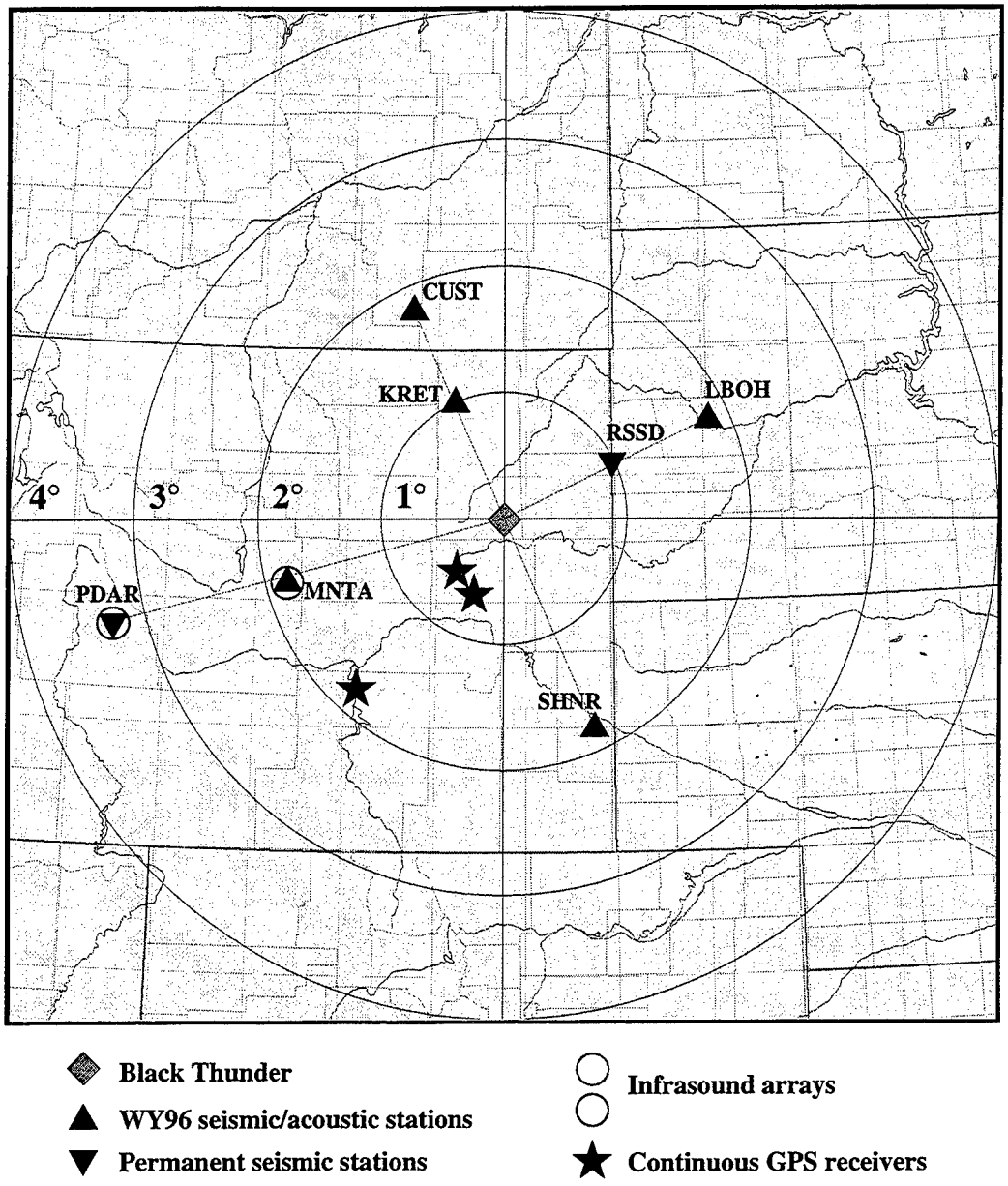

Figure 5 The 1996 Black Thunder regional deployment. The WY96 seismic stations consist of 3-Component STS2 broadband seismometers. The seismometers will be making continuous recordings digitized at 100 sps. The acoustic sensors are DNA pressure gauges. The W96 infrasound array will be deployed 200 km to the west of Black Thunder (at MNTA). This array will consist of 3 sensors arranged in a triangle 100 m on a side. The continuous GPS receivers are ZX2's digitizing the signal at 1 sps.

CONCLUSIONS AND RECOMMENDATIONS

The key question which we are attempting to address with our research is: Can a robust discriminant be developed which will discriminate large numbers of industrial, multiple, explosions from nuclear explosions and earthquakes? It seems that the generic ATFD is robust with misclassification probabilities ranging from 0.5 to 3.5%. The ATFD is easily adapted to a wide range of deployments (from single stations to arrays and networks) and thus easily automated.

In the coming year we will broaden the scope of our test of the ATFD by analyzing data at greater ranges and in regions not closely studied before:

- Examine data collected by the Saudi Network (*Vernon et al., 1996*)
- Examine CNET data
- Examine J. Pulli's NORESS Ground Truth Database to test ATFD at greater range

We will examine more recordings of single explosions (*e.g.* those recorded in Wyoming in 1995 by *Stump et al. (1995).*

We will further examine wavelet based time-frequency expansions and bring a wavelet based ATFD on line.

We will continue our analysis of tightly constrained mining events and dual (seismic and acoustic) monitoring technology by analyzing the data collected in Wyoming this summer. With these data we will address the question of the linearity of ripple-fired wavefield superposition, the range to which ripple-fired events can be detected and improve our understanding of outliers. This experiment will enable us to test the utility of continuous GPS for event detection.

REFERENCES

Hedlin, M.A.H., Minster, J.-B. & Orcutt, J.A., 1989, The time-frequency characteristics of quarry blasts and calibration explosions recorded in Kazakhstan, U.S.S.R., *Geophys. J. Int.*, **99**, 109-121.

Hedlin, M.A.H., Minster, J.-B. & Orcutt, J.A., 1990, An automatic means to discriminate between earthquakes and quarry blasts, *Bull. Seismol. Soc. Amer.*, **80**, 2143-2160.

Hedlin, M.A.H., Vernon, F.L., Minster, J.-B. & Orcutt, J.A., 1995, Regional Small-Event Identification using Seismic Networks and Arrays, *proceedings of the 17th Seismic Research Symposium on Monitoring a CTBT*, Scottsdale, AZ, Sept, p 875-884. PL-TR-95-2108, ADA 310037

Seber, G.A.F., 1994, *Multivariate Observations*, Wiley series in probability and mathematical statistics, John Wiley & Sons, Inc.

Stump, B.W., Pearson, D.C., Edwards, C.L & Baker, D.F.., The LANL Source Geometry Experiment, *proceedings of the 17th Seismic Research Symposium on Monitoring a CTBT*, Scottsdale, AZ, Sept, p684-693. PL-TR-95-2108, ADA 310037

Vernon, F.L., Mellors, R.J., Berger, J., Al-Amri, A.M. & Zollweg, J., 1996, Initial Results from the Deployment of Broadband Seismometers in the Saudi Arabian Shield, the *proceedings of the 18th Seismic Research Symposium*, Annapolis, MD, Sept 4-6.

SEISMO-ACOUSTIC STUDIES AT TXAR

Eugene Herrin and G. G. Sorrells
with contributions from
Jessie Bonner, Valeriu Burlacu, Nancy Cunningham, Paul Golden, Chris Hayward,
Jack Swanson, Karl Thomason and Ileana Tibuleac

Southern Methodist University
PL Contracts # F19628-95-C-0184 and F 19628-93-C-0057
Sponsored by AFTAC and ARPA

ABSTRACT

Data from the TXAR array showed that infrasonic signals from explosions caused ground motion that was detected on the seismic sensors (seismo-acoustic signals). Experiments recording acoustic and seismo-acoustic signals from quarry blasts in Central Texas confirmed a theoretical transfer function between the two types of signals in the band of interest (0.5 - 5.0 Hz). Four infrasonic stations were established at TXAR using porous hose arrays and inexpensive, low-frequency acoustic sensors collocated in boreholes with the seismometers. A number of different designs of the hose arrays were tested in order to maximize the acoustic signal-to-noise ratios. Acoustic and seismo-acoustic signals have been detected from a large number of mining explosions at regional distances from TXAR. As many as 75% of the regional signals detected at TXAR are now thought to result from commercial explosions, so that identification of these events is an essential part of routine analysis. Detection of acoustic and seismo-acoustic signals from both surface and underground explosions has been used as a positive discriminant that allows the construction of a ground-truth data base to be used in testing purely seismic discriminants.

Keywords: Seismic, acoustic, seismo-acoustic, infrasonic, explosions (surface and underground), discrimination, ground-truth data base.

Objective

The detection of seismic, acoustic and seismo-acoustic signals from both surface and underground mining explosions at regional distances from TXAR provides positive identification of the source. Using these observations we are building a ground-truth data base that can be used to test purely seismic discriminants. This same approach can be used at seismic arrays to be constructed in areas of particular interest for CTBT monitoring.

Research Accomplished

During GSETT2 a large number of teleseismic and regional signals were detected at the Lajitas, Texas, station (now TXAR) and reported to the National Data Center. Figure 1 shows the number of teleseisms detected during the test period sorted by day of week and hour of day. There is no clear pattern of occurrences.

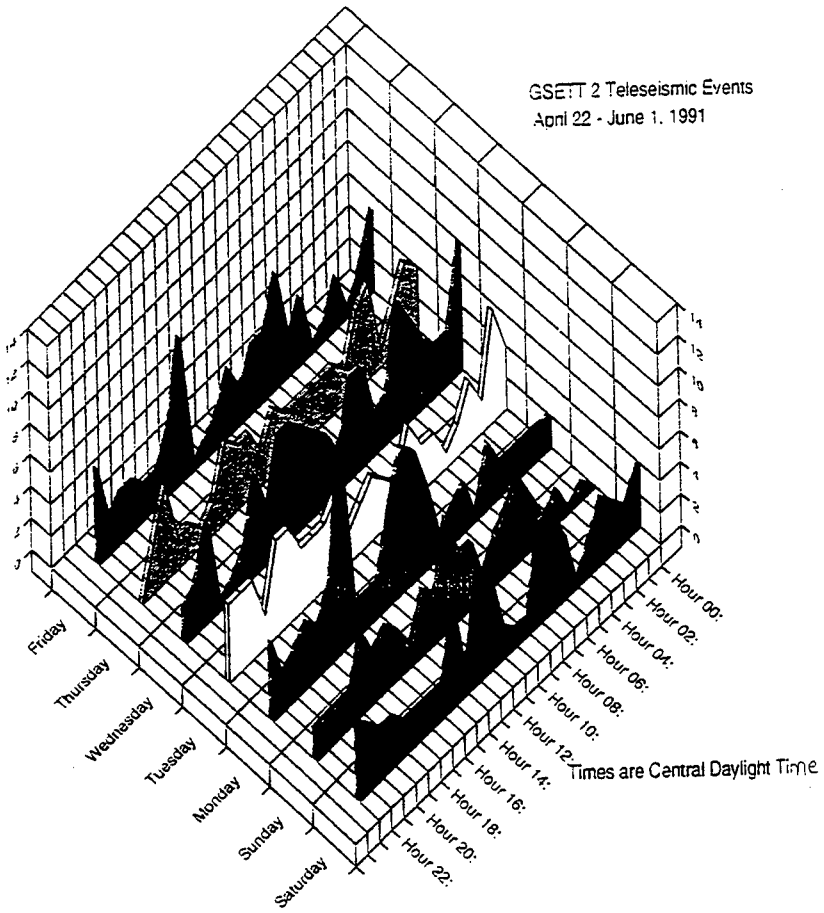

Figure 1

In Figure 2 the number of regional events similarly sorted reveals a clear pattern of activity that peaks during the daylight hours of working days. We now estimate that up to 75% of the regional detections at TXAR are from commercial explosions up to m_b 3.5. Under a CTBT, commercial explosions of larger than about m_b 2.5 to 3.0 must be identified using data from arrays located in areas of particular interest.

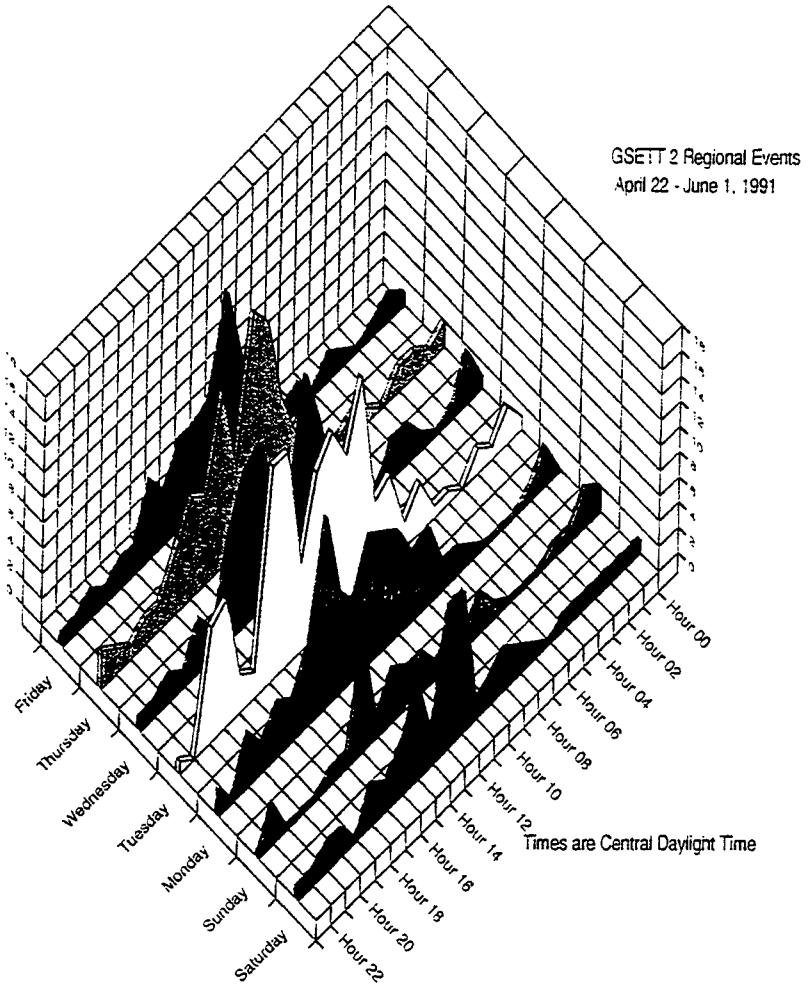

Figure 2

Investigations at the Lajitas station and experiments carried out in Central Texas using quarry blasts have confirmed that low-frequency (0.5 to 5 Hz) acoustic signals can be detected at regional distances from commercial explosions on both acoustic and seismic arrays. The acoustic wave causes ground motion that is recorded by the seismic systems (seismo-acoustic signals). Detection of seismic, acoustic and seismo-acoustic signals at TXAR with appropriate arrival times, azimuths and phase velocities clearly identifies the source as an explosion. Figure 3 shows the location of the seismic elements in the TXAR array. Acoustic pipe arrays were located at the four underlined elements. A small, inexpensive acoustic sensor was placed in the boreholes that house the seismometers and electronic systems. One of these sensors is shown in Figure 4.

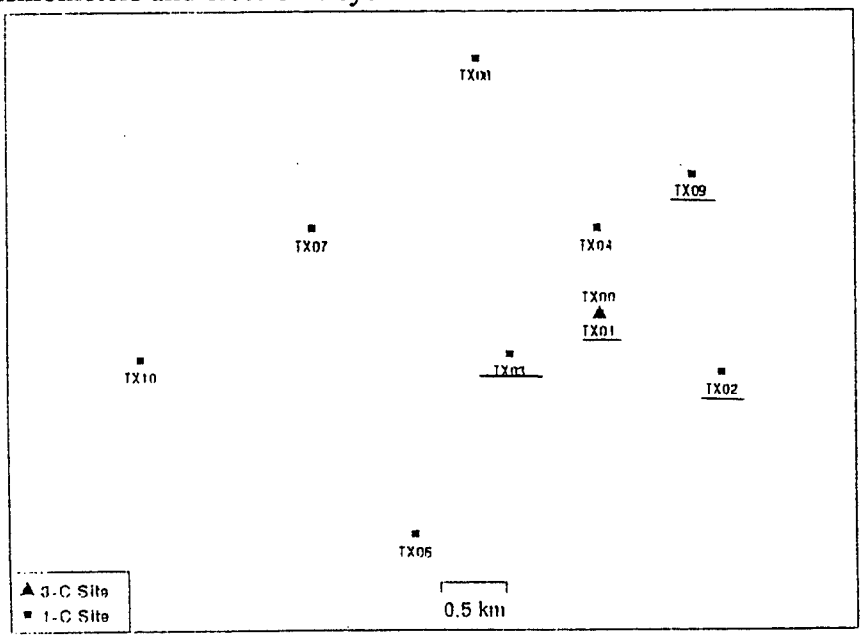

Figure 3

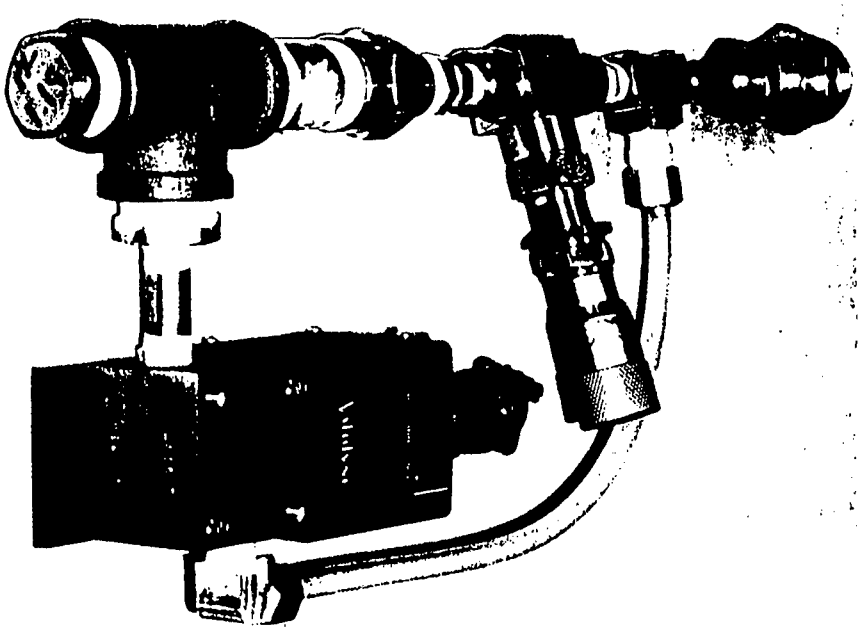

Figure 4

Figure 5 shows the acoustic signal recorded at TXAR for an m_b 2.0 surface explosion in the Micare' coal mining district of northern Mexico.

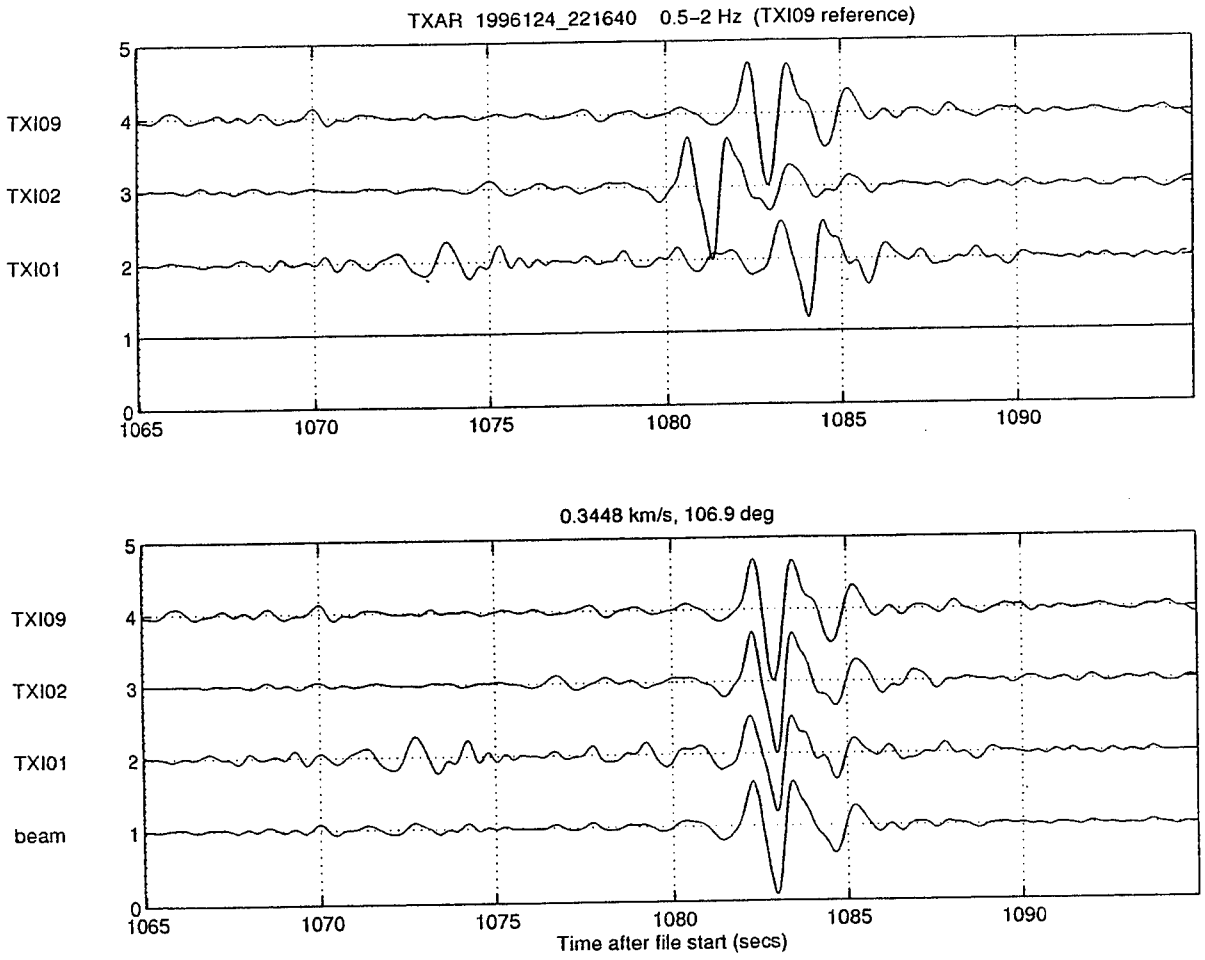

Figure 5

Figure 6 shows the seismo-acoustic signal seen on the 9 element seismic array, the array beam and the result of application of an adaptive, pure-state filter to the signal. These recordings clearly identify the event as an explosion.

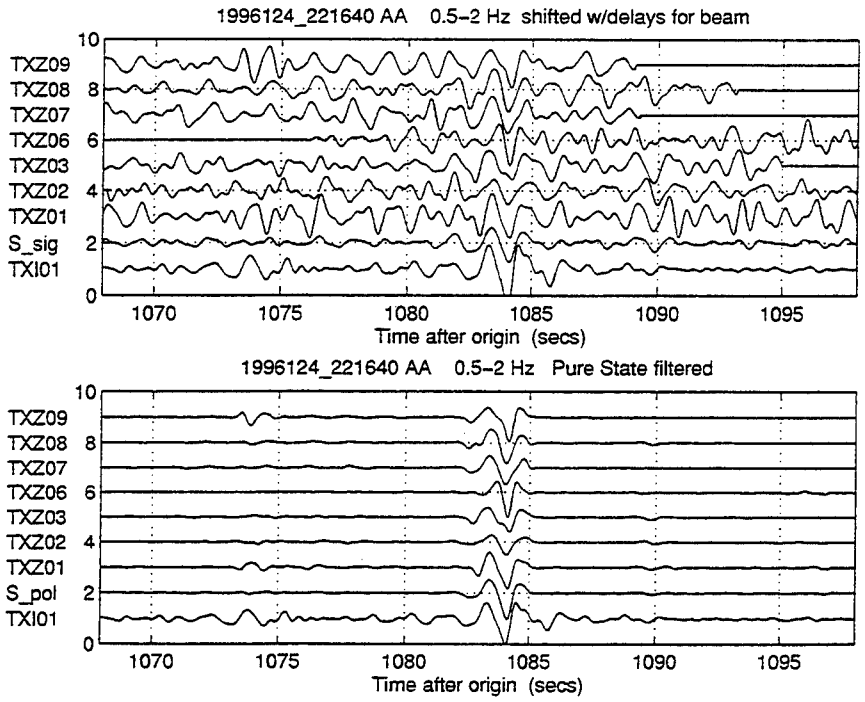

Figure 6

Figure 7 shows the acoustic signal from an underground m_b 3.0, explosion in the same mining district.

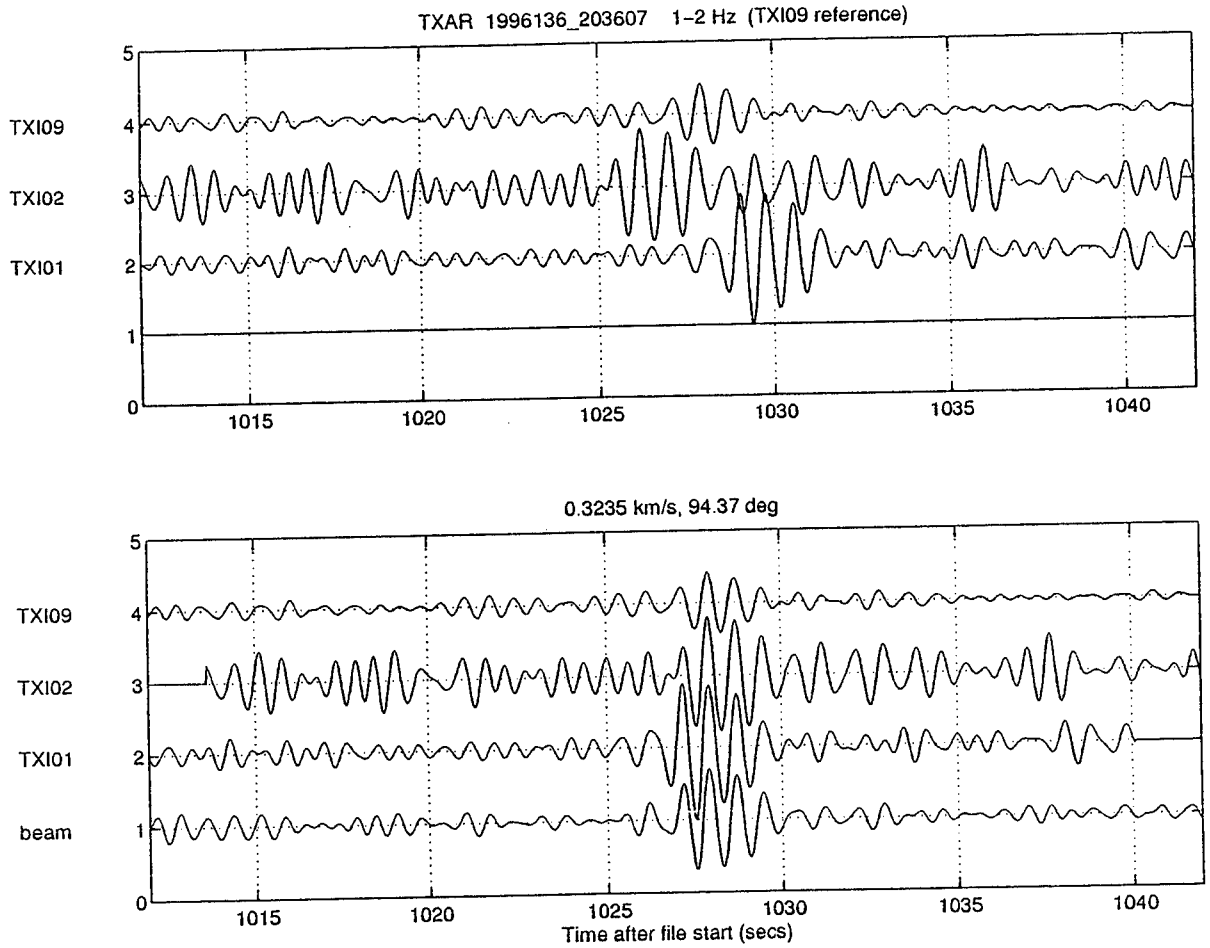

Figure 7

Figure 8 shows the seismo-acoustic signal, the array beam and pure-state filtered record. This event is clearly identified as an explosion. Collateral information lead us to conclude that the event is a vented, underground explosion with small, if any, delays in the firing sequence. A number of events from mining districts in Mexico and the Western United States have been positively identified by the detection of associated seismic, acoustic and seismo-acoustic signals. These identified events then become, along with earthquake aftershock sequences, part of a ground-truth data base that can be used to test seismic discriminants.

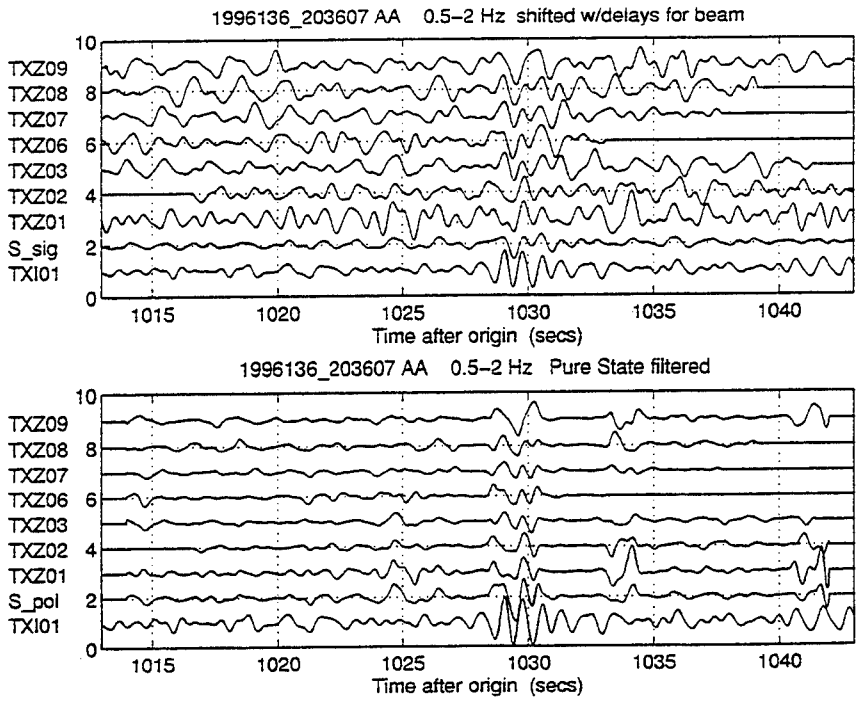

Figure 8

In order to increase the detection capability of the 4-element acoustic array at TXAR, we have been experimenting with changes in the geometry of the porous-hose arrays connected to the infrasonic sensors. One simple change in the hose array led to a 10 dB reduction in the acoustic background noise in the 0.5 to 5.0 Hz band. The collocation of the acoustic and seismic sensors makes possible the estimation of the transfer function of the acoustic array for signals of interest. Figure 9 is a diagram showing as blocks the acoustic array and seismo-acoustic response functions. The latter function depends upon the seismometer response, which is well known, and the earth response to the acoustic signal for which we have an experimentally verified theoretical model. Deconvolution of these two effects provides an estimate of the acoustic signal that can be used, along with the acoustic sensor output, to calculate the array transfer function. Figure 10 shows the amplitude and phase response of one of the acoustic pipe arrays. The linear trend in the phase response corresponds to the pure signal delay in the pipes. This technique is being used to evaluate a number of acoustic array geometries.

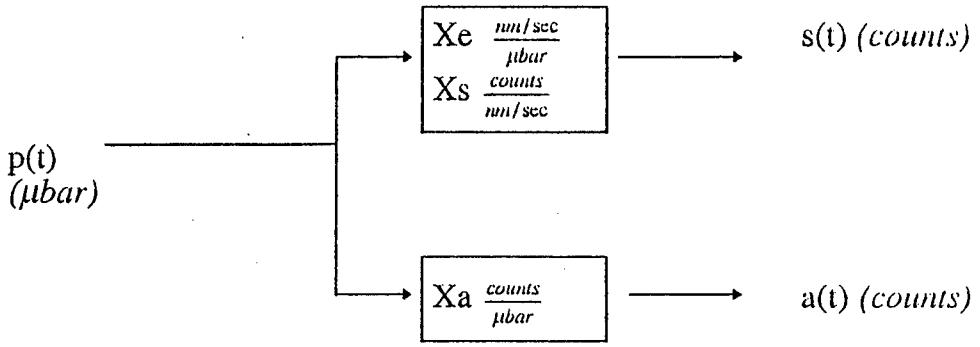

Figure 9

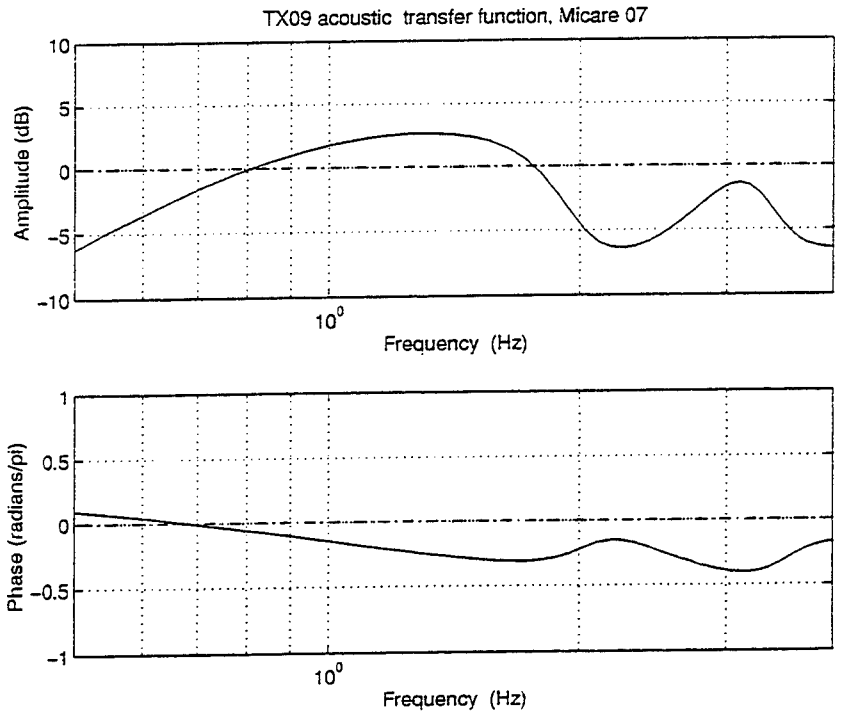

Figure 10

Conclusions and Recommendations

The use of seismic, acoustic and seismo-acoustic detections has been clearly established as a means of positively identifying surface and vented underground explosions. These identified events then become part of a ground-truth data base. This procedure can be used at collocated seismic and acoustic arrays that detect explosions m_b 2.5 or larger from regional sources.

Work now in progress includes:
Pipe array design studies
Evolution of the use of the pure-state filter
Seismo-acoustic detector algorithms
Development of a ground-truth data base for TXAR.

Attenuation at GSETT-3 Stations and the Lg/P Discriminant

Richard D. Jenkins, Thomas J. Sereno, Donna J. Williams, and Aaron A. Velasco
Science Applications International Corporation
10260 Campus Point Drive
San Diego, California 92121

Contract No. F19628-95-C-0097
Sponsored by U.S. Department of Energy

ABSTRACT

Recent studies have shown that the high-frequency Lg/P ratio can be an effective discriminant at regional distances. However, this ratio must be recalibrated for each new source region. We will derive regional wave attenuation models for up to 10 subnetworks of the International Data Center (IDC) primary network, and use them to evaluate the transportability of the Lg/P discriminant to uncalibrated regions.

We use the Detection and Feature Extraction (`DFX`) program at the IDC to make frequency-dependent amplitude measurements of regional phases in the time- or frequency-domain. We use a 10-s window based on the observed arrival time for Pn, Pg and Sn. A group velocity window from 3.0 to 3.6 km/s is used for Lg. Time-domain measurements are made on coherent and incoherent beams for arrays and on the vertical for 3-component stations in seven overlapping frequency bands. We developed a new program called `AmpInv` that inverts these amplitudes for attenuation and source models. `AmpInv` will be used to develop path corrections for regional phases using data from the Group of Scientific Experts Third Technical Test, called GSETT-3. Fourteen IDC subnetworks have been identified, of which we will select ten based on the amount of data that are available and the geologic environment. These subnetworks consist of IDC primary and auxiliary stations within 40 degrees of each other. Five of them are in geologically-stable regions, six are in tectonic regions, and the other three are in a mixture of the two regions. Eleven subnetworks have >200 regional phases in the IDC Reviewed Event Bulletin (REB) between January 1, 1995 and June 1, 1996. In addition, we will use local and regional bulletins (called Gamma Bulletins) contributed by National Data Centers (NDCs) to supplement our data sets in areas with sparse coverage. Many of these events are too small to satisfy the REB event definition criteria. In these cases, we will associate arrivals in the REB with events reported in the Gamma Bulletins.

We developed all software needed for this study, investigated alternative amplitude measures, and compiled a data set for the Australian subnetwork during the first year of this two-year project. During the second year, we will compile the data sets for the other IDC subnetworks, estimate regional wave attenuation using `AmpInv`, and evaluate the accuracy and transportability of the Lg/P discriminant. We will obtain "ground-truth" identification for as many of the events as possible, and we will use knowledge of the local natural and industrial seismicity when this information is not available.

KEY WORDS: Discrimination, Frequency-Dependent Attenuation, Regional Seismicity, Lg/P Ratios, Transportability, Regionalization, Software Development.

OBJECTIVE

Identification of small events is the most difficult technical problem for seismic verification of a Comprehensive Test Ban Treaty (CTBT). Previous empirical studies have shown that the high-frequency Lg/P ratio is one of the most promising discriminants at regional distances [e.g., *Bennett et al.*, 1989; *Baumgardt and Young,* 1990; *Chan et al.,* 1990; *Dysart and Pulli*, 1990; *Baumgardt et al.*, 1992; *Wuster*, 1993]. However, these studies are based on co-located earthquakes and explosions in limited geographic regions, and their results must be recalibrated for each new source region. Our main objective is to develop and apply distance corrections so we can evaluate the transportability of the Lg/P discriminant to uncalibrated regions.

We will develop software to invert frequency-dependent regional wave amplitudes for source and attenuation parameters, and apply it to data from up to 10 stations in the International Data Center (IDC) primary network. The attenuation models will be used as path corrections to the Lg/P discriminant. We will evaluate the identification accuracy of this discriminant at each of the IDC stations and generalize the results in terms of geologic and tectonic environment.

RESEARCH ACCOMPLISHED

This report summarizes our progress in the first year of this two-year project. More detail is provided in our annual report [*Jenkins et al.*, 1996]. We began compiling data sets for our attenuation study and to develop software for measuring amplitudes and inverting them for attenuation and source parameters. We have not yet derived attenuation models or evaluated the accuracy of the Lg/P discriminant. However, we have developed procedures which we will follow to accomplish these tasks.

Data Sets

The prototype IDC at the Center for Monitoring Research (CMR) in Arlington, Virginia, supports the Group of Scientific Experts Third Technical Test called GSETT-3 (for an overview of GSETT-3, see *Kerr* [1993]). The final analyst-reviewed results are maintained in the Reviewed Event Bulletin (REB). This bulletin currently includes over 31,000 events and will be the primary source of data for this study. We require event, arrival, and waveform data to calculate the attenuation models. In addition, the IDC also maintains a database of small, local events reported by National Data Centers (NDCs) in what is called the Gamma Bulletin. We use events in this bulletin to supplement our REB data set in areas of sparse coverage. The Gamma Bulletin may also be used to provide "ground-truth" since most of the events are identified by the contributing NDC. This ground-truth identification is needed to evaluate the accuracy of the Lg/P discriminant. We may consider other event bulletins such as the Preliminary Determination of Epicenters (PDE) bulletin produced by the United States Geological Survey (USGS) as needed.

Station Selection. Our goal is to select up to 10 IDC primary stations in a variety of tectonic environments as shown in Figure 1. For the purposes of this study, we combine Cenozoic Continental, Paleozoic and Mesozoic, Proterozoic, and Archean into a single "stable" category and consider this and "tectonic" as our only categories of interest. Most IDC primary stations have other primary and auxiliary stations in close proximity. We give preference to these stations since events recorded at multiple stations improve the resolution of the attenuation model. For this reason, we form subnetworks of primary and auxiliary stations. We group primary and auxiliary

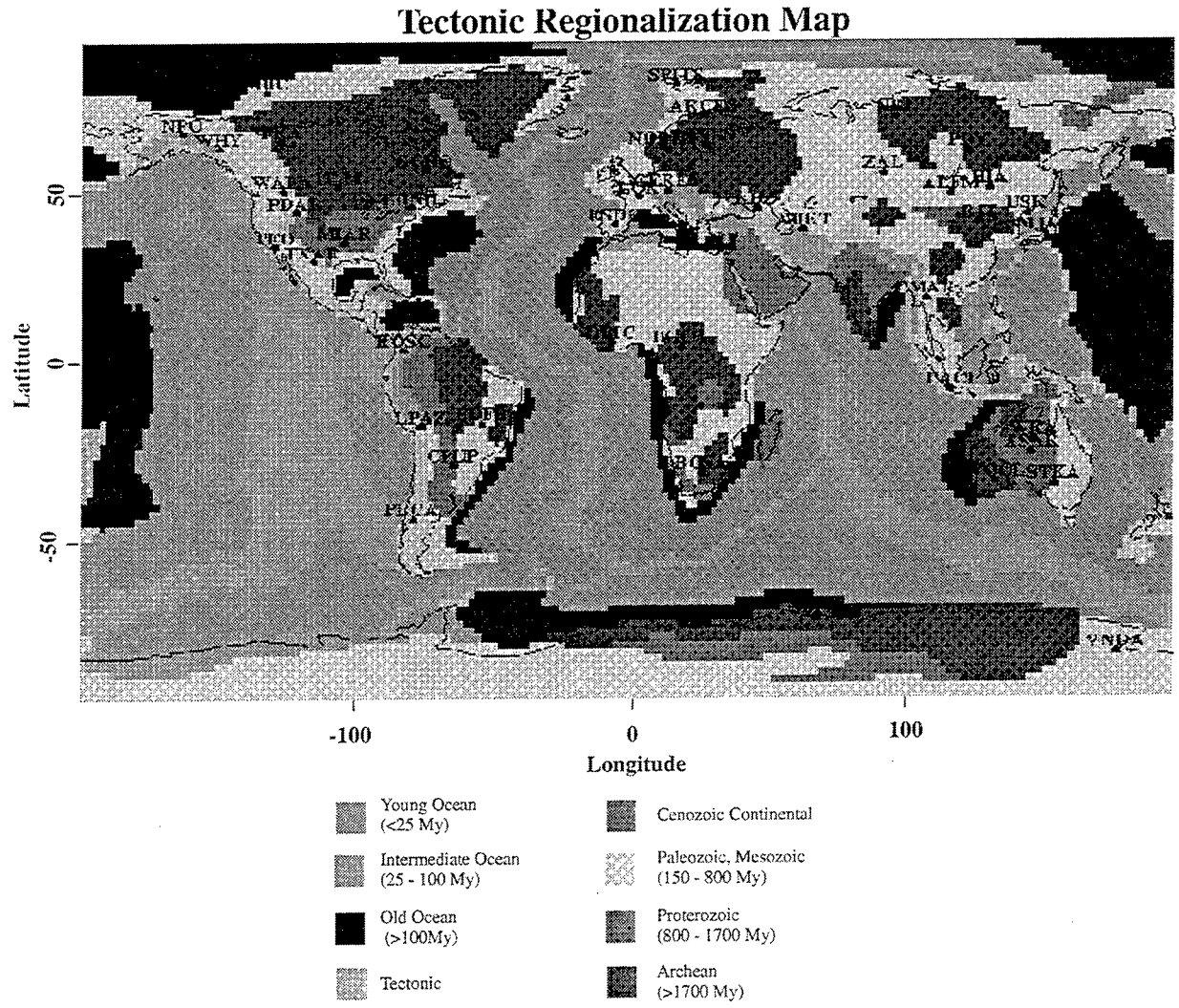

Figure 1. Tectonic regionalization map showing locations of current IDC primary stations. This tectonic map is based on a 2° by 2° grid provided by *O. Gudmundsson* of the Australian National University [personal communication].

stations into subnetworks if they are within 40° of each other. We query the REB database for regional arrivals (e.g., Pn, Pg, Sn, Lg) for each subnetwork subject to the following constraints: time period of January 1, 1995 to June 1, 1996, distance less than 20°, and depth less than 40 km. Our main criteria for selecting the 10 subnetworks is quantity of regional phases available in the REB, the number of events recorded by multiple stations (shared events), and the tectonic environments (i.e., either stable or tectonic). We compiled a list of 14 possible subnetworks of which we will choose 10. The number of Pn, Pg, Sn, and Lg arrivals in the REB, total number of multiple-station events, the tectonic environment, and IDC station labels are summarized in Table 1 for each subnetwork.

The first five subnetworks are located in tectonically-active regions. Some networks (e.g., Alaska/ Northwestern Canada, Central Africa, and South America) contain stations mixed in both stable and tectonic regions. Of course, many of the events recorded by the subnetworks in stable regions occur in tectonic zones. For example, most of the events recorded by the Australian subnetwork

are from events in subduction zones to the north. However, the regional paths are primarily through stable continental material. This is discussed in more detail below.

Table 1: SubNetworks of IDC Primary and Auxiliary Stations.

SubNetwork	Pn	Pg	Sn	Lg	Shared Events	Tectonic Name	Stations
E. Caucasus/Hindu Kush/ E. Med. Sea	209	24	60	29	14	Tectonic	ABKT, KBZ, KVAR, NIL, BGIO
Pacific Rim	1299	60	402	93	240	Tectonic	MJAR, OGS, TSK
Spain	273	23	62	67	60	Tectonic	ESDC, PAB
Thailand	265	86	23	84	278	Tectonic	CMAR
Western USA	1150	334	227	502	267	Tectonic	PDAR, PFO, WALA, BBB, DUG, EDM, ELK, MNV, NEW, PGC, PMB, PNT, RSSD, TUC
Alaska/NW Canada	1315	154	440	438	285	Mixed	WHY, YKA, NPO, MBC, DAWY, DLBC, INK
Central Africa	53	1	29	12	30	Mixed	BGCA, DBIC, AAE
South America	642	12	105	70	175	Mixed	BDFB, CPUP, LPAZ, PLCA, ROSC
Antarctica	39	0	22	9	19	Stable	MAW, VNDA, CSY
Australia	3683	75	2064	339	1028	Stable	ASAR, STKA, WOOL, WRA, ARMA, CTA, FITZ, FORT, MEEK, NWAO, QIS, RMQ, TOO, WARB, YOU
Central Asia	197	21	71	84	19	Stable	ALFM, BJT, HIA, NRI, PDY, ZAL, ARU, ULN, USK
North America Shield	452	34	159	159	54	Stable	LBNH, SCHQ, ULM, DRLN, EEO, EYMN, FCC, FRB, GAC, LMN, LMQ, RES, SADO, TBO
South Africa	48	15	31	38	9	Stable	BOSA, LSZ, TSUM
Southern USA	551	60	75	190	133	Stable	MIAR, TXAR, ALQ, TKL, TUL

Waveform Data Selection. Waveform data are obtained from the IDC primary and auxiliary stations for arrivals associated with events in the REB. Supplemental data are selected for arrivals that we predict are associated with events in the Gamma Bulletin. Most of these events are too small to be reported in the REB because of the strict event-confirmation criteria used during GSETT-3. However, these additional events may be valuable for filling in areas of sparse coverage. We use the exhaustive grid-search technique called the Global Association (GA) System of *Le Bras et al.* [1994] to associate signals at IDC primary and auxiliary stations with events in the Gamma Bulletin.

To assess the distribution of each data set, we plot ray-paths for regional phases recorded by stations in the subnetwork. As an example, Figure 2 shows Pn and Lg ray-paths for our Australian subnetwork. We use these maps to evaluate whether or not we need to add or subtract data to obtain adequate coverage of a region. In this example, there are many more Pn phases from events originating in the Java Trench to the north than from events to the south or east. We may want to remove some or all of the Java Trench events to avoid biasing our results for paths from that source region. One approach would be to only use data from Java Trench events with high signal-to-noise ratio. Alternately, we may omit events from the Java Trench so that our attenuation estimates are made solely from events within the continent of Australia. We will evaluate which strategy is most effective.

(a)

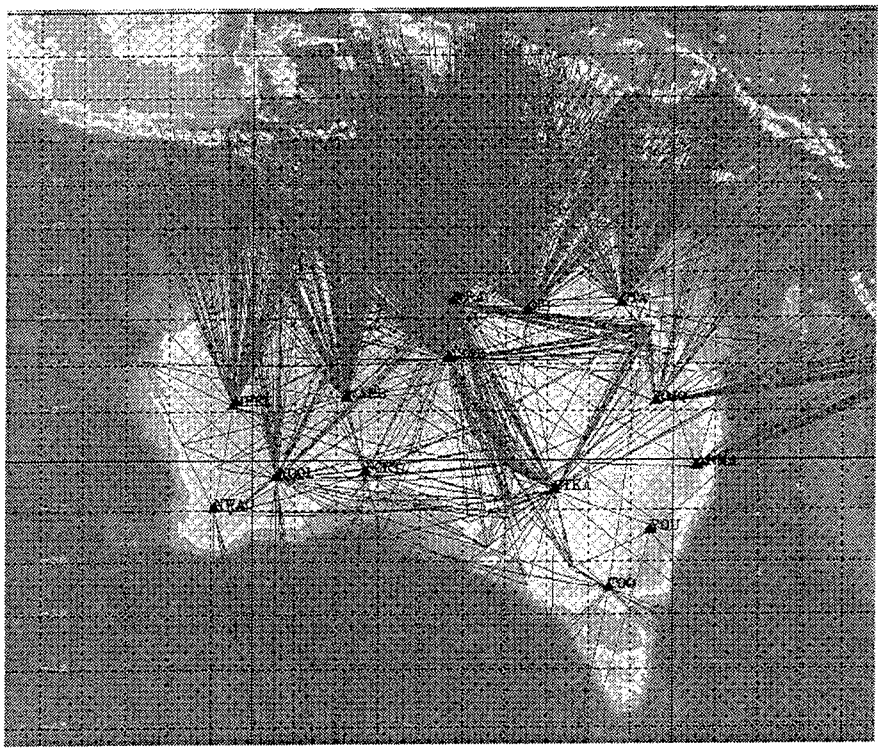

(b)

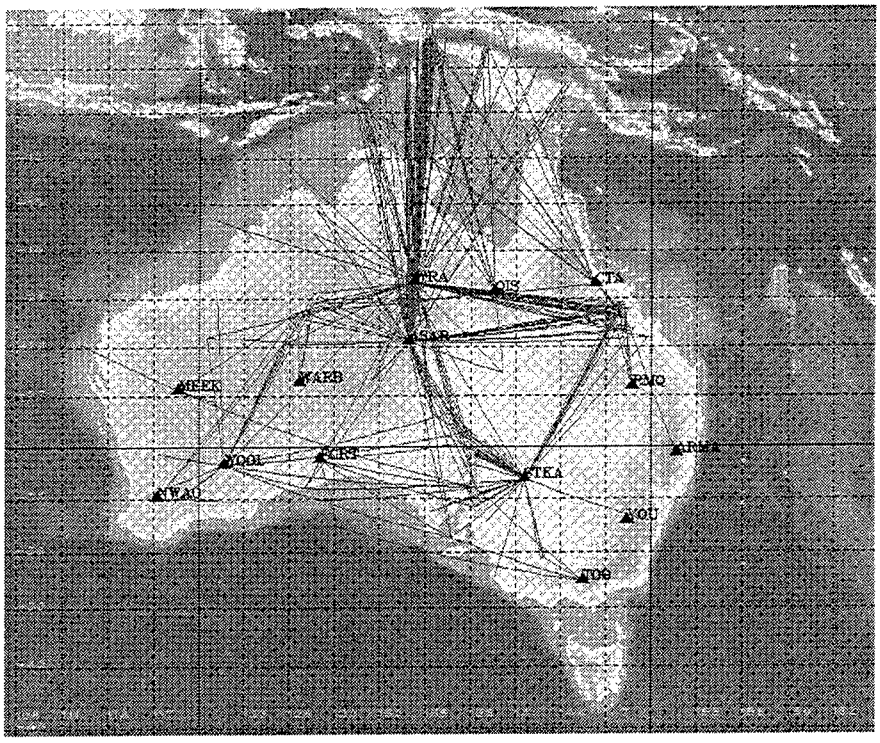

Figure 2. Example from the Australian subnetwork showing regional events recorded by IDC primary and auxiliary stations as reported in the Reviewed Event Bulletin. This data set covers the time period of January 1, 1995 to June 1, 1996. Many more regional phases come from events to the north than from events to the south or east. (a) Pn ray-paths and (b) Lg ray-paths.

Attenuation Models

We plan to estimate attenuation models for up to 10 subnetworks of IDC primary stations. Here, we outline our procedures for selecting a preferred amplitude measurement type and determining attenuation models for each subnetwork.

We started development of software to invert frequency-dependent regional wave amplitudes for attenuation models. Figure 3 shows the major software components. `DFX` was developed for the International Data Center (IDC) to perform seismic signal detection and feature extraction [*Wahl*, 1996]. It will be used in this study to compute frequency-dependent regional wave amplitudes in the time and frequency domains. `AmpInv` is a new program being developed under this contract to invert regional wave amplitudes for attenuation models.

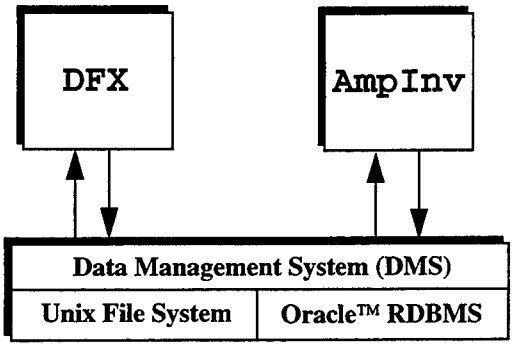

Figure 3. `DFX` and `AmpInv` are the two major software components for this project. Both programs interface with the IDC's Data Management System.

Amplitude Measurements. We evaluate the consistency and robustness of several types of automated amplitude measurements for regional phases. We investigate three types of time-domain amplitude measurements. These are root mean-square (*rms*), short-term average (*stav*), and the average absolute amplitude in the time window after removing the *rms*. These measurements are made on both coherent and incoherent beams in up to seven overlapping frequency bands (each one octave wide) from 0.5 Hz to 16.0 Hz. For both 3-component and array stations, measurements will be made on vertical data channels but we may evaluate other channels as well (e.g, radial, transverse, and combined horizontal). We also make frequency-domain measurements from amplitude spectra. For array stations, the spectra will be array-averaged. The same time window is used for frequency- and time-domain amplitude measurements. Amplitude measurements for the preceeding noise are made so that the quality of the signal can be evaluated before it is used in the inversion. We evaluate the different amplitude measures by comparing the variance with respect to our derived attenuation models. Our preferred amplitude measurement for each phase is the one with the lowest variance.

We compute the time-domain measurements discussed above using 10-second signal windows for Pn, Pg, and Sn starting 0.3 seconds before the analyst-verified onset time in the REB. A group velocity window of 3.0-3.6 km/sec is used for Lg. Noise windows are 5.0 seconds and start 5.5 seconds prior to the signal window. Figure 4*a* shows a regional seismogram recorded by the Alice Springs array (ASAR) in Australia for an M_L=3.6 event in south-central Australia at a distance of about 500 km. The analyst-reviewed onset times are superimposed. The group velocity window for Lg is based on epicentral distance and an estimate of the event origin time. Figure 4*b* shows that this time window captures the analyst-reviewed Lg onset time most of the time. It shows

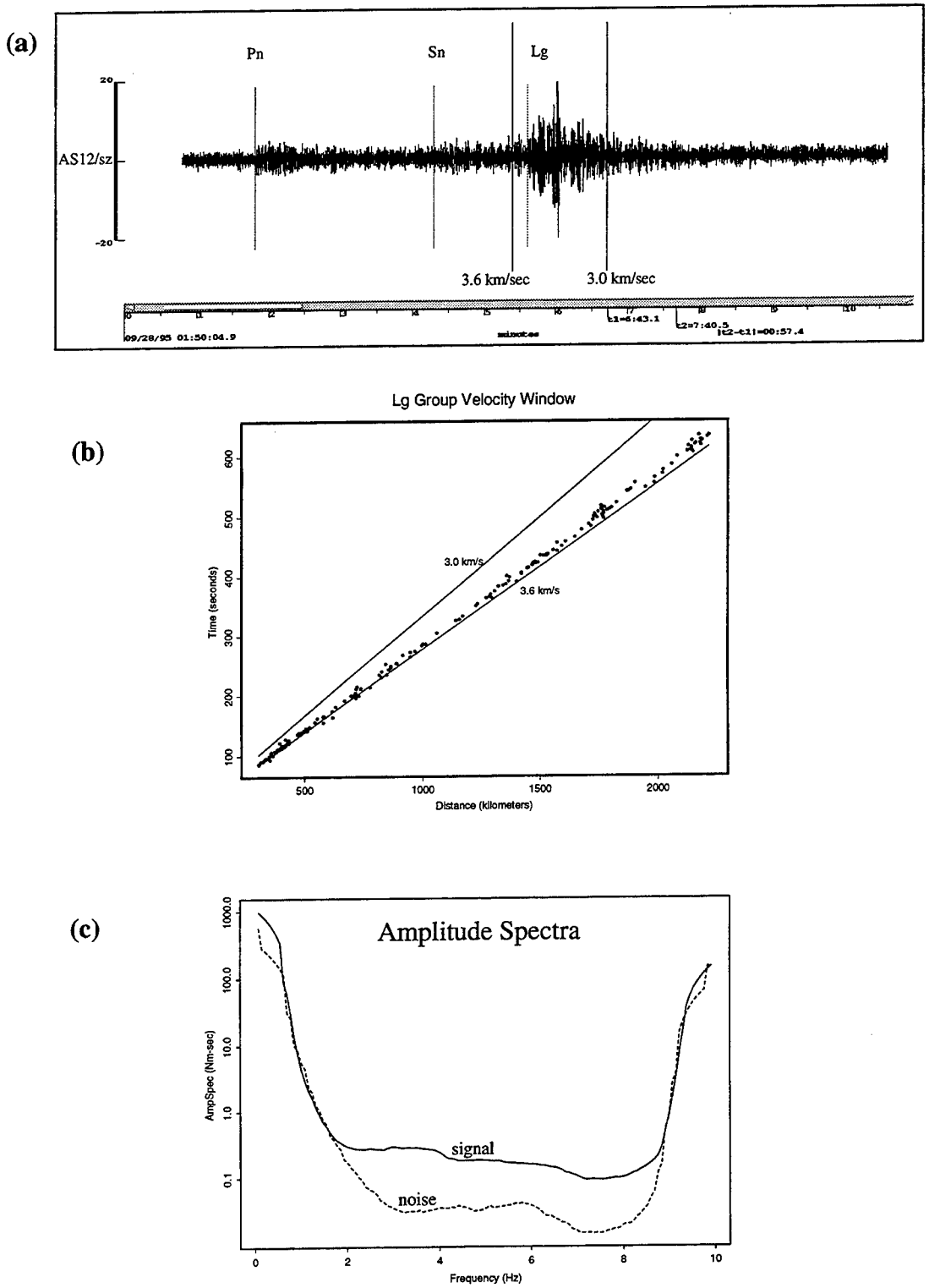

Figure 4. (a) Example of waveform from one of the elements of the ASAR array. The majority of the Lg energy is included in the 3.0-3.6 km/s group velocity window. (b) Arrival times for 210 Lg phases in the IDC database recorded by stations in Australia. Most arrivals are included in the 3.0-3.6 km/s group velocity window. (c) Signal and noise amplitude spectra for the Pn arrival shown in (a).

arrival times for 210 Lg arrivals recorded by stations in Australia. Amplitude spectra are computed using the same time windows as those used for time-domain measurements. Figure 4*c* shows smoothed and instrument-corrected signal and noise spectra for the Pn arrival in Figure 4*a*. We use these spectra to determine which frequencies to include in the inversion.

We have computed approximately 6000 amplitude measurements for regional phases recorded at Australian stations. These measurements are stored in an Oracle database and will be used to evaluate the amplitude measurement types.

Amplitude Inversion. Our parameterization and inversion method are described in detail by *Sereno* [1990]. Briefly, the frequency-dependent (either time-domain or spectral) amplitude of the *kth* wave recorded at the *ith* station from the *jth* source is parameterized as:

$$\log A_{ijk}(f) = \log A^0_{jk}(f) + B_k(\Delta_{ij}, \Delta_0, f) + \delta_{ik} \quad (1)$$

where $A^0_{jk}(f)$ is the amplitude at a reference distance Δ_0, $B_k(\Delta_{ij}, \Delta_0, f)$ is the attenuation from the reference distance to the epicentral distance Δ_{ij}, and δ_{ik} is a station correction. The amplitude at the reference distance is expressed in terms of the material properties at the source and the receiver, source parameters such as the seismic moment, the shape of the source spectrum, and a wave-dependent excitation factor. We use the *Mueller and Murphy* [1971] and *Brune* [1970, 1971] models to parameterize the shape of the source function.

The attenuation is parameterized in terms of a power-law distance dependence with a frequency-dependent exponent:

$$B_k(\Delta_{ij}, \Delta_0, f) = -\log e \cdot \alpha^0_k \cdot f + n_k(f) \cdot \log(\Delta_0/\Delta_{jk}) \quad (2)$$

where the first term accounts for anelastic attenuation from the source to the reference distance, and the second term is the total attenuation from the reference distance to the epicentral distance. The total attenuation includes geometrical spreading, scattering and anelasticity. It is difficult to separate these terms since the geometrical spreading of regional phases is a complicated function of the crustal and upper mantle velocity structure [e.g., *Sereno and Given*, 1990]. Fortunately, it is not important to separate these terms for application to the Lg/P discriminant. The exponent, $n_k(f)$, is parameterized as a linear function of frequency.

The system of equations governing the relationship between the data (log amplitudes) and model parameters is formulated by subtracting theoretical data computed from an assumed starting model from the observed data, and solving iteratively for the model perturbations that minimize the data residuals in the least-squares sense.

Our new software called `AmpInv` is being written in the C language, and is summarized in Figure 5. Several parameters including the database account, signal-to-noise ratio thresholds, phase-dependent frequency limits, a starting model and other parameters that control `AmpInv` are set by the user in a ASCII parameter (or par) file. Event and amplitude information are obtained directly from the IDC Data Management System or DMS. This new software may invert any amplitude measurement type stored in the IDC database. This includes time-domain measurements stored in the *arrivalamp* table or frequency-domain (i.e. amplitude spectra) measurements indexed in the *fsdisc* table [*Swanger et al.*, 1993]. Synthetic amplitudes may optionally be generated for testing purposes or for evaluating parameter resolution. Only data that satisfies user-specified constraints on signal-to-noise ratio are included in the inversion. An iterative approach using a singular value

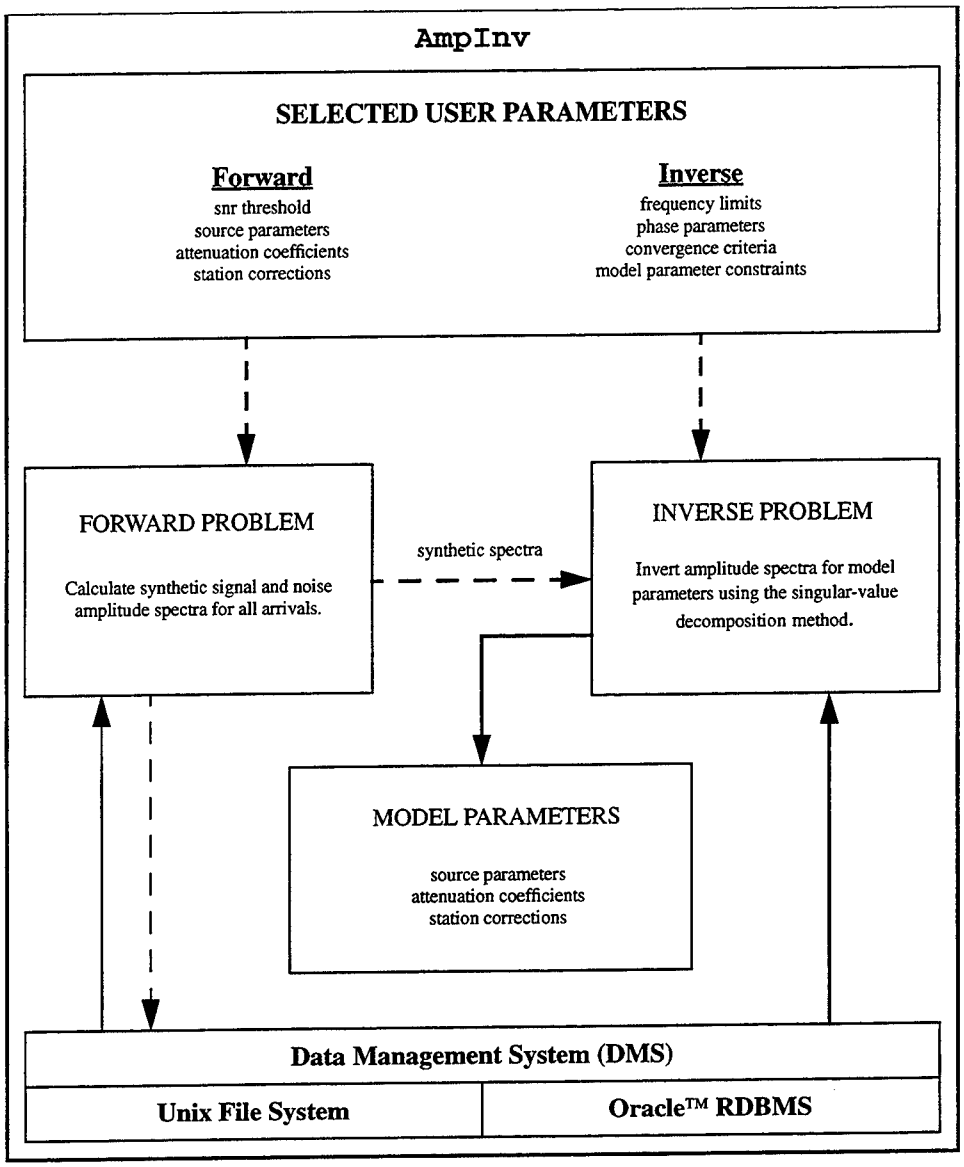

Figure 5. Flow chart for the `AmpInv` program. `AmpInv` will invert regional wave amplitude spectra for source and attenuation parameters. It will also generate synthetic amplitude spectra by solving the forward problem. Dashed lines represent switches which may be turned on/off. `AmpInv` will interface with the DMS.

decomposition (SVD) method is used to estimate source and attenuation parameters. Our convergence criteria include the maximum number of iterations, the condition number of the singular values matrix, and the variance between the observed and predicted data. The new model parameters are written to an output model file.

CONCLUSIONS AND RECOMMENDATIONS

We have completed nearly all of the software development needed for this project. During the next year we will finish compiling our data sets, estimate frequency-dependent attenuation for IDC subnetworks, and evaluate the accuracy and transportability of the Lg/P discriminant.

REFERENCES

Baumgardt, D., and G. Young, Regional seismic waveform discriminants and case-based event identification using regional arrays, *Bull. Seismol. Soc. Am., 80*, 1874-1892, 1990.

Baumgardt, D., J. Carney, M. Maxson and S. Carter, Evaluation of regional seismic discriminants using the Intelligent Seismic Event Identification System, *Tech. Rep. SAS-TR-93-38*, ENSCO, Inc., Springfield, Virginia, 96 pp., 1992.

Bennett, J., B. Barker, K. McLaughlin, and J. Murphy, Regional discrimination of quarry blasts, earthquakes, and underground nuclear explosions, *Final Rep. GL-TR-89-0114*, 146 pp., 1989. ADA223148

Brune, J., Tectonic stress and the spectra of seismic shear waves from earthquakes, *J. Geophys. Res., 75*, 4997-5009, 1970.

Brune, J., Correction to tectonic stress and the spectra of seismic shear waves from earthquakes, *J. Geophys. Res., 76*, 5002, 1971.

Chan, W., R. Baumstark, and R. Cessaro, Spectral discrimination between explosions and earthquakes in central Eurasia, *Tech. Rep. GL-TR-90-0217*, 38 pp., 1990., ADA230048

Dysart, P., and J. Pulli, Regional seismic event classification at the NORESS array: seismological measurements and the use of trained neural networks, *Bull. Seismol. Soc. Am., 80*, 1910-1933, 1990.

Jenkins, R.D., A. Velasco, D.J. Williams, and T.J. Sereno, Procedures for Estimating Attenuation at GSETT-3 Stations and Evaluating the Lg/P Discriminant, *Tech. Rep. SAIC-96/1137,* Science Applications International Corporation, July 1996.

Kerr, A. (ed.), Overview GSETT-3, Report prepared by the *GSE Working Group on Planning*, 9 pp., October, 1993.

Le Bras, R., H. Swanger, T. Sereno, G.Beall, R. Jenkins, and W. Nagy, Global Association Design Document and User's Manual, *Tech. Rep. SAIC-94/1142*, SAIC, 67 pp., 1994.

Mueller, R. and J. Murphy, Seismic characteristics of underground nuclear detonations, *Bull. Seismol. Soc. Am., 61*, 1675-1692, 1971.

Sereno, T.J., Attenuation of regional seismic phases in Fennoscandia and estimates of arrival time and azimuth uncertainty using data recorded by regional arrays, *Tech. Rep. SAIC-90/1472,* Science Applications International Corporation, 115 pp., 1990.

Sereno,T.J., and J. Given, Pn attenuation for a spherically symmetric earth model, *Geophys. Res. Lett., 17*, 1141-1144, 1990.

Swanger, H., J. Anderson, T.J. Sereno, Jr., J. Given, D. Williams, IMS Extensions to the Center Version 3 Database (Rev. 1), *Tech. Rep. SAIC-93/1123,* SAIC, 103 pp.,August 27, 1993.

Wahl, D., Programmer's Guide for the Detection and Feature Extraction Program (DFX), *Tech. Rep. SAIC-96/1069,* Science Applications International Corporation, 77 pp., April 1996.

Wuster, J., Discrimination of chemical explosions and earthquakes in central Europe - a case study, *Bull. Seismol. Soc. Am., 83*, 1184-1212, 1993.

DISCRIMINATION OF EARTHQUAKES AND EXPLOSIONS USING THREE-COMPONENT REGIONAL RECORDS CORRECTED FOR THE FREE SURFACE EFFECT

W.-Y. Kim, A. Lerner-Lam[1] and P. Richards[1]
Lamont-Doherty Earth Observatory of Columbia University, Palisades, NY 10964
([1] also, Department of Earth and Environmental Sciences, Columbia University)

F49620-95-1-0026

Sponsored by AFOSR

ABSTRACT

High-frequency regional records from small earthquakes (magnitude < 4.5), and comparable magnitude chemical explosions, are analyzed to find a reliable seismic discriminant in southern Russia near Kislovodsk. The digital, three-component seismograms recorded during 1992 by the Caucasus Network operated by Lamont-Doherty Earth Observatory since 1991 in the distance ranges 15 to 272 km are used. Mean vertical-component *Pg/Lg* spectral amplitude ratios in the band 8 – 18 Hz are about 1.3 and 3.2 for earthquakes and explosions, respectively, in this region. These ratios are much higher than those observed in tectonically stable eastern U. S. where Kim et al. (1993) reported the mean *Pg/Lg* ratios of 0.5 and 1.25 for earthquakes and explosions, respectively in the similar high frequency band. We find that the vertical-component *Pg/Lg* spectral ratio in the frequency band 8 – 18 Hz serves quite well for classifying these events. A linear discriminant function analysis indicates that the *Pg/Lg* spectral ratio method provides discrimination power with a total misclassification probability of about 7.1%.

The *Pg/Lg* spectral ratios of rotated, three-component regional records improve the discrimination power of the spectral ratio method over the vertical-component *Pg/Lg* ratios. But we find that an even better discriminant is the *Pg/Lg* spectral ratio of the three-component regional records corrected for the free surface effect. In the frequency band 8–18 Hz, the free surface corrected three-component *Pg/Lg* spectral ratio provides discrimination power with a total misclassification probability of only 2.6%. Free surface corrected and network averaged *Pg/Lg* spectral ratios provide transportability of the spectral ratio method to various regions worldwide.

The *Pg/Lg* spectral amplitude ratio method we used is sufficiently reliable and robust that it can be used in discriminating chemical explosions (especially numerous mining and quarry blasts) from small regional earthquakes in the routine analysis of regional earthquake monitoring networks.

Keywords: regional wave propagation, seismic discrimination, Caucasus region

OBJECTIVE

Main objective of this research is to improve our knowledge of seismic sources and structure in central Asia including Iran, Caspian Sea and Caucasus Mountains, by analyzing regional high-frequency signals recorded at IRIS/JSP North Caucasus Network and other regional networks.

Our goals are; 1) to characterize seismic sources in the region and to evaluate reliable seismic discriminants, and 2) to determine crust and uppermost mantle velocity structure beneath the Caucasus Network and to locate accurately small events in the region.

Results of our work assist in the identification of seismic events at regional distances for CTBT monitoring.

RESEARCH ACCOMPLISHED

The discrimination of small earthquakes from large chemical explosions (from mines and quarries) based on seismic signals recorded at regional distances (10 – 1000 km) is an important issue facing numerous regional seismic networks. The seismic discrimination problem becomes especially severe in an area with poorly known seismicity such as southern Russia near Kislovodsk. It would be extremely useful to have a reliable and robust criterion that could be used to discriminate earthquakes from explosions in the context of global seismic monitoring.

Most of the previous work on seismic discrimination has focused on separating large underground nuclear explosions from earthquakes in the context of a future comprehensive test ban (e.g., Evernden et al., 1986; Taylor et al., 1989). In most earlier studies, data available for discrimination analyses were limited to frequencies below 10 Hz, and previous work on regional signals from earthquakes and explosions in the western U.S. suggested that *P* and *S* waves from earthquakes often had stronger high frequencies (that is, up to 10 Hz), than signals from explosions (e.g., Bennett & Murphy, 1986; Chael, 1988). There do not appear to be any robust discriminants based upon regional data for small events in the passband below 10 Hz. However, at significantly higher frequencies, the *Pg/Lg* spectral ratio shows great promise. Thus, Kim et al. (1993) reported that the mean *Pg/Lg* spectral ratios in the band 1 – 25 Hz are about 0.5 and 1.25 for earthquakes and explosions, respectively, in the eastern U. S. ($\Delta \approx 10$ - 610 km). Further, they found that the high-frequency *Pg/Lg* spectral amplitude ratio in the frequency band 5 – 25 Hz was an adequate discriminant for classifying these events. In the eastern U. S., the *Pg/Lg* spectral amplitude ratio method provides discrimination power with a total misclassification probability of about 1% (Kim et al., 1993).

In this paper, we report our findings of a robust discriminant for earthquakes and explosions in southern Russia. Figure 1 depicts the Caucasus Network operated during November 1991 - summer of 1994 by Lamont-Doherty Earth Observatory under the IRIS/Joint Seismic Program. The network consists of six stations around Kislovodsk in southern Russia. The network was deployed to record seismic events in the region to study wave propagation beneath the Caucasus mountains in particular and southern Russia and the Middle East in general. The region covered by the network includes areas that differ greatly in their attenuation properties, as previously known from WWSSN stations south of the Caucasus (e.g., Kadinsky-Cade et al., 1981). The network has also provided abundant high-frequency signals from small events, both natural and manmade. Within a degree of the center of the network, over half of the events recorded can be associated with active quarries, or roughly 150 events per year. These data are useful for characterizing discriminants of chemical explosions from earthquakes, a critical issue facing a proposed Comprehensive Test Ban Treaty (e.g., Stump et al., 1994).

The regional signals from small seismic events in the northern Caucasus region are characterized by *Pg* and *Lg* onset arrivals with group velocities of about 5.8 km/s and 3.2 km/s, respectively at distances of a few tens to about 200 km. This *Lg* group velocity, which is somewhat slower than the global average of 3.4 - 3.5 km/s, indicates lower than normal *S*-wave speeds in the crust around the Caucasus Network. Although spectrograms can provide effective discrimination, their interpretation is usually a matter of expert judgement that cannot obviously be

turned into a simple objective algorithm, applicable on a routine basis to large numbers of events. Our observations of high-frequency (1-25 Hz) regional signals from earthquakes and explosions in southern Russia indicate that high-frequency seismograms show distinctively different patterns in the spectral content of *P* and *S* signals, between earthquakes and explosions. Such high-frequency seismograms suggest that the *Pg/Lg* spectral amplitude ratio can be made the basis of an objective discriminant.

In the following sections, we report our measurements of the *Pg/Lg* spectral amplitude ratio, using high-frequency digital seismograms from earthquakes and chemical explosions recorded by the Caucasus Network (Figure 1); and we evaluate their discrimination capability, paying particular attention to the improvements attainable with three-component records, as compared to conventional *Pg/Lg* spectral ratios based only on vertical-component data.

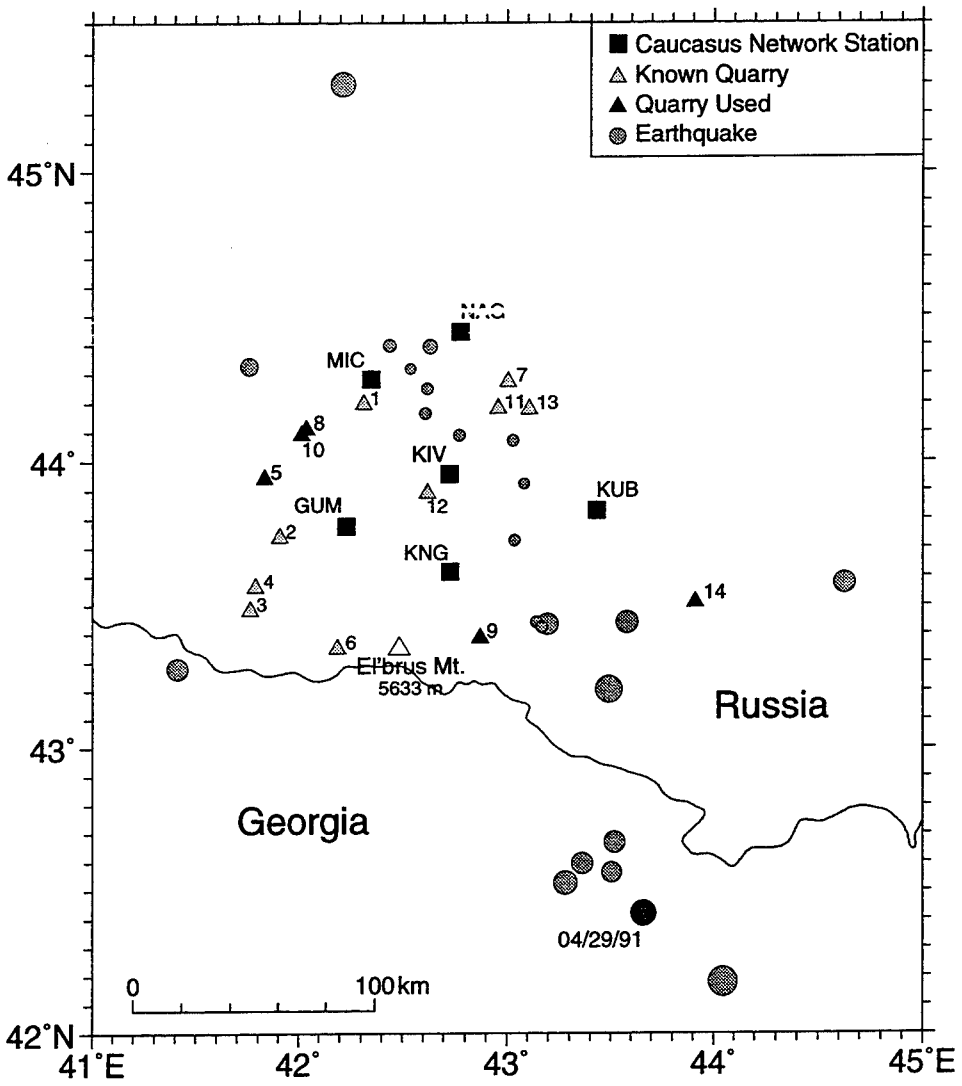

Fig. 1. Locations of earthquakes (*solid circles*), mines and quarries identified and used in this study (*solid triangles*), other known quarries (*open triangles*) and Caucasus Network stations (*shaded squares*). Circle size is proportional to the magnitude of the earthquakes.

Applications of Discriminant Analysis

We present the analysis of digital seismograms from 25 explosions (presumably quarry blasts) and 25 earthquakes to obtain a specific discriminant. Most of the earthquakes are in the magnitude range 1 to 4 and are reported by the Joint Seismic Program Center (JSPC) or the U.S. Geological Survey (PDE). All quarry blasts are from three known quarry sites. Locations of mines and quarries in the region are depicted in Figure 1. Accurate locations of the Tyrnauz mine in the south of the network (Stump et al., 1994) as well as other mines and quarries are obtained from a map provided by V. Khalturin (personal comm., March 1994). Only explosions for which we had information about the blast characteristics or events whose signals were clearly identified as quarry blasts are included in the sample data for the explosion group. Distance ranges of the data are 15 to 272 km with means of 98 and 74 km for earthquakes and explosions, respectively.

The *Pg/Lg* spectral amplitude ratios at discrete frequency points are obtained for each record employing the method described in Kim et al. (1993). Network averaged *Pg/Lg* ratios for 25 earthquakes and 25 explosions are then obtained for each event by averaging the discrete frequency values from all stations. Earthquake and explosion populations are well separated in the frequency band 8 to 18 Hz and a sampled version is used in the discrimination analysis.

To test the discriminant power of the high-frequency *Pg/Lg* spectral ratio, we performed multivariate discriminant analysis on $\log_{10}(Pg/Lg)$ spectral ratios for the data set of earthquakes and explosions. Details of the linear discriminant function is given for example, Seber (1984) and Kim et al. (1993).

Network Averaged Vertical-Component Pg/Lg Ratio

The sample data sets consisting of 25 earthquakes and 25 explosions were analyzed using the linear discriminant function. For each event, network averaged vertical-component $\log_{10}(Pg/Lg)$ ratios at frequencies of 8, 10, 12, 14, 16 and 18 Hz are used. Assuming equal prior probabilities for the two groups, we find that three earthquakes and an explosion are classified incorrectly and the misclassification probability is 0.071 and the Mahalanobis D-squared measure is $\Delta^2 = 8.67$. Eearthquake records from various paths in the southern Russia near Kislovodsk have a mean vertical-component *Pg/Lg* spectral ratio of about 1.3, while the explosion records show a mean of about 3.2 in the frequency bands 8 - 18 Hz.

Network Averaged Three-Component Pg/Lg Ratio

The Caucasus Network and many other modern seismograph stations are now equipped with three-component broadband sensors. Although high-frequency regional signals on the vertical-component show reasonable discrimination power for classifying earthquakes from explosions, there is interest in the evaluation of three-component records to see if they can provide improved discrimination. We have therefore examined *Pg/Lg* spectral ratio methods to discriminate the earthquakes from explosions using regional three-component records. Our first approach was simply to rotate the observed NS- and EW-component seismogram pairs to obtain radial (R) and tangential (T) components. Then the *Pg/Lg* ratios of three-component records are formed for each station by defining

$$\frac{Pg}{Lg} = \frac{\sqrt{Pg_Z^2 + Pg_R^2}}{\sqrt{Lg_Z^2 + Lg_R^2 + Lg_T^2}} \qquad (1)$$

where subscripts indicate the component. For example, Pg_Z indicates spectral amplitude of P waves (mostly Pg) on vertical-component (Z), Lg_Z indicates spectral amplitude of Lg waves on radial-component. A single three-component *Pg/Lg* ratio is obtained for each station from eq. (1) and the network mean $\log_{10}(Pg/Lg)$ is obtained by averaging over stations for each event.

The network averaged $\log_{10}(Pg/Lg)$ ratios of the three-component records from the

earthquakes along various paths in southern Russia have a mean three-component *Pg/Lg* spectral ratio of about 0.73, while the explosion records show a mean of about 2.2. These mean *Pg/Lg* ratios are slightly lower, about a factor of 1.6, than the vertical-component data, due mainly to the inclusion of *Lg* waves on radial and tangential components.

We repeated the multivariate analysis using three-component *Pg/Lg* ratios. Discriminant function analyses for the three-component data suggest that the use of three-component records reduces the scatter of the mean $\log_{10}(Pg/Lg)$, particularly for the explosions. The Mahalanobis D-squared measure is $\Delta^2 = 14.07$ indicating a greater separation between earthquake and explosion populations than was the case with vertical-component data. The discriminant function analysis indicates that all events in the sample data are classified correctly and the total misclassification probability is 0.0304, suggesting that the three-component *Pg/Lg* ratios improve the discrimination power of high-frequency regional data by about 4% over the use of single vertical-component *Pg/Lg* ratios (92.9% versus 97.0%).

Removal of Free Surface Effect on Regional Records

Although high-frequency *Pg/Lg* spectral ratios of regional signals on vertical-component records show reasonable discrimination power for classifying earthquakes from explosions – and rotated three-component records are apparently a significant improvement – the success of such discriminants in trial regions does not always warrant their applicability to various other regions world-wide. The key to the successful discrimination of various types of seismic sources is the clear observation of the signals radiated from the seismic sources. One of the most important problems is correction of the effects of the source-receiver paths on observed regional signals. The source-receiver path effects include, for example, attenuation along the paths, different geometrical spreading of *P* and *S* waves, local receiver site responses and interaction of the incoming wave field with the free surface.

The effect of the free surface in the neighborhood of the receiver on the recorded regional signals is significant and its main effects are amplification of incoming waves. However, unlike other path effects, it can be removed by a relatively simple real transformation (House & Boatwright, 1980; and Kennett, 1991). Recently, Kennett (1991) showed that a set of approximate free surface correction operators can be formed to remove the free surface effects over the slowness bands for the main regional phases.

For a *P*-wave, with pulse shape $P(t)$ and particle motion having (x, y, z) components $P(t)$ (sin i, 0, -cos i), incident upon a free surface perpendicular to the z (depth) direction, the motion of the free surface itself is (Aki and Richards, 1980; page 190),

$$\frac{P(t)\left[\frac{4\alpha p}{\beta^2}\frac{\cos i}{\alpha}\frac{\cos j}{\beta}, 0, \frac{-2\alpha}{\beta^2}\frac{\cos i}{\alpha}\left(\frac{1}{\beta^2}-2p^2\right)\right]}{\left(\frac{1}{\beta^2}-2p^2\right)^2+4p^2\frac{\cos i}{\alpha}\frac{\cos j}{\beta}} = [R(t)\ 0, -Z(t)] \qquad (2)$$

where α = surface *P*-wave velocity, β = surface *S*-wave velocity, i = angle of incidence of the *P*-wave, j = angle of incidence of the *S*-wave, p = slowness and $\sin i/\alpha = \sin j/\beta = p$. Note that $Z(t)$ is conventionally measured positive upward, opposite to the depth direction; and $R(t)$ is positive away from the source. The ground motions in a homogeneous half-space for a *P*-wave incident upon a free surface are depicted in Figure 2.

The motion of the incident *P*- and *SV*-wave can then be recovered as a linear combination of the radial, $R(t)$, and vertical, $Z(t)$, components available from three-component records. Thus, equation (2) can be used to show that

$$P(t) = \frac{\cos 2j}{2\cos i} \cdot Z(t) + \frac{\beta}{\alpha}\sin j \cdot R(t). \qquad (3a)$$

The corresponding result for an incident *SV*-wave is

$$SV(t) = \frac{\cos 2j}{2\cos j} \cdot R(t) - \sin j \cdot Z(t), \qquad (3b)$$

which has long been used by those studying earthquake source functions to infer the *S*-wave pulse shape from three-component data (House and Boatwright, 1980). The incident *SH*-wave is simply one half of the recorded tangential-component.

If the incident *P*-wave is contaminated by *SV* motion due to local horizontal layering, then eq (3a) gives precisely the right combination of *R* and *Z* to eliminate the contribution from *SV*. Similarly, eq. (3b) removes contaminating *P* (due to horizontal layering) from the *SV* trace.

An example of three-component records of an explosion from Tyrnauz mine recorded at station MIC (Δ = 108 km) is shown in Figure 3. The rotated seismograms, *Z*, *R* and *T* components, show that *P* waves on the *Z*-component as well as *Lg* waves on the *R*- and *T*-components have comparable amplitudes (Figure 3). However, when free surface effects are removed from the rotated seismograms by successively applying free surface correction operators appropriate for major regional phases (*Pn*, *Pg* and *Lg*), the recovered incident wavevector estimates allow us directly to compare the *P*-, *SV*- and *SH*-wave amplitudes on different traces.

The composite incident wavevector traces in Figure 3 are obtained by applying transformations (3ab) sequentially to successive group velocity windows along the trace. Successive windows used are indicated in Figure 3 with corresponding slownesses. Assuming α = 4.5 km/s and β = 2.6 km/s appropriate for the region, signals in the group velocities greater than 5.2 km/s are transformed with an approximate *Pn* slowness, p = 0.08 s/km ($i \approx 25°$), signals in the group velocities 5.2 - 4 km/s are transformed with an approximate *Pg* slowness, p = 0.14 s/km ($i \approx 40°$) and signals in the group velocities 3.3 - 2.6 km/s are transformed with an approximate *Lg* phase slowness, p = 0.34 s/km ($j \approx 60°$). The *SV* transformation is sensitive to the slowness used, since the free surface correction factor for *R*-component in (3b) varies rapidly for slownesses $1/(\sqrt{2}\beta) < p < 1/\beta$. When the precise slownesses of the incoming waves are not

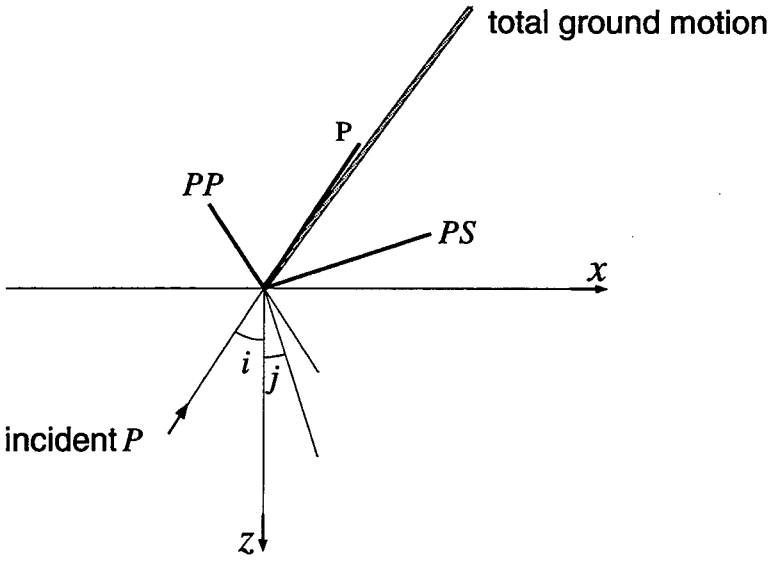

Fig. 2. Sketch of ground motions in a homogeneous half-space for a *P*-wave incident upon a free surface with unit amplitude and an angle of incidence $i \approx 33.37°$ (= 0.1 s/km), surface *P* and *S* velocities: α = 5.5 km/s and β = 3.1 km/s, respectively. The total ground motion of the free surface (*shaded line*) itself is shown above the surface level $z = 0$ and has amplitude 2.03 times the incident wave with an apparent angle of incidence $i' = 36.12°$. Scattered waves *PP* and *PS* which are downgoing waves, are plotted above the level $z = 0$ indicating the directions of true particle motion. The amplitudes of particle motions are indicated by their length.

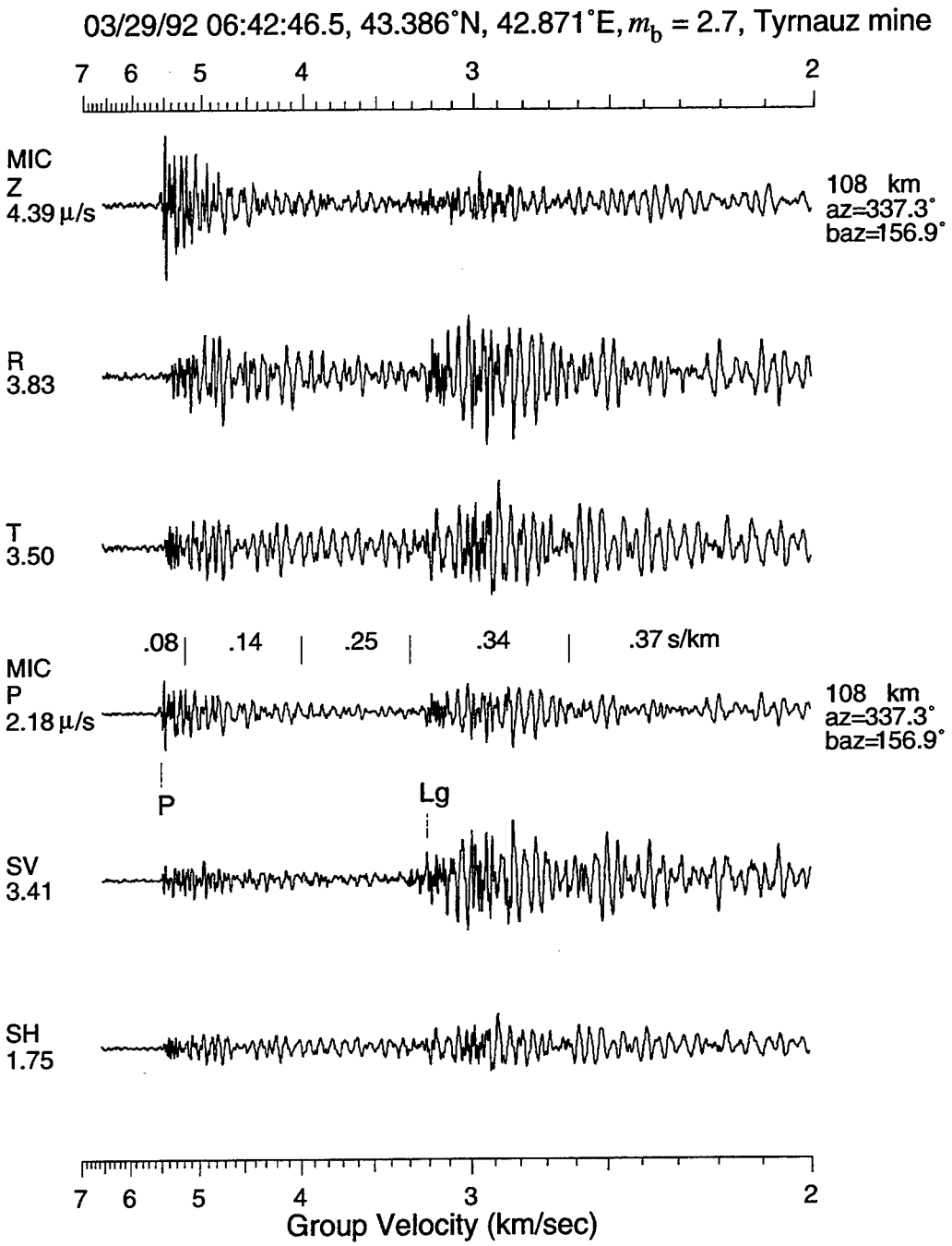

Fig. 3. (*Upper three traces*) Rotated three-component records from an explosion in Tyrnauz mine (*Z*, *R* and *T*). The *P* waves are on the *Z*-component, while *S* waves are dominantly on the *R* and *T* components. (*Lower three traces*) Composite incident wavevector component traces (*P*, *SV* and *SH*) produced by applying free surface correction operators successively along the trace. The breaks between different slowness bands are marked by vertical bars and the slowness (in s/km) used in each group velocity window is indicated. All traces are plotted with the same amplitude scale. Trace peak to peak amplitudes in μ/s are given in each trace.

available for correct transformation, our experience suggests that a reasonable choice of the slowness is when the *P*-wave on the *SV*-trace after the transformation has comparable amplitude to the *P*-wave on the *SH*-trace, since *P* waves on both traces are derived from scattering, for example from heterogenieties other than horizontal layering. Similarly for *Lg* signals from the explosions, a reasonable choice of the slowness is when the *Lg* waves on the *P*-trace are comparable to the *Lg* waves on the *SH*-trace. For the *P*-trace, the Z-component is Hilbert transformed before the transformation (3a) for slownesses greater than $1/\alpha$ (Kennett, 1991).

The composite incident wavevector traces show that indeed the *P* waves are mainly on the *P*-wavevector component, while *S* waves (*Lg*) are dominantly on the *SV*-wavevector component (Figure 3), hence the amplitudes of major crustal phases reveal clearer radiation characteristics from the source. In particular, the relatively small *SH* in the regional *S* waves clearly indicates the signal being generated by an explosion source. A very useful result of the free surface correction is that we can make direct comparison between the *P*-, *SV*- and *SH*-wave amplitude in a particular group velocity window and so get closer to the radiation characteristics from the source. This is of potential significance for discriminating different types of sources and we examine the usefulness of free surface corrected data in the following section.

Network Averaged Free Surface Corrected Three-Component Pg/Lg Ratio

We examined the *Pg/Lg* spectral ratio method to discriminate earthquakes from explosions using the free surface corrected regional three-component records. The *Pg/Lg* ratios from the free surface corrected *P*- and *SV*- and *SH*-seismogram of three-component regional records are obtained for each station by defining

$$\frac{Pg}{Lg} = \frac{Pg_P}{\sqrt{Lg_{SV}^2 + Lg_{SH}^2}} \tag{4}$$

where Pg_P = spectral amplitude of the *P*-wave on the *P*-seismogram, Lg_{SV} = spectral amplitude of the *Lg*-wave on the *SV*-seismogram and Lg_{SH} = spectral amplitude of the *Lg*-wave on the *SH*-seismogram. A single *Pg/Lg* ratio is obtained for each station, and the network mean *Pg/Lg* ratio is obtained by averaging over stations for each event. The separation of the spectral ratios of earthquake and explosion groups appears to be similar to the vertical-component *Pg/Lg* ratios, but the separation between the two groups is greater at high frequencies (10 - 20 Hz).

The sample data sets consisting of 25 earthquakes and 25 explosions were analyzed using the linear discriminant function as in the previous sections. The linear discriminant function that best separates the two types of source yields $\Delta^2 = 15.15$, higher than either of the two values obtained above. Assuming equal prior probabilities for the two groups, and applying the previous classification rule to the earthquake and explosion data, we find that two explosions are classified incorrectly and the total misclassification probability is very low, namely 0.0258.

The discriminant score for each event is plotted in Figure 4 with respect to the network mean free surface corrected $\log_{10}(Pg/Lg)$ spectral amplitude ratio of each event. It is shown in Figure 4 that the earthquake records from various paths in southern Russia have a mean free surface corrected three-component *Pg/Lg* spectral ratio of about 0.32 in the frequencies 8-18 Hz, while the explosion records show a mean of about 1.0. These mean *Pg/Lg* ratios are lower than the vertical-component or three-component data discussed earlier by about a factor 2 to 3 and there is a clearer separation of *Pg/Lg* spectral ratios of the earthquake and explosion populations.

The free surface corrected *Pg/Lg* spectral ratios at frequencies 5 - 20 Hz indicate that for the earthquakes, the radiated seismic amplitudes are partitioned into *P* and *SV-SH* waves with a ratio 1:3, while for the explosions, *P* and *SV* waves have comparable amplitudes. Use of the free surface corrected *Pg/Lg* spectral ratio improves the discrimination power of high-frequency regional data by about 4.5% over the use of single vertical-component ratios (92.9% versus 97.4%).

Discussion and Conclusions

The *Pg/Lg* spectral amplitude ratio using the vertical-component records in the frequency band 8–18 Hz provides discrimination power with a total misclassification probability of about 7.1%. In a lower frequency band, 2-10 Hz, *Pg/Lg* ratios show poor results and the separation between explosions and earthquakes is less clear. The *Pg/Lg* spectral ratios using three-component regional records corrected for the free surface effect improve the discrimination power of the spectral ratio method. In the frequency band 8–18 Hz, the free surface corrected three-component *Pg/Lg* spectral ratio provides discrimination power with a total misclassification probability of only 2.6%.

In case that free surface effects cannot be corrected with confidence, then the *Pg/Lg* spectral ratios of rotated, three-component regional records may be used as a discriminant. The use of rotated three-component records improves the discrimination power of the spectral ratio method over the vertical-component *Pg/Lg* ratios. In the frequency band 8–18 Hz, the three-component *Pg/Lg* spectral ratio provides discrimination power with a total misclassification probability of about 3%.

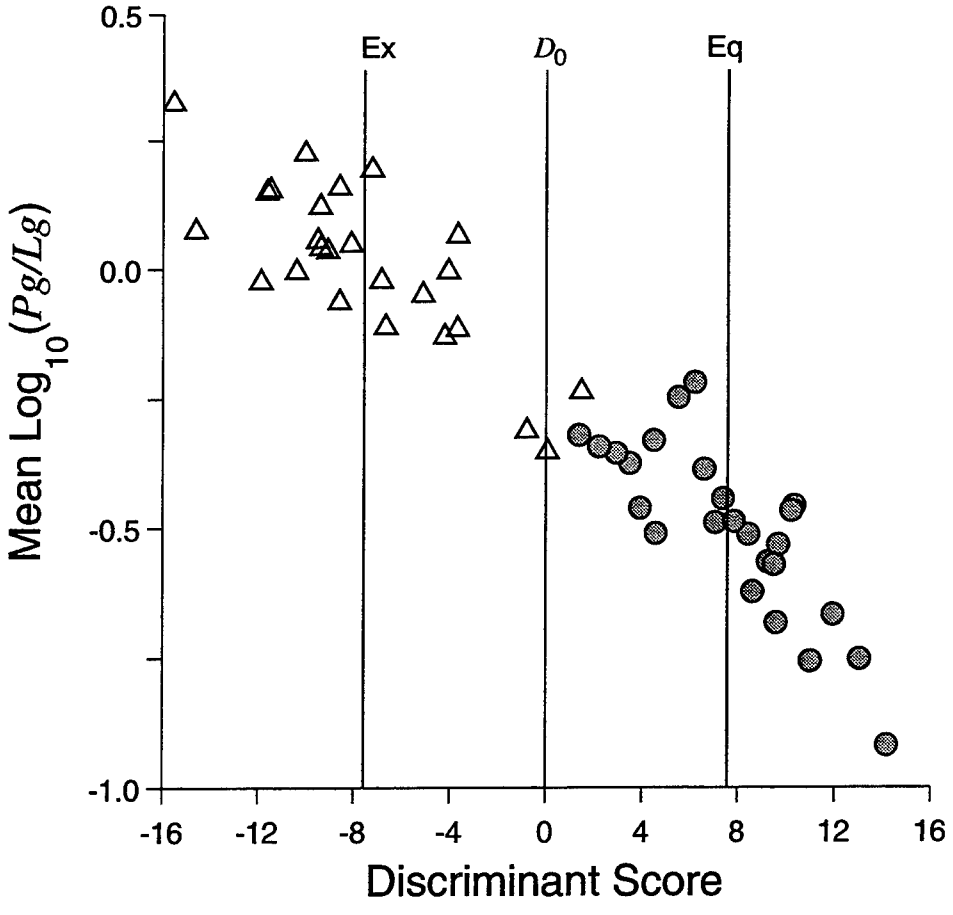

Fig. 4. Discriminant scores of earthquakes (*shaded circles*) and explosions (*triangles*), of the sample data from the free surface corrected three-component records, are plotted with their mean network averaged $\log_{10}(Pg/Lg)$ ratios. Vertical lines denoted as Ex and Eq are the projection of the multivariate mean of the earthquake and explosion population, respectively. The vertical line D_0 is the classification line.

We have shown that the *Pg/Lg* ratio is an adequate discriminant for explosions from earthquakes (magnitude smaller than 4.5) in southern Russia, and that the discrimination is improved by the use of three-component data together with a free surface correction. The stability of the *Pg/Lg* ratio in discriminating multiple-hole, ripple-fired explosions from small regional earthquakes is significant for seismic monitoring in southern Russia. Our results demonstrate the importance of data at frequencies up to at least 20 Hz.

RECOMMENDATIONS AND FUTURE PLANS

A key to the portability of the *Pg/Lg* spectral ratio discriminant to various parts of the world is the correction of regional signals for their source-receiver paths effects. We have shown that the free surface effect can be easily removed from the regional records and the free surface corrected *Pg/Lg* ratios using three-component records improve the discrimination power of the *Pg/Lg* ratio method. Further, the dependence of the frequency content of *P* and *S* waves on specific propagation paths and local structure at the receiver is reduced by using the network averaged *Pg/Lg* ratio.

The area around the Caucasus Network was not an ideal region to make free surface corrections, because of site effects associated with low velocity near-surface layering. Application of the free surface correction to data acquired at a good hard rock site gives better separation of *P*, *SV* and *SH* signals on different traces. For such sites, we would therefore expect even better discrimination performance of the free surface corrected *Pg/Lg* ratio, and we recommend that the method should be applied to various regions for establishing a robust discrimnant for CTBT.

Acknowledgments

Drs. Vitaly Khalturin and Florence Riviére provided us with locations of known quarries in southern Russia. We thank Drs. G. Abers & Danny Harvey for production of catalog used here. Mr. V. Aharonian helped in the vertical-component data analysis.

References

Aki, K. and P. G. Richards (1980). *Quantitative Seismology: Theory and methods*, vol. 1, W. H. Freeman and Co., 1980.

Bennett, T. J. and J. R. Murphy (1986). Analysis of seismic discrimination capabilities using regional data from western United States events, *Bull. Seism. Soc. Am.*, **76**, 1069-1086.

Chael, E. P. (1988). Spectral discrimination of NTS explosions and earthquakes in the southwestern U. S. using high-frequency regional data, *Geophys. Res.Lett.*, **15**, 625-628.

Kadinsky-Cade, K., M. Barazangi, J. Oliver, and B. Isacks (1981). Lateral variations of high-frequency seismic wave propagation at regional distances across the Turkish and Iranian Plateaus, *J. Geophys. Res.*, **86**, 9377-9396.

Evernden, J. F., C. B. Archambeau and E. Cranswick (1986). An evaluation of seismic decoupling and underground nuclear test monitoring using high-frequency seismic data, *Review Geophys.*, *24*, 143-215.

Kennett, B. L. N. (1991). The removal of free surface interactions from three-component seismograms, *Geophys. J. Int.*, **104**, 153-163.

Kim, W. Y., D. W. Simpson and P. G. Richards (1993). Discrimination of regional earthquakes and explosions in eastern United States using high-frequency data, *Geophys. Res. Lett.*, **20**, 1507-1510.

Seber, G. A. F. (1984). *Multivariate Observations*, John Wiley & Sons, Inc., New York, 686pp.

Stump, B. W., F. Riviére-Barvier, I. Chernoby, and K. Koch (1994). Monitoring a Test Ban Treaty presents scientific challenges, *EOS Trans.*, Am. Geophys. Union, **75**, 265-273.

Taylor, S. R., M. D. Denny, E. S. Vergino and R. E. Glaser (1989). Regional discrimination between NTS explosions and western U.S. earthquakes, *Bull. Seism. Soc. Am.*, **79**, 1142-1176.

Study of statistical classification approach to discrimination between weak earthquakes and chemical explosions recorded by Israel local seismic network

A.F. Kushnir, E.V. Troitsky, L.M. Haikin, A. Dainty***
** Moscow IRIS Data Analysis Center/SYNAPSE Science Center; International Institute of Earthquake Prediction Theory and Mathematical Geophysics RAS*
***Phillips Laboratory USAF*

EOARD Special project SPC-95-40-45
Sponsored by AFOSR

ABSTRACT

Discrimination between weak regional or local earthquakes and explosions remains a serious challenge for state-of-the-art CTBT monitoring. In particular, the known fact that discrimination features proved to be efficient in one seismic region are often useless in another region is a serious obstacle for refinement and standardization of source discrimination techniques. Another important unsolved task in seismic discrimination is to estimate the probability of event misclassifications inherent to the seismic region under investigation

In recent years success has been achieved in techniques for discriminating between earthquakes and explosion sources by artificial neural networks. Nevertheless, the potential of the conventional statistical discrimination approach is not exhausted yet. There exist powerful methods for selection of the most informative discrimination features (providing the minimum discrimination errors) from a larger amount of parameters which *a priori* seem to be relevant to the problem. Statistical discrimination theory also possesses a variety of methods for reliable estimation of misclassification probabilities based on learning observations. These methods are not at present used widely in seismic discrimination practice to choose appropriate wavetrain parameters and to ensure the reliability of earthquake-explosion discrimination in a given region.

In this paper we make an attempt to implement the methods mentioned above for discrimination between earthquakes and chemical explosions recorded by Israel local seismic network. A learning set of 28 earthquakes and 25 explosions with magnitudes 1.1–2.6 recorded at distances of 30–200 km. was used for this study. A large number of discrimination parameters based on the relative power spectral distribution of P and S phases was extracted from the event wavetrains and processed by special statistical procedures with the purpose of selecting the most informative features and estimating the probability of discrimination errors. Estimates of the power spectrum of seismic noise at intervals preceding the event wavetrains were used to improve the quality of discrimination feature measurement in conditions of poor signal-to-noise ratio typical for recordings of weak events.

The feature selection procedures allow us to extract by an automatic procedure the 8 most informative features. Implementation of noise refinement and feature selection procedures provides a decrease of misclassification probability (estimated with the help of a statistically consistent cross validation procedure) from 11.5% to 7.5%.

Keywords: Discrimination, Statistics, Feature Selection, Israel.

OBJECTIVE

Automatic discrimination of weak explosions and earthquakes at local distances is an important problem for CTBT monitoring in regions where commercial mining operations and quarry blasting generate a large number of seismic recordings on a daily basis. Development of reliable discrimination techniques to solve this problem involve selection of regionally dependent parameters which have to be automatically extracted from seismograms, and estimation of misclassification probabilities intrinsic for a given region.

RESEARCH ACCOMPLISHED

Description of the processing technique. Two general statistical approaches may be distinguished in the seismic discrimination problem *(Shumway, 1995)*: *waveform discrimination approach*—implementation of the statistically optimal hypothesis testing technique to discrimination between random time series; and *feature extraction-feature discrimination approach*—implementation of adaptive statistical hypothesis testing for discrimination between relevant numerical features extracted from seismograms based on heuristic considerations. In this study we concentrate on the second approach. As the discrimination features in this approach we use various power or spectral characteristics of seismograms that are typically different for earthquakes and explosions. The discrimination problem is solved by application of modern statistical pattern recognition techniques to the feature set. Numerous investigations in discriminate analysis *(Deev, 1970; Levin and Troitsky, 1970; Raudis, 1976; Tsvang et. al., 1993)* demonstrate that selection of a small number of the most informative features is extremely useful in this approach. A few carefully selected features may provide a smaller error classification probability compared to the full set of features. This is the so-called "pick-effect" or "multivariate effect".

Procedure for feature selection. Feature selection is based on processing of learning sets of vectors $x_l(j)$; $l \in 1,2$ is the number of classes; n_l the number of vectors in the learning sets; $j \in 1,n_l$. Initially each vector consists of p features chosen as relevant for a given discrimination problem. The feature selection procedure consists of p steps. At intermediate steps only some $k<p$ features are involved, the $x_l(j)$ are k-dimensional vectors of the features of this step. We use as a base for feature selection a stochastic distance between two k-dimensional probability distributions of learning sets, the Mahalanobis distance

$$D(k)= (m(k,1) - m(k,2))^T S^{-1}(k) (m(k,1) - m(k,2)), \qquad (1.1)$$

where: $m(k,1)$, $m(k,2)$ are the sample mean vectors of the two classes for k features; $S(k)$ is the sample covariance matrix calculated for these features using learning data for the both classes. At the first step of the selection procedure p values of the $D(1)$ functional are calculated for every feature. The maximum from these p values is attained for some $j(1)$ feature which is thus selected. At the second step $p-1$ values of the $D(2)$ functional are calculated for the feature pairs. The first member of every pair is always the previously selected feature $j(1)$, the second member are any rest feature. The second feature is selected as providing a maximum of these $D(2)$ values. At the k-*th* step of the selecting procedure values of the $D(k)$ functional are calculated for a set consisting of $p-k+1$ feature vectors. The first $k-1$ components in these vectors are the features which have been selected at the previous steps, the k-*th* component is any feature from the

remaining ones. The procedure described rearranges the initial order of features in the learning vector set to provide the most rapid increase of the Mahalanobis distance. To select the most informative subset of the features the estimate of misclassification probability $P(k)$ is calculated at each step k $(k = 1,2,...,p)$ of the selection procedure using the Kolmogorov-Deev formula *(Deev, 1970)*

$$P(k) = (1/2)[1 - T_k(D(k)/2\sigma(k)) + T_k(-D(k)/2\sigma(k))], \qquad (1.2)$$

where $\sigma^2(k) = [(t+1)/t][r_1+r_2+D(k)]; \quad t=[(r_1+r_2)/r_1 r_2]-1; \quad r_1=k/n_1; r_2=k/n_2$

$$T_k(z) = F(z) + (1/(k-1))(a_1 - a_2 H_1(z) + a_3 H_2(z) - a_4 H_3(z)) f(z),$$

$F(z)$ is the distribution function of the standard normal distribution; $f(z)$ is the probability density function of this distribution; $H_i(z)$ is the Hermitian polynomial with order $i \in 1,2,3$; a_j, $j \in 1,...,4$ are coefficients depending on k, n_1, n_2 and $D(k)$.

The method is based on the observation that in practice the Mahalanobis distance $D(k)$is a monotonically increasing function of k tending to a finite limit as $k \to p$. In this case the function $P(k)$ has a minimum at a some step k_0 between *1* and p. Thus the most informative set of features, with indices $j(1), j(2),..., j(k_0)$, is the set selected at the steps $1,...,k_0$ of the procedure described. These features give the minimum total misclassification probability for the given set of learning observations.

Cross validation procedure for estimation of misclassification probability. Estimation of misclassification probability by the Kolmogorov-Deev formula provides a fast and effective procedure of feature selection *(Levin and Troitsky, 1970; Raudis, 1976)*. However, due to the asymptotic method of its derivation it often gives higher probabilities of misclassifications than achieved in practical experiments with mediate (several dozen) learning vectors. The most realistic estimate of misclassification probability is provided by examination of the learning vector sets with the "cross validation" procedure *(Fukunaga and Kessel, 1971)*. In our experiments, to make classification decisions we used the conventional linear discrimination function (LDF)

$$L = \mathbf{x}^T \mathbf{S}^{-1} (\mathbf{m}(2) - \mathbf{m}(1)) - (1/2)(\mathbf{m}(2) - \mathbf{m}(1))^T \mathbf{S}^{-1} (\mathbf{m}(2) + \mathbf{m}(1)), \qquad (1.3)$$

It is, of course, possible to implement more sophisticated statistical discrimination rules or artificial neural network algorithms. In all cases the cross validation algorithm became the same as described below. For this reason we regard the probability of misclassification estimated with the LDF as a reliable upper bound for the real error probability.

In the cross-validation method at each step one of the learning vectors $\mathbf{x}_l(j)$, $j \in 1,n_l$, $l \in 1,2$ is eliminated from the learning data set. The remaining vectors are used as the data for LDF adaptation (learning). The eliminated vector is then classified by this learned LDF. If this vector is classified incorrectly, i.e. attributed to a class *2* instead *1* or vice versa, the appropriate count v_{12} or v_{21} is increased by one. The eliminated feature vector is then returned to the learning data set and the next vector $\mathbf{x}_l(j)$ is extracted. This procedure is repeated with the all n_1+n_2 learning vectors. The values $p_{12}=v_{12}/n_1$, $p_{21}=v_{21}/n_2$, $p_0 = (v_1 + v_2)/(n_1+n_2)$ are asymptotically unbiased estimates for probabilities of misclassification from class 1 to class 2, from class 2 to class 1, and total classification error. The LDF values for both classes produced by the cross validation

procedure can be ranked in magnitude. The two ranked LDF sequences allow us to investigate the physical reasons for misclassifications due to outliers of the feature values.

Description of experimental results. The statistical classification approach described above was applied to discrimination of earthquakes and explosions in the region of Israel. We are grateful to Dr. V. Pinsky of the Israel Geophysical Institute for a set of seismograms of weak events recorded by stations of the local Israel seismic network. The set consists of recordings of 28 earthquakes with magnitudes 1.1–2.6 and 25 chemical explosions with magnitude 1.3–2.6, with each event recorded by several stations of the network. For every event we selected two vertical seismograms: one recorded by a nearby station (distance less than 100 km) and another by a far station (mostly from 100 km to 200 km). The location of earthquake and explosion epicenters and stations used in the study is shown in Fig. 1. Fig. 2 shows sets of earthquake and explosion waveforms recorded at near and far distances; onsets of P-waves are aligned, seismograms are ordered according to epicenter distances and scaled to the waveform maximum. Comparison of the waveforms indicates that earthquake and explosion seismograms reveal some visual differences which are more explicitly manifested at far distances. From Fig. 2c and 2d we conclude that earthquakes have more powerful S-waves relatively to P-waves in comparison to explosions. This is evident for the majority of event wavetrains in spite of rather poor signal-to-

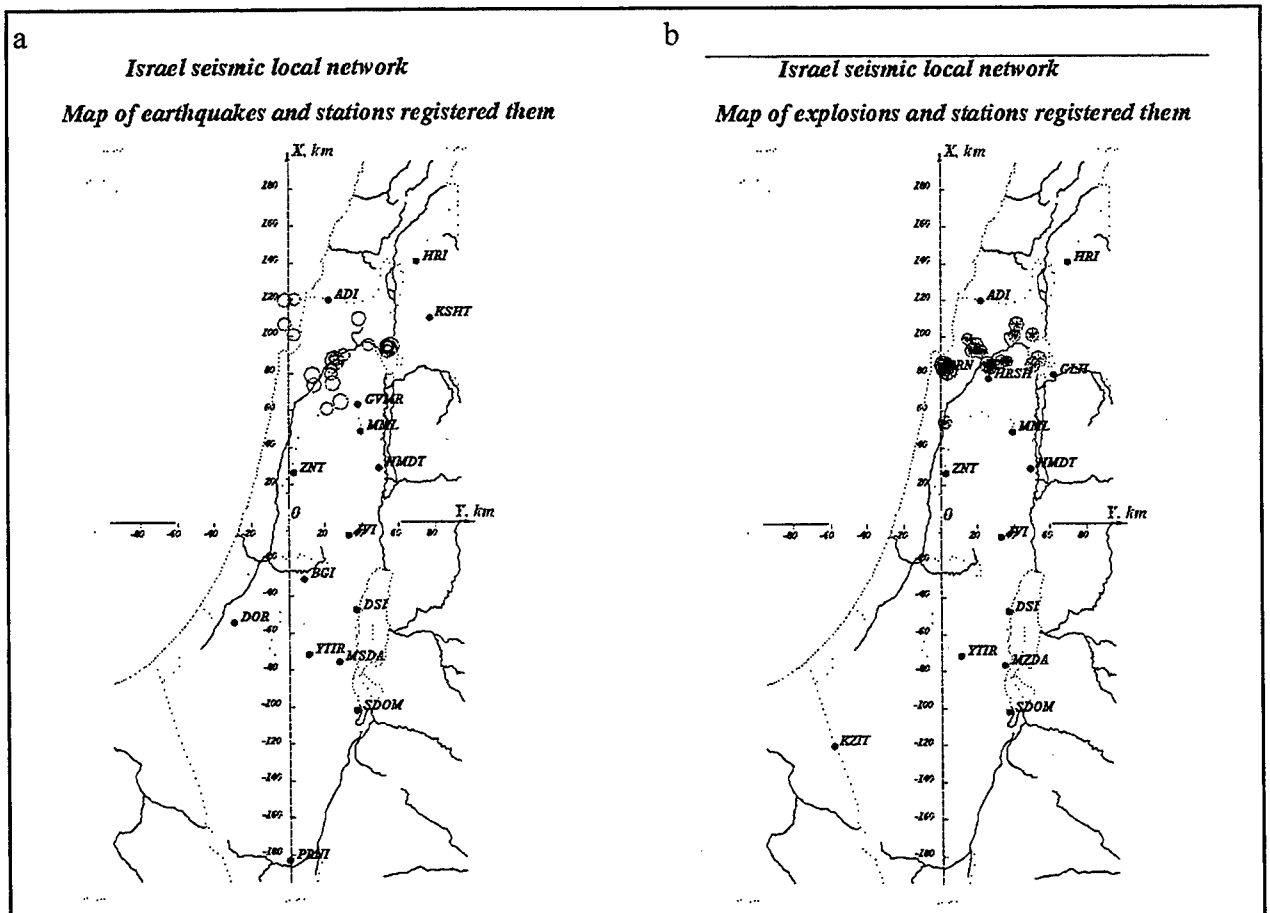

Fig. 1. Location of Israel local network stations and seismic events used in source discrimination study. a,b: Location of stations recording earthquakes and explosions

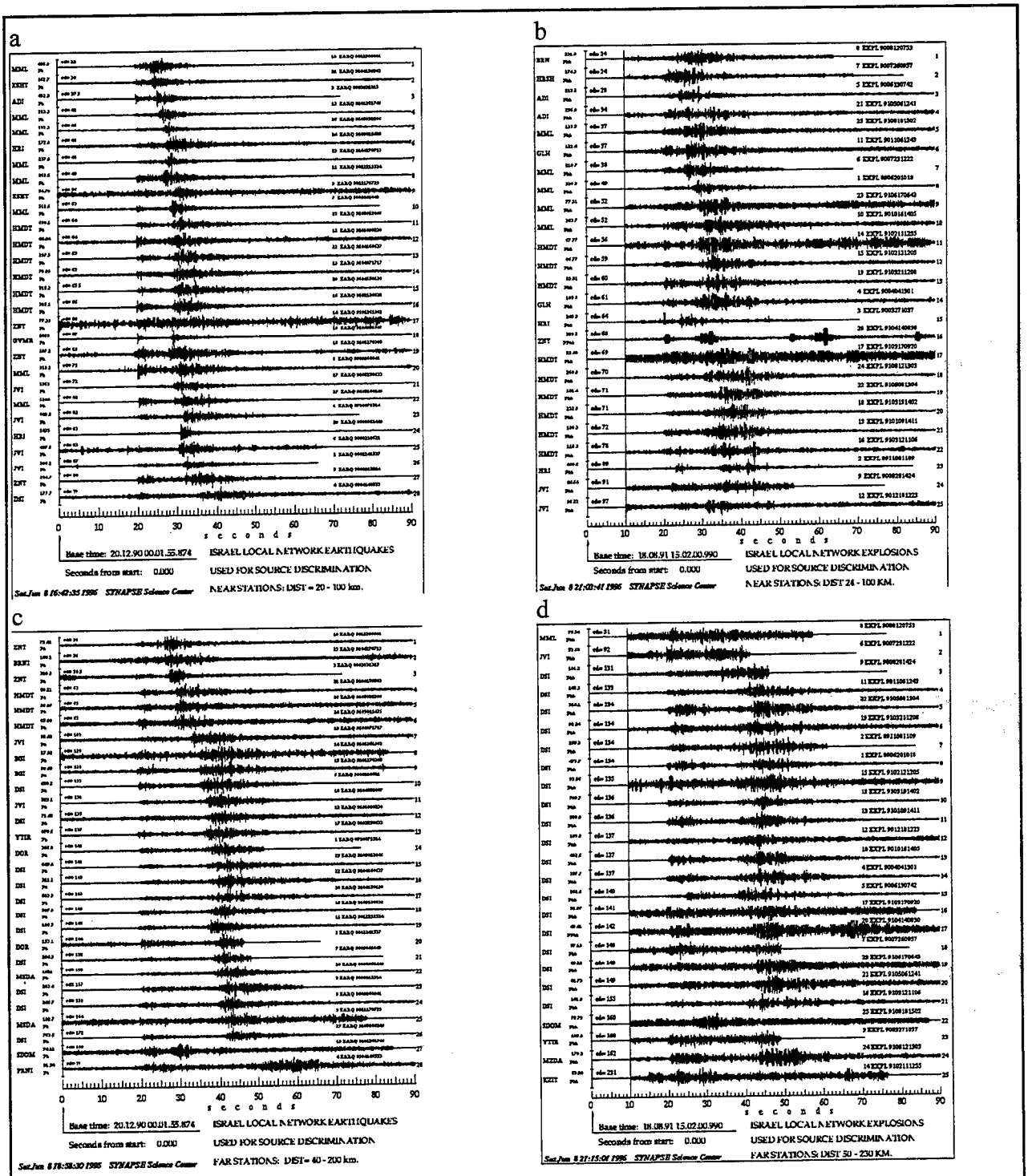

Fig. 2. Set of event seismograms used in discrimination study. a,b Earthquake and explosion seismograms at near distances: 20-100 km. c,d Earthquake and explosion seismograms at far distances: 70-200 km.

noise ratio for some seismograms. Note that for the near distances (Fig. 2a,b) this divergence of earthquake and explosion seismograms is not so explicit. The example depicted is encouraging

enough in our opinion to prompt developing an automated procedure for discrimination of weak local earthquake and explosions.

We designed such a procedure in the framework of the Seismic Network Data Analysis (SNDA) System, a problem-oriented programming shell developed at the Moscow IRIS Data Analysis Center/SYNAPSE Science Center. The procedure was designed using SNDA macro language and comprises routines for extracting discrimination features from event waveforms and processing feature vector sets by feature selection, classification and cross-validation algorithms described above. We use as discrimination features different ratios of P- and S-wave average and peak power in the following frequency bands: Δ_0 = (1-15), Δ_1 = (1-3), Δ_2 = (3-6), Δ_3 = (6-10), Δ_4 = (10-15) Hz. We also used the frequencies of maximum power. The following ratios are calculated: $av(P,\Delta_i)/av(P,\Delta_0)$; $av(S,\Delta_i)/av(S,\Delta_0)$; $i \in 1,...,4$; $av(S,\Delta_i)/av(P,\Delta_i)$; $max(S,\Delta_i)/max(P,\Delta_i)$; $i \in 0,...,4$, where $av(\bullet,\Delta_i)$ and $max(\bullet, \Delta_i)$ denote average power and peak power of the corresponding phase in the corresponding frequency band. Besides the power ratios we measured the ratio of peak value of power spectral densities for P and S phases in the total frequency band Δ_0 and the frequencies f_{mp} and f_{ms} for which the peak values are attained. Thus 21 physically meaningful features of the event wavetrain are measured, reflecting the phase power distribution through the total frequency band Δ_0 (i.e., the spectrum shapes of phases) and the spectral ratios of S and P phases in different frequency bands. Note that all these features are relative and do not depend on event magnitudes or scale factors.

To make the feature measurement procedure more robust to the influence of seismic noise, average noise power is measured in the same frequency bands Δ_i in a noise window preceding the P-wave onset. The noise power values are subtracted from the corresponding signal phase power values. This ensures more precise feature measurement of an event wavetrain even if the signal-to-noise ratio in the event recording is poor. Fig. 3 illustrates the procedure used for automatic feature measurements. Vertical bars in Fig. 3b mark the limits of the frequency bands used; in Fig. 3c mark noise, P-phase and S-phase time intervals used for feature measurements; and in Fig. 3(d) mark positions of current phase power peaks for different frequency bands. Note that phase peak power is measured as averaged power within a 1 sec. interval around the time of absolute maximum power.

The processing of sets of feature vectors starts by identifying pairs of strongly statistically dependent features with mutual correlation coefficient exceeding 0.75. For every such pair one of the features (providing minimum 1-dimensional Mahalanobis value) is eliminated from the feature vectors. For example, ratios of maximum and averaged phase powers appeared to be strongly correlated for some frequency bands. The second processing step is implementation of the feature selection and cross validation procedures described above. Fig. 4 and Fig. 5 illustrate results of these procedures applied to the seismograms recorded at "far" distances of 100-200 km (Fig. 2c,d). Fig. 4a shows the Mahalanobis distance and the theoretical estimates of misclassification probability. Points on these curves correspond to feature subsets consisting of 1, 2, ...,16 features selected to provide the most rapid increase of Mahalanobis distance. We see that this curve becomes flat after the 8-th step and the misclassification probability has a minimum at this step. The list of features ranked according to their discrimination power allows the choice of 8 optimal features providing the minimum misclassification probability. After

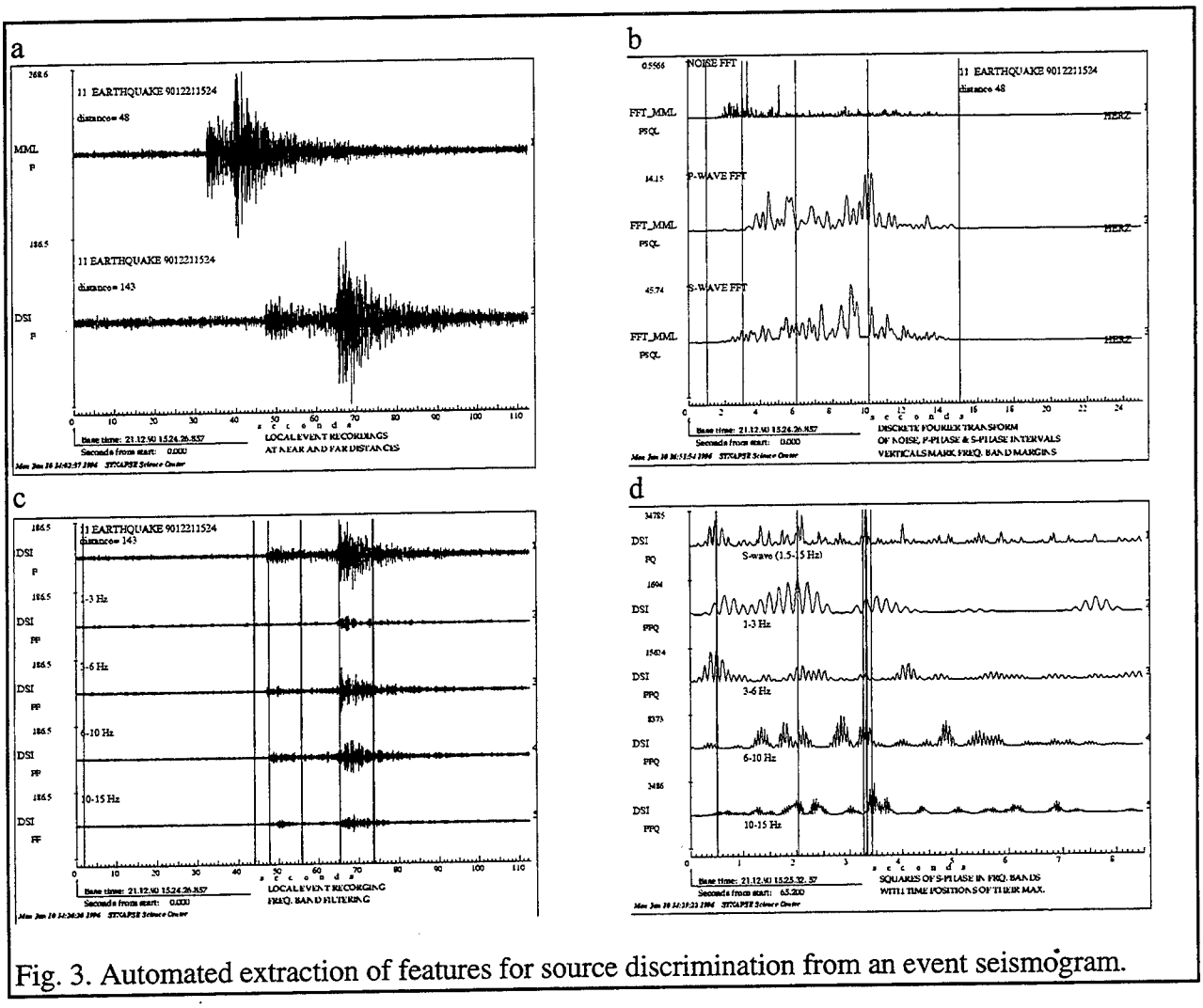

Fig. 3. Automated extraction of features for source discrimination from an event seismogram.

processing "far" earthquakes and explosion seismograms (Fig. 1, 2c,d) the following features were selected:

ratios of maximum S power to maximum P power in the bands (1-3),(3-6),(6-10)Hz;
ratio of average S power to average P power in the band (10-15) Hz;
ratios of average S power in the bands (6-10) and (10-15) Hz to total S phase power;
ratios of average P power in the bands (1-3) and (6-10) Hz to total P phase power.

If to take into account that ratios of maximum and average powers are as a rule strongly correlated, and thus can be used interchangeably, we conclude that the conventional discrimination feature, S/P power ratios for different frequency bands, typically employed for seismic source discrimination were automatically selected by our statistical procedure for all 4 partial frequency bands used in the experiment. Portions of total S power at high frequencies and total P power at low frequencies also appeared to be important for discrimination in this study.

Fig. 4b shows values of selected features depicted as traces versus event numbers. The first 28 vectors belong to the earthquake set, the next 25 to the explosion set. Some differences in the trace images for earthquake and explosion intervals are noticeable, but a great dispersion of the feature values are evident, especially for explosions. Fig. 4c,d display results of cross

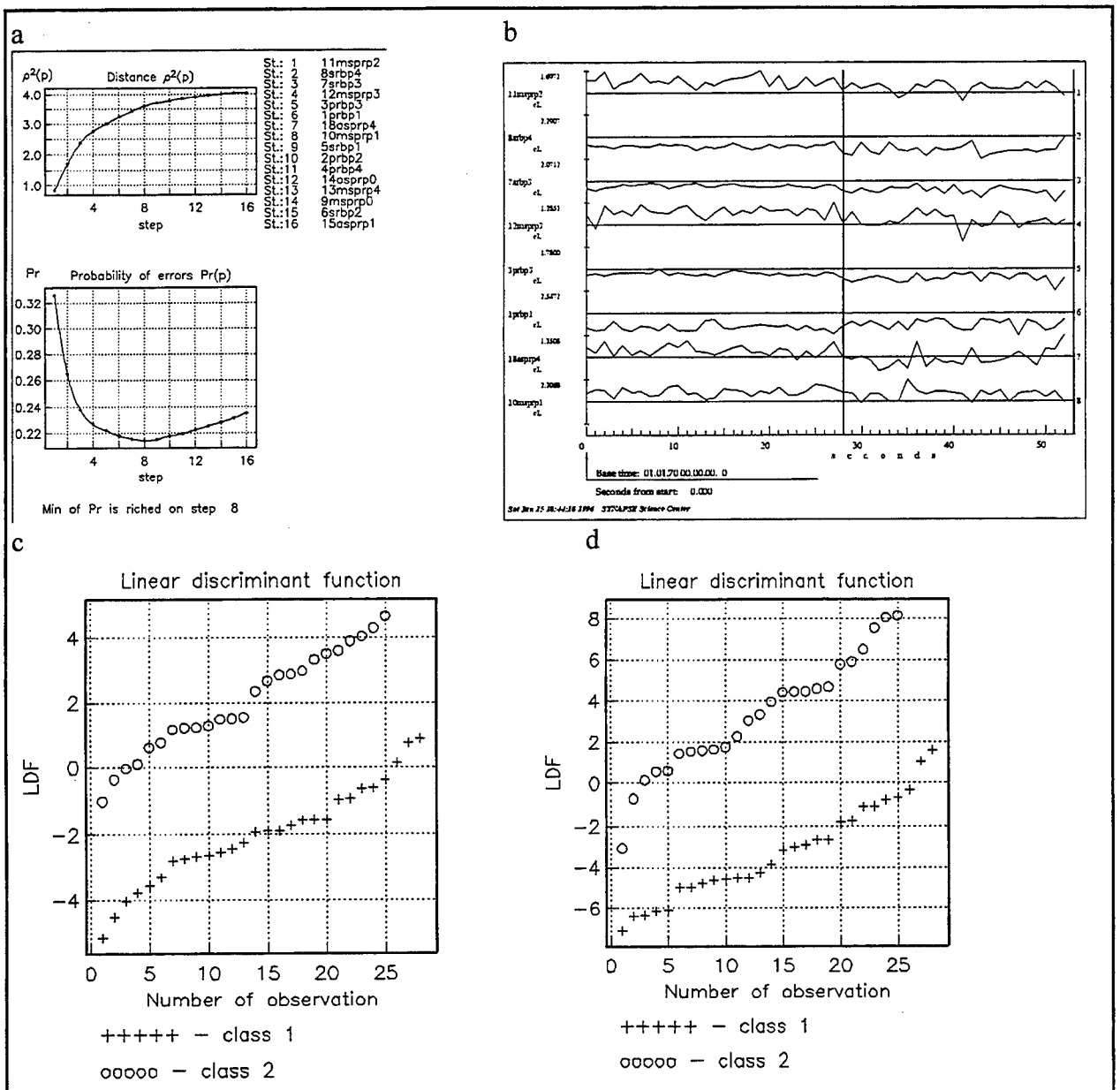

Fig. 4. Discrimination of local event source using statistical discrimination functions with preliminary feature selection. a. Results of feature arrangement and selection in accordance with their information power for discrimination. b. Traces of selected feature values for different classes (abscissa is event number, not seconds as labeled): 1-28 - earthquakes, 29-53 - explosions. c, d, Results of discrimination for total set (16) and selected set (8) of features; Total probabilities of errors are: $P_0(16) = 11.5\ \%$, $P_0(8) = 7.5\ \%$

validation processing of the earthquake and explosion feature vectors. Fig. 4c shows the results obtained for 16 features (the remainder after deleting strongly correlated elements from the total feature set); Fig. 4d the results for the 8 features selected as most informative. The values of the linear discrimination function (LDF) arranged for each class in increasing order are plotted (class 1 is earthquakes, class 2 is explosions). The decision making threshold for LDF equals zero, thus

the number of wrongly classified events is 6 in Fig. 4c and 4 in Fig. 4d. The estimates of misclassification probability are then: 11.5% for the total feature set and 7.5% for the selected feature set.

Fig. 5 presents so called scattering diagrams for 5 selected features. The diagrams comprise points with coordinates equal to values of two features for all the events under study. On all diagrams feature "srb3" (portion of S-power contained in the band 6-10 Hz.) is the Y-axis. In diagram (a) the feature "srb3" is matched with the feature "msprb2" (ratio of maximum S

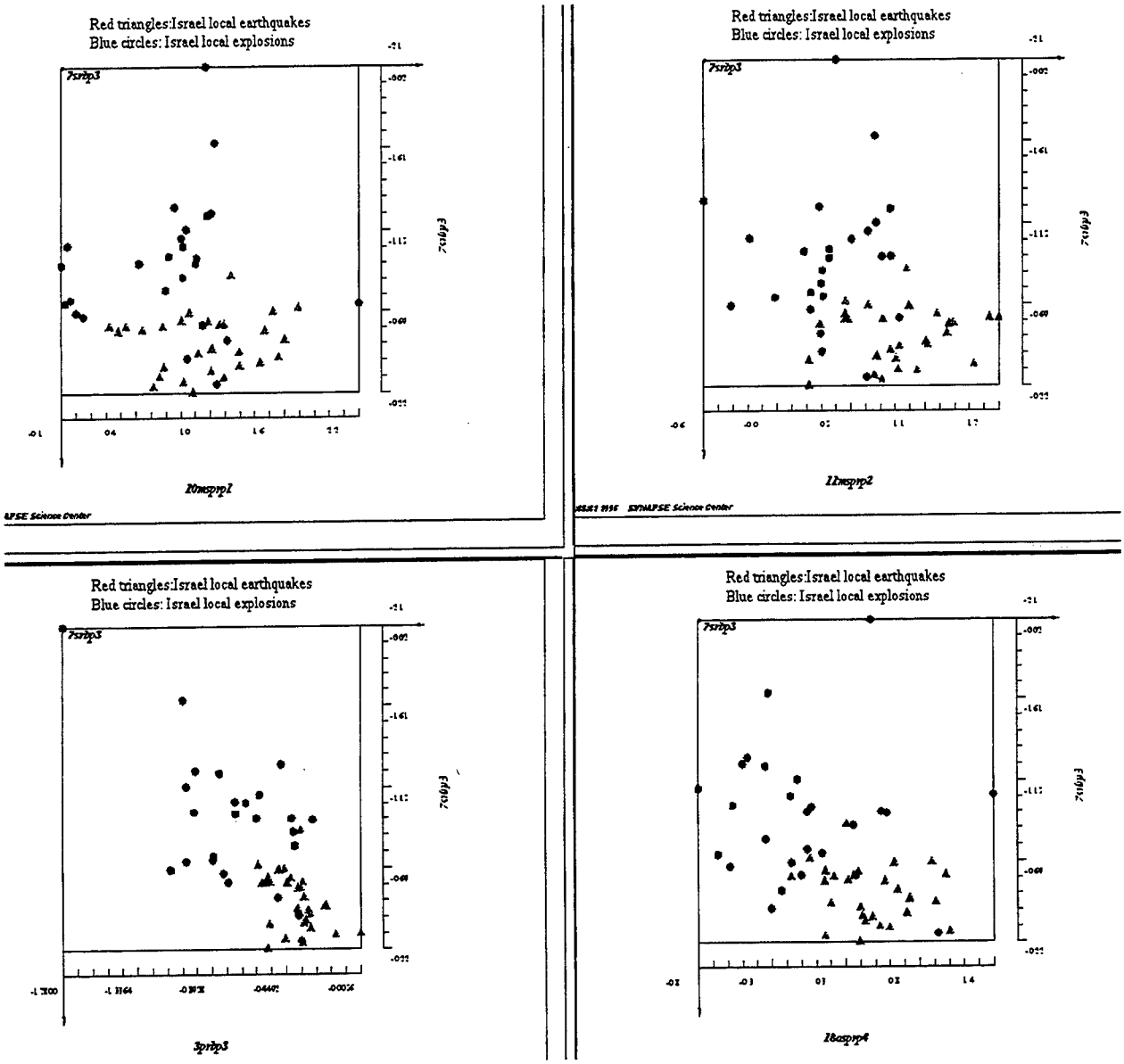

Fig. 5. Scattering diagrams of feature pairs from the selected feature set. Features: a. msprb2 - srb3; b. msprb1 - srb3; c. asprb4 - srb3; d. prb3 - srb3 (explanation of feature labels given in text). Circles denote explosions (25 events); triangles denote earthquakes (28 events). All diagrams exhibit good clustering of points belonging to different classes with a probability error of about 10%.

power to maximum P power for the band 3-6 Hz); in diagram (b), with the feature "msprb1" (same as "msprb2" but for the band 1-3 Hz); in diagram (c), with the feature "asprb4" (ratio of average S power to average P power for the band 10-15 Hz); and in diagram (d), with the feature "prb3" (portion of P power in the band 3-6 Hz). In all diagrams the earthquake and explosion points form explicit clusters; the explosion cluster is more scattered then the earthquake one. In each diagram the clusters can be almost entirely separated one from another by a straight line or, in case (d), by two straight lines. The best separations provide numbers of wrongly attributed points not exceeding 4 or 5. This graphic analysis confirms the results of the thorough statistical analysis aimed at estimating a misclassification probability potential in the region based on a given set of earthquake and explosion recordings.

CONCLUSIONS AND RECOMMENDATIONS

1) A statistical approach seems to be helpful for selection and precise measurement of seismogram features optimal for discrimination of earthquakes from explosions at local distances.

2) Cross validation procedures have to be used for consistent estimation of misclassification probability intrinsic to a given region, especially in the case of number of learning observations of earthquakes and explosions not large.

3) Discrimination efficiency of local events tends to improve with increasing distance of the recording station from the event source. Comparing the results from the nearby stations (not presented here) with the far stations, we find the misclassification probability of events recorded at distances of about 60 km is 11.5% while for the same events recorded at distances of about 140 km it is 7.5%.

ACKNOWLEDGEMENTS

The events were recorded by the Israel Seismic Network (ISN) which is operated by the Seismological Division of the Institute for Petroleum Research and Geophysics (IPRG), Israel. The database supplied with ground truth information was collected by Dr. Y. Gitterman (IPRG) and used in the discrimination study: Gitterman, Y. and T. van Eck, 1993. Spectra of quarry blasts and microearthquakes recorded at local distances in Israel, Bull. Seism. Soc. Am., 83, 1799-1812. The waveforms and ISN bulletin information were prepared and transferred by Dr. V. Pinsky (IPRG).

REFERENCES

A.D. Deev (1970) Representation of statistics of discrimination analysis and their asymptotic expansion for space dimension comparable with sample size. *Docl. Acad Nauk USSR*, v.195, 759-762 (in Russian)

K. Fukunaga, D.L. Kessel (1971) Estimation of classification errors. *IEEE Trans. on Comp.* v.C-20, N12, 136-143.

B.R. Levin, E.V. Troitsky (1970) Total probability error in classification of normal populations differing in vectors of means. *Automatics and Telemechanic*, n.1, 54-56. (in Russian)

Sh. Yu. Raudis (1976) Limitations of sample size in classification problem. *Statistical Problems of Control, Publ. of Institute of Physics and Mathematics AN Lit. SSR*, Vilnius, n.18 (in Russian)

R.H. Shumway (1995) Statistical approach to seismic discrimination. E. Husebye, A. Dainty (eds.) Monitoring of Comprehensive Test Ban Treaty, 791-805, NATO ASI Series, Kluwer Academic Publishers.

S.L. Tsvang, V.I. Pinsky, E.S. Husebye (1993) Enhanced seismic discrimination using NORESS recordings from European events. *Geophys. J. Intern,* v.112, 1-14

CRUSTAL WAVEGUIDE EFFECTS ON REGIONAL PHASES IN CHINA AND SOUTHEAST ASIA

Thorne Lay, Guangwei Fan, and Arthur Rodgers
University of California, Santa Cruz
Contract #F19628-95-K-0014
Sponsored by DOE

ABSTRACT

This research is intended to enhance seismic discrimination capabilities in China and Southeast Asia, as well as in the Middle East, by assessing the influence of large- and intermediate-scale crustal waveguide heterogeneity on regional waveforms. We are focusing on the influence of along-path variations of surface topography, Lg Q, crustal thickness, crustal and mantle lid velocity structure, and sedimentary basin thickness on Pn, Sn, and Lg phases and discriminant ratios such as Lg/P. Our immediate effort has been to assemble large data bases from earthquakes and explosions in each of the study areas, and then to seek empirical relationships between seismic discriminants and crustal waveguide observables. We seek to go beyond simple maps of relative propagation efficiency to establish any correlations with controlling crustal structure so that we can develop a basis for predicting effects in areas that have poor raypath coverage; an important effort for CTBT monitoring in many regions.

We will show the results of the first year of analysis of data for China and the Middle East in this presentation. At present we have accumulated large data bases and are commencing the empirical analysis. The raypath coverage is rather limited when we restrict our attention to larger, well-located events. These events offer the opportunity to examine the effects of varying focal mechanism and source depth on the regional phases, and we will isolate these effects by considering events with similar paths.

Key Words: Regional Seismic Phases, China, Middle East, Seismic Discriminants

Objective This research is directed at enhancing the confidence in regional seismic wave discriminants used in monitoring a Comprehensive Test Ban Treaty. Our approach involves analysis of large numbers of signals, emphasizing common seismic discriminant measures, seeking empirical relationships with independently observed properties of the crustal structure on each path. The intent is to develop empirical relationships when possible that will reduce the scatter in discriminant measures for a given region, and will provide predictive capabilities for assessing the likely energy partitioning on a new path which has not been previously calibrated.

Research Accomplished There are two main research efforts supported by this contract. Regional phase analysis and assessment of effects of crustal waveguide properties are being conducted separately for China and Southeast Asia (Guangwei Fan) and for the Middle East (Arthur Rodgers). In the first year of this effort, large data sets have been assembled for each region, and results of preliminary path analysis will be presented at the annual review meeting. The motivation for this work is the previous analysis of energy partitioning in the regional signals for nuclear explosions in Eurasia (Zhang and Lay, 1994 a,b), and for earthquake and explosions signals in Eurasia (Zhang et al., 1994). The first of these studies established that there are quite strong correlations between simple measures of regional phase signal strength (rms amplitudes) for Sn and Lg phases and simple measures of the along-path topographic characteristics (Figure 1). While various measures of the surface topography give comparable correlations (due to the large covariance in the topographic measurements), it appears that for these explosion signals, order of magnitude fluctuations in relative Sn/Lg amplitudes can be related to path properties, providing a stable basis for applying path corrections to reduce the scatter in the data. Earthquake signals display larger scatter due to a variety of factors (source depth, source mechanism, greater diversity in paths sampled), but Zhang et al. (1994) demonstrated that in central Eurasia there are systematic correlations with crustal properties, including topographic measurements, crustal thickness, sedimentary basin thickness and models of crustal attenuation. At higher frequencies the correlation with path properties persists, and in some cases is even stronger (e.g. Zhang et al., 1996). In the two regions being studied under the current research effort, we are conducting similar analysis of the relationships between regional phase waveform variations and along-path properties, seeking to establish empirical rules that can be applied to reduce the scatter in regional discriminants (mainly an earthquake population in most areas), so as to enhance the performance of the discriminant (detection of an outlier with distinctive source process).

There is complex, diffuse seismicity throughout the China-Southeast Asia region (Figure 3), which poses major challenges for calibration of regional phase behavior over a broad region with a very sparse distribution of high quality seismic stations. This motivates the development of both maps of regional phase propagation efficiency (the conventional approach) and our approach of seeking more general empirical relationships which can reduce scatter in discriminant measures over a wide region with a diversity of tectonic structures and path effects.

Our initial data collection was targeted at events for which a focal mechanism had been determined by the Harvard CMT procedure. This is for the events in the region larger than magnitude 5.0, which corresponds to those with relatively good source locations (although not necessarily good depths). For this data set we requested all regional broadband recordings out to distances of 20 degrees from the IRIS data center. The resulting path coverage is shown in Figure 4, with there being a relatively high-quality observation for each path that is indicated. Two aspects of the China research are immediately apparent. The first is that many of the events are recorded by only a few stations, so there is relatively little opportunity to revise the source parameters based on regional wave analysis. The

other aspect is that the path coverage is non-uniform in much of the region, but western and southwestern China can be relatively well sampled with existing data. Key stations are the CDSN stations, but it is not clear which of these will ultimately contribute data to the IDC, so our focus here is on the systematic regional characteristics and path influences rather than specific station calibration.

A few example waveforms from the broadband recordings in China are shown in Figure 5. Station LZH has a good azimuthal distribution of sources, as does WMQ. We are just beginning to sort out path and source influences on the waveforms by establishing empirical correlations with individual path properties.

The other region which we are analyzing is the Middle East, with the event and station distribution for our initial data set being shown in Figure 6. This is the data set collected by Rodgers et al. (1996), who have performed preliminary mapping of Sn and Lg propagation efficiency in the region. Our analysis, which is just beginning on the heels of that work, will extend the analysis to include all phases in the regional signals and to seek correlations with path properties that may provide insight into the general variability of the regional signals and hopefully corrections that will reduce the spread of discriminant measures.

Conclusions and Recommendations

We are in the data processing phase of this investigation of regional phases in China and the Middle East, and it is too early to assess whether there are significant new perspectives of the influence of regional phases. It is clear from our inspection of the data that there is great variability in the observations, and simple guidelines as to regions of blockage or propagation inefficiency are probably not adequate for an operational approach to CTBT monitoring in these regions. This encourages to persist with the attempt to attain a more detailed empirical understanding of the control on regional phase energy and the associated behavior of discriminants that will be used to identify clandestine explosions.

References:

Rodgers, A. J., J. F. Ni and T. M. Hearn (1996). Propagation characteristics of short-period Sn and Lg in the Middle East, preprint.

Zhang, T., and T. Lay (1994a). Analysis of short-period regional phase path effects associated with topography in Eurasia, *Bull. Seism. Soc. Am.*, 84, 119-132.

Zhang, T., and T. Lay (1994b). Effects of crustal structure under the Barents and Kara Seas on short-period regional wave propagation for Novaya Zemlya explosions: Empirical relations, *Bull. Seism. Soc. Am.*, 84, 1132-1147.

Zhang, T., S. Y. Schwartz, and T. Lay (1994). Multivariate analysis of waveguide effects on short-period regional wave propagation in Eurasia and its application in seismic discrimination, *J. Geophys. Res.*, 99, 21929-21945.

Zhang, T., T. Lay, S. Schwartz, and W. R. Walter (1996). Variation of regional seismic discriminants with surface topographic roughness in the Western United States, *Bull. Seism. Soc. Am.*, in press.

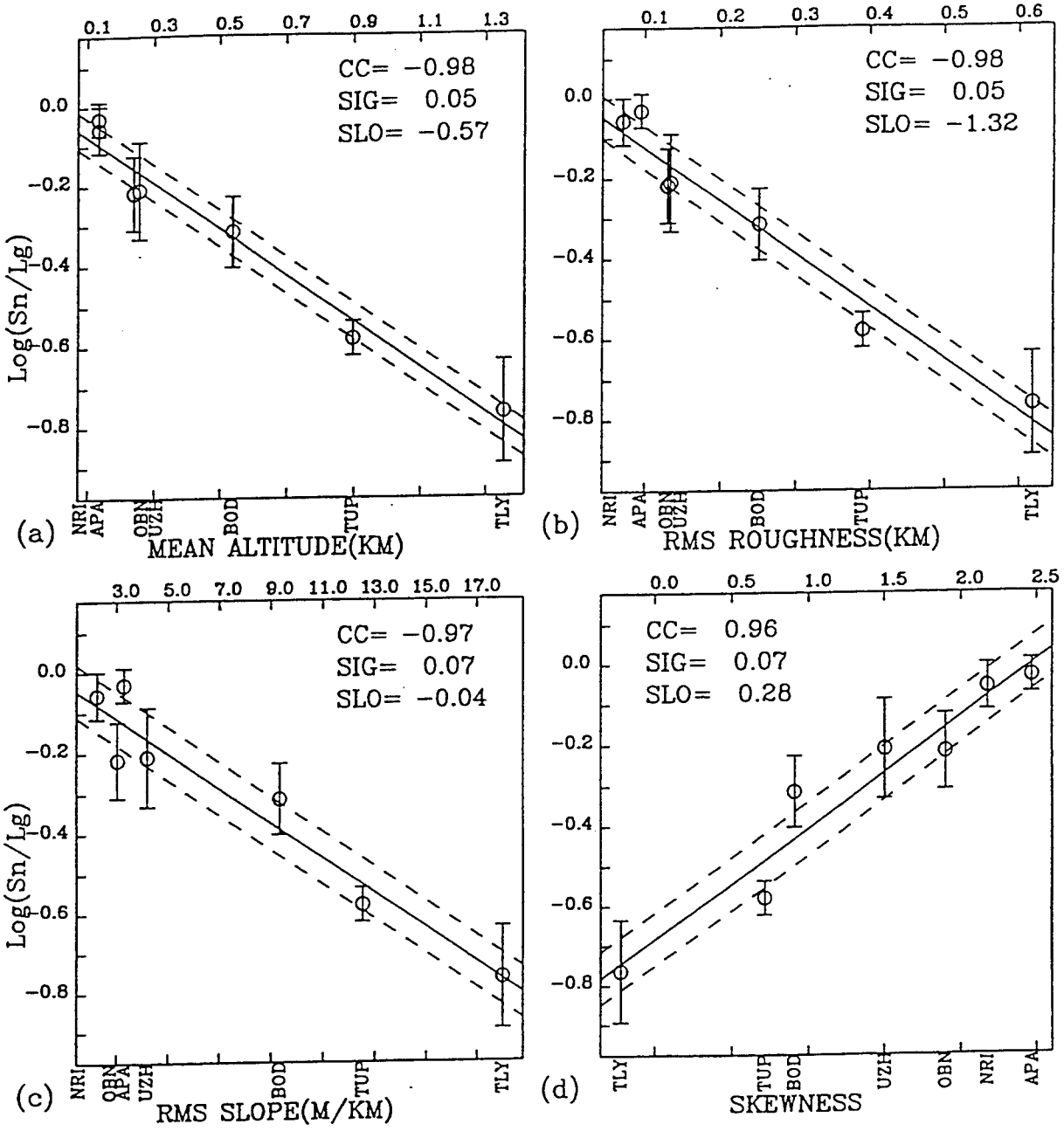

Figure 1. The relationship of Sn/Lg with topography for nuclear explosions at the Semipalatinsk test site recorded at broadband stations in the former Soviet Union. Each circle is the average relative value observed for many explosions on that path, with the error bar indicating the standard deviation. The logarithmicamplitude ratios are compared to (a) mean altitude, (b) rms surface roughness, (c) rms surface slope variation, and (d) skewness of the altitude on the corresponding path. Note that path effects appear to have a huge influence on the regional phase behavior, and that gross measures of the waveguide such as surface topography may provide a means by which to reduce the path-induced scatter. From Zhang and Lay (1994a).

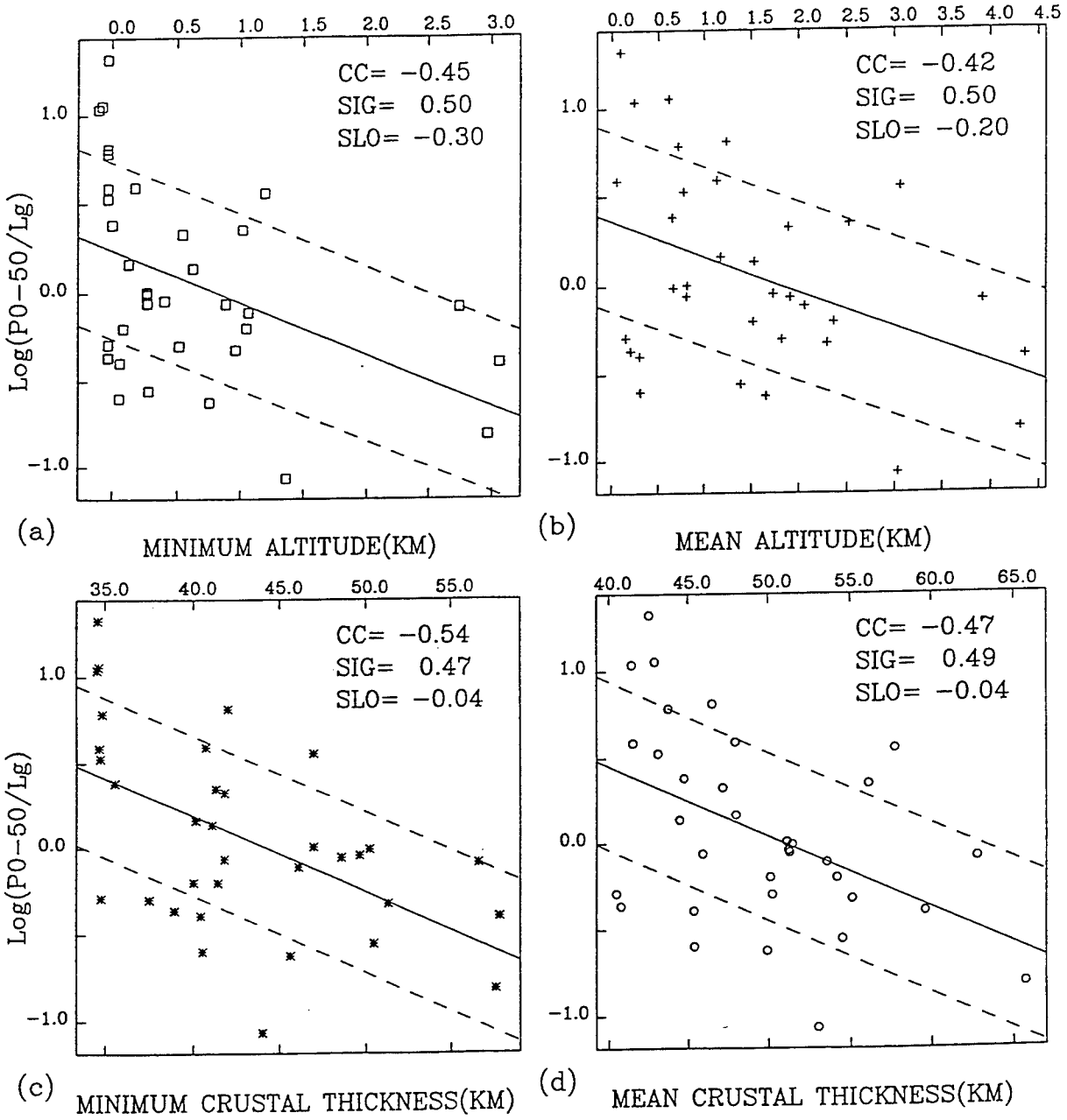

Figure 2. Log P/Lg ratio variations with (a) minimum altitude on the path, (b) mean altitude on the path, (c) minimum crustal thickness on the path, and (d) mean crustal thickness on the path for earthquake data in central Eurasia. CC stands for linear correlation coefficient, SIG is standard deviation of the linear regression, and SLO is slope of the linear regression. P0-50 refers to the RMS amplitude in a 50 s window beginning with the P onset. From Zhang et al. (1994).

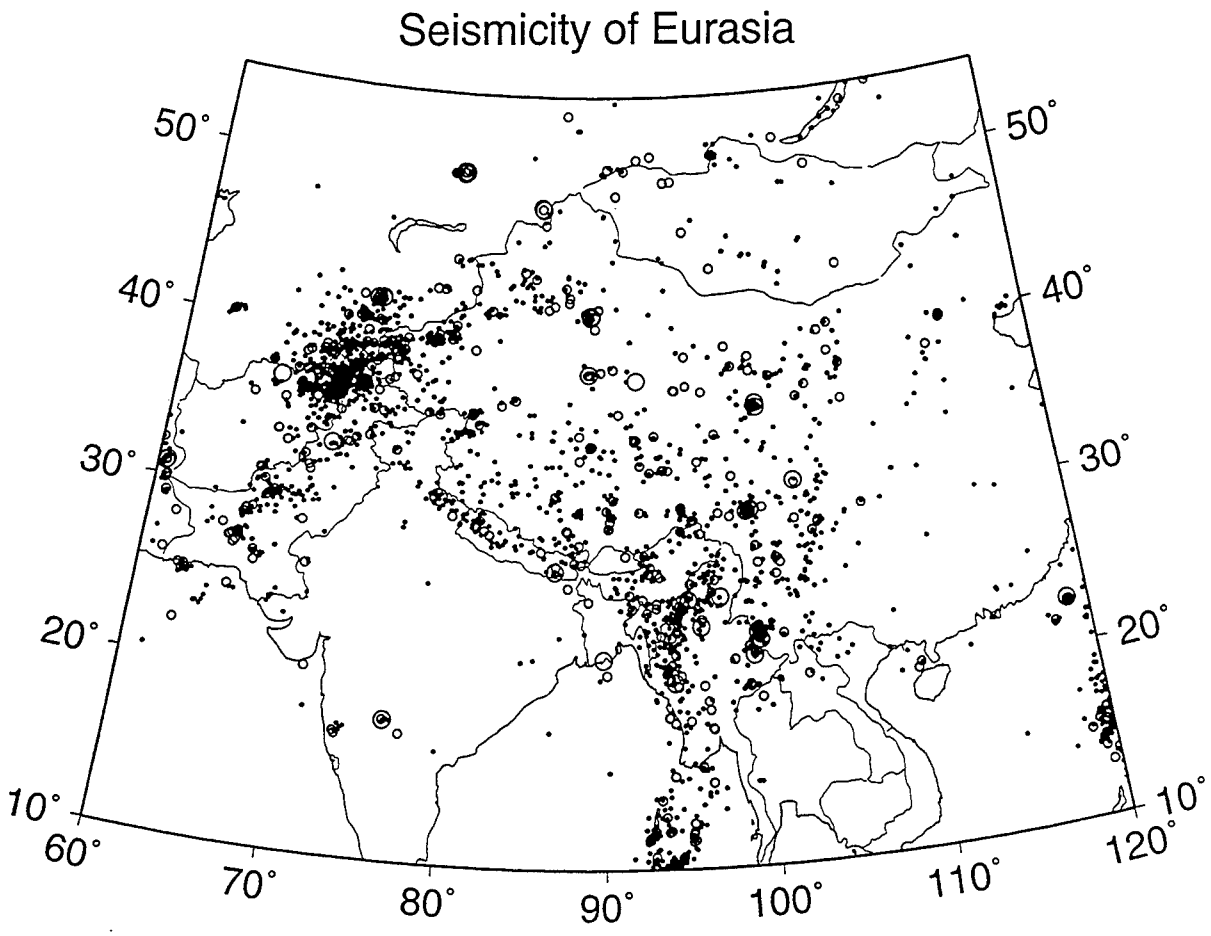

Figure 3. Seismicity distribution of central Eurasia from the Preliminary Determination of Epicenters by the NEIC. This illustrates seismicity in the past ten year period where there have been broadband stations deployed in the region. The dots indicate events with magnitudes less than 4.0. Small circles indicate events with magnitudes from 4.0-5.0. Large circles are events larger than 5.0.

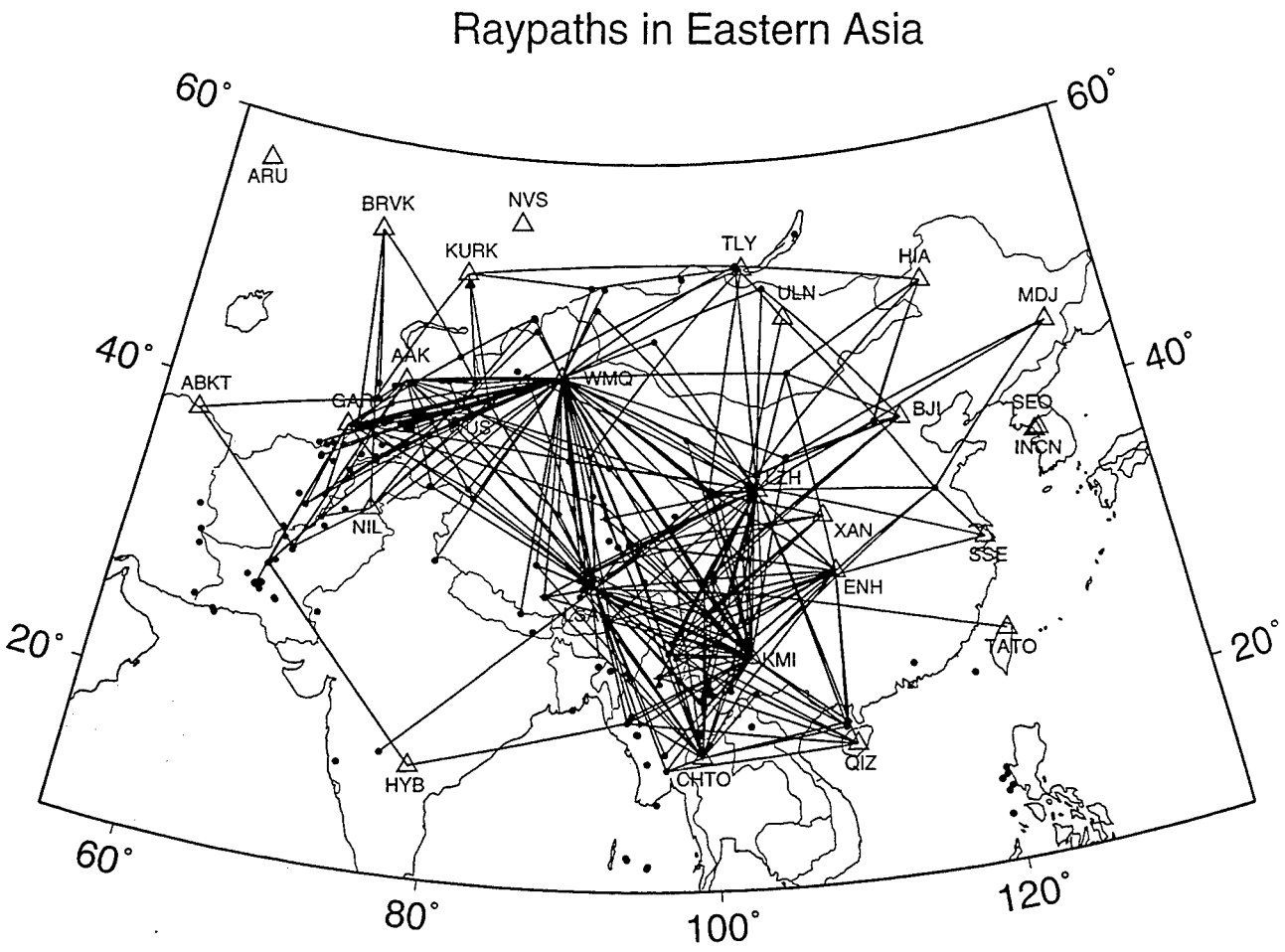

Figure 4. Current path coverage for regional phases recorded at broadband and high frequency channels in China and Southeast Asia. These events all have known CMT focal mechanisms and relatively accurate source locations.

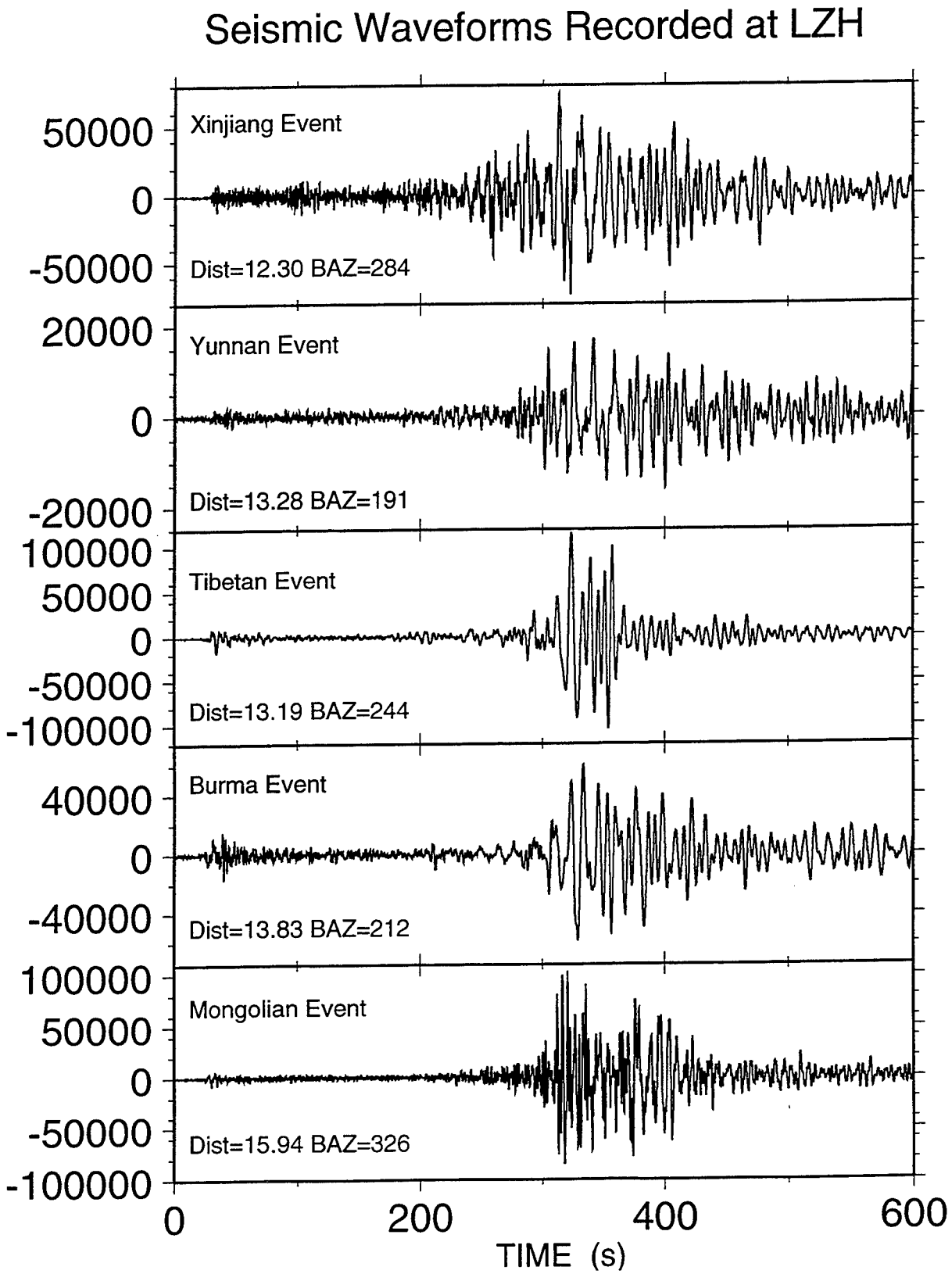

Figure 5. Example of broadband regional signals recorded in western China.

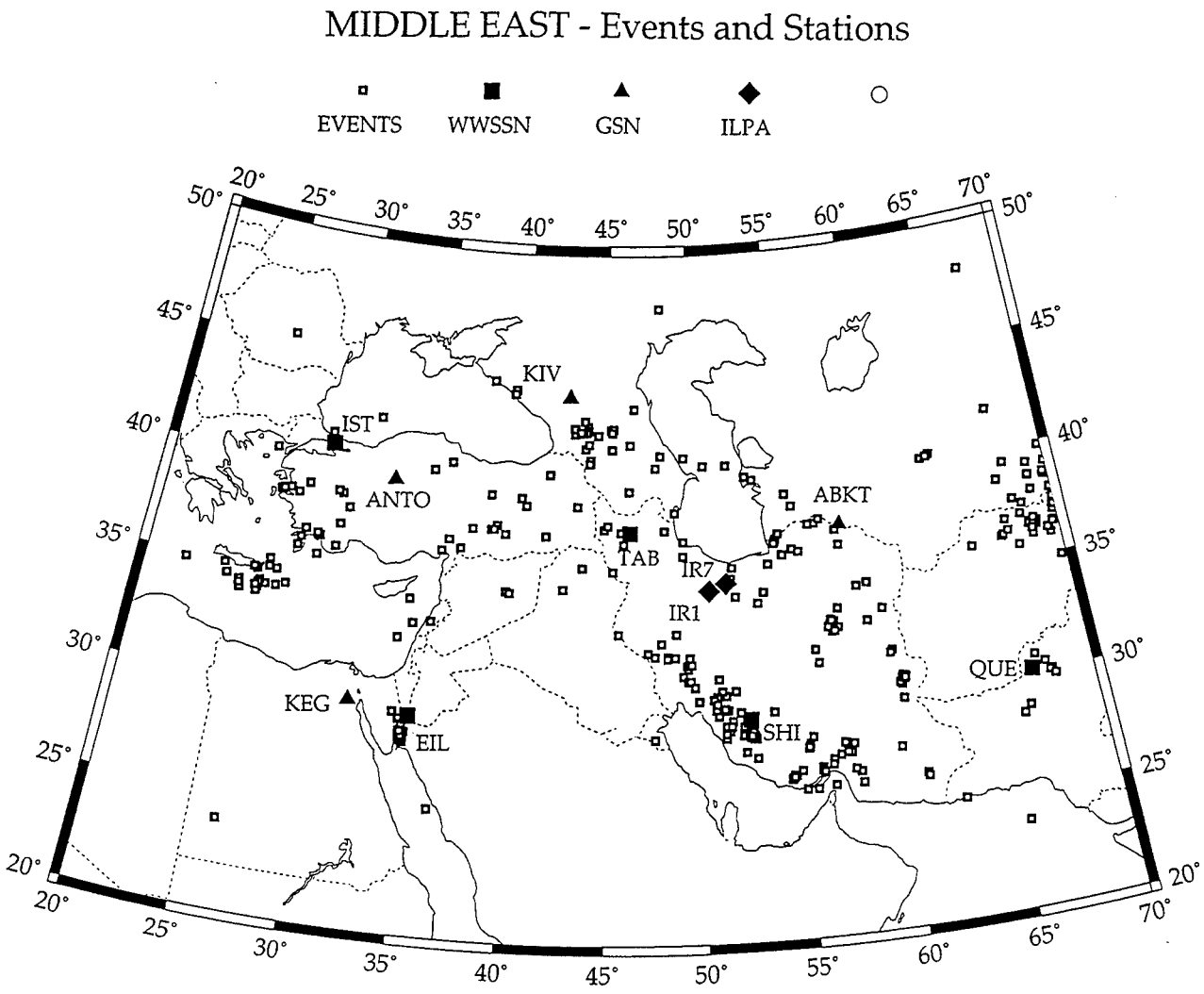

Figure 6. Distribution of sources and receivers providing regional waveforms for the Middle East region (from Rodgers et al., 1996). Path effects on these signals are being analyzed, along with collection of additional data in the region.

Discrimination of Small Earthquakes and Explosions

Y. Li, M. N. Toksöz and W. L. Rodi

Earth Resources Laboratory
Department of Earth, Atmospheric, and Planetary Sciences
Massachusetts Institute of Technology, Cambridge, MA 02139

Contract No. F49620-94-1-0282
Sponsored by AFOSR

ABSTRACT

The discrimination of seismic events as small as magnitude 2.0 at regional distances is of critical importance to achieving the goal of monitoring the Comprehensive Test Ban Treaty (CTBT). Although many discriminants work well for large earthquakes and explosions, little has been learned about their performance for smaller events. In this study, we explore the performance of Pg/Lg and Lg spectral ratio discriminants on smaller events using waveforms of 14 earthquakes and 10 industrial explosions with magnitudes between 1.6 and 3.8 in New England, recorded by short-period stations at distances up to 250 km. We find that the Pg/Lg discriminant fails to separate the small explosion and earthquake populations, but Lg spectral ratio appears to be a good discriminant for these events. Our analysis indicates that the Lg spectra observed from industrial explosions have much larger amplitudes at lower frequencies, while earthquakes have higher amplitudes at higher frequencies, which is reversed from the situation for large earthquakes and explosions. To understand the physical basis of the Lg spectral ratio discriminant for small magnitude seismic events, we performed numerical modeling experiments to study the effects of source properties, depth, and attenuation. Synthetic seismograms demonstrate that the lower frequency content of small explosions, relative to earthquakes, is partially explained by their shallower depth. The energy from a near-surface explosion experiences greater high frequency attenuation in shallow, low Q, layers and greater trapping of low frequency energy in lower velocity layers. Furthermore, the separation between earthquake and explosion Lg spectra is enhanced by two source effects: the shorter source duration of small earthquakes and the extended duration of explosions that are multiply detonated. These modeling results, together with our empirical study of New England events, suggest that Lg spectral ratio is a promising method for discriminating seismic events of small magnitude.

Keywords: Seismic, Discrimination, CTBT, Earthquake, Explosions, Lg Spectral Ratio, Waveform Modeling

OBJECTIVES

The objective of this project is to characterize the source properties of seismic events, as a function of event type and magnitude, with the ultimate goal of developing effective regional discriminants. In previous work we applied the EGF method to estimate source time functions for a wide variety of events (earthquakes, chemical and nuclear explosions, mining tremors) over a large magnitude range (0.9–6.6), and discovered that the source time function duration could discriminate earthquakes and explosions in certain magnitude ranges, including very small events (magnitudes of 3.0 or less) but not including events in the magnitude range 3–4.5.

To achieve the goal of monitoring a CTBT, it is critical to discriminate seismic events as small as magnitude 2.0 (Murphy, 1995). Although many methods work well for discriminating larger earthquakes and explosions, little has been learned about their performance on the smaller events. The objective of our present work is to understand the physical basis of our previous results for small events, and to compare them to the behavior of discriminants based on Lg.

RESEARCH ACCOMPLISHED

In our previous studies (Toksöz et al., 1993; Li et al., 1994, 1995a,b) we applied an empirical Green's function (EGF) method to characterize seismic sources and estimate source time functions for explosions, earthquakes, and mining tremors covering the magnitude range 0.9–6.6. Figure 1 displays source duration vs. event magnitude for all the events we have studied to date. We see that the earthquake and explosion populations appear to obey different source scaling relations. For magnitudes between 3.5 and 4.5, the earthquake and explosion populations overlap due to the crossover of two scaling relations with different slopes, indicating that simple source duration is not a good discriminant in this magnitude range. However, for M = 5 and greater, source durations of nuclear explosions are about a factor of 5 to 10 shorter than those of the earthquakes (Figure 1). Thus source duration, like other discriminants such as P/Lg, Lg spectral ratio, and mb-Ms (e.g., Pomeroy et al., 1982; Bennett and Murphy, 1986; Taylor et al., 1988), works as a good discriminant for larger earthquakes and explosions.

For the small (M<3) events we analyzed, the discriminant also works but in an opposite way. The source durations of quarry and construction blasts are significantly longer than those of earthquakes with similar magnitudes (Figure 1). This is consistent with the results of Herrin et al. (1994), who found that Lg spectra of small magnitude earthquakes in the Vogtland area have relatively higher peak frequencies compared to explosions with similar magnitudes. Possible explanations for these observations from small earthquakes and explosions are source, depth, and attenuation effects, i.e.,

1. Smaller earthquakes and explosions may have significantly different source dimensions over space and time. For example, the source duration of industrial blasts is often controlled by shooting practices, such as multiple detonation and ripple firing.

2. Explosions typically are detonated at shallow depths (<1 km) while earthquakes occur at depths of a few kilometers or more.

3. Explosions are typically in a near-surface medium with high attenuation while earthquakes occur in a medium with lower attenuation.

In this study we explore the performance of the P/Lg discriminant and Lg spectral ratio discriminant on the smallest events from our previous work. These include earthquakes and industrial explosions with magnitudes between 1.6 and 3.8 in New England recorded by short-period stations of the M.I.T. seismic network at regional distances.

Figure 3 shows velocity seismograms of one quarry blast (M=2.0) and one earthquake (M=2.8) at Littleton, Massachusetts, recorded at station DNH, which is about 80 km from the epicenters (see Figure 4). As we expected, the small earthquake has a much richer high frequency content compared to the explosion. Bandpass filtered seismograms, using 2–4 and 6–8 Hz bands, are also shown in Figure 3. For the explosion, the Lg peak amplitude on the 2–4 Hz trace is about 5 times greater than that on the 6–8 Hz seismogram. In contrast, the Lg peak amplitude on the 2–4 Hz seismogram is about 2 times smaller than that on the 6–8 Hz seismogram. The Fourier spectra of the Lg phases from the filtered traces (bottom of Figure 3) show this same pattern, with the explosion displaying relatively more low frequency energy. Since the two events have very similar epicenters and are recorded at a common station, we believe that the observed differences between their Lg spectral patterns are mainly caused by differences between the sources themselves and by effects related to focal depth differences, as opposed to propagation along different paths. This suggests that Lg spectral ratios may generally discriminate between small earthquakes from explosions.

It is interesting to compare this result to an example with large events. Figure 2 shows Lg spectra of one Xinjang earthquake (931002, m_b6.2) and one Lop Nor explosion (900816, m_b6.2) recorded at station ARU about 25 degrees away. We see that the Lg spectral ratio between higher (0.4 to 2 Hz) and lower (0.04 to 0.2 Hz) frequency bands is much higher for the explosion than for the earthquake. That is, the large explosion has relatively higher peak frequencies compared to the large earthquake, which is reversed from the small event example of Figure 3. Again, the two events have similar propagation paths and, considering also the lower frequencies used, the Lg spectra are probably dominated by the source effect. The behavior of Lg spectral ratios for small vs. large events suggests that the source scaling relations for source duration may be true in general.

Next, we apply the Lg spectral ratio discriminant to 10 explosions (M=1.6 to 2.7) and 14 earthquakes (M=2.2 to 3.8) in New England (see Figure 4). The spectral ratio Lg(2–4Hz)/Lg(6–8Hz) plotted against epicentral distance and magnitude are shown in Figure 5. We find that the Lg spectral ratio separates well the earthquake and explosion populations, although the magnitude and distance ranges containing both types of events are limited. We note that Pg/Lg at either 2-4 Hz or 6-8 Hz does not separate the small explosion and earthquake populations.

To understand the physical basis for the Lg spectral ratio discriminant for small magnitude events, we performed tests with synthetic data to study the various effects listed above: source properties, depth, and attenuation. Synthetic seismograms were computed using the discrete wavenumber algorithm of Mandal and Toksöz (1990) and a 1-D structure comprising three crustal layers over a half-space (Table 1). Seismograms were computed for an explosion source at 0.1 km depth and a thrust earthquake at a depth of 4 km. The source-receiver distance is 80 km. We

selected both source time functions to be a triangle pulse with time duration of 0.1 s. The synthetic velocity seismograms for the explosion and earthquake are shown in Figures 6b and 6c, and the Lg spectra are displayed in Figures 7b and 7c. From the seismograms and Lg spectra we can see that, for the same source pulse, the explosion has much higher amplitudes at lower frequencies (< 4Hz) while the earthquake has higher amplitudes at higher frequencies (> 6Hz). Since the explosion is detonated in the more attenuating surface layer, and ray paths go through this layer twice, there is a greater loss of high frequency energy from this source compared to the earthquake, which is in the second layer of the model. There may also be an enhancement of lower frequency energy from the explosion due to the trapping of energy in the shallow layer.

We also calculated synthetics for a multiply detonated blast at a depth of 0.1 km (Figures 6a and 7a). The multiple explosion has 10 subevents with delay times varying between 0.08 to 0.12 s and a total source duration of 1.0 s. We see that multiple firing increases the energy at lower frequencies and decreases it at higher frequencies, thus increasing the difference from the earthquake synthetic.

As shown in Figure 1, the source duration for a small earthquake is typically 2 to 3 times shorter than for an explosion with similar magnitude. To examine how a sharper source pulse for earthquakes affects the Lg ratio discriminant, we recalculated the earthquake synthetic with the triangle source pulse reduced to 0.05 s in duration (Figures 6d and 7d). As expected, the energy content shifts to higher frequency, further enhancing the difference between the earthquake and explosions.

We applied the Lg(2-4Hz)/Lg(6-8Hz) discriminant to the synthetic data from all four cases. The Lg spectra in the two frequency bands are shown for the multiple blast, single blast, and earthquakes with differing source durations in Figures 8a–8d, respectively. The Lg spectral ratio between the two frequency bands clearly separates the explosions and earthquakes. The greatest separation is between the multiple explosion (Figure 8a) and the earthquake with a shorter source duration (Figure 8d).

CONCLUSIONS AND RECOMMENDATIONS

The Lg spectral ratio, using frequency bands of 2–4 Hz and 6–8 Hz, discriminates earthquakes and industrial explosions in New England at magnitudes below 3 and epicentral distances up to 250 km. The Pg/Lg discriminant is not effective on these events, however. The success of the Lg spectral ratio discriminant is consistent with our previous work that showed that the source time duration of M<3 earthquakes is 2 to 3 times shorter than that of explosions of similar magnitude.

Based on numerical modeling of earthquake and explosion seismograms in New England, we conclude that the lower frequency content of small explosions, relative to earthquakes, is partially attributable to their shallower depth. The energy from near-surface explosions experiences greater high frequency attenuation in shallow, low Q layers and greater trapping of low frequency energy in lower velocity layers. The separation between earthquake and explosion Lg spectra is enhanced by two source effects: the shorter source duration of small earthquakes and the extended duration of explosions that are multiply detonated.

These results imply that source time duration and Lg spectral ratio are promising discriminants for small earthquake and explosions. The Lg discriminant is particularly interesting since Lg spectra

are more directly and easily measured. For future work, therefore, we recommend that Lg spectral discriminants be tested on a large number of events from different regions to assess their general effectiveness and transportability. Of particular importance is to learn their effectiveness on events of magnitude 3 and greater, and at greater distances. To better understand the physical basis for the Lg spectral ratio discriminant, and to provide the knowledge needed to adapt the discriminant to different regions, we recommend further numerical modeling studies aimed at determining how Lg spectra are affected by vertical layering in the crust, and 2-D and 3-D scattering by topographic and geologic features.

REFERENCES

Bennett, T., and J. Murphy, 1986. Analysis of seismic discrimination using regional data from western United States events, *Bull. Seis. Soc. Am., 76*, 1069-1086.

Herrin, E., Burlacu, V., Gray, H.L., Swanson, J., Golden, P., and Myers, B., 1994. Research in regional event discrimination using Ms:mb and autoregressive modeling of Lg waves, *Proceedings*, 16th Annual Seismic Research Symposium, Thornwood, New York, Phillips Laboratory, Hanscom AFB, Massachusetts, 152–158. PL-TR-94-2217 , ADA284667

Li, Y., Rodi, W., and Toksöz, M.N., 1994. Seismic source characterization with empirical Green's function and relative location techniques, *Proceedings*, 16th Annual Seismic Research Symposium, Thornwood, New York, Phillips Laboratory, Hanscom AFB, Massachusetts, 231–237. PL-TR-94-2217 , ADA284667

Li, Y., Toksöz, M.N., and Rodi, W., 1995a. Source time functions of nuclear explosions and earthquakes in central Asia determined using empirical Green's functions, *J. Geophys. Res., 100*, 659–674.

Li, Y., Rodi, W., and Toksöz, M.N., 1995b. Discrimination of earthquakes, explosions, and mining tremors using the empirical Green's function method, *Proceedings*, 17th Annual Seismic Research Symposium, Scottdale, Arizona, Phillips Laboratory, Hanscom AFB, Massachusetts, 78–87. PL-TR-95-2108

Mandal, B. and Toksöz, M.N., 1990. Computation of complete waveforms in general anisotropic media – results from an explosion source in an anisotropic medium, *Geophys. J. Int., 103*, 33–45.

Murphy, J. R., 1995. An overview of seismic Discrimination issues relevant to CTBT monitoring, *Proceedings*, 17th Annual Seismic Research Symposium, Scottdale, Arizona, Phillips Laboratory, Hanscom AFB, Massachusetts, 88. PL-TR-95-2108

Pomeroy, P.W., J.B. Best, and T.V., McEvilly, 1982. Test ban treaty verification with regional data – a review, *Bull. Seis. Soc. Am., 72*, S89-S129.

Talyor, S.R., N.W.Sherman, and D.D. Marvin, 1988. Spectraal discrimination between NTS explosions and western United States earthquakes at regional distances, *Bull. Seis. Soc. Am., 78*, 1563-1579.

Toksöz, M.N., Li, Y., and Rodi, W., 1993. Seismic source characterization with empirical Green's function and relative location techniques, *Proceedings*, 15th Annual Seismic Research Symposium, Vail, Colorado, Phillips Laboratory, Hanscom AFB, Massachusetts, 398–404. PL-TR-93-2160, ADA271458

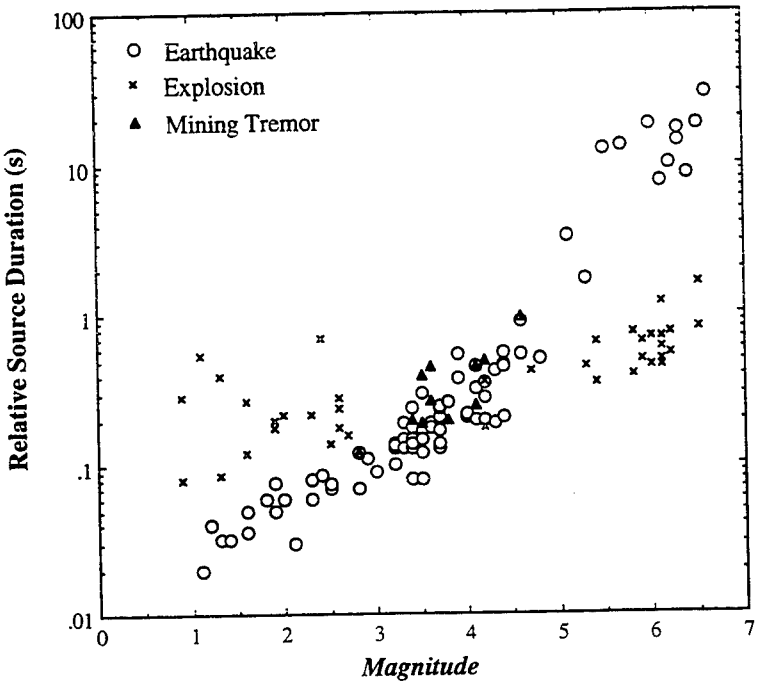

Figure 1: Source duration vs. magnitude for earthquakes (circles), explosions (squares), and mining tremors (triangles), determined by EGF analysis (Li et al., 1995b). For events having magnitude less than 3 or greater than 4.5, the source duration is a good discriminator between earthquakes and explosions. In the remaining magnitude range (3.0 to 4.5) the earthquake, explosion and mining tremor populations overlap.

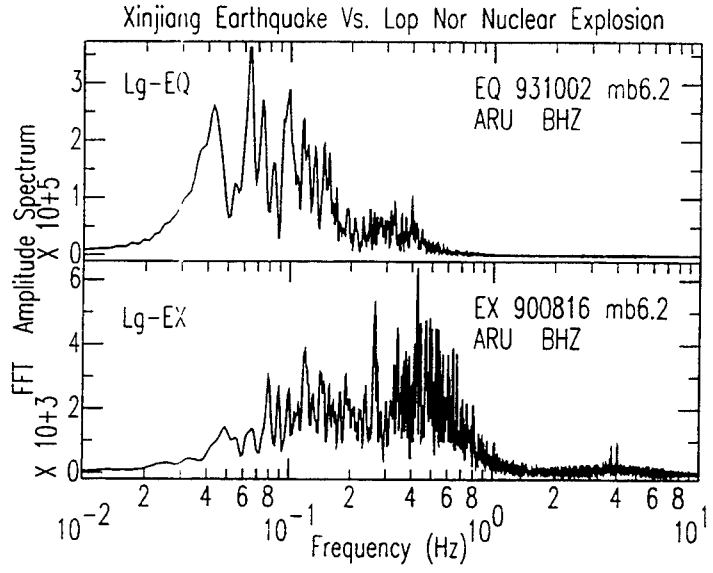

Figure 2: The Lg spectra for an m_b6.2 earthquake in Xinjang (931002) and an m_b6.2 Lop Nor nuclear explosion (900816) recorded at broadband station ARU.

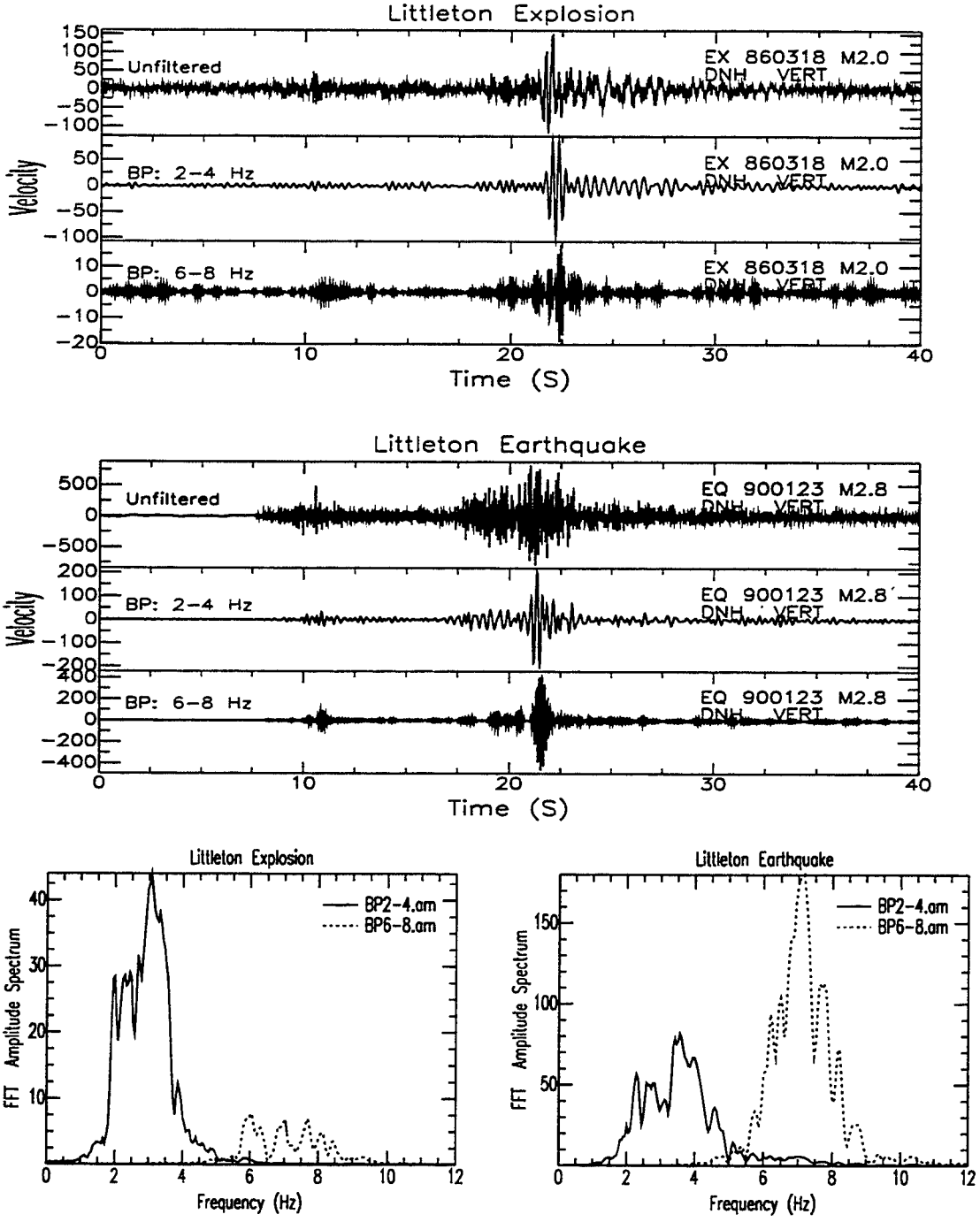

Figure 3: Short period, vertical component seismograms recorded at station DNH (distance 80 km) for a Littleton explosion (top) and a nearby earthquake (middle). Unfiltered, bandpass filtered from 2-4 Hz, and bandpass filtered from 6-8 Hz waveforms are displayed in velocity. Lg spectra of the two frequency bands are plotted for the explosion (bottom left) and the earthquake (bottom right). Note that the Lg spectral ratios between the two frequency bands are different for the explosion and the earthquake.

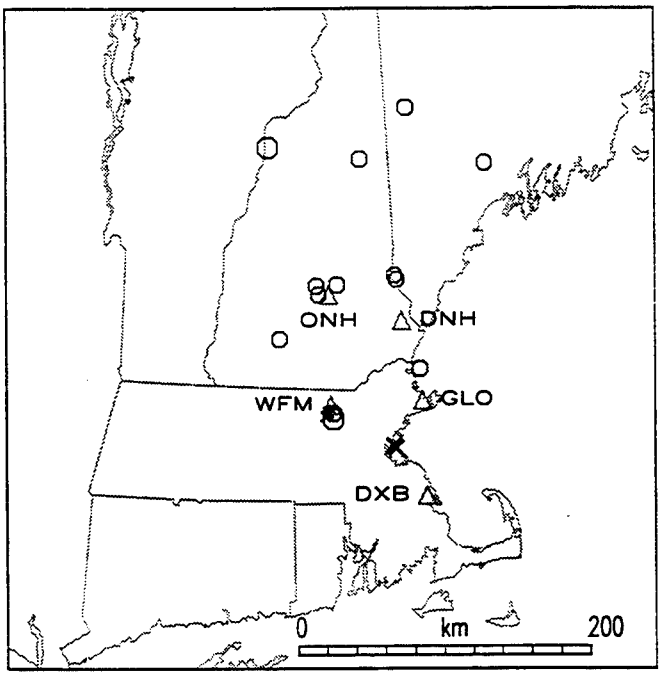

Figure 4: Map of New England showing locations of 10 explosions (crosses) and 14 earthquakes (circles) and 5 M.I.T. seismic stations (triangles) used in this study. The distance from the Littleton earthquakes and explosions (close to station WFM) to station DNH is about 80 km.

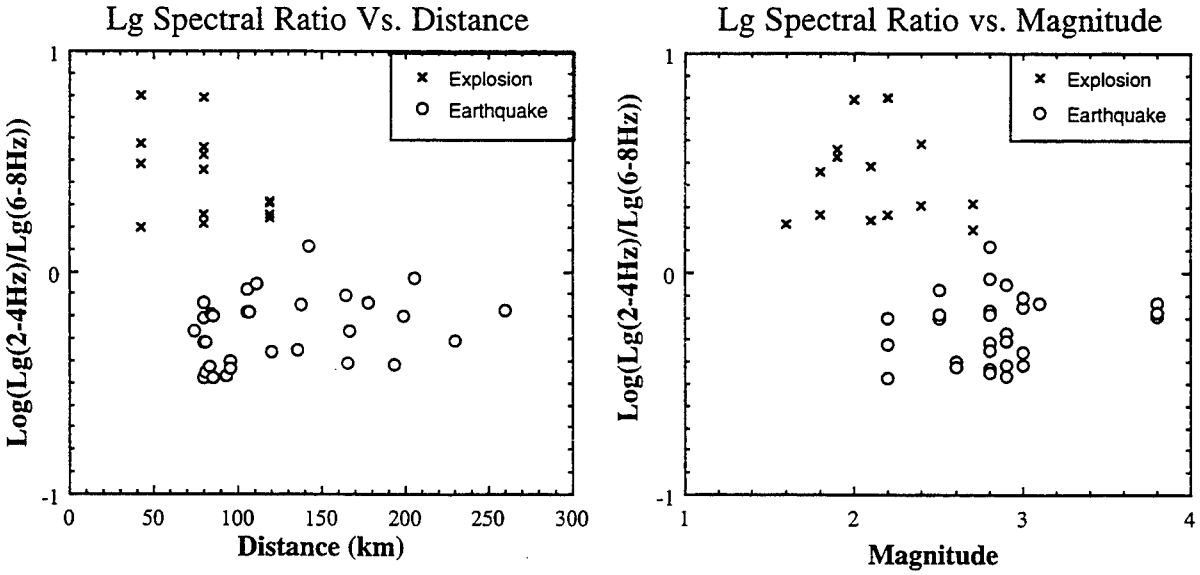

Figure 5: The Lg spectral ratio (2-4Hz)/(6-8Hz) versus epicentral distance (left) and magnitude (right) for explosions (crosses) and earthquakes (circles). The Lg spectral ratio well separates the small earthquake and explosion populations.

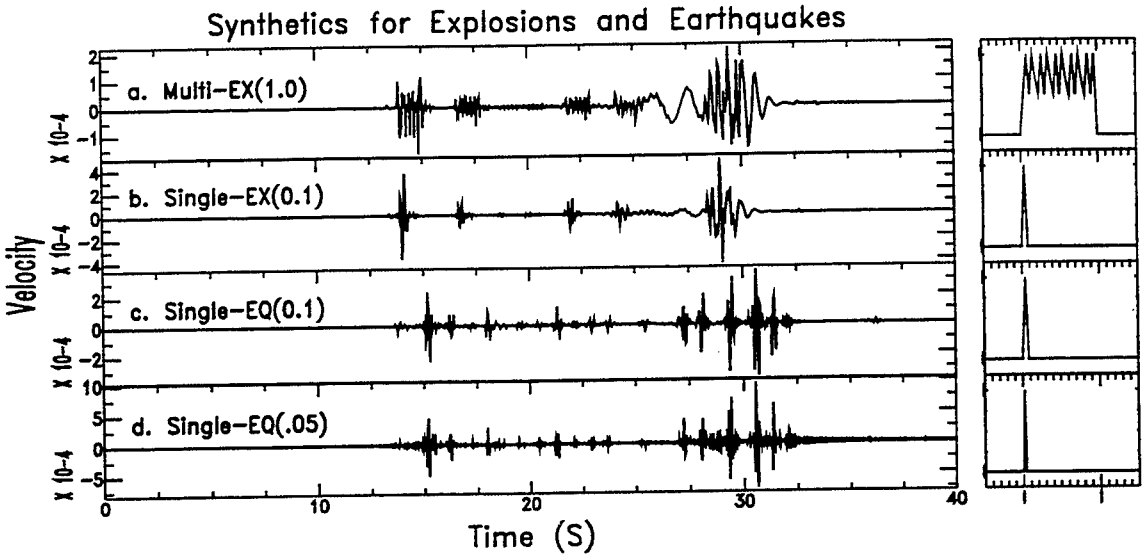

Figure 6: Synthetic velocity waveforms for a multiple explosion (a), a single explosion (b), and a thrust earthquakes with a source duration of 0.1 s (c) and 0.05 s (d). The left column shows the source time functions used in the calculation of the synthetics.

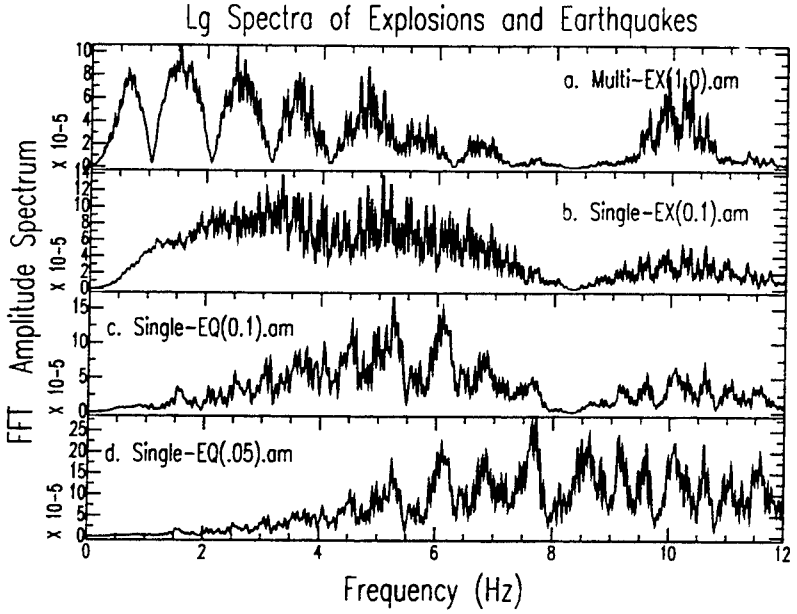

Figure 7: Fourier spectra of the Lg phase for a multiple explosion (a), a single explosion (b), and two thrust earthquakes (c and d) with different source durations. Note that the explosions are richer in lower frequency energy and earthquakes have more higher frequency energy.

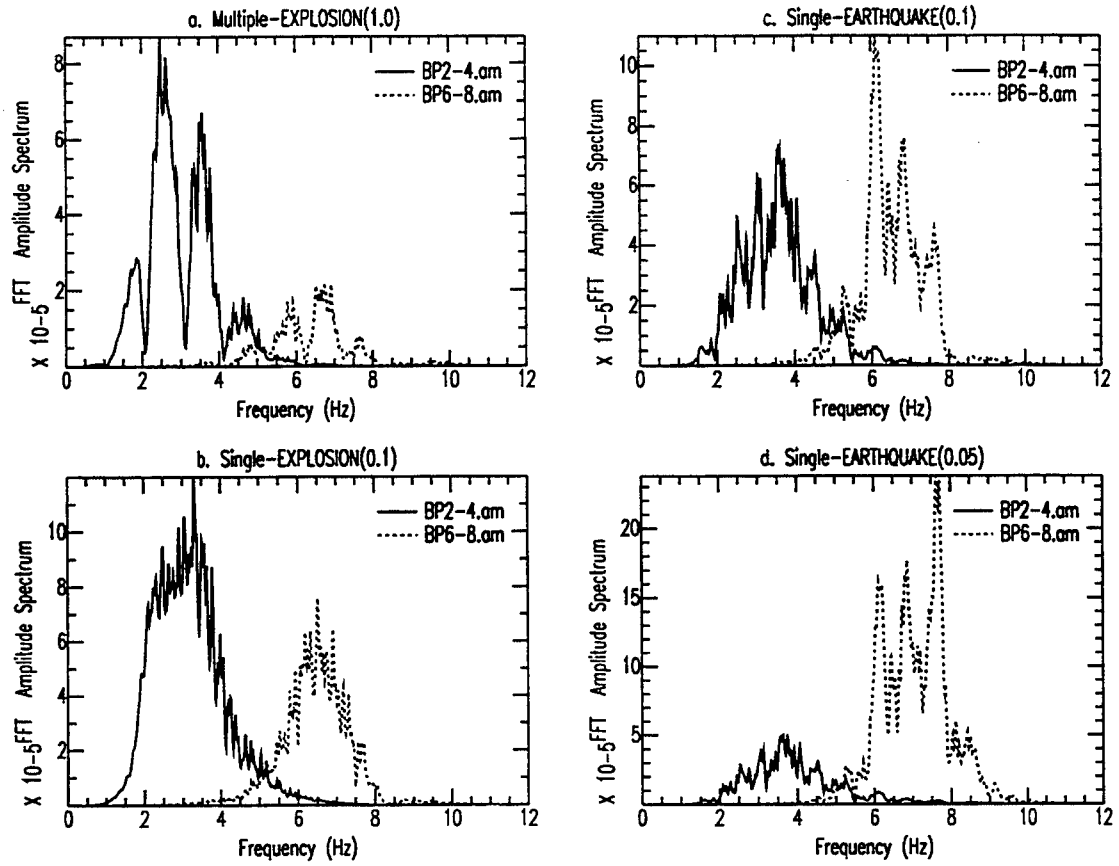

Figure 8: The Lg spectra of two bandpass filtered signals (2-4Hz and 6-8 Hz) for a multiply detonated explosion (a), a single explosion (b), and two earthquakes with source duration of 0.1 and 0.05 s (c and d).

Table 1. Velocity Structure Used in This Study

Layer	Thickness (km)	V_p (km/s)	V_s (km/s)	Density (g/cc)	Q_p	Q_s
1	1.0	5.31	3.07	2.4	70	35
2	12.0	6.06	3.50	2.6	100	50
3	22.0	6.59	3.80	2.7	1000	500
4	∞	8.10	4.68	2.8	∞	∞

Application of Soviet PNE Data to the Assessment of the Transportability of Regional Discriminants

J. R. Murphy, D. D. Sultanov*, B. W. Barker, I. O. Kitov*, and M. E. Marshall
Maxwell Laboratories, Inc., S-CUBED Division
11800 Sunrise Valley Dr., Suite 1212
Reston, Virginia 22091
Contract No. F19628-95-C-0109
Sponsored by AFTAC

Abstract

In order to discriminate the regional seismic signals produced by underground nuclear explosions from those produced by earthquakes, rockbursts and conventional mining explosions of comparable magnitude, it is necessary to know the range of nuclear explosion signal variation that can be expected as a function of source and propagation path conditions over the entire ranges of these conditions which may be encountered in global test monitoring. However, most research conducted to date has focused on analyses of regional signals recorded from explosions conducted at the few major nuclear test sites and these sample only limited ranges of the variables of interest. On the other hand, the extensive Soviet PNE testing program provides a source of regional seismic data recorded over much broader ranges of source and propagation path variables. More specifically, over 120 tests were conducted in this series and these explosions were detonated in a wide variety of geologic emplacement media (e.g., salt, clay, sandstone, granite, limestone) and are representative of wide ranges in yield (0.01 to 300 kt) and source depth (130 to 2860 m). Moreover, because of the tremendous geologic and tectonic diversity represented within the territories of the former Soviet Union, regional data recorded from these tests sample propagation path characteristics encompassing a range extending from tectonically active to stable continental interior regimes. S-CUBED is working with scientists from the Russian Institute For Dynamics of the Geospheres (IDG) to improve regional seismic discrimination capability by using data recorded from these Soviet PNE tests to derive improved, quantitative bounds on the ranges of seismic signal characteristics which can be expected from underground nuclear explosions which might be conducted under the wide variety of source and propagation path conditions which must be considered in global test monitoring. In particular, a digital database of regional seismic data recorded from selected Soviet PNE events at the Borovoye station in Central Asia has been acquired from IDG for use in this study and these data are being systematically analyzed to define the effects of source and propagation path variables on the spectral characteristics of the different observed regional phases. The results of these analyses are being used to derive improved constraints on the transportability of various proposed regional discriminants as they apply to underground nuclear explosions conducted over a wide range of testing conditions.

Key Words: Seismic, Discrimination, Regional, Soviet, PNE

* Institute For Dynamics of the Geospheres, Russian Academy of Sciences

Objective

The principal objective of this research program is to improve regional seismic discrimination capability by deriving improved, quantitative bounds on the ranges of seismic signal characteristics which can be expected from underground nuclear explosions which might be conducted under the wide variety of source and propagation path conditions which must be considered in monitoring a Comprehensive Test Ban Treaty. In order to reach this objective, we are working with scientists from the Russian Institute for Dynamics of the Geospheres (IDG) to conduct detailed analyses of regional seismic data recorded from selected Soviet PNE events which encompass the widest currently available ranges of explosion source conditions and propagation path variables.

Research Accomplishments

During the past year, our research has focused on the analyses of regional seismic data recorded from selected Soviet PNE events at the Borovoye station in Central Asia. At this time, Borovoye digital data recorded from 63 different Soviet PNE tests have been assembled, carefully reviewed and calibrated, and merged into a uniform database. These data represent a range of epicentral distances extending from 2.8 to 30 degrees, and sample a wide variety of explosive source conditions. Detailed information regarding the yields, depths of burial and geologic emplacement conditions have also been collected for each of these PNE tests and these data have been assembled into a comprehensive database which can be associated with the corresponding seismic database.

One of the unique features of this Borovoye database is that it provides samples of regional seismic data recorded at a fixed station from underground nuclear explosions at nearly constant distances, but along different azimuths. For example, Figure 1 shows the locations of seven selected Soviet PNE events located at comparable distances from Borovoye which sample about 180° in azimuth. The source characteristics of these explosions are listed in Table 1 where it can be seen that they sample a variety of source media and a wide range in source depth. The vertical component data recorded at Borovoye from the six explosions of Table 1 which are located at a nearly constant distance of about 8° are plotted as a function of apparent group velocity in Figure 2. These data are plotted in order of increasing station to source azimuth in this display and it can be seen that they exhibit some significant dependence on azimuth which are presumably related to propagation path differences. The most obvious is that the ratio of broadband amplitude level in the 5 to 6 km/sec group velocity window (i.e. Pg) to that in the 6 to 8 km/sec group velocity window (i.e. Pn) is much

Table 1

Source Characteristics of Selected Soviet PNE Events

Date	Yield, kt	Depth, m	Source Medium	Epicentral Distance, Degrees
08/15/73	6.3	600	Clay	10.5
09/19/73	6.3	615	Argillite	7.6
10/26/73	10	2026	Dolomite	8.3
10/04/79	21	837	Clay	7.7
12/10/80	15	2485	Sandstone	8.8
08/25/84	8.5	726	Clay	8.9
06/18/85	2.5	2859	Argillite	7.1

larger for explosions located to the north of Borovoye than for those located south and west of the station. Moreover, if we associate the 3 to 4 km/sec group velocity window with Lg, it can be seen that the broadband Lg/P amplitude ratio varies from significantly less than 1.0 (e.g. 12/10/80) to significantly greater than 1.0 (e.g., 10/26/73) for these explosions at an essentially constant distance from Borovoye. Thus, these data once again illustrate that propagation path variability can have a significant effect on some proposed regional discriminants.

Of course, the variability illustrated in Figure 2 can be different in different frequency bands and incorporates effects of yield, depth of burial and source medium. Therefore, these data have been bandpass filtered in an attempt to identify the effects of specific source and propagation path variables on the spectral compositions of the different regional phases. For example, Figure 3 shows comparisons of the Pn, Pg and Lg spectra determined from the Borovoye recordings of the two southern PNE events of Figure 1. In this case, the two explosions have very similar propagation paths to Borovoye, and have essentially the same yields and depths of burial, but one (08/15/73) was detonated in clay, while the other (09/19/73) was detonated in argillite. It can be seen that this difference in source medium has a pronounced and consistent effect on the regional phase spectra, with the explosion in clay having a notably lower source corner frequency, consistent with the results of our previous teleseismic analyses.

A second illustrative example is presented in Figure 4, where the regional phase spectra corresponding to southern (08/15/73) and northern (08/25/84) PNE events with comparable yields and depths of burial in clay media are compared. In this case, the overall shapes of the regional phase spectra are quite similar for these explosions with similar source conditions, but the relative phase excitation

levels are notably different. In particular, the Pg/Pn spectral ratio for the 08/25/84 northern explosion is much larger than that for the 08/15/73 southern event over the entire frequency range extending from 0.5 to 10 Hz. This is consistent with the corresponding time domain difference noted in Figure 2 and presumably relates to variations in the regional phase propagation paths. Note, however, that the Lg spectra are essentially identical in this case, indicating that at least some characteristics of the crustal wave guides along these two azimuths must be similar. This example illustrates the fact that the regionalization task is complex and strongly dependent on the specific regional phase under investigation.

The most consistently effective regional discriminant that has been discovered to date is the Lg/P spectral ratio, which has been found to be significantly lower at high frequencies for underground explosions than for earthquakes and other source types. However, since this discriminant involves two different regional phases, it is recognized that it can be sensitive to source conditions and propagation path effects. Therefore, it is important to quantify these effects over the widest possible range of potential nuclear test conditions. Figure 5 shows the range of the Lg/Pn spectral ratios computed using the six Borovoye recordings of Figure 2, which are representative of an average epicentral distance of about 8°. It can be seen that although the variability is large for this sample of explosions, all the ratios decrease to a value of less than about 1.0 above 3 Hz, consistent with previous observations from other underground nuclear explosions. Thus, this appears to be a fairly robust feature of underground explosion sources. Additional work will be required to assess the dependence of this discriminant on epicentral distance and other variables.

Conclusions and Recommendations

Over the past year, we have been working with scientists from the Russian IDG on a research program directed toward the derivation of improved, quantitative bounds on the ranges of regional seismic signal characteristics which can be expected from underground nuclear tests which might be conducted under the wide variety of source and propagation path conditions which will need to be considered in monitoring any eventual Comprehensive Test Ban Treaty. Research conducted to date has focused on analyses of regional seismic data recorded at the Borovoye station from a representative sample of Soviet PNE events. It has been shown that these regional signals display significant variations which correlate with source and propagation path characteristics and, therefore, they should be applicable to critical assessments of the transportability of various regional discriminants. Work is continuing on the formulation of parametric models which can account for this observed variability in regional phase characteristics.

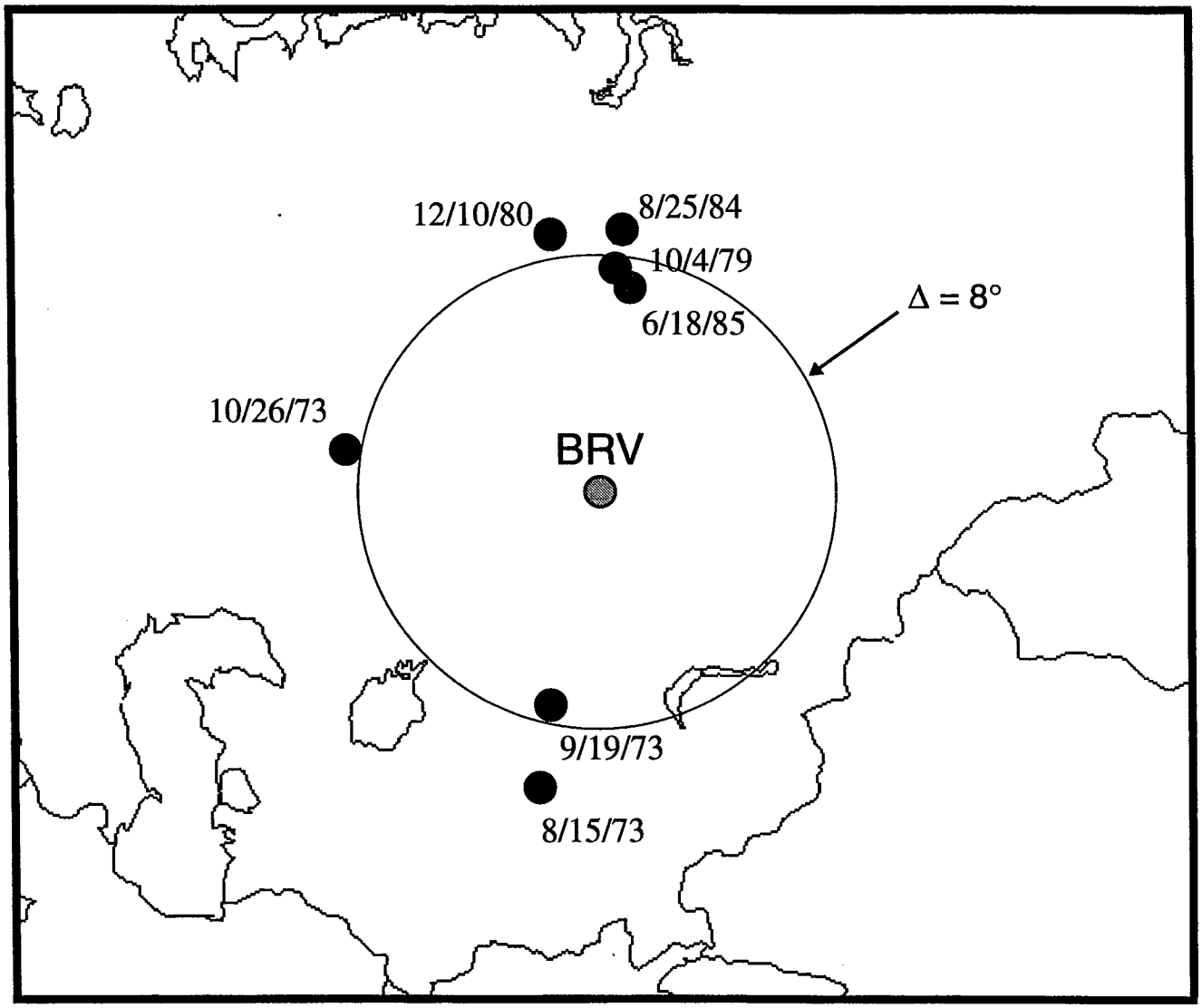

Figure 1. Locations of some selected Soviet PNE events for which regional seismic data have been recorded at the Borovoye (BRV) digital station.

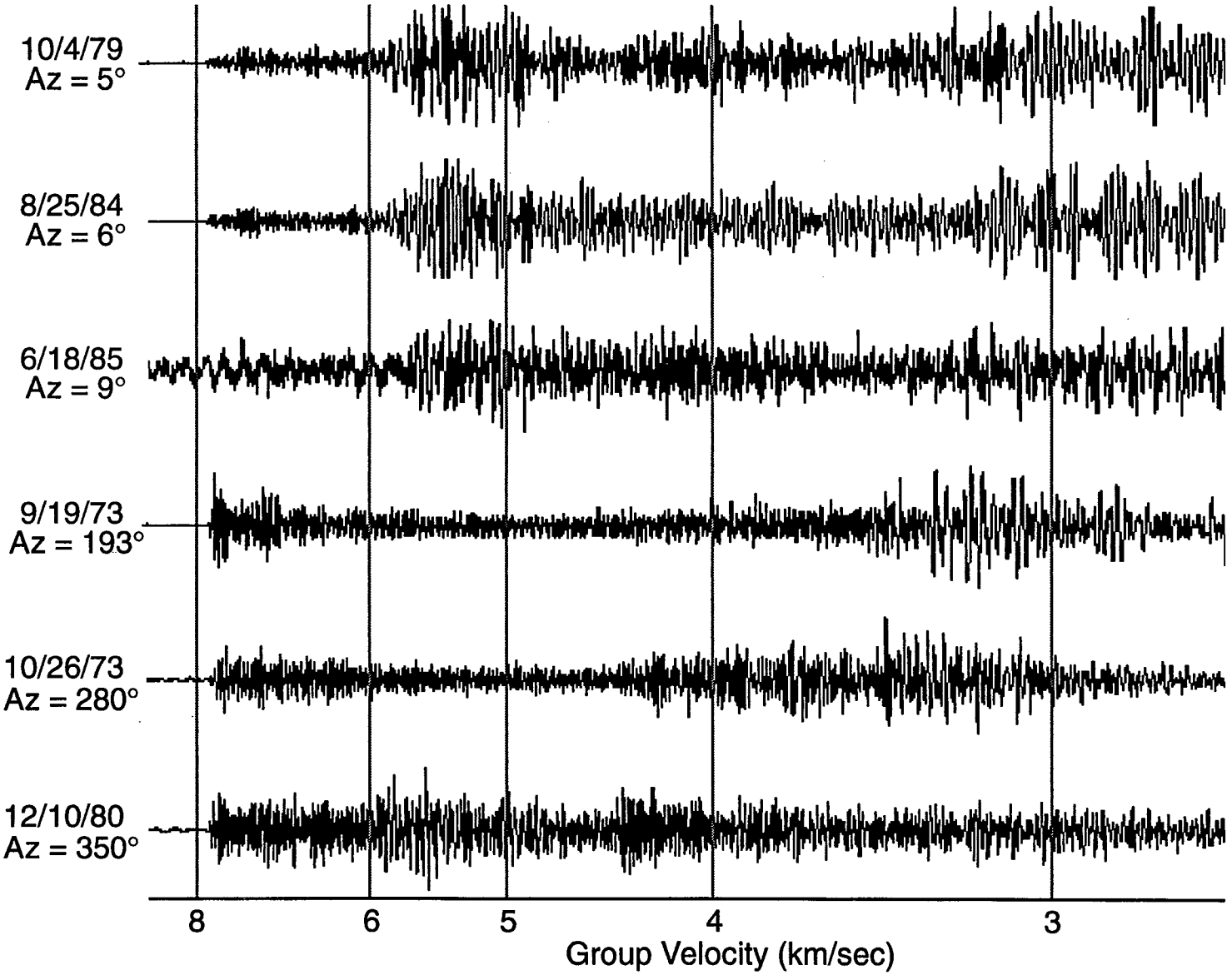

Figure 2. Vertical component regional signals recorded at Borovoye from six Soviet PNE events located at a common epicentral distance of about 8 °. Note the strong dependence of the P_g/P_n ratios on the azimuths of the source locations with respect to this station.

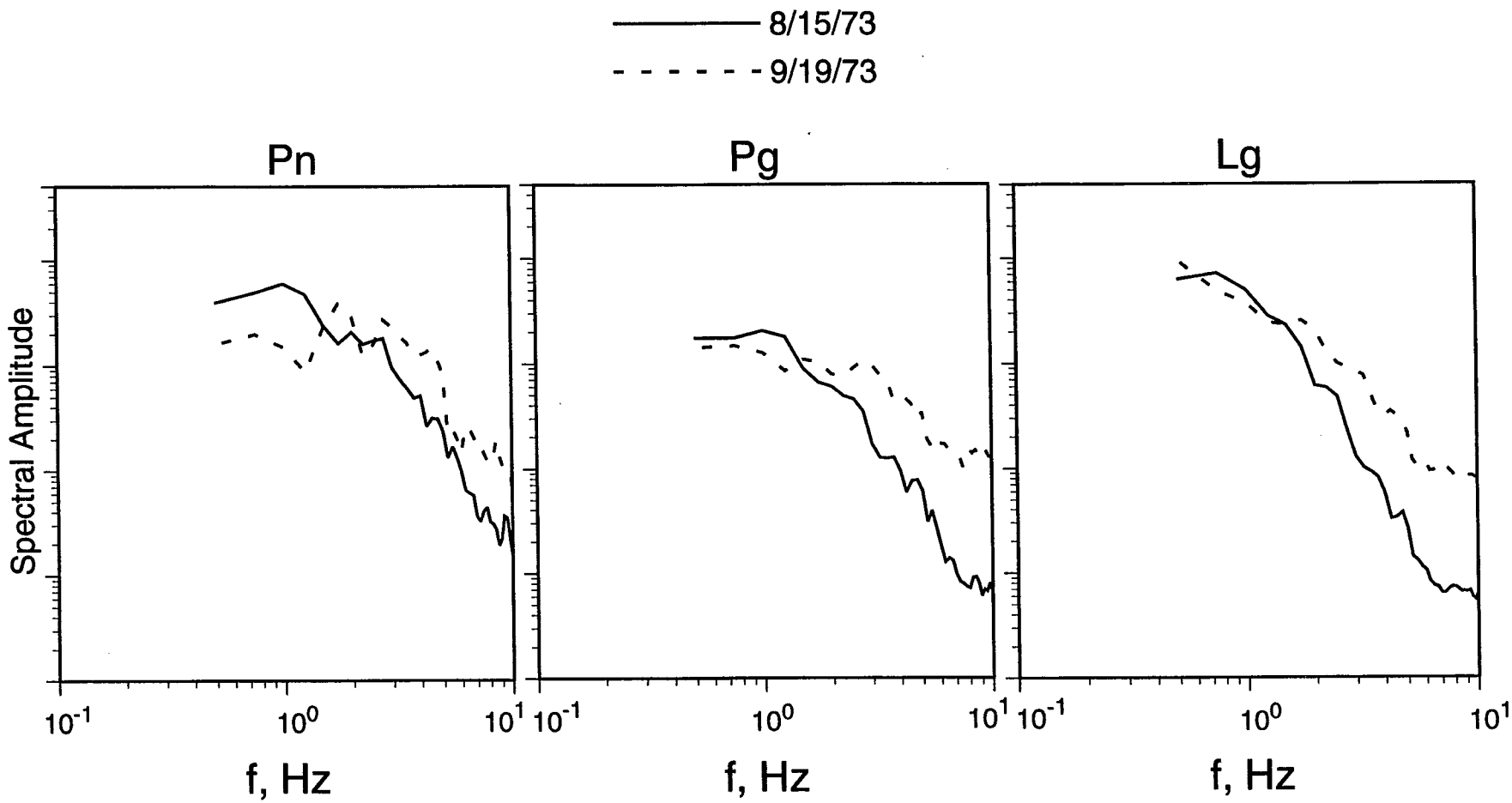

Figure 3. Comparison of regional phase spectra determined from the Borovoye recordings of two Soviet PNE events with essentially the same yields, depths of burial and regional propagation paths, but different source media. It can be seen that the source corner frequency associated with the explosion in clay (8/15/73) is significantly lower than that associated with the explosion in argillite (9/19/73), consistent with the results of previous teleseismic analyses.

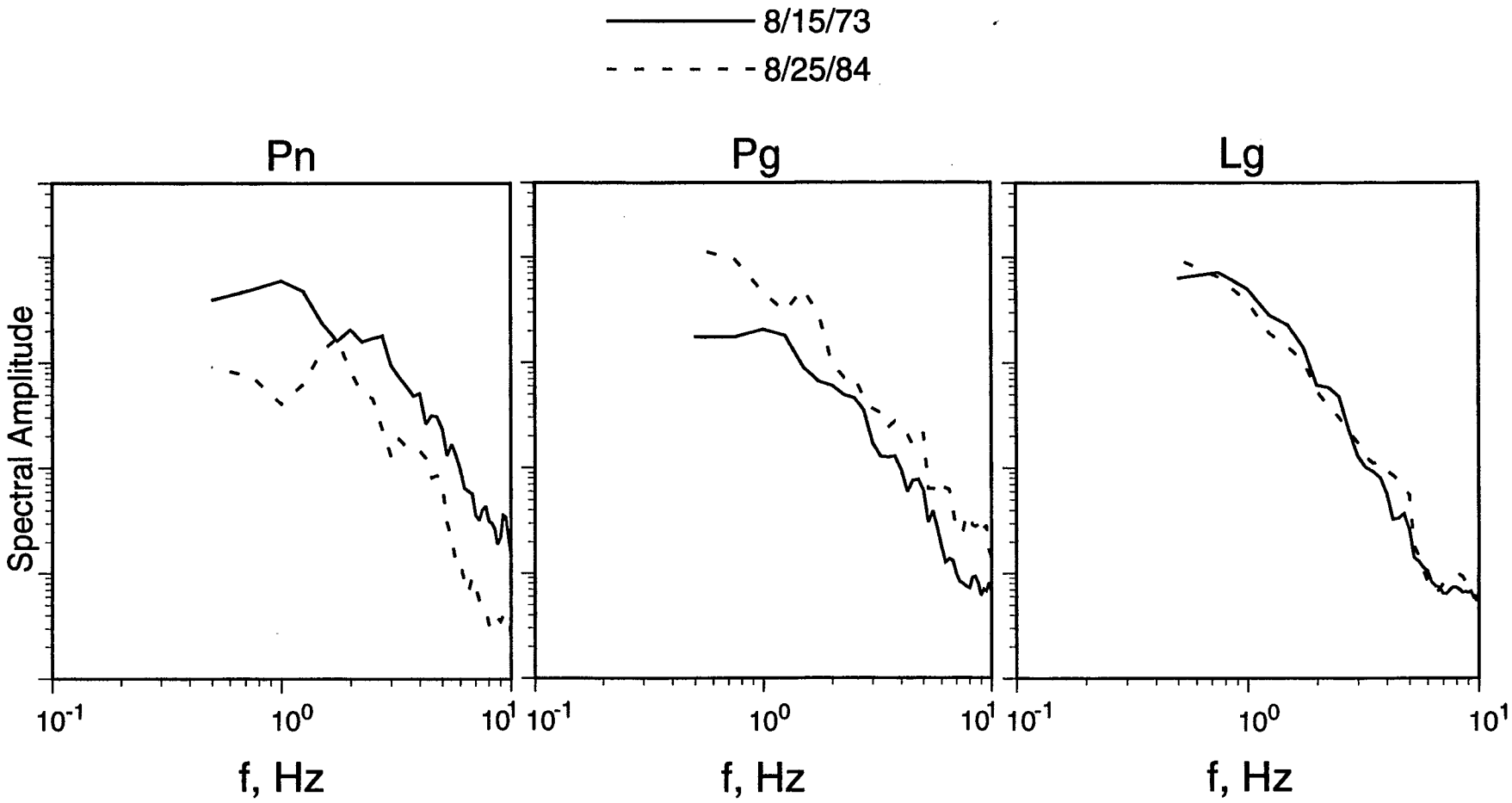

Figure 4. Comparison of regional phase spectra determined from the Borovoye recordings of two Soviet PNE events with comparable yields, depths of burial and source media (clay), but different regional propagation paths. It can be seen that, although the shapes of the individual phase spectra are similar for these two explosions, the Pg/Pn ratio for the northern event (8/25/84) is significantly larger than that for the southern event (8/15/73), consistent with the azimuthal dependence noted in Figure 2.

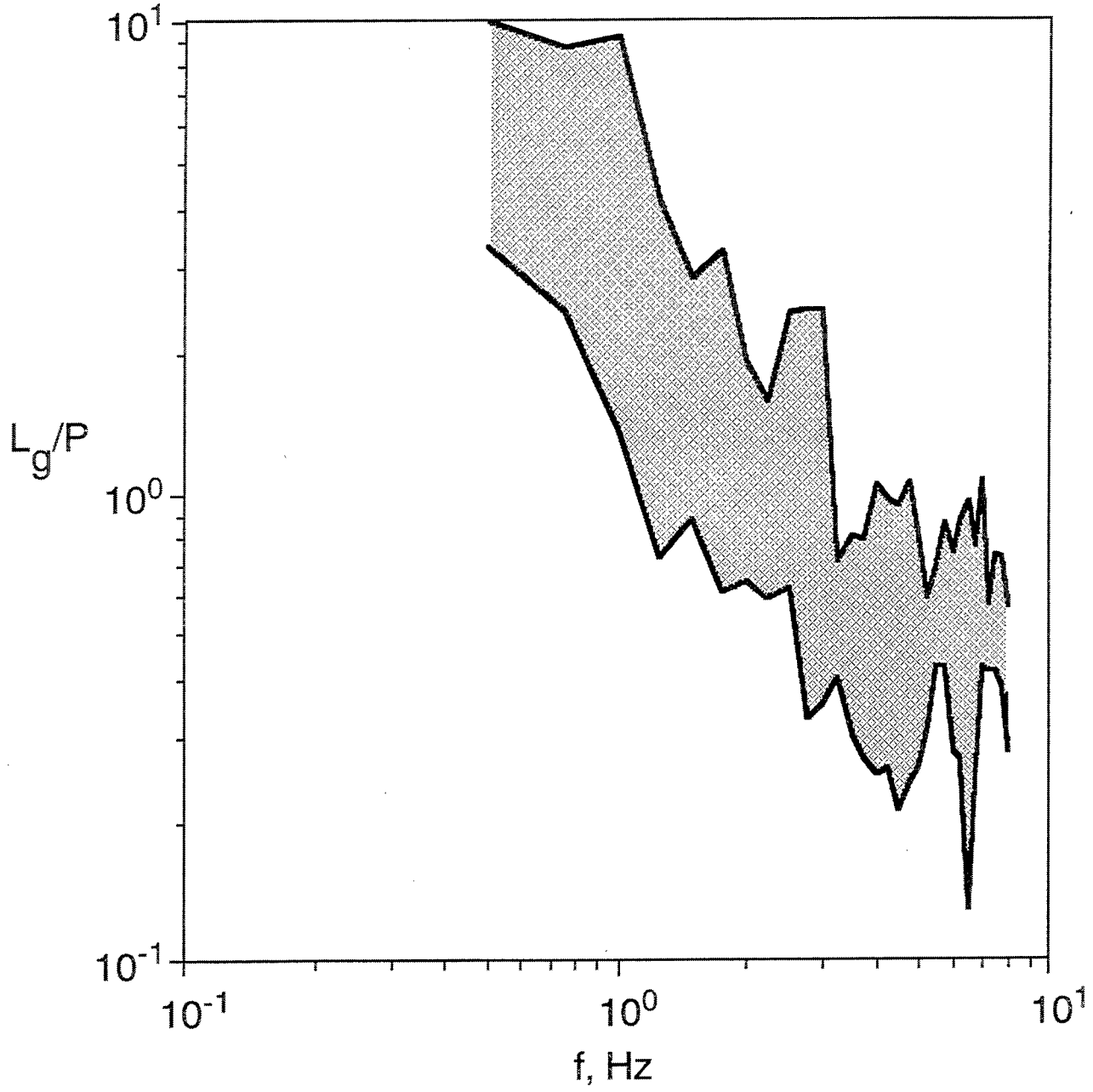

Figure 5. Range of Lg/P spectral ratios computed from the six Borovoye Soviet PNE recordings of Figure 2. Note that all these ratios are less than about 1.0 above 3 Hz, consistent with previous observations from underground nuclear explosions.

TRANSPORTABLE SEISMIC DISCRIMINANTS: STABLE ESTIMATES OF SPECTRAL RATIOS

Jay J. Pulli
Radix Systems, Inc.
6 Taft Court, Rockville, MD 20850
pulli@radix.com
Contract No. F19628-95-C-0175
Sponsored by DOE

ABSTRACT

This research addresses the issue of discriminant transportability, that is, the development of discriminants which can be successfully applied to events in a variety of geographic areas. The failure of discriminants to work in new areas of study is often attributed to changes in the path effect (Q, phase blockage, scattering, focusing/defocusing, etc.). These are certainly important contributing factors, especially since all discriminants are based either on the temporal or spectral nature of the regional phases. Our studies have shown that even in one geographic area, the comparison of seismic spectra for discriminant development can result in unstable estimates and therefore large variances in the actual discriminants. For example, spectral interference from multiple quarry shots results in spectral nulls which appear at frequencies which are different for *Pn* and *Lg* waves. Spectral ratios computed in these circumstances have large variances and thus often fail to identify the seismic source. Most of this is due to the lack of coherence between *Pn* and *Lg*. We are studying a variety of ways of comparing seismic spectra with the goal of developing a stable estimate of the relative excitation of *Pn* and *Lg* which reflects the source characteristics. The first step is the analysis of an existing database of about 200 events which have been studied using previously developed parameterizations. The new methods are being compared with these old parameterizations in order to evaluate discrimination capability. The second step is the testing of these discriminants with new ground truth databases being compiled as part of the DOE/CTBT research program.

KEY WORDS

Discrimination, signal processing, discriminant transportability, ground-truth databases

OBJECTIVE

The primary objective of this research is to assess the utility of a variety of methods for comparing spectra (e.g. spectral ratios, cross-spectra, transfer function estimation, and statistical methods) for the purpose of regional seismic event identification. The goal is to develop a stable, low variability method of spectral comparison for application to the problem of discriminant transportability. Specific objectives are:

- to apply these methods to an existing database of about 200 regional events which have already been studied using parameterizations of the *Lg/Pn* and *Sn/Pn* spectral ratios;
- to compare the identification performance of these new methods with that of the older parameterizations;
- to apply these methods to new events in other areas, specifically the Middle East and North Africa, which are being compiled as part of the overall DOE CTBT research effort.

RESEARCH ACCOMPLISHED

Background

For over ten years it has been known that there are observable differences in the regional phases *Pn*, *Sn*, and *Lg* for earthquakes and explosion sources (e.g. Dysart and Pulli (1987), Baumgardt and Ziegler (1988), Hedlin *et al.* (1990)). These differences were noted in the (relatively) high-frequency band of the data, using events recorded at the newly installed NORESS, ARCESS, and FINESA arrays. Specifically, it was noted that the *Lg/Pn* and *Sn/Pn* spectral ratios above 10 Hz provided excellent discrimination capability. Research then focused on a variety of methods to parameterize and process these observed differences, including statistical methods (Shumway, 1996), neural network methods (Dysart and Pulli, 1990), and fuzzy logic (Sereno and Wahl, 1993).

However, when these discriminants were applied to events in new areas of interest, their ability to identify source types was shown to be inferior when compared to events from the original source area. In hindsight this was not unexpected, given the area-to-area variation in propagation effects which can change the spectral content of the regional phases. Some of these effects, such as anelastic attenuation, can be independently measured and modeled for application to the observed spectra. Other effects, such as *Lg* blockage and the focusing/defocusing of regional phases due to velocity perturbations are more difficult to correct. Scattering also contributes to spectral variation (Dainty, 1996), although recent developments in the measurement of scattered waves (coda) show promise for source identification (Mayeda and Walter, 1996).

An additional consideration is the actual comparison of the *Pn*, *Sn*, and *Lg* phase spectra. Spectral ratios are typically used for spectral comparison and these formed the basis of our early studies. To parameterize the spectral ratios, we computed the mean values of *Lg/Pn* and *Sn/Pn* over a variety of frequency bands: 0-20 Hz to characterize the broadband spectra as well as 2-5 Hz, 5-10 Hz, and 10-20 Hz. A closer examination of this calculation illustrates the difficulty of the estimation. *Figure 1* shows the *Lg* and *Pn* spectra for an explosion at the Koashva Nostoch apatite mine in the Apatity area. The *Lg* spectrum peaks around 2 Hz, then quickly decays by a factor of 10, after which there is a smooth decay with frequency. The Pn spectrum however shows evidence of spectral scalloping as is often seen in quarry explosions. This is presumably due to ripple firing (if the firing pattern is delayed by enough time to appear in the pass band of the data) or the total length of the firing pattern. When we calculate the Lg/Pn spectral ratio, these peaks and troughs of the spectra result in an estimate which shows simply artifacts of the spectral ratio and not a true comparison of the relationship of the spectral energy in each phase.

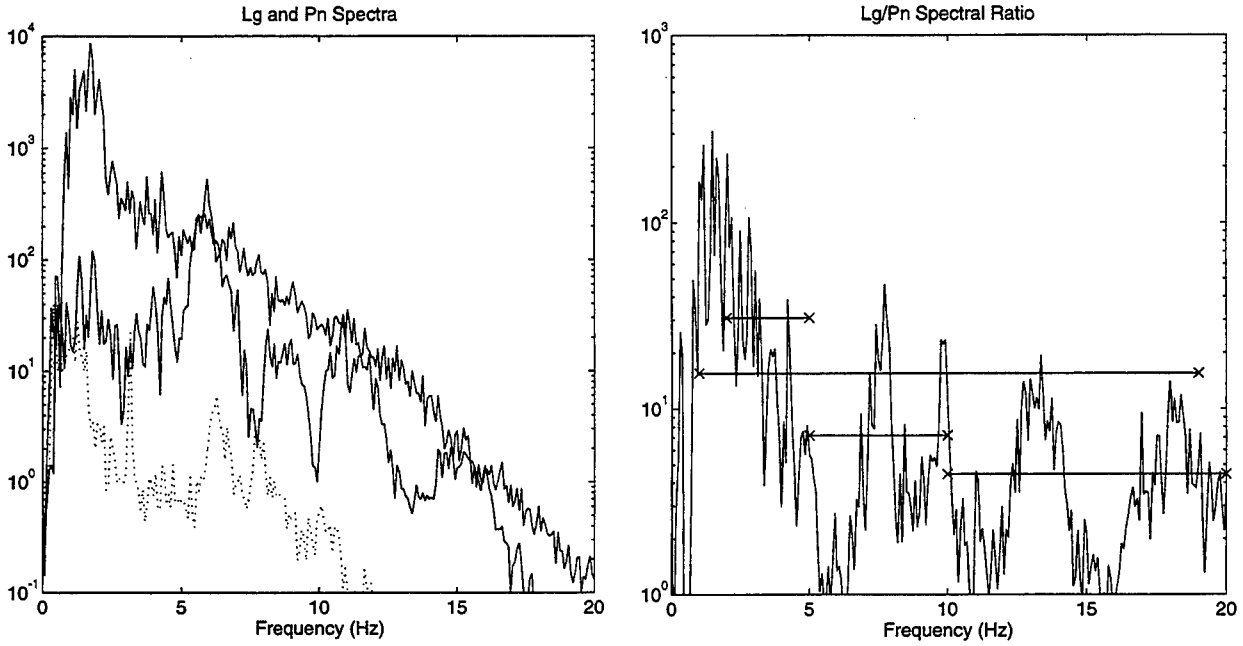

Figure 1. Lg and *Pn* spectra (left) as well as *Lg/Pn* spectral ratio (right) for an explosion at the Koashva Nostoch apatite mine in the Apatity area (GTDB event number 2066). The spectral ratio has been parameterized as mean values across the entire band as well as from 2-5 Hz, 5-10 Hz, and 10-20 Hz. In this case, the parameterization is clearly not representative of the data.

Our earlier estimates of spectral ratios also did not correct for the path effect. Clearly the path effect is important for spectral comparisons of events at varying distances. *Figure 2* illustrates this using a simple exponential decay model for *Pn* and *Lg* waves, each of which has a Q value of 1000. Since the *Lg* waves propagate at a slower velocity than the *Pn* waves, the effect of Q (energy loss per cycle) is greater. At a distance of 180 km, *Lg* decays approximately 50 times as much as *Pn* at 20 Hz. At 380 km, this difference increases to nearly three orders of

magnitude. The estimation of path corrections to the observed spectra is seen as a crucial part of the overall DOE/CTBT effort.

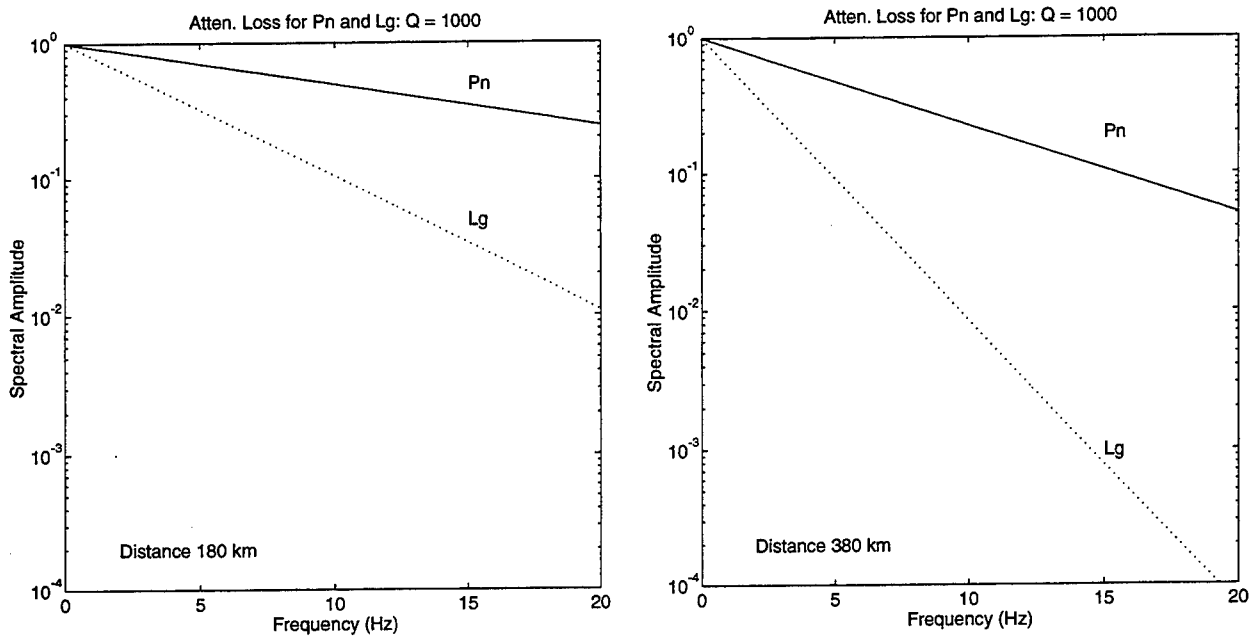

Figure 2. Model calculation of the decay of Pn and Lg for a common Q value of 1000, propagated to distances of 180 km (left) and 380 km (right).

Software and Data Processing

Software used during this research effort has been written in the MATLAB® technical computing environment. The software consists of scripts or functions (so-called *m-files*) which call the built-in MATLAB® routines to perform basic vector and matrix computations. These scripts can be linked to previously compiled C or FORTRAN objects, or can be translated to ANSI C using a supplied compiler. Toolboxes, which combine numerous *m-files*, are also available which perform groups of functions, such as signal processing, image processing, system identification, and neural computing. This computing environment was chosen to take advantage of signal processing routines already developed for other projects, and because the binary data files (*mat-files*) and ASCII *m-files* can be moved from platform-to-platform (UNIX, PC, Macintosh) without translation.

The starting point is a CMR Version 3.0 database (*.wfdisc*, *.origin*, and *.w* files; see Anderson *et. al*, 1990). The C-program *css2matlab* reads a user-specified *.wfdisc* file and generates *mat-files* for each *.wfdisc* entry with file names *station_channel.mat* (e.g. *ARA0_sz.mat*). Each *mat-file* contains variables with names corresponding to those in the CMR Version 3.0 definition, as well as other comments which are used by subsequent plotting routines. At this point, the programs *gram.m* and *zoom.m* are used to display a single channel of data and select windows for the noise, *Pn*, *Sn*, and *Lg* phases. The program *extract_arcess.m* (as well as programs for the NORESS, GERESS, FINESA, and ILPA arrays) are used to extract the

waveform segments and produce matrix variables of the phase waveforms across each array. For the regional data of interest to this project, waveform segments consist of 512-points for each channel, corresponding to 12.8 seconds for the typical 40 samples/second digitization. Once the waveforms have been extracted, *event* files (e.g. *e2002.mat*) are created which contain all of the relevant information, including that from the *.origin* file if available. Event names correspond to the *.wfdisc* prefix name in order to remain consistent with the Ground-Truth Database convention (Grant *et. al*, 1993).

Signal processing is accomplished with a variety of developed *m-files* which typically consist of four versions: compute, plot, process, and hardcopy. For example, there is *compute_spectra.m*, *plot_spectra.m*, *process_spectra.m*, and *hardcopy_spectra.m*. The *compute* version performs the actual calculation, the *plot* version plots the results, the *process* version batches all *event* files for the *compute* version and saves the result to each *event* file, and the *hardcopy* version batches all plots to a specified printer. *m-files* have been developed to perform a variety of these signal processing functions, including spectra, power spectral density, cepstra, coherence, cross-spectra, multiple-filter analysis, spectral ratios, and beamforming, as well as three-component analysis.

Software and user manuals are specified as a contract deliverable for this project, and are thus available to anyone upon request. Plans are underway to create a Web page which will contain both the software *m-files* and the event *mat-files* for downloading.

Databases Examined

Our earlier studies of regional seismic event identification utilized the parameterization of the *Pn*, *Sn*, and *Lg* spectra discussed above (mean values over broad and narrow bands). Waveform windows of the regional phases were not saved as part of the effort, just the parameterizations of the spectra. In order to address this new research, we dearchived all of the old data and used the software described above to re-pick phase windows and create event files consisting of the waveform segments of pre-event noise, *Pn*, *Sn*, and *Lg* phases. These databases include:

- NORESS events from 1985 - 1988
- Ground Truth Database 1: Vogtland earthquakes and explosions
- Ground Truth Database 2: Steigen earthquake data swarm
- Ground Truth Database 8: Apatity mining-induced tremors
- Ground Truth Database 9: Apatity mine blasts
- ILPA Database for Region 4: Regional earthquakes

The analysis of additional ILPA database events in underway. Although in the new area of interest, the data for these events is of lower frequency (sampled at 20 samples/second) which makes comparisons difficult. The souce types are all earthquakes, so direct comparison of source types is not possible. Newer databases are currently being compiled as part of the overall program effort, and should be available during the second half of the program.

Example 1: Mining Explosion at the Rasvumchorr Apatite Mine

This event (from GTDB Dataset 9, event 2047) is an example of one which produces a high degree of coherence between the *Pn* and *Lg* waves. Recording made at ARCESS are shown in *Figure 3*. The *Pn* wave consists of a simple, compact pulse peaking at about 5 Hz. Spectral nulls occur at 4, 8, and 12 Hz (*Figure 4*). The *Lg* spectrum is remarkably similar, with more energy in the low frequency band and similar spectral nulls at the higher frequencies. The high frequency null however occurs at a slightly lower frequency (by about 1 Hz), contributing to an osscillatory spectral ratio. Across most of the band, the *Lg* is consistently about 5 times larger than the *Pn*.

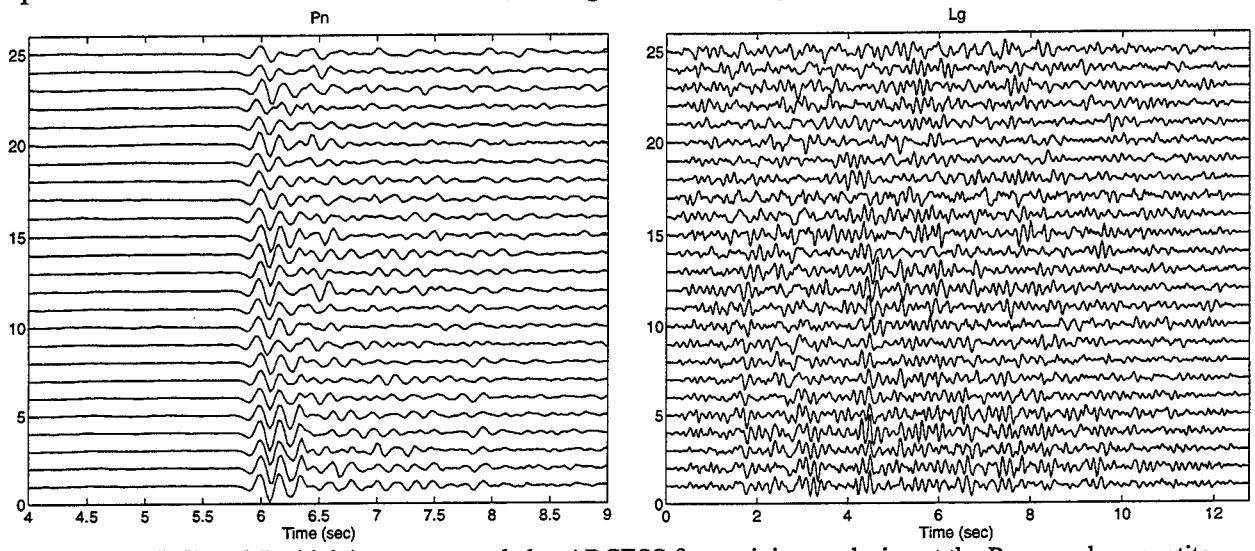

Figure 3. Pn (left) and *Lg* (right) waves recorded at ARCESS for a mining explosion at the Rasvumchorr apatite mine (GTDB Dataset 9 event 2047).

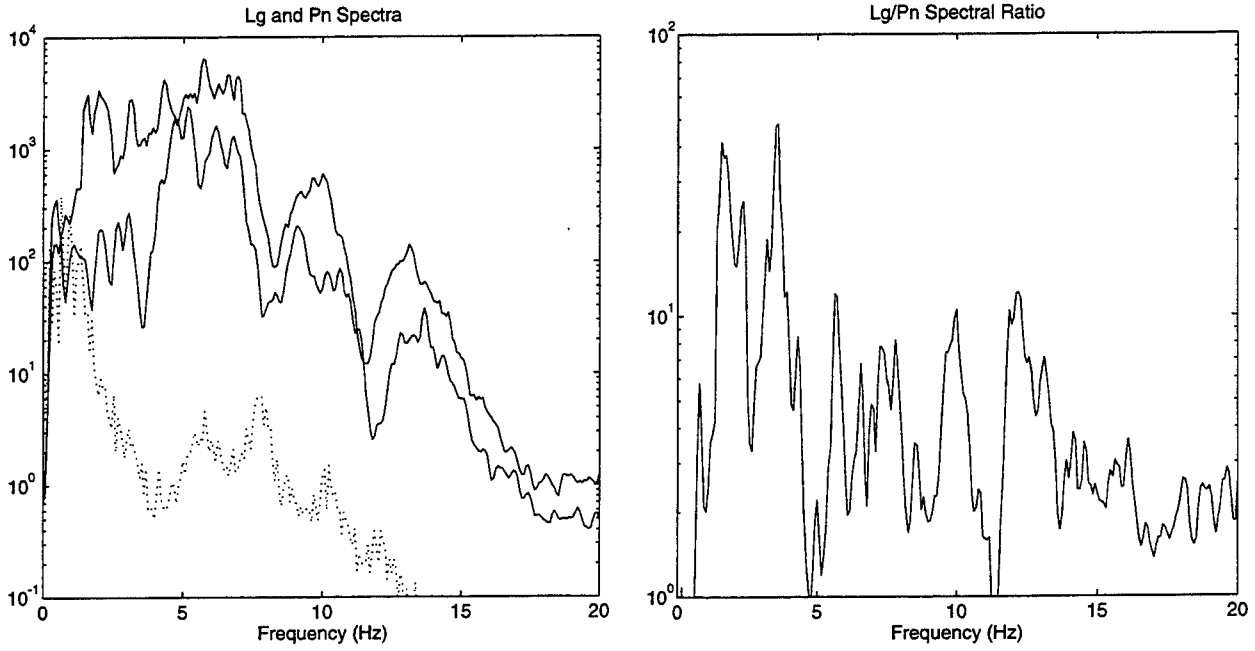

Figure 4. Lg and *Pn* spectra (left) and *Lg/Pn* spectral ratio (right) for the Rasvumchorr apatite mine explosion using the data from *Figure 3*. The spectra track well as a function of frequency, though there is some breakdown in the location of the large spectral null at about 12 Hz.

Example 2: Mining-Induced Earthquake at Apatity

This event produced signals which are more complex than those of the previously discussed mine blast, though both are in the same area. The *Pn* wave train appears to consist of a number of arrivals of similar frequency but differing amplitudes. Channel 1-6, comprising the ARCESS A and B rings, also show a strong arrival about 0.5 seconds after the largest wavelet. The *Lg* wave train is of much lower frequency than the nearby quarry explosion and shows little evidence of spectral scalloping. The resulting spectral ratio is thus dominated by the complexiety of *Pn*.

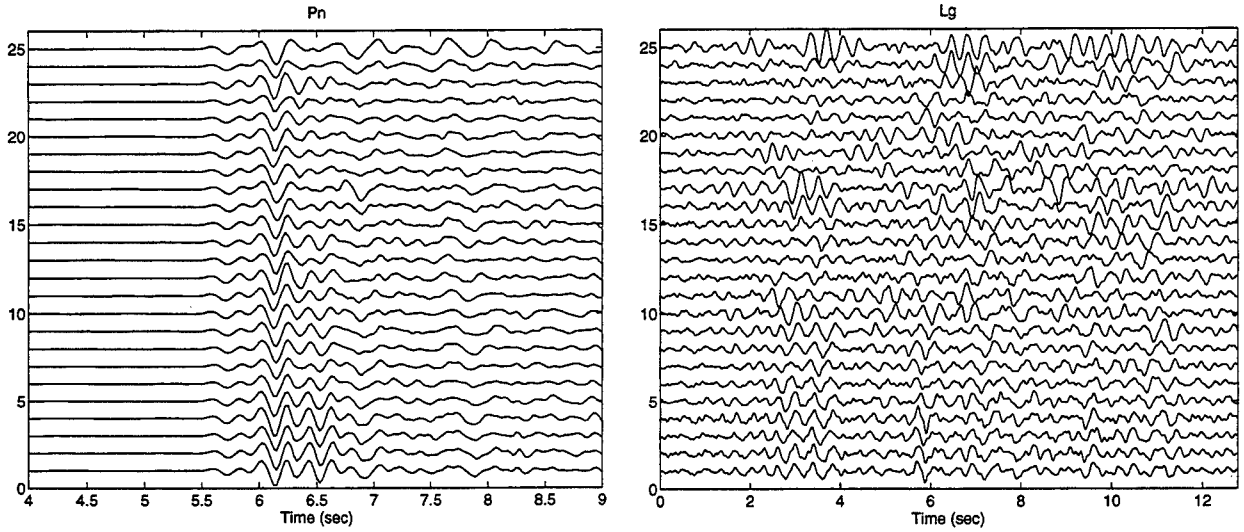

Figure 5. Pn (left) and *Lg* waves (right) recorded at the ARCESS array for a mining-induced earthquake in Apatity (GTDB Database 8 event 2002). The *Pn* wavetrain appears to consist of a number of simple pulses of the same frequency but differing amplitudes.

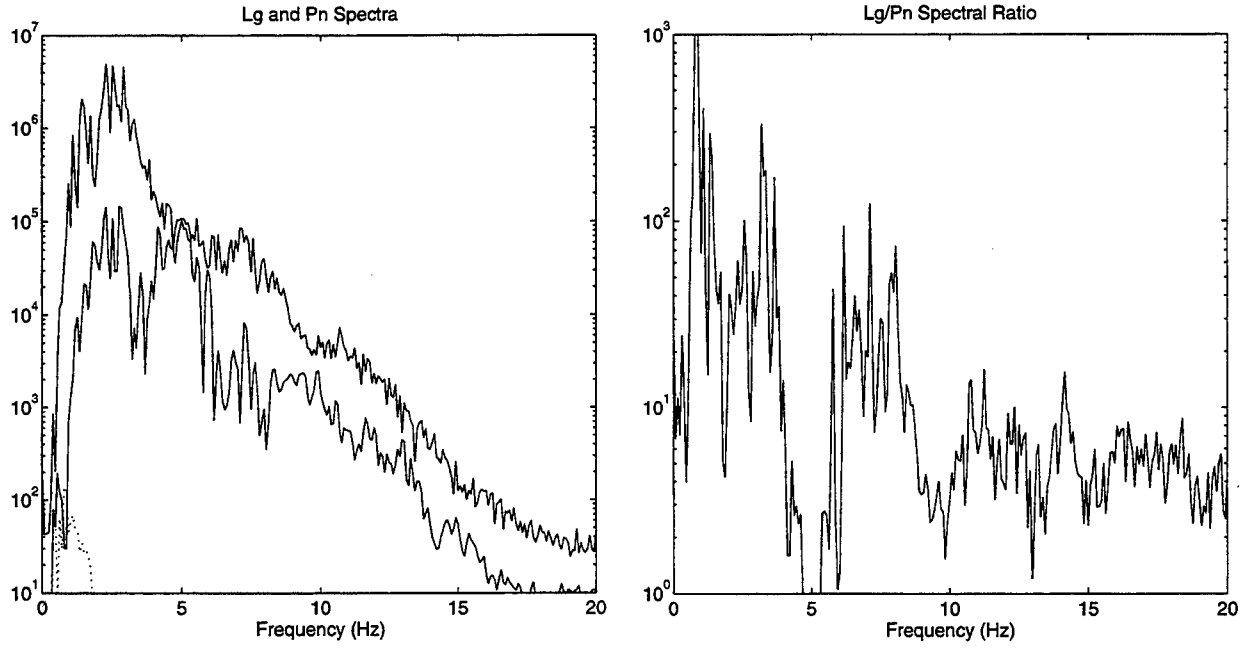

Figure 6. Lg and *Pn* spectra (left) and the *Lg/Pn* spectral ratio (right) for the Apatity mining-induced earthquake.

CONCLUSIONS AND RECOMMENDATIONS

There are numerous ways to compare signal spectra: spectral ratios, cross-spectra, transfer functions, system identification methods, and statistical methods. We have applied a variety of techniques to an expanded database of regional events with the objective of stabilizing the comparison in order to minimize the variance and improve the transportability of the measurement. We have found that no one technique works best for all events: the stability of the spectral comparisons is event dependent, even for events in the same source area. Much of the instability can be attributed to the nature of the *Lg* waves. The *Lg* wave trains show little broadband coherence with the *Pn* or *Sn* waves. However, narrowband correlations do exist. We are currently investigating methods to phase match the spectra in order to take advantage of these narrowband correlations, and will report on their success at the poster session.

REFERENCES

Anderson, J, W.E. Farrell, K. Garcia, J. Given, and H. Swanger (1990), Center for Seismic Studies Version 3 Database: Schema Reference Manual, Center for Seismic Studies Technical Report C90-01, 61 pp.

Baumgardt, D.R. and K.A. Zeigler (1988), Spectral evidence for source multiplicity in explosions: application to regional discrimination of earthquakes and explosions, *Bull. Seis. Soc. Amer., 78*, 1773-1795.

Dainty, A.M. (1996), The influence of seismic scattering on monitoring, in Husebye and Dainty, eds., Monitoring a Comprehensive Test Ban Treaty, NATO ASI Series, Kluwer Academic Press, 836 pp.

Dysart, P. and J. Pulli (1987), Spectral study of regional earthquakes and chemical explosions recorded at the NORESS array, Center for Seismic Studies Technical Report C87-03.

Dysart, P. and J. Pulli (1990), Regional seismic event classification at the NORESS array: seismological measurements and the use of trained neural networks, *Bull. Seis. Soc. Amer., 80*, 1910-1933.

Grant, L., J. Coyne, and F. Ryall (1993), CSS Ground Truth Database: Version 1 Handbook, Center for Seismic Research Technical Report C93-05.

Hedlin, M., J.B. Minster, and J.A. Orcutt (1990), An automatic means to discriminate between earthquakes and quarry blasts, *Bull. Seis. Soc. Amer., 80,* 2143-2160.

Mayeda, K. and W.R. Walter (1996), Moment, energy, stress drop, and source spectra of western United States earthquakes from regional coda envelopes, *J. Geophys. Res., 101*, 11,195-11,208

Pulli, J. (1996), Extracting and processing seismic signal parameters for regional seismic event identification, in Husebye and Dainty, eds., Monitoring a Comprehensive Test Ban Treaty, NATO ASI Series, Kluwer Academic Press, 836 pp.

Sereno, T.J. and D.D. Wahl (1993), A fuzzy-logic approach to regional seismic event identification and application to the Novaya Zemlya event on 31 December 1992, in The Novaya Zemlya Event of 31 December 1992 and Seismic Identification Issues, 15th Annual Seismic Research Symposium , PL-TR-93-2160, ADA271458.

Shumway, R.H. (1996), Statistical approaches to seismic discrimination, in Husebye and Dainty, eds., Monitoring a Comprehensive Test Ban Treaty, NATO ASI Series, Kluwer Academic Press, 836 pp.

Outlier Detection without Ground Truth

Stephan R. Sain, H. L. Gray, and Wayne A. Woodward
Southern Methodist University
Dallas, TX

ARPA CONTRACT NO: F19628-95-C-0098

ABSTRACT

We consider the difficult task of using seismic signals (or any other discriminants) for detecting nuclear explosions from the large number of background signals such as earthquakes and mining blasts. Wang et al. (1996) attack the problem in terms of outlier detection, i.e. modeling the background as a mixture distribution and looking for outliers (nuclear events) from that mixture. However, those authors only considered the case in which at least some fraction of the training sample was labeled, i.e. ground truth was available, and the number of distinct classes of events was known. In the current paper we extend these results to the case in which no events in the training sample are labeled and also to the case in which the number of event types represented in the training sample is unknown. In order to accomplish this task, a preliminary clustering of the training sample data is necessary. We also briefly consider the case in which some observations in the training sample and in the potential outlier are missing.

In practical application, the seismic events in a given region may be detected at a number of stations. Due to the fact that several features will be observed at several stations, it may be important to be able to compress data across stations in a manner that does not lose important information. Procedures for data compression that apply to the setting in which the outlier population is considered to be a mixture of event types are also discussed.

Keywords: outlier detection, discrimination, mixture distributions, likelihood ratio

OBJECTIVE

The objective of this research is to develop statistical methodology for automated detection of the occurrence of unusual or rare events, i.e. outliers. In order for this methodology to be effective it must work in the environment of large data sets with a substantial amount of missing data cells, and additionally, an effective algorithm must operate in real time or near real time and should not require ground truth data for training.

RESEARCH ACCOMPLISHED

1. Introduction

Monitoring a comprehensive test ban treaty involves the difficult problem of differentiating the seismic signal of nuclear events from the large number of seismic signals of earthquakes, mining explosions, etc. This problem is made even more difficult due to the lack of information concerning the behavior of nuclear signals in many regions of the earth. The distinguishing characteristics of small nuclear explosions are regional in nature. Therefore, the features that characterize such events are not transportable from region to region around the world. Certainly, in many regions there is no previous data on nuclear tests. Furthermore, in many regions, little information is available on non-nuclear events.

Wang, Woodward, Gray, Wiechecki, and Sain (1996) frame the problem of detecting nuclear events in terms of detecting outliers (nuclear events) from a mixture population (earthquakes, mining explosions, etc.) Specifically, the authors assume that the training data is a sample of size n from a mixture distribution whose density is given by

$$f(x) = \sum_{i=1}^{m} p_i g_i(\boldsymbol{x}; \boldsymbol{\mu}_i, \boldsymbol{\Sigma}_i) \tag{1}$$

where m is the number of components in the mixture, $g_i(\boldsymbol{x}; \boldsymbol{\mu}_i, \boldsymbol{\Sigma}_i)$ is the density associated with the ith component, the p_i, $i = 1, \ldots, m$ are the mixing proportions, and $\boldsymbol{x}$ is a d-dimensional vector of feature variables. A typical scenario might be the case in which the mixture population consists of events associated with earthquakes and mining explosions. The authors developed a modified likelihood ratio test that required no distributional assumptions concerning the outlier distribution. This is a useful practical solution because of the lack of regional training samples for nuclear events. Using the bootstrap to model the distribution of the test statistic and calculate critical values, the authors showed that this test has essentially as high a detection probability as the standard likelihood test in which complete information concerning the distribution of the outlier population is known.

However, Wang et al. (1996) made assumptions concerning the training sample that may not be appropriate in practice. Specifically, it was assumed that the associated source component population is identifiable for $n_L \leq n$ members of the training sample where $n_L > 0$. Letting n_i denote the number of labeled (i.e. the source of the event is known) observations associated with component i, the authors assumed that the n_i, $i = 1, \ldots, m$ are random variables following a multinomial distribution and that they contain information about the mixing proportions. The

parameters are estimated via the EM algorithm (see Redner and Walker, 1984 and McLachlan, 1982, and this algorithm further assumes that each n_i is sufficiently large to provide initial estimates of μ_i and Σ_i.

In practice, no ground truth may be available, and it may well be the case that we may not even know the number of component populations in the mixture distribution of the training sample. Also, it often occurs that some data will be missing, i.e. we will not always have all features measured at each of the events in the training sample or in the potential outlier. Finally, in a relatively new region, the training sample may actually contain a few unusual non-nuclear events (malfunctioning ripple-fired mining explosions, mine collapses, etc.) that do not belong to any component population of the appropriate mixture distribution.

In this report, we study the problem of detecting a nuclear event or other rare or unusual seismic signals in new or relatively unexplored regions for which training samples do not satisfy the assumptions imposed by Wang et al. (1996).

2. The Procedure

In this section a procedure is presented for detecting outliers in a region for which limited information is available concerning the training sample of non-nuclear events. We extend the work of Wang et al. (1996), to develop an outlier-detection procedure that applies to the case in which no labeled training data (i.e., no ground truth) are available in a region.

(a) Data Types

(i) Known number of components and no missing data

Here we assume that the training sample is known to contain a fixed number of event types (i.e. m in (1) is known.), and we assume that no data are missing. The event groups in the training sample represent the types of non-nuclear seismic activity in the region, e.g. earthquakes and mining blasts.

Let

$$\boldsymbol{X}_1, \ldots, \boldsymbol{X}_n \in \Pi$$

denote the training sample of size n from the mixture population. In the notation of Redner and Walker (1984) the sample is of Type 1, i.e. it consists only of unlabeled observations. A new observation, $\boldsymbol{X}_{n+1}$, is obtained, and given the training sample we want to test the hypotheses

$$H_0 : \boldsymbol{X}_{n+1} \in \Pi$$

$$H_1 : \boldsymbol{X}_{n+1} \notin \Pi .$$

Wang et al. (1996) recommend the use of a modified likelihood ratio statistic, W, for testing the above hypotheses. They show that the rejection region is of the form $W \leq W_\alpha$ for some W_α picked to provide a level α test. Since the null distribution of W has no known closed form, the nonparametric bootstrap is used to approximate it. Specifically, B bootstrap samples are obtained. Each bootstrap sample is obtained by resampling from the training sample to obtain a sample of size $n+1$, and for each bootstrap sample the test statistic W_b^* is obtained where $b = 1, \ldots, B$. We then define W_α to be the (100α)th percentile of the W_b^*.

It should be noted that the maximum likelihood estimates involved in evaluating W are obtained using the EM algorithm (McLachlan, 1982 and Redner and Walker, 1984). This

procedure is iterative in nature and requires initial values of the parameters estimates. Additionally, under the present scenario it is assumed that no initial estimates for the parameters, μ_i and Σ_i, of the component distributions or the mixing proportions, p_i, are available. Wang et al. (1996) assumed that a sufficient amount of labeled (ground truth) data are available to provide initial estimates. In our setting, this information is not assumed to be available and a clustering approach is used to group the data into distinct classes from which initial estimates can be obtained. The initial estimates are then taken from the data assigned to each of the unknown classes.

(*ii*) *Number of components unknown and no missing data*

It will often be the case that the number of components, i.e. distinct classes, in the population of the training sample will not be known. In this section we propose a modification of the procedure in (*i*) which is appropriate when the number of components is unknown. We consider the use of Akaike's AIC (Akaike, 1974) for purposes of determining the number of components m in the mixture. Specifically, for $m = 1, \ldots, M$ we calculate

$$\text{AIC}(m) = -2\ln(L_{max}(m)) + 2(\#\text{ of free parameters})$$

where $L_{max}(m)$ is the maximized likelihood of the training sample under the assumption that there are m components and M is a sufficiently large integer. $L_{max}(m)$ is obtained via the EM algorithm as discussed in the previous section. For each m, $m = 1, \ldots, M$, we use the clustering discussed previously to obtain m initial clusters to provide starting values for the EM algorithm from which $L_{max}(m)$ is obtained. AIC is calculated for $m = 1, \ldots, M$, and the number of components, m_{AIC}, associated with the minimum AIC is chosen. The test statistic for the data, W, is then calculated based on m_{AIC} components.

To obtain the distribution of W we again use the nonparametric bootstrap. The bootstrap samples are selected as before, and for the bth bootstrap sample we find $m^*_{\text{AIC}}(b)$ using AIC and calculate W^*_b on this basis. We then take W_α to be the (100α)th percentile of the W^*_b, $b = 1, \ldots, B$ as before.

It is well known that in general AIC does not provide a consistent estimator of the model order, and that the selected model order has the tendency to increase as sample size increases thus leading to overly complicated models. To compensate for this, in the simulations and data analysis in the next sections, and as an alternative to AIC we consider the use of BIC (Akaike, 1977) given by

$$\text{BIC} = -2\ln(L_{max}(m)) + \ln(n)(\#\text{ of free parameters}) .$$

BIC imposes a more severe penalty than does AIC and in some cases provides a consistent estimator of the model order.

In Section 3 we will investigate the use of AIC and BIC in order to determine their performance in the context of the bootstrap-based likelihood ratio outlier test considered here.

(*iii*) *Missing data*

In either (*i*) or (*ii*) it may be the case that some of the data are missing. Miller, Gray and Woodward (1993) studied outlier testing in the setting in which the training sample is from a multivariate (non-mixture) population when some data are missing. They considered the use of the EM algorithm versus simple mean replacement for dealing with missing data, and their findings were that the performance of mean replacement (at least for no more than 20% missing) was comparable with the full EM algorithm at a fraction of the computation requirements. Based on these findings, we considered strategies for dealing with missing data in the mixture setting considered here. These strategies require a preliminary clustering based on a modified distance measure that allows for missing data. We have investigated a mean-replacement procedure which shows to work well when the percentage of missing cases is relatively small (about 10%). When missing data is more prevalent, improved techniques may be needed. These could include use of a modified mean-replacement procedure or the use of the EM algorithm.

(*b*) *Cleaning the Training Sample*

While it is assumed that the training data contain no nuclear events, the procedure we propose includes an examination of the training sample for unusual events (i.e. events which are in fact outliers themselves such as mine collapses) that should be examined and possibly removed before the training sample is used for testing new, and possibly nuclear, events.

After the initial estimates are obtained, each point in the training sample is considered individually by using the other $n-1$ points as a pseudo training sample. The modified likelihood ratio test developed in Wang et al. (1996) is used to test each point and determine the probability that each point belongs to the assumed mixture population. Any point with a significant result (very small probability of inclusion in the mixture - say 0.01 level) at this phase is labeled as an outlier and is removed from the training data set. After checking each point, the remaining points are then used as a "clean" training data set for testing future events as potential outliers from the mixture population.

3. Simulations

In this section the effect of unlabeled data, unknown number of components and missing data on the detection probability of the outlier test based on W is examined using a simulation study based on the procedures described previously. In the simulations of this section, the training data are from a mixture distribution as in (1) with $m = 2$ and where the component distributions are each bivariate normal. Specifically, components 1 and 2 are distributed

$$N\left(\begin{pmatrix}0\\0\end{pmatrix}, \begin{pmatrix}1 & 0.5\\0.5 & 1\end{pmatrix}\right) \tag{2}$$

and

$$N\left(\begin{pmatrix}2\\2\end{pmatrix}, \begin{pmatrix}1 & -0.5\\-0.5 & 1\end{pmatrix}\right)$$

respectively with $p_1 = p_2 = 0.5$. For the simulation, training samples of size $n = 60$ are generated from this mixture population, and outliers are generated from the populations

$$N\left(\begin{pmatrix} 1+k-5 \\ 1-k+5 \end{pmatrix}, \begin{pmatrix} 1 & 0.5 \\ 0.5 & 1 \end{pmatrix}\right), \tag{3}$$

where $k = 1, ..., 9$.

In Table 1 we show the results for the case of known components and for various degrees of labeling. The table shows detection probability results for the case in which all training sample observations are labeled using the technique based on W. The estimates shown are the proportion of the 1000 replications for which an outlier was detected. In general, the lack of labeling information from the class labels of the training data leads to no detectable decrease in detection probability as would be expected. This suggests that in these types of settings, although lack of labeling may degrade our estimates of the components of the mixture, it does not seem to have a dramatic effect on the estimated mixture distribution itself.

		k								
% Unlabeled	Sig. Level	1	2	3	4	5	6	7	8	9
0	.062	1.00	.979	.799	.260	.031	.249	.756	.983	1.00
10	.074	1.00	.979	.796	.282	.037	.291	.768	.977	1.00
25	.068	1.00	.981	.783	.254	.032	.264	.767	.985	1.00
50	.061	1.00	.980	.790	.255	.032	.249	.758	.985	1.00
75*	.061	.999	.980	.767	.232	.030	.237	.746	.972	1.00
100	.066	1.00	.986	.761	.261	.032	.251	.747	.981	.999
S.E.	.007	0.015								

* Several of these (18) lacked sufficient data in a group for starting values.

Table 1. Significance levels and power of outlier test with some data unlabeled and number of components assumed to be known. ($n = 60$, 1000 replications)
Training sample population : 2-component mixture in (2) with $p_1 = p_2 = 0.5$
Outlier populations: specified by $k = 1, ..., 9$ as in (3)

In order to examine the implications on the outlier test of not knowing the number of components, in Table 2 we show power corresponding to that shown in Table 1 when m is assumed to be unknown and is estimated by either AIC or BIC. In these simulations we generated 100 replicates of size $n = 60$ from the two-component distribution in (2) for which none of the observations were labeled and for which the number of components was assumed to be unknown in the analysis stage. It can be seen in Table 2 that there is some loss in power when compared to the known component, 100% unlabeled case in Table 1. However, the powers are not dramatically smaller. The power results using AIC and BIC are very similar.

		k								
Criterion	Sig. Level	1	2	3	4	5	6	7	8	9
AIC	.08	1.0	.98	.70	.27	.04	.21	.70	.96	1.0
BIC	.09	1.0	.98	.75	.23	.01	.17	.67	.97	1.0
S.E.	.02	.05								

Table 2. Significance levels and power of outlier test with all data unlabeled and the number of components assumed unknown. ($n = 60$, 100 replications)
Training sample population : 2-component mixture in (2) with $p_1 = p_2 = 0.5$
Outlier populations: specified by $k = 1, \ldots, 9$ as in (3)

4. Example using Seismic Data

The data for this example are based on an analysis of earthquakes and mining explosions from the Vogtland region near the Czech-German border by Burlacu and Herrin (1996). These data were taken from the ground truth database compiled by Grant, et al. (1993). These measurements are new to the seismic community and involve fitting a third order autoregressive process to the S wave. The power spectral density is estimated and the strength and frequencies of the real and complex poles are calculated. These are useful features since distributed surface explosions (i.e. ripple-fired mining blasts) tend to be lower frequency with a sharper spectrum (strong pole) and earthquakes tend to have higher frequency and a more distributed spectrum (weak pole). These features are incorporated into a promising screening process to identify mining blasts. In the analysis here, the complex frequency and pole strength associated with an AR(3) fit to the data are used as feature variables.

Table 3 contains information on the events used in this study. Note that event number 25 is listed in the ground truth data base as an explosion, although some controversy has surrounded this event. For this example, the ground truth information is not used. Rather, the source for each event is assumed to be unknown, although it is assumed that the data set is composed of observations from two sources (earthquake and mining blast). Finally, it is also assumed that no nuclear events are present in the training sample.

Event #	Date	Lat(N)	Long(E)	Depth	M_1	Y(kg)	Or.time	Q/X
1	031191	50.207	12.685	0	1.98	3,265	12:03:24	EX
2	032191	50.207	12.685	0	2.05	3,982	12:04:15	EX
3	032291	50.207	12.685	0	2.03	2,835	12:33:25	EX
4	032391	50.207	12.685	0	1.99	2,025	12:00:56	EX
5	032491	50.296	12.225	12.9	2.18	-	05:05:04	EQ
6	032491	50.279	12.228	12.9	1.50	-	05:35:21	EQ
8	032491	50.278	12.220	12.4	1.65	-	09:38:33	EQ
9	032491	50.294	12.223	12.7	2.07	-	14:33:28	EQ
10	032491	50.293	12.224	12.5	1.80	-	15:00:45	EQ
11	032491	50.293	12.224	9	1.73	-	15:41:04	EQ
12	032591	50.298	12.222	12.9	2.37	-	14:54:14	EQ
13	032591	50.292	12.213	12.4	1.54	-	22:31:46	EQ
15	050291	50.207	12.713	0	1.93	3,575	11:06:10	EX
19	051991	50.360	12.371	0	2.06	-	03:22:10	EQ
20	052391	50.207	12.713	0	2.12	3,135	11:01:05	EX
21	052591	50.207	12.713	0	2.13	3,135	11:01:29	EX
23	052891	50.207	12.685	0	2.01	3,575	11:03:51	EX
24	062091	50.207	12.685	0	1.98	1,998	11:01:17	EX
25	062091	50.293	12.803	0	1.80	-	11:45:35	EX
26	062291	50.207	12.685	0	2.15	2,886	10:58:34	EX
27	062791	50.207	12.685	0	1.93	3,515	11:04:40	EX

Table 3. Information on the 27 Vogtland events

These data show a clear separation between the groups, and only one iteration of the cluster analysis is necessary, i.e. no observations in the training sample were determined to be outliers.

The leave-out procedure described in Section 2b was applied to the data and only event 25 shows a significant result (p-value < 0.01), which leads to the conclusion that event 25 is an outlier to the mixture distribution of earthquakes and explosions. Results for all other points support their membership in the mixture and are consistent with the ground truth information. New events in this region should now be tested using this "clean" data.

5. Data Compression

Gray, Woodward, and Yücel (1995) and Fisk (1995) have extended outlier detection results to the case in which readings are obtained at multiple stations but for which the population of the training sample was assumed to consist of a single event type. They considered several multi-station approaches including a full-vector approach in which the data were not compressed but the data on d features and m stations was simply considered to be a multivariate observation vector of length dm. Other strategies included a weighting across stations in which the weights were computed in such a way as to minimize the variance of the new variable. Another approach consisted of the obvious strategy of declaring an event to be an outlier if any of the individual station-based tests finds the event to be an outlier. This test involved a Bonferoni-based

adjustment to assure that the overall significance level is no larger than α. The full-vector approach was shown via simulations to be the most desirable approach, but it may be impractical when dm is large. In the current research we are developing improved data compression procedures and are extending these results to the case in which the outlier population is considered to be a mixture of event types. More specific results will be given at the poster session.

6. Concluding Remarks

In this report we show that outlier detection based on a mixture training sample of totally unlabeled data can be successfully accomplished even when the number of components is not known and when some data are missing.

It is desirable to assign labels to events in the training sample after the clustering and estimation of component parameters is accomplished. We first consider the case in which the training data consist of two components. Each point in the training sample is tested as an outlier from each of the two training sample components and corresponding p-values obtained are associated with each component. Based on these p-values, each training sample member would be assigned a component membership or will be left unassigned when membership is not clear as defined by some predetermined p-value. Use of tests based on a focused critical region can be used to increase our ability to assign component membership based on the position of the training sample value being tested with respect to the locations of the corresponding component centroids. When the distribution of the training sample has more than two components, the testing can be based on considering the components two at a time. Actual "naming" of components can be done by an analyst, or by a defined statistic and/or auxiliary variables.

REFERENCES

Akaike, H. (1974), "A New Look at the Statistical Model Identification," *IEEE Transactions on Automatic Control* 19, 716-723.

Akaike, H. (1977), "On Entropy Maximization Principle," *Applications of Statistics*, Ed. P.R. Krishnaiah, Amsterdam: North-Holland, 27-41.

Berlacu, R. and Herrin, E. (1996), "Discrimination between Earthquakes and Ripple-Fired Explosions based on a Parametric Spectral Approach," unpublished manuscript.

Fisk, M.D., Gray, H.L., and McCartor, G.D. (1995),"Statistical Methodiology and Assessment of Seismic Event Characterization Capability, Mission Research Corporation, Phillips Lab TL-TR-95-2156. ADA305487

Grant. L., Coyne, J., and Ryall, F. (1993), "CSS Ground Truth Database: Version 1 Handbook," *Scientific Report*, C93-05, Center for Seismic Studies.

Gray, H.L., Woodward, W.A., and Yücel, Z.T. (1995), "Outliers with Multiple Stations," Southern Methodist University Technical Report #286, Department of Statistical Science, February, 1995.

McLachlan, G.J. (1982), "The Classification and Mixture Maximum Likelihood Approaches to Clustering," in *Handbook of Statistics, Vol. 2,* P.R. Krishnaiah and L.Kanal (Eds.). Amsterdam: North-Holland, 199-208.

Miller, J.W., Gray, H.L., and Woodward, W.A. (1993), "Discriminant Analysis and Outlier Testing when Data are Missing," Semi-Annual Technical Report Four, Contract No. F29601-91-K-DB25, Advanced Research Projects Agency, Nuclear Monitoring Research Office, August 19, 1993.

Redner, R.A. and Walker, H.F. (1984), "Mixture Densities, Maximum Likelihood and the EM Algorithm," *SIAM Review*, **26**, 195-239.

Wang, S., Woodward, W.A., Gray, H.L., Wiechecki, S., and Sain, S.R. (1996), "A New Test for Outlier Detection from a Multivariate Mixture Distribution," *Journal of Computational and Graphical Statistics*, Submitted.

CONCLUSIONS AND RECOMMENDATIONS

In this report a method has been presented which modifies and generalizes previous work on outlier detection. The following new features should make these results applicable in the expected operating environment:

1. Ground truth data not required.
2. Number of event classes need not be predetermined.
3. Data are compressed to eliminate computational problems while still yielding near optimal detection.
4. Previous missing data methodology can be adapted to this new methodology.

Some additional development is required to make the methodology proposed here operational in the case of mixture distributions. These results should be completed over the next few months. In addition, as much real data as possible will be processed.

DISCRIMINATION OF SEISMIC SOURCES USING THE ISRAEL SEISMIC NETWORK

Avi Shapira, Yefim Gitterman and Vladimir Pinsky
Institute for Petroleum Research and Geophysics, P.O. Box 2286, Holon, Israel

Contract F19628-95-K-0006
Sponsored by the U.S. Department of Energy

ABSTRACT

Sixty nine quarry blasts and local earthquakes, recorded by the Israel Seismic Network (ISN) are used to test different analytical discrimination procedures. The seismic events are within the magnitude range M_L=1.0-2.6 and distances between 10 to 320 km from the stations.

The most commonly used discriminants are based on the enhancement of the surface waves of an explosion which are characterized as low frequency motions. The seismic energy ratio between low frequency (1-6 Hz) and high frequency (6-11 Hz) bands showed an overlap between quarry blasts and earthquakes. When averaging the ratios obtained at different stations from different azimuths and distances, the resolving power is enhanced and the two classes of seismic events are separated. We also computed r.m.s. spectral amplitudes in five equal, sequential frequency windows within the 1-11 Hz band and applied multiparametric automatic classification procedures (i.e. Linear Fisher Discriminator, Artificial Neural Network and the King's cluster algorithm) to the station averages of those data. The preliminary results of a lay-one-out test showed a low rate of classification mistakes for all of the methods.

We developed and tested a new multi-station discriminant which is based on the Low Frequency Spectral Modulation (LFSM) method. The LFSM is associated with ripple-firing in quarry blasts and with the bubbling effect in underwater explosions. The method demonstrates a distinct azimuth-invariant coherency of spectral shapes in the frequency range (1-12 Hz) for a broad range of distances (up to 320 km) and for arbitrary delay times. The coherency of modulated spectra for different stations is measured by semblance statistics, commonly used in seismic prospecting, for the phase correlation in time domain. After modification, the statistics being applied to spectra at different stations, provided good distinction between earthquakes and explosions. The analysis is based on smoothed (0.5 Hz window) FFT spectra of the whole signal without picking out separate wave phases.

Another new discriminant is based on velograms (signal envelopes versus group velocity). We measured velocities Vms and Vmp at which the velogram reaches its local maxima Smax, Pmax within the range 1-4 km/sec and 4-8 km/s, respectively. It is observed that the empirical relationship between Vms and the distance R (in the 10-150 km range) differs for blasts and earthquakes. The effect could probably be attributed to the different excitation of surface waves from these two types of seismic events and/or different S-wave group velocities for shallow and deep sources. A simple statistic, derived from the $V_{ms}(R)$ parametric approximation, provides true identification of the events. As part of the investigation we tested the P_{max}/S_{max} ratio, which worked properly only for a small number of relatively strong events ($m_b > 2$).

Key words: regional discrimination, seismic network, spectral semblance and ratios, velogram

OBJECTIVES

The primary objective of this research is to utilize efficiently advantages of the dense regional Israel Seismic Network (ISN) as a multichannel, spatially distributed system, for discrimination of low magnitude events (mb<2.5) in the Middle East region. This issue is very important for CTBT monitoring, especially when considering small nuclear tests which may be conducted under evasive conditions.

RESEARCH ACCOMPLISHED

During the period of this report, we focused on application of conventional single station/array methods, such as P/Lg and spectral short period ratios, to Regional Dense Seismic Networks (RDSN), as well as on the development of principally new RDSN oriented algorithms, based on different spectral and space-time characteristics of seismic radiation in explosions and earthquakes (i.e. spectral semblance statistics and multi-channel velogram analysis). These developments are followed by the integration of different approaches into a multidimensional discrimination procedure for the achievement of the highest automatic performance in routine RDSN operations.

Data. The study is based on 39 regionally recorded quarry blasts with ground truth information and 30 earthquakes (M_L=1.0-2.6). All these events occurred in the Galilee region of Israel in relatively close proximity to each other. Seismograms were collected from ISN stations located within 10-310 km of the epicenters (see Fig. 1). All seismograms are from short period (1 Hz) vertical seismometers digitally recorded (50 samples per sec.) in a bandpass of 0.2-12.5 Hz.

Spectral discriminants. We computed the Fourier spectra for ten specific stations (in the 10-100 km distance range). Computations were made for a time window of 20-30 sec. The analyzed window for an event is the same for all stations and includes the whole signal. The spectra were instrument corrected and smoothed by a triangle operator in the 0.5 Hz window.

Energy ratio. A number of known regional discriminants are based on spectral differences between earthquakes and explosions. Different kinds of spectral ratios are used (see e.g. review of Blanford, 1995): ratios of separate phases, e.g. P to S, in selected narrow bands; ratios of peaks, r.m.s., or averaged amplitudes (or power) in different frequency bands for the same phase, mainly Lg. The performance of these short period discriminants varies from region to region and should be tested on a ground truth database in every case study.

It is commonly observed in Israel that seismograms of explosions are richer in low-frequency energy as compared to earthquakes. The phenomenon is caused by the dominant surface waves generated by quarry blasts and associated with the regional crustal structure of widespread unconsolidated subsurface sediments. We utilize this effect by the spectral ratio, R_E, of seismic energy in the low-frequency range (1-6 Hz) and high-frequency range (6-11 Hz).

The ratios determined for a subnetwork of ten ISN stations are presented in Fig. 2. A small overlap between quarry blasts and earthquakes is observed for specific stations. If the ratios for different events are averaged over all ten stations covering a relatively broad azimuth and distance range, the resolving power is significantly enhanced and the two populations of seismic events are fully separated. Several earthquakes from the small area in Lake Kinneret (the Sea of Galilee), placed exactly on the Dead Sea fault (Fig. 1), show anomalous high ratios (Fig. 4). In general, we may suggest that seismograms yielding an average ratio R_E>6 are associated with quarry blasts.

Automatic discrimination (preliminary results). An additional discriminant can be achieved using an Integrative Approach, based on a number of different physical signal features, which can be realized in the form of an automatic discrimination procedure, such as the Fisher Linear Discrimination Function (LDF) (Tsvang et al., 1993) or Artificial Neural Network (ANN) (Dowla et al., 1990). We started tuning LDF and ANN by application of the r.m.s. spectral amplitudes in several equal sequential spectral bands, averaged for the set of stations. The discriminators were checked by application of the "lay-one-out" procedure to the 69 events. The experiment showed good discrimination performance. For five spectral bands (1-3, 3-5, 5-7, 7-9 and 9-11 Hz) two classification errors were counted for LDF and no errors for ANN. In addition, we examined the performance of an algorithm based on the Cluster Analysis procedure (King, 1967), separating the dataset into several subsets without any preliminary knowledge of its structure. The algorithm resulted in five errors for the case of implying five bands and one mistake for the case of four specific spectral bands: 1-3, 3-5, 5-7 and 9-11 Hz.

Spectral semblance. One of the main features used in the identification of industrial explosions is spectral modulation (SM) caused by ripple firing. Most of the studies are based on time-independent patterns for a single station or array, presented in spectrograms or sonograms of the whole seismogram (e.g. Hedlin et al., 1995; Kim et al., 1994), or in spectra of different regional phases (e.g. Der and Baumgardt, 1995). These discriminants are concerned mainly with spectral maxima at high frequencies (more than 10 Hz) reciprocal to a delay time. Another multi-station approach based on the azimuth-invariant SM, considered jointly for regional network stations, is discussed by Gitterman and van Eck (1993). This approach was also implemented for the identification of underwater explosions in the Mediterranean using an SM caused by the bubbling phenomenon (Gitterman and Shapira, 1994). The method utilizes low frequency (1-12 Hz) minima and demonstrates the distinct coherency of spectral shapes for broad ranges of azimuths and distances (10-320 km) and delay times (20-100 msec).

The LFSM approach is efficient in identifying explosions with a low SNR. A number of quarry blasts recorded at remote stations with SNR<1 for P-waves and SNR1.5-2 for S and coda waves show clear SM patterns, presented by coherent minima (or nulls) and maxima (Fig. 5). Spectral scallops depend strongly on ripple-firing parameters, e.g. the frequency of the first null, dominant in our frequency-limited recordings, is determined mainly by the duration of ripple-firing (Gitterman and van Eck, 1993; Barker et al., 1993). Similar plots for earthquakes demonstrate the irregular character of spectral shapes and minima for different azimuths (Fig. 6).

The coherency of spectral shapes for different stations can be quantitatively assessed by "semblance" and "cross-correlation" statistics commonly used in seismic prospecting for phase correlation of seismic traces in the time domain (e.g. Neidell and Taner, 1971). After some modification (including spectra logarithming and subtraction of the average), the statistics were applied to the spectra. The statistics values obtained are higher for blasts (0.7-0.9) than for earthquakes (0.1-0.4) (see Fig. 3). As may be expected, correlation between the two statistics is observed. For the above mentioned earthquakes from the Sea of Galilee, we obtained anomalous high semblance values of 0.4-0.65; however, the two sets of seismic events are still separate. The same result is observed on the semblance versus energy ratio plot (Fig. 4).

Discussion. A quarry blast may be considered as a point source, therefore the interference pattern is uniform in different directions, providing the azimuth-independent SM and high "semblance" values. Frequencies of spectral minima for different stations, caused by nulls of the

interference transfer function, have small random shifts (Fig. 5a). It is maintained (Der and Baumgardt, 1995) that the Doppler effect could be responsible for this phenomenon which can even suppress the nulls (Blanford, 1995). We consider this azimuthal effect, caused by the spacing of individual shots in a quarry blast, as minor, and the shifts are determined mainly by the spectrum slope of a single shot explosion at a station site (Gitterman and van Eck, 1993).

The Doppler effect could be relevant in the case of earthquakes which are actually line sources and the stochastic superposition of sub-events along the rupture also produces some kind of SM - "scalloped spectra" (Bakun et al., 1978). The time-independent SM alone does not prove ripple-firing; it can be acquired during propagation in the case of shallow earthquakes and the low velocity stratified media with sharp boundaries along the path (Hedlin et al., 1989). These detrimental effects can be misleading when observed at one station or array, but this is negligible in the azimuth-invariant modulation patterns observed at regionally distributed stations. Due to the directivity effect, the interference pattern for an earthquake will be azimuth-dependent, therefore we observe non-coherence of spectra (Fig. 6) causing low semblance values.

Our results provide a positive answer to questions such as: are short delay (20-30 msec) ripple-fired events capable of generating SM below 20 Hz and can this feature be used for discrimination of distant regional (0-400 km) events (Hedlin et al., 1995). The LFSM approach can help in the case of disappearing high frequency scalloping (above 5 Hz), as for spectrograms of mine explosions in central Chile at distances greater than 100 km (Beck and Wallace, 1995).

Velogram analysis. Earthquakes usually have deeper foci than explosions with different physical properties of the media and surface and, therefore, their respective wave fields possess different kinematic characteristics. The experimental fact emphasized in many studies (Kafka, 1990, Walter et al., 1996) is that explosions in the vicinity of the source generate very slow (1.5-2 km/s) fundamental surface Rayleigh waves, Rg with low frequencies and high amplitudes as compared to earthquakes. Alexander et al. (1995), using data from quarry blasts, showed that Rg scattering into body phases shifts the total dispersion of the wavetrain towards lower group velocities. In spite of the above analysis, no direct study using group velocity measurements for discrimination has previously been performed. Our discrimination technique is based on velograms, determined by the Short Time Average (STA) transform of the original seismograms using a group velocity section instead of the conventional time section (Fig. 7). This approach is inspired on one hand by Kim et al. (1994), who used a group velocity section obtained over a seismic short period network to demonstrate the effect of inhomogeneous crust, and, on the other hand, by Husebye and Ruud (1995) in which seismic network intensity curves were utilized for an automatic epicenter location procedure. The kinematic group velocity discriminator is compared with the conventional dynamic P/S discriminator which may also be obtained from velograms.

The processing scheme for each channel is illustrated in Fig. 8. In the first step, the STA is computed from digital seismograms; then for the sequence of velocities $V_j=V0+j*dV$ (j=1,...,J), the velogram $Q(V_j)$ is obtained from the STA as: $Q(V_j) = STA(R/V_j)$, where R is the distance from the source. In this study the window length for the STA was 1 sec, moving over seismograms with a 0.02 sec step equal to the digitizing interval. Time $T_j=R/V_j$ is the travel-time associated with the beginning of the moving window. Group velocity V was in the range of 0.1-

10 km/s, computed in steps dV=0.1 km/s. For noise reduction, all the original seismograms were filtered in the frequency range 1-10 Hz using a Butterworth filter.

The velogram characterizes the distribution of seismic wave intensity versus group velocity. The intensity peaks in the study were characterized by maximum velogram values P_{max} and S_{max} (see Fig. 8) in group velocity intervals 4-8 km/s and 1-4 km/s, corresponding to P and S-Lg-Rg wave groups. It was found that Vmp does not resolve events, whereas V_{ms} has a tendency to be slightly larger for earthquakes than for explosions over a wide range of distances: 10-200 km. The experimental points were fitted by equation Vms = a+b*ln(R) (see Fig. 9). The coefficients a and b can serve as a compact characteristic of event type.

The results are presented in Fig. 10a which shows separation of the two populations of seismic events and also demonstrates the linear relationship between coefficients a and b, close to C=b+0.33*a for both types of events. The distribution of C values obtained from the analysis of velograms from all the events is presented in Fig. 10b. Using the criterion C = 0.69, we obtain almost complete separation between earthquakes and explosions. One mistake was accounted for by the extremely low magnitude explosion, absolutely invisible at distances R > 28 km.

Testing of a P/S discriminant. Using the velograms of the ISN individual channels, we tested a dynamic P/S discriminant in which P=P_{max} and S=S_{max}, (see example in Fig. 8). That statistic characterizes the ratio of velogram intensities in the specified group velocity intervals 4-8 km/s for P and 1-4 km/s for S. It is expected that the P/S for explosions will be greater than that for earthquakes. In practice, this appeared to be true for only a limited number of ISN stations and only for strong events with a good SNR at distances greater than 100 km. Only 18 events of the data set fall into this category, i.e. 8 explosions and 11 earthquakes. Figure 11a shows the P/S ratios at various distances; no distinction between earthquakes and explosions may be observed here. Six stations for which this tendency was evident were selected, all of them at distances greater than 100 km from the source. Figure 11b shows the P/S ratios for these stations for various events. From Figure 11c we can see that, except for one or two events, the average P/S ratios obtained for each event at the various stations, enable us to distinguish between earthquakes and explosions. The combined P/S and C criteria (P/S are average values) for the 18 events are shown in Fig. 12. The joint (P/S,C) vector parameter evidently enhances resolution power of the individual discriminants; however, the applicability and reliability of the dynamic P/S discriminant is much less than that of the kinematic parameter C.

Discussion. The enhanced excitation of short period regional surface waves from shallow events is well known and widely used to facilitate discrimination between explosions and earthquakes. However, during the past decade, many investigators have demonstrated the deficiencies of using amplitude and spectral ratios. In this study we deal with the same seismological phenomenon, but analyze it in a different manner, i.e. using velograms. As may be expected, the classic approach of searching for the P/S waves ratios, presented here in terms of the velogram P_{max}/S_{max}, depends heavily on the characteristics of the uppermost crust. We have developed a procedure which seems less sensitive to crustal variations, yielding a reliable and simple discriminant. In our case study, the threshold C=0.69 is successful; however, we have no reason to assume that the same value is valid for other regions. This study clearly indicates that the "C discriminant" is far more reliable than amplitude ratios of different seismic phases, even over a network of seismic stations; it has the disadvantage, however, of being determined from a network of stations rather than from a single observatory.

CONCLUSIONS AND RECOMMENDATIONS.

1. The resolving power of the single-station discriminants (spectral and P/S ratios) was enhanced by averaging over the dense ISN.

2. Application of principally new RDSN oriented algorithms, based on different spectral and space-time characteristics of seismic sources: spectral semblance statistics and multi-channel velogram analysis, provided further improvement of discrimination results.

3. In the next stage we shall focus on integration of different approaches into a multidimensional discrimination procedure to achieve high automatic performance in routine operations of RDSN and investigate the transportability of the developed discriminants.

REFERENCES.

Alexander, S.S., R.C. Hsu, S.L. Karl, I.N. Gupta, and D.H. Salzberg, 1995. New techniques for estimating depth and other diagnostic source characteristics of shallow events from regional observations of P, Lg and Rg signals. Proceedings of 17th Seismic Research Symposium on Monitoring a CTBT, AZ, 821-830, PL-TR-95-2108, ADA310037.

Bakun, W.H., R.M. Stewart and C.G. Bufe, 1978. Directivity in the high- frequency radiation of small earthquakes, Bull. Seism. Soc. Am., 68:1253-1263.

Barker, T.G., K.C. McLaughlin and J.L. Stevens, 1993. Numeral simulation of quarry blast sources, SSS-TR-93-13859, S-Cubed, LaJolla, CA.

Blanford, R.R., 1995. Regional seismic event discrimination, in: E.S. Husebye and A.M. Dainty (eds.) a Comprehensive Test Ban Treaty, NATO ASI Series, Series E: Applied Sciences - Vol. 303, 689-719.

Beck, S.L. and T.C. Wallace, 1995. Broadband seismic recordings of mining explosions and earthquakes in South America, Proceedings of 17th Seismic Research Symposium on Monitoring a CTBT, AZ, 157-163, PL-TR-95-2108, ADA310037.

Der, Z.A. and D.R. Baumgardt, 1995. Source finiteness, signal decorrelation, spectral scalloping and identification of multiple delayed explosions, Proceedings of 17th CTBT Symposium, Scottsdale, AZ, 723-732.

Dowla, F., S. Taylor and R. Anderson, 1990. Seismic discrimination with artificial neural networks: preliminary results with regional spectral data, Bull. Seis. Soc. Am., 80, 1346-1373.

Gitterman, Y. and T. van Eck, 1993. Spectra of quarry blasts and micro- earthquakes recorded at local distances in Israel, Bull. Seis. Soc. Am., 83:1799-1812.

Gitterman, Y. and A. Shapira, 1994. Spectral characteristics of seismic events off the coast of the Levant, Geophy. J. Int., 116:485-497.

Hedlin, M., J.G. Minster and J.A. Orcutt, 1989. The time-frequency characteristics of quarry blasts explosions recorded in Kazakhstan, USSR, Geophys. J. Int., 99:109-121.

Hedlin, M., F. Vernon, J.G. Minster and J.A. Orcutt, 1995. Regional small- event identification using networks and arrays, Proceedings of 17th CTBT Symposium, 12-15 September 1995, Scottsdale, AZ, 875-8, PL-TR-95-2108, ADA310037.

Husebye, E.S. and B.O. Ruud, 1995. Waveform synthetics in 3D and fully automatic event locations. Proceedings of 17th Seismic Research Symposium on Monitoring a CTBT, 12-15 September 1995, AZ, 389-400, PL-TR-95-2108, ADA310037.

Kafka, A.L., 1990. Rg as a depth discriminator for earthquakes and explosions: a case study in New England, Bull. Seism. Soc. Am., 80, 373-395.

Kim, W.Y., D.W. Simpson and P.G. Richards, 1994. High-frequency spectra of regional phases from earthquakes and chemical explosions, Bull. Seis. Soc. Am., 84: 1365 - 1386.

King B .F., 1967. Step-wise clustering procedures. Journal of the American Statistical Association, 62, 86-101.

Neidell, N.S. and M.T. Taner, 1971. Semblance and other coherency measures for multichannel data, Geophysics, 36:482-497.

Pully, J.J., 1995. Extracting and processing signal parameters for regional seismic event identification. In: E.S. Husebye and A.M. Dainty (eds.), Monitoring a CTBT, NATO ASI Series, Series E: Vol. 303, 741-754.

Tsvang, S.L., V.I. Pinsky and E.S. Husebye, 1993. Enhanced seismic source discrimination using NORESS recordings from Eurasian events, Geophys. J. Int., 112, 1-14.

Walter, W.R., S.L. Hunter and L.A. Glenn, 1996. Preliminary report on LLNL mine seismicity deployment at the Twentymile Coal Mine. CTBT Seismic Monitoring Project Task S7.2, Deliverable #2, UCRL-ID-122800.

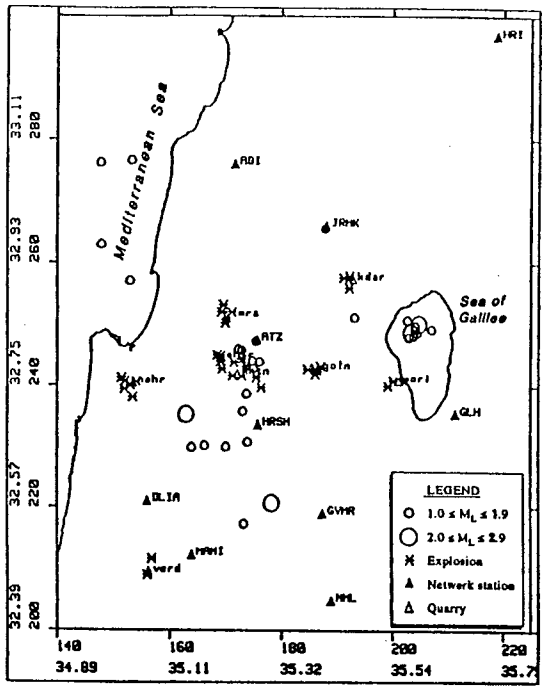

Fig. 1. Locations of ISN stations, quarries and seismic events.

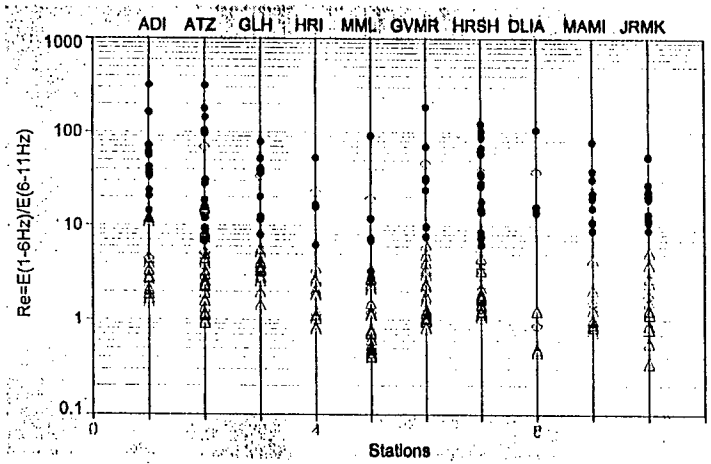

Fig. 2. Energy spectral ratios for individual stations: Δ - earthquakes, • - quarry blasts, ◊ - average values.

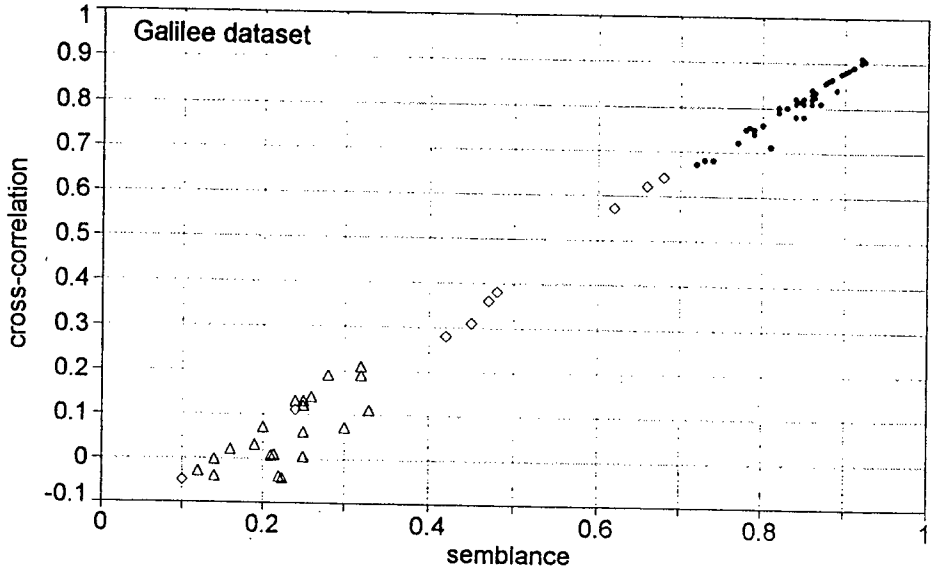

Fig. 3. Discrimination results of joint application to the Galilee dataset of the two spectral statistics: cross-correlation and semblance of spectra at the network stations (Δ - earthquakes, • - quarry blasts, ◊ - earthquakes from the Sea of Galilee).

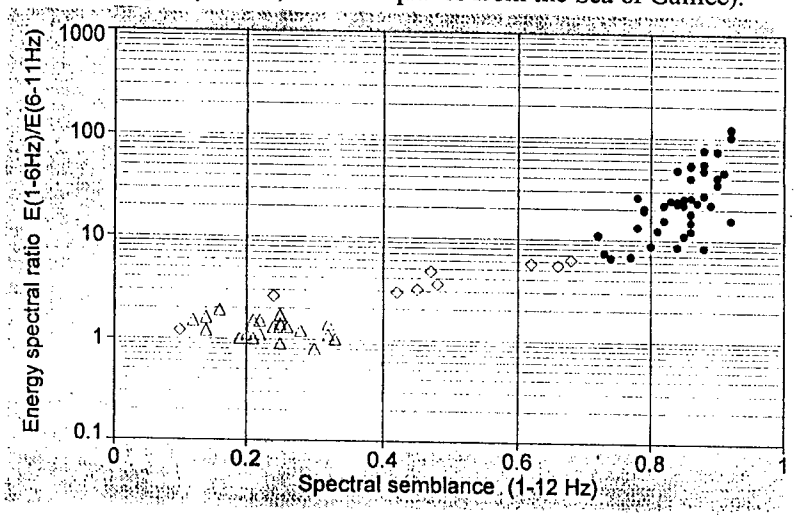

Fig. 4. Discrimination results of joint application to the selected dataset of the two spectral statistics: semblance and energy ratio (Δ - earthquakes, • - quarry blasts, ◊ - earthquakes from the Sea of Galilee).

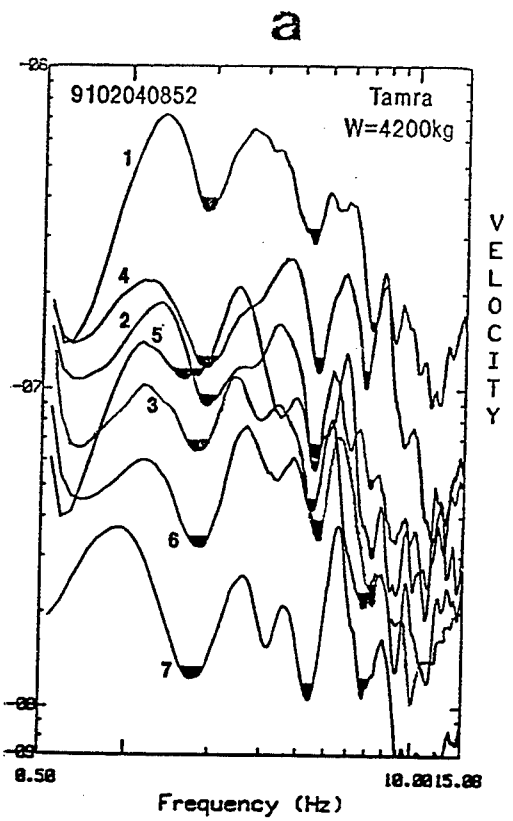

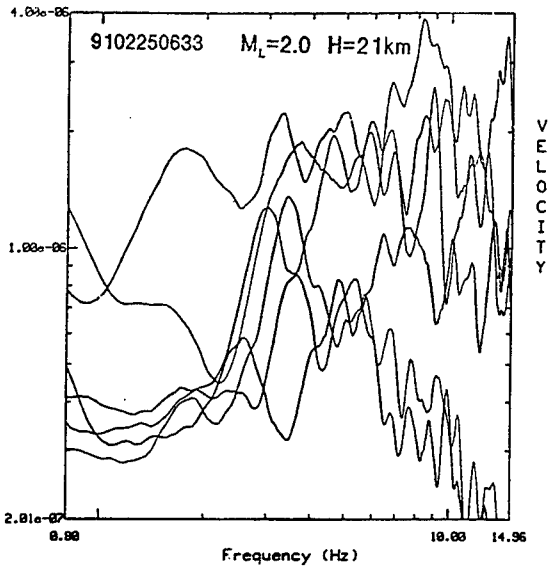

Fig. 6. Example of earthquake recordings showing irregularity of spectral shapes and low frequency minima (nulls) for a broad azimuth range (66-354°) of ISN stations.

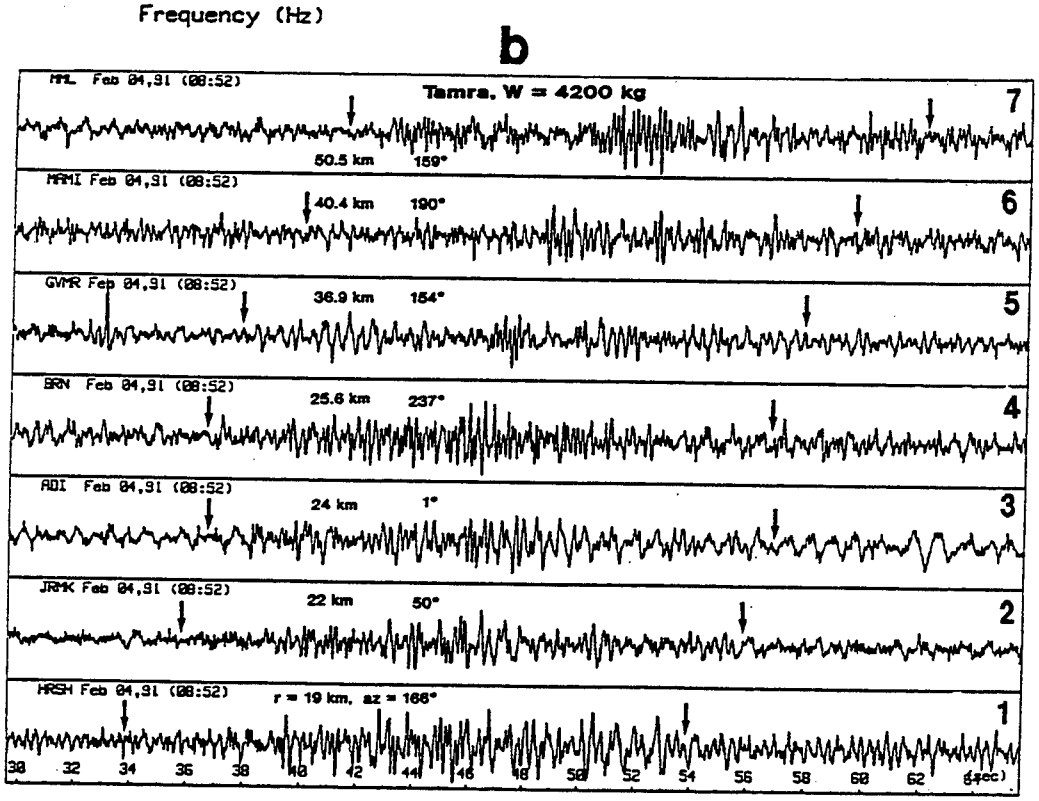

Fig. 5. Example of distinct low frequency, azimuth and distance-independent spectral modulation (a) for low SNR<2 recordings of a quarry blast (b). FFT spectra are instrument corrected and smoothed by a triangle operator in the 0.5 Hz window.

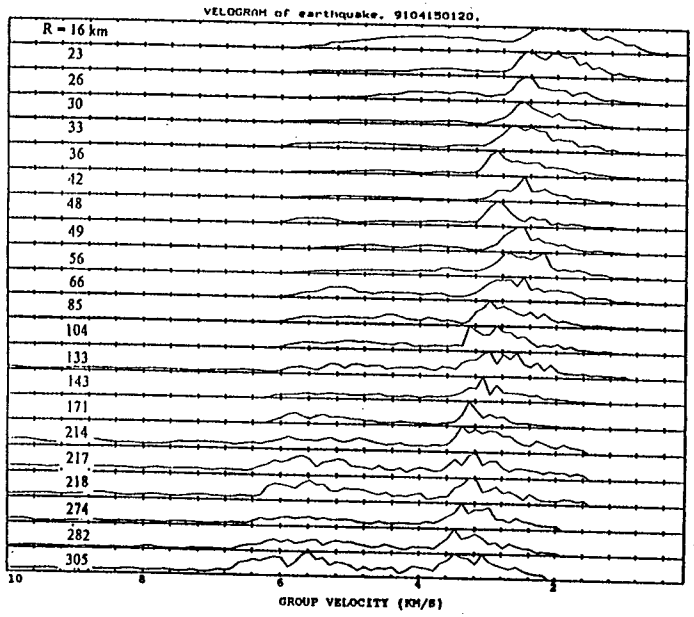

Fig. 7. Velogram section for an earthquake Q (a) and an explosion X (b).

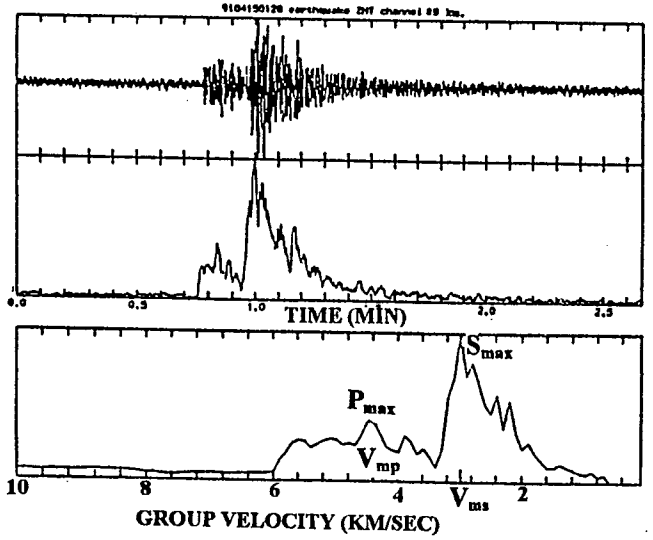

Fig. 8. Example of data processing for an earthquake Q record at the station ZNT (85 km from the source): (1) band-pass (1-10 Hz) filtered digital seismogram; (2) 1-second length STA; (3) velogram.

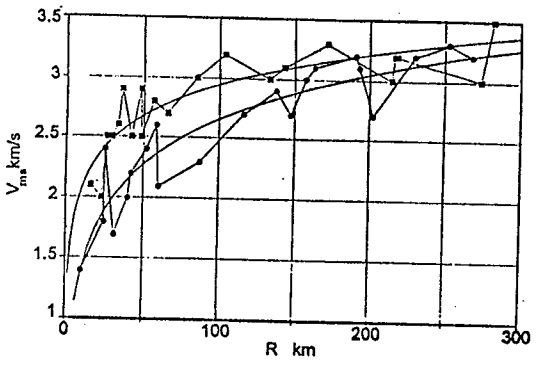

Fig. 9. V_{ms}-distance curves for an earthquake Q (□) and an explosion X (•), and the corres-ponding least squares fit curves V_{ms}=a+b*ln(R). Q: a=1.16, b=0.389; X: a=0.793, b=0.487.

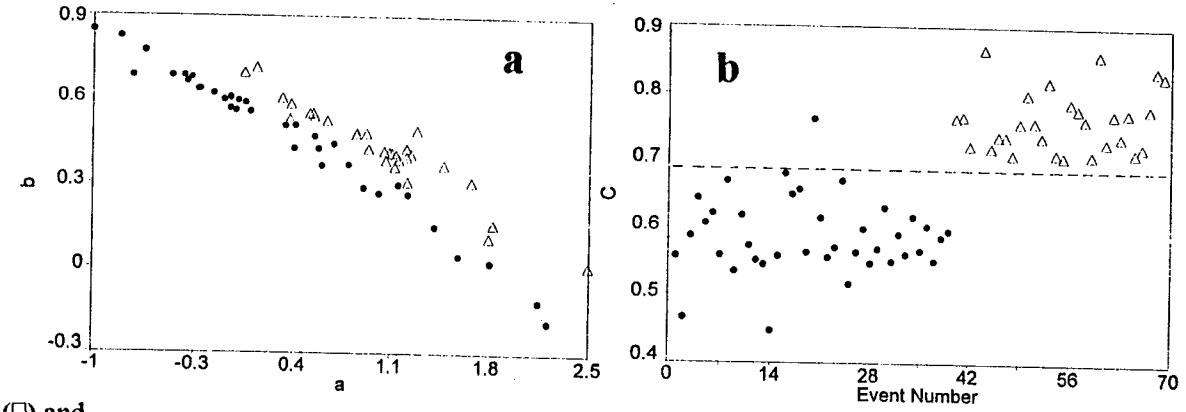

Fig. 10. V_{ms}(R) fit curve parameters for earthquakes (Δ) and explosions (•): a) pairs (a,b); b) c = a + 0.33b.

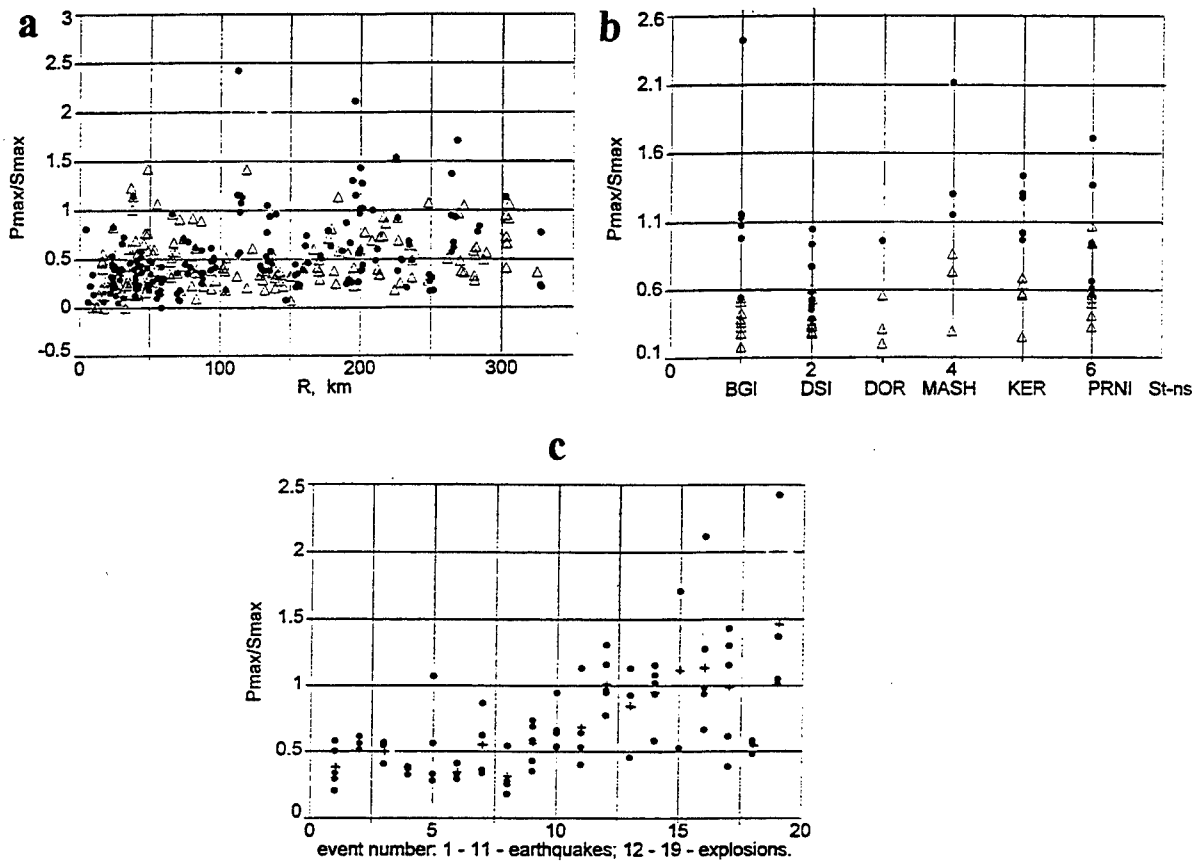

Fig.11. Velogram Pmax/Smax for the Galilee strong events: 11 earthquakes (Δ) and 8 explosions (•): a) distance dependency; b) for selected stations; c) averages (+) for selected stations.

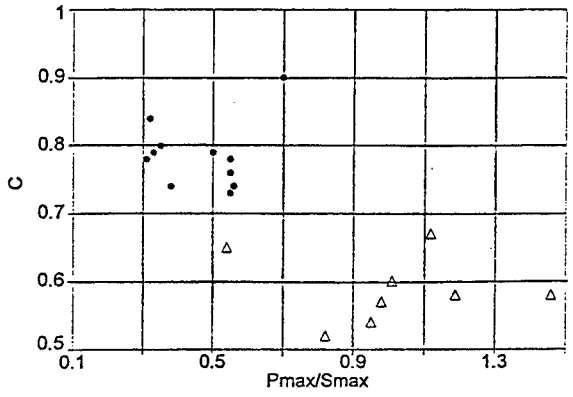

Fig. 12. Joint (P/S, C) discriminator for a subset of relatively strong Galilee events: 8 explosions (•) and 11 earthquakes (Δ).

A Transportable Regional Discriminant Using a Maximum Likelihood Analysis of Surface Waves

J. L. Stevens and K. L. McLaughlin
S-CUBED Division of Maxwell Laboratories
P. O. Box 1620, La Jolla CA 92038
619-587-8442, FAX 619-755-0474, stevens@scubed.com
Contract No. F19628-95-C-0110
Sponsored by AFTAC

ABSTRACT

We develop a method for regionalization of surface wave magnitudes, replacing the traditional Ms measurement with a new type of magnitude, the scalar moment, derived from the equations for surface waves from point sources in layered media. This has the effect of minimizing the frequency dependence, depth dependence, and distance dependence of the magnitude, and allows worldwide regionalization so that the magnitude is a consistent measure of source size for any source and receiver location.

Automatic surface wave processing has been implemented at the Prototype International Data Center since May, 1995, using a program, Maxsurf, developed by S-CUBED. We developed a new program Maxpmf, based on Maxsurf, with the addition of a phase-matched filtering module, to estimate moments in automatic processing mode from approximately 7000 waveforms recorded at the GSETT 3 primary stations (3-Component long period and broadband stations and arrays). Regionalized earth models were developed on a 10 degree grid for phase velocity, group velocity, attenuation coefficients and surface wave source and path amplitude factors. The phase and group velocity models were refined using a tomographic inversion of travel time residuals from the large data set. The improved dispersion curves are a good enough fit to the data over most of the world's surface to successfully compress waveforms using phase-matched filtering for an arbitrary path. The regionalized group velocity curves are used for identification of surface waves by comparing measured and predicted dispersion curves.

Maximum likelihood magnitudes were calculated for a data set of 175 events using amplitude levels from nondetections as measured noise levels. The results demonstrate the need for a high level of quality control if maximum likelihood magnitudes are to be meaningful. In particular, noise levels from nondetections must be measured as accurately as signals, and the results can be severely distorted by low amplitudes from stations that are not operating properly.

Keywords: surface waves, Rayleigh waves, earthquake/explosion discrimination, Ms, moment, maximum likelihood

OBJECTIVES

The primary objective of this research program is to develop and test a transportable regional discriminant based on a maximum likelihood analysis of surface waves. This is to be accomplished by implementing and extending the method developed by Stevens and McLaughlin[1]. This method applies phase-matched filters to data, recovers spectra, flattens the spectrum with a frequency dependent amplitude correction, and recovers a spectral magnitude (scalar moment). This procedure is to be applied to a large data set and its range of applicability, limitations, and discrimination capability determined.

Specifically, we are looking for the following:

1. An accurate measure of surface wave amplitude, similar to Ms, that has the same value at all distances and frequencies.
2. A mechanism for regionalizing the magnitude to account for regional differences in dispersion, attenuation, and excitation.
3. A method for determining an upper bound on the magnitude in cases where no surface wave is measureable.
4. A discriminant similar to m_b:Ms, but more robust, with a wider range of applicability and with the ability to use nondetections as well as measured amplitudes.
5. Automation of the surface wave identification and measurement process to the maximum extent possible.

RESEARCH ACCOMPLISHED

We have developed an automatic surface wave processing/phase-matched filtering program and applied it to a large data set at the Prototype International Data Center in Arlington, VA. The program, Maxpmf, is based on the automated processing program Maxsurf with the addition of a phase-matched filtering module. Maxsurf, developed by S-CUBED, is used to identify and measure all surface waves the appear in the IDC bulletin.

Automatic surface wave processing

Surface wave identification is accomplished in the following way: for each origin identified through short period arrivals, the data in the surface wave arrival time window (approximately 5 km/sec to 2 km/sec) is extracted and the following tests are performed:

1. A set of narrow-band filters are applied to determine the group velocity dispersion as a function of frequency.
2. The observed dispersion is compared with the predicted dispersion based on ray tracing through a regionalized earth model.

---

[1] Stevens, J. L., and K. L. McLaughlin (1988), "Analysis of surface waves from the Novaya Zemlya, Mururoa, and Amchitka test sites, and maximum likelihood estimation of scalar moments from earthquakes and explosions," S-CUBED technical report submitted to AFTAC, SSS-TR-89-9953, September.

3. The azimuth to the origin is estimated based on polarization filtering for three-component data, and beam azimuth for array data.
4. If these tests show the characteristics of a surface wave then an arrival is added to the bulletin. The amplitude is measured by digitally replacing the instrument with a KS36000 long period instrument and measuring the amplitude of the arrival near 20 seconds period.

Phase-matched filtering

The phase-matched filtering module adds the following:

1. A phase-matched filter is derived from ray tracing through a regionalized phase-velocity model consistent with the group velocity model described above.
2. The phase-matched filter is applied to the data to compress it to within a narrower time window, the data is windowed, and transformed back to the frequency domain. This results in a more accurate spectrum with noise windowed out.
3. The spectrum is divided by a theoretical explosion spectrum for the path. The amplitude spectrum depends on the earth structure near the source and receiver and the attenuation along the path. Again these functions are derived from a regionalized earth model.
4. The spectral ratio is averaged over a frequency band, typically 0.02 to 0.05 hz to give a single number, the scalar moment. For an explosion, the spectral ratio is flat as a function of frequency, and the resulting scalar moment will therefore be independent of frequency. This makes the scalar moment ideal to use for a regional magnitude, because it has the same value (in principle) whether measured at 10 seconds period at 1000 km, or at 25 seconds period at 10000 km. For an earthquake, the ratio depends on the source mechanism and depth, and in general will not be flat, however the frequency dependence is reduced and the scalar moment can be measured at any frequency. The estimated scalar moment is related to the double couple moment of the earthquake through a distribution function which can be calculated theoretically.

Figures 1 and 2 below show an example of waveform compression using phase-matched filtering. The original wave train had a duration of about 800 seconds and was compressed to within a time window of about 200 seconds. The compressed signal is offset from zero by about 50 seconds. The amount of compression can be improved and the offset reduced by improving the regionalized dispersion model. The ability of the current model to compress waveforms is quite remarkable given the relatively coarse 10 degree grid used for ray tracing.

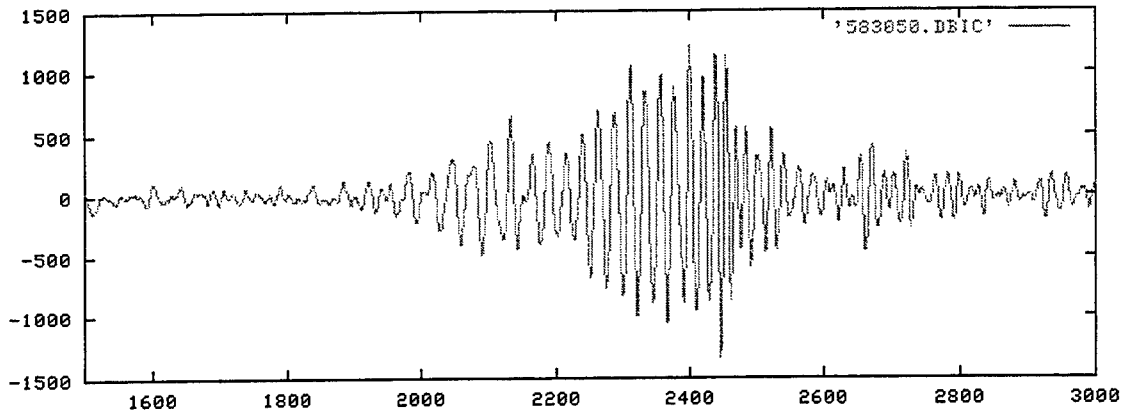

Figure 1. Surface wave from earthquake recorded at station DBIC.

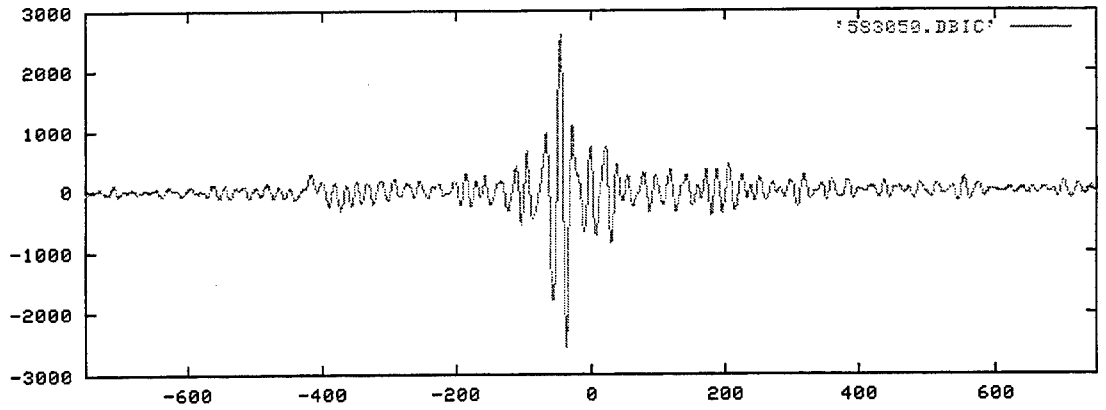

Figure 2. Surface wave from earthquake recorded at station DBIC after phase-matched filtering. The surface wave is compressed into a narrower time window allowing noise to be filtered out.

Regionalization

In order to perform the processing described above, we need to be able to determine the phase and group velocity and attenuation coefficients along any source to receiver path, and the surface wave amplitude factors at the source and receiver. We started with a set of group velocity dispersion curves from AFTAC, and integrated these to obtain phase velocity dispersion curves. To date, we have used only generic models for the amplitude factors and attenuation coefficients, but expect to improve these in the next phase of this project. Note that although this procedure sounds more complicated than measuring Ms, Ms is really an equivalent measure using constant (average) values worldwide for amplitude factors, attenuation coefficients and dispersion.

The group velocity curves from AFTAC turned out to be inadequate for accurately predicting dispersion curves, primarily because of a poor model for dispersion in subduction zones. Consequently, we spent some time improving the models. To do this, we ran Maxpmf on a data set of approximately 4000 seismograms, examined the observed dispersion curve visually to remove inaccurate data points, and used these to perform a

tomographic inversion of group velocity at all grid points. To fill in some gaps in coverage and add some additional data points, we also included in the inversion several hundred paths obtained during development of surface wave path corrections from a large data set of historical underground nuclear tests.[2] Figure 3 below shows the paths used for tomographic inversion of group velocity residuals. Because the tomographic inversion leads to a different dispersion curve for each grid cell, we did not use the results directly, but instead used them as a guide to improve the dispersion models. The final model, which uses a total of 8 dispersion models on a 10 degree grid worldwide, predicts dispersion accurately for frequencies of less than 0.02 to 0.06 hz. The group velocity model at a period of 50 seconds (0.02 hz) is shown in Figure 4.

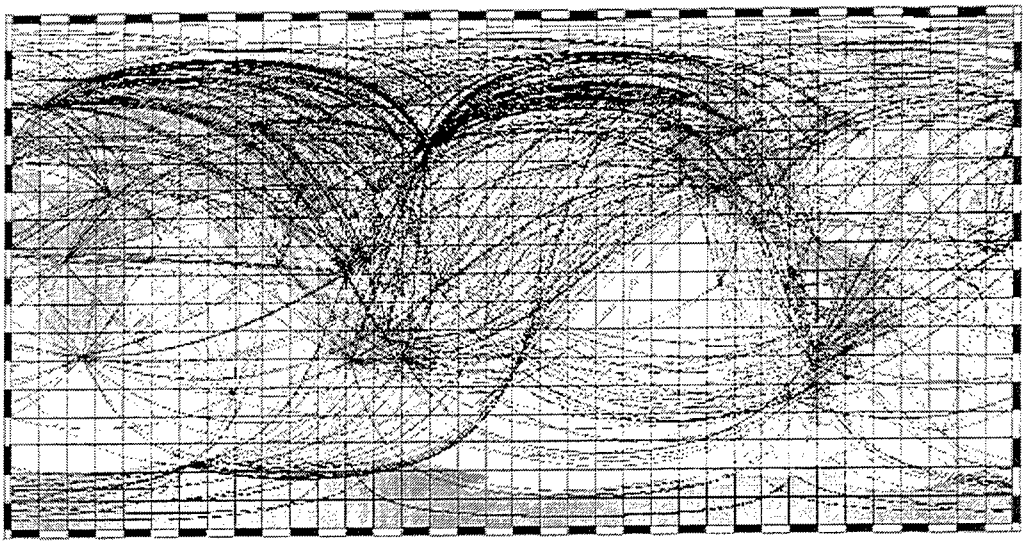

Figure 3. Great circle paths used for tomographic inversion of group velocity residuals.

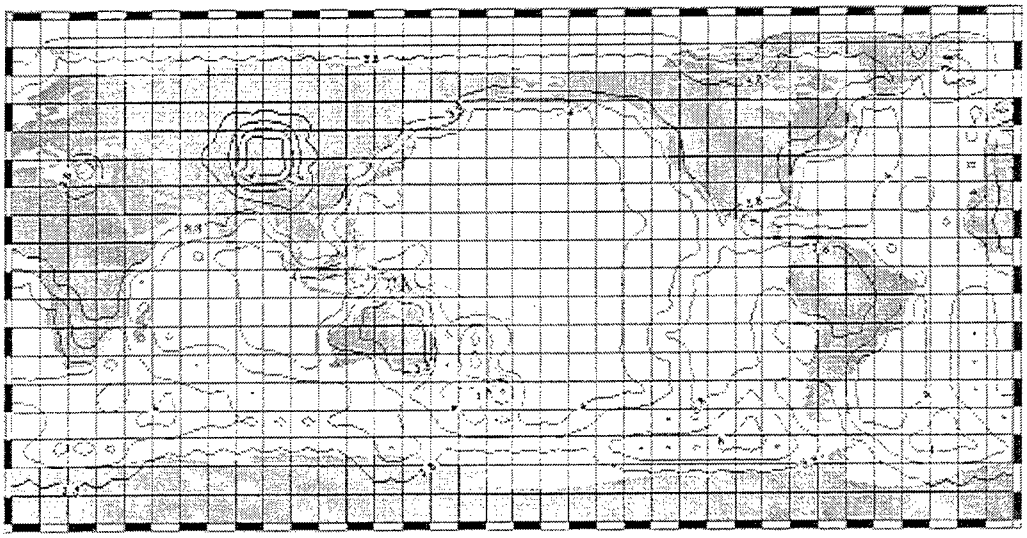

Figure 4. Contours of group velocities at 50 seconds period.

[2] Stevens, J. L. (1986), "Estimation of scalar moments from explosion-generated surface waves," *BSSA, 76, 123-151.*

Maximum likelihood magnitude/moment

There are two major reasons for developing maximum likelihood magnitudes. The first is to determine station corrections to reduce the variance in network magnitudes. The second is to be able to use nondetections to get a better estimate of the magnitude by including a noise estimate in the magnitude calculation as an upper bound on the magnitude at that station. While in principle this is a straightforward procedure, there are practical problems that require careful attention to detail in order to make it work. Station corrections will vary according to the source region, so station corrections derived using a large volume of data from one area will be biased and possibly inaccurate for events in other areas. Similarly, if noise estimates are to be used as an upper bound on the magnitude, it must in fact be an upper bound on the magnitude. We have found that with automatic processing it is very easy to inadvertently use low amplitude data from stations that are not operating properly and that this seriously distorts the maximum likelihood magnitude.

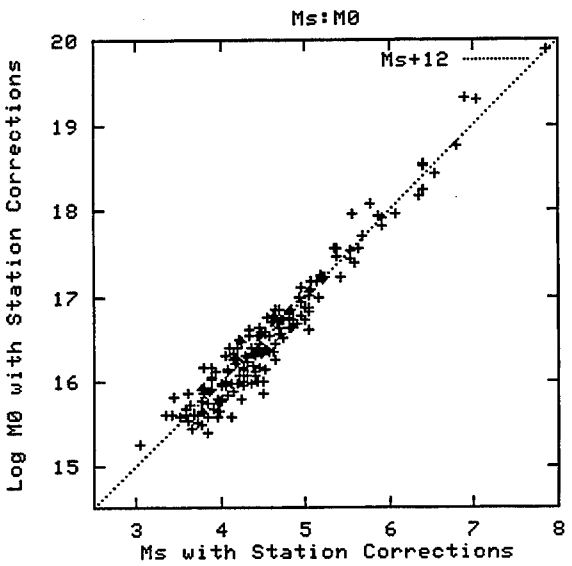

Figure 5. Station corrected network averaged Log Moment and Ms. Log Moment and Ms are similar measures of path corrected surface wave amplitude differing by approximately 12.

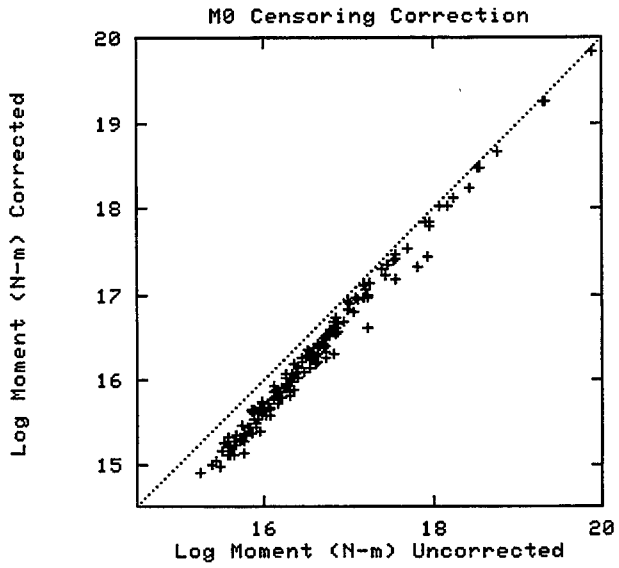

Figure 6. Log Moment with and without censoring correction. The censoring correction uses measured amplitudes of nondetections as noise estimates.

Figure 5 shows the relation between Ms and log scalar moment (M0). These are similar measures of surface wave amplitude corrected for distance to give an estimate of the strength of the source as a surface wave generator. Both have global station corrections and give similar values with some scatter and a constant offset of approximately 12. Figure 6 shows the effect of the censoring correction. Here we have used the measured scalar moment as an upper bound on the moment for all data that did not satisfy the surface wave tests. The results show a gradual decrease in M0 with the censoring correction as a function of decreasing M0. This is to be expected since more noise estimates are included in the estimates for smaller events. However, the censoring

correction shown here has too strong an effect. It does not completely go away even for the largest events. This is due primarily to problems with data quality and to the fact that the surface wave identification tests were designed to be conservative and fail to identify some data that contains surface wave signals. For example, some of the data is clipped, some contains small gaps, and some has high noise levels on the horizontal components. Any of these problems will cause the data to fail the polarization azimuth test and therefore identify signal as noise. Consequently additional quality control is needed, and a less conservative test is desirable in order for the censoring correction to be meaningful.

Discrimination

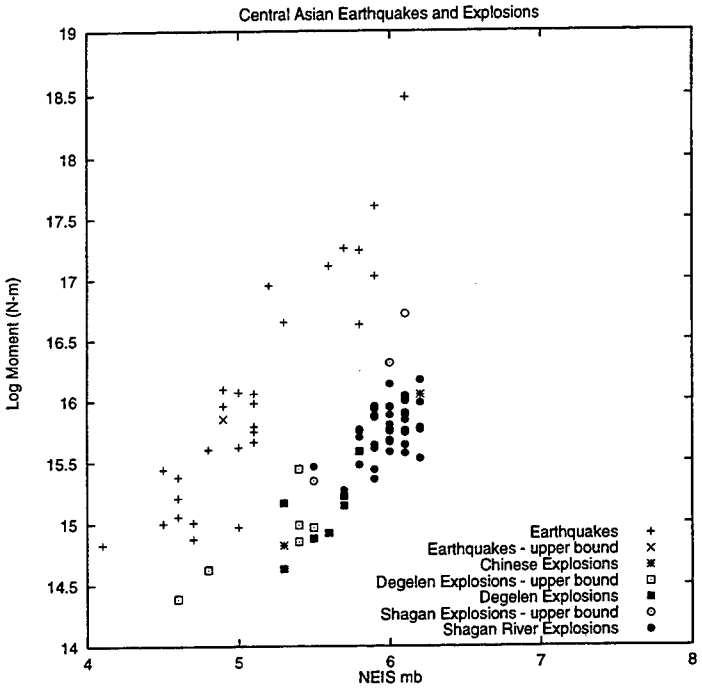

Figure 7. Plot of NEIS m_b vs. log Moment for a data set of central Asian earthquakes and explosions. The open circles are an upper bound on log moment for events for which no surface wave data was visible either because of low signal/noise or an interfering event.

The most important function of surface wave magnitudes in a CTBT context is for discrimination. Figure 7 shows a plot of mb vs. Log Moment for a data set of central Asian earthquakes and explosions (from Stevens and McLaughlin[1]). Maximum likelihood moments were calculated for all events. For this data set, the data was carefully examined to remove any bad data. Data that did not visibly contain surface waves was treated as noise. Maximum likelihood magnitudes were calculated for all events, and an upper bound on the network magnitude was determined for all events with no useable surface wave data. This occurred for several small events, and for a couple of larger explosions where the surface waves were overwhelmed by surface waves from large earthquakes. The earthquakes and explosions clearly separate into distinct populations, and even the explosions with no surface wave data are clearly discriminated from the earthquake population for this data set. This is important, because surface waves are so much smaller

for explosions than for earthquakes of a corresponding magnitude, that being able to use negative information substantially reduces the magnitude threshold for which explosions can be discriminated using the mb:M0 (or mb:Ms) discriminant.

Figure 8 is a plot of IDC m_b vs. log Moment derived from IDC data for a data set from early 1996 plus the Chinese underground nuclear test of June 8, 1996. The Chinese test is well separated from the earthquake population. Also shown on the plot is the line log M0 = mb+11 which is an approximate discrimination line between the two populations.

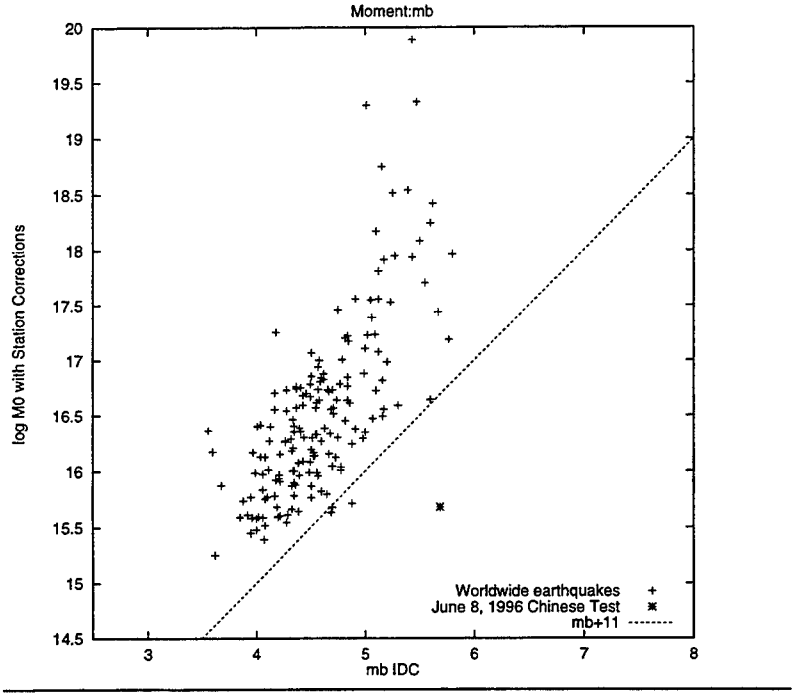

Figure 8. Log M0 vs. mb derived from IDC data for early 1996 plus the Chinese underground nuclear test of June 8, 1996

CONCLUSIONS AND RECOMMENDATIONS

1. Regionalization of phase and group velocities can be used to estimate phase and group velocities along any path. Even the relatively coarse 10 degree grid used in this study is adequate for surface wave identification and phase-matched filtering. Further improvements are possible with a finer grid and improved earth models. Regionalization also appears to be practical for surface wave attenuation and source and receiver amplitude factors.
2. Automatic surface wave processing with a small amount of operator review works well for identification and measurement of surface waves and calculation of Ms and scalar moments.
3. Maximum likelihood magnitudes and moments with station corrections but without censoring can be easily calculated and automated.

4. Inclusion of censoring within maximum likelihood magnitudes requires a much higher level of quality control to ensure that the magnitudes are not contaminated by poor quality data and improperly operating stations.
5. Scalar moments derived from surface waves appear to provide an effective discriminant when used in the same manner as the Ms:mb discriminant. The advantage of scalar moments over Ms is that they can be regionalized and used at any distance range. With proper quality control, and upper bound can be determined for the moment of any event. The effect of these improvements is to reduce the magnitude threshold for which the surface waves can effectively discriminate earthquakes from underground nuclear explosions.

LLNL's Seismic Magnitude and Discrimination Research

William R. Walter, Kevin M. Mayeda, David B. Harris, Howard J. Patton, Alan Sicherman, Craig Schultz, Peter Goldstein, Dan McNamara and Jerry Sweeney
Geophysics and Global Security Division, Lawrence Livermore National Lab

Sponsored by U.S. Department of Energy, Contract W-7405-ENG-48
Comprehensive Test Ban Treaty Research and Development Program, ST482B

ABSTRACT

The ability to verify a Comprehensive Test Ban Treaty (CTBT) depends in part on the ability to seismically detect, characterize, and discriminate between potential clandestine underground nuclear tests and other seismic sources, including earthquakes and mining activities. Teleseismic techniques are effective on the largest seismic events but regional techniques are necessary to push detection and discrimination levels down to small magnitudes. While regional signals can offer stronger signals and broader bandwidth, they are also strongly affected by source and path variability. Regional magnitude and discrimination techniques therefore need to be calibrated in each geophysically distinct subregion of a tectonically complex area such as the Middle East and North Africa. The goals of Lawrence Livermore National Laboratory's (LLNL's) seismic magnitude and discrimination research are to test and calibrate the most promising algorithms in regions of high monitoring interest, improve our understanding of their physical basis, and use this information to develop new and more effective techniques.

In this report we outline our tested procedure to calibrate regional discriminants and magnitude scales in the Middle East and North Africa. The procedure involves building a set of known earthquakes and explosions using auxiliary information (e.g., local and global catalogs, time and spatial clustering, depth, etc.) which is independent of the algorithms to be tested. The known events are then used to calibrate magnitude scales, map out regions of regional phase blockage, determine phase and discriminant distance corrections, and evaluate discriminant performance. Since the nuclear tests in this region are limited in distribution and only a very few regional seismograms are available, we are making use of mining and industrial chemical explosions to test discriminants. In aseismic and non-mining regions, as well as in regions where auxiliary information is inconclusive, we will need to rely on our physically based models of discrimination.

Key Words: seismic, magnitude, discrimination, Middle East, North Africa

OBJECTIVES

To evaluate and improve the capability to seismically verify the anticipated Comprehensive Test Ban Treaty (CTBT) in the Middle East and North Africa (ME&NA) and other regions of interest.

RESEARCH ACCOMPLISHED

As part of the overall Department of Energy CTBT Research and Development program, LLNL is pursuing a comprehensive research effort to improve our capabilities to seismically characterize and discriminate potential underground nuclear tests from other natural and man-made sources of seismicity. We present three aspects of our magnitude and discrimination research: (1) our procedure to test and calibrate the algorithms; (2) studies to improve our physical understanding and modeling capability; and (3) statistical methods to assess our progress.

Magnitude and Discrimination Calibration Procedure

LLNL is characterizing the Middle East and North African regions shown in Figure 1a. As a starting point, we show the results of the best known teleseismic discriminant, M_S:m_b, which performs quite well (Figure 1b). We used the NEIC monthly PDE catalog for the explosions and for a limited period of earthquakes (1985-1995). We supplemented the meager explosion data set with M_S values from Marshall et al. (1979). M_S and m_b values were available for only 2% of the 48,000 shallow (<50 km) earthquakes over the 11 year period. While more stations and improved processing could increase this number, M_S measurements require long-period surface waves to be visible at many stations which is difficult to achieve for the m_b<4 events which make up almost 90% of the catalog. Clearly, thousands of events per year need to be identified and characterized with other methods, including accurate locations, depths, and regional discrimination. This is the focus of the DOE CTBT R&D program at LLNL.

To evaluate and calibrate regional discriminants, we have developed a procedure and successfully tested it in a trial region. Here we emphasize the magnitude and discrimination aspects of the procedure, but it is actually closely intertwined with the regional characterization procedure described by Dowla et al. (this volume). First, we use the global catalogs to collect waveforms from earthquakes with independently determined locations to estimate velocity structure and regional phase propagation characteristics. As shown in Figure 2, S_n and L_g blockage can have a significant impact on discrimination capability. Next, we collect independent moments (e.g. Harvard CMT) or waveform model for moments (e.g., Walter, 1993) to tie our regional coda magnitude scales to a physically based parameter. Then we evaluate empirical distance corrections for both the magnitude scale and the discriminants as illustrated in Figure 3. Finally, we start to build up "ground truth" libraries of known earthquakes and explosions using auxiliary information (not discriminants to be tested) to evaluate discrimination performance. For earthquakes we use location, depth, focal mechanism and size to assess source type. Because underground nuclear explosion data is so limited, particularly at regional distances, we make use of mine blasts as known explosions. We use spatial and temporal clustering analysis as illustrated in Figure 4 to identify mine blasts (Harris, 1991), when direct reporting is unavailable or inconclusive.

Once we have calibrated the magnitude scales, corrected path effects, and obtained ground truth events, we evaluate discriminant performance. The best discriminants are combined in an integrated magnitude and discrimination analysis tool as illustrated in Figure 5. The specific path corrections, discriminants, and ground truth data change in each geophysically distinct region. This tool and its associated calibration parameters and data can then be incorporated in the Department of Energy Knowledge Base and delivered to the National Data Center for evaluation.

Physical Basis of Discrimination Studies

In aseismic regions or places without ground truth explosion data, we will need to rely on our physical understanding and models to assess the regional discrimination performance. As one aspect of this work we are comparing the western U.S. results of the potential discriminant M_0:m_b in the only other region of the world with significant amounts of regional nuclear explosion data, the E. Kazakhstan test area. Preliminary results in Figure 6 show good agreement with theory and the western U.S. results for explosions. The picture for earthquakes is more complex. We are also continuing research on several other topics including: (1) why mine collapses are outliers for some discriminants and not others; (2) quantifying the effect of source material properties on explosion discriminants; and (3) quantifying the effect of earthquake radiation patterns on P/S amplitude and slope discriminants.

Discriminant Performance Assessment

We are working with statisticians at LLNL and PNNL to better assess discrimination performance as well as to quantify the improvements provided by the CTBT R&D Program. Figure 7 shows an example of the tradeoff between false alarms versus missed violations for the L_g/P_g discriminant in the western U.S. under some very simple assumptions, and indicates the improvement achieved by use of higher frequencies. As discrimination results become available for ME&NA we will use similar techniques to assess performance.

CONCLUSIONS AND RECOMMENDATIONS

The ME&NA is a challenging and tectonically complex area, requiring calibration in each of many geophysically distinct subregions. LLNL has developed and tested an empirical calibration procedure and has used it to start characterizing the magnitude and discrimination behavior in the ME&NA, and other areas of monitoring interest. For regions without sufficient empirical data, accurate physically based discriminant models are needed and are being pursued at LLNL.

References

Goldstein, P. (1996) Slopes of P to S wave spectral ratios: a broadband regional seismic discriminant and a physical model, *Geophys Res. Lett.*, **22**, 3147-3150.

Harris, D. B. (1991). A waveform correlation method for identifying quarry explosions, *Bull. Seism. Soc. Am*, **81**, 2395-2418.

Marshall, P. D., D. L. Springer, and H. C. Rodean, (1979). Magnitude corrections for attenuation in the upper mantle, *Geophys. J. R. astr. Soc.*, **57**, 609-638.

Mayeda, K. and W. R. Walter (1996). Moment, energy, stress drop, and source spectra of western United States earthquakes from regional coda envelopes, *J. Geophys. Res.*, **101**, *11,195-11,208.*.

Patton, H. J. and W. R. Walter (1993). Regional moment:magnitude relations for earthquakes and explosions, *Geophys. Res. Lett.* **20**, 277-280. and 1994 Correction, *Geophys. Res. Lett.* **21**, 743.

Rodgers, A. J., F. Ni, and T. M. Hearn, (1996). Pn, Sn, and Lg propagation in the Middle East. (submitted to *Bull. Seism. Soc. Am.*).

Taylor, S. R., M. D. Denny, E. Vergino and R. Glaser (1989). Regional discrimination between NTS explosions and western U.S. earthquakes, *Bull. Seism. Soc. Am*, **79**, 1142-1176.

Walter, W. R. (1993). Source parameters of the June 29, 1992 Little Skull Mountain earthquake from complete regional waveforms at a single station, *Geophys. Res. Lett.* **20**, 403-406.

Walter, W. R., K. Mayeda, and H. J. Patton (1995). Phase and spectral ratio discrimination between NTS earthquakes and explosions Part 1: Empirical observations, *Bull. Seism. Soc. Am.*, **85**., 1050-1067

Zhang, T., T. Lay, S. Schwartz, and W. R. Walter (1996). Variation of regional seismic discriminants with surface topographic roughness in the western U.S. *Bull. Seism. Soc. Am.*, **86**, 714-725.

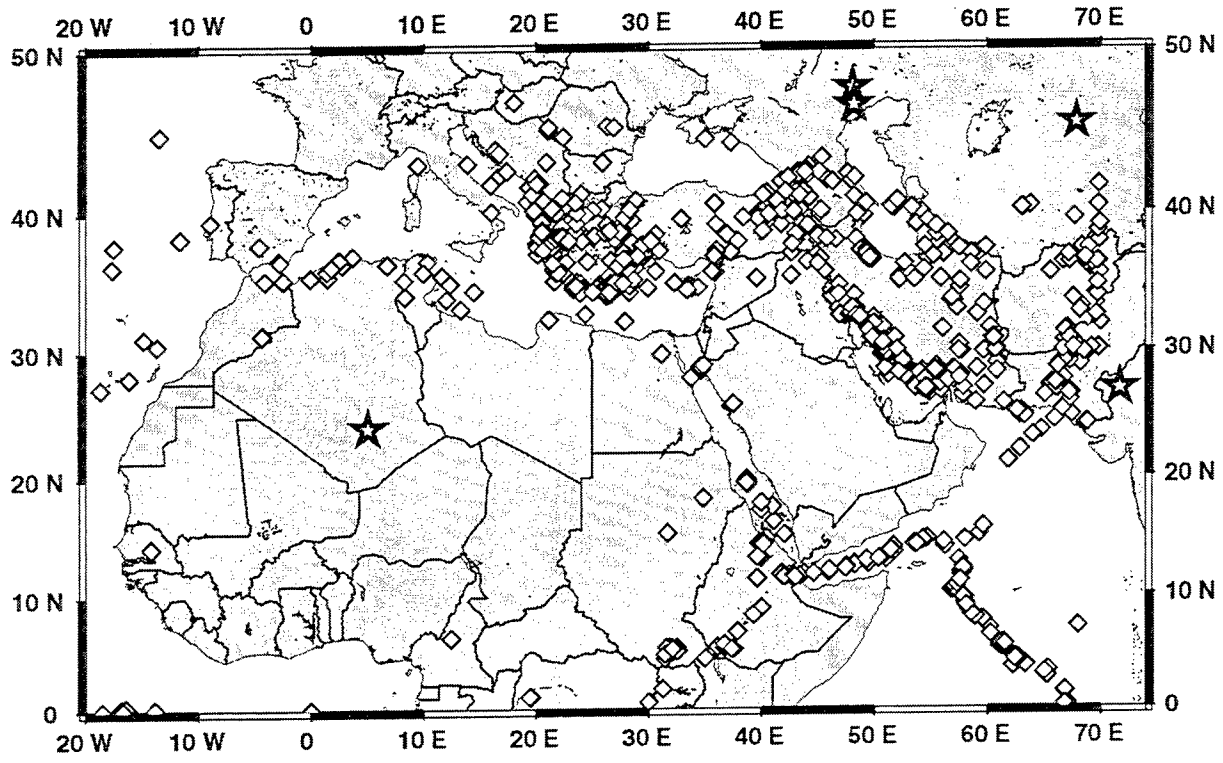

Fig 1a. Map showing main locations of underground nuclear tests (stars) and 1985-1995 earthquakes (diamonds) with NEIC M_S and m_b values in the Middle East and North African region.

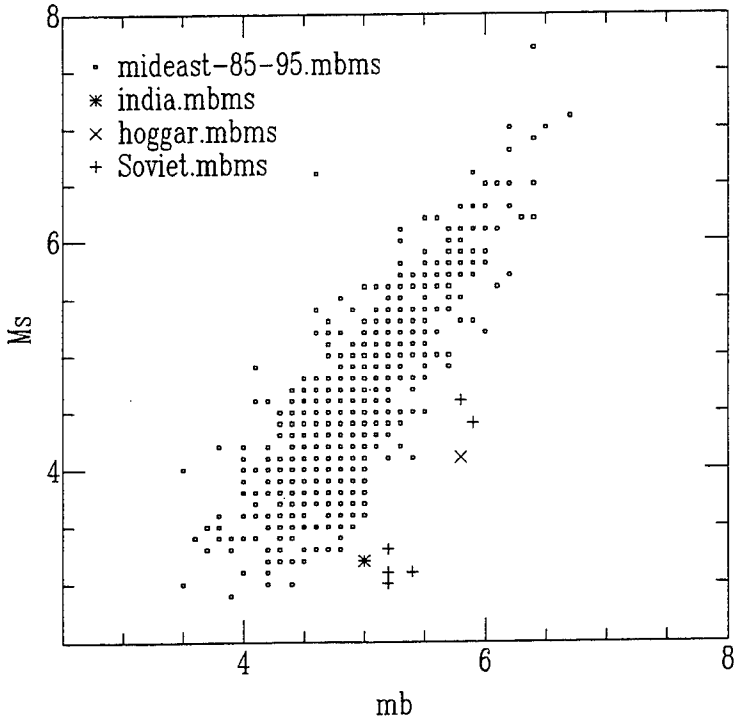

Fig. 1b. Plot of Ms:mb for the data shown in figure 1a. The earthquake-explosion separation is quite good. However there are very few measurments for events with m_b<4 and M_S <3. In fact, out of 49,000 events in the 1985-1995 NEIC catalog, 4126 with m_b>4, only 932 have both M_S and m_b. Thousands of events per year will need to be identified using other techniques.

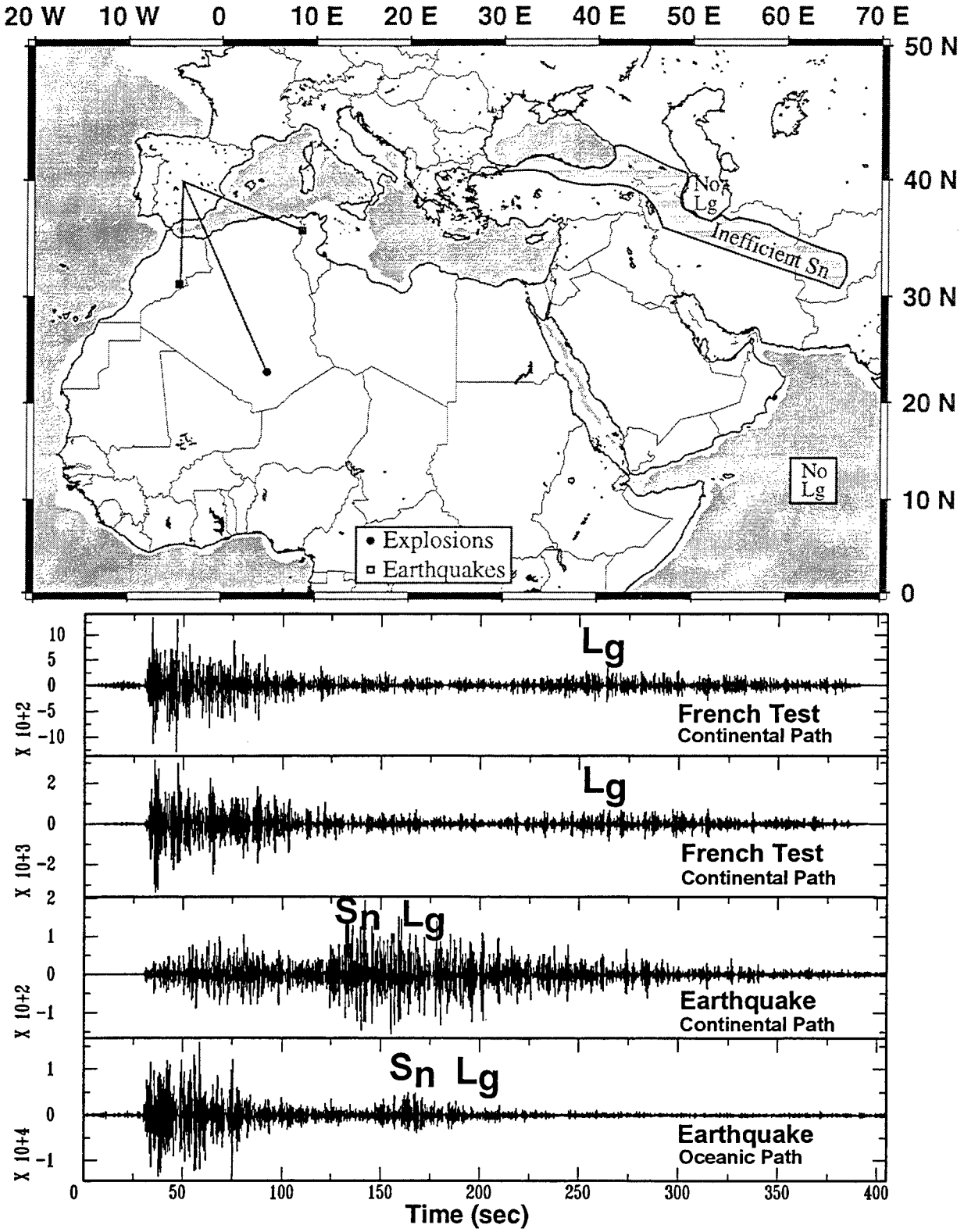

Fig. 2. Top map of event paths and areas of regional S phase blockage. Shaded zone indicates water depth greater than 1 km approximating oceanic crust which blocks L_g. Striped area is S_n blockage zone mapped by several studies (e.g. Rodgers et al., 1996). LLNL is refining these boundaries. Lower plot shows band passed (1-5 Hz) seismograms of African events recorded in Spain. Note the low L_g/P_g for the explosions is a source effect while the relative amplitude of S to P for earthquakes depends on the path. Regional S phase blockage complicates use of P/S discriminants in this region.

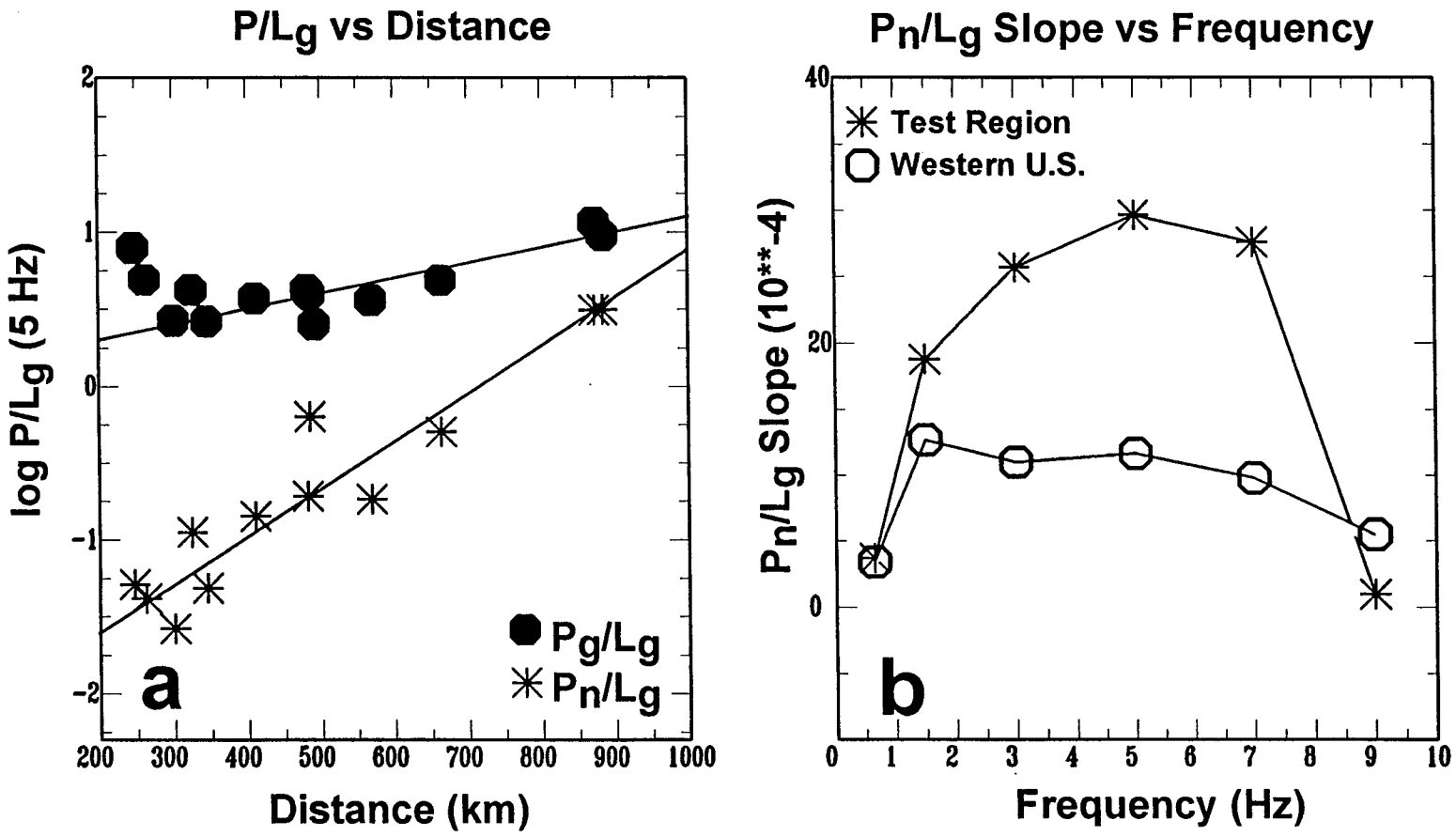

Fig. 3. Example of simple empirical discriminant distance corrections obtained as shown on the left by fitting a line to earthquake P/S amplitudes as a function of distance. Two examples are shown for the 4-6 Hz passband, P_g/L_g (●) and P_n/L_g (✳). Distance corrections need to be empirically determined for each region since they can vary greatly as shown on the right. The right hand plot shows P_n/L_g corrections as measured by the slope of the ratio amplitude versus distance for several different frequency bands. The results for this test region (✳) differ significantly from the Western U. S results (○) obtained by Zhang et al (1996).

Space and Time Clustering Identifies Mine Blasts

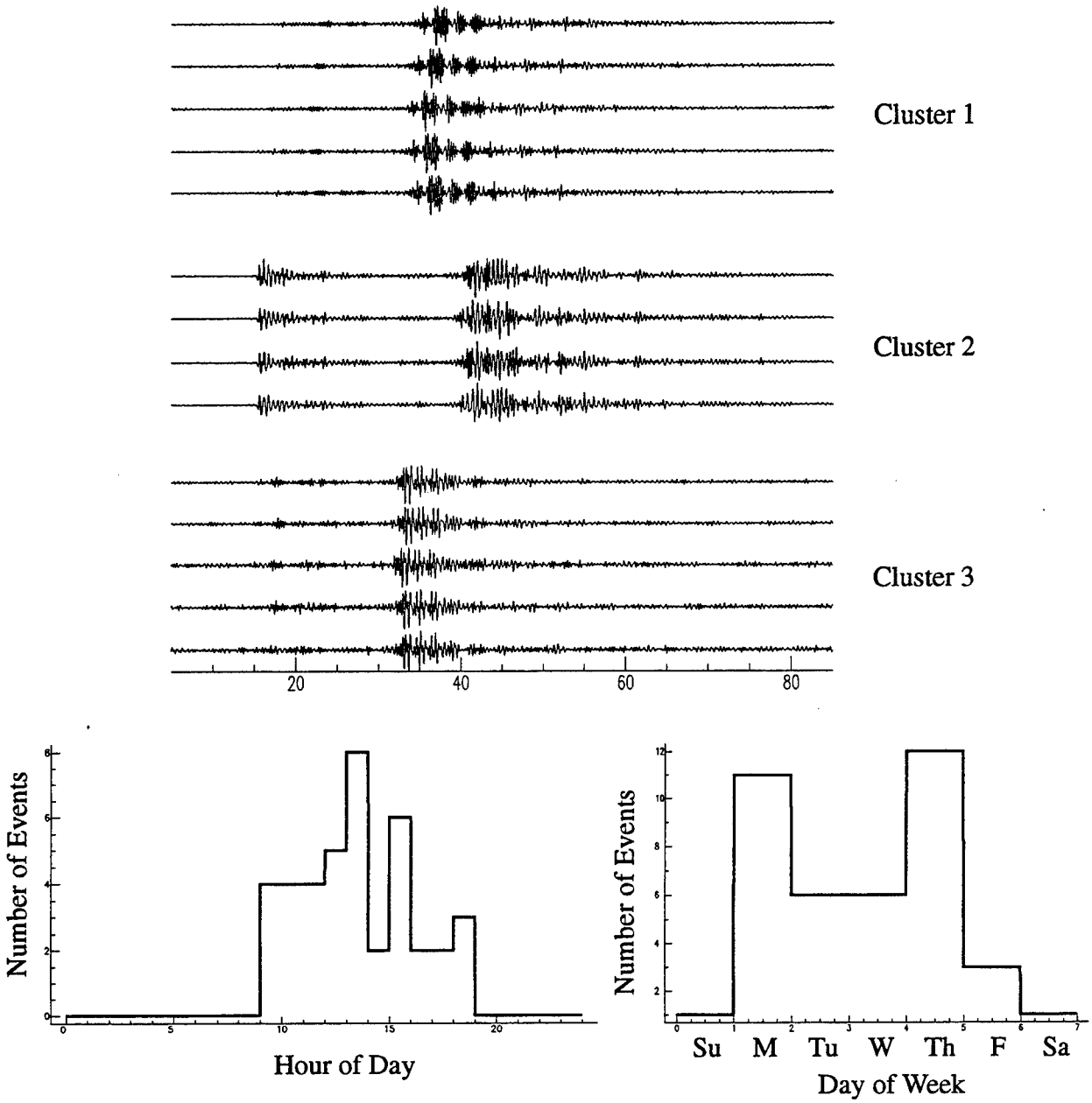

Figure 4. Spatial and temporal clustering of mining explosions provides a "bootstrap" mechanism for constructing a "ground truth" set of explosions for testing discriminants. The top figure shows waveforms from three clusters of local events observed at station MDT in Morocco. The events of cluster 2 are at the correct range to be explosions at phosphate mines near Khouribga. The clusters were defined by an algorithm operating on waveform correlations measured for all pairs of events in a group of 215 detections. Some 40 events were aggregated into 6 clusters; the histograms in the bottom Figures show how these events were distributed as a function of time of day and day of the week. The mid-day and working-day groupings support the interpretation that these are mining explosions (not earthquakes).

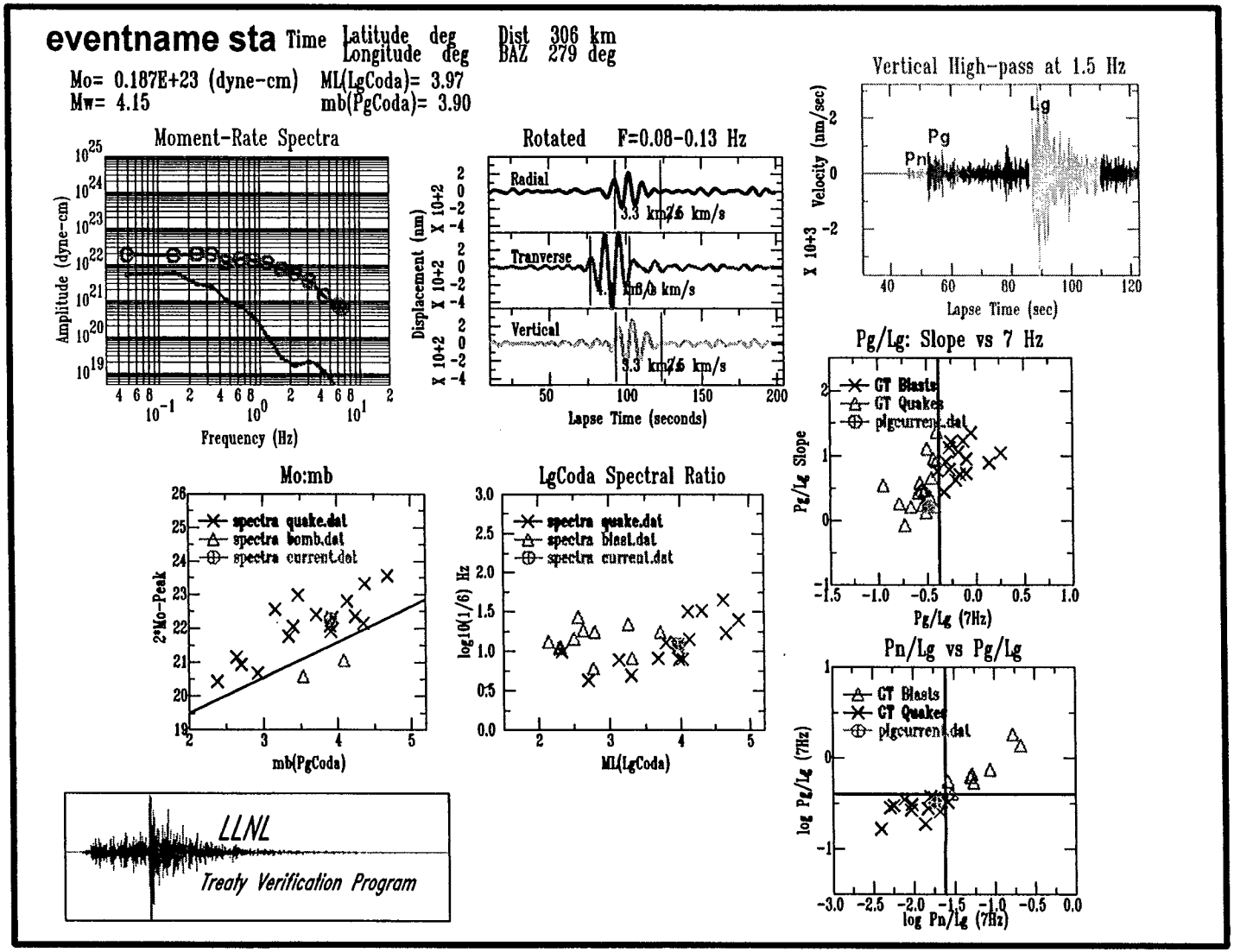

Fig. 5. LLNL has developed an integrated magnitude and discrimination analysis program, which we calibrate in each geophysically distinct region. The event source spectra and magnitudes are determined using regional coda (Mayeda and Walter, 1996) at the top left. The longer period data show the relative amplitudes of the Rayleigh and Love waves at the top center. The top right shows the high frequency regional phase windows. The lower plots compare the current event to a set of ground truth earthquakes and explosions for a set of tested discriminants (e.g. Walter et al., 1995; Goldstein, 1995). This example event is an earthquake.

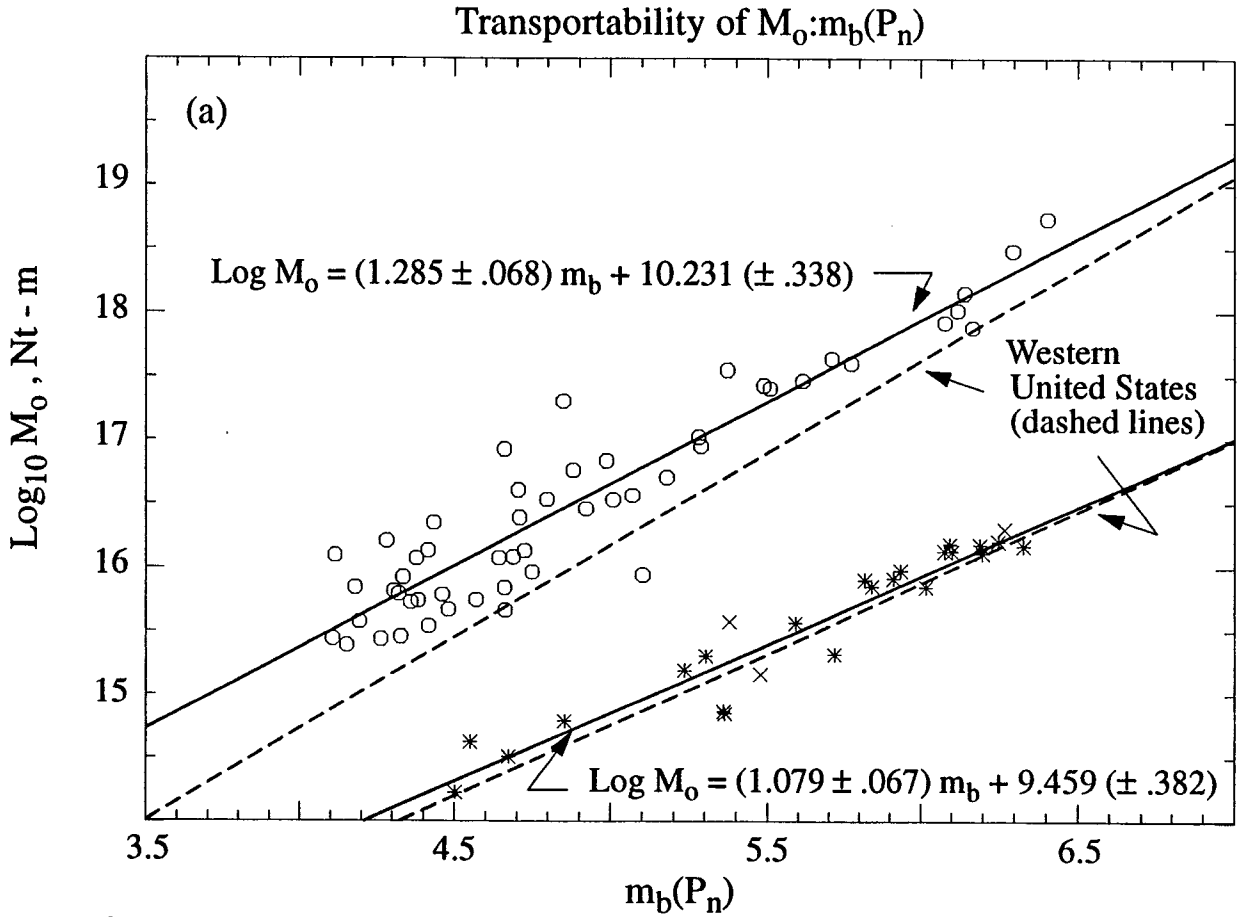

Fig. 6. As part of LLNL's physical basis studies to help us understand transportability and modeling issues, we tested the Mo:mb potential discriminant in the only other region with significant regional data from nuclear explosions, central Asia. The data points (circles, earthquakes; stars and x's explosions) are measurements for sources in central Asia and the former test site in Kazakhstan, where the solid lines with annotated equations are linear fits to these data The comparison is with western United States results (Patton and Walter, 1993). Here the magnitude is based on amplitudes of the regional Pn phase, and the magnitude scale has been calibrated in both regions against the teleseismic mb. The excellent comparison between explosions, detonated in very different materials, is expected based on a theoretical model presented by Patton and Walter. To gain such a close agreement between the explosions, the western U. S. mb(Pn)'s had to be adjusted for the magnitude bias between test sites by shifting the dashed lines to the right 0.35 magnitude units. This discriminant is still under development for application under operational conditions (Priestley, Patton and others. unpublished data).

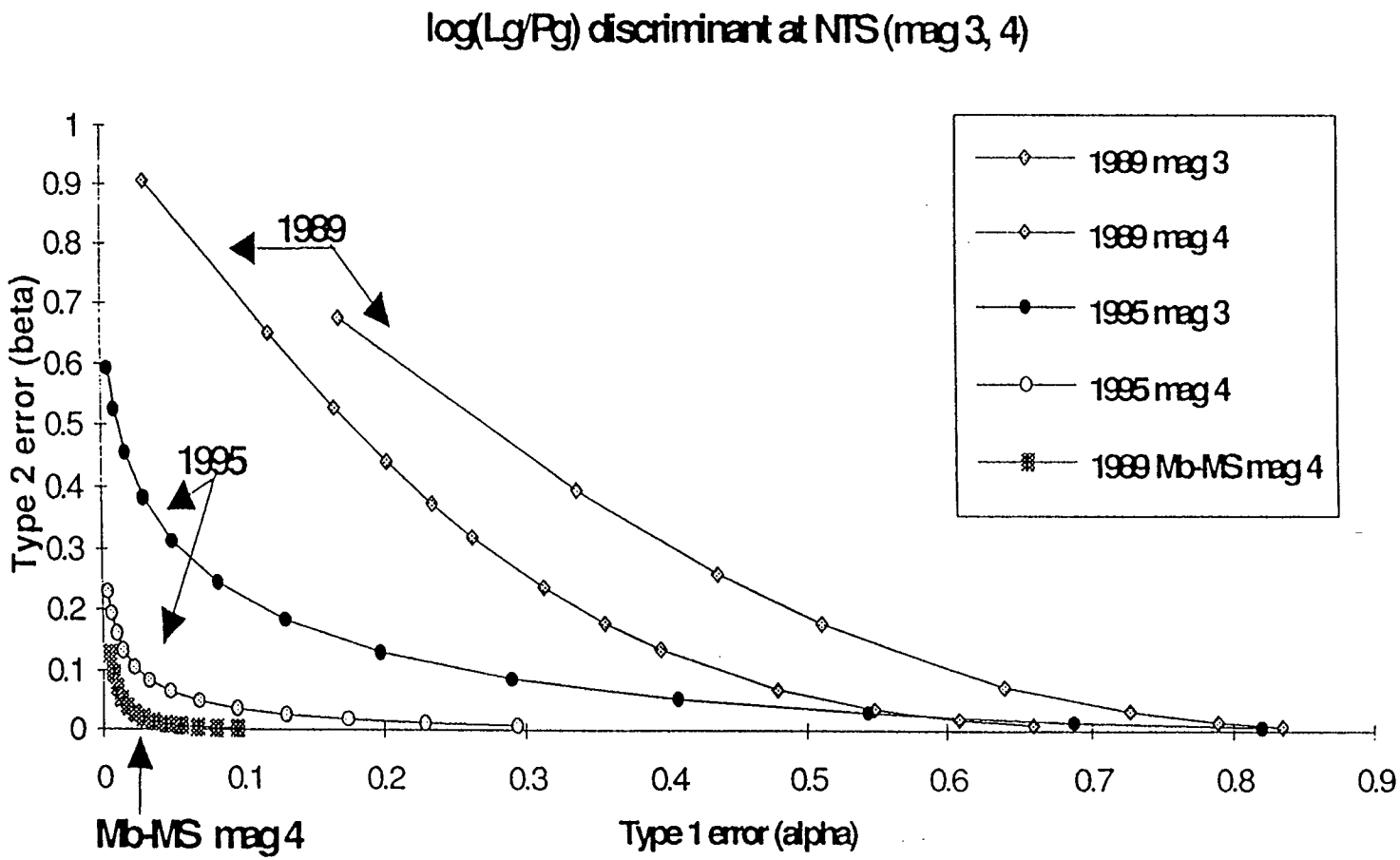

Fig. 7. A plot showing curves for the probability of a false alarm (type I error, calling an earthquake an explosion) versus the probability of a missed violation (type II error, calling an explosion an earthquake) for the L_g/P_g discriminant in the western U.S. Closer to the origin is better but for overlapping earthquake and explosion populations there is a tradeoff between the errors. The 1989 curves are the Taylor et al (1989) amplitude data based on the WWSSN SP passband which emphasizes frequencies near 1-2 Hz. The 1995 curves are the Walter et al. (1995) data which used a 6-8 Hz passband. This roughly shows the improvement achieved by moving to higher frequencies for L_g/P_g discriminants (though a small amount may come from the smaller geographic range of the 1995 earthquakes). The curves are also divided by magnitude range, with the true challenge and utility of the regional discriminants occurring at the magnitude 3 level (for comparison the regional Ms:mb curves from Taylor 1989 for magnitude 4 are shown). These curves are obtained by making simple assumptions to fit distributions to the data, obtain likelihood plots, define decision lines and calculate error probabilities (Sicherman, unpublished data).

The Performance of Some Regional Seismic Discriminants Applied to the Middle-East

Bradley B. Woods and Chandan K. Saikia
Woodward-Clyde Federal Services, Pasadena, CA

Sponsored by AFOSR, contract No. F49620-94-C-0046

ABSTRACT

We are investigating the portability of a variety of regional seismic discriminants to the Hindu-Kush region, and westward into the Middle East. The discriminants to be analyzed are the ratio of integrated short-period, vertical component, P-wave to long-period energy (predominantly surface wave) summed over all three components (E_{sp-Pz}:E_{lp-3}) vs. distance , the ratio of integrated short-period vertical component energy between the P- and S-wavetrains (E_{sp-Pz}:E_{sp-Sz}) vs. distance, and the ratio of m_b to scalar seismic moment (M_0), which we have used in lieu of the M_L:M_0 discriminant as the region lacks extensive near-regional network coverage necessary for M_L measurements. Unlike the southwestern U.S., from which data was used to develop these discriminants, the present study region has significant deep (mantle) seismicity owing to the major orogeny occurring in the area. As no explosion data are available for this region, the analysis of the discriminants involves comparisons of these data to earthquake data from other calibrated areas. For earthquakes within the crust, E_{sp-Pz}:E_{lp-3} values for this area lie generally within the same energy ratios vs. distance space as that for for other the western U.S. and central Asia earthquakes (Woods and Saikia, 1995). The deeper events exhibit little or no surface wave, so they have significantly higher ratios which makes them appear explosion-like (or can be considered outlyers from the general earthquake population). The deep events, however, often do display large amplitude, long-period S-waves, which, if included in he long-period energy window, pull the E_{sp-Pz}:E_{lp-3} ratios down towards the general earthquake population. At short periods the near-regional recordings of deep earthquakes also have strong initial motions, often with the P-wave dominating the wavetrain. Thus outliers to the crustal earthquake population will be deep events or explosions. Consequently accurate source depth estimation is necessary to use in conjunction with these energy ratio measures as source discriminants in regions with deep seismicity. The short-period P:S ratio can be used as a depth discriminant, itself, by identifying deep earthquakes from shallow ones, of course this would potentially mean mis-classifying an explosion as a deep earthquake. The M_L:M_0 discriminant is deterministic, requiring Green's functions that reflect the crustal structure of a region with which to invert waveform data to obtain the source parameters for any event. To this end we have modeled broadband regional records at NIL and those recorded by the PASCAL array in Pakistan. A refined 12-layer velocity structure has been developed which produces well-constrained source mechanisms have been obtained for deep and shallow events. It was found that m_b:M_0 ratios for the earthquakes analyzed lie within the general central earthquake population for this measurement. Refinements to the wavetrain-energy-ratio discriminants also have been made which yield better source-type separation.

OBJECTIVE:

We are investigating the portability of regional seismic discriminants which were developed from the analysis of data for southwestern U.S. earthquakes and NTS explosions. The discriminants being used here are the ratio of integrated short-period P-wave (E_{sp-Pz}) to long-period energy (predominantly surface wave) summed over the three components (E_{lp-3}) (Woods and Helmberger, 1996), the ratio of integrated short-period vertical component energy between the P and S wavetrains (E_{sp-Pz}:E_{sp-Sz}) (*ibid*), and the ratio of m_b to scalar seismic moment (M_0) (Patton and Walter, 1993), which we have used in lieu of the M_L:M_0 discriminant (Woods *et al*, 1993) as the region lacks extensive near-regional network coverage necessary for M_L measurements. The E_{sp-Pz}:E_{sp-Sz} ratio is akin to a time-domain short-period Lg:P discriminant (Taylor *et al*, 1989). Besides determining whether or not these discriminants are effective for seismic events in other tectonically active regions, it will be possible to calibrate the effective discriminant parameters for these different regions, so that an event from any such area can be incorporated into a unified database. Previous analysis of the performance of these discriminants has been limited to regions of primarily crustal seismicity. This study examines events in the Hindu-Kush region and westward into Iran (Figure 1). This region contains considerable deep (mantle) seismicity due its orogenous nature which extends down to depths of at least 225 km. Although no large explosion data exist for this region, it is a good test case for determining the discriminants' performances for a wide range of earthquake depths. Further refinement of the wavetrain energy ratios is also an important aspect of this work.

The energy ratio discriminants are empirical and only require the velocity records, whereas the m_b:M_0 discriminant is deterministic in that it involves waveform inversion for source parameters, which in turn requires establishing crustal models for these regions. Besides being used for source inversion, such Green's functions can be used to calibrate paths with respect to specific regional phases used for magnitude measurements and other discriminants. These path calibrations are particularly useful for regions where no large explosions have taken place, as it is then possible to predict waveforms for such sources, thus helping to establish criterion for a "first-blast" in the region.

RESEARCH ACCOMPLISHED:

Figure 1 plots the locations of earthquakes used in this study and the stations at which they were recorded; earthquakes symbol types correspond to that of the station (large symbol) which recorded them. Three of these four stations are are part of the IDC network. Other temporary array data, PAKN (located near NIL) and KNET (centered about AAK) have been analyzed, but have not been included in the figure. We have obtained between 50 and 70 events for each station. The bulk of the events comes from the Hindu-Kush region which contains a lot of deep seismicity (d > 100 km). Earthuqakes in Iran are primarily crustal in nature, while those under the Caspian Sea (Northwest corner of map) appear to be fairly deep and within the mantle (d > 50 km). Thus we have available a wide range of sources depths to compare their behavior with respect to the energy ratio discriminants.

Figure 2 plots typical examples of vertical component records for typical shallow (d=26 km), intermediate (d=77 km) and deep (d=151 km) earthquakes in three columns, respectively. The top trace is the broadband velocity record. Below that are the short-period

($f \geq 1$ Hz) and long-period ($0.033 \leq f \leq 0.125$ Hz) records along with their respective integrated energy curve. It can be seen that the waveforms and energy curves have different characteristics. The shallow event has a lot of short-period energy arriving throughout the Pnl and S-Lg wavetrain and consequently the energy curve appears ramp-like. The deep event has more prominent early arrivals and the energy curve is very step-function-like at the S-wave arrival. The intermediate-depth event is intermediate in nature in this respect. At long-periods the shallow event has a prominent surface wave which yields a sharp jump in its energy curve. The intermediate depth event also exhibits a Rayleigh wave, but it is smaller in comparison and the energy is more ramp-like, due in part to the signal to noise ratio. The deep event appears to have no discernible surface wave, but rather the prominent arrival is an S-wave. Such S-waves are a common feature of deep events in this region and are predicted by waveform modeling (Woods and Saikia, 1995). Further, the long-period phase's arrival coincides with that of the short-period S-wave arrival implying that it is in fact the direct long-period S-wave. This phase arrives outside of the surface wave time-window, so it would not contribute to the long-period energy level as defined for the discriminant. Consequently E_{lp-3} for deep events are low in comparison to crustal earthquake values for a given E_{sp-Pz}:E_{sp-Sz} level.

Figure 3 plots E_{sp-Pz}:E_{lp-3} vs. distance for NIL and PAKN data. Each data point represents one source-receiver pair. Earthquakes have been separated by depth. It is clear that the deep events, in general, have higher energy ratios than the shallower events for the reason discussed previously. Thus this discriminant produces two types of outliers: explosions and deep earthquakes. In areas with deep seismicity this discriminant requires source depth information to differentiate between deep earthquakes and explosions. One can modify the long-period time window used, however, to include long-period S-wave energy which would then give such deep events E_{sp-Pz}:E_{lp-3} ratios more in line with shallower earthquakes. Conversely, the E_{sp-Pz}:E_{lp-3} ratio could be used to estimate source depth: events lying outside of the crustal earthquake population (outliers), would be classified as deep, sub-crustal events. A secondary test for a prominent Rg wave or other late arriving shallow waveguide energy could potentially be used to cull-out explosions. Comparison of analogous plots for the other stations yields similar results.

Depth does not appear to significantly affect short-period P:S ratios. Figure 4 plots the E_{sp-Pz}:E_{sp-Sz} ratio vs. distance for earthquakes recorded by NIL. Although the largest energy ratio values are for deep events, there is a lot of scatter with some deep events having very low E_{sp-Pz}:E_{sp-Sz} values as well. Similar results hold for the other stations as well.

Besides investigating these discriminants' performance on data from differing tectonic regimes, we have investigate potential refinements to these discriminants. For the E_{sp-Pz}:E_{lp-3} discriminant improved performance was obtained by normalizing the energy ratios by magnitude, or

$$E'_{sp-Pz} = E_{sp-Pz} \times 10^{(m-m_o)},$$

where m is the magnitude (m_b or M_L), and m_o is chosen arbitrarily to be m=5. Figure 5 (a) and (b) plot the original and magnitude-normalized E_{sp-Pz}:E_{lp-3} values for TERRAscope data. Significantly better separation of earthquake from explosions was obtained using the magnitude-normalized values. Source depth effects also became much more apparent after the normalization procedure was applied to the Hindu-Kush/Middle East events. A similar normalization was tried on the E_{sp-Pz}:E_{sp-Sz}, but did not help its performance in any way.

Using regional M_0 lowers the long-period measurement threshold to m_b=4, which is near the threshold for teleseismic m_b measurements, making it a practical extension of the teleseismic m_b:M_S discriminant. Figure 6 plots m_b vs. M_0 for earthquakes in the Hindu-Kush region along with central Asian earthquakes and explosions for comparison. Moments have been determined by for events recorded by the PAKN temporary array as well as taken from other studies, while m_b's are from the PDE catalog, or in the case of Yunan, China events, from a regional bulletin. The Hindu-Kush events fall right within the general earthquake population.

An improvement in the E_{sp-Pz}:E_{sp-Sz} discriminant was found by using higher frequency bands. Figure 7 compares short-period P:S integrated energy ratios for four NTS explosions and three of the largest Little Skull Mtn. aftershocks for records convolved with a short-period Wood-Anderson instrument vs. records high-pass filtered at 4 Hz. In general the higher frequency energy ratios are larger in value than those the lower passband ones. More importantly, this separation is significantly larger for the explosions. Thus using higher frequency bands should improve the performance of this discriminant in general.

CONCLUSIONS AND RECOMMENDATIONS:

The m_b:M_0 ratio appears to be the most effective of the discriminants analyzed, but it requires considerable path calibration and has a fairly high magnitude threshold, particularly for sparse network coverage. In regions with deep seismicity the E_{lp-3}:E_{lp-3} discriminant needs complimentary source depth information, so that it can distinguish between crustal earthquakes and explosions. It can be used as a fast depth discriminant itself, with the caveat that the event could also be an explosion.

The E_{sp-Pz}:E_{sp-Sz} ratio needs further refinement to make it effective an effective discriminant, although increasing the passband from about 0.5 Hz to 3 Hz does improve its performance. Several procedures currently being analyzed include weighting more heavily the early arriving energy of the P-wave a and S-wave relative to the rest of the short-period Pnl and S-Lg wavetrains, and incorporating the SH-component into the ratio of P to S energy. With the extensive data now gathered for this region and the many events for which multiple observations are available, we will analyze the short-period behavior of these events more thoroughly in terms of source, radiation pattern and propagation effects. For comprehensive seismic monitoring of smaller events (M≥3.5) better understanding of such issues is necessary in order to produce effective short-period discriminants.

REFERENCES:

Patton, H. J. and W. R. Walter, 1993. Regional moment:magnitude relations for earthquakes and explosions, *Geophys. Res. Let.*, **20**, pp. 277-280.

Saikia, C. K., B B. Woods, L. Zhu, H. H. Thio, and D. V. Helmberger, 1996. Path calibration, source estimation and regional discrimination for the Middle East: Application to the Hindu-Kush Region, Woodward-Clyde Fed. Services, PL-TR-96-2069, 129 pp.

Taylor, S. R., D. D. Denny, E. S. Vergino, and R. E. Glaser, 1989. Regional discrimination

between NTS explosions and Western U.S. earthquakes, *Bull. Seism. Soc. Am.,* **79** pp. 1142-1176.

Woods, B. B., S. Kedar, and D. V. Helmberger, 1993. M_L:M_0 as a Regional seismic discriminant, *Bull. Seism. Soc. Am.,* **83**, pp. 1167-1183.

Woods, B. B. and C. K. Saikia, 1995. The Portability of some regional seismic discriminants and related broadband waveform modeling, Proceedings of the 17th Annual Seismic Research Symposium, PL-TR-95-2108, pp. 138-147.

Woods, B. B. and D. V. Helmberger, 1996. Regional seismic discriminants using wavetrain energy ratios, submitted to *Bull. Seism. Soc. Am.*

THIS PAGE LEFT
INTENTIONALLY
BLANK.

USE OF THE CEPSTRAL STACKING METHOD (CSM) FOR IMPROVED SOURCE DEPTH DETERMINATIONS FROM COMBINED SINGLE-STATION AND ARRAY OR NETWORK OBSERVATIONS AT REGIONAL DISTANCES

Shelton S. Alexander and Chih-Chieh Yang
The Pennsylvania State University

AFOSR Grant No. F49620-94-1-0179

ABSTRACT

The Cepstral Stacking Method (CSM), developed earlier in this project as part of a broader effort to develop effective regional discriminants, has been extended to combine single-station stacking with array or network stacking to obtain improved estimates of depth-phase delay times (hence depth). The procedure consists of first stacking (product or sum) cepstra of overlapping time windows in the P and P-coda signal at each regional station and then stacking (product or sum) these individual stacked cepstra over all regional stations. The combined stacking suppresses spurious delay times common to all sub-windows at a single station (e.g. P to S conversions at major crustal interfaces or locally-scattered incoming signals at the receiver) and further enhances the desired pP - P and sP - P depth phases. As in the single-station case, product-stacking over a local array or distributed network generally is more effective than sum stacking, although sum-stacking allows S/N weighting when there is a large variation in signal-to-noise ratios among the stations used.

Modifications that potentially can enhance the effectiveness of the CSM have also been investigated; they include noise reduction through band-pass filtering or noise power subtraction before computing the sub-window cepstrum and time-domain envelope normalization before computing cepstra of sub-windows.

Through various tests on crustal events with independently-known source depths, effects of sub-window length and percent overlap of successive sub-windows on the signal-to-noise of depth-phase cepstral peaks have been investigated for both product- and sum-stacking. Shorter sub-window lengths (15 - 20 seconds) give significantly better results than longer windows for product-stacking, while longer sub-windows give slightly better results for sum-stacking. An overlap of 60-75 percent appears to give the best results for product-stacking and there is little dependence on overlap for sum-stacking.

Results to date indicate that, with reasonable signal band-widths and signal-to-noise levels, accuracies in source depth of about 1 km or better can be achieved rapidly and routinely using the CSM on regional signals from explosions or earthquakes.

OBJECTIVE

The objective of this aspect of the study is to develop the capability to determine source depths reliably and accurately for shallow (crustal) earthquakes and explosions recorded at regional distances. If source depths accurate to about 1 km or better can be determined rapidly and routinely for all events larger than magnitude 2.5, a large fraction of crustal earthquakes could be eliminated from further consideration under a CTBT, because only the shallowest events (less than about 5 km) could include possible explosions. Focal depths from regional travel-time observations (hypocenters) typically are not accurate, especially when there are only a few stations, none of which is close to the epicenter; because of the complexity of regional signals, direct identification of depth phases (pP - P and sP - P) typically is not feasible. The CSM overcomes this difficulty and provides reliable and accurate depth-phase delay times for small events for which reliable teleseismic depth phase determinations cannot be made. The current research is focused on further developing the CSM approach, taking advantage of new local arrays (Alpha arrays) and distributed regional stations.

RESEARCH ACCOMPLISHED

Within the research project's broader goal of developing effective regional discriminants for Iran and other areas of interest, the main emphasis of recent work discussed here has been on further evaluation and extension of the Cepstral Stacking Method (CSM) for accurate source depth determinations. Earlier work on source depth in this project was focused on the development and testing of the CSM for application to single regional stations (e.g. Alexander, et al., 1995; Karl, 1995; Alexander, 1995).

The CSM enhances depth phases for a single station, because each sub-window in the P and P-coda total window contains the same, or nearly the same, (pP - P) and (sP - P) delay times, whereas delay times for distinct crustal phases appear in at most a few sub-windows; by stacking the cepstra (product or sum) of these sub-windows the common depth-phase delay times are enhanced while crustal-phase delay times are not. Figure 1 illustrates how the method works for a regional earthquake in Iran recorded at the ILPA array station IR1; the prominent depth-phase cepstral peak at 7.1 seconds is verified by independent teleseismic pP - P delay times that agree within 0.1 seconds of this time. Extension of the CSM by stacking individual-station, stacked cepstra over a local array or regional network of stations was found to result in significant further enhancement of depth phase delay times. The reason for further enhancement is that other cepstral peaks ("noise") in individual-station, stacked cepstra that may result from receiver site effects such as P to S conversions at sharp boundaries beneath the station, discrete local scatterers, multipathing, or random noise generally are not in common among separated stations and consequently are suppressed after stacking, compared to the common depth-phase delay times. As in the single-station case, product stacking was found to be more effective than sum-stacking over an array or network; however, if some stations have a poor signal-to-noise ratio relative to others, sum-stacking may be more appropriate, because S/N weighting can be used.

As an example, Figure 2 compares several individual-station, product-stacked cepstra and the combined array-stacked cepstrum for a magnitude 4.6 earthquake in the Yellow Sea recorded regionally (distance of approximately 470 km) at the KS array in Korea. The combined stack has a single, sharp peak at about 2 seconds. Similarly, Figure 3 shows the individual-station, product-stacked cepstra and the combined stack for widely-separated regional stations in China for the same event; the combined, four-station stack has a single dominant peak at about 2.1 seconds, in close agreement with the KS array-stacked result. If this is the pP delay time, the source depth is approximately 5-6 km; the depth is approximately 4 km if the delay time is sP. Comparable enhancements for regional events have been found using the ILPA array in Iran and the TXAR Alpha array in Texas.

As part of this study Yang (1996) implemented and tested other modifications of the CSM that may be useful in enhancing the desired delay times. Effects of noise can be reduced by bandpass filtering the signal, keeping only frequencies where the S/N in the power spectrum is greater than some chosen level; the tradeoff is a reduction in the band-width of the remaining signal, which limits the time resolution of the depth-phase cepstral peak(s). Subtracting the noise power obtained from a noise window ahead of the first P arrival from the power spectrum of each sub-window before computing the sub-window cepstrum is another alternative for suppressing noise effects; this should be done when the S/N is low over the entire frequency band. An new envelope-normalization approach was implemented for reducing cepstral peaks from prominent crustal phase delay times relative to depth-phase cepstral peaks; it consists of computing the envelope of the input signal and dividing the input signal by the envelope before applying the CSM. An example comparing the CSM results using each of these procedures and the conventional approach where none of these procedures is used is shown in Figure 4 for a single KS array station. Figure 5 shows the corresponding combined stacking results for the KS array. All appear to work, but none consistently outperforms the other for the events analyzed, all of which have relatively high S/N.

As part of this study Yang (1996) also carried out tests to determine the dependence of the CSM results on sub-window length and percent overlap of successive sub-windows. It was found that in terms of signal-to-noise ratio (SNR) of the cepstral peak the sum-stacked results are relatively insensitive to either sub-window length or percent overlap. In contrast the SNR of the product-stacked cepstral peak has a strong dependence on both; the SNR increases as the sub-window length decreases and as the percent overlap increases. Tables 1 and 2 for an Iranian regional earthquake illustrate these dependencies. Because product-stacking is more effective than sum-stacking, relatively short sub-windows and overlaps of 60-75 percent should be used, based on the tests carried out. However, the sub-window length must be greater than the (unknown) depth-phase delay time; using a sub-window length of 20 seconds or greater would allow the CSM method to work for events anywhere in the crust in most regions of interest.

CONCLUSIONS AND RECOMMENDATIONS

1. Combined single-station and array or network cepstral stacking gives improved estimates of depth-phase delay times (hence source depth) for regional events.

2. Product stacking is more effective in enhancing depth-phase delay times than sum-stacking for both single-station and array or network applications of the CSM.

3. Shorter sub-window lengths (15 - 20 seconds) give significantly better results than longer windows for product-stacking, while longer sub-windows give slightly better results for sum-stacking.

4. A sub-window overlap of 60-75 percent appears to give the best results for product-stacking and there is little dependence on overlap for sum-stacking.

5. Modifications to the CSM that reduce the effects of noise and reduce the influence of delay times from large crustal phase arrivals appear to be useful, but need more study, especially for small events with marginal S/N.

6. Results to date indicate that, with reasonable signal band-widths and signal-to-noise levels, accuracies in source depth of about 1 km or better can be achieved rapidly and routinely using the CSM on regional signals from explosions or earthquakes.

Further work is needed to establish the threshold minimum magnitude for which the CSM can be used to obtain reliable source depth for regional events in areas of interest. It should also be applied to additional events for which independent estimates of source depth are available (e.g. teleseismic pP or sP; aftershock monitoring; known explosions). The CSM for both individual stations and arrays or networks should be implemented and tested for near-real-time, automated depth determinations for regional events.

REFERENCES

Alexander, S. S., 1996, A New Method for Determining Source Depth From a Single Regional Station, Seis. Res. Ltrs., Vol. 67, No. 1, p. 63.

Alexander, S. S., R. C. Hsu, S. L. Karl, I. N. Gupta, and D. H. Salzberg, 1995, New Techniques for Estimating Source Depth and Other Diagnostic Source Characteristics of Shallow Events From Regional Observations of P. Lg and Rg signals, Proc. 17th Seis. Res. Symposium on Monitoring a Comprehensive Test Ban Treaty, PL-TR-95-2108, Env. Res. Paper, No. 1173, 821-830.

Karl, S. L., 1995, Magnitude and Source Depth Estimates for Earthquakes and Explosions in Iran--Regional Observations, B.S. Thesis in Geosciences, The Pennsylvania State University, 185 pp.

Yang, C. C., 1996, Investigation of Cepstral Stacking Methods for Time Delay Extraction, M.S. Thesis (EE), The Pennsylvania State University, 113 pp.

Table 1. Comparison of SNRs of product- and sum-stacked cepstral peaks for different sub-window lengths for the regional Iranian earthquake recorded at IR1 (Figure 1a).

	SNR (Product stack)	SNR (Sum stack)
Sub-window length=60sec.	41.0	4.3
Sub-window length=50sec.	101.9	3.8
Sub-window length=40sec.	178.0	3.4
Sub-window length=30sec.	287.5	2.7
Sub-window length=20sec.	537.9	2.1

Table 2. Comparison of SNRs of product- and sum-stacked cepstral peaks for different sub-window overlap percentages for the regional Iranian earthquake recorded at IR1 (Figure 1a).

	SNR (Product stack)	SNR (Sum stack)
Overlap percentage=60%	287.5	2.7
Overlap percentage=40%	125.4	3.1
Overlap percentage=20%	47.2	3.0
Overlap percentage=10%	42.8	2.9
Overlap percentage= 0%	38.3	2.9

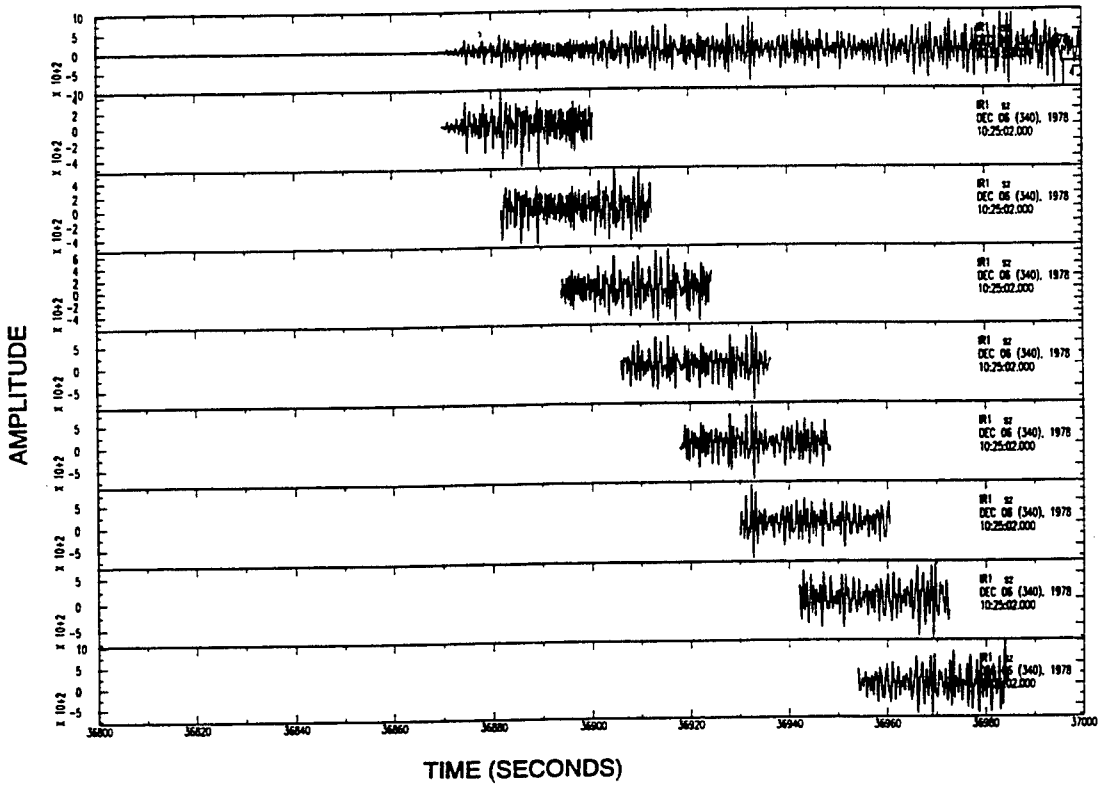

Figure 1a. Iranian earthquake recorded regionally by ILPA array station IR1 with sub-windows (30 seconds) and overlaps (60 percent) used for cepstral stacking.

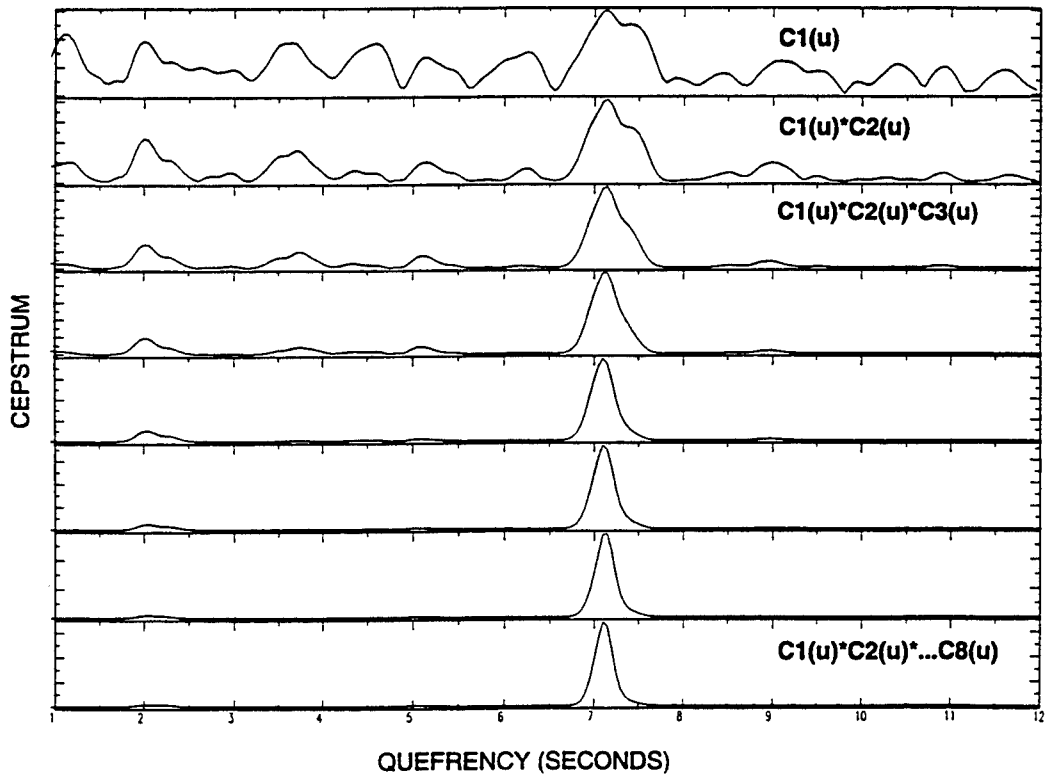

Figure 1b. Step by step product stacking of cepstra for successive sub-windows shown in Figure 1a showing how the depth-phase delay of 7.1 seconds is enhanced.

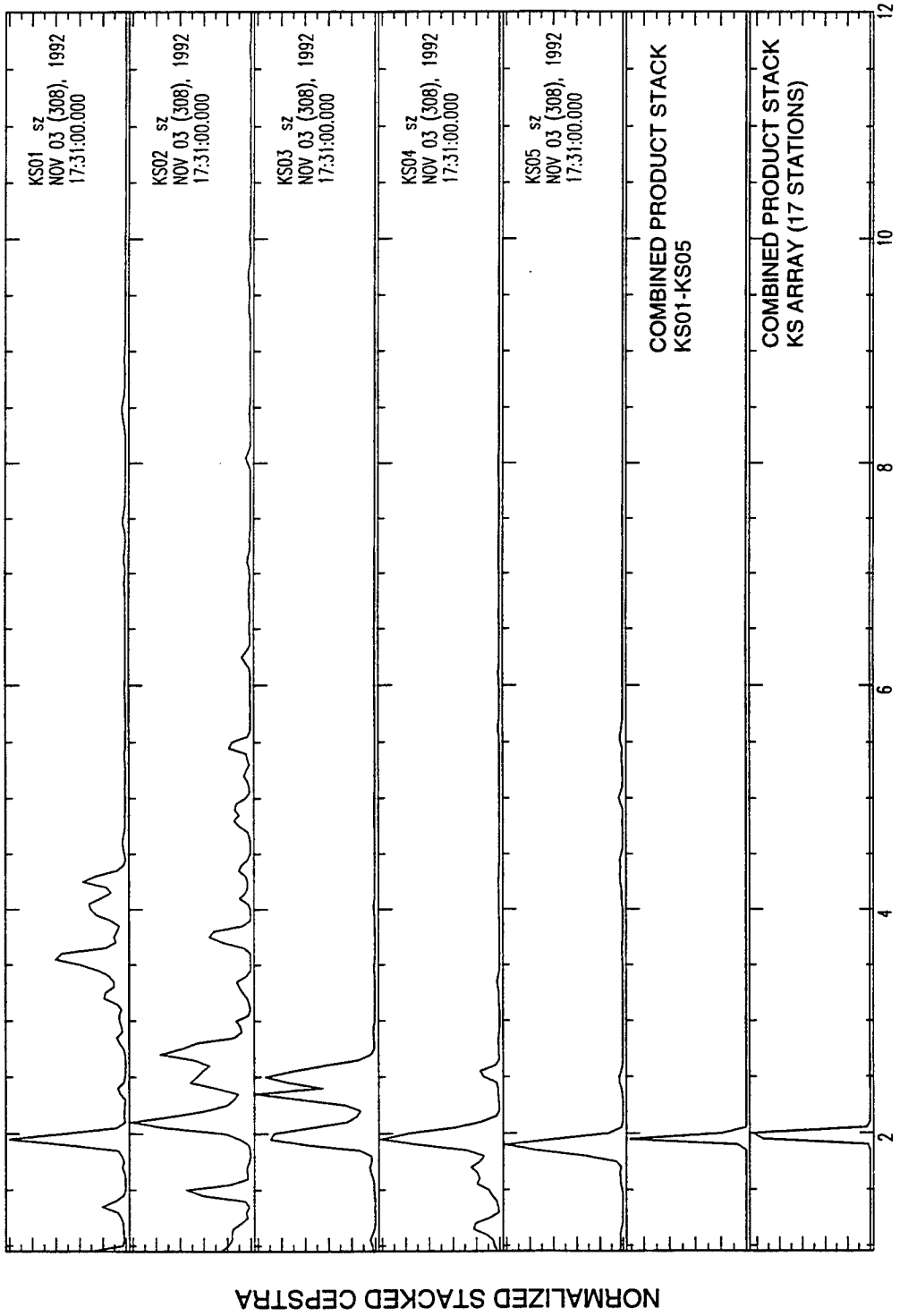

Figure 2. Individual-station, product-stacked cepstra for a magnitude 4.6 regional earthquake in the Yellow Sea (distance approximately 470 km) recorded at the KS array in Korea (top 5 panels). Combined product-stacked cepstra for the five stations and for the entire KS array are shown (bottom two panels) showing a prominent depth-phase cepstral peak at about 2 sec.

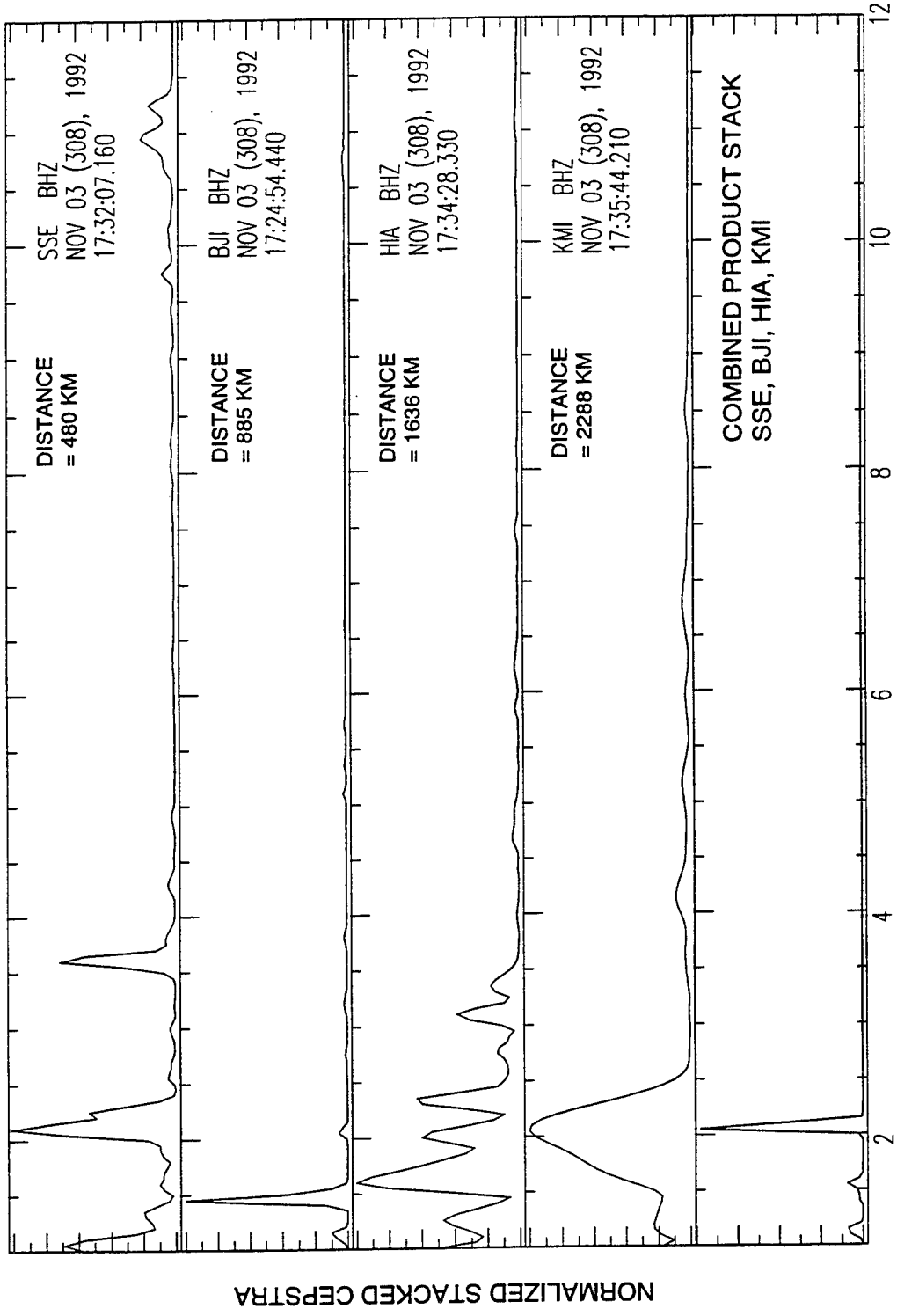

Figure 3. Individual-station, product-stacked cepstra for the magnitude 4.6 regional earthquake in the Yellow Sea recorded at four widely-separated regional distances in China (top 4 panels). The combined product-stacked cepstra for the four regional stations (bottom panel) has a prominent depth-phase cepstral peak at about 2.1 seconds in close agreement with the results for the KS array (Figure 2).

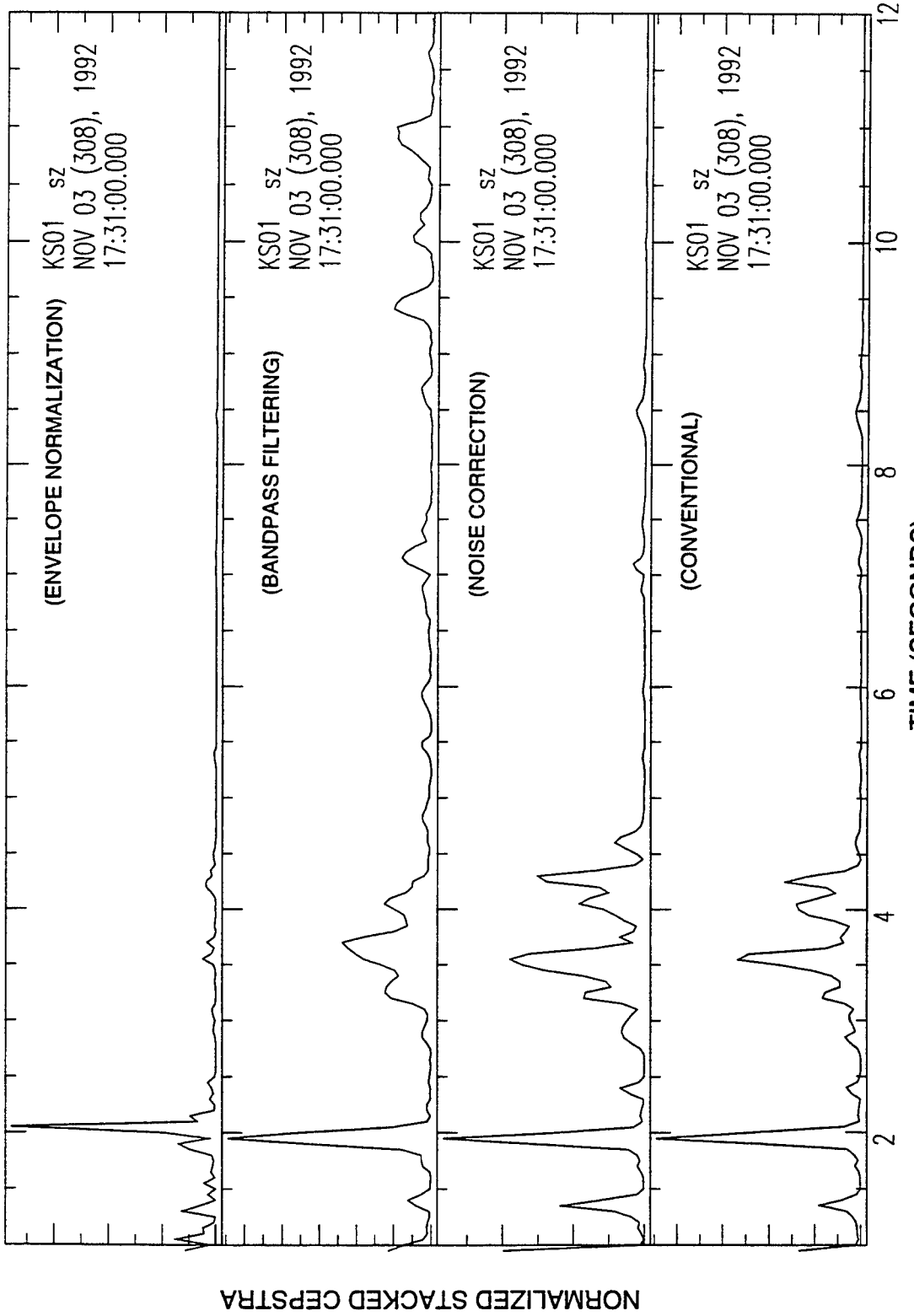

Figure 4. Comparison of the conventional and modified CSM approaches for KS array station KS01 for the 3 November 1992 Yellow Sea earthquake.

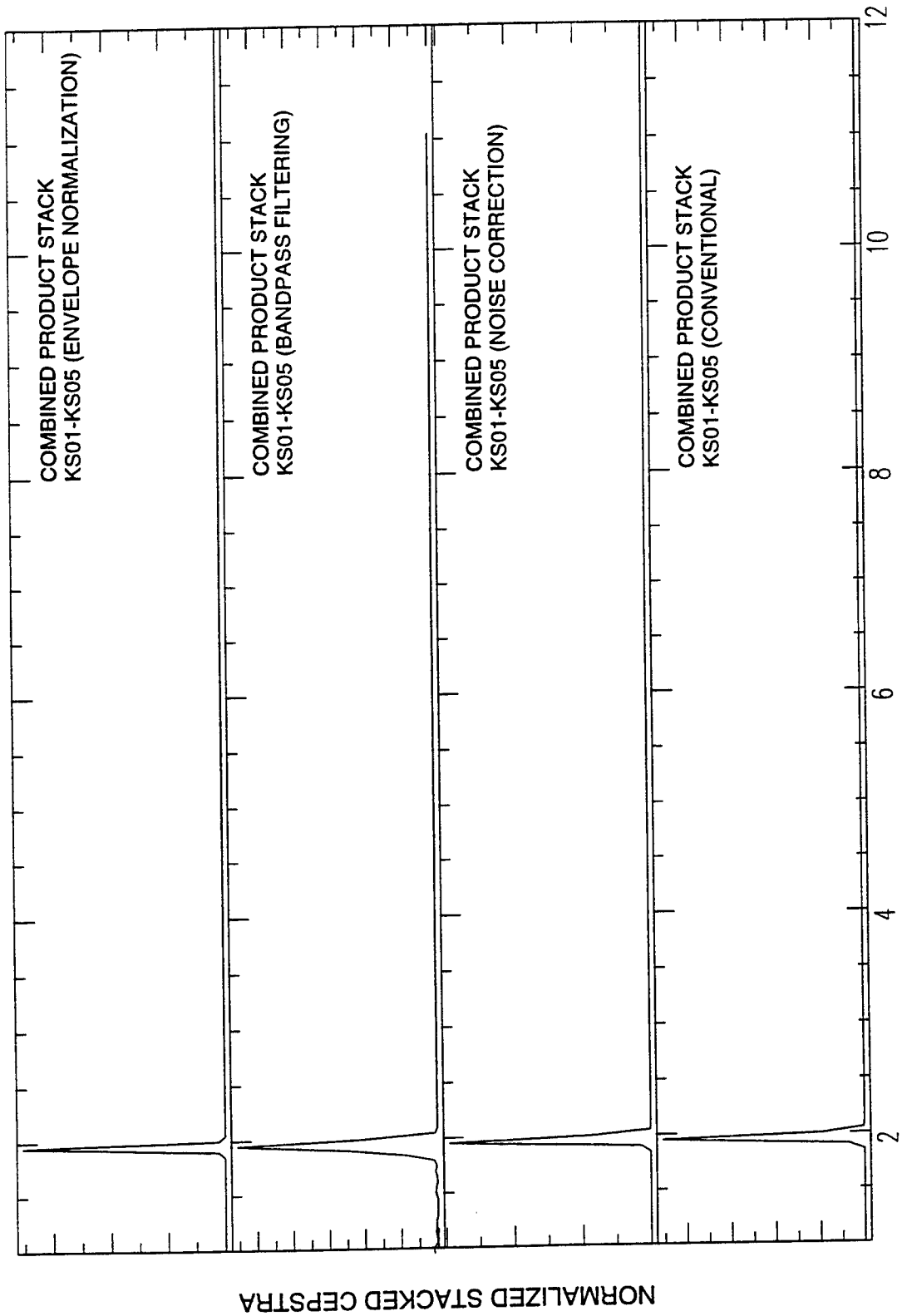

Figure 5. Comparison of the combined product-stacked cepstra for the conventional and modified CSM approaches using all stations in the KS array for the 3 November 1992 Yellow Sea earthquake.

MULTIWAVELET BEAMFORMING- A NEW SEISMIC ARRAY DATA PROCESSING METHOD

Lorie K. Bear & Gary L. Pavlis
Department of Geological Sciences, Indiana University
1005 East Tenth St.
Bloomington, IN 47406
Grant # F49620-95-1-0366
Sponsored by AFOSR / AASERT

ABSTRACT

We have developed a new seismic array data processing method which produces statistical confidence intervals for slowness vector estimates. The slowness vector, which is typically transformed into bearing and velocity, is a key parameter used for identifying seismic phases and for event source location. Estimates for the slowness vector are typically found using some variant of time-domain or frequency-domain beamforming. A major failing of existing methods is that they lack an objective measure of the precision of their estimates. Our method, multiwavelet beamforming, is closely related to both time-domain and frequency-domain beamforming. The primary advantage to multiwavelet beamforming is that we are able to produce multiple estimates of the slowness vector which are approximately statistically independent. We use a special set of integration kernels we call the Lilly and Park wavelets to transform the seismic data in a manner analogous to applying a windowed Fourier transform. For a range of possible slowness vectors we calculate semblance, a measure of signal coherence, using the multiwavelet transforms. The semblance is then a function of the assumed slowness vector and the particular wavelet. For each wavelet we determine a slowness vector estimate by finding the slowness value associated with the maximum semblance. We calculate confidence intervals by applying the jackknife statistical method to the ensemble of separate slowness vector estimates.

key words: beamforming, array processing, wavelets, jackknife statistical method

OBJECTIVE

The key measurement in seismic array data processing is the slowness vector. The slowness vector, which is typically transformed into bearing and velocity, is used for phase identification and event source location (e.g. Mykkeltveit and Bungum, 1984). The most common, and simplest, methods for determining slowness vectors are frequency-domain (classical) and time-domain beamforming. A major shortcoming of existing methods is that they provide no objective measure of the possible error in the estimated slowness vector. In this report we present a new beamforming method which produces an objective, quantitative measure of uncertainty directly from the waveform data.

RESEARCH ACCOMPLISHED

We are able to produce direct measures of uncertainty because our method produces multiple estimates for each slowness component. These multiple samples allow us to calculate confidence intervals using standard statistical methods. This new method combines aspects of both time-domain and frequency-domain beamforming and incorporates concepts drawn from such diverse topics as wavelet transforms, multiple spectral estimation, and statistics.

Integral Transforms

The characteristics of a seismic signal can fundamentally be described by time location and frequency content. These two properties can be studied simultaneously by using a moving window Fourier transform. The windowed Fourier transform of signal s(t) for frequency f and time t is

$$\mathcal{F}[s](f,t) = \int_{t-T/2}^{t+T/2} s(\xi)g(\xi - t)\cos(2\pi f\xi)d\xi + i\int_{t-T/2}^{t+T/2} s(\xi)g(\xi - t)\sin(2\pi f\xi)d\xi$$

$$= \int_{t-T/2}^{t+T/2} s(\xi)g_{f,e}(\xi - t)d\xi + i\int_{t-T/2}^{t+T/2} s(\xi)g_{f,o}(\xi - t)d\xi \qquad (1)$$

where g(t) is a chosen taper of length T (Kumar and Foufoula-Georgiou, 1994). The integration kernel for the transform is $g_f(t) = g_{f,e}(t) + ig_{f,o}(t) = g(t)\cos(2\pi ft) + ig(t)\sin(2\pi ft)$.

Within the last ten years there has been an explosion of interest in developing a special class of kernel functions called wavelets. Wavelets are functions developed so that their time lengths match the scale of the frequencies to be studied (Kumar and Foufoula-Georgiou, 1994). It is well known that a function which is finite in time cannot also be finite in frequency due to the uncertainty principle. Lilly and Park (1995) use a novel approach to develop functions which are finite in the time domain and have their energy concentrated into a given frequency band.

The Lilly and Park wavelets are real time series (w_m) with M samples and sampling rate Δt. They are defined to concentrate energy within a frequency range defined by a center frequency f_c ,and a bandwidth $2f_w$ (where $f_w \leq f_c$). The fraction of total energy contained in the frequency band can be represented as

$$\lambda = \frac{\int_{-(f_c+f_w)}^{(f_c+f_w)} |W(f)|^2\,df - \int_{-(f_c-f_w)}^{(f_c-f_w)} |W(f)|^2\,df}{\int_{-1/2\Delta t}^{1/2\Delta t} |W(f)|^2\,df} \quad \text{where} \quad W(f) = \Delta t \sum_{m=-P+1}^{R} w_m e^{i2\pi f \Delta t} \tag{2}$$

(P is the closest integer $\geq {}^{M}/_{2}$ and R is the closest integer $\leq {}^{M}/_{2}$.)

Lilly and Park (1995) calculate a set of wavelets by rewriting Equation 2 as an eigenvalue equation of the form

$$\mathbf{A}\,\mathbf{w} = \lambda\,\mathbf{w} \tag{3}$$

and solving for **w**. This equation has M orthogonal solutions of eigenvectors $\mathbf{w}^{\{k\}}$ and associated eigenvalues λ_k which we order so that $\lambda_1 > \lambda_2 > \lambda_3 > \ldots > \lambda_M$. The wavelets $\mathbf{w}^{\{k\}}$ are normalized such that $\sum_{m=1}^{M}\left(w_m^{\{k\}}\right)^2 = 1$. We only use the wavelets $\mathbf{w}^{\{k\}}$ which have λ_k close to one, since these functions have almost all their spectral energy within the frequency band of interest. The number of such wavelets is dependent on the width of the frequency band and how long the wavelets are in time (Lilly and Park, 1995).

The wavelets occur as even and odd pairs where the pairs emphasize different portions of the frequency band (Figure 1). Since the pairs of wavelets are functions that are 90 degrees out of phase, we can combine them into complex functions of the form $\boldsymbol{w}_f^{\{j\}} = \{\mathbf{w}_{f,e}^{\{j\}} + i\mathbf{w}_{f,o}^{\{j\}}\}$ where f is the center frequency, $\mathbf{w}_{f,e}^{\{j\}}$ is the j^{th} even wavelet, and $\mathbf{w}_{f,o}^{\{j\}}$ is the j^{th} odd wavelet.

The multiwavelet transform with kernel $\boldsymbol{w}_f^{\{j\}}$ and time length T = MΔt is

$$\mathcal{W}^{\{j\}}[s](f,t) = \int_{t-T/2}^{t+T/2} s(\xi)\mathbf{w}_{f,e}^{\{j\}}(\xi - t)\,d\xi \; + \; i\int_{t-T/2}^{t+T/2} s(\xi)\mathbf{w}_{f,o}^{\{j\}}(\xi - t)\,d\xi \tag{4}$$

Note that Equations 1 and 4 have the same form.

Beamforming

Classical beamforming (e.g. Mykkeltveit and Bungum, 1984) uses windowed Fourier transforms to slant-stack array data in the frequency domain. For a given slowness vector **u** = (u_{ew} , u_{ns}) and array station *n* there is a plane-wave time delay $\tau(\mathbf{u},n) = -\mathbf{u}\cdot\mathbf{x}_n$, where $\mathbf{x}_n$ is the vector position of the station with respect to a local Cartesian system. For N stations, the NxN spectra covariance matrix **C**(f,t,**u**) has components

$$C_{nm}(f,t,\mathbf{u}) = \mathcal{F}[s_n](f,t+\tau(\mathbf{u},n))\cdot\mathcal{F}[s_m]^{*}(f,t+\tau(\mathbf{u},m)) \tag{5}$$

where $\mathcal{F}[s_n]$ is the windowed Fourier transform for station *n* and * denotes the complex conjugate transpose.

A common measure of the overall coherence between the station signals is semblance (Husebye & Ruud, 1989)

$$S(f,t,\mathbf{u}) = \frac{P_{beam}(f,t,\mathbf{u})}{P_{avg}(f,t,\mathbf{u})} = \frac{\mathbf{d}^T\mathbf{C}(\mathbf{u})\mathbf{d}}{|\mathbf{d}|^2\cdot tr(\mathbf{C}(f,t,\mathbf{u}))} \tag{6}$$

where **d** is an Nx1 vector of station weights such that $\sum_{n=1}^{N} d_n = 1$. We uniformly weight the station data such that $d_n = {}^1/_N$. We can calculate the semblance values over a range of slowness vectors which covers all possible velocities and bearings for a given phase. An estimate of a seismic phase's slowness components is obtained by choosing the slowness vector which corresponds to the point of maximum semblance. To compensate for the discrete nature of this slowness grid, we use a center of mass calculation to determine the slowness component estimates (Bear and Pavlis, 1996).

What we will call multiwavelet beamforming can be couched in the same mathematical constructs as classical beamforming by substituting

$$C_{nm}^{\{j\}}(f,t,\mathbf{u}) = \mathcal{W}^{\{j\}}[s_n](f,t+\tau(\mathbf{u},n)) \cdot \mathcal{W}^{\{j\}}[s_m](f,t+\tau(\mathbf{u},m)) \tag{7}$$

for the spectra covariance matrix. In practice, though, the formation of the covariance matrix is inefficient when taking time delays into account.

It is straightforward to incorporate the time delays when forming the slowness grids in the time domain. Standard time-domain beamforming of array data (e.g. Pavlis and Mahdi, 1996) can be localized in the frequency domain by applying a band-pass filter, with center frequency f, to the data. If $\phi_f(t)$ is the time-reversed filter of length T, then the filtered signal can be written

$$\mathcal{C}[s](f,t) = \int_{t-T/2}^{t+T/2} s(\xi)\phi_f(\xi - t)d\xi . \tag{8}$$

The average station power is

$$P_{avg}(f,t,\mathbf{u}) = \frac{1}{N}\sum_{n=1}^{N} P_n(f,t,\mathbf{u}) \quad \text{where} \quad P_n(f,t,\mathbf{u}) = \int_{t-L/2}^{t+L/2} \left|\mathcal{C}[s_n](f,\xi+\tau(\mathbf{u},n))\right|^2 d\xi . \tag{9}$$

and the beam power is

$$P_{beam}(f,t,u) = \int_{t-L/2}^{t+L/2} \left|b(f,\xi,u)\right|^2 d\xi \quad \text{where} \quad b(f,t,\mathbf{u}) = \frac{1}{N}\sum_{n=1}^{N} \mathcal{C}[s_n](f,t+\tau(\mathbf{u},n)). \tag{10}$$

The semblance is then defined as in Equation 6.

The summing over time L is done to smooth the power estimates as the signal cycles back and forth from local maxima to local minima. This averaging is necessary to produce a stable solution, but introduces an arbitrary free parameter in the form of the length L. Consider the station power used in multiwavelet beamforming

$$P_n^{\{j\}}(f,t,\mathbf{u}) = \left|\mathcal{W}^{\{j\}}[s_n](f,t+\tau(\mathbf{u},n))\right|^2 . \tag{11}$$

Since the wavelets are even and odd functions, the wavelet transform can be considered a convolution, or filtering, operation where $\mathbf{w}_{f,e}$ and $\mathbf{w}_{f,o}$ are two filters with 90 degree phase differences. Thus $P_n^{\{j\}}(f,t,\mathbf{u})$ is an envelope of the real part of the wavelet transform (Kanasewich, 1981) and varies relatively slowly. This implies that the power estimate will be relatively stable. We use this method to stabilize the power estimates $P_n^{\{j\}}$ and $P_{beam}^{\{j\}}$ instead of time-averaging and then calculate the semblance.

Jackknife Method

The distinct advantage of multiwavelet beamforming over existing methods is that we are able to produce J slowness component estimates for a given signal- one for each complex wavelet. These estimates can be thought of as samples drawn from some unknown distribution. We can assume that these samples are approximately independent if we make standard assumptions about the noise field (Bear and Pavlis, 1996). We are particularly interested in estimating a parameter θ which defines a "center" of the distribution and the variance in that estimate. We use the jackknife statistical method (Thomson and Chave, 1991) to calculate a sample variance s^2 of the estimate of our parameter, $\hat{\theta}$.

Work by Hinkley (1977) has suggested that if the distribution of the data is close to normal, then we can use the usual method of producing a 95% confidence interval

$$\theta = \hat{\theta} \pm s \cdot t_{0.975} \tag{12}$$

where $t_{0.975}$ is the 0.975 quantile of the Student t distribution with *J-1* degrees of freedom.

It is important to note that in any real application there is some limit as to how well the slowness vector can be estimated. Some possible limiting factors are the data sampling rate as it compares to the aperture of the array and the sampling interval between slowness values used to calculate semblance. This limit effectively places a floor on the width of the confidence interval. How this floor should be determined, though, is beyond the scope of this report.

Application

To demonstrate our approach, we will analyze data from the Geyokcha array (Al-Shukri et al., 1995). This array operated in Turkmenistan on the northern border of Iran from August 1993 to November 1995. We used a subset of the array which consists of 12 stations with three-component Streckeisen STS-2 sensors arranged as shown in Figure 2. All the data used in this paper comes from the triggered data stream which was recorded at 250 sps. We used only the vertical components and removed the DC bias from each trace.

We produced a set of Lilly and Park wavelets for the band of 0.5 - 3.5 Hz with 125 samples and $\Delta t = 0.016$ sec. We use the 10 real wavelets with energy fraction greater than 0.9 and thus produce 5 estimates for the slowness vector. These five estimates take advantage of the fact that the quantile values of the Student t distribution change relatively slowly for 4 or more degrees of freedom. The wavelets are shown in Figure 1.

We apply our processing method to a controlled simulation with 100 similar synthetic events. We started by using a trace with a very high signal-to-noise ratio recorded at station ORGH of the array. This trace had a maximum first arrival amplitude of a = 1820 nm/s. We then produced a simulated plane-wave signal as if this waveform traveled across the array with a given azimuth and slowness (Figure 3a). We arbitrarily used an azimuth of 166 degrees and slowness magnitude of 0.158 s/km.

We produced 100 sets of noise recorded at the array where each trace had the same number of samples as the plane-wave traces. The synthetic traces for each station *n* were then defined as

$$s_{n,t} = \frac{3\sigma}{a} p_{n,t} + \eta_{n,t} \tag{13}$$

where $p_{n,t}$ was the plane-wave trace for station *n*, $\eta_{n,t}$ was a noise segment recorded at station *n*, and σ is a measure of the noise amplitude defined as

$$\sigma = \left(\sum_{t=1}^{T} \left(\eta_{n,t} - \bar{\eta}_n \right)^2 \Big/ T-1 \right)^{1/2} \quad \text{where T is the number of samples.} \qquad (14)$$

This is, on average, comparable to a 3-to-1 signal-to-noise ratio for the broadband signal (Figure 3b).

We performed our signal analysis in the frequency band 0.5 - 3.5 Hz. (Figure 3c). Note that the signal-to-noise ratio is lower than 3-to-1 in this frequency band. We calculated semblance values over a 50 by 50 grid of slowness values between -0.3 and 0.3 s/km. We used these semblance values to determine our five slowness vector estimates for each synthetic event.

Our goal in creating 100 samples of the 'same' event was to test whether jackknife intervals created for our slowness vector components would approximate 95% confidence intervals. For each of the 100 sets of estimates we produced jackknife confidence intervals for the mean and the median. To evaluate the results, we created the plots shown in Figure 4. In part (a) we see that for the east-west slowness component 96 out of 100 of the jackknife intervals for the mean contained the known value while 90 of the intervals for the median contained the known value. In part (b) we see 98 of the 100 north-south slowness intervals for the mean contained the known value, while 87 of the 100 intervals for the median did.

An interesting observation we can make is that there is a noticeable bias in the mean estimates- particularly for the north-south slowness component. Vernon et al. (1994) noted that the noise field at Geyokcha has a high-velocity directional component with a northeastern bearing. Thus, it is not surprising that at these low signal-to-noise ratios the noise field would bias the slowness estimates. Perhaps a more interesting observation is that the bias is hardly detectable in the median estimates. We feel that this illustrates how the complex Lilly and Park wavelets each interact with the data differently. Some of the wavelets interfere constructively with the noise field while others interfere destructively with the noise field. The median, unlike the mean, naturally minimizes the effects of the outlying estimates by only using the inner samples when the data is sorted. This implies, however, that the median is less efficient in its use of data and probably explains the poorer performance of the median confidence intervals.

Work by Hinkley (1977) suggested that for small data sets from significantly non-normal distributions, the validity of the jackknife intervals as confidence intervals was compromised. We can use a quantile-quantile plot to compare our set of estimates to the normal distribution (Figure 5). Where the plot is linear, the standardized distributions are the same (Kleiner and Graedel, 1980). It is interesting to compare the normal portion of the slowness values with the multiwavelet beam pattern centered on our known slowness vector $\mathbf{u}^{known}$ (Figure 5). The beam pattern components are plotted as $S(f,t,u_{ew}^{known},u_{ns})$ vs. u_{ns} and $S(f,t,u_{ew},u_{ns}^{known})$ vs. u_{ew}. Note how the portion of the distribution of slowness values that matches the normal model corresponds to the peak of the beam pattern in a systematic way. We suspect this results from interference effects at these low signal-to-noise ratios. That is, when the wavelet interaction with a noise field leads to an effective signal-to-noise ratio much less than unity, the estimated slowness value can fall anywhere on the slowness grid.

CONCLUSIONS AND RECOMMENDATIONS

The jackknife intervals obtained from the mean estimator are an objective measure of the uncertainty in slowness vector estimates. The mean jackknife intervals are conservative since they weight all data equally, even gross outliers, and our simulation suggests that they closely approximate true 95% confidence intervals. On the other hand, we recommend that the actual estimates be taken from the median or some other estimator which minimizes the effects of outliers, particularly when the jackknife intervals are large. In our simulation, the median effectively reduced the bias introduced from the noise field in low signal-to-noise conditions.

It should be relatively simple to implement multiwavelet beamforming as an automated tool. The machinery built up for time-domain beamforming can easily be changed to accommodate our method and the number of computations per time window should decrease since we do not need to time average the power estimates. This technique should become a standard tool for routine array analysis to produce objective error estimates with no human intervention.

REFERENCES

Al-Shukri, H.J., G.L. Pavlis, and F.L. Vernon, III, Site effect observations from broadband arrays, *Bulletin of the Seismological Society of America, 85* (6), 1758-1769., 1995.

Bear, L. K., and G. L. Pavlis, Jackknife estimation of slowness vector confidence intervals using multiwavelet seismic array processing, *Bulletin of the Seismological Society of America*, in review.

Hinkley, D.V., Jackknife confidence limits using Student t approximations, *Biometrika, 64* (1), 21-28, 1977.

Husebye, E.S., and B.O. Ruud, Array seismology- past, present, and future developments, in *Observatory Seismology*, edited by J. J. Litehiser, pp. 123-153, University of California Press, Berkeley, 1989.

Kanasewich, E.R., *Time Sequence Analysis in Geophysics*, 480 pp., University of Alberta Press, Edmonton, Alberta, Canada, 1981.

Kleiner, B., and T.E. Graedel, Exploratory data analysis in the geophysical sciences, *Reviews of Geophysics and Space Physics, 18* (3), 699-717., 1980.

Kumar, P., and E. Foufoula-Georgiou, Wavelet analysis in geophysics: An introduction, in *Wavelets in Geophysics*, edited by E. Foufoula-Georgiou, and P. Kumar, pp. 1-43, Academic Press, San Diego, California, 1994.

Lilly, J.M., and J. Park, Multiwavelet spectral and polarization analyses of seismic records, *Geophysical Journal International, 122* (3), 1001-1021., 1995.

Mykkeltveit, S., and H. Bungum, Processing of regional seismic events using data from small-aperture arrays, *Bulletin of the Seismological Society of America, 74* (6), 2313-2333, 1984.

Pavlis, G.L., and H. Mahdi, Surface wave propagation in central Asia: Observations of scattering and multipathing with the Kyrgyzstan broadband array, *Journal of Geophysical Research, 101* (B4), 8437-8455, 1996.

Thomson, D.J., and A.D. Chave, Jackknifed error estimates for spectra, coherences, and transfer functions, in *Advances in Spectrum Analysis and Array Processing*, edited by S. Hayken, pp. 58-113, Prentice-Hall, Englewood Cliffs, New Jersey, 1991.

Vernon, F.L., D.J. Harvey, G.L. Pavlis, W.-Y. Kim, G.A. Abers, and G.S. Wagner, Array studies in the Joint Seismic Program (abstract), *EOS, Transactions, American Geophysical Union, 75* (44), 1994.

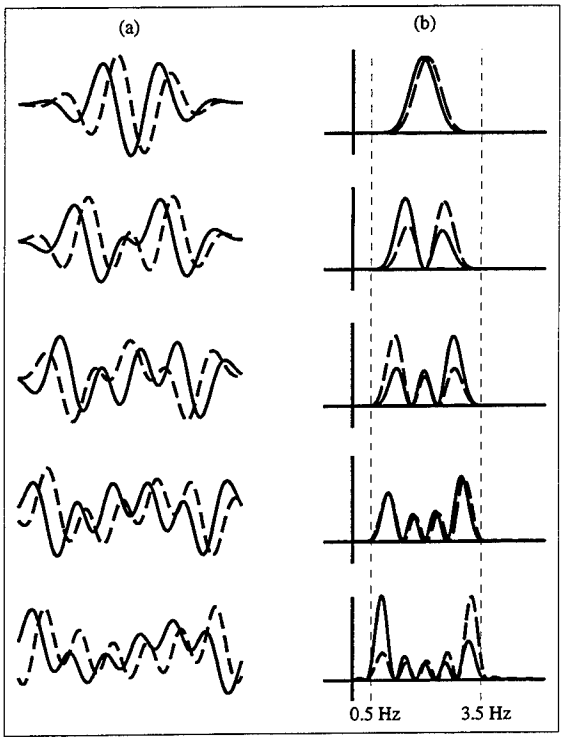

Figure 1 : Ten real Lilly and Park wavelets (a) in the time domain and (b) their frequency power spectra. Wavelets from top to bottom go from higher to lower lambda values.

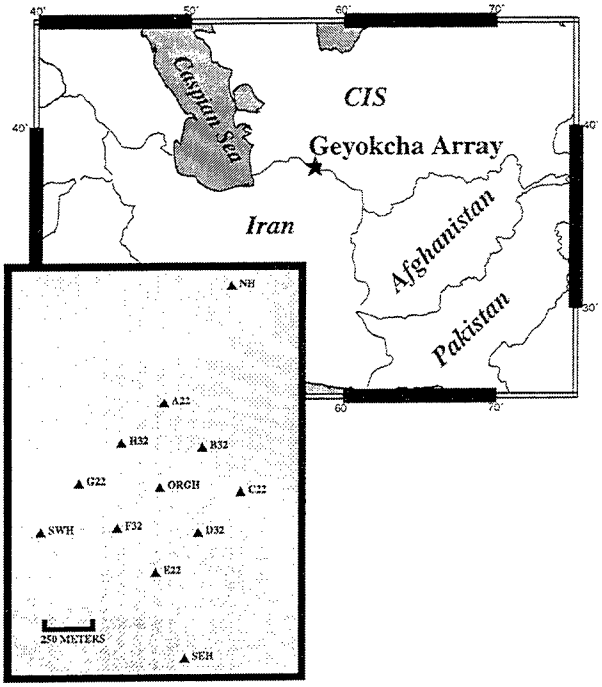

Figure 2 : The Broadband stations of the Geyokcha Array

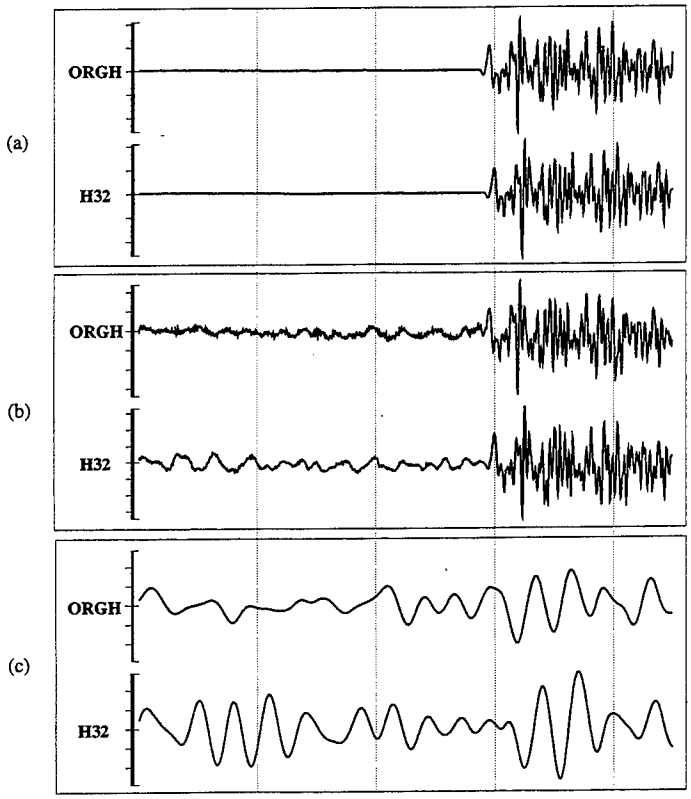

Figure 3 : Vertical records from two stations for one of the simulated events- (a) the plane-wave signal, (b) the plane-wave signal with noise added, and (c) traces in (b) filtered to 0.5 - 3.5 Hz. Time marks denote seconds.

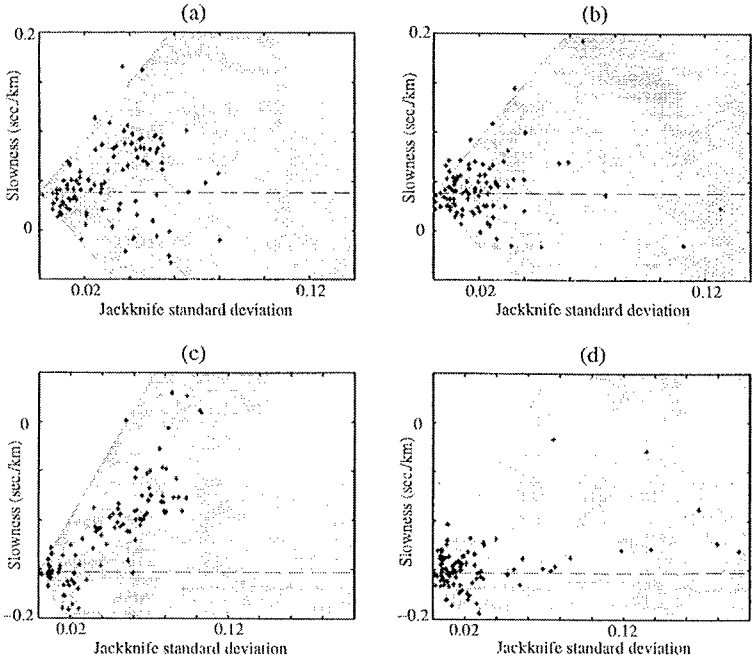

Figure 4 : Plots of estimates for parameter θ vs. the jackknife standard deviation for (a) east-west slowness, θ = mean, (b) east-west slowness, θ = median, (c) north-south slowness, θ = mean, and (d) north-south slowness, θ = median. The shaded area signifies where the jackknife intervals contain the known value (which is plotted as a dashed line).

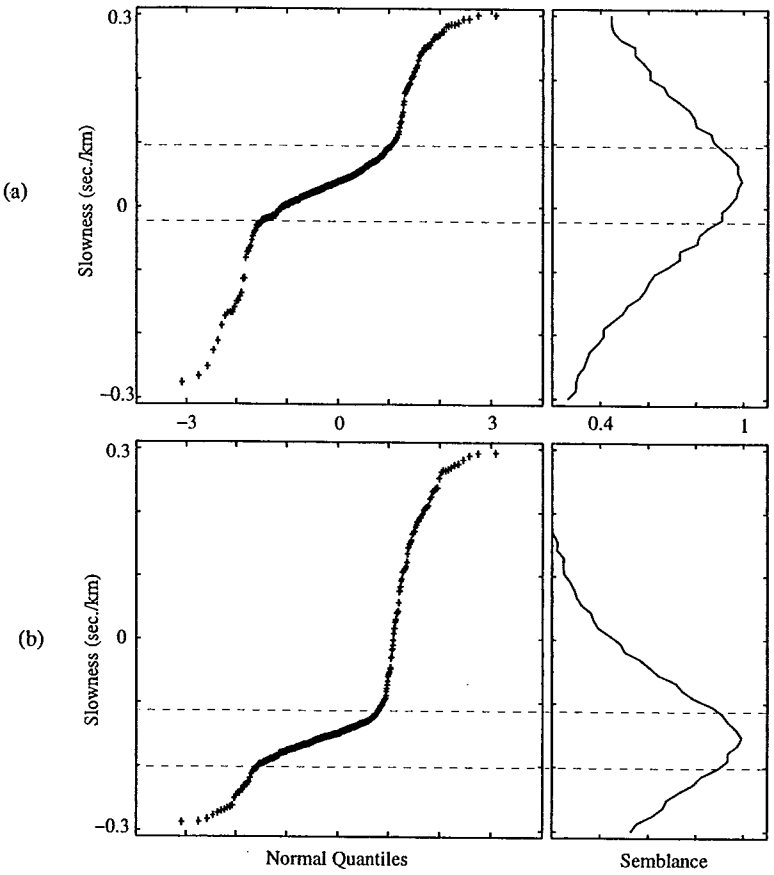

Figure 5 : Quantile-Quantile plots compared to one-component beam patterns for (a) the East-West and (b) the North-South slowness components.

Event Location by Long-Period Surface Waveform Matching - Application to Earthquakes in Northeastern China and Korea

John J. Cipar

Earth Sciences Division
Phillips Laboratory (PL/GPE)
29 Randolph Road
Hanscom AFB, Massachusetts 01731

AFOSR Seismology Task 2309G2

8 July 1996

ABSTRACT

This paper reports on an experiment to test the utility of long-period surface waveform matching for event location. The goal is to develop a location technique for small-magnitude events for which only the surface waves emerge from the ambient noise. The method compares the observed data to realistic synthetics in the time domain over a grid of trial locations. A prerequisite is that the event depth and focal mechanism are known independently. Five magnitude 4-5 earthquakes occurring in northeastern China and Korea that were recorded well at regional distances by the CDSN were selected for study. A single earth model was assumed for the entire region, an assumption justified by previous work. A single model also mimics a realistic CTBT monitoring situation in which the earth structure is imperfectly known. The surface wave locations for the five earthquakes were shifted from 2-60 km southeast from the PDE locations. These mislocations can be attributed to a combination of an earth model that is 2-5% too fast relative to the observations and to a large station gap east of the events. Alternatively, the PDE locations could be in error for similar reasons. This study points up the need for well-characterized "ground-truth" events for regional calibration.

Key words: Seismic Locations, Earth Structure, China, Korea, CTBT

OBJECTIVE

A key part of seismic discrimination is the determination of the location of an event. An answer to the question of whether an event occurred, for example, at sea or in an active mining complex, has a critical bearing on use of other assets such as on-site inspections or satellite imagery. For events large enough to have clear P and S arrivals, normal location methods used with appropriate travel time curves provide the most accurate locations. Events of interest for CTBT monitoring, on the other hand, are often small, with the first arrivals, in particular low-amplitude Pn, buried in ambient earth noise. Often, the only recognizable signal consists of the Lg phase on short-period seismographs and the Rayleigh and Love surface waves on the long-period.

In this paper, I explore the use of regional-distance Rayleigh and Love surface waves recorded on long-period seismographs for event location. My approach is to compute realistic surface wave synthetic seismograms over a grid of trial locations and to compare those synthetics directly to the observed seismograms in the time domain. A prerequisite is that the focal mechanisms and depth have been determined independently. The magnitude 4-5 earthquakes studied in this paper occurred in northeastern China and Korea (Cipar, 1995; 1996). A key assumption in this paper is the use of a single earth model to represent the entire region, which reduces the number of free parameters in the inversion. More importantly, it mimics the condition in which the earth model is only generally known, which is the case for most regions of the globe.

RESEARCH ACCOMPLISHED

Data Preparation and Analysis. I have selected recent earthquakes that occurred in northeastern China and the Korean peninsula for analysis (Table 1). An important selection criterion was that the events were recorded by the Chinese Digital Seismographic Network (CDSN; Table 2). This network provides excellent on-scale recordings of moderate-size earthquakes at regional distances. Five events that had adequate signal-to-noise ratio on two or more stations were selected from the waveform database maintained by the Incorporated Research Institutions for Seismology (IRIS). The largest event was the 25 July 1994 Yellow Sea earthquake (Ms = 5.0) for which the USGS centroid moment tensor solution has been determined. The other four events were too small to allow a reliable long-period moment tensor solution. Of particular interest in the context of CTBT monitoring is the mb 4.0 event that occurred in North Korea. This event is too small to be clearly observed at teleseismic distances, thus regional observations are crucial when determining location and source parameters.

For each event, the long-period seismograms were first detrended and windowed to isolate the surface wave signal, and then high-pass filtered with a three-pole Butterworth filter with a corner frequency of 0.01 Hz. I prefer to work with data that have suffered as little processing as possible. In particular, I use observed data that still retain the instrument response, and compare the data directly to synthetics that have been convolved with the appropriate instrument response. The instrument response acts like a causal filter, producing seismograms that are similar to familiar analog records. To equalize the data to a common

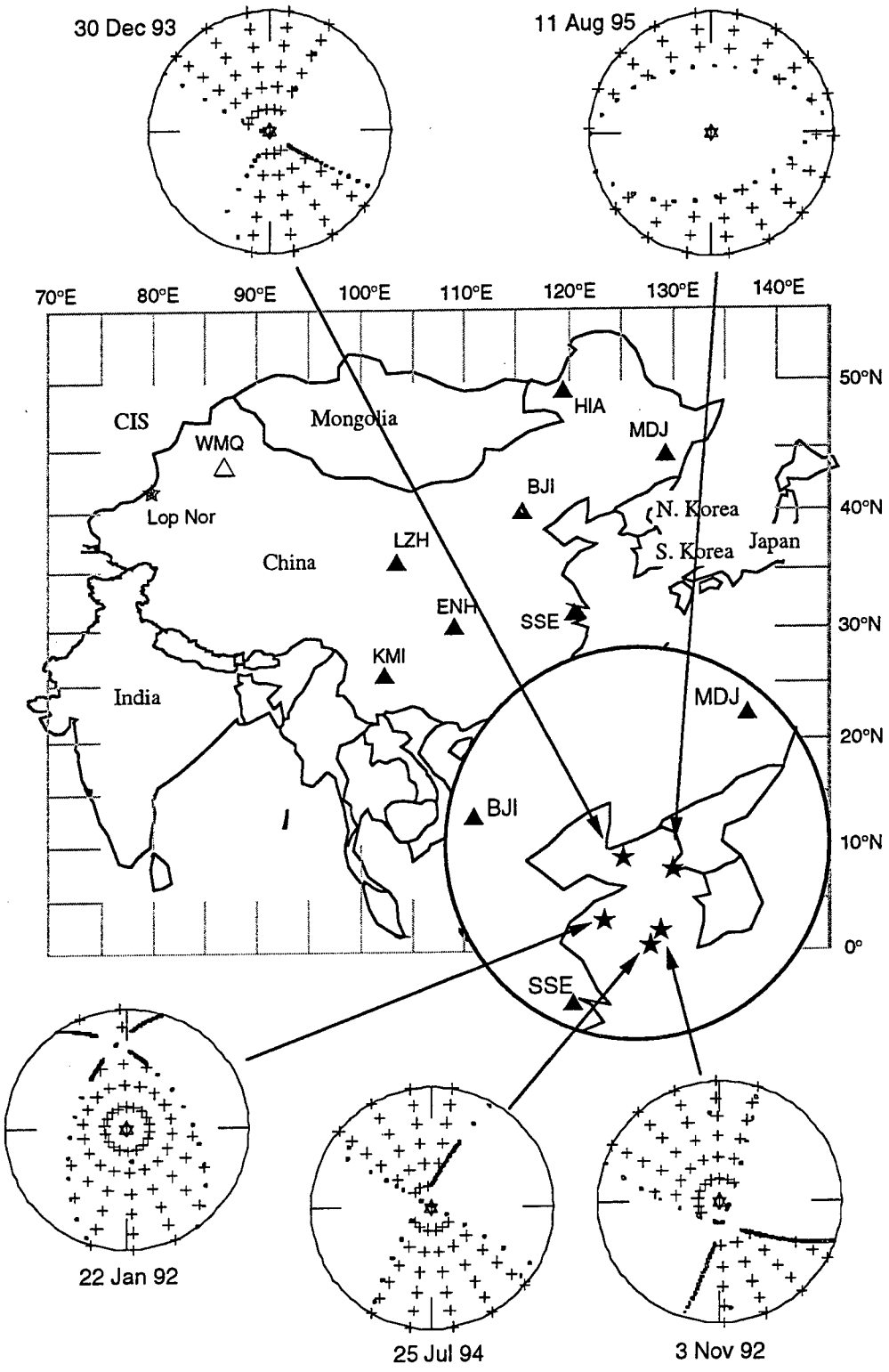

Figure 1. Map of eastern Asia showing the CDSN stations (triangles). The Chinese test site at Lop Nor is shown as an open star. The inset shows the events studied in this paper (stars) and nearby CDSN stations. Focal mechanisms for the earthquakes studied in this paper are shown with compressional quadrants indicated by plus (+) signs (Cipar, 1996).

response, I first remove the original response by deconvolution, then convolve the response of a specific station, in this case the LHZ component at the CDSN station MDJ. This procedure is done in one pass in the frequency domain, and works especially well for stations with similar instrument response functions such as most of the CDSN stations, in which the only effect is a scale change. CDSN stations are currently being upgraded to full compatibility with other IRIS stations with a major change in instrumentation. Station HIA was upgraded before the 11 August 1995 North Korean earthquake. In addition, the IRIS station INCN (Inchon, South Korea) was operating for that event. The IRIS response is given in units of velocity, unlike the CDSN that is in units of displacement. The IRIS velocity response has a much wider bandwidth than the original CDSN displacement response For these stations, I deconvolved the velocity response, integrated, and convolved the CDSN response. Instrument-corrected horizontal seismograms were rotated to radial and transverse components. The synthetics were computed using reflectivity (Fuchs and Muller, 1971) as displacement seismograms and convolved with the CDSN instrument response for the LHZ component at station MDJ. In this fashion, observed and synthetic seismograms are directly comparable to each other in the time domain.

Seismic Model. The Green's functions used in the inversions in this paper were computed with an improved version of the A8 model for northeastern China and the Yellow Sea (Cipar, 1995). The model used in this paper A8b2 (Figure 2), has a thinner crust (35-km versus 40-km for A8), higher Pn velocity (8.04 km/sec), and higher velocities in the sediments than A8. In addition, A8b2 uses the IASPEI91 upper mantle velocities (Kennett, 1991). Synthetics computed using model A8b2 show significantly better fits to observed data for the 3 November 1992 Yellow Sea earthquake, than synthetics computed with model A8.

A crucial point in this paper is that the same crustal model is used for all stations and earthquakes. The rationale for this is three-fold. First, the dominant frequency of the CDSN LH seismograms is approximately 40 sec, with a wavelength of 140-150 km. This wavelength effectively averages over small-scale variations in crustal structure. Second, inversions for the 3 November 1992 earthquake attained good agreement between synthetics and observed data with a single model, suggesting that in northeastern China the crust can indeed be approximated by a single layered model. Third, use of a single structural model reduces the number of free parameters in the inversion. The approach in this paper is to assume a single crustal model for the entire region, then invert for the earthquake location.

Locations. The surface wave location algorithm compares 3-component CDSN long-period (LH) seismograms in the time domain to synthetics computed with model A8b2 over a grid of trial locations. The synthetic Green's functions for the eight fundamental faults were computed at 50-km intervals over the distance range 300-1850 km, and stored on disk. For a given trial location, distances and azimuths were computed to each station and the nearest synthetic (in distance) was retrieved from the disk. Because the synthetics were computed at 50-km intervals, the distances could differ from the true distances by as much as 25 km. To correct for this discrepancy, the synthetics for each station were propagated to the correct trial distance by time shifting using the phase velocity for model A8b2, taking into account attenuation and geometrical spreading. The eight Green's functions were weighted according to the focal mechanism (Cipar, 1996 and Table 3) and combined to create realistic synthetics. Observed and synthetic seismograms were windowed using a group velocity window

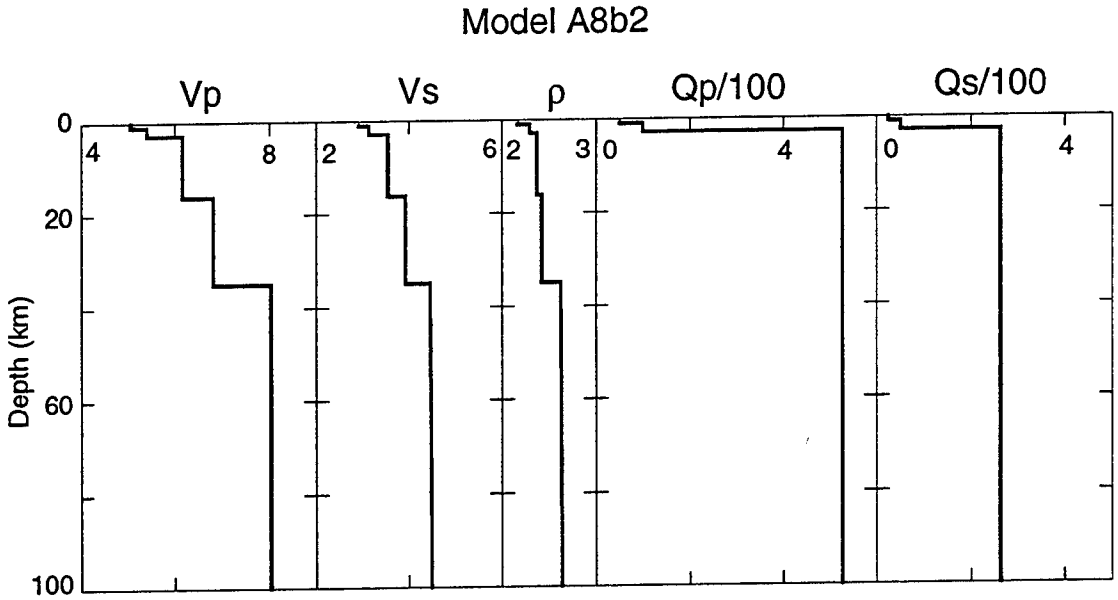

Figure 2. Model A8b2 displayed as a function of depth.

between 4.5 and 2.8 km/s, isolating the surface waves. The L2 norm was used to compared observed and synthetics in the time domain (Menke, 1984). Details of the algorithm are given in Cipar (1995). For each earthquake, a subset of 3-6 CDSN stations was available for analysis. The grid search for the optimal location was done over a 2x2 degree grid centered on the PDE epicenter, at a sampling interval of 0.05 deg, approximately 5.5 km. The time shift feature of the algorithm was not used for the location calculations, thus the synthetics could not "slide" in time to best match the observed seismograms. A zero time shift implies that model A8b2 is the best average model for the region encompassing the earthquakes and stations.

The results of this experiment for the five earthquakes are shown in Figure 3. The large X indicates the PDE location, while the large star shows the best waveform matching location. The star and boxes mark the grid locations with the ten best fits. The vector between the PDE and surface wave locations (in terms of distance and azimuth) are given in upper right-hand corner of each panel. With the exception of the 11 August 1995 North Korean earthquake, all the waveform matching locations show a consistent southeast offset of 20-60 km. It is reasonable to assume that the PDE locations are approximately correct, despite the relatively small size of these events and the lack of close-in stations. Note that the CDSN stations are located predominantly to the west of the earthquakes, leaving a large station gap (~180 deg) to the east. Assuming, for the moment, that the PDE locations are correct, the southeastward shift of the waveform locations indicates that the synthetics generally arrive too early relative to the observations. The consistent southeast offset provides a positive time shift to the synthetics, which allows them to better match the observed data. This, in turn, implies that model A8b2 is too fast compared to the earth.

I can estimate the average travel time bias by noting that the average offset between the PDE and waveform matching locations (excluding the North Korean event) ranges between 20 and 62 km. Dividing by the surface wave group velocity (3.6 km/s for a Love

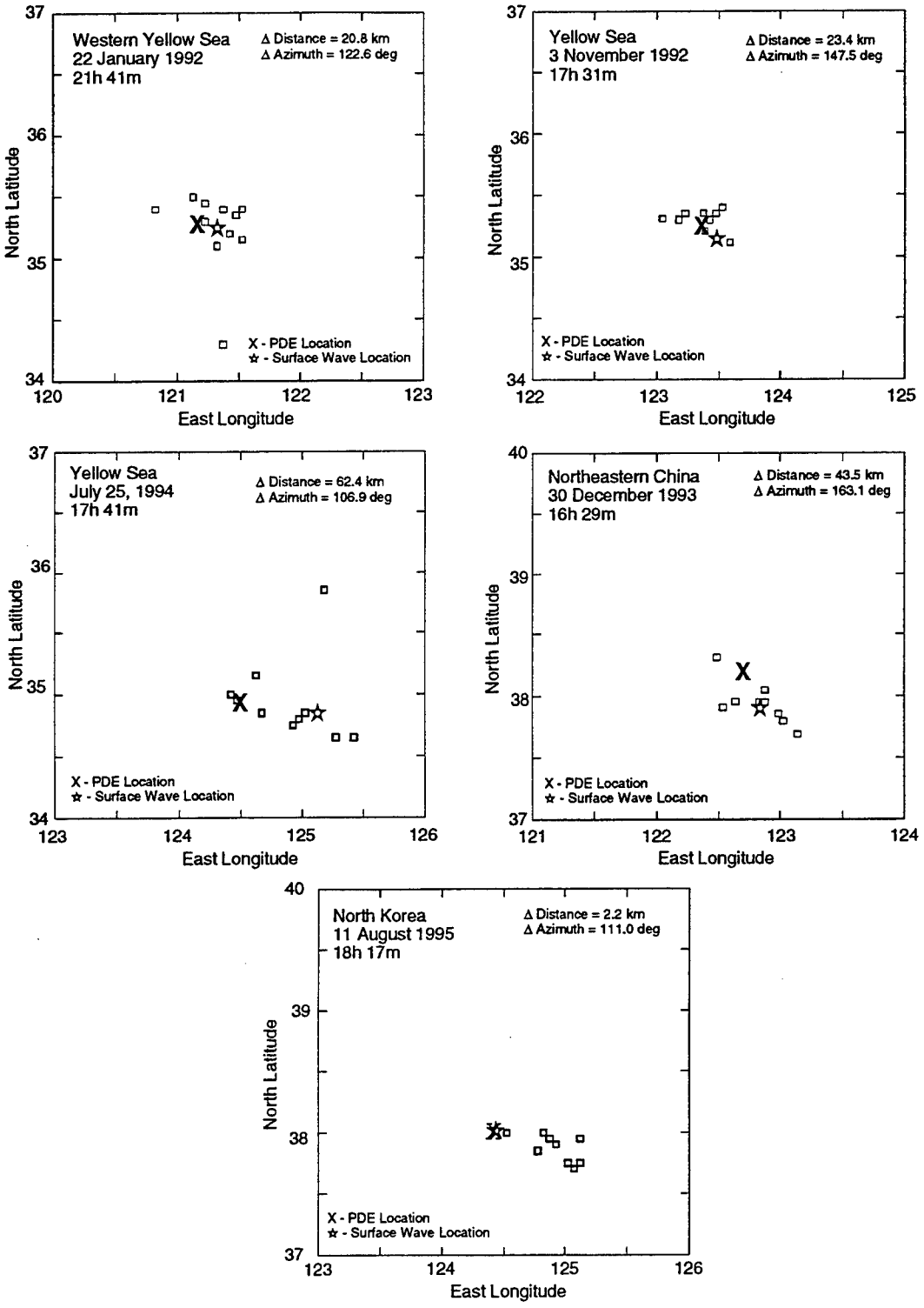

Figure 3. Comparison between PDE location (X) and surface wave locations (star) for the events studied in this paper. Boxes indicate the ten best fitting trial solutions. The change in distance and azimuth between the PDE and surface wave locations is indicated.

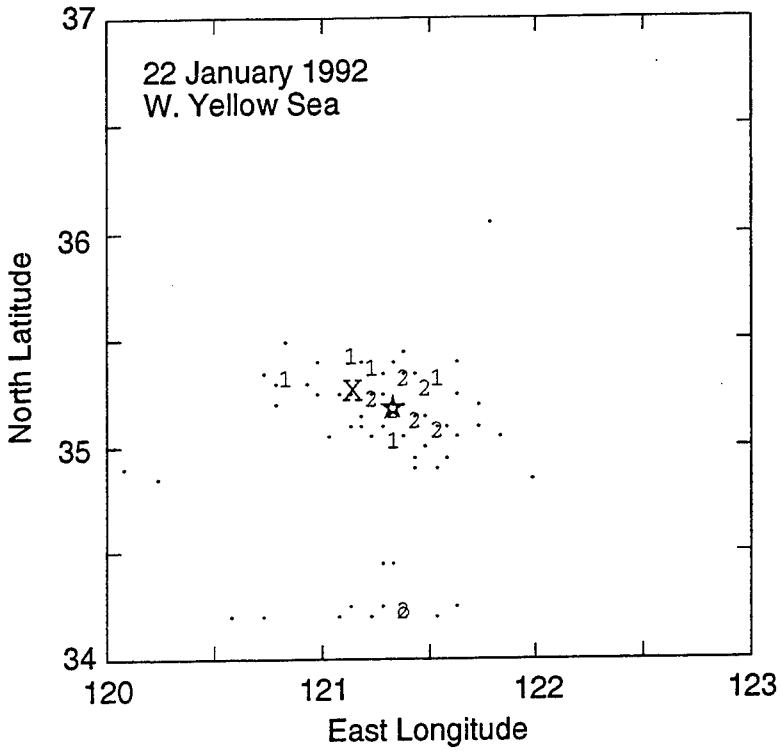

Figure 4. Plot of PDE (X) and surface wave (star) locations for the 22 January 1992 western Yellow Sea earthquake. Dots and numbers indicate the spatial stability of the solution.

wave at 40 s), the average time correction is 10 s. Travel paths to the western stations are on the order of 800 to 1800 km, with total surface wave travel times of 220 to 500 s. Thus, the location bias can be accounted for by a 2-5% decrease in the model A8b2 shear velocities, the model parameters that control the surface wave group velocity.

The North Korean earthquake of 11 August 1995 is exceptional in that its misfit is 2.2 km, which means that the grid point closest to the PDE location produced the best L2 norm fit. Both the PDE and surface wave locations put the epicenter in the northern Yellow Sea, off the west coast of North Korea. Note in Figure 3 that the boxes indicating the "ten-best" grid locations are distributed to the southeast of the PDE location, consistent with the results for the other earthquakes. It is hard to explain the reason for the good fit for this event in light of the 20-60 km offsets for the other, larger earthquakes. One explanation is that both the surface wave and PDE locations are incorrect for this event (I assume that the PDE location is correct for the other events), and that the true location is ~20-40 km to the northwest.

Another test of the surface wave location method is the stability of the solution. Ideally, the method will produce one well-defined minimum in the observed-synthetic misfit function. The solution stability is illustrated in Figure 4 for the 22 January 1992 western Yellow Sea earthquake. The PDE epicenter is marked by the large X, and the best-fitting solution by a star. The other symbols (dots and numbers) indicate different levels of the L2

norm misfit function with "2" being the best. Note that the best-fitting solution (star) is near the center of the main cluster of good solutions. Clearly the algorithm found a pronounced minimum in the misfit function.

CONCLUSIONS AND RECOMMENDATIONS

The mislocations between the PDE and surface wave epicenters shown in Figure 3 can be attributed to a combination of an incorrect earth model and a large gap in station coverage. In this sense, the surface wave location method behaves like other location algorithms where good station coverage with an incorrect earth structure can place the event in the proper location, although with high residuals (the difference between observed and calculated travel times) and/or incorrect origin time or depth. Conversely, a large gap in station coverage, with an incorrect model, will lead to incorrect location, origin time, and depth, albeit with low residuals For the earthquakes in this paper, the large eastern gap coupled with a fast earth model pushed the surface wave locations to the east relative to the PDE locations. Conversely, the PDE locations may be wrong since these events are relatively small with few, if any, close-in observations.

This experiment in event location using surface waves underscores the need for ground truth events in which the source parameters (location, depth, origin time, focal mechanism, etc.) are known independently. Several spatially distributed, well-characterized events would allow improved determination of the underlying average earth structure as well as measurement of specific station residuals that account for departures from the average model. Note that having ground-truth events is crucial to improving conventional body-wave travel time locations.

The work reported here used long-period surface waves (T ~ 40 s) to avoid, as much as possible, velocity perturbations due to crustal heterogeneity and multipathing caused by scattering. The trade-off when using long-period waves is poor resolution in time and thus location. Higher frequency surface waves (T ~ 10-20 s) are well observed on broad-band seismographs at regional distances, but are subject to variations in crustal structure on the order of 10s of kilometers. One approach to using these signals would be to compare observed and synthetic envelopes rather than the actual waveforms. It is important to test this method in a region in which the structure and event location are known. An ideal place would be southern California, which has abundant, well-characterized earthquakes and numerous seismograph stations.

Acknowledgments. I wish to thank Keith Priestley and Katharine Kadinsky-Cade for critically reading the manuscript. Mary Martyak edited the final draft. The assistance of Stephan Koester and the Data Management Center of the Incorporated Institutions of Seismology in providing the data used in this report is gratefully acknowledged. This work was supported under the AFOSR Seismology Task 2309G2 at the Earth Sciences Division, Phillips Laboratory.

Table 1. Earthquake Information

Earthquake	Origin Time h:m:s	Latitude (deg N)	Longitude (deg W)	Depth (km)	mb	Ms	Ml (BJI)	Location
22 January 1992	21h 41m 25.9s	35.351	121.109	33 N	5.1	4.8	5.5	W. Yellow Sea
3 November 1992	17h 31m 23.7s	35.328	123.312	10	4.8	-	5.0	Yellow Sea
30 December 1993	16h 29m 49.8s	38.257	122.656	33 N	4.6	-	4.8	NE China
25 July 1994	17h 41m 50.6s	35.015	124.447	10 G	5.0	5.0	-	Yellow Sea
11 August 1995	18h 17m 44.4s	38.029	124.441	10 G	4.0	-	3.8	N Korea

Table 2. CDSN Station Information

Station	Latitude (°N)	Longitude (°E)	Elevation (m)	Location
BJI	40.0403	116.1750	43.0	Beijing
ENH	30.2800	109.4975	487.0	Enshi
HIA	49.2667	119.7417	610.0	Hailar
HKC	22.3036	114.1719	0.0	Hong Kong
INCN	37.4833	126.6333	410.0	Inchon, South Korea
KMI	25.1500	102.7500	1952.0	Kunming
LZH	36.0867	103.8444	1560.0	Lanzhou
MDJ	44.6164	129.5919	250.0	Mudanjiang
SSE	31.0956	121.1867	10.0	Sheshan

Table 3. Focal Mechanisms

Earthquake	Stations Used	L2 Norm	Depth (km)	Strike (deg)	Dip (deg)	Rake (deg)
22 January 1992	BJI, HIA, LZH, MDJ	0.64982	12	197	54	127
3 November 1992	BJI, ENH, MDJ, HIA,SSE, LZH	0.82777	15	18	84	166
30 December 1993	ENH, HIA, LZH, MDJ	0.94557	15	29	90	177
25 July 1994	HIA, LZH, MDJ, SSE, KMI	0.95097	12	210	82	179
11 August 1995	HIA, MDJ, SSE	0.37372	9	72	47	258

References

Cipar, John J. (1995). A Grid Search Algorithm to Determine Earthquake Source Parameters - Application to the 1992 Yellow Sea, China, Earthquake, PL-TR-95-2082, Env. Res. Paper 1171, 8 June 1995, ADA 302221

Cipar, John J. (1996). Earthquake Focal Mechanisms in Northeastern China and Korea Determined by the Grid Search Algorithm, PL Technical Report, PL-TR-96-2152, July, 1996.

Fuchs, K. and G. Muller (1971). Computation of Synthetic Seismograms with the Reflectivity Method and Comparison with Observations, *Geophys. J. Roy. Astron. Soc., 23,* 417-433

Kennett, B. L. N. (Editor) (1991). *IASPEI 1991 Seismological Tables,* Australian National University, 167p.

Menke, William (1984). *Geophysical Data Analysis: Discrete Inverse Theory,* Academic Press, 260p.

Performance Estimates of the CD Proposed International Seismic Monitoring System

John P. Claassen

The Cooperative Monitoring Technologies Department, Sandia National Laboratories

Sponsored by the U.S. Department of Energy, CTBT Research and Development Program, ST485D

Abstract

An enhanced version of NetSim and an expanded supporting database were used to predict the detection and location performances of the International Seismic Monitoring System (ISMS) proposed in Working Paper 330 by the Ad Hoc Committee on a Nuclear Test Ban Treaty. The primary goals of this effort were to estimate the levels of performance of the proposed ISMS and to predict the enhancements in location accuracy as would be provided by station and regional calibrations.

An estimate of the detection threshold indicates that the primary network alone with all of its upgrades is capable of detecting a fully coupled 1 kiloton nuclear shot contained in consolidated rock anywhere on the earth. Further, the best detection thresholds appear in central Eurasia and range from 3.25 to 3.5 magnitude units. The threshold estimates were based on a 3P at 99% network detection criterion. Location performance estimates indicated that conventional location methods using regional and station calibrations are capable of achieving location accuracies better than 1000 square kilometers with 90% confidence largely everywhere for events with magnitudes at or above the detection threshold of the primary network. The poorest accuracies primarily appear on some of the islands in the southern oceans and in portions of Antarctica. For events having a magnitude of 4.25 the predicted location accuracy exceeds 100 square kilometers in almost the entire northern hemisphere, over a large portion of Africa, and a small portion of South America. Better accuracies than these are possible at larger event magnitudes. Regional and station calibrations yield net reductions in the elliptical areas of uncertainty by factors better than 6.0 using conventional location methods. Further location improvements can be achieved through the use of the secondary arrivals, by the use of additional stations, and through the use of other location methods.

Key words: seismic network modeling, detection thresholds, location accuracy, calibrations, propagation models

Introduction

Network modeling is a methodology to predict and assess the performance of a collection of monitoring stations. As a scientific-engineering-statistical discipline, network modeling brings insight, understanding, and integrity into activities which plan and assess proposed and existing monitoring networks. For modeling to have meaning and significance it is important that the physical and statistical aspects of the source, propagation, detection, location, and discrimination processes be appropriately integrated to realize useful predictions and assessments. To confirm or deny the adequacy of either network models or network processing methods, the predictions must eventually be subjected to the test of actual network observations and the actual network observations to the test of the predictions. Calibrating stations and regions and measuring network performance are the primary methods by which to realize this objective. Validated simulation models in a given geology permit the extension of performance estimates into new or aseismic areas of the globe which have a similar geology. On the basis of these comparative and calibrative experiences the predictive models or the real-time processing models and their supporting parameters may undergo modification to yield improved predictions and network performance, ultimately bringing improvements to the operation of networks.

The primary goals of this modeling effort were 1) to estimate the detection and location capabilities of the primary and auxiliary networks as defined in the May 28, 1996 Draft of a Nuclear Comprehensive Test Ban Treaty [1] and 2) to assess the importance of station and regional calibrations in improving the location capability of the combined primary and auxiliary networks.

The Approach

To address these goals, the original version of NetSim [2] and its supporting environments were enhanced. These enhancements produced a new location methodology for NetSim based on more realistic physical and statistical premises. A modification was introduced to permit location performance estimates of one network conditioned on the detection levels of a another network. Improvements in the detection model assigned frequency dependent variances to the station noise spectra and the station (array) gain. To more appropriately account for the differences in regional propagation on a global basis and the contributions of the various regional phases, existing regional propagation models were altered to reflect different qualities in the propagation attributable to tectonic, stable, and very stable geological conditions (See the next paragraph). A station noise database [3], which supports the modeling computations, was extended and as duplicate noise estimates became available noise spectra were more carefully selected on the basis of consistency of estimates by different investigators and with noise levels across adjacent sensor bands at the same station. A friendly versatile graphical interface (NetCon) was also developed to plot the performance estimates in numerous ways. An option to filter the graphical data was provided to smooth the irregular boundaries often associated with performance levels (Irregularities in the contour direction can adversely impact contour seeking routines). A zoom capability was also introduced for closer looks at the predicted performance levels.

Several options to color fill the contours were provided to ease the interpretation of the graphical results.

To appropriately account for the differences in propagation on a global basis it was necessary to use propagation models which are region dependent. Region dependent propagation models were extrapolated from the Scandinavian models developed by Sereno [4] to all parts of the globe by using the Q variations of Lg propagation as an indicator of the quality of propagation of the other regional phases. This assumption may be overly simplistic but does permit implementing region dependent models because Lg Q is reasonably well known worldwide, primarily as a result of efforts by researchers at St. Louis University (See, for example, [5]). The Scandinavian models were scaled to low (Lg Q = 900) and high (Lg Q = 300) attenuation regions assuming that the Scandinavian craton represented a medium (Lg Q=600) attenuation region. This scaling approach was used in the interim because frequency dependent regional models for propagation in distinct geologies of the world, other than Lg, have not been addressed or when addressed have not been developed in a manner compatible with NetSim.

These enhanced modeling tools were applied to predict and plot the detection and location performances of the networks defined in Working Paper 330 and to assess the improvements in event location induced by regional and station calibrations. When interpreting the resulting performance contour plots, use the color filled and labelled contours and the minimum contour level and contour interval appearing in the upper right hand corner of the graphs. The network detection threshold estimate was based on the 50 primary stations in their final state (See Figure 1 for the locations of the primary stations). The location performance estimates were based on observations by both the primary and auxiliary networks (The locations of the auxiliary stations are shown in Figure 2). The network detection criterion required that 3 or more stations detect P arrivals with a 99% probability. This detection criterion was specifically used because it admits only a 1% probability in missed detections as opposed to the historical 10% value. To account for the different station noise levels, the detection and location performance estimates were based on the actual station spectral noise statistics when available. For those primary stations for which noise data were not available, noise statistics similar to those of the GTSN (Global Telemetered Seismic Network) stations, which are recognized as very low noise stations, were assigned. For those auxiliary stations whose noise data were not available, the noise statistics were assumed to be similar to those of the GTSN stations after raising them by 10 dB to reflect the noisier characteristics usually associated with the auxiliary stations. The actual gain characteristic of an array station was used when available. The gain characteristics of the NORESS array were interpolated to estimate the gain of the new regional arrays to be installed in the primary network. The gain of large teleseismic arrays whose characteristics were not available was assumed to be somewhat larger than the square root of N (no. of elements) at SP (short period) frequencies less than 2 Hz, the square root of N between 2 and 4 Hz, and the quadratic root of N (the non-coherent gain) at frequencies above 4 Hz. The location performance estimates were based on location modeling parameters which are though to reflect conditions before and after regional and station calibrations. The "before and after" modeling parameters are stated in Tables 1 and 2, respectively.

A Presentation of the Findings

An estimate of the detection performance level of the primary network with all of its station upgrades is illustrated by the contour graph of Figure 3. This result shows that the detection threshold varies from magnitude 3.25 to below 4.25 over the globe. The best detection levels appear in central Eurasia where the threshold ranges from 3.25 to 3.5 and the poorest appear in Antarctica and on some of the islands of the southern oceans. Assuming that the predictions are valid, the actual network detection levels are probably better than shown here since the contributions of the secondary arrivals were not included in the threshold estimates. On the basis of earlier studies [6] it can be stated that if three or more arrivals, two of which are P arrivals from distinct stations, are required to admit a network detection with 99% probability, the detection threshold can be reduced by approximately 0.25 magnitude units.

The contour graphs of Figures 4 and 6 portray the location performance of shallow contained shots having a magnitude of 4.25 everywhere and having a magnitude equal to the detection threshold of the primary network (See Figure 3), respectively. The location performances are stated in terms of location accuracy when given in square kilometers with 90% confidence and are based on the use of the arrival time picks and bearings associated with the P arrivals only. Both graphs indicate that events can be located with accuracies better than 1000 square kilometers largely everywhere. The poorest predicted accuracies occur in the Antarctica and on some of the islands in the southern oceans. The best accuracies are somewhat better than 100 square kilometers and largely appear in the northern hemisphere. For events having a 4.25 magnitude, the areas having the best accuracies (See Figure 4) encompass almost all of the northern hemisphere, a large portion of Africa, and a small portion of South America. Greater accuracies than these are possible at larger event magnitudes. For event magnitudes at the detection threshold (See Figure 3), the best accuracies (See Figure 6) occur in limited areas of the northern hemisphere. It is important to realize that these accuracy estimates are conservative. Improvements in the accuracy are possible by using the secondary arrivals in addition to the P arrivals. Additional location accuracy is also possible by using other location methods.

The contour graphs of Figures 5 and 7 estimate the factors by which location uncertainty ellipses can be reduced in area in going from a uncalibrated state to a calibrated state for an event magnitude of 4.25 and for event magnitudes at the detection threshold of the primary network, respectively. Both results imply that improvements in location accuracy by a factor of 6 to 6.5 are possible. These results simply document the improvement possible when conventional location methods are augmented with regional and station corrections.

Conclusions

The following conclusions can be withdrawn from the above findings ...

- The primary network alone and in its mature state is capable of detecting a fully coupled 1 kiloton nuclear shot contained in consolidated rock anywhere on the

earth

- The lowest detection thresholds produced by the primary network appear in central Eurasia where the threshold ranges from 3.25 to 3.5 magnitude units
- Slightly lower thresholds (0.25 magnitude units lower) than the ones shown are possible when secondary arrivals are included in a network detection criterion requiring at least three arrivals two of which are P arrivals from distinct stations
- Conventional location methods using regional and station calibrations are capable of achieving location accuracies better than 1000 square kilometers with 90% confidence largely everywhere for events having a magnitude at or above the detection threshold of the primary network. The poorest accuracies primarily appear on some of the islands in the southern oceans and in portions of Antarctica
- For events having a magnitude of 4.25 the predicted location accuracy exceeds 100 square kilometers in almost the entire northern hemisphere, over a large portion of Africa, and a small portion of South America. Better accuracies than these are possible at larger event magnitudes
- Regional and station calibrations yield net reductions in the elliptical areas of uncertainty by factors better than 6.0 using conventional location methods. Further location improvements can be achieved through the use of the secondary arrivals, by the use of additional stations, and through the use of other location methods

References

[1] Draft of the Nuclear Comprehensive Test Ban Treaty, Ad Hoc Committee on a Nuclear Test Ban of the Conference on Disarmament, Working Paper 330, Geneva, Switzerland, May 28, 1996

[2]Sereno Jr., Thomas J., Steven R. Bratt, and Gaymond Yee, NetSim: A Computer Program for Simulating Detection and Location Performance of Regional Seismic Networks, Report SAIC 90/1163, Science Applications International Corporation, March 1990

[3]Wada, M. M. and J. P. Claassen, Background Noise Spectra for Global Seismic Stations, In preparation, Sandia National Laboratories, June 1996

[4]Sereno Jr., Thomas J., Attenuation of Regional Phases in Fennoscandia and Estimates of Arrival Time and Azimuth Uncertainty Using Data Recorded by Regional Arrays, Report SAIC 90/1492, Science Applications International Corporation, September 1990

[5]Xie, J. and B. J. Mitchell, A back-projection method for imaging large-scale lateral variations of Lg coda Q with application to continental Africa, Geophys. J. Int. (1990) 100, 161-181.

[6]Claassen, J. P., Network Modeling and An Evaluation of a CD Proposed ISMS, Report SAND96-0585, Sandia National Laboratories, March 1996

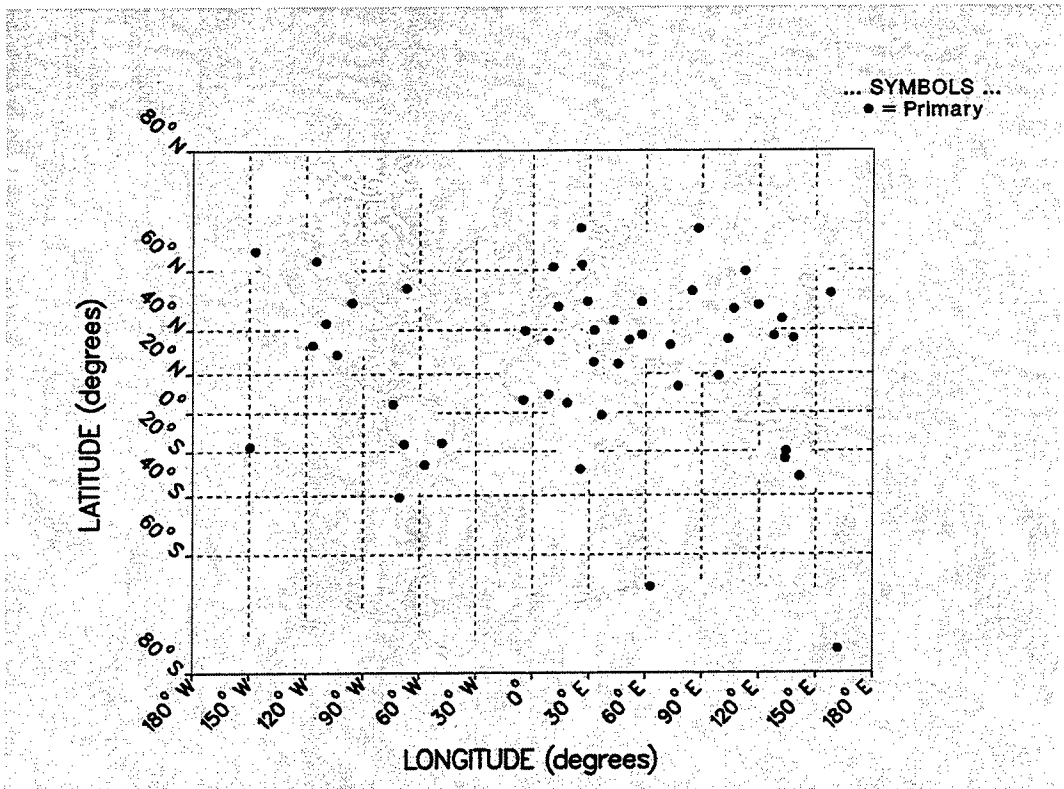

Figure 1. The Locations of the Primary Stations in the CD Proposed ISMS

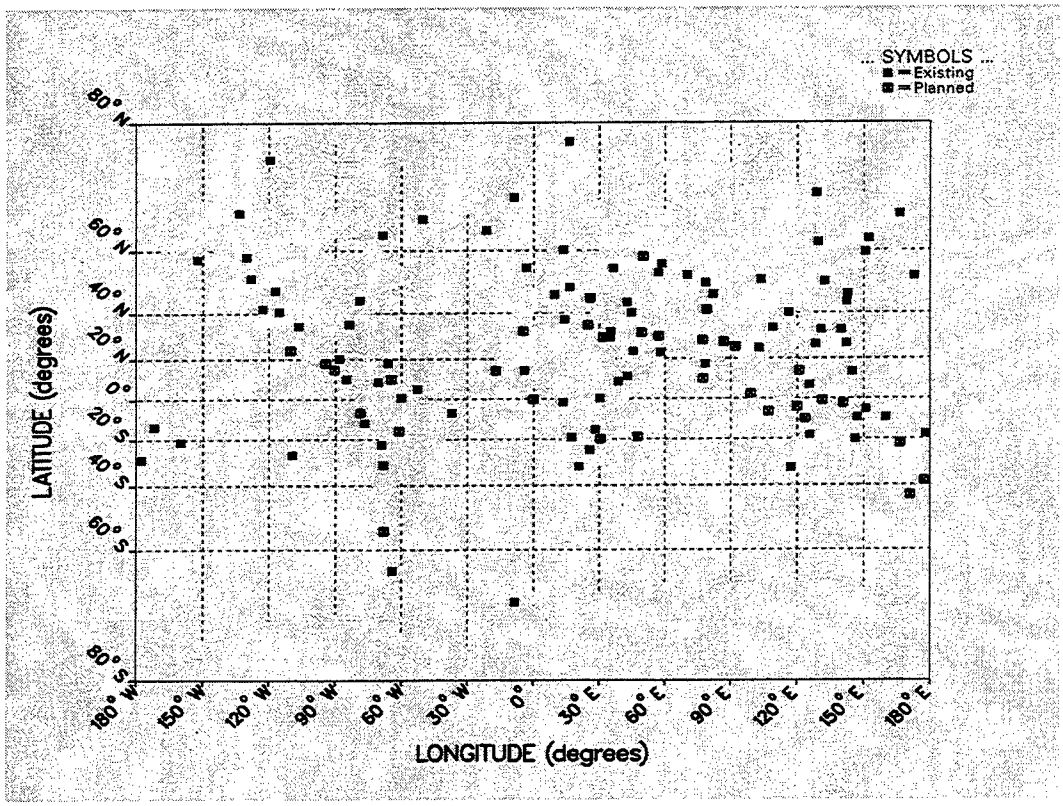

Figure 2. The Locations of the Auxiliary Stations in the CD Proposed ISMS

Table 1: Arrival Time and Bearing Statistics Before Calibration

Phase	Model Error (sec)	Arrival Error* (sec)	Bearing Model Error (degrees)	Bearing Error* *Array Stations* (degrees)	Bearing Error* *Simple Stations* (degrees)
P	2.0	0.15	6	14	20

* Note: These errors are scaled by station SNR

Table 2: Arrival Time and Bearing Statistics After Calibration

Phase	Model Error (sec)	Arrival Error* (sec)	Bearing Model Error (degrees)	Bearing Error* *Array Stations* (degrees)	Bearing Error* *Simple Stations* (degrees)
P	0.75	0.15	2	14	20

* Note: These errors are scaled by station SNR

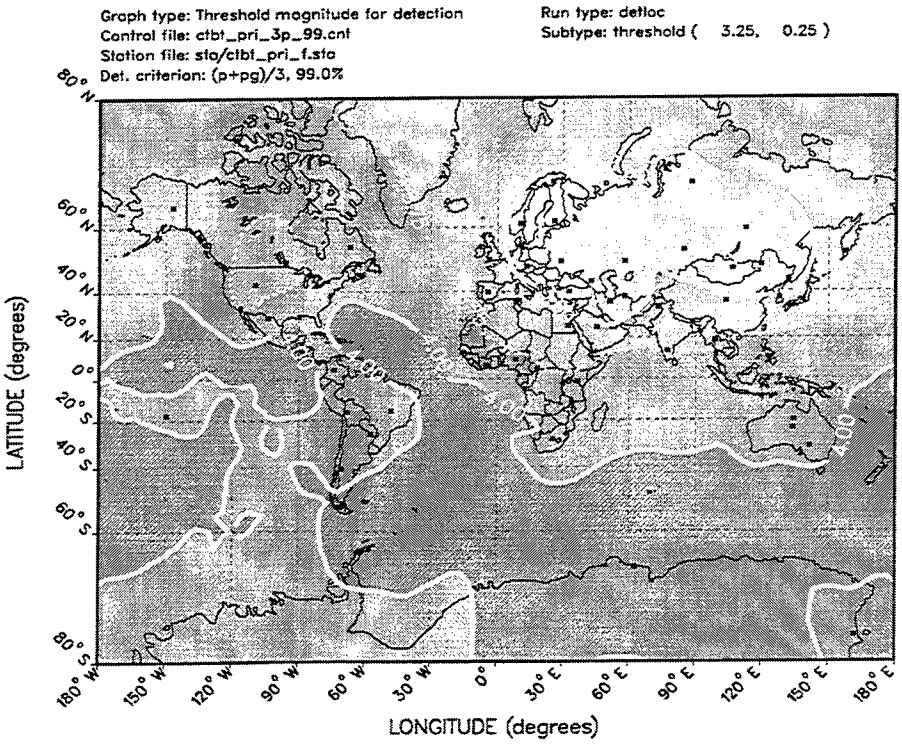

Figure 3. The Detection Threshold of the Primary Network In Its Upgraded State

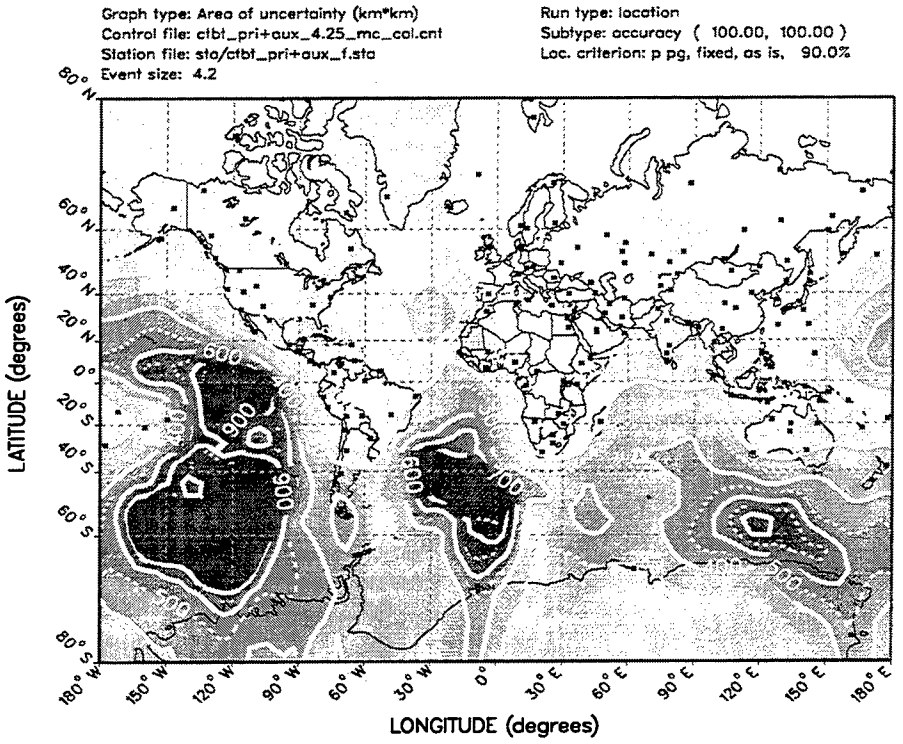

Figure 4. The Location Accuracies in Square Kilometers with 90% Confidence for Events Having a Magnitude of 4.25. The Locations Were Based on Observations by both Networks

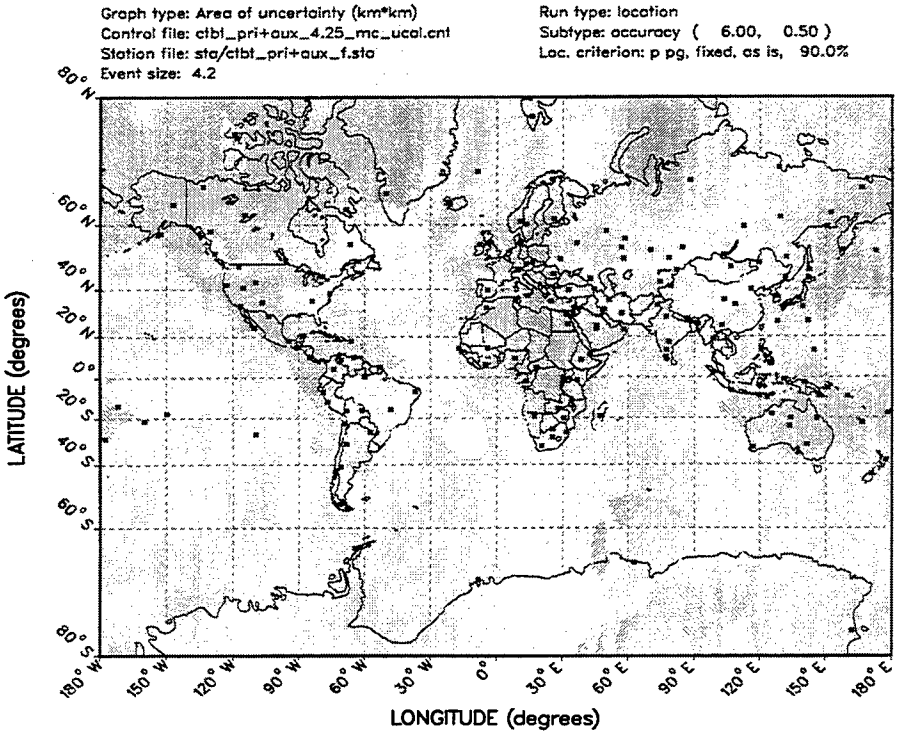

Figure 5. The Reduction in Location Areal Uncertainty After Calibration as Compared to Before Calibration for Events Having A Magnitude of 4.25

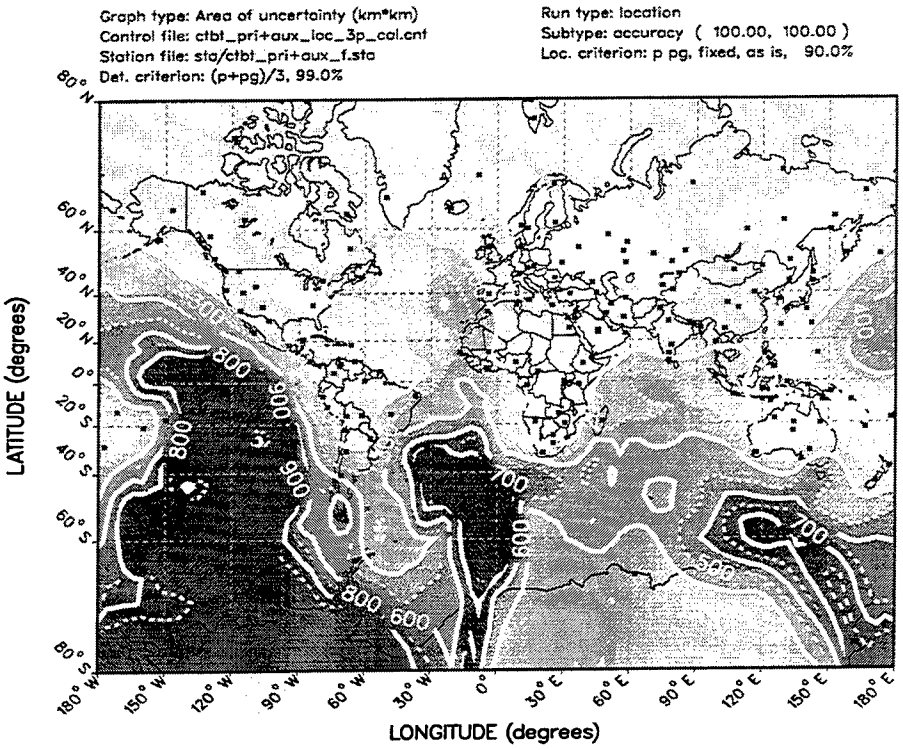

Figure 6. The Predicted Location Accuracy in Square Kilometers for Events Detected at the Threshold of the Primary Network. The Accuracy is Based on Observations by both Networks

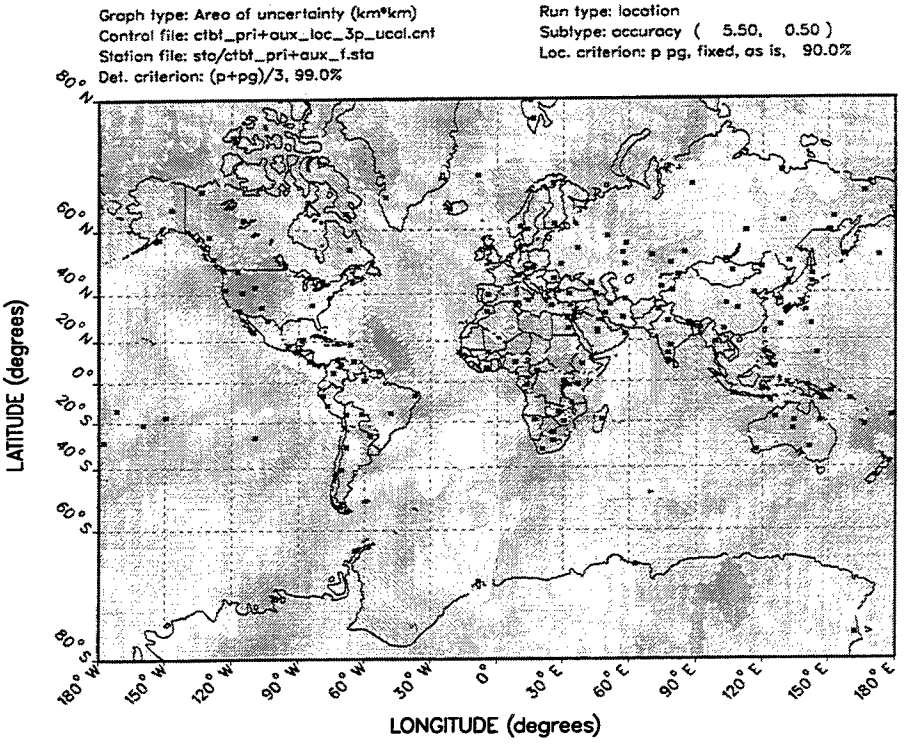

Figure 7. The Reduction in Location Areal Uncertainty After Calibration as Compared to Before Calibration for Events Detected at the Threshold of the Primary Network

Regional Location in Western China

Allen H. Cogbill & Lee K. Steck
Earth & Environmental Sciences Division
Los Alamos National Laboratory

Sponsored by U. S. Department of Energy, Contract W-7405-ENG-36
Comprehensive Test Ban Treaty Research and Development Program, ST482A

ABSTRACT

Accurately locating seismic events in western China using only regional seismic stations is a challenge. Not only is the number of seismic stations available for locating events small, but most stations available to researchers are often over 10° distant. Here we describe the relocation, using regional stations, of both nuclear and earthquake sources near the Lop Nor test site in western China. For such relocations, we used the Earthquake Data Reports provided by the U. S. Geological Survey (USGS) for the reported travel times. Such reports provide a listing of all phases reported to the USGS from stations throughout the world, including many stations in the People's Republic of China. LocSAT was used as the location code. We systematically relocated each event in this study several times, using fewer and fewer stations at each relocation, with the farther stations being eliminated at each step. We found that location accuracy, judged by comparing solutions from few stations to the solution provided using all available stations, remained good typically until fewer than seven stations remained. With a good station distribution, location accuracy remained surprisingly good (within 7 km) using as few as 3 stations. Because these relocations were computed without good station corrections and without source-specific station corrections (that is, path corrections), we believe that such regional locations can be substantially improved, largely using static station corrections and source-specific station corrections, at least in the Lop Nor area, where sources have known locations. Elsewhere in China, we must rely upon known locations of regionally-recorded explosions. Locating such sources is clearly one of the major problems to be overcome before we can provide event locations with any assurance from regional stations. Inasmuch as small events may only be detected at regional stations, it is paramount to find such sources, as they represent "ground truth".

Key words: seismic, location, regional, China

INTRODUCTION

Historically, perhaps the most basic criterion used to discriminate between earthquakes and nuclear explosions was simply the location of an event, for those powers that did test nuclear weapons did so at well-established test sites. For example, the People's Republic of China (PRC) has historically conducted weapons testing at the Lop Nor nuclear test site. As a result, teleseismic discrimination has focused on test sites: events initially located away from the nuclear test sites were largely ignored. Under a Comprehensive Test Ban Treaty (CTBT), however, event location may become more important, for an explosive event located away from both traditional testing areas and away from known mines is suspicious. Indeed, an explosive event located "close" to a mining area could be problematical, depending upon the uncertainty of the estimated location and its proximity to the mine. Reliable estimates of location uncertainty become extremely important under a CTBT.

We report here initial results from a study of the capability to locate seismic events in China, particularly western China, using only regional data. At present, no seismic arrays are available to us to assist in the location of regional events in western China. Thus, we are constrained to use only travel time data from single stations. Our first objective is to estimate the reliability of location methods utilizing only travel times recorded at regional seismic stations.

In order to assess the reliability of our location methods, accurate locations of the seismic sources located must be independently available. For China, this presents an immediate problem, as the only set of accurately-known source locations is the set of nuclear events detonated at the Chinese test site at Lop Nor. We can therefore characterize the capability to locate events from the Lop Nor region, but nowhere else in China. It is possible to utilize well-recorded, large earthquakes having shallow foci as "known" sources, but uncertainties in the positions of such events will always render the location characterization of such areas less certain. This type of inherent uncertainty afflicts any attempt at estimating the location capability of a particular method, such as one utilizing waveform analysis rather than travel-time analysis. Independent studies are ongoing to locate the positions of other types of seismic sources in China, notably mining blasts. The success of the location characterization studies is strongly dependent upon the success of these parallel studies of seismic source location.

RESEARCH ACCOMPLISHED

In the initial stage of this work, we have chosen to test the LocSAT hypocenter location algorithm (Bratt & Bache, 1988) by locating 7 known nuclear explosions at the Lop Nor test site. Observed travel times were taken from the United States Geological Survey's Earthquake Data Reports (EDR). The EDR data are sorted by epicentral distance (from near to far), thus permitting us to easily test the effects of station number and proximity on epicenter location. In the results which follow, we used only the first arrivals, usually indicated in the EDRs as P, with an occasional Pn and some PKP.

Travel times are determined from the AK135 tables, corrected for ellipticity, with no bulk static or source-specific station corrections (SSSC's). Beginning with picks from the nearest 300 stations, we gradually eliminated more distant stations, until only the 3 closest stations remain. Note that we are determining epicenter only, holding depth fixed at 0. We used the closest station as the starting location of the inversion, with *a priori* travel time errors set to 2 sec. Table 1 lists the explosions we have re-located, and Table 2 provides a sample run for one of them. The distribution of regional stations used for relocating the nuclear events is shown in Figure 1, along with the locations of Lop Nor and the former Soviet nuclear test site near Semipalatinsk.

In general, LocSAT epicenters are in good agreement with the EDR locations, which in some cases use upwards of 600 picks. Some systematic differences are to be expected, as the

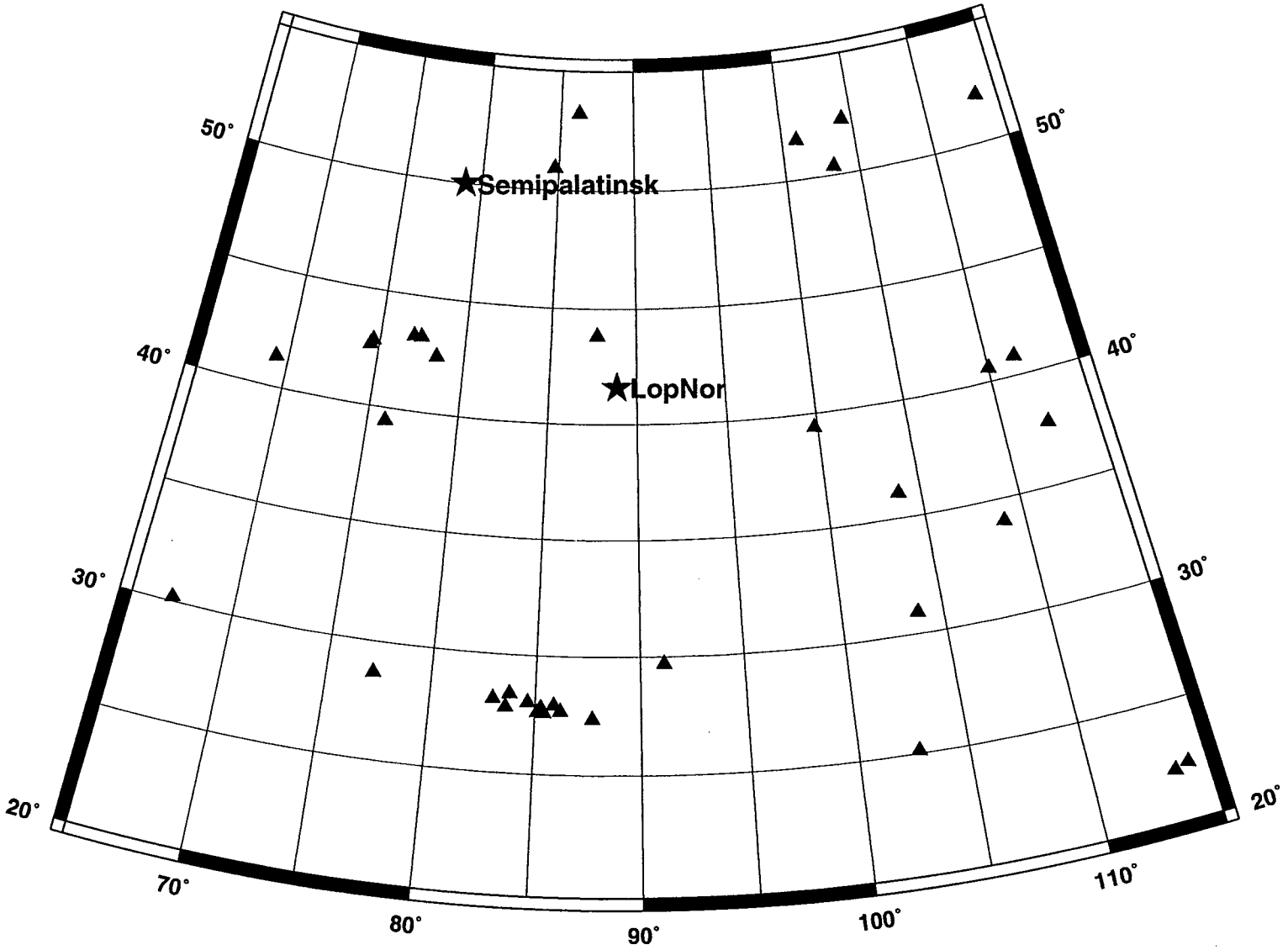

Figure 1. Distribution of EDR stations (triangles) used for relocating nuclear events in this study.

EDR locations use the J-B travel time tables for its locations, rather than AK135. For runs using more than 75 picks, location differences between the LocSAT results and the EDR results were typically less than 5 km in both latitude and longitude. The inversion is typically stable down to 5 stations, at which point average lat/lon errors are still less than 10 km. For 3 and 4 stations, the azimuthal distribution of stations sometimes became unfavorable, resulting in LocSAT solutions diverging dramatically from the EDR locations. This occurred in 3 of the 7 relocations. For the other 4 blasts, LocSAT still performed well, with latitude errors generally less than 22 km and longitude errors less than 10 km. We have also compared the LocSAT epicenters with the those of Gupta (1995), which were derived from a master event relocation based on accurate satellite locations of the June 27, 1973 and October 3, 1984 Lop Nor nuclear tests. Results were very similar to those of the EDR relocations.

Table 1. Nuclear events relocated in this study.

Date	Origin Time	Latitude	Long.	Depth	m_b	Ms
90/05/26	07:59:57.8	41.566	88.688	0	5.4	
90/08/16	04:59:57.6	41.564	88.770	0	6.2	
92/05/21	04:59:57.5	41.604	88.813	0	6.5	5.0
92/09/25	07:59:59.9	41.763	88.387	0	5.0	
93/10/05	01:59:56.6	41.667	88.695	0	5.9	4.7
94/06/10	06:25:57.8	41.527	88.710	0	5.8	
94/10/07	03:25:57.8	41.574	88.680	0	5.9	
95/08/17	00:59:57.0	41.570	88.730	0	6.1	

The relocation of the June 1994 event is enlightening. The details of its relocation are shown as Table 2; Figure 2 shows the spatial distribution of the 10 stations nearest the event. Note that, with the exception of WMQ, located only 2.4° NNW of Lop Nor, regional stations are not located very close to the test site: the next closest station providing data for this study is nearly 9° distant from Lop Nor. One of the implications of this observation is that, for locating events in the Lop Nor region, the details of the travel-time curves from 0-9° may be irrelevant, as no observations in this interval are likely to be available for locating events. In fact, the closest station to Lop Nor available for the June 1994 relocation is FRU, over 10° distant from the event. Figure 2 reveals a relatively good station distribution, despite the fact that 8 reporting stations are grouped very close to one another. Figure 3 shows how the location of the event varies as more stations are eliminated. Even using only 3 stations, the mislocation is only ~7 km. Some of the other nuclear events relocated had very poor station distributions, and consequently their mislocations were greater. Parenthetically, we note that the distribution of reporting stations was quite different from event to event, which is somewhat surprising in view of the fact that all these events were large enough to be well-recorded. We also note that travel times were often reported by PRC-controlled stations, although reporting times from these station commonly showed high residuals, leading us to suspect these times. Note that times from WMQ, the closest station to the events, were never available.

As a first estimate of bulk static corrections, we averaged the EDR station residuals over all events in a large region (10°-60° latitude, 50°-120° longitude) around Lop Nor, and incorporated them into the LocSAT algorithm. Any improvement in epicenter location was very small. However, this set of events contained many regional arrivals having relatively large incident angles (from vertical). A better approach would be to use residuals for events at distances greater than 40°, arriving with much smaller incident angles. These would more accurately model bulk static station corrections. We have estimated these corrections, but have not yet incorporated them into our results.

In addition to relocating several Lop Nor nuclear explosions, we also relocated an m_b=6.2 earthquake that occurred near the Lop Nor test site, as well as several of its aftershocks, ranging

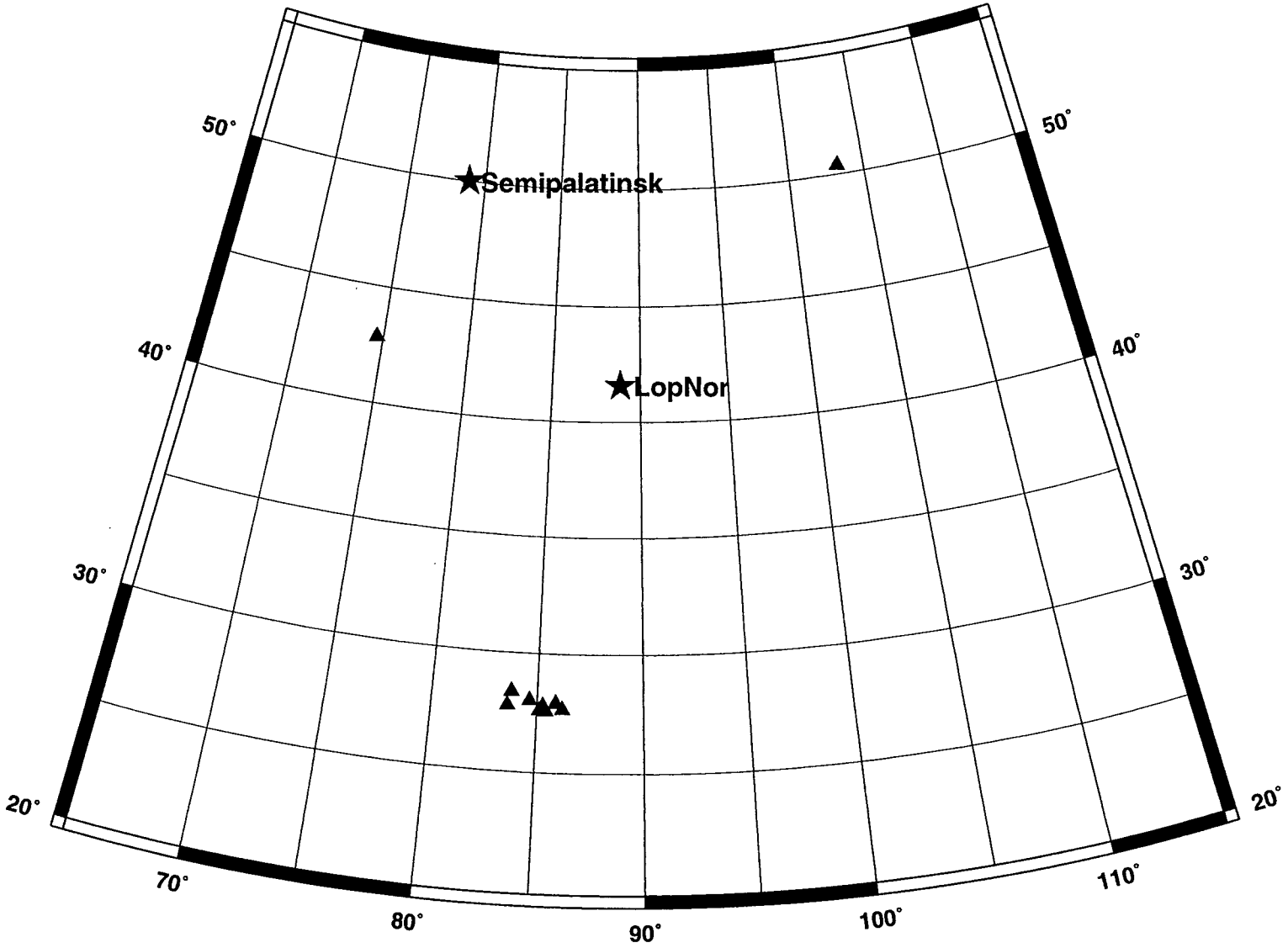

Figure 2. Stations (triangles) available for relocation of the June 1994 Lop Nor event.

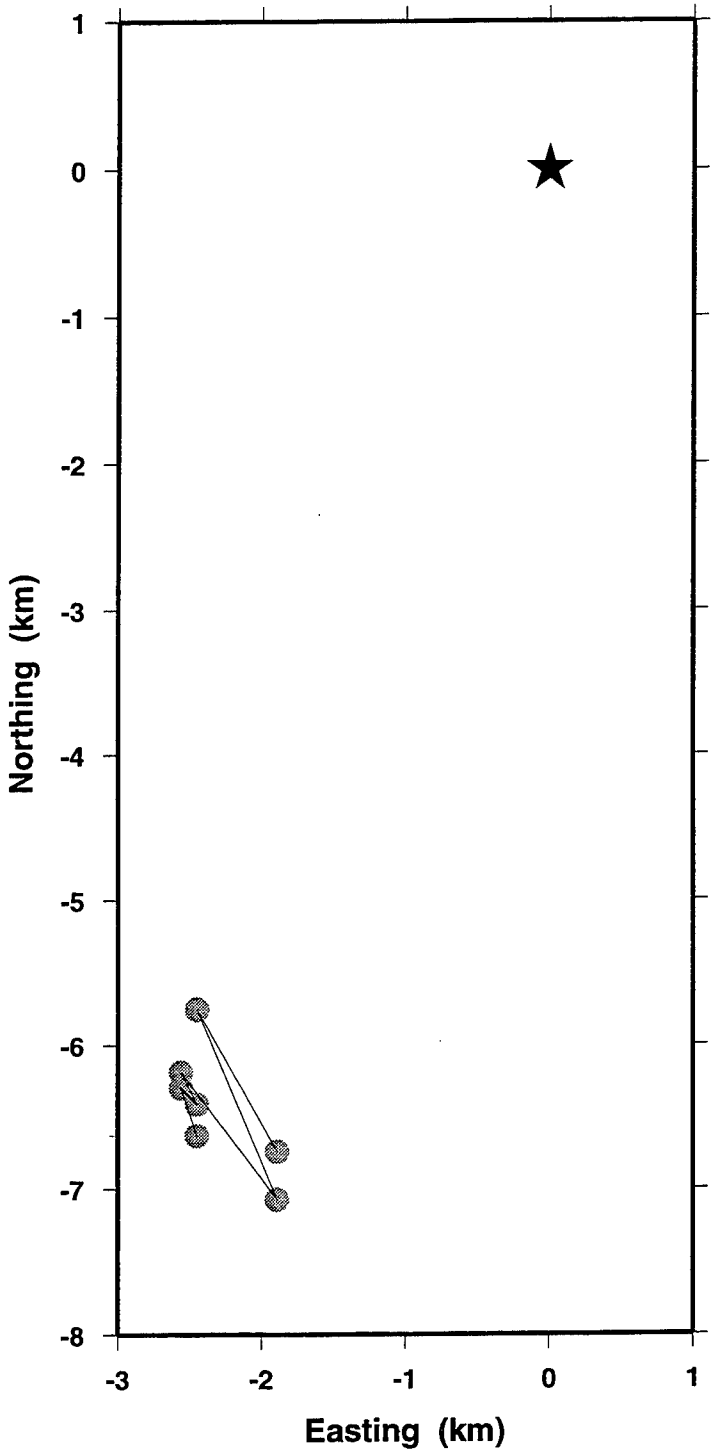

Figure 3. Relocations of June 1994 Lop Nor event. Star is the EDR location, circles are positions of our relocated events. Only 10 nearest stations used. Locations shown use 10,9,...,4 stations in solutions.

in magnitude from 5.8 to 3.8. We followed the same procedure as for the explosions, except that we now allowed depth to vary, and as a result the number of stations could only be reduced to 4. In all cases, LocSAT worked well, finding epicenters to within 10 km in latitude and longitude of the EDR epicenters with as few as 6 stations. However, with depth varying, origin times were off by several seconds, and depths by up to 60 km. Using only 4 or 5 stations, latitude and longitude errors were less than 25 km, with one exception, though depth errors in some cases reached over 100 km and origin time errors approached 8 seconds. In several instances, the inversion using only 4 stations failed. Table 3 lists the earthquakes used and tabulates results from 3 of the 7 earthquakes studied. In general, for both earthquakes and explosions, the error ellipses surrounding the LocSAT location encompassed the reference location, and did not grossly overestimate the errors.

Table 2. Results for the June 1994 Chinese nuclear test. Latitude, longitude, and origin time (ot) errors are the difference between the EDR and LocSAT locations. Other errors shown are estimated by LocSAT (confidence error ellipse and origin time). The confidence level was set to 0.90. Below, the first column shows the number of stations used, and the second shows the maximum azimuthal gap. The sixth, seventh and eighth columns give the ratio of semi-major and semi-minor axes of the error ellipse, the value of the semi-minor axis, and the strike of the error ellipse.

	(°)	(°)	(°)	(sec)		(km)	(°)	(sec)
nsta	az	gap	lat err	lon err	ot err	maj/min	minor	strike	time err
300	49.0	0.005	-0.040	-1.872	1.27	5.5	22.8	0.300
150	49.0	0.026	-0.045	-1.934	1.22	6.5	24.2	0.300
75	65.0	0.028	-0.038	-1.955	1.14	7.6	170.2	0.400
50	65.0	0.058	-0.032	-1.928	1.22	8.6	139.6	0.500
40	76.0	0.071	-0.007	-2.119	1.16	9.6	125.9	0.600
30	76.0	0.087	-0.013	-2.150	1.29	10.4	105.0	0.700
20	76.0	0.072	-0.014	-1.703	1.70	10.7	113.5	0.800
10	145.0	0.069	0.028	-1.709	1.70	18.4	106.2	1.600
9	145.0	0.060	0.022	-1.777	1.68	18.6	106.0	1.600
8	145.0	0.057	0.023	-1.800	1.66	18.9	106.7	1.600
7	145.0	0.058	0.022	-1.794	1.63	19.3	107.8	1.700
6	151.0	0.056	0.023	-1.807	1.59	19.9	109.5	1.700
5	151.0	0.064	0.017	-1.754	1.57	20.7	113.2	1.700
4	155.0	0.052	0.022	-1.837	1.50	22.1	118.3	1.800
3	155.0	0.061	0.017	-1.788	1.55	24.5	133.9	2.000

Table 3. List of 7 earthquakes relocated during this study.

#	Date	Origin Time	Latitude	Long.	Depth	m_b	Ms
1	93/10/02	08:42:32.7	38.190	88.663	14	6.2	6.3
2	93/10/02	09:20:12.3	38.206	89.284	10	4.9	
3	93/10/02	09:43:19.5	38.169	88.605	14	5.8	5.3
4	93/10/02	17:23:33.3	38.171	88.690	14	5.6	5.0
5	93/10/02	19:16:43.0	38.079	88.831	10	3.8	
6	93/10/02	23:49:59.7	38.359	88.878	10	4.8	
7	93/10/07	03:26:58.9	38.214	88.726	11.3¶	5.0	

¶Depth fixed using depth phase.

Table 4. Results are for 3 earthquakes (numbers 1, 7, and 5) from the above sequence, which occurred close to Lop Nor. Latitude, longitude, origin-time (ot), and depth errors are the difference between the EDR and LocSAT locations. Other errors shown are estimated by LocSAT (confidence error ellipse and origin time). The confidence level was set at 0.90. Below, the first column shows the number of stations used, and the second shows the maximum azimuthal gap. The seventh, eighth and ninth columns give the ratio of semi-major and semi-minor axes of the error ellipse, the value of the semi-minor axis, and the strike of the error ellipse.

Earthquake 1 (Mb = 6.2)

	(°)	(°)	(°)	(sec)	(km)		(km)	(°)	(sec)
nsta	az	gap	lat err	lon err	ot err	deperr	maj/min	minor	strike	time err
300	36.0	-0.023	-0.035	-1.372	3.5	1.75	4.8	11.1	3.700
150	36.0	-0.009	-0.037	-0.355	11.0	1.71	5.2	8.8	4.200
75	36.0	0.007	-0.037	-0.374	11.0	1.37	7.3	5.5	4.800
50	36.0	-0.003	-0.052	-1.269	4.0	1.17	9.2	168.4	5.300
40	45.0	-0.004	-0.062	-0.483	10.3	1.16	9.8	171.1	6.400
30	48.0	-0.010	-0.075	-0.345	11.3	1.19	10.1	1.6	7.800
20	52.0	-0.032	-0.041	-4.159	-30.2	1.02	13.2	64.0	1.000
10	99.0	-0.045	-0.069	-4.905	-116.	1.33	15.3	31.8	2.000
9	115.0	-0.049	-0.079	-4.933	-121.	1.83	16.6	55.4	2.100
8	115.0	-0.048	-0.079	-4.924	-120.	1.76	18.1	49.4	2.200
7	115.0	-0.004	-0.060	-1.577	5.6	1.11	20.2	83.9	333.9
6	115.0	-0.010	-0.061	-0.575	14.1	1.17	19.3	84.5	1.400
5	115.0	-0.020	-0.062	-0.647	14.1	1.09	22.2	21.3	1.600
4¶	115.0	-5.640	0.973	-0.647	14.1	1.09	22.2	21.3	1.600

10 stations nearest to Earthquake 1

Station	(°) Latitude	(°) Longitude	(km) Elev	(°) Distance
WMQ	43.8211	87.6950	0.970	5.6731
GTA	39.4106	99.8144	1.341	8.7925
TLG	43.2667	77.3833	0.850	9.9472
KSH	39.4553	75.9800	1.286	9.9789
GUN	27.9106	85.8792	2.900	10.5132
KKN	27.7900	85.2800	1.920	10.7520
DMN	27.6089	85.1058	2.225	10.9656
FRU	42.8333	74.6167	0.655	11.6515
AAK	42.6389	74.4939	1.645	11.6768
LZH	36.0867	103.8444	1.560	12.2975

Table 4 (continued).

Earthquake 7 (Mb = 5.0)

nsta	az (°)	gap (°)	lat err (°)	lon err (°)	ot err (sec)	deperr (km)	maj/min	minor (km)	strike (°)	time err (sec)
75	74.0	-0.029	-0.071	-5.206	-23.1	1.55	9.5	19.4	2.400	
50	74.0	-0.033	-0.079	-5.178	-22.4	1.55	9.7	21.7	2.600	
40	74.0	-0.033	-0.080	-5.180	-22.4	1.52	9.9	22.2	2.600	
30	74.0	-0.033	-0.098	-4.084	-11.6	1.41	10.7	24.5	6.300	
20	74.0	-0.040	-0.103	-5.067	-20.6	1.24	12.7	14.7	3.900	
10	113.0	-0.062	-0.174	-2.556	2.7	1.25	17.7	54.6	36.000	
9	113.0	-0.058	-0.151	-1.593	11.3	1.20	16.4	26.6	1.200	
8	129.0	-0.094	-0.140	-5.688	-38.8	1.14	19.1	48.7	2.000	
7	113.0	-0.059	-0.125	-5.804	-59.2	1.18	20.0	25.7	1.900	
6	245.0	-0.059	-0.127	-5.821	-61.7	1.14	20.4	25.0	1.900	
5	112.0	-0.118	-0.150	-6.339	-103.	3.12	20.2	23.6	3.900	
4¶	112.0	-5.616	1.036	-6.339	11.3	3.12	20.2	23.6	3.900	

¶Convergence error

10 stations nearest to Earthquake 7

Station	Latitude (°)	Longitude (°)	Elev (km)	Distance (°)
WMQ	43.8211	87.6950	0.970	5.6558
GTA	39.4106	99.8144	1.341	8.7391
KSH	39.4553	75.9800	1.286	10.0230
FRU	42.8333	74.6167	0.655	11.6843
SHL	25.5667	91.8833	1.600	12.8905
ZAK	50.3833	103.2833	0.000	15.9820
BTO	40.5983	110.0183	1.120	16.6256
KMI	25.1233	102.7400	1.945	17.6522
IRK	52.2717	104.3100	0.467	17.7763
HHC	40.8494	111.5636	1.169	17.8050

Earthquake 5 (Mb= 3.8)

nsta	az (°)	gap (°)	lat err (°)	lon err (°)	ot err (sec)	deperr (km)	maj/min	minor (km)	strike (°)	time err (sec)
7	184.0	-0.044	-0.035	-5.401	-24.2	2.67	17.1	16.7	4.300	
6	256.0	-0.033	-0.049	-2.609	1.9	2.32	19.7	15.7	23.300	
5[m]	187.0	-0.017	-0.050	3.188	10.0	2.40	19.0	16.5	2.100	
4¶	187.0	-5.751	1.141	3.188	10.0	2.40	19.0	16.5	2.100	

[m] Convergence not attained (maximum iterations reached)
¶ Convergence error

Table 4 (continued)

10 stations nearest to Earthquake 5

Station	(°) Latitude	(°) Longitude	(km) Elev	(°) Distance
WMQ	43.8211	87.6950	0.970	5.8006
GTA	39.4106	99.8144	1.341	8.6855
KSH	39.4553	75.9800	1.286	10.1308
LZH	36.0867	103.8444	1.560	12.1559
XAN	34.0394	108.9214	0.630	16.7340
TIY	37.7131	112.4342	0.850	18.6263
NB2	61.0397	11.2147	0.717	51.7633

CONCLUSIONS AND RECOMMENDATIONS

It is clear from this initial study that well-recorded events (*i.e.*, high S/N for times, good station distribution)in the Lop Nor region can be located rather accurately using only first arrival times at regional distances, even when only a small number of stations are available. Clearly the station distribution is one of the most important parameters controlling the reliability of a location. This result is well-known from a theoretical basis, of course. Also, it seems that, for single-station observations such as those used here, one does not need to be especially close to an event to provide a good estimate of its location. However, the events studied were well-recorded; observed travel times from smaller events are likely to be less reliable, as well as less likely to have a good azimuthal distribution of recording stations, leading to greater error in their locations.

We plan to estimate both static station corrections and SSSCs for all stations of interest. These mostly include not only the stations used by the EDRs, but also digital stations near Lop Nor of interest to CTBT researchers. We hope to be able to attain a location uncertainty of less than 2 km using such methods. Constructing the SSSCs will require estimating local velocity structure at the stations of interest, at least along paths from Lop Nor to the station. Separately, we plan to estimate the effect of noisy first-arrival data with the use of Monte Carlo methods, thus simulating what might be times recorded from a small event in the Lop Nor region.

Finally, we re-emphasize that the characterization of location reliability for regions of the PRC away from Lop Nor is highly dependent upon independent measures of seismic sources' locations in such regions. We plan to work closely with those finding such locations in order to expand our studies to other portions of China. Carefully planned calibration explosions at selected sites could be extremely beneficial, as well.

REFERENCES CITED

Bratt, Steven R. and Thomas C. Bache, 1988, Locating events with a sparse network of regional arrays, *Bull. Seis. Soc. Am.*, **78**(2), 780-798.

Gupta, Vipin, 1995, Locating nuclear explosions at the Chinese Test Site near Lop Nor, *Science & Global Security*, **5**, 205-244.

INVESTIGATION OF ADVANCED PROCESSING TECHNIQUES FOR REGIONAL ARRAY DATA

by

Zoltan A. Der
ENSCO, Inc., Springfield, VA

and

Dr. Robert H. Shumway
University of California at Davis, Davis, CA

Contract No. F19628-95-C-0205
Sponsored by AFTAC

ABSTRACT

In this paper an adaptive approach for automatic identification of regional arrivals is presented. The method is designed to circumvent some difficulties that plagued previous attempts of 3-component polarization analyses to achieve the same purpose. In particular, the methodology is designed to avoid complications due to signal distortion due to near sensor geology and complex arrivals made up of superpositions of multiple independent signal components. The idea is to replace time delay operators and assumed particle motion patterns used in deterministic signal processing with empirically computed sets of transfer functions. The application of this approach requires more than three sensor outputs (such as a 3-component combination). We propose a likelihood ratio formulism for the discrimination problem involving several arrivals. The same formulism also easily lends itself for the computation of receiver operating characteristics for the detection of various arrivals in the presence of various levels of noise. Tests of the techniques on actual events with high S/N ratio are promising. We recommend some modifications to the approach presented in Der et al (1993). Giving more weight to closer-spaced sensors (such as the A and B rings in ARCESS) could reduce the filter lengths, and parametrizations, required to achieve the same results.

Key Words: seismology, arrays, signal processing, statistics, detection, identification

OBJECTIVE

The objective of the work thus far is the facilitation of the automatic recognition of various regional arrivals. This is accomplished by a computational scheme for the adaptive learning of the generalized particle motion patterns as seen by small arrays that may also contain three-component sensors.

The main objectives of the work is to relieve the human operator in seismic monitoring from the effort to identify and locate routine blasting at various quarries, to enable him to possibly identify the sources of seismic waves for the Lg phase alone and to point out unusual events near some quarries that may merit further investigation.

The work presented is relevant to the detection, location, and identification of regional seismic events.

RESEARCH ACCOMPLISHED

General Remarks

In earlier work (Der et al 1993) we have established the fact that the polarization patterns of regional arrivals, unlike simple P and/or S type motion patterns, cannot be fully described by 3 perpendicular components of motion. If this were the case then it would be possible to derive one component of motion from the other two with some simple linear filters, but such was only possible for Pn, and not for the other regional arrivals. Moreover, the particle motions of even supposedly simple "P type" arrivals seem two be quite complex and three dimensional. The complexities in the various regional arrivals can be explained by the facts that all regional arrivals are complex superpositions of multiple reflections in the crust and that each sensor location is also associated with some complex azimuth-slowness dependent transfer functions (site effects) that distort the waveform. The latter arise from geological complexities near each sensor that lead to waveform variations across even very small arrays. These observations lead to the type of general models for regional arrivals that assume that:

a) All of the regional arrivals contain more than the one or two independent (orthogonal) signal components assumed to be present in P and S type arrivals respectively.

b) The waveforms of each sensor in a seismic array (including 3-component combinations) are to be regarded as outputs of such multiple signal components as passed through some sets of multichannel site-effect linear filters. Such multichannel filters are assumed to remain constant for the same regional arrivals for events at the same distance and azimuth from the array.

c) Multiple events at nearly the same locations therefore can be assumed to be

independent replications that contain the same set of multichannel filters and thus can be used to build up statistics used in the detection and identification of various regional arrivals at that distance and azimuth.

While these assumptions are not useful for isolated single events, repeated events at nearly the same location are inevitable consequences mining activity. Thus the basic idea underlying our approach is to replace time delay operators and assumed particle motion patterns used in deterministic signal processing (Kwaerna and Ringdal 1992) with empirically computed sets of transfer functions and a general multi-signal model. Although the plausibility of a multiple-signal multichannel model has been demonstrated for a limited set of Kola peninsula events (Der et al 1993), much needs to be done to extend these finding to other set of events. In that paper it has been shown that Pn contained two signal components instead of one, and Sn and Lg must contain more. This was shown by semi-qualitative comparisons of multichannel predictions of one channel from the rest for a mini-array consisting of a three-component combination and a small tripartite vertical array. This work does not answer following questions however;

a) How many signal components are present in Sn and Lg?

b) How do these things vary with distance and region and arrival?

c) What statistical framework must be set up for detection and discrimination of the various regional arrivals?

d) What is the best minimum sensor configuration is to use?

e) What is the most parsimonious model (both in terms of signal components and time domain filter coefficients) that is still effective?

The method used in Der et al (1993) did not have a quantitative statistical framework, it used a set of multichannel filters which were derived with little spectral smoothing. Such a framework must thus be provided. The determination of the number of effective signal components can be based on statistical criteria such as the Akaike information criterion (e.g. Kaveh and Wang 1991).

Outline of a Theoretical Framework for Regional Arrival Identification

The scheme of identifying a regional arrival type from the comparison of and extrapolated sensor output to an actual one can be reduced to a statistical testing of a set of residuals to determine which one of the regional phase models, defined in terms of multichannel filters, is the most likely one. This is similar to the schemes described by Basseville and Nikiforov (1993) to determine which of a set ARMA models fits a set of data best. The residuals of extrapolation of one output from the rest can be written as:

$$\varepsilon_{k,i} = s_{k,i} - \sum_{j \neq k} \sum_{l=-N}^{l=N} s_{j,i-l} f_{j,l} \qquad (1)$$

where $f_{i,j}$ are the filter weights applied to the traces $s_{i,j}$ with the first sum over all sensors excluding the sensor output k to be extrapolated from the rest. The length of the time-symmetric filter is $2N+1$. The weights can be obtained by solving the well known time domain multichannel filter design equations (Wiggins and Robinson 1965)

$$\begin{vmatrix} r_0 & r_1 & r_2 & . & . & . & . \\ r_1 & r_0 & r_1 & r_2 & . & . & . \\ r_2 & r_1 & r_0 & r_1 & r_2 & . & . \\ . & r_2 & r_1 & r_0 & . & . & . \\ . & . & r_2 & . & . & . & . \\ . & . & . & . & . & . & . \\ . & . & . & . & . & . & r_0 \end{vmatrix} \begin{vmatrix} f_1 \\ f_2 \\ f_3 \\ . \\ . \\ . \\ . \end{vmatrix} = \begin{vmatrix} g_1 \\ g_2 \\ g_3 \\ . \\ . \\ . \\ . \end{vmatrix} \qquad (2)$$

where the r_i are block kxk autocorrelation matrices, subscripts are for each time lag i, where k is the number of input traces, and the g_i are the cross correlation vectors between the inputs and the trace designated as the desired output, and f_i are filter weights. The large matrix is block-Toeplitz in form and is thus amenable to iterative solution methods. These can be obtained by ensemble-averaging the corresponding correlation functions over suites of collocated events for each specific arrival. The weights will be specific to each arrival the sample windows will be centered on. We have implemented the recursive algorithm of Wiggins and Robinson (1965) for use in our work.

We assume that the distribution of residuals for the is zero-mean Gaussian and thus we may test a set of residuals for pairs of hypotheses of the arrival being a Pg or Lg, for example, by the likelihood ratio method. Since the input trace RMS s remains the same for a given data segment to be tested, the increment in the log-likelihood ratio for a single point k can be written for such case (Basseville and Nikiforov 1993)

$$r_k = \frac{\left(\varepsilon_k^0\right)^2 - \left(\varepsilon_k^1\right)^2}{2\sigma^2} \qquad (3)$$

where we are essentially testing for the differences in the two kinds of residuals for determining which of the two (or more) hypotheses is the most likely.

Given this simple framework the methodology can be extended to formulate suitable detection and discrimination operating characteristics (Helstrom 1995). For instance the

presence of Lg plus noise (Hypothesis I) can be tested against the presence of noise alone (Hypothesis II) under various S/N conditions. Obviously the noise models can be derived analogously using noise samples or the assumption of isotropic noise.

Data Analyses

Much of the work was spent on developing a time-domain implementation of the regional phase identification method of Der et al (1993). We find that the original frequency-domain implementation that processes the data in blocks is awkward. Thus we transformed the frequency domain filters that equalize the waveforms into the time domain. These will be applied as convolution filters in a continuous fashion. A drawback of this approach that these filters are non-causal and introduce precursors. Nevertheless, since our purpose is phase identification and the precursors have very little energy this is not a problem.

In the work presented in this report we have used the data set in Der et al (1993) from the Kola mine K2 recorded at ARCESS. We have also assembled data sets from other Kola mines to test our methodology. At this stage of the work we have used broad-band processing ignoring the spectral differences among phases.

As described by Der et al (1993) we design digital filters for predicting, or more correctly, extrapolating the center vertical seismometer waveform from the rest of the mini-array (two collocated horizontals and a tripartite configuration of vertical from the C ring) based on the event compounded spectral matrix derived from a set of events. The filters then can be applied to individual, collocated events, even those not including the learning set. The success of the waveform extrapolation identifies the phase on which the filter was designed. We have concentrated on the Pn and Lg phases which we regard as the key phases in locating an event. The same approach can, and has been, applied to other identifiable regional arrivals as well, such as Sn and Pg (Der et al 1993).

We show the time domain filters for the enhancement of Pn phases in **Figure 1A.** These were designed by inverse Fourier transforming the frequency domain filters in Der et al (1993) and tapering off the ends. These filters are quite complicated, but the relative amplitudes show that it is mostly the two horizontal components that contribute to the prediction. The forms of filters do not lend themselves to easy intuitive interpretation since the observed waveforms, being influenced by distortion due to local geology, are quite complex themselves. Nevertheless the details of original and predicted Pn waveforms (**Figure 1B**) are quite similar, and their cross-products, that would contribute to the cross-correlation coefficients, are predominantly positive in polarity (lowermost traces). **Figure 1C** shows the original A0 vertical compared to the prediction and the smoothed cross-product for the whole recording of the same events. In this display no normalization with respect to the power in the traces of the cross product has been performed and the relative amplitudes of various arrivals still play a role. Nevertheless, it

is clear that the processing enhances Pn relative to the other phases, even in the cases (not shown) where Lg was much stronger than Pn.

Similarly, the filters designed to process the Lg phases are also much more complex than one would expect for simple beamforming, since such filters would contain only a few spikes at the correct time lags. In this case the main contributions come from the rest of vertical traces (**Figure 2A**). The original and predicted Lg waveforms are quite similar again in many details (**Figure 2B**) and their cross-products are again predominantly positive. The waveform matching procedure did not work as well for Lg as for Pn. **Figures 2C** show the original A0 vertical compared to the prediction of Lg and the smoothed cross-product for the whole A0 sensor recordings of the same events. It is clear that the processing enhanced Lg considerably relative to the other phases. Not all of the processed events show enhancement of Lg only as shown here, however, some enhance Sn as well. This can be expected, since both Sn and Lg contain considerable SV components.

The performance of filters designed entirely in the time domain using correlation functions and the recursive block Toeplitz matrix inversion procedure (Wiggins and Robinson 1965) was comparable to the results presented above for Pn even when very short 31 point filters were used. The advantage of such approach is that the filters thus designed are optimum for their time length, instead of being truncated as above. The finding of the most effective and parsimonious filter lengths is the subject of our ongoing work. For Lg the short filters did not work well, we are presently modifying and testing the program to compute longer time domain filters, but shorter than the 160 point filters shown above. The need for testing this is dictated by the fact that the computation of longer filters may make the recursive algorithm to become unstable. We are presently in the process of implementing the likelihood ratio testing algorithm as described above using the filters derived by time domain computations.

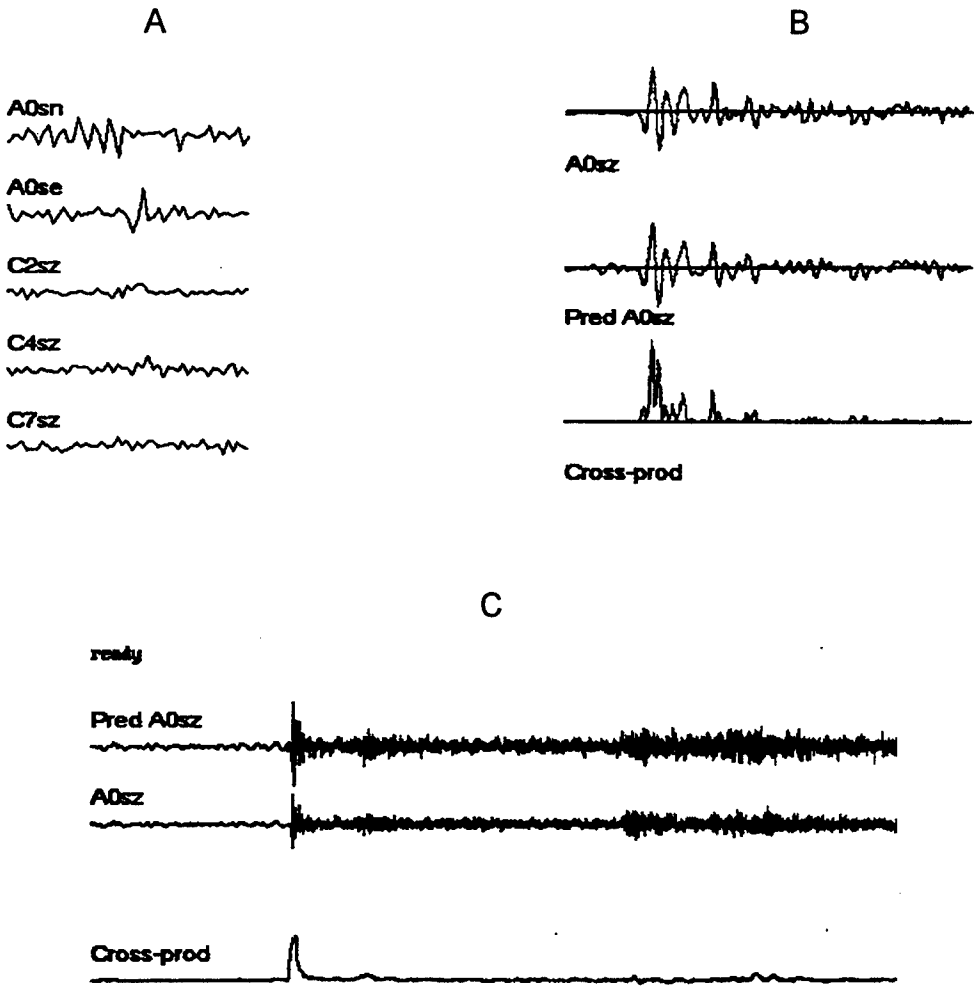

Figure 1. A) Time domain filters for the enhancement of Pn, length 160 points=4 seconds. B) Detail of A0 Pn waveform for event 1990219 (top) vs. the predicted one (middle) and their cross product (bottom). Time length 6.4 seconds. C) Processed trace (top), actual seismogram (middle) and the leaky-integrated cross product. Time length 102 seconds.

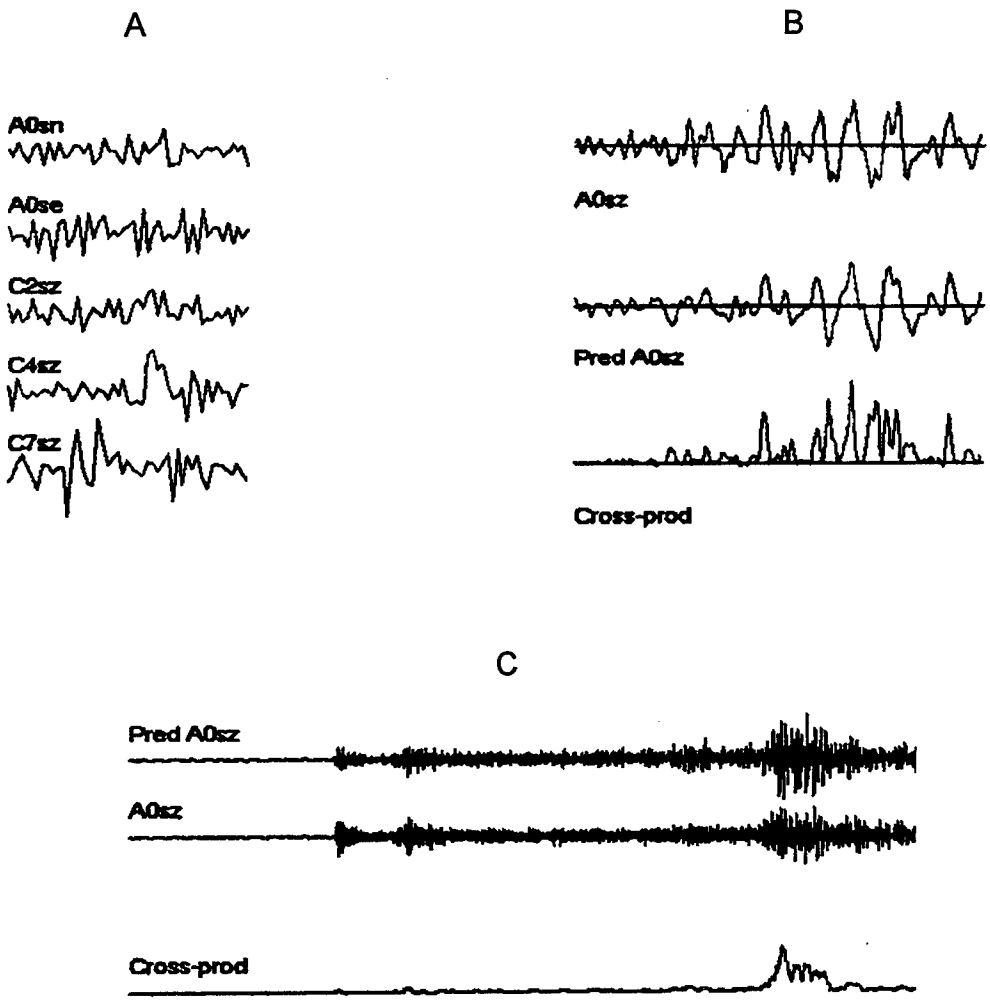

Figure 2. A) Time domain filters for the enhancement of Lg, length 160 points=4 seconds. B) Detail of A0 Lg waveform for event 1990110 (top) vs. the predicted one (middle) and their cross product (bottom). Time length 6.4 seconds. C) Processed trace (top), actual seismogram (middle) and the leaky-integrated cross product. Time length 102 seconds.

References

Der, Z.A., Hirano, M.R., and R.H. Shumway (1990), Coherent processing of regional signals at small seismic arrays. Bull. Seism. Soc. Am., 80B, 2161-2176.

Der, Z.A., Baumgardt, D.R., and R.H. Shumway (1993), The nature of particle motion in regional seismograms and its utilization for phase identification. Geophys. J. Int., 115, 1012-1024.

Basseville, M. and I.V. Nikiforov (1993), Detection of Abrupt Changes. Prentice Hall Information and System Sciences Series. Prentice Hall, Englewood Cliffs, NJ.

Helstrom, C.W. (1995), Elements of Signal Detection and Estimation, Prentice Hall, Englewood Cliffs, NJ.

Kaveh, M. and H. Wang (1991), Threshold properties of narrow-band signal subspace array processing methods. In "Advances in Spectrum Analysis and Array Processing", S. Haykin, Editor, Prentice Hall, Englewood Cliffs, NJ.

Kwaerna, T. and F. Ringdal (1992), Integrated array and three-component processing using a seismic microarray. Bull. Seism. Soc. Am., 82, 870-882.

Wiggins, R. and E. A. Robinson (1975), An iterative implementation of the multichannel filtering problem, J. Geophys. Res., 70, 1885-1891.

CONCLUSIONS AND RECOMMENDATIONS

In this paper an adaptive approach for automatic identification of regional arrivals is presented. We developed a likelihood ratio formulism for the discrimination problem involving several arrivals. The same formulism also easily lends itself for the computation of receiver operating characteristics for the detection of various arrivals in the presence of various levels of noise. Test of the techniques on actual, high S/N events are very promising. Nevertheless, we recommend some modifications to the approach presented in Der et al (1993). First of all, giving more weight to closer-spaced sensors (such as the A and B rings in ARCESS) could reduce the filter lengths (Der et al 1990), and parametrizations, required to achieve the same purpose. Time domain filter design also seems to be more efficient and enables one to design more compact filters.

Evaluation of the Performance of Broadband Networks and Short-Period Arrays in Global Monitoring

Douglas Dreger, Michael Pasyanos, Robert Uhrhammer, and Barbara Romanowicz
UC Berkeley Seismographic Station, Berkeley, CA

Alan Ryall
Lawrence Livermore National Laboratory

Sponsored by Lawrence Livermore National Laboratory

Abstract

A collaborative study between the UC Berkeley Seismographic Station (BSS) and the Lawrence Livermore National Laboratory (LLNL) compares the performance of various seismological monitoring systems in the regional monitoring of a Comprehensive Test Ban Treaty (CTBT). The goals of this study are to determine what role broadband stations will have in the monitoring of a CTBT, to provide a reference of an ideal monitoring situation, and to improve upon the location capability of broadband stations. Central and northern California was chosen as the study area because of the abundant seismicity, the ability to compile a "ground truth" catalog with which to compare the performance, and to provide a reference for phase two of this study which involves the comparison of various seismic systems in remotely monitoring a region. The ground truth catalog contains 239 M>3.0 events and spans all of 1995. The events reported in the Prototype International Data Center (PIDC) Reviewed Event Bulletin (REB) are compared to the control catalog to document the current capability of the IMS. In addition, the REB events are compared to the Berkeley Digital Seismic Network (BDSN) only solutions in the context of assessing relative performance. The BDSN event detections when associated with the control catalog revealed that an upper bound for the BDSN detection rate of magnitude 3 and larger events was approximately 70%. The implication being that even with a sparse network of broadband stations located within the study region a large fraction of small events could go undetected. The REB reported only 17% of the events in the control catalog, however the smallest events in the REB indicate that it is possible to detect and locate events to the M_L 3.5 level. We found that the locations obtained from both systems fall short of the Group of Scientific Experts guidelines (CD/NTB/WP.283, 1995), however magnitude 4.7 and larger events located by BDSN have mislocations within acceptable levels. The magnitudes reported in the REB were found to be biased low (0.5 magnitude units) and it seems that regional calibration of PIDC m_b will be required to provide a globally meaningful and comparative magnitude measure.

Key words: regional monitoring, event locations, magnitudes

Objective

This report summarizes the studies that were conducted in phase one of collaborative research between BSS and LLNL. The primary objective of this research was to evaluate the performance of various seismological monitoring systems, and to ascertain the role that broadband stations might have in the regional monitoring of a Comprehensive Test Ban Treaty (CTBT). The premise of this experiment is that in order to fully understand the current capability of any monitoring system, tests need to be conducted in regions where there is a very high level of "ground truth" information. Northern and central California was chosen as the area of study in phase one (Figure 1) because of the abundant seismicity and the "ground truth" afforded by the dense networks operated by BSS and the USGS. The capability and performance of the IMS as reported in the REB and BDSN are compared to illustrate and document the current capabilities of each system. To fully characterize the detection and location thresholds of the IMS in the study region would require a systematic review of the PIDC waveform data and is beyond the scope of this study. Another component of this study is the evaluation of the ability of the two array stations, PDAR and TXAR, of the primary IMS network to monitor seismicity in California. While LLNL has analyzed a sizable number of events we do not yet have the correct software that will allow us to input station time and azimuth corrections and to locate the events with just the two arrays. This capability should be available soon and will be a component of phase two of this project.

Research Accomplished

Creation of Control Catalog

The control catalog in this study was compiled by determining event locations using the available phase data stored at the Northern California Earthquake Data Center (NCEDC). Events which did not have sufficient phase data on the NCEDC did not enter into the control catalog. This phase data was comprised of P-wave phase picks from the very dense short-period Northern California Seismic Network (NCSN) and both P and S phase picks from the sparse BDSN network of very broadband stations. The control catalog consists of 239 events with magnitudes (M_L) above 3.0 (Figure 2), and the events are generally dispersed throughout central and northern California (Figure 1). On average 29 phase readings per event were used in the control catalog calculations. While the control catalog is considered complete above the magnitude 3.0 level within the networks and north of the UCB-Caltech demarcation (Figure 1), small events near the 3.0 level and events near the edge of the study area may be omitted. All of the BDSN phase picks were analyst reviewed. The same location routine was used in the construction of the control catalog and in the BDSN only calculations to ensure that the results represent only the differences due to the configuration and capability of the various networks. The details of the location methodology can be found in the bulletin of the Seismographic Station (Staff of the BSS, 1995). The events reported in the REB were located by the staff of the PIDC.

Catalog Comparisons

In this section we compare the REB and BDSN catalogs to document current performance of each system. Figure 2 compares the control and REB catalogs for the central and northern California region for the period from January 1, 1995 to December 30, 1995. The events that were listed in the REB are shown as filled symbols. During 1995, 40 of the 239 events were reported in the REB representing approximately 17% of the control catalog seismicity. Figure 2 shows that the REB is only complete above a magnitude of 4.7 (M_L). Between magnitude 4.0 and 5.0 approximately 61% of the events are reported. Seven M<4.0 events were reported in the REB, and in fact, there was one case in 1995 where the REB reported an event that was missed by both the BDSN and NCSN networks. In summary, REB events in the magnitude 3.5 range

demonstrate that the IMS is capable of detecting and locating events to small magnitudes in the study region, however they are currently grossly under reported.

The detection of events M_L<4.5 using only BDSN was inferred by determining the percentage of events in the control catalog which had at least one Murdock-Hutt (1983) event detection. A value of 70% representing an upper bound was obtained. It is noted that the inferred detection or in the case of the REB the reporting rates are upper limits because the control catalog is not complete at low magnitudes and in the outlying regions of the study area. Nevertheless, with consideration of the above caveats, this analysis documents the current performance of both the IMS and the BDSN.

Location Capability

The location capability of both the IMS and BDSN was assessed by associating events reported in the BDSN and REB catalogs with the events in the control catalog.

Figure 3a shows the relative locations of the REB events compared to the control catalog. There are several events which have significant mislocations. Review of the REB detailed logs indicates that the events with the greatest mislocations are the smaller of the events in the Hollister, CA area. The solutions for these events utilized auxiliary stations of the IMS in addition to the closest primary stations such as (PFO, PDAR and TXAR). The largest event in the Hollister area in 1995 has a very good location compared to the control (mislocation of only 1.4 km). This event had 21 stations and 21 defining phases and the closest station used was at a distance of 13.6 degrees. It is interesting to note that in comparison to the events near Hollister the events in the Ridgecrest area generally have very good locations. Many of these events are in the low magnitude 4 range and are of comparable size to the seriously mislocated event in Figure 3a. There are several possible causes of the variations in the quality of REB event locations including signal-to-noise ratios, differences in the level of calibration (i.e. some regions may be better approximated by the models used at the PIDC), use of less calibrated regional stations, analyst biases in the form of picking and station selection, and phase interference from multiple events. For example, the Hollister event which the IDC mislocated by 435 km (Figure 3a) was a double event in which a M_L 3.3 was followed by a 4.0. To compound matters there is evidence of a core phase from a teleseism at the PDAR and TXAR arrays.

BDSN only solutions compared to the control catalog are reasonably good (Figure 3b), however there are several regions where greater than average mislocations occur. These regions include the eastern part of the study area and the Ridgecrest region in the southeast. The increased mislocation in these areas reflects the fact that the BDSN network is located mostly to the west of these areas and consequently there is poor azimuthal coverage. Errors in traveltime picks can "throw" the event either toward or away from the network. Areas that are within the network, namely central California along the San Andreas fault system and the north coast region have comparatively very small mislocations.

Figure 4 summarizes the findings on the relative mislocations of the two networks. In this figure the mislocation is plotted as a function of sliding 0.5 magnitude unit bins. The bold line shows the results for the REB. The very large spike in mislocation at magnitudes of 3.4-3.9 is caused by a single event with a 435 km mislocation (e.g. Figure 3a). When this event is removed the short dashed curve is obtained. The large BDSN mislocations evident on Figure 3b are for relatively small events and are averaged out by the large number of events with small mislocations. One exception is a mislocated Ridgecrest event (M_L 5.4) which is the cause of the spike in the BDSN curve on Figure 4. The horizontal dashed curve shows the 18 km mislocation level and represents a mislocation area of approximately 1000 km^2. The BDSN locations are considerably better as expected and are generally below the 18 km mislocation level above magnitude 4.7. Figure 4 is surprising in that it shows that with even a relatively sparse local

network of broadband stations the CD goals at low magnitudes would be difficult to obtain without first calibrating the region.

To test the ability of a sparse network of broadband stations at monitoring a region a subnet of three stations, namely BKS, CMB and WDC was constructed. There are only a few events that have sufficient phase information for this subnet stored on the NCEDC. As Figure 5a shows, the locations of the Tahoe and Ridgecrest events using this subnet are fairly good and give an idea as to what can be expected when monitoring a region outside a sparse network of broadband stations. There are systematic mislocations in these examples which need to be investigated further and a possible improvement is described below. A more thorough study of remote monitoring with broadband stations is needed before any firm conclusions can be drawn, and will be a component of phase two of the project.

BDSN Azimuth Locations

To investigate whether it would be possible to improve upon the BDSN and sparse network location capability we developed a rather simple program to invert the back azimuth information determined from the three-component broadband data. This routine follows the methodology of Bratt and Bache (1988). The present configuration of this program uses only azimuth information. Essentially this method simultaneously minimizes the arc between the azimuth to an initial location and the measured azimuth at several stations. This procedure continues until convergence below a defined minimum residual level is achieved. In our preliminary tests the iterative process was stopped when the change in location reached the 0.01 km level. Figure 5b shows three examples of the azimuth-only location procedure using the very sparse network configuration of Figure 5a. In each case the event was located outside the BDSN subnet, and the initial location was placed at the centroid of the subnet. The gray curves show the iteration tracks of each inversion. The first iteration essentially "throws" the updated location outside of the subnet. Subsequent iterations converge to the final location (<0.01 km change from the previous iteration). The results for the two cases in eastern California are very good. In comparing Figures 5a and 5b it seems that adding azimuth information could help to reduce the magnitude of the mislocations of events in the Tahoe and Ridgecrest areas. The example for the offshore event results in a substantial mislocation which may be due to multipathing of the P_{nl} waves used to estimate the azimuth. We plan to integrate the azimuth minimization scheme into our traveltime location routines and to test the methodology during phase two of this study which will focus on monitoring southern California seismicity with the BDSN network.

Magnitude Estimation Performance

The performance of the PIDC magnitude estimates were evaluated and a preliminary report was provided for consideration at the panel of experts meeting on PIDC magnitudes (May 2-4, 1996, Arlington, VA). The following summarizes the findings of that report.

Table 1 lists the mean differences between magnitude measures reported by various agencies for events in the study area. Also tabulated is the standard deviation of the mean difference and the number of events which entered into each calculation.

Table 1 - Magnitude Comparisons

Comparison	mean difference	standard deviation	number of observations
ML Comparisons			
UCB_{ML}-$PIDC_{mb}$	0.54	0.18	37
UCB_{ML}-$PIDC_{ML}$	0.52	0.22	25
UCB_{ML}-$PIDC_{Ms}$	0.59	0.33	8
Mw Comparisons			
UCB_{Mw}-$PIDC_{mb}$	0.41	0.13	32

UCB_{Mw}-$PIDC_{ML}$	0.36	0.14	22
UCB_{Mw}-$PIDC_{Ms}$	0.23	0.17	8
UCB_{Mw}-UCB_{ML}	-0.14	0.26	32
mb Comparisons			
$NEIC_{mb}$ -$PIDC_{mb}$	0.12	0.10	25

These comparisons reveal that on average the m_b reported in the REB for northern and central California is 0.54 magnitude units lower than the M_L reported by UC Berkeley using local and regional synthetic Wood-Anderson seismograms (e.g. Uhrhammer et al., 1996). Both m_b and M_L are relatively high frequency measures of magnitude. Another interesting observation is that the M_L reported in the REB is 0.52 magnitude units lower than the M_L reported by UC Berkeley. Both three component and array stations of the IMS primary and auxiliary networks are used in the M_L calculations. Most of these stations are beyond the distance range traditionally used in M_L calculations, and in addition, the lack of calibrated station corrections could be one explanation of the low PIDC magnitudes (R. Stead, personal communication, 1996). The auxiliary stations that are often used to calculate magnitudes are located in the great basin and it has been previously noted that there is a significant difference in local magnitudes calculated by UCB and UNR for this region which cannot be explained by differences in attenuation alone (Uhrhammer et al., 1996). It is possible that other regional differences in structure such as scattering and crustal reverberations could be causing the differences in the two local magnitude measures.

Table 1 also illustrates that the REB M_L and M_S estimates are generally lower than both the UCB M_L and M_w. The REB M_s estimates seem to agree better with the UCB M_w values for the larger events however. The comparison between the NEIC determined m_b and the REB m_b reveals a mean difference of only 0.12 magnitude units. The standard deviation indicates that this difference is not significantly different from zero. Therefore it appears that the REB m_b is not being under estimated at the PIDC and the magnitude discrepancy with the control catalog may actually represent a regional bias, or the impact of uncalibrated station corrections.

Conclusions and Recommendations

Unsurprisingly the performance of BDSN was found to be superior to the IMS in characterizing central and northern California seismicity. The purpose of this study, however, is to demonstrate that in order to fully understand the capability of any seismic recording system it is necessary to compare the performance to "ground truth." The results of this study provide some interesting observations regarding the performance of each of the systems. The question that remains to be answered is how well can a sparse network of broadband stations monitor a region outside the network.

First of all we have shown that both the IMS and BDSN currently have limited capability in reporting the small magnitude events of interest. The REB reported only 17% of the control catalog seismicity, and for magnitudes less than 4.5 the BDSN network detected 70% of the events. Above magnitude 4.5 both systems are currently capable of reliably detecting seismicity in the study region.

Second, we have shown that the locations of events using data from both the IMS and BDSN systems are reasonably well determined at larger magnitudes, but for the smaller events there are problems. The REB mislocations seem to increase with decreasing magnitude suggestive of a signal-to-noise cause, however similar sized events in the Ridgecrest sequence were extremely well located. Other possibilities include station outages, changes in the network configuration, analyst picking bias, and choice of stations used in the inversion. Both the IMS and BDSN

systems fail to meet the CD goals at small magnitudes. The poorly located events using BDSN are mostly smaller events (M 3-4) with the noted exception of the M_L 5.4 Ridgecrest event. Incorporating both traveltime and azimuth information in sparse broadband station locations should improve upon this situation and will be the focus of further study. The large difference in IMS and BDSN mislocation levels at small magnitudes (Figure 4) indicates that auxiliary and gamma stations will factor heavily in the regional monitoring of a CTBT.

Third we have shown that PIDC magnitudes are biased low (0.5 magnitude units) compared to UCB estimates. As Table 1 shows the bias is evident even when several different magnitude measures are compared. On the other hand, the m_b reported by the PIDC compares very well with the m_b reported by the NEIC. This suggests that there may be a regional bias toward low m_b in central and northern California. The comparison of PIDC and UCB M_L also shows a 0.5 magnitude unit bias. These observations are important for ascertaining the actual detection and location capability of the IMS in central and northern California. The regionally derived magnitude measures, particularly M_w, provide robust estimates of the relative size and source energy. Based on the results of this study it is recommended that m_b be "calibrated" (i.e. region specific corrections) using regional magnitudes to provide a more meaningful m_b measure which can be used for comparison purposes on a global scale.

Finally, the results of this study indicate that "ground truth" testing of the IMS will be very important in the evaluation of its performance and to also calibrate the system. Broadband stations of the auxiliary and even gamma levels will be very important in regional monitoring, and to use these data effectively will require region by region calibration.

Acknowledgments

This work was supported by the Lawrence Livermore National Laboratory, through the Department of Energy's Comprehensive Test Ban Treaty Research and Development (CTBT R & D) Program, under the Inter-University Transfer (IUT) Agreement No. B291459.

References

Bratt, S. R. and T. C. Bache (1988). Locating Events with a Sparse Network of Regional Arrays, *Bull. Seism. Soc. Am.*, **78**, 780-798.

Murdock, J. H., and C. R. Hutt (1983). A New Event Detector Design for the Seismic Research Observatories, *USGS Open-file Report,* 83-785.

Savage, M. K., and J. Anderson (1995). A Local-Magnitude Scale for the Western Great Basin-Eastern Sierra Nevada from Synthetic Wood-Anderson Seismograms, *Bull. Seism. Soc. Am.*, **85**, 1236-1243.

Staff of the Seismographic Station (1996). Bulletin of the Seismographic Stations - January 1, 1992 to December 31, 1992, *University of California, Berkeley, Seismographic Station,* **62**, 95 pp.

Uhrhammer, R., S. Loper, and B. Romanowicz (1996). Determination of Local Magnitude using BDSN Broadband Records, *In press Bull. Seism. Soc. Am.*

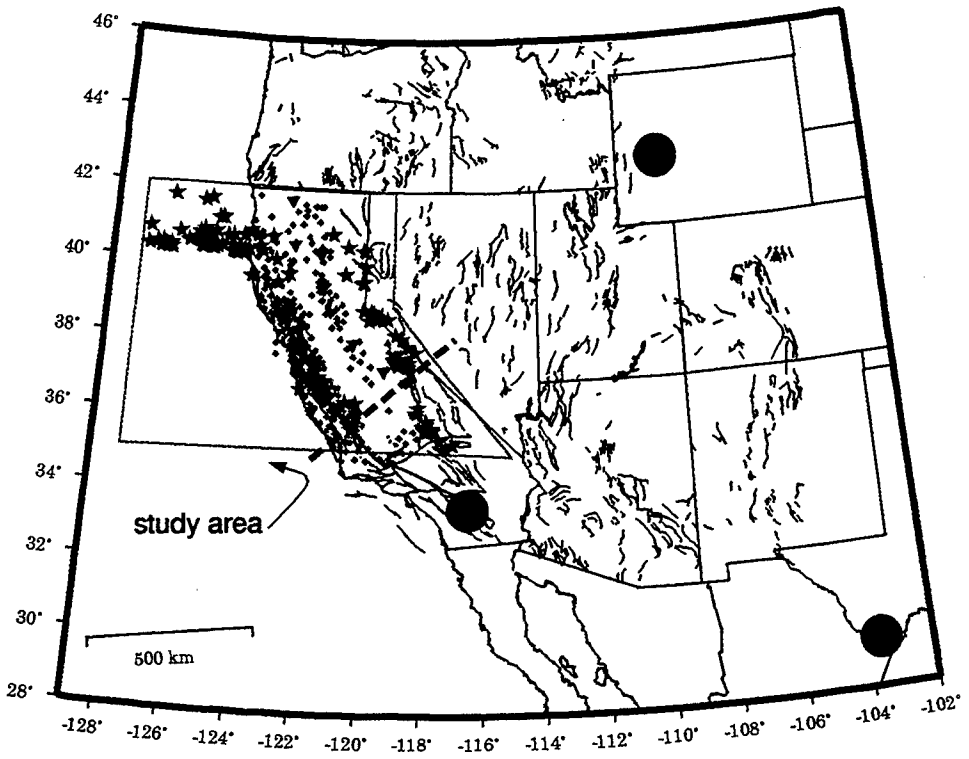

Figure 1. Map showing the location of the study area, GSETT-3 Primary stations (large circles), BDSN broadband stations (triangles), short-period NCSN stations (small circles), and control catalog seismicity (stars). The bold dashed line shows the demarcation between the routine processing regions of UCB and Caltech.

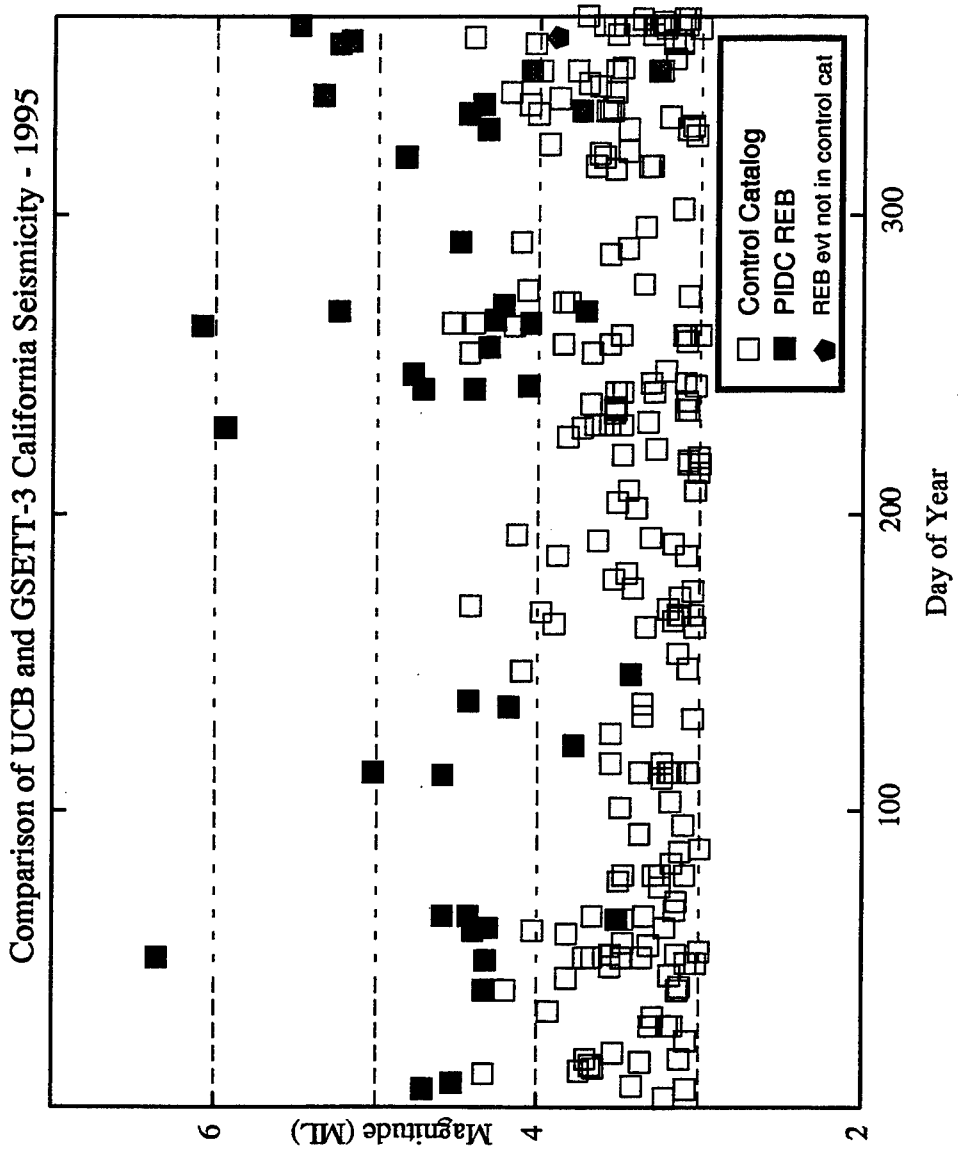

Figure 2. The control catalog seismicity is plotted as a function of both magnitude and day of year. The filled squares show the events which were reported in the PIDC REB. The pentagon is an event in the REB that was missed by both the USGS NCSN and UCB BDSN catalogs.

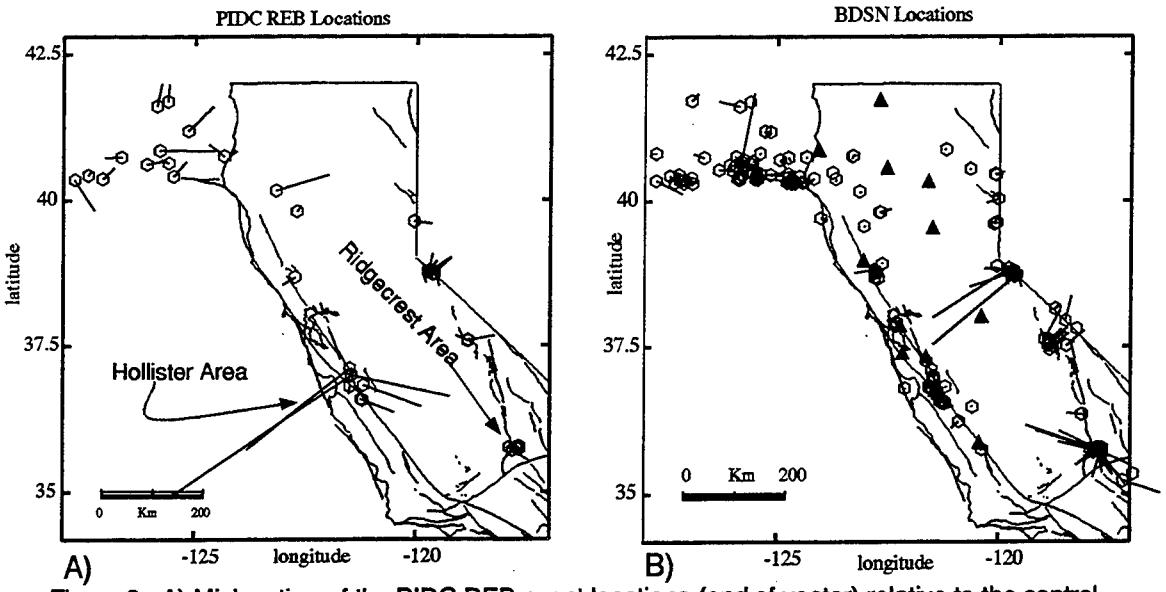

Figure 3. A) Mislocation of the PIDC REB event locations (end of vector) relative to the control catalog (hexagons). B) Mislocation of BDSN only event locations (end of vector) relative to the control catalog (hexagons). BDSN stations are marked by triangles.

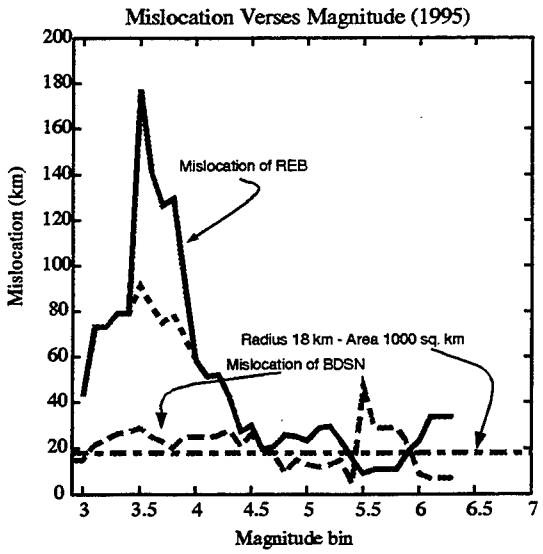

Figure 4. Mislocation relative to the control catalog compared to event magnitude. The average mislocation of events in sliding 0.5 magnitude unit bins for the REB and the BDSN catalogs are compared. The horizontal line shows the 18 km mislocation level.

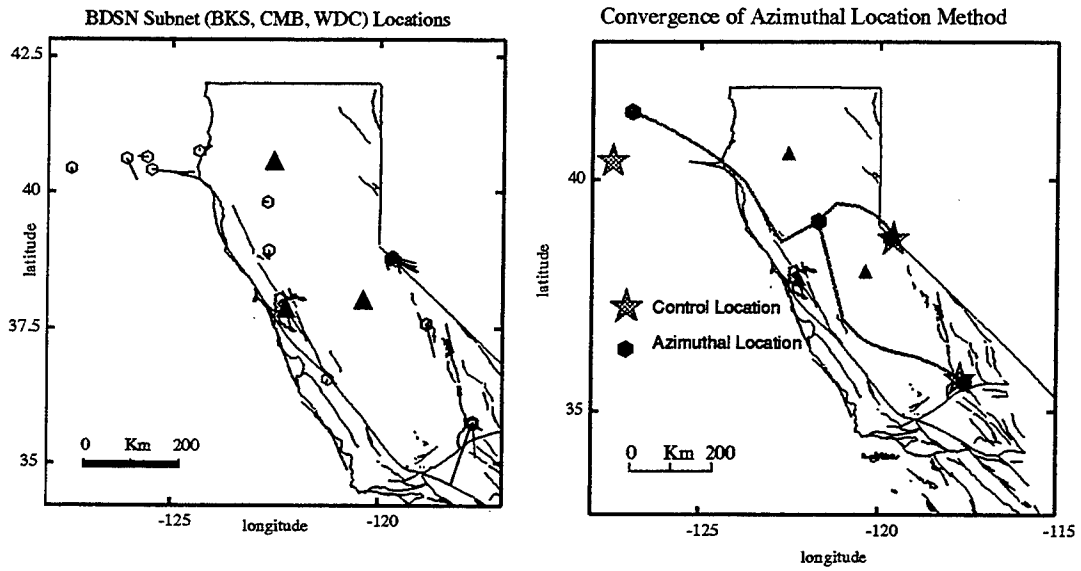

Figure 5. A) Mislocation of events using a sparse subnet of BDSN (triangles). The vector shows the location of the events using only the subnet compared to the control location (hexagons). B) Azimuth only locations for three events using the same BDSN subnet. The stars show the control location and the hexagons show the azimuth-only solution. The hexagon located at the centroid of the subnet is the initial starting location used in each inversion. The gray curves plot the iterative path of the methodology.

SYNERGY AMONG INTERNATIONAL MONITORING SYSTEM TECHNOLOGIES

M.W. Edenburn, M.L. Bunting, A.C. Payne, R.R. Preston, L.C. Trost
Arms Control Studies Department
Strategic Studies and Operational Analysis Center
Sandia National Laboratories

Sponsored by U.S. Department of Energy
Comprehensive Test Ban Treaty Research and Development Program, ST485D

ABSTRACT

Sandia National Laboratories has developed a computer based model called IVSEM (Integrated Verification System Evaluation Model) to estimate the performance of an IMS. The IVSEM project was initiated in June, 1994, by Sandia's Monitoring Systems and Technology Center and has been funded by DOE/NN-20. IVSEM is a simple, "top-level," modeling tool which estimates the performance of a CTBT monitoring system and can help explore the impact of various sensor system concepts and technology advancements on CTBT monitoring. One of IVSEM's unique features is that it integrates results from and accounts for synergy among the various sensor technologies (seismic, infrasound, radionuclide, and hydroacoustic). Specifically, IVSEM estimates the detection effectiveness (probability of detection) and location accuracy of the integrated system and of each technology subsystem individually. The model attempts to accurately estimate the monitoring system's performance at medium interfaces (air-land, air-water) and for some evasive testing methods such as seismic decoupling.

This paper describes the results of an International Monitoring System synergy study using IVSEM. The study compares individual subsystem performance (seismic, infrasound, radionuclide, and hydroacoustic) with integrated system performance for a small, shallow-buried or submerged nuclear explosion. Results from this study show that the integrated system exhibits synergy in that it covers significantly more geographic areas and provides significantly better location accuracy than can any individual subsystem. Results also show that synergy and system performance can be further enhanced by allowing mixed technology detection and location. Allowing mixed technology detection eliminates some detection "holes" and improves detection probability in others. Allowing mixed technology location can reduce location area errors by a factor of ten in some geographic areas.

Key Words: synergy, International Monitoring System, Comprehensive Nuclear Test Ban Treaty, data fusion, sensor system integration, treaty verification, model

INTRODUCTION AND BACKGROUND

An International Monitoring System (IMS) will be an integral part of the Comprehensive Nuclear Test-Ban Treaty (CTBT) presently being negotiated at the Conference on Disarmament. The role of the IMS will be to help ensure verification of compliance with the treaty. The IMS will comprise seismic, infrasound, hydroacoustic, and radionuclide sensor subsystems. These subsystems will work both independently and as an integrated system to detect, locate, and identify nuclear detonations. Working together as an integrated system will be particularly important when conditions make detection most difficult. These conditions include testing of low yield devices, testing at medium interfaces (air-land, air-water), and testing evasively.

Sandia National Laboratories has developed a computer based model called IVSEM (Integrated Verification System Evaluation Model) to estimate the performance of an IMS. We have used IVSEM to illustrate the synergy among monitoring subsystems by applying it to a small, shallow-buried or submerged explosion, and this report will present results of that synergy study.

The IVSEM project was initiated in June, 1994, by Sandia's Monitoring Systems and Technology Center and has been funded by DOE/NN-20. IVSEM is a simple, "top-level," modeling tool which estimates the performance of a CTBT monitoring system and can help explore the impact of various sensor system concepts and technology advancements on CTBT monitoring. One of IVSEM's unique features is that it integrates results from and accounts for synergy among the various sensor technologies (seismic, infrasound, radionuclide, and hydroacoustic). Specifically, IVSEM estimates the detection effectiveness (probability of detection) and location accuracy of the integrated system and of each technology subsystem individually. The model attempts to accurately estimate the monitoring system's performance at medium interfaces (air-land, air-water) and for some evasive testing methods such as seismic decoupling.

IVSEM consists of a FORTRAN core and an IDL graphics interface, which facilitates input and displays results The model was developed for application on a personal computer so that it can be easily transported to other work sites and used by a variety of analysts. Since July, 1995, the model has been reviewed by personnel from DOE, LANL, LLNL, PNL, AFTAC, ARPA, ACIS, ACDA, and the U.S. CTBT delegation in Geneva. The latest version, 1.1, was released to selected government labs, agencies, and their contractors at a user's workshop in July, 1996. The model can estimate system performance for a single event in a few seconds, and it can produce global contour plots of detection probability and location accuracy (in square kilometers) in 5 to 10 minutes when operated on a personal computer with a Pentium processor.

IVSEM makes three sequential computations: 1) individual station detection probabilities are estimated; 2) detection probabilities from individual stations are integrated to estimate system and subsystem detection probabilities; and 3) system and subsystem location accuracy estimates

are made.

Individual station detection probabilities--The model estimates the detection probability for each station within each subsystem. A station's detection probability depends on the event's source strength, the signal's propagation, noise at the sensor, the station's threshold setting, and a statistical test which is specific to the sensor technology used at the station.

System detection probability--Individual station detection probabilities are combined to determine the probability that a specific number of stations within a single technology respond. From these probabilities, we determine the probability that a specific combination of stations respond, for example, a specific system response might be that 1 seismic, 2 infrasound, 1 radionuclide, and 0 hydroacoustic stations respond, and the probability for this specific response might be 0.23. The combination of all possible specific system responses associated with their probabilities is what we call the system detection response. Also associated with each specific system response is a detection effectiveness value for that response. If the detection effectiveness value for a response is 1.0, then that response constitutes a detection. If the detection effectiveness value is 0.0, then that response is not sufficient to constitute a detection. Detection effectiveness values are supplied by the user in the form of a detection effectiveness definition table. The detection effectiveness definition table defines how many responding stations from each technology constitute a detection. Multiplying response probability by response detection effectiveness for each specific response and adding the products over all specific responses results in the system's detection probability. Using a similar process, individual subsystem detection probabilities are also estimated.

System location accuracy--Stations which respond to the event are used in a statistical location analysis to estimate the system's location accuracy in square kilometers. Each station has an associated bearing angle or signal arrival time which the model assumes are random variables with Gausian distributions. The statistical location analysis uses 100 random repetitions. Each repetition randomly selects stations to participate in a location set based on each station's detection probability, assigns each station in the set a randomly selected station-to-event bearing angle (infrasound stations) or signal arrival time (infrasound, seismic, and hydroacoustic stations) and, from these, estimates an event location and a location error. From the 100 random repetitions, the 90th percentile error is selected as IVSEM's location accuracy estimate. This location accuracy process is performed for the system and for each individual subsystem.

SYNERGY STUDY OBJECTIVE AND ASSUMPTIONS

The study's objective is to illustrate synergy among the IMS technologies in both detection and location. Our working definition of synergy is--agents or elements working together to accomplish an effect which none can accomplish individually. This definition is our

condensation of definitions from **The American Heritage Dictionary, Webster's Third International Dictionary, and Webster's New World Dictionary, College Edition**. The agents or elements in the definition refer to individual sensor subsystems in the IMS: seismic, infrasound, radionuclide, and hydroacoustic. Working together as a system, the subsystems can accomplish more that they can accomplish working individually--the system can detect events which individual subsystems cannot detect and it can locate events more accurately than can any individual subsystem.

There are two types of synergy we will consider in describing how IMS subsystems interact. The first type of synergy is what we will call "supplementary synergy." Working independently, individual subsystem will detect events in some geographical areas or media (by geographical area we mean latitude, longitude, and altitude or depth) but not in others. Synergy is achieved if some subsystems cover areas and media that others do not. If detection by any of the four individual subsystem's working independently constitutes detection by the system, then the system will detect events in more areas than will any individual subsystem. This is what we will call supplementary synergy. We implemented supplementary synergy for detection in IVSEM by specifying that detecting an event requires detection by at least three stations of a single nonradionuclide technology or detection by at least one radionuclide station. That is, detections by three or more seismic, or three or more infrasound, or three or more hydroacoustic, or one or more radionuclide stations constitutes detecting an event. This specification was made in IVSEM's user defined detection effectiveness definition input table. We implemented supplementary synergy for location in IVSEM by having IVSEM select the lowest location error estimated for any of the four individual subsystems. For supplementary synergy, we do not mix types of stations when forming a detection or making a location accuracy estimate.

The second type of synergy is what we call "complementary synergy." For this type of synergy, results from individual stations can "cross the subsystem boundary" and work together as mixed station results to form detections or location estimates. To implement complementary synergy for detection in IVSEM, we specify system detection to be detection by any three or more nonradionuclide stations or any one or more radionuclide stations. That is, system detection consists of detection by three seismic stations, or two seismic plus one infrasound, or one seismic plus one infrasound plus one hydroacoustic, or any other combination that adds up to three or more. This specification was made in IVSEM's user defined detection effectiveness definition input table. For location accuracy, complementary synergy is implemented by allowing stations of all types (except radionuclide) to participate together in the location accuracy estimate.

For this study, we compared results from IVSEM using both types of synergy. We assumed a small, shallow buried or submerged nuclear detonation as the event. The event was selected to challenge the monitoring system in that source strength for seismic, infrasound, hydroacoustic, and radionuclide signals were reduced because of the event's shallow depth. Other assumptions for the study are discussed below.

Seismic--The subsystem is comprised of the 50 primary and 120 auxiliary stations specified by Conference on Disarmament document # CD/NTB/WP.330. In IVSEM, only the primary stations are used for detection. The auxiliary stations are used in the location accuracy estimate if the system detects an event. Explosions are assumed to be fully coupled in rock except where stated otherwise. Explosions in the oceans are assumed to be super-coupled which results in an effective magnitude increase of 0.8. The system is assumed to be a mature, well calibrated network in all areas. Arrival time errors, used in the location accuracy estimate have two components: a 0.75 sec. arrival time error and a 0.15/(SNR-1) "model" error. (SNR is signal-to-noise ratio.) These arrival time errors were suggested by John Claassen (Sandia National Laboratories).

Infrasound--The subsystem is comprised of the 60 stations specified by Conference on Disarmament document # CD/NTB/WP.330. We ran the model with 50 km altitude winds typical of October. October is one of the worst months for infrasound detection. Signal arrival time errors used in the location accuracy estimate are assumed to be 2% of travel time. This error was suggested by Rod Whitaker (Los Alamos National Laboratory) as having some, although sketchy, historical NTS test basis. Station-to-event bearing errors are assumed to depend on station-to-event distance as follows: 1.8° between 0 and 3000 km; increasing linearly to 7.0° between 3000 and 10,000 km; increasing linearly to 20.0° between 10,000 and 15,000 km; and, 20.0° beyond 15,000 km. These bearing errors were suggested by Dean Clauter (Air Force Technical Application Center).

Hydroacoustic--The subsystem is comprised of the 6 hydroacoustic and 5 island "T-phase" stations specified by Conference on Disarmament document # CD/NTB/WP.330. Arrival time errors used in the location accuracy estimate are assumed to have two components: a 1 sec. "pick" error (5 sec. for "T-phase" stations) and a travel time error equal to 0.02 multiplied by the square root of station-to-event distance. "Pick" error refers to the accuracy with which arrival time can be picked from a signal profile. These signal arrival time errors were suggested by Dave Harris (Lawrence Livermore National Laboratory) and are very preliminary.

Radionuclide--The subsystem is comprised of the 80 stations specified by Conference on Disarmament document # CD/NTB/WP.330. We ran the model with typical October winds and allowed up to 10 days for detection. October is one of the worst months for radionuclide detection. We assume that all stations are capable of detecting both xenon and barium. Xenon sensitivity is 1 mBq/m^3, and barium sensitivity is 30 uBq/m^3. We allowed the model's built-in algorithms, which depend on depth, to compute vent fractions. The vent fraction for the shallow buried or submerged case being considered was 100% for free xenon, 12% for barium and other aerosols on land, and 65% for barium and other aerosols in the ocean. We also assumed that there was no rain.

RESULTS AND CONCLUSIONS

Figure 1 shows detection probability for each of the individual labeled subsystems. Detection requires detection from 3 stations within the subsystem. Each subsystem has significant holes in its coverage. Figure 2 shows system detection for both supplementary and complementary synergy. The system detection requirement for supplementary synergy is that three or more stations of the same type, or one or more radionuclide stations, must detect the event. The system detection requirement for complementary synergy is that any three or more stations, of any type except radionuclide, or one or more radionuclide stations detect the event. System detection for either type of synergy is significantly better than detection for any subsystem acting alone. Complementary synergy operation gives better detection results than supplementary synergy because it integrates the subsystems by allowing information from stations of different technology types to cross the subsystem boundary and work together to form a system detection. Figure 3 further illustrates supplementary synergy by showing the effects of removing individual subsystems under supplementary synergy. Removing a subsystem decreases system performance except in the hydroacoustic case. The hydroacoustic subsystem does not contribute to detection because the seismic subsystem completely covers detection in the ocean areas due to signal supercoupling for submerged events.

Figure 4 shows estimated location accuracy for each of the individual labeled subsystems. Radionuclide results are not shown because they fall outside plotting range. Figure 5 shows location accuracy for the system. The supplementary synergy figure shows results when the smallest location error among subsystems is used, but mixed stations are not allowed to form a location. The complementary synergy figure shows results when stations of different technology type can be combined to form a location. Notice that complementary synergy gives significantly lower errors than supplementary synergy in many geographic areas, particularly in the oceans. This is a result of allowing hydroacoustic stations to participate in location. Figure 6 further illustrates supplementary synergy by showing what happens to location accuracy when individual subsystems are removed under supplementary synergy. Removing the seismic subsystem causes a significant increase in location error, illustrating the importance of the seismic subsystem to location. Removing the radionuclide subsystem does not change supplementary synergy location accuracy. This is because the radionuclide subsystem does not contribute to system location accuracy in IVSEM.

To conclude, the integrated system exhibits synergy in detection and location because different sensor technologies cover different geographical areas; thus, the integrated system covers more areas than can any individual subsystem. Synergy and system performance can be further enhanced by allowing mixed technology detection and location.

Figure 1. Detection Probability for a Small, Shallow Buried or Submerged Event

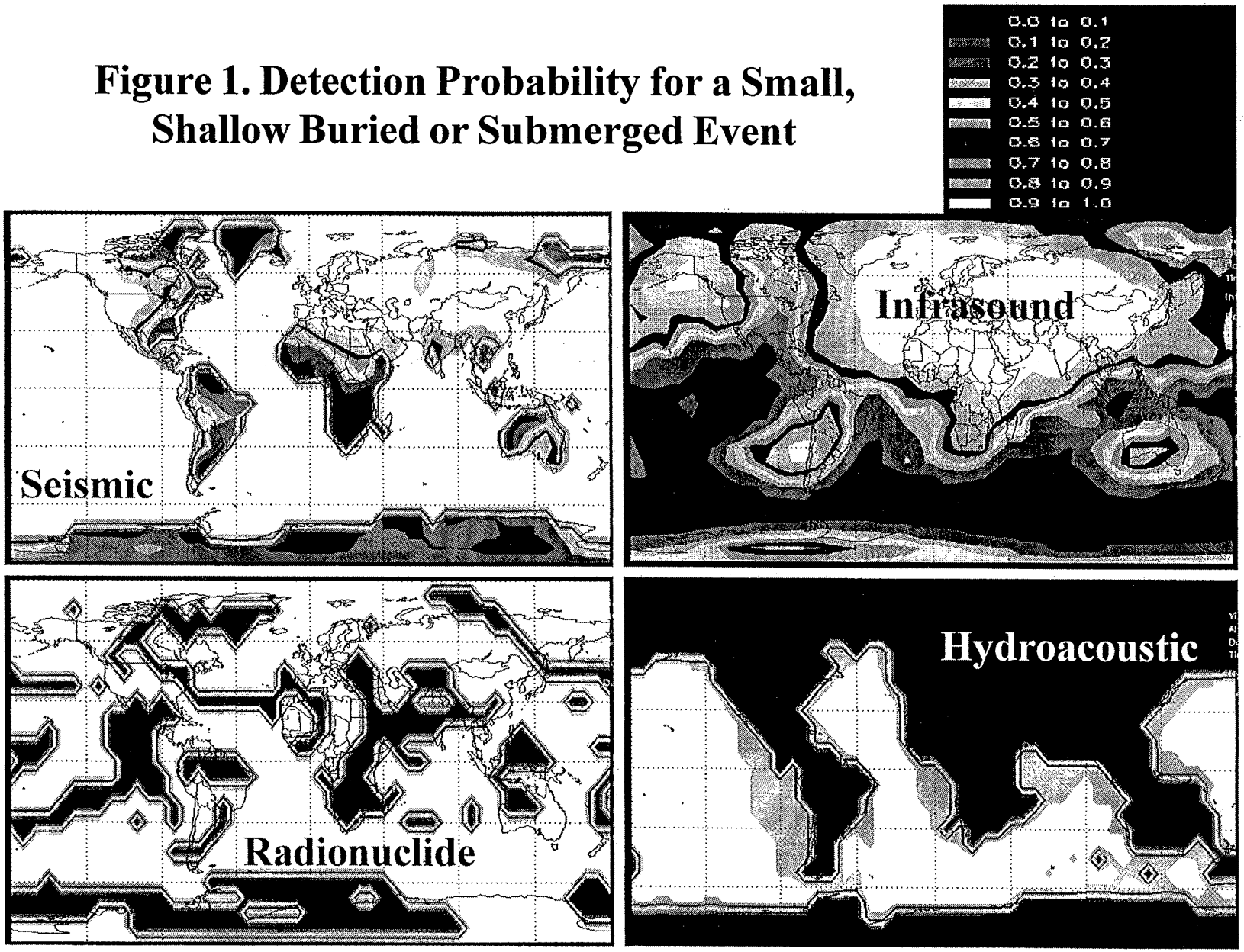

Figure 2. System Detection Probability for a Small, Shallow Buried or Submerged Event

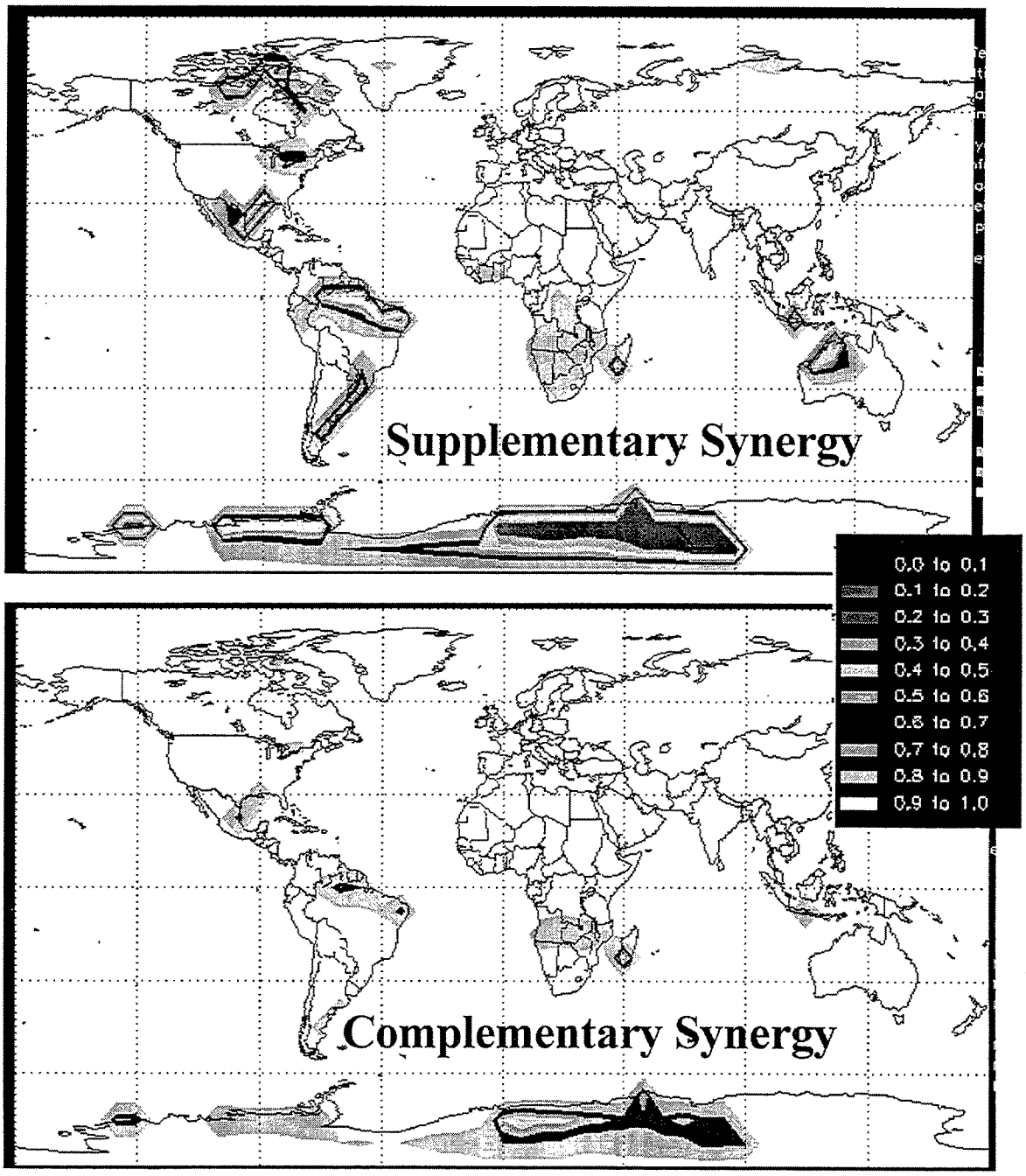

Figure 3. System Detection Probability for a Small, Shallow Buried or Submerged Event when One Subsystem is not Utilized

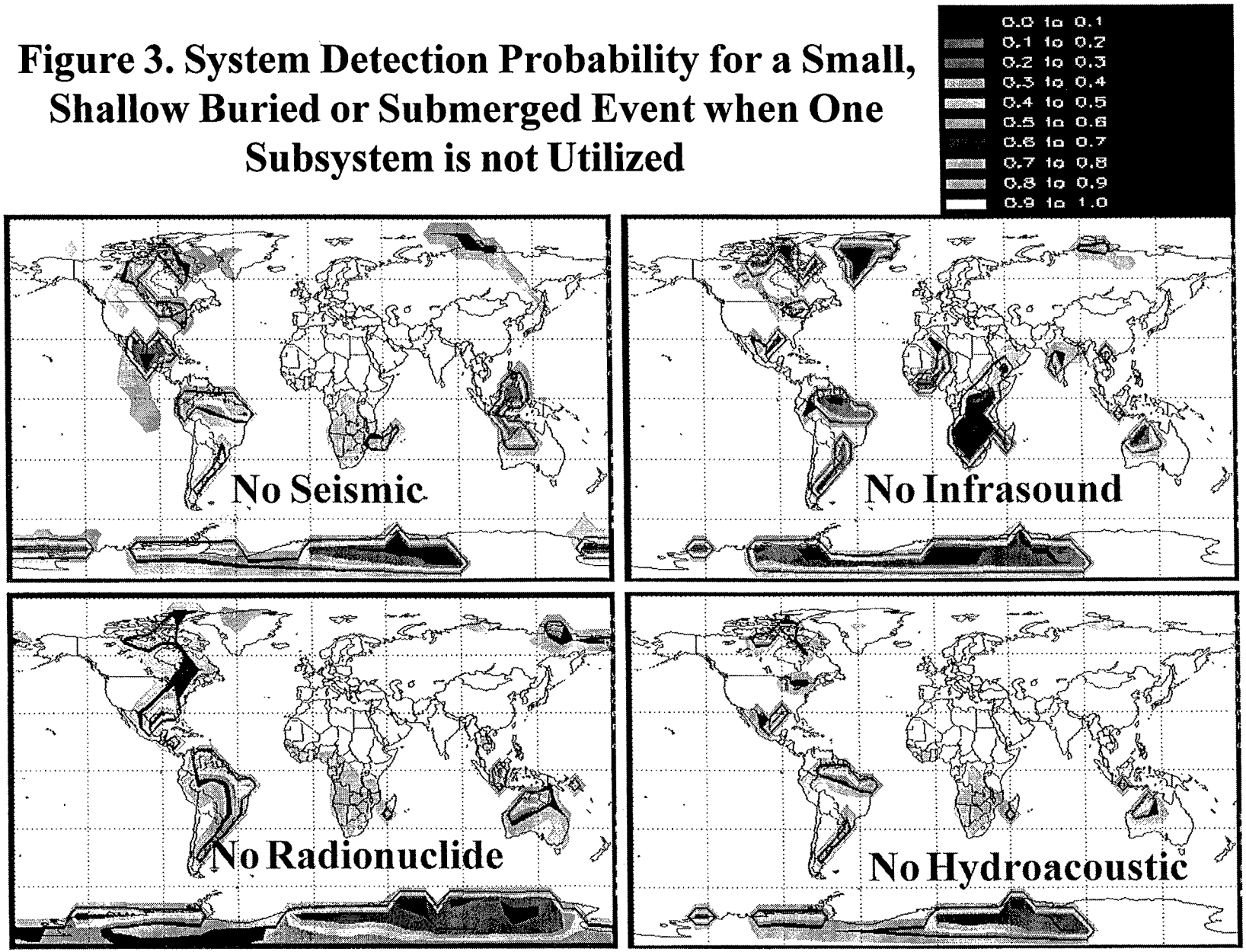

Figure 4. Location Accuracy in Square Kilometers for a Small, Shallow Buried or Submerged Event

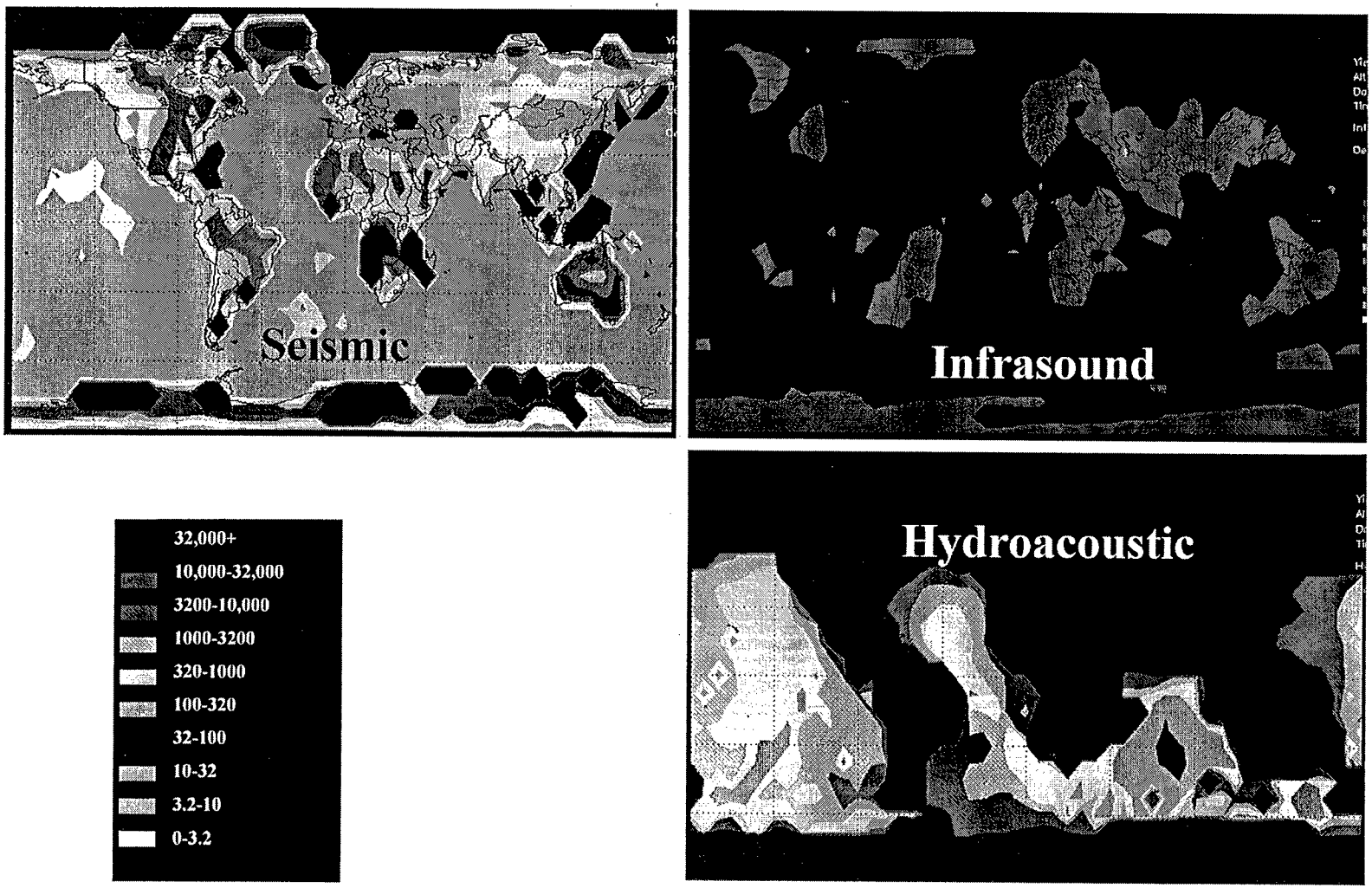

Figure 5. System Location Accuracy in Square Kilometers for a Small, Shallow Buried or Submerged Event

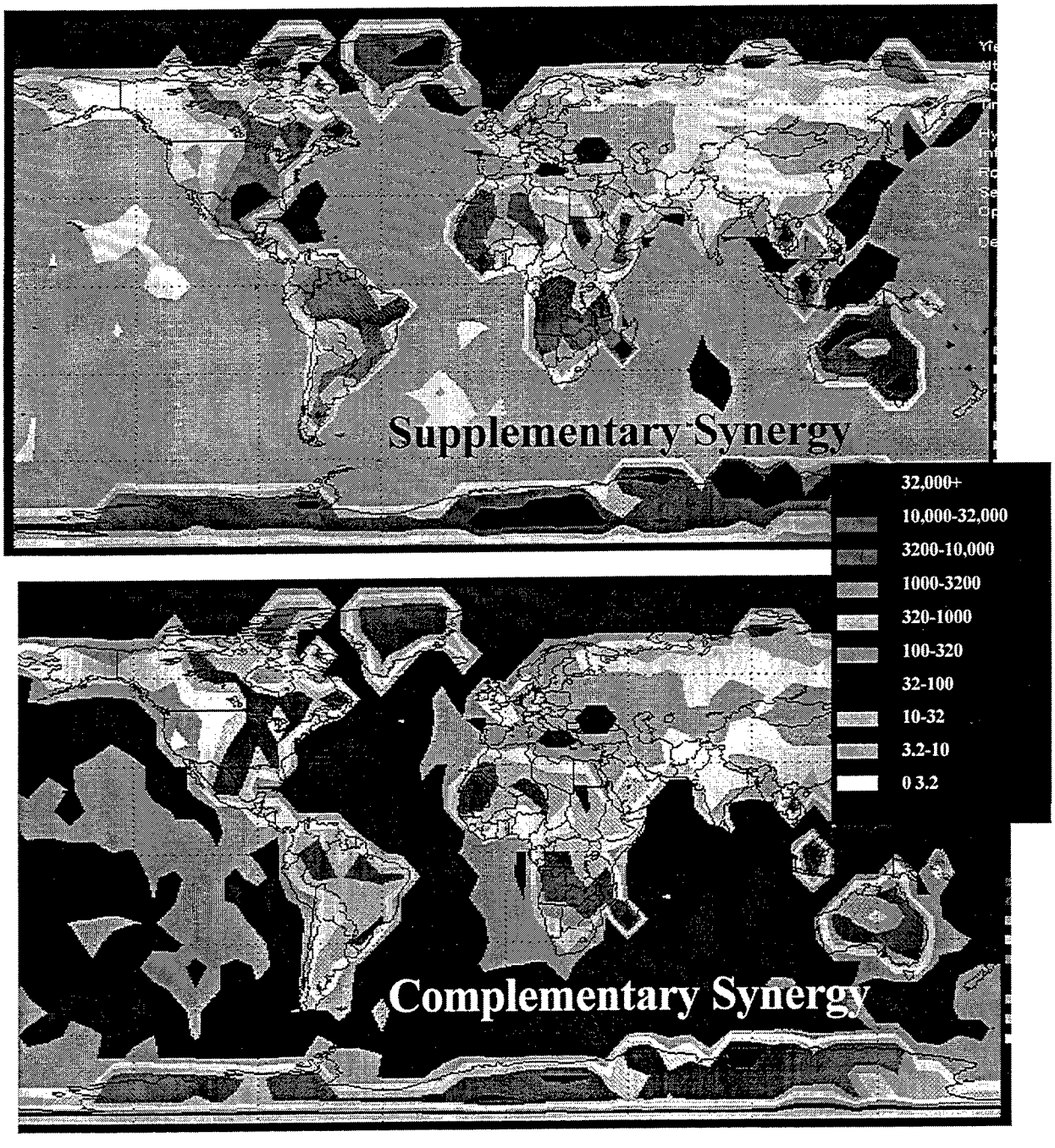

Figure 6. System Location Accuracy in Square Kilometers for a Small, Shallow Buried or Submerged Event when One Subsystem is not Utilized

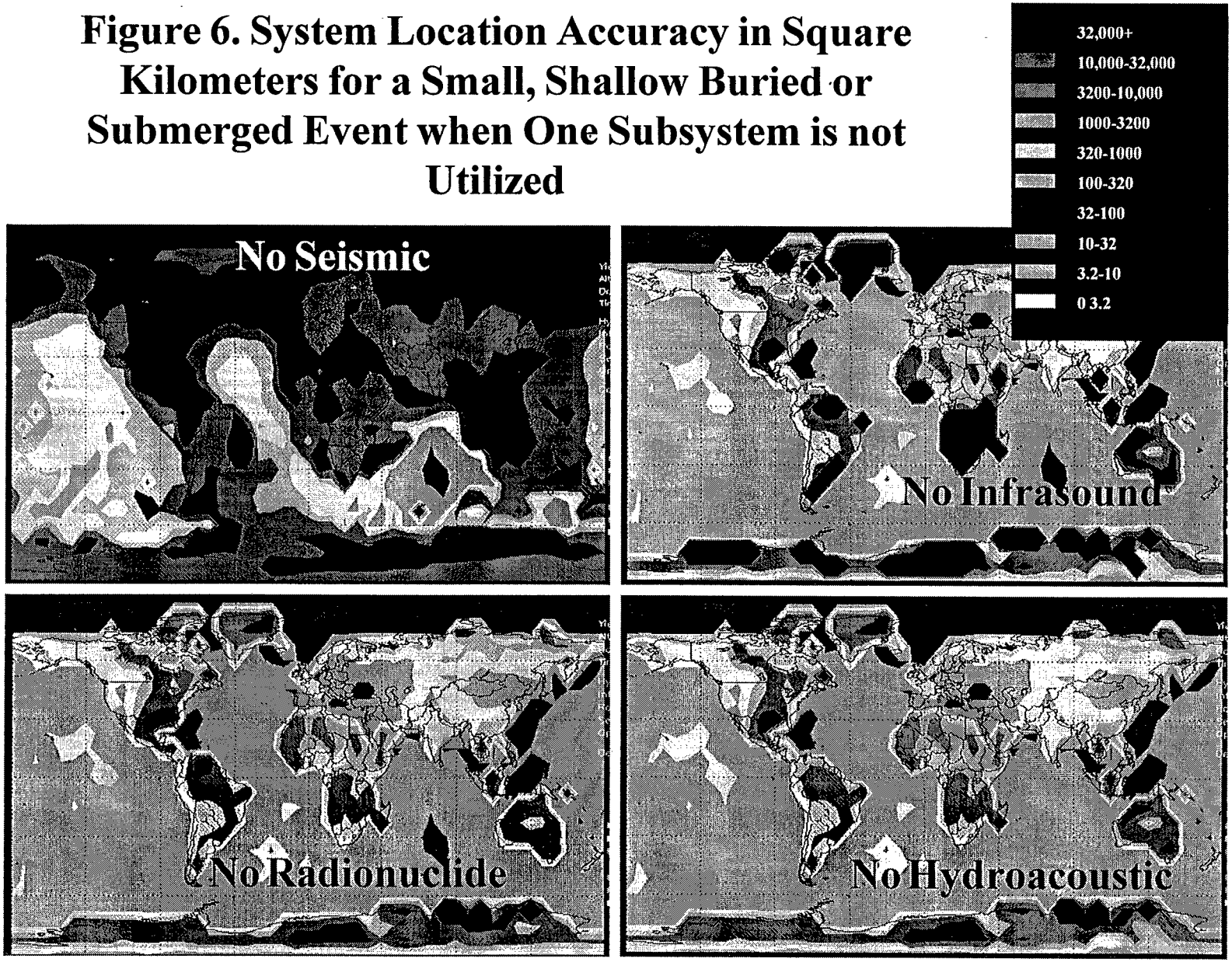

Understanding seismic wave propagation at regional and teleseismic distances

B.L.N. Kennett
Research School of Earth Sciences, Australian National University, Canberra ACT 0200, Australia

Grants: F49620-94-1-0022, F49620-94-1-0110
Sponsored by: AFOSR

ABSTRACT

An individual three-component seismogram contains a large amount of information about the character of the source from which it was generated and the propagation path through the Earth. The major objective of this research program has been the development of techniques which can exploit the information content of regional and teleseismic seismograms to improve both the characterisation of events and knowledge of seismic structure on regional scales.

On regional scales our emphasis has been on systematic mapping of large continental areas using Australia as a testbed for techniques which should be able to be transferred to other regions. The work depends on the use of both the body wave and surface wave components of seismograms at both regional and teleseismic distances. In addition we have undertaken numerical studies of the influence of complex structure on high frequency seismic phases at distances up to 1000 km to understand the conditions which lead to the blockage of crustally guided waves such as Lg.

A significant innovation is the use of a new style of inference scheme for the characterisation of seismic sources by automating the processes of event recognition and identification. Information on the character of sequence of phase detections is combined so as to associate the arrivals associated with an event characterised by an approximate epicentral distance, azimuth and depth.

These studies contribute to the support of a verification regime for a CTBT, by providing improved knowledge of regional structure in different tectonic environments, by improving understanding the influence of complex structure along the propagation path on phases at regional distances, by improving automatic processing of seismic information and by more effective assessment of the location of events compared with major seismic zones to aid in discrimination techniques.

Keywords

Waveform tomography, teleseismic receiver functions, pseudospectral calculations, Lg blockage, phase detection, event characterisation, subduction zones

B.L.N. Kennett

OBJECTIVE

An individual three-component seismogram contains a large amount of information about the character of the source from which it was generated and the propagation path through the Earth. The major objective of this research program has been the development of techniques which can exploit the information content of regional and teleseismic seismograms to improve both the characterisation of events and knowledge of seismic structure on regional scales.

On regional scales our emphasis has been on systematic mapping of large continental areas using Australia as a testbed for techniques which should be able to be transferred to other regions. The work depends on the use of both the body wave and surface wave components of seismograms at both regional and teleseismic distances. The work has combined waveform inversion for surface waves (including higher modes) to determine three-dimensional shear wave structure with the use of teleseismic receiver functions which can provide useful constraints on crustal and uppermost mantle structure. In addition we have undertaken numerical studies of the influence of complex structure on regional seismic phases, to understand the mechanism whereby energy is dissipated from significant phases. The studies have included a simulation of the blockage of the Lg phase by a graben structure such as has been observed in the North Sea.

The major aim of our work with teleseismic events is to improve the characterisation of seismic sources by automating the processes of event recognition and identification. We have been able to develop a new style of inference scheme based on artificial intelligence techniques to combine information on the character of sequence of phase detections so as to associate the arrivals associated with an event characterised by an approximate epicentral distance, azimuth and depth.

We have also undertaken a systematic study of the earthquake distribution in subduction zones to provide effective parametric descriptions for the zones both for structural studies and for incorporation into the knowledge base of a verification regime. Such a representation will allow the rapid comparison of event locations with the major seismic zones around the world.

These studies are designed to contribute to the support of a verification regime for a CTBT in a number of ways. Firstly, by providing improved knowledge of regional structure in different tectonic environments and developing representations of 3-D structure which can be used to incorporate regional corrections into event location and characterisation schemes. Secondly, to understand the influence of complex structure along the propagation path on phases at regional distances (out to 1000 km) to understand the mechanism of phase blockage for crustally guided waves. Thirdly, by improving the capacity of automatic processing of seismic information to minimise the effort required for preliminary event location particularly with a sparse global network. Fourthly by more effective assessment of the location of events compared with major seismic zones to aid in discrimination techniques.

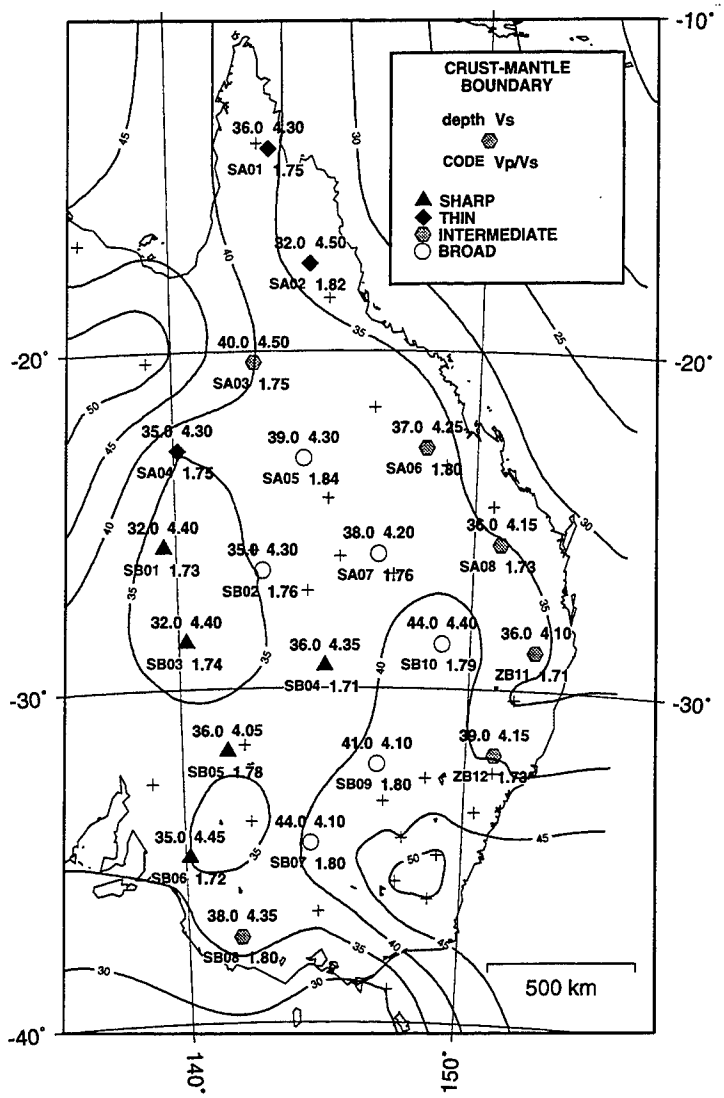

Figure 1. The depth and character of the crust-mantle boundary beneath eastern Australia determined from analysis of teleseismic receiver functions.

RESEARCH ACCOMPLISHED

Determination of regional structure

We have been working on a variety of techniques for the determination of seismic structure in the crust and upper mantle on regional scales. This work has included the analysis of the S body-wave and surface waves on broadband records via waveform tomography in both central Asia and Australia. A effective inversion algorithm due to Nolet (1990) is based on waveform fitting on individual paths to determine the average structure along the paths and then the three-dimensional S wave structure is extracted by a linear inversion of the multiple constraints provided by the various path averages. The analysis of 1200

seismograms recorded in eastern Australia from arrays of broad-band seismic stations has recently been accepted for publication (Zielhuis & van der Hilst 1995). The inter-station spacing of 400 km is sufficient to give good resolution of structure. There is sufficient regional seismicity that adequate data was assembled in less than a year to allow a detailed inversion. In other zones a longer recording duration is likely to be required but this approach provides an efficient way of mapping large continental areas.

In addition to the waveform tomography, we can exploit receiver specific information to build up an improved picture of the crustal and uppermost mantle structure which are not well resolved using longer period data. A valuable tool has been the use of teleseismic receiver functions in which the influence of the source is minimised by deconvolving the radial component of the P portion of a teleseism with the corresponding segment of the vertical component. The resulting receiver function is most sensitive to S wave structure but includes some information on P wave speed. We have developed an inversion procedure based on genetic algorithms which yield very stable estimates of crustal velocity structure. the information compares well with existing data (where available) but has significantly improved knowledge of crustal structure in eastern Australia (see figure 1).

The use of an array of portable broad-band instruments represents a cost effective approach to extending information on regional structure because a variety of techniques can be applied to the same data.

Influence of Complex Structure on Regional Phases

The pattern of seismic wave propagation at distances out to 1000 km from the source is marked by a number of distinct seismic phases with quite complex dependence on seismic structure. One of the most prominent phases, Lg, is largely composed on waves trapped in the crustal waveguide with multiple reflections at the Earths surface and the crust-mantle boundary.

Numerical modelling of the seismic wavefield provides a direct means of investigating the nature of the propagation processes giving rise to the observed arrivals and the influence of source type and depth on the regional wavefield. The calculations have been carried out using the pseudospectral method which allows the calculation of propagation in extended models with high computational efficiency.

Figure 2 shows a sequence of snapshots of the development of the regional wavefield from an explosive source in a model representing the graben structure in the North Sea which combines a crustal thinning with a thick sedimentary basin. The calculations include allowance for attenuation in the sediments. The S wave arrivals are indicated in white and the P wave arrivals in black. In the 56 s window the Lg train is well developed before it impinges on the graben and the Pn wavefront can be discerned approaching the end of the window. In the 70 s frame P wave conversions from the Lg energy can be seen in the sediments and the coherence of the Lg arrival is being disrupted. By the 126 s frame there is little organised S wave energy in the crust and seismograms confirm that the Lg phase has been largely eliminated in its passage trough the graben. The elimination of this

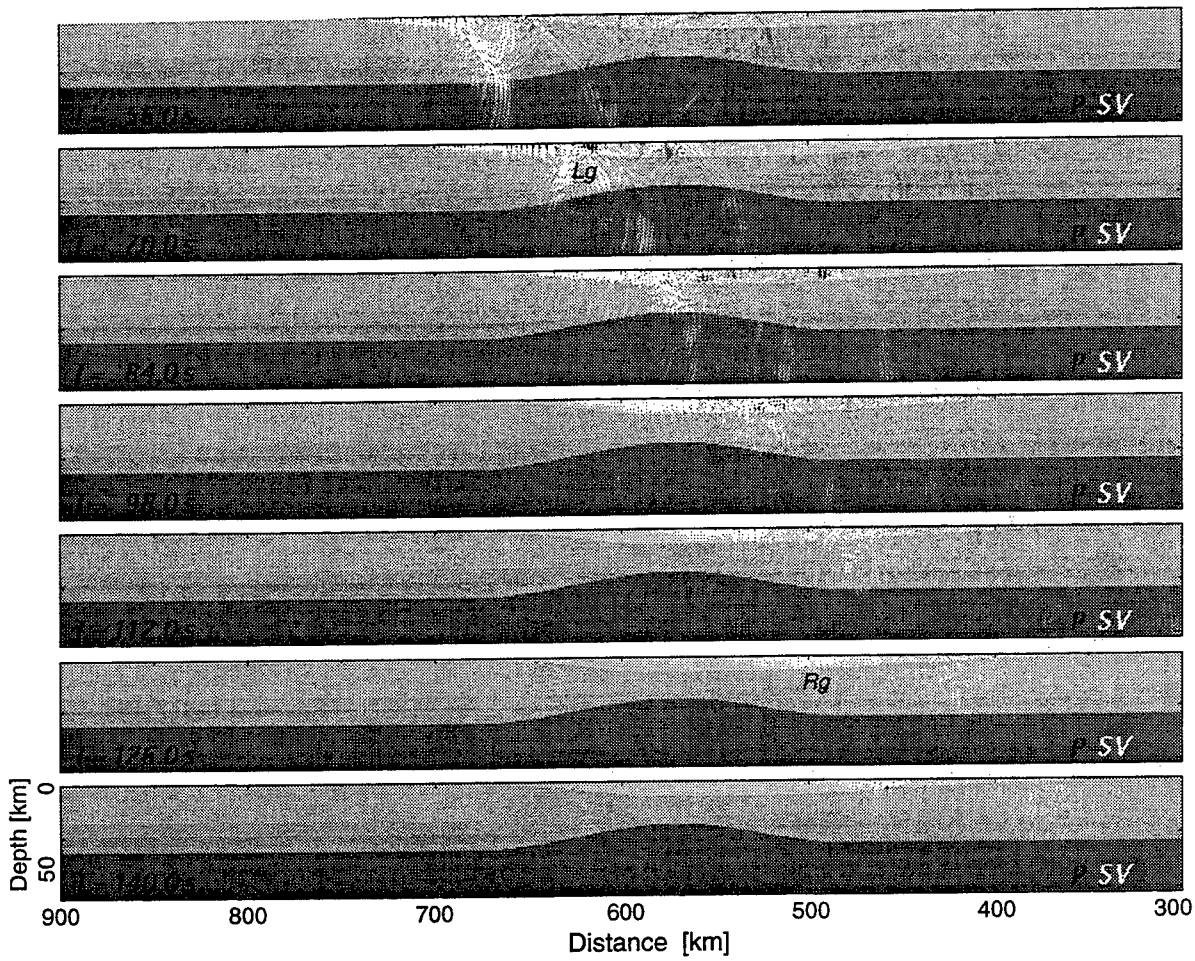

Figure 2. Numerical simulation of seismic waves from a explosive source crossing the graben structure in the North Sea. Note the suppression of the Lg arrival.

major arrival is not due to one single effect but rather the interaction of the squeezing of the wavefield from the crustal pinch which enhances penetration into the attenuative sediments.

Automated Event Recognition

The location of seismic events can be improved if accurate picks can be assigned for later seismic phases, which requires both the detection of an arrival and the recognition of its character.

For smaller seismic events it is desirable to have a phase detection system which is sensitive to the amplitude and frequency of the seismic trace and which can detect subtle changes in wave character. We have therefore found it helpful to supplement an adaptive STA/LTA detector with averaging intervals depending on local frequency (Tong 1995)

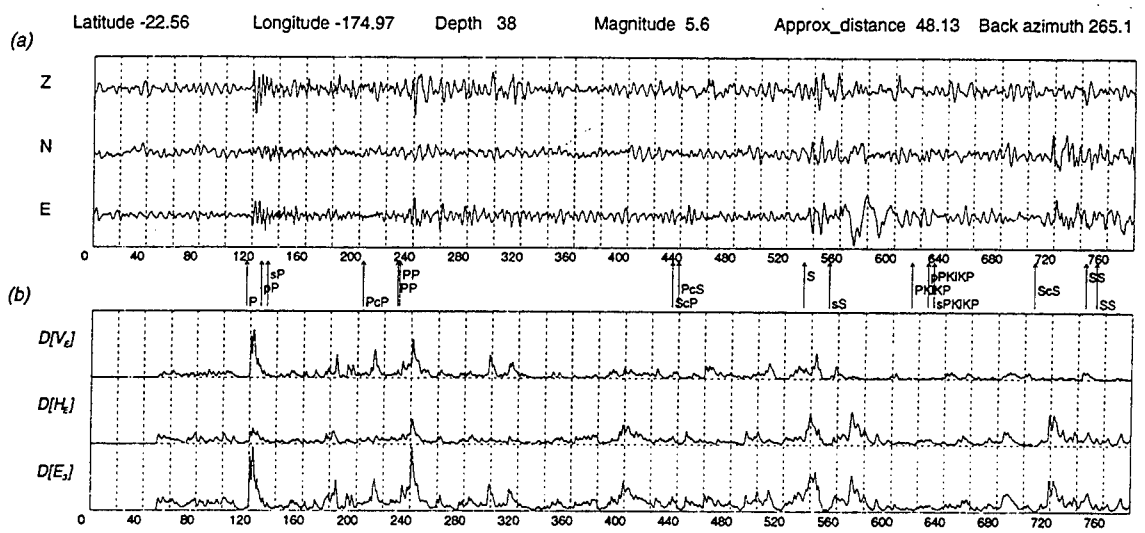

Figure 3. (a) Broad band seismogram for an event in the Tonga subduction zone recorded on a portable seismic recorder in northern Australia. The arrows indicate the expected arrival times of seismic phases from the *iasp91* travel times. (b) the application of phase detectors based on the energy on the vertical component (V_E), the energy in the horizontal plane (H_E) and the total energy (E_3). The strength of the different detectors provides information on the character of the seismic phase. The timing lines are at 10 second intervals

content with either a complexity measure based on the length of the seismic trace between samples or a change in the nature of the coefficients in an AR representation of the data.

The detection and characterisation of seismic arrivals can be combined by analyzing the energy content of 3-component seismic traces as a function of time (Tong & Kennett 1995). A comparison of the energy in the vertical component to the energy in the horizontal plane can be used to separate P and S arrivals and to form the basis of phase-specific detectors (see Figure 3).

The full set of parameters associated with each detection form the basis of an event-recognition system suitable for use in real time. The procedure looks for a combination of key P and S phases and uses the differential time between the phases together with other attributes of the seismic phases. A set of hypotheses on the nature of the phases as well as the depth and epicentral distance of the event are tested to characterise the event. A new technique built on procedures from artificial intelligence ("an assumption tree") is used to provide a rapid means of characterising information into pattern classes even where information is incomplete. As soon as as a contradiction arises between the observed information and the current hypothesis that branch of reasoning is abandoned. This approach provides an effective means of recognizing seismic event patterns and to translate heuristic human experience into an automated environment. An advantage of the approach is that the knowledge bank is maintained outside the testing algorithm so that it is relatively easy to add extra information. The final result is an assessment of the likelihood of different hypotheses based on the fit to the character of all available information.

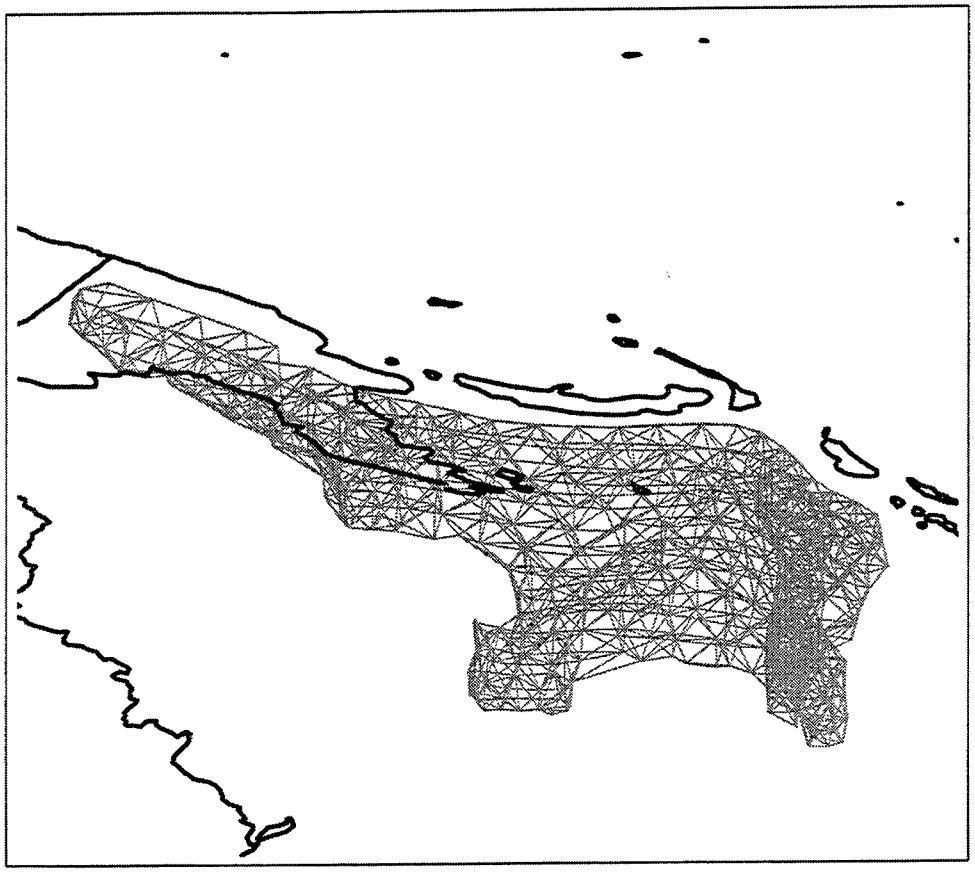

Figure 4. A 3-D tesselation of the New Britain slab viewed from the southeast. The slab shape is derived from the regional seismicity.

The phase recognition scheme makes use of a wide range of phases, and for a single station can give an effective preliminary location particular when a reasonable azimuth can also be estimated from the P onset. Where multiple traces have recorded the same event the consistency of he results are good.

Delineation of seismic subduction zones

Seismic tomography attempts to delineate regions of anomalously high or low seismic wavespeed, based primarily on the arrival times of various seismic waves measured from seismograms. From these observations a model for the structure of the Earth is built to match the observed patterns of the arrival times. Most of the well resolved (large scale) structures in the Earth's upper mantle correlate well with surface geology or tectonics and be adequately described with a 2-D parametrisation. However, many of the smaller scale, less well resolved features are oblique to the Earth's surface. The most notable examples

are subducting slabs, lithospheric plates sinking into the mantle beneath island arcs and orogenic mountain belts, for which a 3-D parametrisation is required.

Figure 4 shows an application of irregular parametrisation in 3-dimensions to the delineation of the subduction zone beneath the island of New Britain in Papua New Guinea. The surface of the slab is represented by a set points which are connected by Delaunay triangulation and the resulting grid is viewed in perspective from the southeast. The deep parts of the slab to the right lie beneath Bouganville Island and the eastern part of New Britain. The shallow parts on the left underlie the volcanoes along the northern shore of New Guinea. The slab volume has been defined from the prolific seismicity of the region.

Similar 3-D grid constructions have now been developed for all the main subduction zones around the world. These three-dimensional representations of slab structure provide a very useful summary of the majority of world seismicity and so allow a quick assessment of the location of an event in verification studies. Further, the slab representations can be included in tomographic studies of upper mantle structure with the shape represented through the complex parametrisation.

CONCLUSIONS AND RECOMMENDATIONS

For regional studies we have been able to demonstrate that it is possible to characterise a broad continental area by using a deployment of portable broad band seismic recorders. The 3-component seismograms can then be exploited via waveform tomography and receiver function analysis. In addition the high frequency waves from local sources can also be analysed to confirm the nature of crustal structure.

Numerical simulation using modelling techniques such as the pseudospectral method can carry wavefields hundreds of wavelengths away from the source and so provide information on the wave that changes in crustal structure interact with the wavefield. The circumstances that lead to Lg blockage will generally involve both a disruption of the crust-mantle boundary and the presence of sediments.

For events at distances of 10° or more away from a broad-band receiver we have been able to build an automated processing system which recognises and characterises an event by the pattern of key P and S phases and secondary phases. A novel inference system enables the incorporation of a knowledge base of phase attributes which can be used in assessing the likelihood of phase associations. The output of the procedure is a characterisation of the event in terms of detected arrivals and an estimate of the epicentral distance and depth, which should be of value for forming preliminary event locations for a sparse global network.

We have also developed a 3-D parametrisation of all the major subduction zones, based on their seismicity patterns which should be of value in testing hypotheses about event location in a verification regime as well as being of use in the delineation of upper-mantle structure.

Acknowledgements

This report is based on the work of a number of members of the Seismology Group, notably Alet Zielhuis, Rob van der Hilst, Takuo Shibutani, Takashi Furumura, Oli Gudmundsson, Malcolm Sambridge and Cheng Tong

References

Kennett B. L. N., 1995. Event location and source characterization, in *Monitoring a Comprehensive Test Ban Treaty*, eds E. S. Husebye & A. M. Dainty, Kluwer, Dordrecht.

Tong C. (1995). Characterization of seismic phases - an automatic analyzer for seismograms, *Geophys. J. Int.*, **123**, 937-947.

Tong C. and B. L. N. Kennett (1995). Towards the identification of later seismic phases, *Geophys. J. Int.*, **123**, 948-958.

Zielhuis, A. & van der Hilst, R., 1995. Three-dimensional shear structure in the upper mantle beneath eastern Australia from Skippy portable arrays, *Geophys. J. Int.*, in press

PRACTICAL ANALYSIS OF SEISMIC ACTIVITY IN NORTHWESTERN CHINA DURING SEPTEMBER 4 - 7, 1995

W. Y. Kim, G. L. Vsevolozhsky, T. L. Mulder, and P. G. Richards[1]

Lamont-Doherty Earth Observatory of Columbia University,
Palisades, NY 10964
([1] also, Department of Earth and Environmental Sciences, Columbia University)

Contract number F49620-94-1-0057

Sponsored by AFOSR

ABSTRACT

We have analysed natural and artificial seismicity in detail in northern Kazakhstan and northwestern China for September 4-7, 1995, using a broadband seismographic network with 7 stations (which constitutes a large aperture array) together with a 21-element, medium aperture cross-array. This time interval appeared to be a very interesting one for exploring the capabilities of the Kazakhstan network. Our primary objective was twofold: to determine the detection capabilities of the Kazakhstan network, and to look for a possible underground nuclear explosion in the Lop Nor region. To accomplish this, natural and anthropogenic seismic activity in the region was determined with the use of the Kazakhstan network.

For the time period of September 4-7, 1995, we located 25 events that were not reported on either the PDE or REB bulletins. These events were mostly regional events associated with mining activities and had magnitude ranges of 2.5 to 3.5. We have identified major mines and quarries in northern central Asia; these are Ekibastuz in northeastern Kazakhstan, Kuzbass region near Novosibirsk, Russia, and an area east of Kurchatov. Minor mines and quarries are also identified in northern Kazakhstan near Kokchetav and Dzhetygara. We also found a single event that was in the PDE and REB, and which (from its seismic characteristics and in the absence of any other information) might be regarded as a problem event because it could not easily be identified using data from far regional ranges. While this event (September 4, 1995; 18h 43m; m_b = 3.9, PDE) occurred approximately 200 km northwest of the Lop Nor test site, at a time and place atypical for previously known nuclear tests, the relatively large *P* phases at stations in Kazakhstan suggested an impulsive nature for the event which is not typical for earthquakes in this region. The eight-station broadband seismograph network in Kazakhstan provides important high-quality digital seismogram data for detailed studies of earth structure and seismic sources. The very low microseismic noise levels at most of the station sites, as well as, their prime location at the center of Eurasia make the network an important contribution to the global seismic monitoring system for the NNPT and a CTBT.

KEYWORDS: China, discrimination, arrays, CTBT monitoring

OBJECTIVE

Our primary objective was twofold: to determine the detection capabilities of the Kazakhstan Seismographic Network, and to look for a possible Underground Nuclear Explosion (UNE) in the Chinese test site, Lop Nor region. To accomplish this, natural and anthropogenic seismic activity in the region was determined with the use of the Kazakhstan Seismographic Network which consists of eight broadband stations and a 21-element medium aperture seismic array.

Results of our work assist in evaluating the detection and location of problematic events in an area poorly covered by seismic stations for Comprehensive Test Ban Treaty.

RESEARCH ACCOMPLISHED

Introduction

Starting in the summer of 1994, a cooperative project in seismic data acquisition and analysis began in Kazakhstan which includes scientists from the Institute of Geophysical Research, National Nuclear Center, Republic of Kazakhstan; the Complex Seismological Expedition, Talgar, Kazakhstan; and the Lamont-Doherty Earth Observatory in the U. S. under the auspices of the Joint Seismic Program of the IRIS Consortium. One of the main objective of the joint project is to provide seismic data to the scientific community from low-noise sites, located in the center of the Eurasian continent. From July to October, 1994, eight broadband seismographic stations were established in vaults in Kazakhstan, and a centralized digital recording system was installed for an existing 21-element borehole seismometer array at Kurchatov city on the former nuclear test site near Semipalatinsk. These are low-noise sites with high sensitivity for teleseismic recording, originally developed by the Soviet Union in the 1960's and 1970's as part of an extensive program to monitor global seismicity and nuclear explosions in particular (see Kim et al., 1996). Table 1 and Figure 1 both describe elements of the Kazakhstan Network and show their location.

Table 1. Seismograph Stations in Kazakhstan Deployed in 1994*.

Station name	Station code	Lat (°N)	Long (°E)	Elev (m)	Sensor type	Site geology
Aktyubinsk†	AKT	50.433	58.017	400	STS-2	Paleozoic basic rock
Borovoye	BRVK	53.058	70.283	315	STS-2	Granite
Chkalovo†	CHK	53.676	70.615	240	CMG-3	Granite
Kurchatov†	KUR	50.715	78.621	240	STS-2	Sandstone
Makanchi†	MAK	46.808	81.977	600	STS-2	Andesite
Talgar	TLG	43.249	77.223	1120	CMG-3	Granite
Vostochnoye†	VOS	52.723	70.980	450	CMG-3	Granite
Zerenda†	ZRN	52.951	69.004	420	STS-2	Granite
Cross-array†	KUR21	50.622	78.531	203	K-213	Sandstone

* All sites are now operated by the Institute of Geophysical Research (IGR), NNC, Republic of Kazakhstan, except Talgar which is operated by the Institute of Physics of the Earth (IPE), Moscow, Russia. Borovoye Observatory was under the Institute for Dynamics of Geosphere (IDG), Moscow, Russia until summer of 1992.

† These sites/stations were operated by the Ministry of Defense, Russia until May 1994.

The continuous, 40 samples/s, broadband waveform data, acquired by the eight-station broadband seismic network in Kazakhstan, are archived at IRIS DMC for the period from Aug 94 - Dec 95. These data are available from DMC by using the XRETRIEVE application program or by using an e-mail data request format, BREQ_FAST. The waveform data from the selected events ($m_b(P) \geq 5.5$) acquired at the 21-element cross-array are also available from DMC starting from Feb 1995.

In this paper we describe the seismicity recorded during September 4-7, 1995, to see if any signals originating near the Lop Nor test site might have the characteristics of a small underground nuclear explosion (UNE). Therefore in our analysis we paid particular attention to regional and local events. We qualitatively assessed performance of the network as a whole, and determined which sites were sensitive to particular types of events. In our analysis we considered recent Lop Nor nuclear tests, earthquakes in the region, and known chemical explosions from sources with *S-P* times similar to those of UNEs from the Lop Nor test site.

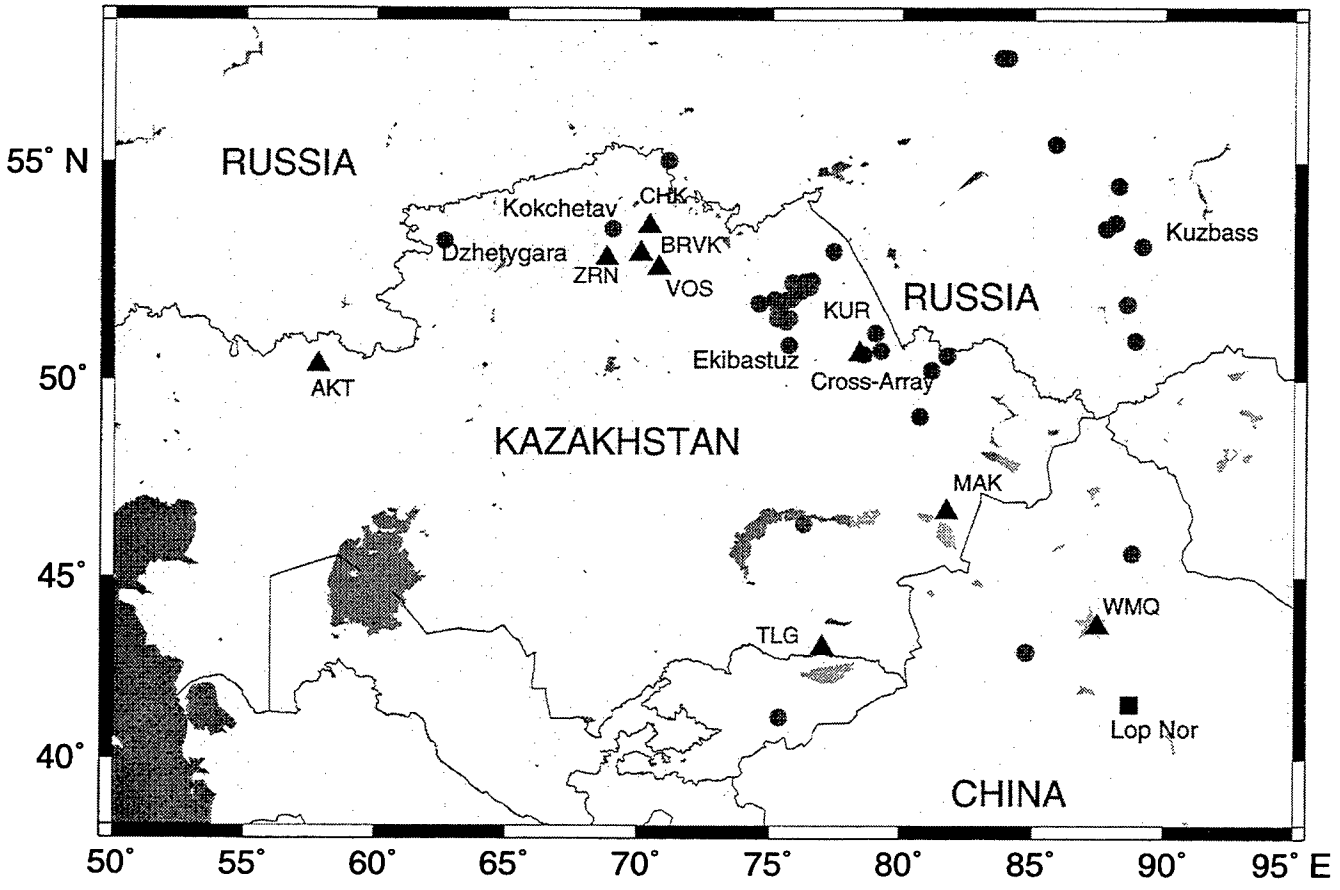

Figure 1. Locations of 8 broadband seismographic stations (*closed triangles*) in Kazakhstan deployed during July-Oct. 1994. Seismic events during Sept 4-7, 1995 which were detected and located are plotted with circles. Active mining areas which generated seismic signal during this period is indicated. They are from west to east; Kuzbass, Ekibastuz, Kokchetav and Dzhetygara. A problem event on September 4, 1995 is indicated by a star. Underground nuclear test site, Lop Nor is shown for reference.

Regional Event Detection and Location

We have carried out an evaluation of the event detection capability of the eight station broadband Kazakhstan network for the period September 4-7, 1995. Seismogram data recorded during this period were processed using a standard four step procedure, which consists of detecting signals, associating the arrivals with known events (PDE and/or REB catalog), event location, and magnitude determination. During September 4-7, 1995, 224 events were reported in the PDE monthly list, of which 108 events were $m_b > 3.0$. Of the 108 PDE events, 60 events were at epicentral distance less than 90°. 112 PDE events were detected and associated at least one station in the Kazakhstan network. During this period, we also detected 36 events which were neither in the PDE nor the REB catalogs, and we located 25 of them. These events were regional events which occurred in central Asia; in northern Kazakhstan, Xinjiang, western China, and in Russia (Figure 1).

For many of the local and regional events, standard location algorithms do not yield a stable solution because there were fewer observations than the location parameters to determine. For those local events, *S* - *P* times were determined and used as an additional constraint for locating the events. Based on the origin times of events, their location, and their waveform character, we determined three major areas where events occur regularly and are associated with industrial activity, e.g. chemical explosions. These events originated in mines and quarries at Ekibastuz in northeastern Kazakhstan, Kuzbass near Novosibirsk, Russia, and quarries located east of Kurchatov (KUR) with *S* - *P* times of approximately 35 s, 100 s, and 29 s respectively, as measured at the Kurchatov (see Figure 1). During the period seven broadband stations were operative with the single exception of the station in Makanchi (MAK) near the Chinese border, which was down due to lack of power. The cross-array in Kurchatov was shut down on September 6, 1996 due power failure resulting from vandalism.

Seismic signals from a typical event (09/04/95, 06h 11m; 12h 11m local time), magnitude ≈ 3.2) from Ekibastuz area is shown in Figure 2. The vertical-component waveforms recorded at five broadband stations are plotted. Notice that *P*-wave amplitudes at stations BRVK, CHK and ZRN in the distance ranges 382-461 km are much weaker than at the station VOS ($\Delta = 326$ km) in the same azimuth. Seismic signals from events (presumably quarry blasts) located near Kokchetav city in northern Kazakhstan (Fig. 1) were detected with an *S*-*P* time of 11 s as measured at station ZRN. Figure 1 shows locations of sources in the region with respect to all stations of the network.

During our evaluation we have determined that two groups of stations, one at Borovoye, and another at Kurchatov, contributed the most to the event location procedure. Stations at TLG and AKT have not been much help in locating events due to their isolation from the rest of the network and their higher ambient noise levels.

It has been established that with the existing set of seismic waveform analysis tools (many programs produced by the IRIS Joint Seismic Program Center at University of Colorado), and data from the group of stations in the Borovoye area (namely VOS, CHK, BRVK, ZRN), most of the local and regional events in northern Kazakhstan could be located with reasonable location errors. The solutions for epicenters inferred from the cross-array, and the broadband station KUR, using a standard inversion location procedure from *P* and *S* arrival times plus back azimuth and slowness from the array, appear to be stable at local distances.

An Impulsive Event

After the data were processed for event detections, and the arrivals were associated with known events (PDE or REB lists), or located, we continued analysis to determine if there had been an event which might raise concerns as possibly being an explosion from the Lop Nor test site.

Objective features include event locations compared to known seismic sources, event origin times, and character of the waveforms. These were used to compare inferred event locations with

those of the complete PDE or REB catalogs, in order to determine if these events fit the pattern of past activity in the region.

Having analyzed continuous data from the Kazakhstan network for September 4-7, 1995, we concluded that the only event which could be suspected as a possible UNE was that of September 4, 1995, with an origin time of 18:43, and epicentral coordinates of 43.696°N, 87.147°E with the magnitude m_b = 3.9 (PDE). As we will show later, the detection threshold of the Kazakhstan network for events from the Lop Nor test site area would be around $m_b \approx 3.5$ or less, if the nearest station MAK data are available.

We compared this location with known events in the area that establish evidence of protracted seismicity. Lop Nor area had numerous earthquakes in the past, and we can compare the events that occurred close to the event under question. Other events that occurred around the area are:November 8, 1994 (05:31; m_b = 4.9, PDE; 43.20°N, 87.14°E), March 18, 1995 (18:02;m_b = 5.2, PDE 42.42°N 87.20°E), and March 4, 1996 (14:02; m_b = 3.9, PDE; 44.13°N, 87.20°E). Furthermore, to help in classification of these events, we analyzed data from the stations of the Chinese digital seismographic network (CDSN).

Three-component broadband records at KUR (Δ = 1008 km) from the September 4, 1995 (18:43) event are shown in Figure 3. The *P* waves from the event at KUR is very strong and impulsive. Other characters such as, frequency content and amplitude ratio between the *P* and *S* waves, of the three component traces are quite comparable to the signals from the previous underground nuclear explosions from Lop Nor test site at KUR.

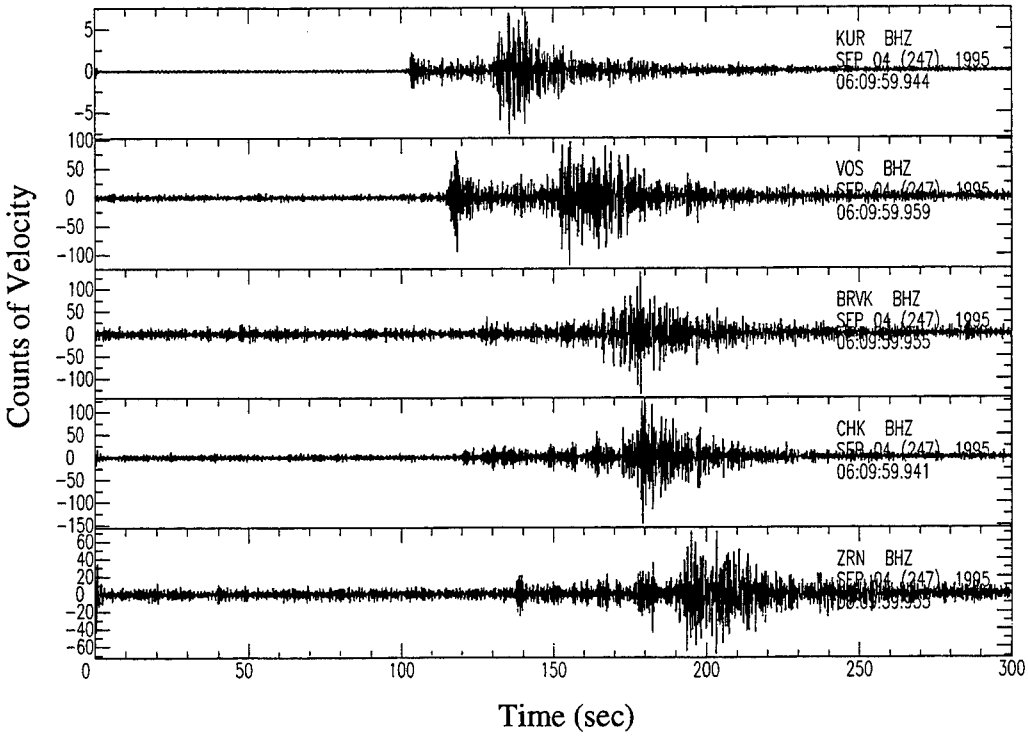

Fig. 2. Vertical-component broadband records from a typical mining explosion from Ekibastuz area in northeastern Kazakhstan. Event on 09/04/95, 06h 11m (12h 11m local time), magnitude ≈ 3.2. Signals are bandpass filtered with cutoff frequencies at 0.5 and 5 Hz.

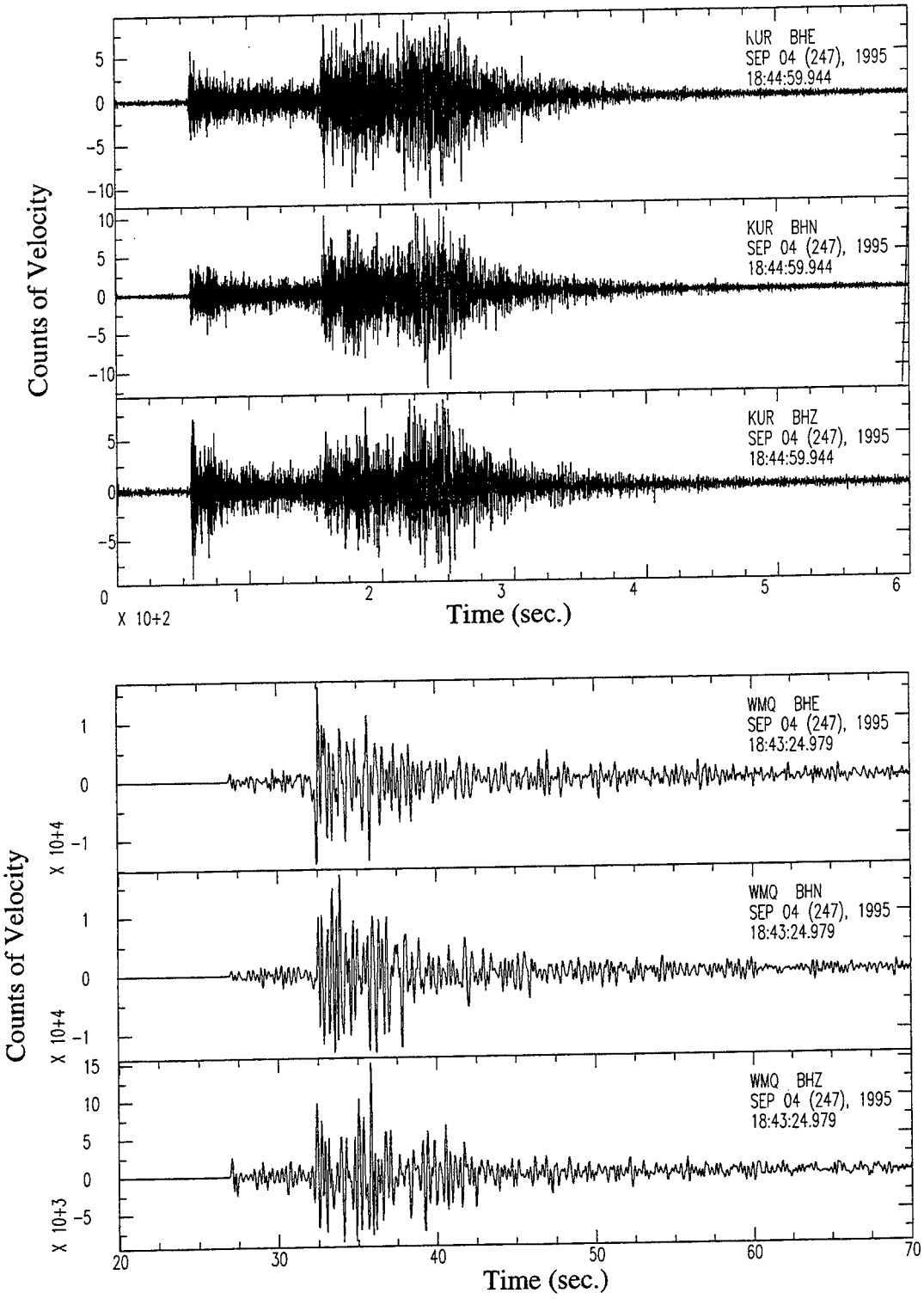

Fig. 3. Three-component broadband records from the event on September 4, 1995 (18:43; m_b = 3.9, PDE) which occurred at 241 km NW of Lop Nor Chinese test site at station KUR (Δ=1008 km, AZ=324°) and WMQ (Δ=46 km, AZ=252°). Notice strong *P* relative to *S* wave at KUR, while the *P*:*S* amplitude ratio is opposite at WMQ.

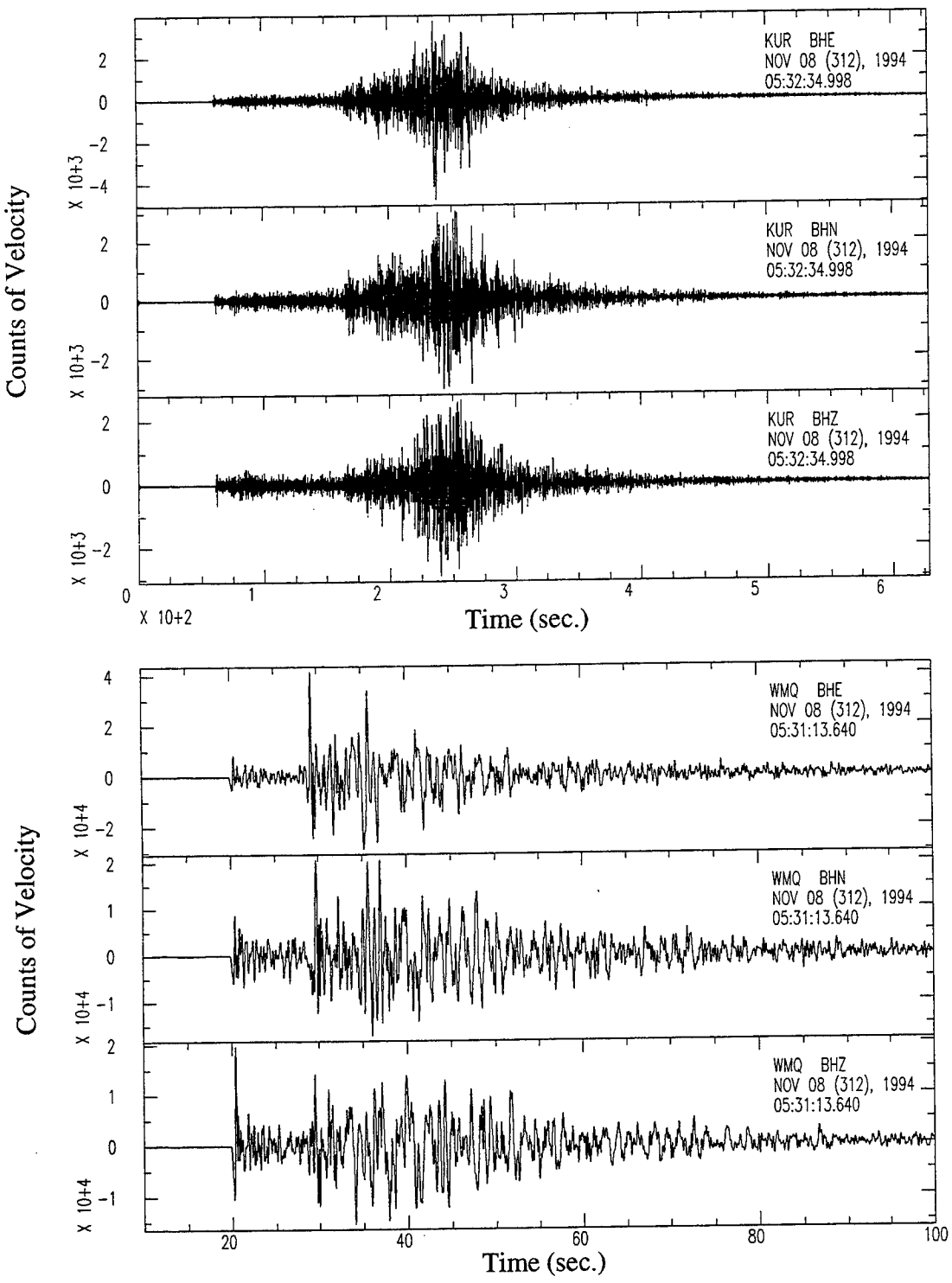

Fig. 4. Three-component broadband records from the event on November 8, 1995 (05:31; m_b = 4.9, PDE; 43.20°N, 87.14°E) which occurred at 195 km NW of Lop Nor Chinese test site (41.75°N, 88.47°E) at stations KUR (Δ=1054 km, AZ=325°) and WMQ (Δ=82 km, AZ=33°). Notice that at WMQ, *P* wave is stronger than from the event on September 4, 95 shown in Figure 3, while at KUR, *P* wave is relatively weaker than *S* waves and it is nearly opposite to the record shown in Figure 3.

Hence, it is difficult to identify the event. The event in question occurred very close to the station WMQ (Urmqui) near the Lop Nor test site (see Fig. 1). The three-component records at WMQ shown in Fig. 3 indicate that the event had strong *S* wave but weak *P* wave indicating a shear dislocation component of the source mechanism. Figure 4 shows three-component broadband records at these two stations from the event which occurred on November 8, 1994 (05:31; m_b = 4.9, PDE; 43.20°N, 87.14°E) near the September 4, 95 event (within about 40 km). For this event, *P* wave at WMQ is stronger than the *P* from the event on September 4, 95 shown in Figure 3, while at KUR, *P* wave is relatively weaker than *S* waves. *P:S* ratios at these two stations are nearly opposite to the records shown in Figure 3. These records suggest great variability of regional signals from the seismic events in western China.

Based on waveforms and the origin time of the event which was near the mid-night in local time, we concluded that the event is likely an earthquake. This exercise underscores the complexities of the event identification in an area poorly covered by the seismographic networks as well as the importance of near distance observation for a problematic event.

Event Detection Capability of the Cross-Array

The cross-array, with an aperture length of 22.5 km and sensor spacings of 2.25 km, is a typical medium-aperture array similar to WAR and YKA. Such arrays give good slowness and azimuth resolution for seismic signals in the distance range 1500 to 10000 km (Classeen, 1985). At Kurchatov, an additional 3-component broadband seismograph near the array complements the cross-array and allows the use of vector characterization of the wavefield to provide phase identification by using, for example, polarization analysis (e.g., Christoffersson et al., 1988).

We have carried out a preliminary evaluation of the seismic event detection capability of the cross-array for July, 1995. There were 1436 events reported in the PDE during July 1995, of which 509 events were $m_b \geq 3$ at epicentral distances less than 90° from Kurchatov array. A conventional seismic detector was applied to channel #21 (array center) based on an STA/LTA ratio with STA=2.5 s, LTA=60 s and trigger ratio of 3.

Of the 494 events with $m_b \geq 3$ in the distance range up to 90°, 334 PDE events were detected and associated, while 160 PDE events were not detected. An additional 10 PDE events with no magnitude were detected. The majority of undetected PDE events had low signal-to-noise ratio, and several events were hidden by the preceding much stronger events. The single channel detection ratio is about 68 % for all PDE events with $m_b \geq 3$, while the ratio is about 92 % for $m_b \geq 4.5$. There were 223 PDE events with $4 \leq$ mb < 4.5, of which 122 were detected, while 101 events went undetected. The detection ratio for smaller PDE events is about 55 %. Detailed event detection is listed in Table 2.

Table 2. Detection capability of the Kurchatov array for July 1995 for events with distance ≤ 90°.

Magnitude (PDE)	Associated	Unassociated	Total	Detection (%)
$3.0 \leq m_b < 4.0$	15	43	58	26%
$4.0 \leq m_b < 4.5$	122	101	223	55%
$4.5 \leq m_b < 5.0$	143	16	159	90%
$5.0 \leq m_b < 6.0$	49	0	49	100%
$6.0 \leq m_b$	4	0	4	100%
Total	334	160	494	68%

On average, there were about 30 - 40 detections/day: up to 50% were PDE events; about 25% were regional events; another 10 % were clear teleseismic events that were not in the PDE. It should be noted that in this preliminary examination of detection capability, we were using only a single channel for the Kurchatov array.

Event detection was also examined by employing a standard array processing method (beamforming). The best beam is found each of the three second windows and its normalized beam power is used as detection criterion. This procedure enhanced many of the previously non-visible signals and the array detection threshold was lowered from $m_b \approx 4.5$ to $m_b \approx 4.0$. In particular, detection in the range of $m_b < 4.0$ increased by approximately 10% and detection in the range $4.0 \leq m_b \leq 4.5$ increased by an additional 5%. Further study is needed to establish optimum signal detection criteria by utilizing consistency of azimuth and slowness of the incoming wave fields.

Concluding Remarks

Installation of broad-band stations in Kazakhstan has allowed us to study Eurasian earthquakes recorded at regional distances with modern digital equipment, and to gain practical experience in an area associated with two former nuclear test sites (Semipalatinsk and Lop Nor) and with significant mine blasting.

We have identified major mines and quarries in central Asia; these are Ekibastuz in northeastern Kazakhstan, Kuzbass region near Novosibirsk, Russia, and an area east of Kurchatov. Minor mines and quarries are also identified in northern Kazakhstan near Kokchetav and Dzhetygara (Fig. 1).

An event on September 4, 1995 (18h 43m; $m_b = 3.9$, PDE) which occurred near the Lop Nor Chinese test site showed an usually impulsive *P* arrivals at stations in Kazakhstan. The event in question occurred very close to the station WMQ (see Fig. 1). The three-component records at WMQ indicate that the event had strong shear dislocation component. Hence, we concluded that the event is likely an earthquake. The origin time is near the midnight in local time. This exercise underscores the complexities of the event identification as well as the importance of near distance observation for a problematic event.

The eight-station broadband seismograph network in Kazakhstan provides important high-quality digital seismogram data for detailed studies of earth structure and seismic sources. The very low microseismic noise levels at most of the station sites, as well as, their prime location at the center of Eurasia make the network an important contribution to the global seismic monitoring system for the NNPT and a CTBT.

The medium aperture, 21-element cross-array, complemented by a three-component broadband seismograph station, at Kurchatov has excellent detection and location potential for various seismic events in near-real time, with high location accuracy. The array can record seismic signals from small events occurring in most of Eurasia, including Russia, Central Asia, as well as, the Middle East and the Far East.

RECOMMENDATIONS AND FUTURE PLANS

Data collected from the broadband stations and the cross-array are archived in Kurchatov and at the IRIS Data Management Center. Plans are also being considered for making the data from some of the sites available in near-real-time for use by groups such as GSE, the IRIS-Spyder system and the USGS NEIC. Additional plans for future activities in this cooperative program include the development of an on-line, near-real-time processing system for the Kurchatov cross-array and possible reactivation of the cross-array and additional stations near Borovoye.

Our practice reported here suggest that such analysis for a particular region provides

invaluable experience for a practical seismic monitoring as well as reveals possible problems associated with the CTBT monitoring for the region in question. We intend to extend our practice for the seismic event detection and identification problems for a poorly known North Korean region.

References

Claassen, J. P. (1985) Design criteria for sizing regional arrays, in Ann U. Kerr (ed.), *The VELA Program: A twenty-five year review of basic research*, pp. 506-515.

Christoffersson, A. E., Husebye, E. S. and Ingate, S. F. (1988) Wavefield decomposition using ML probabilities in modelling single site 3-component records, *Geophys. J. Int.*, **93**, 197-213.

Kim, W. Y., V. Kazakov, A. Vanchugov and D. Simpson, Broadband and array observations at low noise sites in Kazakhstan: Opportunities for seismic monitoring of a Comprehensive Test Ban Treaty, in E. Husebye and A. M. Dainty (eds.), *Monitoring a Comprehensive Test Ban Treaty*, Kluwer Academic Publishers, 467-482, 1995.

Detection of dispersive signals using multitaper double-frequency coherence

Robert Mellors, Frank Vernon, and David Thomson*
SIO - IGPP University of California San Diego, La Jolla, California
ATT Bell Labs, Murray Hill, New Jersey
Contract No. F49620-94-1-0037
Sponsored by AFOSR

ABSTRACT

We demonstrate the use of "double-frequency" coherence estimates to detect weak seismic surface waves. Coherences are calculated between different frequencies of either one or two signals using a multitaper method. The method is effective on signals showing dispersion such as surface waves. We test the algorithm first on a variety of synthetic signals and then on broadband seismic data. It is robust in the presence of noise and we show that dispersive signals can be detected and identified. Double coherence also shows a clear advantage over standard coherence estimates in detecting similarities between two frequency-shifted version of the same signal and in detecting overtones. Phase information between signal components can also be extracted from the double frequency coherence estimates.

Keywords: detection, surface waves, coherence

OBJECTIVES

Detection and identification of weak seismic signals forms an essential element of test ban verification, especially at regional distances of 1° to 20° degrees. For shallow events at these distances, the most prominant section of the wavetrain is often the surface waves. The surface waves are also critical in applying discriminants that depend on comparisons between long- and short period energy such as m_b:m_s ratios. A key characteristic of seismic surface waves is dispersion. In this paper we demonstrate the effectiveness of double-frequency coherence in identifying dispersive wavetrains. In addition, this method provides information about phase relationships between the individual components of the dispersive waves.

Coherence estimates have long been used to evaluate the similarity between time series (e.g. Priestley, 1981; Hinch and Clay, 1968). Our technique has two significant differences from standard coherence estimates. First, we use a multitaper method based on the prolate sphereoidal tapers (e.g. Slepian, 1983; Thomson, 1982; Park et al, 1987) to calculate coherences. Second, coherences are calculated between two different frequencies as well as at one frequency. Previously, Lanzerotti et al. (1987) used multitaper coherence to analyse electromagnetic data and Park et al. (1987) applied it to seismic data.

Because the double-frequency coherence estimate multiplies the spectrum of two signals together, in a sense this detection method resembles a frequency domain version of the Capon (1969) surface wave detection algorithm which used chirp waveforms to perform matched filtering. We first demonstrate our technique using synthetic data and then we apply the algorithm it to seismic data recorded by the Kyrgystan broadband network in Central Asia.

RESEARCH ACCOMPLISHED

The standard definition of coherence γ (e.g. Priestley, 1981) is

$$|\gamma_{ij}(f)| = \frac{|S_{ij}(f)|}{\{S_{ii}(f)S_{jj}(f)\}^{\frac{1}{2}}} \tag{1}$$

where $S_{ij}(f)$is a cross-spectral estimate of time series i and j at a frequency f. Note that if the the raw periodograms are used, the coherence is unity. Therefore, the standard practice is to smooth the spectral estimates over a range of frequencies. This can be done in a variety of ways. The resulting coherence will fall between 0 and 1, with 0 indicating no coherence and 1 indicating perfect similarity. A phase spectrum can also be calculated by taking the arc tangent of the imaginary part of S_{ij} over the real (without taking the absolute values shown in equation (1)). This yields the average difference between the two signals at a given frequency. However, if the coherence at a given frequency is low, the variance of the phase is high.

Thomson (1982) pointed out that coherences can be calculated using multitaper spectral estimates. Multitaper spectral estimates combine weighted spectral estimates from a number of differently tapered versions of the a given signal to yield a spectral estimate. The tapers are are based on the prolate spheroidal series developed by Slepian (1983) and are optimized to minimize leakage from ouside the desired band. The individual tapers are orthogonal and therefore also provide statistically independent estimates of the spectra. Weights are adaptively determined using

an iterative process for each time series. The resulting estimate, $S(f)$ is a combination of all these factors:

$$S(f) = \frac{A}{K} \frac{\sum_{k=0}^{K-1} \lambda_k d_k^2(f) |y_k(f)|^2}{\sum_{k=0}^{K-1} d_k^2(f)} \tag{2}$$

where d_k are the weights of the each spectral estimate, λ_k are the eigen values associated with each taper, and y_k are the discrete Fourier transforms of the tapered data. A is determined using $A = \sum_{k=0}^{K-1} \lambda_k^{-1}$ and K is the number of tapers. This method is especially effective for time series which are either short or have a large dynamic range.

A cross-spectra S_{ij} between two time series i and j can be calculated using:

$$S_{ij}(f) = \frac{A}{K} \frac{\sum_{k=0}^{K-1} \lambda_k d_k^i(f)(y_k^i(f))^* d_k^j(f)^2 (y_k^j(f)^2)}{[\sum_{k=0}^{K-1} d_k^i(f)]^{\frac{1}{2}} [\sum_{k=0}^{K-1} d_k^j(f)]^{\frac{1}{2}}} \tag{3}$$

Consequently, the coherence (magnitude squared) is therefore:

$$\gamma_{ij}^2(f) = \frac{|S_{ij}(f)|^2}{S_{ii}(f) S_{jj}(f)} \tag{4}$$

This yields a coherence estimate between two different signals at one frequency. If only one taper ($K = 1$)is used, the coherence is unity. The smoothing effect of the multiple tapers provides a robust coherence estimate.

Advancing one step further, we can define coherence between different frequencies f_1 and f_2:

$$\gamma_{ij}^2(f_{1,2}) = \frac{|S_{ij}(f_1) S_{ij}(f_2)^*|}{S_{ii}(f_1) S_{jj}(f_2)} \tag{5}$$

This is double-frequency coherence, in that we calculate coherences not only between two signals, but also between different frequencies. If $f_1 = f_2$, the definition reduces to equation(4). If the double-frequency coherence of a single signal with itself is calculated, the result is unity where $f_1 = f_2$ but yields a value between 1 and 0 elsewhere, which shows the amount of coherence between different frequencies. For a dispersive signal, coherence between neighboring frequencies is high.

We tested the multitaper double-frequency coherence with simple signals. The signals were designed to mimic the characteristics of idealized seismic data (surface waves) but with defined frequency and amplitude. Initially pure signals were processed and plotted. The signals were degraded by adding random noise and plotted. We compared the results from the pure signals and the noisy signals to identify robust features in the coherence plots.

The amplitude and phase coherence of the two signals are plotted as two square matrices, with the frequencies (normalized to Nyquist) of one signal on the X axis and the frequency of the other signal on the Y axis. The auto-coherence of random noise (Figure 1, top) shows a diagonal line on both the coherence and diagonal plots since the coherence of a signal with itself at a given frequency is unity and zero-phase. We also plotted the cross-diagonal of the phase coherence plot (unwrapped) to show the phase relationship between different frequencies.

A sine wave that varies in frequency, typical of dispersed surface waves, shows a clear and characteristic pattern (Figure 1, bottom). Random noise has been added using a random number generator. The pattern is dominated by a zone of high coherence near the diagonal and a larger patch of high coherence located near the intersection of the two frequency ranges. A broad zone of low coherence, less visible on Figure 1, is present at the intersection of the two frequency ranges. This patch of low coherence is present where the energy in the frequency band is high but the coherence is low.

The phase diagram is more difficult to interpret. The plots show the differential phase in the these plots, as the value displayed at f_1,f_2 represents the phase difference between the two components because the complex conjugate of one spectra is multiplied by the other. As noted above, only phase values with a high coherence should be interpreted. A difficulty is that the phase values are wrapped, ie, they lie between $-\pi$ and π and should be unwrapped. For frequency ranges where the phase varies quickly, phase unwrapping is difficult. A few first order observations can made, however. First, the plots display a streaky aspect from lower left to upper right. This means that phase differences between adjoining pairs of frequencies vary relatively slowly, ie, the phase difference between f_1 and f_2 is similar to the phase difference between f_3 and f_4. Below the phase diagram is a plot of the unwrapped phase cross-diagonal, from upper left to lower right. The cross-diagonal shows the phase difference between a wide range of frequencies, so it changes rapidly. It clearly shows that the phase difference between the components of the sweep change smoothly, as expected.

Double coherence can also be applied to compare different signals. Figure 2 (top) shows two sweep signals generated with:

$$f(i) = 100 \sin(2\pi i(f0 + \frac{(f1 - f0)i}{600})) \qquad f0 = 0.0 \qquad 0 \leq i \leq 600$$

where $f1 = 0.075$ for the first sweep and $f1 = 0.050$ for the second sweep. Essentially, these signals resemble frequency shifted versions of the same signal, similar to a doppler shift of an acoustic signal. Single coherence indicates little coherence between the two signals, while a linear zone of high coherence lies just above the main diagonal on the double-frequency coherence plot. The offset demonstrates the two signals are coherent at differing frequencies, ie 0.05 Nyquist is coherent with 0.06 Nyquist. The slope $\frac{2}{3}$ of the zone of high coherence is expected from the $\frac{0.050}{0.075}$ relationship between the two sweeps. The phase plot has an area of slowly changing phase corresponding to the zone of high coherence. A similar (but not linear with frequency) relationship would be expected between for seismic surface waves from a single source that travel along paths with different velocity structure thereby causing differing dispersion. Extended sources can also cause frequency shifts of a signal.

Figure 2 (bottom) shows a sweep with overtones:

$$f(i) = 50 \sin(2\pi i(f0 + \frac{(f1 - f0)i}{600})) + 50 \sin(5\pi i(f0 + \frac{(f1 - f0)i}{600}))f0 = 0.0 \qquad 0 \leq i \leq 600$$

The added overtone signals appear as a pair of lines of high coherence sloping away from the main diagonal with a slope $\frac{2}{5}$ and $\frac{5}{2}$ corresponding to the frequency difference between the signals.

Because seismic surface waves can contain overtones similar to this, and which depend on source characterics such as depth, we are investigating whether these overtones can be detected in real data (such as higher mode surface waves).

We tested the algorithm with seismic data recorded by the Kyrgyzstan seismic network in Central Asia. Figure 3 (top) shows the coherence of the surface waves from a large teleseism. Since this data has a very high signal-to-noise ratio, the coherence and phase plots appear very similar to the synthetic tests. Note the zone of high coherence along the diagonal flanked by two distinct zones of coherence slightly off the diagonal. It is possible that these off-diagonal zones (near 0.09 Nyquist) may represent higher modes or possibly multipathing.

Test with a smaller event (magnitude 4.0 20 degrees away in China) however also included a zone of high coherence (Figure 3 - bottom) in the frequency band of the surface waves. This event was difficult to see in unfiltered data and the surface waves were obvious only in filtered data. The two panels represent pre-event and event sections.

CONCLUSIONS AND RECOMMENDATIONS

Double coherence can be used to detect dispersive signals such as surface waves. In addition, various characteristics of the dispersive signal such as the presence of overtones, and frequency shifts between signals can be easily discerned. The next steps are clear. First, the detection capability must be quantified and thresholds defined so that the presence or absence of dispersive waves can clearly stated. We propose to achieve this by using the coherence as a filter. We first define frequency ranges which possess a coherence about a certain level, and then rebuild the signal including only the coherent frequencies (using both coherence and phase information) and eliminating non-coherent energy. This should greatly improve the signal-to-noise ratio, aiding detection and identification. Second, we propose to further investigate the phase information combined with the coherence. In principal, it should be possible to determine the phase relationships between the frequency components of the signal. We also wish to explore the ability to determine source effects from the coherence plots. In effect, this technique breaks a signal down into its individual components and clearly shows the relationship between the components, so all possible information contained in the signal has been extracted.

References

CAPON, J., R. J. GREENFIELD, AND R. T. LACOSS, *Long-period signal processing results for the large aperture seismic array*, Geophysics, 34, pp. 305-329,1969.

HINCH, M. J., AND CLAY, C. S., *The application of the discrete Fourier transform in the estimation of power spectra, coherence, and bespectra of geophysical data*, Revs. of Geophysics, 6, pp. 347-363, 1968.

PARK, J. J., F. L. VERNON III, AND C. R. LINDBERG, *Multitaper spectral analysis of high-frequency seismograms*, J. Geophys. Res.,92, pp.12,675-12,684, 1987.

PRIESTLEY, M. B..,Spectral analysis and time series , Academic Press, 890 p. 1981.

SLEPIAN, D.,Some comments on Fourier analysis, uncertainty, and modeling, SIAM rev., 25, pp. 379-393, 1983.

THOMSON, D. J.*Spectrum estimation and harmonic analysis*, IEEE Proc., 70, pp. 1055-1096, 1982.

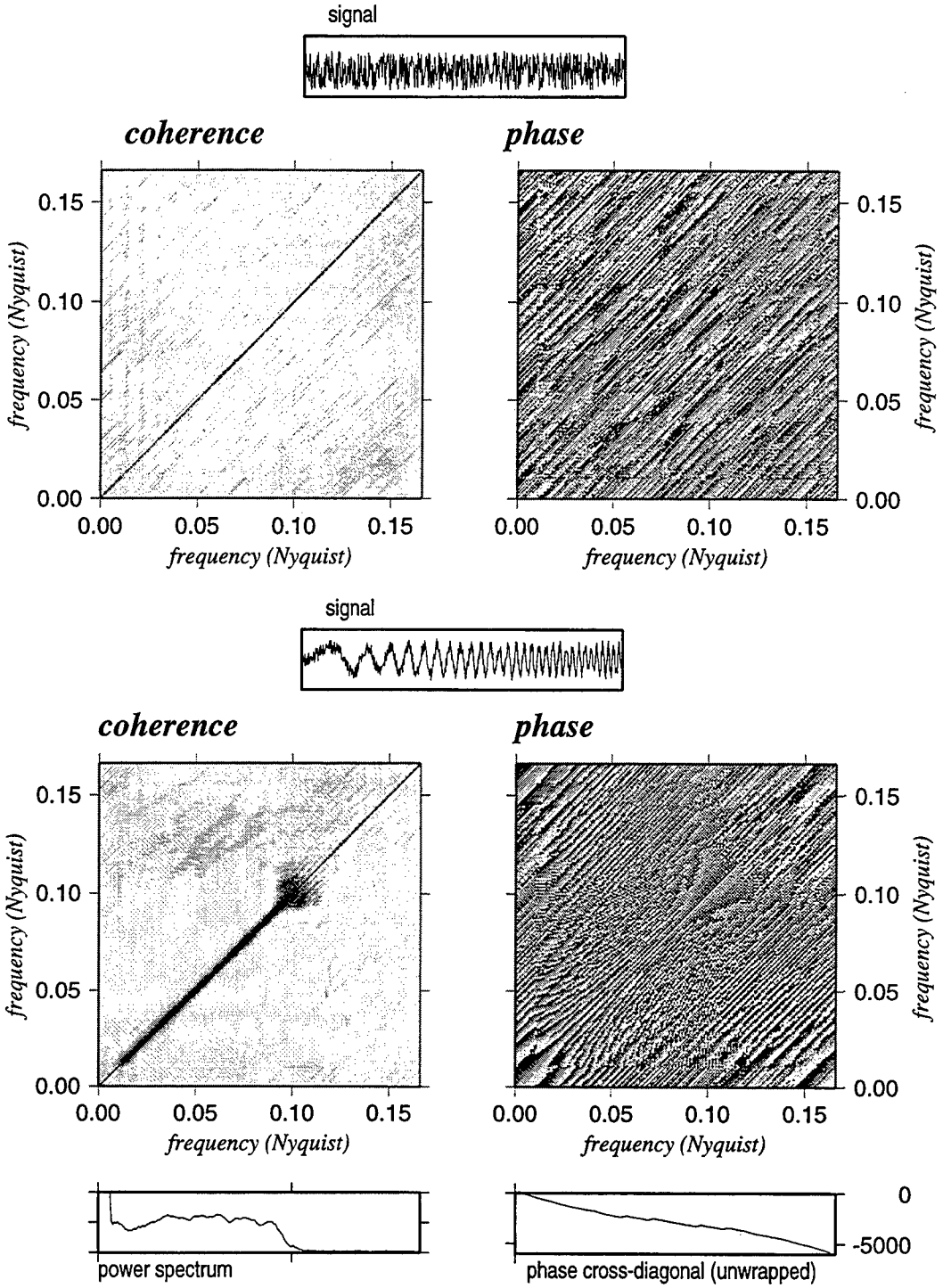

Figure 1. (**top**) Coherence plot (left) and phase plot of random noise generated by a random number generator. The same signal is plotted with itself, so the diagonal line shows that the signal is coherent with itself at a given frequency. Below the phase plot is the unwrapped cross-diagonal (top left to lower right) (**bottom**) Coherence plot of a simple sweep signal with noise added. Below the coherence plot we show the power spectrum of the signal. The left side shows the phase plot.

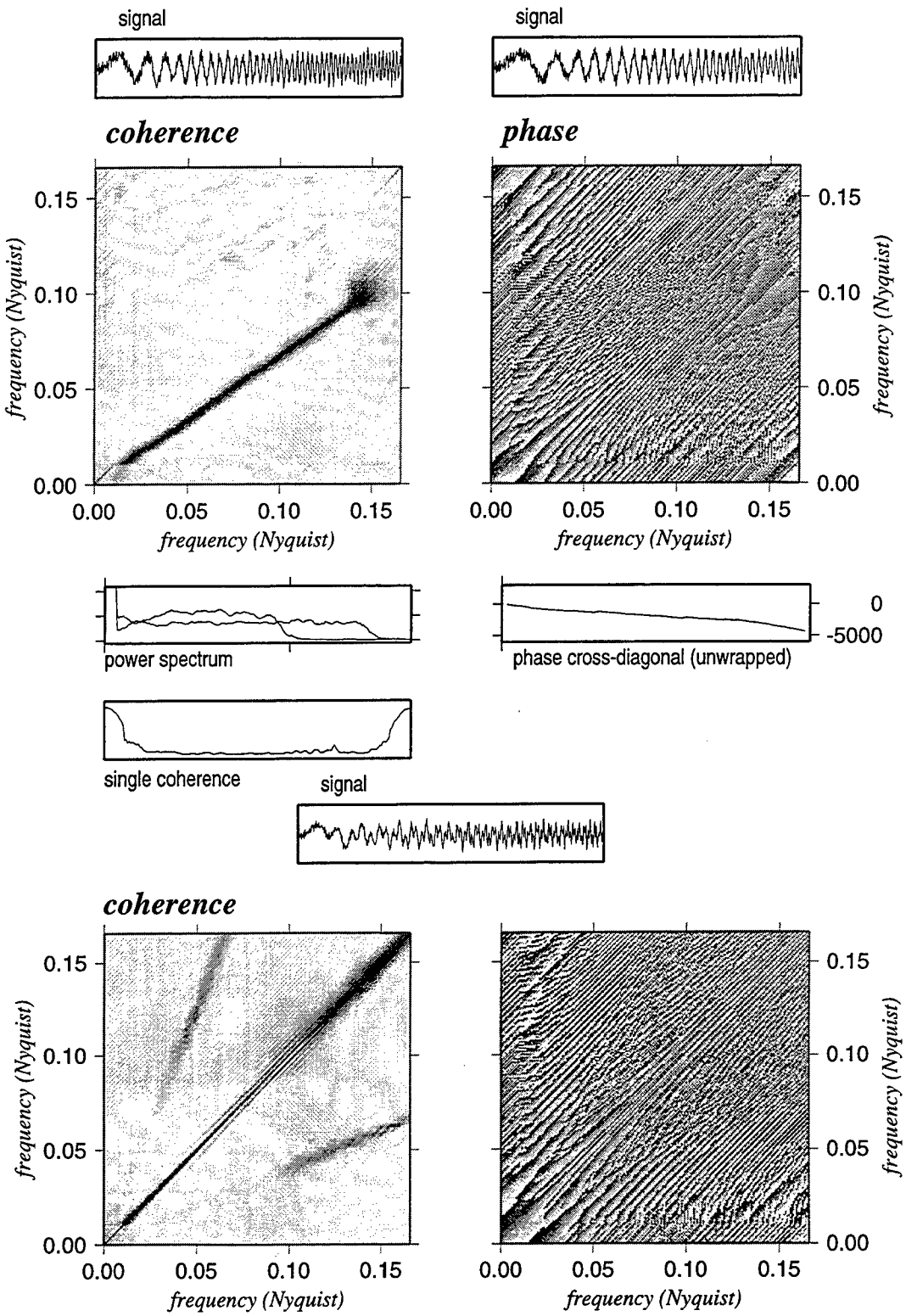

Figure 2. (**top**) Coherence plot (left) and phase plot (right) of two sweep signals with different ending frequencies. Note that the signals are coherenent, but at different frequencies, ie, 0.15 Nyquist is coherent with 0.10 Nyquist. Below is the power spectrum of the two signals and a standard "single" coherence plot for comparison. (**bottom**) Plots of a signal composed of a sweep combined with simulated "overtones" of the same sweep causing two easily discernable sidelobes.

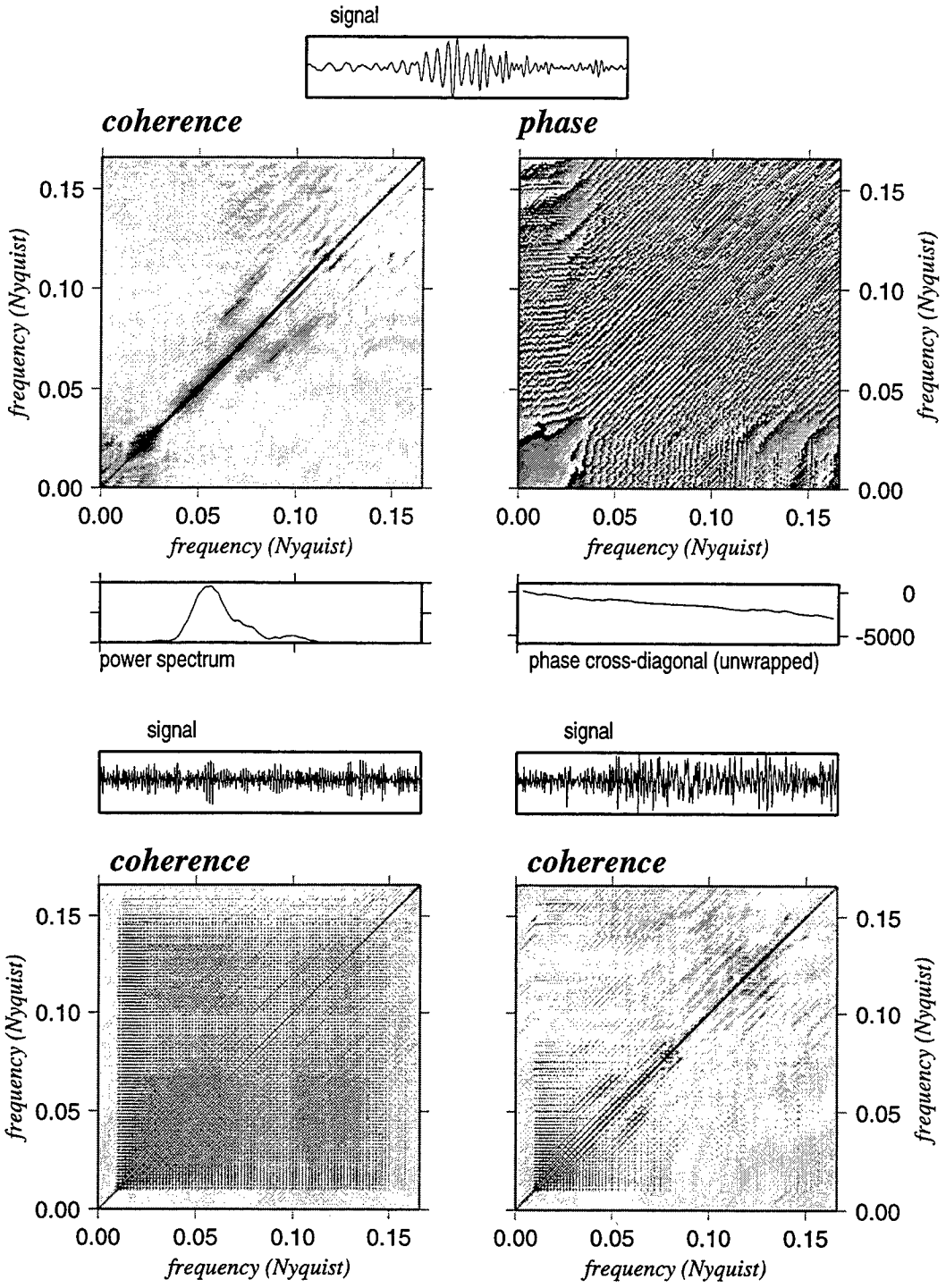

Figure 3. (**top**) Real seismic data of the surface waves from a large teleseism. (**bottom**) Two coherence plots of seismic data from a small (Ml 4.0 event 20 degrees away). The left plot show the pre-event noise and the right plot include the P wave, S wave and surface waves.

Detection Analyses of Low Yield Soviet PNE Explosions

J. R. Murphy, D. D. Sultanov*, B. W. Barker, I. O. Kitov*, and M. E. Marshall
Maxwell Laboratories, Inc., S-CUBED Division
11800 Sunrise Valley Dr., Suite 1212
Reston, Virginia 22091
Contract No. F19628-94-C-0083
Sponsored by ACDA

Abstract

A central issue which needs to be addressed in assessing the seismic monitoring capability required to adequately verify any eventual Comprehensive Test Ban Treaty (CTBT) concerns the definition of the threshold level of explosion yield down to which seismic events will have to be detected and identified. For example, since it has been experimentally demonstrated that it is possible to reduce the amplitude of the radiated seismic signal of an underground nuclear explosion by at least a factor of 70 by employing the cavity decoupling evasion scenario, it follows that a truly comprehensive monitoring of underground nuclear tests down to the 1 kt level will require the detection and analysis of seismic signals corresponding to fully tamped nuclear explosions with yields of about 14 tons. However, it is difficult to directly assess the detectability of such small nuclear tests, since there are no regional seismic data available which have been recorded from nuclear explosions in this yield range. In this study, S-CUBED is working with scientists from the Russian Institute for Dynamics of the Geospheres (IDG) to use regional seismic data recorded from the extensive Soviet PNE testing program to better quantify the detectability of small, evasively tested underground nuclear explosions. This is being accomplished by theoretically scaling regional seismic data recorded from selected Soviet PNE tests at the Borovoye station in Central Asia to obtain estimates of the corresponding seismic signals which would be expected from small cavity decoupled nuclear explosions at those same source locations. Preliminary results of analyses of such synthetic data suggest that it will be difficult to detect cavity decoupled nuclear explosions with yields in the 1 kt range, even at low noise regional stations such as Borovoye. Moreover, it has been found that the relative detectability of such explosions at a fixed regional distance can vary by as much as an order of magnitude depending on the specific source and propagation path conditions associated with a particular test. These analyses are continuing in an attempt to derive more reliable assessments of the nuclear test detection capability of various proposed CTBT monitoring networks.

Key Words: Seismic, Detection, Regional, Soviet, PNE, Cavity Decoupling

* Institute For Dynamics of the Geospheres, Russian Academy of Sciences

Objective

The principal objective of this research program is to derive improved estimates of the seismic detectability of small, evasively tested underground nuclear explosions, for use in assessments of the monitoring requirements which will be associated with any eventual Comprehensive Test Ban Treaty (CTBT). In order to accomplish this objective, we are working with scientists from the Russian Institute for Dynamics of the Geospheres (IDG) to analyze regional seismic data recorded from selected, low yield Soviet PNE tests which sample a wide range of the source and propagation path variables of potential interest in global treaty monitoring.

Research Accomplishments

The difficulty of the seismic monitoring task associated with any eventual CTBT depends very strongly on the designated monitoring threshold. That is, since no practical seismic monitoring system will ever insure detection of all conceivable underground nuclear tests, it is necessary to establish a monitoring threshold value which represents some compromise between system cost and various political and military considerations. For example, the proposed design goal of the International Monitoring System currently being discussed in Geneva is to detect and identify all seismic events corresponding to non-evasively tested underground nuclear explosions having yields greater than about 1 kt. On the other hand, the ultimate monitoring goal of the corresponding U.S. National Technical Means system has often been expressed in terms of confidently detecting all evasively tested underground nuclear tests having yields greater than a few kilotons. Thus, since it has been experimentally demonstrated that it is possible to reduce the amplitude of the radiated seismic signal from an underground nuclear explosion by at least a factor of 70 by employing the cavity decoupling evasion scenario, it follows that a truly comprehensive monitoring of a 1 kt threshold will require the detection and analysis of seismic signals corresponding to fully tamped nuclear explosions with yields of about 14 tons. This constitutes a problem since there are no regional seismic data currently available which have been recorded from nuclear tests in this yield range which can be used to directly assess the detectability of such events. Therefore, we have proceeded by theoretically scaling observed regional seismic data from low yield tamped nuclear explosions in order to simulate the corresponding signals which would be expected from cavity decoupled explosions at those same source locations.

The scaling procedure used to derive the synthetic regional seismic data analyzed in this study has been described in detail in a number of previous reports. In this approximation, if the elastic radius of the source of the tamped

reference explosion of yield W_T is denoted as rel_2, then the elastic radius for the corresponding cavity decoupled explosion is

$$rel_1 = \frac{rel_2}{(DF)^{1/3}}$$

where DF denotes the low frequency decoupling factor. Thus, assuming a nominal full decoupling factor of 70, the value of DF to be used in scaling to a 1 kt fully decoupled explosion is simply 70 W_T. In general, the source scaling operator is frequency dependent and acts as a high pass filter in applications of interest in the present study. This fact is illustrated in Figure 1 which shows the source spectral ratio required to scale a 1 kt tamped recording to the corresponding estimate of a 1 kt fully decoupled recording. In this example, the scaling operator reduces the low frequency spectral amplitude level by the nominal factor of 70, while reducing the 10 Hz spectral amplitude level by only about a factor of 10.

The analyses of detectability conducted to date have focused on the Borovoye station recordings of 12 Soviet PNE explosions located in the epicentral distance range extending from about 7 to 11 degrees. The map locations of these explosions with respect to the Borovoye station are plotted in Figure 2, where it can be seen that they sample about 180° in azimuth. The source characteristics of these selected explosions are listed in Table 1 where it can be been that they sample a variety of source media and a wide range of source depth. The broadband Borovoye recording of the 10 kt PNE event of 10/26/73 is shown in Figure 3, together with the results of theoretically scaling it to correspond to 1 kt tamped and 1 kt fully decoupled explosions at that same source location. Note that in progressing from the observed to the simulated 1 kt decoupled recording, the Lg/P ratio decreases significantly, consistent with the frequency dependent nature of the source scaling illustrated in Figure 1. That is, because the dominant frequency of the Lg phase is lower than that of the P phase, the broadband Lg amplitude level is reduced more by the scaling procedure than is the P wave amplitude level.

All of the Borovoye recordings from the 12 Soviet PNE events of Table 1 have been theoretically scaled to simulate the corresponding signals expected from 1 kt cavity decoupled explosions at those same source locations using the procedures illustrated in Figure 3. These synthetic data, together with the original pre-signal noise windows, were then bandpass filtered and signal/noise ratios as a function of frequency were determined for each of the 12 simulated decoupled explosions. The results are summarized in Figure 4, where the means and upper and lower bounds corresponding to the six explosions at an average epicentral distance of about 8° (left) and to the six explosions at an average

Table 1

Source Characteristics of Selected Soviet PNE Events

Date	Yield, kt	Depth, m	Source Medium	Epicentral Distance, Degrees
06/18/85	2.5	2859	Argillite	7.1
09/19/73	6.3	615	Argillite	7.6
10/04/79	21.0	837	Clay	7.7
10/26/73	10.0	2026	Dolomite	8.3
12/10/80	15.0	2485	Sandstone	8.8
08/25/84	8.5	726	Clay	8.9
04/19/87	3.2	2015	Limestone	10.4
08/15/73	6.3	600	Clay	10.5
10/03/87	8.5	1000	Salt	10.5
07/21/84	13.5	846	Salt	10.6
10/17/78	23.0	593	Sandstone	10.7
09/02/81	3.2	2088	Limestone	11.0

epicentral distance of about 10.5° (right) are compared. It can be seen that, in both cases, the range of the ratios is quite large, reflecting the large signal variability associated with differences in source and propagation path parameters between these selected PNE events at nearly constant distances. Moreover, it can be seen that the average signal-to-noise ratios are on the order of 0.1 over much of the frequency band extending from about 0.3 to 9 Hz, which suggests that such clandestine tests would be very difficult to detect in this regional distance range, at least under the prevailing noise conditions at the relatively quiet Borovoye station. Current efforts are focusing on analyses of the expected detectability of these estimated signal levels at other low noise stations where the frequency dependent noise levels have been well documented.

Conclusions and Recommendations

Over the past year, we have been working with scientists from the Russian IDG to use regional seismic data recorded from the extensive Soviet PNE testing program to better quantify the detectability of small, evasively tested underground nuclear explosions. Data recorded at the Borovoye station from 12 of these PNE events located in the epicentral distance range extending from about 7 to 11 degrees have been theoretically scaled to simulate the signals which might

be expected from 1 kt cavity decoupled nuclear explosions at those same source locations. Preliminary analyses of these synthetic data indicate that it will be difficult to detect such evasively tested nuclear explosions in this regional distance range at least under the prevailing background noise conditions at the Borovoye station. These analyses are continuing in an attempt to derive more reliable assessments of the nuclear test detection capability of various proposed CTBT monitoring networks.

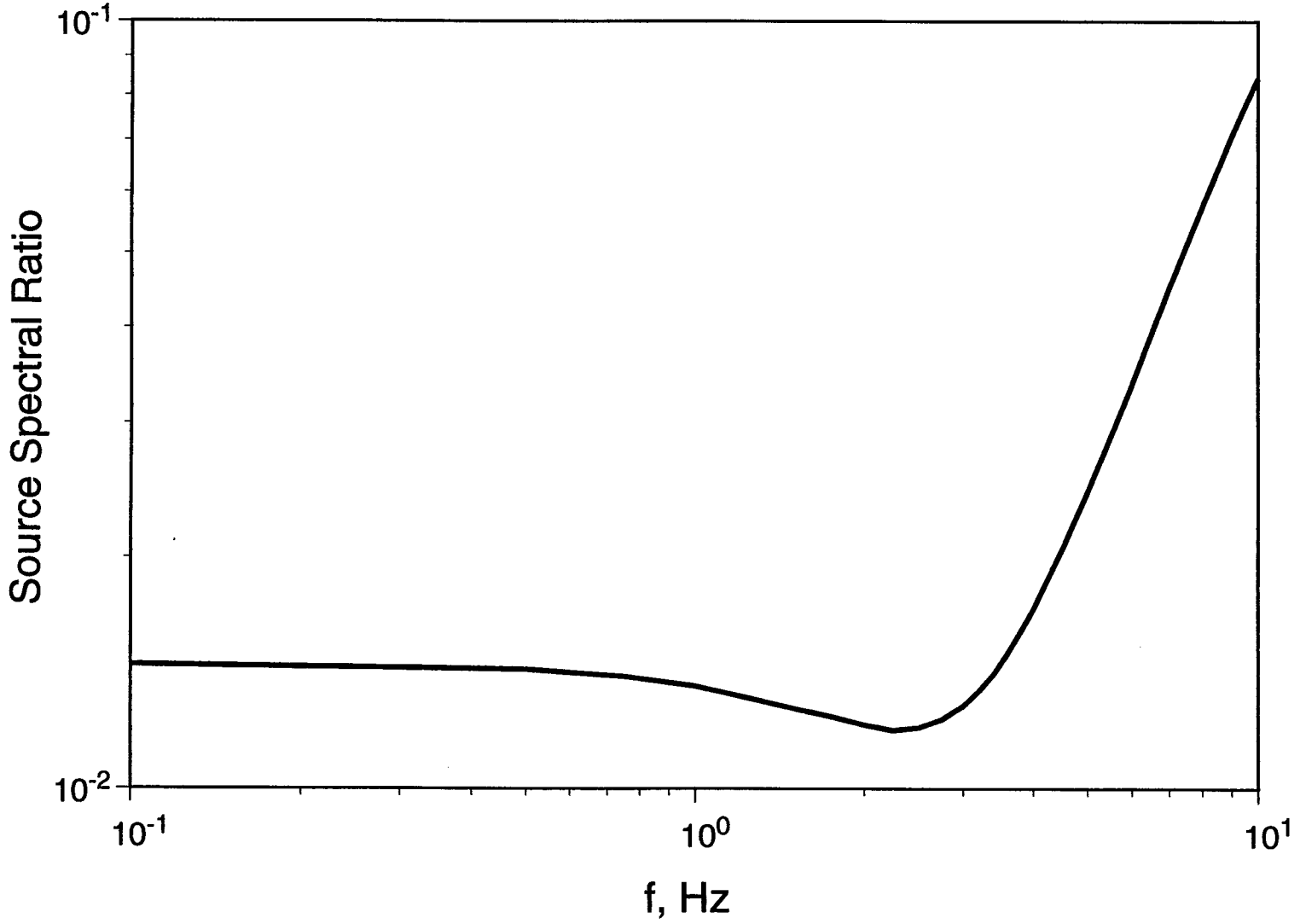

Figure 1. Theoretical seismic source spectral ratio of a 1 kt cavity decoupled explosion to a 1 kt tamped explosion.

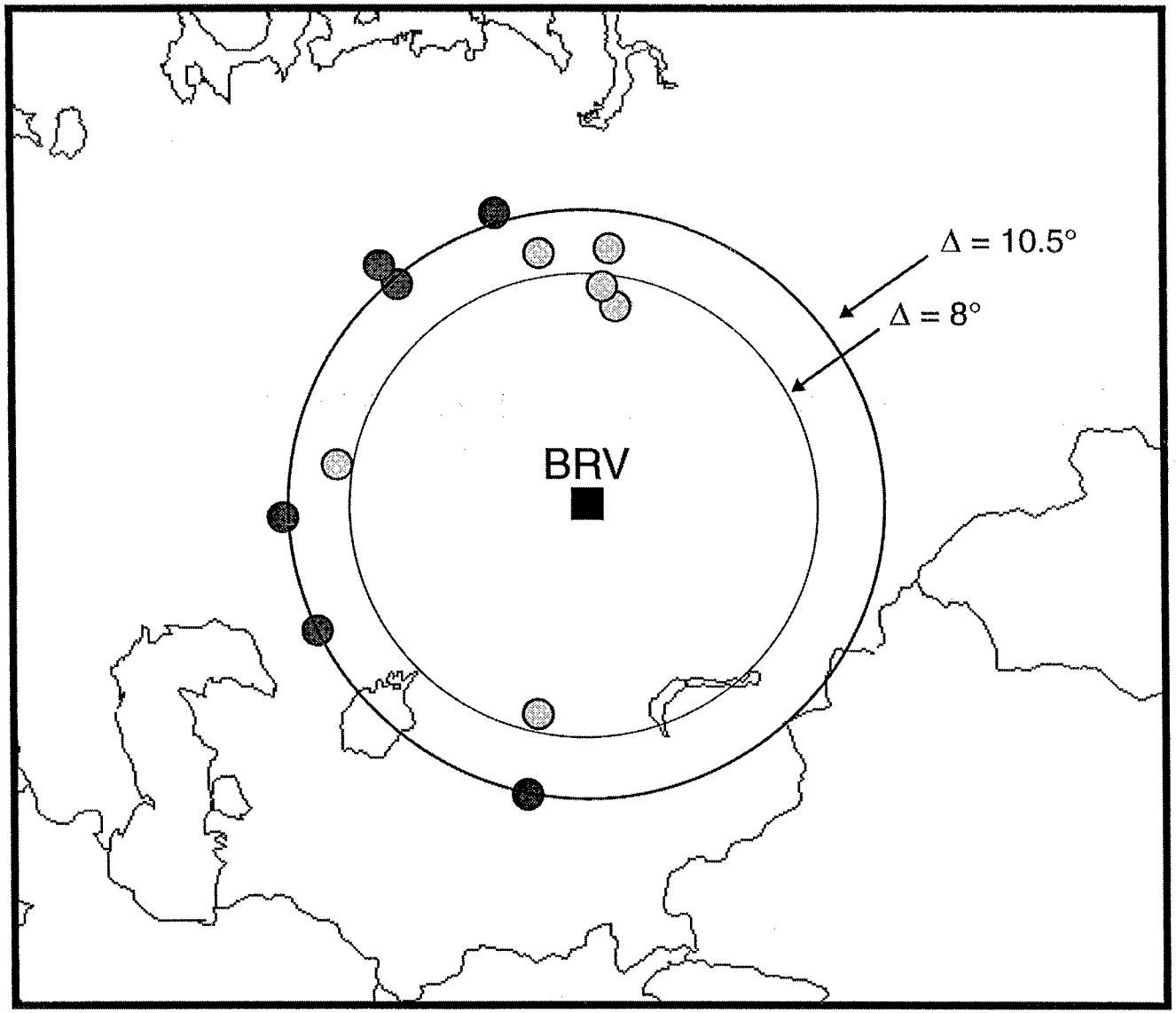

Figure 2. Locations of selected Soviet PNE events with respect to the Borovoye (BRV) station. The open circles correspond to six explosions at an average epicentral distance of about 8 °; the filled circles correspond to six explosions at an average epicentral distance of about 10.5 °.

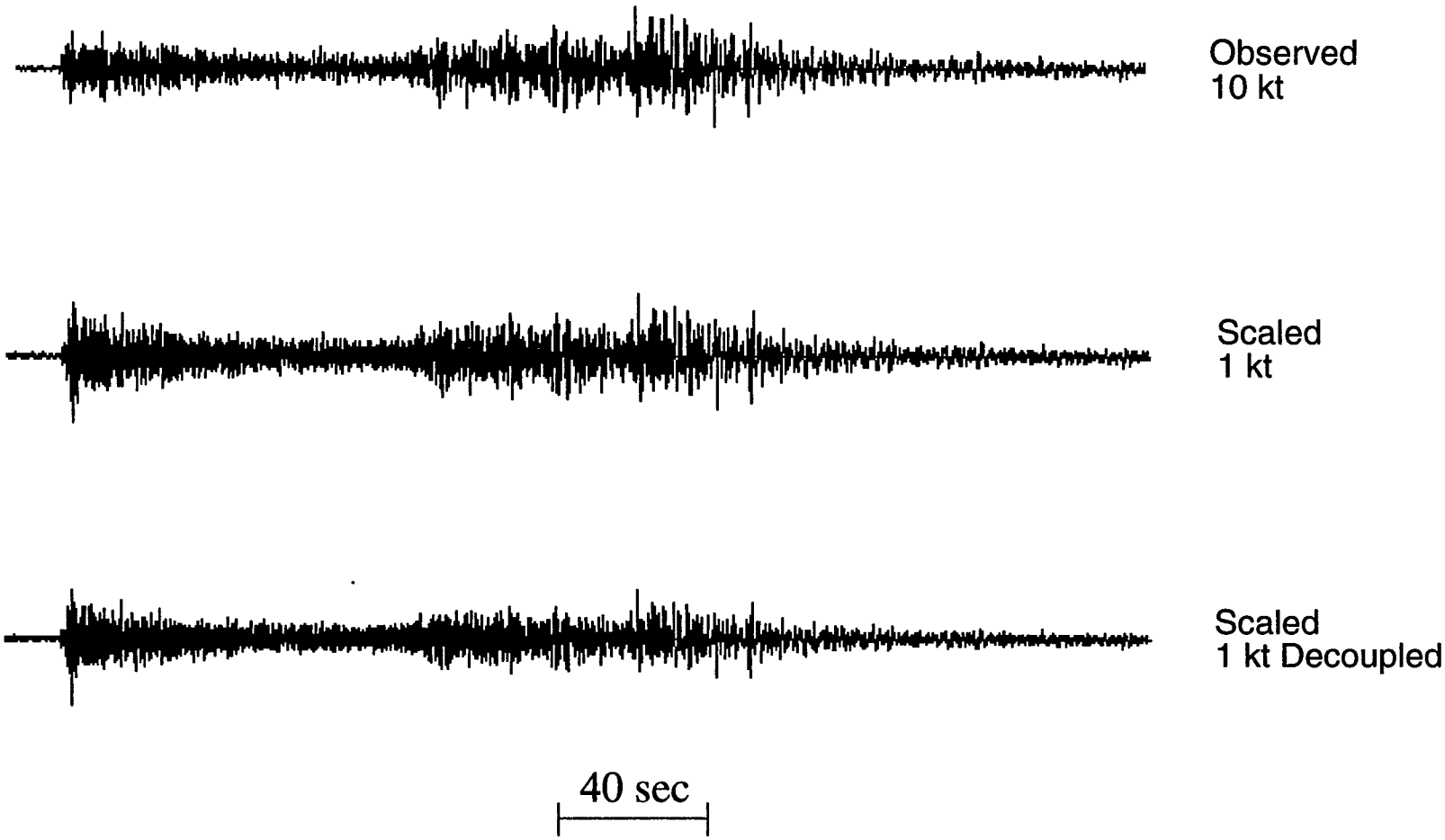

Figure 3. Comparison of observed and theoretically scaled broadband seismograms corresponding to the vertical component Borovoye recording of the Soviet PNE test of 10/26/73.

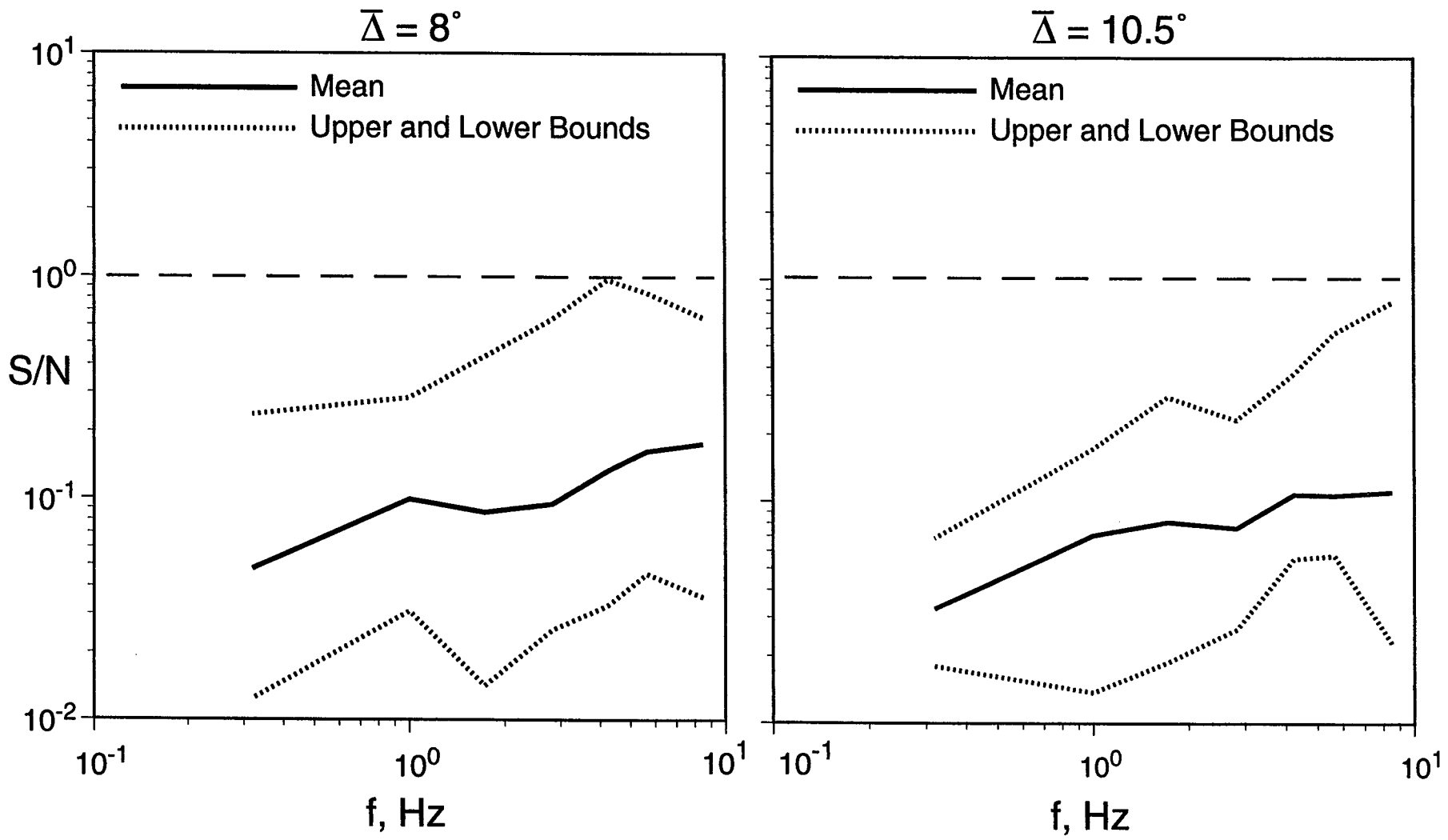

Figure 4. Estimated frequency dependent signal to noise (S/N) ratios at the Borovoye station corresponding to six different simulated 1 kt cavity decoupled explosions at average epicentral distances of both 8° (left) and 10.5° (right).

Path Calibration, Source Estimation and Regional Discrimination for the Middle East

Chandan K. Saikia, B. B. Woods and H. K. Thio
Woodward-Clyde Federal Services, Pasadena, CA 91101
Contract F19628-95-C-0093
Sponsored by ARPA

ABSTRACT

We have analyzed observations of earthquakes occurring in the Hindu-Kush regions to establish a basis for location and discrimination using the new broadband station NIL (β station), which is located near the site of the PKAR (α array) in Pakistan. Preliminary analyses of the regional data at NIL in terms of the $E_{SP\text{-}Pz}$:$E_{LP\text{-}3}$ discriminant by our seismic discriminating module produces a plot not unlike those produced by a similar analyses of TERRAscope data for the southwestern US. NTS explosions plot consistently higher than regional earthquakes in the TERRAscope data. In the NIL earthquake population, deep events appear like explosions as they have weak surface waves relative to the body waves. An identical problem occurs for the m_b:M_s discriminants for events in this region. Thus estimating the source depth for a deep event ($M_w \geq 4$) in this region becomes crucial for a successful implementation of the discrimination module. For a sparse network, finding reliable hypocentral locations of seismic events using travel time data is difficult, especially for events recorded by only one or two stations. For such situations path calibration becomes an integral part of event identification. We selected 5 crustal and 5 sub-crustal events ($M_w > 4$) which were recorded by temporary local arrays in Pakistan (PAKN) located near and to the northeast of NIL and in Kyrgyzstan (KNET) to calibrate regional paths. Several 1-D models were developed to fit the local waveform data and a useful library of Green's functions was generated for use in the source parameter inversion. The source depth of the shallow events was constrained by the ratio of Pnl to surface wave amplitudes. The depth constraint for the deep events was provided by the time separation between sPmP and P waves. Teleseismic and far-regional synthetics predicted by standard earth models and the local source inversion parameters compared quite well for events with $M_w \geq 4.5$, although the depth phases (pP and sP) were not always clear for shallow events. The analysis of small events become problematic even for stacked array data although upper-mantle triplication arrivals still provide reasonable estimates of location (50 km). A comprehensive review of these 10 master event locations relative to those estimated by ISC and AFTAC reveals the importance of local data, especially for depth controls. In addition to these 10 events and those reported in the monthly bulletins of ISC and PDE, the PAKN array recorded many small events. Many of these small events (from 10 to 20 daily with M_L's > 3) are deficient in long-period signals and about 75% of them are also observed at AAK station located in the middle of the KNET array.

A similar study is also in progress in the western Mediterranean region for monitoring North Africa. Using few selected master events (M_w >4.7), we have developed crustal models for the various local (MEB, GFA, MDT) and GSETT-3 (PAB, VSL, TBT) stations and used these models to determine their source mechanisms using regional waveform modeling. We also determined single-station mechanisms which are consistent to those obtained by multi-station data. Deep events in this region show the same features in the $E_{SP\text{-}Pz}$:$E_{LP\text{-}3}$ discrimination as experienced in the Hindu-Kush region.

OBJECTIVE A recent review of effective regional discriminants and their transportability indicates that a discriminant rule established in one region does not readily apply to another. For example, the present m_b:M_s technique has difficulty in identifying seismic events in the Hindu-Kush region, a region of complex geology (Blandford, personal communication). These difficulties have been traced to deep crustal events and upper-mantle events which have correspondingly weaker M_s than shallow events, making them fall in the explosion population. Similarly, the $E_{SP\text{-}Pz}$:$E_{LP\text{-}3}$ ratio vs. distance discriminant (Woods and Helmberger, 1996) has difficulty when applied to three-component broadband seismograms from the stations NIL (Figure 1); deep earthquakes appear as explosions as they lack long-period fundamental-mode surface waves. For an automated IDC event identification sub-system to perform well in the regions of deep seismicity, especially in North Africa and Middle East, toward CTBT, we need to develop complementary discrimination tools which will be able to distinguish the deep events from the group of outliers that separates from the shallow and intermediate depth earthquake population ($M_w > 3$). To this end, development and performance testing of automated discrimination modules that contain appropriate path calibrations for North Africa and the Middle East is the primary objective of this work.

RESEARCH ACCOMPLISHED

Source Parameters from Regional Seismograms: Significant progress in lowering the magnitude threshold to M_w 4.0 has been made recently in retrieving source mechanism from regional broadband seismograms (Zhu and Helmberger, 1996). Figure 2 shows the locations of 10 events along with their focal mechanisms obtained by using this direct grid-search technique. The data set comes from two broadband arrays: the KNET array (Pavlis and Mahdi, 1995) and the Pakistan Himalayan array, PAKN (Sandvol et al., 1994). All the velocity seismograms from the two arrays were integrated and band-passed filtered between 5 to 100s for source parameter inversion. The dots indicates the locations and mechanisms as determined by thee two arrays (solid) as compared to the two station (AAK and SBRA) solution (grey). Note that SBRA is near GSETT-3 station NIL which has recently become operational.

The depth is a non-linear parameter in the source inversion procedure. For crustal events, we found that the source mechanisms are very stable over a large depth range. Figure 3 shows the crustal source estimates determined from two arrays, both separately and together. For all the events, they have well defined minima except for the event 311.1758 (Jul day: 311; Origin time: 17h 58m) which is a relatively small event (Mw=4.5). One of the best recorded shallow earthquake is the earthquake 328.2311 (Mw=5.1) which occurred at about an equal distance between the two arrays. Figure 4 shows the observations and the synthetic fits for the best source depth of 10 km. The surface waves (Love vs Rayleigh) are about equal size indicating a mixed mechanism and the overall fit is excellent as indicated by the low misfit error. The relative strengths of two types of surface waves plays a key role in fixing the depth. The depth resolution and fit between the synthetic and data are generally better in comparison to the crustal events. Part of the reason is that they do not generate surface waves which helps to constrain the focal mechanism. Another reason is that the inversion uses the P and SV waves separately, so the S-P times are not employed to constrain focal depths. To refine a deep event's location and mechanism we conduct a depth grid search with no relative time shifts allowed, see Figure 5. A detail discussion of all these features can be found in Saikia *et al* (1996). Presently, we are using these 10 events to understand various waveform characteristics of a pool of new data from events in the magnitude range $4 > M_w > 3$ recorded both by the PAKN array and a

permanent broadband station, AAK, to the north.

Regional Modeling: The geological structure between the two arrays (KNET and PAKN), is probably amongst the most complex on the earth. It contains high mountains, the western Himalayan syntax, major boundary faults, sutures and two subduction zones. Mapping of 3-D structure, while interesting, is quite impossible given the current data coverage and resources. However, one can idealize the structure in a manner that allows the best use of the two permanent broadband stations NIL and AAK in future efforts by the IDC system in locating events and identifying their source types. Several crustal models have been developed using the direct waveform modeling, we relied on two methods to generate synthetic seismograms: the frequency-wavenumber method which yields complete wavefield, and generalized ray theory (GRT) which provides quick estimates of timing and synthetics. These two methods are highly complementary when used in conjunction.

A particularly important phase that was observed on both broadband data sets for deep events is the phase sPmP which follows an S-wave and changes mode. This can become critical and develop a head wave sPn, see Figure 6, as noted by Zhao and Helmberger (1994) in the Garm observation. Generally, the seismograms recorded at KNET array show more scatter compared to the seismograms recorded at PAKN array, especially in the short-period wave propagation, but even then the sPn phase is quite clear at KNET. The separation between direct P and sPn is depth diagnostic in depth estimation and since we need to have strategic tool to identify deep events amongst the outliers in Figure 1, we conducted a series of numerical experiments to develop a better appreciation of the sPn phase and its relationship to the direct SV wave. Figure 6 shows part of this effort where column (a) contains the motions produced by phases arriving at the surface layer leaving the source as S, and column (b) contains results of (a) plus the moho reflected sPmP ray. The phase sPn which becomes visible at about 350 km dominates the long period beyond 400 km as can be seen in Figure 5 The broadband features of sPmP are strongly influenced by the surface structure at the bounce point while the local PL waves following S are more sensitive to the receiver structure. Allowing these two surface conditions to vary produces reasonable fits to many of the broadband records, Saikia *et al* (1996).

Analysis of Short-Period Array Data: We have also examined the quality of P and pP waveforms of 10 master events recorded teleseismically by five short-period arrays, namely ASP and WRA (Alice Spring and Warramunga, Australia), GBA (Gauribidanur, India), CHG (Chiang Mai, Thailand) and GET (Egress, Germany) arrays. Of these five arrays, the GBA array is located in the upper-mantle range of 22-26°, and the CHG array is located in the range of 29-33° which is a transition to the teleseismic range. The Australian arrays are located at about 82° away from the selected events. In general, array data are used for detection, location, discrimination and yield estimation of low-yield events (Baumgardt and Der, 1994; Fisk et al., 1994), but for regions like the Middle East, we are using array data to explore their utility in estimating the source depth of earthquakes. By examining waveform data, we noticed that depth phases are distinctly observed as well separated from the direct P waves for deep events. Depth phases arrive close to the direct P when the events are shallow, and sometimes when the array location is in the upper mantle triplication range, the interaction is even more complicated as was observed in the GBA array data (Figure 7). Arrivals from the 400 and 600 km discontinuities also appear in this distance range. Analysis of limited array data indicated that the short-period teleseismic data alone cannot provide sufficient control for source

depths of the Pakistani earthquakes, especially for low-magnitude events. The ASP array seems to be naturally calibrated in amplitude (agrees very well with local data) and is quite useful in predicting the true strengths of events from the Hindu-Kush region.

Event Triggered Algorithm and Possible Discrimination (Mw>3.0): The PAKN array operated for a period of about 3 months in 1992. During this brief period, this array picked up many events (10 to 20 events daily), not reported in the ISC monthly bulletin. We are in the process of archiving these additional data, and locating those events which have simultaneously been recorded at AAK station using the HYPOCENTER program. Events are small (Mw < 4.0) and the signal-to-noise ratio is poor, especially at long periods. To detect and locate these events and to automatically pick P and S travel times, we are using an event-triggered algorithm developed by Prof. H. Kanamori (personal communication) which is a part of an automated source retrieval system operating at TERRAscope stations. It uses velocity seismograms and computes two average energy values, called short-time (STA) and long-time (LTA) energy averages. The quantity STA is estimated by moving a specified length of time window along the time series and is assumed to increase in strength when it includes the P or S onset. The quantity LTA measures the strength of noise over a length of time window prior to the P or S arrivals. Users provide tolerance values for the STA/LTA ratios for P and S waves above which the algorithm will identify the occurrence of the individual waves. Once P wave is detected, the algorithm determines the azimuth of the event by minimizing the energy in the Pnl window using the transverse motion. For large events (Mw > 4.0), the algorithm appears to be smart enough to determine the azimuth to within 20°. However, for smaller events the P window is contaminated by site-specific scattered energy and determination of the azimuth becomes somewhat difficult. We plan to include this event-triggered algorithm in the IDC off-line subsystem; its objective is to provide initial estimate of epicentral distance based on an assumed source depth for the discriminants.

Works Related toward Monitoring North Africa: Contrary to the Hindu-Kush region, many seismic stations of this area report to the ISC, thus helping to provide path calibration and location information of even relatively small earthquakes. We have developed crustal and upper-mantle models for the western Mediterranean region to provide path calibration for various local and regional GSETT-3 stations so that events from the North Africa can be monitored. We found the crustal thickness to vary in the area: 37 km under Algeria, 20 km under the western Mediterranean and 28 km under southern Spain. We obtained these estimates by inverting average surface-wave group velocities along various paths. The upper-mantle under Algeria is comparable to model TNA of Grand and Helmberger whereas the upper mantle under Spain has a more shield-like character.

Using the phase velocity corrections based on the calibrated structure models, we have determined focal mechanisms and source depths of several master events (Figure 8). These solutions are consistent with those obtained by teleseismic waveform analysis *e.g.* the Harvard CMT solutions whenever the latter is available. The depths of our solutions are also consistent with those obtained using the teleseismic depth phases, whole-record regional waveform inversion, and depth phases recorded by short-period arrays like the Sonseca array in Spain. We have also inverted the complete waveforms recorded at PAB (TOL) separately (Figure 9) and find that single-station source mechanisms are as reliable as those obtained by modeling waveforms from several stations for events down to a magnitude 4.5.

An important phenomenon related to the seismic discrimination is the blockage of Lg waves. Strong blockage occurs in seismograms recorded along the paths that cross the Mediterranean sea compared to those that do not (Figure 10), which is in contrast with the Pakistan region where no Lg blockage or strong Sn attenuation is observed.

Finally, the seismic discrimination analysis, using the $E_{SP\text{-}Pz}$:$E_{LP\text{-}3}$ discriminant, of all waveforms that we have compiled for this region also indicates that the deep earthquakes do separate from the shallow earthquakes (Figure 11), similar to the deep Pakistani earthquakes. These deep earthquakes occur throughout the Mediterranean around the Strait of Gibraltar, the Calabrian and the Hellinc arcs.

CONCLUSIONS AND RECOMMENDATIONS

Attempts at calibrating teleseismic and regional paths has proved to be quite difficult. Therefore, we wanted to ascertain what we can achieve using the PAKN array, by using the broadband seismograms from NIL (in fact we used the SBRA station from the PAKN array as a proxy for NIL) and AAK stations alone to retrieve the source information. We used the ISC locations of the master events as initial locations and used the two stations SBRA and AAK to determine source parameters. For most of the events, just two-station source parameter inversion estimates seem compatible with those estimated by the full network. A comparison of these results can be found in Tables 6.1 and 6.2 of Saikia *et al* (1996). Our current effort is toward developing an automated system which will use broadband data from a single station (say from the PAKR α array) to locate an event and identify its source type.

Our source depth location study is comprehensive, making use of travel-time data, analysis of regional broadband waveforms with respect to depth phases, and the strength of P_{nl} waves relative to the surface waves, and analysis of teleseismic depth phases. The method that we have developed is highly effective for events with magnitude down to M_w of 4.0 which are not always recorded at teleseismic and far-regional distances, especially their depth phases.

Unlike the southwestern US experience, the Hindu-Kush region has seismicity spread over the entire crust and into the upper mantle which makes seismic discrimination more difficult, especially for the $E_{SP\text{-}Pz}$:$E_{LP\text{-}3}$ and related discriminants. Deep events excite very little long-period surface waves and consequently deep earthquakes appear as explosions. However, considering all events which do not agree with the shallow earthquakes criterion, we have added an extra step to our discrimination tool which invokes regional waveform modeling to determine their depths. Any event that cannot be proven deep could be an explosion or an outlier. For this discrimination tool to be successful, we will require at least two broadband stations, for example NIL and AAK for the Pakistani events, with continuous data streams; thus it is necessary to integrate the short-period PAKR array with a broadband station and add AAK station to the β stations.

The PAKR array is surrounded by seismicity of varying magnitude. Accurate locations of small magnitude events and the behavior of applicable regional discriminants are highly valuable in identifying the source of these low-magnitude events. In general, the PAKN array seismograms are deficient in long-period for $M_w < 4.0$ making the application of $E_{SP\text{-}Pz}$:$E_{LP\text{-}3}$ discriminant difficult. For any seismic discriminants to be useful, it is necessary to establish how well these discriminants can perform in distinguishing source types of the low-magnitude events. By completing our analysis

of the archived low-magnitude events recorded by the PAKN array, we expect to contribute immensely toward this understanding.

REFERENCES:

Baumgardt, D. and Z. Der (1994). Investigation of the transportability of the P/S ratio discriminant to different tectonic regions, PL-TR-94-2299, Scientific Rept #1, Phillips Laboratory, Hanscom AFB, MA 66p. ADA 292944

Fisk, M. D., H. L. Gray, and G. D. McCartor (1994). Preliminary assessment of seismic CTBT/NPT monitoring capability, PL-TR-94-2300, Scientific Rept #1, Phillips Laboratory, Hanscom AFB, MA, 39p. ADA 293188

Pavlis, G. L. and H. Mahdi (1995). The spatial stability of Rayleigh wave amplitudes and path dependent propagation characteristics of central Asia, Proceed. 17th Seis. Res. Symp., PL/AFOSR/DoE, held at Scottsdale, AZ, 291-298. PL-TR-95-2108, ADA 310037

Saikia, C. K., B. B. Woods, L. Zhu, H. K. Thio and D. V. Helmberger (1996). Path calibration, source estimation and regional discrimination for the Middle East: Application to the Hindu-Kush, PL-TR-96-2069, Scientific Rept #1, Phillips Laboratory, Hanscom AFB, MA,120p.

Sandvol, E., J. Ni and T Hearns (1994). Seismic azimuthal anisotropy beneath the Pakistan Himalaya, Geophys. Res. Lett., 21, No 15, 1635-1638.

Woods, B. B. and D. V. Helmberger (1996). Regional seismic discriminants using wavetrain energy ratios, Bull. Seis. Soc. Am., (accepted).

Zhao, L-S. and D. V. Helmberger (1994). Source estimation from broadband regional seismograms, Bull. Seis. Soc. Am., 84, 92-104.

Zhu, and D. V. Helmberger (1996). Advancement of source retrieval from broadband regional seismograms, Bull. Seis. Soc. Am (accepted).

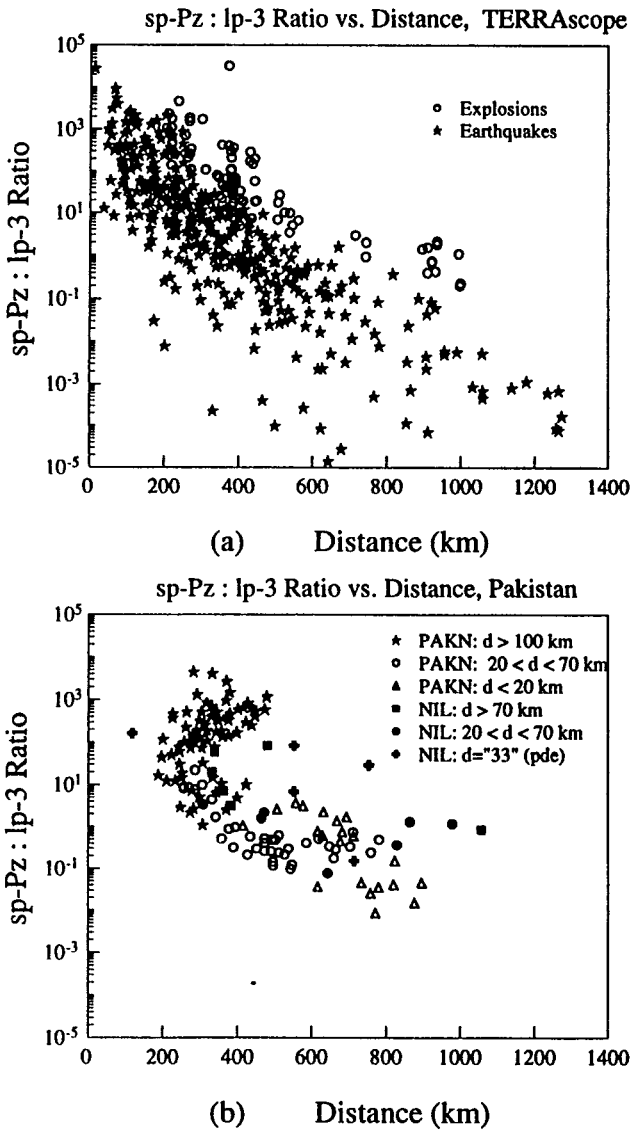

Figure 1. (a) Short-period:long-period energy ratio vs. distance for TERRAscope data. (b) The energy ratio discriminant for data recorded by stations in Pakistan.

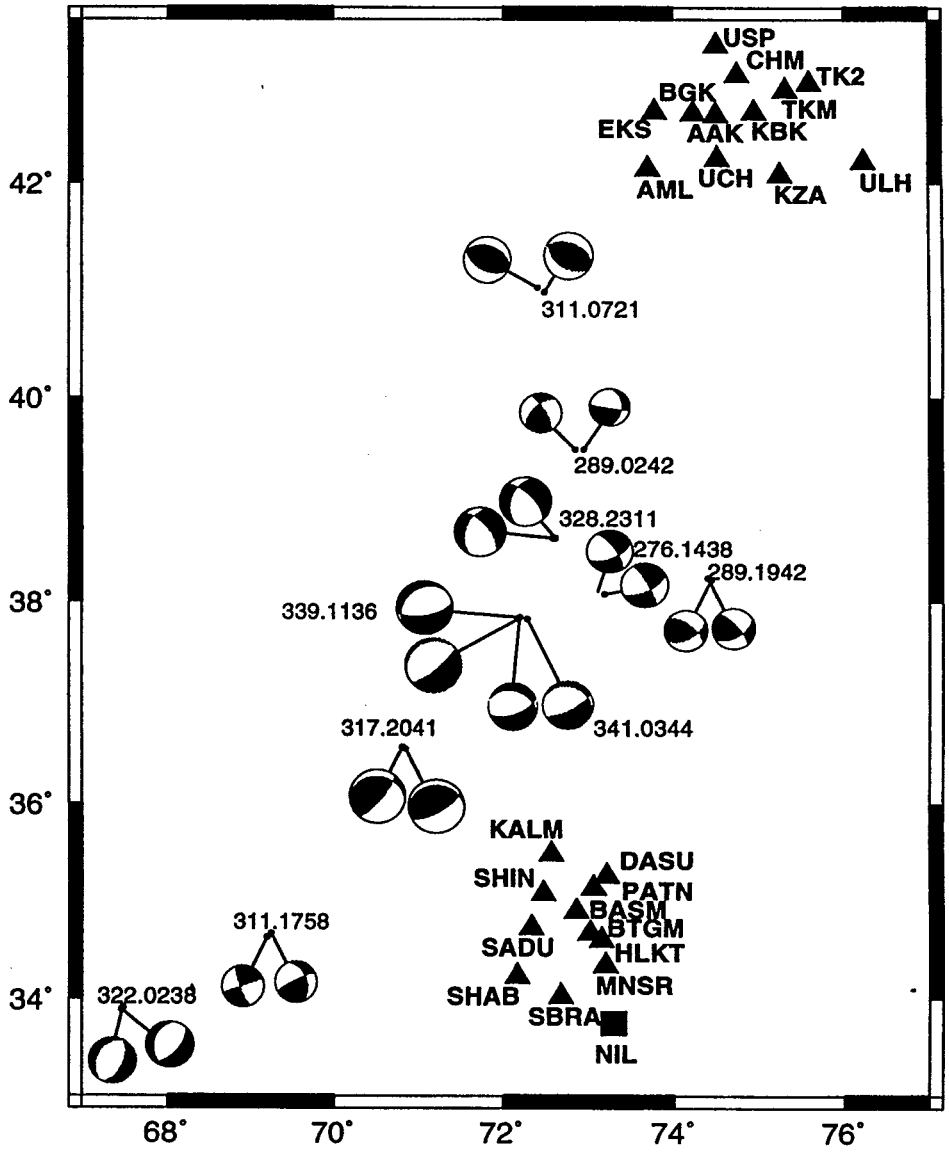

Figure 2. Map of the Hindu-Kush area showing the mechanisms determined using the KNET and PAKN arrays (black) and the mechanisms determined using two stations, AAK and SBRA, only.

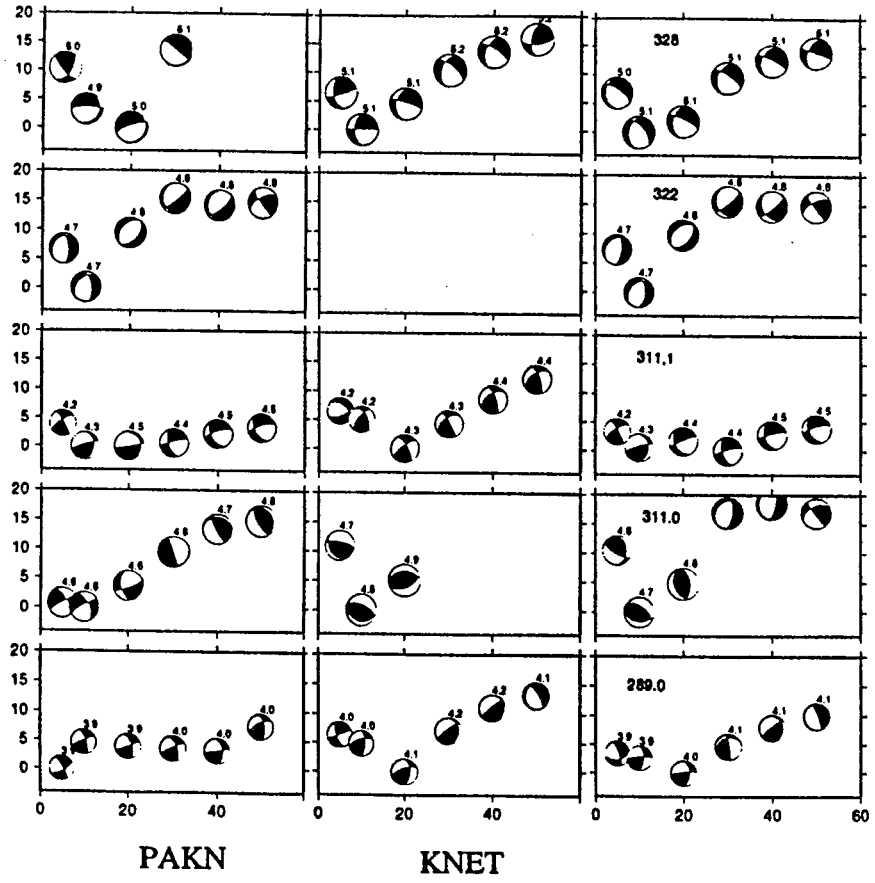

Figure 3. Display of misfit errors for crustal events as a function of depth. Solutions using the separate arrays are given on the left with the joint solution on the right.

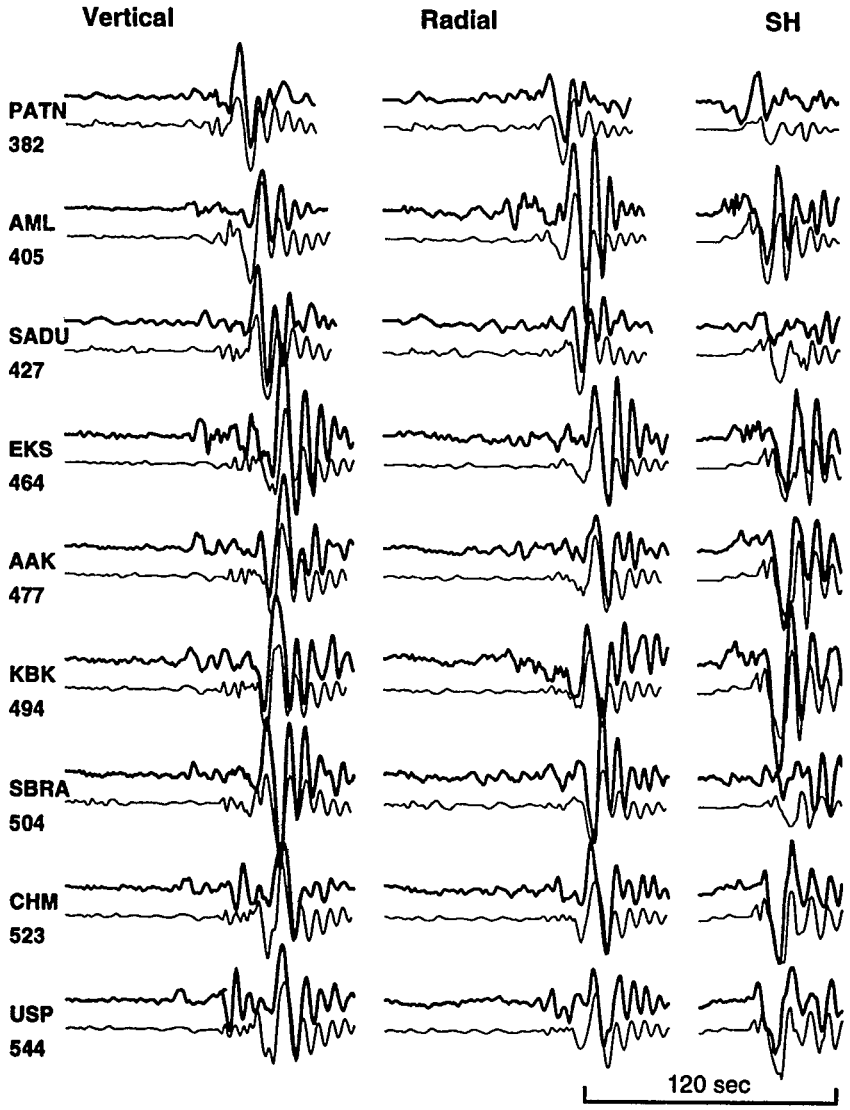

Figure 4. Comparison of the best fitting synthetics (bottom) vs. observations (top) for the 328.2311 event.

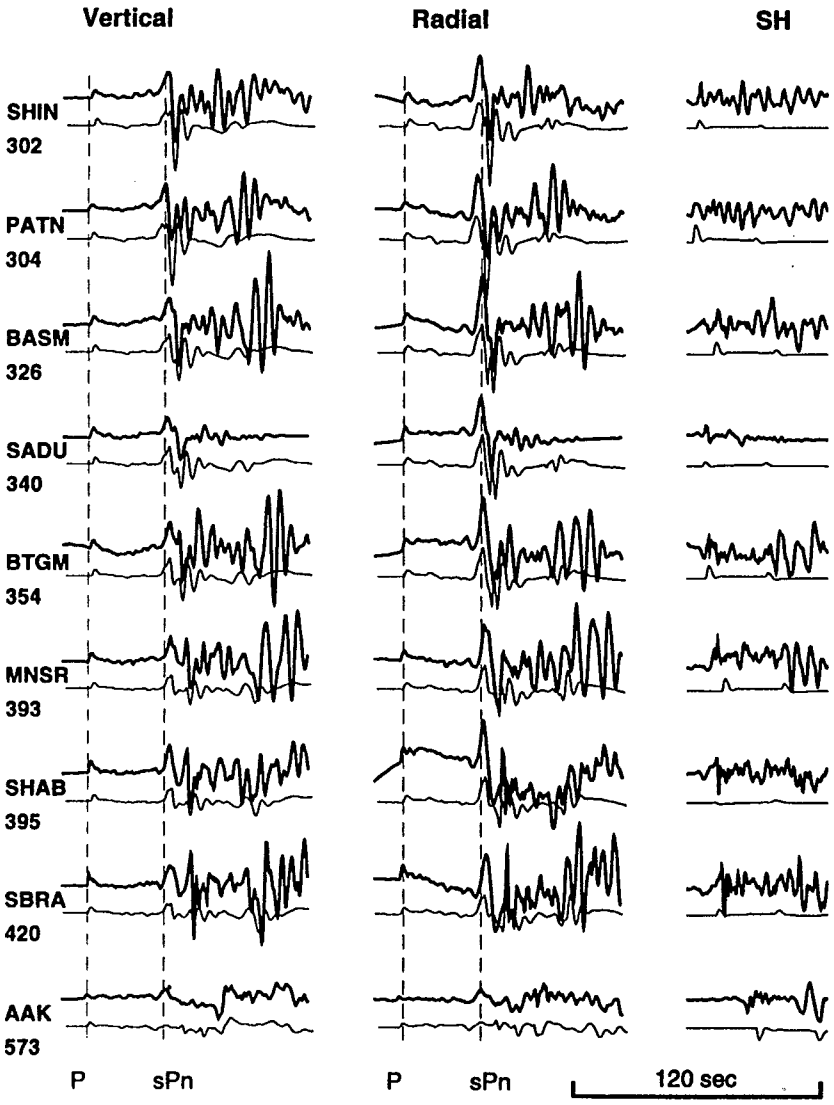

Figure 5. Observed seismograms and synthetics for a deep event (341.0344) .

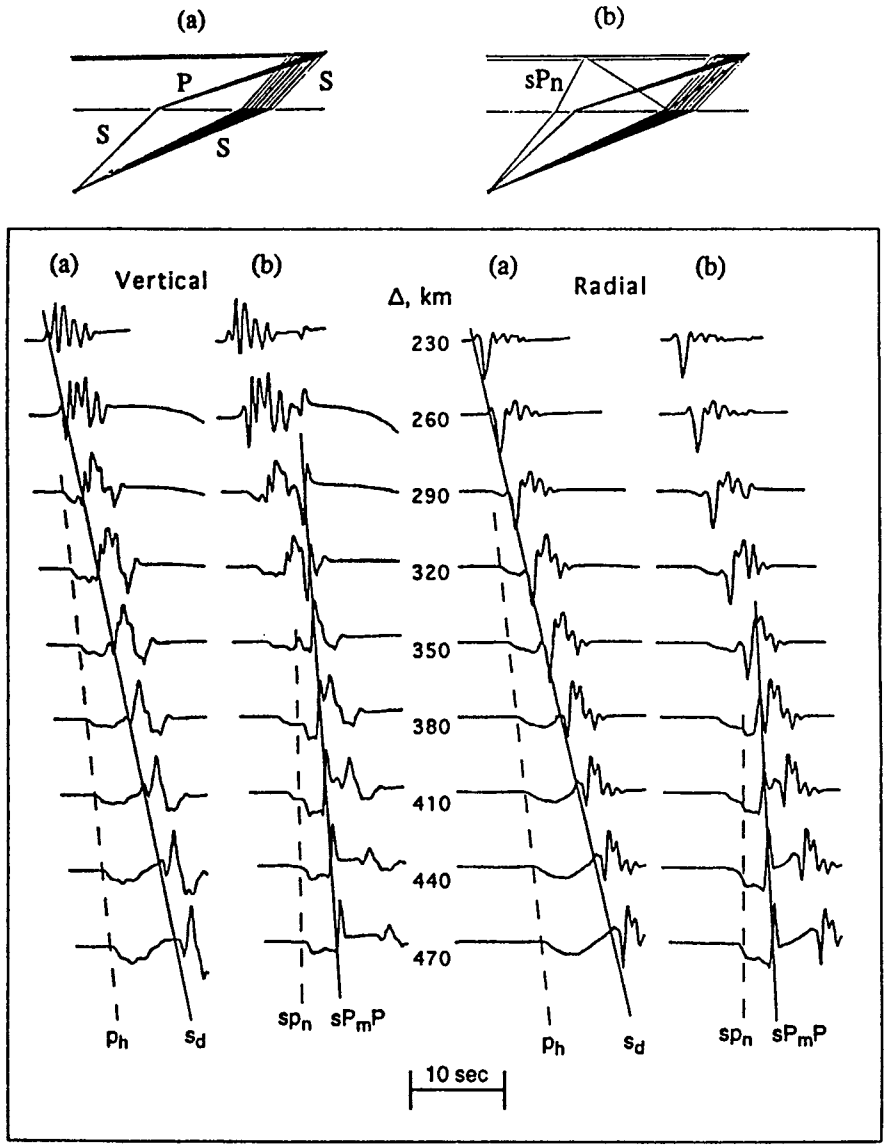

Figure 6. GRT synthetics constructed from two ray sets (a) and (b) as displayed in the top panel.

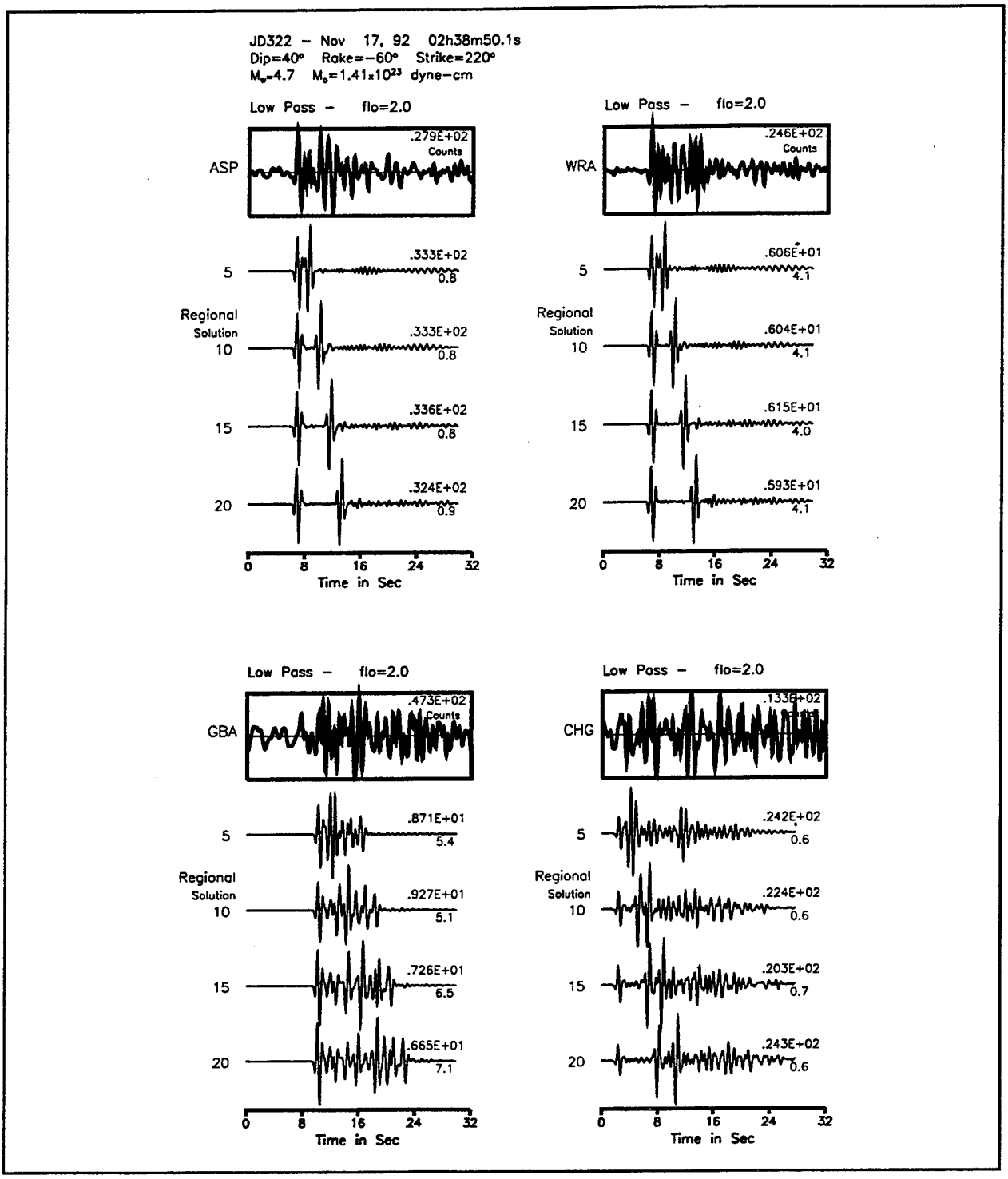

Figure 7. Comparison between data and a suite of synthetic seismograms at ASP, WRA, GBA and CHG for event 322.0238. The depth of each synthetic waveform is given at the left of the trace. The number at right and below the trace is the ratio of observed to synthetic peak amplitude. Peak amplitudes are in counts. Note the clear depth phase recorded at ASP.

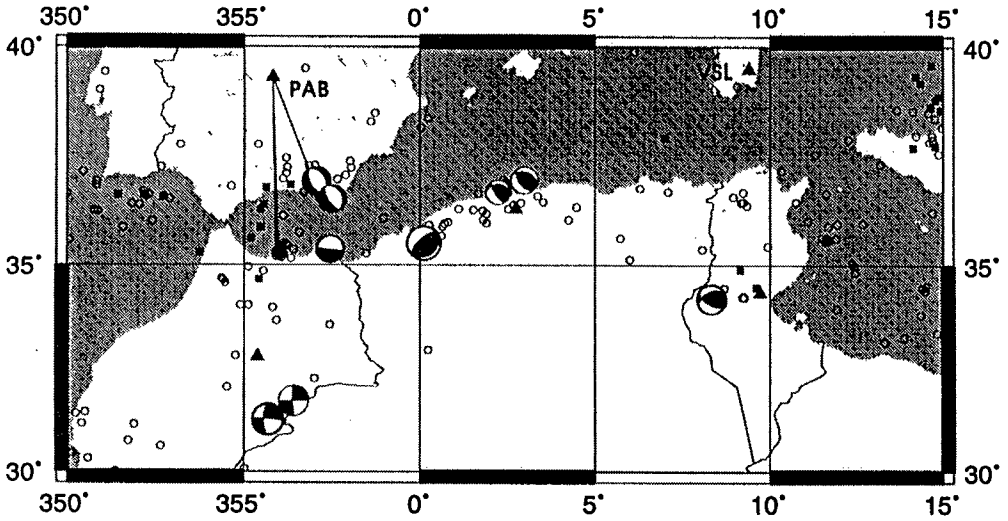

Figure 8. Map of the Western Mediterranean region with the focal mechanisms of the master events. Stations are represented by triangles, crustal earthquakes are open circles and subcrustal earthquakes (> 33 km) are black squares. The paths to station PAB correspond to the seismograms in figure 10.

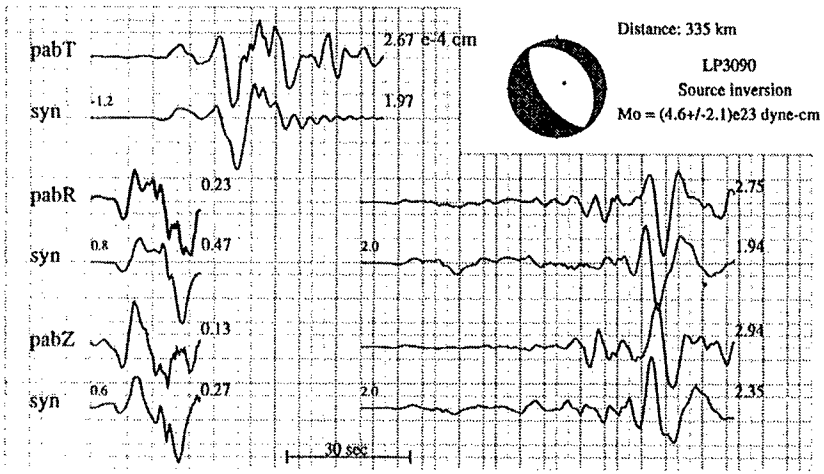

Figure 9. Results from a single station source inversion for an event in Southern Spain recorded at PAB.

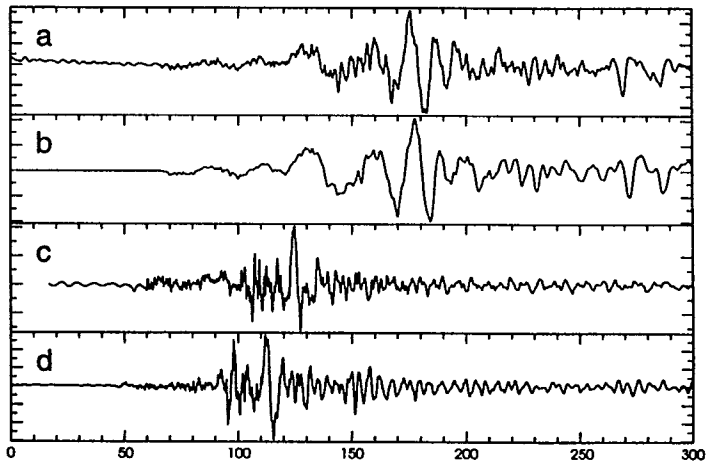

Figure 10. A comparison of seismograms recorded at station PAB for two events in North Africa (a and b) and two events in Southern Spain (c and d). The paths are shown in figure 8.

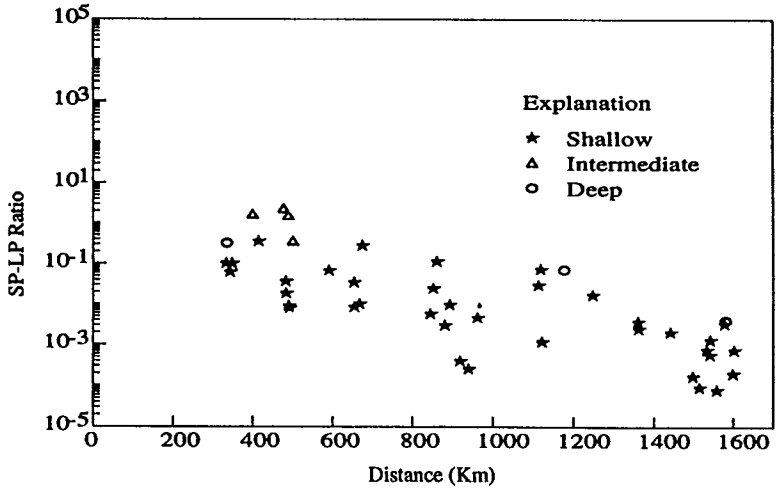

Figure 11. Short-period:long-period energy ratio vs. distance for events in the Western Mediterranean.

SCANLOC: Automatic seismic event location based on local seismic network data

B.M. Shoubik, A.F. Kushnir, L.M. Haikin**, A. Dainty****
** Joint Institute of Physics of the Earth RAS*
*** Moscow IRIS Data Center/SYNAPSE Science Center*
**** Phillips Laboratory USAF*

EOARD Special Project SPC-95-40-45
Sponsored by AFOSR

ABSTRACT

In this paper we use the principles of seismic emission tomography to create an automatic event location procedure based on data from a seismic network or array. Previously this method has been used for localizing microseismic activity in active seismic zones. The essence of our approach is to look for a "bright spot" by seismic beam scanning the area under investigation. An advantage of the method is it does not require detection and parameter measurement of seismic phases.

Implementation of the principle varies depending on the epicenter distance and the seismic network scale (regional network, local network, or array with aperture of several dozen km). In array data analysis it might be effective to use coherent stacking in the beamforming procedure. However, coherent stacking is likely to prove ineffective in regional and local seismic network data processing. Accordingly, incoherent analysis methods in the grid scanning technique are used in this paper.

Results of experimental processing of Israeli local network data show that the method allows determination of event epicenters with errors which do not exceed 1-2 scanning grid steps (in our experiments 5-10 km). The computation time for scanning a square of size 255 km x 255 km processing data from 10-20 sensors with sampling rate 50 Hz does not exceed 10-20 sec for a SPARC-2 workstation. Thus, a near real-time automatic location technique could be designed on this basis.

Keywords: Location, Automatic, Seismic Emission Tomography, Incoherent Stacking, Signal/Noise Estimation Functional, STA/LTA

OBJECTIVE

Robust methods for automatic event location and origin time determination of numerous small earthquakes and mining explosions at local and regional distances is an important part of modern CTBT monitoring technology. The goal of this research is to design a reliable method for fast automatic event location based on local seismic network data. This is important for monitoring in industrialized or seismically active regions. The major effort is to eliminate any need in the location procedure for the analyst verification of seismic wave phase detection and parameter estimation that is routine practice in conventional monitoring systems.

RESEARCH ACCOMPLISHED

Traditional methods for seismic event location (and evaluation of other event parameters) are based on detection, identification and precise measurement of seismic phase parameters by individual processing of recordings from every seismic network station (Kennett, 1996). Automatic methods designed using this paradigm have low computational efficiency because of the difficulty of designing algorithms which adequately reproduce the operations of a skillful geophysicist. Taking a different point of view, recording the event wavefield by a network consisting of identical sensors allows us to consider the set of recordings from all receivers as a multichannel seismogram. In some sense this seismogram is similar to those conventionally used in seismic prospecting and deep seismic sounding. Powerful tools for optimal processing of multichannel data have been developed, and some of them can be used in solving the problem of seismic event location. Similar approaches to automatic analysis of seismic data are under investigation by a number of research groups (Ryzhikov et al., 1995; Young et al., 1995; Ringdal and Kværna, 1989) and promising results have been obtained, demonstrating that new techniques specifically oriented to computer implementation are useful for solving many traditional problems in seismology.

We have developed a new automatic event location technique based on processing of multichannel recordings from local and regional seismic networks. The approach is based on the seismic emission tomography technique, initially used for localizing microseismic activity zones in seismic regions (Shoubik et al., 1991; Shoubik and Kiselevich, 1993; Gurevich et al., 1994). This method performs automatic event location and origin time determination without preliminary detection and identification of seismic phases and estimation of their parameters. The essence of the method is to scan the medium volume under study by a beam formed from the seismic network recordings. The volume is partitioned into an equidistant scanning grid and beam power coefficients at every point of the grid calculated. The coefficient values are the relative energy of seismic waves radiated from grid units (small volumes of the medium under study). The "Signal/Noise Estimation" (*SNR*) procedure is used for these calculations.

The processing algorithm is based on a linear additive model of signals and noise at the network sensors:

$$f_m(t) = \alpha_{mijk}\, \phi_{ijk}(t-\tau_{mijk}) + \varepsilon_m(t) \qquad (1)$$

where: $m = 1,2,...M$ is the number of the sensors; $f_m(t)$ is the seismic time series at the m-th sensor; t is receiver time; α_{mijk} is the amplitude decay factor due to geometric spreading, angle of

incidence and attenuation (absorption and scattering) of the signal at the m-th sensor; $\phi_{ijk}(t)$ is a signal emitted from the source volume element with coordinates X_i, Y_j, Z_k; τ_{mijk} is the time delay determined by the signal travel time; $\varepsilon_m(t)$ is the sum of seismic noise and signals emitted from other sources not coinciding with X_i, Y_j, Z_k. The location problem is reduced to a comparative assessment of the energy of signals (ϕ_{ijk}) radiated by different elements (ijk) of the volume under study (V). In order to assess the energy of the highly correlated components $\phi_{ijk}(t-\tau_{mijk})$ which are present in the multichannel recording $f_m(t)$ two functionals are most commonly used: Semblance (S) and Signal to Noise Ratio (SNR) (Katz et al., 1986). Let us designate

$$A_{ijk}(t_n) = \{ \sum_{m=1}^{M} \beta_{mijk} f_m(t_n + \Delta_{mijk}) \}^2 \quad (2)$$

$$B_{ijk}(t_n) = \sum_{m=1}^{M} \{\beta_{mijk} f_m(t_n + \Delta_{mijk}) \}^2 \quad (3),$$

then the Semblance functional is equal to:

$$S_{ijk} = \sum_{n=1}^{N} A_{ijk}(t_n) / M \sum_{n=1}^{N} B_{ijk}(t_n) \quad (4)$$

and SNR functional is equal to:

$$SNR_{ijk} = \sum_{n=1}^{N} (A_{ijk}(t_n) - B_{ijk}(t_n)) / \sum_{n=1}^{N} (M B_{ijk}(t_n) - A_{ijk}(t_n)) \quad (5)$$

where: β_{mijk} is an amplitude normalizing factor theoretically or experimentally chosen to approximate the reciprocal value of the amplitude decay factor α_{mijk} for the signal radiated from the medium element at X_i, Y_j, Z_k (i.e., $\beta_{mijk} \sim 1/\alpha_{mijk}$); N is the number of samples in the time window for which the estimate of an average correlated signal power is calculated; Δ_{mijk} is an estimation of τ_{mijk}, the time delay of the signal due to propagation from the ijk volume element to the m-th receiver, computed for the *a priori* medium velocity model.

It can be shown that for a linear additive model (1) and uncorrelated random noise in different sensors, the Semblance S converges to the ratio of the coherent signal power to the total average seismogram power, varying from 0 to 1; the Signal to Noise Ratio SNR converges to the ratio of the coherent signal power to the noise power, varying from 0 to infinity. If the ith medium element contains the seismic source the SNR value calculated for this element exceeds the SNR values calculated for neighboring grid points. The set of SNR values (5) calculated for every point X_i, Y_j, Z_k of the scanned medium surface area or the scanned medium volume (2D or 3D SNR-map) reflects the spatial distribution of seismic sources in the region under study.

The method described above may be thought of as scanning the medium by a sounding beam from the seismic network "antenna". Actual implementation of these principles will vary depending on the epicenter distance and the seismic network scale (regional network, local network, array with aperture of several dozen km). Seismic array data typically exhibits consistency (correlation) between signals recorded on different array sensors in a certain

frequency range. In this situation it would probably be effective to use coherent stacking in (2) to scan the medium area. However, this is likely to be ineffective in regional or local seismic network data processing; incoherent analysis in the grid scanning should be used. In this case the original waveforms (1) should be replaced in (2) and (3) by some low frequency signal model such as the envelope function, STA/LTA function or similar function produced by an appropriate one-channel signal phase detector.

The automatic event location method described is implemented in the SCANLOC computer software package. The main procedures of this package are:

- Forward modeling using an *a priori* velocity model of a layered medium. The procedure calculates the time delay matrix for the required number of seismic phases and for a given set of grid points and station coordinates.
- One-channel frequency filtering and signal detecting. If incoherent stacking is used the procedure calculates a low frequency signal model based on the original waveform.
- Grid scanning procedure. The procedure calculates the 2D or 3D *SNR*-map, i.e., the set of *SNR* values (5) for all grid points. This *SNR* map reflects the spatial distribution of seismic emitters in the area under study. The quality and accuracy of the event location can be assessed by the maximal *SNR* value and estimation of *SNR* dispersion.

An efficient method of scanning through the grid points was implemented in the package. The computing time for processing data from 10-20 stations with sampling rate 50 Hz and about 3000 grid points does not exceed 10-20 sec for a SPARC-2 workstation. This means it is possible to develop a near real-time automatic location technique.

The SCANLOC package was used to locate earthquake epicenters for 19 events recorded by the Israel local seismic network. We acknowledge Dr. V.I. Pinsky of the Israel Geophysical Institute (IGE) for supplying us with the set of earthquake seismograms used in this study. A short description of the data is given in (Kushnir et al., 1996). The data processing was performed by a SCANLOC package installed in the SNDA Programming Shell (Kushnir et al., 1995). Table 1 contains the event coordinates (Xcat, Ycat) from the catalogue file using a conventional location procedure implemented at IGE, the coordinates (Xm1, Ym1) of maxima from the *SNR*-maps, and the coordinates (Xm2, Ym2) of the nearest to maximum map points as a measure of the dispersion (width of the peak). The coordinates are given in a local orthogonal system with the geographical coordinates of the center (0,0) coinciding with the epicenter of the first processed event: LAT = 32.671N, LON = 35.260E. Event date and time are given by a 10 digit event label containing the year, month, day, hour, minute (2 digits each). The scanning area was 255km x 255km, 2601 grid units with a 5 km interval. In the processing we used a homogeneous velocity model with velocities of P and S waves Vp = 6.2 km/sec and Vs = 3.4 km/sec. These velocities were estimated from regression analysis of onset times of P and S phases measured at seismograms of the numerous local earthquakes and explosions recorded by the Israel network. The STA/LTA function was used as the low frequency signal model. The last column of the table shows the location error rounded off to integer km.

TABLE 1. EVENT LOCATION DATA

No	Event Date	M	Xcat	Ycat	Xm1	Ym1	Xm2	Ym2	Error
1	8710071514	1.9	0.0	0.0	0.0	0.0	0.0	5.0	0
2	8802241537	1.5	0.844	5.101	-5.0	5.0	0.0	0.0	4
3	9008210621	1.8	-10.13	-0.882	-5.0	-15.0	-10.0	-5.0	15
4	9009160941	1.6	-26.08	32.196	-30.0	35.0	-30.0	30.0	5
5	9011170729	1.2	0.937	13.419	0.0	10.0	5.0	10.0	3
6	9012211524	1.5	29.113	20.227	30.0	20.0	30.0	25.0	0
7	9101090230	1.1	1.124	12.199	5.0	10.0	-5.0	10.0	4
8	9101261746	2.6	1.218	12.310	0.0	15.0	-5.0	15.0	3
9	9101270305	1.5	5.994	15.195	-5.0	15.0	5.0	15.0	10
10	9102120832	1.4	19.470	20.647	25.0	20.0	20.0	20.0	5
11	9102250633	2.0	4.319	-9.980	5.0	-10.0	0.0	-15.0	1
12	9104071717	1.3	30.332	19.344	30.0	20.0	35.0	15.0	1
13	9104150120	2.4	31.268	19.679	35.0	15.0	35.0	20.0	5
14	9104150503	1.5	29.403	17.234	30.0	20.0	-35.0	5.0	3
15	9104160637	1.9	30.614	19.234	40.0	20.0	45.0	20.0	10
16	9104270713	1.3	29.956	20.119	30.0	20.0	30.0	15.0	1
17	9105012046	2.2	29.774	18.233	35.0	15.0	40.0	20.0	6
18	9105032206	1.0	30.244	17.680	35.0	15.0	30.0	20.0	5
19	9105160249	1.7	-26.050	45.395	-35.0	45.0	-30.0	45.0	11

It may be seen that 80% of the location errors do not exceed the scanning grid interval (5 km).

Fig. 1 illustrates some processing results for the first event from Table 1, 8710071514. The deployment of stations recording the seismograms is shown in Fig. 1a. The circle on the map marks both the origin of coordinates and the event epicenter, as discussed above. The event seismograms are shown in Fig. 1b. The seismograms are ordered according to the station-epicenter distance. The SCANLOC output *SNR*-map is presented in Fig. 1c in the form of a mesh perspective diagram.

CONCLUSIONS AND RECOMMENDATIONS

1) The new SCANLOC technique for event location based on local seismic network data was developed and tested. The processing is founded on the principles of seismic emission tomography. The results of experiments with Israel local network data confirms the high reliability and precision of weak local event epicenter location by this technique. The software written can serve as the basis for developing a near real-time location tool for seismic monitoring at local and regional distances.

2). It is possible to refine the medium velocity model within the framework of the event location method. The peak value of the calculated *SNR* map can serve as a performance criterion of the velocity model used: a better velocity model provides a greater peak.

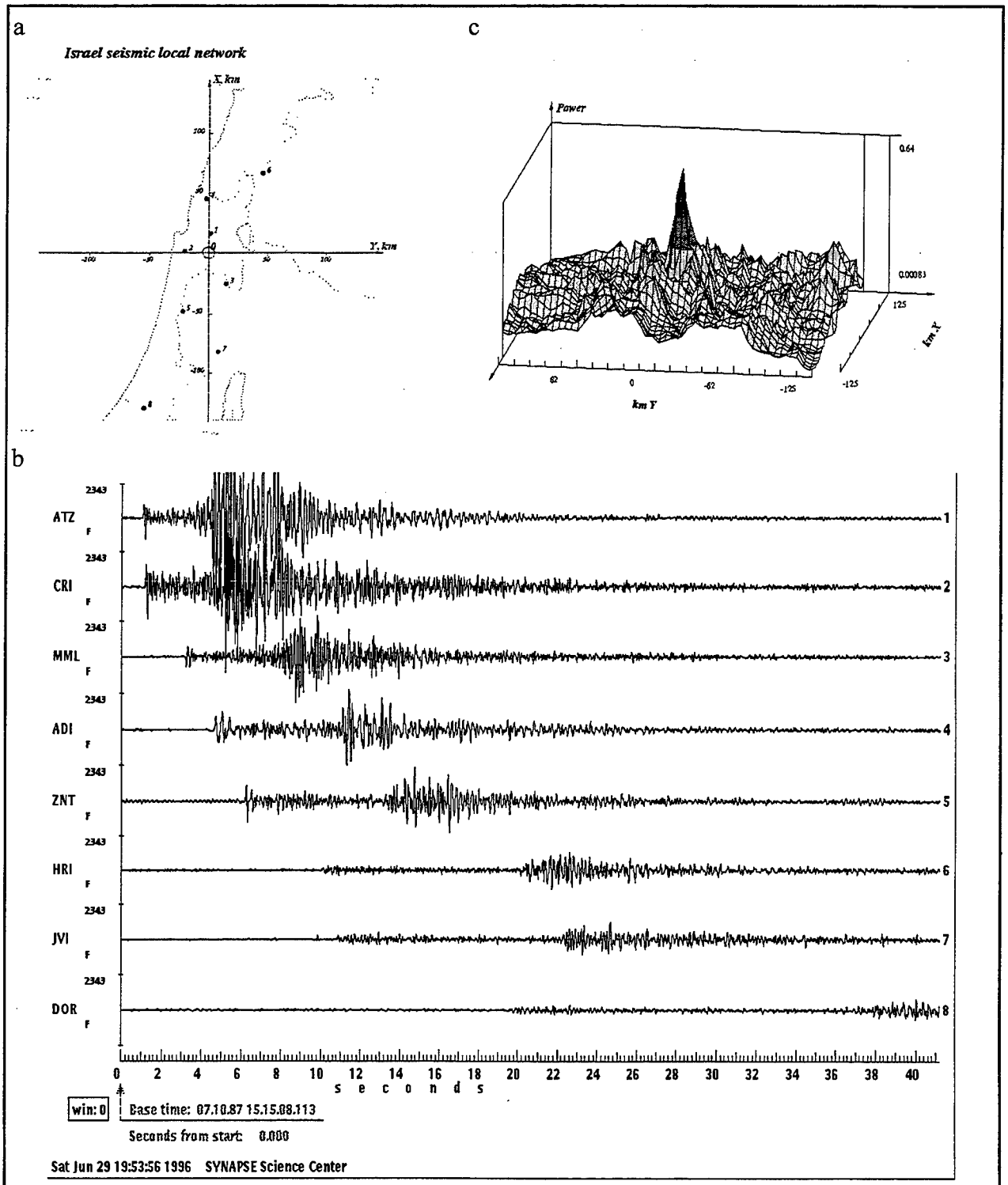

Fig.1. Epicenter location of event 8710071514. a) Stations of the Israel local network recording good seismograms. Circle shows the event epicenter determined by IGE. b) Seismograms. c) Estimation of event epicenter coordinates. The maximum value of the *SNR* is at (X=0.,Y=0.). This estimate of the epicanter coincides with the coordinates from IGE.

3). The processing approach can be implemented for coherent and incoherent multichannel seismogram analysis. The precision of weak event location can be increased by implementing one-channel seismic phase detectors which are more sensitive than the conventional STA/LTA detector used in our experiments.

ACKNOWLEDGEMENTS

The events were recorded by the Israel Seismic Network (ISN) which is operated by the Seismological Division of the Institute for Petroleum Research and Geophysics (IPRG), Israel. The database supplied with ground truth information was collected by Dr. Y. Gitterman (IPRG) and used in the discrimination study: Gitterman, Y. and T. van Eck, 1993. Spectra of quarry blasts and microearthquakes recorded at local distances in Israel, Bull. Seism. Soc. Am., 83, 1799-1812. The waveforms and ISN bulletin information were prepared and transferred by Dr. V. Pinsky (IPRG).

REFERENCES

V.A.Gurevich, V.L.Kiselevich, B.M.Shoubik (1994) ASET - Array based Seismic Emission Tomography, IRIS Newsletter, Vol.XIV, No 1, 10-11.

S.A.Katz and B.M.Shoubik (1986) Implementation of Multichannel Adaptive Filters in Seismic Researches. Publication of Institute of Physics of the Earth, RAS, Moscow, "Nauka", pp.221 (in Russian).

B.L.N.Kennett (1996) Event location and source characterization, in E.Husebye, A.Dainty (eds.) "Monitoring a comprehensive test ban treaty", Kluwer Academic Publishers, Dortrecht, 501-520.

A.F.Kushnir, E.V.Troitsky, L.M.Haikin, A.Dainty (1996) Study of statistical classification approach to discrimination between weak earthquakes and chemical explosion recorded by Israel local seismic network, Presented to 18th Seismic Research Symposium on Monitoring of Comprehensive Test Ban Treaty,

A.F.Kushnir (ed), L.M. Haikin, V.M. Lapshin, B.M. Shoubik, E.V. Troitsky (1995) Seismic monitoring with small aperture arrays under strong noise conditions: algorithms, technique, system design and experimental data processing. Scientific report on AFOSR Special Project SPC-94-4039.

B.M.Shoubik, V.L.Kiselevich (1993) Microseismic activity in hydrothermal areas and problems of the seismic monitoring., in: "Concepts of the natural and engineering media monitoring". RAS, Moscow, "Nauka" (in Russian).

B.M.Shoubik, V.L.Kiselevich, A.V.Nicolaev and L.N.Rykounov (1991) Microseismic activity in hydrothermal areas, in: "Physics basis of the seismic methods", Publication of Institute of Physics of the Earth, RAS, Moscow, "Nauka", 143-158 (in Russian).

F. Ringdal and T. Kværna (1989) A multichannel processing approach to real time network detection, phase association and threshold monitoring, Bulletin of the Seismological Society of America, Vol.79, 1927-1940.

G.A.Ryzhikov, M.S.Birulina and E.S.Husebye (1995) Automatic event location using local network data, Proceedings of the 17th Annual Seismic Research Symposium on Monitoring of Comprehensive Test Ban Treaty 12-15 September of 1995, 393-400, PL-TR-95-2108, ADA310037.

C.J.Young, J.I.Beiriger, J.R.Trujillo, M.M.Withers, R.C.Aster, L.Astiz and P.M.Shearer (1995) WCEDS: A Waveform Correlation Event Detection System, Proceedings of the 17th Annual Seismic Research Symposium on Monitoring of Comprehensive Test Ban Treaty 12-15 September of 1995, 931-940, PL-TR-95-2108, ADA310037.

Location and Signal Identification With *Broadband Arrays* at Regional and Teleseismic Distances

Terry C. Wallace
Mark A. Tinker

Southern Arizona Seismic Observatory
Department of Geosciences
University of Arizona
Tucson, Arizona

Grant F19628-95-K-0007

Sponsored by Philips Laboratory

ABSTRACT

One of the most important problems in monitoring a Comprehensive Test Ban Treaty (CTBT) is the detection and location of small seismic events. Standard location procedures which utilize a finite set of travel times are limited by identification methodology. Further, for small events, the travel times may come from very heterogeneous data sets; a few stations at local, regional and teleseismic distances. One way to improve the location methodology is to make use of the "entire" waveform. Here we develop methodologies for utilizing the broad band waveforms from a sparse network.

We use a polarization filter which parameterizes the three component ground motion into an ellipse. We use the vertical and horizontal axis of the ellipse to determine back aziumth and resolution of the back azimuth determination. The filter is a sliding window, and allows the determination of polarization for P, S and Rayleigh waves. We have begun testing the proceedure on an archive of broad band recordings from a sparse array in the Andes of South America. The events in the archieve include both industrial explosions and earthquakes.

Preliminary results indicate that by utiling different frequency bands it is possible to combine body and surface wave azimuthal estimates. We are exploring ways to combine the different estimates to achieve the most robust location. We are also beginning to use "envelope" analysis to determine distances.

OBJECTIVE

Seismic arrays have become the central tool for event detection in the context of monitoring a nuclear weapons treaty (Mykkeltveit et al., 1990), and much work has been done developing methodologies for large, dense, short-period arrays such as NORESS, ARCESS, and GERESS. However, in the context of a global monitoring treaty, it is likely that there will be *some* dependence on sparse regional networks of three-component broadband seismic stations. Although there has been some work on event location with sparse broadband networks (for example, Thurber et al. 1989; Walck and Chael, 1991), the full power of the data has not been utilized, namely using phases other than *P* and *S*. Waveform processing procedures which have been developed for arrays need to be expanded to encompass disparate data sets. For example, a small seismic event may be well recorded on a few broadband seismic stations at regional distance, and a few at teleseismic distance. The standard procedure for locating the event is to "pick" travel times from the various stations and invert for the hypocenter. Such a process ignores the rich travel-path information contained within individual waveforms. Shearer (1994) has shown that the GSN can be treated as an "array" and that events can be located by comparing a complete long-period seismogram with a catalogue of events.

Our objective in this project is to develop processing techniques for broadband sparse arrays. In particular, we have three tasks: (1) a polarization filter for mid-period Rayleigh waves (periods of 5 to 15 sec) to improve on back azimuth determination (2) develop "stacking" algorithms for stations which are spaced 1000's of kilometers apart. (3) combine information from the body and surface wavetrains to improve location.

RESEARCH ACCOMPLISHED

Walck and Chael (1991) studied procedures for seismic event location using a very sparse seismic network. They showed that augmenting travel time data (arrival times of *Pn*) with back azimuth information can improve location However, near-surface geology can strongly affect the back azimuth estimates; unfavorable conditions (thick sedimentary stacks, complex structure) can introduce substantial errors for relatively high-frequency (2–8 Hz) body wave arrivals. These errors are introduced because the back azimuth is determined from the *polarization* of a given seismic phase. If waves are deflected off azimuth by irregular geology, the polarization will reflect the off-azimuth path of approach. Suteau-Henson (1991) documented the strong site dependence for "clean" polarization by studying short-period three-component elements of NORESS and ARCESS.

Several procedures have been proposed to improve the azimuthal estimates. These include making the azimuth measurement over a very short time interval (Christofferson et al., 1988) and using multiple phases. Unfortunately, these procedures will not improve the azimuth determination at many sites where complex structure is present; the frequency range of the analysis always has a *low-pass* cut-off greater than 1 Hz. Vsevolozhsky and Wallace (1994) show that when the passband used for the analysis has a *high-pass* cut-off of 5 sec, the azimuthal determinations dramatically improve. However, this is problematic for small events because no energy exists in this passband for typical regional distance body waves. The advantage of using broadband data is that it allows azimuthal information to be determined at a spectrum of frequencies. This allows the different phases to be utilized; the combined information can be "average" to improve location estimates.

Flinn (1965) showed that it is possible to use principal-component analysis to characterize the polarization of seismic waves; he showed that the retrograde elliptical motion of Rayleigh waves made it possible to discern their onset. Jurkevics (1988) extended Flinn's method to arrays. The polarization of the seismic waves is rotated into principal directions, which lie along the eigenvectors of the covariance matrix **C**:

$$\mathbf{C} = \begin{bmatrix} \sigma_{nn} & \sigma_{ne} & \sigma_{nz} \\ \sigma_{ne} & \sigma_{ee} & \sigma_{ez} \\ \sigma_{nz} & \sigma_{ez} & \sigma_{zz} \end{bmatrix}$$

where σ_{ij} represents the zero-lag cross power:

$$\sigma_{ij} = \frac{1}{N} \sum_{i=1}^{N} x_i y_j$$

The eigenvectors define a polarization ellipsoid. For *P* waves the dominant eigenvector is assumed to lie in the direction of propagation; for *SH* waves the dominant eigenvector is perpendicular to the direction of propagation. We have developed an signal processing module which determines the polarization of seismic waves based on determining the eigenvectors of the covariance matrix. We use a sliding window which determines the direction of the principle horizontal direction of P, S and Rayleigh waves. These three waves type give independent estimates of source azimuth.

We have begun testing the algorithm on a large archive of broadband recordings from a sparse array: the University of Arizona is involved in the operation of a temporary deployment of a broadband seismic array in Bolivia. Figure 1 shows the location of 19 stations deployed in April 1994. (The deployment is a cooperative project between the University of Arizona, Carnegie Institute of Washington, and Lawrence Livermore National Laboratory.) The stations consist of Streckeisen STS-2 or Gulrup -3ESP broadband sensors and Reftek (24 and 16 bit) digital recorders. Data were recorded in a continuous stream (10 samples/sec) and a triggered mode (50 samples/sec). This array was operational for approximately 18 months; more than 3000 seismic events at local and regional distances were detected. This data catalogue is an excellent test bed to develop procedures for incorporating long-period waveform information in event location.

During this the first year of this contract we have accomplished two objectives: (1) we have developed the test bed archive, and (2) we have begun testing the robustness of the algorithm. Figure 1 shows a representative analysis. The seismic event, which was located approximately 9 degrees from the BANJO array had a magnitude of 5.0, produced a well recorded surface wave train. Shown in the figure are the back-azimuth determinations for successive windows in the wavetrain. Figure 2 shows the details of the wavefrom; the surface wavetrain used in the analysis is approximately 50 seconds long. The back-azimuth determinations are represented by vectors, where the direction is projection of the principle horizontal eigenvalue from the elliptical polarization. The length the of vector is proportional to the ratio of the two horizontal eigenvalues; if the polarization was perfectly elliptical with no tangential component the vector would very long. If the horizontal eigenvectors are equal in length then back-azimuth vector has zero length.

The back-azimuth vectors in figure 1 are for different time windows. The grey scale for the vectors is proportional to the relative timing of the windows; the darkest vectors correspond to the beginning of the waveform and the white arrows are at the end of the waveform. The epicenter, represented with the star, has some uncertainty in location. However, it is apparent that azimuthal determination is best resolved in the first 50 seconds

of the waveform. The analysis is detailed in figure 2 where the back-azimuth determination is shown as a function of the time window.

Figure 3 shows the filter analysis for the body wave train. The azimuthal determinations are much better resolved, although there is still considerable uncertainty. Note that there are both P waves (azimuth determination towards the epicenter) and S waves (azimuthal determination perpendicular to a line connecting the epicenter and recording station) in the wavetrain.

The next step in the analysis is to develop a methodology to average the information in both the surface and bodywave. In the next year we intend to investigate several schemes, including a least squares fit, an L1 norm and sum of all the vectors.

CONCLUSIONS AND RECOMMENDATIONS

Combining the surface and body wave information in regional event location holds promise how improving poorly recorded events. Preliminary work indicates that one of the most important constraints is spectral bandwidth. It is essential to have broadband data so that surface wave information can be resolve. In the next year we intend to:

(1) Combine the surface and body wave analysis.

(2) Add information determined from teleseismic recording.

REFERENCES

Christofferson, A. E. Husebye, S. Ingate (1988). Wavefield decomposition using ML-probabilities in modeling single site 3-component records, *Geophys. J.*, 93, 197–213.

Flinn, E. A. (1965). Signal analysis using rectilinearity and direction of particle motion, *Proc. IEEE, 53*, 1874–1876.

Jurkevics, A. (1988). Polarization analysis of three-component array data, *Bull. Seism. Soc. Am., 78*, 1725–1743.

Mykkeltveit, S., F. Ringdal, T. Kvaerna and R. Aleurine (1990). Application of regional arrays in seismic verification research, *Bull. Seism. Soc. Am., 80*, 1777–1800.

Shearer, P.M. (1994). Global seismic event detection using a matched filter on long-period seismograms, *J. Geophys. Res., 99*, 13,713–13,725.

Suteau-Henson (1991). Three-component analysis of regional phases at NORESS and ARCESS: Polarization and phase identification, *Bull. Seism. Soc. Am., 81*, 2419–

Thurber, C., H. Given and J. Berger (1989). Regional seismic event location with a sparse network: Application to eastern Kazakhstan, USSR, *J. Geophys. Res., 94*, 17,767–17,780.

Vsevolozhsky, G. and T. C. Wallace, Seismic source location with a very broad band single station, to be submitted to *Seism. Res. Lett.*

Walck, M. and E. Chael (1991). Optimal back azimuth estimation for three component recordings of regional seismic events, *Bull. Seism. Soc. Am., 81*, 643–666.2440.

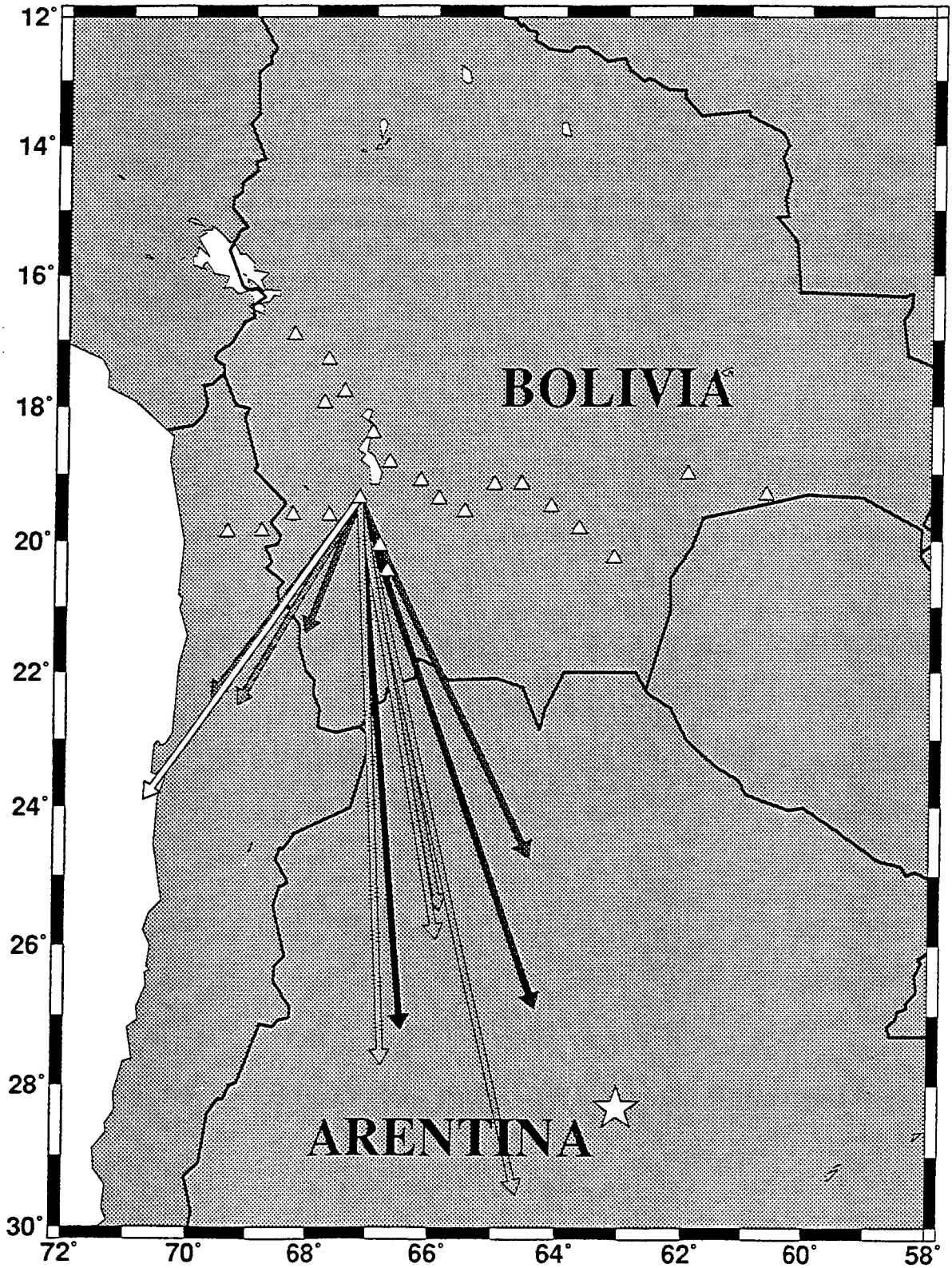

Figure 1. A map showing the back-azimuth vectors determined from the surface waves recorded at station DOOR (see Figure 3). The vectors were determined using a 10 second sliding time window along 5 second time increments. The color of the vector represents what 10 second portion of the surface waves were used in the inversion with black being the beginning and white being the end. The length of the vector is an indication of the "quality" of the determination. The longer the vector, the more robust the back-azimuth. The star is the epicenter determined by a body wave inversion.

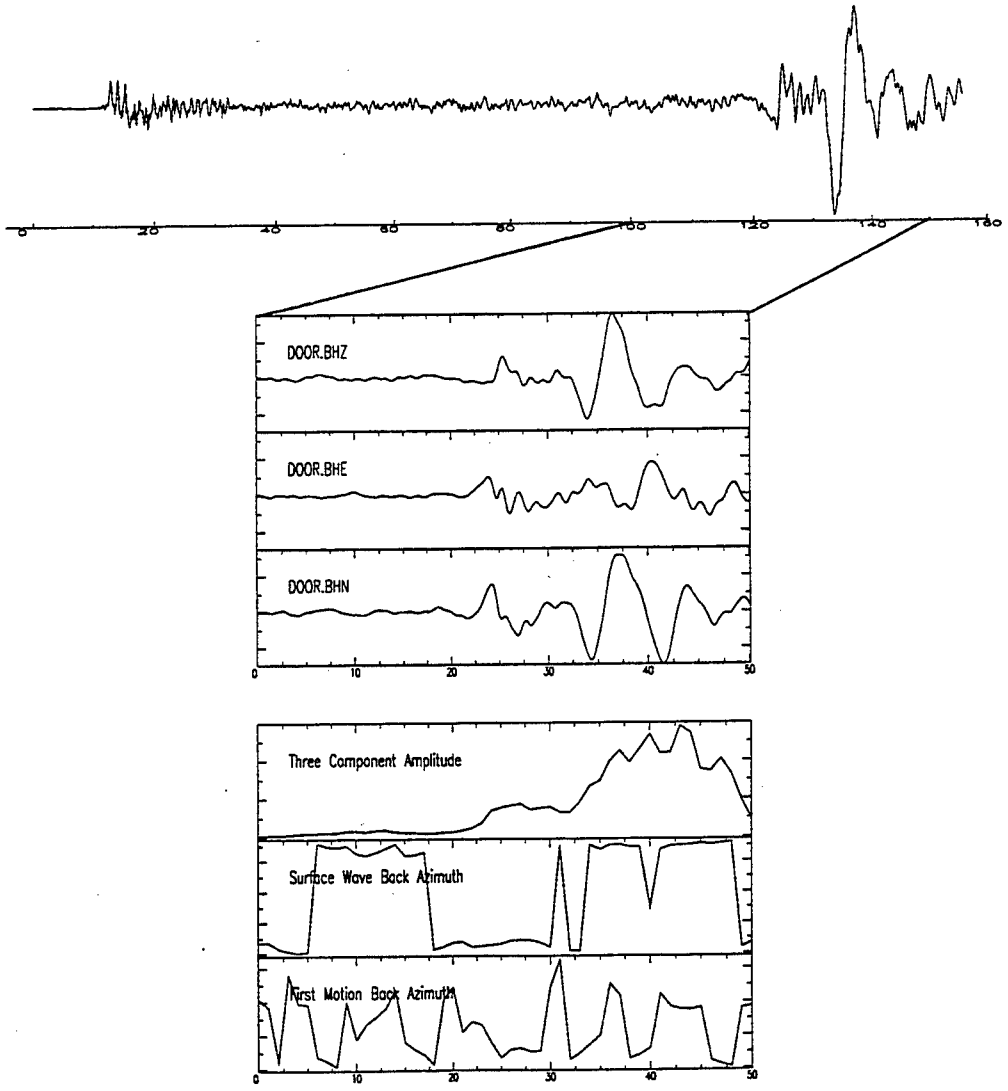

Figure 2. *Top:* An unfiltered broadband vertical component recorded at station DOOR. The P-wave and Rayleigh wave (surface wave) arrivals are very distinct. *Middle:* The 3-component surface waves filtered between 5 and 15 seconds. *Bottom:* The 3-component amplitude for the surface waves and the back-azimuth determined as a function of time for both the surface waves and P-waves. The bottom of each of the back-azimuth plots is 0° (North) and the top 360°.

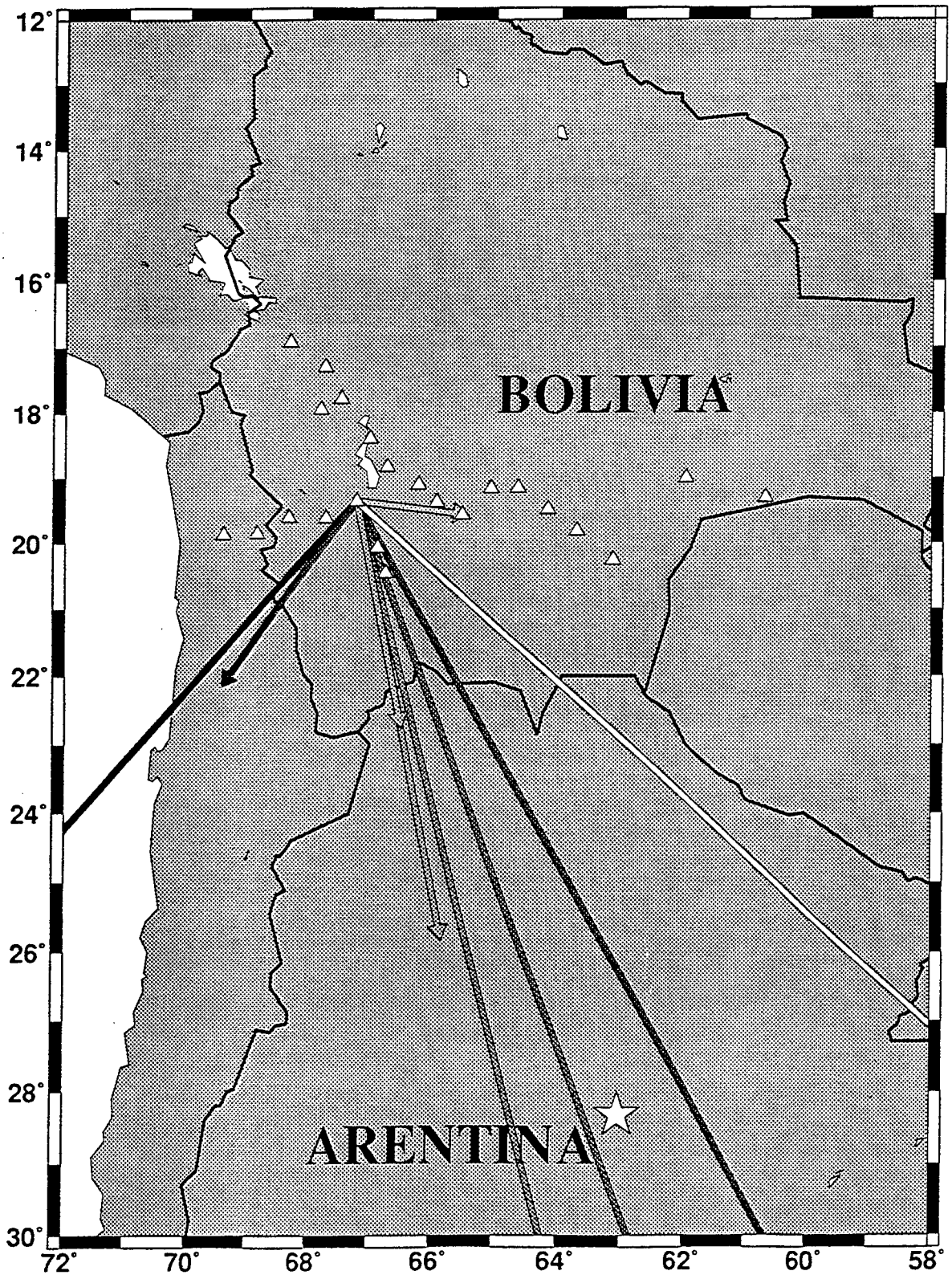

Figure 3. The same as Figure 1, except for P waves.

The Waveform Correlation Event Detection System Project: Issues in System Refinement, Tuning, and Operation

Christopher J. Young, Judy I. Beiriger, J. Mark Harris, Susan G. Moore, Julian R. Trujillo
Sandia National Laboratories
Mitchell M. Withers, Richard C. Aster
New Mexico Institute of Mining and Technology
Sponsored by U.S. Department of Energy
Comprehensive Test Ban Treaty Research and Development Program, ST485D

ABSTRACT

The goal of the Waveform Correlation Event Detection System (WCEDS) Project at Sandia Labs has been to develop a prototype of a full-waveform correlation based seismic event detection system which could be used to assess potential usefulness for CTBT monitoring. The current seismic event detection system in use at the IDC and USNDC is very sophisticated and provides good results but there is still significant room for improvement, particularly in reducing the number of false events (currently being nearly equal to the number of real events). Our first prototype was developed last year and since then we have used it for extensive testing from which we have gained considerable insight. The original prototype was based on a long-period detector designed by Shearer (1994), but it has been heavily modified to address problems encountered in application to a data set from the Incorporated Research Institutes for Seismology (IRIS) broadband global network. Important modifications include capabilities for event masking and iterative event detection, continuous near-real time execution, improved Master Image creation, and individualized station pre-processing. All have been shown to improve bulletin quality. In some cases the system has detected marginal events which may not be detectable by traditional detection systems, but definitive conclusions cannot be made without direct comparisons. For this reason future work will focus on using the system to process GSETT3 data for comparison with current event detection systems at the IDC and USNDC.

Keywords: event detection, waveform correlation, event masking, master image

OBJECTIVES

The Waveform Correlation Event Detection System (WCEDS) Project at Sandia was initiated to assess the viability of developing an improved seismic event detection system for CTBT monitoring based on the correlation of full waveforms. This type of project is warranted because although the current system (Global Association or GA) is highly sophisticated and is a vital part of the current monitoring pipeline, the quality of the bulletin produced shows substantial room for improvement. The number of *missed* events (i.e. those which must be associated by an analyst) has continued to decrease and is now approaching 10% of the final total of real events, but the number of *false* events (i.e. those that are not real and which must be disassociated by an analyst) is still large, being nearly equal to the final total of real events (pers. comm., R. Le Bras, June, 1996). This leads to a significant loss of efficiency in the system because analysts must screen all of the events to find those that are potentially important. Many approaches to improving event detection could be investigated, of course, but to create the most sensitive detector possible a full waveform approach is especially attractive.

INTRODUCTION

The WCEDS Project was initiated in the Spring of 1995 with the goal of developing a prototype which could be used to assess viability for CTBT use. By May of 1995 a rudimentary prototype was available, which was then refined based on the results of repeated testing with a set of continuous data from the Incorporated Research Institutions for Seismology (IRIS) broadband global network. Details of the initial prototype development and testing were given in a presentation at the 17th Phillips Lab Symposium (Young et al., 1995).

In the ensuing year, we have made several important refinements to the prototype and learned a great deal about the strengths and weaknesses of a waveform correlation-based system. In this paper we will summarize some of the most important new features of the present version of the detector, discuss ongoing and planned work, and provide an assessment of the potential value of the system based on what we have learned so far.

REVIEW

The detector is a grid-based automatic system which examines continuous seismic data streams for matches with some portion of a master set of waveforms which we refer to as the *Master Image* (MI). The complete grid covers the entire surface of the Earth. To understand how the detector works, think of it as creating a waveform profile for each grid point at a given time and comparing this observed profile with the expected profile if an event had indeed happened at that point and time. Prior to forming the profiles, the waveforms are processed with filtering and an STA/LTA algorithm to enhance phases relative to noise. We refer to this as *pre-processing* because it occurs prior to execution of the detector itself. The detector then runs continuously at some specified time discretization interval.

To improve the efficiency of the algorithm, at each potential origin time all possible distance correlations for each processed waveform are pre-calculated and stored in an array which we call the C matrix:

$$C_{ij} = \sum_{k=1}^{N_t} M_{ik} D_{kj} \qquad \text{(EQ 1)}$$

Where D is the data matrix whose columns are the observed waveforms, M is the MI matrix whose rows are the expected waveforms, and N_t is the number of time points. The detector output at each grid point is then determined by summing elements in C:

$$O = \sum_{j=1}^{N_s} C_{ij} \qquad \text{(EQ 2)}$$

Another way to think of this is that to calculate the detector output for each grid point, the detector follows a particular summation path through the columns of C.

NEW RESEARCH ACCOMPLISHED

Event Masking and Iterative Event Detection

As might be expected, fundamentally changing the basis of event detection creates a new set of problems. One of the most basic is the problem of the sidelobes produced by the correlation. If the observed signal and the master signal each have multiple phases, then the cross correlation function will show sidelobes in addition to the true correlation peak. We refer to these sidelobes as *false correlations* because they are due to correlations of an observed phase with the wrong master phase. To understand how false correlations occur, consider a simple hypothetical system with three phases: A, B, and C. For a data set we will use a waveform from one station at which all three phases are observable and distinct.

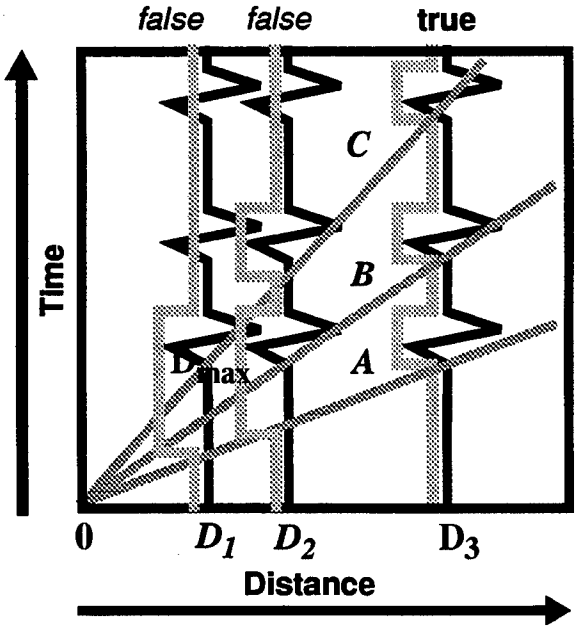

FIGURE 1. True and false correlations, 3 phase system: fixed origin time

As Figure 1 shows, in addition to the true correlation at the correct origin time at distance D3, there are lesser but significant false correlations at D2 and D1. For any given distance, there will also be false correlations both before and after the true origin time (Figure 2). This means that there will be certain *incorrect* grid and time points for which false correlations will occur, and if the output at any of these points exceeds a detection threshold a false event will be declared at that

point. Perhaps more importantly, it will be very difficult if not impossible, to detect any real events of smaller magnitude which may have occurred nearby in time.

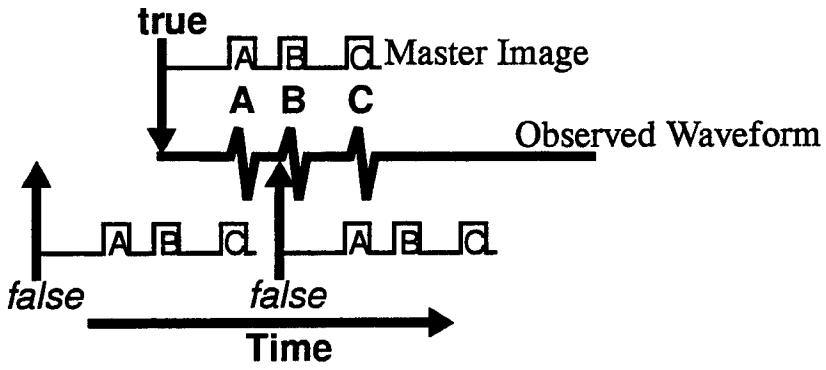

FIGURE 2. True and false correlations, 3 phase system: changing origin time

To solve this problem it is necessary to remove all the effects of a given event, both true and false, once it has been detected. If this can be accomplished then events with intermingled phases could be detected through an iterative process of detection and masking. The most obvious solution would be to zero the waveforms where phases have been observed for a detected event. This does imply removing data, but it is important to realize that this is really no different than what goes on in trigger-based systems such as GA. Virtually no system will allow the phase observed at a given time to be associated with more than one event: a choice must be made (this is the topic of "conflict resolution", e.g. Beall et al., 1995). Once a trigger has been associated with a given event it is effectively removed from further consideration which is equivalent to zeroing the waveform from which it came.

We chose another approach, however, because in our system the censored waveforms would have to be re-correlated with the MI and this is a computationally expensive process. Instead, we elected to mask the correlations in the C matrix that are associated with a detected event and then recompute the output (O; Equation 2) at the grid points. We wish to note however, that as we have continued to refine the code we have greatly increased the speed at which the C matrix can be computed and iterative calculation of C may now be viable.

In order to mask properly, it is necessary to determine which stations and which phases at those stations contributed to the event detection. Fortunately, this is straightforward in the WCEDS scheme (details are provided in Young et al., 1996). Once this information is available, all possible correlations between observed phases and MI phases are calculated and stored in masking matrices, referred to as the X matrices. There will we an X matrix for each origin time, just as there is a C matrix for each origin time. The grid is then searched again over the specified time interval, but in this case the correlation sums are calculated from the C matrices masked by the X matrices. If any other grid points are found to exceed the detection threshold then the largest output point will be found, an event will be declared, X information will be determined, and so on. Using this iterative technique, we have conducted several tests in which multiple events with intermingled phases were successfully detected within the same time interval.

Continuous Near Real Time Execution

While the above results are encouraging, bulletin completeness is not the only criteria which must be considered for a monitoring system: near real time response is also essential. For this reason event detection systems used for continuous monitoring divide data into small segments to insure that events are detected as soon as possible. The minimum length of the segment which can be processed is constrained by the requirements of the detection system. In our case, to run the detector for even one potential origin time, we must have data from that origin time through the time span of the MI or all of the potentially available phases may not contribute to the correlation. Presumably systems that need very quick response times would have to use shorter MIs.

Let us consider how the processing of segments could occur by considering an 8 hour interval of data with 4 events in it.

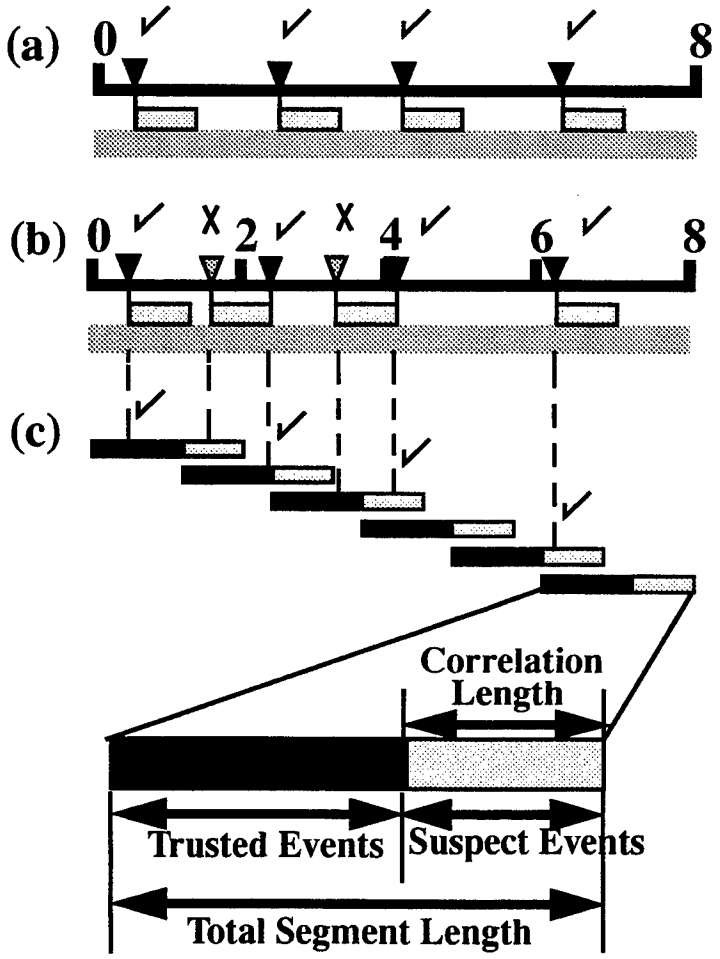

FIGURE 3. Continuous execution models

If we process the data as a single long interval (Figure 3a) then all of the events present should be built properly, but the time delay in declaring the events is too large, particularly for an event occurring early in the interval. An obvious solution is to divide the interval into smaller segments and process these as they become available; in this case we could choose four 2 hour segments (Figure 3b). The difficulty with such a system is caused by events which occur near the end of a segment, and this is a common occurrence for a global network when segment lengths are short.

Such an event may have phases which correlate in more than one segment and consequently the event may not be built properly. In this case two of the real events have correlations in multiple segments and as a result we declare two extra false events. Unless there is some communication between the processing of the segments, we cannot recognize these as false events.

To deal with this problem we chose to implement the concept of overlap or *look back*. The process is illustrated in Figure 3c. The MI has a correlation time length associated with it (the number of columns in the MI defines the time span), so it is apparent that we can trust any detected events whose origin times fall more than that time length before the end of the current segment. These events will have secondary peaks due to false correlations that will be examined as the detector runs through the current time segment, but the true correlation will also be examined and will be preferred because it must have a greater value than any of the false correlation points. Hence the true point will be found, and all of its correlations will be correctly masked and the detector will be able to find nearby smaller events. The difficulty comes in situations when it is not possible to guarantee that the detector will have had the opportunity to check the true correlation point and prefer it to one of the false correlation points. Any events detected in the segment following the trusted event segment fall in this category. As soon as it is possible to correlate with any phase corresponding to an event whose true origin time lies outside of the segment currently being processed, events built must be labelled as suspect. Note however, that these events still must be built and masked because whether or not they are real, the correlations related to them may corrupt the association process in the current time period.

The key to continuous processing in our system is to treat the trusted events and the suspect events differently when the detector moves on to the next time period. Except for this modification the processing is as discussed above: events are built and stripped away until no grid point in the segment exceeds the detection threshold. When the detector is ready to move on, the next segment to be processed must overlap the previous segment by the correlation time length of the MI, i.e. by the length of the suspect event interval. As we begin processing the next interval, we start with an X matrix created from the previously detected trusted events, but we discard the suspect events and the related masking. Now we begin processing as above, except that what was the suspect interval in the previous segment is now part of what will be the trusted interval in the current segment. Thus, any of the discarded events which were legitimate will be rebuilt while false events will be rejected in favor of the corresponding true events. In this manner the process continues one segment at a time, perhaps building false events but correcting them before they are added to the final bulletin.

Master Image Refinements

In the initial stages of the project, we chose to use travel-time based MIs rather than empirically derived images (stacks) a la Shearer because of the difficulty in controlling the number, width, and weighting of the phases in the latter. To form the travel-time based MIs we convolved the IASPEI travel time curves (Kennet and Engdahl, 1991) with a shaping function to give them finite correlation widths chosen to match the observed widths in the processed data. For the most part, MIs formed in this manner yielded satisfactory results, but in fact the MIs were not truly correct. In addition to compensating for processed phase width, the width of the phases used in the MI should also be wide enough to 1) compensate for limited origin time sampling, 2) compensate for limited origin depth sampling, and 3) compensate for inaccuracies in the MI distance against which the waveform for a given station is correlated (due to both the discrete sampling provided by the grid and to the discretization interval of the MI). Origin time and depth effects are straight-

forward. To correct for origin time discretization, one simply widens all intervals by half of the time discretization at which the correlations are to be calculated. The depth discretization is a more complicated effect but can be approximated by a similar uniform widening dependent on the depth range to be spanned by each MI.

The distance discretization effects require a more complex phase and distance dependent adjustment of the correlation widths.

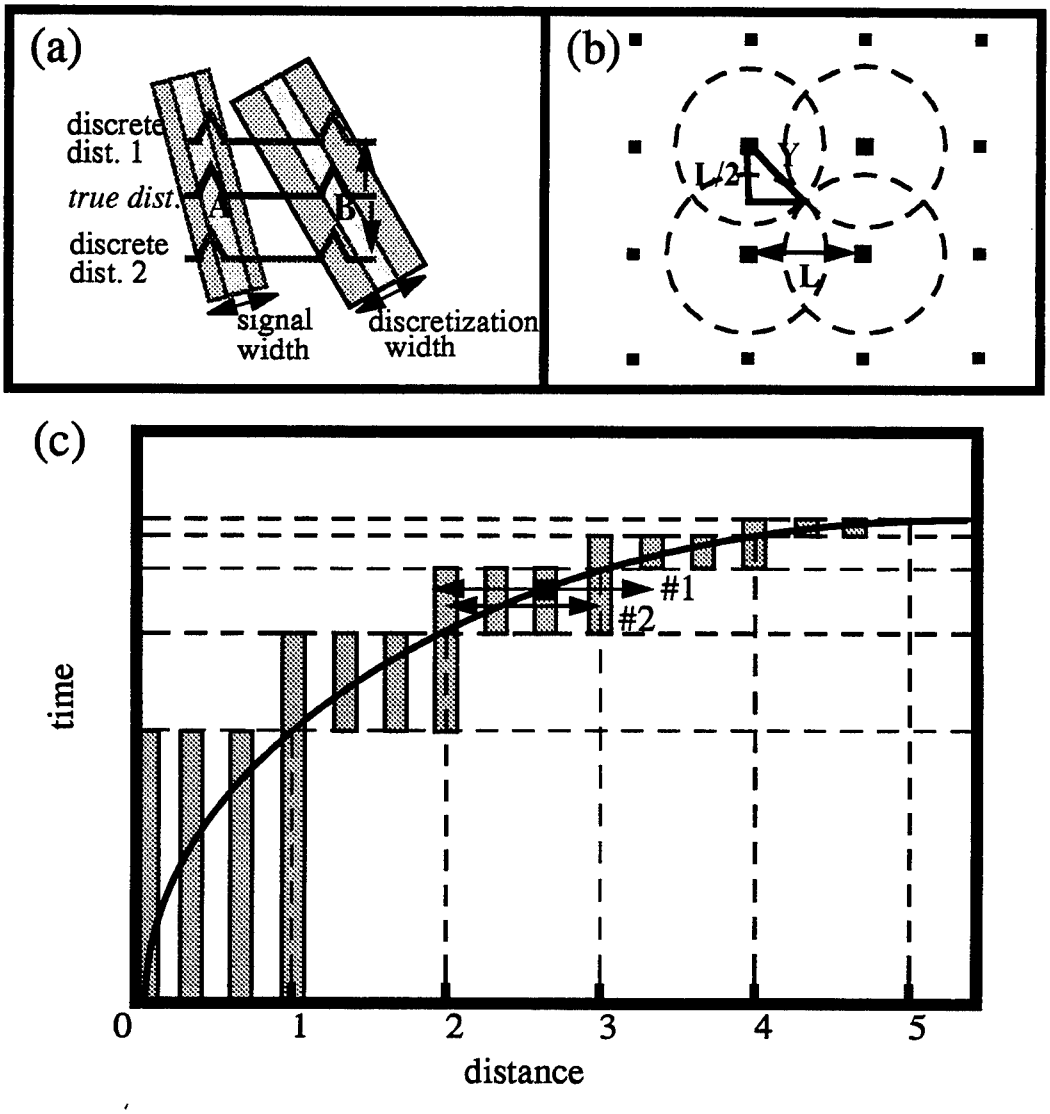

FIGURE 4. Master image correlation widths and distance discretization

Unless an event happens to occur exactly at a grid point and stations happen to lie at integer multiples of the MI distance discretization from that point, observed waveforms will be correlated with MI waveforms for *incorrect* distances. As shown in Figure 4a, to compensate for these effects the MI correlation width should be widened. Note that the necessary discretization width is related to the slope (slowness) of the phase: the greater the slope of the phase, the wider the dis-

cretization width. For a uniformly spaced grid of spacing L the largest possible distance shift due to grid discretization, Y, is:

$$Y = L/(\sqrt{2}) \qquad \text{(EQ 3)}$$

As is shown in Figure 4b. On top of this one must apply the effect of the distance discretization in the MI; all grid point to station distances must be rounded to the nearest distance represented in the MI before correlation. To understand these effects, consider an example where a station is 72.6 degrees from an event and the grid spacing is 2 degrees (Y ~ 1.4). The possible range of distances to the nearest grid point are 71.2 degrees to 74.0 degrees. However, if the discretization interval of the MI is 1 degree, then the range of distances to the nearest grid point for purposes of correlation is 71 degrees to 74 degrees. Given a set of travel time curves, the grid spacing, and the MI distance discretization, one can generate the required correlation widths for stations at every distance. The process is illustrated in Figure 4c.

Station-specific Processing

As mentioned above, prior to correlation the data streams are pre-processed to enhance phases relative to noise. In our original version of the code, all data streams were pre-processed in the same manner. This led to performance problems for some time segments due to the varying quality of the data at each station. We have now implemented a pre-processing control file which allows individualized control over the processing and weighting for each station:

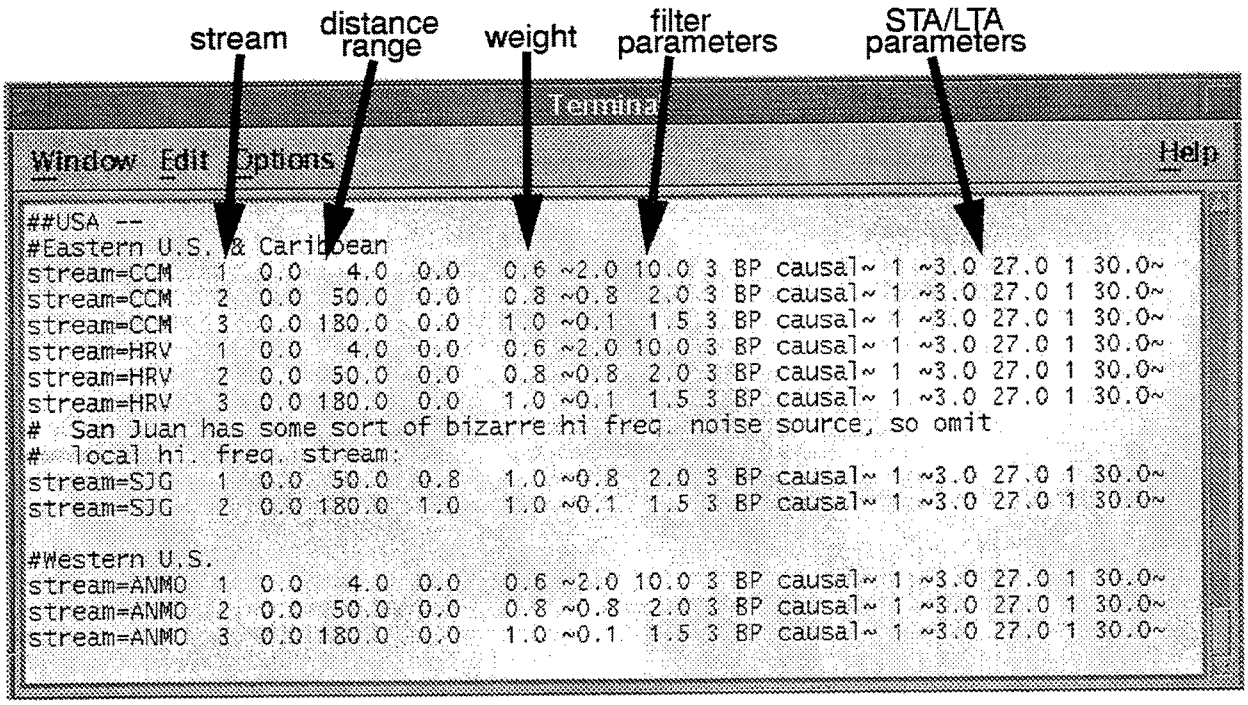

FIGURE 5. Pre-processing control file

With the new structure, the user has full control over the number of processed streams which will be formed for the correlation for each station, the distance range over which they will be used for correlation with the MI, the weighting for each stream, the filter parameters, and the STA/LTA parameters. The user can use these controls to preferentially filter out known noise sources, down-

weight less-reliable stations, etc., which can greatly improve the performance of the system. Changes in frequency content with distance can be taken advantage of by using sets of band-pass filters and specifying the precise distances at which the filtered streams will be correlated (note that more than one stream can be correlated at a given distance).

As is shown in Figure 5, the new structure also provides the user with the opportunity to take a regional approach to the problem. Groups of stations from similar regions can grouped together for parameter control and comparison. The groups of stations can then be down- or up-weighted to control their effect on the overall detector output.

CONCLUSIONS AND RECOMMENDATIONS

Much was accomplished in the first year of the WCEDS Project. We developed a sophisticated detector prototype which we used to run an extensive series of tests on waveform data from the IRIS broadband global network. The problems we encountered during these tests led us to add important new capabilities to the original code including event masking and iterative detection, continuous execution with lookback, creation of better Master Images, and individualized station pre-processing. Each of these capabilities improved the quality and completeness of the bulletin produced by the system.

The potential value of the system for CTBT monitoring, however, is still not clear. In some situations, the detector has successfully built small events which might not be detectable by trigger-based systems such as GA, but in others it has missed events which should be detectable by many existing systems. Perhaps the single greatest reason for the lack of a clear conclusion about the usefulness of WCEDS has been our inability to make direct comparisons with existing systems. To do this we must be able to process the data from GSETT3, and this has only recently become available to us. Once the necessary modifications have been made to process this data we should be able to make direct comparisons with GA on the same data set and this should make the value provided by a full waveform system should become much clearer. Our primary goal in the current year is to make this comparison.

Access to GSETT3 data should also provide us with the means to address another important idea: the possible use of waveform correlation for event screening. As mentioned above, one of the major problems facing the current system is that it generates a very large number of false events whose validity cannot be determined with the information available in the database. Yet these events can easily be determined to be false when the waveforms are viewed by analysts, suggesting that waveform correlation might provide a means to improve automated screening. We will pursue this idea once GSETT3 data is available to us by computing correlation products for all of the events (true and false) in the IDC bulletin and looking for an obvious difference. This is in fact a much easier problem than has been addressed in the WCEDS project because many of the difficult issues which we have had to solve (e.g. false correlations) are not relevant.

REFERENCES

Beall, G., R. Le Bras, W. Nagy, T. Sereno and H. Swanger (1995). Global association system phase 2: conflict resolution, *SAIC document #SAIC-95/1029*, 46 pp.

Kennet, B. L. N. and E. R. Engdahl (1991). Traveltimes for global earthquake location and phase identification, *Geophys. J. Int.*, **105**, 429-465.

Shearer, P. M. (1994). Global seismic event detection using a matched filter on long-period seismograms, *J. Geophys. Res.*, **99**, 13713-13725.

Young, C., J. Beiriger, J. Trujillo, M. Withers, R. Aster, L. Astiz, and P. M. Shearer (1995). WCEDS: a waveform correlation event detection system, *17th Seismic Research Symposium on Monitoring a CTBT.* PL-TR-95-2108, ADA 310037

Young, C. J., M. Harris, J. Beiriger, S. Moore, J. Trujillo, M. Withers, R. Aster (1996). The waveform correlation event detection system project, phase I: issues in prototype development and testing, *SAND report*, in press.

Single-Station Seismic Event Location: How Non-Horizontal Structure Affects Apparent Azimuth

Lian-She Zhao and Cliff Frohlich
Institute for Geophysics
The University of Texas at Austin
8701 North MoPac
Austin, Texas 78759-8397

AFOSR Contract No. F49620-94-1-0287

ABSTRACT

If we attempt to locate small (M~3) regional seismic events using waveforms recorded at a single station, the event back azimuth is the most poorly determined location parameter. In some cases, the apparent back azimuth–the direction where the P-group phases exhibit the minimum tangential-component energy–may differ from the true source back azimuth by 10°-20°. This is significant since a back azimuth discrepancy of 10° at an event-station distance of 100 km corresponds to a location error of 17 km.

We here show that dipping near-station crustal layers can explain these discrepancies. Using a generalized ray approach, for sources at representative azimuths we construct synthetic seismograms for P-group arrivals that incorporate the principal direct, converted, and reflected phases from a dipping Moho with a dip of 5° or 10° of a normal layer-over-half-space model. These model observations indicate that the greatest discrepancies in apparent azimuth occur when signals arrive at azimuths of 80°-120° from the up-dip direction, with a maximum 15° for a dipping layer with dip of 10°.

At stations where these apparent discrepancies occur and sufficient observations are available, we are investigating whether inversion methods such as grid-search or simulated annealing can determine the thickness and orientation of dipping layers, and whether the layer geometry so found adequately explains the observed azimuthal discrepancies. We are also investigating how dipping near-station layers affect the apparent polarization of S-group phase arrivals, possibly producing polarization discrepancies which might be misinterpreted as evidence for mantle anisotropy.

Key Words: Event Location, Waveform Modeling, Crustal Structure, CTBT

OBJECTIVE

Our objective is to develop practical methods for locating small (M~3) regional seismic events using single-station waveform data; this is essential for the successful implementation of the Comprehensive Test Ban Treaty. Locating small events requires determining event distance, focal depth, and azimuth. Previously we have proposed a procedure to determine receiver structure using teleseismic body waveforms (Zhao and Frohlich, 1995, 1996; Zhao et al., 1996), and then determine source depth and distance for the events using grid search method (Zhao and Helmberger, 1994) to match the three component whole waveforms (Zhao and Frohlich, 1995). The apparent back azimuth of the event is obtained by determining the direction of minimum tangential-component energy for P-group waveforms, which should possess only P and SV phase arrivals. In our experience, focal depth and distance are generally well-determined using this procedure, while back azimuth is the usually the most poorly determined parameter. Thus, we here evaluate how much dipping crustal layers affect the apparent back azimuth of regional seismic events. We also are investigating methods for improving azimuth determination by routinely incorporating dipping crustal layers into the synthetic waveforms that we compare with observations.

RESEARCH ACCOMPLISHED

Single Station Seismic Event Location–The Problem

When observations are available from only one or a few stations, the comparison of observed and synthetic waveforms is the most effective way to locate small seismic events; this involves the determination of event distance, focal depth, and azimuth with respect to the observing station. While the comparison are computationally designed to find a "best" location, in practice this is meaningful only when variation in the location parameters strongly affects identifiable "key features" of the waveforms. For event distance, the key features are the time intervals separating major wave groups, such as the P group, the S group, and the surface wave group; these intervals do depend strongly on the details of crustal structure–thus distance is nearly always well-determined. For focal depth, the key features are surface waveforms and the relative times of secondary phase arrivals within the P group and the S group; these represent surface and layer reflections/conversions which depend strongly on an accurate knowledge of near-event and near-station crustal structure. In our previous research (Zhao and Frohlich, 1995; 1996; Zhao et al., 1996) we describe efficient methods for determining near-station crustal structure; in the majority of situations, where crustal structure is flat-layered and regionally homogenous, these are sufficient to accurately determine focal depths for regional events (Figure 1).

For event back azimuth, the key feature we utilize is the polarization of the P-group phases. In flat-layered structures both P and S_V are polarized in the vertical plane extending between the station and the event; thus, we determine the apparent back azimuth as the direction in which tangential-component energy is minimized for the P-group phases (Figure 1); of the two such minimum-energy directions, one can be eliminated by checking first motion direction. Unfortunately, this procedure doesn't work very well even for teleseismic signals. For example, our determination of the apparent back azimuth of station ISA in Southern California from a Caribbean earthquake ($m_b = 6.3$) differed by 16° from the back azimuth corresponding to the location determined by the ISC (Figure 2). What is responsible for this discrepancy?

Our hypothesis is that these polarization discrepancies occur because the near-station crustal structure does not consist of simple flat layers. In Tibet, for example, the optimum near-station crustal structure determined using teleseismic waveforms by a receiver function method (Zhao and Frohlich, 1996) doesn't always provide an acceptable fit between

waveforms and synthetics for regional events when the regional events occur in different azimuths than the teleseismic events (Figure 3).

Synthetics Seismograms for Crustal Structures with Dipping Layers

To evaluate the effect on non-flat crustal layers on P-group polarization, we have used a generalized ray approach to construct synthetic waveforms arriving at a station overlying structure with dipping layers. The program correctly accounts for amplitudes, time delays, and polarization of P-to-S conversions and reflections. The program can generate synthetics for model with any numbers of dipping layers. For simplicity we determine synthetic waveforms for a crustal model with a single dipping Moho layer (Figure 4). Even when the layer dip angle is only a few degrees, the time delays and amplitudes are significantly different for rays arriving from the up-dip and the down-dip directions. This may explain why, when we used teleseismic events and determined crustal structure in Tibet using a receiver-function approach (Zhao and Frohlich, 1996; Zhao et al., 1996) we obtained different flat-layered crustal structures when the teleseismic events arrived from different azimuths.

However, for dipping layers P-to-S conversions produce no tangential-component signal for phases arriving from a pure up-dip or down-dip azimuth; this requires phases arriving from oblique azimuths. To evaluate how this affects the use of the minimum tangential-energy criterion for determining event azimuth, we constructed P-group synthetics for phases arriving at oblique azimuths (Figures 5 and 6) and determined the apparent azimuth by rotating the waveform components to find the minimum-tangential-energy direction. For a Moho with a dip of 10°, the difference between real and apparent azimuth reached a maximum of 15° for events at an oblique azimuth of 100°. The discrepancy exceeded 5° for all azimuths between 30° and 140°.

Our ongoing modeling efforts focus on determining dipping structures which can explain the azimuth discrepancies for stations in California (e. g., Figure 2), where we have independent locations which give us information about the "true" location of regional earthquakes. We are currently investigating what kind of data is required to invert teleseismic or regional data to determine the directions and dips of non-flat layers.

We are also modeling S-group phases to determine how dipping layers affect the apparent polarization of arriving phases. This is of interest because apparent polarization shifts might be incorrectly interpreted as evidence of anisotropy in the crust.

CONCLUSIONS AND RECOMMENDATIONS

We conclude that the presence of dipping near-station crustal layers significantly affects the apparent azimuth of P-group phase arrivals. When layer dip angles are 5° to 10° the discrepancy between back azimuth and the back azimuth of minimum tangential-component energy is typically between about 5° and 15°. Thus, to obtain reliable single-station locations, it will be necessary to account for dipping-layer effects at stations in regions where the crust varies laterally. Our preliminary research indicates that for a dipping-layer geometry we can construct reasonable synthetic seismograms using generalized ray methods, and it may be possible to use these synthetics in inversion schemes to determine the amount and orientation of dipping layers.

REFERENCES

Zhao, L.-S. and C. Frohlich. Determination of near-station crustal structure and the regional seismic event location problem, *Proceedings, 17th Annual Seismic Research Symposium*, PL-TR-95-2108, Air Force Office of Scientific Research, 941-950, 1995.

Zhao, L.-S. and C. Frohlich. Teleseismic body waveforms and receiver structures beneath seismic stations, *Geophys. J. Int., 124*, 525-540, 1996.

Zhao, L.-S. and D. V. Helmberger, Source estimation from broadband regional seismograms, *Bull. Seismol. Soc. Am., 84*, 91-104, 1994.

Zhao,. L.-S., M. K. Sen, P. Stoffa and C. Frohlich. Application of very fast simulated annealing to the determination of the crustal structure beneath Tibet, *Geophys. J. Int., 125*, 355-370, 1996.

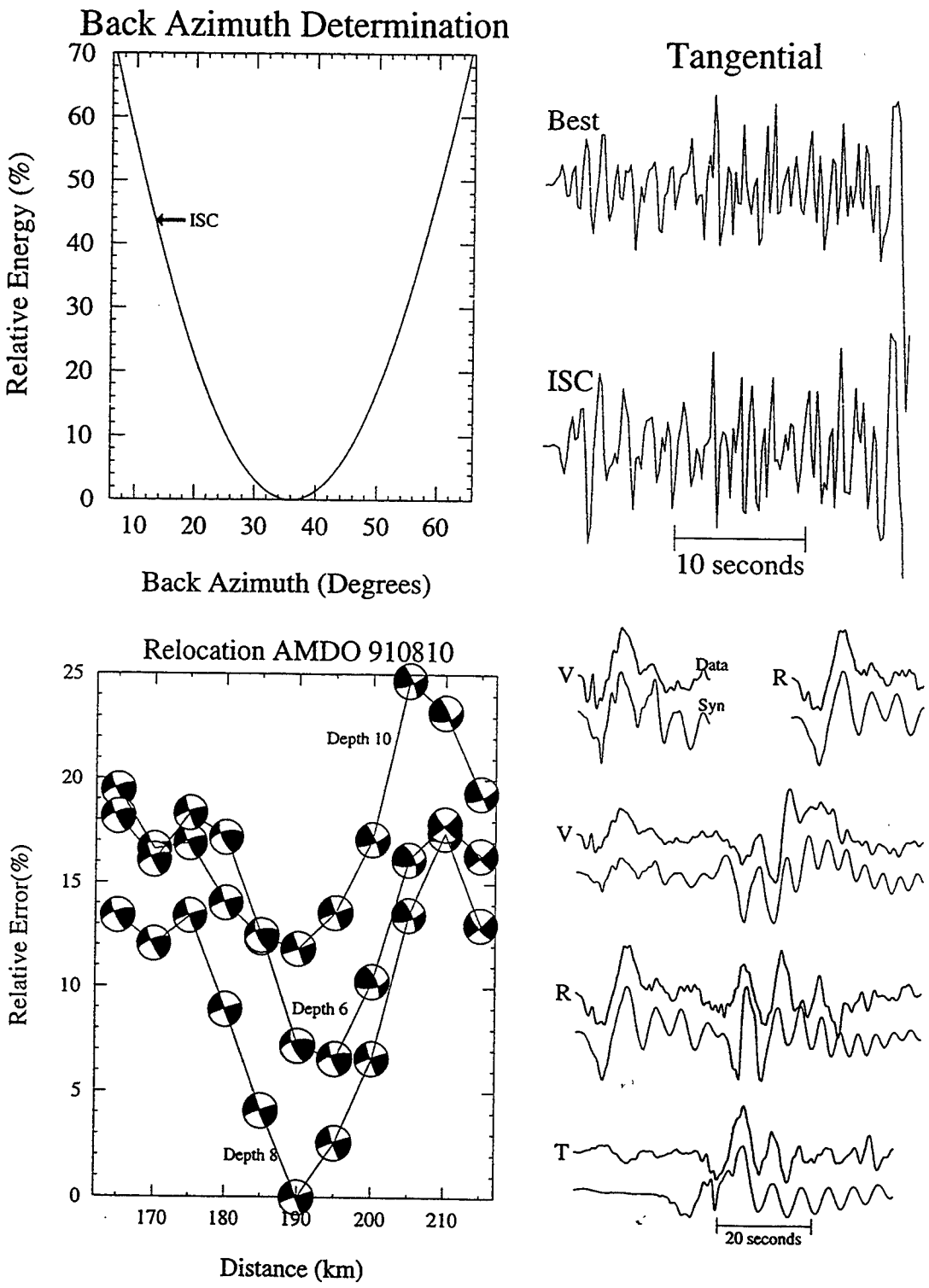

Figure 1. Illustration of single-station location accomplished by comparison of observed and synthetic waveforms. The earthquake (m_b ~ 3.0) occurred on 10 August 1991 and was recorded by station AMDO in Tibet. (Top) A back azimuth of 36° corresponded to the direction of minimum tangential-component energy for P-group phases; this was significantly different from that corresponding to the location reported by the ISC. After determining near-station crustal structure using a receiver-function method and data from a teleseismic earthquake in Alaska, a grid-search over various mechanisms, depths, and distances (bottom left) found that observed (upper traces, bottom right) and synthetic (lower traces, bottom right) were most similar for a depth of 8 km and an event-to-station distance of 190 km.

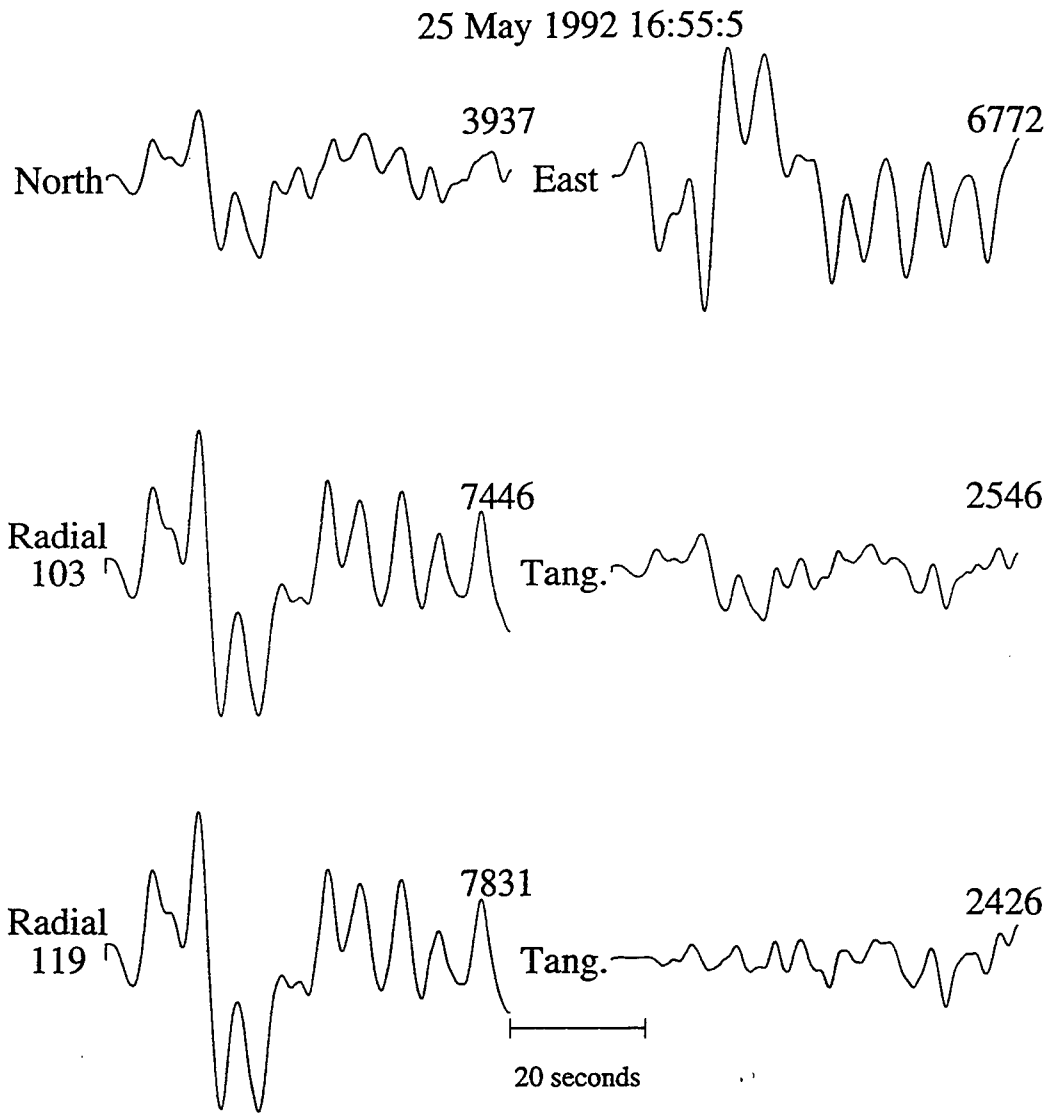

Figure 2. P waveforms recorded at station ISA in California for a Caribbean earthquake with m_b of 6.3 occurring on 25 May 1992. The back azimuth corresponding to the ISC location was 103° (middle trace), whereas the minimum-tangential-energy back azimuth was 119° (bottom trace). We suggest that near-station dipping crustal structure may be responsible for this discrepancy.

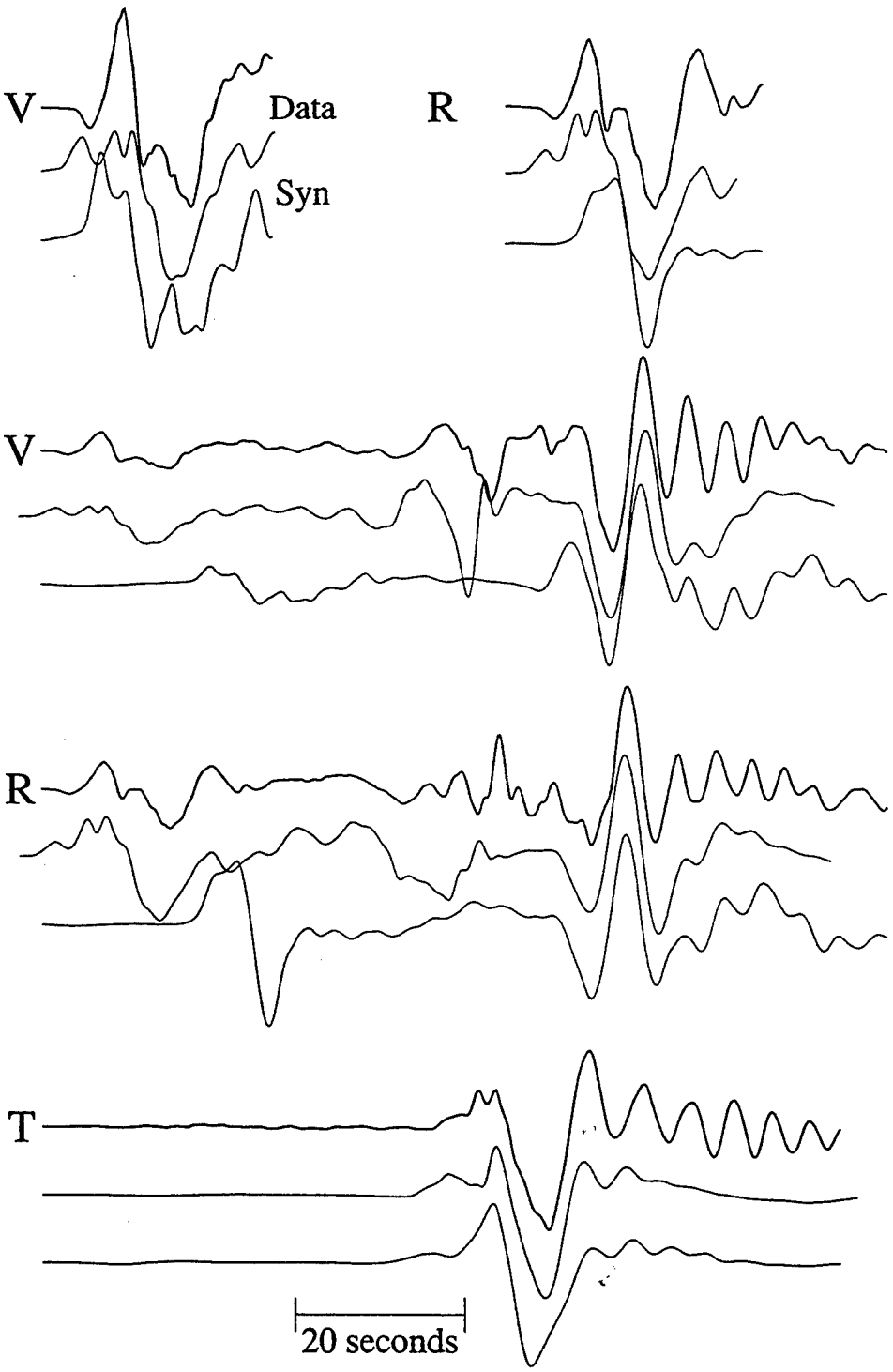

Figure 3. In some cases, the fit is poor between observations and synthetics constructed for crustal models determined from receiver-function methods and teleseismic data. Top traces are vertical- (V), radial- (R), and tangential- (T) component waveforms for an earthquake (m_b = 5.9) recorded at station AMDO in Tibet. Bottom traces are synthetics for the crustal structure determined by receiver-function methods as in Figure 1; note especially the poor fit for the radial component data. Middle traces are for synthetics determined for a crustal model determined specifically for this data using a grid-search procedure.

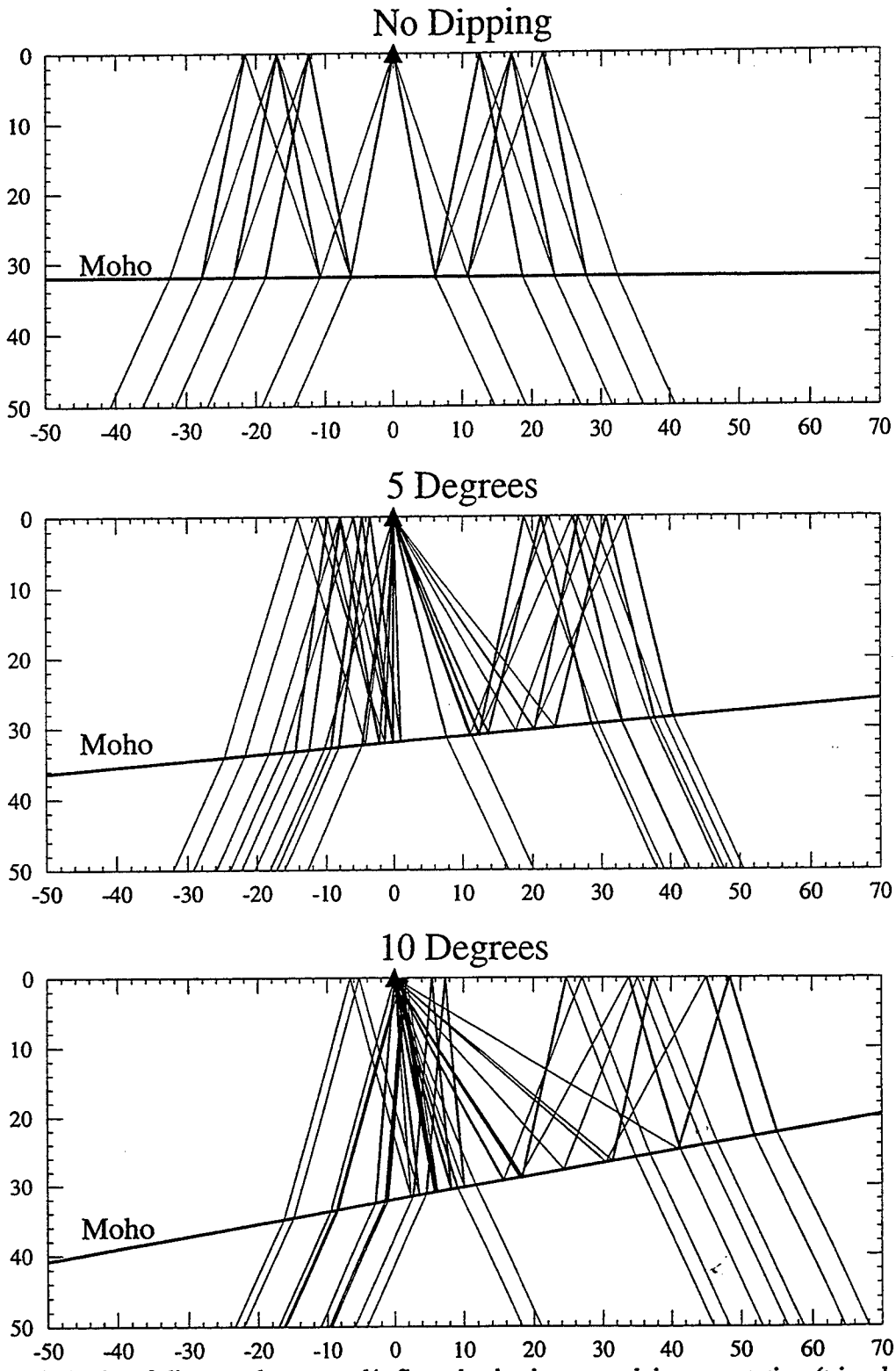

Figure 4. Paths of direct and converted/reflected seismic rays arriving at a station (triangle) overlying a flat layer (top), a layer with a dip of 5° (middle) and 10° (bottom). Thin lines are P segments, thicker lines are S segments; figure includes only the direct, converted, and twice-reflected rays within a single layer above the "Moho." Note that the ray paths and angles of incidence at the station are significantly different for phases arriving from the down-dip (left) and up-dip (right) directions. The crustal model used has a P velocity, S velocity, and density 6.2 km/sec, 3.7 km/sec, 2.7 g/cm3 for the crust, and 8.2, 4.5, and 3.3 for the mantle; in all cases the Moho/mantle boundary is 32 km beneath the station.

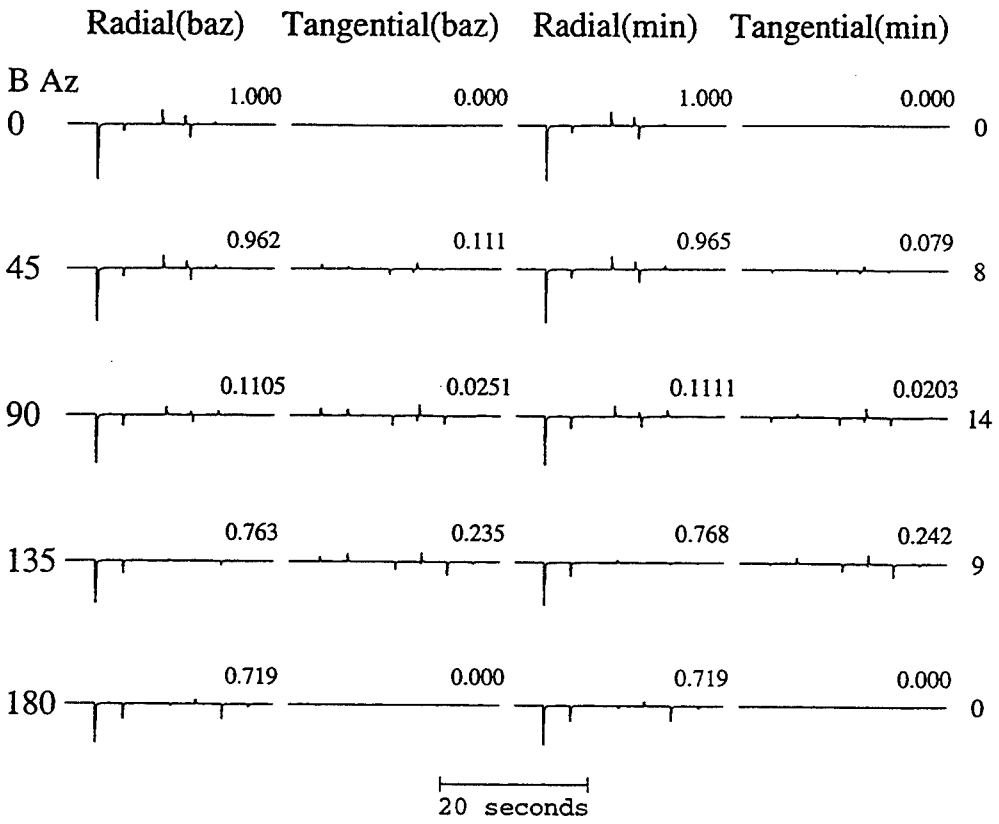

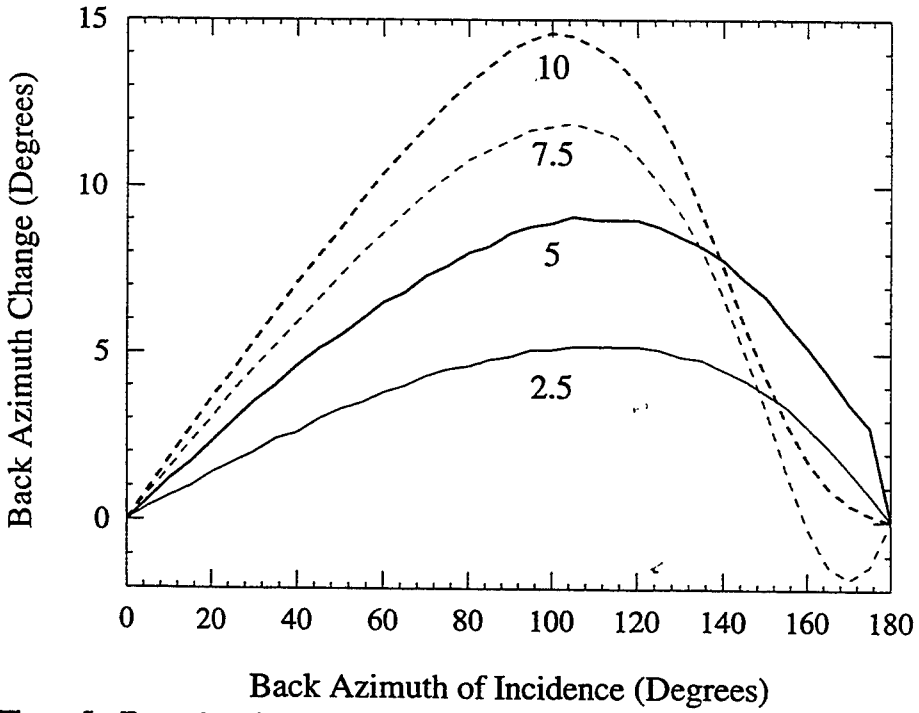

Figure 5. Examples of P-group synthetics calculated for a crustal layer overlying a Moho with a dip of 10°. (Top) Calculated synthetics for phases arriving from the up dip (back azimuth of 0°) and down dip (180°) directions, as well as the oblique back azimuths of 45°, 90°, and 135°. On the left are radial and tangential components corresponding to the true source location direction; on the right are the apparent radial and tangential components corresponding to the direction of minimum tangential-component energy. Numbers above each synthetic are the maximum amplitude, normalized to the radial-component, 0° back-azimuth case. (Bottom) Difference between true and apparent back azimuth (true back azimuth - apparent back azimuth) versus true back azimuth of source signal. The cases are for Moho dip of 2.5°, 5°, 7.5°, and 10°.

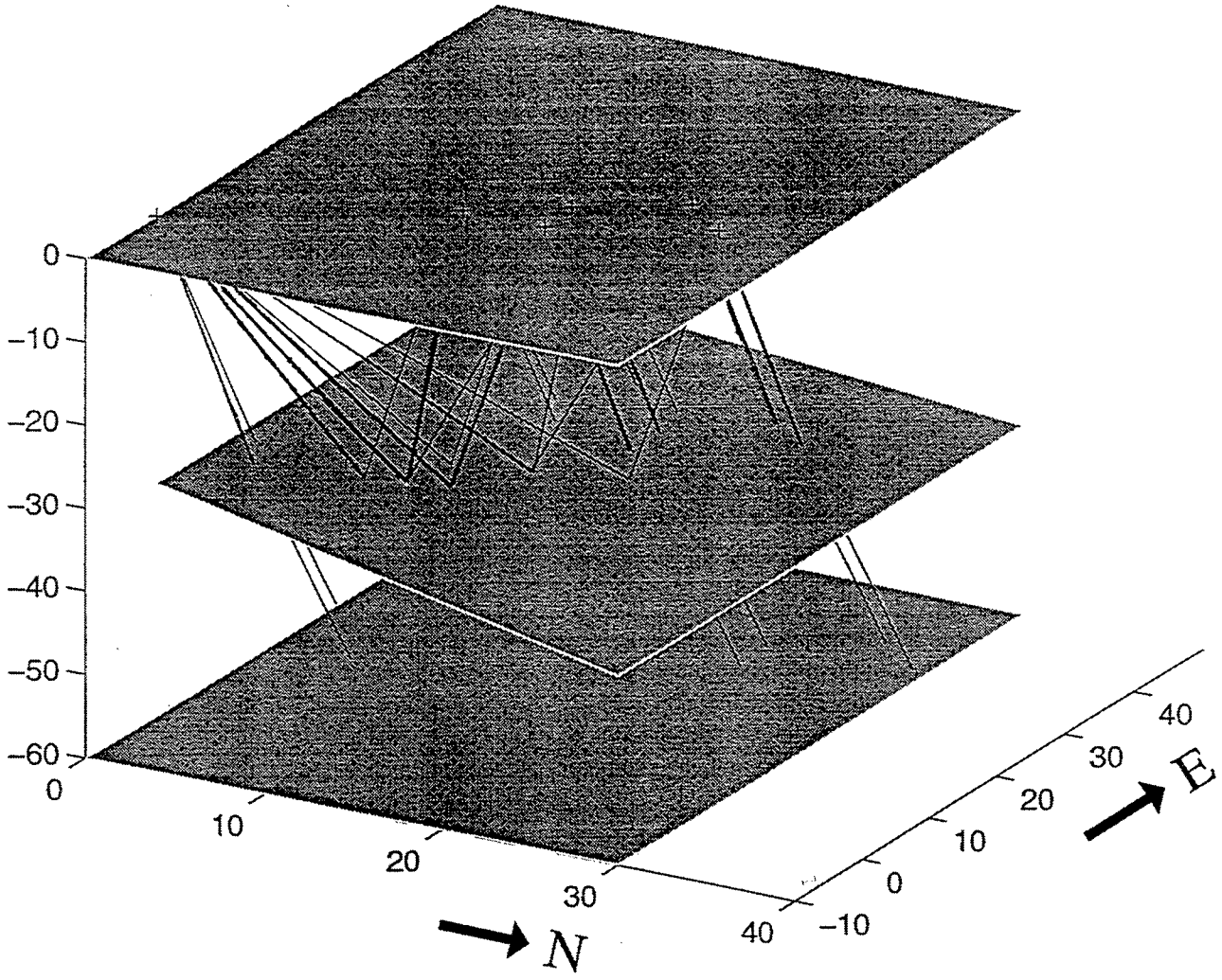

Figure 6. The discrepancy between actual and apparent azimuth may occur because refraction from dipping layers causes signals from a localized, distant source to arrive at the recording station from a range of directions. In this three dimensional representation, the station is at the upper left, the refracting layer dips down to the north (right), and the distant source is to the east.

EMPIRICAL IDENTIFICATION OF DEPTH-RELATED *P* PHASES AT REGIONAL DISTANCES

J. E. Zollweg and D. M. Childs
Boise State University

CONTRACT NUMBER F49620-94-1-0086
Sponsored by Air Force Office of Scientific Research

ABSTRACT

Data from aftershocks of the 1981 Elk Lake, Washington earthquake were examined for *P* phases showing depth dependence. Paths to stations in northern, central, and eastern Washington at distances of 130 to 285 km are structurally complex. Travel-time curves and synthetic seismograms were produced by 2D raytracing through published models and composites we constructed. The travel-time curves and synthetics usually did not correlate well with observed seismograms and were of little use in identifying phases. P_n was found to propagate poorly, even for events with magnitudes near 4. P_g was rarely identifiable. P_mP was well-observed only in one particular azimuth range. These phases do not appear to be good candidates for use in regionally-based depth determination, based on our data set. We also attempted an empirical approach based on plotting seismograms at single stations as functions of depth. Phases that exhibit depth dependence were found at 15 of 34 stations examined. At no single station could two *P* phases be found whose time difference could potentially be used to estimate focal depth. However, some same-azimuth pairs of stations show time differences between phases that are a function of event focal depth.

Key Words: *P* phases, depth-related phases, depth determination, regional phases

Objective

Focal depth determination of seismic events recorded at regional distances is potentially an important means of discriminating between small explosions and earthquakes. We are investigating the frequency with which identifiable crustal phases are recorded, the resolution of depth determination using depth-related phases, and the frequency with which any given station can make such determinations.

1. INTRODUCTION

Discrimination between explosions and earthquakes in a Comprehensive Nuclear Test Ban monitoring scenario is in part dependent on accurate event location. A largely unsolved problem in location is the determination of focal depth for small events recorded at regional distances. Focal depth is an important discriminant in its own right. Most explosions and rockbursts occur at depths less than 3 km, while most natural earthquakes occur at depths greater than 4 km. Focal depth determination at regional distances depends on the ability to either directly identify depth-related phases such as P_mP, or else find some other characteristic of the recorded seismograms that can be shown to be depth-related.

We are examining earthquake sequences in the U. S. Pacific Northwest. Our efforts to date have been directed toward the 1981 Elk Lake, Washington earthquake sequence (see Figure 1). We have concentrated on a group of the larger aftershocks having a good distribution in depth. We have found that most depth-related phases predicted by crustal studies are unidentifiable on the seismograms, in part because the complicated structure leads to multiple phase arrivals within very short time windows. Propagation of other phases (particularly P_g) seems to be blocked at relatively short distances. However, by plotting the observed seismograms at single stations as functions of focal depth, we have been able to identify depth-dependent phases at nearly half of the stations examined. In nearly all of the observed cases of depth-related phases, only one depth-related phase is apparent at each station. This problem has led us to examine the time differences between depth-related phases at pairs of stations along the same azimuth as measures of focal depth. We have found some cases where such time differences are functions of depth. In some other cases, however, the observed relationships are difficult to interpret.

In the following sections we describe our efforts to identify depth-related phases from forward modelling based on crustal structure studies, and then discuss the more empirical approach we adopted when the modelling approach proved a disappointment. We note that we have examined only one earthquake sequence in detail and studies of other sequences may still show the forward modelling approach to be of use.

2. REGIONAL CRUSTAL PHASE IDENTIFICATION UTILIZING FORWARD MODELLING

We attempted to identify regional crustal phases based upon predicted arrival times. Theoretical travel time plots were produced using the raytracing program *RAYINVR* (Zelt and Smith, 1992). The plots were compared to data from the 1981 Elk Lake, Washington earthquake sequence (Grant *et al.*, 1984). Use of different velocity models was necessary due to variations in velocity structure for station groups lying to the north, northeast, and east of Elk Lake (Figure 1).

Four earthquakes (magnitude 3.0 - 4.5) of differing focal depths between 7.8 and 10.3 km were

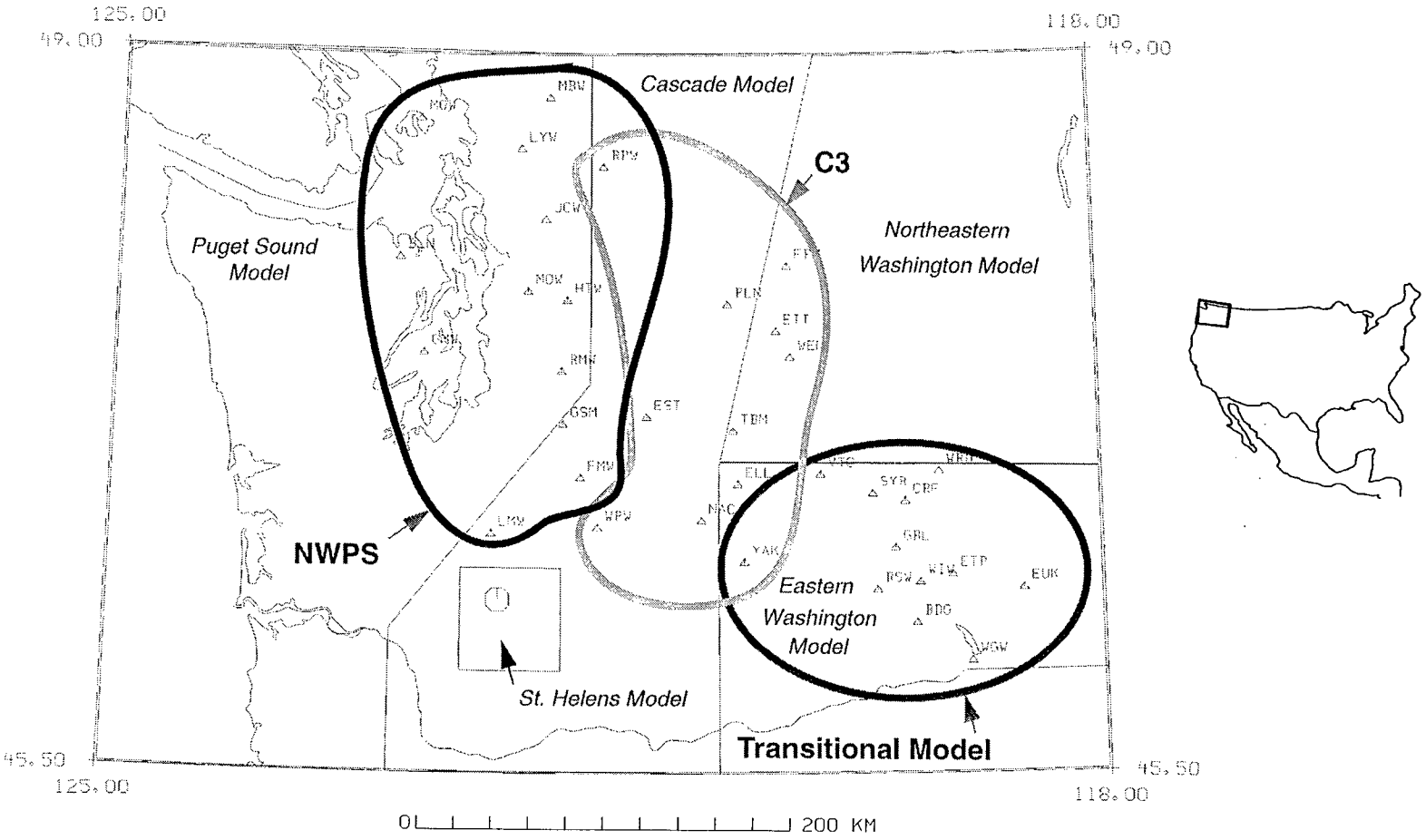

Figure 1. Regions of validity of the University of Washington velocity models (italicized) used in routine seismic event location. Recording stations whose data have been examined in this study are shown by triangles. Station groups are enclosed by solid lines according to the corresponding velocity model used to predict crustal phase arrivals. The epicenter of the 1981 Elk Lake main shock is shown by an octagon.

studied in detail. These earthquakes have well constrained epicenters and depths, estimated to be accurate within about 0.5 km in a relative sense. Their focal depths are representative of the range found in the Elk Lake sequence. Travel time and ray trace plots were created for each event using *RAYINVR*. Phases modelled included critically refracted, reflected, and direct *P* and *S*, as well as *S*-to-*P* reflection boundary conversions. Velocity models were used corresponding to three station groups lying to the north, northeast, and east of Elk Lake. Models were based upon current interpretations of crustal refraction and earthquake data and are discussed below. A total of 34 stations was chosen from the University of Washington's seismic network to form the three station groups. Epicentral offsets range from 35 to 285 km. To identify regional crustal phases 5 to 10 seconds of data around the observed first arrivals were plotted together by station groups. These were then compared with the appropriate travel time curves both by their calculated arrival times and by visual inspection, the latter being a means of accounting for station delays. Observed data were bandpass filtered with corners at 1 and 10 Hz.

Due to structure variations along the three azimuthal paths it was necessary to use several 1D and 2D velocity models. Both C3 (University of Washington's standard processing model for events in the Cascades), and NWPS (the velocity model for the Puget Sound region reported by Miller *et al.*, 1995) are existing models. We developed a transitional model for mixed paths through the Cascades into eastern Washington from the University of Washington's C3 and E3 models (E3 is the University of Washington's standard processing model for events in southeastern Washington), as well as other studies of crustal structure in Oregon and southeastern Washington (Leaver *et al.*, 1984; Glover, 1985; Catchings and Mooney, 1988).

An amplitude-normalized record section overlying travel time curves from a transitional velocity model (Cascades to eastern Washington) is shown for the aftershock of 14 February 1981 2127 UTC (magnitude 3.8, depth 7.8 km) in Figure 2. Trace plots were also made for other velocity model/station groupings and for aftershocks at other depths, but the observations we present based on one aftershock were found to apply to the other events over the full range of focal depths studied.

Observations are as follow:
1. P_n is weak, very emergent and often not visible at all on some of the smaller events. This can be seen at all of the station groups.

2. P_g as predicted by model C3 is seen at a few stations. It is recorded poorly, if at all, at eastern Washington stations. Predicted arrivals for model NWPS have considerable error; what appear to be the proper phases arrive one to two seconds early.

3. Relatively strong P_mP arrivals as predicted by model C3 are seen at some stations. P_mP may also be present on records of several eastern Washington stations.

4. The remaining reflected and critically refracted phases often arrive close together (within one second or less), hampering efforts to identify distinct phases. This can be seen in Figure 2 from offsets of 130 to 245 km.

5. *S*-to-*P* conversions are not obvious in the observed data.

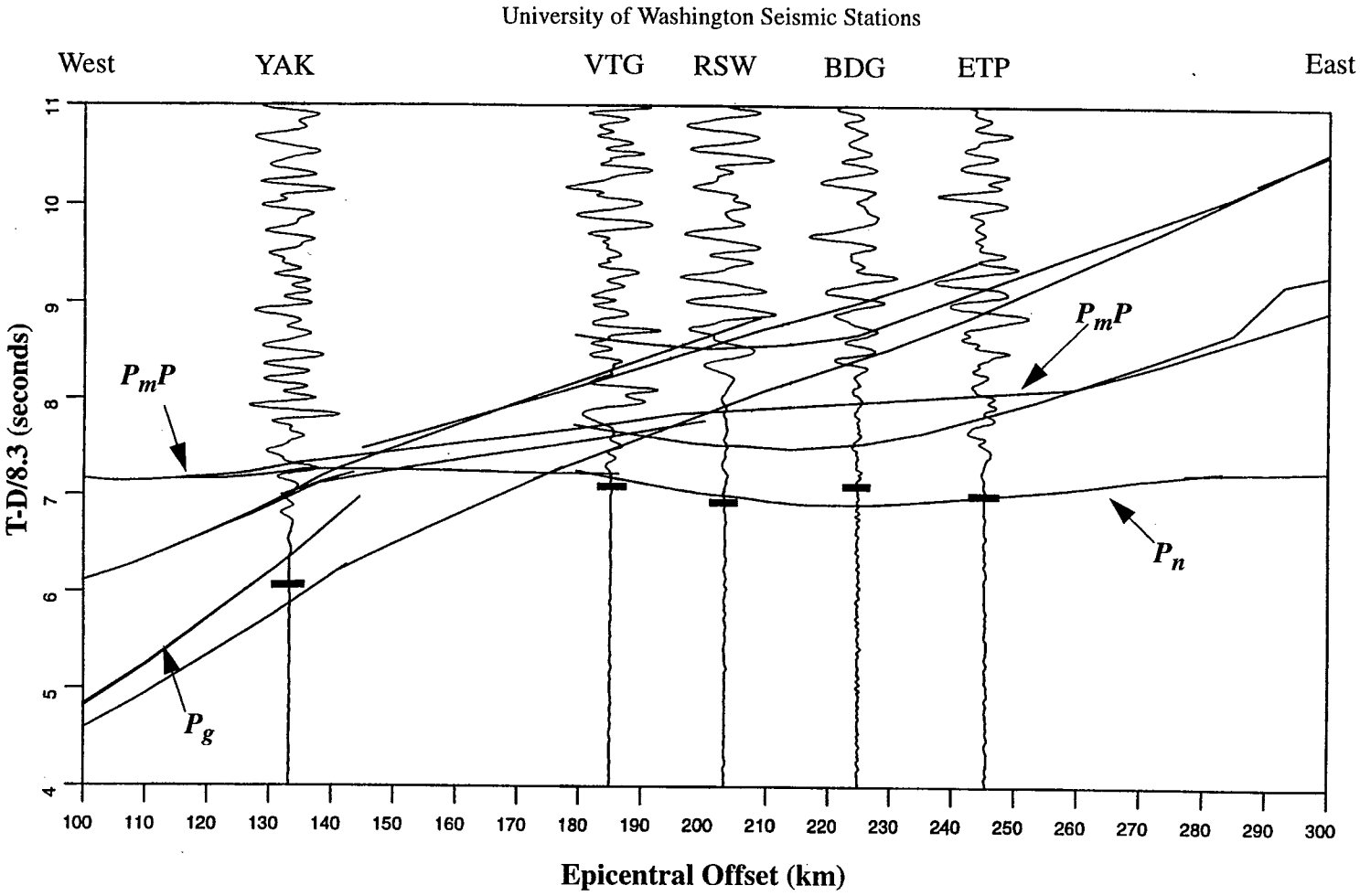

Figure 2. Travel time plot for Elk Lake aftershock of 14 February 1981 2127 UTC, (magnitude 3.8, depth 7.8 km) at eastern Washington stations, utilizing a transitional 2D velocity model. Observed times of first arrivals are noted by bars across traces. Note weak and emergent P_n arrivals and generally poor correspondence between predicted and observed arrivals.

6. Synthetic seismograms were produced but were oversimplified when compared to the actual data, and did not aid in the identification of regional crustal phases.

3. EMPIRICAL IDENTIFICATION OF DEPTH-RELATED PHASES

Since the forward modelling described in the previous section appears to hold only modest promise, we attempted a more direct empirical approach. Since the Elk Lake earthquakes are well-located in a relative sense, we plotted seismograms in depth order at individual stations. The seismograms were arbitrarily aligned on the expected time of the P_g phase, whose travel time is virtually insensitive to depth at distances greater than a few focal depths. We found that of the 34 stations examined, 15 had arrivals that appear to be functions of focal depth. An example is shown in Figure 3. We note that the depth-related phases are usually negative functions of increasing depth; this may be diagnostic of either reflections or refractions but not of direct waves. We have not attempted to positively identify the observed depth-related phases at this time; we are not optimistic of success in doing so in light of the forward modelling results. The stations are too widely separated to attempt identification based on apparent velocity.

At nearly all stations at which depth-related phases were observed, only one such phase was apparent. Since P_n and P_g were recorded poorly (if at all) at most stations, it appears that depth information can only rarely be developed from time differences between various P phases observed at a single station. A two-station methodology appears to offer some promise, however.

Two-Station Time Differences

We sought pairs of stations having depth-related phases and which were situated at different distances along the same azimuth from Elk Lake. Time differences between individual events' depth-related phases at these stations are themselves functions of focal depth, as long as the depth-related phase observed at both stations is not the same (P_n time differences, for instance, would be constant). The effects of minor differences in the stations' azimuths were computed and corrections made to the observed time differences, but for the station pairs selected this was a second order effect and our conclusions would not be affected if this correction were not made.

Figure 4 shows examples of depth-related time differences which are monotonic functions of focal depth. The changes in time difference with depth are small, but well within the observable range. Assignment of relative focal depths to an accuracy of the order of 0.5-1.0 km would appear to be possible using these curves as calibration; the accuracy could possibly be increased if methods such as cross-correlation were employed rather than direct picking by an analyst. These particular plots show fairly typical data for cases where there is a relationship between depth and the two-station time difference. Not all stations show clear trends. An explanation for trendless difference plots is that the observed depth-related phase in each pair is the same at both stations.

Finally, not all the plots are directly interpreted. Some show strong maxima or minima (see Figure 5 for examples). In these plots, a given time difference may correspond to two different focal depths.

Discussion

The empirical approach to identification of depth-related phases from a calibration set, coupled

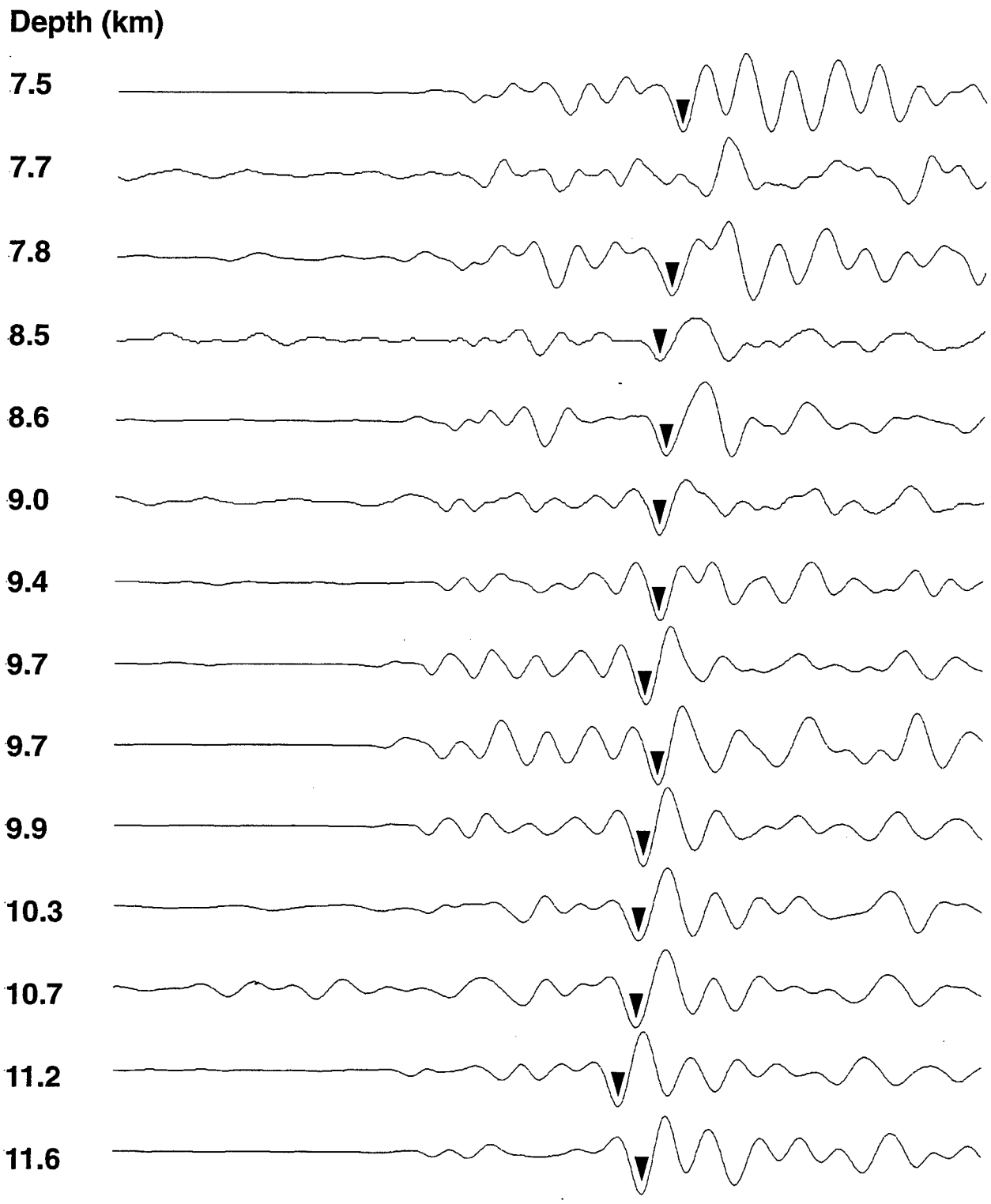

Figure 3. Phase picks from station HTW plotted in order of increasing hypocenter depth. Depths in (in km) are listed to the left of the traces. Traces are: bandpassed at 1 to 3 Hz with a two pole Butterworth filter; 6 seconds in length; amplitude normalized and aligned according to calculated P_g arrival times using a velocity of 6.0 km/s.

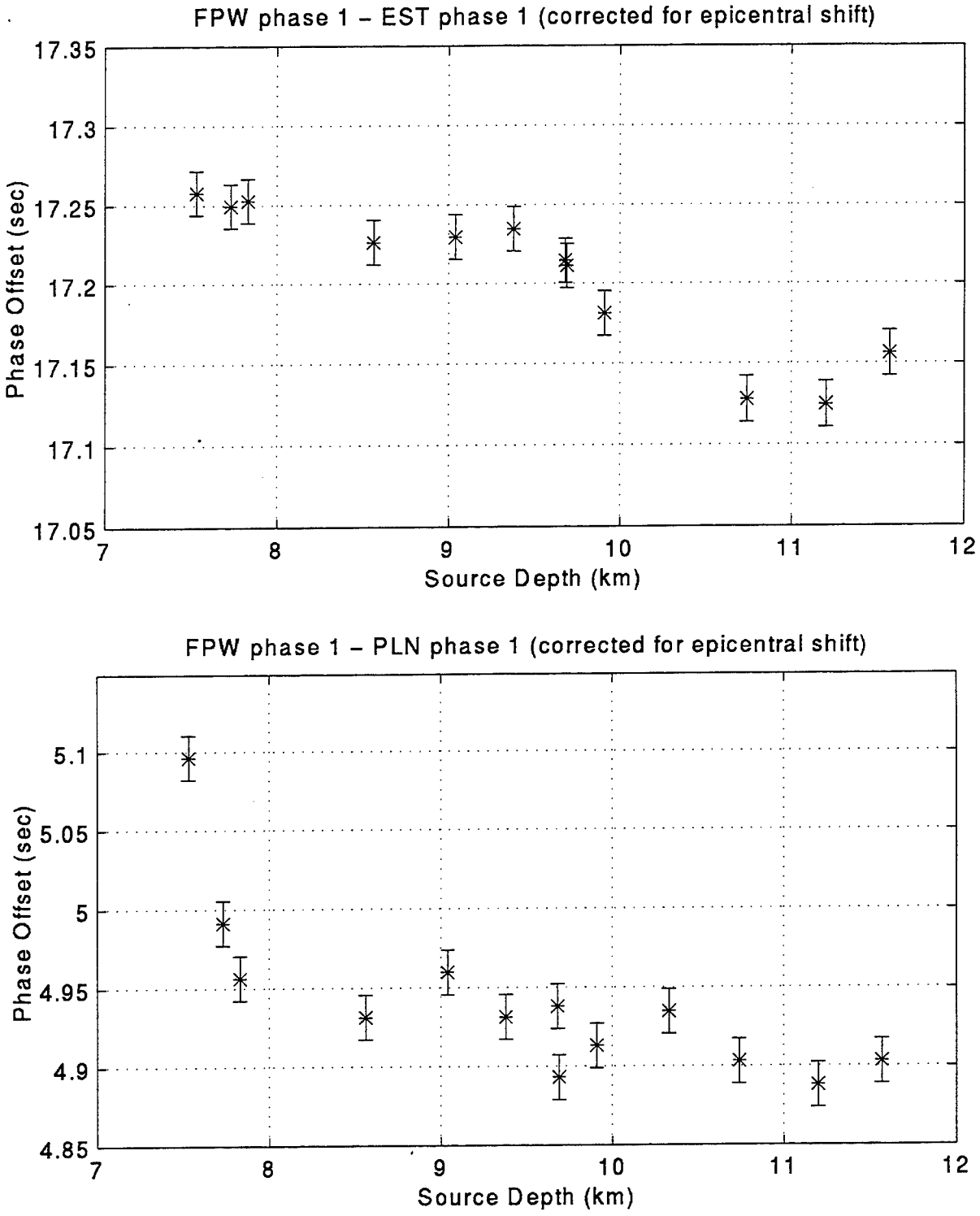

Figure 4. Phase offset plots between stations FPW and EST (top), and FPW and PLN (bottom). Error bars represent a standard deviation of +/- .014 s. Both plots are corrected for epicentral shift. Notice clear depth dependent trend where phase offset decreases with depth.

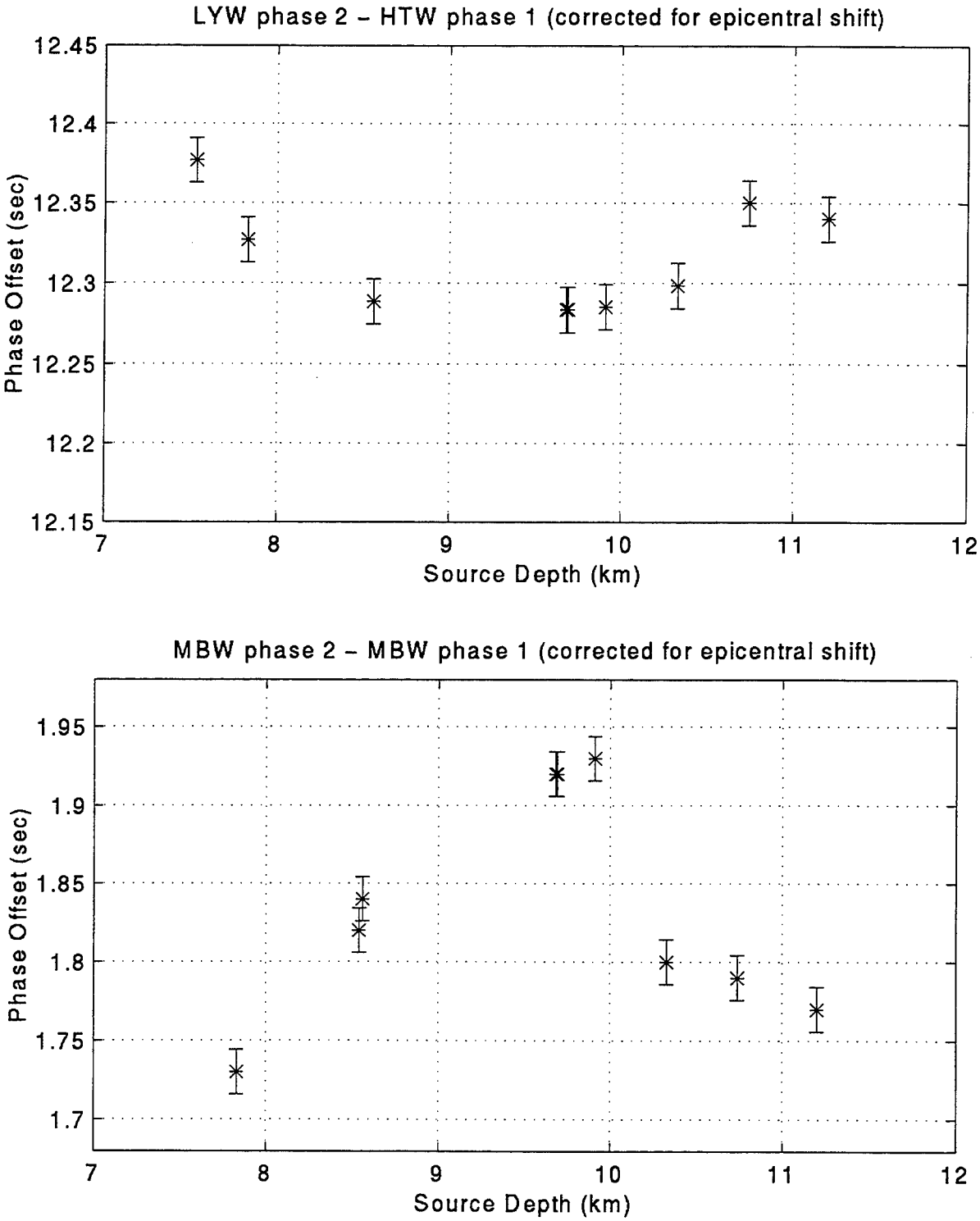

Figure 5. Phase offset plots between station LYW phase 2 and station HTW phase 1 (top), and MBW phase 2 and MBW phase 1 (bottom). Error bars represent a standard deviation of +/- .014 s. Both plots have been corrected for epicentral shift. Notice that equal phase offsets may correspond to two different depths.

with the use of the two-station time-difference method, appears to hold promise as a method for improving focal depth determination using a limited number of stations. There is a limitation in the need to observe similarity between the waveforms for different events at the same station, which almost certainly will limit the depth range over which precise time differences may be determined. Another limitation is the need for a calibration set of events with known focal depths. We are nevertheless encouraged that development of robust methodology that can be of practical use appears to be possible.

Conclusions and Recommendations

Regional phases that have been commonly thought to be useful in focal depth determination (such as P_n, P_g, and P_mP) do not appear to be prominent phases in the data studied to date, making it difficult to estimate depth from a single station. Raytracing techniques using the results of crustal studies have been of notably little use in identifying regional P phases at the distance ranges (130 - 285 km) investigated to date. We have found an empirical technique useful in identifying depth-related P phases from source areas small enough that the seismograms are similar. A two-station, same-azimuth time difference technique shows some promise for use in determining depths of regional events.

The implication for CTBT monitoring is that reliance on P_n, P_g, and P_mP in structurally complicated areas may not be appropriate. While depth-related phases have been found, they are apparent at a minority of the stations examined to date. Finally, although the depth-related phases observed to date appear to be capable of fairly good depth resolution over a small area like an aftershock zone, we do not yet know whether they can be traced over a larger region.

REFERENCES

Catchings, R. D., and W. D. Mooney (1988), Crustal structure of the Columbia Plateau; Evidence for continental rifting, *Journal of Geophysical Research* **93**, 459-474.

Glover, D. W. (1985), *Crustal Structure of the Columbia Basin, Washington from Borehole and Refraction Data*, M. S. Thesis, University of Washington.

Grant, W. C., C. S. Weaver, and J. E. Zollweg (1984), The 14 February 1981 Elk Lake, Washington, earthquake sequence, *Bulletin of the Seismological Society of America* **74**, 1289-1309.

Leaver, D., W. D. Mooney, and W. M. Kohler (1984), A seismic refraction study of the Oregon Cascades, *Journal of Geophysical Research* **89**, 3121-3134.

Miller, K. C., G. R. Keller, J. M. Gridley, J. H. Luetgert, W. D. Mooney, and H. Thybo (1995), Crustal velocity structure in western Washington: Relationship to geology and seismicity, *Seismological Research Letters* **66**, 40.

Miller, K. C. and G. R. Keller (1993), *Proposal to Collaborate with the USGS Deep Continental Studies Group on the North Deployment of the Pacific Northwest Refraction Experiment*, Technical Report, 232 p.

Zelt, C. A., and R. B. Smith (1992), Seismic traveltime inversion for 2-D crustal velocity structure, *Geophysical Journal International* **108**, 16 - 34.

Zollweg, J. E., and D. M. Childs (1995), Knowing the depth of a shallow event, how often can we find depth phases at regional distances?, in J. F. Lewkowicz, J. M. McPhetres, and D. T. Reiter (eds.), *Proceedings, 17th Seismic Research Symposium on Monitoring a Comprehensive Test Ban Treaty*, Air Force Phillips Laboratories. PL-TR-95-2108, ADA 310037

Estimates of Infrasonic Array Gain Patterns

W. Thomas Armstrong, Rodney W. Whitaker
Geoanalysis Group - ESS-5, Los Alamos National Lab
Sponsored by U.S. Department of Energy, Contract W-7405-ENG-36
Comprehensive Test Ban Treaty Research and Development Program LA426

ABSTRACT

Infrasonic array gain patterns are discussed and estimated for the infrasonic frequency range and array geometries under consideration by the Conference on Disarmament in the International Monitoring System (IMS). The larger array spacing being considered for the IMS infrasonic arrays is found to be appropriate in maintaining directivity of the steered beam at lower frequencies. A modestly filled array is found to offer great improvement in narrow band side-lobe suppression at higher frequencies, allowing the benefit of greater directivity of the steered beam at these higher frequencies. Narrow band side-lobe suppression is considered of importance in mitigating frequent, naturally occuring "micro-barom" signals in the southern hemisphere.

Keywords: infrasound, array patterns

OBJECTIVES

The United Nations Conference on Disarmament (CD) has recommended an infrasonic network as one of the International Monitoring System's (IMS) technological monitors of compliance of the Comprehensive Test Ban Treaty (CTBT), presently under negotiation. An important step in assessing and optimizing infrasonic arrays for the IMS is to evaluate the directional detection capability of the arrays. Infrasonic array gain patterns are discussed here and then estimated for the infrasonic frequency range and array geometries under consideration by the CD in the IMS.

RESEARCH ACCOMPLISHED

Pattern Calculation

An infrasonic array usually consists of sensor elements arranged in a 2-D configuration, with each sensor providing a single "channel" signal. Signals from the sensors are typically "steered" to a particular direction; ie, the signals are delayed or "lagged", and then summed, so as to reinforce a sensed disturbance propagating with a particular heading and trace speed across the array. The lag is determined by the geometrical range and bearing of the sensor with respect to a reference location, and in relationship to the trace propagation velocity vector:

$$\tau_i = \frac{r_i \cos(\theta_i - \varphi)}{c}, \tag{1}$$

where r_i and θ_i are the range and bearing of the i^{th} sensor, and c and φ are the trace speed and heading of the propagating disturbance. With the channel signals given by $s_i(t)$ or s_i, and the lagged signals given by $s_i(t+\tau_i)$ or $s_i(\tau_i)$, the summed "composite" signal or "beam" can be written as

$$\hat{s} = \frac{1}{N}\sum_{i=1}^{N} s_i(\tau_i), \tag{2}$$

where N is the number of elements in the array. This composite signal represents the optimized signal for plane wave disturbances and stationary, spectrally-uniform, noise.

The signal-to-noise ratio SNR is defined to be the ratio of mean-squared signal to mean-squared noise, wherein the noise is assumed to be uncorrelated with the signal and stationary. The "gain" of the array is defined as the ratio of the composite SNR to the individual sensor SNR, wherein equal weighting of the sensors is assumed. For noise uncorrelated between sensors and ideal beam steering, the gain of an array is simply N. For the purposes of this paper, a normalized gain for non-ideal beam steering is given by the mean-square of (2); ie, the power of the composite signal. A normalized gain of 1 represents the maximum ideal array gain of N.

The average signal (across channels) is simply the zero-lag composite signal, designated as

$$\hat{s} = \frac{1}{N}\sum_{i=1}^{N} s_i \,. \tag{3}$$

In general, the average signal will emphasize the "vertically propagating" disturbances, or common mode signals which arrive simultaneously at all sensors. Indeed, the traditional impulse response of an array embodies this approach [the reader is referred to the work by Wilson, Olson, Spell, and others on the subject of array performance estimates].

Given the lags for a steered composite signal of (2), the gain pattern is calculated by assuming propagating disturbances from all other headings, but forming the composite signal with these original steered lags. The "off-beam" signals may be written as $s_i'(t)$ or s_i', in which the signal at each sensor location is simply the same signal delayed by the lags associated with the off-beam propagation velocity vector; ie,

$$s_i'(t) = s_i\left(t - \tau_i'\right) \text{ or } s_i\left(-\tau_i'\right). \tag{4}$$

The resulting composite signal for this off-beam signal, formed with the original beam lags, is then given by

$$\hat{s}' = \frac{1}{N}\sum_{i=1}^{N} s_i\left(\tau_i - \tau_i{}'\right), \tag{5}$$

and the normalized gain is given by

$$g = \hat{s}'^2 . \tag{6}$$

For the purpose of simplicity, a sinusoidal waveform is used for the signal. Hence,

$$s_i\left(\tau_i - \tau_i{}'\right) = \exp\left(i2\pi f(\tau_i - \tau_i{}')\right), \tag{7}$$

where f is the frequency of the wave. Patterns of normalized gain are then given as polar plots for all off-beam signals. The trace propagation speed is taken as a fixed value of 330 m/s.

Gain Pattern Estimates

The first array considered is a "centered-triangle", depicted in Figure 1. Figures 2, 3 and 4 present the normalized gain patterns for this array with a spacing of d = 200 m and for frequencies of 0.1, 0.3 and 1.0 Hz. This array and frequency range are in accordance with the array geometry and approximate frequency band under consideration by the CD for the IMS infrasonic network. The array spacing first examined here of 200 m approximates the spacing of arrays previously used in association with higher frequency infrasonic monitoring at ~ 1 Hz. It is observed in figures 2, 3 and 4 that this array has negligible directivity in it's beam steering at low frequencies and has poor side-lobe suppression at high frequencies.

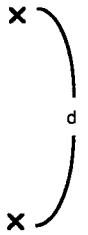

Figure 1. Centered-triangle array geometry.

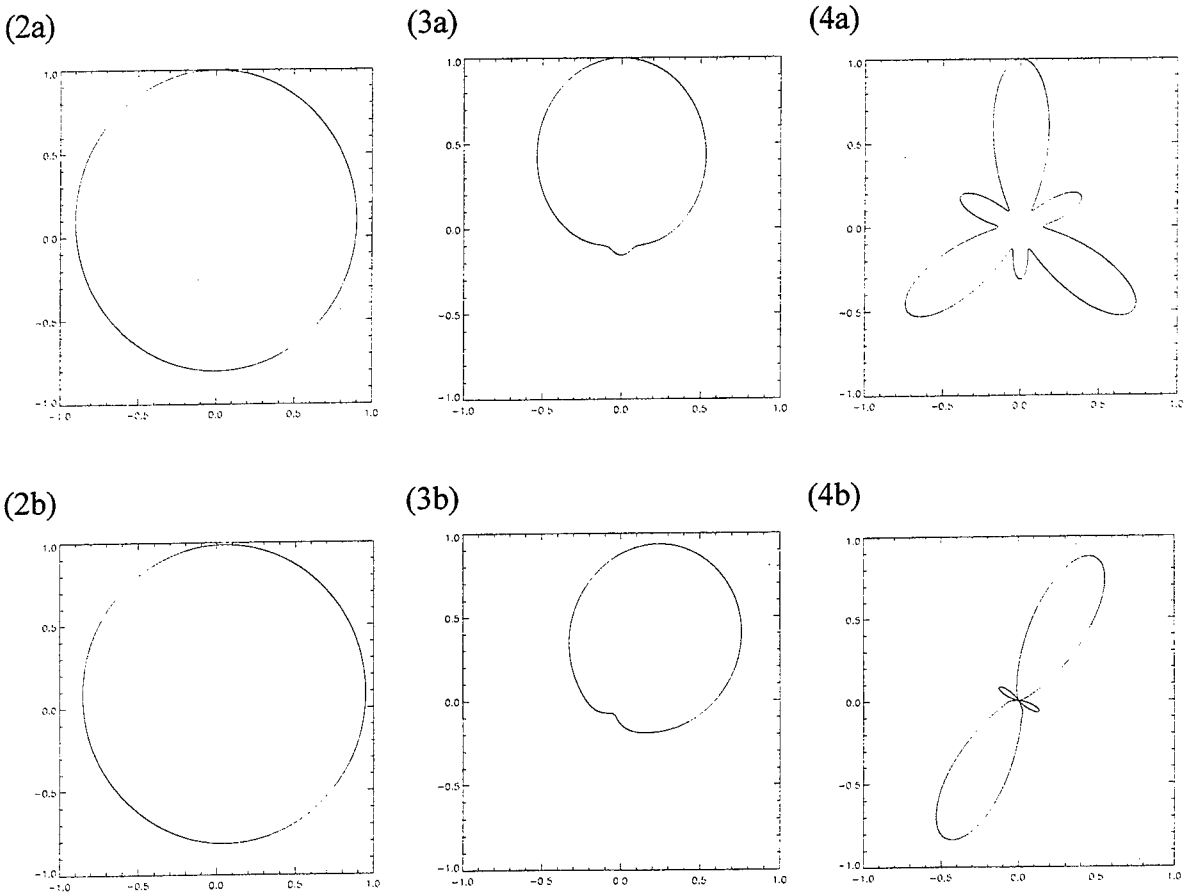

Figures 2, 3, 4. Gain patterns are shown for the centered-triangle 4-element array of figure 1 with 200 m spacing. Figures 2, 3, and 4 show patterns for 0.1, 0.3, and 1.0 Hz, respectively. Subframes a and b show pattern variations for 0° steering and 30° steering, respectively.

Gain patterns for the same array is again considered in figures 5, 6 and 7, but with spacing of the elements of d = 1000 m. The prior frequencies of 0.1, 0.3 and 1.0 Hz are retained. This spacing

approximates the array size proposed for the IMS infrasonic network. With this larger spacing, it is observed that reasonable directivity of the steered beam is now obtained at low frequencies. However, side-lobe suppression is still poor at higher frequencies.

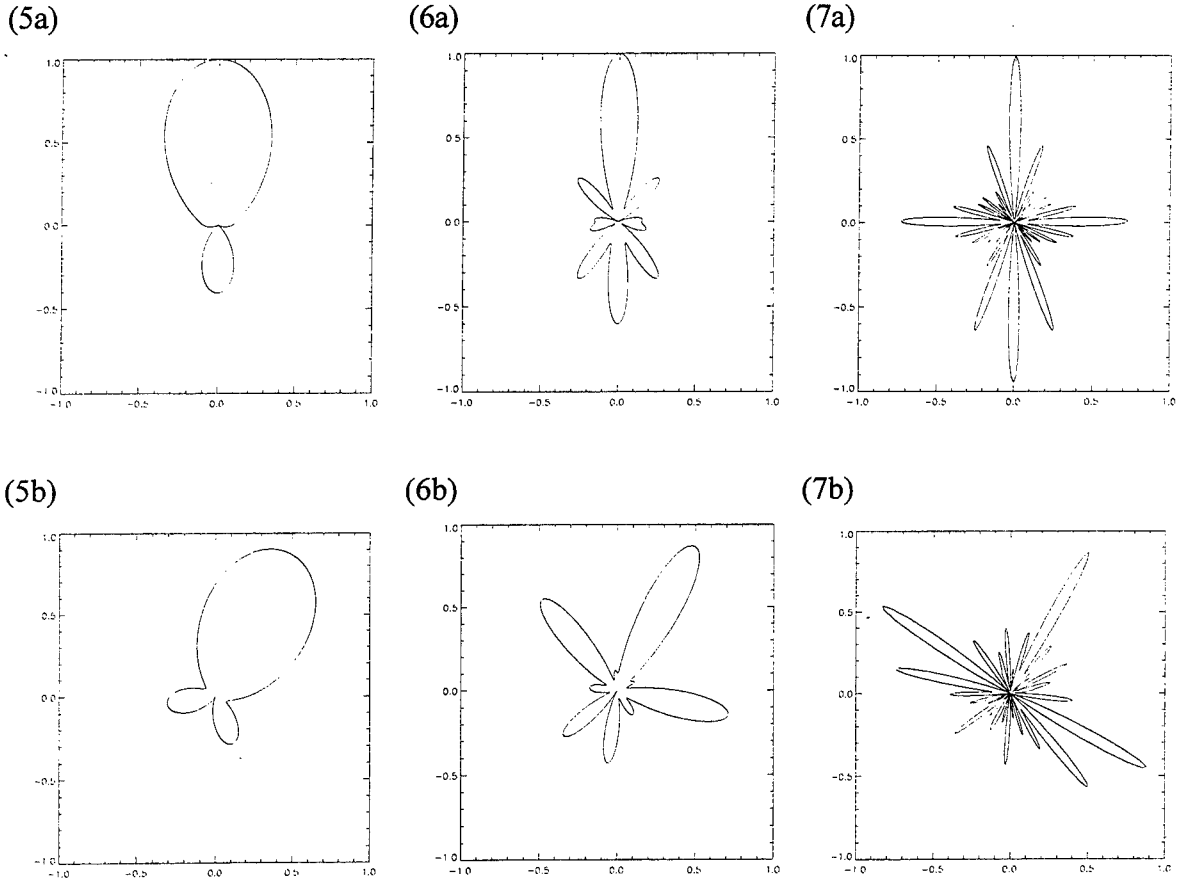

Figures 5, 6, 7. Gain patterns are shown for the centered-triangle 4-element array of figure 5 with 1000 m spacing. Figures 5, 6, and 7 show patterns for 0.1, 0.3, and 1.0 Hz, respectively. Subframes a and b show pattern variations for 0° steering and 30° steering, respectively.

A final array considered here is shown in figure 8. This filled centered-triangle array geometry is simply a combination of the previous small and large centered-triangle arrays. The combination of an inner and outer triangular array combination is again similar to a 7-element array previously proposed for the IMS infrasonic network. This array differs slightly from the proposed IMS array in having the inner triangle rotated 60° so as to be aligned with the outer triangle. The differences in the gain patterns for the two arrays are insignificant, while in-line elements are preferable for ease of installation. The resulting gain patterns for the "filled" array of figure 8 are shown in figures 9, 10 and 11. These patterns exhibit moderate directivity in the low frequency steered beam, as well as good side-lobe suppression at higher frequencies. Also expected and seen in earlier patterns, the width of the beam narrows sharply with increased frequency.

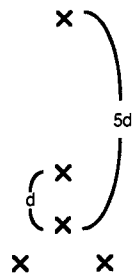

Figure 8. Filled centered-triangle array geometry.

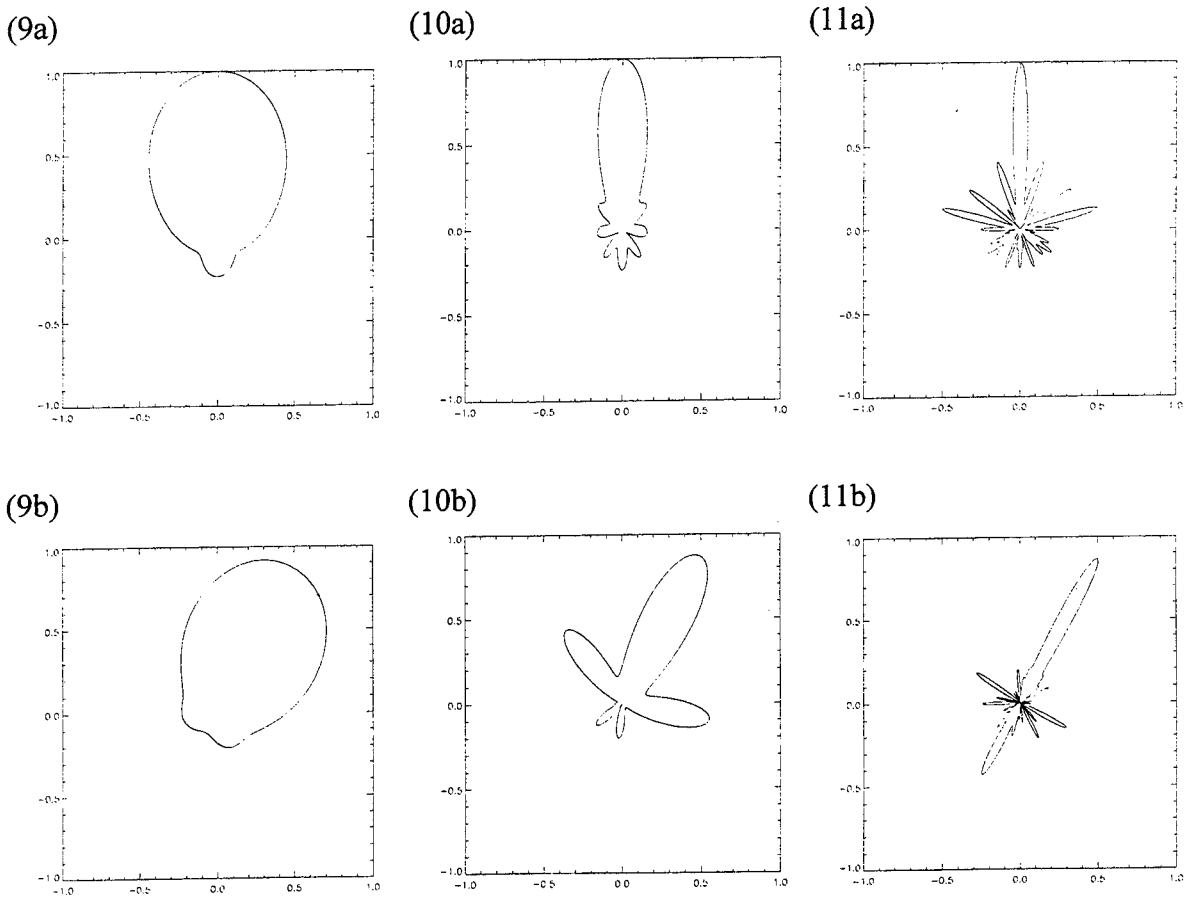

Figures 9, 10, 11. Gain patterns are shown for the filled centered-triangle 7-element array of figure 8 with 200 m inner spacing and 1000 m outer spacing. Figures 13, 14, and 15 show patterns for 0.1, 0.3, and 1.0 Hz, respectively. Subframes a and b show pattern variations for 0° steering and 30° steering, respectively.

CONCLUSIONS AND RECOMMENDATIONS

Though the gain pattern estimates presented here are expected to be representative of actual array performance, some variations of these results can be anticipated. First, the signal processing assumed here is a simple composite signal. Actual signal processing will likely consist of some form of correlation of signals, in which a finite window period will be applied to the signal. Hence, additional signal structure will be utilized in identifying the signal from the noise. In particular, modulation of the signal is anticipated to assist in suppression of side-lobes. In effect, processing of finite bandwidth signals will promote improved directivity of the array. Although sensitivity to narrow band side-lobes will still exist as indicated here, overall sensitivity in the direction of beam steering will be improved with increasing bandwidth.

Another difference in actual signal processing will be the steering of the beam not only in azimuth, but also in trace speed. Changes in the gain patterns are expected which would be achieved with complimentary change in frequency.

After considering these approximations made in the present gain pattern estimates, several conclusions are made. The use of a steered beam is important in estimating off-beam gain. The steered beam helps greatly in evaluating side-lobes of the gain pattern at low and intermediate frequencies. The larger array spacing being considered for the IMS infrasonic arrays is appropriate in maintaining directivity of the steered beam at lower frequencies. A modestly filled array offers great improvement in the side-lobe suppression at higher frequencies, allowing the benefit of the greater directivity of the steered beam at these higher frequencies. Narrow band side-lobe suppression is considered of importance in mitigating frequent, naturally occuring "micro-barom" signals in the southern hemisphere.

SEISMOACOUSTIC STUDIES IN THE NORWEGIAN SEA

Donna K. Blackman and John A. Orcutt
Institute of Geophysics and Planetary Physics
Scripps Institution of Oceanography CA 92093-0225
Contract No. F49620-94-1-0041
Sponsored by AFOSR

ABSTRACT

Archived data from U.S. Navy hydrophone arrays (SOSUS) are used to study the patterns of seismicity in the Norwegian Sea and to characterize regional T-phases generated at various locations along the plate boundary between Iceland and Svalbard. Data have been archived for the past sixteen months and limitations due to recording problems during the first year have now been rectified. In this report we discuss the aims of the project and the events that have occurred during the time period of the archive. At the meeting we will present more detailed analysis of the SOSUS data and we expect to have initial results on modeling T-phase generation at the seafloor.

A swarm of events occurred on the northern Mohns ridge over a period of 12 days starting late November, 1995. This activity is probably related to rifting along the plate boundary and perhaps to associated volcanic activity. Twenty five swarm events, ranging in magnitude from 2.7-4.8 mb, were detected by regional seismic arrays; no similar events were listed in the bulletins based on the global seismic network. This fortuitous, though not surprising, occurrence provides important detailed data for comparative studies of event detection using the hydrophone arrays that monitor the Norwegian Basin versus detection of oceanic sources by the seismic arrays on land (NORESS, ARCESS and the Spitsbergen array).

OBJECTIVE

The goals of our investigation in the Norwegian Sea are to assess the usefulness of SOSUS as a tool for seismology and to increase understanding of seismoacoustic wave propagation in ocean basins. Comparison of earthquakes recorded by the U.S. Navy hydrophone arrays versus those recorded by the seismic arrays in Norway allows us to quantify the sensitivity of the two systems with regard to regional oceanic events. Analysis of earthquake epicenters determined using the hydrophone arrays illustrates the accuracy with which T-phases can be used for locating low frequency events in the ocean. Modeling of T-phase generation is still in the 'basic research' stages but we consider it an essential step towards understanding the partitioning of energy between the ocean and the underlying crust at the seafloor interface. Our growing catalogue of T-phase arrivals for various types of events at different basin localities provides the data necessary to constrain models of T-phase gen-

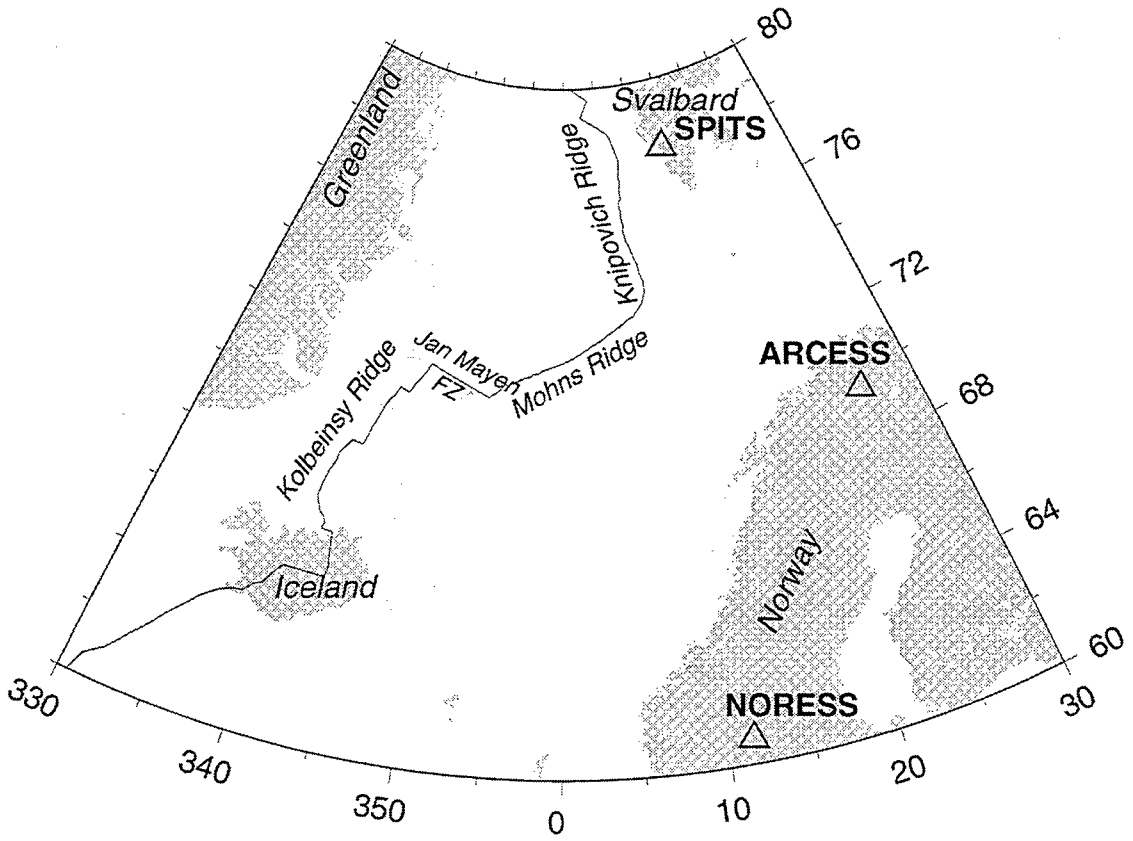

Figure 1. Tectonic setting of the Norwegian Sea seismoacoustic study area. Plate boundary is shown by solid line with spreading centers (Kolbeinsey, Mohns and Knipovich Ridges) and transform faults (Jan Mayen) labeled. The Norwegian seismic array locations are indicated by the triangles. Sixteen channels of beamformed hydrophone data from this area are being archived for characterization of local, regional and teleseismic arrivals.

eration.

The Norwegian Sea offers a unique setting for assessing SOSUS use for seismology due to the existing combination of seismic activity, instrumentation and varied oceanographic conditions. The different seismic sources in the region provide a range of signal types and locations (e.g. Vogt, 1986; Figure 1): large oceanic earthquakes from transform faults along the plate boundary between Iceland and Svalbard; smaller oceanic earthquakes associated with rifting and volcanic eruptions along the spreading ridges of the plate boundary; mining explosions on land; slope failure events on the continental shelf. Several types of recordings of Norwegian Sea seismic activity are available from instruments whose capabilities dovetail each other: the Global Seismic Network (GSN); the seismometer arrays in Norway and on Spitsbergen; and the SOSUS acoustic arrays.

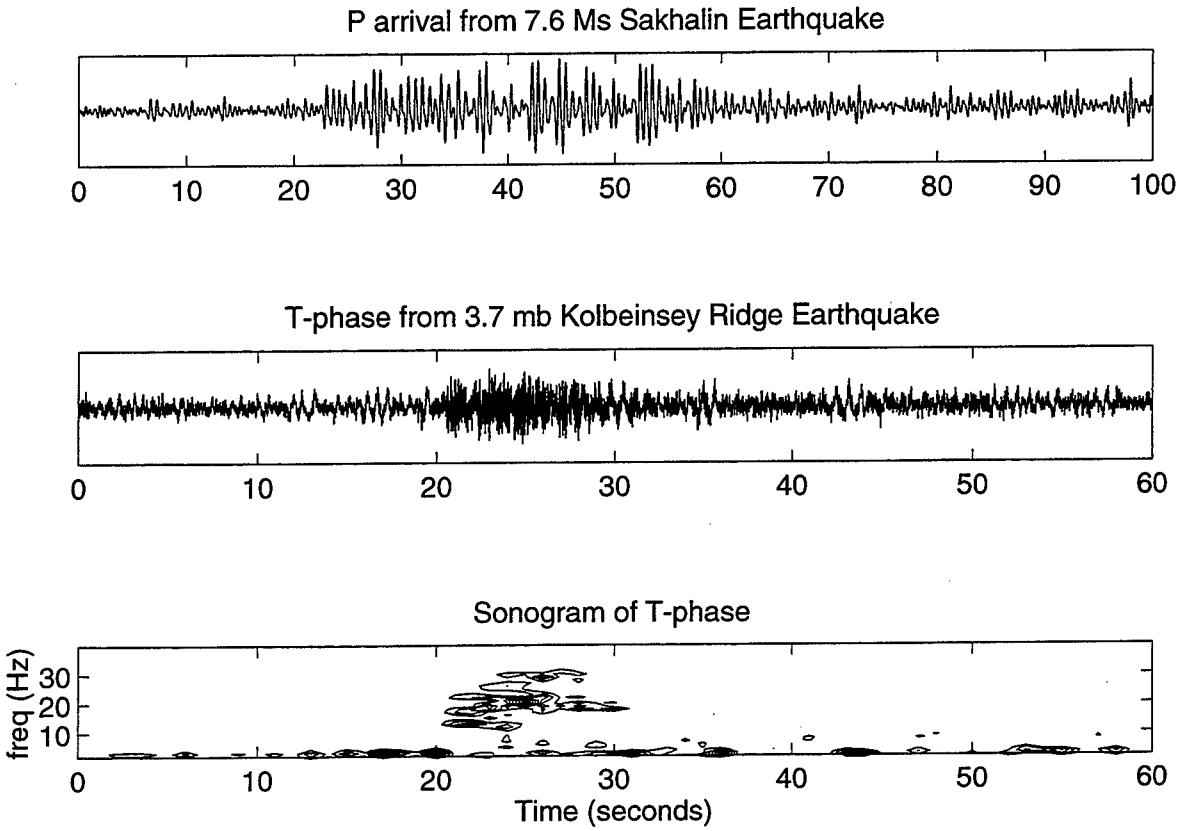

Figure 2. Data from SOSUS hydrophone array. Top panel shows time series of beam data for a teleseismic event (range 50-60 degrees). These data have been filtered with 2nd order Butterworth with pass band 1-4 Hz. The lower two panels show a T-phase arrival from a regional event. Time series is low-pass filtered (5th order Butterworth w/cut at 40Hz). Time window for spectral estimate in sonogram is 1 second.

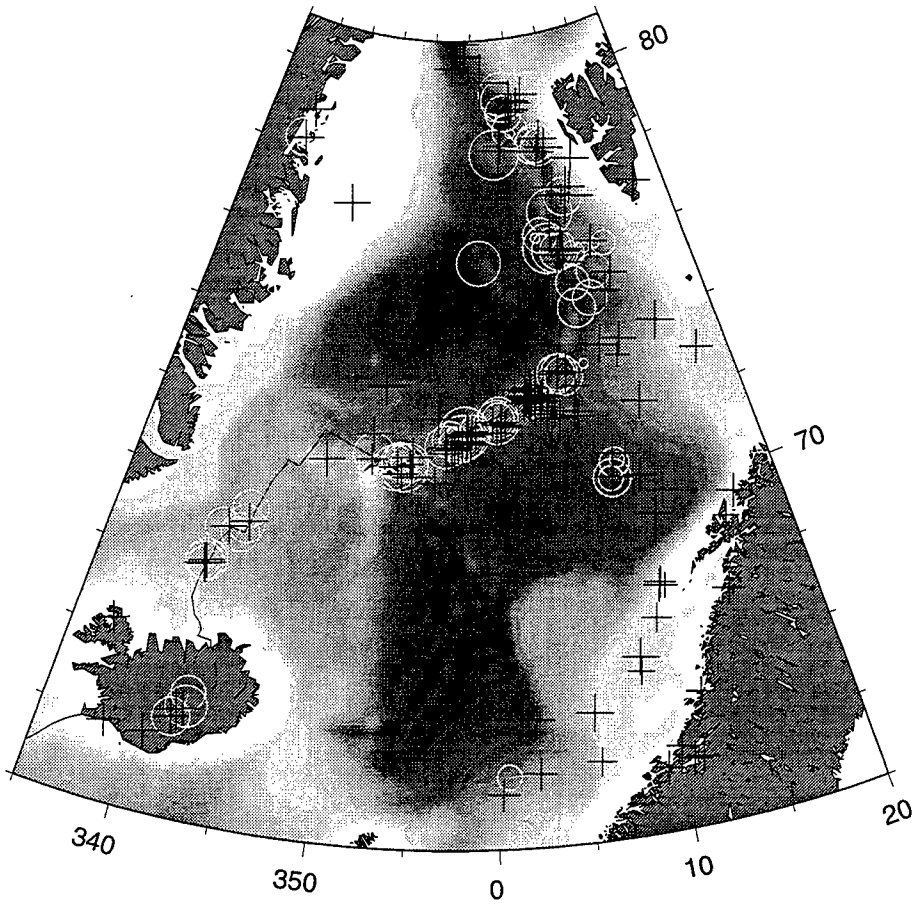

Figure 3. Earthquake epicenters listed by CMR (+) and DMC (white o) for the period 15Feb96-22May96. 54 events are listed in both bulletins; when locations do not match the DMC and CMR symbols are connected by a white line. Symbol size is proportional to event magnitude. Smallest circles simply show location where no magnitude was listed. The size of these smallest circles corresponds to a scaled circle for 1.0 mb. The largest symbol is for 5.1 mb.

RESEARCH ACCOMPLISHED

The hydrophone array data for this project has been archived by the Naval Research Lab since mid February, 1995 (Nishimura and Conlon, 1994). Sixteen channels can be recorded by this system and we are currently monitoring pre-formed beams only; single hydrophones may be monitored in the future on some channels. We continue to focus our efforts on the Mohns ridge, a known source of frequent, low-level seismic activity, and the Jan Mayen transform fault, along which larger earthquakes are generated. Our choice of archived beams reflects this emphasis and we monitor several beam directions from more than one location. During the first eight months of recording, we obtained data useful for initial work but, due to wiring diagram problems at the acquisition site, noise and electronic crosstalk between channels reduced the full usefulness of the archive. Most of

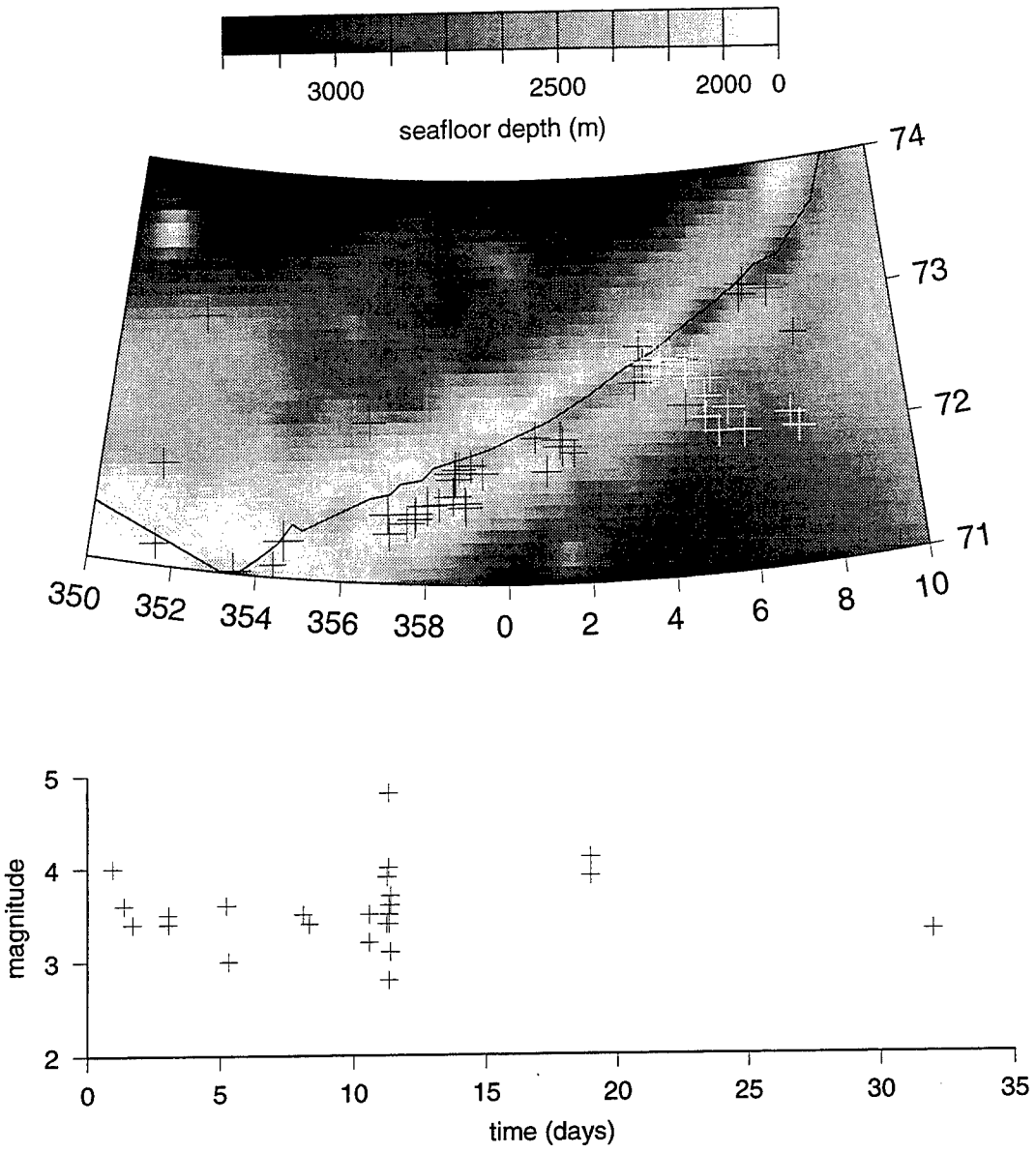

Figure 4. Swarm of events starting late Nov 1995. CMR locations are shown (+) along the northern Mohns ridge. White +'s indicate events 27Nov-30Dec95. Rift valley is shown by darker gray in the center of the shallow ridge. Solid line marks spreading axis. Time history of swarm events is shown in the lower panel. Activity ceases abruptly following day 12 on which the largest (4.8 mb) event occurred followed by several smaller events.

these wiring problems were sorted out in November, 1995, and by February, 1996, a GPS clock was integrated into the system so that a reliable time stamp is now present for each record.

The initial data can be used to compare the number of earthquakes in the study area that are recorded by the SOSUS arrays with that listed in the Center for Monitoring Research (CMR) Bulle-

tin. The events recorded by the hydrophone arrays can be approximately located through beamsteering with the archived beams. The statistics vary with time period and the length of our time sample is still fairly short but it is clear that the SOSUS system records many more events along the ridges in the Norwegian Sea than are reported in the CMR bulletin. Earthquake activity has varied over the period Feb95-May96. Last year (Blackman and Orcutt, 1995) we reported more SOSUS recordings from the southern Mohns Ridge than from the northern Mohns Ridge (although part of this result probably reflects our choice of archive beams). In the past year, some of the most intense low-level activity has been on the northern Mohns as discussed below.

The hydrophone data record both regional T-phases and teleseismic body waves. An example of a teleseismic P arrival from the 27May95 Sakhalin earthquake (7.6 Ms, range 55° from Jan Mayen Island) is shown in Figure 2. This arrival can be seen in the raw beam data but filtering significantly improves the signal-to-noise ratio for the 1-4 Hz frequency range. An example SOSUS recording of a 3.7 mb event on the Kolbeinsey Ridge is also shown in Figure 2.

Daily reports of seismic events in the Norwegian Sea are sent via email by CMR allowing us to continually monitor activity. Event magnitudes are estimated by CMR to range from 2.7 Ml to 4.8 mb for the time period corresponding to the SOSUS archive in this region. Figure 3 shows the distribution of earthquakes listed by CMR as well as those listed by IRIS Data Management Center (DMC) based on the Global Seismic Network (GSN). CMR lists 171 events, DMC lists 75 events and 54 events are listed by both bulletins. There does not appear to be a consistent pattern in the 28% of events listed by DMC that are not listed by CMR. The magnitude estimates and locations differ somewhat between the bulletins for co-listed events in this time period. On average, their epicenters match to within about 20 km although two events have a DMC location more than 100 km from the CMR location (Figure 3).

A swarm of events is listed by CMR as occurring on the Mohns ridge near 72.5°N, 4°E during the period 27Nov-30Dec, 1995 (Figure 4). Throughout the first ten days of the period, activity in the magnitude 3-4 range occurred with an earthquake reported about once a day on average. On days 11-12 of the swarm, activity appears to have reached a maximum with a 4.8 mb event being followed by 8 smaller events on 8 Dec alone. Only 3 more events were detected by the land arrays during the subsequent 20 days as shown in the lower panel of Figure 4. Preliminary work shows that many events are recorded by SOSUS during this time period and more quantitative analysis of the hydrophone data (spectral characterization of the arrivals, location of events where possible) will be undertaken at NRL this summer. These results will provide an important comparison of the detection levels for oceanic events on SOSUS vs on the seismic arrays on land.

INTERIM CONCLUSIONS

Upgrades in the acquisition and recording system late 1995/early 1996 appear to have brought the quality of the Norwegian Sea SOSUS archive to a level appropriate for modern seismoacoustic investigation. Problems encountered during the first year of data archiving limit our initial analysis to comparison of the number of regional oceanic events detected by SOSUS vs that detected by the land seismic arrays. Although only a first step, these results do provide useful information on the

general detection levels of these two systems in this area. More complete characterization of T-phases generated/recorded at different sites and our ability to locate events using these phases is a main focus of our work in the coming months.

REFERENCES

Blackman, D.K., J.A. Orcutt, D.W. Forsyth, 1995, Recording teleseismic earthquakes using ocean bottom seismographs at mid-ocean ridges, Bull. Seis. Soc. Amer. 85, 1648-1664.

Blackman, D.K. and J.A. Orcutt, 1995, Seismoacoustic studies of the Norwegian Sea, Proceedings of the 17th Seismic Research Symposium. **PL-TR-95-2108, ADA 310037**

Nishimura, C.E. and D.M. Conlon, 1994, IUSS dual use: monitoring whales and earthquakes using SOSUS, Mar. Tech. Soc. 27, 13-21.

Vogt, P., 1986, Geophysical and geochemical signatures and plate tectonics, in B.G. Hurdle (ed), *The Nordic Seas,* Springer-Verlag, New York, p413.

An Automated Radioxenon Analyzer for Possible CTBT Monitoring "The Xenon Xephyr"

T.W. Bowyer, K.H. Abel, C.W. Hubbard, A.D. McKinnon,
M.E. Panisko, R.W. Perkins, P.L. Reeder, R..C. Thompson, R.A.Warner
Pacific Northwest National Laboratory

Sponsored by U.S. Department of Energy, Contract DE-AC06-76RLO-1830
Comprehensive Test Ban Treaty Research and Development Program, ST583

ABSTRACT

A fully automatic radioxenon analyzer has been developed and demonstrated for the collection and quantitative measurement of the four xenon radionuclides, Xe-131m (11.9 d), Xe-133m (2.2 d), Xe-133 (5.2 d), and Xe-135 (9.1 hr), in the atmosphere. These radionuclides are important signatures in monitoring for compliance to a Comprehensive Test Ban Treaty (CTBT). The activity ratios of these radionuclides permit discrimination between radioxenon originating from nuclear detonations and those from nuclear reactor operations, nuclear fuel reprocessing or losses from medical isotope production and usage. Stable xenon and associated radioxenon components are continuously and automatically separated from the atmosphere at flow rates of about 7 m^3/hr by sorption bed techniques, and aliquots collected during 6- to 12-hr time periods are automatically analyzed by electron-photon coincidence spectrometry to provide sensitivities in the range of 20 to 100 $\mu Bq/m^3$ of air. This sensitivity is 100-1000 times better than would be achievable with reported laboratory-based procedures for the short-time collection intervals of interest. The large sensitivity improvement over reported laboratory techniques is due to: a 10- to 25-fold higher sampling rate, a 3- to 4-fold higher counting efficiency, a 10^3 to 10^4 lower background, the immediate analysis of the radioxenons following collection and purification, and the complete elimination of radon from the separated atmospheric xenon samples. Spectral data from the measurements are automatically analyzed for radioxenon concentrations, and the analyses and the gamma-ray spectra are automatically transmitted to data centers.

Key Words: xenon, radioxenon, Xenon Xephyr, noble gas, CTBT, PNNL

An Automated Radioxenon Analyzer for Possible CTBT Monitoring "The Xenon Xephyr"

T.W. Bowyer, K.H. Abel, C.W. Hubbard, A.D. McKinnon,
M.E. Panisko, R.W. Perkins, P.L. Reeder, R..C. Thompson, R.A. Warner
Pacific Northwest National Laboratory

OBJECTIVE

To help ensure compliance with a Comprehensive nuclear Test Ban Treaty (CTBT), it is important that monitoring technologies for detection of covert nuclear testing be available. Monitoring methods which are being developed and/or enhanced by the DOE include seismic, hydroacoustics, infrasound, and radionuclide technologies. While seismic, hydroacoustic, and infrasound signals may provide evidence that an explosion has occurred, only detection of short-lived fission products can provide absolute confirmation that the event was nuclear. If a covert nuclear test were performed by evaders of a CTBT, they may attempt to carry it out in a manner which minimizes signatures associated with such an event. For example, conducting a test underground, underwater, or over the ocean in a rainstorm could minimize or eliminate some signatures, including the emission of particulate radionuclides. Under such conditions, only the noble gas radionuclides may enter the atmosphere in significant quantities. Of the noble gas radionuclides, the xenon radionuclides are by far the most abundant at a few days after a detonation. Therefore, their measurements could provide confirmation that signatures from other monitoring technologies were indeed nuclear events, or without these they could provide both detection and confirmation of a nuclear detonation.

Based on the radioxenon activity ratios from subsurface weapons test venting and reactor leakage shown in figure 1, it is clear that excellent differentiation is possible provided selective and sensitive radionuclide measurements can be made. For example, the ratio of Xe-133m to Xe-133 (see figure 1a) is about 100-fold higher for vented material from a nuclear detonation than from a reactor. The ratio from reactors is equal to what is present in fuel at equilibrium, but since some time is required for radioxenon emission following leakage from fuel, the Xe-133m to Xe-133 ratio may be considerably less. Therefore, by measuring this Xe-133 isomer ratio it should be possible to detect a very small amount of vented radioxenon in a relatively large ambient reactor background. Also, there is a 10^4-fold higher Xe-135 to Xe-133 ratio in vented radioxenon from a nuclear detonation than that observed near operating nuclear reactors (see figure 1b). Thus the measurement of these three xenon radionuclides provides a very sensitive method of detecting vented material from a nuclear explosion.

RESEARCH ACCOMPLISHED

Our automatic radioxenon analyzer (The "Xenon Xephyr") allows rapid separation of atmospheric xenon from about 7 m^3 of air per hour and prompt subsequent radioxenon measurement. The demonstrated sensitivities for the radioxenons are about 100 $\mu Bq/m^3$ based on a 6-hr collection and a 24-hr analysis period. These measurements of extremely low concentration levels require a very low background and highly selective and efficient counting system which is provided by the beta (and/or conversion electron) gamma (or x-ray) coincidence detection systems as described below. While sensitivity requirements for possible radioxenon monitoring of a CTBT are not specified, it is clear that high sensitivities will be essential to detect the very low yields which will be prohibited by a "zero yield" test ban.

To achieve the maximum sensitivity with a practical automatic radioxenon analyzer it was necessary to: (1) provide a high sampling rate, (2) employ a high efficiency detector system capable of

measuring all of the airborne radioxenons simultaneously, (3) minimize the background count rate, (4) completely eliminate radon in the separated xenon samples, and (5) conduct short cycles of continuous separations with prompt subsequent analysis of the aliquots to provide timely reporting and avoid serious decay of the radioxenons (especially the 9.1-hr half-life Xe-135).

A primary requirement for our automatic radioxenon analyzer was that it automatically and continuously separate xenon gas from the other atmospheric gases at a flow rate of 4,000 to 10,000 liters of air per hour, with minimum energy consumption and with no consumables. It also included the objective of automatically measuring the xenon radionuclides in consecutive aliquots collected over 6-hr periods. This will permit continuous separation and analysis at a monitoring site without the need for an operator or frequent maintenance.

An essential requirement of the separation process is the total separation of radon from the xenon gas product. The ambient atmospheric concentration of Rn-222 of about 10 Bq/m^3 is about 10^5 times greater than the desired detection sensitivity for Xe-133; therefore, it could cause a serious interference if it were not removed prior to analysis.

The sampling and subsequent analysis of atmospheric xenon with the Xenon Xephyr is accomplished in three steps. First, xenon is adsorbed from an air stream on a cooled, activated charcoal at a flow rate of ~110 standard liters per minute (slpm). Second, the xenon trapped on the charcoal bed is thermally desorbed and purified to remove traces of radon and CO_2. Third, the purified sample is transferred to a nuclear counting system, counted, and then assayed using a residual gas analyzer, so that the stable xenon concentration can be determined. Figure 2 shows a simplified schematic illustration of the Xenon Xephyr. The vertical dotted lines represent separations of the three steps used in the trapping, purification, and analysis of the radioxenons. Much of the detail related to the redundant pieces of hardware necessary for 100% duty cycle of this system have been left out of the figure.

Xenon Trapping: Xenon is highly adsorbed on activated charcoal at low temperatures (<-100° C). We trap the xenon from a stream of compressed atmospheric air by passing it through a bed of cooled charcoal. In order for the charcoal work with maximum efficiency, all of the water vapor and CO_2 must be removed from the air stream. Past measurements of ambient levels of atmospheric radioxenons have generally involved drying of the air followed by collections at temperatures of -70 to -80°C on activated charcoal beds (Bernstrom, *et al.*, 1983; Kunz, 1989; Kunz, 1995; Pence, *et al.*, 1978) with flow rates on the order of 3 to 7 slpm.

The main compressor (a) forces air at ~550-700 kPa (80-100 psig) at a rate of ~110 slpm through a heat exchanger (b) cooled by off-gas from the output of the cooled, activated charcoal trap and through a 100% duty cycle industrial air drying system (c) filled with 13X molecular sieve. The molecular sieve is used to remove the water vapor and CO_2 from the air stream. The total flow through the air drying units is monitored and kept constant through the use of a mass flow controlling unit (d), just down stream of the air dryers. Each one of the drying columns is large enough to handle 110 slpm for approximately 5 hours before it must be regenerated. The dryer regeneration is accomplished by heating the molecular sieve in the drying units to a high temperature and flowing dry, CO_2-free air through it for at least one hour. The "purge" air used to regenerate the dryers is fed by the output of the main charcoal trap.

After the dry air stream emerges from the air drying unit, it passes though a cryogenic air chiller (e). This air chiller is capable of lowering the output temperature of a room temperature air stream to -125 °C at >110 lpm. The air stream is cooled to provide the cooling necessary for the "radon pre-trap" (f) and the main charcoal trap (g).

The 5-cm long radon pre-trap is used to eliminate much of the radon which is pulled through the system along with the other atmospheric gases. Since the radon pre-trap has a relatively small diameter (~1 cm) the contact time with the air stream is very short, and so xenon is not held appreciably. The radon, however, is held much more strongly than xenon on cooled charcoal, and hence a large amount of radon is retained on this trap. Since the radon pre-trap continually adsorbs radon throughout a normal run, it must be regenerated periodically. We have determined that a regeneration time of ~2 hrs at ~300°C while under vacuum is sufficient for the regeneration of this trap.

Detailed laboratory analyses have shown that with ~110 slpm flow through the main charcoal trap (g) (20-cm long × 10-cm diam. held at -125°C) the xenon begins to break through bed after approximately 6 hrs. This corresponds to a total of about 40,000 liters of air. Once the xenon has also been adsorbed by the charcoal at low temperatures, it remains adsorbed even at room temperatures for long periods (>days).

Since the charcoal is held at a low temperature during the 6-hr trapping process, other atmospheric gases are adsorbed on the charcoal. To remove as much of these gases as possible while not losing a significant amount of xenon, a vacuum is pulled (~few hundred Pa) on the trap for approximately 30 minutes after the trapping step. We have determined most of the xenon (>90%) is retained on the charcoal bed under these operating conditions.

Xenon Purification: The xenon is desorbed from the charcoal trap (g) by heating and purging with a nitrogen carrier gas (h) maintained at ~200 cc/min with mass flow controllers (i-j). In order to facilitate xenon desorption, internal heaters are used to increase the temperature of the charcoal in the trap to ~300°C, while the nitrogen flows through the trap. A series of three additional traps (k-m) are used for further purification and to facilitate the transfer of the xenon into the counting system. Further heating of his trap under vacuum for several hours is used to regenerate this trap.

The first of the purification traps (k) contains 5A molecular sieve cooled to -40°C. This trap removes any radon which was not trapped in the radon pre-trap (f) and has the capability of removing additional CO_2 which may not have been adsorbed in the drying units (c).

The second trap (l) after the main charcoal trap contains a mixture of ascarite and silica gel (71% ascarite - 29% silica gel). This trap removes any traces of CO_2 which may have not been adsorbed by the drying columns (c), or adsorbed in the post-radon trap (f). The silica gel is used to remove H_2O produced in the reaction which removes the CO_2. The 25-cm long × 10-cm diam. bed can remove >70 liters of CO_2 with >98% efficiency.

The last trap in the xenon purification step, the "final charcoal trap" (m), contains the same material as the main charcoal trap, though its dimensions are much smaller. The dimensions of this trap are approximately 6-cm long × 0.6-cm diam. These dimensions were determined to be sufficient to trap all of the xenon flowing from the main charcoal trap at ~200 cc/min carrier gas flow when its temperature is kept below -100°C. Once the xenon is trapped in the final charcoal trap, it is transferred to the xenon quantification step by heating the final charcoal trap to ~400°C and letting the gas (typically >33%-50% xenon) expand into a pre-evacuted gas cell scintillation counter.

The entire desorption/purification process takes ~3 hrs at ~200 cc/min nitrogen carrier flow, while transferring >90% of the xenon trapped on the main charcoal trap onto the final charcoal trap.

Xenon Quantification: The xenon quantification step consists of electron-photon coincidence counting of the radioxenon gas in a gas cell scintillation counter (n), subsequent gas composition analysis via a residual gas analyzer (o), and final transfer to one of several pre-evacuated archive bottles.

The gas mixture is transferred from the final charcoal trap by first evacuating one of four gas cell scintillation counters and then opening a small dead volume valve between the cell and the trap. The gas cell's internal volume is 10 cc or less, and the volume of the combination of the final charcoal trap, tubing and valves downstream of the final charcoal trap is much smaller. We have observed transfer efficiencies >80% of the xenon gas from the final charcoal trap into the counting cell. The gas in the counting cell is counted by requiring a beta particle and/or conversion electron to be detected in coincidence with a gamma or x-ray in the NaI(Tl) spectrometer.

Measurement Procedure: A primary concern in radioxenon monitoring for compliance to a CTBT is the detection of nuclear explosion related radioxenon in the presence of ambient radioxenon. Essentially all ambient radioxenon is from reactor leakage, whereas the nuclear weapons radioxenon of interest would be from rapid (a few minutes) venting of a subsurface detonation or other nuclear detonation where particulate release was minimized or eliminated.

The decay of the three xenon radionuclides of primary interest, Xe-133m, Xe-133 and Xe-135, as well as that of Xe-131m, is by coincidence emission of a beta particle and/or a conversion electron in coincidence with a gamma ray or a cesium or xenon x-ray. In order to simultaneously measure these with very high sensitivity and selectivity, it is necessary to measure the energy of the photon in coincidence with the electron with high efficiency. To accomplish this in a manner which was compatible with the automatic separation process, a gas cell scintillation counter was developed. This scintillation counter consists of a hollow cylinder with a 1-mm wall thickness, 1-mm thick end sections, and a volume of several cc. It is viewed at each end with 2-cm diameter photomultiplier tubes. To record an event in the gas cell scintillation counter, a coincidence event must be observed by each phototube.

The photons are detected in one of two NaI(Tl) crystals completely encasing the gas cell scintillation counters. The laboratory prototype employs 7.6-cm thick × 12.7-cm diam. detectors, though a new detector has been designed which increases the geometric solid angle coverage considerably (see figure 3). It will accommodate four gas cell scintillation counters for the simultaneous counting of four xenon gas samples. The xenon gas samples which are collected during consecutive 6-hr periods are transferred into the gas cell scintillation counters and their xenon radionuclide content measured by beta and/or conversion electron - gamma or x-ray coincidence counting. Since a beta and/or a conversion electron event in a given gas cell triggers storage of an associated gamma ray or x-ray as part of a specific gamma-ray spectrum, four spectra or more could be measured simultaneously without interference. We have observed that using beta and/or conversion electron and gamma or x-ray coincidence counting provides a 10^3- to 10^4-fold background reduction over standard gamma-ray spectrometry. Since essentially all of the beta and conversion electron emissions are observed in the gas cell scintillation counter, the gamma-ray and x-ray counting efficiencies are not significantly reduced by requiring a coincidence event. Figure 4 illustrates an beta coincidence gamma-ray spectra of a Xe-133 spike taken with our prototype counting system with and without the coincidence requirement. This shows the Xe-133 photopeak at 81 keV and the associated x-ray peak which is due to both xenon and cesium x-rays at 30 to 34 keV. The extremely low gamma-ray background provided by the coincidence requirement permits xenon measurement of just a few disintegrations per hour.

Another counting system which has not yet been fully tested will consist of a gas cell scintillation counter which will be located in the center of a large annular intrinsic germanium detector. This system uses more electrical power than the NaI(Tl)-based system, but may reduce the background (perhaps an additional 10-fold) and provide better suppression interference from radioactive

contaminants in the xenon gas. This system has been simulated by placing the gas cell scintillation counter on the top surface of a large intrinsic germanium detector and operating this detector system in the same coincidence counting mode as that required with the NaI(Tl) detector system. Studies are underway to determine optimal detector geometry and cost/power/sensitivity trade-offs for such a detection system.

Figure 5 shows a CAD rendering of an engineering field model which is scheduled to begin initial testing in August, 1996 and should be ready for field tests in early 1997. All of the operations will be automatic and computer-controlled, including state-of-health, remote programmability, transmission of gamma-ray spectral data and a calculation of the radioxenon concentrations, if required. The spectral data, together with gas composition and radionuclide composition, permit calculation of the radioxenon concentrations and all of these data are automatically transmitted to a data center at the conclusion of each analysis. However, if the radioxenon concentrations are found to exceed specified limits at any time during the counting period, these preliminary data can be automatically transmitted.

CONCLUSIONS AND RECOMMENDATIONS

A near real-time automatic xenon radionuclide analyzer has been developed which permits the continuous measurement of atmospheric Xe-131m, Xe-133m, Xe-133 and Xe-135. By measuring these concentrations, it is possible to differentiate between vented material from a subsurface or other nuclear detonation where particulate radionuclide release is minimal and emission from nuclear reactors, fuel reprocessing, and medical isotopes production and usage. This is the first automatic system developed for the measurement of atmospheric xenon radionuclides and allows a 100- to 1000-fold greater sensitivity for the short collection/analysis periods of interest than previously reported laboratory-based analytical methods. The current system design incorporates the following specifications: continuously separates xenon from the atmosphere at a flow rate of ~110 slpm for 6-hr periods, measures the Xe-131m, Xe-133, and Xe-135 with a sensitivity of 20 to 100 $\mu Bq/m^3$ during a subsequent 24-hr period, automatically transmits gamma-ray spectra and radionuclide concentrations to appropriate designated organizations, reports abnormally high concentrations of xenon radionuclides as soon as statistically valid data have accumulated, operates automatically, and all functions are remotely programmable.

REFERENCES

Bernstrom, Brita, Lars-Erik DeGeer, Matning Av Sma MangderXenon133 I Luft. FOA Rapport, C-20515-A1, November (1983).

Bowyer, T.W., K.H. Abel, W.K. Hensley, M.E. Panisko, R.W. Perkins. Ambient Xe-133 Levels in the Northeast U.S., submitted for publication in Journal of Environmental Radioactivity (1995).

Kunz, C.O. Separation Techniques for Reactor-Produced Noble Gases, pp. 209-217. Noble Gases, A Symposium Held in Las Vegas, Nevada September 24-28, (1973).

Kunz, C., "Xe-133 Ambient Air Concentration in Upstate New York." Atmospheric Environment, Vol. 23, No. 8, pp. 1827-1833 (1989).

Pence, D.T, C.C. Chou, J.D. Christian, W.J. Paplawsky, Noble Gas Separation With the Use of Inorganic Adsorbents. 15th DOE Nuclear Air Cleaning Conference, CONF 780819, Pt. 1, pp. 512-519, (1978).

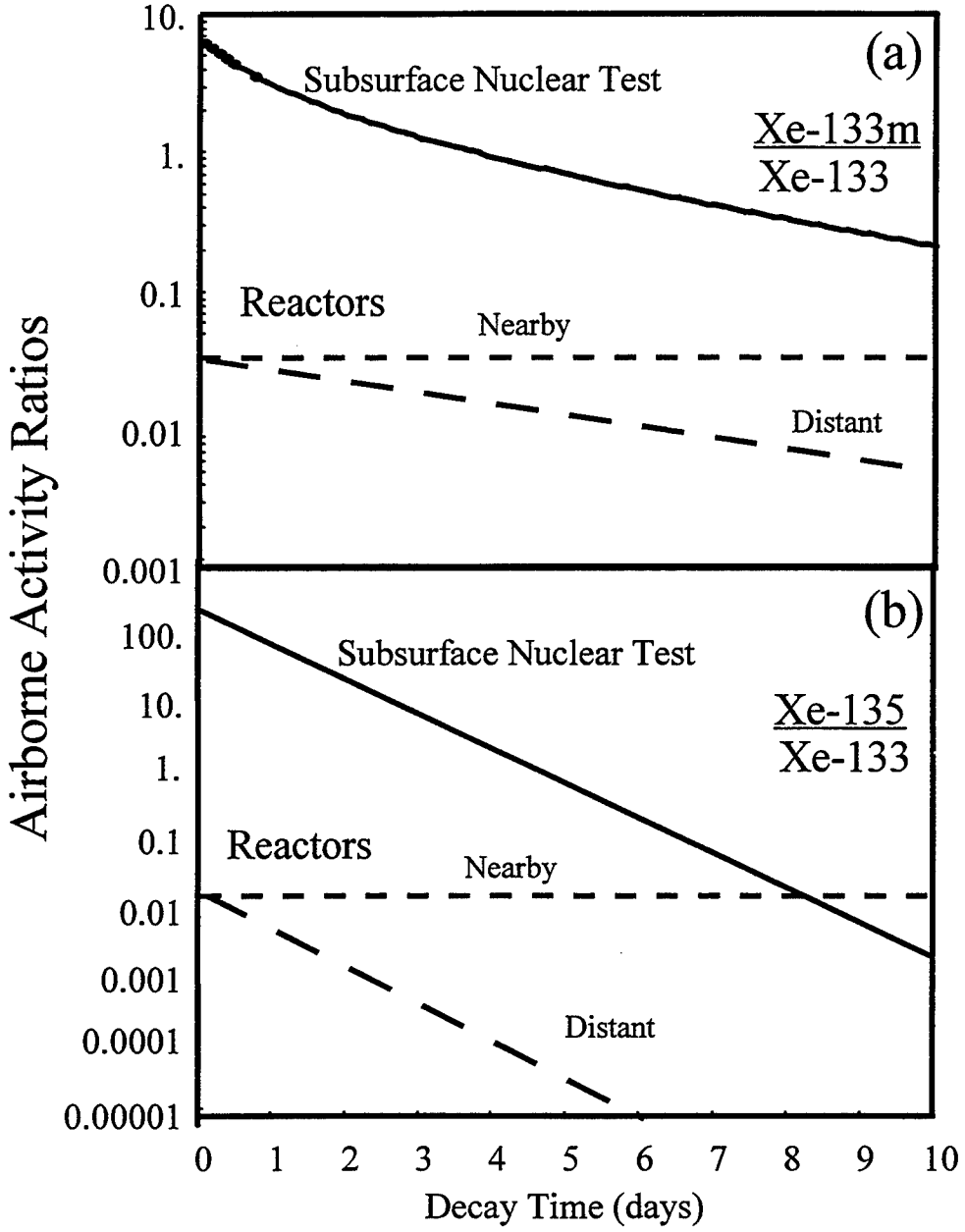

Figure 1. Expected airborne activity ratios for the radioxenons from subsurface nuclear tests and reactors. Measurement of the ratios should easily give an indication of the source of the radioxenon detected in the Xenon Xephyr's counting system.

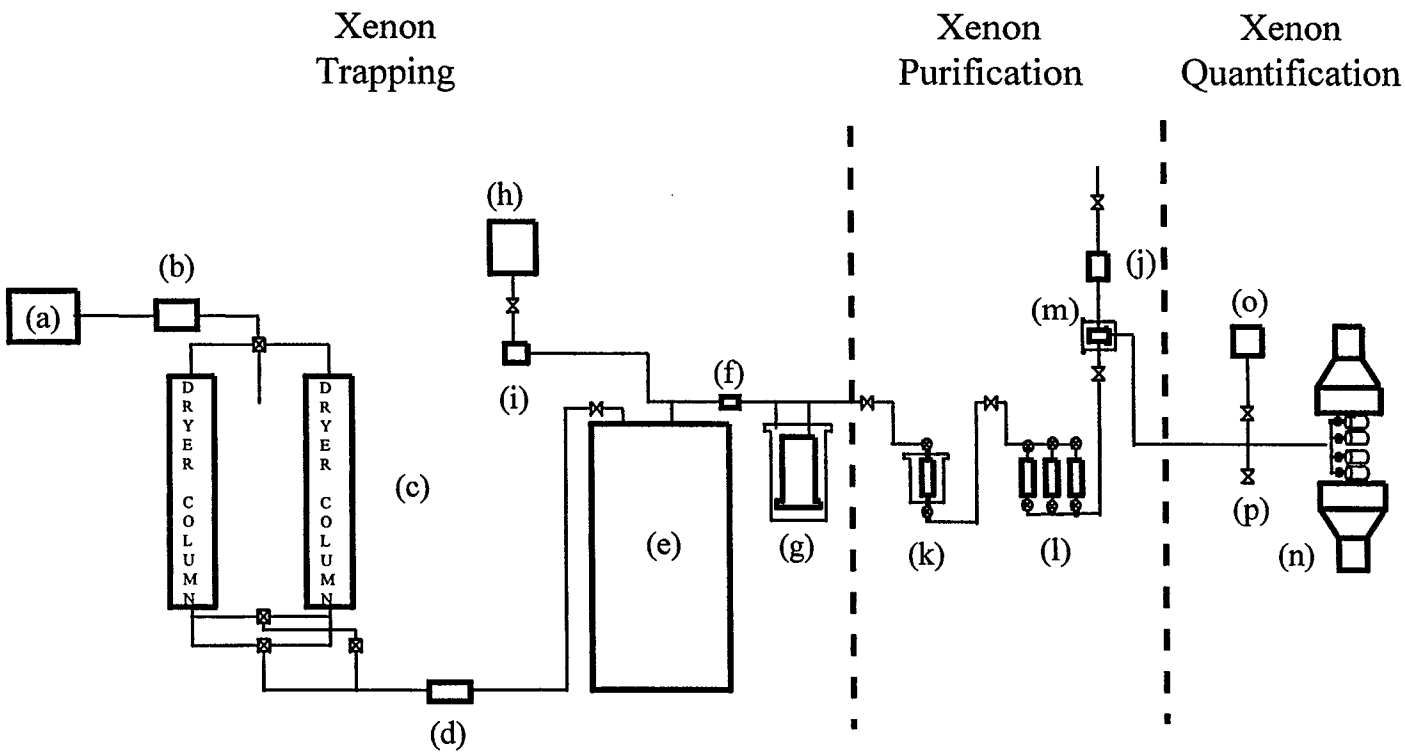

Figure 2. Simplified schematic illustration of xenon purification and analysis system. The text describes the labelled components.

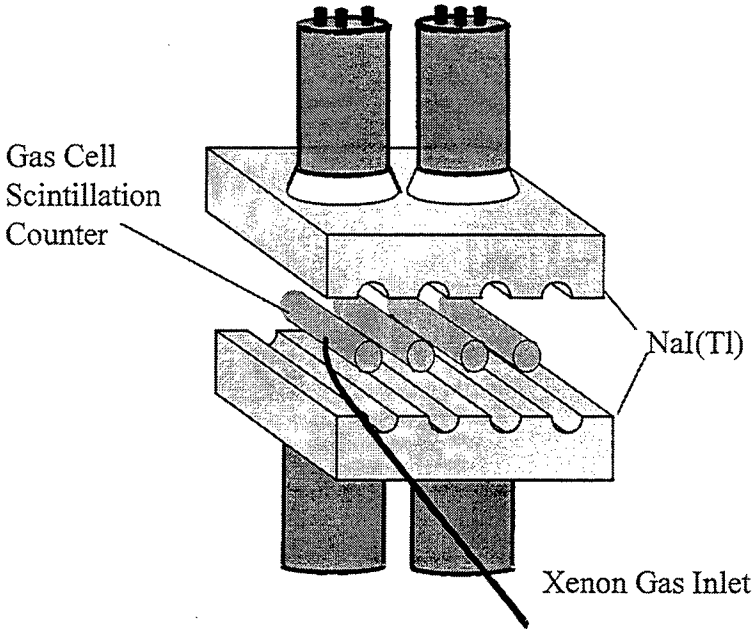

Figure 3. Exploded illustration of the beta-gamma coincidence spectrometer showing a typical xenon gas inlet, the NaI(Tl) crystal, and four gas cell scintillation conters (shown without phototubes for ease of viewing).

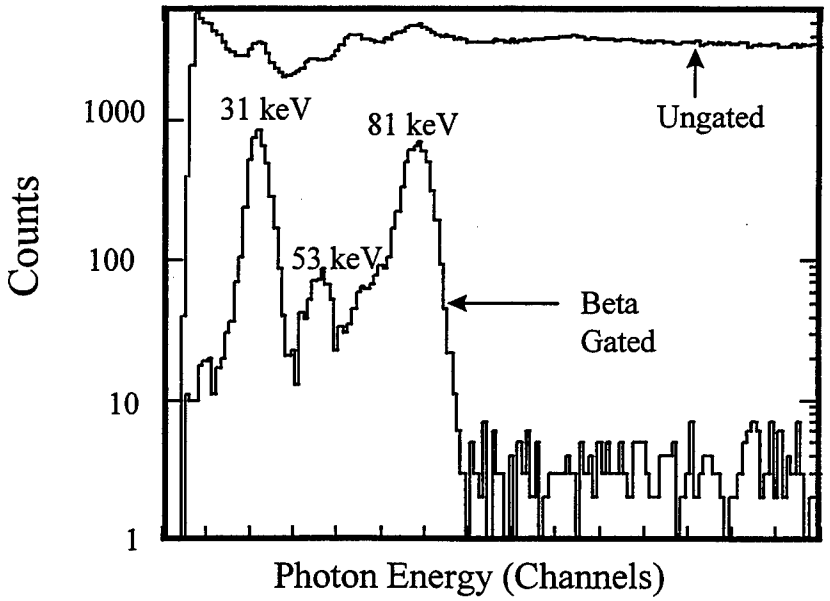

Figure 4. Gamma-ray spectrum of Xe-133 source taken with prototype NaI(Tl) detection system with and without beta gate.

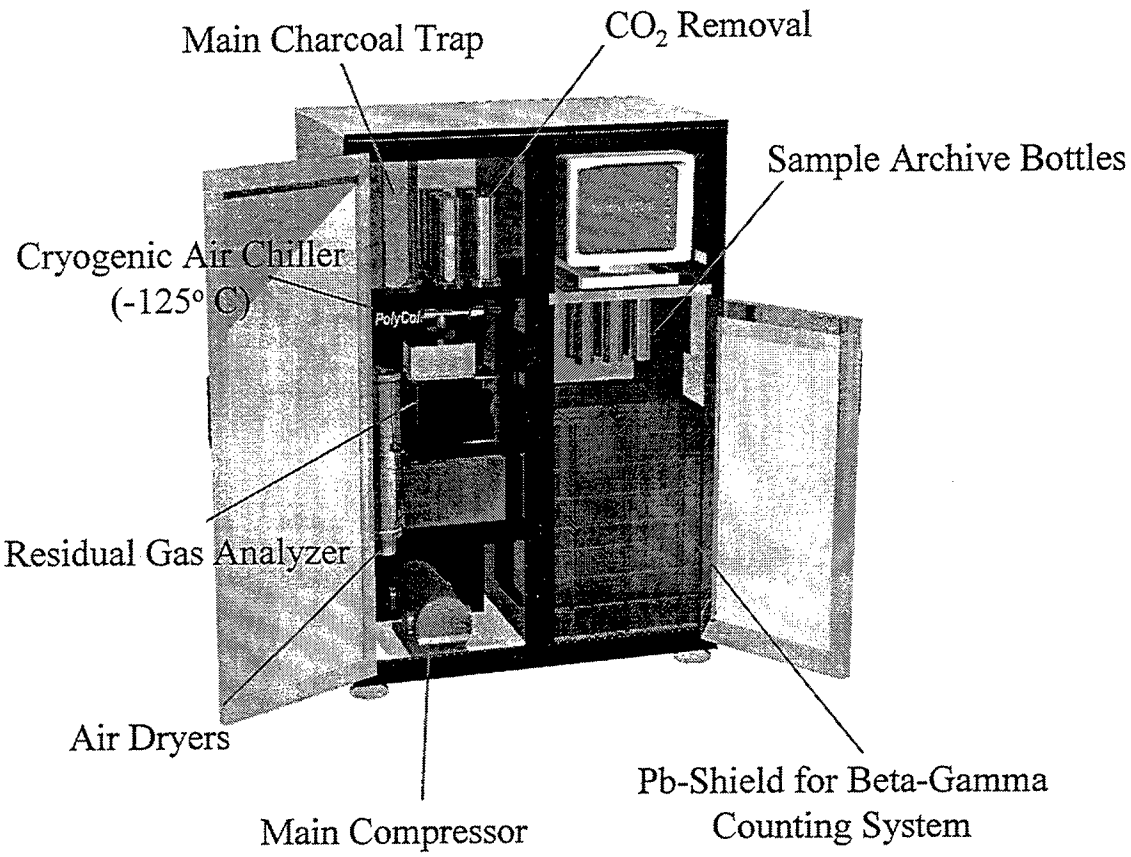

Figure 5. CAD drawing of Xenon Xephyr system.

IMS Hydroacoustic Network Site Selection and Performance

D. Clarke*, D. Harris*, T. Hauk*, E. McDonald**, G. Orris**, J. White*, R. Wong**

*Lawrence Livermore National Laboratory
**Naval Research Laboratory

*Sponsored by U. S. Dept. of Energy, Contract W-7405-ENG-48
Comprehensive Test Ban Treaty Research and Development Program, ST483B* & ST763**

ABSTRACT

The DoE has supported the formulation and defense of U. S. positions on ocean monitoring for the Comprehensive Test BanTreaty through research on suitable sensor sites, source characteristics of nuclear explosions underwater and in the low atmosphere, and expected performance of proposed networks. The work conducted by DoE-sponsored contractors had significant impact at negotiations in Paris and Geneva. DoE contractors contributed to site selection through detailed examination of local bathymetry at the sites, through sophisticated attenuation calculations that predict blockage, and to network selection by timely calculations of IMS hydroacoustic network location performance. DoE especially contributed an appreciation of the significance of hydrophone stations for detecting and locating explosions conducted above the water surface. Work on this issue is continuing at LLNL for explosion sites in shallow water (such as above continental shelves). Current work includes detailed placement of hydrophones at the four new IMS hydrophone sites (NRL), construction of more sophisticated models for predicting network performance and for generating travel time corrections for location algorithms (BBN, see Farrell et al., this volume), and on signal processing methods for associating hydroacoustic signals to events defined and located by seismic and infrasound networks (LLNL).

Key Words: Hydroacoustic monitoring, ocean monitoring

This work was performed (in part) under the auspices of the U. S. Department of Energy by the LLNL under Contract W-7405-ENG-48.

OBJECTIVE

DoE-sponsored hydroacoustic monitoring research this year has provided direct support for IMS hydroacoustic site selection, network performance evaluation, and source physics characterization. DoE's objective has been to support the formulation of U. S. proposals for the IMS network and to provide technical justification for those positions at negotiations in Geneva and Paris.

RESEARCH ACCOMPLISHED

Site Selection

Current Conference on Disarmament (CD) opinion favors a strategy of combining hydroacoustic, infrasound and seismic networks to provide detection, location and identification capabilities in the broad ocean areas. Each technology contributes where it has a particular advantage, complementing the others. The hydroacoustic component of the IMS network is focused on the Southern Hemisphere, where the lack of landmass results in relatively poor seismic network capability and presents some difficulty in finding suitable infrasound sites (see Figure 1). The hydroacoustic network is much more sparse than the seismic and infrasound networks. The sparsity of the network is due to the greater cost of deploying hydrophone systems and to highly favorable propagation conditions in the efficient acoustic waveguide (the SOFAR channel) present in much of the oceans.

Two types of hydroacoustic stations are proposed: hydrophone stations and T-phase (island seismic) stations. Hydrophone stations are much more sensitive than T-phase stations, but also far more costly. Consequently, hydrophone stations are placed in the Southern Hemisphere where distances between stations are largest and their greater sensitivity is used to best advantage. The island seismic stations are sited largely in the Northern Hemisphere to extend coverage northward. In all cases, station sites were chosen to avoid the cold water regions of the high latitudes, especially the area south of the Antarctic Convergence (Figure 1). Orris et al. [1995] pointed out that stations in sites with cold surface water temperatures would not observe near-surface explosions in warm-water regions well; path attenuation is severe because the SOFAR channel is replaced by a surface duct in cold water regions. Acoustic energy propagating there is confined close to the surface where interaction with the rough surface and/or ice causes significant signal loss.

Several principles guiding network geometry design were agreed in Geneva. To the extent possible, stations were arranged in triangles enclosing major ocean basin, because location by triangulation is accurate in the interior of networks. Wherever possible, sites were chosen to give wide-area coverage; the best sites (e.g. Cape Leeuwin, Australia) permit observation of two major ocean basins with a single hydrophone station. In special circumstances, sites were chosen to provide coverage in blockage-prone regions; areas such as the northwest Indian Ocean which has especially complex bathymetry.

LLNL and NRL examined more than two dozen candidate sites for local blockage; detailed bathymetry was examined on local maps, hydrophone positions were picked to avoid the more obvious bathymetric features, and a sophisticated long-range propagation model was used to esti-

mate coverage from the site. Figure 2 shows the (representative) analysis developed for the Diego Garcia site. A major blockage feature (the Chagos Bank) in the vicinity of Diego Garcia atoll forced the location of a hydrophone nearly 150 kilometers west of the island to provide coverage of the northwest Indian Ocean. The ray-trace and attenuation calculations performed by NRL clearly show the blockage effect of the Bank and the fact that two hydrophones positions selected for the site provide effective coverage of the Indian Ocean. NRL is now undertaking a more detailed optimization of hydrophone positions for the four new IMS hydrophone stations using more detailed bathymetry and three-dimensional propagation models.

Network Performance

After the acoustically and logistically suitable sites were enumerated, different combinations of sites were evaluated as candidate networks. One criterion used in Geneva was the location capability of the network. While the hydroacoustic network would be used in combination with the seismic or infrasound networks for location, the hydroacoustic-only location capability provides an estimate of the contribution offered by that IMS component to the complete solution. LLNL developed a simple model to estimate location error, using propagation along great circle paths and a perturbation approach (the Cramer-Rao bound) to map arrival-time errors into location errors. Two sources of error were assumed: a picking error that was small for hydrophone stations and larger for T-phase stations, and an error contributed by uncertainty in the sound velocity. The standard deviation of the error induced by velocity uncertainty was conservatively estimated to be 0.3% of the total travel time along any given path (an approach suggested by Geneva experts). Figure 3 shows an estimate of the location error for underwater explosions expressed as the area of the error ellipse (at 1 σ) for the full IMS network (including T-phase stations, and one primary seismic station, Tahiti, known to observe T phases). The network has acceptable performance in the wide ocean areas, but, due to blockage by continents, generally poor performance around land masses. The weakness of the hydroacoustic network are offset by the high density of ship traffic in coastal waters, and the proximity of these waters to land-based seismic and infrasound stations.

The T phase stations were incorporated in the IMS hydroacoustic network as a low-cost alternative to hydrophone stations (seismic stations may cost up to 10 times less than a fixed-cable hydrophone station). Experience with some T phase stations (Tahiti, Raratonga) suggests that good ones are capable of observing small, well-coupled explosions. The relative sensitivity of T phase and hydrophone stations is unknown, but it is expected that average T phase stations may be up to 100 times less sensitive. One way of testing this hypothesis is to compare observations of undersea earthquake made at adjacent island seismic and hydrophone stations. There are few experimental sites with such adjacent sensors; Ascension Island and San Nicolas Island are two. LLNL has begun comparing data from these two sites; a representative data sample is shown in Figure 4 for a magnitude 4.3 ridge earthquake observed by the Ascension sensors at a range of 5700 kilometers. The hydrophones clearly record the T phases, but the seismometers on the island do not. Other, closer earthquake T phases have been observed by Ascension seismometers [Holly Given, personal communication], suggesting either a detection threshold with an azimuthal dependence or that this event is just below the detection threshold.

The sensitivity of T phase stations is a concern for observing explosions conducted above the

water surface. It is well known empirically and from sophisticated coupling calculations [1995, Clarke et al.; 1995, Clarke] that hydroacoustic signals should be about 1000 times smaller for a 1 kiloton explosion conducted 30 meters above the ocean surface than for a similar explosion conducted at the SOFAR axis depth. An explosion decoupled in this manner would still produce a signal detectable by hydrophones, but not necessary by island seismic stations. Figure 5 displays the loss of location coverage in the Southern Hemisphere caused by the failure of the island seismic stations to observe events. Due to the sparsity of hydrophone stations in the Pacific, the capability of the network is minimal in the South Pacific.

Signal Processing

Explosions above the ocean surface are expected to be observed by infrasound and hydrophone stations, but may not be located well by infrasound stations alone. Infrasound stations, which are arrays, are anticipated to provide good direction estimates, but not good arrival time estimates. If hydrophone observations can be associated to the infrasound-defined events, the hydroacoustic arrival times will provide accurate constraints on event locations. At the low signal levels anticipated for explosions in the low atmosphere, the background of transient hydroacoustic signals may complicate association. Some ability to screen background signals may simplify automatic processing. Direction estimation using two hydrophones may provide the necessary screening capability. Figure 6 shows about 20 minutes of data recorded at the Ascension hydrophones in which acoustic signals from several events are intermixed, complicating association. In this case, it is possible to estimate the direction of the various incoming acoustic waves using simple incoherent processing to measure relative arrival times. The envelopes of waveforms from two hydrophones are shifted to align expected signals arriving from two different (seismically defined) event locations. The coincidence of the envelopes identifies which signals associate with each of the two events. Work is underway to estimate the reliability of such direction estimates.

CONCLUSIONS AND RECOMMENDATIONS

Detailed modelling for hydrophone placement at each of the four new IMS hydroacoustic stations needs to be completed and is being undertaken by NRL. More sophisticated long-range model development for network performance projection and construction of knowledge base components (e.g. travel-time calibrations) is needed and being undertaken by BBN (see Farrell et al., this volume). Source coupling and hydroacoustic signatures in shallow water conditions must be developed and are being undertaken by LLNL.

References

Clarke, D. B., J. W. White, D. B. Harris (1995) , "Hydroacoustic Coupling Calculations for Underwater and Near-Surface Explosions," UCRL-ID-122098, LLNL, Sept. 1995.

Clarke, D. B. (1995), "Pressure Time Histories Derived from Hydroacoustic Coupling Calculations: The Transition to Long Range Linear Acoustics," UCRL-ID-122595, LLNL, Dec. 1995.

Orris, G. and B.E. McDonald (1994), "Modeling Hydro-Acoustic Comprehensive Test-Ban Treaty Monitoring Networks," 17th Seism. Res. Symp. on Monitoring a CTBT, Scottsdale, AZ. PL-TR-95-2108, ADA 310037.

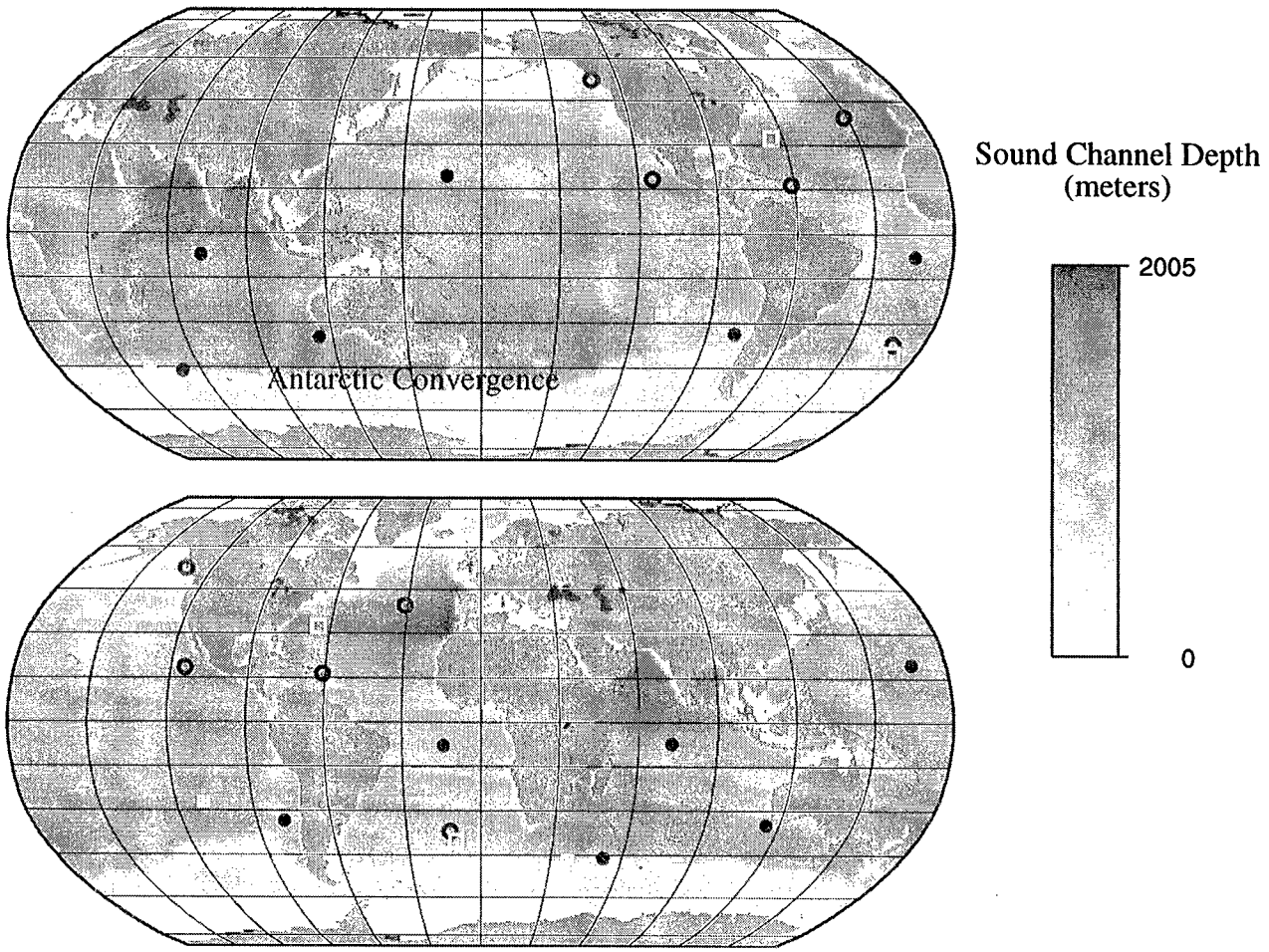

Figure 1 Stations in the IMS hydroacoustic network were placed in sites which avoided low surface water temperatures, especially waters south of the Antarctic Convergence. This design criterion assures good propagation characteristics, since relatively warm surface temperatures lead to a well-developed waveguide for underwater sound (the SOFAR channel). The map shows the depth to the axis of the SOFAR channel; shades approaching white indicate a shallow axis (cold surface temperatures), and relatively poor propagation. Hydrophone stations are indicated with solid symbols and T-phase (island seismic) stations with open symbols. The round symbols are the IMS stations and the square symbols are alternates.

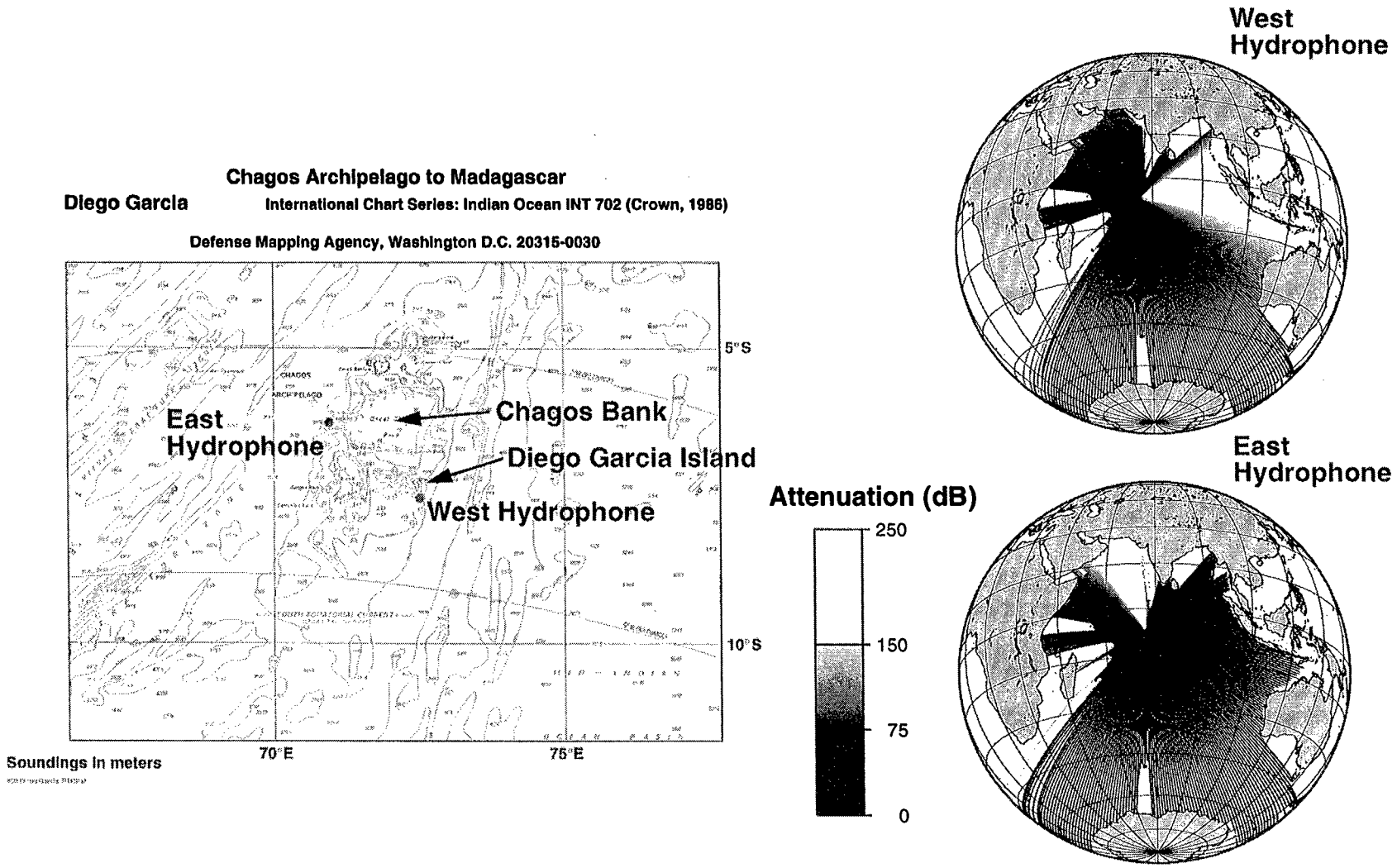

Figure 2 Site selection entailed an examination of local bathymetry for features that could block propagation. For example, Diego Garcia Island is located on the flank of the Chagos Bank, a major shallow feature that effectively blocks propagation. Hydrophone positions were picked on either side of the Bank to avoid the worst blockage effects. The NRL acoustics branch ran calculations of attenuation from each of the sites (shown to the right) to verify that the configuration provided good coverage of the north Indian Ocean. More sophisticated three-dimensional modelling of propagation using higher resolution bathymetry is now underway to optimize the placement of the hydrophones.

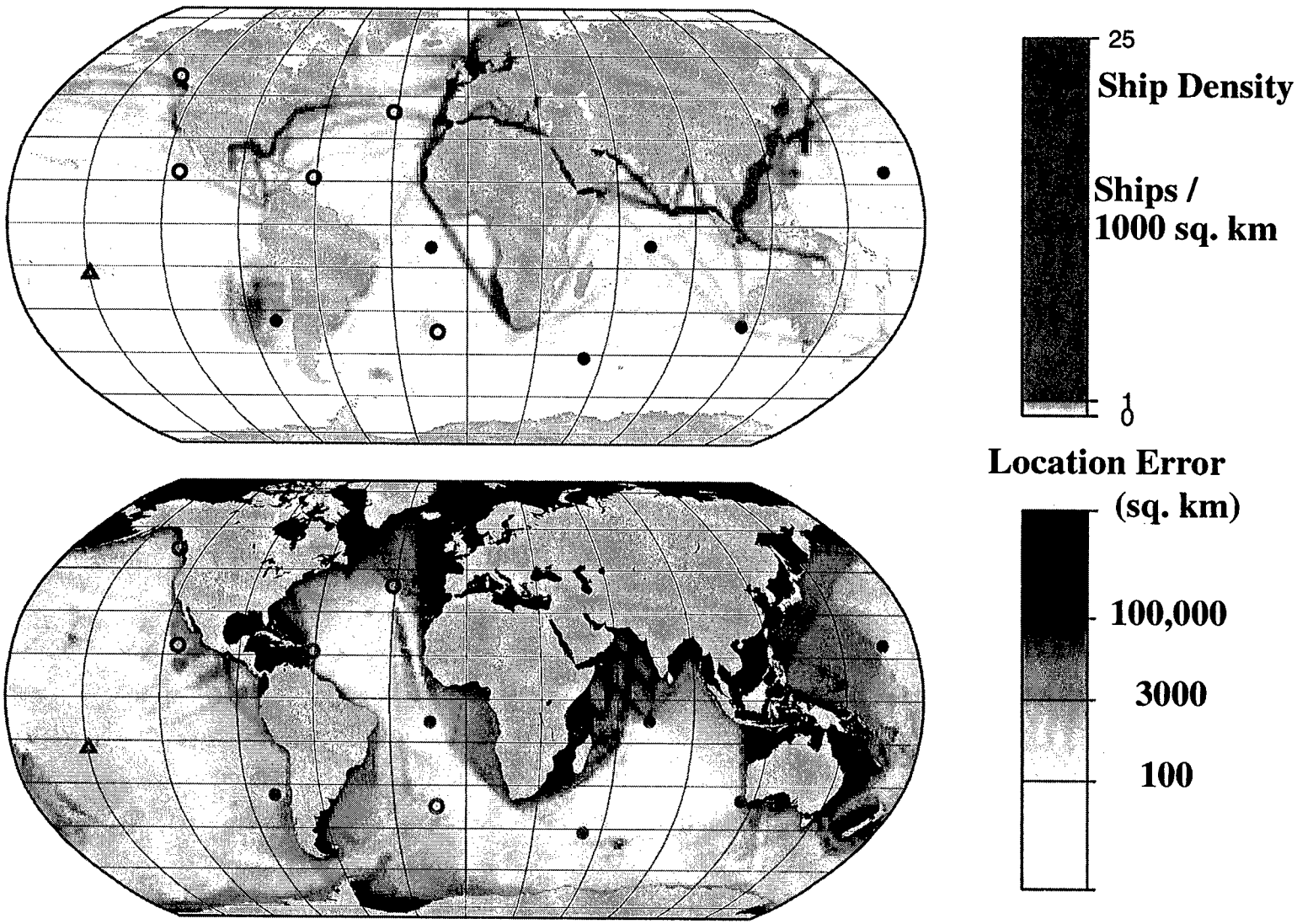

Figure 3 IMS Hydroacoustic location coverage is good in the wide ocean areas for underwater explosions. Poor coverage in areas surrounding the continents is largely offset by high ship density in coastal waters. Hydrophone stations are indicated with solid symbols, T-phase (island seismic) stations with open symbols.

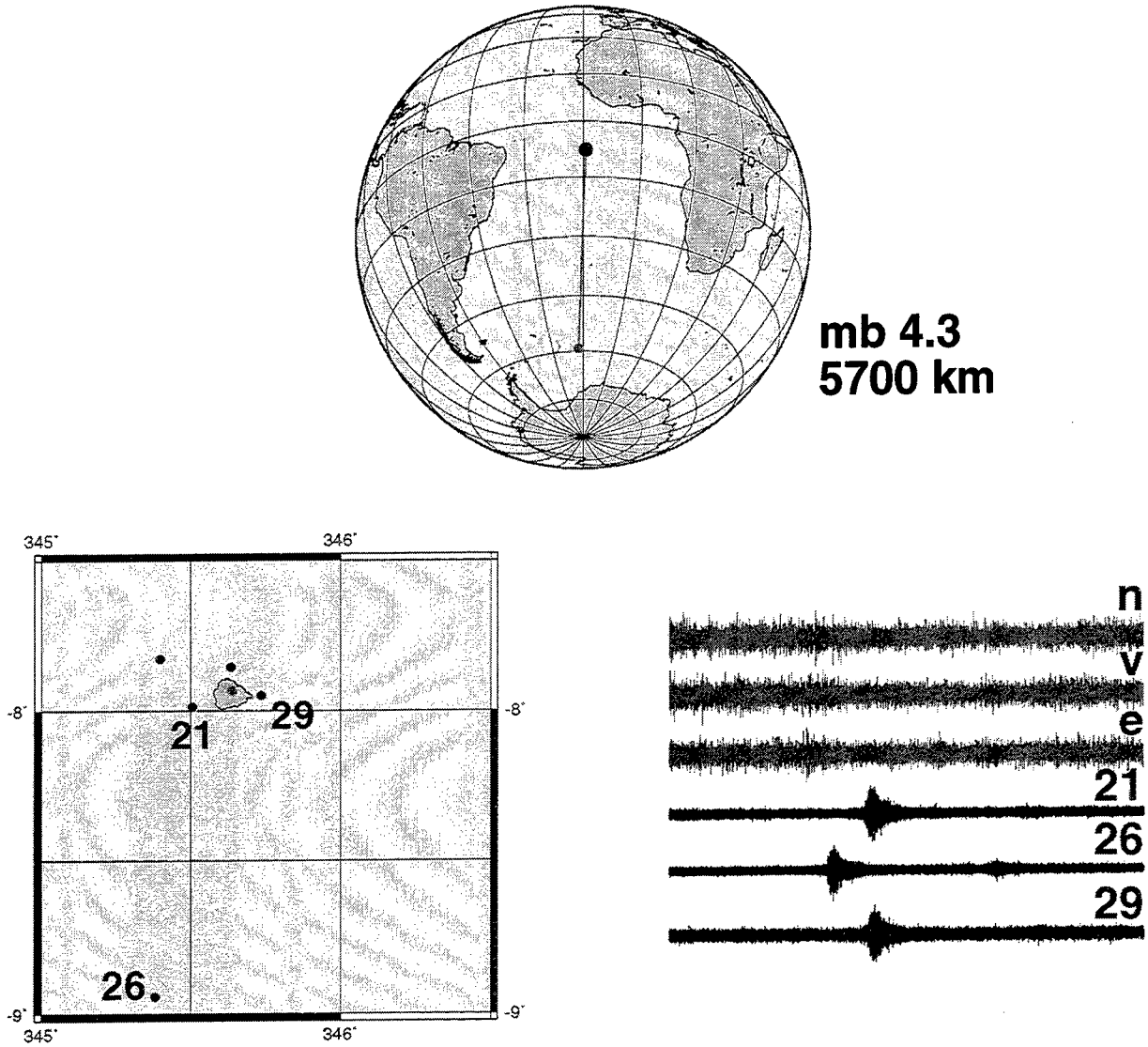

Figure 4 Island seismic (T-phase) stations appear to be less sensitive than hydrophones for detecting waterborne acoustic waves. This figure contrasts waveforms from the IRIS station ASCN (top three traces) with those from three MILS hydrophones (bottom three traces) for a magnitude 4.3 undersea ridge earthquake in the South Atlantic at a range of 5700 kilometers. Even when filtered into a band favorable for observation of the T-phase (5-20 Hz), the seismic data show no signal. The lack of sensitivity may pose no problem for detecting and locating underwater explosions, but may limit the usefulness of island seismic stations for observing explosions above the water surface.

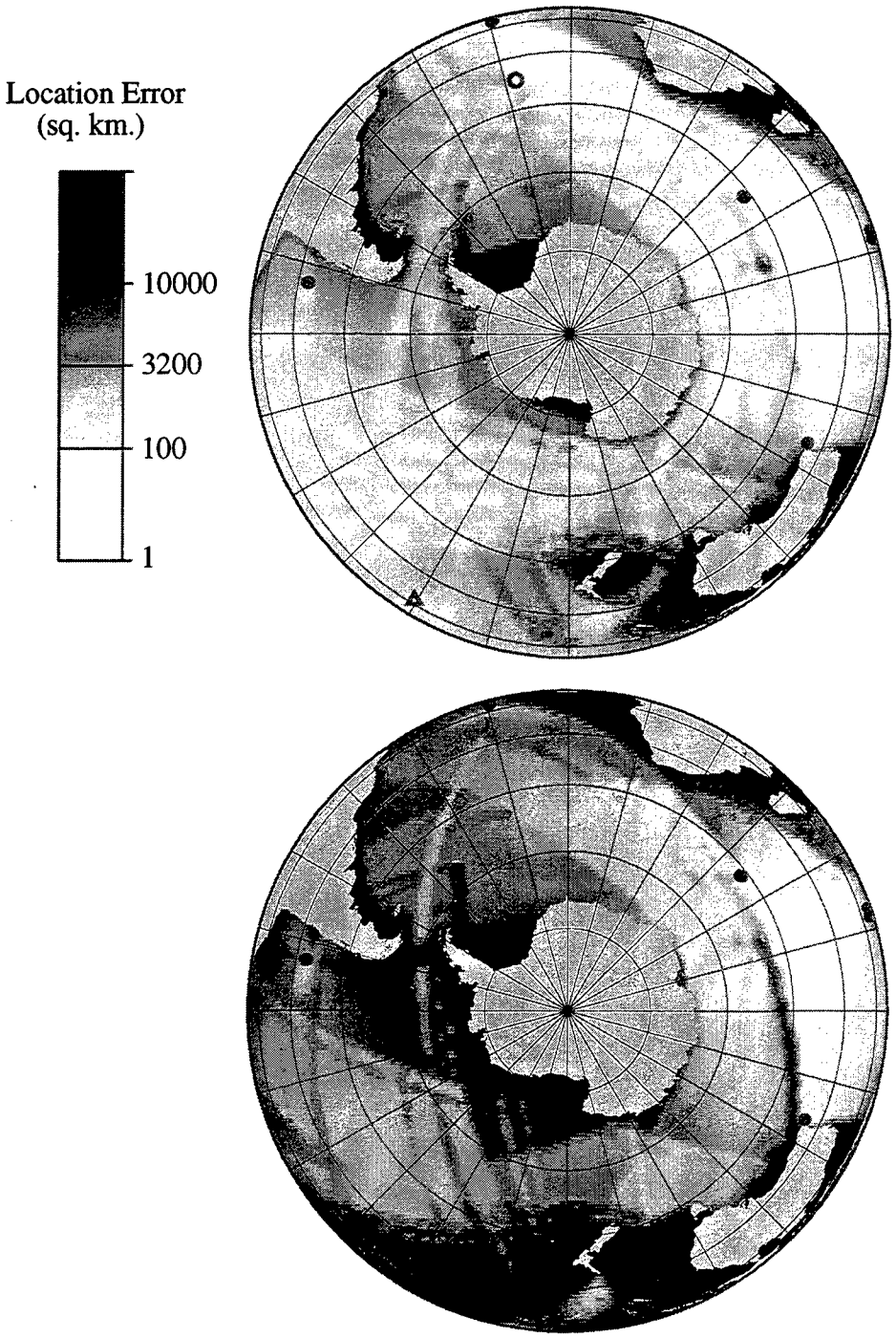

Figure 5 IMS location coverage with (above) and without (below) the island seismic stations, estimating location capability for underwater explosions and explosions in the low atmosphere, respectively. The conservative .3% rule (see text) has been used to estimate the area of uncertainty of location algorithms. The south Pacific is not as well covered by the hydrophone stations as are other oceans.

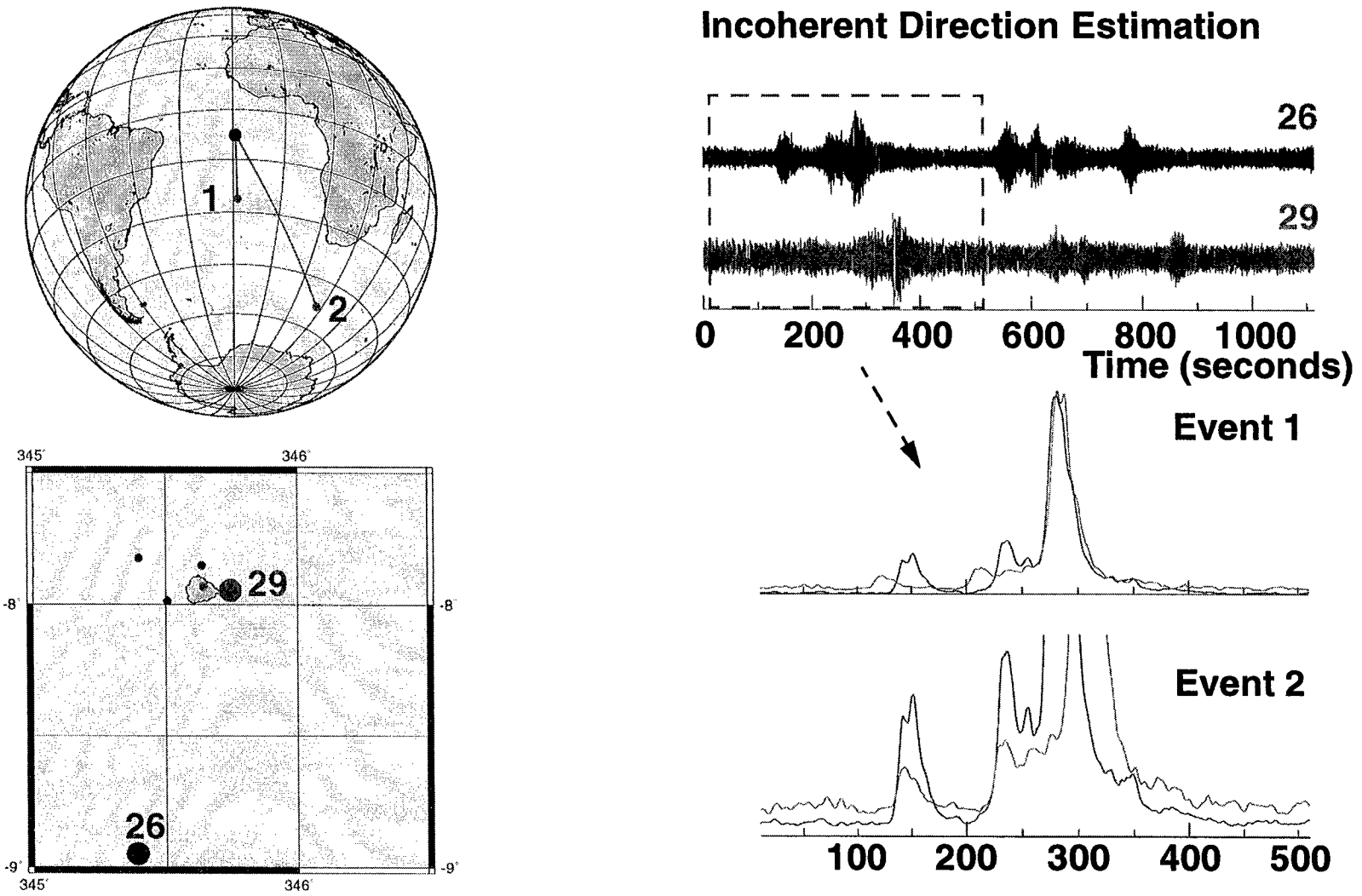

Figure 6 Direction estimation using two hydrophones at the same site may assist hydroacoustic signal association with events built and located from seismic and infrasound observations. Four of the six hydrophone stations in the IMS network have at least two hydrophones, emplaced to prevent nearby islands from blocking the acoustic "field of view." Relative arrival times of signals at the two sensors can be used to estimate direction, which can help sort out nearly-overlapping signals. This figure shows signals recorded at two hydrophones from events at different directions. The envelopes of the signals are shifted to show alignment expected for the two source locations, a simple form of incoherent direction estimation that associates signals to their sources.

Observations of T phase Arrivals from North Pacific Events

Catherine D. deGroot-Hedlin & John A. Orcutt
IGPP, Scripps Institution of Oceanography, University of California, San Diego

Sponsored by the Department of Energy

F19628-95-K-0011

ABSTRACT

We have assembled a large suite of T-phase observations recorded at Point Sur, in an attempt to understand how acoustic energy from underwater earthquakes is coupled to the sound channel and how the sound propagates from source to receiver. We show results for a wide range of event locations in the North Pacific. We find that T-phases observable at Point Sur are generated only in a limited number of geographical regions, the Aleutian Islands and Kodiak Island regions, south of Japan, and the southern portion of the Kuril Islands region. A signal to noise (SNR) measure was determined for each event. We found that there were no clear patterns in the SNR when all the events were examined together. We narrowed the region of study to a small cluster of events in the Andreof Island region of the Aleutian Island chain in order to eliminate variables such as source mechanism, transmission path, and event depth. For this limited data set, we found that the SNR was more strongly dependent upon event magnitude, however, there was still a considerable degree of scatter. We suggest that this scatter is due to near source effects, such as the slope of the seafloor in the region of the events.

keywords: hydroacoustic propagation, T-phases, energy coupling, suboceanic earthquakes

OBJECTIVE

The objective of out research is to analyze hydroacoustic signals from oceanic earthquakes recorded by hydrophones and hydrophone arrays, in order to understand the coupling of energy to the SOFAR channel and the propagation of acoustic energy from source to receiver. The generation of detectable hydroacoustic phases for any underwater event depends on a complicated combinaton of source effects, such as event magnitude and depth and source mechanism; near-source effects, such as the slope and depth of the land/ocean boundary near the source; and path effects, i.e. whether the event lies within a shadow zone for a particular receiver, and source to receiver distance. In order to successfully discriminate oceanic nuclear tests from submarine earthquakes, it is important to distinguish between source signatures and propagation effects. Both the sound speed within the waveguide and seafloor bathymetry, which limits the depth of the waveguide, strongly affect T-phase energy recorded on hydrophones. We plan to integrate theoretical predications of propagation effects with observed acoustic arrivals. Goals include

(a) determining the physical mechanisms by which acoustic energy from sources with varying depths is coupled into the sound channel,

(b) determining the effects of variations in bathymetry and temperature profiles along the travel path on the received signals, and

(c) comparing synthetic responses to data to see if source signatures of various T-phase arrivals can be accurately modelled.

This last step includes the assembly of a suite of hydroacoustic array data from a large number of underwater seismic events, in order to obtain optimal azimuthal coverage from source to receiver, as well as a wide range of source depths and source parameters. In this paper we examine a suite of hydroacoustic data from the North Pacific as recorded by a hydrophone located near Point Sur.

RESEARCH ACCOMPLISHED

We assembled a suite of 96 recordings at Point Sur for events in the North Pacific. The recording were obtained from the Center for Monitoring Research (CMR) for an 8-10 minute band about each expected T-phase arrival. Event parameters were obtained from the near-real-time Earthquake Bulletin, provided by the National Earthquake Information Service (NEIS). In order to quantify signal strength, a signal-to-noise ratio (SNR) measure was determined for each recording as follows. Each trace was de-meaned and filtered to 0.1 - 0.5 Hz since most of the T-phases are observable only at the lowest frequencies. For this filtered trace, the signal variance was determined over each 30 second band, with steps of 2 seconds between bands. The square root of the maximum variance divided by the minimum variance is taken as the signal to noise ratio. In general, signals were observable for events with calculated SNRs of greater than about 1.6. An example of the calculation of the SNR is shown in figure 1.

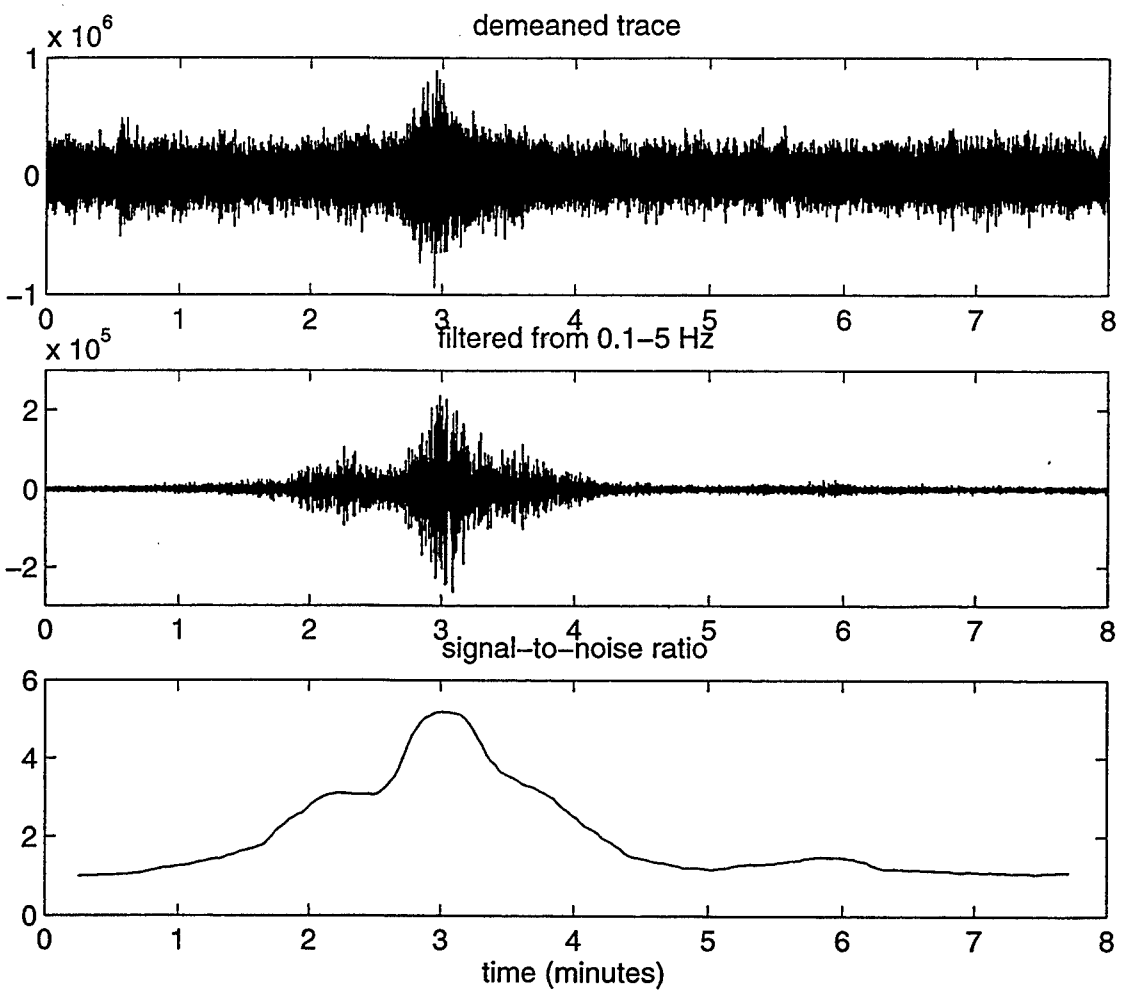

Figure 1. The method of calculation of the SNR is shown here. The de-meaned trace for the Aleution Island event of April 21, 1996 is shown in the top panel. The trace was filtered to 0.1 to 5 Hz, shown in the center panel. The SNR as a function of time is shown in the bottom panel. The method of calculation of the SNR is outlined in the text. The signal to noise ratio for this event was determined to be 5.1.

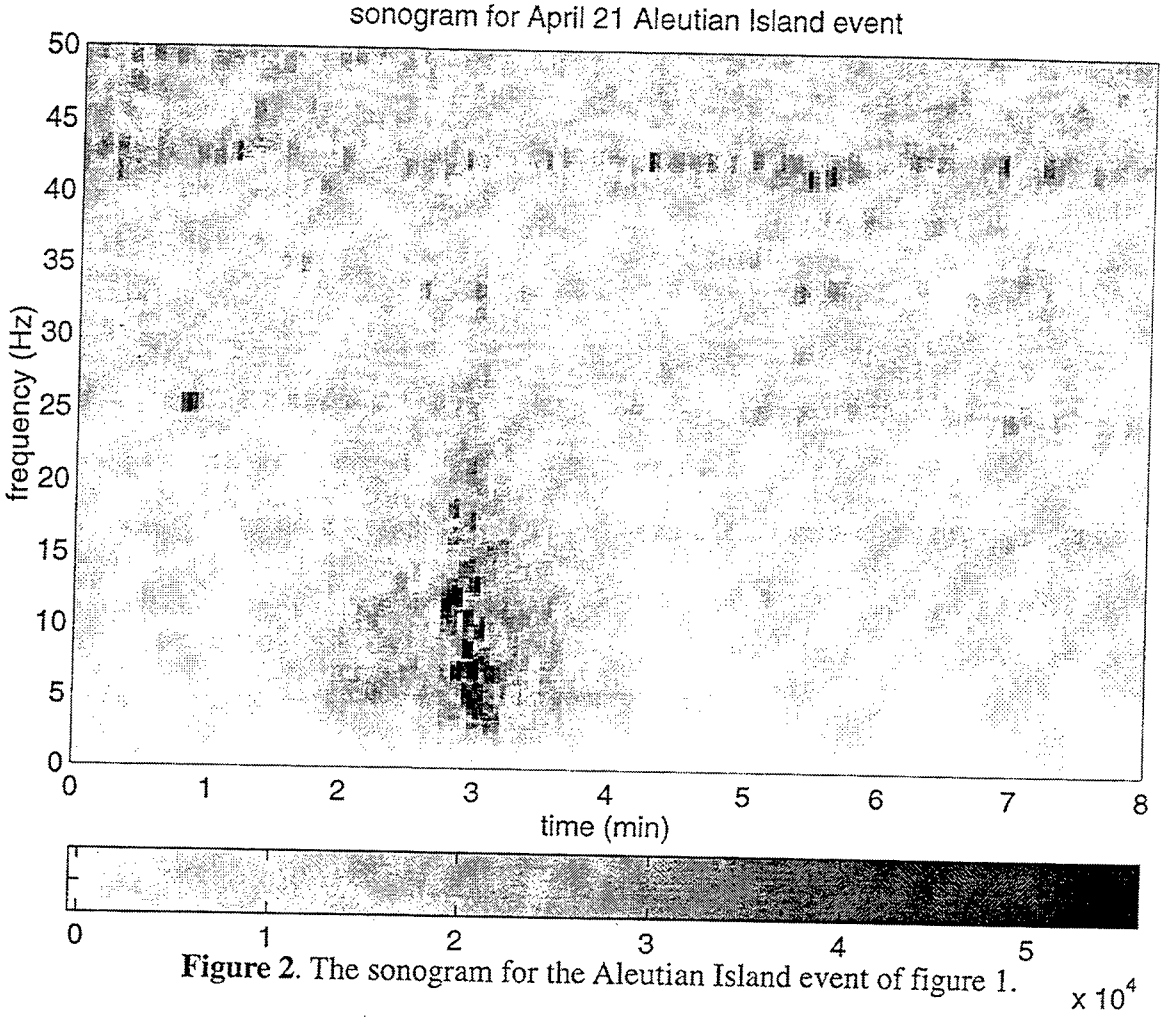

Figure 2. The sonogram for the Aleutian Island event of figure 1.

Figure 2 shows a sonogram for the trace shown in the top panel of figure 1. The sonogram confirms that the signal is most clearly observable at the lowest frequencies. At higher frequencies the signal s drowned out by the higher noise levels. For the larger SNR events, such as this one, T-phases are observable at frequencies up to 25-30 Hz.

The SNR ratios were calculated for each event within the suite and are shown as a function of geographic location below. The spatial patterns in the SNR indicates that T-phases observable at the Pt Sur hydrophone are generated in a limited number of geographical regions, the Aleutian Islands and Kodiak Island regions, south of Japan, and the southern portion of the Kuril Islands region.

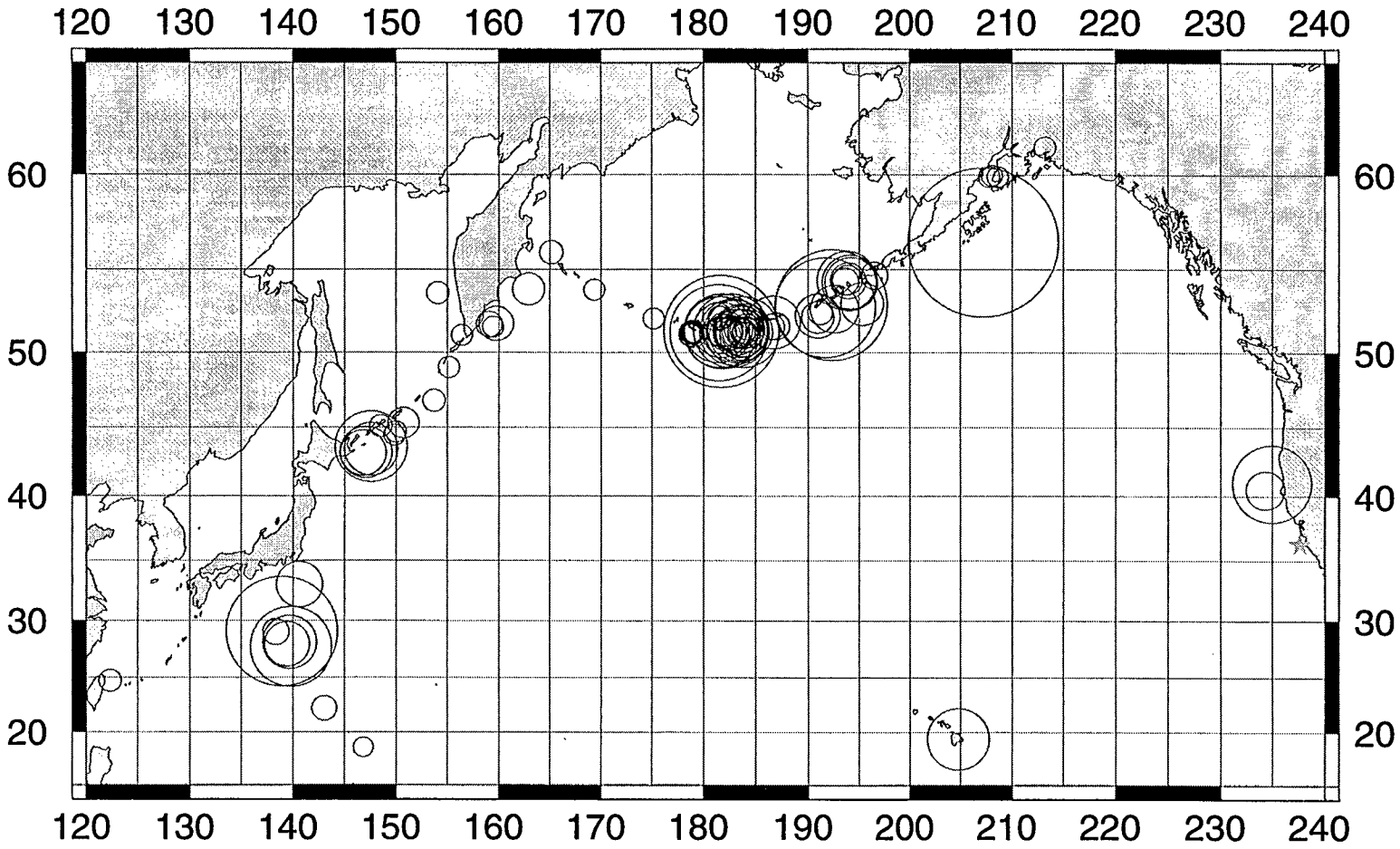

Figure 3. The signal-to-noise ratios (SNR) for T-phases of 96 North Pacific events as recorded at the Pt. Sur hydrophone. All events of the North Pacific that have been examined are shown here, including a number of events for which no signal was observable. The symbol size is proportional to the SNR, which varies from 1 (no signal) to 8 (large signal).

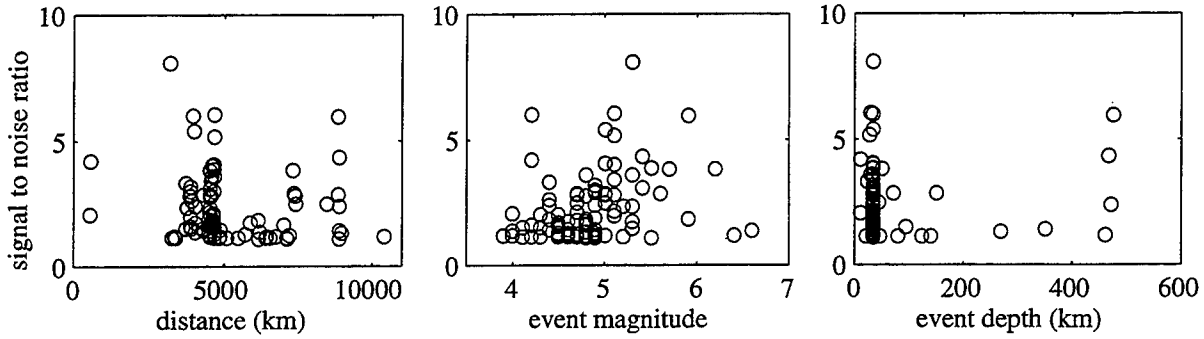

Figure 4. SNR as a function of distance, event magnitude, and event depth.

In figure 4, we show the SNRs as a function of each of distance, event magnitude, and event depth. No clear patterns are evident in any of these plots. The biggest surprise is in the plot of SNR vs event depth, in that one would not expect ANY T-phases to be observable for deep events. Instead, at least three events generate observable T-phases, all in the region south of Japan.

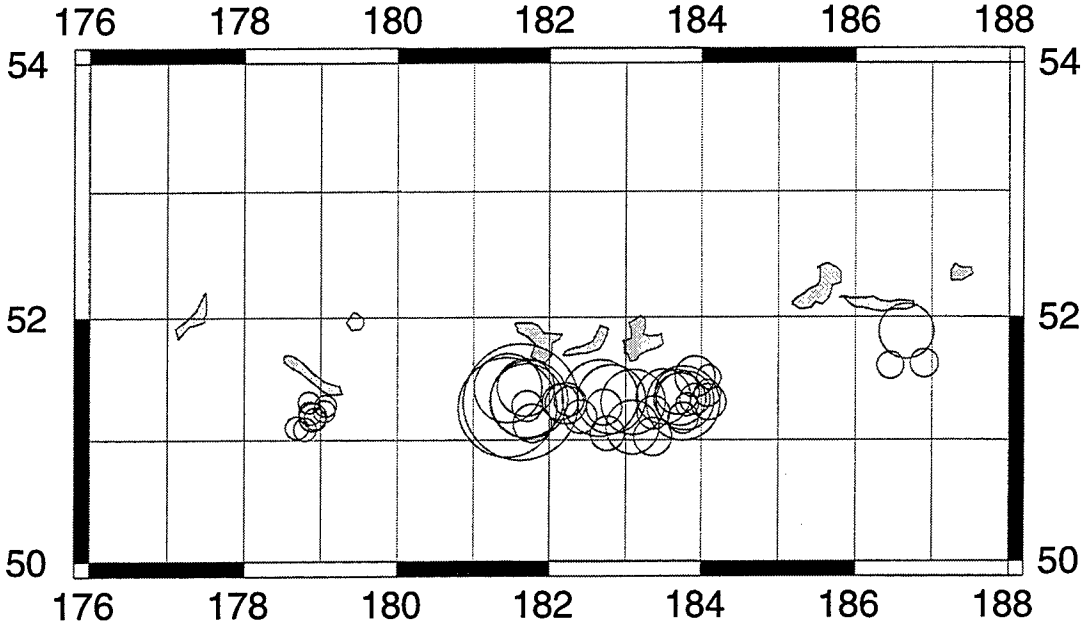

Figure 5. SNRs for the Andreof Island events.

In order to make more sense of the data, we confined our attention to a cluster of events in the Andreof Island region, within the Aleutian Island chain. The SNRs for 43 events to the south of the Aleutian Islands are shown in figure 5 (events to the north of the Islands and thus in the shadow zone were not included). All but one of the events has a given depth between 28 and 33 km. Source mechanisms for all these effects should be the same, ie due to the subduction of the Pacific plate at the Aleutian trench. Thus we have eliminated complications due to path effects, souce mechanism, and event depth. Even at this small scale, a spatial pattern is evident in the SNRs. The events furthest to the east do not generate T-phases that are detectable at Point Sur.

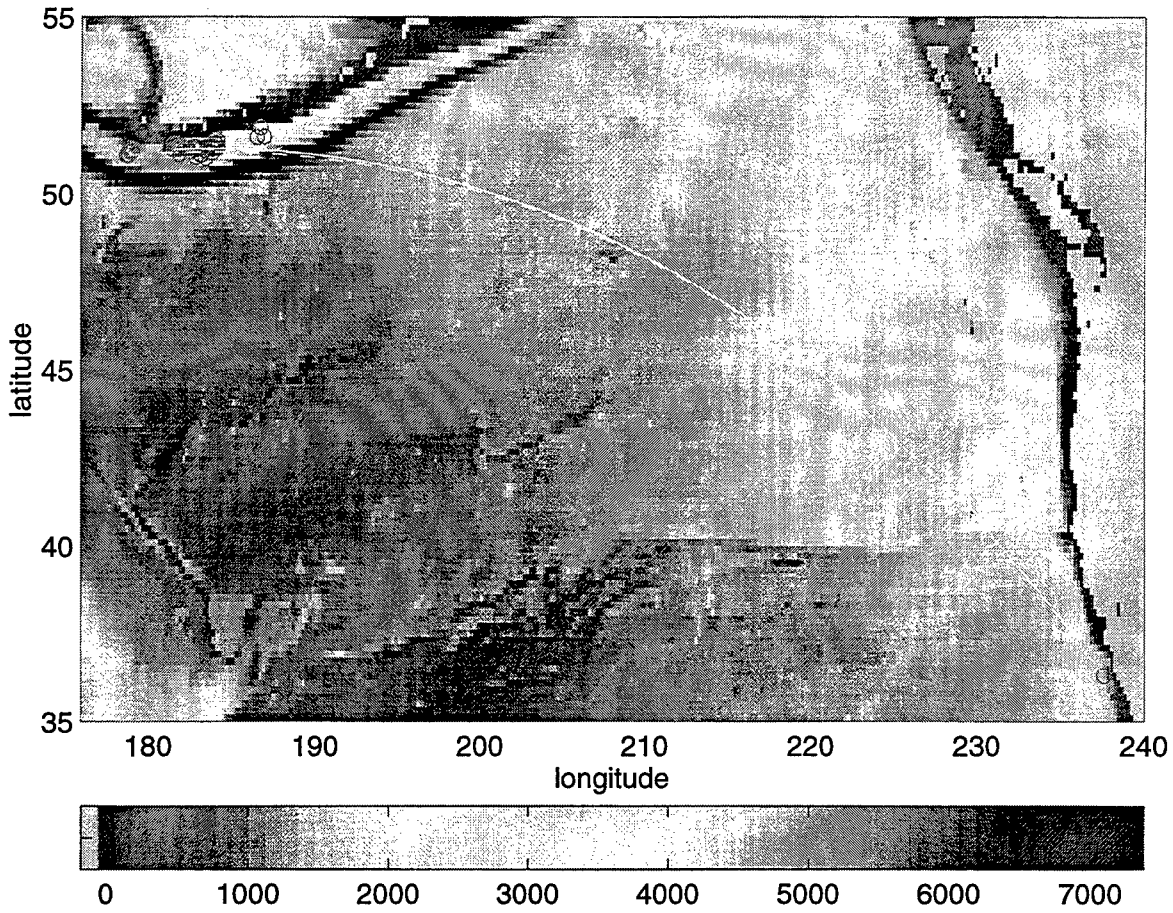

Figure 6. Depth map of the Northeast Pacific showing Andreof Island event locations.

A depth map of the Northeast Pacific showing Andreof Island event locations and geodesic paths for two events is shown in figure 6. Note that all travel paths follow virtually the same trajectory. The solid path is for a magnitude 5.1 event, with SNR of 5.1 at the receiver. The dotted path is for a 5.0 event slightly further to the east with an SNR of 1.4 at the receiver, ie the signal was not observable. In this case the differences in seismic source to T-phase coupling must be due to near-source effects.

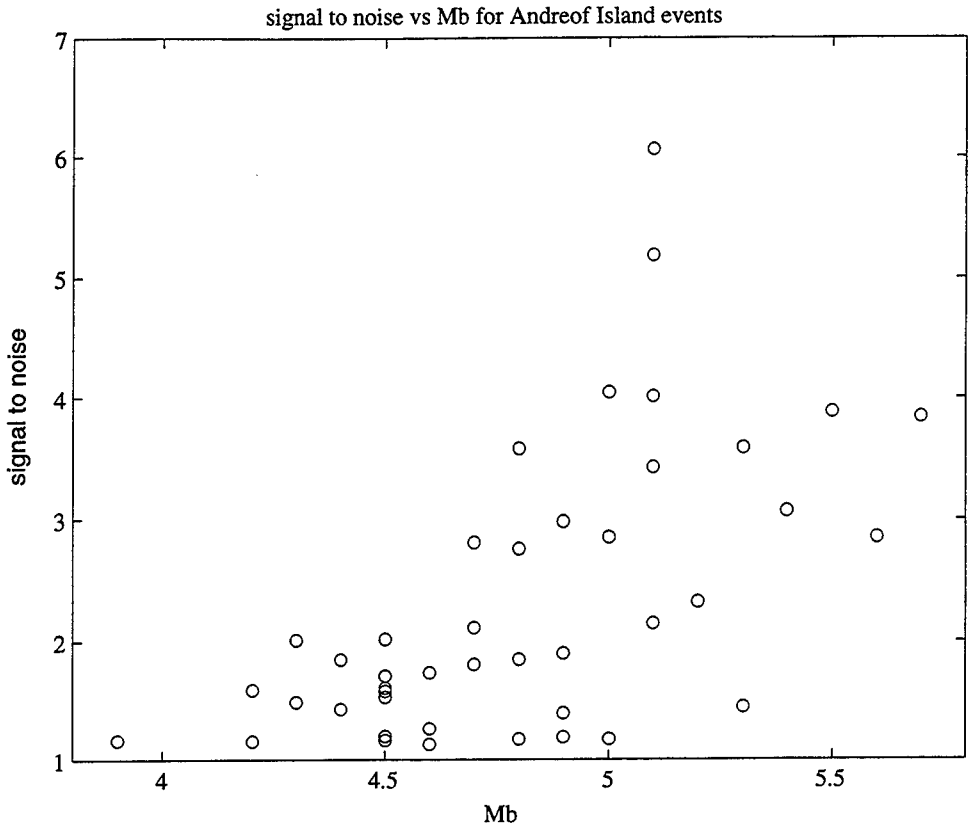

Figure 7 SNR vs magnitude for the Andreof Island events.

A plot of SNR vs magnitude for the Andreof Island events is shown in figure 7. This plot indicates that larger T-phases are generated by larger events, as expected. However, there is still considerable scatter, possibly due to near-source effects, as mentioned above.

CONCLUSIONS AND RECOMMENDATIONS

Examination of a widely distributed set of suboceanic events indicates that T-phases are observable at Point Sur for only a limited number of geographical regions. When all these events are examined together, signal strength is cannot be determined simply on the basis of event magnitude, depth, or source-receiver distance. Conversion of seismic energy into acoustic energy transmitted in the ocean waveguide is highly complicated, depending on source effects, near-source effects, and path effects. In order to isolate the effects of event magnitude and near-source bathymetry, we narrowed the study to a cluster of 43 events in the Andreof Island region. We found that the T-phase signal strength was more strongly dependent upon event magnitude. However, the scatter within the SNR/event magnitude relation is attributed to near-source bathymetry. More observations are necessary to confirm the conclusions made here. Data from the Wake Island hydrophone is available and will be examined. However, accessible hydrophone coverage is poor since each hydrophone is sensitive only to events within limited regions, and should be improved. Future plans include modelling the coupling of sub-seafloor events to the oceanic column given realistic topographies and ocean temperatures, in order to determine the importance of near-source effects in the generation of T-phases. The importance of refraction of acoustic energy due to lateral variations in bathymetry will be determined.

Development of the Hydroacoustic Coverage Assessment Model (HydroCAM)

Ted Farrell, Kevin LePage and Greg Duckworth
BBN Systems and Technologies

Contract No. F19628-95-C-0174

Sponsored by the Department of Energy

ABSTRACT

A model for predicting the detection and localization performance of hydroacoustic test-ban monitoring networks has been developed. The model accounts for major factors affecting global-scale acoustic propagation in the ocean, such as horizontal refraction from bathymetric features and horizontal changes in sound speed, travel time variability due to spatial and temporal fluctuations in the ocean, and detailed characteristics of the source. Graphical user interfaces are provided to setup the models and visualize the results. The model produces maps of network detection coverage and localization area of uncertainty, as well as intermediate results such as predicted path amplitudes, travel time and travel time variance. Although much of the software is recently developed C++ code, a large body of existing models and databases developed by the US Navy, NOAA, DOE and other institutions have been integrated. The result is a flexible system with the ability to produce quick results, using simple geometric propagation models and low-resolution oceanographic databases, as well as the ability to produce results using research grade propagation models and high-resolution databases. Travel time predictions from the model have been favorably compared to measured data. The model is currently being exercised to resolve issues necessary for the future development of the hydroacoustic knowledge base. This paper describes the capabilities of the model and outlines some of the design tradeoffs made during the development.

Keywords: CTBT, hydroacoustics, network, localization, oceanography, performance prediction

OBJECTIVE

The primary technical issues for hydroacoustics are derived from the need to provide discrimination and improved location estimates. Both of these functions rely on the ability to detect events of interest. In general, the high source levels from nuclear tests and the efficiency of acoustic propagation in the SOFAR channel should result in excellent detection performance. In addition, the channel sound speed in many areas is relatively constant so that energy in the channel travels along stable geometric paths, resulting in predictable travel time and localization performance. However, recent experiments using acoustics to monitor the temperature of the oceans has shown that rays following great circle paths are inadequate to describe the signal structure for propagation between sources and receivers half a world apart. Additional challenges occur at shorter ranges when the channel is partially or completely blocked by bathymetric features, when energy is horizontally refracted as it traverses into colder Antarctic waters, when the continuously changing temperature and salinity structure of the ocean is accounted for, or when atmospheric sources do not fully couple their energy into the SOFAR channel. For a sparse global network where information from each sensor is critical to the performance of the network (like the currently proposed International Monitoring System, IMS) an accurate prediction of the detection and localization coverage needs to account for these effects. When the IMS becomes operational, processing and interpretation of hydroacoustic data will require a knowledge database that contains accurate ocean characteristics, travel times, path amplitudes and ultimately spectral characteristics of received waveforms. The goal of this effort is to leverage the large investment in oceanographic databases and models, made in the past by the US Navy and others, to develop a tool capable of addressing these technical issues.

The specific goals for this year were:

1. To develop the initial version of a comprehensive model for evaluation of the ability of underwater sensors to detect and localize the detonation of nuclear devices in or above the ocean.

2. To validate this model by comparing its predictions with measured data.

3. To apply the model to demonstration problems of operational interest.

The user community for this product is expected to include PL/GPE, DOE, and AFTAC, as well as researchers at the national laboratories and universities. In the remainder of this paper, we describe the capabilities of the current model, outline studies that have been undertaken using the model, and present recommendations for additional research.

RESEARCH ACCOMPLISHED

HydroCAM is a hydroacoustic network performance prediction program that runs on Unix workstations. It contains an assortment of oceanographic databases, acoustic propagation models, network performance models, and software for visualizing and interpreting results at each stage in the prediction process. Because we took advantage of the best existing models and databases, the components of HydroCAM are in a variety of data formats and software languages, from FORTRAN-77 to C++. The user interface makes all of this transparent, and provides a capability to perform these functions:

- Access, analyze, and display a variety of oceanographic databases.
- Create geographic databases containing acoustic modes and waveguide parameters.
- Predict global-scale acoustic propagation paths and their characteristics.
- Assess network detection coverage and localization performance.
- Include spatial and temporal signal processing characteristics of receiver systems.
- Predict source effects on acoustic signals received at long ranges.

The following sections describe the functionality in each of these areas.

Using Environmental Databases

Compared to the crust and mantle of the earth, characteristics of the worlds oceans are well known. In a sense, the US Navy, NOAA, and other oceanographic institutions have solved the "regionalization" problem for the worlds oceans. Oceanographic databases are available at a variety of temporal and spatial resolutions, from raw data to analyzed statistics, all in a variety of formats. The critical element is the ability to rapidly access, visualize, analyze and incorporate this data into propagation and network performance models. The databases included in HydroCAM are listed in Table 1. They contain information on environmental factors affecting low frequency ambient noise (shipping densities), high frequency ambient noise (ocean surface wind speed and rainfall), and acoustic propagation (sound speed profiles, bathymetry and sediment characteristics).

Database Name	Database Description	Temporal Resolution	Spatial Resolution (min)
ETOPO5	Bathymetry	N/A	5
GDEM	Sound speed profiles	Seasonal	30
WOA94	Temperature and Salinity	Monthly	30 and 300
HWS	Historical Wind Speed	Monthly	60
HITS	Historical Temporal Shipping	Monthly	Variable
GDS	Global Daily Summary (Temp/Precip)	Daily	Variable

Table 1 - Environmental databases included in HydroCAM

HydroCAM allows users to interactively extract, visualize and analyze data for a given region with a graphical user interface. It also enables predictions of the modal characteristics and acoustic propagation to be performed without regard for the specific database format or the input formats required by the propagation model.

Characterizing the Ocean Waveguide

Two general options for characterizing the ocean waveguide are provided. The first assumes that all energy propagates in the SOFAR channel. In this case, the oceanographic characteristics at the SOFAR depth (which varies according to geographic location and season) are automatically extracted and provided to horizontal propagation models. The second, more accurate, approach is to treat the vertical component of the problem with the method of normal modes.

In this approach, the environmental data *at each location on a geographic grid* is used to calculate the mode structure in each of these "cells". Two models are available for computing the mode structure at each point; a well known normal mode code called Kraken from NJIT, and a WKB approximation developed by BBN. Kraken calculates exact eigenvalues for as many modes as are necessary locally, while the WKB code rapidly calculates approximate eigenvalues for only those modes requested. Since it is expected that received signals will contain energy from the first several modes only, the WKB should result in a significant time savings. After the mode structure has been determined, the local phase speed, group speed, modal attenuation and slowness variance [1] are computed. The results are placed into four geographic grids, which are provided as inputs to the propagation models. Figure 1 shows an example display of a group speed grid at 10 Hz. To produce these "derived databases" involves extracting environmental data from a diverse set of databases and running a set of software packages on tens of thousands of geographic locations, a task that was previously required manual intervention at many intermediate steps. With the new software interfaces, thousands of model runs and management of the data has been automated. New environmental databases that include seasonal fluctuations and new data collected in the Southern Hemisphere, have also been integrated, resulting in the ability to produce better knowledge grids of the ocean characteristics with significantly less effort.

Predicting Propagation Paths

Acoustic paths are calculated in 2 steps; first the path itself is calculated, then the travel time, travel time variance and amplitude along the path. We evaluated five candidate path models: (1) a geometric path model on a spherical earth model for reference, (2) an ellipsoid (geodesic) model, (3) the horizontal ray/vertical mode model developed by NRL [8], (4) a horizontal ray bender model, and (5) the 3-D raytrace program HARPO [9]. Studies early in the year comparing predicted travel times using spherical paths and ellipsoid paths to measured travel times from the September 1995 French nuclear tests resulted in the elimination of the spherical model. The 3-D raytrace model was also eliminated after we obtained acceptable travel time predictions using the other models

with significantly less computational load. The remaining models are part of the baseline capability of HydroCAM. Once raypaths are calculated, the travel time, amplitude and travel time variance along each path are calculated by performing path integrals of the appropriate grid database quantity along the path. For example, travel times are calculated by integrating the inverse of the group speed database along the predicted path.

Output products at this stage include plots of the paths and their characteristics. If the predictions are run to a grid of sources (eigenray mode), plots of the path data at the endpoints on the grid are produced. These grids are used to determine network performance as described in the following section. The grids are also used to investigate the ray stability and the sensitivity of predicted travel times, amplitudes, modal content and horizontal multi-path to environmental variability and database interpolation.

The option for extracting sound speed profiles and bathymetry in a vertical plane along the path is often used to investigate blockage. In addition, this environmental information can be passed on to state of the art vertical plane propagation models such as the Range-dependent Acoustic Model (RAM) developed by NRL. This capability is used for determining detailed propagation characteristics along the paths, effects of bathymetric features on loss mechanisms and mode structure, and the detailed structure of the arrival from a specified source. Figure 2 shows examples of some of the data products produced by the geodesic path model.

Evaluating Network Performance

The performance of a network is described in terms of the ability to detect and locate sources. The detection performance of a single sensor is measured by the signal to noise ratio observed at the sensor output

$$SNR = ESL - TL - (NL - AG) + PG, \qquad (1)$$

where ESL is energy source level, TL is transmission loss (path attenuation), NL is noise level, AG is receiver array gain (receiver spatial processing gain), PG is the receiver temporal processing gain, and all quantities are in dB. TL is calculated by the path model described above, ESL by the source model described in the next section, and NL, AG and PG are provided in data files for each receiver in the network.

SNR is usually defined as the peak value of the receiver output relative to the background level, and may be calculated for a complete event, or for a single component phase. It can be related to a number of other performance metrics, such as detection probability and arrival time accuracy. However, transformation into detection probability requires a model for the receiver output statistics and specification of a detection threshold. Since these are usually determined empirically, we have opted to produce SNR only.

Single-receiver SNR may be used to display the detection coverage or combined with SNR estimates for receivers at other locations to compute the performance of the

hydroacoustic network as a whole. Many related data products are available, including geographic plots of:

- SNR for a specific receiver, corresponding to different event locations (for evaluation of existing assets)
- SNR for a specific event location, yield and depth/height for various receiver locations (for evaluation of alternative locations for new sensors).
- The minimum SNR seen by all receivers in the network
- The Mth largest SNR value seen by the network
- The number of receivers receiving the event above a specified SNR threshold. This plot is particularly useful for interpreting localization solutions.

The metric for localization coverage is area of uncertainty (AOU), which summarizes the effect of all the uncertainties in the localization calculation, including model uncertainties, e.g., uncertainties in the assumed propagation speeds. At the current time, the AOU model is based on localization using arrival time of one specific phase at multiple receivers. Additional measurements, such as bearing, can be readily added to the algorithms. The size of the AOU is a function of the accuracy of the travel time model, the ability to correctly measure the arrival time of the modeled phase, and the sensor-event geometry. This year, the effort focused on modeling the effects of sensor geometry and the travel time model. Uncertainties in propagation speeds are included in the travel time variance calculations of the path model, using world-wide statistics of the sound speed derived from WOA94 and a perturbation model for the slowness variance of propagating modes [1] . Measurement uncertainties, which depend on signal-to-noise ratio and the specific signal shape, are currently modeled parametrically, as an independent "picking" error added to the travel time error. Measurement uncertainties and the biases due to horizontal refraction will be investigated in the coming year.

The primary output products of the localization model are geographic plots of the AOU and specialized display formats showing contributing receivers and path characteristics for a particular source location. Figure 3 shows an example AOU prediction for the IMS network.

Investigating the Effects of Different Sources

The performance of the network and the details of the arrival structure depend on the characteristics of the source. DOE funded research at LLNL and NRL has produced a combined hydrodynamic and non-linear acoustic model of the pressure signature from underwater and low-atmosphere nuclear bursts called CALE/NPE [2]. The principal development effort for the source portion of HydroCAM was to couple the source functions produced by this model to the linear acoustic propagation models contained in HydroCAM. Standard models that predict the pressure signature of low-level conventional explosions are also being integrated. [3]

The source function is provided as pressure time series vs depth at a range where the acoustic propagation becomes linear (typically about 10 km from the burst). HydroCAM reads these files and calculates the complex pressure and the ESL over a cylindrical surface in the water column as a function of depth and frequency. This data is used as a "starter field" for the linear propagation model; i.e. the complex pressure is the input to a range dependent propagation model which estimates the complex propagation transfer function, and hence transmission loss (TL) at multiple frequencies along selected bearings from the event position. The result is the estimated received energy spectral level, for each frequency, to any selected range and depth along these radials.

Output products include displays of the source time series, spectral characteristics and ESL. In addition, plots of the received energy in a vertical plane along any geographic path can be produced. There are many uses for these products, including investigation of potential evasion scenarios, and potential discrimination methods. As an example, the pressure signatures calculated by CALE/NPE contain the most important physical characteristics of underwater and atmospheric explosions. When coupled with the long-range models provided in HydroCAM, the predicted spectral characteristics of the received waveforms may provide important discrimination/estimation clues. In addition, the effects of different environmental conditions at the source, such as bursts on a continental shelf, can be investigated.

Including Receiver Characteristics

The primary receiver characteristics that affect network performance are the ambient noise background at the sensor location, the transfer function of the sensors, and the characteristics of any spatial and/or temporal processing. Ocean ambient noise over most of the frequency range of concern, 1-200 Hz, is principally due to distant shipping, resulting in a noise field concentrated near the horizontal which varies in both azimuth and frequency. HydroCAM accounts for ambient noise using a table of noise level vs frequency and azimuth for each station in the network. These tables can be produced from measured data at the location if available, otherwise standard underwater noise models, such as the Wenz model [4] are used.

Some stations may have different sensor capabilities. For example, the island seismic stations in the proposed IMS are likely be on the order of 40 dB less sensitive than hydrophones placed directly in the SOFAR channel [5]. These effects, along with additional losses due to hydrophone sensitivity, scalloping loss, any other system SNR losses are accounted for in a loss table vs frequency. "Picking errors" are characterized by an arrival time variance term for each station, which is added to the travel time variance calculated by the path model. Typical values are 5 seconds for island seismic stations and 1 second for hydroacoustic stations [5].

In general, acoustic receivers can range in complexity from single omnidirectional hydrophones to arrays of hydrophones in various configurations. The spatial processing

advantage produced by an array is measured by its array gain, which is the noise level of a beam output relative to an omnidirectional hydrophone. In other situations where single hydrophones are located close to bathymetric features, it may be more convenient to model the effect of the feature as a directionality inherent in the sensor. In HydroCAM, the spatial characteristics of the receiver in both of these cases are specified either by a table of noise level versus azimuth and frequency, which represents the beam output in each direction, or by a table of array gains vs frequency and azimuth, which is applied onto the omnidirectional noise table described above. Array gains must be calculated offline using the location and orientation of the array and the beamforming parameters, such as spatial shading functions, number of beams formed, and pointing directions.

HydroCAM Validation and Applications

One of the objectives of this year's effort is to validate the baseline model using measured data. Travel time measurements taken during the Heard Island Feasibility Test [6], the French nuclear tests in 1995, and an explosion off the coast of Australia in 1960 [7] favorably compare with predictions from the model. The first two travel times are predicted within 3 seconds (~0.04% of the total travel time) using the geodesic model and sound channel axis parameters. Successful prediction for the third case requires the horizontal refraction model. Additional travel time comparisons as well as validation of the amplitude and travel time variance models will be made during the coming year.

A number of issues which affect the design of the network and the ability to produce an accurate knowledgebase have been studied using the model. The studies include:

- Travel time bias using annual average vs monthly average sound speeds
- Conditions when waveguide parameters (i.e. phase speed) are needed vs sound channel parameters
- Sensitivity of travel time variance predictions to several models of slowness fluctuations
- Predicted performance of the IMS under annual average environmental conditions.

Details of these studies will be provided in the project Final Report.

CONCLUSIONS AND RECOMMENDATIONS

A baseline hydroacoustic network performance prediction model has been developed. Verification of the model is underway. In the coming years, the model should (1) be used to investigate issues necessary for producing the hydroacoustics knowledge base needed in operational systems, (2) be certified by comparison of predicted travel times, travel time variances and amplitudes to measured data, (3) potentially be integrated with models for other techniques, such as infrasound.

REFERENCES

[1] T.R. Farrell and K.D. LePage. *Travel time variability and localization accuracy for global scale monitoring of underwater acoustic events.* JASA 99(4), April 1996.

[2] D.B. Clarke, *Pressure Time Histories Derived from Hydroacoustic Coupling Calculations: The Transition to Long Range Linear Acoustics.* LLNL Report UCRL-ID-122595, December 1995.

[3] J. Wakeley, *Pressure Signature Model for an Underwater Explosive Charge,* US Navy Journal of Underwater Acoustics Vol 27, No2. April 1977.

[4] G.M. Wenz, *Acoustic Ambient Noise in the Ocean, Spectra and Sources.* JASA 34(12), December 1962.

[5] D.B. Harris, Personal Communication.

[6] JASA 96(4). October 1994. This issue contains a collection of papers describing the Heard Island Feasibility Test (HIFT).

[7] Shockley et al. *SOFAR Propagation Paths from Australia to Bermuda: Comparison of Signal Speed Algorithms and Experiments,* JASA 71(1), January 1982.

[8] McDonald et al. "Comparison of Data and Model predictions for Heard Island acoustic transmissions", JASA **96** (4), October 1994, p 2360.

[9] R.M. Jones, J.P. Riley, and T.M. Georges, *HARPO: A Versatile Three-Dimensional Hamiltonian Ray-Tracing Program for Acoustic Waves in an Ocean with Irregular Bottom.* NOAA Wave Propagation Laboratory, October 1986.

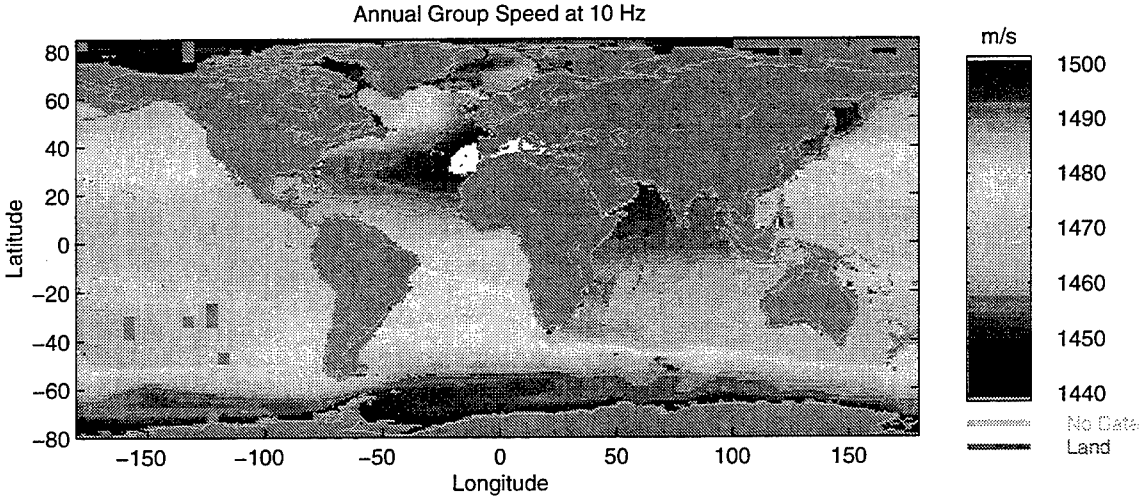

Figure 1: Calculated group speeds at 10 Hz for the worlds oceans. These calculations were produced using annual average sound speed profiles from the WOA94 database and running the Kraken normal mode program at each of 36705 geographic locations.

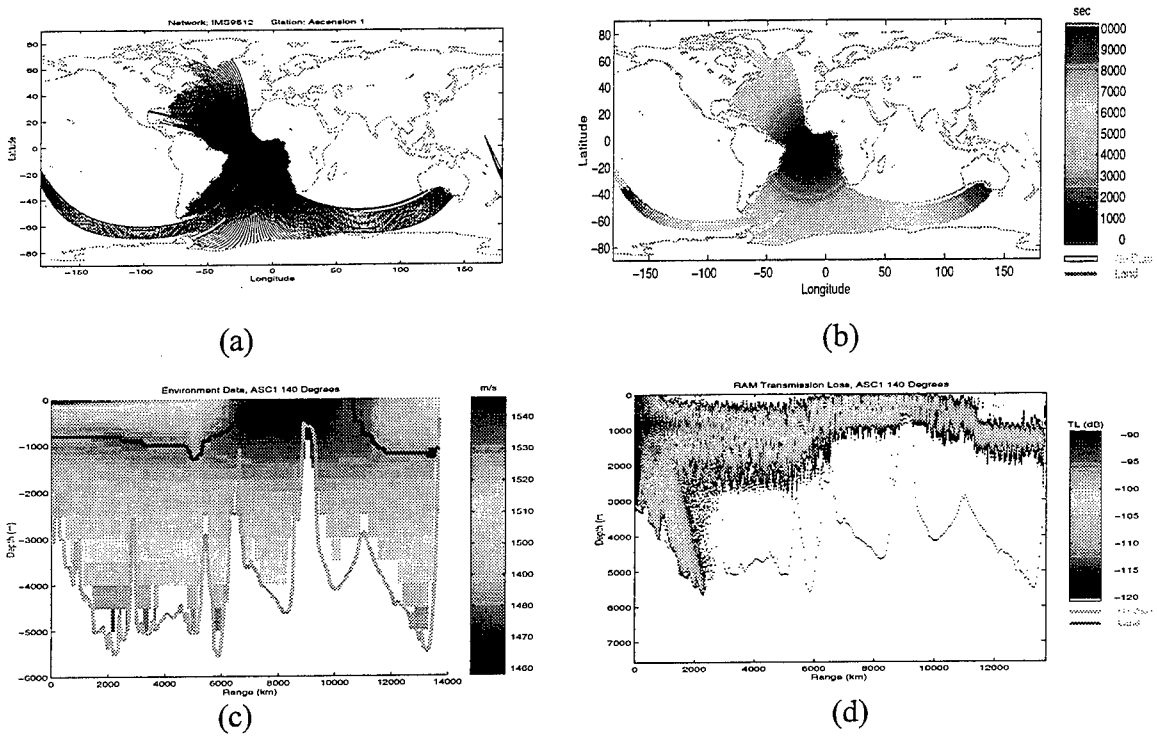

Figure 2: Example output products of the path model, clockwise from the top left plot: (a) locations of the acoustic paths from a receiver at Ascension Island, (b) travel time along these paths, (c) sound speed and bathymetry along one of the paths in (a) ending near Australia, (d) transmission loss in a vertical plane along the path used in (c).

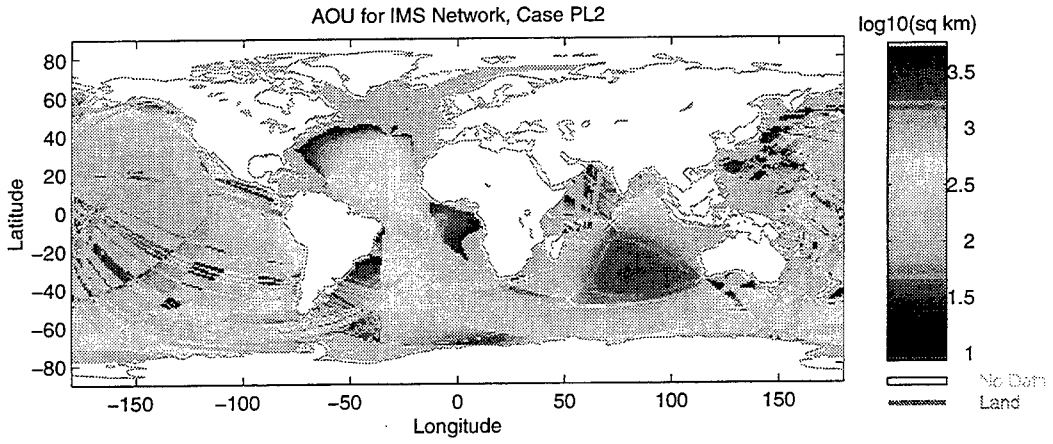

Figure 3: Example output product from the network performance model. Localization Area of Uncertainty calculated for the candidate IMS hydroacoustic network. Sources were placed at every location on a 1 degree by 1 degree grid. This example includes the travel time variances using historical statistics of the ocean sound speed, but ignores the effects of horizontal refraction.

DOE Aerosol Radionuclide Monitoring System for the CTBT

H.S. Miley, S.M. Bowyer, C.W. Hubbard,
R.W. Perkins, R.C. Thompson, R.A. Warner
Pacific Northwest National Laboratory

Sponsored by U.S. Department of Energy, Contract DE-AC06-76RLO 1830

Comprehensive Test Ban Treaty Research and Development Program, ST-271

ABSTRACT

Radionuclide monitoring, though slower than vibrational methods of explosion detection, provides a basic and certain component of CTBT verification. Measurement of aerosol radioactive debris, specifically a suite of short-lived fission products, gives high confidence that a nuclear weapon has been detonated in or vented to the atmosphere. The variable nature of wind-borne transport of the debris requires that many monitoring stations cover the globe to insure a high degree of confidence that tests which vent to the atmosphere will be detected within a reasonable time period. These multiple stations will constitute the nodes of a network, requiring network-wide infrastructure including control, communications, data standardization, calibration, quality assurance, and maintenance. While the treaty language will likely simply specify the basic measurement requirements, a superior and more cost-effective network would result from the use of standardized, completely automated equipment which allows much simpler general network operations.

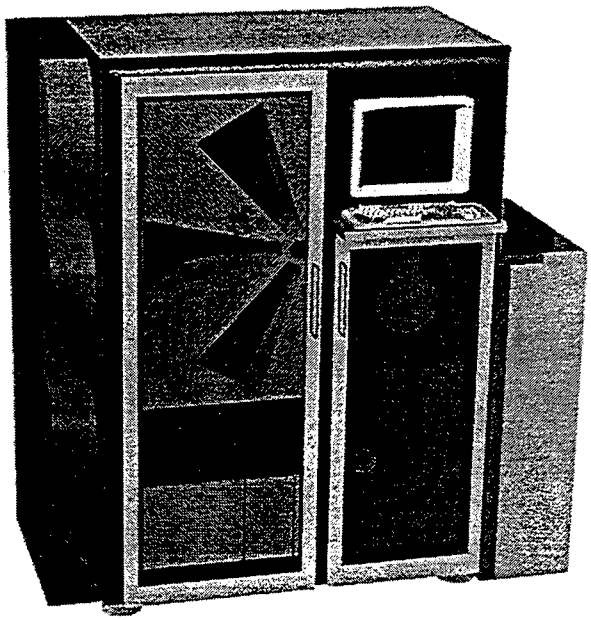

Figure 1. Mark IV Aerosol Monitoring System

To fulfill both the primary CTBT measurement requirements and the secondary infrastructure requirements, a system has been developed at PNNL to automatically collect and measure radioactive aerosol debris, then communicate spectral data to a central data center. This development has proceeded through several design iterations which began with sufficient measurement capability (<10 $\mu Bq/m^3$ ^{140}Ba-^{140}La) and resulted in a system with a minimal footprint (1 m x 2 m), minimal power requirement (2500W), and support of network infrastructure needs. The Mark IV prototype (fig. 1) is currently the subject of an Air Force procurement with private industry to partially fulfill US treaty obligations under the CTBT. It is planned that the system will be available for purchase from a manufacturer in late 1997.

Key Words: CTBT, aerosol, particulate, radionuclide, DOE, fission, nuclear, weapon, debris, monitoring, network, atmospheric, vent.

OBJECTIVE

The objective of the research activity reported here is to develop CTBT verification technology for remote, automatic near-real-time collection and measurement of radioactive aerosol debris. This system must achieve or exceed CTBT-mandated sensitivity as a primary objective and should provide robust network infrastructure as a secondary goal. Figure 2 shows several features of the system.

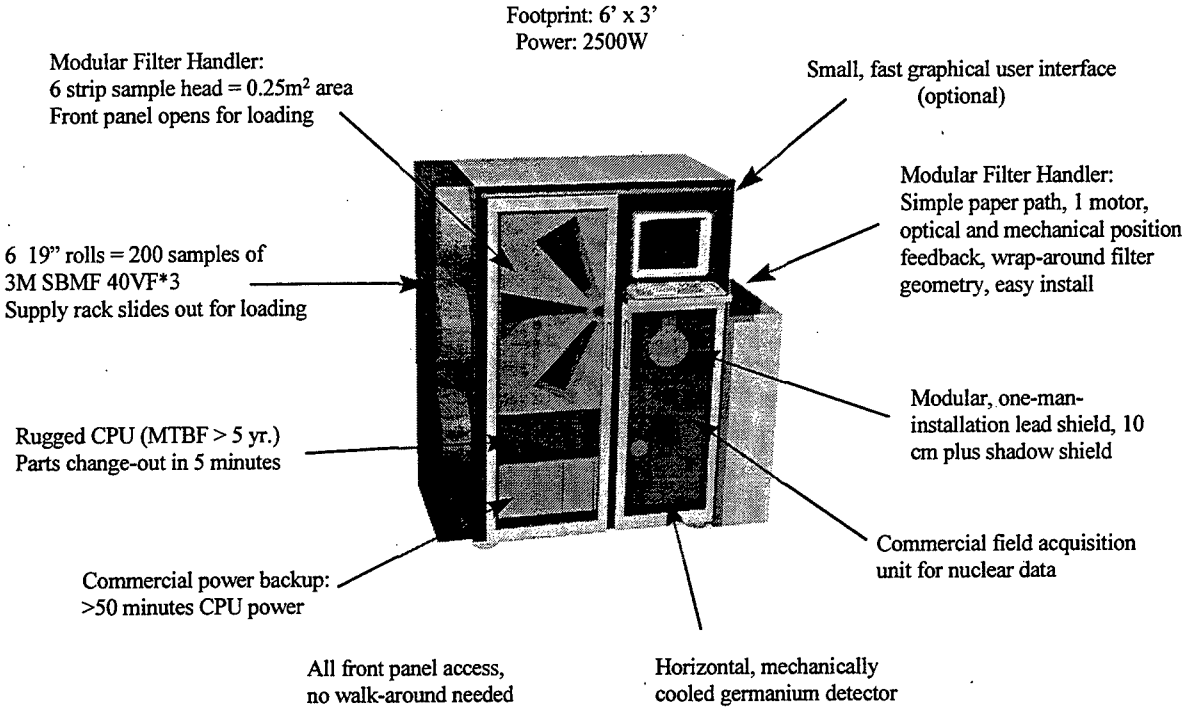

Figure 2. System Features

While vibrational methods of detecting, locating and quantifying explosions are important, radionuclide detection provides absolute physical evidence of even a small nuclear weapons test: physical traces of the weapons itself are collected on a filter or in a gas sample. This is possible because large quantities (10^{23} fission atoms per kT) of radionuclides are released in atmospheric nuclear weapons tests. Even when diluted and decayed by many days of mixing/transport in the atmosphere, these fission atoms may be observed at continental distances down wind. Certain characteristic radionuclides can be detected and used to conclusively identify a weapons test. The system reported here is sensitive to quantities as small as about 10^5 fission atoms. When gathered with 20,000 m^3 of air during a 24 hour period, this represents 5 fission atoms per cubic meter.

In order to meet CTBT radionuclide measurement needs, several developments have been undertaken. First, a method of drawing a sufficient volume of air through a high-efficiency filter medium is required. The radionuclides on the filter should be allowed to decay for a period to reduce the interfering effect of natural airborne radionuclides (radon decay products). Also the filter should be sealed to prevent contamination and introduced to a shielded radiation detector.

These operations should be done automatically to reduce the labor cost of operators and improve the quality assurance aspects of the work.

In addition, an automated system can eliminate much of the cost of logistical support. This can be accomplished by State-of-Health (SOH) sensors which can predict failures, identify failed components, and most importantly, verify proper operation of a system which has sent signals indicating a potential treaty violation. By selecting an appropriate computer architecture, the sensors can be continuously monitored and logged. In addition, the logs are available for review at any time to remote operators. With this capability, a network can be established consisting of many intelligent monitoring stations which allow a central data center to receive daily radionuclide data in a low-cost, automatic way, while facilitating a central logistical center to routinely monitor the physical operation of the stations without costly, frequent site visits. In fact, unskilled local operators will need only to restock filter paper once or twice a year and return a few filters to regional labs for quality assurance work.

RESEARCH ACCOMPLISHED

To develop such a system, researchers began with standard laboratory techniques used in 30 years of aerosol weapons debris sampling at Pacific Northwest National Laboratory (PNNL). These methods involved the use of an expensive cotton based filter requiring high velocity for good efficiency, a 15 hp pump which creates 125 dBA of noise, hydraulic presses to compress the filter into a good counting geometry, a 3 to 5 day decay period, and large laboratory-based detectors for good detection efficiency. Unfortunately, these pieces are not suitable for true field work, where size, power, complexity, and automation are all strident issues.

Measurement System Approach: Instead, a solution was sought which employed a more suitable filtration media, low-power pumps, no shape-changing hydraulic presses, and the largest practical mechanically cooled germanium detector. Germanium detectors are crucial to this application, since their high resolution greatly reduces the interference caused by the decay products of radon, a ubiquitous natural radioactive gas. Other detectors, like NaI(Tl), allow the signals from ^{214}Bi, ^{214}Pb, ^{212}Bi, ^{212}Pb, and ^{208}Tl to greatly raise the continuum background that fission products must rise above to be detected, and they blur the fission product peaks with the interfering peaks as seen in figure 3. Mechanical coolers for germanium detectors have been available from manufacturers for several years which eliminate the need for a liquid nitrogen supply and consume only about 1 kW of electrical power.

Past methods of large volume aerosol collection have employed pumps requiring several kilowatts of power. An alternative filtration method involves the use of large-surface-area, low-pressure-drop filters. Large surface areas allow a lower velocity at the face of the filter to sample a given volume, and therefore require less energy per standard cubic meter (SCM), since the frictional energy is related to the square of the velocity. Reducing the frictional energy loss of the air stream is manifested in a smaller pressure drop across the filter, which in turn means that a lower-pressure-drop pump can be used. After a market survey of filter media, a specific combination of parameters was found which consumed only about 1 kW to filter over 20,000

SCM/day through a 0.25 m^2 high-efficiency filter while producing <75 dBA of noise. While this represented a tremendous improvement over pre-existing laboratory methods, a large filter should be compressed to achieve the best possible sensitivity.

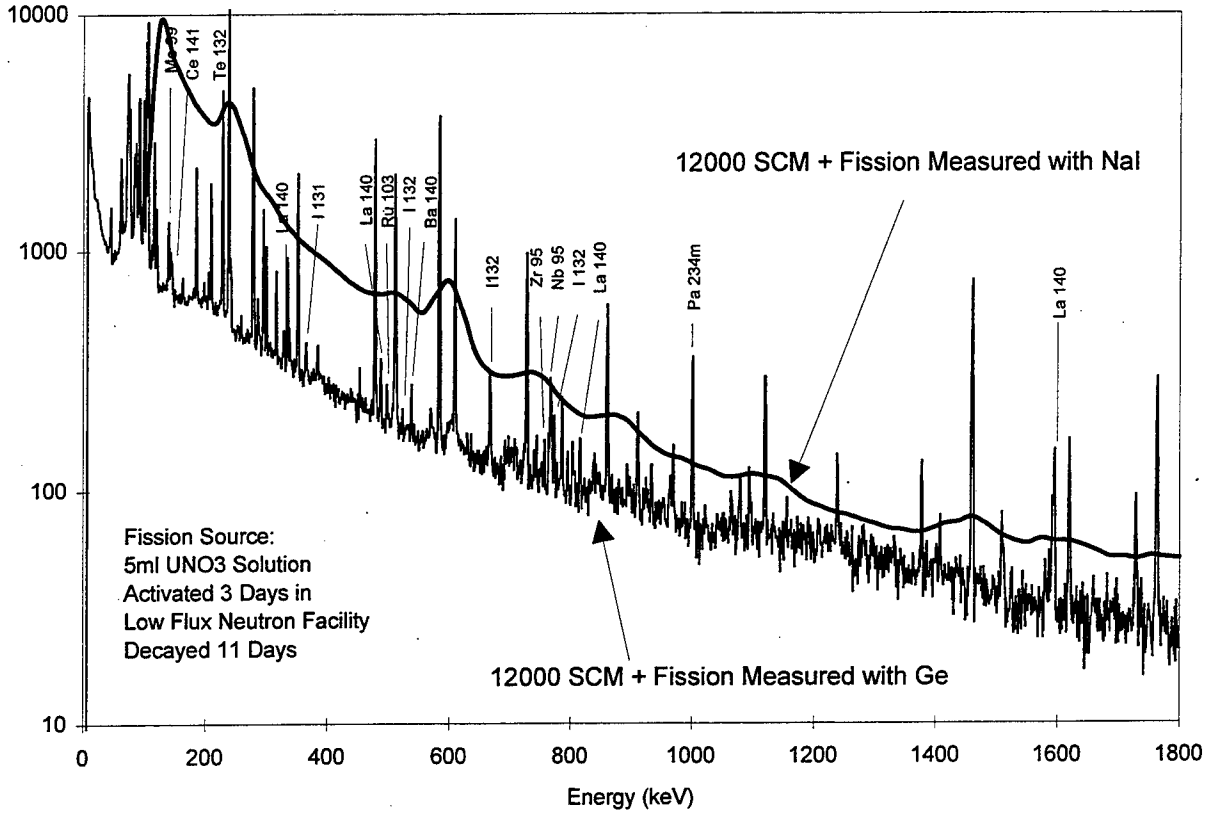

Figure 3. Comparison of Germanium and NaI Detectors on Fission + Radon-Daughter Spectrum

Hydraulic presses are used in the laboratory to compress samples to improve the geometric detection efficiency. A large filter as described above would ordinarily be folded over several times to achieve a roughly spherical shape, then compressed into a wafer perhaps 5 cm in diameter and 0.5 cm thick. However, the complex physical manipulations required, both folding and compression, do not lend themselves to automation, particularly where cross contamination is a concern. For this reason, a method was sought to compact the 0.25 m^2 filter without folding or physical compression. The solution was a segmented sample head with six 10 cm x 40 cm filter strips simultaneously exposed to an air stream. At the end of the collection period, the six independent strips are sandwiched together and sealed. This bundle is then wrapped around the detector and a gamma-ray spectrum is acquired. The segmented sample head concept is the subject of a patent application currently under review.

While this approach is a compromise between complexity and sensitivity, it has been demonstrated that additional sensitivity can always be gained at the cost of power and noise by simply increasing the volume sampled or reducing the size of the filter presented to the detector.

The pump selected for this technology is actually more properly called an industrial fan. The required pressure for filtration is so low (6 inches of water or $1/64^{th}$ of an atmosphere) that a 1 hp rotary fan is sufficient. In fact, this hardware is so common that this component and many others in the system are obtained through industrial hardware distributors.

Sensitivity: The sensitivity of the measurement system is roughly determined by several simple factors: air volume, detector size, shielding and detector/sample geometry, and radon-daughter decay time. The air flow rate is about 20,000 SCM/day, the detector size is measured as 90% (of the detection efficiency of a 3" x 3" NaI(Tl) detector at 1332 keV), and the geometry of the source is a 10 cm x 40 cm x 2 thick cm strip wrapped around an aluminum can ~11 cm in diameter centered about the detector. We note that the air volume is expected to be ~20000 SCM/day compared to ~27000 SCM/day for previous systems (due to thicker filter paper), the detection geometry is about 15% better, an off-setting effect. Thus the sensitivity should be about the same as previous systems, or <10 μBq/SCM of $^{140}Ba/^{140}La$. A note about the detector size is also in order. The 90% size specified is designed to (1) provide the required sensitivity, (2) fit the ~11 cm diameter rotating filter cylinder (see figure 4), and (3) meet the price goals for the system.

Automation and State-Of-Health Sensors: While the above section describes the sampling approach, much more is involved with automating the system. First, the segmented sample head allows commercially-available filters strip rolls to be drawn in and exposed to air flow for a programmable period. Then the exposed filters are sealed between polyester strips as they are pulled out of the segmented sample head. The filter samples are then drawn around a horizontally mounted detector (fig. 4). The driver for the entire process is a single motor which applies torque to a pair of crepe-rubber-coated drive shafts. The relationships between motor torque, drive-to-drive compression, dust coating, and slippage have been investigated. The result is a drive system which has a robust engineering safety factor when totally loaded with dust, yet minimized power and size.

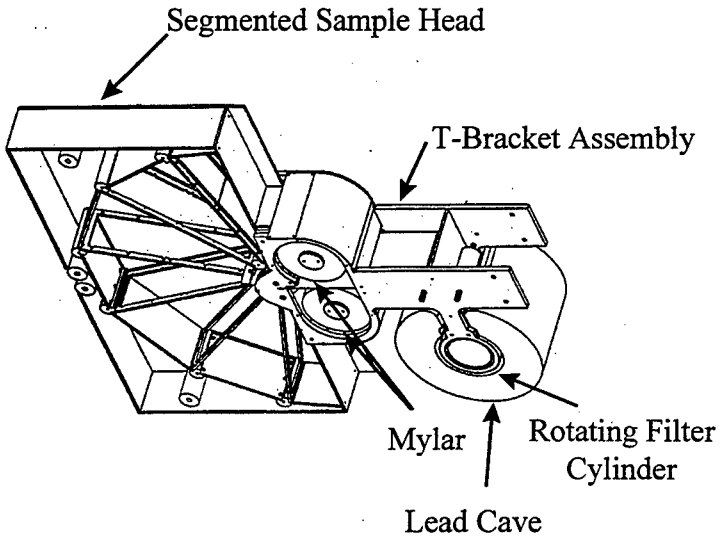

Figure 4. Filter Handling Mechanism

The above mechanisms fulfill most of the basic sampling and measurement needs and provide a degree of automation, but a number of auxiliary sensors and systems are needed to finish the measurement and provide SOH data. First, an optical position sensor guarantees that each filter is positioned uniformly with respect to the detector. Barcodes are also printed on this polyester encapsulation strip (fig. 5) for easy computer and human identification of exposed filter. An anemometer and differential pressure transducer are used to integrate air flow and detect possible filter clogging and filter breakage. Rotary encoders are used to compare motor revolutions to paper advance to detect slippage. Motor currents are measured to predict failures and to note excessive resistance to turning. A suite of temperatures is measured to provide diagnostic data to remote interrogators. All of these sensors are routinely monitored and logged, as is every system command, every state change, and every process error, for maintenance and security reasons. Finally, a small meteorological station communicates over an RS-232 line to log local weather data every ten minutes.

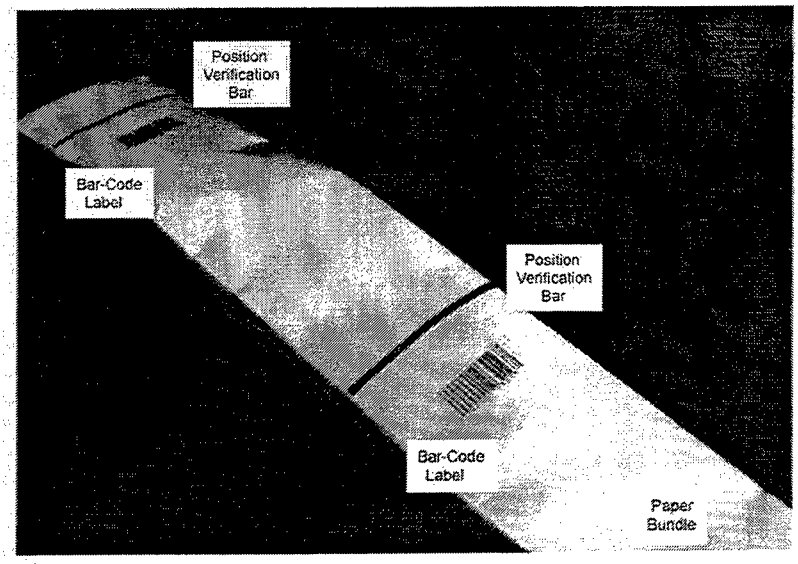

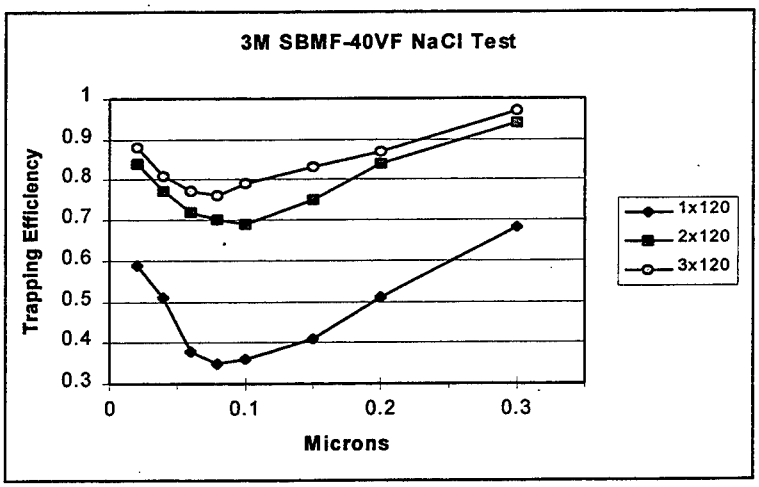

Figure 5. Filter Bundle and Filter Efficiency vs. Layers

Control System: The automation requires a certain degree of control sophistication. While this could actually be provided by a small programmable logic device common in industry, the two-way communications requirement and operator interface demand that a computer run a real-time operating system (QNX) able to support common communications methods (TCP/IP) and multiple-platform graphical user interfaces (X-Windows).

The programming method chosen for this is an approach called a State Machine. The State Machine allows all possible systems conditions to be defined as states, and all possible actions as transitions. In this way, the system behavior can be designed by those without programming skills, and system modifications become easy to implement. A simple programming loop checks the current state once per second to determine if conditions (like a time-out) warrant a transition.

The control program then calls subordinate processes to perform transition activities, like advancing a filter.

The State Machine would be a simple series of steps with the last step pointing back to the first except that power failure recovery steps can be optimized for the duration of a power failure, and therefore cause the State Machine to have multiple choices for several transitions, based on how long the power has been off in a power failure. This feature saves days of down time due to short (<20 minute) power failures, and assures that the maximum use is made of all air sampled.

Because the computer process architecture is modular (see figure 6), any sub-process can be halted and replaced remotely without interrupting normal operations. In addition, any crashed process will restart automatically without a system crash. And in the event of a system crash, the operating system itself supports communications such that the system can be connected to, diagnosed, and restarted without a site visit.

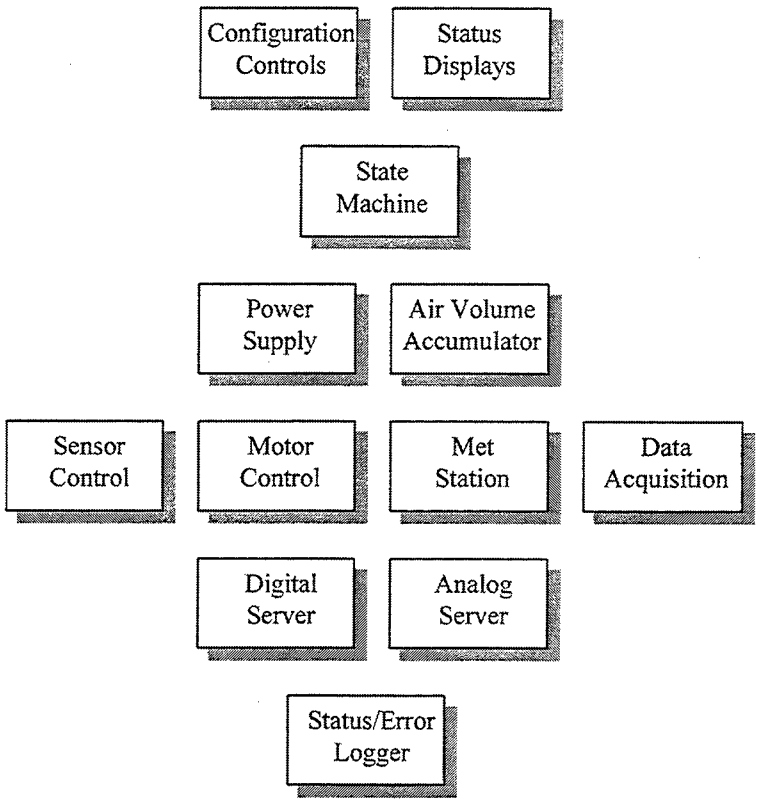

Figure 6. Software Modules

Maintainability: Because of the remote locations of many of the CTBT monitoring sites, the system must be easy to maintain. Simple queries of the system from a central logistics facility can determine if the system requires maintenance beyond the yearly filter restock/maintenance period. The query should also permit a visiting technician to have a good idea of any maintenance problem and appropriate replacement parts. Routine maintenance is limited to cleaning dust off surfaces and to applying a thin film of lubricant to one set of gears. To facilitate these and all other logistical operations, the system is designed for front panel access. Certain major activities would be much easier with a standard walk-around, but all activities, including installation are possible using front panel access only.

It is envisioned that a logistics operator in a central logistics facility will be able to observe a computer-generated world map, instantly inspect all nodes for functionality, including scheduled periodic maintenance, then simply click on a functional or non-functional node icon to query logged SOH data, calibration certificates, maintenance records, and current attributes which may actually initiate a communications link directly to the node. While the requisite software does not

currently exist to do this infrastructure task, it is under investigation so that the appropriate characteristics can be built or selected into the node.

CONCLUSIONS AND RECOMMENDATIONS

The automation of a high sensitivity CTBT aerosol monitoring system has had numerous important side benefits. Monitoring which meets or exceeds expected CTBT sensitivity requirements is obviously of primary importance. Low labor costs, low down-time, ease and centralization of logistics; all are reasons to have an automated design for a global network which supports a robust network infrastructure.

The Mark IV aerosol monitoring system is currently being readied for testing at PNNL (see fig. 7).

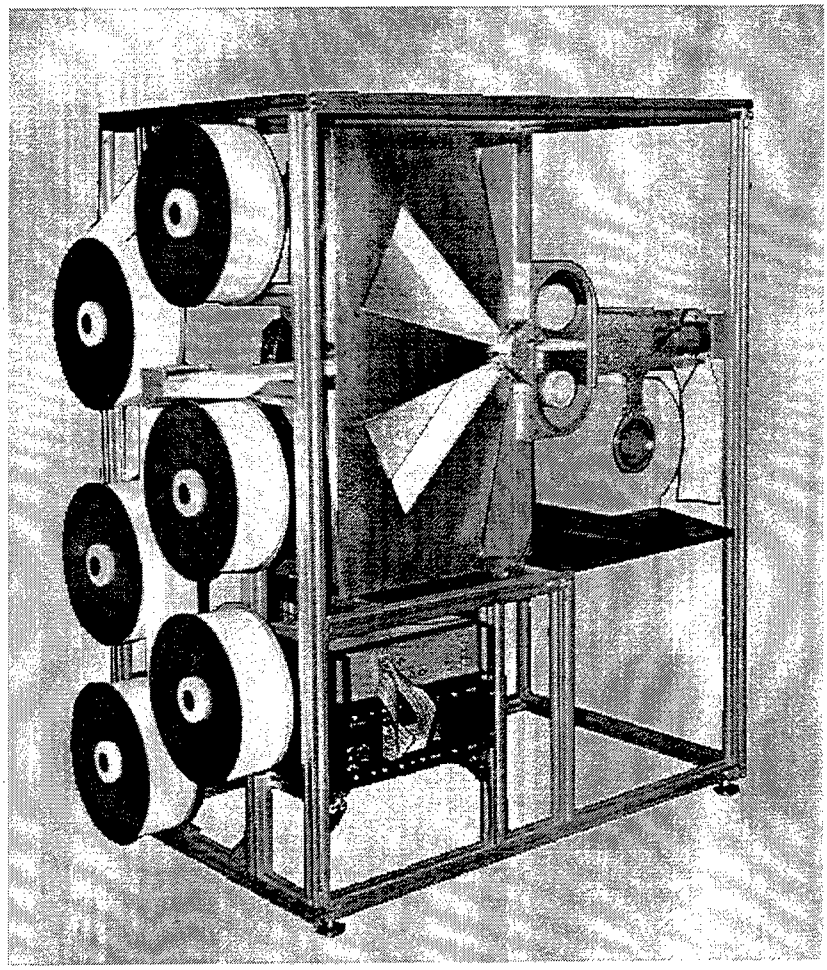

Figure 7. Current Status of Mark IV System

Results of the LLNL On Site Inspection Research Project

J. J. Sweeney, C. Carrigan, W. Pickles, C. Schultz, and A. Smith
Lawrence Livermore National Laboratory

Sponsored by U.S. Department of Energy, Contract W-7405-ENG-48
Comprehensive Test Ban Treaty Research and Development Program, ST484B

ABSTRACT

In the initial stage of our research into on-site inspection (OSI) methods to support a possible Comprehensive Test Ban Treaty (CTBT), we identified four immature technology areas that could be used in the CTBT which we felt could be brought up to an implementation status relatively quickly and cheaply. Three of the methods, aftershock monitoring, noble gas monitoring, and detection of disturbed ground with imagery, are directly applicable to OSI. The fourth method, low frequency electromagnetic pulse (EMP) monitoring, is applicable to "transparency"—methods used during an announced explosion to improve confidence that the explosion was non-nuclear. Our study of aftershocks has shown that there are similarities between the aftershocks from underground nuclear tests at the Nevada Test Site and seismicity associated with mine caving operations, like those at the Henderson Mine in central Colorado. Other mine-caving operations, such as those at Twentymile mine in north-central Colorado, have aftershocks more characteristic of earthquakes. We have been working on methods to improve our ability to locate microseismic events in areas of complex geology and topographic relief. In our noble gas monitoring effort we have demonstrated, using results from the Non-Proliferation Experiment (NPE), that even the short-lived xenon-133 isotope could reach the surface in detectable quantities from an underground nuclear explosion. We have also developed optimal sampling strategies for collecting gases. In the EMP effort, monitoring of several different chemical explosion/mining environments revealed that low frequency EMP is uncommon. Our review of the literature and further analysis of the NPE data suggests that hydrofracturing may be a possible source of the EMP from underground nuclear and chemical explosions. Overhead imagery of the NPE, looking at the ratio of 690 to 420 microns of visible light, suggested that plant stress over a large area of the surface over the detonation point was due to ground shock. We have recently verified the shock effect on plant stress with a series of carefully controlled experiments. Results of all of the above work will play an important role in the preparation phase of the CTBT, once the treaty has been signed.

Key Words: On-site inspection, noble gas monitoring, aftershocks, plant stress, low frequency electromagnetic pulse

OBJECTIVE

Under a comprehensive test ban treaty the initial detection capability for treaty violations will come from the international monitoring system (IMS). However, in some instances, such as for underground explosions, the IMS will not be able to provide conclusive evidence of the nuclear nature of the event. In these cases an on-site inspection (OSI) may be called on under the treaty to gather evidence to determine the nature of the event.

The objective of our OSI research project is to identify phenomenology to be utilized during inspections and to develop techniques and procedures for use during an OSI. Our project encompasses techniques that would be employed after the occurrence of an ambiguous event as well as so-called "transparency" methods that would be used during an on-site visit to the site of a declared explosion to improve confidence in its non-nuclear nature.

There are many possible OSI methods that could be employed. We have focused on improving the effectiveness of a few methods which we believe are critical to the success of an OSI: aftershock characterization, noble gas seepage, and the detection of disturbed ground. Added to this is one method applicable to transparency: low-frequency electromagnetic pulse. Current status of the research on each of these methods is outlined below.

OSI RESEARCH ACCOMPLISHED

Aftershocks

The initial search area for an OSI, as delimited by the international monitoring system, may be as large as 1000 km^2. Clearly, an important immediate concern of the OSI will be to refine the search to a smaller area. One way to do this is by monitoring for aftershocks with a local seismic network. The network will have to be designed to rapidly handle a large number of events and provide accurate location determinations. Our research has focused on the characterization of aftershocks from a variety of explosion and mining settings and the application of improved event location methods for the complex settings of the mining environment.

Underground nuclear explosions can generate aftershocks just as those occurring after large earthquakes; however, the explosion aftershock sequence includes varying numbers of events with predominantly low frequency energy (Jarpe et al., 1994; Ryall and Savage, 1969). High frequency aftershocks have corner frequencies greater than 20 Hz, whereas low-frequency events have corner frequencies of a few Hertz. Since low-frequency aftershocks are associated with underground explosions, detection of such events during an OSI could help focus the efforts of the inspectors.

To find out if low frequency events occur in other settings, we have examined mining environments and volcanic areas. A deployment around the Henderson mine in central Colorado detected many low-frequency events. These were associated with surface rockfalls in the collapse crater on the surface. Figure 1 compares these waveforms to Non-Proliferation Experiment (NPE) aftershocks and to seismic events associated with long-wall mine of the Twentymile Mine in Colorado. The rockfalls produce a very gradual amplitude increase over a few seconds, much longer than emergent events from the NPE. In the Twentymile Mine, the main events and aftershocks are associated with roof collapse following long-wall mining. Unlike the caving operation at Henderson and underground explosions, these aftershocks are impulsive with very clear onsets and high frequency energy.

Location of emergent events using relatively few stations requires robust algorithms to achieve good location accuracy. The events can occur both above and below stations, a condition not allowed in most traditional location programs. We are experimenting with

routines developed by Lou Estey, formerly of the US Bureau of Mines, Harley Benz (Benz, et al., 1996), and with grid search methods to achieve a stable solution. Initial results indicate that additional modifications to the codes will be needed to obtain stable location solutions without having to constrain depth. In addition to the above, we are also looking for and evaluating commercial systems to use for aftershock detection and characterization in an OSI context.

Noble Gas Seepage. We have demonstrated that gases released from a detonation cavity can be detected by surface sampling along natural faults and fractures within a period of weeks to months following a deep underground explosion (Carrigan *et al.*, 1996). We put tracer gas bottles of ^3He and SF_6 in the explosive-filled detonation cavity of the NPE to produce a gas source following detonation. Both gas tracers were detected on the surface of Rainier Mesa by sampling fractures and faults that existed prior to the detonation. The SF_6 tracer was detected first, fifty days after the detonation at the surface about 500 m from surface ground zero of the NPE. The helium tracer was detected at the same station 375 days following the detonation. Detailed numerical flow and transport models, based on the computer program NUFT (Nitao, 1995), show that the observed delay in the arrivals of the two gases at the surface is best explained by a mechanism which combines diffusion of gas into porous rock and barometric pumping of gas through fractures. The much greater gas diffusivity of helium relative to SF_6 means that it is absorbed into the pore space more readily, so it isn't transferred as quickly through the fractures, thus the heavier SF_6 arrives at the surface earlier. We have been able to closely fit our numerical simulations of the transport of both tracers to our observations of the tracer arrivals on Rainier Mesa. In effect, we have used the observations to calibrate our models of transport so that they can be used for predicting the transport of radionuclides from a nuclear explosion.

In the case of an underground nuclear explosion, the gases of interest are certain trace radionuclides of argon and xenon that are exceedingly rare and represent extremely good indicators of the occurrence of a clandestine test. These trace gases have very short half lives (5.3 days for ^{133}Xe and 34.8 days for ^{37}Ar) permitting a detection window of several months to a year following a suspected underground event. (Background levels are very low, so extremely small amounts these gases can be detected.) Under the conditions of the NPE, we predict that radionuclide gases would reach the surface at detectable levels within 50 to 80 days following a one-kiloton nuclear event. Our models of radionuclide gas transport assume the conditions identical to the NPE explosion with the addition that we take into account the solubilities of both xenon and argon in groundwater. Both of these radionuclides are more soluble in groundwater than are the NPE tracers. The effect of solubility is to permit the storage of tracer gas in the water-filled part of the pore space which delays and diminishes of amount of tracer reaching the surface from the detonation site. However, our models indicate that the decrease in quantity will not be enough to prevent detection of these radionuclides at the surface. We consider these predictions to be conservative because we have used conservative estimates of the ^{37}Ar and ^{133}Xe source values.

In addition to evaluating the detectability of rare radionuclides from well-contained underground tests, we have worked on optimizing sampling techniques that would be used during an on-site inspection (OSI). This is important since large (100 liter) gas samples will be required for radiological counting purposes during an OSI, and we need to know if there will be dilution by influx of atmospheric gases during sampling. Our optimization effort has involved both field experiments and numerical modeling. Results of our modeling are illustrated in Fig. 2. The figure shows cross sections of two models representing extremes of the types of situations that will be encountered during an OSI. In one case (left cross section), a sample tube has been inserted in a narrow (1 mm) fracture that comes to the surface. As a 100 liter sample is withdrawn from the soil, most of the gas removed initially is soil gas. However, as the withdrawal continues, air from the atmosphere is drawn down

the fracture to the sampling tube, as indicated by the plume around the tube. Thus, atmospheric air is drawn up into the sample of the soil gas; this results in dilution of any tracer present in the soil gas. For the limiting case of uniform soil (right cross section) with no fractures, infiltration does not appear to be a problem for this size of sample; in this case concentrations in the sample are four times greater than those obtained in cross sections with 1 mm fractures. Some infiltration occurs but significant amounts of atmospheric air are never captured in the sample for a tube emplaced at this depth (2.1 m). From the plot of concentration versus time in the figure, we also find that the depth of the sample tube inlet in the fracture can significantly affect the concentration of tracer gas extracted in a 100 l sample with deeper inlets, resulting in a decrease in trace gas dilution by the entrained air from the atmosphere. While the model suggests that fractures are problematic for infiltration of air which can dilute large samples, we also know that fractures are necessary for getting the gas to the surface and that sampling stations on surface fractures provide the best sites for detection (Carrigan et al. 1996). The use of deeper sampling tubes such as can be emplaced by a truck-mounted hydraulic ram are suggested by our modeling.

Using radon detectors with built-in pumps, we have withdrawn 100 l samples from sites sampled earlier near the NPE that were the most prolific producers of tracer signals. Using the soil-produced radon concentration as a means of monitoring infiltration, we find that radon concentrations were not strongly diluted even at our stations on suspected faults. Thus, our field sites appear to more closely correspond to the case of a uniform, unfractured medium in which infiltration is less of a problem. In addition, new field work is attempting to measure the degree of infiltration directly by releasing a xenon tracer beneath a tarp on the surface. If the gas drawn out has been significantly diluted, the xenon level in the sample will be elevated above atmospheric values. These results in conjunction with our simulations, which can treat more cases than can be sampled, are critical for developing optimized techniques for gas sampling during an on-site inspection.

Detection of Disturbed Ground. Analysis of multi-spectral images of the surface of Rainier Mesa over ground zero before and after the NPE showed a broad region of apparent plant stress (Pickles, 1995). The pattern of plant stress similar to the variation in peak ground motion on the mesa due to the underground explosion, so the natural conclusion is that the plant stress was caused by ground shock. In order to confirm the supposition that plant stress can be caused by ground shock, we decided to carry out some simple controlled experiments on a group of trees of the same species, age, and health that have lived through exactly the same daily environmental conditions.

The objective of the field experiments was to establish the existence of shock-induced plant stress, gain some idea of the relative magnitude of the shock effect compared to dehydration stress effects, and to provide direct plant physiological measurements and remote sensing ratio images from the same plants at the same time. The experiments were done on the grounds of a large commercial nursery near LLNL. Dr. Greg Carter, a scientist from NASA-Stennis Science Center who has had extensive experience in remote sensing of plant stress, collaborated in the design and conduct of the experiment.

In the field experiments, we measured plant physiological responses and obtained multi-spectral imagery of trees that were purposely physically shocked under highly controlled conditions. Sixteen *Alnus Rhombifolia*, or white Alder, trees in 15 gallon plastic pots which had been under carefully controlled conditions for over a year were selected for the study. Shock was induced in the plants by picking them up and dropping them from three different heights. The free fall and subsequent shock of hitting the ground was designed to simulate slap down conditions that the earth surface experiences following a large underground explosion. Plant physiological measurements and multi-spectral images were obtained on twelve trees that were dropped as well on a control group of four randomly-selected adjacent trees that were not dropped. We also subdivided the experiment to provide information about the magnitude the shock-induced plant stress effects relative to

the plant stress effects that would occur if water were withheld from the trees. Water was withheld from two plants in each group of dropped and undisturbed trees while the others continued to be treated exactly as they had been for the previous 17 months.

Measurements were made using equipment provided by NASA-SSC and by LLNL. The NASA-SSC equipment is the same that Greg Carter has used in previous plant stress studies on a wide variety of species. Physiological plant stress measurements included a leaf water potential, plant photosynthesis rate, and leaf reflectance with a high resolution visible light and infrared spectrometer system. Images at five separate spectral bands with 1 nanometer width in wavelength acceptance were taken with the new NASA handheld specially filtered ccd camera. LLNL provided the shock measuring instrumentation to record the time-dependent levels of shock in each plant tested. This experiment marks the first time that hyper-spectral imagery and plant physiology measurements have been acquired at the same time on the same plants under controlled conditions.

At the time of writing of this abstract, we have only just finished the field tests and started the data analysis. Preliminary results indicate that shock-induced stress effects are shown by the water potential measurement, which is a standard plant physiology measurement. The shock effect was observed on at least one day in the trees that were additionally stressed by withholding their normal daily watering, but not on the trees watered normally. This is a quantitative confirmation of the shock induced plant stress effect. Shock-induced plant stress is actually a well known fact to the nursery personnel who participated in this experiment. Surprisingly, in our experiment, the trees that recovered most completely and quickly from the water withholding were those trees that had received the shock stress.

These experiments provide us with a unique and very complete time dependent data set. This experimental data directly ties remote sensing data with physiological data on the same plants at the same time. Analysis of the data for this project will give us a better understanding of basic shock-induced plant stress effects and the potential for application of the phenomenon to CTBT-OSI requirements.

TRANSPARENCY RESEARCH ACCOMPLISHED

Low Frequency Electromagnetic Pulse. Low frequency electromagnetic pulse (EMP) signals have been observed from underground nuclear explosions of several kilotons or greater within several kilometers of ground zero (Sweeney, 1989). Observations during the NPE underground chemical explosion showed that a low frequency EMP can be produced by an underground chemical explosion, but there are significant differences in duration and frequency content of the signal when compared to that from an underground nuclear explosion (Sweeney, 1994). These results suggest that EMP measurements could be used during cooperative zero time inspections to confirm the nature of announced explosions. During the past two years we have been carrying out research to better understand the nature of the low frequency EMP from all types of chemical explosions, the fundamental cause of the EMP, and the limits on the practical use of low frequency EMP measurements for confidence-building applications.

To date we have performed low frequency EMP measurements in four different mining/experiment environments in addition to the NPE. In each case, to minimize preparation and field expenses, the EMP measurements were tied to other LLNL field experiments designed to observe shock and seismic effects. Because of this, the experiments were not optimally designed to answer questions about low frequency EMP, but the data still provide important limiting cases for our understanding of the phenomena.

During FY1995 we monitored large underground chemical explosions at the Henderson mine near Idaho Springs, Colorado, large ripple-fired chemical explosions at the Carlin gold mine near Ely, Nevada, and the Kuchen series of small high explosive detonations in a borehole at the Nevada Test Site. During FY1996 we monitored a series of

explosions carried out in an abandoned mine near Lynchburg, New Mexico. In all cases, no EMP was observed that could be attributed to the chemical explosion.

At Henderson mine, the sensors were about 1.5 km away from the explosive source, which ranged up to 1500 lbs of high explosive. Because of the geometry of the mine, this was the closest we could get without being underground in the mine. At the open-pit Carlin mine, sensors were located within the mine, but out of range (0.5-1 km from the blast) of flying debris from the surface explosions, which contained a total charge of over one million pounds. The Henderson results are consistent with our understanding of the dependence of the EMP with yield and its attenuation with distance (Sweeney, 1995); they also demonstrated important practical limitations to deployment of sensors in a mining environment. The Carlin experience showed that a large ripple-fired chemical explosion does not create an EMP equivalent to the total charge detonated (the sum of all the charges in all the boreholes)—if it did, we would have easily detected an EMP from our instruments.

The Kuchen series were 100 pound chemical explosions detonated in boreholes at depths of 65-90 m using the same arming and firing system as used during underground nuclear explosions. The non-observance of an EMP from these explosions confirmed our previous estimates about the yield-distance dependence of signal strength (Sweeney, 1995). However, during each phase of the Kuchen series we observed, at a distance of 20 m from ground zero, low frequency EMP signals clearly generated by the arming and firing system. In the Lynchburg series, our sensors were again located as close as possible to the detonation without being within the mine itself; in this case at the mine portal and on the surface above the detonation—about 150 m away. No EMP was observed from any of the explosions, the largest being over 4000 pounds, although we observed strong signals caused by the local ground motion and the passage of the air blast out of the portal.

We have also been reviewing the literature on electromagnetic signals related to rock fracture. There have been a large number of observations of high-frequency EMP from a wide variety of materials by the material properties community and other observations during explosions in boreholes and fracturing of rocks in the laboratory. A group of Russian investigators have developed a theory that attributes EMP generation during fracture to the actual propagation of the fracture tip. This suggests that during a chemical explosion hydrofracturing caused by gas pressure in the cavity could be the source of an EMP. Pressure data taken during the NPE shows a duration of high pressure in the cavity (Heinle, et al., 1994) that is quite similar to the duration of the EMP (Fig. 3). This evidence to supports the hydrofracture source explanation. During a nuclear explosion (Fig. 3, top) the EMP is much shorter in duration and is probably caused by nuclear processes. Any hydrofracture effects, if present, may be masked by the stronger nuclear-related pulse.

Our research on low frequency EMP has allowed us to make some estimates of the character and detection limits of signals from underground nuclear and chemical explosions. We have some idea of what to expect of possible EMP from chemical explosions in a wide variety of mining situations. Low frequency EMP from chemical explosions is probably a complicated phenomena that may depend on rock type and local heterogeneities, but our experience suggests that the EMP signature of an underground nuclear explosion is probably unique.

CONCLUSIONS AND RECOMMENDATIONS

On-site inspections will probably be a component of a CTBT. Our work will benefit international monitoring by helping make OSIs more effective in two ways: (1) an effective OSI regime will give confidence to the requesting party that a violation can be found and assures the inspected party that the inspectors will only search for relevant evidence; and (2) a carefully constructed OSI capability will help keep costs to a minimum. During the past two years, our understanding of the four technology areas discussed above has

advanced considerably. Our knowledge of these potential OSI methods has now advanced to the state where we can make specific recommendations for field-deployable systems and analysis methods.

REFERENCES CITED

Benz, H.M., B. A. Chouet, P. B. Dawson, J.C. Lahr, R.A. Page, and J.A. Hole, 1996, Three-dimensional P and S wave velocity structure of Redoubt Volcanoe, Alaska, J. Geophys. Res., 101, 8111-8128.

Carrigan, C.R., Heinle, R.A., Hudson, G.B., Nitao, J.J. and Zucca, J.J., 1996, Trace gas emissions on geological faults as indicators of underground nuclear testing, to appear in *Nature*.

Heinle, R.A., B.C. Hudson, and M.A. Hatch, 1994, Cavity pressure/residual stress measurements from the Non-Proliferation Experiment, in Proceedings of the Symposium on the Non-Proliferation Experiment, DOE Conf-9404100, edited by M.D. Denny, Lawrence Livermore National Laboratory, Livermore, CA, pp. 6-36 to 6-53.

Jarpe, S., P. Goldstein, and J. Zucca, 1994, Comparison of the Non-Proliferation Experiment aftershocks with other Nevada Test Site events, in Proceedings of the Symposium on the Non-Proliferation Experiment, DOE Conf-9404100, edited by M.D. Denny, Lawrence Livermore National Laboratory, Livermore, CA, pp. 8-34.

Nitao, J.J., 1995, Reference manual for the NUFT flow and transport code, version 1.0, UCRL-ID-113520, Lawrence Livermore National Laboratory, Livermore, CA.

Pickles, W.L., 1995, Observations of temporary plant stress induced by the surface shock of a 1-kt underground chemical explosion, UCRL-ID-122557, Lawrence Livermore National Laboratory, Livermore, CA.

Ryall, A. and W. U. Savage, 1969, A comparison of seismological effects for the Nevada underground test BOXCAR with natural earthquakes in the Nevada region, J. Geophys. Res., 74, p. 4281.

Sweeney, J.J., 1989, An investigation of the usefulness of extremely low frequency electromagnetic measurements for treaty verification, UCRL-53890, Lawrence Livermore National Laboratory, Livermore, CA.

Sweeney, J.J., 1994, Low frequency electromagnetic measurements at the NPE and Hunter's Trophy: a comparison, in Proceedings of the Symposium on the Non-Proliferation Experiment, DOE Conf-9404100, edited by M.D. Denny, Lawrence Livermore National Laboratory, Livermore, CA, pp. 8-21 to 8-23.

Sweeney, J.J., 1995, Low frequency electromagnetic signals from underground explosions—on site inspection research progress report, UCRL-ID-122067, Lawrence Livermore National Laboratory, Livermore, CA.

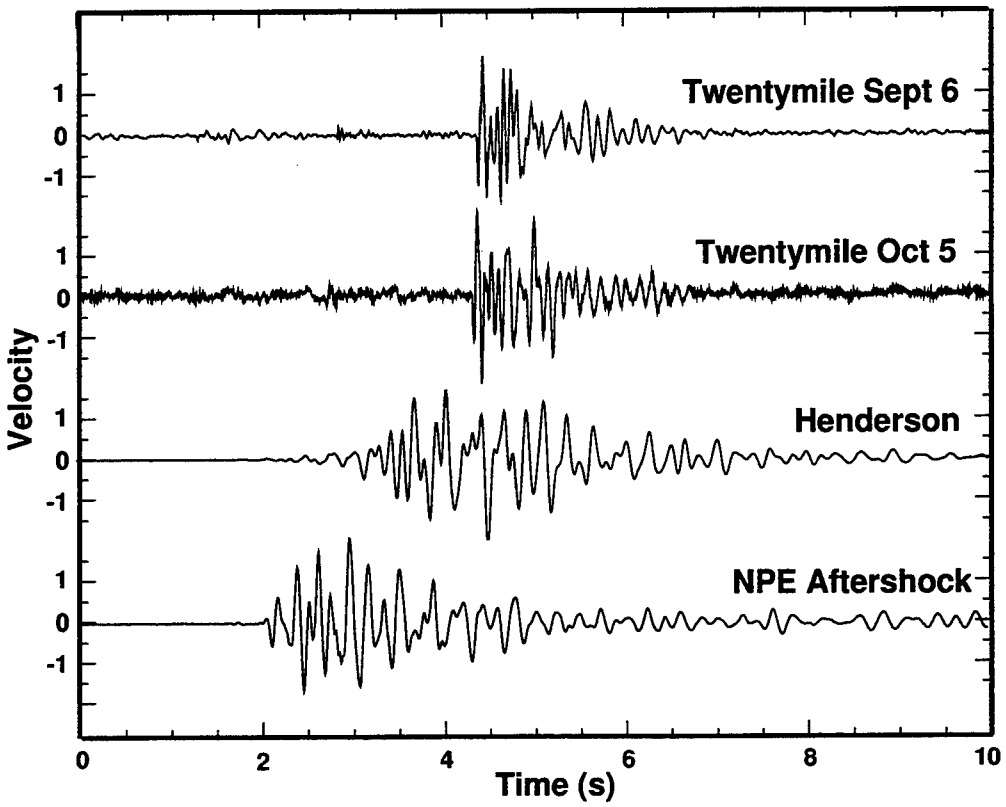

Figure 1. Aftershocks recorded in different settings. The top two signals are aftershocks typical of those recorded after main collapse events at the Twentymile mine. Note that these events are impulsive and have relatively high frequency energy. The lower two aftershock events are typical of those recorded at the Henderson mine and after the NPE. For the lower two events, note the emergent character and relatively low frequency energy content.

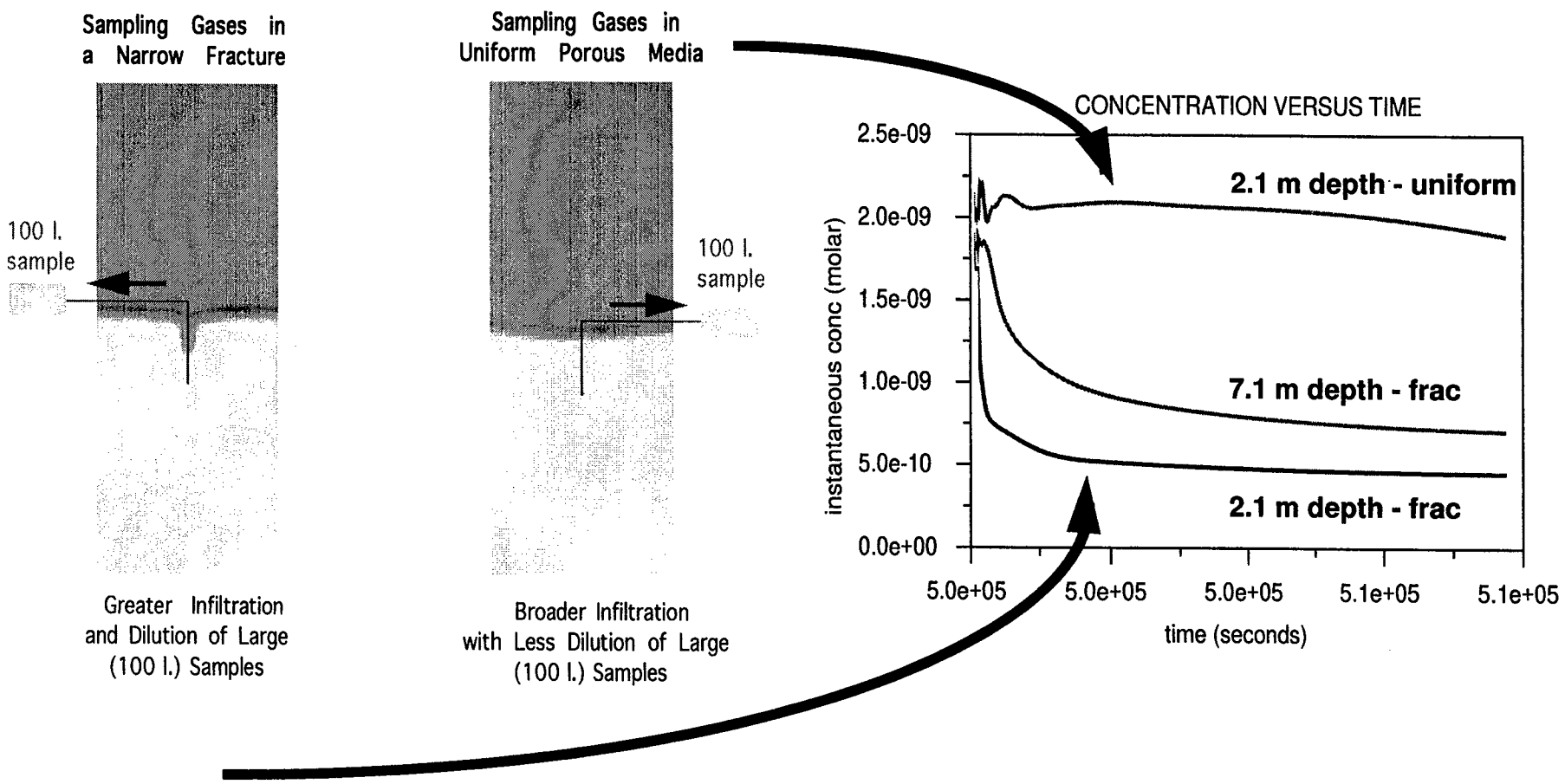

Figure 2. Results of model simulations of atmospheric infiltration while gases are being sampled. At left, sample is taken from a tube inserted into a narrow fracture. In the middle, the sample is taken from a uniform porous medium, with no fracture. The plot shows how concentration of a tracer gas is diluted over time by atmospheric infiltration in each case.

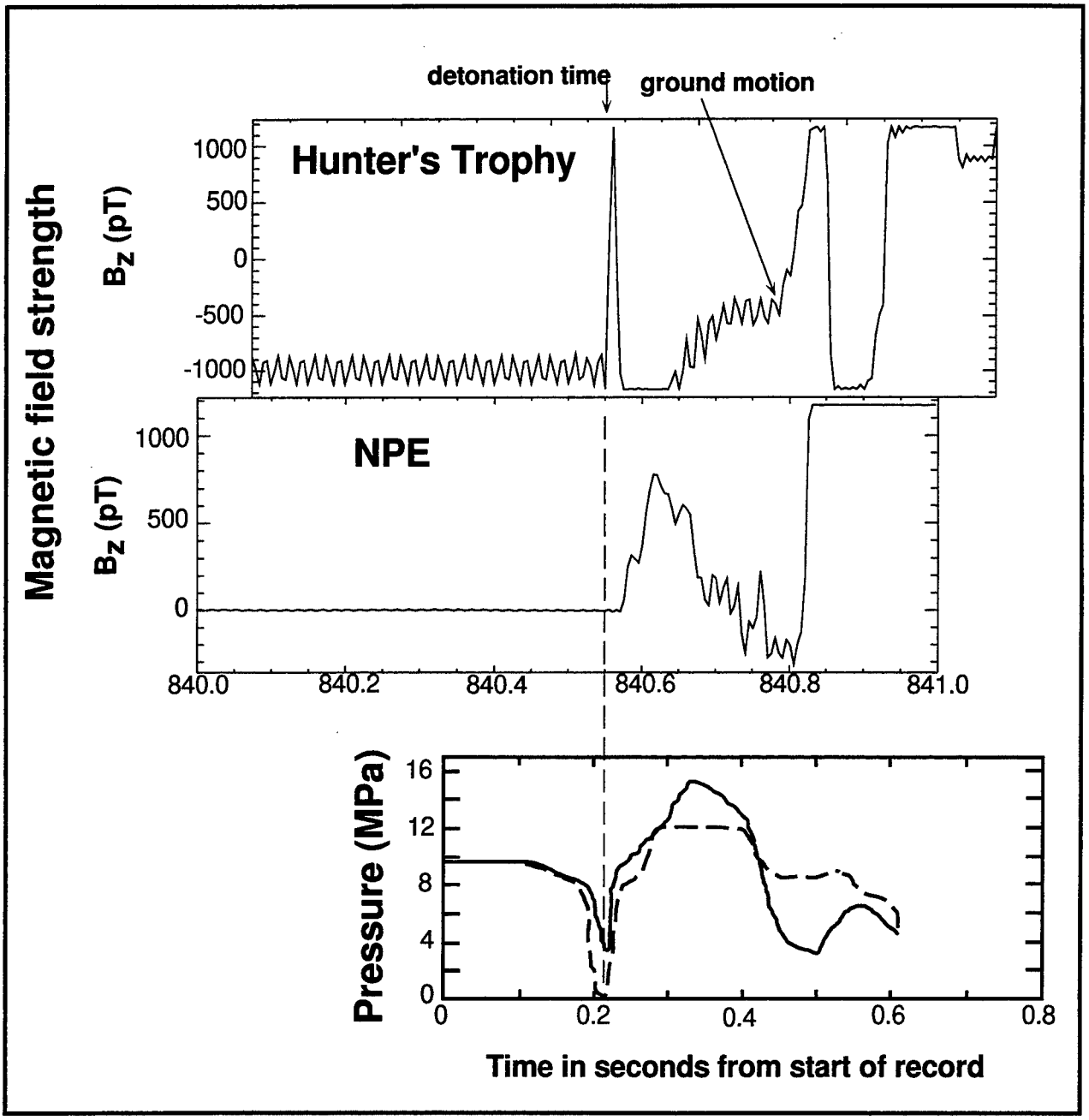

Figure 3. Low frequency magnetic field signals from a nuclear explosion (top - Hunter's Trophy) and a chemical explosion (middle - NPE) compared with the cavity pressure curve from the NPE (bottom - after Heinle et al., 1994). Note the similarity in duration and shape of the magnetic promt-time signal from the NPE with the pressure curves (the two pressure curves are from sensors at two different distances from the cavity). These curves are very different from the short-duration, high frequency pulse seen at detonation time from the nuclear explosion.

THIS PAGE LEFT
INTENTIONALLY
BLANK.

Physical Mechanisms of Quarry Blast Sources

T.G. Barker, K.L. McLaughlin and J.L. Stevens
S-CUBED Division of Maxwell Laboratories, Inc

Contract No. F19628-95-C-0112
Sponsored by DOE

ABSTRACT

Quarry mining practices vary considerably within the United States and worldwide, the variations reflecting the materials that are to mined, the means for removing and processing the materials, operator preferences, safety considerations and constraints imposed by nearby population and structures. Models of quarry blasts that can be used to develop efficient and robust methods for discriminating quarry blasts from other source must reflect the varied practices. The objective of this contract is to validate and extend the models using near-source and regional data, and numerical simulations, and to use the models to determine the sensitivity of proposed regional discriminants to varied mining practices.

Research in this program has focused on two efforts: (1) modeling the near-field and regional data taken at the Black Thunder Mine (Stump, et al, 1996), and (2) making 3 dimensional numerical simulations to investigate the effects of geometry, with comparisons to data collected at the Chemline quarry in central Texas (Bonner, et al.,1996). We have analyzed two large cast blasts and a coal shot from the Black Thunder Mine, and investigated the role of the firing pattern in the cast blasts on the time series and the role of site response on azimuthal variations. Several 3D numerical simulations were performed using the geometry of the central Texas quarry. These calculations used a recursive grid refinement scheme (McLaughlin and Day, 1994) which allowed resolution of the quarry shape to 5m while accurately propagating 1 to 5 Hz seismic signals to several km.

Keywords: Seismology, seismic discrimination, quarry blasts

OBJECTIVES

The objective of this project is to develop models for quarry blasts, validated by near-source and regional data. The models will then be used determine the sensitivity of proposed regional discriminants to varied mining practices.

RESEARCH ACCOMPLISHED

Research in this program has focused on two efforts: (1) modeling the near-field and regional data taken at the Black Thunder Mine (Stump, et al, 1996), and (2) making 3 dimensional numerical simulations to investigate the effects of geometry, with comparisons to data collected at the Chemline quarry in central Texas (Bonner, et al.,1996). We have analyzed two large cast blasts and a coal shot from the Black Thunder Mine, and investigated the role of the firing pattern in the cast blasts on the time series and the role of site response on azimuthal variations. Several 3D numerical simulations were performed using the geometry of the central Texas quarry. These calculations used a recursive grid refinement scheme (McLaughlin and Day, 1994) which allowed resolution of the quarry shape to 5m while accurately propagating 1 to 5 Hz seismic signals to several km.

CONCLUSIONS AND RECOMMENDATIONS

The character of the seismograms at the Black Thunder Mine is strongly dependent on the firing pattern, which has a long duration (several seconds) and on near surface low velocity earth structure. There are strong variations at recording sites on reclaimed land compared to those on unmined land. Analysis of more shots should allow us to discriminate site effects from geometrical effects due to the mine.

The 3D calculations show the linear effects of the quarry shape on the seismic signals. The simulations predict SH and P-SV patterns and ratios of vertical to horizontal motions consistent with observations and predict P-SV polarity reversals. The radiation patterns are not explained by a simple reduction in the component of the moment tensor normal to the bench.

Numerical Calculation Series

Several numerical experiments, diagrammed in Figure 1 and summarized in Table 1, were performed. First, an explosion source was placed in the upper 10 m of a laterally homogeneous layered half-space with no quarry present (shot _0). This "control" calculation could be compared with a wavenumber integration code for testing and validation. Next, the quarry pit was inserted into the finest grid (level 8 with 5 m resolution) by setting the elastic modulii of the appropriate cells to zero (shot_1). This implicitly forces the free surface boundary condition upon the topographic representation of the quarry pit. The explosion sources are inserted into the calculation by specifying the diagonal moment tensor components of appropriate cells with the relevant time delays. Each source was given a time function with a rise time of 0.25 seconds in order to remove spurious high frequencies from the calculation. This is equivalent to applying a lowpass filter to the resulting synthetic seismograms. Both single shots ($2.5*10^9$ Nt-m total explosion moment) and multiple shots ($1.0*10^{11}$ Nt-m total explosion moment) with ripple firing were simulated. Most simulations were run to between 3 and 4 seconds duration requiring between 48 and 72 hours of CPU time on an SGI R4000 workstation. Three components of velocity were saved on the free surface at every 160 or 640 m and every 0.01 or 0.04 sec. Several calculations were performed with the linear gradient velocity model (Table 2) instead of the original model of Bonner et al. (1996) (shot_0a, shot_1c, and shot_1d). No significant differences were seen in the results from the calculations with the linear gradients. conducted with the explosion source 10 m behind the quarry face rather than 5 m behind the quarry face.

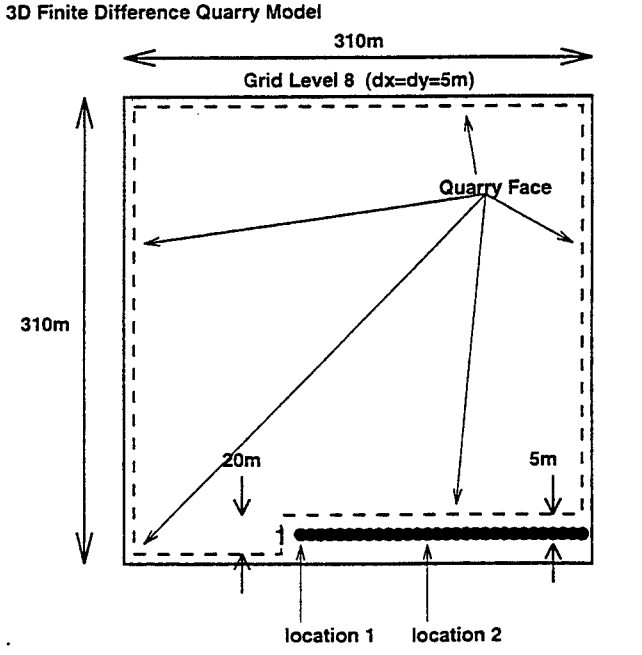

Figure 1. Diagram of the quarry models and shot locations used to simulate 3D wave propagation. The line of multiple shots 5m behind the bench is indicated by filled circles. Two single shot locaions #1 and #2 are labeled.

One calculation (shot_1e) was performed with lower P velocities in the upper layers

consistent with a Vp/Vs = 2 in order to test the sensitivity of the results upon the Poisson's ratio of the material. In order to test the sensitivity to the location of the shots behind the quarry face two locations were chosen for the single shots (see Figure 1). One calculation (shot_1d) was

Table 1. 3D Finite Difference Calculations

Run	Quarry Present Quarry Face	Velocity Model	Multiple/Single Shot Shot Location	Burden
shot_0	No	Original	single	-
shot_0a	No	Linear Gradient	single	-
shot_0b	No	Linear Gradient with Vp/Vs=1.67 in upper layers	single	-
shot_1	Yes South	Original	multiple fired ripple west-to-east	5 m
shot_1a	Yes South	Original	single - location 1	5 m
shot_1b	Yes South	Original	single - location 2	5 m
shot_1c	Yes South	Linear Gradient	single - location 1	5 m
shot_1d	Yes South	Linear Gradient	single - location 2	10 m
shot_1e	Yes South	Linear Gradient with Vp/Vs=1.67 in upper layers	single - location 2	5 m

In order to separate the effects of the ripple fire from the single shot and test the sensitivity of the radiation patterns upon location along the bench, we performed several single point explosion simulations listed in Table 1. It is easier to examine the individual phases of the point sources on the seismograms since they do not have the long source duration associated the ripple fire. Synthetic seismograms at a distance of 2 km from a single shot located 5 m behind an outside bench corner (shot_1a) are shown in Figure 2. The radiation patterns are shown in Figure 3. Note that the transverse radiation (Love Wave) pattern is shaped like a "figure 8" with the maxima oriented along the axis of the bench. The radial and vertical radiation (Rayleigh waves) are slightly larger in the directions across the quarry. These patterns are similar to the patterns observed by Bonner et al. (1996) although the synthetic Rayleigh wave patterns (shot_1a) do not have as large an amplitude pattern as the observed Rayleigh wave radiation patterns from the real quarry.

In summary, we have completed a set of three-dimensional elastic finite difference calculations (using the S-CUBED program TRES) designed to simulate the observations of mine blasts in central Texas by Bonner, et al. (1996). The calculations show the linear effects of the quarry shape on the seismic signals. The simulations predict SH and P-SV patterns and ratios of vertical to horizontal motions consistent with observations and predict P-SV polarity reversals. The radiation patterns are not explained by a simple reduction in the component of the moment tensor normal to the bench.

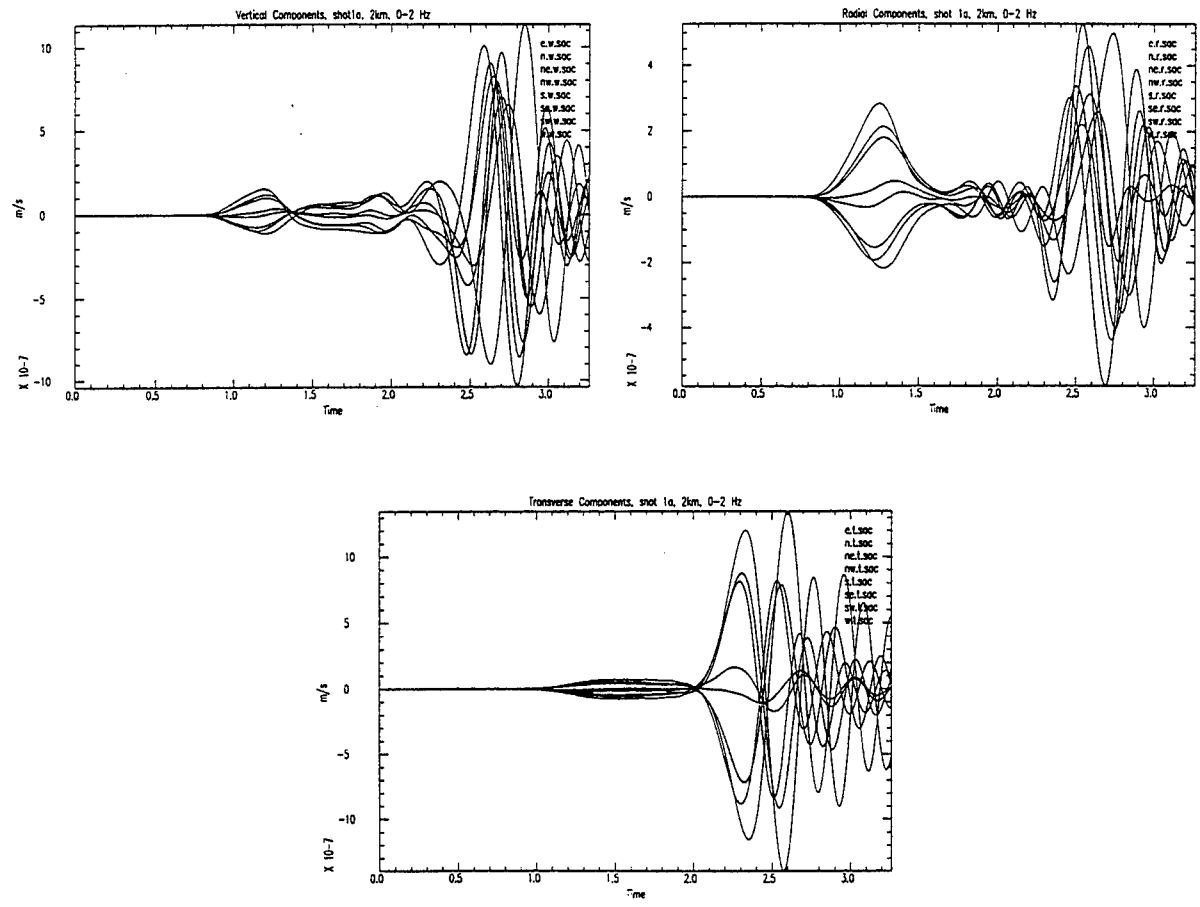

Figure 1. Vertical, radial, and transverse synthetic seismograms at a distance of 2 km from simulation shot_1a. Seismograms have been lowpass filtered at 2 Hz.

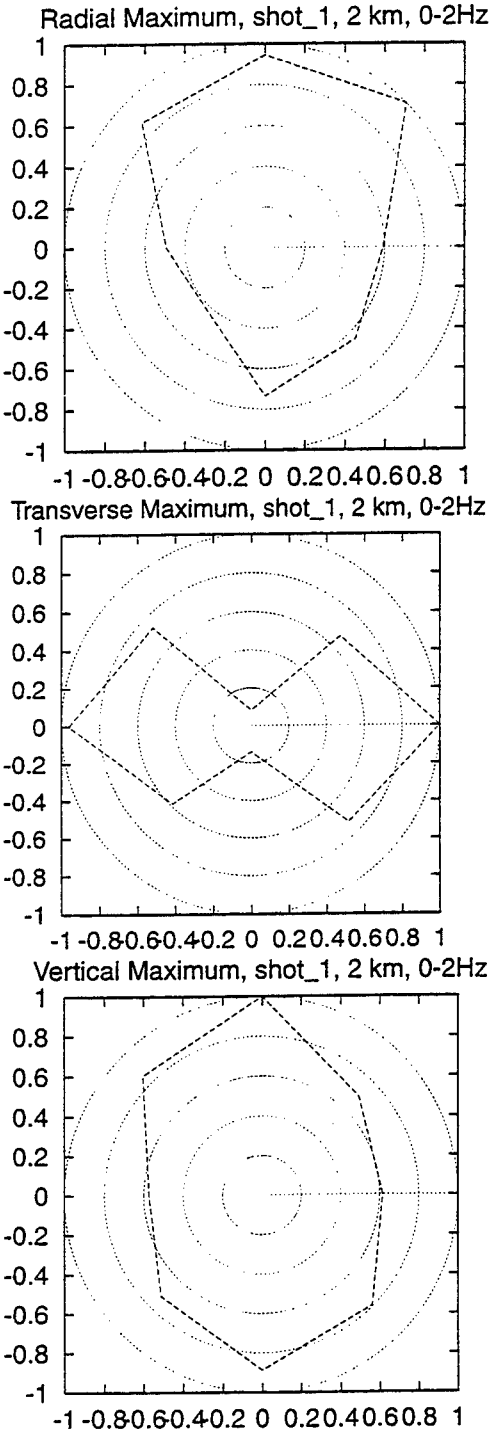

Figure 3. Radiation patterns are the maxima of the envelopes of the seismograms of Figure 2, Shot_1a.

Black Thunder Mine Series

Data for three shots described in Stump, et al. (1996) were made available to us by Dr. Craig Pearson at LANL. The shots are two large cast shots, and a single, contained coal shot. In Figure 4, we show the locations of the near-field recording sites relative to the cast shot done on Julian days 167 and 174 of 1996. Descriptions of the sensors can be found in Stump, et al. (1996). The plot shows the location of the pit (stippled area) at the time of these shots. Mining operations have proceeded from north to south, and the land is reclaimed after coal is removed. Thus, the highwall is on the south side of the pit. The cast blasts originated at the same location, with shot 167 (4.7 million lbs) propagating to the right, ending at the edge of the pit, and shot 174 (2.3million lbs) propagating to the left. The coal shot (day 236) is west of shot 167.

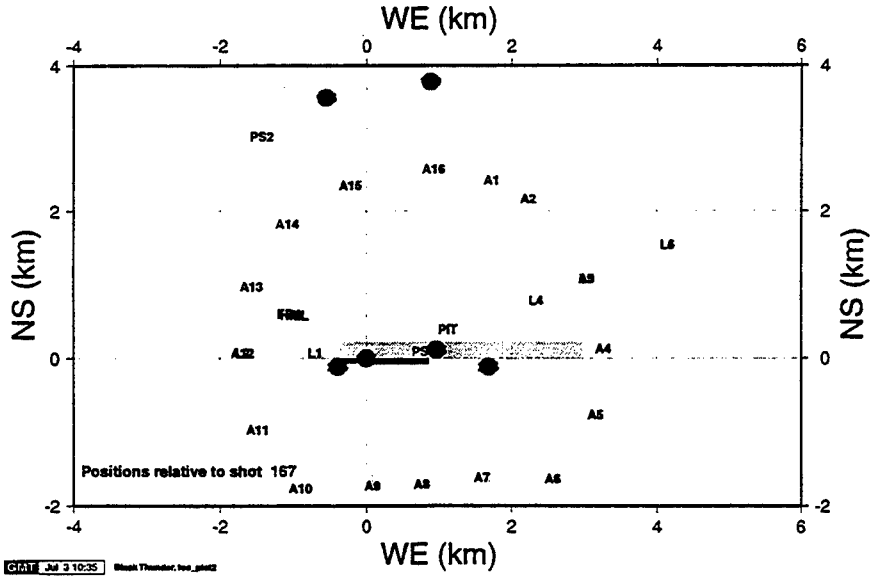

Figure 4. Locations of shots (circles) and recorders (triangles) relative to shot 167. The pit is shown as the stippled area.

We have focused on two aspects of the data: the differences between the coal and cast blasts and the azimuthal patterns. Coal shots are used to bulk (fracture) material prior to removal. This is accomplished by exploding vertical shot holes which cause the material to lift and drop, with little horizontal movement. These shots are usually ripple fired to minimize ground roll, but shot 236 was shot simultaneously, especially for this experiment. The cast shots are the standard ripple-fired, distributed shots which cast material horizontally from the highwall into the pit. Thus, the primary differences in coal and cast blasts from the point of view of this program are:

1. The coal shots have no horizontal movement and very little net vertical movement, while the cast shots have both. The effects of mass movement on seismic signals was investigated theoretically by Barker, et al. (1995). The horizontal motion produces a horizontal force in the direction of the mass movement, and a corresponding radiation

pattern. The vertical motion is causes band-limited signals peaked around between 0.2 and 1 Hz.

2. The coal shot (in this case) is localized temporally and spatially, while the cast shots are distributed. The finite duration of the signal (usually several seconds) has the effect of low-passing the data with a corner frequency of the inverse of the duration.
3. The cast shots occur on the side of the face to be removed, while the coal shot was detonated in the bottom of the pit. The geometrical effects have studied in the numerical experiments discussed above and in Barker, et al. (1994).

To investigate the role of the source time history, we convolved the firing pattern of the cast blasts with the coal shot. If there are no geometrical effects or effects due to mass movement, then the convolved results should match the cast shots. That is, if the firing pattern of the cast blast is $F_{cast}(t)$, the seismogram from the cast blast is $S_{cast}(t)$, and the seismogram if the coal shot is $S_{coal}(t)$, then we would have $S_{cast}(t) = S_{coal}(t) * F_{cast}(t)$. In Figure 5, we show the convolutions and seismograms for both cast blasts (167 and 174) at station A6. It can be seen that the firing pattern accounts for much of the differences between the coal and cast blasts, in particular the signal duration and peak amplitude. When recordings from other shots in the series become available, we can perhaps be more quantitative.

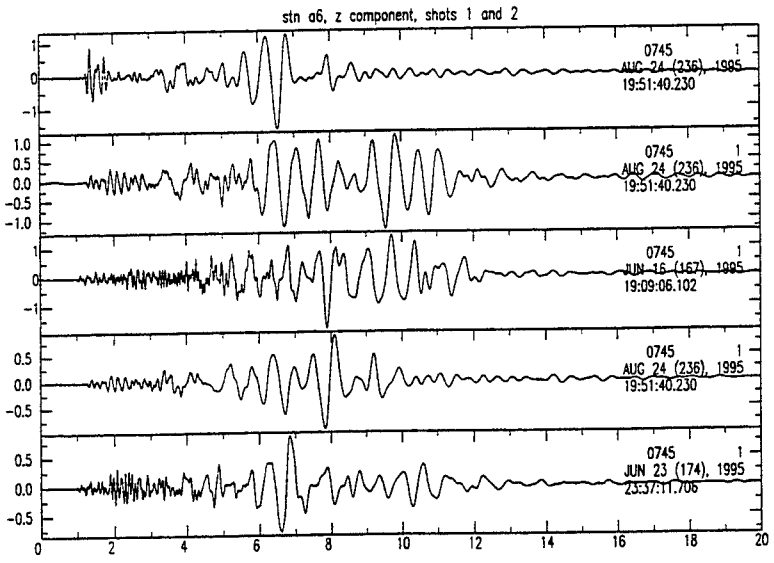

Figure 5. Time series from top are (1) the coal shot, (2) the coal shot convolved with the firing pattern for cast blast 167, (3) cast blast 167, (4) the coal shot convolved with the firing pattern for cast blast 174, (3) cast blast 174.

Figure 6 shows the radiation pattern of the transverse component from shot 167 at the "A" stations (Figure 4). Shown are the peak amplitudes, which are typically found in the Rayleigh wave and have frequencies near 1 Hz (see the seismograms in Figure 5). The station labels are shaded differently to indicate whether they are on reclaimed land (stations A1 to A4

and A14, A15) or unmined land (stations A5 to A13). The pattern for shot 174 is quite similar, with small amplitudes associated with reclaimed land and large amplitudes associated with unmined land.

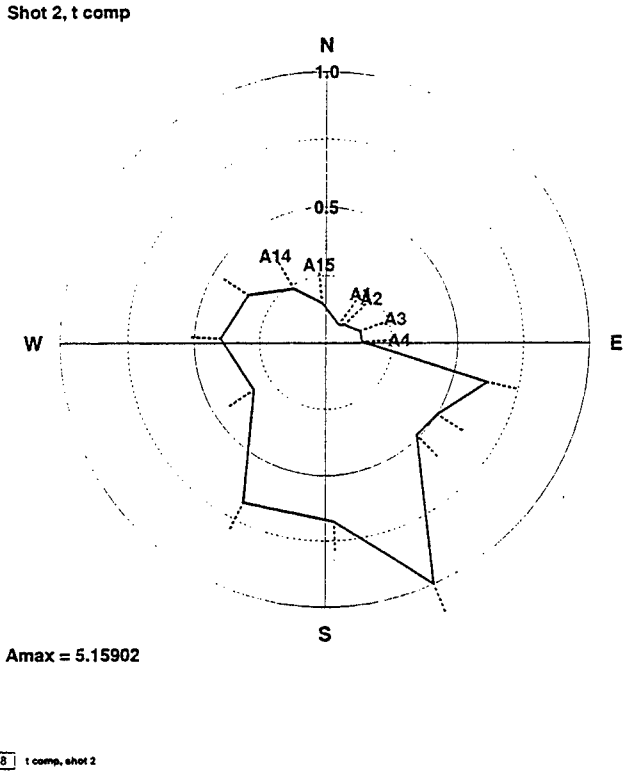

Figure 6. Radiation pattern of the transverse component from shot 167 at the "A" stations.

It is not possible with this limited data set to determine whether the radiation patterns are due primarily to path and propagation effects or to the geometry of the shots and the pit. We plan to examine data from additional Black Thunder shots and recordings of mining activity outside the mine at these stations to determine effective station corrections and site responses.

References

Barker, T.G., K.L. McLaughlin and J.L. Stevens (1993), "Numerical simulations of quarry Blast Sources", S-CUBED Technical Report to Phillips Laboratory, SSS-TR-93-13859 ADA265517

Bonner, J., E. Herrin and T. Goforth, 1996, "Azimuthal Variation of Rg Energy in Central Texas", submitted to *Bull. Seism. Soc. Am.*

McLaughlin, K.L. and S.M. Day (1994), "3D finite difference Modeling of Seismic Wave Propagation", *Computers in Physics*, Nov-Dec, 1994.

Stump, B.W., D.C. Pearson, R.L. Martin, P.E. Harben, C.L. Edwards, D. Baker, K. Kihara, K. Dalrymple, J.P. Lewis, D. Rock and R. Boyd, "The Black Thunder regional Seismic Experiment", LANL Report LAUL-95-3980.

Seismic Investigations of Rockbursts

T. J. Bennett, M. E. Marshall, K. L McLaughlin, B. W. Barker
and J. R. Murphy
Maxwell Laboratories, Inc., S-CUBED Division
11800 Sunrise Valley Dr., Suite 1212
Reston, Virginia 22091
Contract No. F 19628-94-C-0083
Sponsored by AFOSR

Abstract

Rockbursts or mining-induced seismic events present some interesting problems for seismic monitoring of potential nuclear explosion tests under a Comprehensive Test Ban Treaty (CTBT). Such events are frequent and occur in mining areas throughout the world at depths similar to those of nuclear tests. Theoretical and observational results suggest that some traditional discriminants, such as M_S-versus-m_b, might not be effective for some types of rockbursts. Another potential problem is that deliberate triggering of mine tremors might provide an evasion opportunity for nuclear explosion testing. Because many rockbursts are relatively small, regional discrimination techniques are important to their identification. Therefore, we have been conducting investigations of how regional discrimination methods can be applied effectively to the identification of rockbursts.

In some mining areas rockbursts occur quite regularly and are regarded as routine, while in other areas they are unusual and their unexpected occurrence can be catastrophic. In some of our prior work we investigated observations from several large events, including several in unusual source areas. Our recent investigations have focused primarily on rockbursts from areas where their occurrence is considered routine. In particular, we have been analyzing the characteristics of the regional signals from rockbursts in three repetitive source areas: (1) the South African gold-mining region, (2) coal-mining regions in Poland, and (3) a coal mine in eastern Kentucky. We have conducted bandpass filter analyses on samples of rockbursts from each of these source regions and determined L_g/P ratios as a function of frequency. Our results indicate that the L_g/P ratios tend to be fairly consistent between events from region to region and are generally larger than similar ratios for underground nuclear tests over a range of frequencies. Such differences appear to offer the best opportunities for discrimination.

Key Words: Seismic, Discrimination, Mechanism, Rockbursts, Earthquakes, Explosions, Regional, South Africa, Europe, North America, Evasion.

Objective

Rockbursts and related mine tremors present several challenges for seismic discrimination. Unlike earthquakes, which often occur at focal depths well below those normally associated with underground nuclear explosion tests, rockbursts are located in approximately the same depth range as nuclear tests; and, therefore, standard discriminants based on focal depth are not useful. Observations from several rockbursts suggest relatively weak long-period surface waves which could significantly reduce the effectiveness of the M_S-vs-m_b discriminant often used to distinguish between earthquakes and explosions. Therefore, the frequent occurrence of rockbursts and related events in mining regions throughout the world poses a potential problem for seismic monitoring at the levels currently considered of interest for the CTBT. Our principal objective has been to identify and test regional discriminants which can help facilitate the identification of these numerous rockbursts. For this purpose we have been pursuing analyses of empirical data from rockbursts in a variety of different mining, tectonic, and propagation environments. We have also been investigating theoretical techniques for modeling several of the varied rockburst mechanisms and their associated regional seismic signals in an effort to better characterize those types of rockbursts which are likely to be problematic for seismic discrimination. Finally, there is evidence in mining case histories that activation of rockbursts might be deliberately triggered, thereby providing an opportunity to conceal a clandestine nuclear test if the timing and size can be adequately predicted. We have been continuing to seek historical evidence supporting this predictive capability, and we plan to use the results of theoretical model studies to further assess mining conditions which might be required to effect such evasion scenarios.

Research Accomplished

As we have described at recent review meetings and in research reports, rockbursts or related mine tremors appear to present some unique problems for seismic discrimination under a CTBT. After investigating rockbursts and their seismic signals over the past few years, we have gained new insights with regard to rockburst occurrence around the world, physical processes and seismic mechanisms producing rockbursts, and the characteristics of the regional seismic signals which they generate. This understanding should be useful in determining the discrimination problems related to rockbursts in various areas and in identifying procedures to distinguish them from other source types based on their seismic signal characteristics.

Rockbursts occur in mining regions throughout the world. Over the course of our investigations, we have reviewed the behavior of seismic signals from rockbursts in several different source regions including (1) South Africa, (2) Central Europe, (3) Eastern U.S., (4) Western U.S., and (5) Russia. In some of these areas rockbursts are regarded as routine, and they occur frequently; while in other mining areas rockbursts are irregular and the unexpected occurrence of such events can be surprising and catastrophic. In prior reports (cf. Bennett et al., 1994, 1995) we have described several instances of catastrophic mine collapses (e.g. in 1989 in eastern Germany, in 1995 in Wyoming, and in 1995 in the Ural mountains of Russia) which are regarded as unusual for the regions where they occurred. In the most recent phase of this research program, we have focused primarily on observations from three areas where rockburst occurrence is routine. These source areas are (1) South Africa, (2) Central Europe, and (3) Eastern U.S. Because rockburst events are so frequent in these areas, we have been able to collect waveforms from several events in each source area enabling us to analyze the consistency of the observations from within specific source areas. Furthermore, in some of these areas, rockbursts occur in several different mines which permits us to look more closely at possible differences related to mining practice or sensitivities to propagation path differences.

For each of these more regular source areas, we have computed L_g/P ratios as a function of frequency -- a discriminant measure which has shown indications of promise in several prior investigations. In each area we utilized waveform data from a single high-quality seismic station located in the near-regional distance range (< 500 km). These stations were selected because they

consistently recorded good regional phases with generally high signal-to-noise ratios over a range of magnitudes for even the small rockburst events of interest. At larger ranges the weaker signals limit the useful frequency band for such small events, although the largest rockbursts often seem to produce fairly strong signals at larger regional distances (~ 1000 km). For each of the areas, we have performed a discrimination analysis comparing the frequency-dependent L_g/P ratios for the rockbursts with similar observations from nuclear explosion tests. The nuclear explosions are from other source regions, but the recordings are at comparable distance ranges to the rockbursts observations.

South Africa

Rockbursts, or mine tremors as they are called in South Africa, occur in association with deep (2 - 3 km) gold mines in an arcuate zone extending approximately 250 km from east of Johannesburg to the west and southwest into the Orange Free State. This zone is the site of large (magnitudes often greater than 5) and frequent induced seismicity. In an earlier study we analyzed regional signals recorded at the DWWSSN station at Silverton (SLR) from selected small events in this zone. More recently we have been collecting and analyzing regional seismograms from mine tremors in this area recorded at the high-quality digital station BOSA at Boshof (cf. Figure 1). This station is an IDC alpha station and records numerous regional events. For our analyses we have selected samples of these events from the IDC or NEIS catalogs. Figure 1 shows the locations of 21 events within the last two years with magnitudes in the range from 3.5 M_L to 5.1 M_L which we have been working with. The locations of the events within the seismic zone vary and indicate association of the tremors with at least three or four distinct mining areas within the overall zone. Epicentral distances to BOSA cover a range from about 160 km to 390 km. For these events we have performed bandpass filter analyses (as described at previous meetings and in prior reports) on the broadband vertical-component records at BOSA. From the bandpass filter output, we measured the maximum signal amplitudes in the L_g and P group velocity windows and computed L_g/P ratios as a function of the filter center frequencies. As part of a separate research project reported elsewhere, we are currently seeking to refine amplitude spectral measurement procedures to identify more robust discrimination methods for application to regional phase spectral ratios and to help understand the physical basis for the L_g/P discriminant.

Figure 2 shows the average L_g/P ratio as a function of filter center frequency for 10 South African mine tremors. The 10 events include five in the Orange Free State mining area at an average epicentral distance of 163 km and five in the Far Western Rand mining area at an average distance of 326 km. For the plot in Figure 2, we grouped all 10 events. In general, the average L_g/P ratios for the South African mine tremors lie well above one. From a high value near four just above 1 Hz, the average L_g/P ratios show a gradual decline to values above two at high frequencies. The L_g/P ratios were somewhat larger for the mine tremors in the nearer mining area over most of the frequency band analyzed. Additional analyses are needed to determine whether such differences are significant and whether they can be related to propagation effects or variation in mining practice. The L_g/P ratio measurements for the two subsets overlap at the one sigma level, and at high frequencies the mean values for one subset fall within one sigma of the mean of the alternate subset.

For comparison we show in the figure the average L_g/P ratios determined from the same bandpass filter analysis applied to 10 NTS underground nuclear explosions measured at the four Lawrence Livermore Laboratory stations at ranges between 230 km and 410 km. The average L_g/P ratios for the NTS nuclear explosions have values somewhat greater than one at frequencies from 0.5 Hz to 2 Hz but fall off to below one at frequencies above 3 Hz. At the lowest frequency there is no difference in the average L_g/P ratios between the South African tremors and the NTS nuclear tests, but above 1 Hz there is a clear separation between the average values. The L_g/P ratios for the NTS nuclear explosions are fairly consistent between events and as a result the sigma values are fairly low over most of the frequency band. The scatter about the mean L_g/P

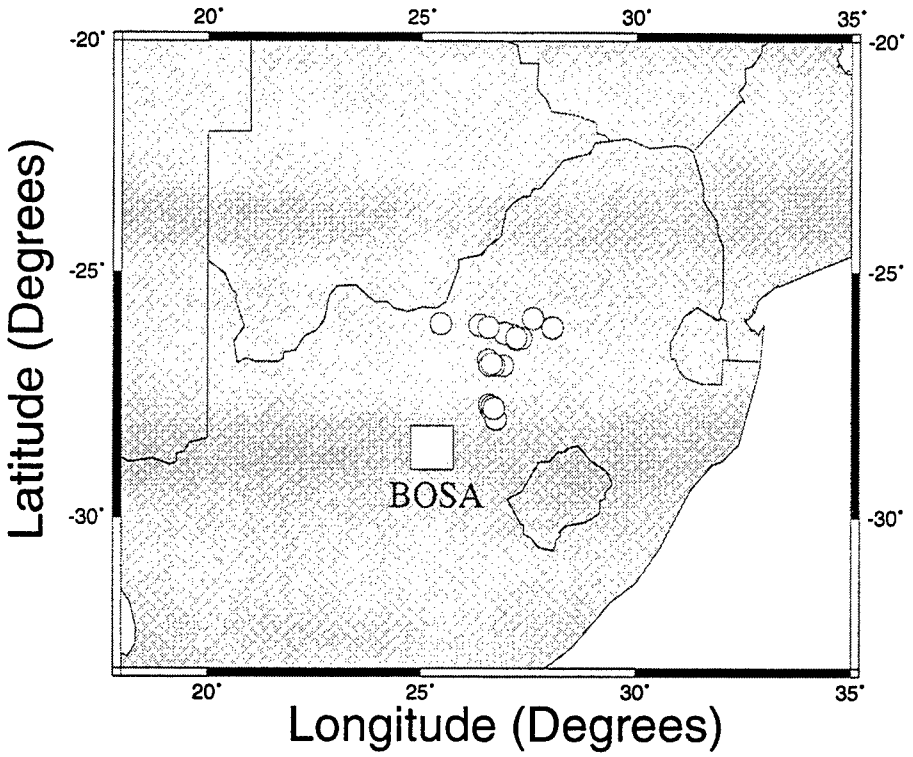

Figure 1. Locations of 21 South African mine tremors relative to station BOSA.

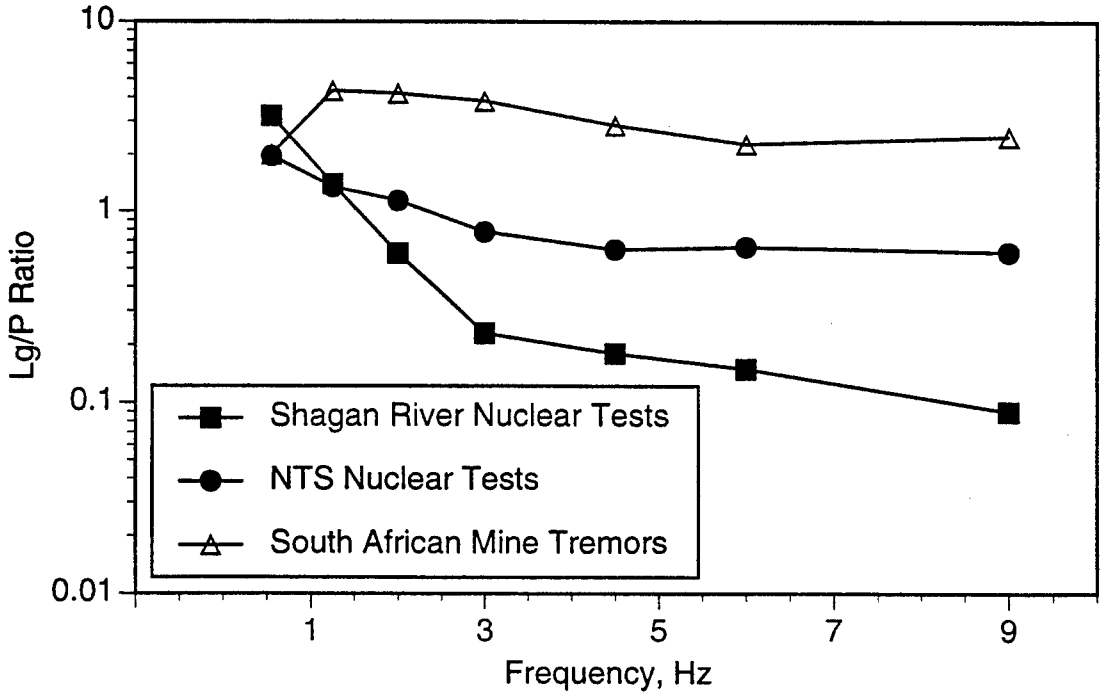

Figure 2. Comparison of average Lg/P ratios as a function of frequency for 10 South African mine tremors and 10 NTS and 10 Shagan River nuclear tests.

ratios is considerably larger for the South African mine tremors at all frequencies, and this is reflected in larger sigma values. Nevertheless, at frequencies of 2 Hz and above the two populations are completely separate at the one sigma level.

As a second comparison we also show in Figure 2 the average L_g/P ratios previously determined from the same bandpass filter analysis applied to 10 nuclear explosions at the former Soviet test site at Shagan River observed at the CDSN station WMQ. The epicentral distance in this case (~ 950 km) is much larger than for our South African mine tremor observations. The average L_g/P ratios from the Shagan River explosions fall well below the mine tremor ratios except at the lowest frequency. The L_g/P scatter was also found to be small for this explosion sample. The observed differences appear to provide the basis for a possible discriminant. The figure also suggests significant differences in average L_g/P ratios between nuclear tests in the two different source areas. This problem is currently under investigation within a separate research project to better understand the physical basis for the L_g/P ratio discriminant measures, as noted above.

Central Europe

Rockburst activity in Poland occurs principally in two zones. The eastern zone of induced seismicity (cf. Figure 3) is associated with coal mining in Upper Silesia and includes the surface mines in the vicinity of Belchatow. The western zone includes seismicity associated with coal mining in Lower Silesia and copper mining near the town of Lubin. The induced seismic activity in these areas has been frequent and occasionally large (with magnitudes approaching 5). In a prior study we analyzed regional signals from several of these events recorded at the Grafenburg array station GRFO. In our more recent investigations we have collected and analyzed the regional signals at the GERESS array, an IDC alpha station, for selected events from the two Polish mining regions. Figure 3 shows the locations of 40 events in the last two years which we have analyzed. The events were selected from the IDC or NEIS catalogs and include distance ranges to GERESS from 290 km to 365 km for Lower Silesia events and ranges from 360 km to 450 km for the Upper Silesia events. The magnitudes for the events cover a range between 2.6 M_L and 4.1 M_L. The same bandpass filter analyses as described above were performed on the vertical-component records at a selected GERESS array element (normally GEC2), and L_g/P ratios as a function of frequency were determined.

Figure 4 shows the results of the L_g/P measurements determined from the bandpass filter analysis applied to 20 Polish rockbursts. The events included 10 events from the Upper Silesia area and 10 from the Lower Silesia/Lubin source area. The average L_g/P behavior for the Polish rockbursts is very similar to that which we saw in Figure 2 for the South African mine tremors. The ratios are high (near four) at low frequencies and slowly decreases to values somewhat below two at the higher frequencies. There again appear to be some differences in the ratios between the two source areas. In this case the average ratios are seen to be somewhat higher at most frequencies for the rockbursts in the more distant source region, viz. Upper Silesia. The sigma values were again found to be fairly large for the rockburst L_g/P ratios, so that differences between the two source areas are probably not significant. On the other hand, the differences in L_g/P ratios between Polish rockbursts and the nuclear explosion tests are probably significant. Although the observations again overlap at the one sigma level at lower frequencies, above about 2 Hz the sigma values are lower; and there seems to be significant separation between the source types.

Eastern U.S.

Rockbursts have historically occurred at numerous mines around the eastern U.S. These events associated with coal mining are called mine bumps and have been particular problems at some mines. In this study we have focused on the rockburst activity at a single coal mine in eastern Kentucky. This mine has had a long history of mine bump activity and has been notably active in recent years. For our investigation we have analyzed waveform data recorded at the high-quality digital station BLA in Blacksburg, Virginia, an auxiliary station in the IDC network.

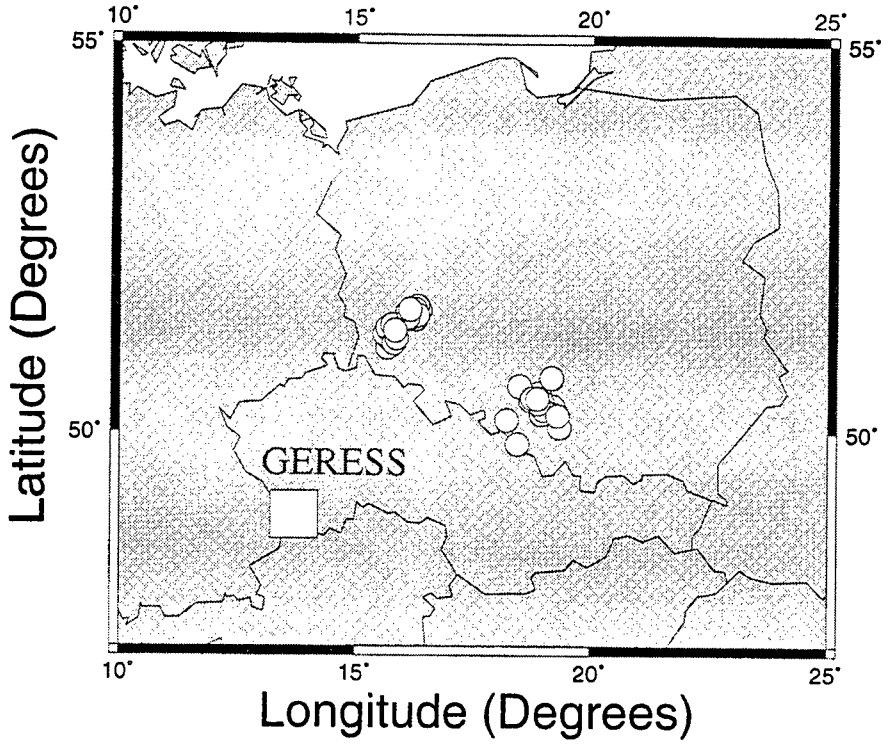

Figure 3. Locations of 40 Polish rockbursts relative to Geress array.

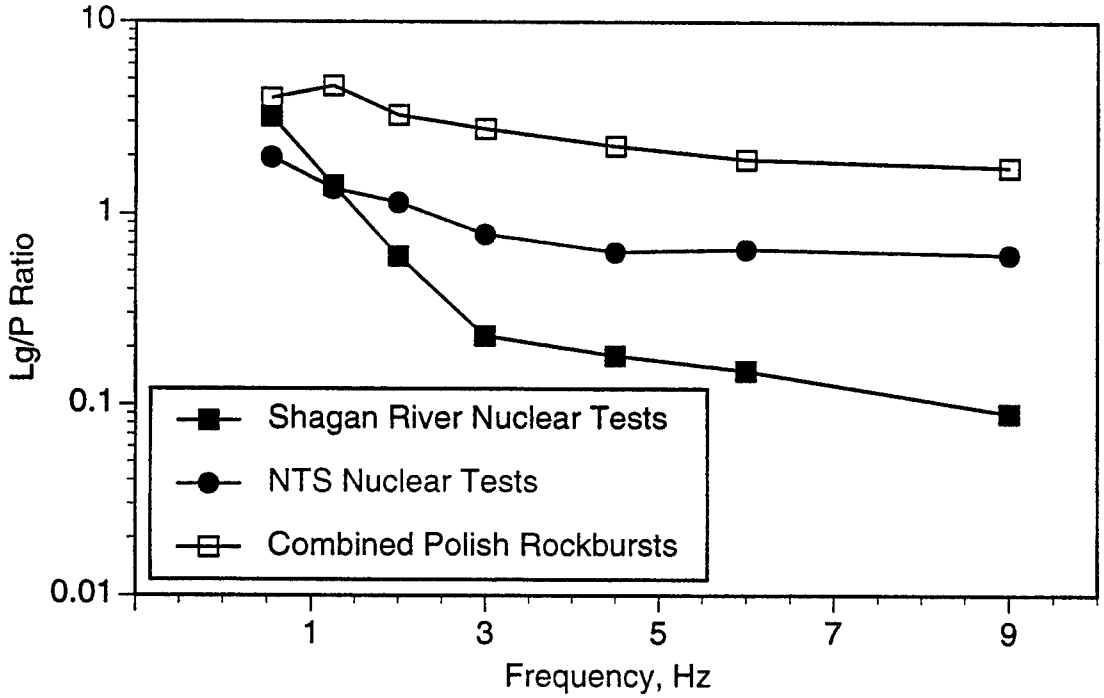

Figure 4. Comparison of average Lg/P ratios as a function of frequency for 20 Polish rockbursts and 10 NTS and 10 Shagan River nuclear tests.

Figure 5 shows the location of the mine relative to station BLA. Waveform data recorded at BLA for 19 bumps occurring in the last two years were kindly provided by Martin Chapman at Virginia Tech and Carol Finn at AFTAC. The epicentral distance from BLA to the mine is about 235 km, and the selected events cover magnitudes from approximately 2.3 M_L to 4.3 M_L. We again applied the same bandpass filter analyses to the broadband, vertical-component records at BLA for these events and measured the L_g/P ratios as a function of frequency.

For the eastern Kentucky coal mine bumps, we performed the bandpass filter analysis and measured the L_g/P ratios for 11 events. The average ratios versus filter center frequency are show in Figure 6. The average L_g/P ratios start out at high values in the 4 - 5 range at lower frequencies but drop off more rapidly above 3 Hz. Thus, at higher frequencies the average ratios for the eastern Kentucky mine bumps approach values near one. Comparing to the nuclear explosion L_g/P ratios, we see much less separation between the explosion average and the average for the eastern Kentucky mine bumps at high frequencies. However, the scatter about the mean for the eastern Kentucky mine bump observations is much smaller than for the rockbursts described above from the other source areas. This reduction in scatter may be attributable to the common propagation path or uniformity of rockburst mechanisms from within the eastern Kentucky mine in contrast to more diverse source mechanisms and propagation conditions from the multiple mines in other rockburst source regions. In any case, although the average L_g/P ratios are not so well separated for the eastern Kentucky bumps and nuclear explosions, as a result of the smaller sigma values there is total separation in the ratios at the one sigma level over the broad band of frequencies from 0.5 Hz to 4.5 Hz. Even with the reduced scatter in the observations, the proximity between the L_g/P average ratios for the mine bumps and NTS explosions at the highest frequencies (viz. 6 Hz and 9 Hz) causes them to overlap somewhat at the one sigma level. So, for eastern Kentucky we again see differences in L_g/P ratios between rockbursts and underground explosions; but the frequency bands most useful for discrimination there may be different.

Conclusions and Recommendations

Rockbursts pose some unique problems for seismic discrimination under a CTBT. Rockbursts are expected to be frequent in many areas at magnitudes which are likely to be of interest in treaty monitoring. Observations and theoretical studies seem to confirm that some rockburst mechanisms are inefficient in generating long-period Rayleigh waves, which could cause such events to look like explosions with respect to the traditional M_S-versus-m_b discriminant. However, a promising discriminant for rockbursts appears to be their consistently large S/P or L_g/P ratios. We have found in the studies reported here for three mining areas (viz. South Africa, Central Europe, and Eastern U.S.) that rockbursts show a consistent pattern in L_g/P ratios as a function of frequency which should in many cases distinguish them from potential nuclear explosion tests. One weakness in our empirical comparisons is that the nuclear explosion and rockburst source areas are not the same, so we have been forced to ignore some possible propagation differences. Additional research (both theoretical and empirical) is needed to improve understanding of rockburst behavior in regions with little or no experience and to resolve issues related to rockburst predictability and the potential for concealing nearby simultaneous nuclear tests.

References

Bennett, T. J., M. E. Marshall, B. W. Barker, and J. R. Murphy (1994). "Characteristics of Rockbursts for Use in Seismic Discrimination," PL-TR-94-2269 , ADA290881

Bennett, T. J., K. L. McLaughlin, M. E. Marshall, B. W. Barker, and J. R. Murphy (1995). "Investigations of the Seismic Characteristics of Rockbursts," PL-TR-95-2169, ADA304549

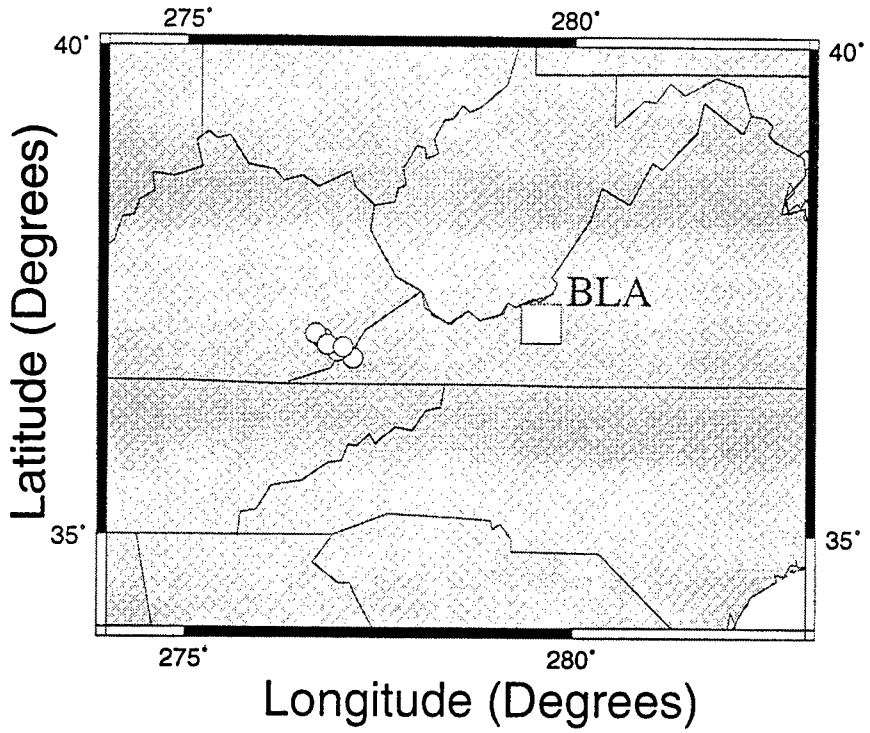

Figure 5. Locations of 19 eastern Kentucky mine bumps relative to station BLA.

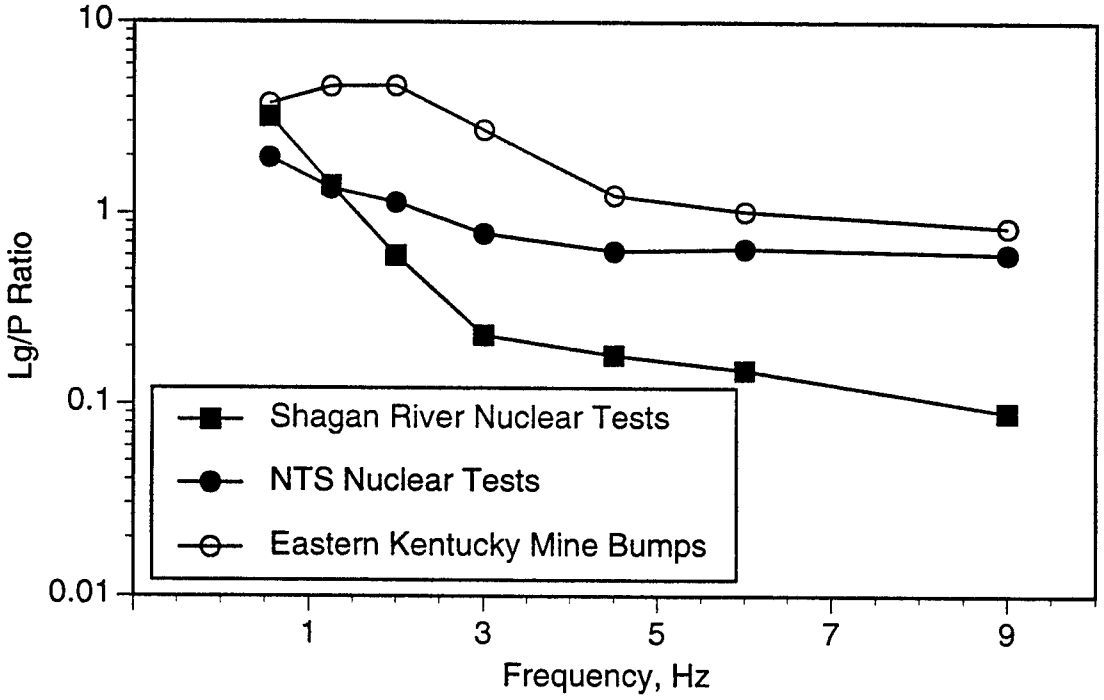

Figure 6. Comparison of average Lg/P ratios as a function of frequency for 11 Eastern Kentucky mine bumps and 10 NTS and 10 Shagan River nuclear tests.

Seismic Characterization of Commercial Blasting Practice in an Open-Pit Gold Mine

L. A. Glenn, S. P. Jarpe, and P. Goldstein
Geophysics and Global Security Department
Lawrence Livermore National Laboratory
University of California

Sponsored by U.S. Department of Energy, Contract #W-7405-Eng-48
Comprehensive Test Ban Treaty Research and Development Program, ST482B

ABSTRACT

Under the right conditions, chemical explosions can appear on seismic records as nuclear explosions. Therefore, as part of the DOE's Field Program, we have conducted an investigation of surface mining blasts in metamorphic rock in the Carlin, NV area, for which extensive ground truth was obtained. Coda amplitudes were derived for 61 blasts from seismic records obtained at station ELK, located roughly 80 km from the mine. Of the 61 blasts, 48 were production shots, 5 were waste shots (meaning that their purpose was to break up overburden, rather than directly produce ore) and 8 were combined shots, in which a waste shot was directly followed or preceded by a production shot. The objectives of this investigation were to: 1) assess the effectiveness of spectral methods for identifying ripple-fired quarry blasts and for detecting a nuclear explosion fired simultaneously with these quarry blasts, and 2) determine whether the seismic magnitude of the quarry blasts could be related to explosion parameters such as total yield, duration of blast, or number of delays. Two spectral discriminants were used to identify ripple-fired explosions and both were tested by superimposing a simulated fully decoupled one kiloton nuclear explosion on each of the commercial blasts. The main result was that both discriminants consistently identified ripple firing, with a relatively small number of false alarms, provided appropriate thresholds were set. In most cases, when the decoupled explosion was superimposed it was easily identified as not being ripple fired, but this may be due to the relatively small magnitudes of the quarry blasts. We were unable to correlate the total yield of the quarry blasts, nor any other shot parameters, with the seismic amplitude.

KEY WORDS: Explosions, Spectral Discrimination, Quarry Blasts, Magnitude

INTRODUCTION

It is well known that chemical explosions can appear on seismic records as nuclear explosions under the right conditions. It is obviously important, in monitoring a comprehensive test ban treaty (CTBT), to be able to distinguish one from the other since mines throughout the world routinely employ chemical explosives in large quantities. In conventional mining practice, large-scale explosions are normally conducted in what is known as ripple-fired mode. With this technique, an array of holes is drilled, filled with explosives, tamped, and then fired in a spatial and temporal sequence designed to obtain maximum efficiency in rock comminution while, at the same time, reducing to a minimum ground motions in areas proximal to the mine and material thrown into the air. It is easy to show that the seismic signature from this kind of explosion can, in principle at least, be distinguished from that produced by an underground nuclear explosion (UNE). In the former case, and for simple shot patterns and delays, a regular, time-independent spectral modulation is predicted in the signal, where the characteristic frequency is inversely proportional to the programmed delay. Spectral modulation has been observed by several investigators [Stump and Reamer (1988), Smith (1989), Hedlin et al. (1989, 1990), Chapman et al. (1992), Kim et al. (1994)]. When the shot patterns are not simple and the delays sufficiently irregular, however, the spectral modulation may diminish or disappear altogether. A significant fraction of supposedly ripple fired blasts reported in the above-cited literature could not be identified as having been ripple fired via spectral analysis.

As suggested by the conventional practice, ripple firing also is predicted to reduce the amplitude of the seismic signal by up to several orders of magnitude. It has been argued [Richards (1994)] that the great majority of mining blasts are unlikely to be confused for underground nuclear explosions because only about 10 to 30 chemical explosions per year in the U. S. are detected teleseismically with magnitudes greater than 3.0 (and, by extension, the number worldwide would presumably not be significantly greater). However, clandestine nuclear explosions would likely be carried out in large cavities; assuming, conservatively, that a decoupling factor of 50 is achieved in such a cavity, a kiloton nuclear explosion would produce an m_b of 2.1 in tectonically active areas (based on the scale developed by Vergino and Mensing (1990) for the Nevada Test Site). Clearly, a very large number of mines worldwide perform explosions at this level. Hence, even the verification of a kiloton threshold might require discriminating between many mine explosions each day and the (hopefully) occasional attempt at evasion.

RESEARCH ACCOMPLISHED

Identifying Ripple-Fired Quarry Blasts

Under a CTBT many mining events will need to be identified. It will also be important to know how likely it is that such events could be used to hide a simultaneously detonated nuclear explosion. In this report, we test two techniques for identifying ripple-fired quarry blasts at a gold mine in the Carlin, Nevada region and simulate the effects of superposing a kiloton, decoupled nuclear explosion on these quarry blasts.

A potential CTBT evader might attempt to use commercial blasting to conceal underground testing. One tactic for so doing is to simultaneously detonate the nuclear explosion with a conventional quarry blast in such a way that the seismic signal from the explosion would be indistinguishable from that of the quarry blast alone. Our main objective in the current investigation was to determine whether it was feasible to identify this attempt at evasion by using spectral analysis of the combined seismogram.

We obtained the cooperation of the Newmont Gold Company (NGC), which operates an extensive open-pit gold mining operation in the Carlin, NV area. Their largest pit is called Gold Quarry, in which they conduct two to three explosions each week, with yields ranging from 25-150 tons. This seemed to be an excellent range in which to test the combined-explosion scenario. Since the body-wave magnitude is conventionally related to yield by an expression of the form: $m_b = a + b \log_{10} W$, where a and b are constants, it is easy to show that the yield decoupling factor, $f_W = f^{1/b}$, where f is the amplitude decoupling factor. A fully decoupled nuclear explosion would have f at least equal to 50 [Glenn and Goldstein (1994)] and, typically, $0.8 < b < 0.9$, so that f_W would then be in the range $77 < f_W < 133$. In other words, a one kiloton decoupled explosion would produce the same seismic amplitude as a tamped explosion with yield in the range $7.5 < W < 13$ tons, which would fit very well in the yield range exhibited at Gold Quarry.

In the period between April 11 through September 20, 1995 we recorded 70 Gold Quarry blasts at the LLNL permanent seismic station ELK, located 80 km to the east of the mine [Jarpe *et al.* (1996)]. We also recorded the blasts at several close-in sites, which allowed us to positively identify the time and location of the blasts and we obtained blasting logs, which provided detailed information on shot geometry, amount of explosive in each hole, and the time interval between explosions in adjacent holes (delays). Of the 70 blasts recorded at ELK, we were able to obtain coda amplitudes from 61. Of the 61, 48 were production shots, 5 were

waste shots (so-called because their purpose was to break up overburden rather than directly produce ore), and 8 were combined shots, in which a waste shot was directly followed or preceded by a production shot. 34 out of the 48 production shots were of multiple pattern, in which the orientation of the rows of charges, or the delays between rows, varied within a shot.

The seismic records at ELK were analyzed by constructing high-resolution spectograms and binary sonograms to identify events that were characterized by time-independent spectral modulation. Each spectogram consisted of a time sequence of spectral amplitudes obtained by windowing a 2 second segment of data, applying a 5% Hamming taper, computing the auto-correlation function, and finally calculating the maximum entropy power spectrum. We used a 1 second overlap between successive windows. Color spectograms were obtained by converting the spectral amplitudes to integers between 0 and 255 and assigning a separate color to each integer. Binary sonograms were then computed by taking the difference between spectograms smoothed over a 10 Hz bandwidth and the corresponding unsmoothed spectograms, and then setting all negative values to zero (white) and positive values to unity (black). Time independent spectral modulation is represented by continuous horizontal bands in both spectograms and sonograms that are not present in pre-event noise. A similar proceedure was first employed by Hedlin *et al.* (1989).

Two methods were employed to automatically test for time independent spectral modulation. Wüster (1990) integrated the binary sonograms in discrete frequency windows over a time domain that included the pre-event noise. The resulting integrals were normalized to approximate a bounded, continuous, band limited function, I_W. Peaks in I_W that exceeded a given threshold, and were not present in pre-event noise, were taken to signify a ripple-fired explosion. The second discriminant was based on the method developed by Hedlin *et al.* (1990). In our modification, we computed the maximum-entropy power spectra of the Wüster integrals to obtain time-independent amplitude functions, A_H, which were then thresholded to obtain the discriminant. Figures 1 and 2 show binary sonograms, together with plots of I_W as a function of frequency and A_H as a function of quefrency, for a typical production shot and a typical waste shot.

To evaluate the scenario in which an underground nuclear explosion is caused to occur during a ripple fired mine blast we superimposed a simulated fully decoupled 1 kiloton explosion on each of the seismic records obtained from the Gold Quarry. The simulated explosion was created by convolving a scaled source function from the 1 kiloton Non-Proliferation Experi-

ment (NPE) with an empirically derived Green's function obtained from NPE data at a range of 85 km, the same approximate distance as the Gold Quarry is to ELK. The source function for the decoupled explosion was derived from the NPE source [Goldstein and Jarpe (1994)] by dividing the long-period amplitude by a factor of 100, and assuming a flat spectrum to $f = 15$ Hz, which then decayed as f^{-2} at higher frequencies.

When we used the Wüster discriminant, 45 of the 70 blasts passed a signal-to-noise test both before and after adding the decoupled explosion. Using a decision threshold of 0.75, after Wüster, 39 of the 45 were classified as ripple fired before the decoupled shot was superimposed and all 39 failed the ripple-fire test after superimposition.

We determined the threshold for the modified Hedlin discriminant by comparing the Gold Quarry blasts with our database of nearby shallow earthquakes recorded at ELK. Figure 3 shows $\tilde{A}_H$, the peak value of A_H, plotted as a function of magnitude for both quarry blasts and earthquakes. All 70 blasts lie above the line $\tilde{A}_H = 0.17$, which was taken to be the threshold for identifying a ripple-fired explosion (even though a small number of earthquakes are misidentified with this criterion). When the simulated decoupled explosion was superimposed, all but 2 of the 70 blasts failed the ripple-fire test.

Effect of Shot Parameters on Seismic Magnitude

Magnitudes for the Gold Quarry blasts were calculated from data recorded at ELK using the coda method of Mayeda (1993) because it was found that, for explosions at the Nevada Test Site (NTS), the random errors (standard deviation) in the single-station coda magnitudes were a factor of 6 smaller than for other single-station magnitude measurements. Also, because of the relatively short distance between Gold Quarry and ELK, P_n-phase amplitudes were not readily available. ELK station recordings were used to calibrate the coda magnitude scale. For each NTS explosion, we determined the network averaged P_n-phase amplitude, A_{P_n}, as well as A_{C2}, the average (of the two horizontal recordings at ELK) of the distance corrected "coda amplitude" measurements in the 1-2 Hz band [Mayeda and Walter (1995)]. The distance corrections were made assuming that coda amplitude is proportional to $r^{-\gamma}$, where r is the epicentral distance and γ is 0.3. From the measured values of A_{P_n} we determined $\bar{m}_b$, the (four-station) network averaged $m_b(P_n)$, using the correlation obtained by Denny *et al.* (1987). We then calculated the best fitting relationship between the logarithm of A_{C2} and $\bar{m}_b$ and used this relationship to derive m_b for the Gold Quarry blasts.

Figure 4 plots this magnitude as a function of total yield for the 61 blasts for which coda amplitudes could be measured. A regression line through these data indicates no correlation between magnitude and yield. We have also plotted the regression line derived by Vergino and Mensing (1990) for explosions at the NTS. All the Gold Quarry blasts fall below this line and its extrapolation. We also searched for a correlation between magnitude and the number of delays, the total shot duration, and the average energy release rate (total yield divided by total duration of blast). The latter parameter had the greatest measurable effect, but the correlation coefficient was only 0.32.

CONCLUSIONS

We identified ripple-fired quarry blasts in the Carlin, Nevada gold mining region using techniques that search for spectral modulation in the seismic records. When combined with a simulated 1 kiloton decoupled nuclear explosion, most of these quarry blasts did not appear to be ripple-fired. However, eeven though the yield of many of the quarry blasts was significantly larger than the decoupled nuclear explosion, the magnitude of the decoupled explosion was larger than virtually all of the quarry blasts. Some combined events may have been identified as being ripple-fired because of a relatively large high- to low frequency spectral amplitude ratio in the ripple-fired explosion. Also, our analysis required a simulated nuclear explosion to be superimposed on the commercial blasts since it was obviously neither possible nor desirable to produce the real thing. The methodology used in deriving the simulated nuclear explosion requires further analysis and testing and more work needs to be done in assessing the portability of these methods and in dealing with outliers.

Even though considerable care was taken in obtaining ground truth for each of the quarry blasts, we were unable to find strong correlation between any of the shot parameters, including the total yield, and seismic amplitude. Although some of the blasts, especially some of the waste shots, produced magnitudes nearly equal to those of underground nuclear explosions of the same yield, most were at least one magnitude unit lower and some of the production shots were lower by two magnitude units. This also explains why spectral analysis was relatively successful in identifying a simulated decoupled nuclear explosion fired simultaneously with the quarry blasts.

References

Chapman, M. C., G. A. Bollinger, and M. S. Sibol (1992). Modeling delay-fired explosion spectra at regional distances, *Bull. Seism. Soc. Am.*, **82**, 2430-2447.

Denny, M. D., S. R. Taylor, and E. S. Vergino (1987). Investigations of m_b and M_S formulas for the western United States and their impact on the $M_S : m_b$ discriminant, *Bull. Seism. Soc. Am.*, **77**, 987-995.

Glenn, L. A. and P. Goldstein (1994). Seismic decoupling with chemical and nuclear explosions in salt, *J. Geophys. Res.*, **99**, No. B6, 11723-11730.

Goldstein, P. and S. P. Jarpe (1994). Comparison of chemical and nuclear-explosion source spectra from close-in local and regional seismic data, *Symposium on the Non-Proliferation Experiment: Results and Implications for Test Ban Treaties*, Lawrence Livermore National Laboratory publication CONF-9404100, 6-98.

Hedlin, M. A. H., J. B. Minster, and J. A. Orcutt (1989). The time-frequency charcateristics of quarry blasts and calibration explosions recorded in Kazakhstan, USSR, *Geophys. J. Int.*, **99**, 109-121.

Hedlin, M. A. H., J. B. Minster, and J. A. Orcutt (1990). An automatic means to discriminate between earthquakes and quarry blasts, *Bull. Seism. Soc. Am.*, **80B**, 2143-2160.

Kim, W. Y., D. W. Simpson, and P. G. Richards (1994). High-frequency spectra of regional phases from earthquakes and chemical explosions, *Bull. Seism. Soc. Am.*, **84**, 1365-1386.

Mayeda, K. (1993). m_b (L_g coda): a stable single station estimator of magnitude, *Bull. Seism. Soc. Am.*, **83**, 851-861.

Mayeda, K. and W. Walter (1995). Moment, energy, stress drop and spectra of Western U. S. earthquakes from regional coda envelopes, *J. Geophys. Res.*, in press.

Richards, P. G. (1994). Blasting activity of the mining industry in the United States, *Symposium on the Non-Proliferation Experiment: Results and Implications for Test Ban Treaties*, Lawrence Livermore National Laboratory publication CONF-9404100, 2-16.

Smith, A. T. (1989). High-frequency seismic observations and models of chemical explosions: implications for the discrimination of ripple-fired mining blasts, it Bull. Seism. Soc. Am., **83**, 160-179.

Stump, B. W. and S. K. Reamer (1988). Temporal and spatial source effects from near-surface explosions, *10th Annual AFGL/DARPA Seismic Research Symposium*, Fallbrook, CA.

Vergino, E. S. and R. W. Mensing (1990). Yield estimation using regional $m_b(Pn)$, *Bull. Seism. Soc. Am.*, **80**, 656-674.

Wüster, J. (1990). Discrimination of chemical explosions and earthquakes in central Europe – a case study, *Bull. Seism. Soc. Am.*, **83**, 1184-1212.

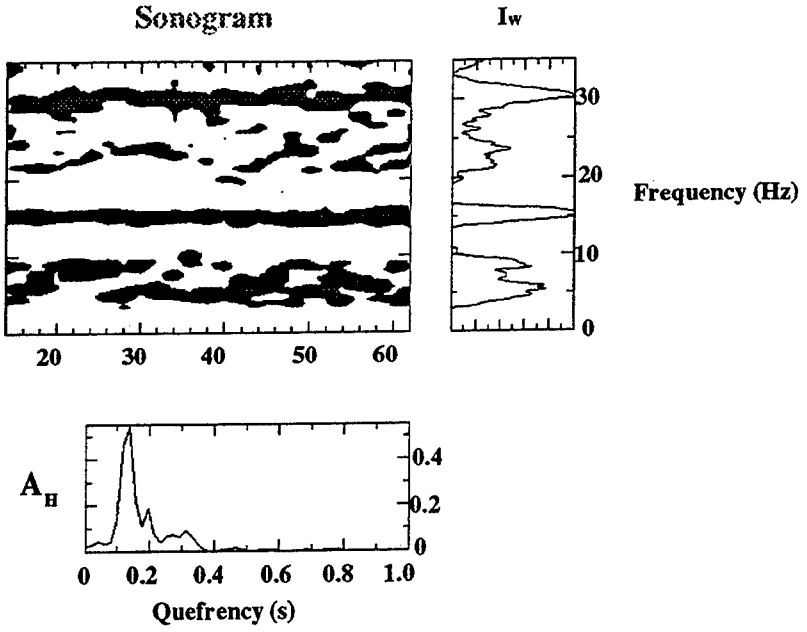

Figure 1. Spectral discriminants applied to a typical production shot.

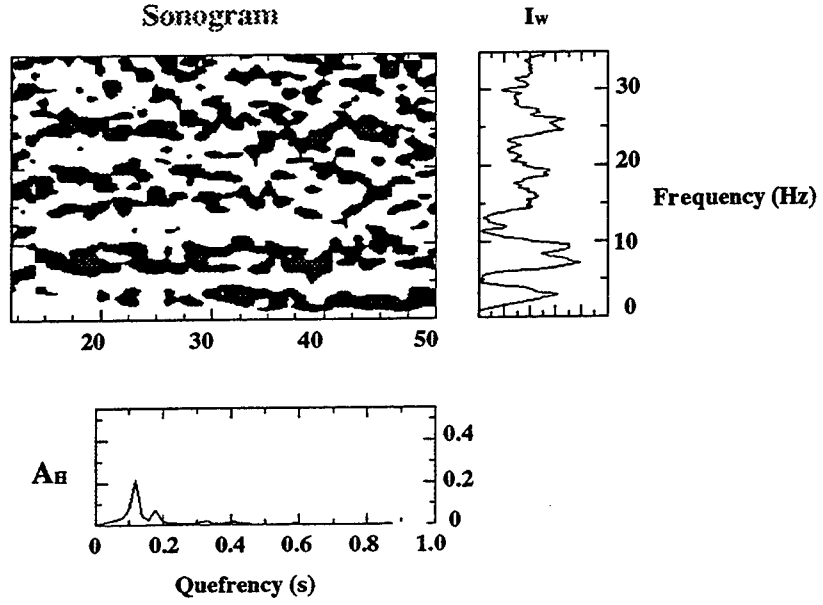

Figure 2. Spectral discriminants applied to a typical waste shot.

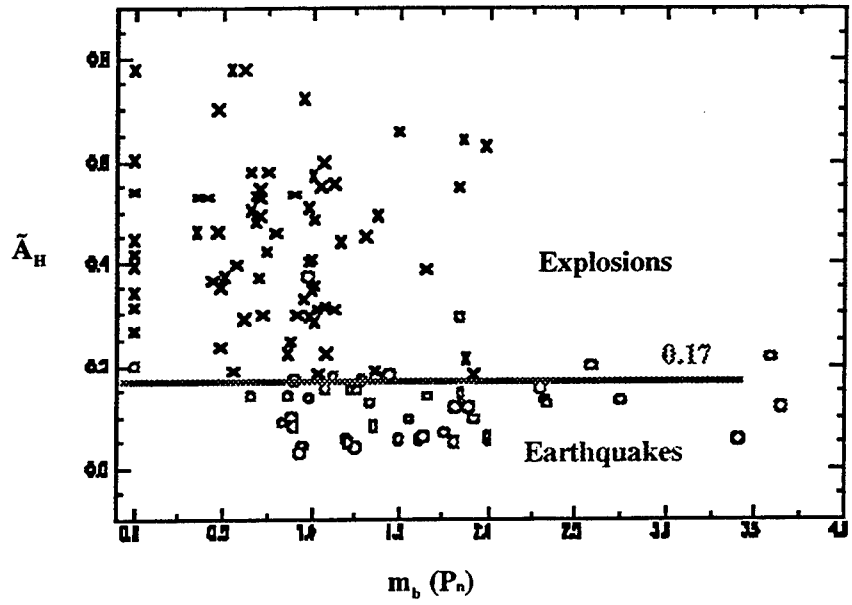

Figure 3. Peak value of modified-Hedlin method amplitude as a function of magnitude applied to discriminate quarry blasts from nearby shallow earthquakes.

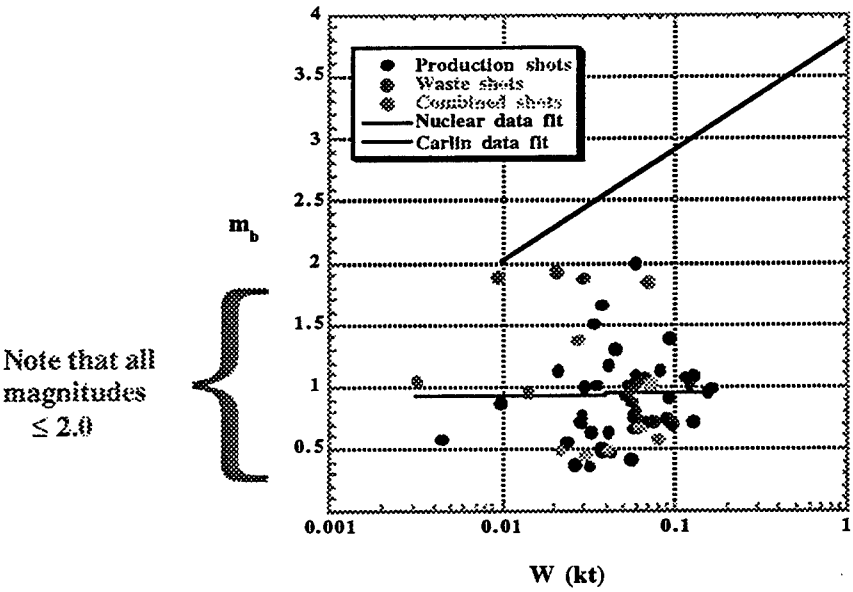

Figure 4. $m_b(P_n)$ as a function of total yield for 61 Gold Quarry blasts recorded at ELK in the period April - September 1995. The Nuclear data fit derives from *Vergino and Mensing (1990).*

STATISTICS ON MINE BLASTING AND BLASTING SIGNALS FOR THE FORMER SOVIET UNION

Vitaly I. Khalturin, Tatyana G. Rautian, and Paul G. Richards[1]
Lamont-Doherty Earth Observatory of Columbia University
([1]also, Department of Earth and Environmental Sciences), Palisades, NY 10964

F19628-95-C-0100, sponsored by DOE

ABSTRACT

We have documented the frequency of occurrence of mine blasts of different seismic signal strength for 23 regions of the former Soviet Union (FSU). Our goal has been to gain a practical appreciation of the numbers of mine blast signals likely to be detected teleseismically, and at regional distances, by seismograph networks used to monitor compliance with a Comprehensive Test Ban Treaty. We believe our survey includes all regions of major mine blast activity in the FSU. Knowledge of mine blast statistics is needed in order to plan efforts in discrimination, recognizing that in general it is more difficult to tell the difference, from seismic data, between underground nuclear and chemical explosions, than between underground nuclear explosions and earthquakes. If the number of strong mine blast signals is large, the effort to analyse such signals could swamp discrimination programs, and/or could result in the need for special monitoring of certain mining regions.

For 22 of the 23 regions we have studied, it appears that only on the order of 50 blasting events per year have K (energy class) value of 9 or greater – corresponding to m_b around 3.35 or greater. Also, the slope of the frequency-magnitude relation is much steeper for mine blasting signals in these regions, than for earthquakes (the b-value is greater than 2 for blasting, and around unity for earthquakes). This latter result is good from the perspective of concern over very large blasts – because it implies there are very few such events. It also indicates that the number of blast signals rises very rapidly as one considers events with magnitude below about m_b 3.25.

However, the remaining one of the 23 regions turns out to be the site of blasts of significantly larger magnitude. This is the Kuzbass region, ranging over latitudes 53° – 55° and longitudes 86° – 88.5°, together with mining at (53.6°N, 91.1°E) near the town of Abakan. Mine blasts with K values around 10 and somewhat above (m_b around 4) occur on the order of twice a month at a small number of mine operations within this region.

As a related project, we have studied the seismicity described in standard bulletins that report earthquake activity in the FSU, and have estimated the numbers of mine blast events, mistakenly presumed to be earthquakes, that are contained in such bulletins.

Keywords: mine blasting, seismic discrimination, CTBT monitoring

OBJECTIVE

Our goal is to document the rates of occurrence of chemical explosions of different sizes, in as many mining regions as possible, but with a focus on the observability of blasting signals originating in the former Soviet Union, Australia, Canada, possibly China, Korea, and the U.S.

The size of a chemical explosion is expressed commonly in terms of charge size. But in this project we are more interested in size expressed in terms of seismic magnitude, whether local, regional, or teleseismic, since our concern is with the observability of blasting activity. We are particularly interested in estimating the numbers of chemical explosions that occur in different regions and that are detected teleseismically with $m_b > 3$. Underlying our work, is the fact that mine blast signals are less easily discriminated from nuclear explosion signals, than are earthquake signals, so mine blast signals may require more sophisticated analysis in programs of CTBT monitoring and verification. Therefore, large numbers of detectable mining blasts would represent a problem for those who must routinely identify the nature of seismic sources (earthquake, mining blast, underground nuclear explosion). Our project will help estimate the extent of this problem, by making surveys of the observability of mine blast signals of various sizes.

RESEARCH ACCOMPLISHED

Prior to starting this project in June 1995, we had preliminary indications for the U.S. that, in practice, only around 10 to 30 mine blasts appeared to be detectable teleseismically with $m_b > 3$. This number was surprisingly low, since, using magnitude-yield relationships for contained single-fired tamped explosions, one would expect from knowledge of the amounts of chemical explosives used, that thousands of U.S. blasts would be teleseismically detectable each year by sensitive arrays (Richards *et al*, 1992; Richards, 1995). The REB during GSETT-3 has reported about one U.S. blast each week (E. Bergman, personal communication), confirming our preliminary indications for the U.S., concerning the low numbers of observable blast events.

To carry out our FSU survey we have acquired six types of information, as follows:

- coordinates of active quarries and mines in the different regions of our study;
- lists of times at which representative blasts, and large blasts, occurred;
- information on total charge size, and, if possible, of blasting patterns (numbers of holes, charge size and timing of delays);
- regional magnitudes for mining blasts;
- information on the teleseismic observability of mining blasts; and
- pertinent seismograms, for our own analysis.

We now have information for 23 mining areas in the FSU, as listed in Table 1. For several of these areas we have detailed information on several tens of specific quarries/mining operations, and on hundreds of specific mining blasts.

Region	Lat (°N)	Lon (°E)
AZGIR	45-55	45-59
APATITY	67-71	33-35
GULF of FINLAND	55-62	20-30
UKRAINE	47-51	22-40
CARPATHIANS	45-50	20-30
KOMI	63-67	55-59
URALS	54-59	57-63
CRIMEA	44-45	34-35
ANAPA	36-38	44.5-45.5
NORTH CAUCASUS	42-45	38-43
GEORGIA (GRUZIA)	41-44	42-45
ARMENIA	39-42	44-47
AZERBAIJAN	38.5-39.5	46.3-47.7
SOUTH CENTRAL KAZAKHSTAN	40-45	67-73
SOUTHEAST.KAZAKHSTAN	42-45	76-79
TADJIKISTAN	38-40	67-70
KURSK	50-53	35-38
KUZBASS	52-56	86-93
BAIKAL	48-58	100-120
TRUBKA MIRA	60-65	104-119
EASTERN SIBERIA		
PRIMORIE	43-56	123-139
CHUKOTKA	60-72	165-195

Table 1: The name and location of 23 areas of blasting activity in the former Soviet Union

Our project has now been underway for 13 months, and we have four research results to report. The first two results were already indicated in our report last year when this project had just begun — and are now confirmed based upon orders of magnitude more data. Briefly, these two results are that

(1) almost all routine blasting activity in the FSU, at magnitude levels that have any significance in the context of CTBT monitoring, occurs at specific times of day, usually during the hours at the end of the working day; and

(2) for 22 of the 23 areas we have studied, the frequency of occurrence of seismic signals from blasting has a high "*b* – value", of around 2, and only a quite limited number of blasts (approximately 50 per year) have magnitude greater than about 3.35.

We are documenting these two results with numerous tables and figures for our first annual

technical report. We have two other two research results, which are quite new. These results can be briefly stated as follows:

(3) the blasting that occurs in the Kuzbass mining region is significantly different from all others we have studied, in that explosions routinely occur (on a weekly basis) up to about magnitude 4;

(4) the occurrence of blasting activity in many regions of the FSU has contaminated bulletins of natural seismicity (that is, lists of earthquakes). We have been able to make preliminary estimates, in a number of areas, of the number of events routinely reported as earthquakes, that we believe instead to be chemical explosions (usually quarry or mine blasts).

Further discussion of the Kuzbass region now follows.

Mine blasts in the Altai-Sayan region, including the Kuzbass

The location and names (where known) of 24 mining operations in the Altai-Sayan region of Russia is given in Table 2, and a map of these 24 mines appears as Figure 1. The Kuzbass is part of the Altai-Sayan region, and is indicated by the dotted rectangle of Fig. 1, within which are the first 13 mines listed in Table 2.

#	Name of mine (if known)	Latitudes		Longitudes		nearby town (if known)
1	Tashtagol-S	52.70	52.85	87.84	87.97	Tashtagol
2	Tashtagol-N	52.85	53.00	87.90	88.20	Tashtagol
3	Krasnogorsky	53.40	53.70	87.65	87.98	Mezhdurechensk
	Tomusinsky					Mezhdurechensk
	Sibirginsky					Mezhdurechensk
	Mezhdurechensky					Mezhdurechensk
4	Oldgerassky	53.70	53.95	88.05	88.25	Mezhdurechensk
5	Osinnikovsky	53.35	53.47	87.33	87.45	Osinniky
6	Kaltansky	53.48	53.57	87.33	87.53	Kaltan
7	Baidayevsky	53.87	54.05	87.30	87.60	
8	Taldinsky	54.07	54.20	87.05	87.23	Leninsk-Kuznetsky
	Mschohovsky					Leninsk-Kuznetsky
9	Imeny Vakhrusheva	53.90	54.25	86.33	86.64	Kiselevsk
	Krasnobrodsky					Kiselevsk
	Novo-Sergiyevsky					Kiselevsk
	Kiselevsky					Kiselevsk
	Novosergievsky					Kiselevsk
10	Listvyansky	53.50	53.60	86.70	86.95	Novokuznetzk
11	Kolmogorsky-2	54.30	54.40	86.70	86.90	Belovo
12	Kolmogorsky-1-1	54.40	54.65	86.33	86.70	Leninsk-Kuznetsky
	Kolmogorsky-1-2					Leninsk-Kuznetsky
13	50 years of October	54.17	54.32	86.15	86.32	Belovo
14	Beresovsky	55.50	55.65	86.10	86.30	
	Chernigovsky					
	Kedrovsky					
15		54.60	54.75	91.00	91.35	
16	Abakansky-1	53.55	53.80	90.80	91.50	Abakan
17	Abakansky-2	53.40	53.60	91.20	91.70	Abakan
18	Krasnokamensky	54.15	54.25	93.25	93.35	
19		51.10	51.30	90.00	90.60	
20		51.50	51.75	94.45	94.65	Kyzyl
21		52.35	52.45	92.35	92.45	
22		50.35	50.45	97.65	97.75	
23	Abazinsky	52.55	52.65	90.10	90.20	Abaza
24		53.00	53.20	91.90	92.20	

Table 2. Coordinates of mines in the Kuzbass and Sayan regions

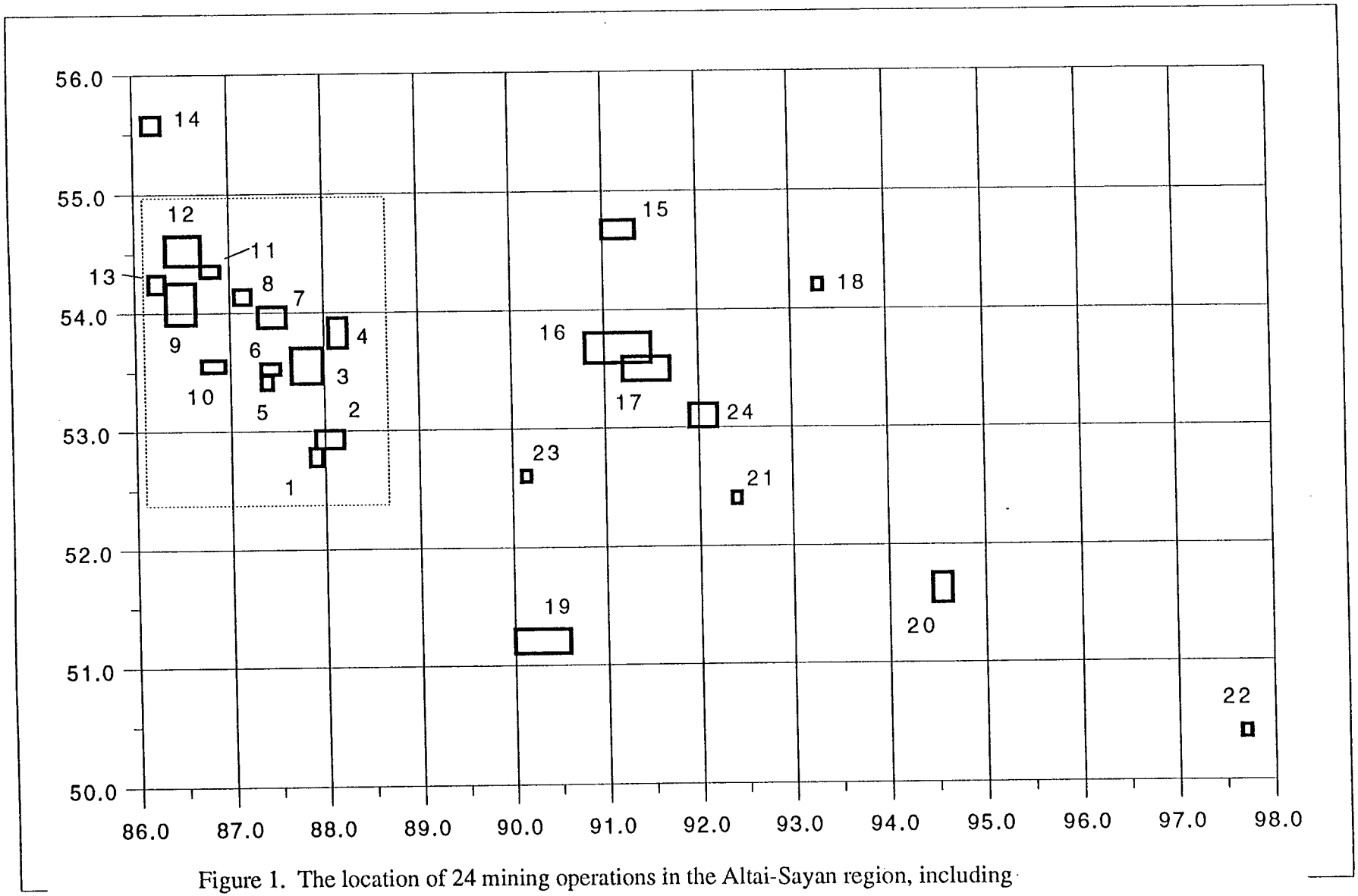

Figure 1. The location of 24 mining operations in the Altai-Sayan region, including the Kuzbass (shown as the region within the dotted rectangle containing mines numbered from 1 to 13). Mine numbers are keyed to Table 2.

We have obtained two groups of data on specific blasts in this region. The first group consists of 803 blasts in 1989–1990 plus 22 blasts in 1991–1993, for which epicenters and energy class K (rounded to the nearest integer) have been determined by the local seismographic network. Epicenter errors have been estimated and are typically about 10 km. K appears to be linearly related to magnitude (m_b), via the rule $K = 9 + 2.32 * [m_b - (3.32 \pm 0.25)]$ so that a K value of 9 indicates m_b around 3.1 to 3.6 and a K value of 10 indicates m_b around 3.6 to 4.

Of these 825 blasts, 29 had K values around 10. These 29 large blasts, all in the years 1989, 1990, 1992, could presumably be detected teleseismically. They are listed in Table 3 and their locations are shown in Figure 2. 22 of the 29 shots are clustered in two locations, namely around (53.6°N, 87.8°E) and (53.6°N, 91.1°E), and 7 are scattered over a wide area.

date	hr	min	sec	lat N	lon E
1989-Jan-09	8	44	39.7	53.69	91.06
1989-Jan-20	10	53	29.1	53.61	87.88
1989-Jan-23	8	55	17.1	53.69	91.00
1989-Mar-24	9	21	20.1	53.69	91.04
1989-Apr-11	8	14	13.4	53.67	91.11
1989-Apr-12	9	44	8.8	53.66	87.88
1989-Apr-13	9	11	3.9	53.66	87.85
1989-Apr-20	6	39	26.0	53.85	88.18
1989-May-25	9	56	31.0	53.65	87.87
1989-Jun-01	7	50	33.8	53.61	91.24
1989-Sep-18	9	12	55.5	53.63	87.83
1989-Sep-26	6	51	42.6	53.54	91.45
1989-Nov-25	8	40	54.9	54.54	86.46
1989-Dec-21	8	13	14.1	53.65	87.87
1989-Dec-21	9	21	40.7	53.80	91.00
1990-Mar-13	8	30	24.8	51.25	90.13
1990-Jun-20	9	3	12.7	53.65	91.09
1990-Jul-06	6	15	15.8	53.71	99.14
1990-Aug-17	8	1	48.1	53.68	87.85
1990-Sep-13	7	59	41.3	53.67	91.10
1990-Sep-27	8	51	51.9	53.64	87.83
1990-Oct-04	8	41	13.5	53.71	91.11
1990-Oct-26	10	15	34.9	53.66	87.90
1990-Nov-02	8	13	10.6	53.76	90.98
1990-Nov-17	8	52	24.1	53.63	87.84
1990-Nov-26	9	5	42.4	53.74	91.10
1990-Dec-04	13	30	29.0	54.73	91.31
1992-Mar-20	7	47	23.0	50.40	97.70
1992-May-29	6	38	13.0	52.40	92.39

Table 3. 29 large mining blasts (teleseismically observable?) in the Kuzbass/Abakan region

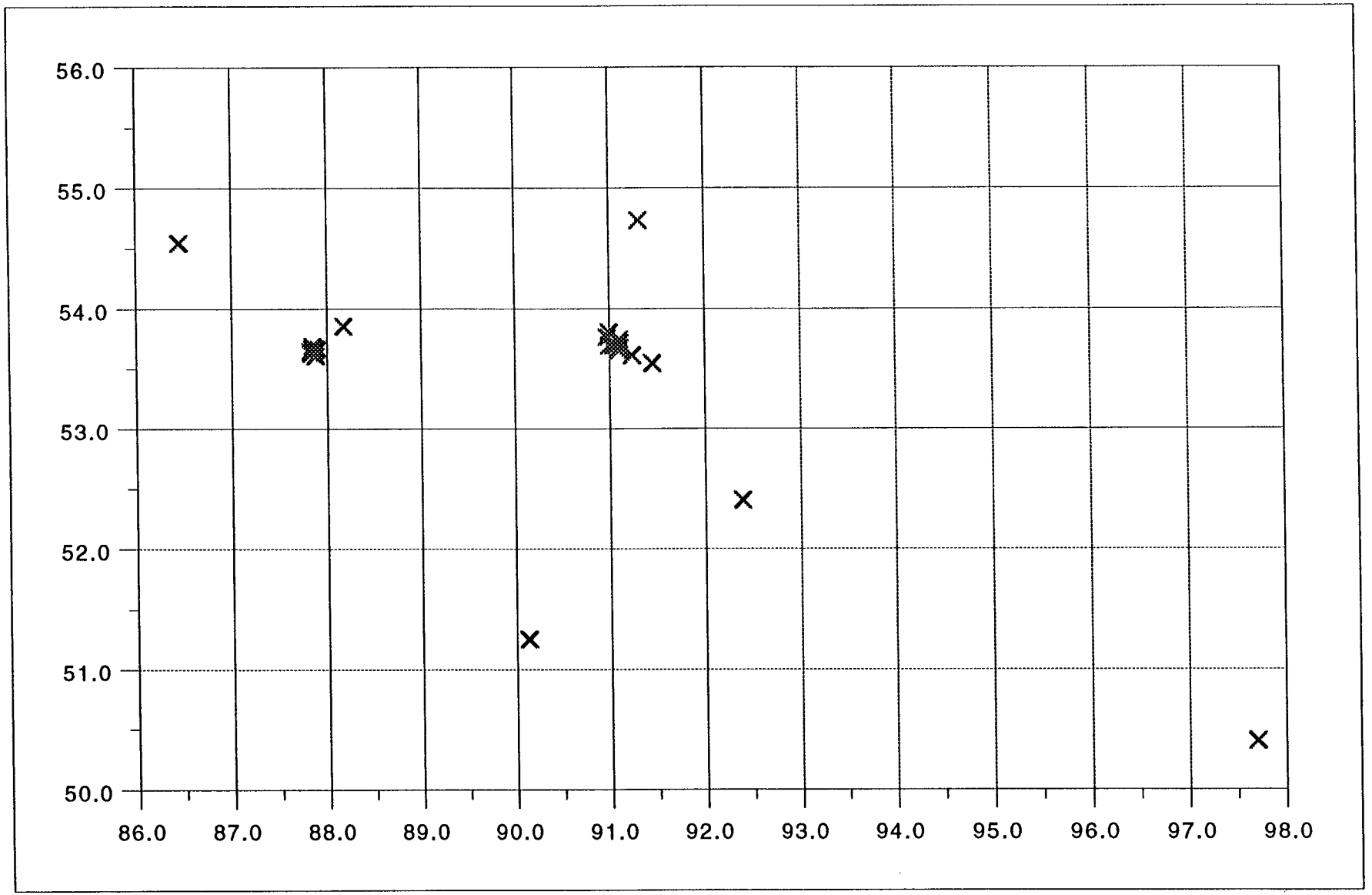

Figure 2. The locations of 29 blasts with K (energy class) around 10. Every blast appears to occur at the location of a particular mine operation shown in Figure 1.

The second group of data concerns a set of 370 events recorded by the Cheremushki seismographic station at (52.8°N, 91.5°E) and having $S - P$ times from 1 s to 15 s during the time period July 1991 to May 1993. The hypocentral distance R in km from this station can be estimated as R = ($S - P$ in sec) times 8.1 km/sec. 40 of these 370 events had K values in the range $9.5 \leq K \leq 10.5$ (with none greater than 10.5).

From both groups of data, we find that the specific mining operations, routinely having the largest seismic signals, from the list of mines in Table 2, are mine #3 in the Kuzbass region and mines #16 and possibly #17, further to the east near Abakan. [The town of Abakan is at (53.43°N, 91.25°E).] These three mines appear to account for about 75% of the largest shots. The remainder are scattered among several different mines.

We believe these largest explosions can be observed teleseismically as well as regionally. We plan further research, using regional and teleseismic signals, to see what efforts in discrimination may be needed to identify these blasts — for example, to see if they are distinctively different, seismically, from single-fired contained explosions.

RECOMMENDATIONS AND FUTURE PLANS

Our survey of mine blasting in the former Soviet Union is almost completed. We expect to acquire further lists of blasting events, and associated information on charge size and signal strength, for additional regions including Australia, Canada, and the U.S. Again, we shall document the observability of these events, paying particular attention to any blasts observed teleseismically, and for them we shall compare values of magnitude assigned on different scales. We are also documenting the occurrence of large single-fired chemical explosions, several of which occurred in the nuclear weapons program of the former Soviet Union.

We recommend that the Kuzbass mining region of Russia, and the region near Abakan further to the east, be made the subject of special studies in seismic discrimination and in the development of relationships between regional and teleseismic magnitudes.

ACKNOWLEDGEMENTS

We appreciate the assistance Dr. Natalya N. Mikhailova from the Institute of Seismology of the Kazakhstan Academy of Sciences, and Dr. Anna A. Godzikovskaya from the Hydroproject Institute in Moscow.

REFERENCES

Kim, Won-Young, Vladimir V. Kazakov, Alexey G. Vanchugov, and David W. Simpson, Broadband and array observations at low noise sites in Kazakhstan: opportunities for seismic monitoring of a comprehensive test ban treaty, in *Monitoring a Comprehensive Text Ban Treaty*, pp 467–482, eds. E.S. Husebye & A.M. Dainty, Kluwer Academic, 1996.

Richards, Paul G., Douglas Anderson, and David Simpson, A Survey of Blasting Activity in the United States, *Bulletin of the Seismological Society of America*, **82**, 1416–1433, June 1992.

Richards, Paul G., Blasting Activity of the Mining Industry in the United States, in *Proceedings of a Symposium on the Non-Proliferation Experiment: Results and Implications for Test Ban Treaties*, sponsored by LLNL/Dept of Energy, CONF-9404100, pp. 2-16 to 2-35, April 1994, Rockville, Maryland, ed. M.D. Denny, 1995.

LARGE MINING BLASTS FROM THE KURSK MINING REGION, RUSSIA[1]

William Leith
U.S. Geological Survey
Reston VA 22092

Alexander Spivak and Leonid Pernik
Institute of the Dynamics of Geospheres
117979 Moscow, Russia

USGS/UC-LLL M.O.A. B291532
Sponsored by the U.S. Department of Energy

ABSTRACT

We present information on blasting practice and history at the Kursk mining region of the Russian Republic of the former Soviet Union, as part of an overall program of study of this mining region which includes field recording of mining blasts on modern digital seismic equipment and analysis of the recorded data. Because there are both similarities and differences in blasting between the U.S and Russia, the Russian data are important both in that they provide some insight into variations from the U.S. and because they can be used directly to estimate the assets needed to effectively monitor the seismicity of Russia and the former Soviet Union. Mines conducting blasts over 300 tons at Kursk are limited to the surface iron-ore mines at the Lebedinskiy, Mikhaylovskiy and Stoilensky Mining and Metallurgical Combines. In recent years, the Lebedinskiy and Mikhaylovskiy mines have dominated the largest charge sizes of Soviet blasts, and are therefore of interest as targets for seismic monitoring research. Blasting at these mines is carried out by the open cast method, in deep surface excavations. Most of the blasts are detonated on alternate Thursdays, and are detonated at 12:00 or 12:30pm, local time. Blasts at Kursk have traditionally been conducted using a "conventional" geometry, in which an entire row of spaced charges is detonated at once. This method, which is very efficient at crushing and displacing the rock but results in large amplitude ground motion near the source, has dominated the blasting at Kursk for decades. More recently, the Kursk mines have started to use a second method or geometry, which we call "reduced-shaking", in which individual rows are blasted in a series of charge-delayed holes. In the Russian application of this method at Kursk, charges are fired so that short, diagonally oriented rows, each consisting of only a few holes, are fired sequentially. This is similar, but not identical to common U.S. "ripple-fire" blasting practices, and results in a much decreased local ground motion. By 1994, both blasting geometries were being used for mining iron ore at the Kursk mining combines. Blasts from the four principal mining combines were recorded in August and September, 1995. A detailed description of the field recording program and initial results can be found in Technical Report No. 2 of the referenced contract, and the seismic data are available from the archive of mine blast data maintained by Lawrence Livermore Laboratory. Current efforts focus on the analysis of the seismic recordings and the videotaped blasts, and on the acquisition of additional data, particularly broadband recordings. It appears that Kursk cast blasts in the range of 300-1200 tons total charge, detonated in the "reduced-shaking" blast geometry, are recorded well above the noise levels at 600 km, with magnitudes ranging from 2.5 to 3.5.

OBJECTIVE

Monitoring a comprehensive nuclear test ban by seismic means may require identification of seismic sources at magnitude levels where industrial explosions (primarily, mining blasts) may comprise a significant fraction of the total number of events recorded, and may for some countries dominate the seismicity. Thus, data on blasting practice have both political significance for the negotiation of treaties involving seismic monitoring of nuclear tests, and operational applications in terms of establishing monitoring and inspection needs on a mine-by-mine basis.

While it is generally accepted that mining explosions contribute to seismicity at lower seismic magnitudes (less than about magnitude 3.5), the rate of mining seismicity as a function of seismic magnitude is unknown for most countries outside the U.S. This results in a large uncertainty when estimating the task of discriminating nuclear explosions from chemical explosions and earthquakes by seismic means, under a comprehensive nuclear test ban. This uncertainty directly affects estimates of seismic network enhancements required to achieve treaty verification requirements at magnitudes less than about 3.5.

This report presents some details of blasting practice and history at one mining combine in the Russian Republic of the former Soviet Union (FSU), as part of an overall program of study of this mining region including field recording of mining blasts on modern digital seismic equipment. These preliminary data illustrate that there are both similarities and differences in blasting between the U.S and Russia. These Russian data are important both in that they provide some insight into variations from the U.S. and because they can be used directly to estimate the assets needed to effectively monitor the seismicity of Russia and the former Soviet Union.

Before its breakup in 1991, the former Soviet Union (FSU) conducted most of the largest known chemical explosive blasts (for a review of blasting in the former Soviet Union, see Leith and Bruk, 1995a). While the largest of those blasts (up to 13kt) were rare explosions for excavation projects (principally dam building), the mining industry of the FSU routinely detonated blasts in excess of 1 kt. The FSU is a leading producer of many commodities mined with explosives, including iron ore. In 1987, the Kursk region was the second largest iron ore producing region in the former Soviet Union (next to Krivoy Rog, Ukraine), and accounted for about 10% of world iron ore production and 20% of Soviet iron ore production.

RESEARCH ACCOMPLISHED

Geologic Setting

The city of Kursk is located in the center of a broad belt of banded iron ore deposits in European Russia, some 600 km south of Moscow (Figure 1). The region is known geologically as the Kursk Magnetic Anomalies (or KMA), because of the strong magnetic anomaly pattern generated by the magnetized iron ore deposits. While the KMA were discovered in 1778, the iron ore deposits were completely covered by sediments ranging from 37 to 500 meters thick. Geophysical studies began in 1883, and the first cores of banded iron formation were recovered in 1923 (Alexandrov, 1973).

The KMA cover an area of about 170,000 square kilometers. There are two principal belts of banded iron formation; one to the southwest of the city of Kursk, the Belgorod belt; the other to the northeast of Kursk, the Oskol' belt. Several of the ore bodies have enormous dimensions: for example, the Yakovlevo deposit (Belgorod region) has been traced more than 50 kilometers along strike, ranging from 200 to 400 meters in thickness. The reserves of the KMA are estimated to be 13 times that of Krivoy Rog, the next largest iron reserve of the former Soviet Union (in Ukraine),

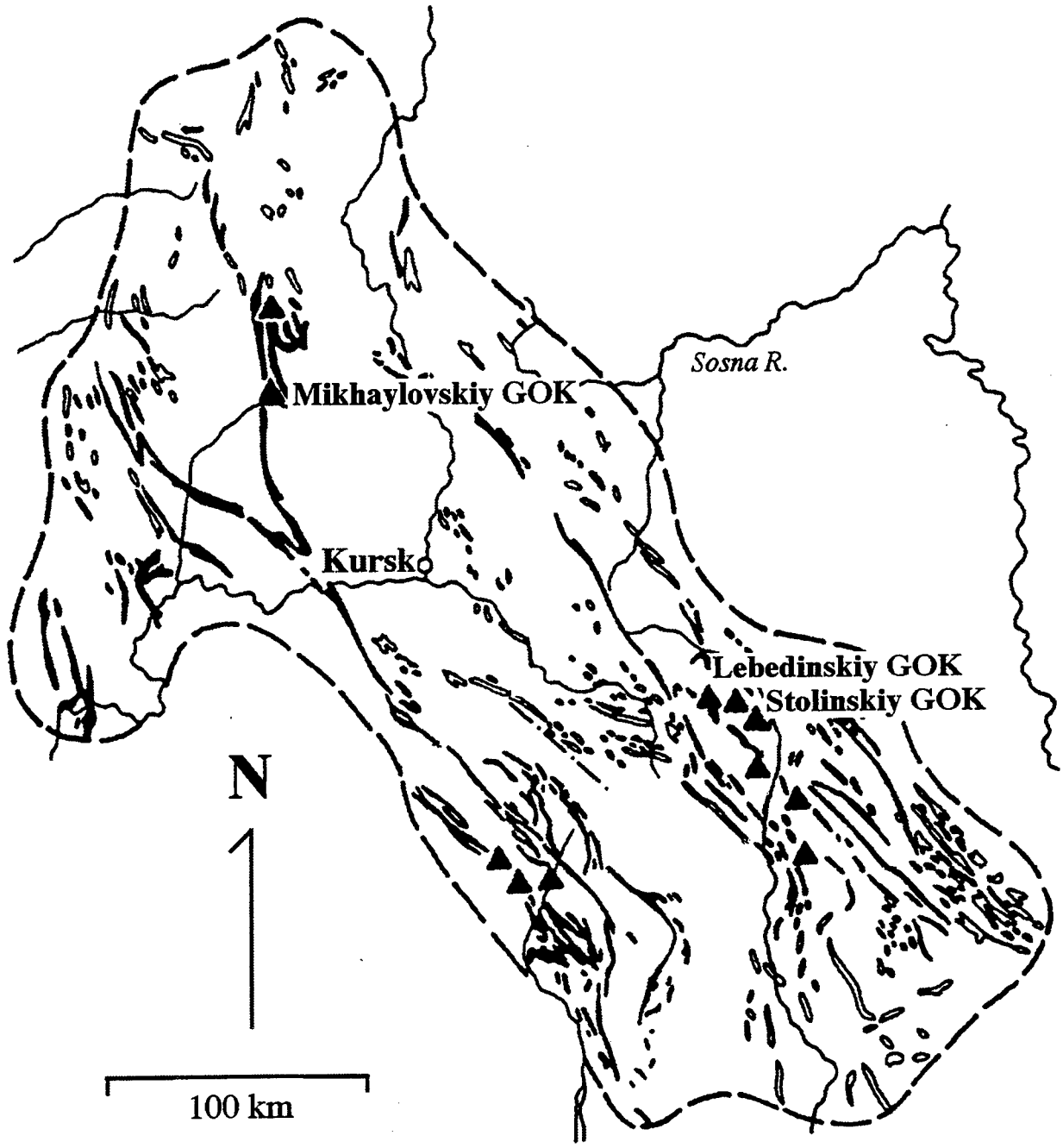

Figure 1. Map of the Kursk region, showing the distribution of banded iron formation (filled bands are higher grade iron ore; unfilled bodies are lower grade ore) and the locations of the principal mining combines (triangles). Note the locations of the Lebedinskiy, Mikhaylovskiy, and Stolinskiy mining/metallurgical combines (GOKs).

and almost 17 times larger than those of the Lake Superior region in the U.S. and Canada (Alexandrov, 1973).

Kursk Mining Operations

Mines conducting "strong" blasts (over 300 tons) at Kursk are limited to the surface mines at the Lebedinskiy, Mikhaylovskiy and Stolinskiy Mining and Metallurgical Combines (see Leith and Bruk, 1995a). Blasting at these mines is carried out by the open cast method, in deep surface excavations. In recent years, the Lebedinskiy and Mikhaylovskiy mines have dominated the largest charge sizes of Soviet blasts, and are therefore of interest as targets for seismic monitoring research.

Table 1 gives statistics for strong blasts at the Kursk mines in 1993. It is not known how much variability there is in blasting practices at these mines over periods of years, but comparison with previously published data (Leith and Bruk, *op.cit.*) indicates that blast size and frequency have decreased since the 1980s. Blasting has been further diminished at Kursk in the last few years as a result of deteriorating economic conditions. This has resulted in both lower total charge sizes and some weeks or months passing without blasts.

Table 1. Total numbers of blasts and "strong" (>300 tons) blasts at Kursk in 1993.

mining operation	total charge	blasts (blasts>300t)
Lebedinskiy	250-1400 t	34 (30)
Mikhaylovskiy	200-500 t	50 (40)
Stolinskiy	100-700 t	25 (12)

Large Blasts at the Lebedinskiy Combine in 1992

In recent years, the Lebedinskiy combine has detonated the largest blasts in the Kursk region. As noted above, blasting here is conducted in surface mines by the open cast method, in mines cut relatively deep through the surface deposits. A geological cross-section is shown in Figure 2. Note that this mine is also located in close proximity to active, deep underground mine workings at Gubkin, and is therefore an ideal target for a seismological mine monitoring experiment.

Table 2 lists large blasts detonated at the Lebedinskiy Combine during the first six months of 1992. Several features of these blasts are worth noting. First, most of the blasts were detonated on alternate Thursdays, and all but two were detonated at 12:00 or 12:30pm, local time. This pattern of regular blast timing at a single mining combine is typical of Russian blasting practice, and has been noted at several of the largest Russian mines (e.g., Apatity, Tyrnauz, Kuzbass, and others).

Blasting Geometries

Blasts at Kursk have traditionally been conducted using a "conventional" geometry, in which an entire row of spaced charges is detonated at once (Figure 3a). This method, which is very efficient at crushing and displacing the rock but results in large amplitude ground motion near the source, has dominated the blasting at Kursk for decades. This type of blasting is now apparently only rarely used in the United States because of damage to structures near mines as a result of the near-source ground motion. Detailed blasting data for mines in the Magadan Oblast' of the Russian Far East, for the years 1989-1992 indicate that this blasting pattern was exclusively

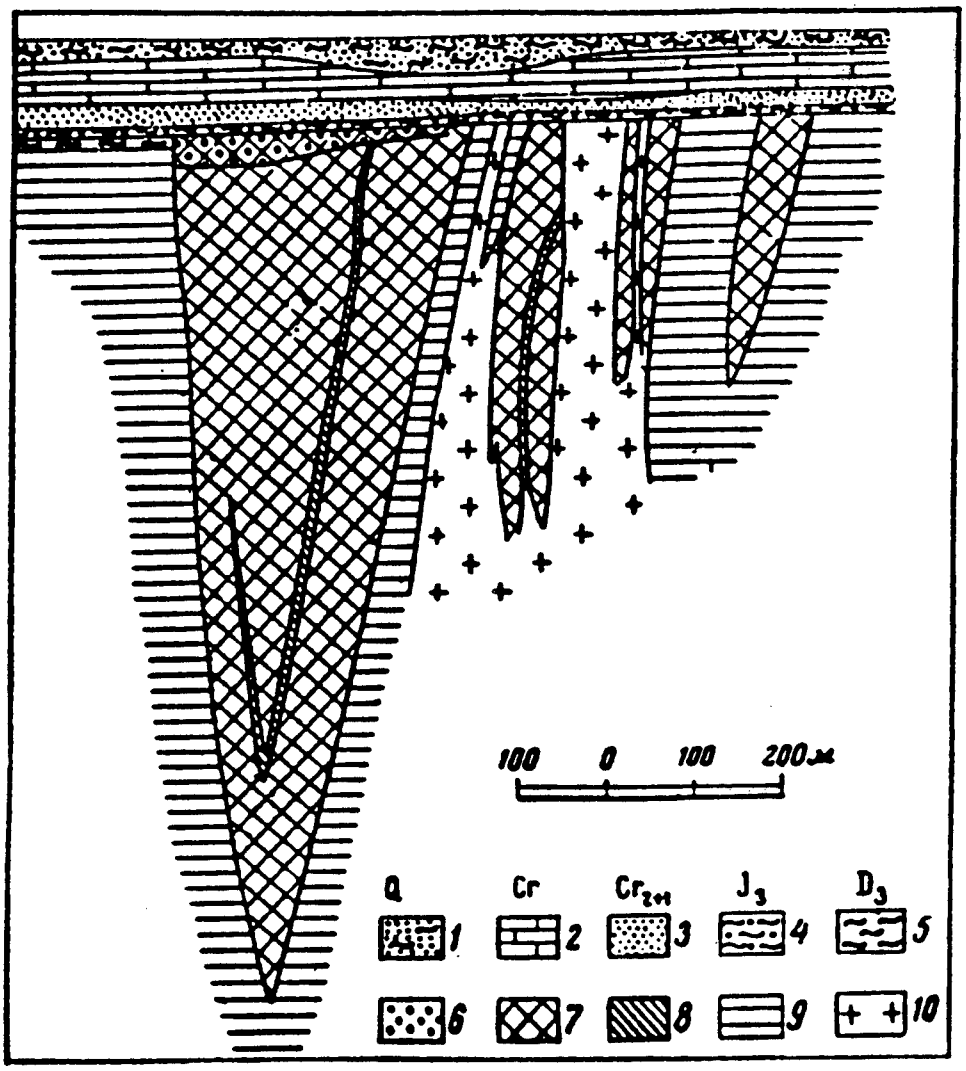

Figure 2. Geological cross-section of the Lebedinskiy iron ore deposit, Kursk mining region (from Laznika, 1993). The thick cover layers have been stripped back to expose the iron ores for surface mining. These deposits are also mined nearby in underground workings, at significant depths.

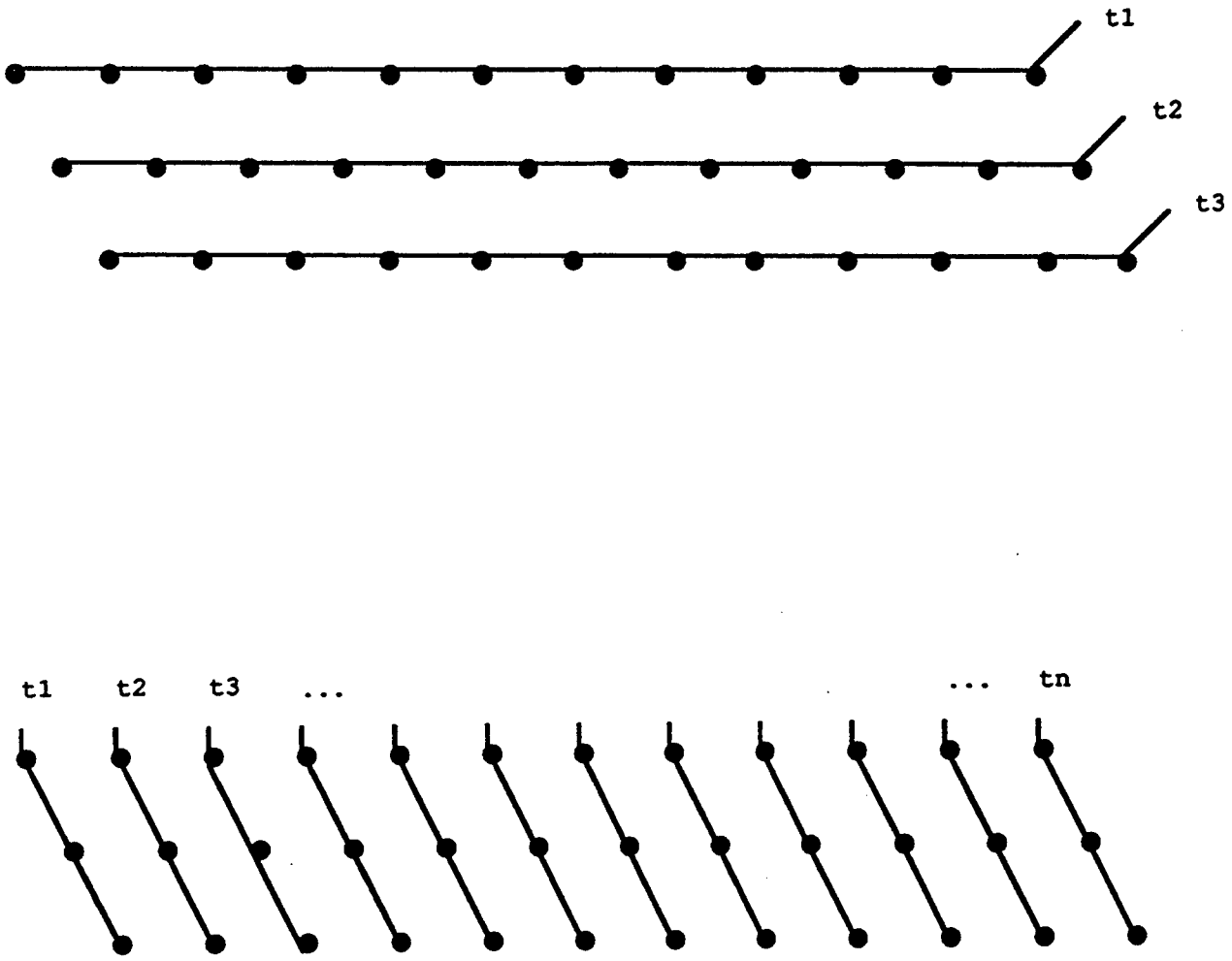

Figure 3. Typical blast geometries: Upper figure shows the charge/delay geometry of a typical "conventional" mining blast, in which successive charge rows are detonated with no delay along the row; Lower figure shows the charge/delay geometry of a "reduced shaking" blast, in which charge rows are detonated on the diagonal, down the rock face, with a short (e.g., 10 msec) delay between rows.

used for mining in this region, which includes both coal and metal mining (Leith and Bruk, 1995b).

Table 2. Blasts at Lebedinskiy mining combine, Feb-Jun, 1992

date	day	time (Mos.)	tot. chg.(t)
92/02/06	Th	12:00	871.7
92/02/21	Fr	12:00	1248.1
92/03/05	Th	12:30	1110.0
92/03/19	Th	12:00	979.0
92/04/02	Th	12:00	1319.6
92/04/16	Th	12:00	946.6
92/04/30	Th	12:30	786.7
92/05/08	Fr	9:00	290.6
92/05/14	Th	12:00	694.0
92/05/22	Fr	12:00	1221.7
92/06/11	Th	13:22	1568.5
92/06/25	Th	12:00	1273.5

In the last 1-2 years, the Kursk mines have started to use a second method or geometry, which we will call "reduced-shaking", in which individual rows are blasted in a series of charge-delayed holes. In the Russian application of this method at Kursk, charges are fired so that short, diagonally oriented rows are fired sequentially, each consisting of only a few holes (see Figure 3b). This is similar, but not identical to common U.S. "ripple-fire" blasting practices, and results in a much decreased local ground motion. By 1994, both blasting geometries were being used for mining iron ore at the Kursk mining combines.

Since the breakup of the former Soviet Union, economic conditions have deteriorated, affecting most of the major industries. This has included the mining industry, where production has fallen dramatically since 1990. Likewise, the consumption of explosives has also fallen: In 1990, approximately 2 million metric tons of explosives were detonated in Russia; by 1994, that number had fallen to about 700,000 metric tons. Economic conditions have affected blasting practices through the unavailability (or high cost) of explosives, and has resulted in both fewer blasts and smaller total charge sizes.

There is also apparently a trend to reduce the local seismic shaking at some mines, as evidenced by the increasing use of the "reduced shaking" blasting geometry for some of the blasts at the Lebedinskiy combine. It is not known whether this is becoming more common at other mines, for mining other mineral commodities, and whether its use will soon dominate the mining industry in populated areas of Russia.

Example of charge geometry for the blast of 16 August, 1994

Table 3 list the blast parameters from a large, complex blast that was detonated at the Lebedinskiy mining combine in 1994. In this blast, which was detonated at 12:00pm on Tuesday, 16 August, 1994, 318 tons were detonated in five individual "blocks", separated laterally by 500 to 1000 meters. Each block was blasted in a conventional charge geometry (see above), and there was a delay of about 1 second between each block. A diagram of one block's charge geometry is shown in Figure 4.

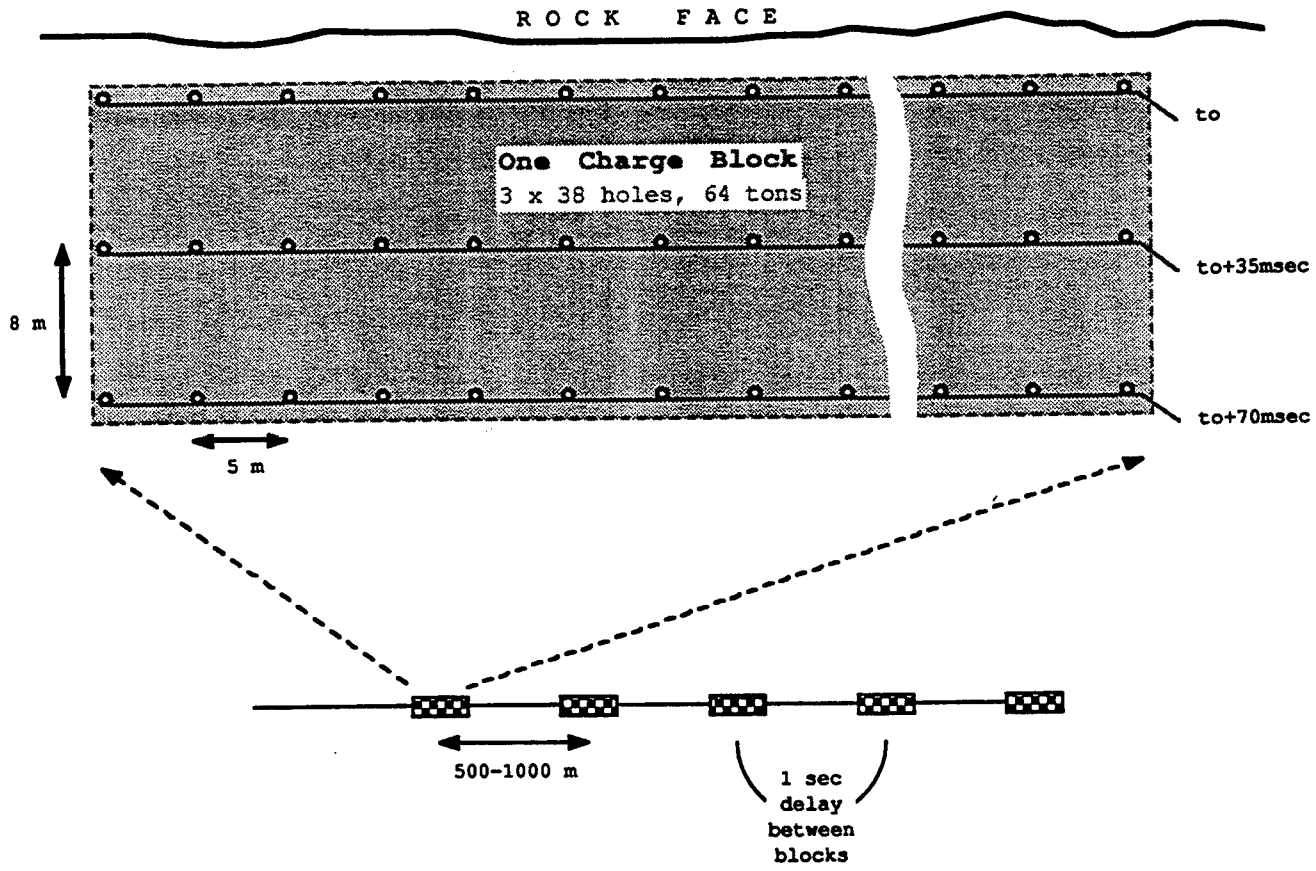

Figure 4. Example of the detailed charge geometry for a single block of the 18 Aug. 1994 blast at Lebedinskiy combine, KMA mining region, Russia. This blast was composed of a series of 5 such charge blocks, each separated by 500-1000 meters, and detonated with a delay of about 1 second.

Table 3. Charge geometry for a single block of the 18 Aug. 1994, blast at Lebedinskiy combine, KMA mining region.

charge rows	3
hole diameter	250mm
holes per row	~38
charge per hole	560kg
charge per row	~21 t
hole depth	16.5m
charge length	12m
row separation	8m
hole separation	5m
delay interval	35msec
delays per block	3
charge per block	~64 t

Seismic Recordings

Blasts from the four mining combines were recorded in August and September, 1995. Table 4 (following page) shows the source-station combinations for which we have either digital or a/d converted data. A detailed description of the field recording program and initial results can be found in Technical Report No. 2 of the referenced contract. Data are available from the archive of mine blast data maintained by Lawrence Livermore Laboratory.

Figure 5 shows an example of the raw and filtered traces of the broadband recording of the blast of 8 September 1995 (Mikhaylovsky combine), recorded at Mykhnevo station, 600 km to the north. The blast was recorded well above the noise level, and its magnitude was estimated at 2.8.

CONCLUSIONS AND RECOMMENDATIONS

This paper describes work in progress on under the referenced agreement between the Lawrence Livermore Laboratory and the U.S. Geological Survey. Current efforts focus on the analysis of the seismic recordings and the videotaped blasts (see Table 4), and on the acquisition of additional data, particularly broadband recordings. It appears that Kursk cast blasts in the range of 300-1200 tons total change, detonated in the "reduced-shaking" blast geometry, are recorded well above the noise levels at 600 km, with magnitudes ranging from 2.5 to 3.5.

REFERENCES

Alexandrov, E.A., 1973, The Precambrian banded-iron formations of the Soviet Union, *Economic Geology*, v.68, p.1035-1062.

Laznika, P., 1993. *Precambrian Empirical Metallogeny*, v. 2, part a.

Leith, W. and L. Bruk, 1995a, A review of blasting activity in the former Soviet Union, in *Proceedings, Symposium on the non-Proliferation Experiment*, U.S. Department of Energy, p. 2-36 - 2-44.

Leith, W. and L. Bruk, 1995b, Blasting in the Magadan Oblast', Russia, 1989-1992, Technical Report No. 3 on AC94-1A-3003, *U.S. Arms Control and Disarmament Agency*, 10 pp.

Richards, P., D.A. Anderson and D.W. Simpson, 1992, A survey of blasting activity in the United States, *Bull. Seis. Soc. Am.* v.82, n.3, p.1416-1433.

Vanecek, M., ed., 1994, *Mineral Deposits of the World*, Elsevier (Amsterdam).

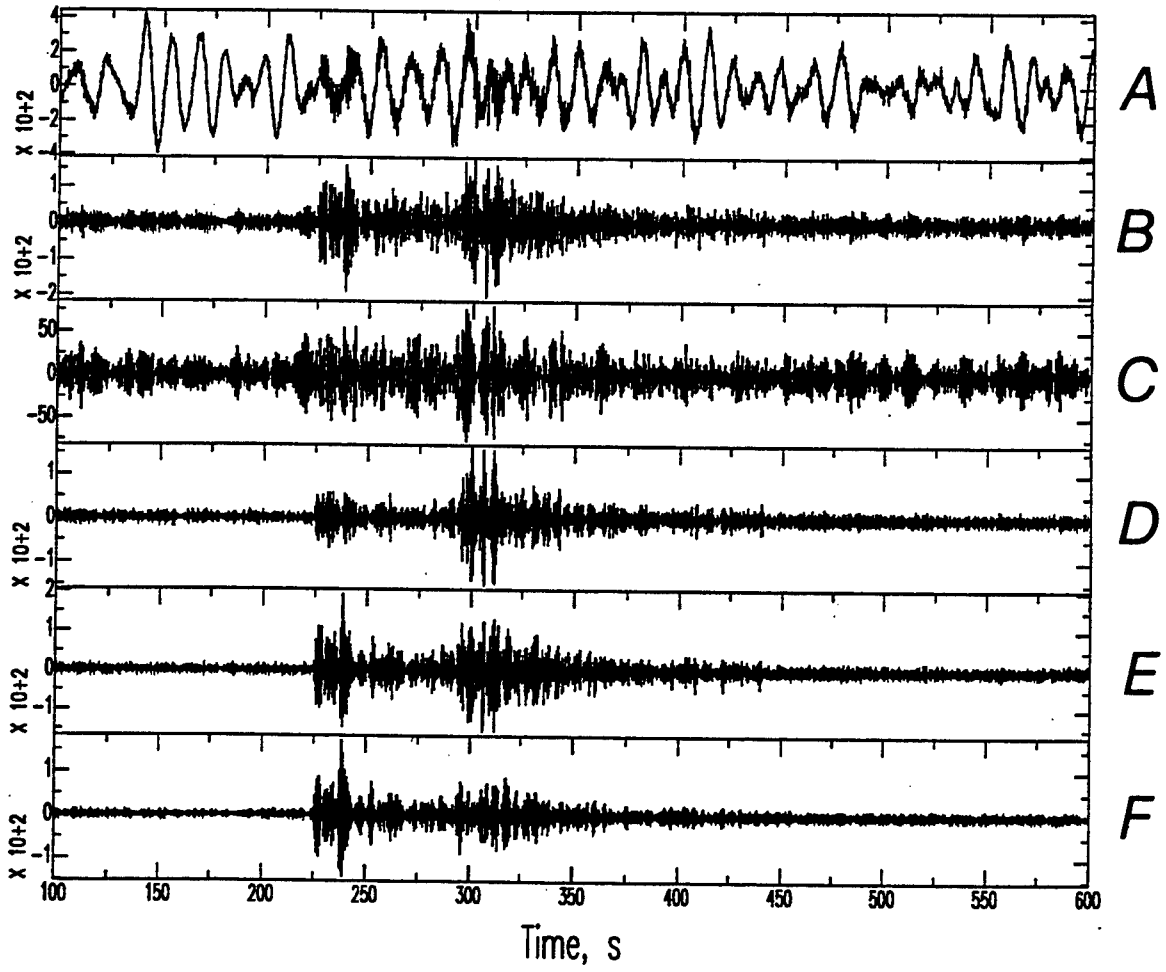

Figure 5. Example of the raw and filtered traces of the broadband recording of the blast of 8 September 1995 (Mikhaylovsky mining combine), recorded at Mykhnevo station, 600 km to the north. Trace A is unfiltered. Traces B-F are filtered as follows: B: 0.7 Hz to Niquist; C: 0.7-1.4 Hz; D: 1-2 Hz; E: 1.4-2.8 Hz; F: 2 Hz to Niquist.

Table 4. List of blasts from the Kursk mining region recorded during August-September, 1995

date	day	time	source loc.	station	dist. (km)	charge (t)	note
4-Aug-95	216	10:08	Stoilensky	Mikhnevo	~500	N/A	REFTEK recording
10-Aug-95	222	8:15	Lebedinsky	Mikhnevo	~500	N/A	REFTEK recording
18-Aug-95	230	9:57	Stoilensky	Svoboda	~130	155.6	REFTEK recording
24-Aug-95	236	8:10	Lebedinsky	Svoboda	~130	834.2	REFTEK recording
24-Aug-95	236	8:10	Lebedinsky	Elets	~150	834.2	analog SP recording
24-Aug-95	236	8:10	Lebedinsky	Mykhnevo	~500	834.2	REFTEK recording
24-Aug-95	236	8:10	Lebedinsky	Tim	~65	834.2	analog SP recording
24-Aug-95	236	8:10	Lebedinsky	Turdey	~240	834.2	analog SP recording
26-Aug-95	238	~20:00	Gubkin	Svoboda	~120	N/A	REFTEK recording
1-Sep-95	244	~8:00	Mikhaylovsky	Svoboda	~60	106	video, REFTEK rec.
1-Sep-95	244	~8:00	Mikhaylovsky	Tim	~130	106	video, analog record.
1-Sep-95	244	10:00	Stoilensky	Svoboda	~130	872	video; charge details
1-Sep-95	244	10:00	Stoilensky	Tim	~65	872	video, analog record.
2-Sep-95	245	20:00	Gubkin	Svoboda	~120	10	REFTEK record
7-Sep-95	250	8:31	Lebedinsky	Svoboda	~130	710	video; charge details
7-Sep-95	250	8:31	Lebedinsky	Tim	~65	710	video, analog record.
7-Sep-95	250	8:31	Lebedinsky	Bol. Ogarevo	~270	710	video, analog record.
7-Sep-95	250	8:31	Lebedinsky	Lamskoe	~180	710	video, analog record.
8-Sep-95	251	8:00	Mikhaylovsky	Mikhnevo	~340	N/A	broadband recording
8-Sep-95	251	8:00	Mikhaylovsky	Svoboda	~60	N/A	clipped; analog rec.
10-Sep-95	253	N/A	Lebedinsky	Mikhnevo	~500	N/A	REFTEK record.

Approximate Station Coordinates

Code	Location	Latitude	Longitude	Source
OBN	Obninsk	55.18.20	36.34.12	Sta. Book.
MHV	Mykhnevo	54.57.49.4	37.45.99.5	GPS
	Elets	52.35.00	38.15.00	map
	Tim	51.45.00	37.00.00	map
	Svoboda	52.05.00	36.15.00	map
	Mikhaylovsky	52.22.00	35.27.00	map
	Lebedinsky	51.15.00	37.40.00	map
	Stoilensky	51.15.00	37.45.00	map
	Gubkin	51.20.00	37.50.00	map

The White Pine Mine Explosively Induced, Controlled Collapse Experiment

D. Craig Pearson, Brian W. Stump, W. Scott Phillips
Geophysics Group - EES-3, Los Alamos National Lab

Sponsored by U.S. Department of Energy, Contract W-7405-ENG-36
Comprehensive Test Ban Treaty Research and Development Program, ST482A

ABSTRACT

On September 3, 1995, the White Pine Mine, which is owned by Copper Range Company, conducted the first of a planned series of explosive removal of existing pillars in their underground mining operations. The purpose of this operation is to evaluate the effectiveness of pillar rubbilization and roof collapse for planned in-situ leaching of the copper ore from the rock mass. This type of seismic source is unique in that a large, delay fired, explosive source was expected to be followed by collapse of the rock immediately above the explosion into the void created.

Characterization of this type of mining source is of interest to the CTBT R&D Seismic Program due to its unique properties. These include the controlled nature of the source in time, location, and magnitude, the fact that the source is located in an active region of underground mining, and that natural collapse of large portions of this mine have occurred in the recent past. The Mine operator is concerned with the characterization of the vibration induced by both the explosive and implosive components of the procedure and determination of the depth to which chimneying of the roof proceeded.

This current report will document 1) the reasons for conducting both the explosively induced collapse and the Los Alamos National Laboratory CTBT R&D Experimental Field Program experiment, 2) the local and regional seismic, acoustic, and videographic data acquired, 3) analysis of the explosion/collapse seismic signal generated, 4) analysis and location of the aftershocks associated with the collapse, and 5) conclusions made concerning this type of mining explosion in relation to verification of a Comprehensive Test Ban Treaty.

Key Words: induced, controlled, mine collapse, local and regional seismology

OBJECTIVES

The purposes of this experiment were to 1) document a type of mining activity which is engineered to produce regional seismic signals similar to unplanned mine collapse events (Taylor, S. R., 1994, Walter, W. R., *et al*, 1996) and 2) determine the locations and temporal occurrence of aftershocks induced by the pillar removal process.

RESEARCH ACCOMPLISHED

The Mine

The White Pine Mine is located near Lake Superior on the Upper Peninsula of Michigan in the vicinity of the town of White Pine, Michigan. The southern shore of Lake Superior is approximately 9 kilometers to the north of the townsite. The area is sparsely populated. Tourism, harvesting of pulp wood for paper milling, and declining levels of copper mining are the major industries in the area.

The terrain varies from relatively flat lake coastal regions incised with small rivers at elevations ranging from 600 to 110 feet above sea level to semi-mountainous to the west and south with elevations ranging from 1100 to 1800 feet. Vegetation is dense and poses a high degree of hardship for deployment of seismic equipment. Weather conditions are also extreme with high temperatures and humidity in the summer and very low temperatures and large amounts of lake effects snow pack in the winter.

The primary mineral being mined is copper which was hydrothermally emplaced into folded and faulted, low grade metamorphosed, meta-sandstones and meta-shales of Cambrian age. Figure 1 shows a map view of a model of the local geological structure at the horizon of the ore body. The well known White Pine Fault is a large normal fault that strikes at 131 degrees (South-east) and dips steeply at 221 degrees (South-west) and is evident in the lower left quadrant of Figure 1. The White Pine fault dissects a large anticlinal structure which plunges at approximately 10 degrees along a strike of approximately 130 degrees (South-east).

The underground workings at the mine, shown as a map view in Figure 2, are extensive, with rough dimensions of 8 km by 9 km. Historically, portions of the mine have collapsed "naturally" and are denoted by dark black areas in the figure. The naturally collapsed area in the north central portion of the mine has collapsed slowly over a period of many years. The collapsed area south west of the White Pine Fault failed catastrophically, producing a locally felt earthquake and extensive damage to underground mine structures (St. Don, personal communication 1995). The controlled collapse documented here is the first of its type in the White Pine Mine.

Recently discontinued operations at the mine relied on ore removal by the room and pillar mining technique with subsequent movement of the ore to the surface for processing. A number of factors have led to the recent decision to discontinue the room and pillar operation and to begin investigation into the effectiveness of pillar rubblization and in-situ leaching of the ore body remaining in the pillars.

The initial pillar removal operation was conducted on September 3, 1995 at 5:39 PM local time (246:21:39:38 UTM). Prior to the shot, LANL personnel fielded a seismic network designed to characterize the near source wave propagation effects and to determine the locations of aftershocks

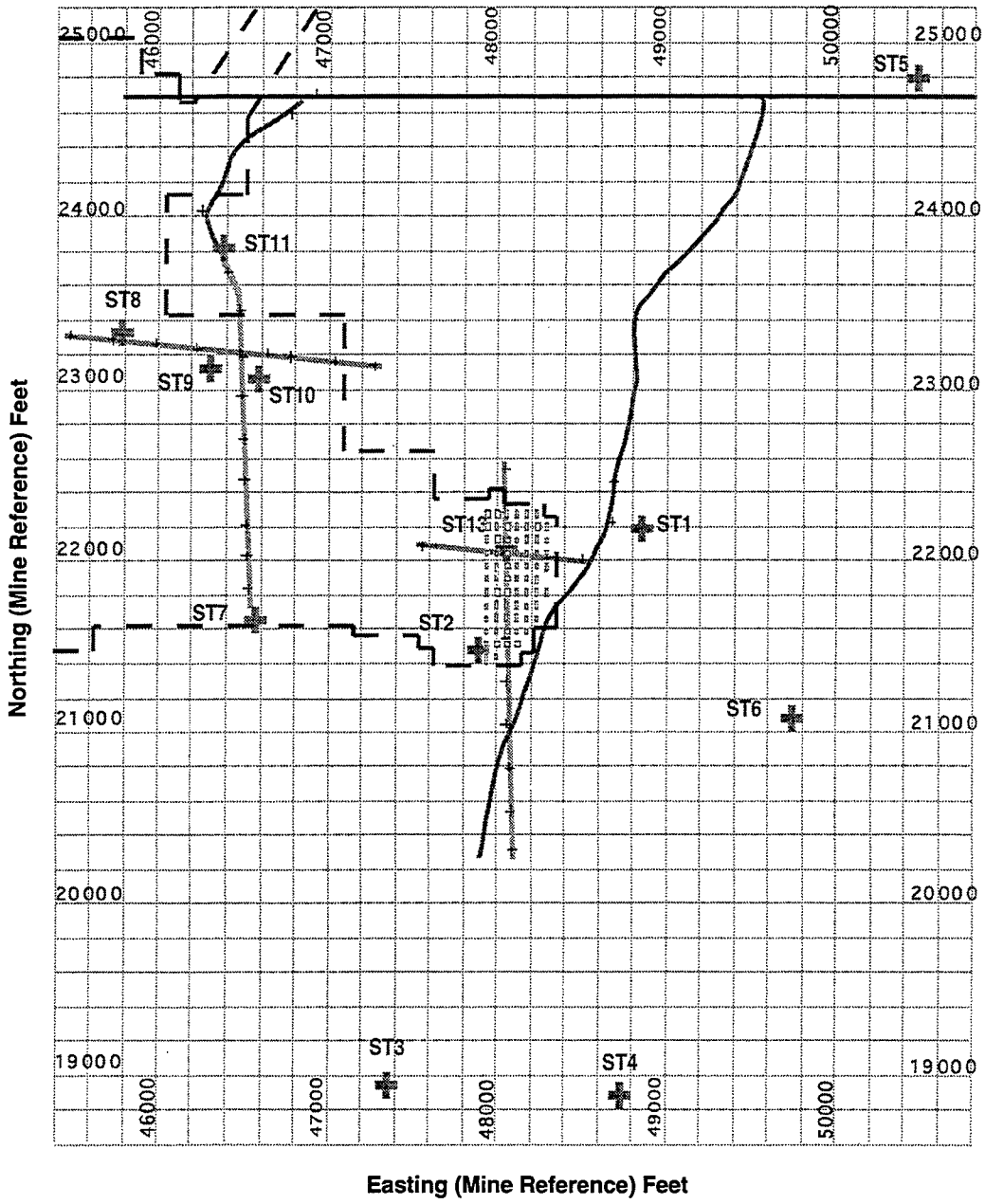

Figure 3: Experimental design for the White Pine Mine Explosively Induced Collapse Experiment. Only that portion of the underground mine that underlies the near source seismic network is outlined with a dashed line. The pillars that were blasted are also shown in the center of the figure. Seismic stations were located along existing roads and survey lines due to the density of vegetation in the area.

component, 1 Hz, Mark Products Model L4-3C geophones were fielded at each station and a 3 component, Terra Tech SSA-302 accelerometer was fielded at ST2. All stations were programmed to record event triggered data using a STA/LTA algorithm with the exception of ST13 (near surface ground zero) which recorded continuously. All channels were initially programmed to record with unity gain to avoid clipping. In addition to the seismic stations, a Hi-8 video camera was deployed at ST13 to document surface motion and acoustic signals.

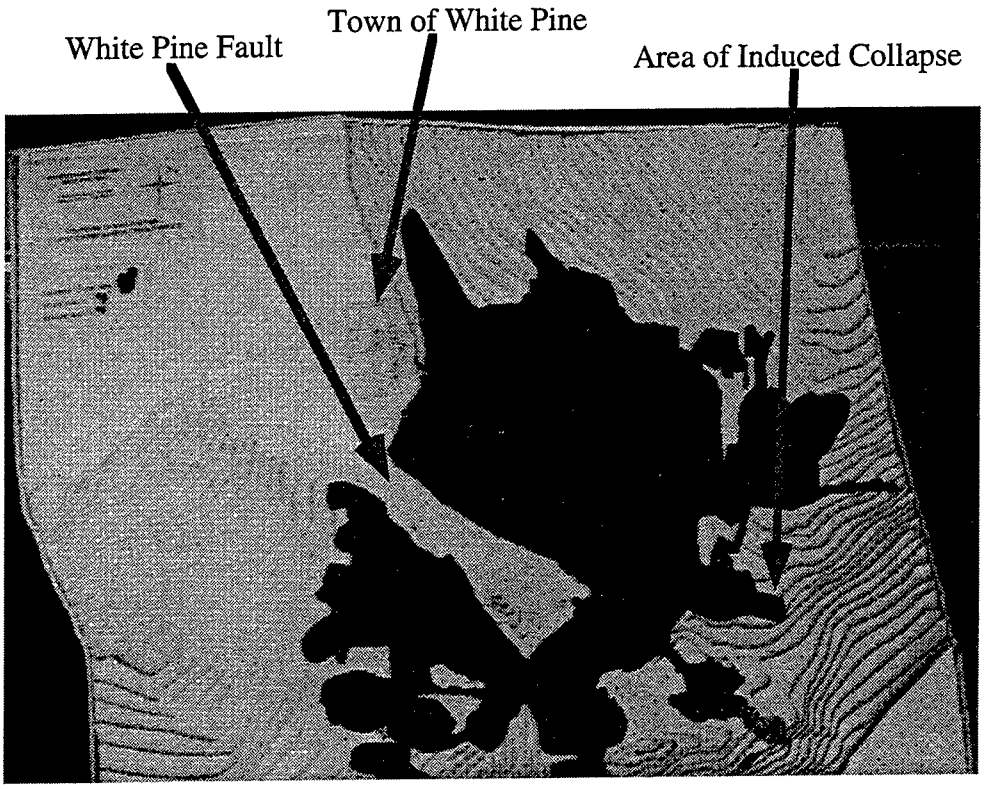

Figure 1. A photograph of a three dimensional model of the White Pine Mine. The White Pine, Michigan townsite, the White Pine Fault, and the area of induced collapse are identified. Structural components readily identifiable are the anticlinal fold which plunges to the south-east and the large displacement White Pine normal fault on the south-west limb. Contour interval 100 feet.

associated with stress redistribution following the explosive pillar removal. Seventy-two (72) pillars with average dimensions of 6.1m by 12.2m were loaded with an average of 1,807 lbs of explosive per pillar for a total explosive source of 130,068 lbs. A millisecond delay firing pattern, 325 milliseconds in length, was used to minimize vibration effects at the surface and propagate the collapse toward the unmined faces. Note that this preliminary test event was designed to be only 1/4 the size of future full scale panel blasts (St. Don, 1995).

Data Acquisition

The areal extent of the seismic network is shown in Figure 3 while pertinent station location information relative the ground zero station are listed in Table 1. The network was designed primarily to aid in the determination of the extent to which chimneying of the overlying rock propagates following the pillar removal. The level at which the explosion occurred is approximately 330 m below the surface.

Twelve stations of the seismic network were distributed in azimuth and range out to approximately 1000 m (3 Depth of Burial). The thirteenth seismic station was located at a range of approximately 5 km to primarily record the electrical shot break signal and secondarily to characterize the wave-field as it propagates away from the source region. Each station was instrumented with a six channel, Refraction Technology Model 72A-08 data logger which was continuously locked to GPS broadcast timing signals for adequate timing accuracy. Three

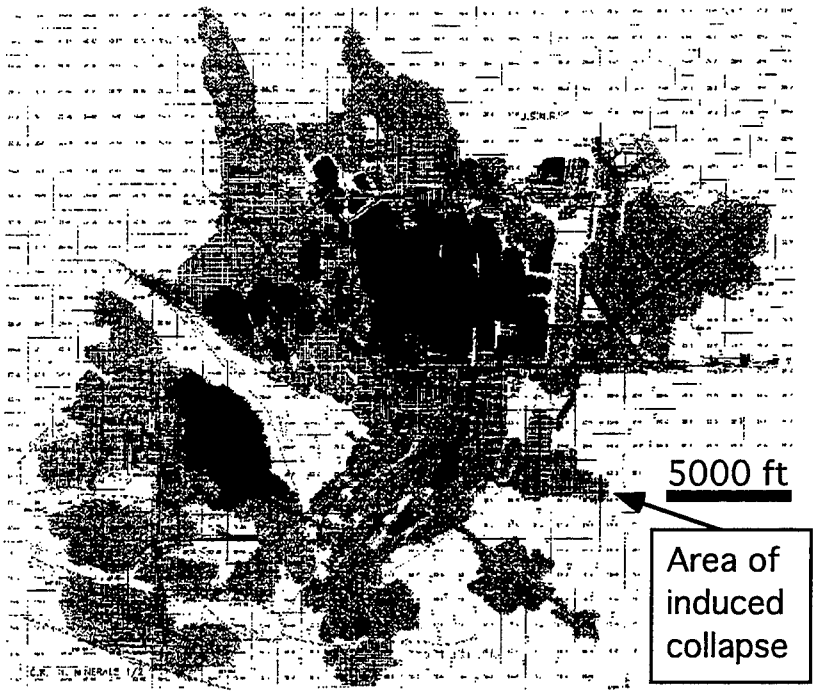

Figure 2. A plan view of the extent of underground workings at the White Pine Mine. Hachured areas indicate room and pillar mined areas while black indicates failed pillar areas in the mine. The failed area outlined in the lower left quadrant on the hanging wall of the White Pine Fault was a catastrophic event which generated regional signals in January of 1989. All other failed areas have experienced slow failure which does not generate large seismic events.

Table 1. Azimuths and distances from ST13 (surface ground zero) to other stations. Magellan Map Datum WGS84.

STATION NAME	BACK AZIMUTH	RANGE (km)	Latitude (deg min)	Longitude (deg min)
ST1	78	0.244	46 43.80	89 29.91
ST2	152	0.201	46 43.68	89 30.03
ST3	191	0.976	46 43.27	89 30.26
ST4	166	0.986	46 43.26	89 29.93
ST5	39	1.104	46 44.23	89 29.53
ST6	119	0.585	46 43.62	89 29.70
ST7	253	0.459	46 43.71	89 30.45
ST8	298	0.782	46 43.98	89 30.64
ST9	299	0.620	46 43.95	89 30.52
ST10	303	0.542	46 43.94	89 30.45
ST11	314	0.727	46 44.06	89 30.50
ST12	300	3.067	46 44.63	89 32.17
ST13	0	0	46 43.78	89 30.10

All seismic stations triggered on the induced collapse event and continued to trigger during the aftershock sequence. The seismic traces recorded at ST12 were contaminated with strong 60 Hz noise induced by ground loop with the electrical firing system. Due to the fact that there was no noticeable expression of the collapse at the detonation point, the video camera deployed at ST13 was recovered within 1 hour of the event to verify that the explosives had detonated and the collapse had occurred. During recovery of the camera, Stump noted that aftershocks could be felt and heard at ST13.

Data acquisition parameters were changed approximately 12 to 14 hours following the main collapse by increasing the pre-amplifier gain. Stations at 2 to 3 depth of burial surface ranges were increased to a gain of x32 and stations at less than 2 depths of burial were increased to a gain of x8. Data acquisition continued for approximately 36 to 40 hours following the main collapse.

Local and Regional Seismograms

High quality three component velocity seismograms were acquired at each of the local stations. Figure 4 shows the Vertical, North/South, and East/West velocities at station 13 (surface ground zero) which have been corrected for instrument response and their associated spectra. At surface ground zero, the vertical component of motion is a factor of 5 larger than the horizontal components. At this scale, the individual explosive sources in the pillars are not resolved but failure of the pillars is indicated by the high frequency arrivals on the vertical component. These failure signals are followed by a long period signal which indicates an initial upward motion associated with release of the material above the working level. Detailed analysis of the data following the collapse event shows that distinct aftershocks are occurring immediately afterward (as with the explosive signals, these aftershock events are not resolved at the graphic level shown). The spectra shown below the time series in Figure 4 indicate the peaked nature of the vertical component at surface ground zero. Horizontal spectra at surface ground zero are essentially flat to 5 Hz and exhibit spectral modulation similar to the vertical component.

Figure 5 shows the Vertical, North/South, and East/West velocities at ST10 which have been corrected for instrument response and their associated spectra. Station 10 was at a surface range of 0.5 km from surface ground zero and exhibits the effect of slant range on the relative amplitudes of the vertical and horizontal traces. In the 0.7 to 3 Hz band, the horizontal components exhibit larger amplitudes than that of the vertical component. Longer period first motions of all components are consistent with a collapse event located to the south-south-east of ST10.

Regional seismograms of the White Pine Induced Collapse were recovered from stations at ranges from 200 to 1000 km. Figure 6 shows the Vertical, North/South, and East/West velocities at station EYMN (range 202 km, 313 degrees azimuth) and their associated spectra. High signal to noise ratio body and surface waves are evident in the data which have been high pass filtered at 0.75 Hz. Spectra of the regional components indicate that in the 1 to 2 Hz band, the vertical component has the largest amplitude. Detailed analysis of the first motion shows that the compressional P arrival is very impulsive with a dominate frequency of 1 to 2 Hz.

Aftershock Locations

All data recorded by the 12 station network were used to associate aftershock events which triggered at least 3 stations. This *computational* association process and subsequent *analyst* event

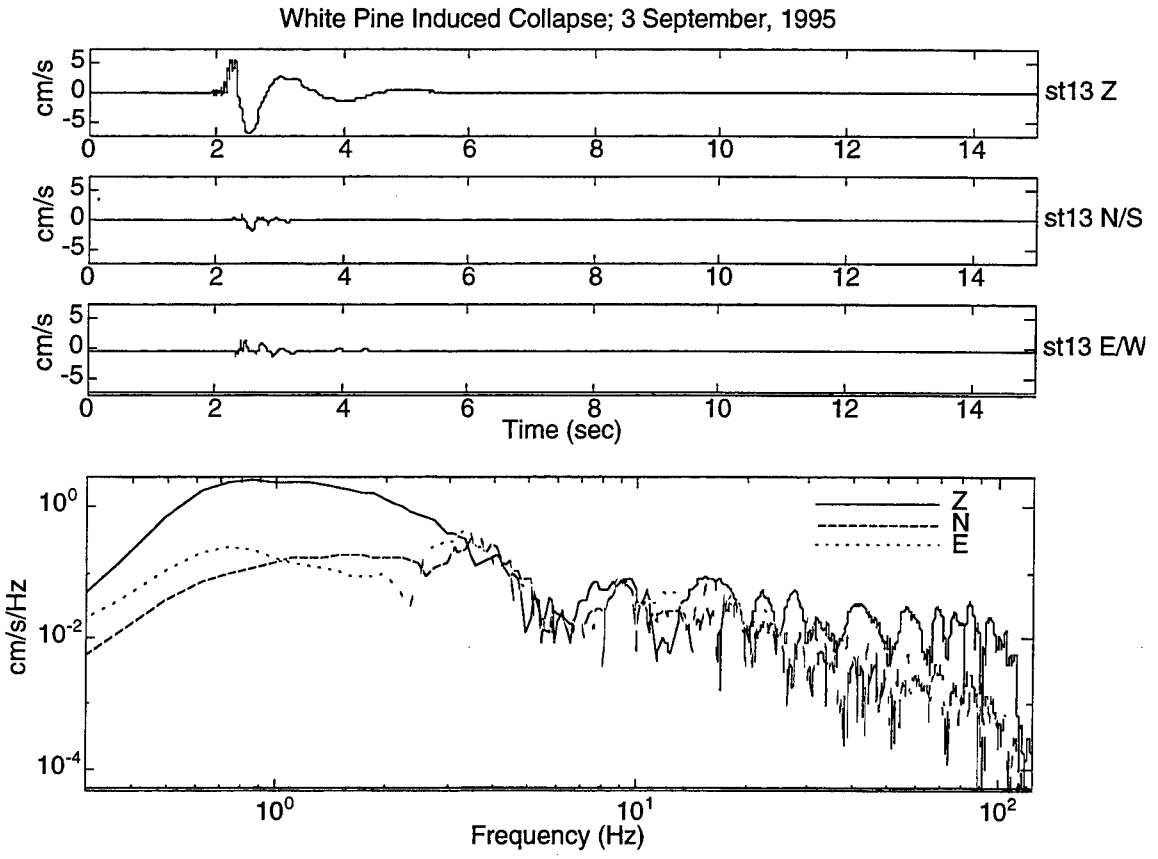

Figure 4. Three component seismogram and spectra of the collapse event at ST13 (surface ground zero) with instrument response removed. Note the high frequency failure events leading to the longer period collapse signal on the vertical component and the peaked nature of the vertical spectrum.

creation and quality control provided a set of 85 aftershocks which were located. Both P and S phases were picked and classified according to quality and polarity for each station and each event.

A velocity model was created based on reflection surveys provided to LANL by the White Pine Mine. This model was used in conjunction with the shot break information recorded at ST12 and first motions at each station to provide station corrections due to static effects of elevation and weathered layer thickness. A relative location algorithm was employed with the known location of the collapse event used as the master event.

Results of the aftershock location exercise are shown in Figure 7. Both a plan view and a cross-sectional view are shown. Station locations are indicated by stars (note that stations ST3 and ST4 are not shown on the map view), aftershock locations are indicated by circles with black filled circles for events greater than 250 feet above the working level, gray filled circles for events at the working level to 250 above the working level, and open circles for events located below the working level. Further analysis of those events located below the working level indicates that these events are most likely multiple events that made it difficult to pick associated phases.

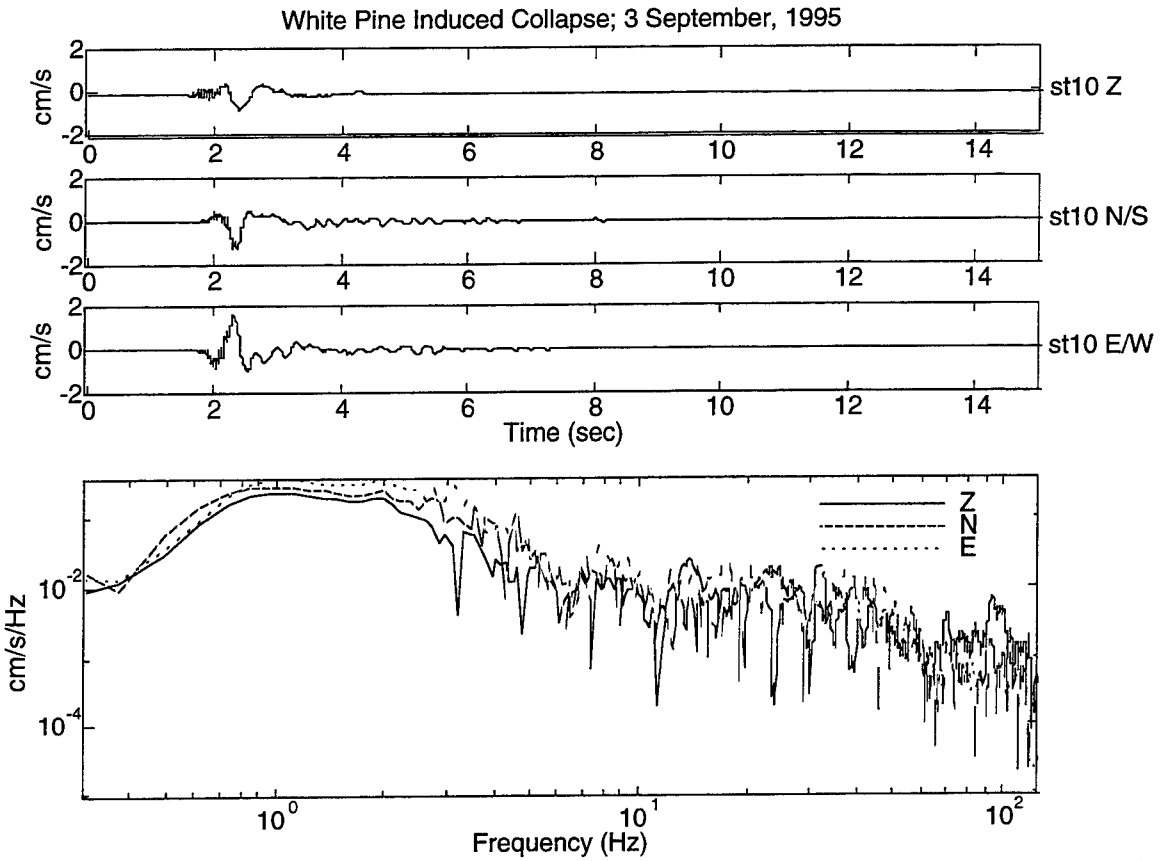

Figure 5. Three component seismogram and full record spectra of the collapse event at ST10 with instrument response removed. Note the high frequency failure events leading to the longer period collapse signal on all components and the similar nature of all spectra.

The frequency of aftershock occurrence decayed rapidly following the collapse event with more than 90% of the high quality aftershocks located occurring within 4 hours of the collapse. The remaining 10% of the high quality aftershocks located occurred during isolated swarms of activity through the remaining 36 hours of network operation. It should be noted that the largest of the aftershocks recorded were more than 2 orders of magnitude smaller in amplitude than the collapse event.

CONCLUSIONS AND RECOMMENDATIONS

The explosively induced collapse of a panel in an underground room and pillar mine indicates that this type of controllable event will generate seismic signals which will propagate to at least near regional distances (as great as 1000 km). Findings by the mining personnel indicate that the event behaved as planned and further work in the pillar rubbilization pilot project will proceed.

Near source monitoring of the mining collapse show that the observed ground motion agrees well with previous work on mining collapses. The individual explosive charges emplaced in the pillars do not produce strong seismic signals, however, the failure of the

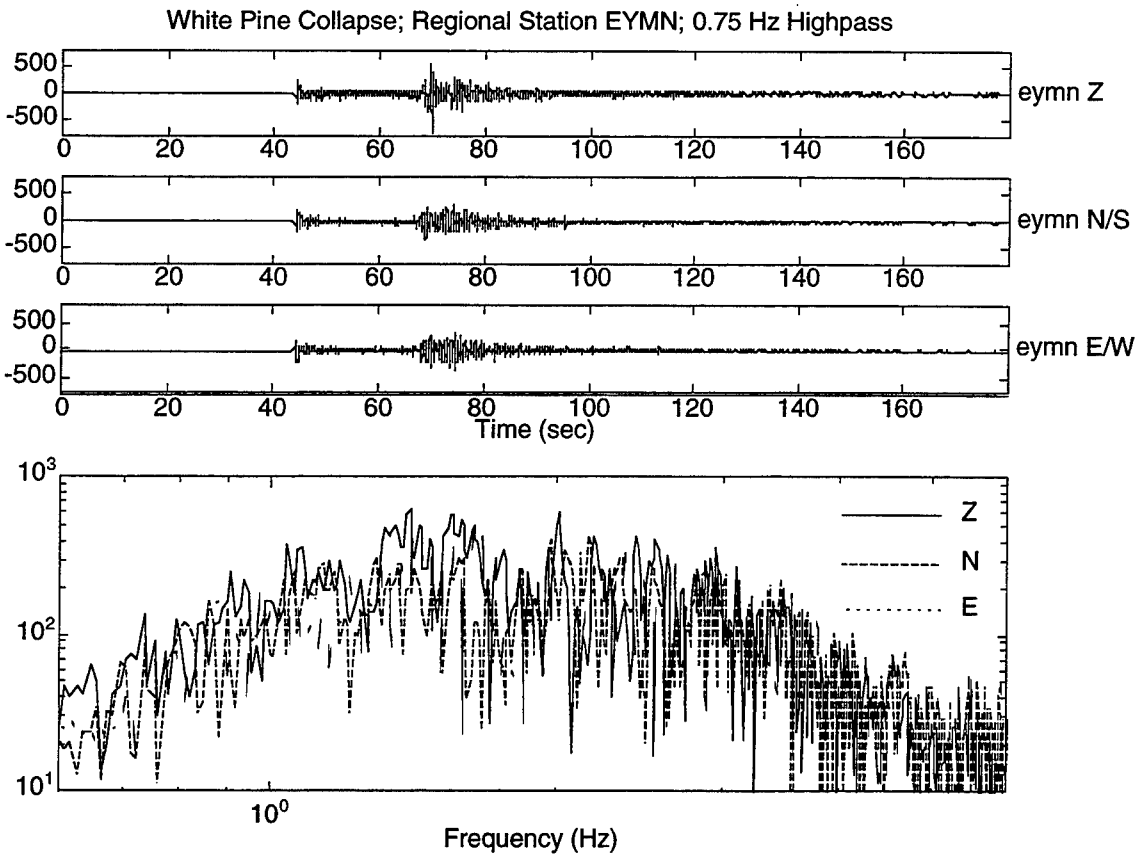

Figure 6. Three component regional seismogram and spectra of the collapse event at station EYMN (range 202 km, 313 degrees azimuth), high pass filtered at 0.75 Hz. Full waveform spectra indicate that the vertical component is peaked between 1 and 2 Hz as was the case in the on-site measurements.

pillars and the material above the working level do produce strong seismic signals. Work continues on determination of local and regional magnitude associated with the White Pine collapse event and the relationship of this magnitude to the area collapsed. It can be concluded that the explosive component of the induced collapse source does not produce regional seismic signals but that the resulting collapse can be expected to be seen regionally.

Aftershocks that occur following the collapse are at least 2 orders of magnitude smaller in amplitude than the ground motion generated by the collapse. The frequency of occurrence of the aftershocks decays rapidly following the collapse. These two observations could be used to argue that it would be extremely difficult to use aftershocks to improve the location determined by regional observations.

The precision of aftershock locations are very good due in great measure to information provided by White Pine Mine personnel including reflection profiles and access to recording the shot break signal. The cooperation of mining personnel was critical to the success of this experiment.

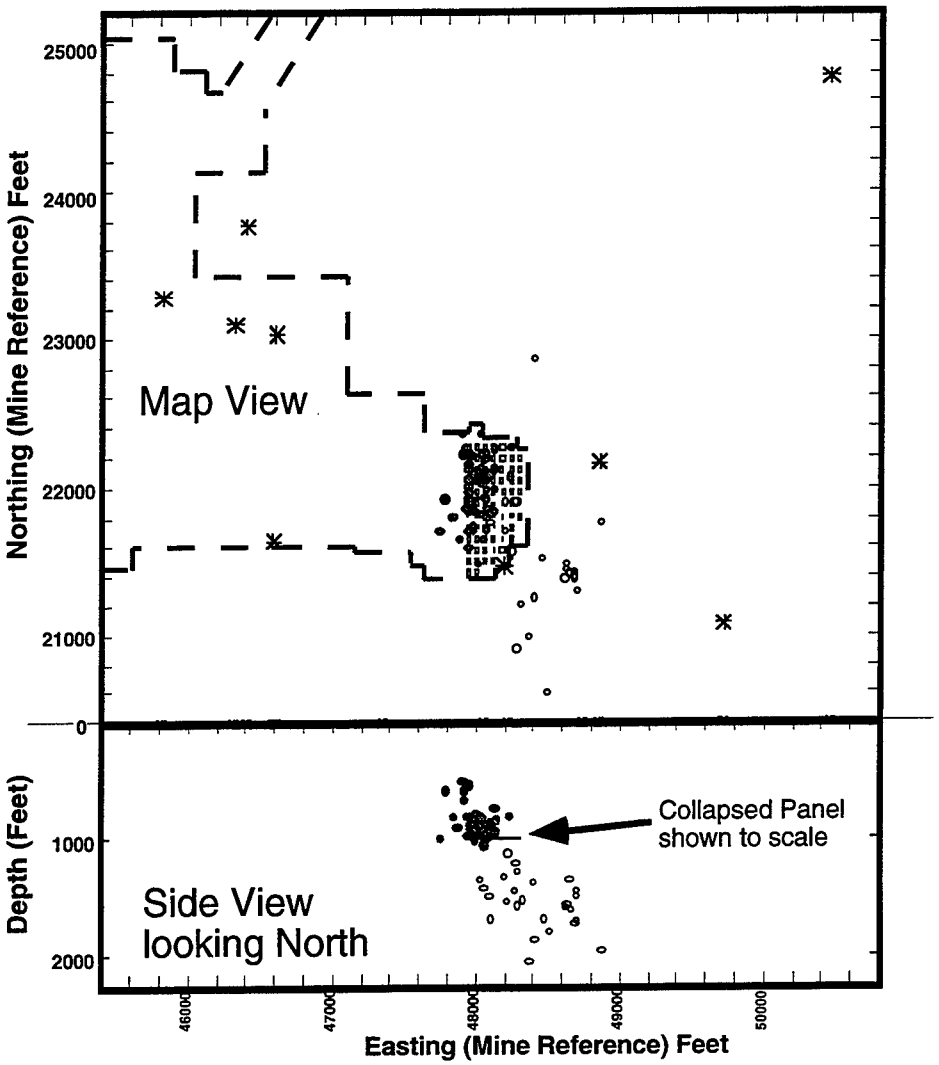

Figure 7. A plan and north looking side view of preliminary aftershock locations for the White Pine Collapse Experiment. Event locations are given by circles where black filled circles locate over 250 feet above the working level, gray filled circles locate from the working level up to 250 feet above the working level, and open circles locate below the working level. Station locations are indicated by the stars.

REFERENCES

St. Don, D. A. (1995), Copper Range Company - Solution Mining Study, Pillar Rubbilization Project 70 Pillar Blast, White Pine Mine Internal Report, 66 pages.

Taylor, S. R. (1994), "False Alarms and Mine Seismicity: An Example from the Gentry Mountain Mining Region, Utah", *Bull. Seism. Soc. Am.*, **84**, 350-358.

Walter, W. R., S. L. Hunter, and L. A. Glenn (1996), Preliminary Report on LLNL Mine Seismicity Deployment at the Twentymile Coal Mine, Lawrence Livermore National Laboratory, Livermore, CA, UCRL-ID-122800, Jan.

BLASTING INDUCED SEISMIC EVENTS IN KOLAR GOLD FIELDS.

C.Srinivasan
Scientist and Head, Seismology Division
National Institute of Rock Mechanics
Champion Reefs - 563 117
Kolar Gold Fields, India

ABSTRACT

Mine induced seismic activity is a common phenomenon all over the world and so also in the century old mines of Kolar Gold Fields in Southern India. Blasting is the usual mining operation carried out daily to break rockmass for production. This alters stress conditions around blasting location and triggers seismic events in the vicinity or in the region where the rockmass attained the brink of instability due to overstressed state. Statistics on mine blasting induced seismic events in different regions of mine working is needed to have better understanding of the mechanism of these seismic events and to distinguish them from other types of events. The influence of blasting on the number of seismic events is quite dominant in this gold mines. This paper attempts to discuss the details of blasting induced seismic events observed and its significance.

Key words : blast, seismic events,trigger, mechanism and instability.

INTRODUCTION

The very high inherent stresses in the rocks of Kolar Gold Fields (KGF) mines give rise to ground control problems and rockbursts of large magnitude. The phenomenon of sudden and violent failure of rockmass in and around the mine workings releasing tremendous amount of energy is termed as rockbursts. Rockbursts belong to that sub-set of seismic events which cause damage to mine workings (Salamon, 1974). The details of seismic events and rockbursts together with their energy and instances of damage for the KGF mines for the year 1989 is shown in Table 1.

Table - 1. Seismic events and rockbursts

Energy of events (ft-lbs)	10^4	10^5	10^6	10^7	10^8
No.of Seismic events	278	21	36	8	2
Instances of damage or number of rockbursts	0	2	2	1	1
Percentage of rockbursts	0	1.8	5.6	12.5	100

The damage to the underground workings depends on the magnitude of the seismic event and its location. A major event far away from the mine workings has no effect on the structure, whereas even small events in the working areas may cause severe damage. The percentage of rockbursts which manifests in damage increases as the magnitude of seismic events increases.

With regard to the mechanics of small and large rockbursts, the seismic equivalence between rockbursts and earthquakes had been determined (Spottiswoode and McGarr,1974) who had observed that mine tremors appeared to be highly similar to natural crustal earthquakes with regard to stress drop, the relationship between moment and magnitude and the relationship between size and magnitude. Richter(1958) has asserted that rockburst are true earthquakes. Brady(1977) has concluded from rock failures that the same physical processes were operative on the small scale (laboratory), intermediate scale (mine failure) and large scale (earthquake) failures.

The seismic investigation carried out in the mines of Kolar Gold Fields using 14 geophones in the seismic network has been used to monitor all the seismic events in the region. The details are described in Srinivasan 1995. The seismic network has recorded more than 12,000 different types of seismic events over the past 15 years. This paper aims at analysing those seismic events induced solely due to mine-blast to understand their significance and differenciate these seismic events for different areas of mine environment.

BLASTING INDUCED SEISMIC EVENTS

Induced seismicity due to blasting is one of the serious hazards associated with mining in highly stressed rock. It has been observed that events induced by mining activity radiate seismic energy in the form of microearthquake having Richter magnitude in the range of -6 to 5 where the smaller events corresponds to seismic events and the larger ones are rockburst.

The frequency of radiated energy ranges from 1 Hz to 1kHz. The part of this frequency spectrum in which most of the energy is concentrated depends upon the size of the event, the frequency decreases with increasing size of the event and the high frequencies tend to be attenuated rapidly with increasing distance from the focus of the event.

In the KGF mining area the majority of seismic events are triggered by routine mining activity such as blasting. It is observed that the incidence of seismic event, during the period of blasting and the period following it, is always higher. This observation was supported by the seismic data for the period from 1981-1990 in Kolar Gold mines as can be seen from figure 1. The induced seismic events from the two significant mines are discussed here in detail.

a) Champion Reef mine.

This mine is the deepest one in the Kolar Gold mines. The mining operations were carried out at a depth of 3.25 km from the surface. During 1987 the total number of seismic events recorded from this mine is found to be 344. 62 seismic events have been recorded during and within one hour after the production blast time. It is interesting to note that 36 seismic events have been reported to have been triggered by blasting in the close vicinity of the blast location. This has been confirmed by the computed focii of the recorded seismic events.

b) Nundydroog mine.

In this mine the mining operation is restricted to 1.5 km and the severity of rockburst problem is less compared to the Champion reef mine. The number of seismic events recorded from this mine during 1987 is 244. Out of this only 84 seismic events have occurred during and within an hour of the production blast. Similar to Champion reef mine, 25 events have been reported to have been triggered by blasting in the close vicinity of the blast location, are the same from the computed source locations of these seismic events.

Table 2 shows the year-wise percentage distribution of seismic events which are triggered due to production blasting from the deeper levels of the Champion reef mine and the Nundydroog mine.

Table- 2. Percentage of Seismic events triggered by blasting

Year	Champion Reef Mine	Nundydroog Mine
1980	27	63
1981	14	52
1982	17	52
1983	15	49
1984	15	52
1985	19	56
1986	19	48
1987	16	48
1988	28	45
1989	23	40
1990	9	38

From the Table-2 it can be seen that the percentage of seismic events triggered in the Champion Reef mine is less compared to that of the Nundydroog mine. This is due to the fact that the mine workings in Champion Reef mine are deeper and the ore body to be mined is associated with faults, dykes and pegmatites, whereas the mine working in Nundydroog mine is shallow and the ore body to be mined is less associated with the geological discontinuities. Due to the lesser concentration of geophone in the Champion reef mine, the percentage of seismic events recorded during the blasting period is comparatively less than the Nundydroog mine.

In mining operation,the rock is strained repeatedly by varying loads which often exceeds the elastic limit because the objective here is to remove the mineral from underground by blasting. Thus due to repeated blasting operation, the redistribution of stresses triggers the seismic events of different magnitude. The knowledge of statistics of mine blasting and its influence on the induced seismic events would help in the safety of workmen and also to discriminate natural and induced seismicity associated with various influencing parameters.

DEEP HOLE BLASTING

The deep hole blasting is carried out in the Nundydroog mines for production of larger tonnage from the mine. This blasting is different from routine blasting operations. The necessity of new developments at shallower depth also provides opportunity for adopting newer techniques in ground breaking. The general details of experiments conducted in deep hole blasting with sub-level caving method between 1800' -2000' levels in Nundydroog mine are as under:

Drilling days	21 days
Length drilled	1760 mtrs
Depth of holes	6.7 to 11 mtrs
Stage of blasting	5 rounds
Single largest charge load	1000 kgs
Total quantity of explosives	3210 kgs
Estimated ground broken	2940 tonnes.

The deep hole blasting experiment with practically no disturbance in the adjoining working places has been successful. The signals from these blasts as picked up by the seismic network has been computed using the following velocity model.

Model 1 : P - wave velocity

" - 6.97 km/sec; X <= 11275 ft
" - 6.53 km/sec; X >= 16950 ft
" - 6.94 km/sec; 11275 < X < 16950.

Model 2 : Uniform P - wave velocity 6.94 km/sec.

The data of known rockburst suggested two different velocity models depending upon whether the field sensors are in close proximity to the source (regional data) or they are situated far away (far-regional data). X denotes X-axis (North-South) of the mining area. As shown in model-1 comprises a P-wave velocity of 6.97 km/sec. in the region extending towards the southern end of the Nundydroog mine (X-coordinate < 11275 ft) and much lower velocity of 6.53 km/sec. over a major part of the Champion reef and the Mysore mine section.(X > 16950 ft.). For the remaining part between the two sections(11275 < X < 16950 ft.) the model has P-wave velocity of 6.94 km/sec. Model-2 consists of a uniform P-wave velocity of 6.94 km/sec. throughout the North-South trending mining area.

The details of computed and actually observed source locations of deep hole blasting (Chemical explosion) is shown in Table-3.

Table 3 Summary of computed and observed Source locations of (Chemical explosion)

Event No.	Date and Time	Actual source coordinates (ft)	Computed source coordinates(ft)
1.	15.5.80 22:16:06	X - 4445	4125
		Y - 6735	6710
		Z - 1895	1781
2.	16.5.80 21:36:38	X - 4225	3997
		Y - 6725	6774
		Z - 1830	1769

The computed sources of deep hole blast using the velocity model show generally good agreement with their corresponding observed values.

LOCAL MAGNITUDE OF SEISMIC EVENTS

Empirical relation for event magnitude is obtained for a region by using the standard equation used for magnitude calculation. The constants in the following equation is computed by knowing magnitudes of different events of a region with the help of other standard recording system:

$$\text{Log } E = a + bM \qquad - 1$$

Where E is the energy and M is the magnitude in Richter scale. For Kolar Gold Fields, the constants a and b is obtained by substituting magnitudes of rockbursts known from the Seismic array station, Gauribidanur which is 110 kms away from KGF. The equation derived by this method is given by

$$\text{Log } E = 13.98 + 0.65\ M \qquad - 2$$

This equation has been verified from the magnitude obtained using the seismogram of KGF rockburst recorded at other seismic array station mentioned above. The magnitude scale used is based on the measured signal duration given by

$$M = - 0.68 + 2.39 \log_{10} D + 0.00217d - 1.097 \log_{10} d \qquad - 3$$

Where D is the duration of the record obtained at seismic array Gauribidanur(Gangrade,1986) and d is the epicentral distance in km.

The magnitude of rockburst are computed using equation 2 and are shown in Table - 4.

Table - 4. Magnitudes of Seismic events

Sl.No.	Date & Time	Magnitude[1]	Magnitude[2]
1.	19.11.91 22:21:31	2.2	2.7
2.	21.11.91 22:30:09	0.9	0.9
3.	22.11.91 20:20:50	1.5	1.5
4.	04.12.91 18:40:40	2.0	2.3
5.	05.12.91 00:17:38	1.7	1.7
5.	07.12.91 11:15:02	1.0	1.3
6.	08.12.91 19:07:01	1.9	2.2
8.	12:12:91 02:42:24	2.6	3.0
9.	15.12.91 13:07:22	2.5	2.7
10.	15.12.91 19:08:27	1.6	1.8

1 - Determined using the relation obtained for KGF region.
2 - Determined using the Seismic Array station data.

As can be seen that the magnitude are agreeing fairly well between the two magnitude relations 1 and 2. Thus using the equation 2 the magnitude computed becomes suitable for the local events in KGF and hence termed as local magniude.

DISCUSSION

The continuous monitoring of seismic activity in and around the Kolar Gold mines has become a formidable tool to understand the phenomenon of rockbursting and the role of geological and mining parameters in inducing the distribution and nature of tremors. Statistical analysis of seismic events reveals that out of the seismic events resulting from mining activity, only few percentage results in rockbursts which

causes damage. The influence of blasting on the number of seismic events is very significant. Analysing waveforms of different types of seismic events including induced due to blasting would help to discriminate them. The existing recording system is analogue and digital recording system would help to do better signal processing analysis to meet the interest of CTBT verification.

FUTURE PLANS

A proposal has been submitted through the EOARD/AFOSR to analyse some seismic events and to determine the source parameters of these seismic events. This analysis would help to understand the source mechanism of seismic events, classification of seismic events of different types recorded in different areas of mine environment and its ground vibration effects in the mine and on the surface structures based on the source parameters determined. An effort will be made to obtain records of selected events from other seismic monitoring stations to allow a comparison of regional seismic signals with close-net station.

ACKNOWLEDGEMENT

The author is thankful to the Director, National Institute of Rock Mechanics, Kolar Gold Fields, for permitting to present and publish this paper in the 18th Seismic Research Symposium to be held at Maryland USA during September 1996. Dr.Anton M.Dainty, Deputy Director,Earth Science Division of Phillip's laboratory is thanked for inviting me to present the paper in the Symposium. Dr.Thomas E.Davis, Liaison Scientist, AFOSR/AOARD is also thanked for arranging WOS visit to attend the Symposium. Finally the whole hearted support from all colleagues of the Seismology Section is sincerely acknowledged.

REFERENCES

Salamon, M.D.G.(1974) - Rockmechanics of underground excavations. Proceeding. Advances in Rock Mechanics, 3rd Congress ISRM, 951-1099.

Spottiswoode S.M. and McGarr A (1974) - Source parameters of tremors in the deep level gold mine (Johannesburg : University of the Witwatersrand, Bernasd Price Institute of Geophysics,).

Richter C.F.(1958) - Elementary Seismology (San Francisco: W.H. Freeman,), 366.

Brady B.T. (1977) - An investigation of the scale invarient properties of failure, Int. J Roch.Mech.Min.Sci 14, 121-6.

Srinivasan C. (1995) - Seismic monitoring of Rockbursts and underground Blastings for assessing the stability of Deep mine workings at Kolar Gold Fields. Proc. 17th Annual Seismic Research Symposium on monitoring a CTBT, 12 - 15 Sept. 1995 PP 581 - 591. PL-TR-95-2108, ADA 310037

Srinivasan C.(1993)- Seismic and Microseismic precursory signals for monitoring and prediction of rockbursts in Kolar Gold Fields, Ph.d thesis, Karnataka Regional Engineering College, Mangalore University, India (Unpublished)

Srinivasan,C. and Shrikant B.S. (1990)- Mine Induced Seismicity in the Kolar Gold Fields ISSN 0016-8696. Gerlands Beitr, Geophysik Leipzig. 99 I.S. 10-20.

Gangrade et.al. (1986)- Earthquakes from Penninsular India: Data from the Gauribidanur Seismic Array for the period Jan-Dec. BARC, Internal report 1385.

Arora S.K. (1981) - A study of rockbursts inside the Gold Mines at Kolar in Southern India, Indo-German workshop on Rockmechanics held at National Geophysical Research Institute, Hyderabad, India.

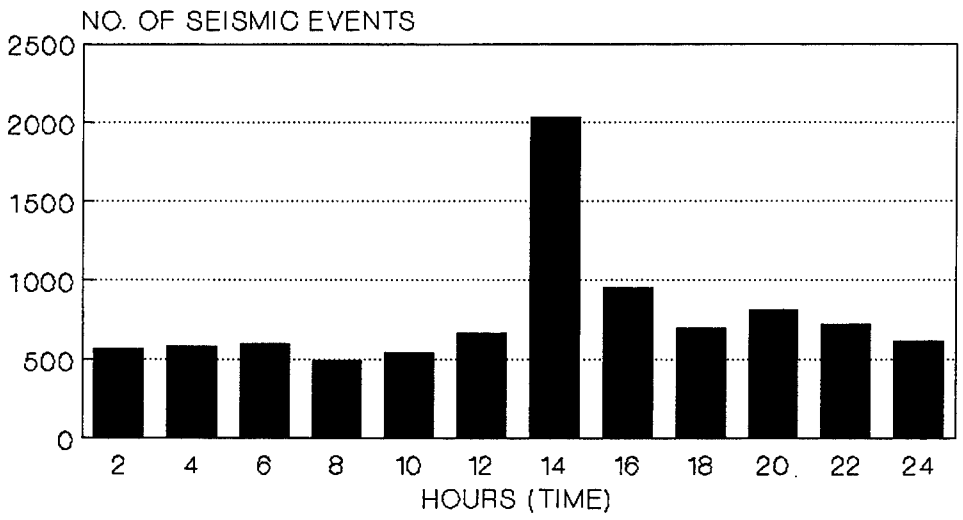

FIG.-1 - SEISMIC EVENTS VERSUS TIME
BLASTING TIME AT 14 & 20 HRS.
SEISMIC DATA FOR THE PERIOD (1981-90)

Design and Utilization of a Portable Seismic/Acoustic Calibration System

Brian W. Stump and D. Craig Pearson
Geophysics Group - EES-3, Los Alamos National Lab

Sponsored by U.S. Department of Energy, Contract W-7405-ENG-36
Comprehensive Test Ban Treaty Research and Development Program, ST482A

ABSTRACT

Empirical results from the current GSETT-3 illustrate the need for source specific information for the purpose of calibrating the monitoring system. With the specified location design goal of 1000 km^2, preliminary analysis indicates the importance of regional calibration of travel times. This calibration information can be obtained in a passive manner utilizing locations derived from local seismic array arrival times and assumes the resulting locations are accurate. Alternatively, an active approach to the problem can be undertaken, attempting to make near-source observations of seismic sources of opportunity to provide specific information on the time, location and characteristics of the source. Moderate to large mining explosions are one source type that may be amenable to such calibration. This paper describes an active ground truthing procedure for regional calibration. A prototype data acquisition system that includes the primary ground motion component for source time and location determination, and secondary, optional acoustic and video components for improved source phenomenology is discussed. The system costs approximately $25,000 and can be deployed and operated by one to two people thus providing a cost effective system for calibration and documentation of sources of interest. Practical implementation of the system is illustrated, emphasizing the minimal impact on an active mining operation.

Key Words: regional seismology, calibration, ground truth, explosion

OBJECTIVE

1. Motivation. The need for calibration of the International Monitoring System (IMS) has been illustrated as locations produced by GSETT-3 have been assessed relative to ground truth information (regional network locations) during the last year (GSE/US/106, GSE/US/108, GSE/FR/22 and GSE/WGE/16). Systematic errors in location can be large and in some instances the actual event location is not contained within the formal error estimates. Bias in locations reflect local and regional variations in the travel time curves for a particular region, inadequate station coverage or problems in depth determination and thus can be location specific. An empirical approach to this problem is the use of events with known location and origin time to develop a set of corrections to the regional propagation model. Once these corrections are established through the analysis of a calibration event, the locations of all other events in the region of interest are improved.

Source information for the purposes of calibration can be provided by locations from local networks although the spatial and temporal characterization in these cases have their own associated errors. A complementary approach to passive calibration is an active one where near-source measurements are made with portable instrumentation at targets of opportunity such as mining explosions. This procedure can provide exact shot time and location for use in improving monitoring system derived locations.

These same calibration procedures (when supplemented with acoustic and video data) can be applied to the characterization of the wavefield generated by the source. Known sources that are documented through this type of extended calibration procedure supply information invaluable in understanding regional seismograms. It is the empirical approach that allows this more rigorous assessment of seismic signals at regional distances.

Mining regions provide an example of the scope of source activity that can benefit from an active calibration exercise that improves the performance of the monitoring network in a specific region. As a result of an experimental program in the last year, an extensive study of mining operations conducted in the Powder River Basin of northeast Wyoming has been undertaken. Within 5000 km^2 there are 15 active mines each producing over 5 Mtons coal/year. This density of possible sources requires precise locations particularly if this information were to be used for an On Site Inspection.

This region has active surface coal mining where large amounts of explosives are used to remove the overburden above the coal as well as to fracture the coal for recovery. As a result of these processes and the large number of mines in the region, there are many seismic signals generated. During 1995, GSETT-3 located 25 events in the basin and in the first four months of 1996 21 events have been formed in this region as reflected in Figure 1.

These results motivate the need for calibration of arrival times as well as signal character from sources in regions of interest. Table 1 compares a number of REB (Reviewed Event

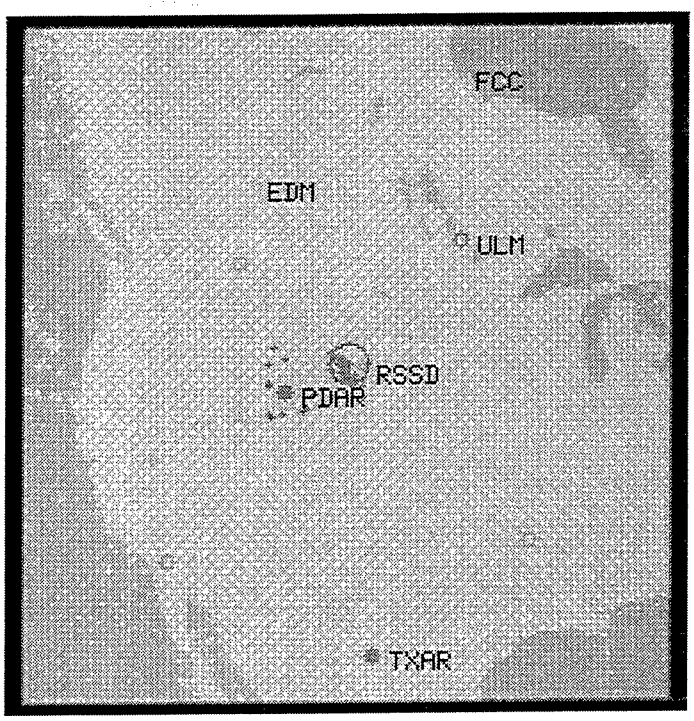

Figure 1: GSETT-3 Events from Wyoming (IDC Home Page). The Cluster of Events in NE Wyoming are in the Powder River Basin

Table 1: Comparison of REB ands Mine Locations

Date Time	REB Lat	REB Long	MINE Lat	MINE Long	DIFF km
950126 234342.8	43.64	-105.32	43.68	-105.27	6
950211			43.64	-105.26	
201835.4	43.56	-105.23			9*
221238.4	44.27	-105.74			80*
222355.6	43.79	-105.54			28*
950317 203727.3	43.56	-105.13	43.64	-105.26	14
950718 1914742.4	43.58	-104.98	43.69	-105.26	25
960311 201336.9	43.61	-105.22	43.64	-105.26	5
960405 201359.0	43.77	-105.34	43.66	-105.27	14

* The ground truth information provided by mine had an imprecise shot time based on the blaster's log and therefore could be associated with any one of three events in the REB.

Bulletin) locations provided by GSETT-3 with ground truth information gathered from one mine in the region. Assessment of the REB locations is only possible as a result of calibration. In this case, the performance of the network is validated with the calibration information while in other regions the calibration data can be used to reduce bias in locations.

2. Calibration Needs. Some have suggested that blaster's logs typically taken by the mines can be used as a source of information on event time and location for purposes of calibration. These documents provide location to the nearest quarter section (0.65 km^2) and time to the nearest 15 or 30 minutes. Many of the largest mining shots have source dimensions that exceed the accuracy of the reported location. Typically, safety issues within the mine, including the clearing of personnel, control the exact shot time and thus the recorded explosion time is the blaster's best estimate, possibly with a reference to his watch. This information, in conjunction with accurate spatial locations within the mine, could be useful for calibration assuming that a recorded signal could be correlated with a particular mine.

Unfortunately, in an active mining region such as the Powder River Basin where individual mines shoot an a daily basis, it may not be possible from the blaster's log to associate a particular regional signal with a single mine unless very precise documentation of the explosion detonation time is undertaken. Table 1 illustrates the problem, where on 11 Feb 95 there were three GSETT-3 events in the Powder River Basin in an approximate 2 hour period and two events within 11 minutes of one another. We were provided with ground truth information from the mine as to precise spatial location of a large cast shot conducted on 11 Feb 95. Typical of blaster's logs (this event was not documented with the calibration instrumentation), the shot time was given as some time around 2200 hours (UTC). With this information, it is difficult, if not impossible, to know with which of the three REB events on the 11th that the ground truth information should be associated. In Table 1 the location difference between each of these three REB events with the ground truthed location is given. Depending on which event is the one generated by the mine, quite different conclusions about the monitoring network performance can be reached. This problem of association can be a problem with blaster's logs but can be avoided with appropriate calibration instrumentation.

The alternative approach to obtaining ground truth information for monitoring system calibration/validation suggested is with a set of simple and easily deployed portable instrumentation. If such a system of equipment could be deployed and operated by one or two people with a minimum of effort then it would provide a cost effective methodology for calibration using sources of opportunity such as those available in an active mining region. This system is described in the next section followed by an illustration of its utilization.

RESEARCH ACCOMPLISHED

3. Example of System The design goals for the calibration system are that it must be deployable by one to two people in approximately one to two hours at a remote site.

The minimum source information it must provide is the origin time and location of the event. Since a supplemental goal of the system is a quantification of the character of the source, in the case of surface explosions, information associated with the design and detonation of the explosions is useful. Video and acoustic measurements that supplement the primary seismometers are included for this purpose. The system should be able to run unattended for hours to days depending on the particular application. The requirement for unattended operation is to accommodate safety issues in the mine at the time of detonation. The ability to record data over the time period of days (excluding video) provides the opportunity to use the system to monitor activity in a mine or mining district for an extended period of time with little or no intrusion on the commercial activities.

The data acquisition system should include six channels, with sample rates as high as 500 samples per second and resolution as high as 24 bits. The high sample rate assures that the system is able to acquire high frequency data which may quantify the detonation times of delay fired mining explosions and the 24 bits assures adequate dynamic range and data with the highest possible bandwidth. An example of a acquisition system that meets these requirements is a Refraction Technology data logger fitted with a large disk to assure long- term stand-alone operation. These data loggers are pictured in Figure 2A and B in two mining operations. Time and location is provided to the data logger by a GPS clock and the entire system is battery powered backed by a solar panel (Figure 2A). This GPS receiver, or possibly an additional handheld GPS, is used to determine the location of the explosion. A single GPS can provide a location accuracy of 20 to 50 m for the explosion and the instrumentation. The location error is much smaller than the size of a typical mining explosion which for some of the larger events can have dimensions in excess of 1 km.

For purposes of recording the near-source, three-component wavefield a 1 to 2 Hz velocity transducer has been found to be adequate. In the demonstration system documented in Figure 2A, a three-component Mark Products L43D velocity transducer is deployed before a large cast blast in the Powder River Basin. Two additional vertical geophones are deployed along a line towards the explosions at 10 to 20 m separation in order to determine the phase velocity of the first arriving P wave for purposes of correcting the arrival time of the first P wave at the observation point back to the explosion. Depending on the spatial separation of these geophones and the explosion, shot times to within one or two tenths of a second of the actual shot time can be obtained. If one wanted to place a geophone on top of the explosion, a very precise detonation time is obtained at the expense of the loss of a geophone.

The sixth channel on the data logger could be assigned to an auxillary acoustic gage. A simple instrument that is capable of recording these source signatures close-in at a modest cost has been proposed by Reinke (1985). These instrument have been found simple to deploy and of adequate dynamic range and bandwidth to make these types of source measurements reliably. This data can provide near-source atmospheric signature information and is used in the supplementary task of source characterization.

Many mining blasts are designed with millisecond delay detonation systems. These designs often lead to complex source signatures which should be documented to allow for removal of the source complexity from the regional seismic observations to improve regional locations. A proven technique for providing this type of information in conjunction with a ground truthing system is deployment of a consumer level Hi-8 video camera which captures 30 frames or 60 fields of data per second. One of these instruments is pictured in Figure 2C ready for a large mining explosion in the Powder River Basin.

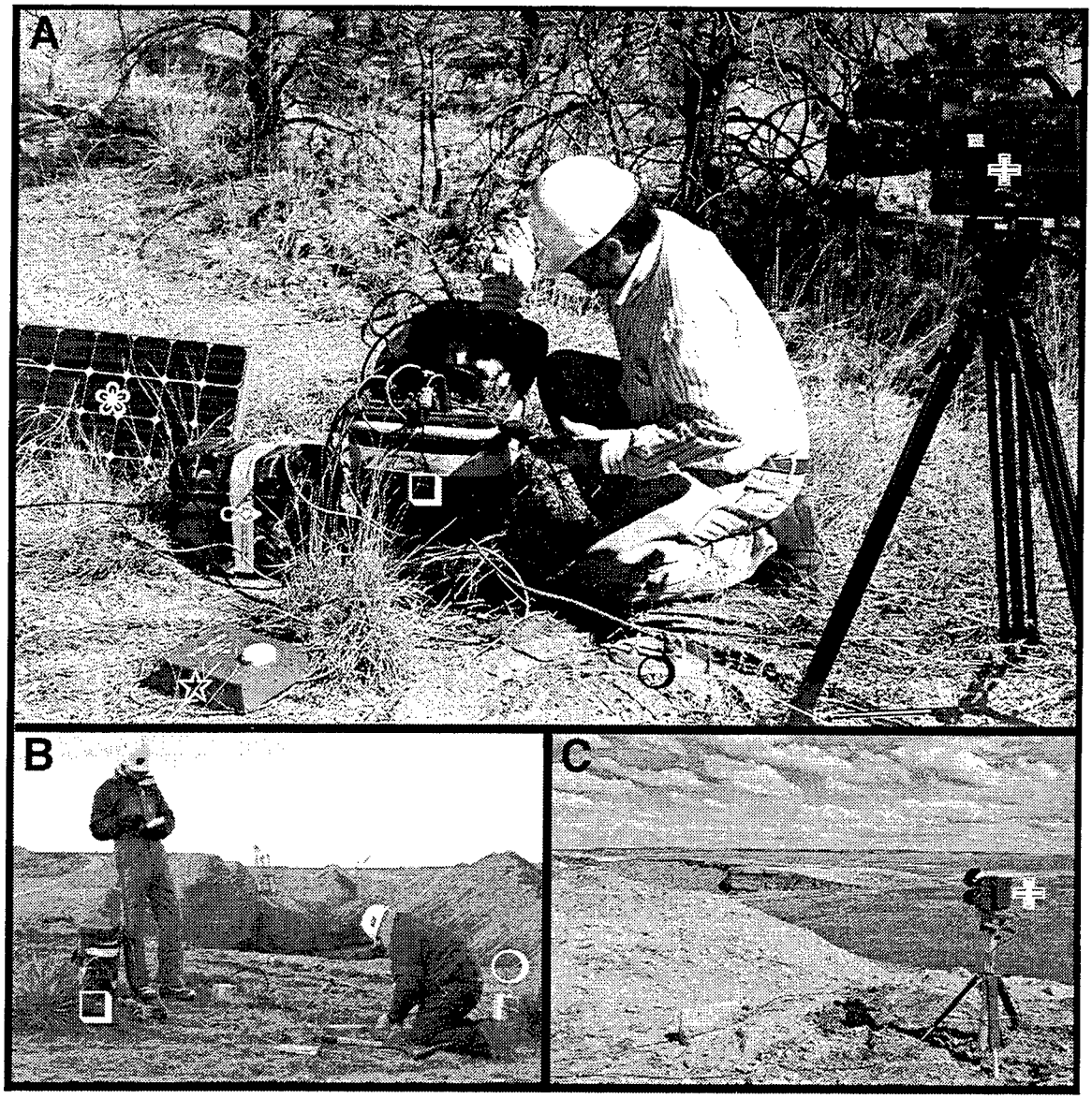

Figure 2 A: The data logger (❑) is attached to the velocity transducer (○) and the GPS receiver (☆). The camera (✙) is to the far right with battery (∞) and solar panel (❀) to far left. B: Installation of the system in a mine just prior to a large cast blast. D: Hi-8 camera (Sony EVW-300) deployment prior to a large cast explosion.

Normally the camera is deployed in the same location as the seismometer and acoustic gage so that the different source phenomena can be correlated for interpretation purposes. It is possible to deploy the camera at a different site if a special perspective of the blasting processes is needed. A number of different cameras in the price range of $1000 to $5000 have been tested such as SONY TR-101 and EVW-300. All are adequate as long as they are Hi-8, which provides improved resolution over standard VHS cameras.

The total cost of this portable system is approximately $25,000 dollars as configured in Table 2. Careful selection of other options from a number of venders could bring the cost closer to $20,000. Thus, a cost effective system that can be used to obtain ground truth information from a number of different sources in widely separated geographical locations with a minimum of impact on the mines and deployable by 1 or 2 people is available.

The system as described is simple to deploy. Practical experience with the installation of this equipment indicates that it can be installed in less than two hours by one to two people. It is completely self contained and thus requires no assistance from the mine in which the measurements are to be made. Even in the case where the equipment is deployed at a location which the mine operators, for safety reasons, would not allow personnel at the time of detonation, the system can operate unattended. In an active region such as the Powder River Basin, the system can be deployed at a number of mines over several days to weeks providing calibration data from a number of spatial locations in a cost effective manner.

Table 2: Portable Ground Truthing Instrumentation Equipment List and Estimated Cost

Component	Possible Manufacturer	Cost
Data Logger, Disk and GPS	Refraction Technology 72A-08	$16,000
3 Component Seismometer	Mark Products L43D	5,000
2 Vertical Geophones	4 Hz Mark Products	200
Acoustic Gage	Validyne Engineering Corp. P305D	2,000
Hi-8 Video Camera	Sony TR-101	1,500
Cables, batteries, solar panels, hand held GPS	miscellaneous	1,000

4. Utilization of Data from System. The instrumentation described in the previous section has been deployed on a number of mining explosions in the last year for the purposes of providing simple ground truthing information as well as documentation of blasting practices within the mines for comparison to the resulting regional signals. Some of the information given in Table 1 resulted from these deployments and has been used to assess the performance of the GSETT-3 locations and error estimates. This type of information offers the advantage over standard gamma data which results from locations utilizing local networks, in that the exact time and location of the sources that generated

the regional data are experimentally documented and do not suffer from their own set of errors. This active calibration procedure provides precise locations that can be compared to those deduced by the monitoring system.

Data gathered by this calibration system can also be used to assess important source processes that lead to the regional signals that will be captured by the International Monitoring System. The fact that a number of different types of measurements are made by the proposed system (ground motion, acoustic and video) allows for the synergism of these different data types into data products that can be used in source interpretation. This combining of the different data sets is illustrated for two separate large explosions at a mine in the Powder River Basin in Figure 3. In these examples, video of the explosion processes recovered at 60 frames/s is combined and time correlated with three-component ground motion and acoustic signals. In addition, a model of the design blasting pattern is also included and time correlated. The synergy of the different data sets (all recovered from the instrumentation described in this paper) provides a time varying record of the explosive processes correlated with the resulting ground motions and acoustic signals. Single frames, with the time listed in the figure, from two mining blasts are included in Figure 3. A description of how these data sets are processed and combined can be found in Stump *et al.,* 1996. This paper is also available on the world wide web along with the time varying images at the address:

www.geology.smu.edu/~dpa.www/blasts.html

Comparing the single frame images from the two mining explosions demonstrates the utility of the measurements made by this portable instrumentation in documenting unusual source processes. The top image is from a shot that detonated in a very regular pattern as exemplified by the relatively equal amplitude of the complete P wave train. The image reproduced in the figure is 2.833 s into the detonation as represented by the vertical bar through the seismograms. The second explosion documented included the accidental simultaneous detonation of a large amount of explosives late in the detonation sequence. This image is at 3.087 s into the detonation with the simultaneous detonation at approximately 4.25 s into the sequence and represented by the large P signal at that time. This peak amplitude is nearly 5 times larger than the peak from the earlier shot (also observed at regional distances) that detonated in a regular pattern thus illustrating how processes in the mining explosion can dramatically affect the seismic waves.

CONCLUSIONS AND RECOMMENDATIONS

There are a number of ways in which accurate spatial and temporal seismic event locations can be obtained for the purpose of calibrating the International Monitoring System and quantifying its performance. Event locations provided by regional networks are one such approach that has been utilized but suffers from the associated errors. In regions where blasting occurs and is documented by mine operators, source location and time information can be used to compare to regional seismic locations. This second procedure depends on the record keeping in the mine and, as illustrated in Table 1, suffers from inaccurate time information which may preclude association of a particular mine blast with a regional signal, especially in areas of active mining.

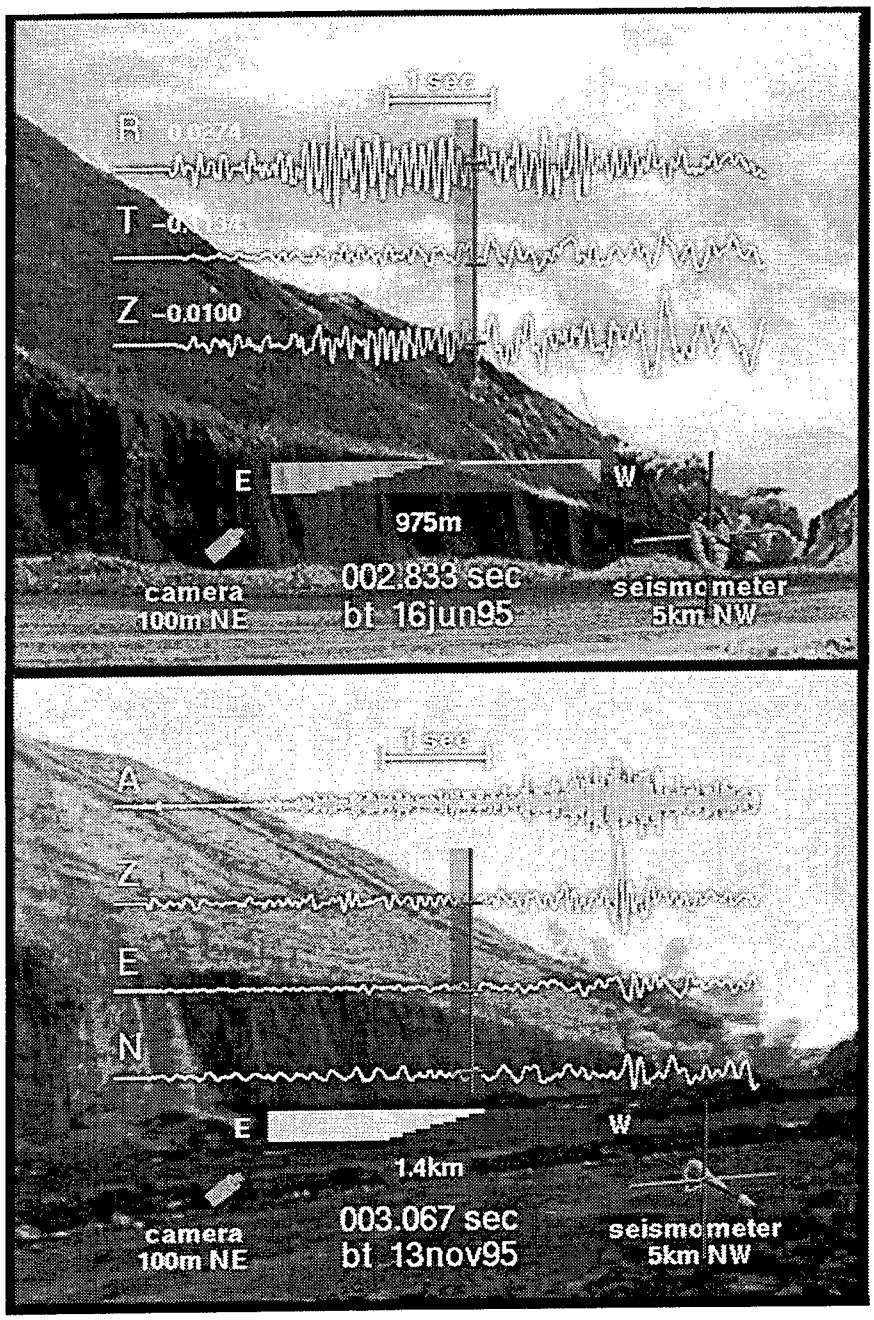

Figure 3: Synergy of ground motion (RTZ or ZNE), acoustic (A), video and models of the design blasting pattern (rectangle in lower center of each figure with individual explosion detonation represented by a change from white to gray). Also included in this figure is the three dimensional particle motion in the lower left hand corner. The two figures are snap shots in time (represented by vertical bar on waveforms) of two large cast blasts. In each case only about one half of the total explosives have detonated at the instant of each image. The 16 June 95 shot detonates in a regular pattern as indicated by the consistent amplitudes in the compressional waves. The 13 November explosion did not detonate evenly but as the data describes a large portion of the explosive array accidentally detonated simultaneously as indicated by the large P wave amplitudes on the vertical velocity record in the lower image.

We propose a third and active approach to the problem of regional calibration. A portable data acquisition system that acquires ground motion for location and shot origin time, and optional acoustic and video data components for phenomenology studies is proposed for temporary deployment in active mines. The system costs about $25,000 and can be easily fielded in less than two hours by one to two people. Without the optional acoustic and video components the system would cost approximately $22,500. This system could be used in a mobile mode to obtain calibration information from a number of sources in different geographical locations in a relatively short time period and at modest cost. Typically the spatial location of the event using this system is within 20-50 m of the source initiation point and within 0.1 to 0.2 s of the initiation time. This information can be used either to provide information for improving the seismic monitoring system through reduction of bias in the locations or validating system performance.

In addition to providing source time and location information, the inclusion of an acoustic gauge and a video camera provides documentation of source processes as well. In preliminary trials of the system, this information has proven to be quite useful in interpreting variations in regional signals from mining sources. The mine operators that we have cooperated with have found that this source information is quite useful to them, as it documents blasting performance, and can identify areas of improvement to reduce ground motion and improve their mining efficiency. The fact that the system is self contained and can operate unattended has allowed its deployment to proceed with little or no impact on mine operators which further enhances the cooperation we have received during its testing.

REFERENCES

FRENCH DELEGATION, Seismological Results of GSETT-3: Comparison of REB and LDG Bulletins for France and Its Borders, 1 January to 31 December 1995, GSE/FR/22

Reinke, R. E. (1985). A Digital Microbarograph System, AFWL-TR-84-142, Kirtland AFB, NM 87117-6008, May 1985.

Stump, B. W., D. P. Anderson and D. C. Pearson, 1996. Physical Constraints on Mining Explosions, Synergy of Seismic and Video Data with Three Dimensional Models, LAUR-96-1141, Los Alamos, NM 87545, April 1996.

UNITED STATES DELEGATION, Contributions of the USNDC to GSETT-3, 1 January - 30 April, 95, GSE/US/106, August 1995.

UNITED STATES DELEGATION, The Use of Auxiliary Stations for Event Location and the Need for Network Calibration, GSE/US/108, February 1996.

Working Group on Evaluation, Summary Report, GSE/WGE/16, February 1996.

THIS PAGE LEFT
INTENTIONALLY
BLANK.

MICROMACHINED SILICON SEISMIC ACCELEROMETER DEVELOPMENT

Carole Craig Barron, James G. Fleming, Stephen Montague, Dale L. Hetherington, Jeffry J. Sniegowski, Brady R. Davies, David L. Armour, and R. Patrick Fleming

Sandia National Laboratories
P.O. Box 5800, Mail Stop 1080
Albuquerque, New Mexico, USA 87185-1080

Sponsored by U.S. Department of Energy,
Comprehensive Test Ban Treaty Research and Development Program, ST4850

ABSTRACT

Batch-fabricated silicon seismic transducers could revolutionize the discipline of seismic monitoring by providing inexpensive, easily deployable sensor arrays. Our ultimate goal is to fabricate seismic sensors with sensitivity and noise performance comparable to short-period seismometers in common use. We expect several phases of development will be required to accomplish that level of performance. Traditional silicon micromachining techniques are not ideally suited to the simultaneous fabrication of a large proof mass and soft suspension, such as one needs to achieve the extreme sensitivities required for seismic measurements. We have therefore developed a novel "mold" micromachining technology that promises to make larger proof masses (in the 1-10 mg range) possible. We have successfully integrated this micromolding capability with our surface-micromachining process, which enables the formation of soft suspension springs. Our calculations indicate that devices made in this new integrated technology will resolve down to at least sub-μG signals, and may even approach the 10^{-10} $G/\sqrt{\text{Hz}}$ acceleration levels found in the low-earth-noise model.

KEY WORDS

Silicon micromachining, microelectromechanical systems, mold micromachining, micromolding, seismic transducers, accelerometers, seismometers, CTBT.

1. INTRODUCTION AND OBJECTIVES

One of the factors inhibiting the effort to collect seismic data for Comprehensive Test Ban Treaty (CTBT) monitoring is the sheer cost, including both the system cost and the deployment cost, of current seismic transducers. Our motivation in pursuing microminiature silicon seismic transducers is twofold. First, such devices would be much less expensive to manufacture than current seismometers, since they could be batch-fabricated in much the same way that electronic integrated circuits are. Moreover their small size would make deployment easier and cheaper as well. Our ultimate goal is to fabricate seismic sensors with sensitivity and noise performance comparable to short-period seismometers in common use. We expect several phases of development will be required to accomplish that level of performance.

We have calculated the best-case performance possible for a seismic acelerometer fabricated in Sandia's experimental "mold-micromachining" technology to be at or very near our most ambitious target specifications. Accordingly, we have actively pursued development of this new micromachining technology, and have this year successfully achieved integration of a micromolded proof mass with compliant surface-micromachined suspension. In this paper we present the design of a prototype device with sub-micro*G* theoretical resolution, and the development of the new fabrication technology required to manufacture these devices. At the symposium we will also present the latest test results from the prototype devices.

2. PROTOTYPE DESIGN

Because the principal axis of interest for seismic measurements is the vertical one, our basic accelerometer design consists of an unbalanced "teeter-totter" platform suspended on opposite sides by two small flexures (Figure 1). This design is a variation on the common "pendulum" design for existing seismic accelerometers, modified to allow differential capacitive pick-offs to be placed to either side of the flexures. We have chosen capacitive pick-offs rather than magnetic coil-based transducers because it is virtually impossible to make a coil in a micromachining process, while parallel-plate capacitors with very small, uniform gaps are a natural in this technology. We also discarded a third possibility, electron tunneling, which has been employed in sensitive accelerometer designs by another micromachining group,[1] because of reliability concerns and because of the $1/f$ noise which limits the performance of tunneling sensors at the very low frequencies which are of interest in seismic monitoring.

The signal-to-noise ratio for the motion of an accelerometer versus thermal-mechanical noise (electronic noise is not usually the limiting factor for seismic transducers) is given by

$$S/N = \sqrt{\frac{a_s^2 m Q}{4\, k_B T \omega_o}},$$

where a_s is the acceleration signal, m the proof mass, Q the so-called "quality factor" (a measure of damping), k_B is Boltzmann's constant, T the absolute temperature in Kelvin, and $w_o = 2\pi f_o$ the natural frequency of the mechanical system.[2] If we insert 10^{-10} $G/\sqrt{Hz}$ for a_s, and the maximum possible Q of 30,000 (corresponding to the intrinsic material damping of a silicon device in an

evacuated package), we obtain a set of pairs of $\{m, f_o\}$ which will give an adequate signal-to-noise ratio. From among these, a potentially feasible pair is $m \geq 10$ mg and $f_o \leq 1$ Hz. In order to achieve these values, it will be necessary to develop a new silicon micromachining technology, as current technologies cannot deliver the combination of large (on this scale at least) proof mass and soft suspension. We have invented a novel fabrication process which addresses these issues — this new "mold" process is described below.

3. SILICON MICROMACHINING TECHNOLOGIES

Silicon micromachining technologies can be divided into three categories — so-called "bulk," "surface," and "mold" micromachining. "Bulk" micromachining generally refers to processes involving wet chemical etching of structures formed out of the silicon substrate and so is limited to fairly large, crude structures. "Surface" micromachining allows patterning of thin films of polysilicon and other materials to form intricate but essentially two-dimensional layered parts (since the thickness of the parts is limited by the thickness of the deposited films). In "mold" micromachining, the mechanical part is formed by filling a mold which was defined by photolithographic means. Historically micromachining molds have been formed in some sort of photopolymer, be it with x-ray lithography ("LIGA") or more conventional UV lithography, with the aim of producing piece parts. Recently, however, several groups including ours at Sandia have independently come up with the idea of forming the mold for mechanical parts by etching into the silicon substrate itself. The following is a quick review of these three micromachining methods intended to clarify the approaches we have taken in fabricating seismic sensor prototypes. Note that the references given here are only examples and are not by any means intended to be a complete survey of the literature.

3.1 Bulk micromachining

The term "bulk" micromachining literally refers to the process of making a mechanical structure out of the bulk material (i.e. the single-crystal silicon substrate). Generally the mechanical structure is formed either by doping-selective[3] or crystallogaphic[4] wet chemical etching. These processes are relatively large-scale and crude compared to the sub-micron photolithographic processes common in microelectronic fabrication, with dimensional variations on the microns to hundreds-of-microns scale. A subcategory of bulk micromachining which offers finer dimen-

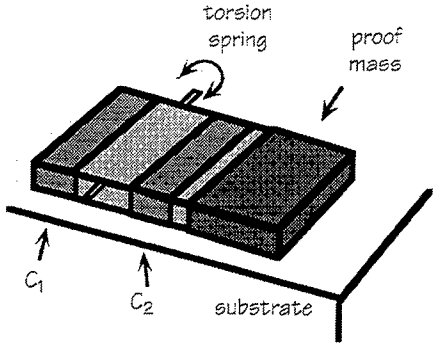

Figure 1. "Teeter-totter" seismic sensor concept.

sional control is dry etching of mechanical structures — again, the part is formed from the single-crystal silicon substrate itself.[5] One of the major advantages of bulk micromachining is that it is relatively easy to fabricate large masses (for accelerometers, for example), but, on the other hand, delicate, sensitive suspensions are difficult to realize. Also, bulk micromachining processes are not particularly compatible with electronics, simply because they aren't planar.

We rejected bulk micromachining as a fabrication strategy for seismic sensors, even though the most sensitive silicon accelerometers to date have been made this way,[1] for several reasons. First, we do not have a mature bulk-micromachining technology at Sandia, and therefore making the prototypes using bulk processes would not leverage well with our other projects. Second, bulk micromachining does not lend itself to monolithic integration with electronics and we are convinced that integrated amplifiers and servo electronics will be necessary in order to achieve the sensitivities required for treaty monitoring.

3.2 Surface micromachining

Surface micromachining uses the planar fabrication techniques common to the microelectronic circuit fabrication industry to manufacture micromechanical devices. The standard building-block process consists of depositing and photolithographically patterning alternate layers of low-stress polycrystalline silicon and sacrificial silicon dioxide. As shown in Figure 2, holes etched through the sacrificial layers provide anchor points between the mechanical layers and to the substrate. At the completion of the process, the sacrificial layers, as their name suggests, are selectively etched away in hydrofluoric acid (HF), which does not attack the silicon layers. The result is a construction system consisting of one layer of polysilicon which provides electrical interconnection and one or more independent layers of mechanical polysilicon which can be used to form mechanical elements ranging from a simple cantilevered beam to complex systems of springs, linkages, mass elements, and joints. Because the entire process is based on standard integrated-circuit fabrication technology, hundreds to thousands of devices can be batch-fabricated on a single six-inch silicon substrate.

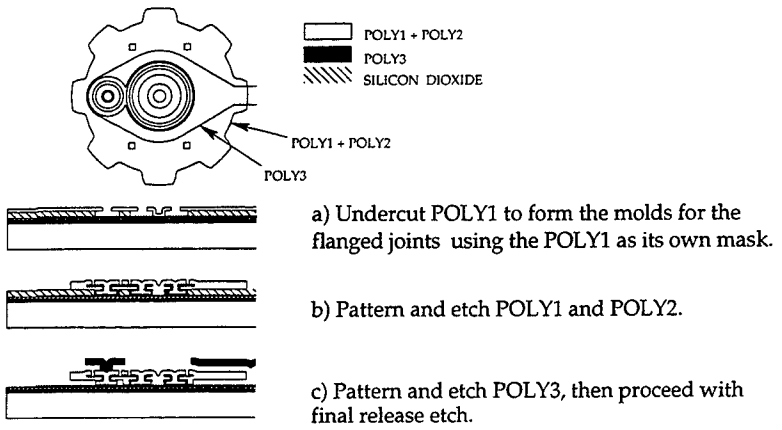

Figure 2: Example surface-micromachining process.[6] These are cross-sections through essential elements of the Sandia microengine gear and joints taken at three stages of completion.

Because surface micromachining takes advantage of the advanced manufacturing processes developed in the microelectronics fabrication industry, it offers the same high degree of dimensional control found in electronic integrated circuit fabrication, and is the micromachining method most compatible with monolithically integrated electronics.[7] The planarity which makes surface-micromachined parts relatively easy to integrate with microelectronics, however, is also the major limitation of surface micromachining — that is, surface-micromachined parts are essentially two-dimensional (since the thickness of the parts is limited by the thickness of the deposited films), and therefore relatively light and compliant. (Typical masses for surface-micromachined components are in the μg range and it is difficult to achieve natural frequencies below 1 kHz.) Sandia's three-level polysilicon process is the world's most sophisticated surface-micromachining technology, and offers integrated electronics as well as complex mechanical parts. We are utilizing surface-micromachining to fabricate the suspension for our seismic transducers.

3.3 Mold micromachining or Micromolding

The principal advantage of all mold micromachining processes are that they make it possible to fabricate high-aspect-ratio parts (i.e. thick relative to surface dimensions). Mold micromachining has generally been used to manufacture piece parts (e.g. gears, etc.), although micromachined structures formed with thick photo-sensitive polymer molds have also been integrated with previously fabricated electronic circuits. Variations on the mold concept include, on the one hand, the well-known "LIGA" process, in which lithography is used directly to form a photoresist mold, and, on the other hand, silicon mold processes, in which the mold is formed by etching into the silicon substrate.

3.3.1 "LIGA" and "LIGA-like" processes

"LIGA" is a German acronym which refers to "lithography, electroplating, and injection molding". The original LIGA process, while it achieves impressive aspect ratios,[8] has only seen scattered application because it requires specialized x-ray lithography equipment. "LIGA-like" processes include ones where the more common UV-exposed photoresist is used instead. These "LIGA-like" processes allow fabrication of thicker parts than can be made using surface micromachining, but are generally limited to much less extreme aspect ratios than the original LIGA process.[9] Both the original LIGA process and the "LIGA-like" processes lend themselves primarily to the fabrication of piece parts which require subsequent assembly into a microelectromechanical system.

3.3.2 Silicon mold processes

The basic concept behind silicon mold processes is that the mold for a micromechanical part is formed by etching into the silicon substrate (Figure 3). Silicon mold processes thus take advantage of the fact that, by etching a high-aspect-ratio mold (that is, one which is much deeper than it is wide) and filling it with a conformal thin film, one can form a mechanical structure that is much thicker than the maximum thickness of the deposited film itself. Our group at Sandia is one of three research groups which have independently conceived of the silicon mold idea and have been pursuing variants on the basic process.[10]

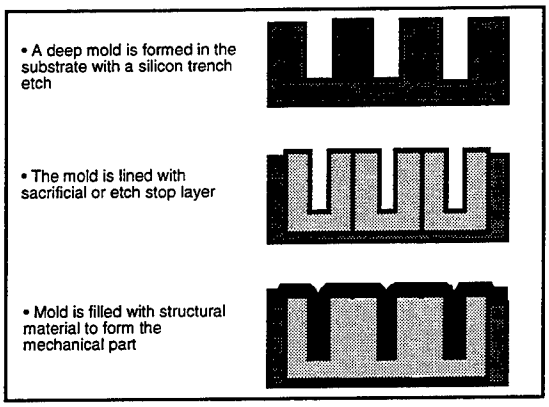

Figure 3. Generalized silicon mold process.

3.3.3 The Sandia mold micromachining process

The first step in the Sandia mold process is to etch the mold pattern into the substrate using a "deep trench" reactive-ion-etching process. The silicon pattern is then transformed into a mold in one of several ways. For example, if the structure will be formed of polysilicon and "released" with a hydrofluoric acid etch, the mold is oxidized at this point. It is also possible to remove the silicon mold by wet etching the silicon, in which case the mold is completed instead by depositing an etch stop layer. The commonality in both cases is that, in the end, the mold-micromachined parts are anchored to the substrate and released in place, like surface-micromachined parts — the mold is not reused. After the mold is formed, it can be filled with any of a number of materials, including most of the thin films common in the semiconductor industry (doped or undoped polysilicon, silicon nitride, tungsten, etc.), as well as plated metals. The wafer is then planarized by an etchback or chemical-mechanical polish (CMP) process. At this point, assuming materials compatibility, it can be taken through a surface-micromachining or electronic integrated circuit fabrication process (or both). Once all the processing is complete, the mechanical parts are released so that they are free to move relative to the substrate.

4. INTEGRATED MICROMOLDING/SURFACE-MICROMACHINING PROCESS

In the past year, we have successfully demonstrated the integration of micromolded silicon proof masses with surface-micromachined suspension springs. Fig. 4 details the integrated process. First, the proof mass mold is formed by etching into the substrate (Fig. 4a), and then oxidizing the mold (Fig. 4b). The pillars, which are spaced throughout the mold on a rectangular grid, are oxidized entirely, so that they will dissolve completely in the final hydrofluoric acid release etch. The mold is then filled with chemical-vapor-deposited (CVD) polycrystalline silicon (Fig. 4c), and planarized with CMP (Fig. 4d). At this point, the planarized wafers are run through our standard surface-micromachining process, which includes the deposition of a layer of sacrificial oxide, patterning of vias through the sacrificial layer to anchor the surface polysilicon parts of the structure (the suspension springs and pickoff/force-feedback contacts) to the substrate, and finally deposition and patterning of the surface polysilicon structures. A scanning-electron micrograph of the finished, partially-released accelerometer structure showing the molded proof mass and surface-micromachined suspension spring and contacts is shown in Fig. 5.

5. SPECIAL INSTALLATION FEATURE OF THE SEISMIC SENSOR PROTOTYPE

The seismic sensor prototype features polysilicon fuses, essentially additional suspension springs formed at regular intervals around the perimeter of the proof mass to hold it in place during the wet-chemical release etch and drying processes. These fuses are blown with the application of short current pulses after the device has completed the manufacturing process. This feature would enable the sensitive transducer to be packaged and installed in the field through high *G*-forces without sustaining any damage, and then "unlocked" once the transducer package is in place. We expect that this capability would enable low-cost installation alternatives.

6. FUTURE PLANS

One of the greatest challenges in the micromachining field is to achieve structures which have been "released"completely, that is structures which are free to move relative to the substrate. The agitation of the wet etch processing tends to break delicate suspensions and solvent residue tends to cause sticking or excessive friction (the combination is popularly called "stiction"). Our future plans for this project include several strategies for implementing a "stiction"-free release of the molded seismic sensor prototypes, including treating the structures with polymeric surface layers

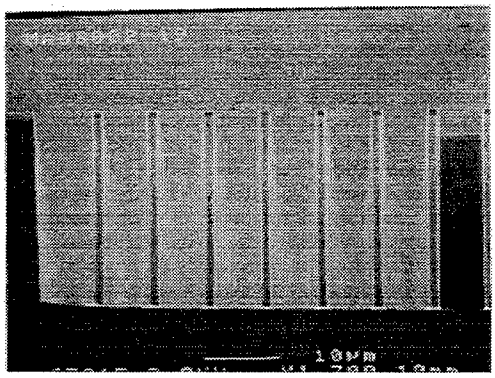

→ Figure 4b. SEM photo of oxidized proof mass mold (in cross-section).

← Figure 4a. SEM photo of etched proof mass mold (in cross-section).

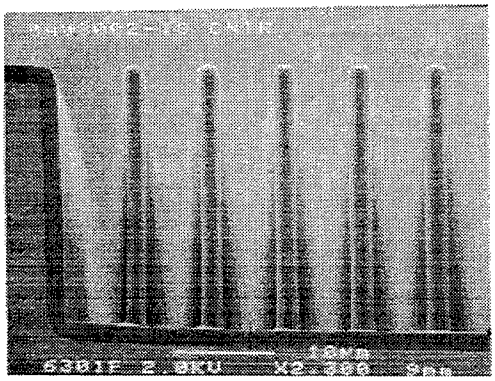

← Figure 4c. SEM photo of etched proof mass mold filled with polysilicon (in cross-section).

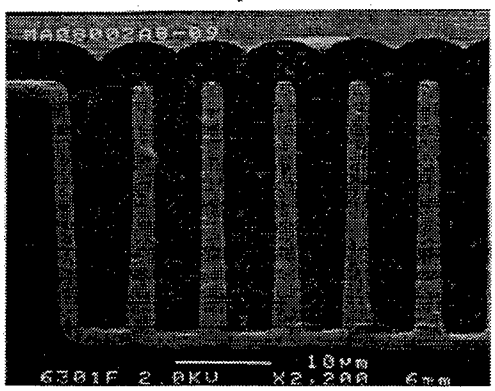

→ Figure 4d. SEM photo of planarized poly-silicon proof mass (in cross-section).

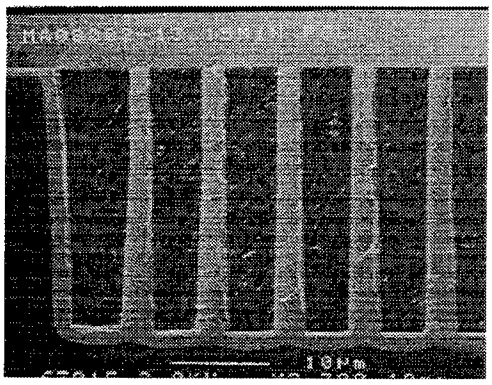

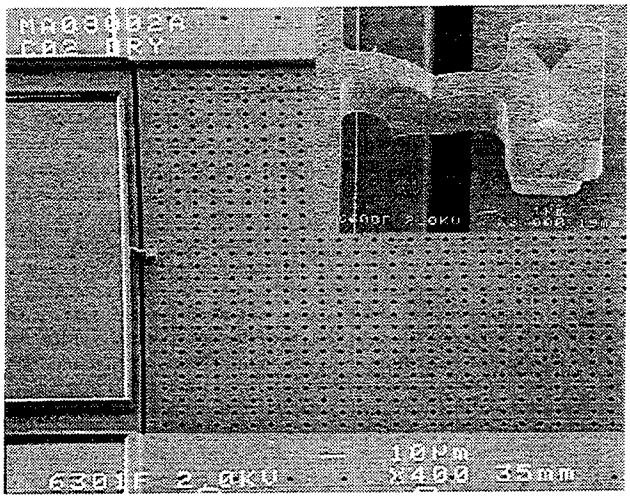

Figure 5: Completed silicon seismic accelerometer prototype manufactured in Sandia's integrated micromolding / surface-micromachining fabrication process. Inset shows close-up of surface-micromachined suspension spring.

to make them hydrophobic[12], and displacing the liquid under the structures with a superfluid (supercritical CO_2)[13]. Both of these methods have been shown to be successful in preventing stiction in other micromachined devices. Once we have completely released devices, we will test the devices, quantify their performance, and redesign them as needed to approach the requirements for a CTBT seismic sensor.

7. SIGNIFICANCE FOR CTBT

Inexpensive micromachined silicon seismic sensors could revolutionize the seismic data-gathering process. The cost savings realized by a micromachined design would result not only from the reduced cost of the sensor itself, but also from lower installation and maintenance costs. A borehole system using current sensor and electronics technologies can be as heavy as 200 pounds (90 kg) and its installation requires a drilling rig. The expense of installing and maintaining an array of such sensors often far outweighs the cost of the sensors themselves. A small, low-cost sensor could also make portable/disposable systems for both cooperative and non-cooperative seismic monitoring viable.

The capabilities and cost of the proposed seismic sensor would also make it attractive for related commercial applications such as low-cost, sensitive earthquake monitors and sensors for oil and gas exploration. The existence of large commercial markets for the sensor would drive manufacturing volumes up and costs down and would attract the interest of commercial sensor manufacturers. The CTBT community, which is in itself a relatively small market, would then benefit from association with these larger commercial applications.

ACKNOWLEDGMENTS

The authors would like to acknowledge the process engineering and fabrication staff of the Microelectronics Development Laboratory for fabricating the prototype seismic sensors. This work was performed at Sandia National Laboratories and supported by the U. S. Department of Energy under contract # DE-AC04-94AL85000.

NOTES AND REFERENCES

1. T. W. Kenny, S. B. Waltman, J. K. Reynolds, and W. J. Kaiser, "Micromachined silicon tunnel sensor for motion detection," Applied Physics Letters, Vol. 58, No. 1, Jan 1991, pp. 100-102.

2. T. B. Gabrielson, "Mechanical-Thermal Noise in Micromachined Acoustic and Vibration Sensors," IEEE Transactions on Electron Devices, Vol. 40, No. 5, May 1993, pp 903-909.

   This equation, strictly speaking, does not hold for the torsional motion of our device, but it turns out that the results one obtains by substituting in the torsional equivalents (moment of inertia for mass, etc.) are to the first order indistinguishable from the linear motion equation given here.

3. L. Spangler and K. D. Wise, "A New Silicon-on-glass Process for Integrated Sensors," IEEE Sensor and Actuator Workshop, Hilton Head, SC, pp. 140-142, June, 1988.

4. K. E. Petersen, "Silicon as a Mechanical Material," Proc. IEEE, vol. 70, no. 5, pp. 420-457, May, 1982.

5. Examples of bulk micromachining using dry etching:

   W.H. Juan and S. W. Pang, "A Novel Etch-Diffusion Process for Fabricating High Aspect Ratio Si Microstructures," 8th International Conference on Solid-State Senosrs and Actuators, Stockholm, Sweden, June 25-29, 1995, pp. 560-563.

   Y. Xu, S. A. Miller, and N. C. MacDonald, "Microelectromechanical Scanning Tunneling Microscope", 8th International Conference on Solid-State Sensors and Actuators, Stockholm, Sweden, June 25-29, 1995, pp. 640-643.

6. The Sandia tri-level polysilicon surface-micromachining technology has been described in

   J. J. Sniegowski and E. J. Garcia, "Microfabricated Actuators and their Application to Optics," Proc. SPIE vol. 2383, pp. 46-64.

   For an earlier review of surface micromachining:

   R. T. Howe, "Surface micromachining for microsensors and microactuators," J. Vac. Sci. Technol. B, vol. 6, no. 6, pp. 1809-1813, 1988.

7. T. A. Core, W. K. Tsang, and S. J. Sherman, "Fabrication technology for an integrated surface-micromachined sensor," Solid State Technology, vol. 36, no. 10, pp. 39+, 1993.

8. H. Guckel, T. Earles, J. Klein, D. Zook, and T. Ohnstein, "Electromagnetic Linear Actuators with Inductive Position Sensing for Micro Relay, Micro Valve and Precision Positioning Applications," 8th International Conference on Solid-State Sensors and Actuators, Stockholm, Sweden, June 25-29, 1995, pp. 324-327.

E. W. Becker, W. Ehrfeld, P. Hagman, A. Maner, and D. Münchmeyer, Microelectronic Engineering, vol. 4,) pp. 35-56, 1986.

9. Examples of "LIGA-like" processes:

M. W. Putty and K. Najafi, "A Micromachined Vibrating Ring Gyroscope," 1994 Solid-State Sensor and Actuator Workshop, Hilton Head, SC June 13-16, 1994, pp. 213-220.

A. B. Frazier and M. G. Allen, "Uses of Electroplated Aluminum in Micromachining Applications," 1994 Solid-State Sensor and Actuator Workshop, Hilton Head, SC June 13-16, 1994, pp. 90-94.

10. Other examples of silicon mold micromachining:

C. G. Keller and R. T. Howe "Hexsil Bimorphs for Vertical Actuation," pp. 99-102, and "Nickel-Filled HEXSIL Thermally Actuated Tweezers," pp. 376-379, 8th International Conference on Solid-State Sensors and Actuators, Stockholm, Sweden, June 25-29, 1995.

C. Keller and M. Ferrari, "Milli-Scale Polysilicon Structures," 1994 Solid-State Sensor and Actuator Workshop, Hilton Head, SC June 13-16, 1994, pp. 132-137.

A. Selvakumar and K. Najafi, "High Density Vertical Comb Array Microactuators Fabricated Using a Novel Bulk/Polysilicon Trench Refill Technology," 1994 Solid-State Sensor and Actuator Workshop, Hilton Head, SC June 13-16, 1994, pp. 138-141.

11. C. G. Keller and R. T. Howe "Hexsil Bimorphs for Vertical Actuation," pp. 99-102, and "Nickel-Filled HEXSIL Thermally Actuated Tweezers," pp. 376-379, 8th International Conference on Solid-State Sensors and Actuators, Stockholm, Sweden, June 25-29, 1995.

12. M.R. Houston, R. Maboudian, and R. T. Howe, "Self-assembled monolayer films as durable anti-stiction coatings for polysilicon microstructures," 1196 Solid-State Sensor and Actuator Workshop, Hilton Head, SC, June 2-6, 1996, pp. 42-47.

13. G. T. Mulhern, D. S. Soane, and R. T. Howe, "Supercritical carbon dioxide drying of microstructures," The 7th International Conference on Solid-State Sensors and Actuators, Transducers '93, pp. 296-299, 1993.

Initial CTBT International Monitoring System Security Findings and Recommendations

R. L. Craft and T. J. Draelos
Sandia National Laboratories
Albuquerque, NM USA

Sponsored by U.S. Department of Energy
Comprehensive Test Ban Treaty Research and Development Program, ST485D

ABSTRACT

An initial security evaluation of the proposed International Monitoring System (IMS) suggests safeguards at various points in the IMS to provide reliable information to the user community. Modeling the IMS as a network of information processing nodes provides a suitable architecture for assessing data surety needs of the system.

The recommendations in this paper include the use of public-key authentication for data from monitoring stations and for commands issued to monitoring stations. Other monitoring station safeguards include tamper protection of sensor subsystems, preservation of data (i.e. short-term archival), and limiting the station's network services.

The recommendations for NDCs focus on the need to provide a backup to the IDC for data archival and data routing.

Safeguards suggested for the IDC center on issues of reliability. The production of event bulletins should employ "two-man" procedures. As long as the data maintains its integrity, event bulletins can be produced by NDCs as well.

The effective use of data authentication requires a sound key management system. Key management systems must be developed for the authentication of data, commands, and event bulletins if necessary. It is recommended that the trust placed in key management be distributed among multiple parties.

The recommendations found in this paper offer safeguards for identified vulnerabilities in the IMS with regard to data surety. However, several outstanding security issues still exist. These issues include the need to formalize and obtain a consensus on a threat model and a trust model for the IMS. The final outstanding security issue that requires in-depth analysis concerns the IDC as a potential single point of failure in the current IMS design.

Key Words: security, data surety, data authentication

INTRODUCTION

The success of the CTBT is critically dependent on the availability of trustworthy data appropriate for compliance decisions. The International Monitoring System (IMS) will be used to collect, distribute, and analyze sensor data. Effective utilization of shared data in an international monitoring environment depends on the participants believing the integrity and authenticity of the data even though they may have had no control over the design, installation, or operation of the monitoring system. When properly implemented, data surety measures such as data authentication can provide assurances of credible sensor data.

In this paper, a brief system overview of the IMS is provided. The core of the paper discusses the data surety issues and safeguards associated with particular elements of the IMS. The paper concludes with general statements about the current state of data surety in the IMS.

SYSTEM OVERVIEW

Figure 1 depicts a notional view of the IMS used to discuss the security issues and safeguard recommendations. Note that the partitioning into blocks represents partitioning of functionality and may not represent the physical partitioning of particular elements of the IMS. The **source** is an event capable of creating **signals** that are detectable by one or more of the IMS **sensor** subsystems (e.g., seismic or hydroacoustic). The sensor subsystem converts these signals into electrical or optical energy and conveys the information to the associated **station**. The station converts the electrical or optical signals into digital format and packages the digitized data into **sensor data** messages bound for the **International Data Center** (IDC). The station also provides time stamp information with each message. On its way to the IDC, a sensor data message flows over communications channels either directly to the IDC or through a **National Data Center** (NDC).

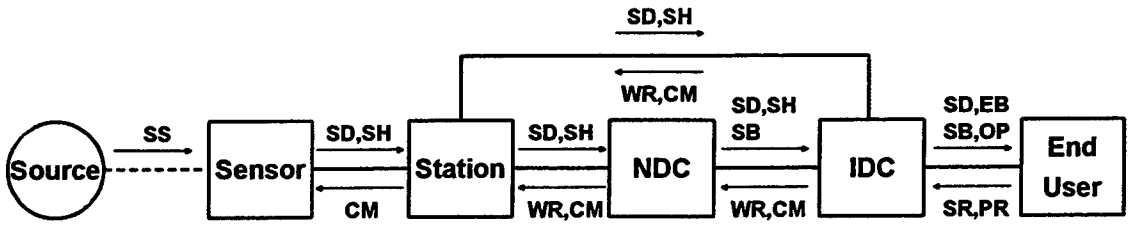

Figure 1. System Architecture and Major Information Flows

The IDC processes worldwide sensor data to determine event locations and to extract other features. If needed, the IDC may issue **waveform requests** to specific stations to retrieve sensor data to help refine the accuracy of location and feature estimates. At regular intervals, the IDC distributes an **event bulletin** listing location and feature information gleaned from sensor data.

To monitor and control the operation of the IMS, two additional information flows are built into the system. The first, the **state of health** message, flows from the sensor to the IDC. These

messages can come from sensors or stations. This information is compiled regularly for the entire system to guide IDC processing and should be available as one of the **other products** produced by the IDC. The second flow, **commands**, originates in the IDC or an NDC and may be used to control certain aspects of station or sensor performance (e.g., when calibrations are performed or how often a station is to sample data).

RECOMMENDED SYSTEM SAFEGUARDS

In this section, recommended system-level safeguards are discussed. The safeguards listed here are ordered first by the node to which there apply (e.g., station or NDC) and then by specific element within that node (e.g., commands, sensor data, etc.). The use of multiple safeguards for each element is intentional, as one goal of these recommendations is to provide "protection in depth".

- **Safeguards at the Sensor and Monitoring Station:**
  There are two primary security objectives to be realized for a station and its sensor(s). First, the integrity and authenticity of signal information must be assured. The possibility of an adversary or environmental factors being able to alter detected signals before they enter the IMS network must be minimized. Second, the availability of this signal information must be guaranteed. Once the information is captured by the sensors and stations, it must be retained until it is securely held within the bounds of the IMS network (i.e., at the NDCs and the IDC). To ensure these objectives, the following sensor and station elements should be addressed with the safeguards specified below:
  - **Sensor Data**
    In order to protect IMS sensor data at the sensor/station, the IMS must:
    - Authenticate the sensor data
    - Protect the integrity of the sensing process
    - Physically protect the authentication mechanisms
    - Deter and detect tampering with sensor/station operation
    - Ensure preservation of sensor data

    In authenticating sensor data, the following design elements should be included:
    - **Authenticate sensor data as soon as possible.** Three options have been proposed for authenticating sensor data -- authenticating at the sensor or station, authenticating it upon arrival at the IDC, and not authenticating it at all. DOE recommends authenticating at the sensor/station as this provides users of the data with greatest assurance that the data has not been corrupted since its creation. As long as a packet of sensor data exists in the IMS its authenticator should never be removed (i.e., even if data must be reformatted for efficient retrieval in the IDC, the user must still be able to go back to the original sensor data packet to ascertain the data's authenticity).
    - **Use public key techniques for this authentication and assign unique keys to each sensor/station**. Two fundamental approaches to authentication can be used: private key and public key. In private key, a secret key is shared between the entity authenticating (or "signing") the data and the entity verifying the signature. In this technique, the ability to verify also gives the verifier the ability to sign. Public key techniques make use of two keys -- a private key held by the signer and a public held

by the verifier. While the public key gives the verifier the ability to ascertain the authenticity of a set of data, it does not give the verifier the ability to forge a signature. If this technique is used and a unique private key / public key pair is assigned to each sensor, users of the sensor data will have the ability to uniquely identify the source of that data.

- **Include a time stamp in the data that is authenticated.** The presence of the time stamp makes it impossible for an adversary to record a packet and to replay it later in place of another packet. Including the time stamp as part of the data to be authenticated binds the time stamp to the sensor data such that neither can be altered without detection.

Protecting the integrity of the sensing process requires the following guidelines:

- **Physically protect the sensor data prior to authentication**. While the details of how to provide the physical protection are properly part of component design, the notion to be gleaned from this recommendation is this: from the time that the signal is captured by the sensor's transducer until it is authenticated, it is vulnerable to potentially undetectable changes. Steps must be taken to assure that these changes cannot be introduced. For the radionuclide detector, this may be realized by simple physical protection of the detector housing. Given the geographically distributed nature of the remaining sensors, this may be a more significant task. For example, if the transducer of a hydroacoustic sensor is placed underwater and its digitizer and authenticator are placed in its station on land, then conduit or other means must be employed to ensure that an adversary cannot inject noise into the signal prior to digitization without detection.
- **Use impartial parties to inspect these physical protection measures during installation**. As a station is being installed, IMS representatives should have the ability to inspect the installations to ensure that they are free from corrupting devices and will faithfully execute their intended functions.
- **Calibrate sensors and stations with great care**. Once stations are operating but before they are validated as part of the IMS, they should be calibrated by IMS representatives (other than the installers) to ensure that the data collected serves as an accurate baseline for that station. To safeguard these baseline readings, the collected calibration data should be signed by the same authentication mechanism that will sign the operational data used by the IMS. As sensor data is received by the IDC, it should be compared against the baseline readings to detect potential tampering.

To physically protect the authentication mechanisms:

- **Create a secure zone around the authentication element**. Rather than giving an adversary direct access to the authentication element, a secure zone should be created that averts (or at least detects) incursion into the zone. For seismic sensors, this may include placing the authentication unit down the borehole and tamper detecting (see next safeguard) the borehole cover. For other sensors, this may require emplacement in a secured housing.

- **Use tamper indication and detection on the authentication element and its physical safeguards.** To protect the integrity of the authentication unit, tamper mechanisms should be employed. Two levels should be considered:
  - Tamper indication (e.g., seals that cannot be removed without destroying them) is useful for limiting access to physical elements of the system. This should be applied to the housing of the authentication unit and should be accompanied by visual inspection during on-site visits.
  - Tamper detection (e.g., door switches or light sensors) is useful for immediate indication of violation of a tamper boundary. This should be applied both to the authentication unit and to physical safeguards used to provide a secure zone around this unit. Detection of tampering should insert indicators into the sensor data message stream.

To deter tampering with sensor/station operation:

- **Trigger short notice, on-site inspections as a result of suspicious sensor/station behavior.** If the countries that host monitoring stations are also responsible for the maintenance of those stations, the IMS must closely monitor station data for any indications of abnormal behavior. This could include loss of data packets, changes from baselines established during calibration, or the presence of tamper indicating bits in the sensor data stream. If tampering is suspected, then on-site inspection of the site should be initiated.

To ensure preservation of sensor data:

- **Put the sensor data into long term storage as soon as possible.** As soon as a sensor's data has been digitized and authenticated, it should be stored in some sort of buffer (hard drive, non-volatile RAM, etc.) at the station. This data should remain in the buffer until received and stored the IDC. In sizing this buffer, the primary consideration will be the length of possible communications outages.
- **Provide alternate means of data retrieval.** In the case where a communication outage might be unusually long, provision should be made for physical recovery of the data from the buffer. The buffer should be sufficiently large to retain its data until a physical recovery can be completed.

- **Sensor/Station Commands**

The use of public communication networks and standard communication protocols to control station operation opens stations to network-based attacks. If an adversary can gain access to a station, then the ability of the station to correctly operate will be in jeopardy. If the adversary can gain this access through the station's network interface, then the possibility exists that the adversary can establish a significant span of control in the IMS.

In order to protect IMS stations from these attacks, the design of the station must:

- Ensure the authenticity of commands received
- Fastidiously control the station's capabilities
- Monitor the effectiveness of these safeguards

In ensuring the authenticity of commands received, the following design elements should be included:

- **Authenticate each command received.** The station must verify (by authentication) the identity of users sending commands as a condition for executing these commands. This verification should be performed on a command by command basis and not on a session basis (i.e., login with password, execute a series of commands, and logout).
- **Use public key techniques and user-unique key assignments to authenticate commands**. In order to facilitate auditing, public key techniques should be employed in authentication. When used with unique key assignments, this will permit the station to uniquely identify the user issuing commands.
- **Time stamp commands from each authorized user**. More than one entity (to include the host nation) will be able to control a given station and its associated sensors. For each such entity, a unique public key / private key pair should be assigned. Each command should be time stamped. The station should not respond to commands whose time stamp is older than a specified period of time. The use of time stamping along with a "live message window" assures that an adversary cannot capture and replay commands at times that suit the adversary's purposes.

To fastidiously control the station's capabilities:

- **Limit the station's network interface to a minimal, well-controlled set of services.** These are component-level design issues, but the goal must be to make sure that only the transactions allowed to occur across this interface are occurring. These design techniques are the same as for firewall designs and may rely, in part, on a small set of custom developed communications utilities written to replace those supplied by the vendor of the station's computer.
- **Limit the number of IMS users able to issue commands to a station.** The motivation behind this is to limit an adversary's points of entry into the station command structure.
- **Limit the functionality available on the station's computer.** When computers are attacked from a network connection, the attacker often starts by gaining access in some way and then continuing to increase his access by using programs/utilities that are resident on the computer. For this reason, the software resident on the station's computer should be reviewed to assure that it has a valid reason for existing. Utilities provided by the computer's manufacturer should be stripped out if not absolutely essential.

To monitor the effectiveness of these safeguards:

- **Audit security critical events at the station**. Certain functions and certain events (e.g., the receipt of commands by a station) must be tracked to ascertain whether legitimate operations are being conducted or whether attacks are being launched. Audit mechanisms should be built into the station software to record these events to an audit file. It should be noted that large amounts of audit data can be generated quickly by audit processes; therefore, care must be exercised in order to ensure enough

information is gathered for adequate monitoring but not so much that the auditor is swamped.

- **Safeguards at the NDC**
  An NDC has two primary roles in the IMS. First, it is a relay point for IMS communications flowing between stations and the IDC. Second, it is the primary user of IMS product data. In addition to these IMS roles, an NDC can be tasked with additional national.

  0f the NDC roles, only the first levies a security requirement (the assured delivery of sensor data) on the IMS architecture. As its user's primary interface to the IMS, the NDC may also have certain requirements for protecting these users' information systems from the rest of the IMS; however, the IMS will take no steps to realize this goal. This responsibility properly resides with the users. To ensure these objectives, the following NDC elements should be addressed with the safeguard specified below:
  - **Sensor Data**
    The IMS design must ensure that the NDC can securely route sensor data. To accomplish this:
    - **Retain the sensor data until it is securely stored in the IDC.** As data from the stations is forwarded through an NDC, the center should retain a copy of the data long enough to ensure that it has been received and stored at the IDC.
    - **Focus on the reliability of the IDC's data storage and routing capabilities.** In support of IMS reliability, the NDC must take those steps necessary to ensure that loss of a storage device or of communications does not result in the loss of sensor data.
    - **Restrict external access to the assets responsible for relaying sensor data.** The goal here is to assure that entities external to the IDC cannot corrupt the relay function of the NDC. Techniques discussed earlier for limiting network access to the station apply here (e.g., limited sets of authorized users, limited, well-studied sets of services available on the interface).

- **Safeguards at the IDC**
  There are two primary security objectives to be realized at the IDC. First, as the IDC will be the ultimate repository of sensor data collected by the IMS, it must be able to guard against the loss of this data and to assure its timely delivery to users in response to subscriptions and requests. Second, the IDC must be able to guard the integrity of the event bulletins that it produces. To ensure these objectives, the following IDC elements should be addressed with the safeguards specified below:
  - **Sensor Data**
    At the IDC, the primary security need, with respect to sensor data, is that the IDC ensure availability of sensor data to itself and to IMS users. To accomplish this:
    - **Focus on the reliability of the IDC's data storage and routing capabilities.** In support of IMS reliability, the IDC must take those steps necessary to ensure that loss of a storage device or of communications does not result in the loss of sensor data. This can be achieved through redundancy (e.g., dual communication paths) or high reliability components.
    - **Backup the data stored at the IDC.** As the IDC is the permanent repository for all IMS sensor data, this data should be backed up as soon as possible and at a location

independent of the IDC itself (to avoid common mode destruction). This should be accomplished in such a way that failure of the IDC still permits sensor data to continue to be stored at the backup site.

- **Limit IMS access to IDC data storage and communication mechanisms**. There are two aspects to this. First, limit the number of IMS users (including IDC operators) who have more than "read access" to the sensor data. Second, make sure that a given user never has other than read access to both the IDC storage and the backup site storage. If a user is able to administer storage at the IDC, he should only be allowed read access to the backup site.

- **Event Bulletins**

  For many treaty signatories, the event bulletins produced by the IDC will be their principal means of assessing compliance. For this set of users, the integrity of the IDC's event bulletins is paramount. In order to protect bulletins from corruption, the design of the IDC must:

  - Protect the processes used to create event bulletins
  - Employ "two man" concepts in bulletin production
  - Control the IDC's external interfaces

  To protect the processes used to create event bulletins:

  - **Limit the number of IDC staffers able to access processes and data critical to event bulletin integrity.** Access to those items that are critical to the proper production of event bulletins (e.g., the pipeline's parameter files) should be kept to the least number of people possible. The goal here is to minimize the exposure of these files.
  - **Audit events that adversely affect these processes and data**. Operations related to these security critical items (e.g., writing/replacing or deleting of parameter files) should be closely monitored by means of audit files. Review and management of these files should be assigned to IDC staff other than those staff members who are authorized to work with these security critical items.
  - **Limit the functionality available to each IDC staffer to only that which is needed in order to execute job responsibilities.** A skilled insider may be the IDC's greatest threat; therefore, no more tools should be placed into his hands than are absolutely required. Analyst workstations should be stripped of any utilities not essential to the analysts' mission. Access to resources and files on network should follow the same principle.

  To employ "two man" concepts in bulletin production:

  - **Make analysis assignments that avoid regional conflicts of interest**. When selecting an analyst to monitor events in a given region, care should be taken to ensure that the analyst is motivated to perform the assigned job in an even-handed manner.
  - **Require independent review of detected events.** To guard against the possibility of an analyst "detecting" an event that does not really exist, a second analyst with different political affiliations should review the events detected by the first analyst.

To control the IDC's external interfaces:

- **Limit the IDC's interface to a minimal, well-controlled set of services.** This is another way of saying "use firewalls, where appropriate, to guard the IDC perimeter." Ideally, this will involve a "proxy server" that sits between the open networks and the IDC computer(s) and that runs a very limited number of custom written (as opposed to vendor supplied), highly inspected programs in order to deliver a very limited set of services to outside entities.
- **Limit the services provided to those that can be satisfied with message passing.** In support of the previous recommendation, the services available should be handled in a request/response fashion. No provision should be made to permit direct access to IDC computing resources.

To make all data, software, parameters, etc. available for inspection:

- **Specify the pedigree of each event in an event bulletin.** Event bulletins published by the IDC should be expanded to include two sets of information for each event. The first set is the parametric data currently published in these bulletins. The second set, available on request, is a specification explaining how these parameters were produced. This specification should include a listing of the source data used at each step in the process, a statement of which programs were used and in what order, and a specification of what parameters were used to control each of these programs. In addition, certified (i.e., signed) versions of these programs and their associated data files should be made available for use by any states party interested in independently verifying results.

- **Other Safeguards**
  - **Split responsibilities in key management.** Authentication does not "solve" any problems; it merely moves the problems to another location -- key management. The intent in doing this is to move the problem to a place where it is more easily managed. Most key management systems centralize the trust in a party trusted by all users of the system's cryptographic capabilities. As no such party appears to exist in the IMS, DOE recommends that a distributed key management approach be employed where trust is spread across multiple parties such that no one party is capable of subverting the key management.
  - **Establish designated chain of succession for use in loss of IDC.** Plans should be made for alternate routing and processing of the IMS data, to handle the event that the IDC becomes inoperable for an extended period of time.

OUTSTANDING IMS SECURITY ISSUES

Work done to date by DOE in assessing the security needs of the IMS and in analyzing the related work that has been performed by the CTBT community points to several key IMS security needs.

First, the kinds of topics that have been discussed in this paper as well as system threats, desired security attributes, probable attacks and associated threat agents need to be discussed by the CTBT community as a whole.

Second, while sensor data authentication is important (even critical) to meeting the security objectives of the IMS, it is not sufficient in itself to safeguard against threats to the system and to realize the desired security features. Other technical and procedural safeguards besides data authentication have been considered by both DOE and NPTO. These need to be discussed within the CTBT community.

Third, no authentication scheme should be accepted as "the answer" until the details of the associated "key management" infrastructure are understood. Authentication is not a "solution"; it merely moves the problem to key management. Assessment of any IMS key management system must accompany assessment of the authentication mechanisms before the security of the solution can be judged.

Fourth, every "secure" system invests "trust" in one or more roles (e.g., system administrator) or entities. It is not clear that a "trust model" has been developed that states how trust is invested in the IMS. The de facto model seems to place a high degree of confidence in the IDC. This can be problematic if the IDC represents the location in the system where certain attacks may be both easy to accomplish and high payoff for an adversary. For this reason, a "distributed trust" approach may be more effective.

Fifth, the current IMS design makes the IDC a potential single point of security failure. Loss of the IDC's routing capability could lead to a complete inability of the IMS to function. Recovery would then seem to be dependent on the NDC's backup capability.

APPENDIX

Additional Reading: Information on the following reports are available on the DOE CTBT web page at URL http://www.CTBT.rnd.doe.gov.

[1] **CTBT International Monitoring System Security Threats And Proposed Security Attributes**, Sandia National Labs Report SAND96-0536, March 1996.

[2] **Authentication of Data for Monitoring a CTBT**, Sandia National Labs Report SAND96-1061, May 1996.

STATISTICAL FRAMEWORK FOR EVENT CHARACTERIZATION AND ASSESSMENT OF SEISMIC CTBT MONITORING CAPABILITY

Mark D. Fisk, Steven Bottone and Richard J. Carlson
Mission Research Corporation
and
Henry L. Gray and Gary D. McCartor
Southern Methodist University

Contract No. F19628-95-C-0101
Sponsored by ARPA

ABSTRACT

This effort focuses on several main areas regarding event characterization within the context of monitoring a Comprehensive Test Ban Treaty (CTBT): (1) development and integration at the Prototype International Data Center (PIDC) of a software system for statistical event characterization; (2) assessment of seismic event characterization performance, using GSETT-3 data from the Primary seismic network, to quantify the availability and utility of event characterization parameters for global monitoring; and (3) investigation of robust multi-sensor fusion techniques for outlier detection and event classification.

To make the event characterization tools and related data products useful and accessible to remote users, we have been developing interactive World Wide Web pages and a subscription service at the PIDC to allow them to perform custom event screening and to receive customized data products on a routine basis. These tools allow users to process, view and download event characterization data products and graphics over the Internet.

The current implementation of the Event Screening Web pages has focused on analysis of seismic events, since seismic processing capabilities at the PIDC are more mature than for the other emerging monitoring technologies. However, event characterization parameters and screening capabilities, based on hydroacoustic, infrasonic, radionuclide and fusion techniques, are being implemented at the PIDC and will be reflected in future versions of the PIDC Web pages.

Using GSETT-3 data from the existing Primary seismic network, we have assessed the availability of useful event characterization data and the utility of the screening tools. For events with useful event characterization data (e.g., depth, Ms-mb and/or regional amplitude ratios), this preliminary set of tools provides an effective means to screen events down to a manageable percentage. There are currently, however, a significant number of events for which these parameters are not available, based on the existing Primary seismic network. Future Primary and Auxiliary stations, as well as new processing capabilities being integrated at the PIDC (Jepsen and Fisk, 1996), are expected to provide useful event characterization data for many events which currently have insufficient data.

We have also been deriving region-specific, frequency-dependent distance corrections for Pn/Lg and Pn/Sn. In addition, we have been performing a study to quantify the relation between the uncertainties in Ms and mb and the number and azimuthal coverage of the observing stations.

Key Words: CTBT, Event Characterization, GSETT-3, Primary Network, Outlier Detection

OBJECTIVE

This effort focuses on developing, testing and delivering a statistical framework to perform seismic event characterization, and on quantifying capabilities with regard to monitoring a Comprehensive Test Ban Treaty (CTBT). Our approach utilizes confidence intervals for depth and Ms-mb to screen events with high confidence that are caused by natural seismicity. Location error ellipses are also used to assess whether events occurred onshore or offshore, or in a given region, at a specified confidence level. (Offshore events will eventually be analyzed using hydroacoustic data.) Due to current limitations in estimating depth and Ms for events below mb ~4.5, further analysis is based on regional seismic discriminants which include high-frequency Pn/Lg and Pn/Sn. Due to regional variations and the lack of calibration data for nuclear explosions in most regions, we have developed a robust multivariate outlier procedure to characterize events relative to previous regional seismic activity. The outlier method, based on the likelihood ratio, has sufficient generality to utilize any combination of seismic and non-seismic parameters from single or multiple stations. Fisk et al. (1993, 1994, 1995a, 1995b) describe the methodology in detail, as well as numerous applications to seismic data. For regions which also have training data for nuclear explosions, we have also developed a classification procedure (Baek et al., 1995; Fisk et al., 1993).

To make these tools and related data products useful and accessible to users of the Prototype International Data Center (PIDC) in Arlington, VA, we have been developing interactive World Wide Web pages and a subscription service to allow users to perform custom event screening and to receive customized data products on a routine basis (Fisk, 1996). These tools allow users to process, view and download event characterization data products and graphics over the Internet.

To obtain meaningful results from the outlier analysis, we have been deriving region-specific, frequency-dependent distance corrections for Pn/Lg and Pn/Sn. To compute accurate confidence intervals for Ms-mb, we have also performed a study to quantify the relation between the uncertainties in Ms and mb and the number and azimuthal coverage of the observing stations.

RESEARCH ACCOMPLISHED

Interactive World Wide Web Pages for Custom Event Screening

To illustrate the functionality of the interactive Web pages for custom event screening, we now provide an example of how a user might apply these tools to analyze a set of events recorded during a given period of time. The map in Figure 1 shows locations of 1759 events which were recorded by the Primary seismic network between 11 January 1995 and 12 February 1995 and were reviewed by seismic analysts at the PIDC. The map has several projection and zoom functions to focus on a region or events of particular interest. Detailed information regarding a particular event or station can be obtained by clicking on the event or station marker, which have hyperlinks to the Reviewed Event Bulletin (REB) or the Network Information pages, respectively.

Associated with the map are text fields (Figure 1) which allow the user to select a region, time period and magnitude range of interest. Once these parameters have been set as desired, the user clicks on the "Retrieve Data" button, which accesses the data from an Oracle database at the PIDC. In addition, the user may specify criteria and confidence levels for defining an event as deep, with Ms-mb in an appropriate range, and whether the event was onshore or offshore, accounting for uncertainties. (Users will be able to further process offshore events using hydroacoustic data, once

relevant data are available.) Users may save their custom criteria and simply load the saved form into their browser to perform similar runs in the future. Criteria can be set differently in various regions if desired.

The screening analyses are executed by clicking on the "Submit Run" button. This produces numerous displays of the results (Figure 2). By clicking on a thumbnail plot on the left of Figure 2, for example, an enlarged plot of hypocentral depth versus event magnitude is displayed, as shown on the right. Green markers correspond to events with 95% confidence intervals deeper than 10 km, in this case, while ones shown in red do not satisfy this condition. Data points on any of these plots may be clicked on to obtain further information, in order to better understand the results.

The events can also be compared to historical events in each region using a multivariate population (or outlier) analysis. Using the form in Figure 3, the user can select which regional event characterization parameters to use, a signal-to-noise criteria, a magnitude cut-off, a minimum training set size and the statistical significance at which an event is not considered a member of the remaining regional population. After the parameters have been set, the analysis is executed by clicking on the "Submit Run" button. Once the analysis is complete, plots of the results can be viewed (Figure 4). As before, a plot is enlarged simply by clicking on the thumbnail size version. These plots show how new

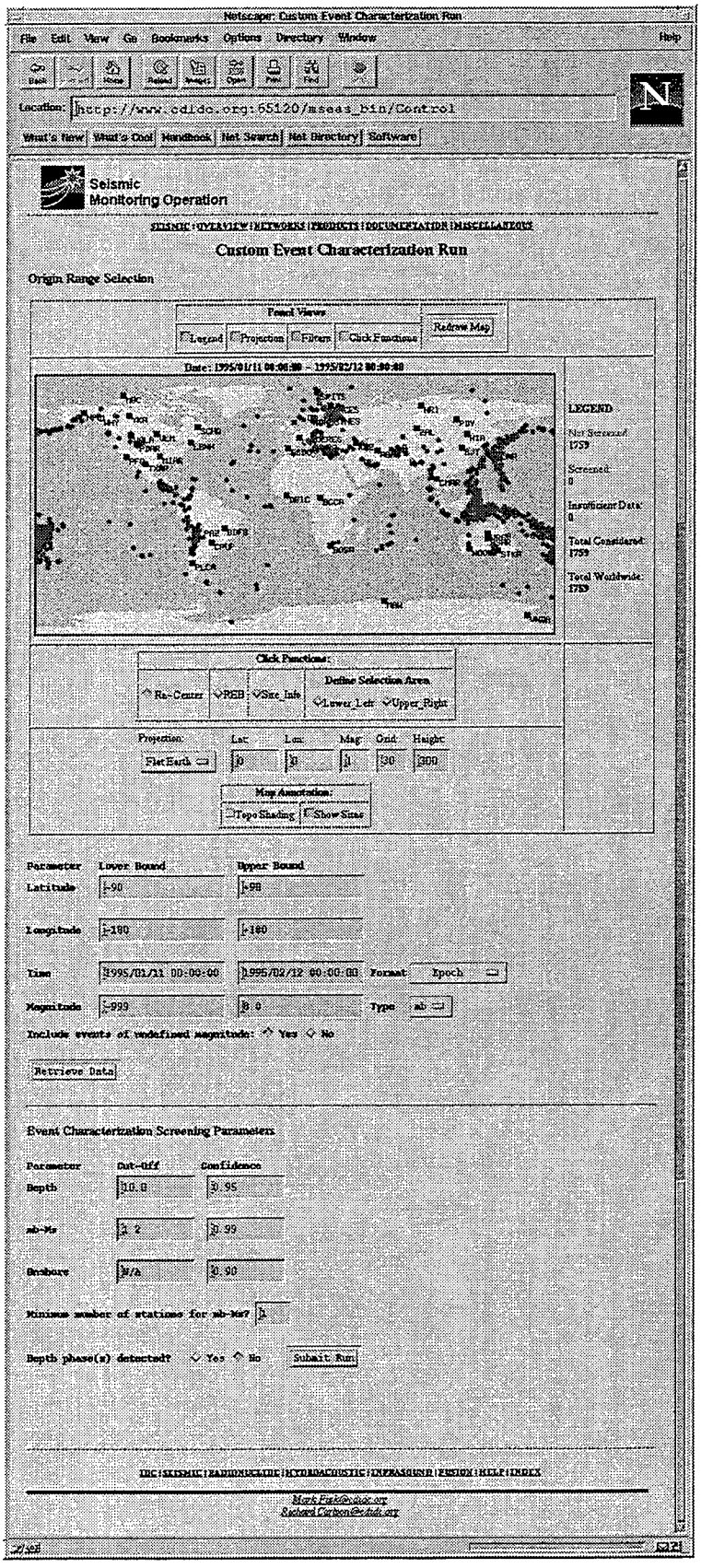

Figure 1. Interactive Web page for custom event screening.

events compare to historical events, as well as to a threshold defined by the user's inputs. Markers to the left of the vertical line correspond to events which are rejected as being a member of the same population in the particular region at the specified significance level. Shown here is an enlarged plot of the population analysis results for station WHY. The circles correspond to the historical events, while the triangles correspond to the new events being tested. In this case all of the new events were consistent with the historical events. As for the other types of plots, the user can click on a marker to obtain the REB entry for the event, the waveforms, and other information.

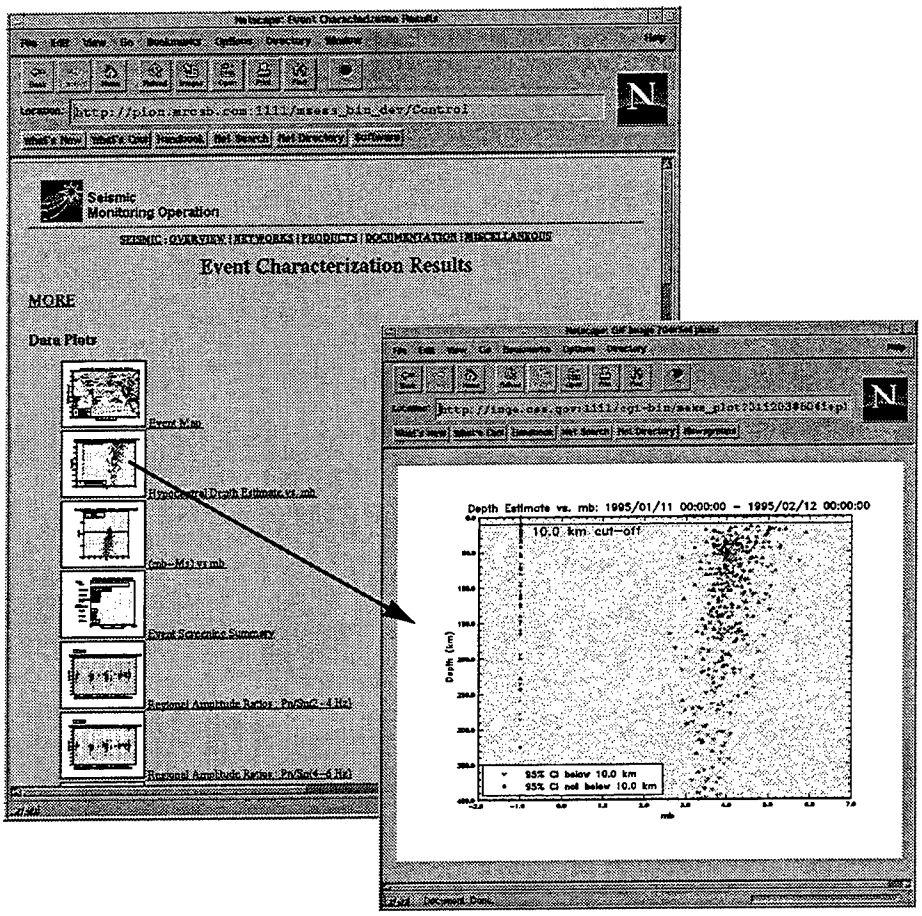

Figure 2. Web page to display a wide range of event characterization data products and screening results.

The map in Figure 1 shows the events before any screening has been applied. The map in Figure 8 illustrates the effect of applying these screening criteria. Events that were screened are shown in green, while those which remain as potentially interesting events are shown in red. The user may examine the effect of the various individual and combined screening criteria by selecting or de-selecting the buttons to the lower right of the map. Of the 1759 events in this case, there are 1108 which were screened out, 182 which have some form of event characterization data but did not satisfy any of the user's screening criteria, and 469 which did not have adequate data to perform any of the tests. This shows how the interactive screening process can be used to reduce the number of seismic events during a given period to a more manageable number for further investigation. The use of additional event characterization parameters, to be computed at the PIDC in the future, should aid in screening a higher percentage of the events.

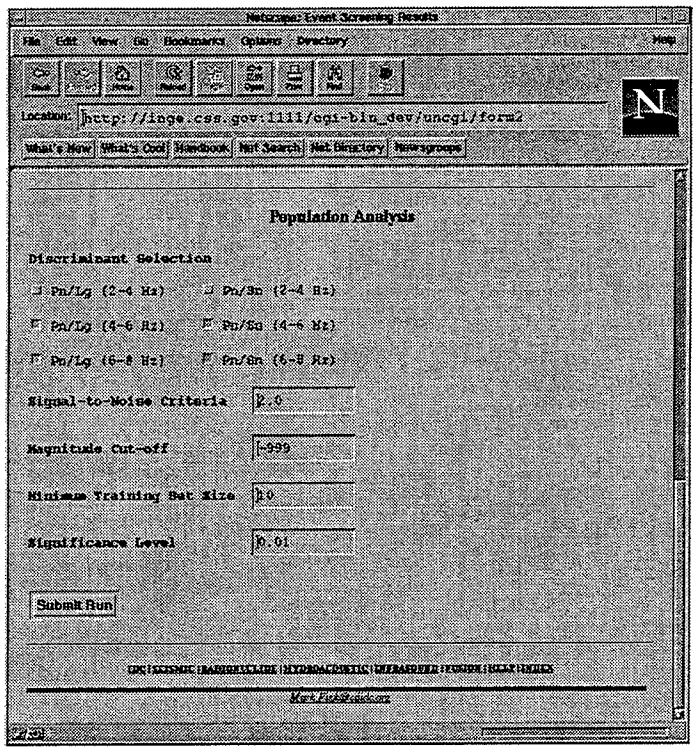

Figure 3. Form to select event characterization parameters and other criteria for the regional population analysis.

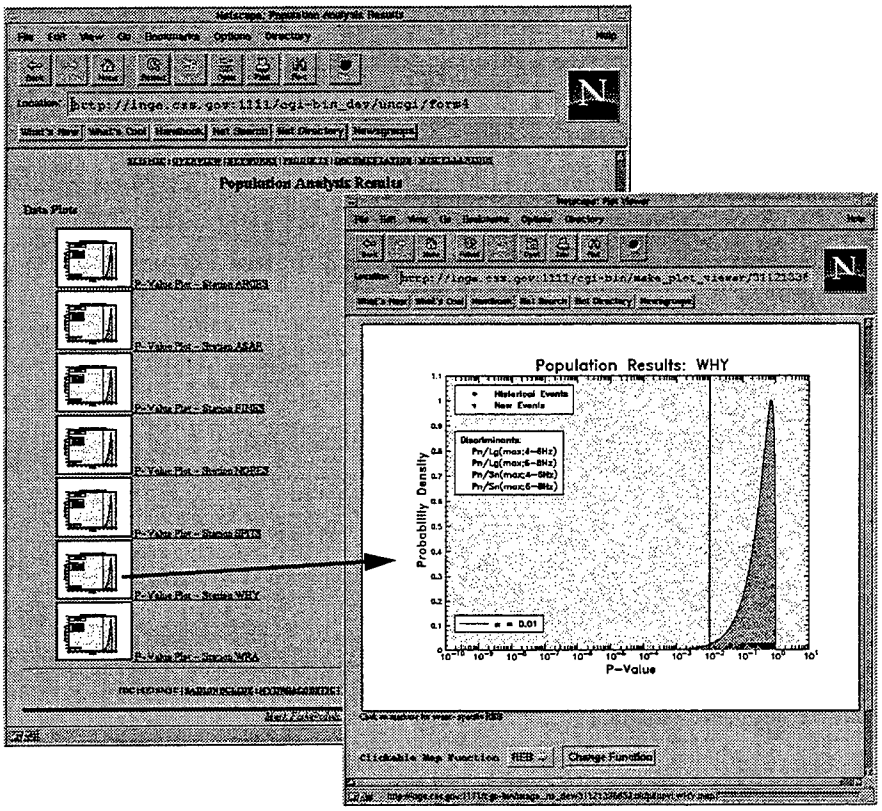

Figure 4. Displays of regional population analysis results.

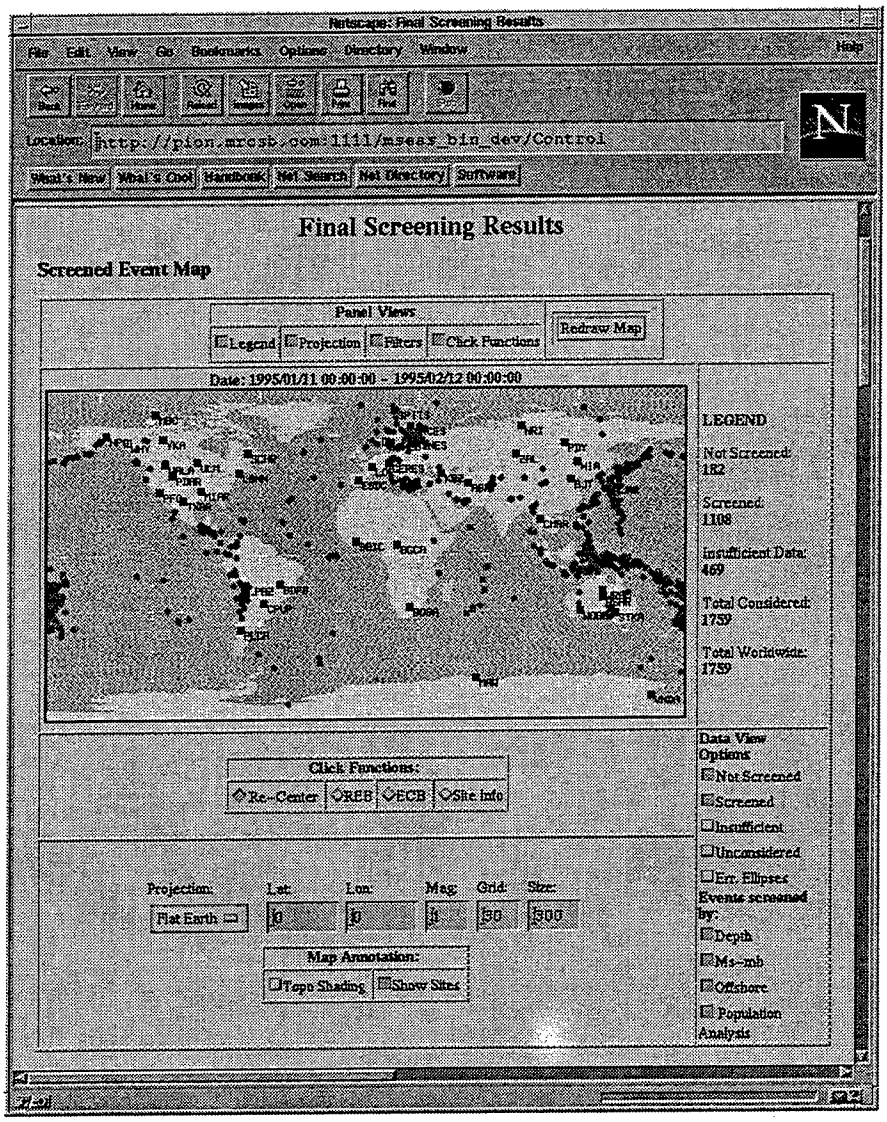

Figure 5. Map display showing seismic events that were or were not screened.

We have also developed top-level summaries for the event characterization Web pages. Associated with these summaries are five levels (or tiers) of event characterization products: (1) an Executive Summary; (2) an Event List; (3) Bulletins; (4) signal parameters; and (5) raw data. The Executive Summary provides high-level information regarding the number of events detected, those which were not screened and those with insufficient data to perform screening tests. In addition, system status is summarized on this page to reflect the IMS network capability and IDC processing capability for the time period in question. The Event List summarizes the totals for events detected in various user-specified regions and by the particular monitoring technique(s) responsible for detecting and characterizing the events. Below this summary is a list of origin information for each event. From the Event List, there are hyperlinks to the Reviewed Event Bulletin (REB) and the Event Characterization Bulletin (ECB), the latter of which we are currently developing. These bulletins provide more in-depth information regarding the details of the corresponding events and various measurements obtained from the raw signals. These Web pages then provide hyperlinks to displays of the event characterization parameters and the raw data.

In conjunction with these Web pages, we have also been implementing an automated subscription service, to allow PIDC users to establish regions of interest and custom event screening criteria, which may vary for different regions. This subscription service is currently being coordinated with David Salzberg of the Center for Monitoring Research (CMR), who is designing a unified service for all subscriptions and on-demand requests via e-mail and the World Wide Web.

Distance Corrections for Regional Amplitude Ratios

We have also been implementing software to compute distance corrections for regional high-frequency amplitude ratios. Pn, Pg, Sn and Lg amplitudes are computed at the PIDC in the 2-4, 4-6 and 6-8 Hz bands by software developed by SAIC. To utilize these data for seismic event characterization, corrections for distance- and frequency-dependent attenuation must be applied.

To correct for attenuation, we derived and applied empirical corrections to the amplitude ratios. To do this, we performed a least squares fit, assuming a standard form of the relation of Pn/Lg, for example, to distance (e.g., Sereno, 1990):

$$Pn/Lg(f)_{corrected} = (\Delta/\Delta_0)^{\alpha(f)}\, Pn/Lg(f)_{uncorrected},$$

where Δ is the epicentral distance of the event, Δ_0 is a reference distance (taken to be 200 km), and $\alpha(f) = af + b$ is a frequency-dependent coefficient, solved for in the least squares procedure. The regression problem is linearized with respect to $\alpha(f)$ by taking the logarithm of both sides of this expression. Corrections for Pg/Lg, Pn/Sn and Pg/Sn are derived in a similar manner.

We currently have six weeks worth of reviewed events, for a total of 776 regional events which have at least one regional amplitude ratio. We are currently using only those amplitude ratios with a signal-to-noise ratio above 1.5. We also plan to use only those events above mb 3.5 once more regional amplitudes are computed, to ensure that mining blasts are not mixed in with earthquakes. Such a mixture could bias the corrections.

Figure 6 (left) shows a Web page which displays thumbnail size plots of the raw regional amplitude ratios versus distance, with curve fits, for the various stations. Also shown are the corrected data. Figure 6 (right) shows an enlarged plot of the data for ARCES. Some Primary stations, such as ARCES, FINES, GERES, HFS and NORES, have a significant amount of data over a broad range of regional distances. This allows for useful corrections to be computed at these stations. There are currently not enough data over a broad enough range of regional distances at most of the other stations to compute valid corrections. Thus, additional regional data are needed to verify and/or improve these empirical corrections at most of the stations. We expect that more regional data will become available in the near future, once the code to compute the regional amplitudes is installed in the automated pipeline at the CMR.

For stations WRA and ASAR, there were some regional seismic events (i.e., within 20 degrees) which occurred beneath the continental structure of Australia, while others were near Indonesia, with propagation paths beneath the Indian Ocean. This is an example of a more general problem of grouping events which occurred in distinct tectonic regions. We plan to separate events seen at individual stations by the tectonic subregions in which they occurred and compute subregion-specific corrections.

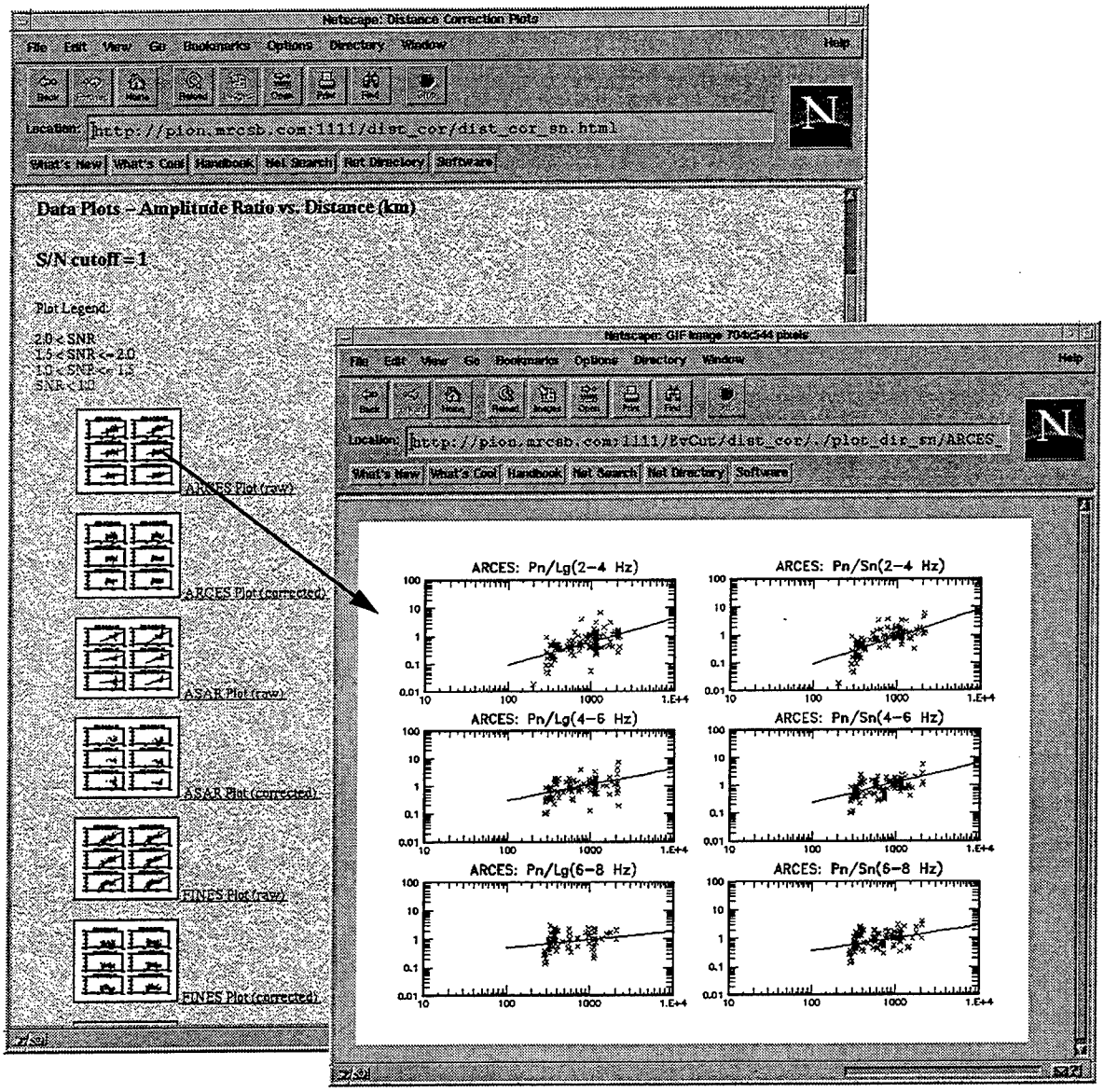

Figure 6. Web page displaying plots of regional amplitude ratios versus distance for each Primary station, along with least-squares fits to the data. An enlarged plot of the data for ARCES is shown on the right.

Magnitude Uncertainty Versus Station Coverage

We have also performed a study to quantify the uncertainties in magnitude estimates for Ms and mb. The objective is to derive appropriate standard deviations in mb-Ms estimates so that a valid confidence interval, treating all relevant uncertainties, may be computed for use in screening seismic events. Dependence on the number of stations used to obtain network-averaged estimates is currently treated. It has also been recognized that station (or quadrant) coverage can affect the uncertainty, due to seismic radiation pattern and propagation effects. Thus, we have focused on quantifying the effect of station coverage on the uncertainties of the magnitude estimates.

We first developed an algorithm to compute station coverage, q, based on the epicentral location of a given event and the locations of the stations used to obtain the magnitude estimates. It is

computed as a number between *1/m* and one, with one corresponding to the *m* stations uniformly surrounding the event. We used all of the events in the REB since 1 Jan 1995 which have Ms measurements based on at least seven stations. There are about 400 events which satisfy this condition. We then computed magnitude estimates, averaged over various subsets of individual stations which observed the events. The residuals, relative to the full network-averaged magnitude estimates, are used to estimate the standard deviations as functions of the number of stations and station coverage, accounting for the fact that the full network-averaged values are also estimates.

Preliminary results of this study indicate that the uncertainty in Ms decreases with increasing station coverage, but not dramatically. For two stations, however, uncertainty in Ms is minimum when the stations are separated by 90 degrees, and increases as station angle goes to 180 degrees, which would be expected for a radiation pattern symmetric about a line. Figure 7 shows a plot of the standard deviation of Ms versus station coverage for Ms estimates based on one through five stations. The decrease in uncertainty with station number falls like the square-root of the number of stations, as expected. There is a general decrease in uncertainty with increasing station coverage, although it is seen that for two stations, there is a minimum in uncertainty for station coverage around 0.75, which corresponds to stations being separated by 90 degrees.

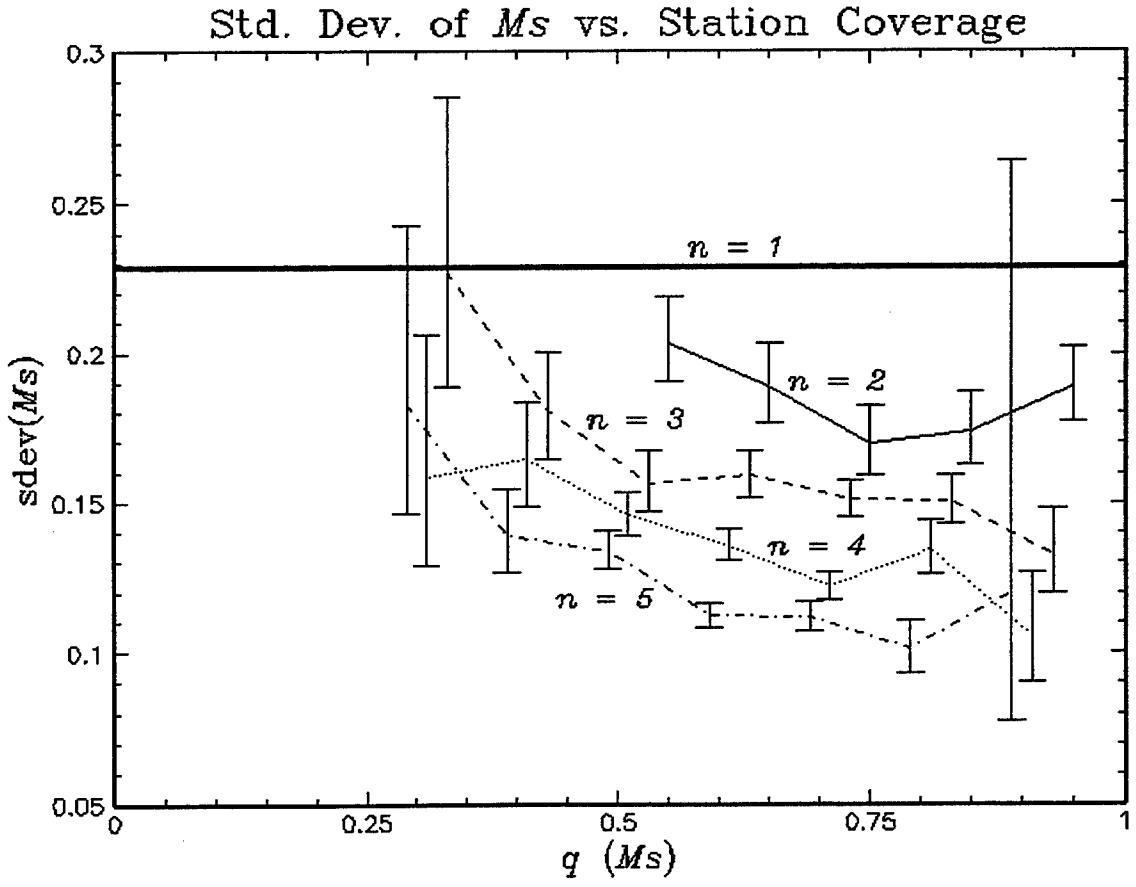

Figure 7. Standard deviation of Ms versus station coverage (q) for Ms estimates based on one to five stations.

CONCLUSIONS AND RECOMMENDATIONS

Much of our recent work has concentrated on developing custom event screening capabilities, accessible via the PIDC World Wide Web site. These capabilities incorporate the statistical tools for event characterization we have developed in the past. For events with useful event characterization data (e.g., depth, Ms-mb and/or regional amplitude ratios), this preliminary set of tools provides an effective means to screen events down to a manageable percentage. There are currently, however, a significant number of events for which these parameters are not available, based on the existing Primary seismic network. Future planned Primary and Auxiliary stations will be needed to provide useful event characterization data for many events. New processing capabilities, to compute additional event characterization parameters, are currently being integrated at the PIDC. These new parameters will also help to reduce the number of events with insufficient data.

The current implementation of the Event Screening Web pages has focused on analysis of seismic events, since seismic processing capabilities at the PIDC are more mature than for the other emerging monitoring technologies. However, event characterization parameters and screening capabilities, based on hydroacoustic, infrasonic, radionuclide and fusion techniques, are being implemented at the PIDC and will be reflected in future versions of the PIDC World Wide Web pages.

Valid distance corrections are vital for utilizing regional amplitude ratios effectively. While there are many published studies for specific regions, we are developing a systematic set of corrections for all regions surrounding the Primary and Auxiliary stations. A significant amount of work remains to collect adequate data sets in many of the regions and to establish corrections for tectonic subregions. We plan to report on our results and make comparisons to previously published results.

We also plan to complete our study of magnitude uncertainty as a function of the number and coverage of observing stations, and report on the results in the near future.

REFERENCES

Baek, J., H.L. Gray, and W.A. Woodward, J. Miller and M.D. Fisk (1995). A Bootstrap Generalized Likelihood Ratio Test in Discriminant Analysis, *Comp. Stat. Data Anal.*, **21**.

Fisk, M.D. (1996). World Wide Web Pages for Custom Event Screening at the Prototype International Data Center, GSE/WGO/Informal 3, February, 1996.

Fisk, M.D., H.L. Gray and G.D. McCartor (1995a). Regional discrimination without transporting thresholds, in press, *Bull. Seism. Soc. Am.*

Fisk, M.D., H.L. Gray and G.D. McCartor (1995b). Statistical Methodology and Assessment of Seismic Event Characterization Capability, PL-TR-95-2156, Phillips Laboratory, Hanscom AFB, MA, ADA 305487

Fisk, M.D., H.L. Gray and G.D. McCartor (1994). Preliminary Assessment of CTBT/NPT Monitoring Capability, PL-TR-94-2300, Phillips Laboratory, Hanscom AFB, MA, ADA 293188

Fisk, M.D., H.L. Gray and G.D. McCartor (1993). Applications of Generalized Likelihood Ratio Tests to Seismic Event Identification, PL-TR-93-2221, Phillips Laboratory, Hanscom AFB, MA. ADA 279479

Jepsen, D. and M.D. Fisk (1996). Progress Report on Event Characterization at the IDC, GSE/WGO/ 17, May, 1996.

Ground Truth Database for Seismic Discrimination Research

Lori Grant Flori Ryall Ivan Henson Wilmer Rivers
Multimax, Inc.
Contract No. F19628-95-C-0094
Sponsored by DOE

ABSTRACT

The goal of the Ground Truth Database (GTDB) is to combine information about seismic events with seismic waveforms to produce research-ready data products. Over time, we will build up a collection of data sets that are easily available in one consistent format.

In completing each data set for the GTDB, we emphasize the importance of careful and consistent seismic data analysis. Most often, the events are grouped into regions and analyzed region-by-region rather than chronologically. This approach results in consistent analysis in which an understanding of one event can be applied to nearby events. The redundancy helps during analysis to tell which observations are consistent for each region and which may be unique for just one event. Once a region is complete, an analysis summary is made.

The GTDB Web page (www.multimax.com) includes seismic bulletins, maps, updates (corrections and new information) and links to related research employing GTDB data sets. Retrieving the data is easy: download individual events from the Web page or FTP whole regions from Multimax's anonymous FTP site (es2.multimax.com).

What you get with each event is an "event-directory" which is a stand-alone data product including seismic waveforms and CSS3.0 table-files containing the auxiliary information necessary and useful to read and interpret the waveforms. Although each event-directory is a stand-alone product, the identification numbers in the database tables are unique, which allows any number of these event-directories to be merged into one large data set or loaded into an RDBMS.

In addition to collecting historical data sets, event clusters identified by in-country sources, and data sets resulting from other studies, we are collecting current events of known type. A software package, ReqData, has been developed to facilitate the collection of data from Internet sites operating an autoDRM. With ReqData, you simply enter an event location and time, a list of stations, and a target autoDRM site. ReqData formats a GSE2.0 request message, which it mails it to the autoDRM. Any available waveforms corresponding to your request are returned to your machine and parsed into CSS3.0 event-directories ready for further processing or analysis.

Keywords: ground-truth, regional waveforms, database, seismic analysis

OBJECTIVES

The objective of the GTDB is to combine information about seismic events with seismic waveforms to produce research-ready data products. Over time, we will build up a collection of various data sets that are easily available and stored in one consistent format. To this end, we are building data sets of several categories:

- Historical data sets of special interest;
- Current events of known type;
- Event clusters verified by in-country sources;
- data sets resulting from other research projects.

RESEARCH ACCOMPLISHED

The next several pages of this report give details of three completed data sets of the GTDB, but first we present a brief description of the GTDB organization and content. To have completed a data set for the GTDB, means the following:

- Identify a list of events from one of the above data set categories;
- Extract segments for available regional waveform data;
- Carefully analyze waveforms, adding phase arrivals and waveform QC notes;
- Correct all database table-files to conform to CSS3.0 format (Anderson *et al.*, 1990);
- Make a seismic bulletin listing event location, phase arrivals, and remarks;
- Put the completed data set in an anonymous FTP site;
- Put documentation for the data set on the GTDB Web page.

To facilitate analysis and processing, GTDB data sets are grouped into geographic regions. Regions comprise data for several events, each stored as an "event-directory" in Unix compressed tar format. Each event-directory includes short-period and/or broad-band seismic waveforms and CSS3.0 database table-files. As an example, the file ev223834.tar.Z contains all data from the ILPA data set, region 7, event 223834, and unpacks into an event-directory, named ev223834, with the following contents:

```
Comments          ev223834.assoc  ev223834.remark ev223834.sitechan ev223834.wftag
QC.dat            ev223834.event  ev223834.sensor ev223834.wfdisc   wf
ev223834.arrival ev223834.origin ev223834.site   ev223834.wfedit
```

We chose to work with this structure for several reasons: 1) Compatibility with analysis and database tools (**geotool** and Datascope); 2) Disk space can be conserved by unpacking only a few events at a time; 3) These are regular files and can be delivered via anonymous FTP without interaction with a RDBMS.

Each GTDB event has been carefully reviewed by Flori Ryall to identify seismic phases and make notes about waveform quality. During analysis, comments about the event are noted in the CSS3.0 *remark* table-file. Notes about data quality for specific waveforms, or for the event as a whole, are noted in the *wfedit* table-file (a Datascope extension to CSS3.0). An analysis summary is written for each completed region.

The ILPA/MAIO Data Set

The Iranian Long-Period Array (ILPA) was operational in the late 70's near Tehran. Seven stations, arranged in a hexagonal pattern of about 50 km aperture, recorded both LP (1 samp/sec) and SP (20 samp/sec) continuous data on Teledyne Geotech KS-36000 instruments. Two sites were equipped with 3-component sensors. Although we do not have a confirmed source type for most events, we pursued this data set because of the location of the ILPA array and because of interest in the data expressed by a number of researchers.

Events to be extracted from the continuous ILPA waveforms were selected from the USGS/ISC bulletin [1] based on query boundaries of: within 20 degrees of ILPA; between 16 May 1978 and 10 October 1979. Another 21 events, which fell outside the query boundaries, but which were used in an earlier study, were added to the list. [2] A Datascope program was used to compare the 635 targeted origins with the existing ILPA waveforms and extract event segments. Windows start 70 seconds before the first expected P arrival and end at 1 km/sec plus 60 seconds. Event-directories resulted for 273 events. [3]

Station MAIO (Mashhad, Iran) was operated by Albuquerque Seismological Lab between 3 October 1975 and 11 October 1978, employing a Teledyne Geotech KS-36000 borehole seismometer. The overlap between the segmented MAIO waveforms and the available continuous ILPA data is 84 days (July-October, 1978). The Mashhad data set, 61 ILPA events for which MAIO waveforms are available, was merged with the ILPA event-directories. Events were grouped into the eight regions outlined in Figure 1 and analyzed region-by-region.

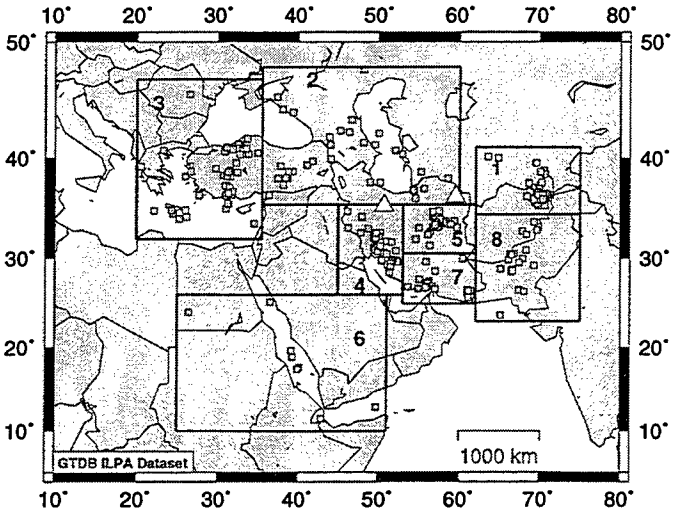

Figure 1: The ILPA/MAIO data set. ILPA is located south of the Caspian Sea; MAIO is about 800 km east. ILPA waveforms exist for the 273 events shown, MAIO for 61. Locations shown are from the USGS/ISC bulletin. Arbitrary regions were drawn to aid analysis.

[1] SQL query of the **events** account on-line at the Center for Monitoring Research (CMR).

[2] The Rodgers *et al.* (1994) data set of 100 events excluded those with no magnitude estimate. One reason for re-segmenting the data was to emphasize regional waveforms by extracting more of the smaller events.

[3] Although ILPA data are continuous, long gaps (days) exist.

Of the 273 events, 190 were large enough to record a signal at ILPA. All together, over 1540 arrivals were consistently timed and named on ILPA waveforms. [4] An additional 159 arrivals were timed on 58 of the 61 MAIO waveforms. The guidelines below were designed and carefully followed by Flori Ryall during analysis of the ILPA/MAIO data set.

- Phases with indistinct and/or ambiguous arrivals were not added.
- Real but unknown arrivals were not added with generic names.
- Phases were timed on unfiltered traces whenever possible. Otherwise phase picks were added after applying band-pass filters to optimize enhancement of the phase of interest.
- Phases identified as Lg, Rg and LR were timed on vertical channels.
- Phases identified as Sn were timed on horizontal channels if available, otherwise on vertical channels.

A number of ILPA recordings displayed a short-period (8-12 sec) fundamental-mode Rayleigh wave. This phase has been read as "Rg", following Press and Ewing (1952) and Ewing *et al.* (1957). It has been suggested that to avoid confusion with the higher-frequency phase observed at relatively short regional distances and also called "Rg", a new name should be found for this classic crustal Rayleigh wave. Suggestions include "RG" and "Rc", but a final decision on a new name is beyond the scope of the present study.

Also of interest in this data set is a very low frequency phase that arrives at about the same time as Sn but is certainly not Sn. This phase was noticed predominantly in regions 4, 5, and 7. To avoid confusion with the standard regional phases, it was not picked as an arrival and is not listed in the bulletin. The plot in Figure 2 displays three waveforms, one from each region where this phase records. The top trace is from region 5, middle from region 4, and bottom from region 7. Traces are band-pass filtered at 0.03 to 0.10 Hz.

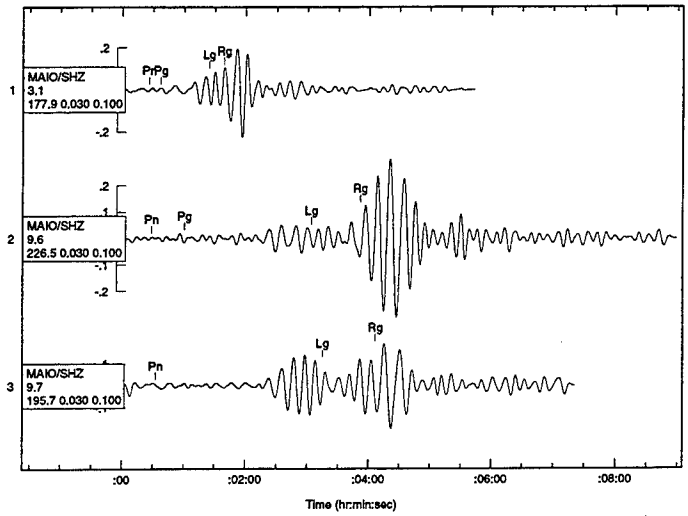

Figure 2: Sample traces from regions 5, 4, and 7.

It was also noted during analysis of this data set that recordings can vary markedly for the same event at the different stations and also between events in the same region.

[4]The aperture of ILPA is too large for effective beaming, so arrivals were timed on individual channels.

The SPANISH Data Set

The Spanish data set is based on event locations from the bulletin produced by the Instituto Geografica Nacional (IGN), Spain. [5] From that bulletin, we identified 5 clusters of interest, totaling 170 events. Four of these clusters are shown in Figure 3, represented by grey squares. The fifth cluster is in the Canary Islands. Events occurred between May, 1993 and July, 1995. For these 5 clusters, all available broad-band waveforms were retrieved from the IRIS database for the following stations: ANTO, AQU, KEG, MEB, PAB, TBT, TTE, VSL. Data were also retrieved for the Spanish Array, Sonseca (station code ESDC).

The Sonseca array has 20 short-period vertical sensors arranged in a filled circular pattern of about 9 km aperture. The reference element is ESLA, and it records 9 channels: three-component broad-band, short-period and long-period. There is also an outer ring of 6 stations recording only long-period data. The Sonseca array did not contribute to the locations of the events in the IGN bulletin before 1996.

The two clusters named "Fuente" and "Puerto" are quarry blasts. Mining regions are represented on the map by circles of 100 km diameter. The two clusters in Morocco, Alhucemas (Al Hoceima) and Melilla, are presumed earthquakes.

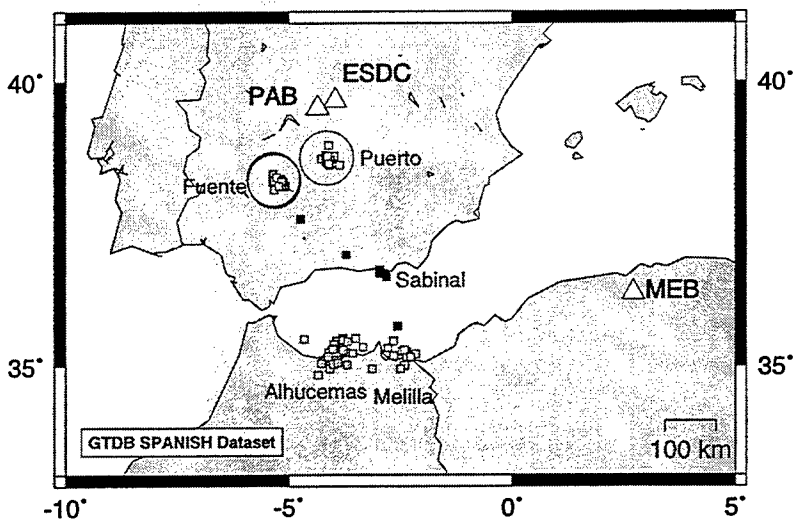

Figure 3: The Spanish data set. Most of the 168 events shown are recorded at ESDC and PAB; several on the Mednet station, MEB. All event locations are from the IGN bulletin. Grey squares show events between 1993 and 1995, black squares show events in 1996.

The nine events shown as black squares in Figure 3 occurred between March and June, 1996. All available broad-band and short-period data within about 30 degrees of these events were retrieved from both the USGS and IDC databases using the ReqData program (described below). Two of these were reported as "felt earthquakes" on the Web page posted by the Andalusian Institute of Geophysics (www.ugr.es/iag/iagpds.html).

[5]The network consists of 30 SP vertical sensors, 2 IRIS stations (PAB and TBT), the Sonseca array, and a subnet in the Canary Islands. Both natural and artificial events are included in the bulletin. IGN cooperates with other data centers including 2 in France, 2 in Morocco, and 1 in Portugal.

The Alhucemas region consists of 53 events ranging in magnitude from ML 2.8 to ML 4.6. The distance to PAB and ESDC is about 4.5 degrees. The procedures below were followed during analysis of this region:

- Events were beamed at Sonseca. Initial Pn was read on the beam but added to the reference station, ESLA.
- Sn was read on the horizontal channels.
- Lg was read on the channel with the best recording. Poorly recorded Lg's were not read, but the quality of the phase was noted in the "Comments" file.
- Surface waves were picked on the short-period channels (usually with a zero-phase 0.05-0.5 Hz filter) unless data gaps at ESLA caused distortion of the filtered signal. In such cases these phases were timed on the long-period channels.
- A phase identified as "Rg" had periods of about 12 seconds and recorded best on the vertical channel.
- A phase identified as LQ had periods of about 14-16 seconds and recorded best on the E-W (i.e., essentially transverse) component.

The Melilla region consists of 15 events ranging in magnitude from ML 2.6 to ML 4.4. Only PAB, MEB, and ESDC recorded these events well enough for analysis. Distances to PAB and ESDC range from 4.5 to 4.9 degrees and for MEB 4.1 to 4.5 degrees. Of the 9 events with MEB data, only 4 had signals large enough to read, and Lg was not evident at any of them. Analysis procedures were similar to those for the Alhucemas region.

Of the 47 quarry blasts in the Fuente region, 31 have available waveforms from both PAB and ESDC, and 8 have waveforms at ESDC only. The bulletin magnitudes range from ML 2.5 to ML 2.9. The distance to ESDC is about 1.7 degrees and to PAB about 1.5 degrees. The initial P arrival was identified as Pg, based on consistent velocity values obtained by frequency-wavenumber (FK) processing of the Sonseca array data using the **geotool** utility. A Pg velocity of 6.6 km/s was obtained from the FK results for a subset of 35 events. Since the distance to PAB was smaller by about 0.2 degrees, the first P arrival was also identified as Pg at that station.

Of the 42 quarry blasts in the Puerto region, 21 have both PAB and ESDC waveforms, and 8 have waveforms at ESDC only. The bulletin magnitudes range from ML 2.5 to ML 2.9. Distance to both PAB and ESDC is between 0.9 and 1.1 degrees. The initial P arrival was identified as Pg, based on consistent velocity values obtained by FK processing. Most of the larger events also recorded a higher-amplitude arrival (possibly PmP) 0.4s - 0.5s after Pg. An average Pg velocity of 6.6 km/s was obtained by FK processing of 21 events. That velocity is high for Pg; it may reflect a mixture of Pg and PmP in the FK processing. Most Pg arrivals are small and emergent at ESDC. The same characteristic is observed for Sg at PAB. A couple of anomalies were noted for the phase Rg. First, Rg has opposite particle motion at the two stations: prograde at ESDC and retrogade at PAB. Particle motions for Pg appeared to be correct, eliminating the possibility that the instrument orientations are in error. Second, FK processing of this phase gave a consistently high average apparent velocity of 4.66 km/s for the Rg of a subset of 21 events.

The IPRG/Galilee Data Set

The Galilee data set, comprising 50 events located in northern Israel, was contributed by the Institute for Petroleum Research and Geophysics, Holon, Israel (IPRG). It was the subject of an earlier study by Gitterman and van Eck (1993) and it has been recently revised under a current DOE contract. IPRG provided the entire data set including:

- Event locations based on the bulletin of the Israeli Seismic Network (ISN). Magnitudes are between ML 1.0 and ML 2.6;
- 713 seismic waveforms. Distances range from 0.4 km to 184 km, averaging 42 km ;
- Event identifications: 30 earthquakes and 20 quarry blasts with known yield;
- Phase arrival time and identifications for 687 phases.

At the time of these events (1987-1991) the ISN employed SP (1 Hz) seismometers. Data were band-pass filtered at 0.2-12.5 Hz and digitally recorded at 50 samp/sec. Figure 4 shows sample traces from one blast and one earthquake recorded at station BGI, which was converted to a broad-band station in 1994 (BGIO, located near Bar Giyyora). All above event parameters and waveforms for this data set have been converted to CSS3.0 format.

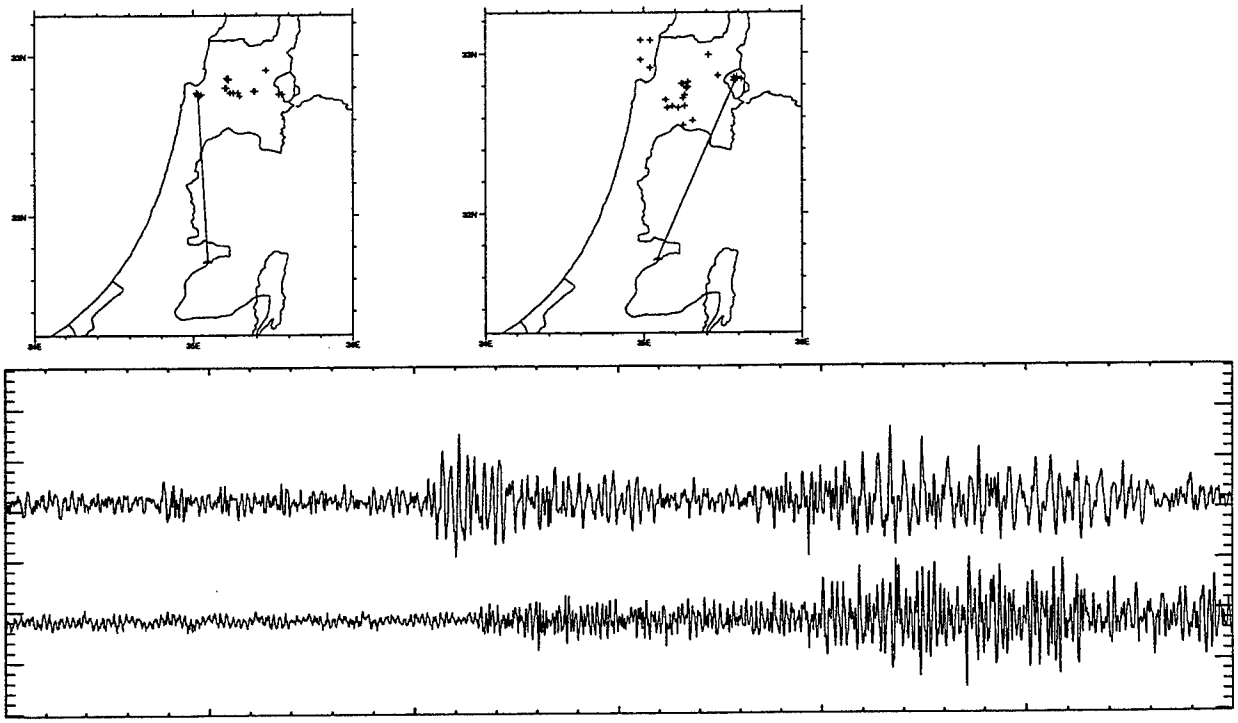

Figure 4: The Galilee data set. Sample traces are from station BGI. The top trace is an ML 2.2 blast at a distance of 115 km. The bottom trace is an ML 2.4 earthquake near the Sea of Galilee at a distance of 134 km. One minute of data is shown. The upper-left map shows all 20 quarry blasts and the path from BGI to the blast shown. The upper-right map shows all 30 earthquakes and the path from BGI to the earthquake shown.

TOOLS

Some of the software tools developed for this project by Ivan Henson may be helpful to users of GTDB data sets and other CSS3.0 formatted data. One of the tools currently available from Multimax's anonymous FTP site is ReqData, a package for requesting and receiving seismic waveform data from Internet sites running an autoDRM (automatic Data Request Manager; Kradolfer, 1993). ReqData comes with a user's guide for installation and operation and with Unix "man" pages for each of the six programs in the package. A brief description of the ReqData package follows.

Parameters to the waveform request program, `reqdata`, are the approximate time and location of events to request, a list of stations and channels to request, and the top-level directory in which to install the resulting event-directory.

After ReqData is installed, the users' incoming email is filtered to catch all GSE2.0 formatted messages. These messages are then removed from the user's mailbox and processed by ReqData conversion programs. All messages not recognized as GSE2.0 are forwarded to the user's regular mailbox. The `gse2css` program converts GSE2.0 messages to CSS3.0 format, and it puts them in event-directories specified by the user at run time.

Figure 5 shows a sample station request window from `reqstat`, the ReqData GUI for managing the responses. To get this popup, select one event from the list of requested events displayed in the `reqstat` main window (not shown). From the station request window,

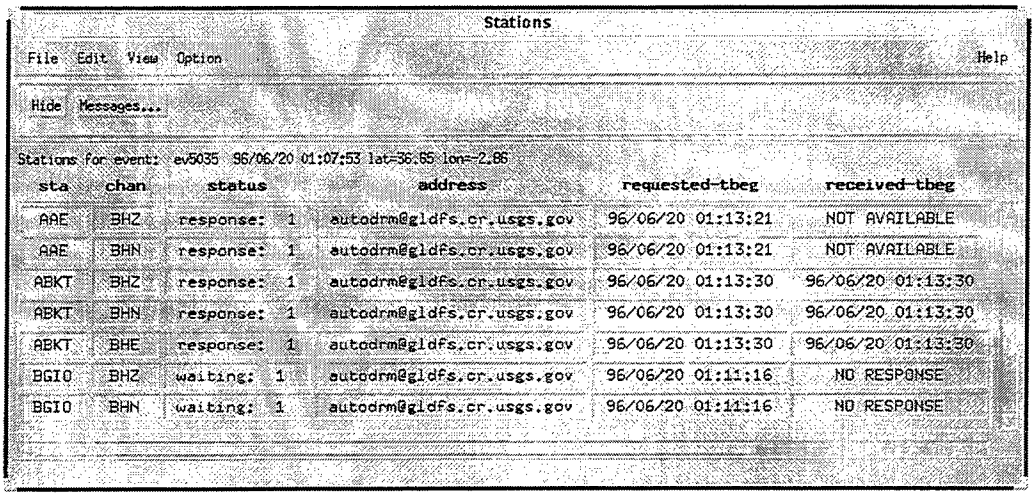

Figure 5: The `reqstat` station request window.

requests can be re-submitted to the same or a different autoDRM. To see a copy of the GSE2.0 autoDRM messages sent and all results from the conversion program, the user can select one of the requests and choose the Messages option.

Two ReqData programs help keep track of the stations available from autoDRM sites: `reqchan` queries an autoDRM for all available stations, and `gse2site` parses the responses and updates the system's CSS3.0 station files as necessary.

CONCLUSIONS AND RECOMMENDATIONS

Now that the methods of retrieving data (ReqData), performing waveform analysis and QC (**geotool**), manipulating database table-files (JSP's Datascope), and distributing of finished products (www.multimax.com) are in place and fully operational, we anticipate the construction of may more useful data sets over the next year.

Updates/feedback/corrections will continue to be an important part of the maintenance of GTDB data sets. Two researchers have already helped make the GTDB better by contributing new information and suggestions after using the ILPA/MAIO data set. Jerry Sweeney has identified 4 of the events in region 5 as "aftershocks of the Ms 7.4 Tabas-e-Golshan earthquake of 9/16/1978" based on a paper by Berberian (1982). We have updated the locations of those 4 events and identified them as "known earthquakes" in the *origin* table-file. After loading the whole ILPA data set into his ORACLE database, Doug Baumgardt made several helpful comments, one of which led to the classification of the event north of the Caspian Sea in region 2 as a nuclear explosion (based on its presence in the **nuclear** account at CMR). Both Jerry Sweeney and Doug Baumgardt presented papers at the Spring SSA meeting based on findings from the ILPA/MAIO data set (Sweeney, 1996; Baumgardt, 1996).

If you have or know of a data set that should be included in the GTDB, we welcome your input. Also, if you have additional information that would complement the current data sets, please forward the information to one of the authors. For additional information or help with GTDB products contact any of us:

Lori Grant lori@otter.mmiwest.com **Flori Ryall** flori@s160.es.llnl.gov
Ivan Henson ivan@multimax.com **Wilmer Rivers** wilmer@multimax.com

ACKNOWLEDGEMENTS

The GTDB is a group effort! We have enjoyed working with the following contributors to the data sets described in this paper. Artie Rodgers, of the University of Santa Cruz, gave initial guidance with the ILPA data set. Conversion of the original ILPA waveforms was performed by Barbara Rueben of Teledyne Brown Engineering under a Phillips Lab contract. Carmen Lopez, of the Instituto Geografica Nacional, Spain, provided the Spanish data. The Galilee data set was provided by the Institute for Petroleum Research and Geophysics, Holon, Israel. Yefim Gitterman and Delaine Reiter helped parse the IPRG data into CSS3.0 format. Many of the ideas behind ReqData resulted from discussions with John Coyne of the Center for Monitoring Research.

REFERENCE LIST

Akasheh, B., Eshghi, I. and Soltanian, R. (1976). The Iranian Long-Period Array (ILPA), *J. Geophysics*, **42**, 159-162.

Anderson, J., W. E. Farrell, K. Garcia, J. Given, H. Swanger (1990). Center for Seismic Studies Version 3 Database: Schema Reference Manual, TR C90-01, September 1990.

Baumgardt, D. R. (1996). Lg Propagation-path Barriers in the Eurasian Continental Cra -ton -Possible Shallow Crust Explanations, Seismological *Research Letters*, **67**, Number 2, March/April 1996, Abstract.

Berberian, M. (1982). Aftershock tectonics of the 1978 Tabas-e-Golshan (Iran) earthquake sequence: a documented active "thin- and thick-skinned tectonic" case, *Geophys. J. R. astr. Soc.*, **68**, 499-530.

Datascope Seismic Analysis Package, IRIS' Joint Seismic Program Center, University of Col -orado, Boulder, Colorado. (http://jspc-www.colorado.edu/software/software.html)

Ewing, M., W. Jardetzky and F. Press (1957). Elastic Waves in Layered Media, McGraw -Hill Inc., 380 pp.

Gitterman, Y., and T. van Eck (1993). Spectra of quarry blasts and microarthquakes recorded at local distances in Israel, *Bull. Seism. Soc. Am.*, **83**, No. 6, 1799-1812.

Henson, I. and J. Coyne (1993). The Geotool Seismic Analysis System, *Proceedings of the 15th Annual Seismic Research Symposium*, Boulder, CO, ed. Lewkowicz, J., and J. McPhetres, PL-TR-93-2160, ADA 271458

Iranian Long-Period Array Final Report (1977). prepared for Albuquerque Seismological Center, USGS, Contract No. 14-08-0001-14031, 8 April 1977, Texas Instruments Inc.

Kradolfer, U. (1993). Automating the Exchange of Earthquake Information, *EOS Trans. Amer. Geophys. U.*, **74**, 442.

Press, F. and M. Ewing (1952). Two slow surface waves across North America, *Bull. Seism. Soc. Am.*, **42**, 219-228.

Rodgers, A., James F. Ni and Thomas M. Hearn (1994). Uppermost Mantle Structure in Southern Eurasia from Pn Tomography and Sn Attenuation, *Proceedings of the 16th Annual Seismic Research Symposium*, Thornwood, NY, ed. Lewkowicz, J., and J. McPhetres.*

Rodgers, A., James F. Ni and Thomas M. Hearn, Pn, Sn and Lg Propagation in the Middle East, *Bull. Seism. Soc. Am.*, submitted January 1996.

Sweeney, J. J. (1996). Interpretation of Crustal Phase Characteristics in Iran and the Sur -rounding Region Determined from ILPA Data, *Seismological Research Letters*, **67**, Number 2, March/April 1996, Abstract.

Wessel, P., and W. H. F. Smith (1995). New version of the Generic Mapping Tools released, *EOS Trans. Amer. Geophys. U.*, **76**, pp. 329.

Wessel, P., and W. H. F. Smith (1995). New version of the Generic Mapping Tools released, *EOS Trans. Amer. Geophys. U. electronic supplement*, http://www.agu.org/eos_elec95154e.html.

* PL-TR-94-2217, ADA284667

MatSeis: A Seismic Toolbox for MATLAB

J. Mark Harris and Christopher J. Young
Sandia National Laboratories
Sponsored by U.S. Department of Energy
Comprehensive Test Ban Treaty Research and Development Program, ST485D

ABSTRACT

To support the signal processing and data visualization needs of CTBT related projects at SNL, a MATLAB based GUI was developed. This program is known as MatSeis. MatSeis was developed quickly using the available MATLAB functionality. It provides a time-distance profile plot integrating origin, waveform, travel-time, and arrival data. Graphical plot controls, data manipulation, and signal processing functions provide a user friendly seismic analysis package. In addition, the full power of MATLAB (the premier tool for general numeric processing and visualization) is available for prototyping new functions by end users. This package is being made available to the seismic community in the hope that it will aid CTBT research and will facilitate cooperative signal processing development.

Keywords: data visualization, signal processing, MATLAB, MatSeis

OBJECTIVE

During the course of CTBT related research efforts at Sandia National Laboratories, several project needs were identified. We determined that proper waveform processing would be very important to the success of a waveform correlation detector. Because our data is stored in an Oracle database, we needed database access to our library of MATLAB signal processing functions. We also noted that the performance of the detector could be verified easily if waveform data could be viewed in a time-distance profile superimposed with the travel-time curves used by the detector. In this format, all types of data are aligned in a natural coordinate system that is visually intuitive. While there are many excellent seismic software packages available, none could address all of our needs. ARS, Geotool, and dbpick are difficult to modify and contain limited signal processing libraries. SAC supports only basic graphing functions and has limited libraries. For this reason, we chose to develop our own MATLAB based software package, now known as MatSeis.

Using MATLAB as a basis has many advantages. It is a popular software package, robust, well supported, and available on many hardware platforms. In addition, it is an excellent prototyping environment, with built-in plotting functions and extensive signal processing functionality. Our data viewing needs could also be met easily with MATLAB graphics functions. MATLAB offers a mature, commercial software package with power and flexibility not available in the alternatives.

We have found MatSeis to be much more useful than we had anticipated. It is now widely used in the CTBT R&D program at Sandia and has been received favorably by others. We are confident this tool will aid others involved in CTBT research.

DEVELOPMENT

We developed MatSeis to meet the above objectives. MatSeis is a Graphical User Interface (GUI) programmed using MATLAB handle graphics. It provides an interactive time-distance profile display as a platform for data viewing and manipulation. Common GUI controls are provided such as menus, push-buttons, and mouse selections, all written in the MATLAB script language and C.

The initial MatSeis prototype was completed very quickly by taking advantage of MATLAB functionality.The prototype consisted of Oracle CSS 3.0 database access routines, a data profile display, and simple plot manipulation controls. Once the power of MatSeis was seen, its functions were expanded and performance improved to make it a more general seismic data visualization, processing, and analysis tool. We developed GUIs for reading and manipulating origin, waveform, travel-time, and arrival data. Interfaces to MATLAB and custom signal processing routines were added. Start-up configuration and system functions such as printing were also developed. Finally, we improved performance by converting often-used routines to compiled C MEX-files.

MATSEIS DESCRIPTION

MatSeis is executed from a command terminal window running MATLAB. The main graphical window has function menus at the top, push-button controls across the bottom, and the main time-distance display in the center. Figure 1 is an example screen print showing both the MatSeis display window and the MATLAB command window.

Since MatSeis is based upon MATLAB, the standard MATLAB environment is available from the command window. In fact, MatSeis is just a collection of functions which are executed in MATLAB. Anything done by a MatSeis GUI may also be done from the command line (although it may be very tedious), and data stored in MatSeis may be accessed on the command line for manual processing. For instance, raw waveform data may be entered directly into a prototype processing routine and the results plotted using MATLAB or entered back into MatSeis.

The main MatSeis display window consists of several linked plots showing the four basic types of data: origins, waveforms, travel-time curves, and arrivals. Origin IDs are displayed at the correct time in the upper plot. The central plot is organized as distance-from-origin vs. time, so

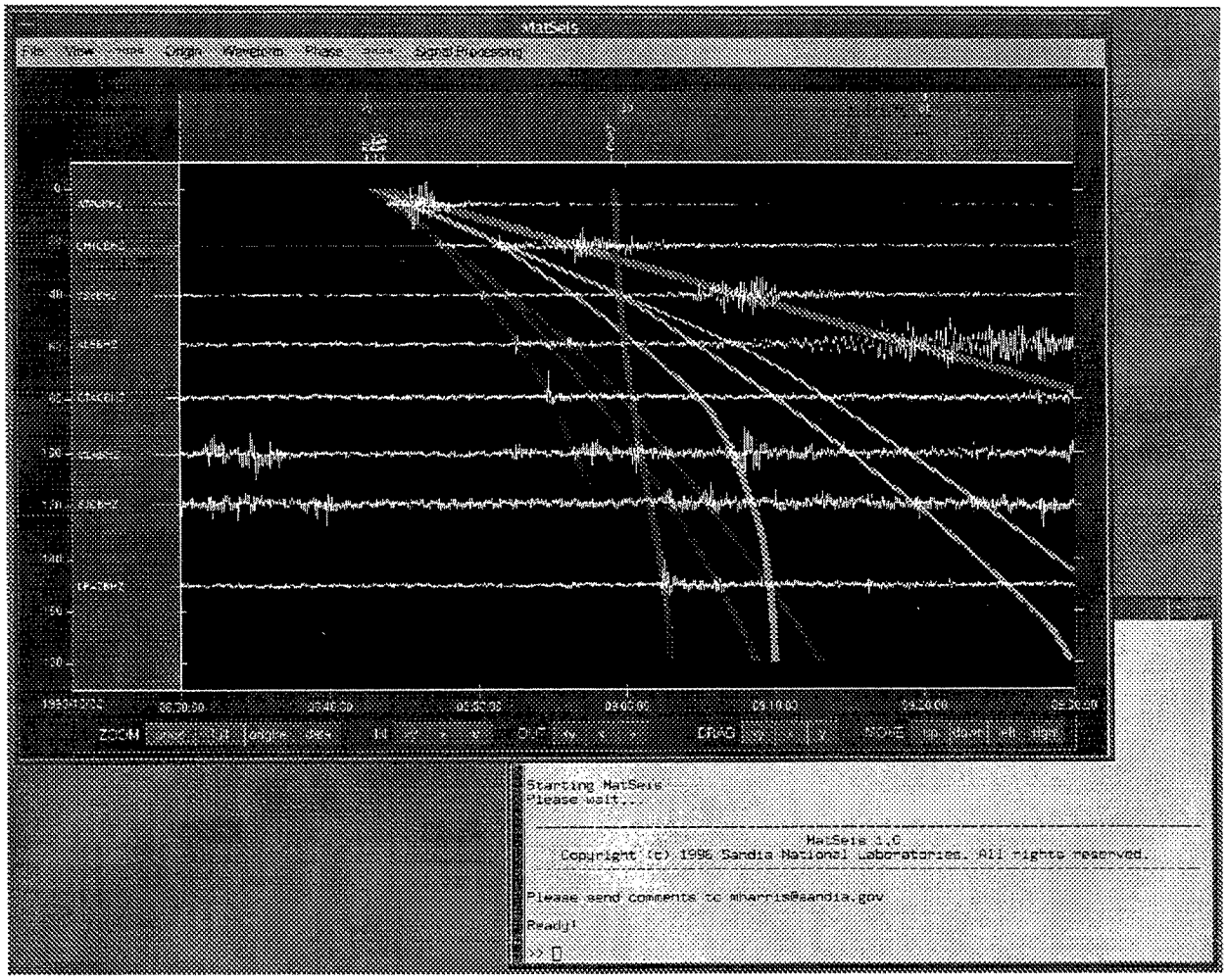

FIGURE 1. MatSeis graphical and command windows.

that travel-time curves are drawn in a familiar fashion. This plot shows waveforms aligned at the correct distance from the selected origin (79). Waveforms are superimposed over the travel-time curves. In this way phase arrival structure in the data is readily apparent.

Plot axis manipulation is easily performed using push-buttons at the bottom of the window. The plot may be resized by zooming in or out using the push-buttons. More detail may be examined by zooming IN on a rectangle drawn with the mouse. The zoom OUT functions expand the view to twice its original size. The DRAG functions allow the plot to be repositioned with the mouse. The MOVE functions move the view one-half screen in the direction selected. A 10-level undo function and several zoom short-cuts are also available.

Pull-down menus organize the functions available in MatSeis. The File and View menus give options for basic administration and window configuration. For example, grid lines on the main plot may be enabled using the *View>Grid Lines* options. A menu for each type of data contains options for reading and manipulating data items. An additional menu provides access to signal processing functions.

Many operations require parameters to be entered before the action is applied. These items may use a setup window like the *Waveform>Read* window shown in Figure 2. Menu items followed by an ellipsis (...) will generate a setup window. Typically, the Apply button must be pressed to execute these actions. Menu items with no ellipsis execute the action immediately.

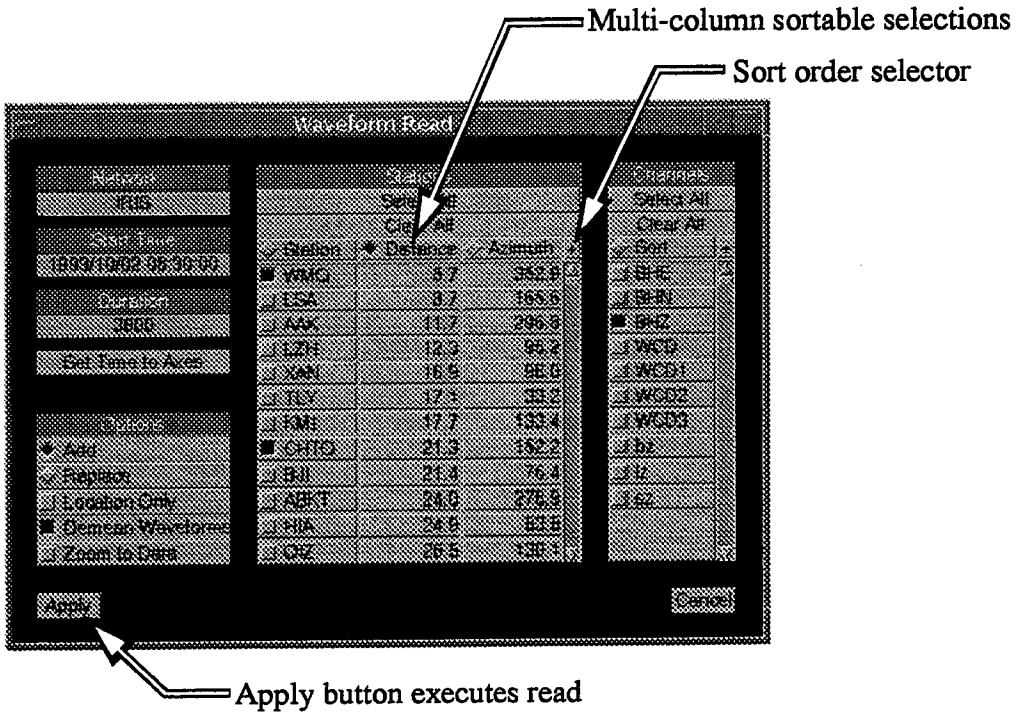

FIGURE 2. Waveform Read window.

In addition to pull-down menus and push-button zoom controls, each data object displayed may be selected with the mouse. When an object is selected by a mouse click, a small popup window appears (see Figure 3). This popup allows manipulation of the object. For instance, if the waveform ALEBHZ is chosen as shown in the figure, it may be selected for signal processing, its color may be changed, or it may be deleted from MatSeis memory.

DATABASE INTERFACE

While MatSeis was originally written to access an Oracle CSS 3.0 database, it is designed to be easily extended to other database types. It currently will also interface with CSS 3.0 flat files, and a set of templates is included for porting to a generic "Local" database. The database type and options are set from the *File>Database Setup* window. The database type may be changed at any time. All data read and write functions will use the database currently selected, so data from different sources may be combined using several read operations.

SIGNAL PROCESSING AND ANALYSIS

Signal processing is an important component of MatSeis. MATLAB provides a rich environment of signal processing functions, and new functions may be rapidly prototyped. MATLAB offers "toolboxes" of functions for many types of processing. Signal processing, statistics, wavelet, neural network, fuzzy logic, and many other toolboxes are available.

Many of the functions in the MATLAB Signal Processing Toolbox have been incorporated into MatSeis. For instance, digital filters may be quickly designed and applied to waveforms using the *Signal Processing>Filters>Filter Design* window (see Figure 4). This GUI combines all the filter design techniques included in the Signal Processing Toolbox, such as Butterworth, Cheby-

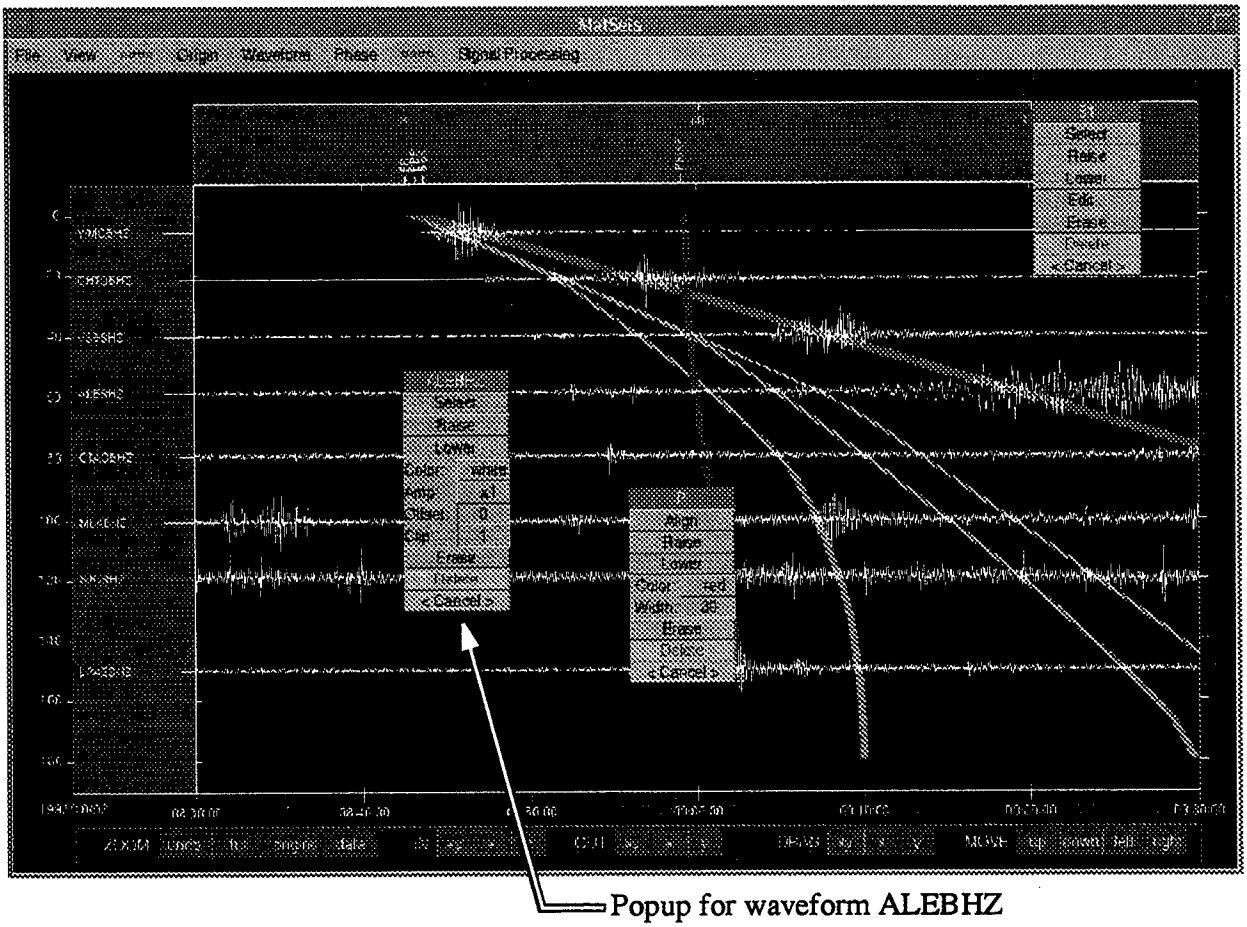

FIGURE 3. Data object popup menus.

shev, Elliptic, and FIR. From the Filter Design window, you may check the filter performance by plotting frequency response, impulse response, and poles and zeros in the z-domain, then apply the filter to selected waveforms. Some typical seismic processing techniques have also been implemented in the current version of MatSeis, such as STA/LTA filtering, beamforming, and polarization analysis.

Waveforms are "selected" for signal processing operations using the waveform popup or the *Signal Processing>Select* options.When selected, the waveform label is highlighted. MatSeis will create new waveforms or replace the originals according to the *Signal Processing>Options* settings. The time segment operated upon may be set using the *Signal Processing>Time Segment* options. Operating upon short time segments will greatly reduce processing time. For example, to refine first arrival picks, you may align the plot on the P travel-time curve, select a time segment containing this curve, then apply a filter only to data containing the P arrivals.

In addition to filtering operations, signal analysis routines are also provided by MATLAB. For example, waveform spectrograms are easily computed using the *Signal Processing>Analysis>Spectrogram* function. See Figure 5 for an example of a spectrogram of about ten minutes of three of the waveforms shown in the previous figures. The plot was first aligned on P, which is clearly seen in all three spectrograms in this example.

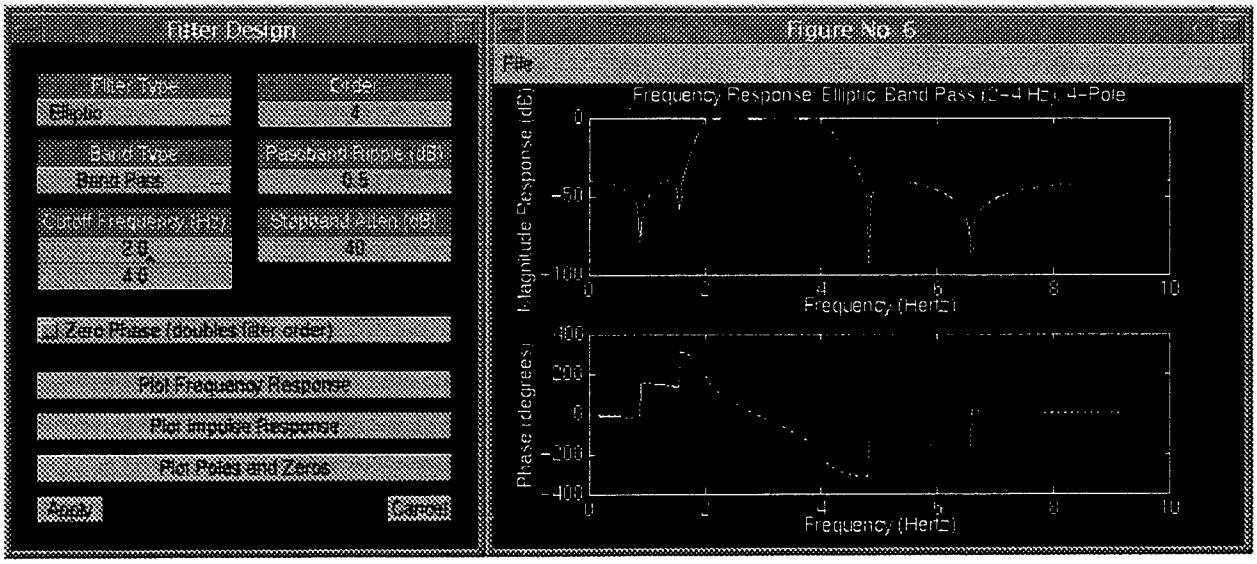

FIGURE 4. Filter Design window and Frequency Response plot.

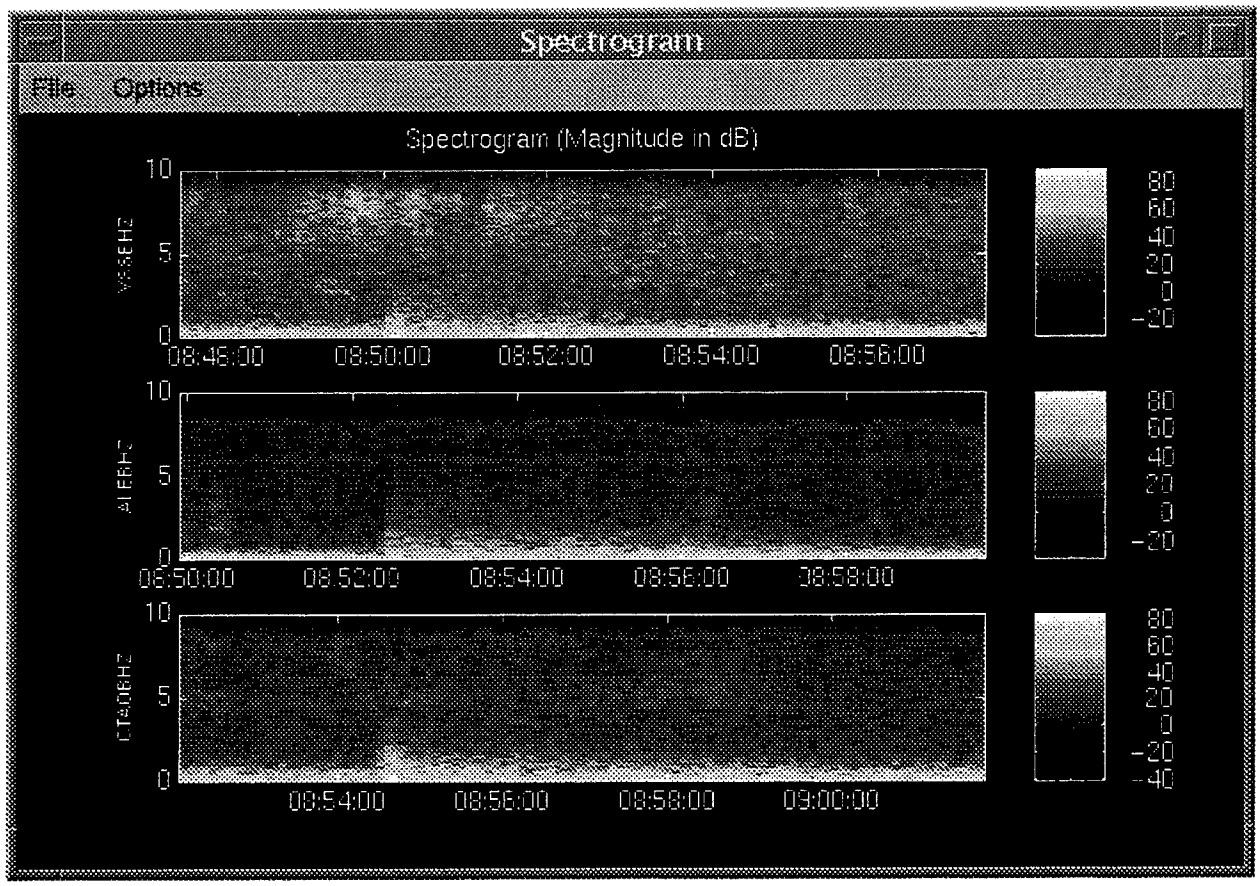

FIGURE 5. Example Spectrogram output.

CUSTOMIZATION AND EXTENSION

MatSeis may be customized to start up with a specific configuration of origins, waveforms, etc. This may be set by environment variables or a configuration file. This technique may be used to spawn MatSeis from another program as a general seismic data viewer.

Also, templates are provided for adding signal processing functions and porting to new databases. New signal processing functions may be added to a custom pull-down menu or called from the command line. The database template files may be modified as needed and then used immediately (this is called the "Local" database).

Users at Sandia and other facilities are currently working to add functionality to MatSeis. Event detection, discrimination, and measurement topics are being addressed. Special functions of interest to the WCEDS project are also being developed, such as calculating the waveform correlation operation directly from MatSeis and generating empirical waveform stacks.

Since MatSeis is distributed as full source code, one can modify existing functionality as needed. New processing routines may be generated easily using examples which are prototyped within MatSeis. It is hoped that this program will encourage enhancements by end users, with feedback of new functions to the original software base at Sandia. Cooperative development will provide more functionality to all users.

AVAILABILITY

MatSeis is freely available to the CTBT community and the seismic community in general. It may be downloaded from the CTBT R&D WWW home page. The MatSeis home page contains links to compiled versions of MatSeis for several hardware platforms. The code may also be compiled for other platforms as needed. Effort has been made to make the code platform independent. Requirements for running MatSeis are MATLAB and the Signal Processing Toolbox. Compiling the source code for a new platform requires a C compiler.

MatSeis documentation and data examples are also provided on the Web page. A user's guide is also included in the distribution. On-line documentation for each function is provided in the usual MATLAB fashion: type help function-name in the command window.

The MatSeis URL is http://www.ctbt.rnd.doe.gov/ctbt/data/matseis/matseis.html, or send e-mail to mharris@sandia.gov.

The MATLAB URL is http://www.mathworks.com.

CONCLUSIONS AND RECOMMENDATIONS

MATLAB has been very useful to the CTBT R&D project team at Sandia. MatSeis has provided better data access, manipulation, and algorithm prototyping than other available packages. Since this software has been well received by other CTBT research groups, it is being made available to the seismic community as a whole. It is hoped that additional features will be added to MatSeis in a synergistic way by any and all users. Sandia will help to make user enhancements available on the MatSeis home page.

REFERENCES

Young, C., M. Harris, J. Beiriger, S. Moore, J. Trujillo, M. Withers, and R. Aster (1996). The Waveform Correlation Event Detection System Project, Phase I: Issues in Prototype Development and Testing, SAND report, in press.

The MathWorks, Inc. (1992). *MATLAB User's Guide*. MATLAB® is a registered trademark of The MathWorks, Inc., 24 Prime Park Way, Natick, MA 01760.

Knowledge Base Interpolation of Path-Dependent Data Using Irregularly Spaced Natural Neighbors

Jim Hipp, Ralph Keyser, Chris Young, Ellen Shepard-Dombroski, Eric Chael
Sandia National Laboratories
Sponsored by U.S. Department of Energy
Comprehensive Test Ban Treaty Research and Development Program, ST485D

ABSTRACT

This paper summarizes the requirements for the interpolation scheme needed for the CTBT Knowledge Base and discusses interpolation issues relative to the requirements. Based on these requirements, a methodology for providing an accurate and robust interpolation scheme for the CTBT Knowledge Base is proposed. The method utilizes a Delaunay triangle tessellation to mesh the Earth's surface and employs the natural-neighbor interpolation technique to provide accurate evaluation of geophysical data that is important for CTBT verification. The natural-neighbor interpolation method is a local weighted average technique capable of modeling sparse irregular data sets as is commonly found in the geophysical sciences. This is particularly true of the data to be contained in the CTBT Knowledge Base. Futhermore, natural neighbor interpolation is first order continuous everywhere except at the data points. The nonlinear form of the natural-neighbor interpolation method can provide continuous first and second order derivatives throughout the entire data domain. Since one of the primary support functions of the Knowledge Base is to provide event location capabilities, and the seismic event location algorithms typically require first and second order continuity, this is a prime requirement of any interpolation methodology chosen for use by the CTBT Knowledge Base.

Keywords: delaunay tessellations, voronoi diagrams, natural neighbors, interpolation, knowledge base

OBJECTIVE

The major objectives of this research are to provide a complete and accurate interpolation scheme capable of evaluating geophysical data important to CTBT verification. This research includes investigating methods of gridding or tessellating data and interpolation methods that provide accurate results given the constraints of sparse data and smoothly varying and continuously differentiable surfaces.

RESEARCH ACCOMPLISHED

Introduction

In this paper we will describe the parameterization techniques and methods of interpolation necessary to satisfy requirements for the proposed CTBT Knowledge Base. As part of its capabilities, the Knowledge Base will require an accurate, robust, and efficient means for interpolating various geophysical parameters required by many related or associated tools needed for automatic data processing, event analysis, and event interpretation.

The Knowledge Base interpolation requirements include the ability to model sparse and scattered data with high accuracy over a smooth surface that possesses both 1st and 2nd order continuity. Of the many interpolation methods which we considered, only natural-neighbor interpolation was found to possess all of the requirements specified for the Knowledge Base. This interpolation method requires the generation of a unique set of triangles to partition the Earth's surface. This partitioning, known as Delaunay tessellation (Delaunay, 1934) constructs a well behaved nodal connectivity over arbitrary data which can then be smoothly interpolated using natural neighbor interpolation techniques.

In the following sections we describe and define the parameterization and interpolation techniques necessary to support the Knowledge Base. First, we define the Knowledge Base requirements relative to data parameterization and interpolation. Next, we define interpolation sufficiency conditions and discuss how these conditions along with the knowledge base requirements led us to choose natural-neighbor interpolation as our preferred interpolatory method. Then we give a brief overview of the tessellation, data searching, and natural-neighbor techniques followed by some current results showing some interpolatory meshes developed from seismicity travel-time data. Finally, we briefly describe future work.

Knowledge Base Requirements

The proposed knowledge base is a vital part of CTBT verification analysis. As a central storage area, it facilitates the integration of and access to information needed to verify compliance with the CTBT. Major tasks in which this information will be used are phase detection and identification, association of detected arrivals with events, event location, event identification and special event analysis (Shepherd-Dombroski, 1996 [draft]). The initial focus of this effort is on path-dependent seismic processing and in particular on event location. Ultimately, hydroacoustic, infrasound and radionuclide data sources will also be modeled.

The Knowledge Base will store much of the information needed for automatic and manual data processing by the USNDC. Most of this information is linked to specific locations on the Earth but the data is generally poorly or irregularly sampled making interpolation into other

areas an important issue. Providing an irregular tessellation and an accurate and robust interpolation method that can handle the highly irregular data point distribution would be extremely useful. This would enable the use of a dense mesh in areas where much data is available, or where seismic activity or test ban treaty surveillance interest is high. On the other hand, the tessellation could be coarsened in regions of little data, activity, or surveillance interest.

The selected interpolation method must allow new data to be added easily and should be based on a local data interpolation method to minimize data error broadcast and diffusion throughout the entire tessellation. Also, the data point insertion should be of two varieties: fixed and variable. Fixed points are true data point specifications that are known to be tied to precise locations. Variable data points, on the other hand, can be smoothed into the mesh and represent a known set of values that apply over an entire region of the Earth. Smoothing the data can help to minimize the mesh distortion and thereby help to decrease the local error in the interpolation.

From the perspective of the knowledge base, successful interpolation will have to satisfy two basic criteria: accuracy and algorithm compatibility. Accuracy refers to the fact that the interpolation must yield values at certain known locations which are within a specified range of tolerance. This can be broken down further into requirements for accurate interpolation of information at known data points (e.g. master events) and for accurate interpolation into areas where there are no known data points but where ancillary information imposes constraints (e.g. tectonic provinces). The algorithm compatibility criteria is simply that interpolated information must satisfy the requirements of current operational algorithms which are deemed mission-critical. As an example, the event location algorithm used at the USNDC requires continuous first and second derivatives from the interpolation to allow proper convergent behavior. Although discontinuities are readily observed in the real Earth, compliance with the derivative continuity requirement is essential to ensure proper performance from the location algorithm. On the other hand, should these real discontinuities require modeling, they can easily be approximated by fixing the gradient along the boundaries edge (this requires data nodes to be placed along the boundary).

In addition to satisfying accuracy and compatibility issues, the data connectivity should be implemented to support fast searching techniques. This will be extremely advantageous, relative to performance, to ensure reasonable response time from the Knowledge Base. In summary, the selected interpolation method must provide the following capabilities:

1) The method should support a sparse unstructured data distribution, as is typically associated with seismic data,
2) The method should allow new data to be added easily and should support both fixed and variable data locations,
3) The method should be based on a local interpolation scheme to minimize error propagation,
4) The method should provide accurate results within a specified tolerance,
5) The method should possess first and second order continuity to support data processing algorithms, and finally

6) The method should provide for rapid searching techniques to maintain reasonable performance margins.

In the next section interpolation sufficiency will be discussed in a general manner and it will be shown that almost all of the requirements specified above correspond to general requirements for an optimum interpolation method and that non-linear natural-neighbor interpolation meets all of these requirements.

Interpolation Sufficiency

Many interpolation methods are available for general use and all vary with how well they fit arbitrary data representations. Generally speaking they can be organized into the two distinct classes of *fitted functions* and *weighted average* methods. Fitted function methods generally require that a set of coefficients to some polynomial be determined by solving a related set of linear equations involving the data and constraints or criteria that control the fit of the function. The fitted function approach summarizes data behavior in a global manner. Weighted average techniques, on the other hand, sum the data influences at an interpolation point from all neighbor points that lie within the interpolation points "influence" region. Weighted average techniques are local in nature and allow local surface trends to be captured which, generally speaking, is not possible with the fitted function approach.

Fitted function techniques are generally much faster than local interpolation schemes in that a single function evaluation is required while weighted average methods require evaluation of the weights at each new interpolation point. On the other hand, fitted function methods are typically poor models for sparse data distributions in that the resulting surface can behave unexpectedly; over- and under-shoot between data points being a typical problem.

Watson (1992) gives an excellent survey of the major types of computational interpolation methods employed today. He also describes five generalizations that define the optimum or ideal interpolation. These generalizations include:

1) The interpolated surface must fit the data to a user specified level of precision.
2) The interpolated surface should be continuous and possess a finite slope throughout the interpolation domain.
3) The interpolated surface should be locally dependent on the data which minimizes datum error propagation throughout the surface and helps to provide surface stability by negating the possibility that a small change in any datum will result in a large or spurious change in the interpolated surface.
4) The tautness of the interpolated surface should be adjustable to provide the user some control in the rate of change of surface to suit the data. Tautness of the surface should be adjusted automatically at each data point as a function of the local surface variability.
5) The interpolation method should behave equally well regardless of data density or pattern. When data density is not homogeneous (e.g. seismic data), methods employing fixed distance or area subsets cannot be used.

Given sufficient data, in both density and accuracy, any interpolation scheme will give good results since the sampled surface is so well defined. At the opposite extreme, however, peaks, valleys, and rapid changes in the data gradients may all be impossible to infer from a sparse

data set. As a result sparse data should be interpolated with methods that incorporate the influence of local gradients. Blending gradients with the interpolated values ensures a continuous and smooth surface throughout the interpolation region.

Of the many available interpolation techniques, natural-neighbor interpolation appears to best fit all of the properties outlined above in Watson's five generalizations. More over, interpolation of seismic data, as required by the Knowledge Base, seems to require that all 5 generalizations be satisfied. The first generalization is necessary to maintain high accuracy. The second and fourth generalizations are required by some data processing algorithms that need first and second order derivative continuity. The third generalization is required by the small scale length features in many of the data sets. The fifth generalization is required since the available data is by default scattered and irregular and contains many large regions with little or no data at all.

Data Tessellations

Proper implementation of a natural-neighbor interpolator requires some form of a triangular tessellation of the data. Delaunay (1934) tessellations, which are triangles on 2-D or 3-D surfaces, are of particular interest because they minimize the maximum angles (or inversely maximize the minimum angles) of the triangles created in the tessellation. Fortune (1992) refers to this property as the maximum-minimum angle property. This property tends to form equilateral triangles and leads to configurations where the average node valence (the number of edges connected to a node) is approximately six. Generally speaking, well proportioned triangles fair better with regard to minimizing local data variability and numerical errors accumulated during the interpolation calculation.

In addition to forming well-shaped triangles, Delaunay triangle sizes are largely determined by the density of the nodal distribution from which they are created. This makes the Delaunay tessellation an ideal selection for tessellating sparse and scattered data.

Many algorithms exist that perform delaunay tessellations. Some of the more popular algorithms include "edge-flipping" (Fortune, 1992), "incremental insertion" (O'Rourke, 1994), and the convex hull algorithms such as Barber's, Dobkin's, and Huhdanpaa's (1993) "quickhull", to name a few. Delaunay tessellations are widely used in the fields of finite element meshing, computational geometry, and computer graphics. The 4th International Meshing Roundtable (1995), Preparata (1985), and Laszlo (1996), all contain excellent descriptions of the uses of Delaunay triangulations and its dual, voronoi tessellations, in the respective research areas previously mentioned.

The CTBT knowledge base currently requires a 2-D tessellation on a 3-D spherical surface (the Earth) that must be global in scope and efficient in construction. Since an "incremental" approach can easily be modified to tessellate a spherical surface, that method was selected over other available approaches. Additionally, "incremental" methods allow for easy data insertion and removal that only affects the tessellation locally near the insertion or removal point. Also, the natural-neighbor interpolation method works by assuming that the point to be interpolated is a new data point to be added to the tessellation. This permits a large subset of code used to perform the tessellation to be reused in performing the interpolation.

An incremental Delaunay tessellator works by first enclosing the region to be tessellated with a minimum set of boundary triangles. This set will completely contain all the data points to be inserted in the region. In a 2-D planar context this is accomplished by defining a rectangle that bounds all points to be tessellated and splitting the rectangle into two triangles. The incremental algorithm then proceeds as follows:

For each new node to be inserted

1) **Find all triangles whose circum-circle contains the new node (a circum-circle is a unique circle that passes through the three nodes of its triangle).**
2) **Remove each triangle whose circum-circle contains the new node to form an enclosing polygon that contains the node.**
3) **Connect each node of the enclosing, or "insertion" polygon to the new node to form new triangles that all share the new node.**

This process is illustrated more clearly in Figures 1 and 2 below.

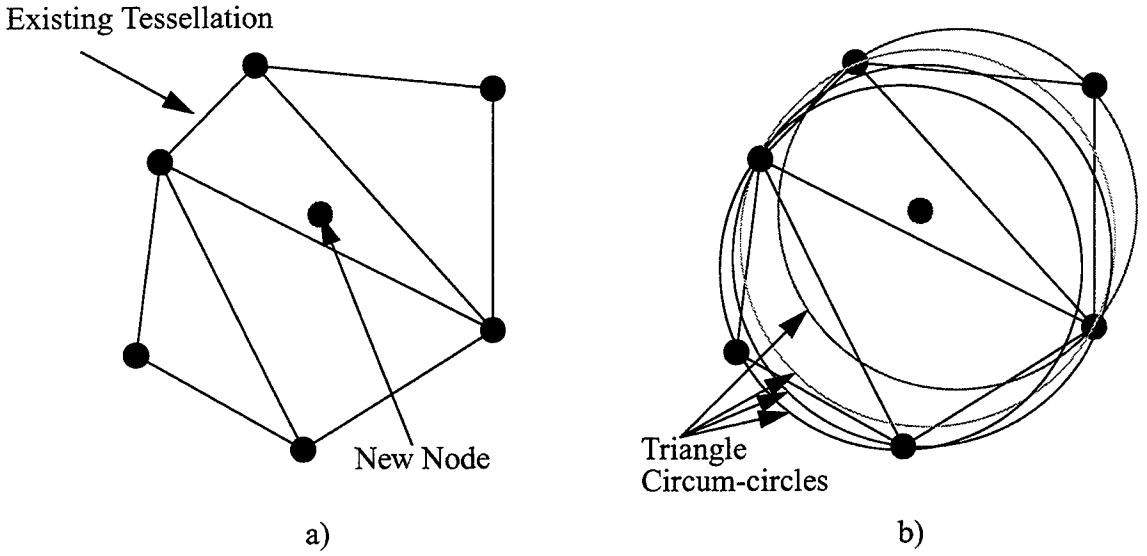

Figure 1. Circum-circle containment of a new node to be inserted in an existing tessellation.

Figure 1 a) shows the original tessellation and the new node to be inserted into the tessellations. Figure 1 b) shows how in this case each circum-circle of the original set of triangles contains the new node. Figure 2 a) depicts the "insertion" polygon after the containing triangles are removed. Finally, Figure 2 b) illustrates the new tessellation after the new node is connected to each node of the insertion polygon.

The incremental tessellator is implemented in a similar fashion on the surface of a sphere except the circum-circles now lie on the spherical surface and are calculated using dot products instead of algebra, as is typically done in the planar 2-D case. Figure 3 shows how the circle is defined by the requirement that the dot-products between the vector to each node of a spherical triangle (V_i) and the vector to the circum-center of the triangle (V_c) must be equal.

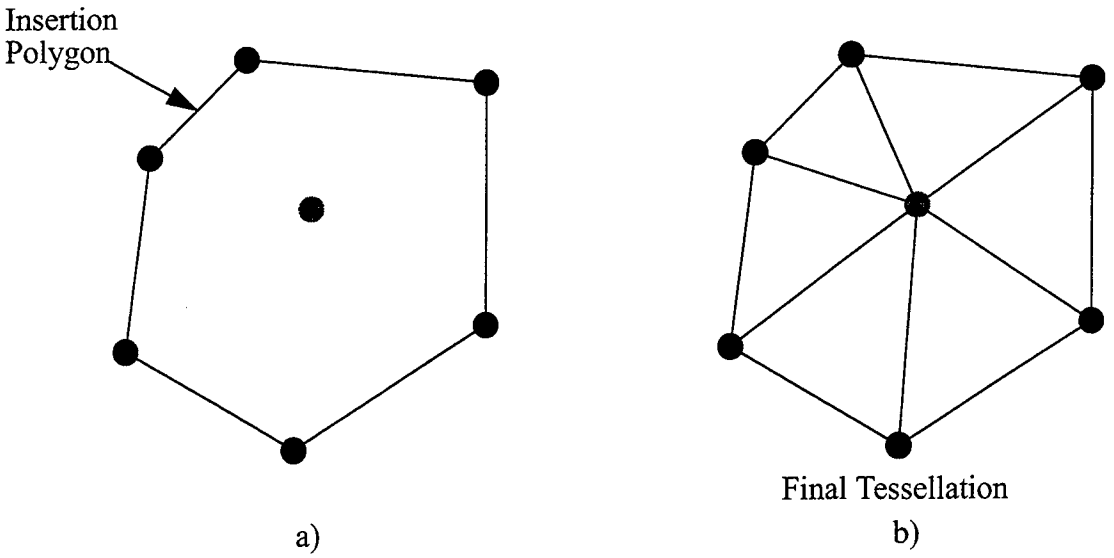

Figure 2. Formation of the insertion polygon resulting in a new tessellation that contains the new node.

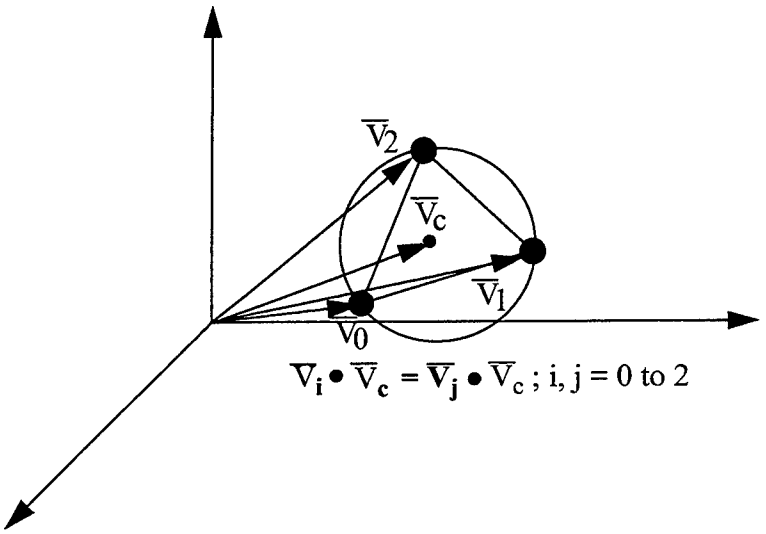

Figure 3. Circum-circle calculation for a triangle whose nodes lie on the surface of a sphere.

Before the data can be tessellated the spherical surface (the Earth) must be divided up into bounding triangles. This is accomplished by forming eight triangles, 4 in each hemisphere, that are comprised of six control nodes located at the poles and 4 equidistant locations about the equator. This provides a complete and bounded surface to begin the insertion algorithm. Once all data points have been inserted the control points can easily be removed and the local neighborhood re-tessellated using "edge-flipping" or any other appropriate approach.

Searching

If the Knowledge Base is to be used in a real time context then finding each interpolation point in the tessellation could be extremely time consuming, especially if a large data set is used. Many search algorithms could be modified to perform the search but most would have to be used in 3-space as the tessellation is a 3D tessellation (a 3D surface). However, one particular method known as the Walking Triangle Algorithm (Lawson, 1977 and Sambridge, 1995) allows the data set to be searched as a 2D data set in linear time. This avoids a global search (typically proportional to the square of the number of nodes) and makes this method ideal for searching a large data set.

The method requires that the edges of each triangle be oriented such that a counter-clockwise traverse of the edges produces an outward-pointing normal when the right-hand rule is used. Figure 4. below illustrates the 'left', 'right' test. The method works by initially guessing a start triangle and subsequently testing each side in turn. If the interpolation point lies to the 'right' of the edge being tested then the interpolation point is not contained by the triangle and the algorithm moves to the triangle shared by the edge just tested. If, however, the interpolation point is to the 'left' of the edge, then the next edge is tested. If all edges of a triangle result in a 'left' test then that triangle contains the interpolation point. The actual test is performed by taking the dot-product of the interpolation point vector with the normal produced by crossing the node 0 vector of the edge being tested with node 1 vector. In this context the direction from node 0 to node 1 is in the counter-clockwise direction around the triangle. If the dot-product is greater than zero then the interpolation point lies to the 'left' of the edge, otherwise it lies to the 'right'.

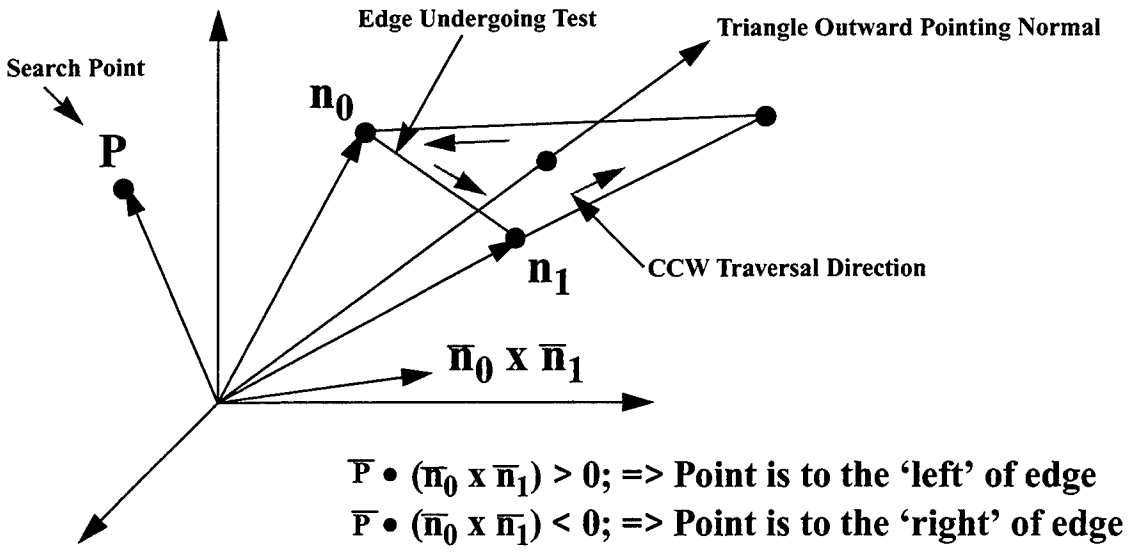

Figure 4. Walking Triangle Search Test.

This method is ideal for use by the current USNDC event location algorithm which is iterative since the previous containing triangle can be used as a new guess for the next event-location search. The searching performance of the algorithm was tested by tessellating 12,000 event locations (provided by 12 years of NEIC seismic event data) with a 26,000 triangle arbitrary tessellation and then searching for the triangles containing the event locations. Typically

between 50 and 100 triangles would be traversed to find each interpolation point. On a 167 MHz Sun Ultra the average search time per interpolation point was approximately 0.007 seconds.

Natural Neighbor Interpolation

Natural-neighbor interpolation, as discussed above, is a local weighted average interpolation method. These methods (in two dimensions) have an interpolation function of the form

$$f(x, y) = \sum_{i=1}^{n} w_i(x, y) f_i$$

where i is summed over all node neighbors that surround the interpolation point (x, y), f_i is the function value at the nodes, and $w_i(x,y)$ is the normalized 'influence' weight attached to neighbor i that influences the interpolation result at (x, y). In natural-neighbor interpolation these weights are referred to as the natural-neighbor coordinates of point (x,y) (Watson, 1992). A brief synopsis of the method by which the natural-neighbor coordinates are calculated will be given here. Refer to Watson (1992) and Sambridge (1995) for excellent treatments of the full procedure.

The natural-neighbor coordinates are best described using a geometric definition. Examine the five nodes in Figure 5a. The dashed lines connecting the nodes represent the Delaunay triangles connecting the nodes whose circum-circles include the interpolation point, X (see **Data Tessellations** section for a description of circum-circle containment).

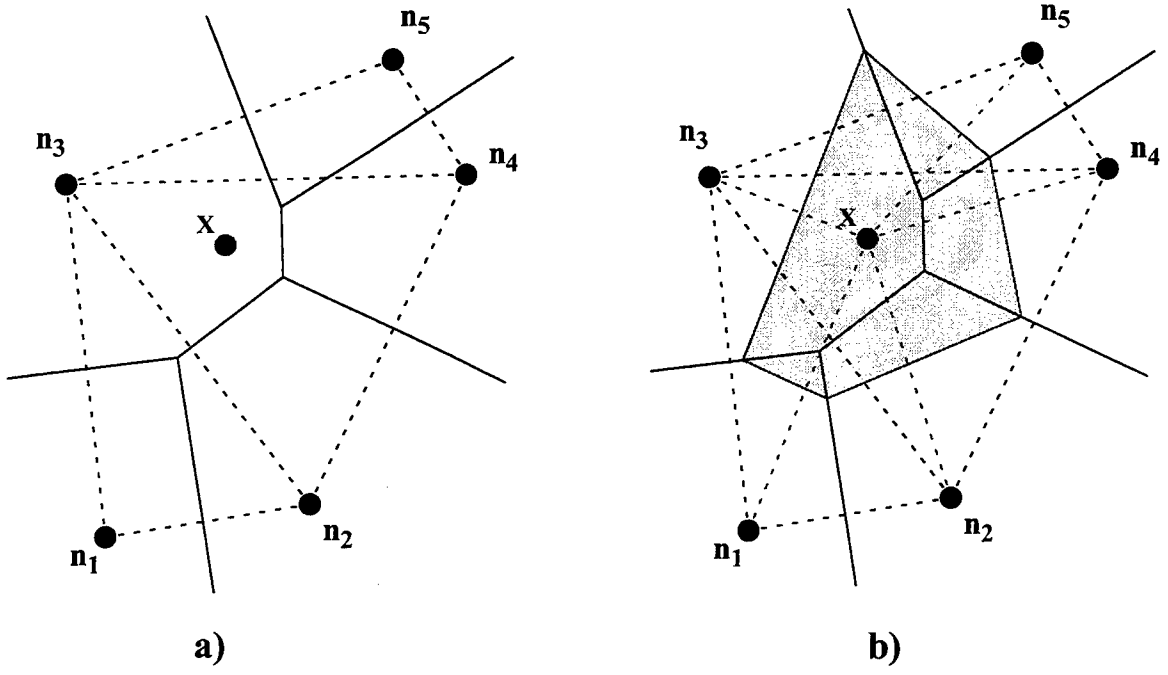

Figure 5. Natural-neighbor coordinate definitions.

The solid lines are the voronoi edges of the nodes, the complete set of which is referred to as a voronoi polygon (Preparata, 1985). Each node in a Delaunay tessellation has exactly one con-

vex voronoi polygon that completely surrounds it. The voronoi polygon can be constructed by passing a perpendicular line through the midpoints of each edge of the Delaunay tessellation. The intersection of those lines form the vertices of the voronoi polygon. In Figure 5a, we have removed outlying edges for clarity.

Figure 5b depicts the result of adding the interpolation point, X, to the tessellation. The shaded portion of Figure 5b represents the new voronoi polygon for the interpolation point. The new voronoi cell about X overlaps all of the original cells of its natural-neighbors. The natural-neighbor coordinate, or weight, for a neighbor node acting on the interpolation point is defined as the ratio of the area of overlap with the neighbor nodes original voronoi cell and the new voronoi cell about X to the total area of the new voronoi cell about X.

Since the nearest-neighbor coordinates are normalized they always lie between 0 and 1. This results in the property that if an interpolation falls exactly on top of a node the function value of the node is returned. The other important property to note is that the interpolation is entirely local and only depends on the nearest-neighbor set of the interpolation point.

This type of interpolation is linear and results in a surface that has continuous first order derivatives throughout the tessellation except at the data points themselves. A completely first and second order continuous interpolation can be evaluated by blending the linear form with the natural-neighbor gradient evaluated at the interpolation point. Watson (1992) describes some simple parametric blending functions that account for the linear interpolant, gradient, and the variability in the data to control the surface tautness.

Results

At present the research has succeeded in implementing the tessellation, smoothing, searching, and interpolation functionality. However, no testing of the algorithms on true Knowledge Base data has been performed as the data is not yet available. This has led us to improvise testing of the tessellation, smoothing, and searching functionality on analogous data sets which are available. As an example, seismicity travel time correction factors were taken from a single station (Albuquerque) to model a mesh density that is smoothed on the travel-time correction gradient. The correction factors are modeled by using a tessellation of all of the seismic event points. Each event point has a nearest neighbor set (voronoi set) whose corrections are weighted by distance to provide an arbitrary field function that approximates the correction factor variability over the Earth.

Once the field function is defined a coarse mesh is prescribed and smoothed over the Earth. Then new points are added and smoothed using the field function as a partial weight. This results in a mesh that densifies within regions of large correction-factor gradient. Figure 4. below illustrates the resulting mesh.

At this point it is not clear how viable mesh smoothing will be. For hydroacoustic interpolation the technique might be very useful because acoustic travel times can be interpolated directly from an already defined mesh. Accuracy and efficiency could be increased by densifying the mesh in regions of large gradients. Seismic data, on the other hand, is more problematic. Regional characterization efforts will yield sets of control points with fixed locations, and these may be embedded in a global coarse mesh which may have null values at many locations. Under these circumstances the global connectivity of the mesh will be used to search for

the triangle containing the point to be interpolated but the interpolation will only be performed if one or more nodes of the containing triangle have non-zero data.

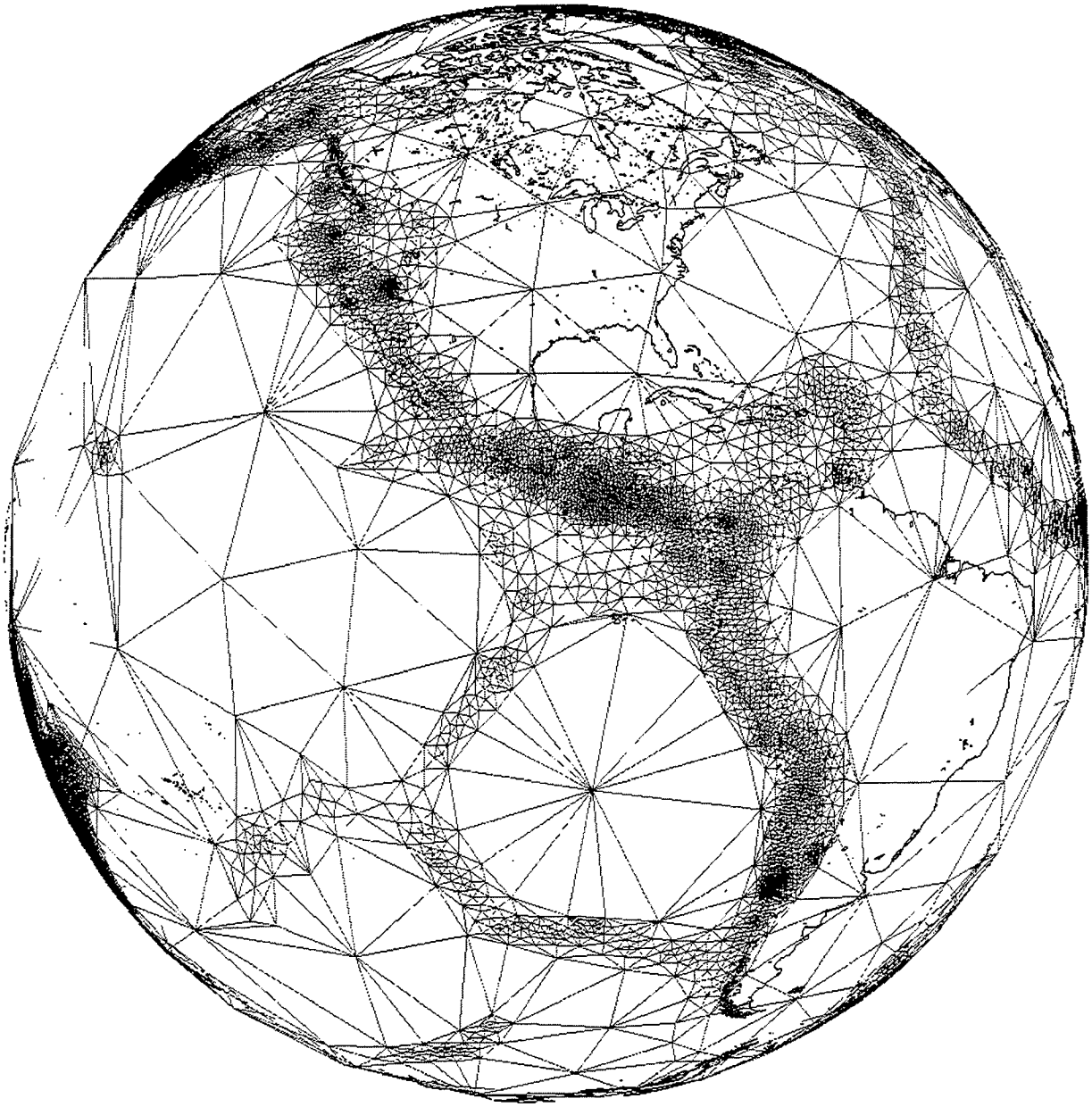

Figure 4. Seismicity map illustrating correction-factor gradient smoothing.

CONCLUSIONS AND RECOMMENDATIONS

This paper described the requirements of the CTBT Knowledge Base relative to seismic event processing and interpolation. We have shown that the methods of Delaunay tessellations and natural-neighbor interpolation more than meet the requirements of the Knowledge Base. The method of Delaunay triangulization is extremely flexible and provides the perfect connectivity network to perform natural-neighbor interpolation. In addition, natural-neighbor interpolation

satisfies the Knowledge Base requirements of accuracy, continuity, and the ability to model sparse and irregular data. Moreover, Watson (1992) has shown that the method of natural-neighbor interpolation meets all the conditions of an ideal interpolator and may be the only means of interpolating sparse and irregular data accurately.

We have briefly described the Delaunay tessellation and nearest-neighbor interpolation methods applied to interpolation on the spherical Earth. We have described an appropriate triangle search technique that is efficient and avoids the use of complex search algorithms and their associated additional memory requirements. Finally, we have shown an example of the meshing technique to model the travel-time correction factor gradient in terms of mesh density.

In the future we intend to use data from the regionalization efforts under way at Los Alamos and Lawrence Livermore Laboratories to begin testing our interpolation and database connectivity algorithms. A major part of this testing will involve connecting the current event location algorithm to the searching and interpolation algorithms to demonstrate both the accuracy of the collected data and the effectiveness of the interpolation.

REFERENCES

Barber, B., Dobkin, D.P., and Huhdanapaa, H., 1993. **"The Quickhull Algorithm for Convex Hull,"** The Geometry centre technical report GCG53. The Geometry Centre, Univ. of Minnesota, Minneapolis, MN 55454.

Braun, J., and Sambridge, M., 1995, **"A Numerical Method for Solving Partial Differential Equations on Highly Irregular Evolving Grids,"** Nature, Vol 376.

Delaunay, B.N., 1934. **"Sur la sphere vide,"** Bull. Acad. Science USSR VII: Class. Sci. Math., 793-800.

Fortune, S., 1992. **"Voronoi diagrams and Delaunay triangulations,"** Computing in Euclidean Geometry, eds. Du, D.Z., and Hwang, F., World Scientific.

Laszlo, M. J., 1996, **"Computational Geometry and Computer Graphics in C++,"** Prentice Hall.

Lawson C. L., 1977, **"Software for C1 surface interpolation,"** Mathematical Software III, ed. Rice. J., Academic Press, New York.

Preparata, F. P., and Shamos, M. I., 1985, **"Computational Geometry: an Introduction,"** Springer-Verlag, New York.

Sambridge, M., Braun, J., and McQueen, H., 1995, **"Geophysical parameterization and interpolation of irregular data using natural neighbors,"** Geophys. J. Int.

Shepherd-Dombroski, E., D. Baur., J., Hipp, J.R., Keyser, R.G., and Young, C. J., 1996 (Draft), **"CTBT Knowledge Base Initial Design"**, Sandia National Laboratories.

Watson, D. F., 1992, **"Contouring: A Guide to the Analysis and Display of Spatial Data,"** Pergamon, Oxford.

"4th International Meshing Roundtable," 1995, Sandia National Laboratories, Sand95-2130.

Development of a Geological and Geophysical Information System and Seismological Studies in the Middle East and North Africa

Dogan Seber, Eric Sandvol, Marisa Vallvé, Graham Brew, Muawia Barazangi

Institute for the Study of the Continents, Cornell University,
Snee Hall, Ithaca, New York 14853

Contract # F19628-95-C-0092
Sponsored by DOE

Abstract

We continue to collect and organize all available seismological, geophysical, topographical, geological, and satellite imagery datasets for the Middle East and North Africa into a digital information system that is quickly accessible via the Internet from Cornell and can be utilized in modeling and display programs. We finalized locating and digitizing published crustal thickness, depth to basement, and crustal velocity and density structures, primarily as interpreted from seismic refraction and reflection, and gravity data. We completed a tectonic map for the Middle East. We are currently working to construct a North Africa tectonic map. We are finalizing metadata entries for all of our databases. All our data are being stored in ArcInfo Geographic Information System (GIS). We are also maintaining a comprehensive bibliography of all the relevant references in a computer database. We continue to update database access tools to extract and visualize on-line databases. We are currently updating our Web page to allow a user to access all our ArcInfo databases and to make searches and custom designed plots on our dedicated Web server.
Our Web address is: **"http://www.geo.cornell.edu/geology/me_na/main.html".**

We are also continuing our efforts on original seismological studies to better understand the crustal structure and regional seismic wave propagation in this region. We have compiled a large seismic waveform database for all the broadband seismic stations in the region. We are studying the crustal structure beneath each station using the receiver function technique. In order to have a better control on errors and resolution limits we have developed a grid search technique that allows us to search and obtain global minima for each layer thickness and velocity. Moho depth was found to be varying from about 8 km in the Afar region to about 55 km in the Caucasus region. We have also finalized a refraction study for a detailed basement structure and velocities in eastern Syria near the Iraqi border. Another seismological study that we conducted was discrimination of chemical explosions in Morocco. Implication of our findings is that source inconsistencies have a significant role in the failure of commonly used discriminants. The 10-15 Hz Pg/Sg ratio test proved to be the most precise and accurate discriminant of the 5 different discrimination tests used.

Key words: Geographic Information System (GIS), digital databases, Middle East and North Africa, Receiver Functions

Objective

It is essential for the implementation and subsequent CTBT monitoring efforts that multidisciplinary information on any given region is readily available and accessible in a digital on-line format via electronic networks for use by concerned researchers and decision makers. New data, both seismological/geophysical and geological, are required to constrain advanced theoretical and modeling efforts in order to better understand the propagation of high-frequency seismic waves produced by very low yield events at regional distances. For these monitoring efforts to be successful, researchers must be able to detect, characterize, calibrate, discriminate, and verify any suspect event for most regions on earth. As important to the success of any monitoring strategy, such data must be swiftly accessible to researchers via networks in order to integrate with real-time recorded events to provide ground-truth for fast verification purposes. Our objectives are to collect and organize all available seismological, geophysical, topographical, and geological datasets for the Middle East and North Africa and to form a digital information system that is accessible via the Internet (except the DMA topography) from Cornell. In cases where there are recent, unstudied data that can be used to constrain some of the existing information and/or provide new information, we study these data and obtain more accurate results and include them in our regional databases as new information.

In implementing these objectives, we are careful to focus on monitoring problems that are addressed or soon will be attacked by the different research groups. It is important that our digital, network-accessible information system is complete, comprehensive, multidisciplinary, unified, easy to update, and of direct relevance to monitor the negotiated CTBT or any other agreements. Because of the unique and considerable contacts between Cornell University and scientists and institutions in most of the countries of the Middle East and North Africa we are able to initiate contacts and assemble large data sets that need to be computerized to serve the ongoing and future work on monitoring the CTBT.

Research Accomplished

We have been focusing our efforts to develop and provide diversified digital databases on the Middle East and North Africa. We are continuing to include published results based on seismic refraction, geologic/tectonic observations, gravity, satellite in our Middle East and North Africa GIS imagery (e.g., Barazangi et al., 1996; Seber et al., 1993; Barazangi et al., 1993). In order to develop a more comprehensive picture of the Moho depth and crustal velocity structure in this region we have modeled teleseismic receiver functions for all broadband stations as well as mapping regional wave propagation using local network data. We studied a detailed refraction data to obtain basement depth and velocities in eastern Syria, and we studied discrimination of chemical explosions in Morocco using Moroccan seismic network.

Developing a GIS database

Our digital databases are growing both in spatial coverage and in size. We now have about 1.2 Gbytes data that we keep on-line excluding satellite imagery and topography data. Under our databases a comprehensive geographic dataset including coastlines, country borders, rivers, cities, roads all to a scale of 1,000,000 is now available. Under geophysical databases we

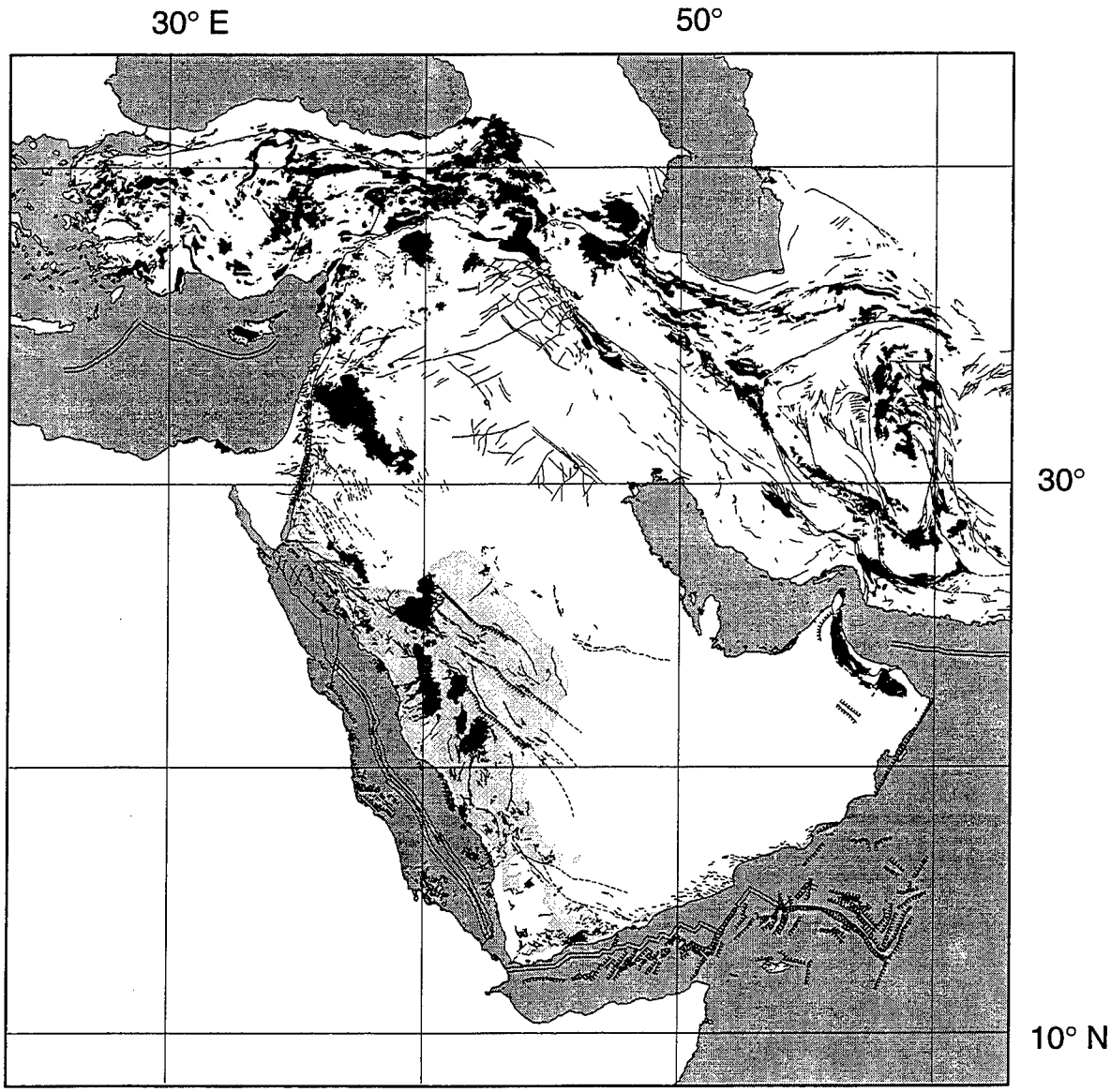

Figure 1. Tectonic map of the Middle East. This map was digitized from several maps and added to our databases. Items digitized include faults (black lines), basement outcrops (light gray), Paleogene, Neogene, and Qua ternary volcanics (dark gray), and ophiolites (black).

complied USGS PDE and ISC seismic event catalogues, global Harvard CMT focal mechanism solutions since 1977 up to February 1996, local seismic station locations as well as broadband station locations in the region. About 60 crustal-scale cross sections in the Middle East, mainly along the margins of the Arabian plate, were digitized and entered into the database system. We complied some local seismic bulletins and entered the data into our GIS. We are currently working and updating a large gravity database for the entire area. Global scale Moho and basement maps were digitized and now available. A 1 km resolution topography/bathymetry dataset was developed and added into the system. Under the geological datasets we compiled a tectonic map of the Middle East from several sources of maps (Figure 1). We are currently developing a tectonic map for North Africa. We also digitized mining sites (active and potential) in Libya, Algeria, Iraq, and Iran. We are currently working on a TM satellite image covering most of the region of interest.

All these databases are kept in ArcInfo GIS format. Each data point in the database is assigned several attributes. This makes the data easy to search, study, and update. Each seismic event, for example, has several attributes describing the location, origin time, depth, magnitude, focal mechanism, etc. By using these attributes it is possible to make a search based on any of the items or just click on the screen on an event to get all the attribute information on it. Items in the tectonic maps also have similar attributes assigned to them. All the faults are labeled as normal, reverse, strike-slip or unknown-type. Volcanics and other units are assigned items such as their ages and the area that they cover.

We have been also developing data access tools. Since ArcInfo software has a slow learning curve, we developed a menu-driven access tool to all of our databases. Using these tools one can search, explore, study, select, print the entire database with ease without having any background knowledge about ArcInfo (Figure 2). It is possible now by using these access tools to make cross sections between two arbitrary points and requesting Moho, basement, topography or any of these items individually.

Another very important issue about developing large scale databases is to develop "metadata" about the compiled data. This becomes very crucial when somebody who is not familiar with the data itself is using them. The metadata give a detailed description about the data resolution, how they were collected/interpreted/processed. We entered metadata to about 80% of the existing data in our GIS. We are currently adding more metadata to finalize this process.

Receiver Function Inversion

We have made estimates of crustal thickness and velocity structure using receiver functions for IRIS GSN, MEDNET, GEOSCOPE and GEOFON broadband stations in the Middle East and North Africa (Figure 3). Over 600 Megabytes of digital broadband data were collected from 24 stations. Receiver functions were created using a waterlevel spectral division with a guassian low-pass filter. We then reviewed each receiver function and eliminated all those receiver functions with poor signal to noise ratios. Of these 24 stations, we have been able to find high quality teleseismic waveforms for 14 stations from which we were able to construct stacked receiver functions. In each of the stacked receiver functions, we have included receiver functions from all azimuths rather than stacking those records that correspond to events from a range of azimuth. This allows us to invert for the average velocity structure beneath each station. In order to avoid destructive interference or artificial broadening of the P-to-S energy, we have stacked events with similar distances between the source and station.

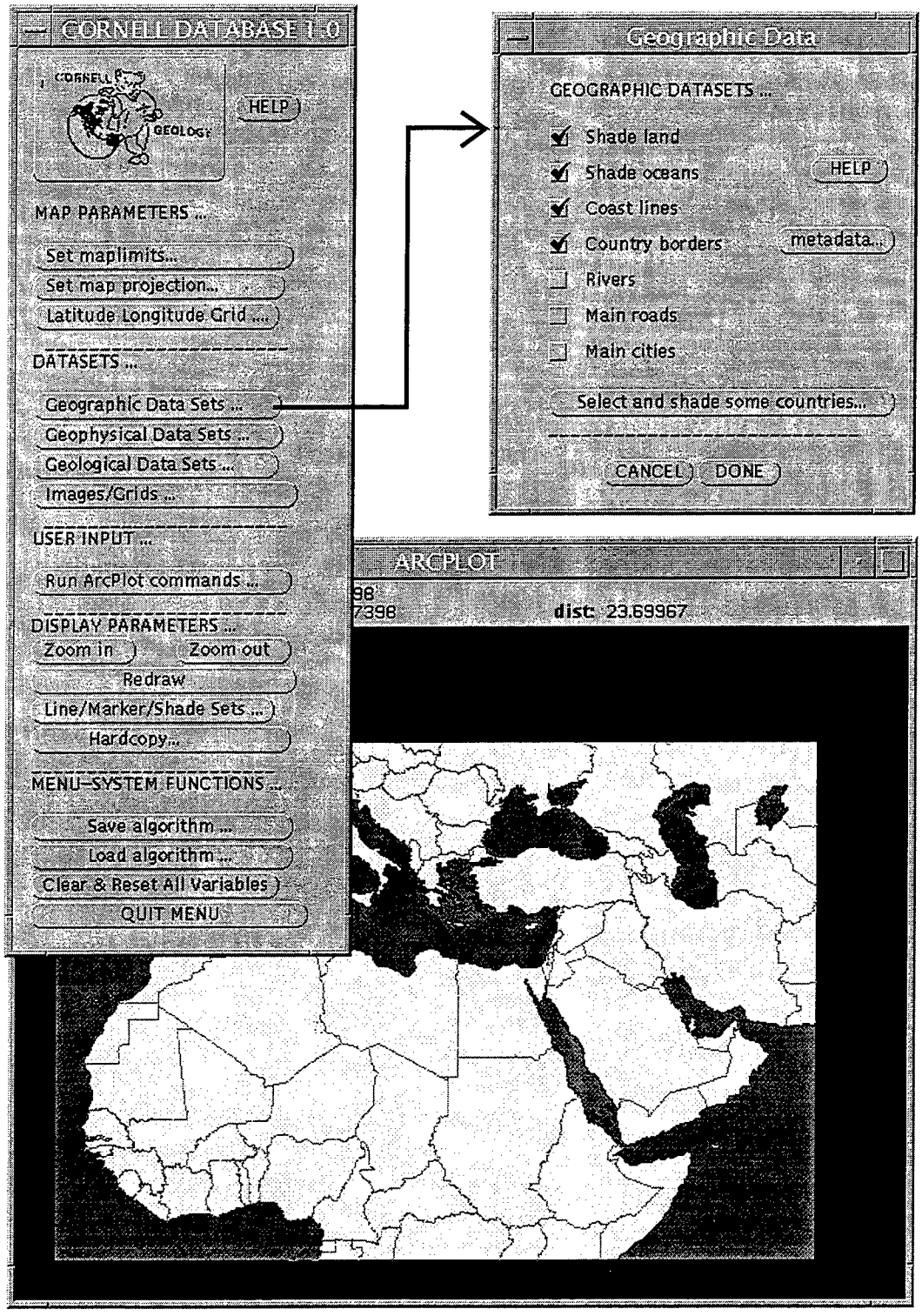

Figure 2. Main menu of data access tools and a sub-menu showing choices of data to be plotted as check marked. Below is the resultant graphical output.

In order to invert the receiver function data for crustal and upper-most mantle shear-wave velocity structure, we employed a grid search scheme using a maximum of six layers in our model. Unlike least-squares inversion schemes our grid search technique guarantees that we will solve only for global minima. By using only 8 to 10 model parameters (4 to 5 layers, varying both the layer thickness and shear-wave velocity) in our inversion, we are able to avoid over-parameterizing the inverse problem. Therefore the receiver function inversion's non-uniqueness problem is reduced, since the number of local minima is limited. We have also been able to make some estimate of the inversion's confidence region by using the error surface derived from our grid search technique. We have found that even though we are only using 4 or 5 layers, we are able to model the receiver function waveforms reasonably well when a longer period gaussian filter (α=1.5 to 1.0) is used. By using only longer period receiver functions (~ 2 to 3 seconds) and relatively small number of layers we should be able to resolve the first order discontinuities within the crust and uppermost mantle.

Crustal thickness in North Africa is found to be generally on the order of 30 to 41 km (Figure 3) except station ATD which is located on exposed oceanic crust. We have found a Moho depth of 8 km at station ATD which is consistent with this being oceanic crust. Data from three coastal stations in North Africa (MBO, TBT, and MEB) contain evidence of very strong lateral heterogeneity and teleseismic P-wave multi-pathing. In the Middle East, our estimated crustal thicknesses compare well with the available seismic refraction profile interpretations. There is some ambiguity in where to interpret the Moho for station KEG. There are two relatively large shear-wave velocity discontinuities: one at 30 km (3.5 km/s to 4.0 km/s) and the other at 40 km (4.0 km/s to 4.5 km/s). Makris et al. (1987) report crustal thicknesses in this region on the order of 31 to 33 km which would correspond to the first discontinuity that we observe in our model. We have also found evidence of a pronounced mid-crustal low-velocity zone in central Turkey beneath station ANTO. There has been no prior indication of a low velocity zone in this region although this is a region where the mantle lid is slow and highly attenuating. It is not clear whether this low-velocity zone is related to heating of the middle crust, some rheological change within the crust or an artifact due to lateral velocity heterogeneity. The thickest crust was found beneath station GNI in the Caucasus Mountains. However, the data at station GNI is of relatively low quality and also shows strong evidence of dipping layers. There is coherent and azimuthally dependent energy on station's tangential receiver function which could best be explained by a dipping Moho or lower-crustal velocity discontinuity.

Refraction Study in Eastern Syria

Original data from a 300 km long reversed seismic refraction profile, with offsets up to 54 km and geophone spacing of 150 meters, were analyzed and interpreted in a study of deep sedimentary structure in eastern Syria. The interpretation was strengthened and refined by data from other coincident sources including seismic reflection data, various well logs and potential field data. The integration of these additional data was necessary to remove the ambiguity of low-velocity zones which is present if the refraction data are used alone. The results established a model of basement depth and sedimentary seismic velocities along a transect crossing the Euphrates graben system in eastern Syria, to a depth of around 9 km (Figure 4). Errors in the depth of the deepest interfaces are less than 200 meters, and seismic velocities are

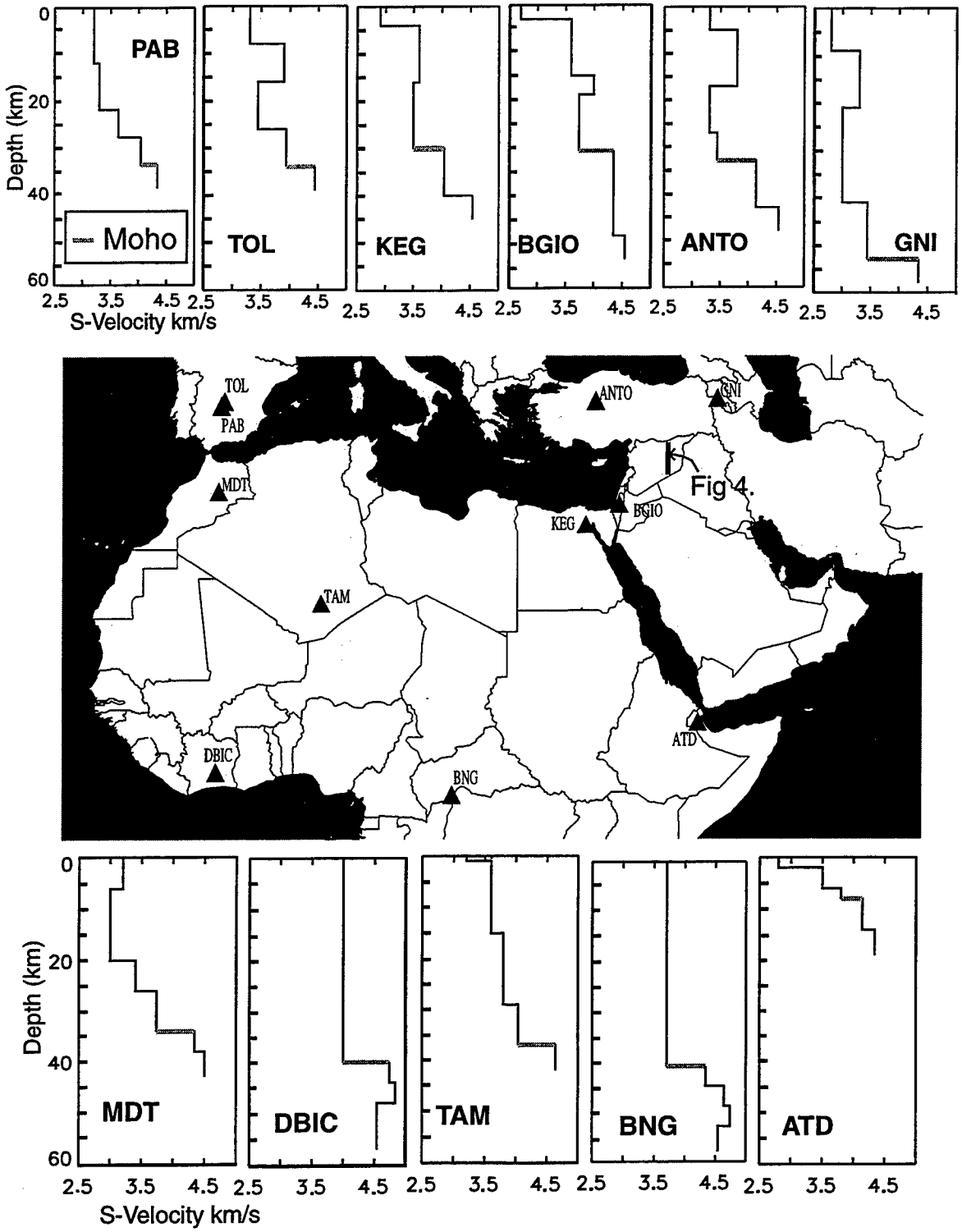

Figure 3. Shear-wave velocity vs depth profiles obtained from the inversion of stacked receiver functions. We have used these models to interpret a Moho depth. The maps shows all broadband stations used in this study.

resolved within ± 0.1 km/s. Basement depth on the north side of the profile is observed to be around 6 km, and in the south it is at least 8.5 km. Detailed knowledge of basement depth and velocityof sedimentary section is essential for a better understanding and modeling of high-frequency regional seismic phases.

Chemical Explosions Discrimination in Morocco

In order to examine the limitations in the techniques for discriminating between chemical explosions and earthquakes at local and regional distances, we have applied several standard heuristics to seismic events in northwest Morocco where little *a priori* information was available. Only short period seismic stations with 1 Hz geophones that recorded both earthquakes and explosions in proportionate numbers were included in the analysis in order to control for station effects and thus to allow direct comparisons between events. Recordings with under a 2:1 RMS signal to noise ratio were eliminated from the population. These criteria eliminated all but high quality seismograms from 8 Oud Zem phosphate mine explosions and 6 earthquakes that occurred in northwest Morocco (Figure 5). The explosions used have similar geographic locations, total charge magnitudes, and presumably ripple fired mechanisms, and yet the seismic recordings are still characterized by a surprising amount of diversity.

Time and path independent modulations, owing to the periodic source mechanism of the ripple fired explosions, rarely unequivocally distinguish the explosions from the earthquakes in the region. Our findings imply that more often than the current literature suggests, source inconsistencies have a role in the failure of common discriminants. Furthermore, crustal seismic velocity and the attenuation structure seemed to shape the seismic signals more than the nature of the source mechanism. The 10-15 Hz Pg/Sg ratio test proved to be the most precise and accurate discriminant of the 5 different discimination test used.

Sn and Lg propagation Efficiency in the Middle East

Collaboration with colleagues in Turkey and Syria have provided a large amount of data from local networks in these two countries. These stations primarily consist of short period, vertical component seismometers. We are using these data to characterize the propagation efficiencies of the regional phases Pn, Pg, Sn and Lg. This work should provide much more accurate maps of the regions of poor propagation. Seismic events from the Aegean sea, Zagros Mountains, Red Sea, and Caucus Mountains have provided us excellent azimuthal coverage for investigating the nature of regional wave propagation in the Middle East.

Bibliography

We continue to build and expand our bibliographic database. References to books, journal articles, reports and other published literature are stored with the usual information on title, date, author, journal, page numbers, etc. and with searchable keywords on the content. This has become a comprehensive database of seismology, crustal structure, geology, and geophysics literature for the Middle East and North Africa. We will continue to update and add to this bibliographic database.

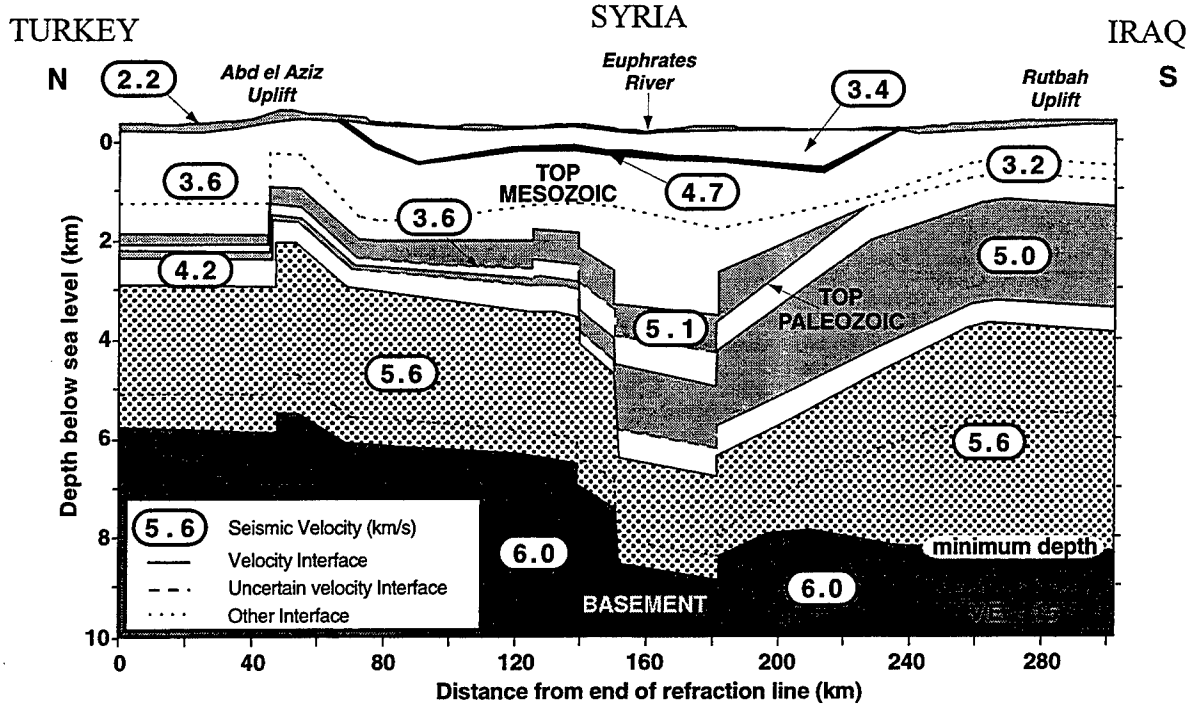

Figure 4: Seismic velocity model along a transect in eastern Syria derived from refraction data and other coincident data sources. See Figure 3 for location.

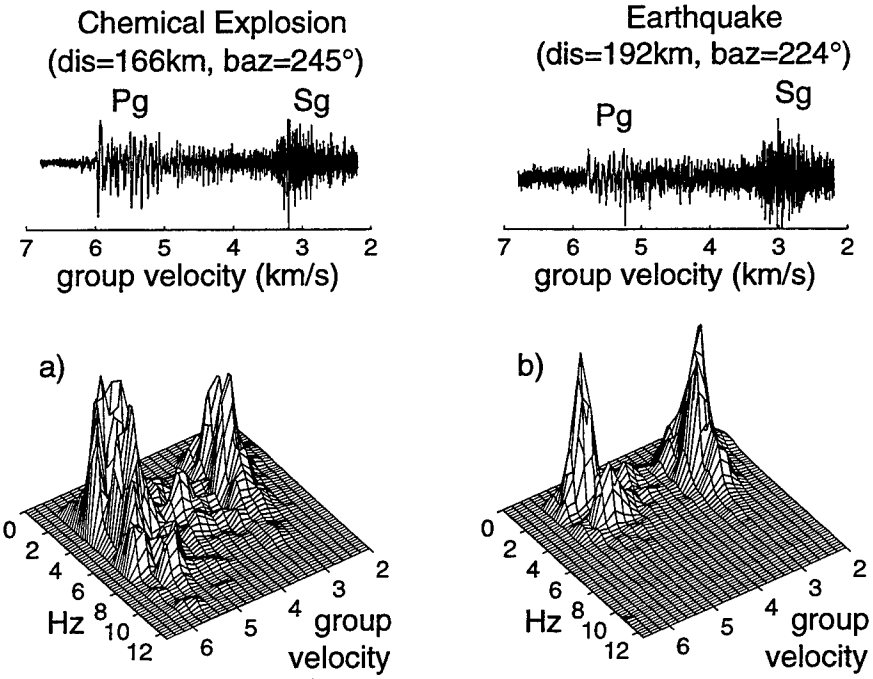

Figure 5. Vertical, short-period seismograms of a chemical explosion from a Moroccan Phosphate Mine and a small earthquake. Both seismograms shown here are from the Moroccan National Network station MSH.

Conclusions and Recommendations

The expanding database of our digital geological and geophysical information system will be useful and support CTBT and nonproliferation monitoring. For example, geophysical and geological datasets can provide important ancillary information on the structure of the crust and upper mantle that may affect the propagation of seismic phases at regional distances. In turn, this bears on the detection, discrimination, calibration, on-site inspection, and yield estimation of nuclear explosions and other suspect events.

To monitor the anticipated multilateral comprehensive nuclear test ban and nonproliferation treaties, we recommend that multidisciplinary information on any given region be readily available and accessible in digital form via the Internet for use by concerned researchers and decision makers. New data, both seismological/ geophysical and geological, are required to constrain advanced theoretical and modeling efforts in order to better understand the propagation of seismic waves produced by very low magnitude events at regional distances. For these monitoring efforts to be successful, researchers must be able to detect, characterize, calibrate, discriminate, and verify any suspect event for most regions on earth. As important to the success of any monitoring strategy, such data must be swiftly accessible in digital form to researchers via networks in order to integrate with real-time recorded events to provide ground-truth for fast verification purposes.

References

Barazangi, M., Fielding, E., Isacks, B., and Seber, D., Geophysical and geological databases and CTBT monitoring: A case study of the Middle East, in Monitoring a Comprehensive Test Ban Treaty, eds. E.S. Husebye and A.M. Dainty, Kluwer Academic Publishers, Amsterdam, 1996.

Barazangi, M., Seber, D. , Chaimov, T. , Best, J. , Litak, R. , Al-saad, D. , and Sawaf, T. , 1993, Tectonic evolution of the northern Arabian plate in western Syria, in E. Boschi et al. (Eds), *Recent evolution and seismicity of the Mediterranean region*, p. 117-140.

Best, J.A., Barazangi, M., Al-Saad, D., Sawaf, T., and Gebran, A., 1990, Bouguer gravity trends and crustal structure of the Palmyride Mountain belt and surrounding northern Arabian platform in Syria, *Geology*, v. 18, p. 1235-1239.

Makris, J., R. Rihm, and A. Allam, 1987, Some geophysical aspects of the evolution and structure of the crust in Egypt, in, El-Gaby, S., and R.O., Greilings (Eds.), *The Pan-African Belt of Northeast Africa and Adjacent Areas*, Friedr. Vieweg & Sohn, Braunschweig, p. 345-369.

Seber, D., Barazangi, M., Chaimov, T., Al-Saad, D., Sawaf T., and Khaddour, M., 1993, Upper crustal velocity structure and basement morphology beneath intracontinental Palmyride fold-thrust belt and north Arabian platform in Syria, *Geophys. J. Int.*, v . 113, 752-766.

ARRAY PROCESSING OF DELAY-FIRED SIGNALS

Robert H. Shumway
Division of Statistics
University of California, Davis

Contract F19628-95-K-0010
Sponsored by AFTAC

ABSTRACT:

We consider frequency and time domain methods for processing delay-fired seismic signals using arrays. Detecting and estimating the delay and duration characteristics induced by ripple fired mine blasts can serve as a basis for discriminating between mining blasts and nuclear or chemical explosions which, in principle, will not contain echo effects.

The time domain model assumes a noise corrupted signal that can be written as a convolution of source, path and instrument responses with a ripple-fired pulse sequence. The pulse sequence is modeled as a seasonal ARMA process, with the period corresponding to the firing delay and the model order proportional to the signal duration. For each element of the array, seasonal ARMA models are fitted with various delay and duration parameters. Values of a Bayesian information criterion (BIC) are plotted as a function of duration and delay to select the ripple firing pattern. The frequency domain approach assumes that the same echo pattern is present on each array element. Cepstra and log cepstra are computed for each array element and the results are stacked using an approach suggested by Alexander et al (1995).

The time domain and frequency domain methods are applied to contrived array data to verify performance under ideal conditions. Ten Scandinavian mining explosions from the same K-2 mine, measured at five channels of the array ARCESS, were obtained and Pn components were extracted from each to serve as a testing set for the two approaches. We compare the results of applying the two approaches to a typical mine blast.

Key Words: *Mining explosions, duration and delay, echo detection, stacked cepstra, seasonal ARMA, model selection.*

OBJECTIVE

Monitoring compliance with a comprehensive test ban treaty (CTBT) depends on the use of close-in arrays for the purposes of detecting and identifying low-yield nuclear explosions. The identification problem is complicated by the fact that mining explosions may be mistaken for nuclear detonations, producing potentially embarrassing false alarms in a CTBT. One particular spectral feature that characterizes some mining explosions is the periodic sequence of pulses that are produced during the delay-firing that is used to break down the cavity. For mine blasts, ripple-firing involves detonation of a number of blasts that are closely grouped in space and time.

The objective of this study is to develop and test data processing techniques for detecting and identifying the echo structure induced by ripple-firing using regional data measured at a seismic array. During the initial phases of the project, we have focussed on time domain techniques involving seasonal ARMA searches and on frequency domain techniques based on the cepstrum (see Baumgardt and Ziegler, 1988, Hedlin et al, 1990 and Alexander et al, 1995).

RESEARCH ACCOMPLISHED

(i) The General Model

A general model for an array of N series, say $y_1(t), y_2(t), \ldots, y_N(t)$ recording a possible mining explosion can be written as

$$y_j(t) = x_j(t) + e_j(t), \tag{1}$$

where the process $x_j(t)$ is a delayed and added signal of the form

$$x_j(t) = \sum_{k=0}^{n-1} a_{jk} s_j(t - \tau_k), \tag{2}$$

$t = 1, \ldots, T, j = 1, \ldots, N$. We assume that the underlying signals $s_j(t)$ are realizations of some underlying signal that is modified by path and instrument response for the jth sensor. The unknown constants a_{jk} and τ_k are, respectively, the amplitudes and time delays of the $n-pulse$ sequence caused by the delay-firing and we assume initial values $a_{j0} = 1, \tau_{j0} = 0$ so that the first pulse is $s_j(t)$. To see that real data can be emulated by the model in (1), consider the realizations from a 5 element array in Figures 1 and 2. Figure 1 is contrived data, constructed by generating a second-order autoregressive signal, modulating, and then adding and delaying using delays $\tau_k = 8, 7, 7, 8, k = 1, \ldots, 4$ and amplitudes $a_{jk} = 1, .9, 1, .6, .7, j = 1, \ldots, 5$. In Figure 2, we show the Pn phase of a typical mining explosion detonated in Scandinavia and simply note that the real data does not differ markedly from the contrived data of Figure 1. We will use the contrived data as a baseline to compare the time and frequency domain methodology. We discuss first a time domain methodology that

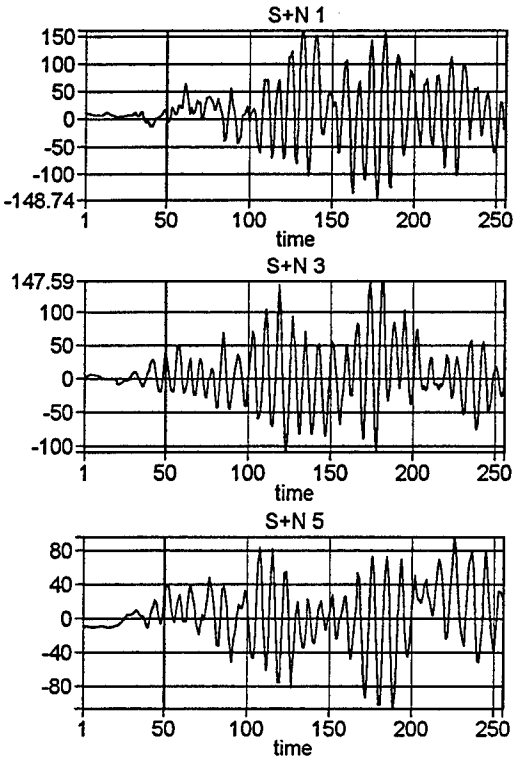

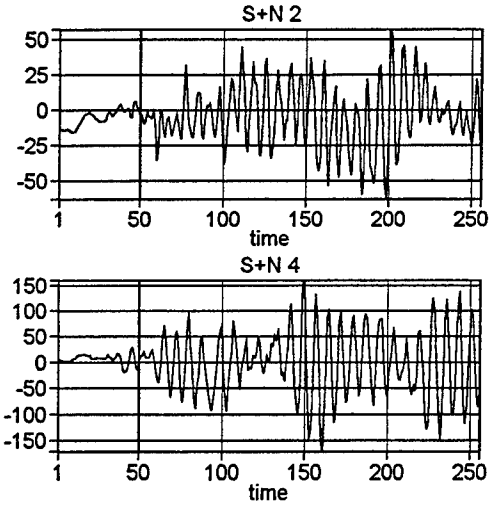

Figure 1: Contrived array with AR signal and noise. Delays are 8, 7, 7, and 8 points respectively.

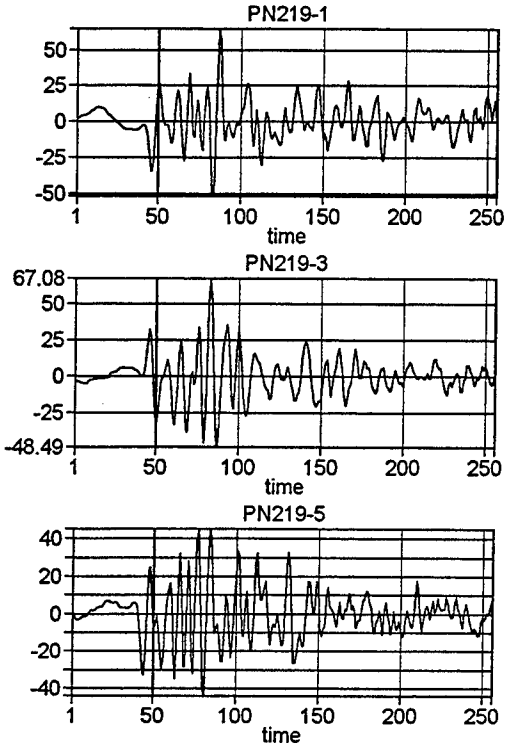

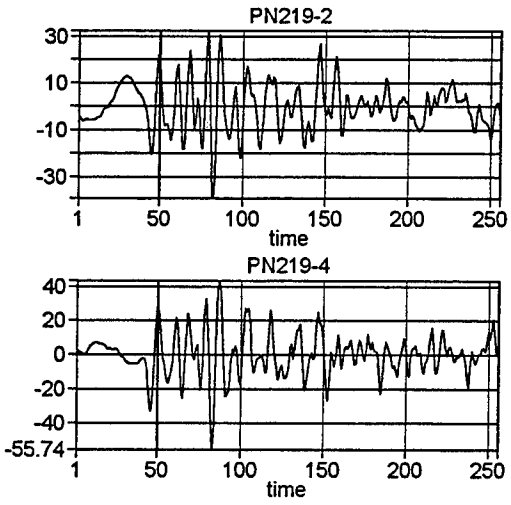

Figure 2: Array data from Pn phase for mining explosion in Scandinavia (20 Hz).

we will refer to as *seasonal ARMA searching* suggested by Shumway and McQuarrie (1994) and then move to a frequency domain method, termed *log cepstral stacking*, that has been suggested by Shelton Alexander (see Alexander et al, 1995).

(ii) Seasonal ARMA Searching

We assume here that the signal satisfies some low-order autoregressive model of the form

$$s_j(t) = \sum_{k=1}^{p} \phi_{jk} s_j(t-k) + \epsilon_j(t) \tag{3}$$

and choose $p = 2$ for most cases, where $\epsilon_j(t)$ are white noise sequences. A simplification of model (1) results if pulses are all assumed to be observed at a constant multiple of some underlying firing delay d. In this case, we may take $\tau_k = kd$ and model the process $x_j(t)$ as

$$x_j(t) = \sum_{k=0}^{n-1} a_{jk} s_j(t-kd), \tag{4}$$

where we have ignored the noise term in the simplification. In this case, $x_j(t)$ in (3) can be identified as a seasonal ARMA process with an ordinary autoregressive (AR) component and a seasonal moving average (MA(d)) component where the order of the seasonal moving average in n and the seasonal factor is d. A reasonable approximation in practice for the path and instrument effects can be attained by fitting an autoregressive model of the form (2) with $p = 2$.

In order to estimate the unknown parameters in the above formulation for a fixed n, d, say $a_{jk}, \phi_{j1}, \phi_{j2}, j = 1, \ldots, N, k = 1, \ldots, n-1$, we use maximum likelihood and compute the value of BIC as a measure of model adequacy. In practice, we obtained

$$BIC(j, n, d) = \log \hat{\sigma}_j^2 + \frac{[(n-1)+2] \log T}{T} \tag{5}$$

separately for each channel, $j = 1, \ldots, N$, and plotted the resulting values as a function of the seasonal component n and the delay d. The variance is computed as the average sum of squared residuals from fitting the seasonal ARMA model implied by (3) and (4), i.e.

$$\hat{\sigma}_j^2 = T^{-1} \sum_{t=1}^{T} \hat{\epsilon}_j^2(t), \tag{6}$$

where $\hat{\epsilon}_j(t)$ is the residual from the fitted model.

Figure 3 shows the result of contouring BIC over all possible delays ($d = s+2$ in the plots) and durations ($n = t$ in the plots). Note that the darker contours represent minima and that there are four contour levels shown on the leftmost scale. Sensors 1,3,and 4 show strong minima at delays of 8 and lesser minima at delays of 4 whereas sensors 2 and 5 show almost equal minima at delays of 4 points. There is also an ambiguity between a delay of 7 and a delay of 8 points that is evident in the second

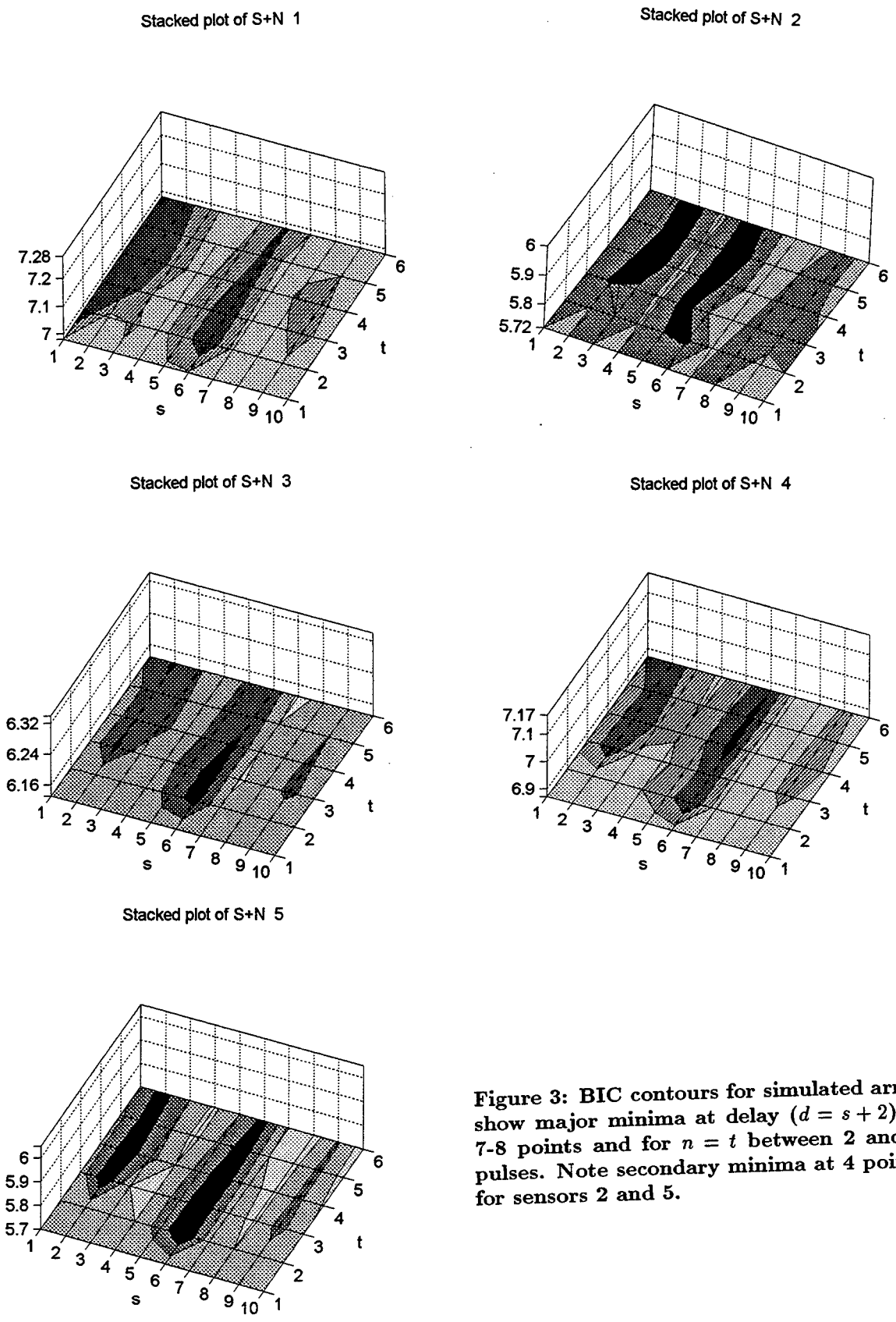

Figure 3: BIC contours for simulated array show major minima at delay ($d = s + 2$) of 7-8 points and for $n = t$ between 2 and 6 pulses. Note secondary minima at 4 points for sensors 2 and 5.

sensor. Note also the elongated nature of the contours, corresponding to difficulty in resolving the duration which could involve from 3 to 6 pulses.

In Figure 4, we see a comparable ARMA search for an actual mining explosion and we note that on sensors 1, 3 and 4 there is an some ambiguity between competing delays of 7 points (.18 sec.) and 5 points (.13 sec). Sensor 5 gives a strong minimum at .18 sec. whereas sensor 2 indicates delays of 5 to 7 points, i.e., .13-.18 sec. Duration seems relatively well specified with somewhere between 4 and 6 pulses.

(iii) Cepstral Stacking

In the frequency domain, we may argue again from the basic signal model given by (1) and (2) in the delay fired case. Assuming that the signal spectra are the same for each j and that the amplitudes are equal over the sensors ($a_{jk} = a_k, j = 1, \ldots, N$), we obtain the signal spectrum as

$$P_{xj}(\nu) = |A(\nu)|^2 P_s(\nu), \tag{7}$$

$1/ \leq \nu \leq 1/2$, where

$$|A(\nu)|^2 = \sum_{j=0}^{n-1} \sum_{k=0}^{n-1} a_j a_k \cos[2\pi\nu(\tau_j - \tau_k)] \tag{8}$$

The spectrum is exhibited as the product of a periodic function and the signal spectrum, with periods proportional to the possible values of $\tau_j - \tau_k, j, k = 1, \ldots, n-1$. If logarithms are taken of the spectrum and the function is expanded, (7) reduces to an additive model in the underlying spectrum and a periodic sequence. Taking the spectrum of the log spectrum, should produce a function with peaks corresponding to the time delay differences. A plot of as a function of time delays is called the *cepstrum*. If $\tau_j - \tau_k = (j-k)d$, the time delay differences are all multiples of the underlying delay for the ripple fired event and one will see peaks at $d, 2d, \ldots, (n-1)d$. Otherwise, one will see peaks at the various paired time differences in the delays. Suppose that we denote the estimated cepstrum at a single element by $\hat{C}_{xj}(\nu)$. Assuming that each sensor observes the same pattern of time delays in the pulses implies that one can average the cepstra over sensors, using, say

$$\hat{C}_x(\nu) = N^{-1} \sum_{j=1}^{N} \hat{C}_{xj}(\nu). \tag{9}$$

Alexander et al (1995) have proposed replacing the stack (9) by the geometric mean and we note that their alternative form

$$\hat{Q}_x(\nu) = N^{-1} \sum_{j=1}^{N} \log \hat{C}_{xj}(\nu) \tag{10}$$

seem to enhance the higher time delays.

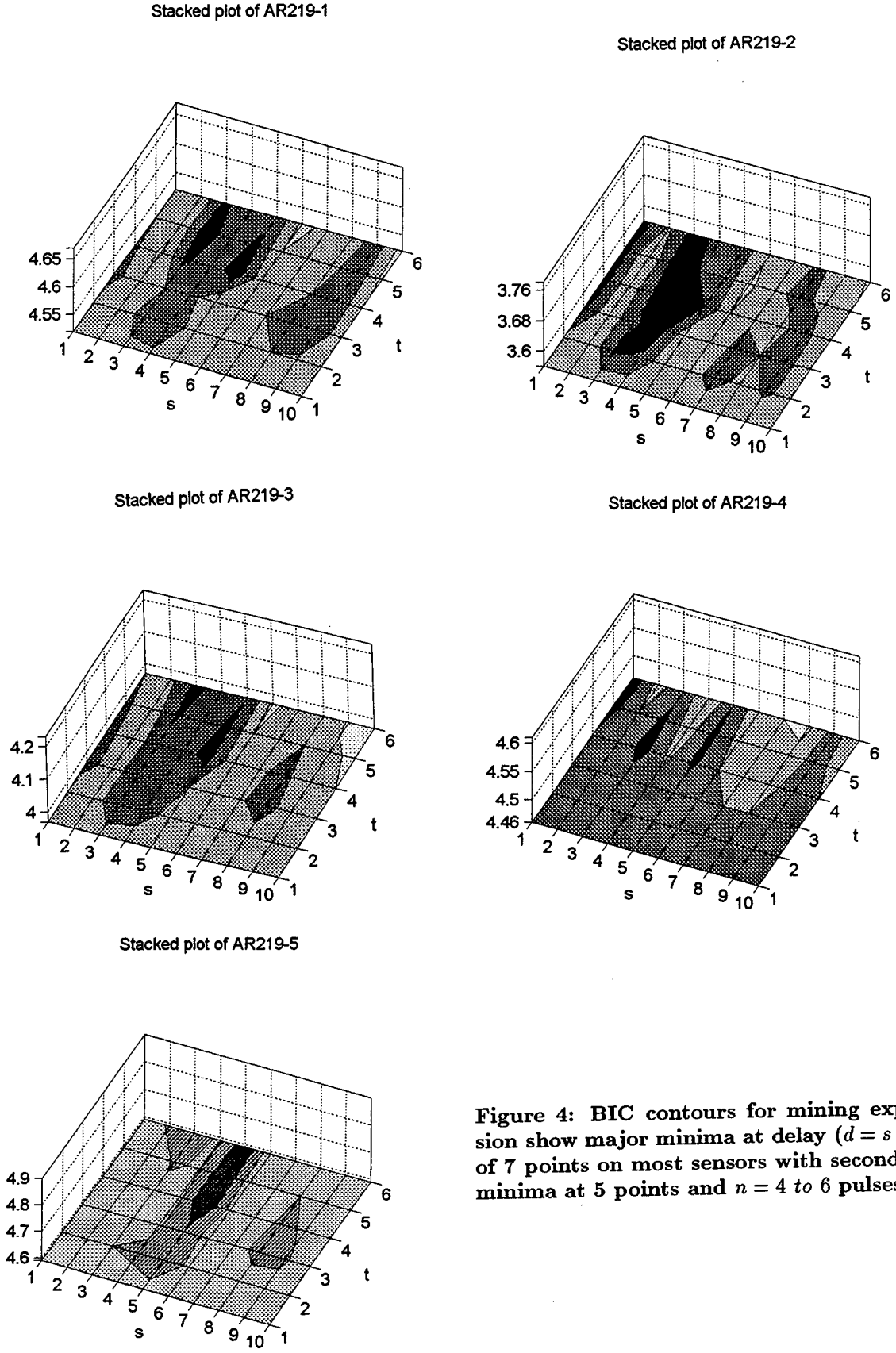

Figure 4: BIC contours for mining explosion show major minima at delay ($d = s+2$) of 7 points on most sensors with secondary minima at 5 points and $n = 4$ *to* 6 pulses.

Figure 5 shows the result of stacking the log cepstra for the contrived data, known to contain delays 8, 7, 7 and 8 points. The first maximum is at 7 or 8 points with successive maxima at 15, 22 and 30. Hence, we note delays that match up quite well with the known inputs. The mining explosion in Figure 6 shows less well-defined peaks and we may infer local maxima at 3, 12, 17, 23 and 29 points. This indicates reflections at 5 or 6 points (.13-.15 sec.) which compares with .13-.18 seconds obtained through the seasonal ARIMA search.

CONCLUSIONS AND RECOMMENDATIONS

While both methods give reasonable results for the contrived case, it is clear that the seasonal ARMA search is somewhat easier to interpret since it is based on the equal reflection model and the contours seem to give more unambiguous explanations of the possible delay-fired structure. Even so, there are aliases that might lead to false reflections and the time delays inferred for the P components are somewhat longer than one would expect. The methodology for the seasonal ARMA search is limited to analyzing single elements and we are in the process of modifying the software so that it will apply to an overall model of the form (3) and (4) with equal reflection coefficients ($a_{jk} = a_k$) and equal signal parameters ($\phi_{jk} = \phi_k$) on each channel. This will yield an overall BIC contour plot based on a single value of (5) and least squares applied to minimize the sum of the variances in (6).

The processing for the single Pn phase has been completed for only two or three of the 10 K2 mine explosions which are all from the same quarry and are measured at 5 elements on the array ARCESS. We are in the process of extracting comparable array data for the Pg, Sn and Lg phases and will complete the analysis of all phases for the 10 events using global versions of the seasonal ARMA search and the cepstral stacking methodologies.

References

Alexander, S.S., R.C. Hsu, S.L. Karl, I.N. Gupta and D.H. Salzberg (1995). New techniques for estimating source depth and other diagnostic source characteristics of shallow events from regional observations of P, Lg and Rg Signals. *17th Annual Seismic Research Symposium on Monitoring a CTBT*, 11-15, Sept., 1995, Scottsdale, Arizona. **PL-TR-95-2108, ADA 310037**

Baumgardt, D.R. and K.A. Ziegler (1988). Spectral evidence for source multiplicity in explosions: Application to regional discrimination of earthquakes and explosions. *Bull. Seismolog. Soc. of Amer.*, **78**, 1773-1795.

Hedlin, M.A.H., J.B. Minster and J.A. Orcutt (1990). An automatic means to discriminate between earthquakes and quarry blasts. *Bull. Seismolog. Soc. Amer*, **80**, 2143-2160.

Shumway, R.H. and McQuarrie, A.D.R. (1994). Statistical discrimination studies for nuclear test verification. Final Report, PL-TR-94-2283, Phillips Laboratory, Directorate of Geophysics, Air Force Materiel Command, Hanscom AFB, MA 01731-3010, **ADA 293572**

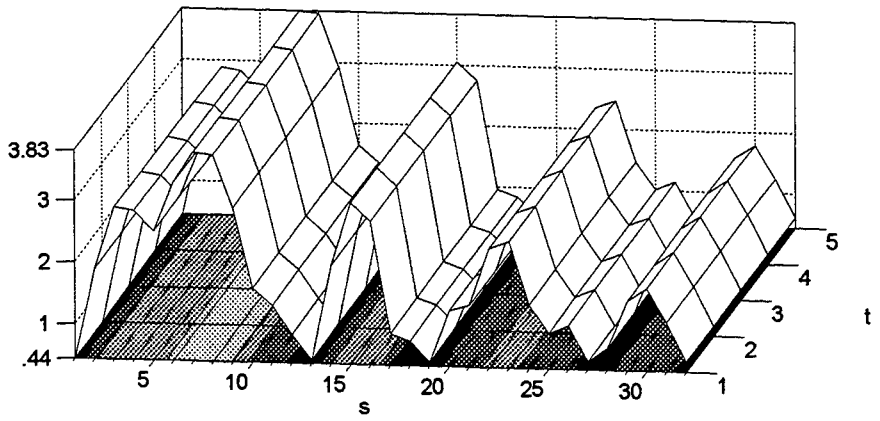

Figure 5: Stacked log cepstra for contrived array data show peaks at 7-8, 15, 22 and 30 points respectively. Observed peaks match known delays in Figure 1.

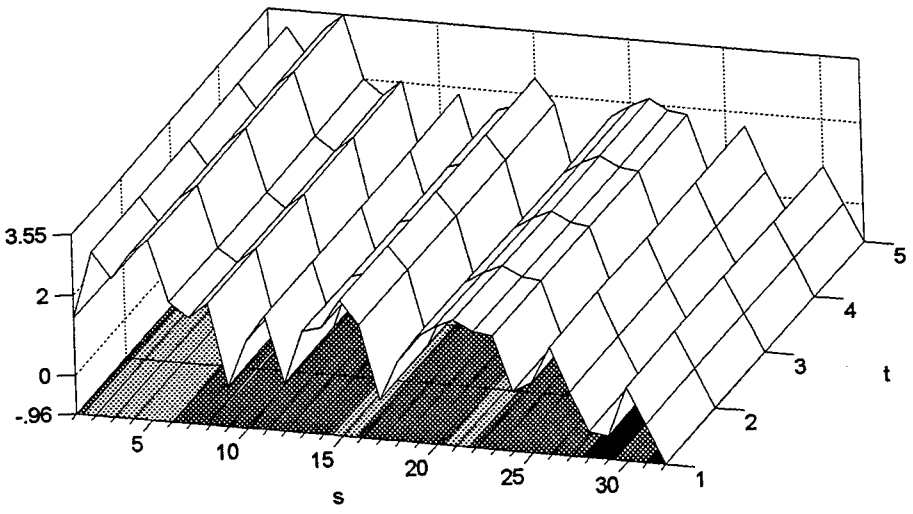

Figure 6: Stacked log cepstra for mining explosion in Figure 2 show maximima at 3, 12, 17, 23, 29. Implies possibly 4 pulses spaced at 5 to 6 points.

Data Visualization for Comprehensive Test Ban Treaty Monitoring

Randall W. Simons, Christopher J. Young, Tony L. Edwards
Sandia National Laboratories

Sponsored by U.S. Department of Energy
Comprehensive Test Ban Treaty Research and Development Program, ST485D

ABSTRACT

The purpose of the Data Visualization Project at Sandia Labs is to prototype and evaluate new approaches to the presentation of data for CTBT monitoring applications. The great amount of data expected to be available, and the complex interrelationships in that data, make this a promising area for scientific data visualization techniques. We are developing a powerful and flexible prototyping environment with which to explore these possibilities. A user-friendly graphical user interface (GUI) should be an integral part of any data visualization tools developed. The GUI is necessary to select which data to visualize, and to modify and explore the displays that are the result of data visualization. Using our prototyping environment, we have produced data visualization displays of various kinds of data and have also experimented with different GUIs for controlling the visualization process. We present here an overview of that work, including promising results, lessons learned, and work in progress. To better understand what is needed, we have identified several data processing/analysis scenarios which we think will be important in CTBT monitoring. These scenarios help us identify what types of information we should display (together or in sequence), and help us focus on isolating the underlying goals. Each display we have produced is put in the context of one or more processing scenarios to help explain why and how it could be useful.

Keywords: data visualization, graphical user interface, GUI, Comprehensive Test Ban Treaty, CTBT, seismology

1. Introduction

The purpose of the Data Visualization Project at Sandia Labs is to prototype and evaluate new approaches to the presentation of data for CTBT monitoring applications. We present here the status of that project, giving examples of the results achieved, including areas for further study and lessons learned. First, we briefly describe the hardware and software we are using to do this work, and some of what we have learned about the strengths and weaknesses of those tools. The next section details our results, including the various map projections used, displays based on data from a CSS database, and displays of other data. In the following section, we identify several data processing/analysis scenarios which we think will be important in CTBT monitoring. These scenarios help us identify what types of information we should display (together or in sequence), and help us focus on isolating the underlying goals. Each display we have produced is put in the context of one or more processing scenarios to help explain why and how it could be useful. Finally, we touch on expectations for future work.

2. Prototype Environment

We are developing prototypes and demonstrations, as opposed to production quality tools. This is a necessary first step, to explore a range of possibilities before recommending specific solutions. The display programs described here were developed on an SGI Onyx workstation and Sun Ultra 1 workstations with Creator3D frame buffers, using AVS Express software.

We have found some limitations with AVS/Express. Although it evolved from a mature product (AVS), Express is a major reorganization and reimplementation and it has not yet reached the stability of its predecessor. We think it works best as a prototyping tool, since it emphasizes flexibility over performance. By keeping functions modular, it simplifies prototyping with plug compatible modules, but combinations of modules cannot be optimized. For example, if two modules are invoked sequentially, each will have to loop through all the data separately, instead of merging the two loops as you would do if programming at a lower level. We continue to evaluate alternatives to cover the areas where Express is weak.

3. Visualization Results

We attempt to describe our work here, but the value of these programs can only be appreciated fully when used interactively on the workstation. Much is lost in the translation from the screen to black ink on white paper. First is the loss of color, which we use extensively to convey information. Second is the loss of dynamic behavior of the user interface, which allows the user to determine what he will look at when. Third is the loss of the ability to manipulate a 3D display to better understand the relative positioning of displayed objects in space.

3.1 Map Projections

Most of the data we are dealing with are inherently geographical, that is, they have locations on or in the earth. There are many ways of displaying maps of the earth. We have found that a few of these projections suffice for all of our display needs, but it is important to choose the right map for each purpose.

3.1.1 Cartesian Coordinates

This map simply uses longitude and latitude directly as (x, y) coordinates. The map shows the entire surface of the earth, but causes severe distortion near the poles. It also distorts shortest paths between points on the surface (great circles). On the plus side, it is easy to read longitude and latitude values off this type of map.

3.1.2 Spherical Earth

This is close to a true representation of the earth, which is nearly spherical. Thus it practically eliminates distortion and avoids "great circle" problems. It is only practical to view one side of the sphere at a time, however, thus requiring 3D rotation to view the back side.

3.1.3 Azimuthal Equidistant Projection

This projection places one location at the center of the map and arranges everything else relative to it. To understand this projection, think of selecting a point on a very elastic globe. Now prick a hole in globe exactly opposite the point you picked and stretch the hole until you have pulled the globe out flat. This projection is good for seeing distance and direction from the center point, since these are not distorted (everything else is). When we place an event at the center of this projection, we call it an event-centered display.

3.2 Visualizing Data from a CSS Database

Many of our visualization displays present data retrieved from a CSS database (Anderson, et. al. 1990). We have used GSETT II data (Group of Scientific Experts 1992), and some GSETT III reviewed event bulletins from the International Data Center.

3.2.1 Multilevel Displays - Events, Stations, Arrivals

This is a continuation of work reported last year by Young, Pavlakos, and Edwards (1995). The key idea throughout all the many iterations of this prototype is that there are multiple displays simultaneously visible and logically linked.

FIGURE 1. Multilevel Display

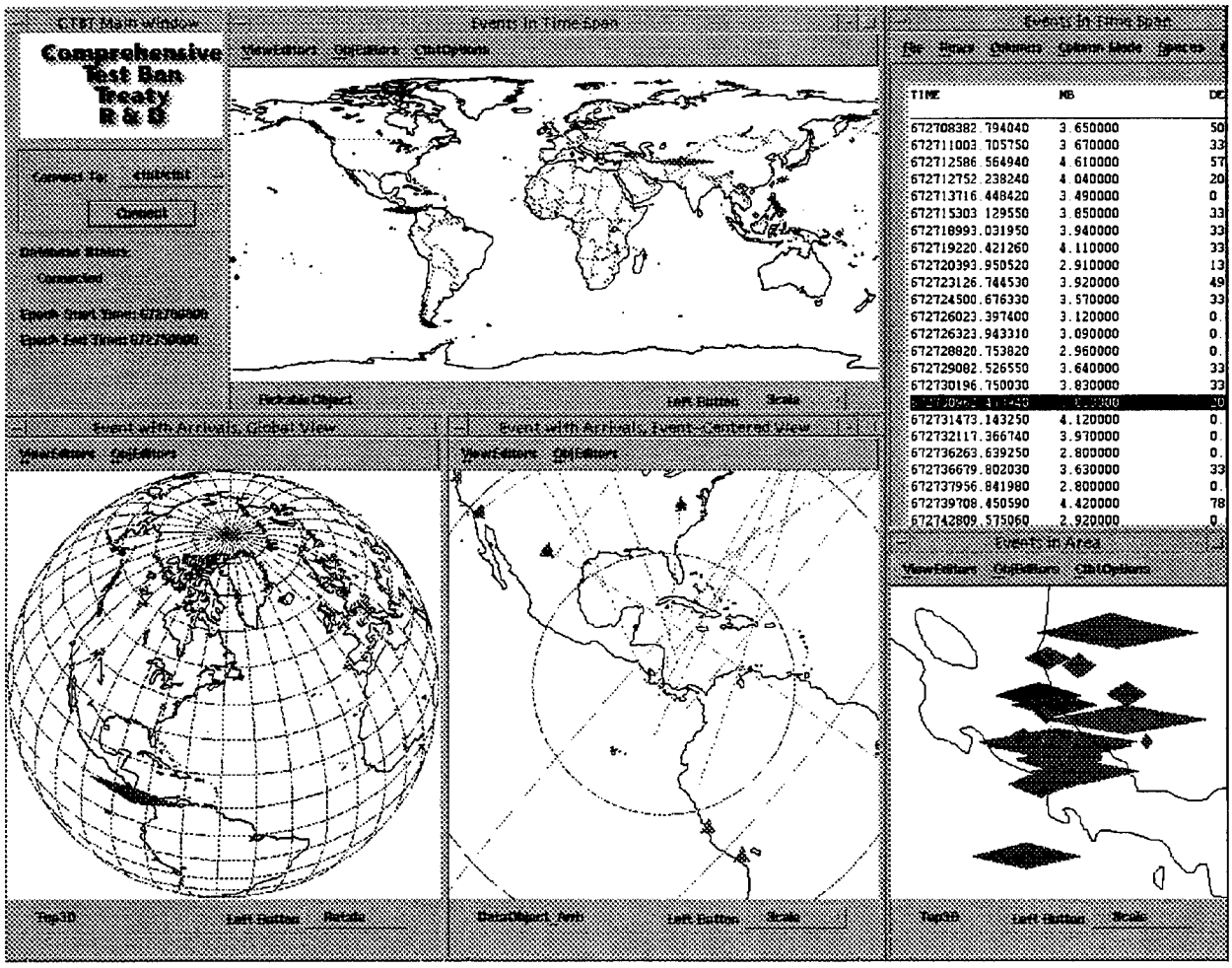

The user begins by connecting to the database he wants and selecting the time span he wants to view events for. The top level display shows a symbol at the location of each event in the user-selected time span, with the color and size of each symbol representing user-selected values (such as magnitude and depth). In addition, there is a corresponding text list of information about the events displayed. Selecting an event brings up a spherical earth display, an event-centered display,

and a display showing other close events in the database. It also highlights the corresponding entry in the text list of events. Selecting an arrival from the event-centered display brings up another display showing azimuth and emergence angle in three dimensions.

We have produced a variant of the multilevel display which could be used for the quick-look application (see next major section). It includes only the top level and event-centered displays, but adds text lists for arrivals seen on the event-centered display.

3.2.2 Animation of Seismic Waves

We wanted to display the propagation of seismic waves as they spread out from an event location. This turns out to be trivial when using an event-centered display. You simply draw a circle with its center at the event location and increment the scale of the circle in a loop. We have not yet identified an application for this utility.

3.2.3 Location/Time Display for Historical Trends

We noticed that when displaying events on a 2D map, it was hard to see them if there were many in the same area (e.g., a series of aftershocks). To make it easier to see all the events we added time as the third dimension. When you first see the display, you are looking straight down along the time axis, so it looks like the simple 2D version. If you rotate the display, however, you see that events are arranged at distances above the surface proportional to the time they occurred. This makes it possible to view events from longer time spans at once and still see each event distinctly. This turns out to be a good way to look for trends over time, such as sequences of events.

FIGURE 2. Location/Time Display

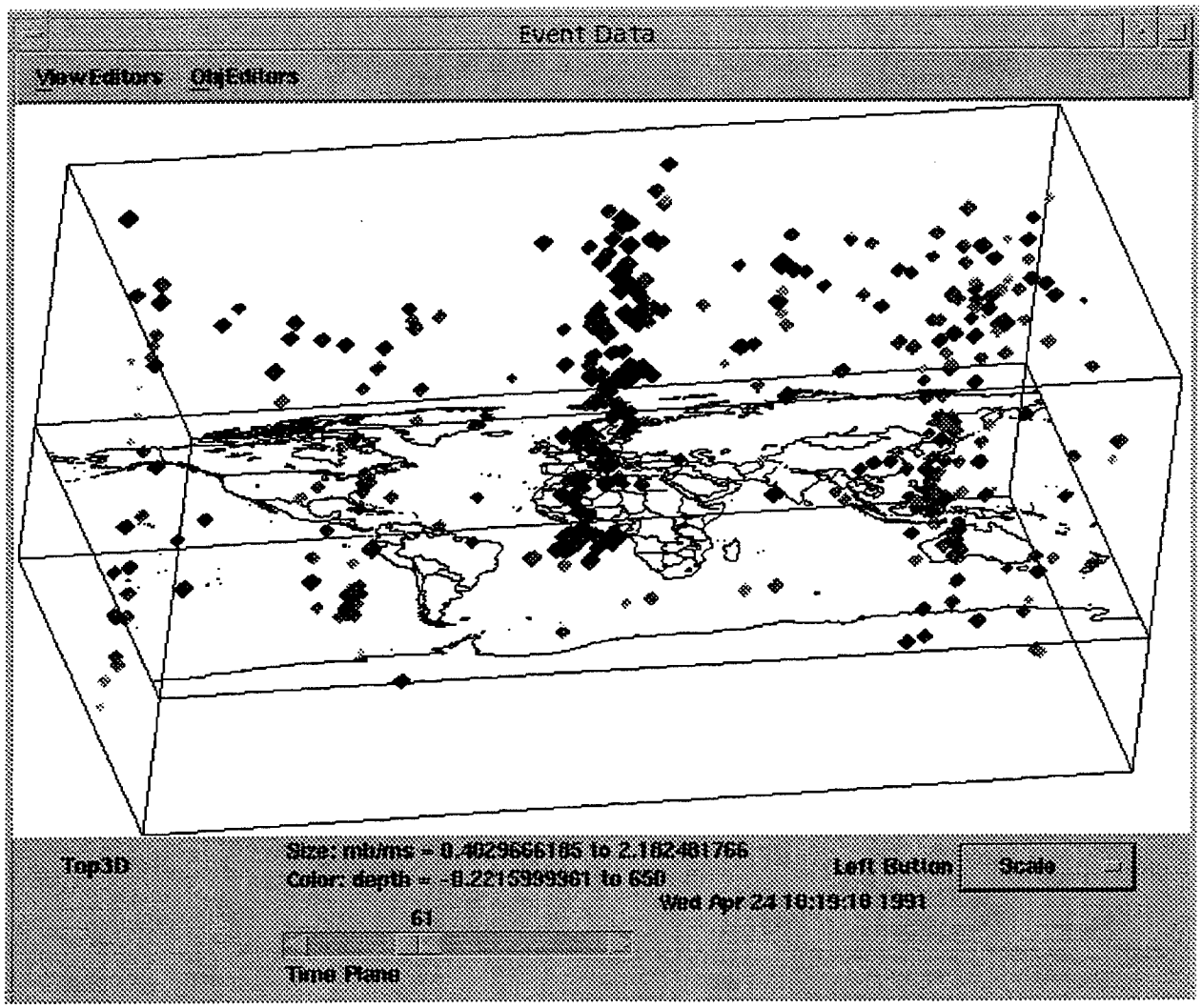

Viewing three dimensions on a two dimensional screen causes some difficulty in seeing how objects are arranged relative to each other. Using a perspective transformation does not seem helpful, perhaps because we are viewing disconnected simple objects instead of complex objects with edges and right angles. We use depth cueing, which dims more distant objects, to help the user's eye sort out what it sees. It also helps to put a wire frame bounding box around the data points, as this seems to give the eye another reference to relate to. Another technique is to drop a line from each object to the base plane. If the base plane contains the map, this helps in locating the object. However, with many objects, the lines can obscure more than they clarify. Instead, we have implemented a moving base plane, which snaps to the origin time of the selected event, so you can easily see exactly where and when that event occurred. 3D glasses might help significantly, but AVS Express does not support generation of stereo views. We are looking into other software to try this.

3.2.4 Goodness of Fit Measures

FIGURE 3. Azimuth Goodness of Fit, Event-Centered View

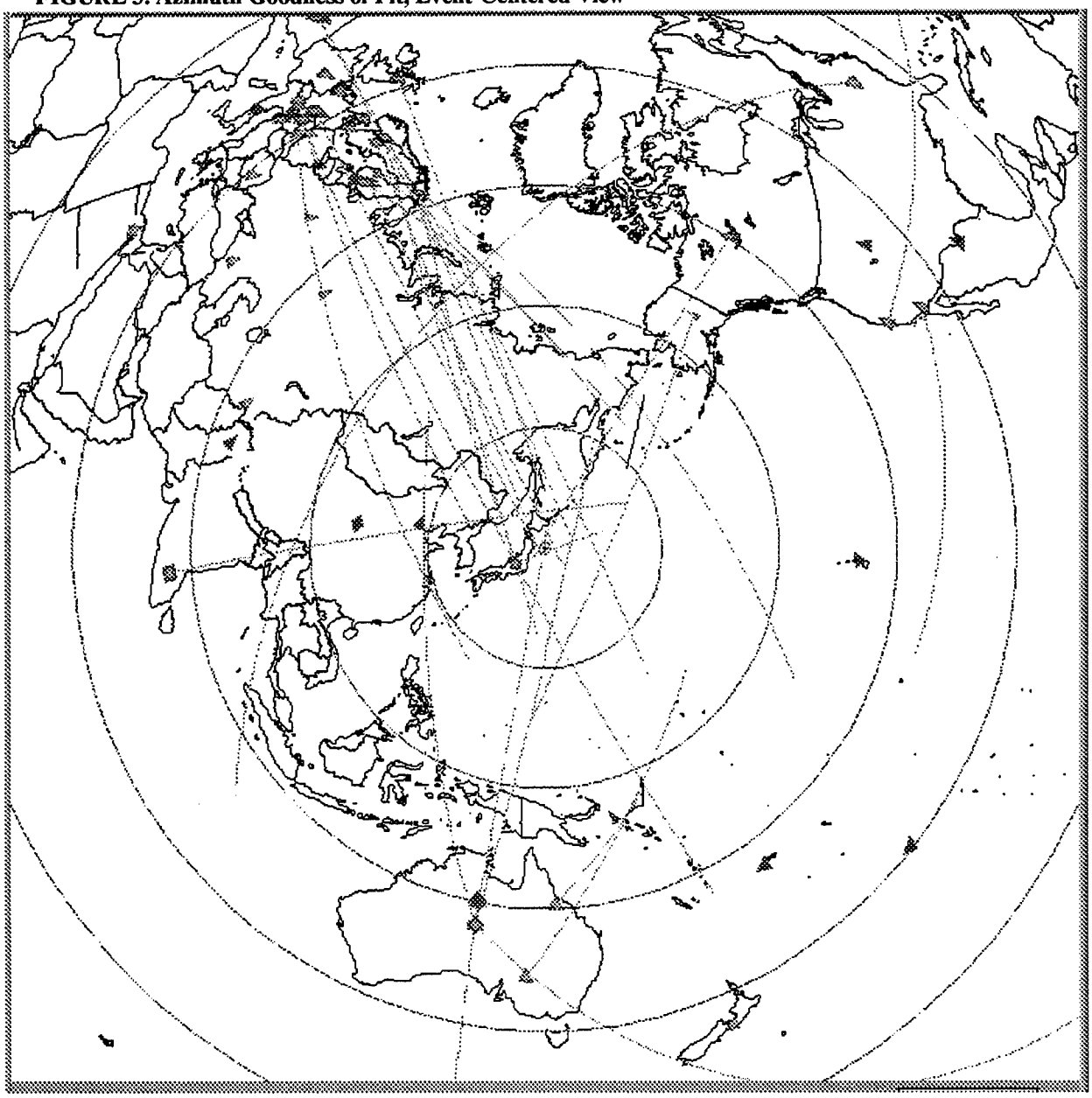

Anderson and Anderson (1995) proposed several goodness of fit measures for evaluating the strength of event association. We developed a program which computes these measures from data in a CSS database and displays the results. In addition to Anderson and Anderson's proposed maximum likelihood magnitude and azimuth goodness of fit measures, we also provide slowness and simplified magnitude goodness of fit measures. Since these measures are one per event, we use a Cartesian map projection with time added as the third dimension. We tried two variations, one which shows each measure in its own separate display, and one which combines selected measures, showing one as size and one as color. We also provide an event-centered display to show details of an event selected from the top level display. This is useful for understanding all the individual station contributions that are combined in a single goodness of fit measure. For example, one can easily see which stations are reporting azimuths with large residuals, and thus cause the azimuth goodness of fit to be large.

All these goodness of fit measures depend on standard deviations determined for the data. Although GSETT II contains such values, it appears they were somewhat arbitrarily assigned, and may be significantly off in many cases. This means goodness of fit measures derived using these erroneous standard deviations must also be considered unreliable.

3.2.5 Generalized Event and Arrival Data Display

The generalized event display allows the user to set the size and color of all event glyphs to any two database values or certain computed values (e.g., magnitude goodness of fit) for all events in a time span. The user can also select an event to show an event-centered display. The generalized arrival display is similar, but displays database values relating to arrivals, and positions the glyphs over the station where the arrival was recorded.

3.2.6 Event and Station Correlation Display

This display shows which stations saw a selected event, or which events were seen by a selected station. Trends visible in this data may help identify good and bad stations, or areas that are more or less visible from given stations.

3.3 Visualizing Other Data

In addition to CSS data, we have created visualization displays of other types of data. Some of these results support other CTBT research projects.

3.3.1 Time/Distance/Depth of Seismic Phases

This display plots arrivals of different phases in time, distance, and depth, color coded by phase. This is simply an extension of the traditional time-distance plot of seismic phases, using results from real events. The addition of depth as the third dimension, and the ability to rotate the 3D scene can lead to better understanding of the data.

3.3.2 Travel Time Surfaces and Cones

This display can plot travel time data (e.g., IASP91, Kennett and Engdahl 1991) for a single seismic phase as a surface in time, distance and depth. Color shading based on the slope of the curve (slowness) at each point makes it easy to see subtle distortions in the surface and better understand how travel times vary with distance and depth.

A single travel time curve for a single seismic phase at one depth can be rotated about the time axis to display as a cone in time and distance. When superimposed on an event-centered display, the surface is the locus of points in space and time where arrivals for that phase may be seen.

3.3.3 WCEDS Output

The Waveform Correlation Event Detection System (WCEDS) (Young, et. al. 1996) is a CTBT research project which attempts to associate and locate events using a novel method for combining full waveform seismic data. Data visualization can help us understand whether and how this new algorithm is working. We first tried plotting a colored glyph at each mesh computation point, and this gave reasonably good results. We then found that converting the data points to a 3D surface with sufficiently high resolution (200x200) produced a striking image that showed

subtle details that were not visible in the colored glyphs, because it is easier to see small differences in a third spatial dimension than small differences in color.

FIGURE 4. WCEDS Output

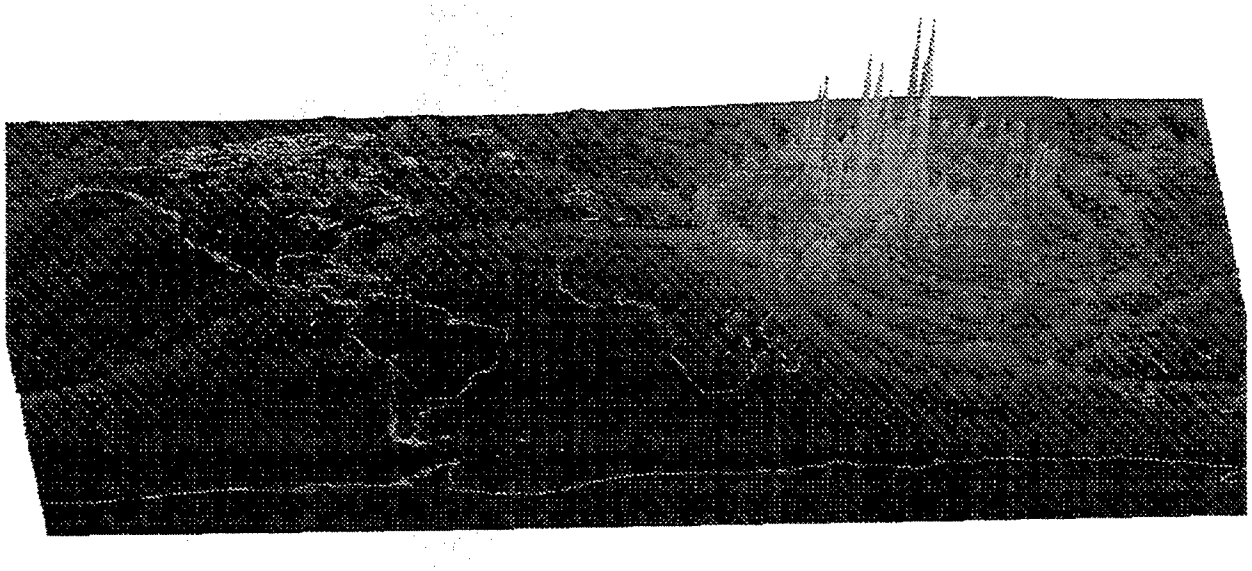

3.3.4 Knowledge Base

The knowledge base is another CTBT research project (Keyser, et. al. 1995) that can benefit from data visualization. Much of the data in the knowledge base is tied to points on the earth's surface. A tessellation of these points creates a mesh which allows searching and interpolating the data (e.g., travel time corrections). Placing and tessellating these control points is an important part of the research, so it is useful to see a clear picture of their locations and the mesh connecting them. A flat map proved unsatisfactory, since mesh lines that crossed 180 degrees West longitude became long lines running the length of the map. A sphere works better, since it avoids introducing this artificial boundary. AVS/Express is especially well suited to this problem, since this type of mesh data is a good match to its internal data types.

FIGURE 5. Tessellation of Knowledge Base Data Points

4. Scenarios/Possible Applications

We have identified several data processing/analysis scenarios within CTBT monitoring where we feel advanced visualization techniques have potential for significant impacts. Existing seismic data processing systems, such as the International Data Center (IDC), National Data Center (NDC), and the AFTAC Distributed Subsurface Network (ADSN), already provide tools that meet some of these needs, but we believe that well-designed data visualization tools can significantly improve efficiency. For each scenario we give a description of the requirements, discuss some possible approaches to meeting these requirements, and then explain how our data visualization results fit with these approaches.

4.1 Monitoring Data Flow, State of Health, and Alerts

4.1.1 Requirements

Within a seismic data processing system, data flow must be monitored from acquisition in the field through automatic processing to review by analysts. This task is made difficult both by the large number of programs which operate on the data during this flow and by the (potentially) large number of stations involved for a global monitoring network. It may not be possible to show information about all stations at once. There is also a need to acquire contextual information about the data presented. Increasingly it looks like questions about processing will be directed towards specific events so a flow monitoring tool should be able to show how the status affects processing of specific events.

Another important task is to monitor the state of health (SOH) of the data acquisition (both in the field and the transfer to local machines). SOH monitoring has some of the same requirements as data flow monitoring. It, too, needs to handle a large number of stations and be able to display contextual information.

Finally, there is a need to quickly identify events that meet immediate reporting requirements as soon as the data becomes available. Much of the information that the operator needs to see regarding calling alerts is in a database, so well-designed database access is a must. A map-type display is a natural because the problem is so fundamentally geographical in nature.

The requirements to monitor data flow, state of health, and alerts are considered together because it has been suggested they could all be done by one person.

4.1.2 Approaches

Using our map displays, we could show symbols for origins and allow the operator to access processing information by interacting with the map(s). At some level more detailed status displays (such as automatic processing status) might be accessed, but perhaps at a lower level than the map. Selecting an origin could trigger an event-level display which would show the level of processing for both the network and the stations. All of the information needed should be available in the database. We could also include some higher-level processing information about the event such as depth and other discriminants which the operator might use to decide how an event should be dealt with (call an alert, send to an analyst, initiate special processing, etc.).

The different versions of the multilevel displays we have experimented with all have this two-level organization with the top level giving information about multiple events, and the next level giving details about a single event.

4.2 Preliminary Event Assessment

4.2.1 Requirements

The preliminary event assessment or "quick look" application requires that for every event in a prioritized list a quick summary of useful information will be presented to an analyst who will then decide how the event should be handled. It must be a quick display because the analyst may have to look at a display for every event (or at least all the important ones), and it must present critical information properly because it is essential that the analyst spend significant time only on the events of interest and deal with the others as quickly as possible.

The type of information presented could be goodness of fit (error ellipse, various residuals) which would allow the analyst to assess the quality of the event association, and discrimination information which would allow the user to assess the potential importance of the event for the mission. Both types of information are needed for the analyst to make the proper decision. Much of the information presented lends itself to graphical displays (especially maps) which could be assessed more quickly by an analyst than simple text displays. Some textual information is certainly useful, but it would be better to have it summoned via a pop-up from a selectable objects on a map display.

4.2.2 Approaches

The multilevel displays start at a global map of events and allow the user to access information about an event at an increasingly fine level of detail. For the quick look application, we could pro-

vide a mechanism to sequentially count through the events (e.g., in order of time of occurrence, but other sortings, such as by magnitude, are possible), changing the subdisplays as the selected event is displayed. This would allow the user not only to see how well an event has been put together but also how it fits with other events occurring before and after.

The goodness of fit displays have options for displaying several measures for multiple events.

4.3 Knowledge Base Review/Editing

4.3.1 Requirements

The knowledge base will be the repository of most if not all of the information needed by automatic data processing software and by analysts for CTBT monitoring. Because most of the data to be stored in the knowledge base is tied to a geographic location, it makes sense to use a tool which is well-suited to displaying geographic information to aid in the display, organization, and editing of the information.

One particular problem which we have identified is the review and editing of the knowledge base grid. This grid must be checked for adequate coverage, for proper interpolation, and referenced to contextual information such as geologic and political boundaries. This implies a fairly complex display which can allow the user to turn on and off several different display options and view in different ways for clarification.

4.3.2 Approaches

We currently have several map displays which could be used to show a grid, including various options to change color and viewing parameters. These displays do not allow editing of the objects displayed however, so modifications would have to be made if the tool was to be used to edit the knowledge base grid.

The WCEDS displays show a grid of output from the WCEDS program, and could be used to display other grids as well. The travel time surface and phase time/distance/depth displays show the power of visualization to help understand large data sets. The knowledge base control point tessellation display is a first attempt to display proposed knowledge base grids overlaying political boundaries.

4.4 Event Reporting

4.4.1 Requirements

In the CTBT monitoring scenario, a decision must be made about the course of action for events of interest. To make this decision, qualified personnel will want access to data from a variety of sources (including seismic) and to a great wealth of contextual information which will allow them to assess the probable significance of the data. Contextual information would include data on seismicity, geologic structure, mines, industrial complexes, population centers, etc. The requirements would be for detailed, high resolution information good down to as little as a few kilometers. The system must be able to fuse many different types of data together and should do this in a flexible manner because so little is known about how mixed data should be presented. An ability to relatively easily handle a new data source is a big plus.

4.4.2 Approaches

Some or all of the AVS/Express map display screens which we have developed could prove useful for event reporting, though their ability to access GIS data sets is not clear (i.e. they may not be able to access the full wealth of knowledge available to a GIS). Express software is flexible, allowing us to relatively easily test whatever options we deem worthwhile. Once concepts have been prototyped using Express, we may want to utilize some of the capabilities provided by a GIS, particularly the availability of lots of contextual information. It may be challenging to deal with the relative inflexibility of the GIS interface. Customization can be difficult and it is not unusual for a user to want a modification which simply cannot be made due to software constraints.

5. Future Work

There are other types of data we expect to be used in monitoring a CTBT, but lack of a sample database populated with complete examples has prevented us from extending to these possibilities. The knowledge base work being done by SNL will give us other types of data to visualize, so this is an area for future expansion. A better understanding of the event reporting scenario requirements will probably lead to new ideas for visualizing the results of seismic data processing and other outputs.

6. Acknowledgments

We would like to thank Kevin Anderson and Dale Anderson of PNNL, and Henry Swanger of SAIC, who visited us to see our displays on the screen, and gave us much insightful feedback. We also thank Ralph Keyser, SNL's CTBT Project Leader, for his ideas and support.

7. References

Anderson, J., W. E. Farrell, K. Garcia, J. Given, and H. Swanger (1990), CSS Version 3 Database: Schema Reference Manual, Science Applications International Corporation, Arlington, VA.

Anderson, K. K., and D. N. Anderson (1995), Statistical Issues in CTBT Verification: Seismic Monitoring Performance Measures, Technical Report PNL-10805, Pacific Northwest Laboratory, Richland, Washington.

Group of Scientific Experts (1992), Second Technical Test, Seismic Parameter and Waveform Data, Washington Experimental International Data Center, Arlington, VA.

Kennett, B. L. N. and E. R. Engdahl (1991), Traveltimes for Global Earthquake Location and Phase Identification, *Geophys. J. Int.* **105**, 429-465.

Keyser, R. G. and H. M. Armstrong (1995), Proposed Conceptual Requirements for the CTBT Knowledge Base, *Proceedings of the 17th Seismic Research Symposium on Monitoring a Comprehensive Test Ban Treaty*, Scottsdale, AZ. PL-TR-95-2108, ADA 310037

Young, C. J., M. L. Harris, J. I. Beiriger, S. G. Moore, J. R. Trujillo, M. M. Withers, R. C. Aster (1996), The Waveform Correlation Event Detection System Project, Phase I: Issues in Prototyping Development and Testing, SAND Report in press.

Young, C. J., C. Pavlakos, and T. L. Edwards, "A Top-down Hierarchical Approach to the Display and Analysis of Seismic Data", *Proceedings of the 17th Seismic Research Symposium on Monitoring a Comprehensive Test Ban Treaty*, Scottsdale, AZ. PL-TR-95-2108, ADA 310037